



First Workshop on
ERS-1
Pilot
Projects

Toledo, Spain
22-24 June 1994

PP03

esa SP-365

ISBN 92-9092-302-4

October 1994

First Workshop on

ERS-1 Pilot Projects

Proceedings

Toledo, Spain

22-24 June 1994

european space agency / agence spatiale européenne

8-10, rue Mario-Nikis, 75738 Paris Cedex 15, France

ESA SP-365

First Workshop on ERS-1 Pilot Projects

Toledo, Spain, 22-24 June 1994

Proceedings published by:

ESA Publications Division
ESTEC, Noordwijk, The Netherlands

Compiled by:

T.-D. Guyenne

ISBN 92-9092-302-4

Price code: E3

Copyright

© 1994 European Space Agency

Printed in The Netherlands

CONTENTS

Welcome Address, <i>J. S. Garrido, Alcalde de Toledo</i>	9
Closing Speech, <i>V. Gomez, Sub-Director of CDTI</i>	11

Session 1. OCEANS

Wind and wave field structures from satellite measurements during mistral events P. Queffelou & A. Bentamy	15
Validation of the second-generation wave forecasting model mu-wave: Comparison with ERS-1, buoy data and WAM forecasts F. Ovidio &al	21
Processing and application of wind scatterometer data and SAR wave spectra in numerical wave and weather prediction J. Sunde &al	29
Numerical analysis of the wind-induced circulation in the Bransfield Strait (Antarctica) using ERS-1/WSC winds M. Espino &al	37
Use of ERS-1 data for wave modelling in Mexican waters F. J. Ocampo-Torres &al	41
Extraction of wave spectra from ERS-1 SAR wave-mode spectra by an improved SAR inversion scheme C. Brüning & S. Hasselmann	45
On the application of ERS-1 data for third-generation wave modelling and shiprouting S. Lehner &al	49
Characterisation and assimilation of ERS-1 scatterometer wind measurements A. Stoffelen &al	53

Session 2. HYDROLOGY

The use of ERS-1 data for spatial surface-moisture determination W. Mauser &al	61
Application of ERS-1 data for the study of soil conditions in Suriname V. A. Achthoven	75
Use of ERS-1 SAR data for soil-moisture assessment K. Dabrowska-Zielinska &al	79

Multi-temporal ERS-1 SAR data in environmental studies: Researching a quantitative approach for soil-moisture retrieval K. Fellah &al	85
Evaluation of soil moisture for the agrameteorological consulting service using ERS-1 data A. Weimann &al	93
Estimation of surface soil moisture from ERS-1/SAR data for hydrological modelling purposes M. Normand &al	97
ERS-1 SAR imagery applied to rural basins hydrological studies: Grassland and lowlands soil wetness characterisation M. Badji &al	103

Session 3. FLOODS

ERS-1 SAR imagery applied to rural basins hydrological studies: Flood inundation mapping and monitoring M. Badji &al	117
A study of flooding on Lough Corrib, Ireland during early 1994 using ERS-1 SAR data J. Matthews & S. Gaffney	125
Assessment of multi-temporal ERS-1 SAR and Landsat-TM data for mapping the Amazon river floodplain Chr. Corves	129

Session 4. ICE

Operational ice monitoring with ERS-1 E.-A. Herland	135
A pilot ice monitoring service using ERS-1 SAR images S. Sandven &al	139
ERS-1 ice monitoring of the Northern Sea Route O. M. Johannessen &al	143
The operational sea-ice charting using ERS-1 SAR images in the Baltic Sea H. Grönvall & A. Seinä	149
Evaluation of real-time use of ERS-1 SAR imagery for icebreaking operations in the Baltic B. G. Häkansson &al	153
Automatic satellite-based sea-ice monitoring system D. Boardman &al	157
Towards a better utilisation of SAR data in sea-ice monitoring M. E. Shokr	163
The potential role of ERS-1 scatterometer data in support of ice navigation R. O. Ramseier &al	169

ERS-1 SAR images and operational mapping of sea ice in the Greenland waters: Preliminary results P. Nielsen &al	175
Parameterisation of lead formation in the Weddell Sea using SAR-derived ice velocity fields M. Thomas &al	183

Session 5. GEOLOGY

Coastal and river dynamics studies by means of space techniques G. Sylos-Labini &al	191
Contribution of ERS-1 data to geological mapping in desert areas - Atacama region, Chili G. Delpont &al	195
Integration of SAR-ERS and other satellite data for applications over the Continental platform of the Black Sea, Danube Delta and Vrancea seismic zone N. Oprescu &al	199
Natural risks evaluation by remote sensing: Lineaments study of the Pastaza Basin, Ecuador P. Ozer &al	205
ERS-1 SAR data as a tool for landform and lineament identification in previously glaciated areas Chr. D. Clark & J. K. Knight	211

Session 6. FORESTS

TREES ERS-1 study '94: Assessment of the usefulness and relevance of ERS-1 for trees J.-P. Malingreau &al	219
Application of the ERS-1 images for assessment of damage to coniferous forest in Poland T. Zawila-Niedzwiecki &al	225
Synergy of remotely sensed data: a European scientific network in the field of remote sensing J. L. van Genderen &al	229
Application of ERS-1 SAR data in large-area forest inventory E. Tomppo &al	235
Applicability of ERS-1 SAR imagery in mapping forest regeneration in burnt areas subject to desertification C. Banninger &al	241
Tropical rainforest investigation in Brazil using ERS-1 SAR data D. R. Scales &al	245
The use of ERS-1 SAR data as a means of assessment for degraded areas and potential aid for agricultural and silvicultural development in the Amazon Forest region F. Lucarelli &al	249
Observation of the tropical forest with the SAR of ERS-1 Chr. Ponsard &al	257

Evaluation of ERS-1 SAR data for forest monitoring in Indonesia (Project TRULI) S. Kuntz & F. Siegert	263
Assessment of the potential of ERS-1 data for mapping and monitoring mangrove ecosystem I. Pons & T. Lê-Toan	273
Retrieval and analysis of temperate forest backscatter signatures from multi-temporal ERS-1 data acquired over hilly terrain A. Beaudoin &al	283
Monitoring fungi diseases in pine forests using ERS-1 SAR data Y. Rauste & E. A. Herland	291

Session 7. TOPOGRAPHY/GEODESY

Contribution of ERS-1 and Spot data to morphologic and bathymetric studies of the North Sea and the Scheldt estuary A.-L. Comhaire &al	297
Detection of sea-bottom topography with ERS-1 SAR.PRI images on the Belgian continental platform L. Vande Velde &al	303
PEGASE Project (mid-1994 status). On the use of ERS-1 altimeter data in the Arctic Ocean Fr. Blanc &al	309
Mean sea level determination in the seas surrounding Greece T. Engelis &al	319
Monitoring lakes in Kenya using ERS-1 altimeter data D. Boardman &al	325
Production of Spot and ERS-1 image maps Fr. Perlant &al	331
Development of an inter-tidal digital elevation model for the UK land-ocean interaction study using ERS-1 SAR data D. Mason &al	337
Topographic and environmental mapping of tidal flats using ERS-1 SAR imagery F. Kennedy & J. Matthews	343
Application and utilisation of datasets obtained by the combination of ERS-1 and multispectral satellite data for monitoring of the Wadden Sea O. Krämer &al	347

Session 8. LAND USE AND INTERFEROMETRY

ERS-1 for land use monitoring in Costa Rica: First results B. Verbist & B. de Roover	355
Possibilités cartographiques offertes par ERS-1 en contexte tropical humide: Exemples en Guyane française (bathymétrie, géologie, urbanisme, etc.) J.-P. Rudant &al	371
The use of ERS-1 data for the detection of urban areas M. Galaup &al	377
Giving an operational status to SAR interferometry D. Massonnet	379

Session 9. SLICKS

ERS-1 SAR imagery of the Rhine-Meuse discharge front – Preliminary results J.-B. Moens & K. Ruddick	385
Pollution monitoring using ERS-1 SAR images T. Wahl &al	389
Automatic satellite-based oil slicks detection and monitoring system D. R. Sloggett & I. S. Jory	395
Operational system for ‘real-time’ oil slick detection based on ERS-1 SAR data A.H.J.M. Pellemans &al	403
Oil spill detection and monitoring with ERS-1 in the ‘Agean Sea’ disaster in La Coruna (2 Dec. 1992) A. de la Cruz	409
Gulf Offshore Satellite Applications Project (GOSAP) E. K. Biegert &al	417

Session 10. AGRICULTURE

Towards the integration of ERS SAR data in an operational system for the rapid estimate of crop acreage at the level of the European Union H.-G. Kohl &al	433
Utilisation of SAR for crop studies in the eastern seaboard region, Thailand S. Vibulsresth &al	443
The use of ERS-1 data for rice monitoring: Examples of Seville, Ebro Delta, Indonesia J. Harms	451

The use of ERS-1 data for crop monitoring J. M. Roques &al	453
Development of neural network techniques for the classification of multi-temporal ERS-1 SAR imagery with respect to agricultural applications M. Davison	469

POSTER SESSION

Landuse classification based on signature analysis and texture-oriented neural network approach S. Carl &al	477
Some results of the PASTA project concerning agricultural classification Ph. Hartl	481
Multitemporal and single image features extraction from ERS-1 SAR image data, with wavelet transforms and unsupervised neural networks M. Mellis & A. Lazzari	493
SAR imagery segmentation and speckle reduction in the Ebro Delta, Spain O. Chic & S. Sugranes	501

PARTICIPANTS

507

WELCOME ADDRESS

Joaquin Sanchez Garrido
Alcalde de Toledo

On behalf of all my corporation colleagues, I warmly welcome you to the city of Toledo for the ERS-1 Pilot Project Workshop starting today.

The city of Toledo was designated part of the World Heritage by UNESCO in 1986. This was in recognition not only of its splendid monuments, which you will have an opportunity to visit over the next few days, but also of its rich historical and cultural past. During one of its particularly flourishing periods, our city was the foremost meeting place for intellectuals from far and wide. Under the Castilian monarchs and Toledan archbishops, our city was instrumental in the dissemination of science throughout Europe. Our streets were trodden by the most renowned astronomers and astrologers, who contributed their learning to the celebrated scientific works commissioned by King Alfonso X. There is even a legend that Toledo was built in a single night by a Mage so that he could contemplate the stars from the seven hills on which it stands.

For some years now our capital has been host to scholars from a vast range of scientific disciplines who have chosen Toledo as the venue for working meetings such as the one you are starting today. These gatherings are giving rise to a substantial corpus of conclusions and agreements which in future will be linked to the name of our capital. We Toledans are very proud to welcome among us, if only for a few days, so conscious are we that all of you are helping to consolidate our city's image as a permanent cultural hub, gradually recovering the standing it enjoyed in bygone days.

Modern communication technologies have brought about an extraordinary revolution in today's world. Changes in our ecology and climate are among the main concerns of contemporary civilisation. That is hardly surprising. We are constantly hearing or reading worrying news for the future of the planet, which is the most precious asset we have inherited. We are duty-bound to hand it down to our children in the best possible condition, so that life can go on. Since July 1991 the ERS-1 satellite has been monitoring the environment, yielding data to give us a better understanding of our climate and changes occurring in it. Observing the growth of crops and vegetation, it is lending a new dimension to the image of our planet. You are here to spend a few days discussing this interesting European Space Agency project. I urge you to do so with composure and rigour, but above all without losing sight of the human dimension of scientific progress. Important aspects of the future of humanity are in your hands. All of us hope that new technologies are going to serve to improve living conditions for future generations. Thank you for the work you are doing.

Once again, we wish you the very warmest welcome. Finally, I wish to thank the European Space Agency and the Centre for Industrial Technological Development at the Ministry of Industry and Energy for having kindly chosen the city of Toledo to host this scientific meeting. I wish all of you every success in your professional and personal lives. Thank you very much, ladies and gentlemen.



CLOSING SPEECH

Vicente Gomez

Sub-Director of CDTI, Madrid, Spain

Ladies and Gentlemen,

It is a great pleasure for me to be here today and to join you for the Symposium closing session.

I do particularly appreciate that Toledo was chosen to host this Symposium and I wish to express my thanks to ESA, who have contributed to help this event take place. As almost one thousand years ago, thanks to you, Toledo is once again a privileged centre for space research and a unique venue of different cultures brought together by science.

Previous Symposia have already proved that ERS-1 had not just met, but even surpassed the expectations of varied groups. During these last days we took the opportunity to see the possibilities of unexpected applications that were unknown when the satellite was designed and prospects for a more extensive range of uses in the field of science and, even more, the use of ambitious technology whose reality has no peer in the world.

On this point, let me encourage you to contribute to major technology transfers by involving users from different fields as much as possible and by offering then convincing results. This is clearly the way to follow our biggest challenger in Earth Observation: to embed remote sensing technology in more and more fields by taking full advantage of these data for scientific, public and commercial applications.

Indeed, ERS-1 marks the beginning of a new era for the European Earth Observation and environmental effort. I think we all now appreciate the foresight and vision of those who were working so hard to make this possible. ERS-2 will provide observation continuity, and beyond, Envisat and Metop will expand observation from space through the next millennium. At present we start to define the future Earth Observation strategy in close consultation with you, the scientific and environmental experts, to submit it for approval at the next ESA Ministerial Council meeting in 1995; I have no doubt, it will be strongly supported by the ESA Member States. The future is guaranteed.

Finally, I would like to stress that this Symposium is an excellent example of highly successful European collaboration and a sign that the investment in space research and technology is well placed.

I hope all those attending have had interesting and fruitful discussions and a pleasant stay in Toledo.



1. OCEANS



WIND AND WAVE FIELD STRUCTURES FROM SATELLITE MEASUREMENTS DURING MISTRAL EVENTS

P. Queffeulou and A. Bentamy
 IFREMER, BP 70, 29280 Plouzané, France
 tel (33) 98 22 42 94 e-mail pierre.queffeulou@ifremer.fr

Abstract. Preliminary results of the project PP2-F17A, "Etude du Mistral en mer à partir des données du satellite ERS-1" are presented. Mistral is a local north-westerly wind blowing over the Western Mediterranean Sea, and involving strong air-sea interactions. Some characteristics of this local wind are observed using combined wind and wave satellite measurements from the ERS-1 scatterometer, from the ERS-1 and TOPEX POSEIDON altimeters, and from the U.S. Special Sensor Microwave Imager. Application of such data to study the wind field structure associated to mistral events is illustrated on two cases.

Keywords: altimeter, mistral, scatterometer, wave, wind.

1. INTRODUCTION

Preliminary results of the pilot project PP2-F17A are presented. The goal of this project is to study wind and wave field structures during mistral events. Mistral is a local wind occurring over the Western Mediterranean Sea, and involving strong air-sea interactions. Some characteristics of this local wind are given in a first part of this paper. Because of their ability to cover quasi-instantaneously narrow area, such as the Western Mediterranean Sea, satellite sensors are useful to study such phenomena. Concerning the sea surface wind speed, the ERS-1 scatterometer is of first interest (Ref.1). Wind information from the scatterometer is available over a 500 km wide swath. This coverage can be extended by using measurements from the Special Sensor Microwave Imager (SSM-I), of the U.S.A. Defense Meteorological Satellite Program, which has a larger swath, about 1400 km. Concerning wave data, to study fetch effect, prevailing in such enclosed sea, radar altimeters are of main interest. In the present study, altimeter wind speed and wave data from both ERS-1 and TOPEX POSEIDON satellite will be used. As soon as data from various sensors and satellites are used together, it is of prime importance to be aware of the homogeneity of the data. A part of the paper is devoted to this aspect. Then two examples of mistral events are analysed in terms of sea surface wind and wave. The first example shows agreement between

satellite wind measurements and available meteorological analysis. The second example illustrates some limits in the modelling of such local events, indicating that improvements are needed in this domain. In the last part of the paper perspectives for further work within the project are presented.

2. MISTRAL

Mistral event corresponds to north-westerly wind blowing over the Western Mediterranean Sea. This occurrence is often associated to particular meteorological situation such as the one illustrated on Figure 1. The

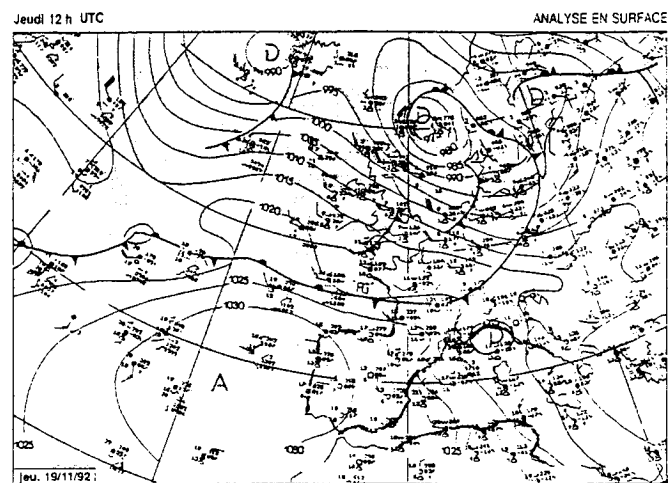


Figure 1: Surface pressure analysis (Météo France).

surface pressure analysis shows a low pressure centre on the north of Europe. Behind the cold front, the cold unstable air flows from the North West and is canalized by the Rhône Valley, due to the natural frontier of the Alps preventing the cold air to flow towards the East. When reaching the sea, over the Gulf of Lion, this flow is often speeded up by the effect of a secondary low pressure centre which is frequently present over the Gulf of Genoa, due to the accumulation of warm air over this area. In the Gulf of Lion the sea

surface temperature is then higher than the air temperature and this creates an unstable atmospheric stratification. When the cold air spread ahead over the sea, the lower layers are warmed by the sea surface, which tends to decrease the stratification and consequently to decrease the friction at the surface. This results in an increase of the wind speed. It is known and it is currently observed by sailors that the sea surface wind speed strongly increases off-shore during Mistral events (Ref.2). Furthermore, the area of strong wind is often very narrow, and this is one of the difficulties in modelling such events. An other difficulty is the strong impact of orography on the air flow, which may be a source of error in modelling (Ref.3). When the thickness of the cold air layer is large enough to spread above the Alps chain, then Mistral extends over the east part of the Western Mediterranean Sea.

3. SATELLITE DATA

Data used in this project are wind data from the ERS-1 scatterometer, and wind and wave data from the ERS-1 and TOPEX POSEIDON radar altimeters. It is also planned to use SSM-I wind measurements, but, now, only one pass has been used.

ERS-1 scatterometer wind data are the off-line products, processed by IFREMER (Ref.4 and 5). These products were validated versus buoy wind measurements and the rms accuracy was estimated to be 1.2 ms^{-1} for wind speed and 15° for wind direction (Ref.4 and 6). The scatterometer resolution is 50 km and the wind vectors are computed on a 25 km grid over a 500 km swath, located 250 km to the right of the satellite ground track. Figure 2 shows an example of such wind data coverage. This scatterometer swath corresponds to the ascending ground track on the left side of the map. In the south west of Sardinia there is an area with no data and, surprisingly, it corresponds to 7 cells for which the land flag is positioned. This was observed on all the swaths investigated over this area, and also on Fast Delivery Products (see figures in Ref.7), which indicates that some land flags used by ESA are erroneous. A second remark is that the land flag is positioned relatively far away from the coast. This might be improved in the future. For the time period we investigated, scatterometer data were only available for ascending passes, so that only one swath every 3 days was of interest for the studied area.

ERS-1 altimeter wind and wave data were the Ocean Products (OPR) processed by the French Processing and Archiving Facility, CERSAT. These products have been validated using comparisons with buoy measurements and with TOPEX POSEIDON data (Ref.8 and 9). The surface wind speed accuracy was found to be about 1.5 ms^{-1} (rms) with a low average bias of 0.4 ms^{-1} , over a $0\text{--}15 \text{ ms}^{-1}$ range. Nevertheless, individual differences can reach relatively high values, up to

6 ms^{-1} , due to the wind speed variability in part and also due to the effect of other geophysical parameters involved with the backscattering, and not taken into account. The bias was also found to depend on SWH.

Concerning SWH, the OPR were corrected using the linear correction (1) given in Ref.9. Once corrected, ERS-1 SWH is shown to be within ESA accuracy specifications, of 10% or 0.5 m, whichever is greater.

$$H_{corr} = 1.19 * H_{OPR} + 0.19 \quad (1)$$

Data from TOPEX POSEIDON were provided by the Centre National d'Etudes Spatiales AVISO group (Ref.10). Cross validation of SWH measurements from ERS-1 and TOPEX POSEIDON showed that, once the OPR are corrected, there is no significant difference between the two satellite data (Ref.8). Wind speed comparison between ERS-1 altimeter and TOPEX Ku band altimeter, as processed by AVISO, showed consistency among the two satellite wind data. Use of collocated measurements from the ERS-1 wind scatterometer and TOPEX POSEIDON altimeters also showed the consistency of the two wind estimates, though the scatterometer wind speed is slightly overestimated, relatively to the altimeter one, for light winds and underestimated for high winds. This scatterometer trend is in agreement with results from validation of the first version of the CERSAT scatterometer products (Ref.4 and 5).

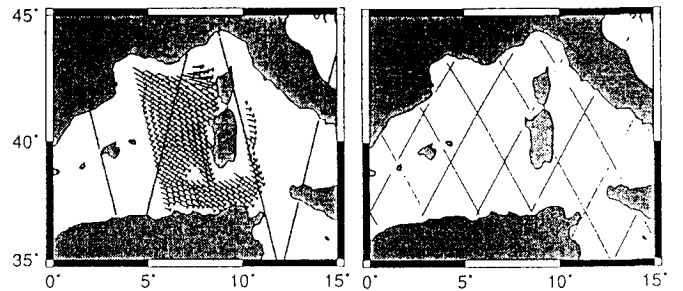


Figure 2: ERS-1 scatterometer swath, and altimeter ground tracks for 3 days (left), and the TOPEX 10-day repeat cycle orbit (right).

During the time period investigated, ERS-1 was on the 35-day repeat cycle orbit. Sample of the area by the ERS-1 altimeter is shown on Figure 2, for 3 days, which constitutes some sub-cycle of the orbit. From one 3-day period to the following one, the ground track pattern is just shifted in longitude. Over a 3-day time period, only one to two ERS-1 altimeter ground track are of interest for the area. For TOPEX POSEIDON, the coverage of the 10-day repeat cycle orbit is shown on the right of Figure 2. Over 3 days, in general only one ground track is of interest for our subject.

SSM-I is a passive multi-frequencies microwave sensor providing measurements of brightness temperature

at 19.3, 22.2, 37.0, and 85.5 GHz. The microwave energy emitted from the ocean surface is related to the wave structure and foam coverage, which in turn, are influenced by the surface winds. An empirical model (Ref.11) was used to relate the surface wind speed to the brightness temperatures. A rain flag is also available and used to discard data polluted by rain effect. Only one case of such wind estimates, with 50 km resolution, is used below.

4. TWO MISTRAL EVENTS

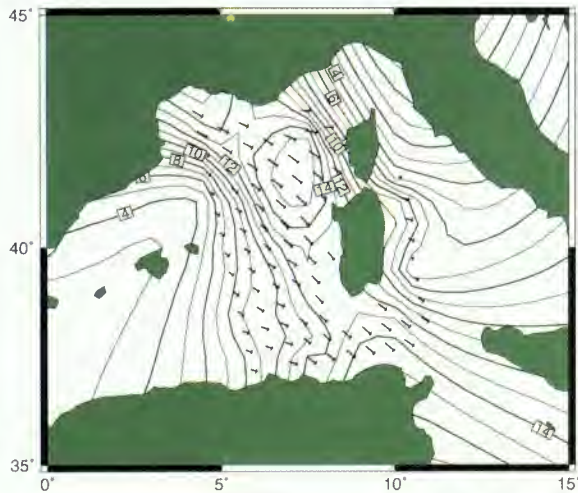


Figure 3: ERS-1 scatterometer wind measurements, Nov. 19, 1992, 21h53.

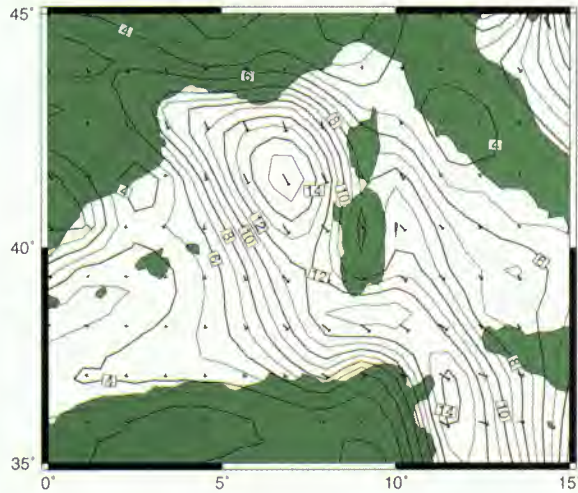


Figure 4: ECMWF surface wind analysis, Nov. 20, 1992, 00h00.

November 19, 1992. For this first example, the scatterometer wind measurement are shown on Figure 3. Wind vectors are represented for only one cell out of two. The scatterometer wind speed contours drawn on

the figure are of course only valid within the swath. Maximum wind speed measured by the scatterometer is 15.9 ms^{-1} and an area of strongest wind is clearly seen, with particular wind gradient on the west side of the maximum. Surface wind analysis from the European Centre for Medium range Weather Forecasting (ECMWF) are in agreement with the scatterometer data (Figure 4), with the exception of a slight shift in the wind direction in the north part of the area.

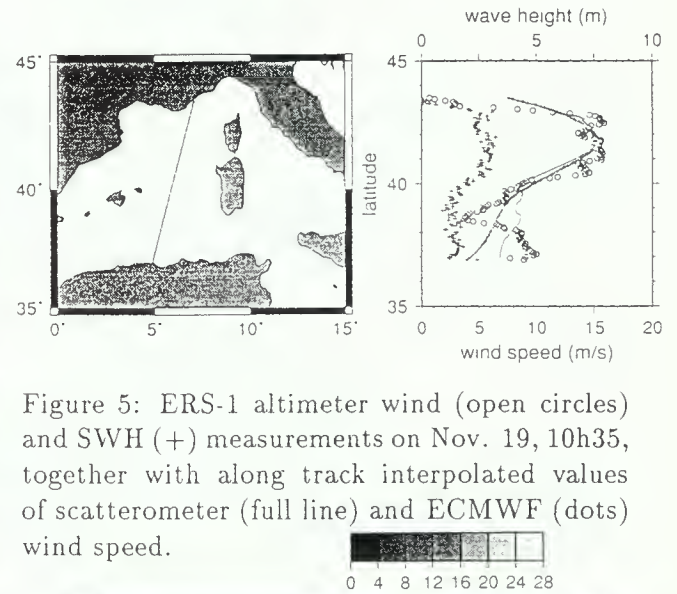


Figure 5: ERS-1 altimeter wind (open circles) and SWH (+) measurements on Nov. 19, 10h35, together with along track interpolated values of scatterometer (full line) and ECMWF (dots) wind speed.

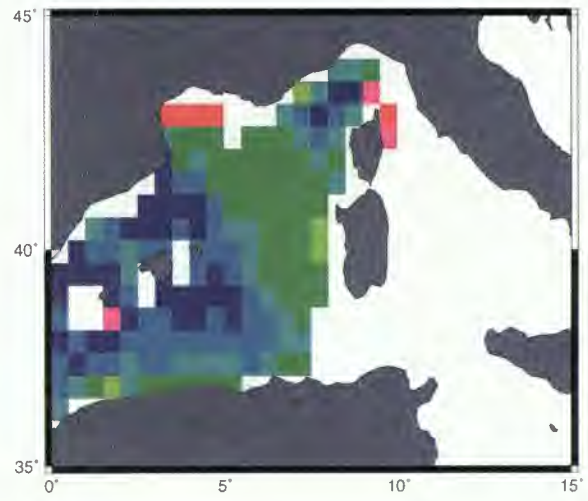


Figure 6: SSM-I surface wind speed, Nov. 19, 1992, 09h21.

An ERS-1 altimeter pass is available at 10h35; the altimeter wind and wave measurements are reported on Figure 5, together with the along track interpolated values from the scatterometer wind field and from the ECMWF wind field. Though there is about a 12 hour time shift, the agreement between various sources is surprisingly good. Note the SWH increase with fetch and wind speed in the north part of the track.

The wind speed measured by the altimeter presents sharper fluctuations than scatterometer and ECMWF data. This may be due in part to the high resolution sample of the altimeter. Note that, on Figure 5, the along track scatterometer interpolated data are not to be taken into account for latitudes lower than 39° because this part is outside the scatterometer swath. Image of the SSM-I wind data for Nov. 19 at 09h21 (Figure 6) also shows the largest wind speeds over a narrow area, the maximum wind speed being slightly higher than the scatterometer and ECMWF estimates.

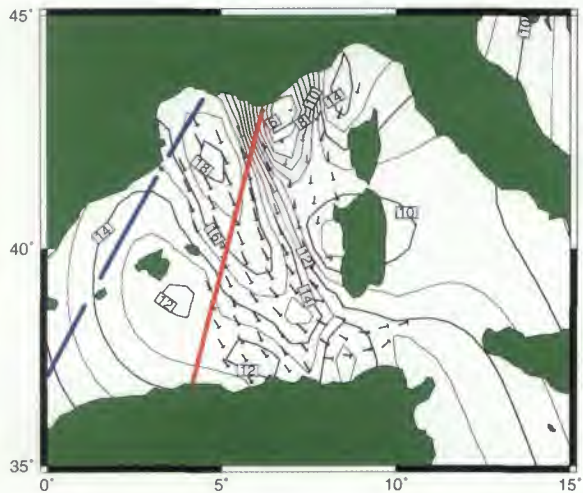


Figure 7: ERS-1 scatterometer wind measurements, Dec. 8, 1992, 21h53.

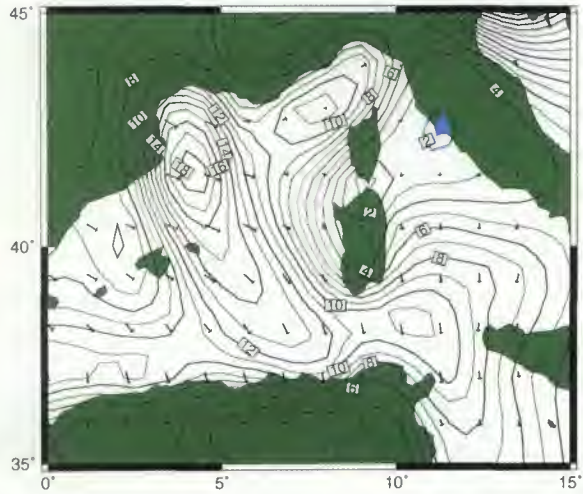


Figure 8: ECMWF surface wind analysis, Dec. 9, 1992, 00h00.

December 8, 1992. Scatterometer measurements of Figure 7 and ECMWF analysis of Figure 8 can be compared. Values of maximum wind speed are in agreement, about 18 ms^{-1} . However strong differences exist

between the two wind fields. There is a significant difference in the wind direction, particularly within the region of maximum wind speed. Just in the east of this area, the scatterometer wind field exhibits some convergence that might be responsible for the strong speed gradient: the scatterometer wind speed fluctuates from 6 ms^{-1} to 18 ms^{-1} , over less than 100 km. Variation of the ECMWF speed in this region is much smoother. High wind speeds are also extending much more towards the South on the satellite data than on the ECMWF analysis.

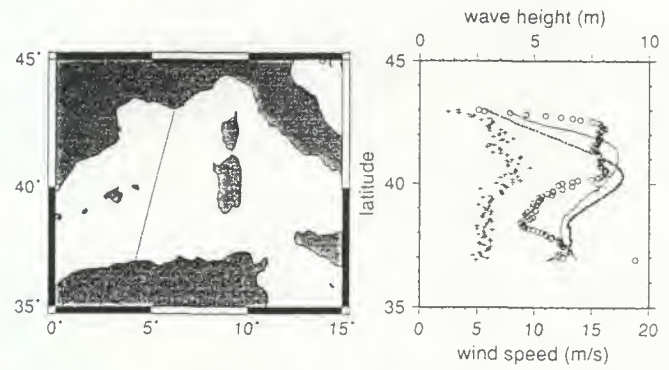


Figure 9: ERS-1 altimeter wind (open circles) and SWH (+) measurements on Dec. 8, 10h37, together with along track interpolated values of scatterometer (full line) and ECMWF (dots) wind speed.

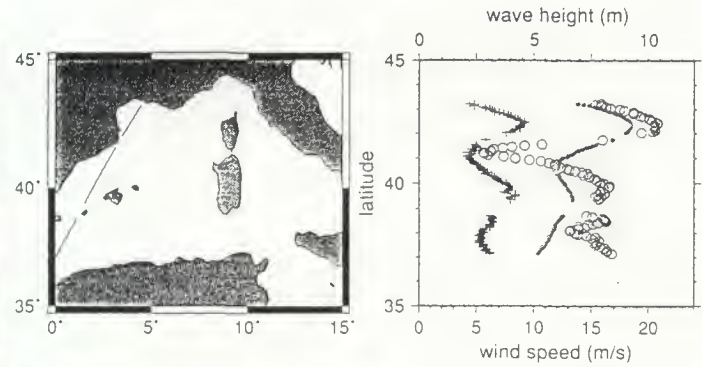


Figure 10: TOPEX altimeter wind (open circles) and SWH (+) measurements on Dec. 8, 20h24, together with along track interpolated values ECMWF (dots) wind speed.

ERS-1 altimeter data are available over the area at 10h37. In the north of the track, (Figure 9) the altimeter measures a larger gradient than the scatterometer which, in turn, indicates a larger gradient than the ECMWF analysis. Fluctuations of altimeter wind speed are largest. Maximum values are 16 ms^{-1} for the altimeter, 17 ms^{-1} for scatterometer and 18 ms^{-1}

for the ECMWF analysis. A TOPEX pass is also available at 20h24, but is situated outside the scatterometer swath, so that only a comparison with the model data is possible. Figure 10 shows obviously that the altimeter measures wind speed fluctuations that are larger and sharper than those estimated by the model, particularly near the coast.

5. FUTURE WORK

The above case studies show the usefulness of combined measurements from various satellite sensors to study wind and wave field structures in Mistral events. The next step of the work is to select and analyse more case studies and to quantify the effects in terms of wind and wave gradients and fetch effect. For this, informations from the imagettes of the ERS-1 Synthetic Aperture Radar, in wave mode, will be also useful. The impact of sea surface thermal structure on the physics of the air-sea interaction and on the satellite measurements will be also investigated. Sea surface temperature measurements from Advanced Very High Resolution Radiometers and from ERS-1 Along Track Scanning Radiometer will be used for this purpose.

REFERENCES

- [1] Guymer T.H. and S. Zecchetto, Applications of scatterometer winds in coastal areas, *Int. J. Remote Sensing*, 14, 1787-1812, 1993.
- [2] Mayençon R., *Météorologie Marine*, 117-137, Editions Maritimes et d'Outre-Mer, 1982.
- [3] Cavalieri L., L. Bertotti and P. Lionello, Wind wave cast in the Mediterranean Sea, *J. Geophys. Res.*, 96(C6), 10739-10764, 1991.
- [4] Quilfen Y., ERS-1 scatterometer off-line products: calibration validation results and case studies, Proceedings of International Geoscience and Remote Sensing Symposium. IGARSS 1993, Tokyo, Japan, August 18-21, 4, 1750-1752, 1993.
- [5] Quilfen Y., ERS-1 off-line wind scatterometer products. IFREMER report ERS-SCAT/IOA/DOS-01, IFREMER, BP 70, 29280 Plouzané, France, 1993.
- [6] Bentamy A., Y. Quilfen, P. Queffeulou and A. Cavanie, Calibration and validation of ERS-1 scatterometer, Technical report, DRO/OS-94-01, IFREMER, BP 70, 29280 Plouzané, France, 1994.
- [7] Zecchetto S. and M. Bortoletto, Examples of mesoscale meteorology in the Mediterranean Sea using ERS-1 scatterometer data, Proceedings Second ERS-1 Symposium - Space at the service of our Environment, Hamburg, Germany, 11 - 14 October 1993, 815-818, ESA SP-361, January 1994.
- [8] Queffeulou P., A. Bentamy, Y. Quilfen and J. Tournaire, Cross validation of ERS-1 and TOPEX POSEIDON wind and wave measurements, submitted to *J. Geophys. Res.*, 1994.
- [9] Queffeulou P., Altimeter wind and wave measurements, CERSAT news issue 2, IFREMER, BP 70, 29280 Plouzané, France, February 1994.
- [10] AVISO User Handbook, Merged TOPEX POSEIDON Products, AVI-NT-02-101-CN, edition 2.1, CLS, 18 av. Edouard Belin, 31055 Toulouse Cedex, France, 1994.
- [11] Goodberlet, M. A., C. T. Swift and J. C. Wilkerson, remote sensing of ocean surface winds with the special sensor microwave-imager, *J. Geophys. Res.*, 94, 14547-14555, 1989.



VALIDATION OF THE SECOND GENERATION WAVE FORECASTING MODEL MU-WAVE : COMPARISON WITH ERS-1, BUOY DATA AND WAM FORECASTS

Fabrice Ovidio, Jean-Raymond Bidlot & Dries Van den Eynde

Management Unit of the North Sea Mathematical Models
Gulledelle 100, B-1200 Brussels, Belgium
Tel. : + 32 2 773 21 11 — Fax : + 32 2 770 69 72
E-Mail : wavesfo@camme.ac.be or wavesjb@camme.ac.be

Weimin Luo & Jaak Monbaliu

Hydraulics Laboratory, Catholic University of Leuven
de Croylaan 2, B-3001 Heverlee, Belgium
Tel. : + 32 016 22 09 31 — Fax : + 32 016 22 52 31

ABSTRACT

The Management Unit of the North Sea Mathematical Models is a Belgian Public Service research institute. Operational wave forecasting for the Belgian coast constitutes one of its responsibilities. The mu-WAVE (HYPAS) model predictions are used by the harbour authorities to help the routing of ships through the very shallow waters of the Southern Bight of the North Sea. A previous validation using buoy data has shown that the model results are satisfactory for an operationally used second generation model. The present validation uses buoy data together with the European Space Agency ERS-1 altimeter and wind scatterometer data to reassess the quality of the coarse and fine grid version of the model, including meteorological forcings. Moreover, the model is compared to the third generation WAM model, implemented on the same grid at the Hydraulics Laboratory Group of the Catholic University of Leuven. In the future, a data assimilation procedure will be developed and embedded in the operational system.

1. MODELS

The mu-WAVE model [Van den Eynde, 1992] is composed of different modules. The core of the system is formed by the second generation wave model HYPAS [Günther and Rosenthal, 1985] which combines the traditional approach of independent calculation of swell energy for each frequency and direction through a ray technique, with a parametrical wind sea model, using the parameters of the JONSWAP spectrum [Hasselmann *et al.*, 1973] and the mean wind sea direction as prognostic variables. Some shallow water effects, such as shoaling, are included in the model.

The well known WAM model [WAMDIG, 1988] is a third generation model which solves the wave transport equation explicitly without any *ad hoc* assumption on the shape of the wave spectrum. The version used is the so called *Cycle 4*.

The models are implemented on two nested grids. The coarse grid (Figure 1) has a 50 km × 50 km resolution (stereographic projection) and covers the entire North Sea to intercept swell generated far away that may travel to the Belgian coast. In mu-WAVE, the open boundaries are

treated as walls where limited fetch laws are applied. One of the goals of the present validation is to assess the impact of these boundary conditions.

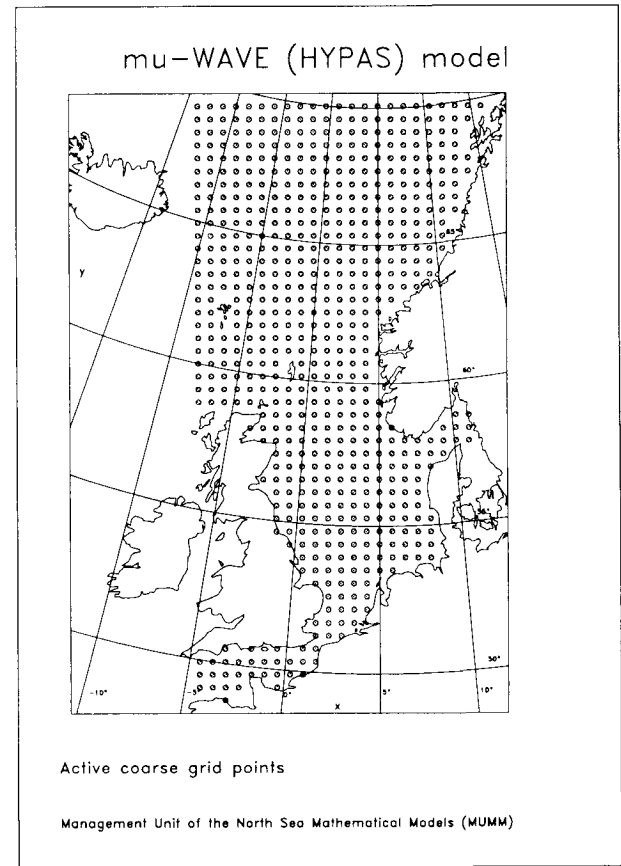


Figure 1. Coarse grid domain

In front of the Belgian coast, a higher resolution is needed to account for the complex bathymetry of the *Vlaamse Banken*. A 10 km × 10 km fine grid is used, coupled to the coarse grid through the open boundaries. In this paper, we only deal with results of the coarse grid model. The validation of the fine grid version will be carried out when we receive additional buoy data.

2. HINDCAST

For this validation exercise, we have chosen a six-month hindcast period running from October 1992 to March 1993. This allows us to test mu-WAVE in various wave conditions, from calm to stormy weather.

The operational model uses the wind fields of the United Kingdom Meteorological Office (UKMO) as forcing. Analysed fields or forecasts are used depending on their availability. They are interpolated to the stereographical coarse grid. The satellite and buoy data have been used to check the quality of these winds (see *infra*) which play a critical role in a wave forecasting system.

Due to the type of physics represented in the mu-WAVE and WAM models, different schemes are used for the time integration of the energy equation. Hence different time steps are also used. A 15 minutes Δt was selected for WAM as a compromise between accuracy and CPU time and mu-WAVE's operational Δt was kept to 30 minutes as a reduction to 15 minutes didn't produce any significant improvement.

3. WIND FIELD ANALYSIS

It is needless to say that the wind forcing quality plays a tremendous part in the successful prediction of the wave energy spectrum. ERS-1, with its altimeter and scatterometer sensors, is an excellent tool to check the meteorological input.

Both altimeter and scatterometer fast delivery products have been used in this work. Comparison with the gridded model forcings is achieved as follows :

- along the altimeter track, groups of eight consecutive observations are constructed, out of which a mean is computed. This procedure smoothes the raw data and leads to data points spacing from about 52 km, which is close to the resolution of the coarse grid. Then each data point is relocated to the nearest model grid point.
- within the 500 km-wide scatterometer swath, wind vectors are produced at nodes separated by 25 km, and each node is centered within a resolution cell of 50 km \times 50 km. Each observation is translated to the closest grid point, at which the scatterometer wind direction is compared to the model wind direction, interpolated linearly in time. Satellite data that differ by more than 45° are discarded. A similar technique has been used by Hoffman (1993). The remaining observations are averaged at each grid point and recombined to a vector field for that subtrack. This data selection method may come as a surprise since we are trying to assess the forecast quality *using* the ERS-1 data, and is used to eliminate obvious spurious wind vectors resulting of a bad ambiguity removal. Indeed, it is well known that the *inherent* ambiguity in the determination of the wind direction using the three σ° is resolved on statistical ground by giving the most probable guess, sometimes leading to wind vectors pointing in the wrong direction.
- using these data it is possible to analyse the

difference between observation and model prediction at each ocean grid point, provided that the satellite data is smoothed *e.g.* using 9-point averages (mainly when dealing with the altimeter data) to avoid spatial irregularities arising from the repetitive sub-track distribution.

We have also analysed data from six buoys whose locations are displayed in Table I. These measurements were provided by Rijkswaterstaat, Service Getijdewateren, The Netherlands. Buoy data give continuous point-wise information and hence are of interest for the validation exercise. An extensive cross-comparison between buoys, satellite and model data has been carried out; some results are presented hereafter.

Table I. Wave stations

Station	Code	Latitude	Longitude
Platform Auk	auk	56°23'59"N	2°03'56"E
Platform k13	k13	53°12'03"N	4°35'18"E
Munitiestort IJmuiden	ym6	52°33'00"N	4°04'00"E
Meetpost Noordwijk	mpn	52°16'26"N	4°17'46"E
Europlatform	eur	51°59'55"N	3°16'35"E
Lichteland Goeree	leg	51°55'05"N	3°40'02"E

A first glimpse of what can be revealed by the statistical analysis is shown on Figure 2, which displays the wind speed time series at station auk during November 1992. Statistics for 4 buoys are presented in Table II. The bias refers to the difference between the mean wind speed at the buoy and the mean model wind speed. The scatter index (S.I.) and the root mean square error (RMSE) are defined as in Zambresky (1989) and Romeiser (1993).

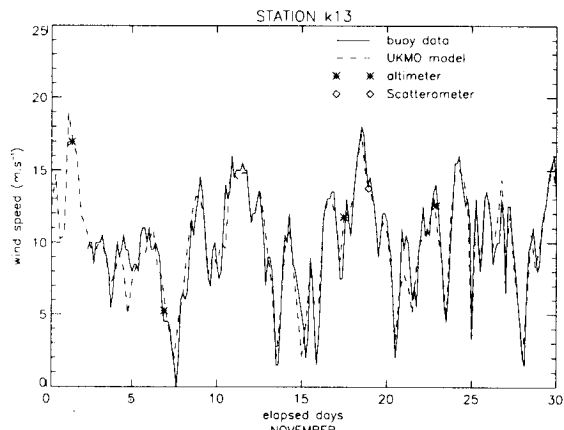


Figure 2. Time series of the wind speed at station k13 for November 1992

Table II. Wind speed, model v buoys; negative bias denotes an overestimation by the model

	Bias (m/s)	S.I.	RMSE (m/s)
auk	-1.02	0.195	1.90
k13	-0.13	0.173	1.46
mpn	0.84	0.205	1.57
ym6	0.16	0.208	1.67

Figure 3 displays the wind speed mean difference between the smoothed satellite observations (altimeter and scatterometer) and the UKMO model winds for the entire study period. Scatter diagrams are presented on Figure 4, while results of the statistical analysis are presented in Table III.

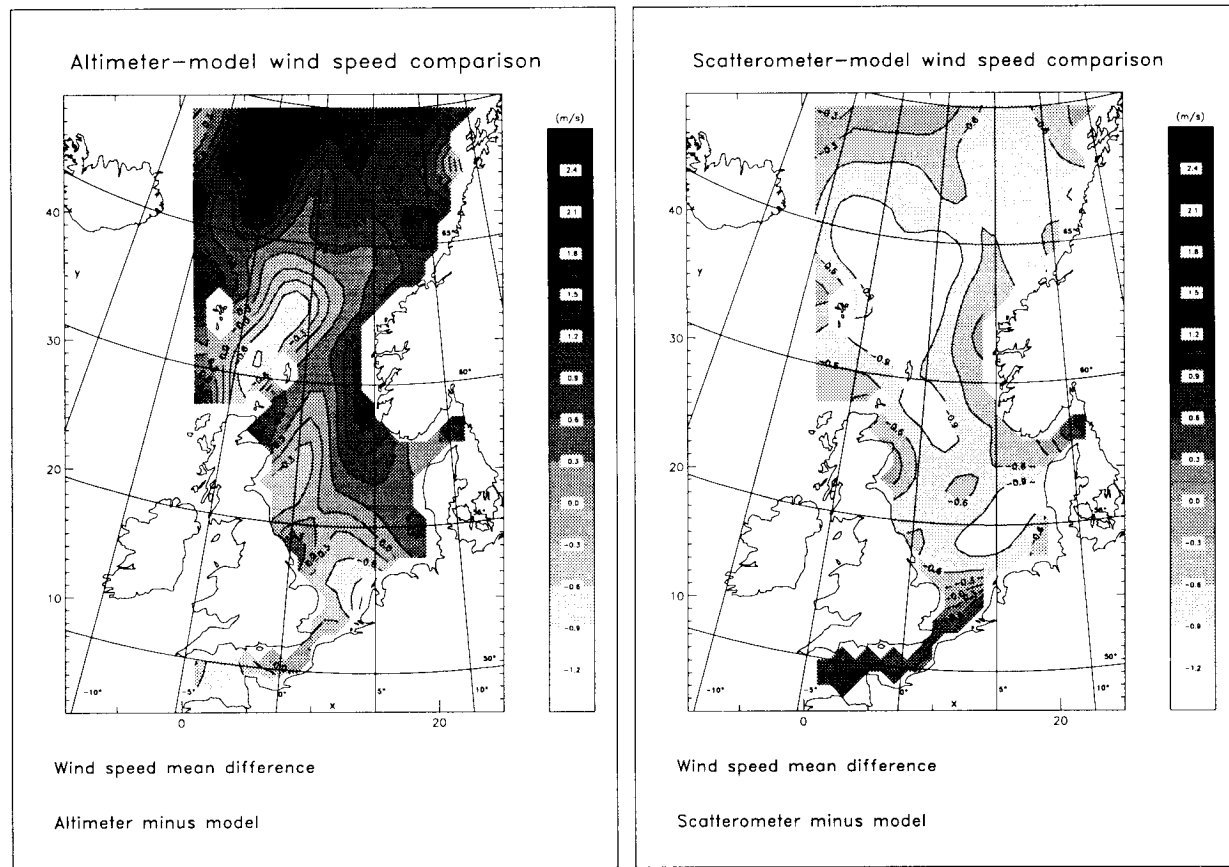


Figure 3. Wind speed mean difference between the smoothed altimeter (left) and scatterometer (right) observations and the model winds for the entire study period.

Table III. Wind data, model ν ERS-1 sensors; negative bias denotes an overestimation by the model, for the wind direction, absolute bias was used

	Alt./Scat.	Bias	S.I.	RMSE
Speed	Alt.	0.79 m/s	0.22	2.20 m/s
Speed	Scat.	-0.63 m/s	0.21	2.24 m/s
Direction	Scat.	13.07°	N/A	16.55°

Comparison with altimeter, scatterometer and buoy data show that the forcings used to drive mu-WAVE globally are of excellent quality. We are particularly pleased with the quality of the analysed winds compared to the buoy measurements. Wind direction has also been investigated, and results (not shown here) were also very satisfactory, with a global (all stations) *absolute* bias of about 22°.

Note that the analysed wind fields are globally underestimated with respect to the altimeter, with a bias of up to 2 m.s⁻¹ in the extreme north of the grid; in this area (during the 6-month test period) the average wind speed was around 11 m.s⁻¹. The agreement in the southern North Sea is good with respect to both altimeter and scatterometer, where the model winds are slightly too high. This overestimation is true in general for the scatterometer measurements, but does not vary much throughout the grid.

The agreement on the scatter diagrams (Figure 4) between the altimeter and model winds is rather good. The scatterometer-model scatter plot shows a larger scatter index. Note that at low (< 4 m.s⁻¹) wind speeds no data is

available.

It is also interesting to compare the satellite winds with the buoy measurements. A limited number of comparison points were found at each wave station (see for instance Figure 2). To achieve this, any satellite observation falling in a 100 km \times 100 km selection zone around one specific buoy was assigned to that buoy, and compared to the nearest buoy-measured data interpolated linearly in time. The results of this analysis are found in Table IV and Figure 5.

Table IV. Wind data, ERS-1 sensors ν buoy; negative bias denotes an overestimation by the satellite; for the wind direction, absolute bias was used

	Alt./Scat.	Bias	S.I.	RMSE
Speed	Alt.	0.36 m/s	0.20	1.65 m/s
Speed	Scat.	0.41 m/s	0.28	2.22 m/s
Direction	Scat.	33.14°	0.91	43.63°

Although a small number of comparison points were found, this analysis is quite interesting. We see, indeed, that the agreement between buoy and altimeter wind speed is rather good up to 20 m.s⁻¹, whereas the scatterometer wind quality seems more precarious, with a fairly large scatter below 12 m.s⁻¹. Whether the altimeter-derived wind speed is more reliable than what is extracted by the scatterometer is far beyond the scope of our project, and requires a broader comparison.

Finally, when compared to buoy measurements, the scatterometer wind direction is satisfactory.

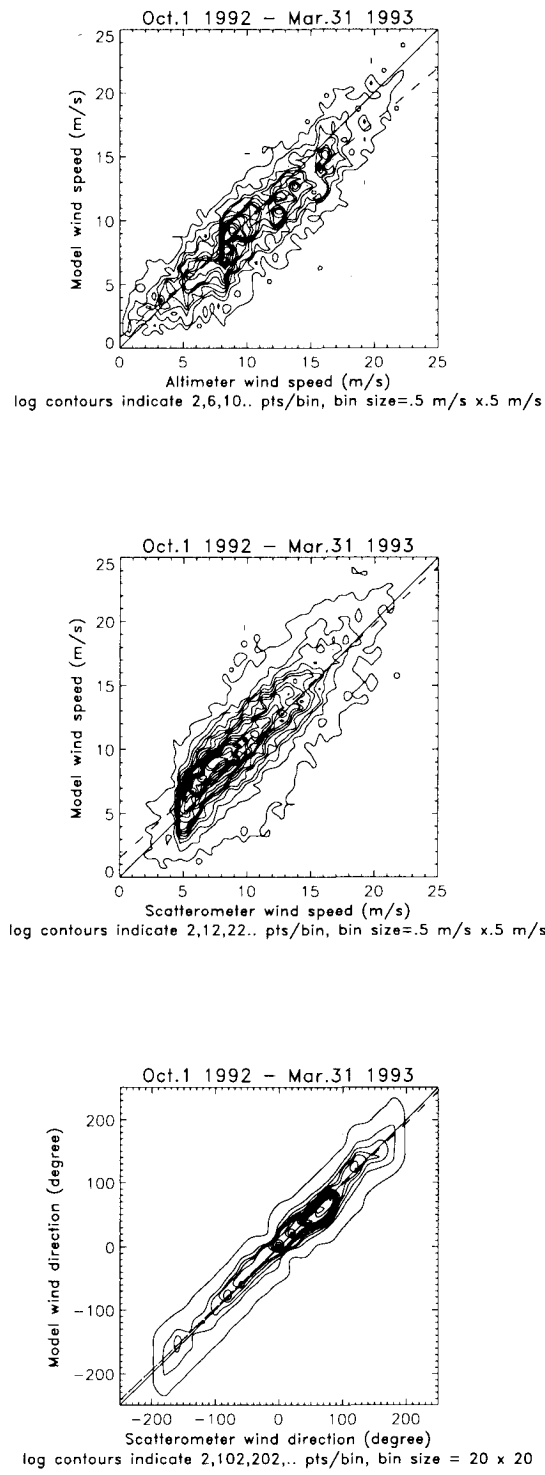


Figure 4. Scatter diagrams for UKMO model wind speeds versus altimeter (top), and versus scatterometer (middle) ; wind direction from UKMO model versus scatterometer (bottom).

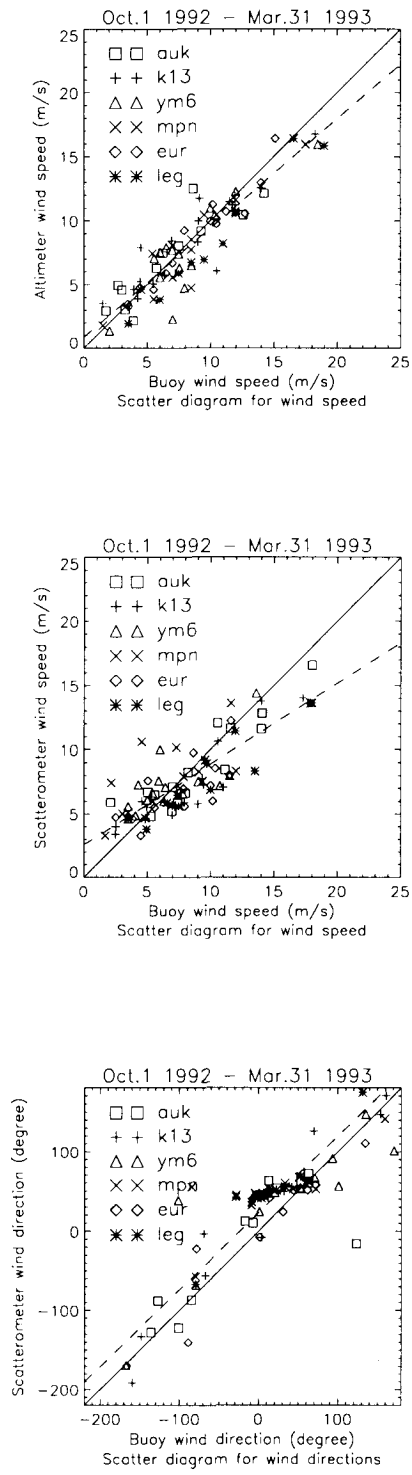


Figure 5. Scatter diagrams for wind speeds from buoy and altimeter (top), buoy and scatterometer (middle) ; wind direction from buoy and scatterometer (bottom).

4. WAVE ANALYSIS

As stated *supra*, the satellite data was used here to check the accuracy of mu-WAVE. We are mainly concerned with the Belgian coastal region, but we also wanted to assess the impact of the open sea boundary conditions used in the model. These were suspected to be a critical element. Indeed, at each open boundary, treated as a wall, limited fetch laws are applied. Of course, energy generated outside the grid is drastically missed. With prevailing westerly wind in the area, this outside generated energy is a matter of concern.

We analysed wave forecasts along selected altimeter sub-tracks. To do so, a potentially interesting sub-track is selected; the criteria for such a selection can be the presence of high waves or the track position with respect to the grid. We present here briefly the example of a track cutting through most of the domain (see figure 6)

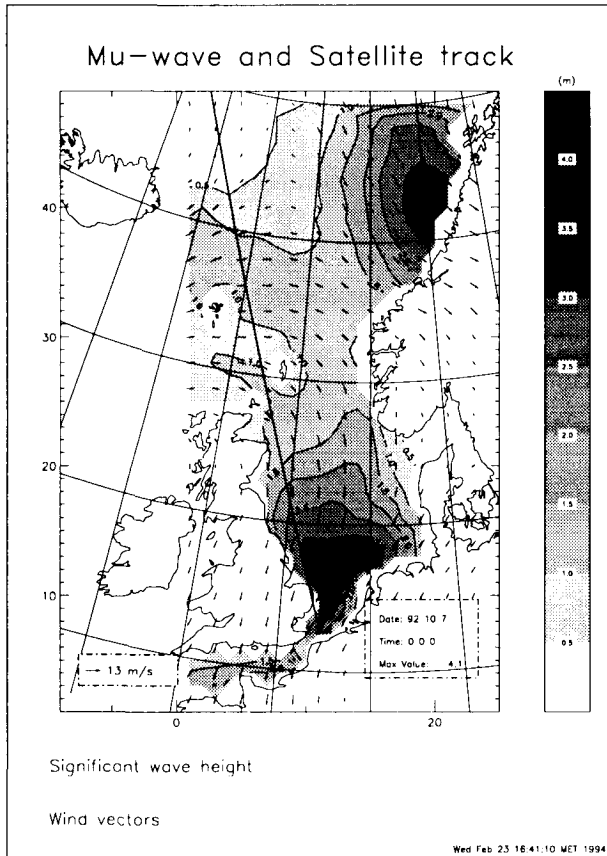


Figure 6. October 7 1992 at 0 GMT. Predicted SWH, wind vectors and the ERS-1 ground track that crossed the domain over 2 hours before that time.

The altimeter data is compared to model forecasts interpolated linearly both in space and time. As the operational model data is available every 6 hours, there's a maximum of 3 hours difference between observation and model results. Similarly, the spatial discrepancy within the coarse grid domain can be up to 37 km which is acceptable since we use 8-point averages of altimeter data, spanning over approximately 50 km. Moreover, tests with a model output every 3 hours did not produce significant changes.

The comparison between altimeter significant wave

height (SWH) data and interpolated model results was carried out for mu-WAVE and WAM. For the track depicted *supra*, this leads to Figure 7, displaying SWH along the satellite track.

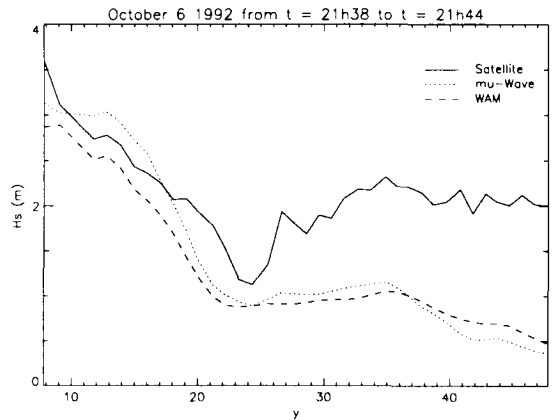


Figure 7. Along track SWH comparison. y is the coarse grid row number (grid bottom = 1 and grid top = 48)

This is a very representative track, where observations and model results are within an acceptable limit from each other up to Northern Scotland ($y=24$) but diverge substantially further to the North. As mentioned earlier, this region is under the direct influence of the open ocean region to the west, where prevailing winds generate wave energy that is bound to propagate into the model domain. From the comparisons, we can see that the open sea boundary condition is an important source of potential error. We are concerned that swell generated in this northern area might be missed by the models. We hope to overcome this situation by assimilating SWH data in mu-WAVE.

In the southern North Sea, where buoy measurements are available, the results of both mu-WAVE and WAM are satisfactory. As an example, Figure 8 displays the SWH time series at station k13 during December 1992.

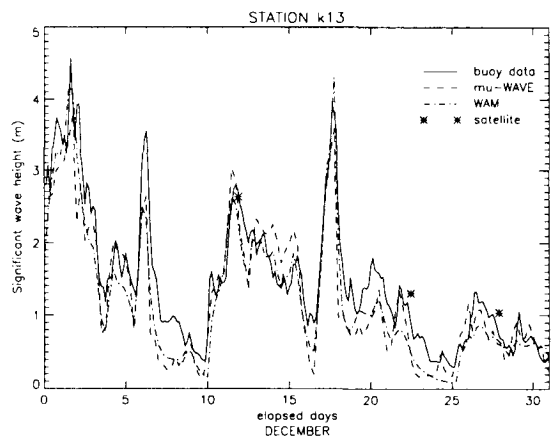


Figure 8. SWH time series at station k13, December 1992

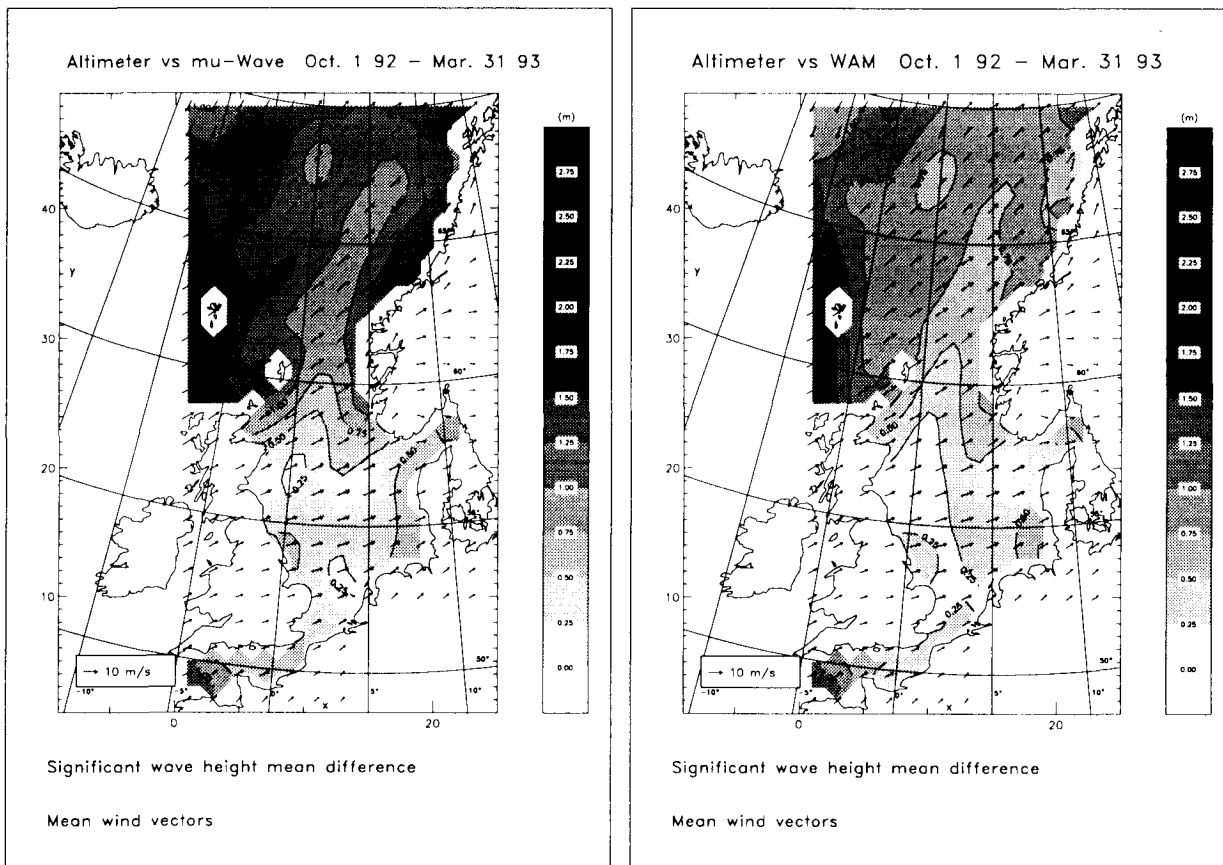


Figure 9. Significant wave height mean difference between the smoothed altimeter observations and the mu-WAVE (left) and WAM (right) results for the entire study period. The model wind vectors averaged over the same time span are also shown (for clarity only half of them are plotted).

A comparison between the predicted significant wave height and the altimeter observations was carried out for the entire 6-month test period. We used the same technique as for the wind speed analysis. For the buoy-altimeter comparison, the selection zone around each buoy was reduced from 100 to 50 km × 50 km. Figure 9 presents the SWH mean difference between altimeter data and mu-WAVE or WAM.

The mu-WAVE model evidently behaves well in the southern North Sea, but, as seen before, the quality deteriorates rapidly towards the western boundary. Notice that the mean wind direction would tend to advect into the grid energy created outside it. This critical underprediction of the wave activity fades eastwards. A better prediction is achieved off the coast of the United Kingdom since no energy created outside the domain can travel into it under prevailing south-westerly winds.

A similar pattern, though less marked, is observed with the WAM model, which has a different approach for the calculation of the energy spectrum and more specifically the boundary conditions.

An extensive statistical analysis was carried out; preliminary results are presented here after. The coarse grid domain was divided in three separate regions, which we called the CHANNEL, the NORTII SEA and the OPEN SEA regions. The reason for this separation is clearly visible in Figures 7 and 9; moreover, it was clear that a fairly narrow zone as the English Channel would contain less (valid) altimeter measurements than the large region off the coast

of Norway. Therefore, the three regions were defined as follows : the CHANNEL region includes the six bottom rows of the grid; the NORTII SEA region extends up to the extreme North of the U.K., where the OPEN SEA region starts. The number of valid altimeter data points (*i.e.* groups of 8 measurements) in these regions are respectively for a one month period in the order of 25, 250 and 1050.

Once again, we used altimeter and buoy data. Unfortunately no wave information was available at station auk, which is the most distant from the coast. Table V presents the results of the comparison between model results and altimeter data; scatter diagrams for the SWH in the NORTII SEA region can be found, as an illustration, in Figure 10. Finally, Table VI displays the results of the model-buoy comparison.

WAM and mu-WAVE generally underpredict the significant wave height seen by ERS-1. The data was analysed monthly (Ovidio *et al.*, 1994) though we only present here the global 6-month results. As already mentioned, the models were least accurate in the OPEN SEA region. A mean SWH bias of 42 cm between altimeter and mu-WAVE is achieved in the NORTII SEA region, which is within an acceptable range.

Table V. Significant wave height data, models v altimeter; positive bias denotes an underestimation by the model;

	Bias (m)		S.I.		RMSE (m)	
	mu-WAVE	WAM	mu-WAVE	WAM	mu-WAVE	WAM
Whole	1,04	0,75	0,54	0,40	1,48	1,14
Channel	0,82	0,79	0,66	0,70	0,93	0,93
North Sea	0,42	0,31	0,38	0,31	0,74	0,63
Open Sea	1,19	0,85	0,55	0,40	1,61	1,23

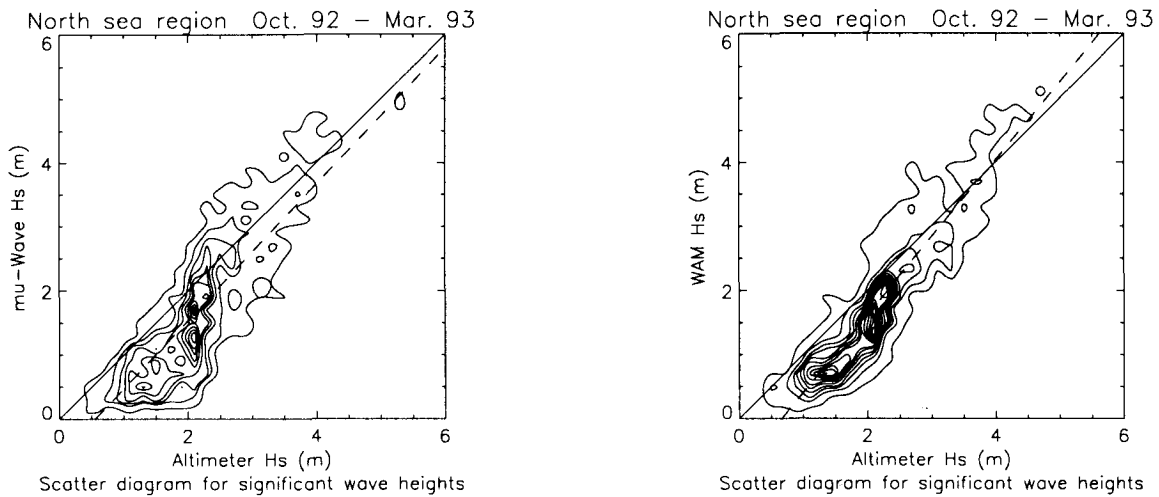


Figure 10. Significant wave height scatter diagrams for mu-WAVE (left) and WAM (right) with respect to the altimeter measurements.

Table VI. Significant wave height data, models v buoys; positive bias denotes an underestimation by the model;

	Bias (m)		S.I.		RMSE (m)	
	mu-WAVE	WAM	mu-WAVE	WAM	mu-WAVE	WAM
k13	0,19	0,27	0,32	0,27	0,45	0,45
mpn	0,18	0,35	0,38	0,53	0,43	0,55
ym6	0,15	0,20	0,38	0,35	0,51	0,46

The validation of both WAM and mu-WAVE has been pursued with the analysis of other wave parameters provided by the buoys. Among these are the low frequency wave height H_f and the mean period T_o . Detailed results will not be presented here. The time series of the mean period at station ym6 in January 1993 is nevertheless presented in Figure 11 to illustrate a persistent difference between WAM and mu-WAVE. Indeed it was shown that, with respect to the buoy data, the latter underestimates T_o , whereas the former overestimates it. The bias is of the order of ± 0.4 s (the sign depending on the model). Scatter indexes were in the range of 0.1 to 0.3 s for both models.

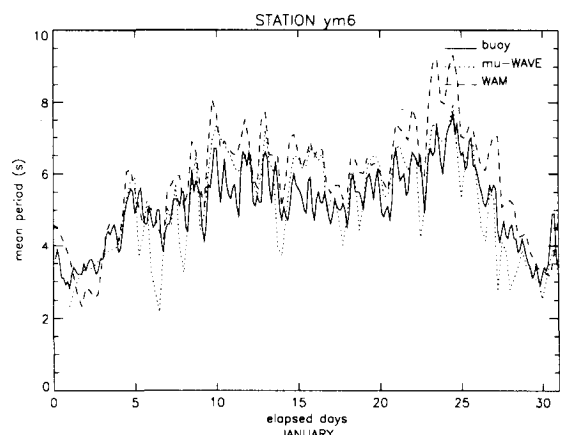


Figure 11. Time series of the mean period at ym6 in January 1993.

5. FUTURE WORK

In the following months, we will carry on with the analysis of the fine grid version of the model. For this purpose, we will use additional buoy data, located near the Belgian coast. The comparison with WAM in the shallow waters of the *Vlaamse Banken* should be quite interesting.

It is thereafter planned to implement a data assimilation procedure in the operational model. Satellite data (mainly altimeter SWH) will be used. We also look upon the possibility to assimilate WAM wave forecasts (as produced for instance by a national meteorological office's global model) along the open sea boundaries.

6. ACKNOWLEDGEMENTS

This work was carried out in the framework of the Pilot Project PP2-B9. The authors wish to thank ESA for providing the altimeter and scatterometer data.

Fabrice Ovidio and Jean-Raymond Bidlot are funded by the Belgian Science Policy Office, Research Program on Remote Sensing (third phase, TELSAT/III) under convention T3/58/011.

Finally, we thank Susanne Hasselmann for authorising the use of the WAM model code.

7. REFERENCES

- Günther H. and W. Rosenthal, 1985, The hybrid parametrical (HYPA) wave model, in *Ocean Wave modelling*, the SWAMP group, Plenum Press, New York, 211–214.
- Hasselmann, K. et al., 1973, Measurements of wind-wave growth and swell decay during the Joint North Sea Wave Project (JONSWAP), Deutsches Hydrographisches Institut, Hamburg.
- Hoffman, R.N., 1993, A preliminary study of the impact of the ERS-1 C band scatterometer wind data on the European Centre for Medium-Range Weather Forecasts global data assimilation system, *J. Geophys. Res.*, **98 C6**, 10233–10244.
- Ovidio, F., J.-R. Bidlot and D. Van den Eynde, 1994, Validation and improvement of the quality of the operational wave model mu-WAVE by the use of ERS-1 satellite data, *Activity Report MUMM/T3/AR02*, MUMM-North Sea, Gulledele 100, B-1200 Brussels, Belgium, 87 pp.
- Romeiser, R., 1993, Global validation of the wave model WAM over a one-year period using GEOSAT wave height data, *J. Geophys. Res.*, **98 C3**, 4713–4726.
- Van den Eynde, D., 1992, mu-WAVE : an operational wave forecasting system for the Belgian coast, *Proceedings of the third International Workshop on Wave Hindcasting and Forecasting*, May 19–22, Montreal, Quebec, Canada, 313–324.
- WAMDIG, the WAM Development and Implementation Group, 1988, The WAM model —a third generation ocean wave prediction model, *J. Phys. Oceanogr.*, **18**, 1775–1810.
- Zambreski, L.F., 1989, A verification study of the global WAM model : December 1987–November 1988, *Report GKSS 89/E/37*, GKSS Forschungszentrum GmbH, Geesthacht, Germany, 86 pp.

PROCESSING AND APPLICATION OF WIND SCATTEROMETER DATA AND SAR WAVE SPECTRA IN NUMERICAL WAVE AND WEATHER PREDICTION

Jens Sunde*), Lars-Anders Breivik*), Baard Haugse*),
Harald Johnsen**), Harald Krogstad***), Magnar Reistad****)

*) The Norwegian Meteorological Institute (DNMI), P.O.Box 43 Blindern, N-0313 Oslo, Norway

**) NORUT Information Technology, N-9005 Tromsø, Norway

***) SINTEF Industrial Mathematics, N-7034 Trondheim, Norway

****) The Norwegian Meteorological Institute (DNMI), Regional Office, Allegt. 70, N-5007 Bergen, Norway

ABSTRACT

At the Norwegian Meteorological Institute (DNMI) ERS-1 wind and wave data has been received operationally since the launch of the satellite. Experience has been gained on utilization of the information in the data analysis of numerical wave and weather prediction. On basis on this a program for further development of the methods for the use of the data has been defined. There are three main objections of the program: Better utilization of the scatterometer wind information in the weather forecast model by development on the assimilation technique; Consistent analysis of wind and waves by coupled analysis of satellite measured wind and wave and weather prediction models; Analysis and assimilation of SAR wave spectra in the wave prediction model. The work was started in 1993 and preliminary results are expected in 1994.

1. INTRODUCTION

As a response to ESA ERS-1 Announcement of Opportunity (AO), 1986, DNMI decided to prepare for operational use of the scatterometer and altimeter information. Since the launch of ERS-1 in July 1991 scatterometer wind and significant wave height information have been received in real time at the Norwegian Meteorological Institute (DNMI). The data has been collocated with and evaluated against operational numerical weather forecast model and ocean wave model data. Both the scatterometer wind information and the altimeter wave heights were found to be of high quality. Routines for assimilation of the data in numerical prediction models were developed. The average impact of the data from test runs were positive, but rather modest. However, the operational wave model at DNMI is currently running with assimilation of significant wave heights from the radar altimeter.

As a successor of the very successful AO project, DNMI in cooperation with the Norwegian Space Centre (NRS) decided to define a ERS data applications program. The aim was firstly to continue the promising work performed on scatterometer information, and secondly

try to apply SAR information in the wave model.

The objective of the first part is to apply the wind scatterometer information operationally in the numerical weather prediction model and to extend the work to perform consistent analyses of the satellite measured wind and wave information in a coupled system of numerical wind and wave models.

The objective of the second part is to deduce wave spectral information from the AMI wave mode and SAR image information, and to apply such information in the ocean wave model assimilation procedures.

In this paper the organization and funding of the satellite application program is presented in section 2. In sections 3, 4, 5, 6, and 7 a closer look into the different program activities is presented before the paper is closed with a conclusion in section 8.

2. ORGANIZATION AND FUNDING

DNMI is responsible for the ERS data application program activities. The program coordinator is employed by DNMI. To execute the program, cooperation is required between three independent Norwegian institutions: Norwegian Meteorological Institute Department of Research in Oslo and Regional Office in Bergen, The Research Institute NORUT Department of Information Technology in Tromsø and The Industrial Research Foundation SINTEF Department of Industrial Mathematics in Trondheim.

The ERS application program is organized in three different projects:

- a) *Improved forecasts of sea surface winds, ocean current and ocean surface waves based on scatterometer wind observations.*

In this project local processing and assimilation technics of scatterometer data in the atmospheric model is developed. Furthermore, preparatory work on a coupled analysis system of wind and wave observations from the ERS scatterometer and altimeter in the numerical

atmospheric and ocean models is performed. DNMI is the main responsible institution for this project.

b) Transformation of SAR image data to wave spectra.

In this project AMI wave mode SAR image spectral information (available on GTS) is transformed to ocean wave spectra. In addition SAR images received at Tromsø Satellite Station are transformed to wave spectra in two steps. NORUT and SINTEF are the main responsible institutions for this project.

c) Assimilation of SAR wave spectra in Numerical Wave Model.

Assimilation technics will be developed to handle the wave information deduced in project b) in the DNMI numerical wave model. DNMI is the main responsible institution for this project.

The ERS application program is jointly funded by Norwegian Space Agency (NRS) and DNMI.

3. SCATTEROMETER DATA IN NUMERICAL WEATHER PREDICTION, NWP

Scatterometer data are locally received at DNMI on GTS in real time. The data are processed by a method 'Prescat' based on the scatterometer model function CMOD4 and a de-aliasing procedure developed at ECMWF and locally modified at DNMI (Breivik and Haugse, 1994). The local modifications are done to limit the use of the first guess background winds from the NWP model without loosing the advantage of having this high quality background information source available. Lokal dealiasing routine gives significantly better 10 m winds than those received on GTS from ESA.

A parallel routine, similar to the operational weather forecast model, was run at DNMI from November to January 1992 -93 to test the impact of ERS-1 scatterometer wind observations on the forecasts (Breivik et al. 1993). The scatterometer data in use at that time were the operational ESA wind vectors derived with, at the time being, the operational model function. An extra data control was run prior to the analyses to take care of 180° aliases. We found a quite small but on average positive impact on the forecast.

In Mars 1994 a new parallel routine was initiated using

the scatterometer wind observations locally retrieved from σ^0 to wind at DNMI. No extra data control on scatterometer data is done, but left to the operational data control prior to the analysis.

Figure 1 shows the results of the data control and analysis. The Figure shows isolines for the analyzed heights of 1000 mb pressure surface together with analyzed scatterometer observations 1200 UTC 9 January 1994. The observations marked with a cross are skipped in the data control prior to the analysis. For this, and for similar cases, the data control works well, handling the part of the observation control not treated by the dealiasing of Prescat. However, there might still be cases were a larger area contains scatterometer winds wrong by 180 degrees. In such cases the convergence check of the multivariate control might not be effective.

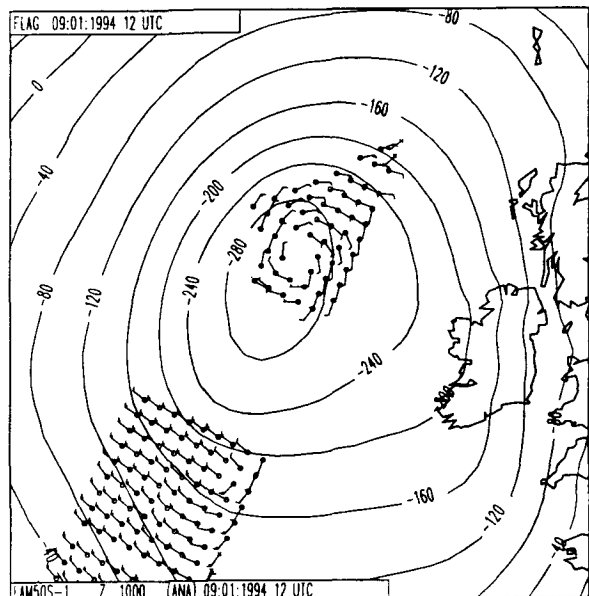


Figure 1.

Isolines of analyzed heights of 1000 mb pressure surface together with analyzed scatterometer observations 1200 UTC 9 January 1994. The observations marked with a cross are skipped in the data control prior to the analysis.

The problems in utilizing the scatterometer winds in the numerical model lay in the possibilities to describe the upper air structures from the surface information. Traditional methods, three dimensional analyses, are not capable of correctly describing the vertical correlations between the increments of the analyzed variables. This is particularly true in the different phases of storm cyclogenesis. It is now generally believed that to fully utilize the information contained in a surface observation, it is necessary to take into account the time

development of the variables in the analyses, i.e. four dimensional analysis. Methods for four dimensional analysis of atmospheric fields need large resources both in development work and later in computing. Presently development takes place in large meteorological centres like ECMWF. The problem can, however, be subdivided. A four dimensional analysis requires a variational approach which needs a specification of each part of a cost function to be minimized. For scatterometer observations the cost function in terms of the distance between the observed value and the analysis should be specified. Considering it as solving for the sea surface a two dimensional part of the four dimensional problem. On this basis the next objective of DNMI's scatterometer data utilization project is development of a two dimensional variational analysis for the wind at the sea surface.

4. ALTIMETER DATA IN NUMERICAL WAVE PREDICTION

Significant wave heights from the ERS-1 radar altimeter have been received at DNMI in real time since July 1991. A method to assimilate significant wave heights into the wave model WINCH has been implemented. WINCH is a regional wave model operationally run at DNMI for the Norwegian areas and the North Atlantic (Reistad et al., 1988). WINCH is a second generation wave model developed by Oceanweather Inc. The WINCH model is a modified version of the SAIL model, which was one of the models in the SWAMP (1985) study. The model produces a full two dimensional wave spectrum at 15 frequency bands and 24 directional sectors on a 75 km grid. The wind at 10 m height is taken from DNMI's numerical weather prediction model. The significant wave height is analyzed in the model area by a Modified Successive Correction method, and the corrected field of significant wave height is used to modify the wave model spectra (Breivik and Reistad, 1994). The altimeter data is now used operationally in the wave model. Verification against independent buoy measurements from in the North Sea has shown that the wave analysis has been improved by assimilation of altimeter data. There is positive impact also on the short forecasts as shown in Figure 2. For forecasts longer than 18 hours the impact is limited. This is to be expected since the wave prognoses are forced by the prognostic wind fields, which presently is independent of the wave assimilation.

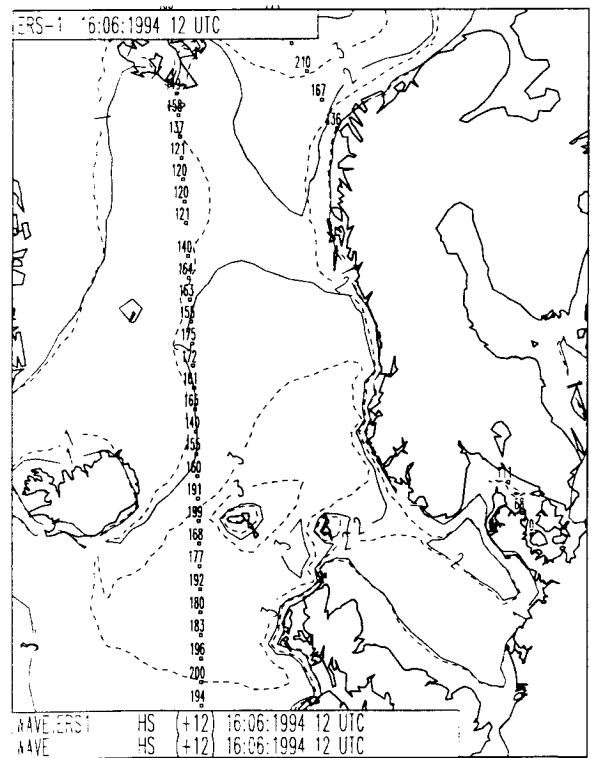


Figure 2.
Isolines of Significant Wave Height, 12 hours prognosis valid 16. June 1994 12 UTC.
Solid line: With altimeter data assimilated.
Broken line: No assimilation.
Plotted together with altimeter observations at verification time.

5. SCATTEROMETER DATA AND ALTIMETER DATA IN COUPLED WAVE/WEATHER ANALYSES

As stated above, the impact of altimeter wave heights assimilation in the wave model on short to medium range forecasts is small. The impact from the analyses gradually decreases throughout the forecast. In the current operational analyses scheme the wind in the wave model is corrected at analysis time and at the next advection time step (2 hours) on basis of the corrected wave field. The input wind from the weather forecast model is not corrected on basis of the wave analysis. We believe that the impact from the observations could be improved if the wind field was consistently corrected in the atmospheric forecast model. The objective of the ERS data utilization project is therefore to define and develop a coupled analysis system of wind and wave observations from the ERS scatterometer and altimeter. The idea is to do this within the two dimensional variational framework briefly described in section 4. The intention is not an independent analysis scheme for scatterometer data in the atmospheric forecast model and

one for wave data in the wave model, but an analysis system for the sea surface taking all relevant data into account and producing consistent wind and wave analyses.

6. TRANSFORMATION OF SAR IMAGE DATA TO WAVE SPECTRA.

6.1 Ocean-SAR inversion based on the ERS-1 Wave Mode product.

The ERS-1 Wave Mode product is distributed daily on GTS to meteorological institutions all over the world. The product consists of a SAR image wavenumber spectrum computed from an approximately 5 by 5 km imagette, and the GTS system appears to distribute about every second recorded spectrum.

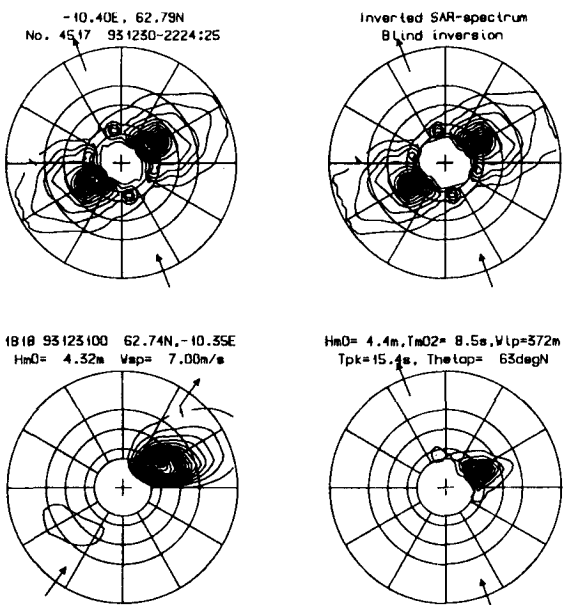


Figure 3.
Example of inverted wavenumber spectrum, SAR Wave Mode (upper left), Wave model input (lower left), improved spectrum (lower right), Corresponding SAR spectrum (upper right). Circles at 100 (outermost), 150, 200, 300 and 400m (innermost).

A major objective of the present project is to apply the Wave Mode spectra in an ocean-SAR inversion algorithm and produce directional ocean wave spectra for assimilation into WINCH. Directional wave spectra along extensive tracks over the model area are well suited for this purpose. Another obvious application of inverted wave spectra is ocean wave climatology in data sparse areas.

However, it has been realised that the ERS-1 Wave Mode spectra suffer from a somewhat imperfect processing which degrades its applicability. Firstly the product is delivered with no indication of its absolute scale, it is not corrected for system transfer functions or indicates how such a correction should be carried out. Moreover, the spectrum is computed from amplitude instead of intensity averaged imagettes, and many spectra contain excessive low frequency noise of unknown origin. Separate spectral analysis of the same imagettes shows no indication of this noise and this analysis has also lead to an improved system transfer function for the spectra (Krogstad, 1994).

Due to the product's rather coarse resolution and limited frequency range, the inversion algorithm has been simplified compared to the algorithm described in section 6.2 for the SAR images received in Tromsø. The ocean-to SAR forward transformation is based on the quasi linear mapping long applied in the field, whereas the inversion is approximately similar to the full algorithm (Krogstad et al., 1994). This inversion algorithm is simple to implement, leads to a stable and robust iteration, and is computationally very fast.

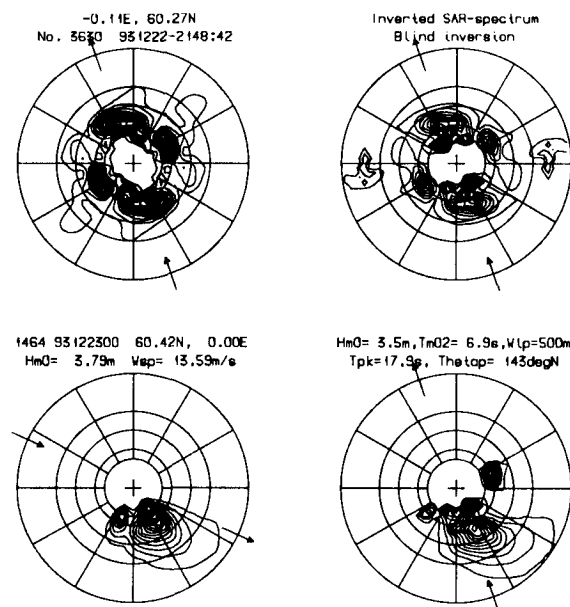


Figure 4.
Example of inverted wavenumber spectrum showing additional swell picked up by the inversion and some low wave number noise.

The wave spectra derived from the inversion algorithm will to some extent be dependent on the inversion strategy, see (Krogstad et al., 1994). Essentially, the inversion applies a certain a priori wave information which in the present case is taken from a neighbouring gridpoint for the wave model. The examples shown in

Figures 3 and 4 do, however, only utilise the wave model spectra as an indication of the wave direction within a 180 degrees sector. The final inverted spectrum is thus defined by the SAR image spectrum where the latter is defined. The inversion in Figure 3 shows a spectrum that is directionally more narrow than the wave model spectrum, and this appears to be a consistent feature most probably due to the finite resolution of the wave model. Figure 4 illustrates how the inversion finds a swell contribution going towards east. This is geographically very likely as the location is heavily exposed to Atlantic swell. However, it also shows some contribution probably due to noise in the SAR spectrum. Low wavenumber noise in the Wave Mode spectra which is erroneously interpreted as wave spectrum contributions is unfortunately rather common.

6.2 Transformation of SAR images to SAR wave spectra.

Directional ocean wave spectra are also extracted from near-real time ERS-1 SAR Image Mode data delivered by Tromso Satellite Station. The SAR wave spectra processing procedure consists of a pre-processing module, an inversion module and a post-processing module. The pre-processing consists of computing the SAR image variance spectra (typically 16 spectra from each image) based on a series of FFT. These spectra are then inverted using a priori information provided by the nearest (in time and space) wave model (WINCH) grid point. Finally the SAR wave spectra are converted to standard wave model spectral representation and distributed to the Norwegian Meteorological Institute for further analysis and assimilation.

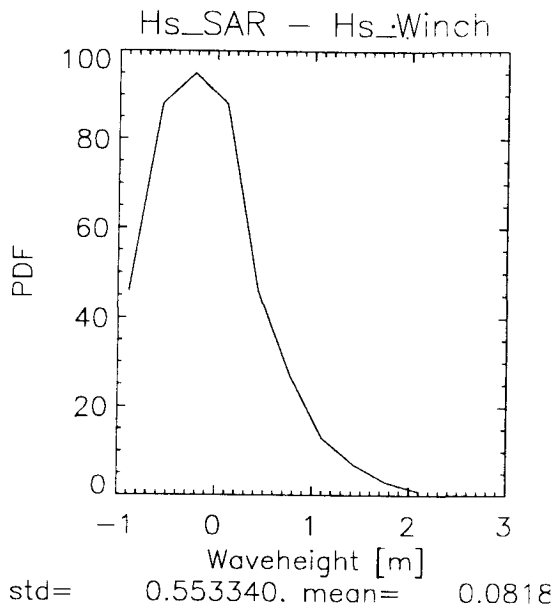


Figure 5a.
Comparison of total Hs of the swell derived from the SAR wave spectra and the WINCH wave spectra.

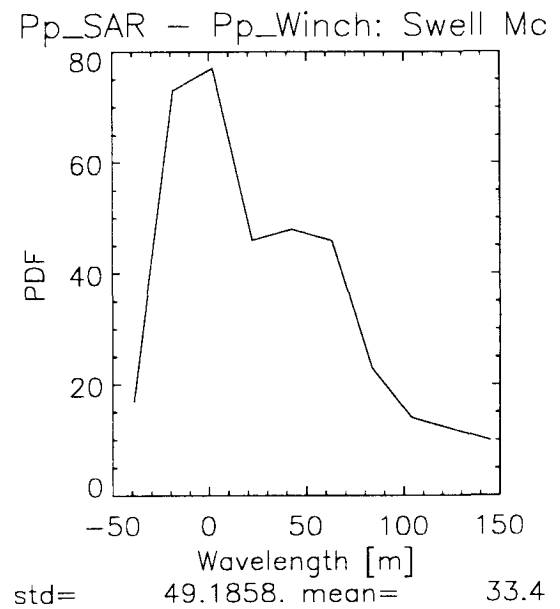


Figure 5b.
Comparison of total peak wave length of the swell derived from the SAR wave spectra and the WINCH wave spectra.

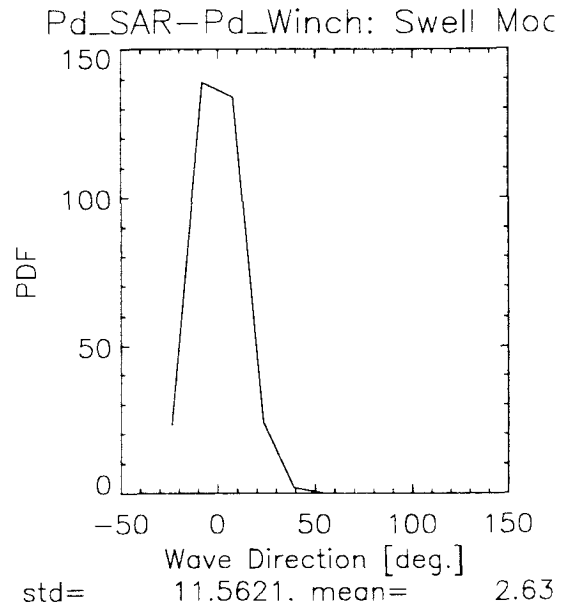


Figure 5c.
Comparison of total peak wave direction of the swell derived from the SAR wave spectra and the WINCH

The inversion procedure is based on a minimization of a weighted mean-square deviation between the observed and the predicted SAR image variance spectra (Engen et al., 1994).

The minimization is done with respect to the directional

wave spectrum under the constraint that the spectrum shall be positive (Krogstad et. al., 1994). The predicted SAR spectra are computed using the full non-linear ocean-to-SAR transform, and a quasi-linear modification is used to compute the update of the input wave spectrum.

Several hundred spectra from the Norwegian Sea have been inverted and validated against in-situ observations and numerical wave model spectra. The results show that the SAR observations have a significant impact on the swell part of spectrum, and often an increase of the peak wavelength is observed. For the wind mode the impact is often small due to the lack of wind mode spectral information in the SAR image spectra. This again is often caused by the poor along track resolution of the ERS-1 SAR system. Figure 5 shows the results of a comparison between wave parameters from SAR wave spectra and the corresponding WINCH wave spectra.

7. ASSIMILATION OF SAR WAVE SPECTRA IN A NUMERICAL WAVE MODEL.

A method to assimilate SAR wave spectra in a numerical wave model is under development. The wave model is the operational wave prediction model WINCH at DNMI, briefly described in section 4.

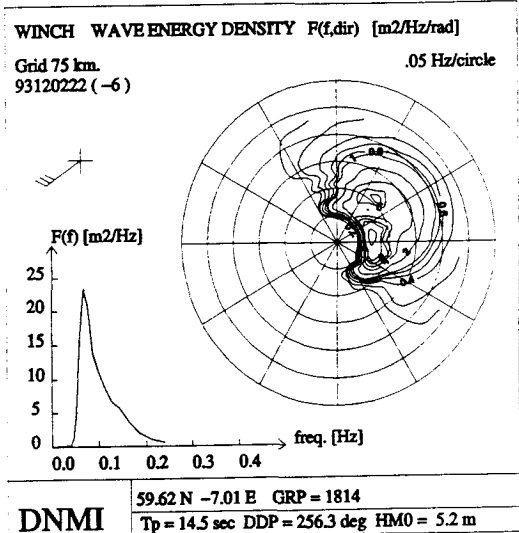


Figure 6a.
Two dimensional SAR wave spectrum inverted from a SAR wave mode spectrum.

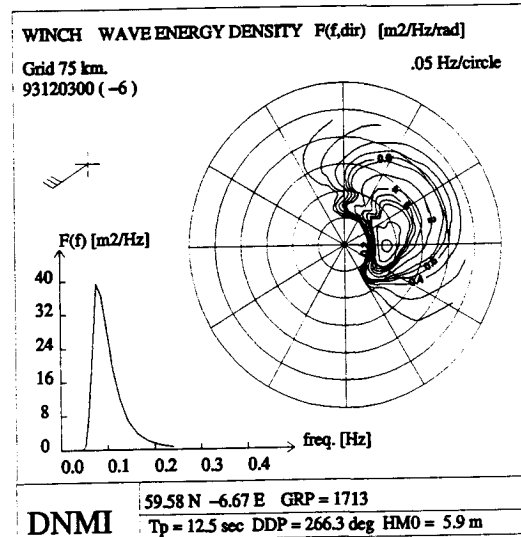


Figure 6b.
Winch model spectrum at nearest time and geographical localization as the SAR spectrum in Figure 6a.

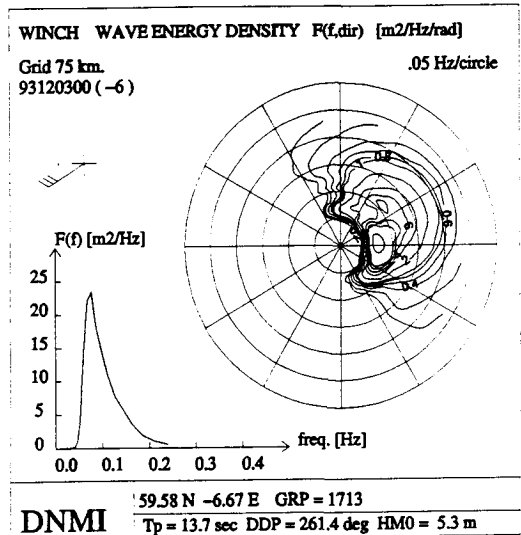


Figure 6c.
Modified wave spectrum after assimilation based on information from Figures 6a and 6b.

Each component of the SAR wave spectra are assimilated using a version of the analysis scheme developed for the weather prediction models at DNMI (Bratseth, 1986). The same analysis scheme is also used for assimilation of ERS-1 altimeter wave heights in the WINCH model. Figure 6a shows a two dimensional SAR wave spectrum inverted from a SAR wave mode spectrum. The wave energy is given in the same

frequency and direction bins as the WINCH model spectra. Figure 6b shows the WINCH model spectrum in the nearest model grid point. The result of the assimilation in the same grid point is shown in Figure 6c. Three SAR wave spectra was assimilated in the WINCH model and the model was integrated forward in time with and without assimilation of the three SAR wave spectra. The impact on the significant wave height 12 hours after the assimilation is seen in Figure 7. In this figure isolines for significant wave height are drawn. The dotted lines are from the run without assimilation and the solid lines are from the run with assimilation.

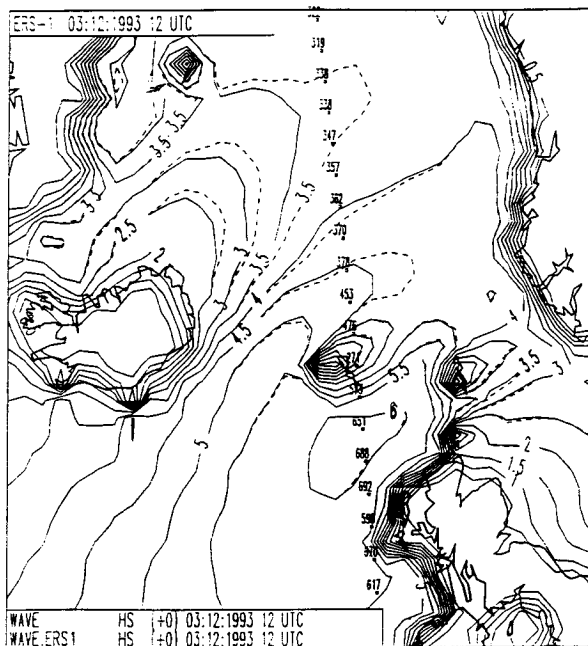


Figure 7.
Isolines for significant wave heights. Impact 12 hours
after assimilation time.
Solid lines: With assimilation of SAR wave spectra.
Broken lines: Without assimilation.

8. CONCLUSION

A well prepared and organized program is executed on applications of ERS data.

The radar altimeter observed significant wave heights are operationally contributing to improved wave analyses and very short range ocean wave forecasts at DNMI. Scatterometer wind observations are of high quality. As a result of this ERS applications program local dealiasing routine gives significantly better 10 m winds than those received on GTS from ESA. Within the next year the scatterometer wind observations are planned to be operationally assimilated in the DNMI numerical weather prediction model. Later a consistent analysis scheme for ERS wind and wave (altimeter and later

SAR) observations will be developed.

The quality of the SAR deduced wave spectra seem promising. However the GTS transmitted wave mode spectra suffer from degraded preprocessing which reduces its applicability. This preprocessing should be improved to reach the same level of quality as the information provided by the TSS/NORUT system. Some very preliminary attempts is performed on the assimilation of the SAR wave spectral information in the wave model. Up to now the results give positive indications of impact. However, more work is needed before final conclusions can be made.

References:

- Bratseth, A.M., 1986: Statistical interpolation by means of successive corrections, Tellus, 38A, 439-447.
- Breivik L-A, B Haugse & M Homleid 1993, Results from Assimilation of ERS-1 Scatterometer Wind Information in an Operational Limited Area Model. In Proceedings of the Second ERS-1 symposium: 'Space at the service of our environment', ESA Publication Division, ESTEC, Noordwijk, The Netherlands.
- Breivik L A & M Reistad 1994, Assimilation of ERS-1 Altimeter Wave Heights in an Operational Numerical Wave Model, To appear in: *Wea. Forecasting*, September 1994.
- Breivik L A & B Haugse 1994, Scatterometer Wind Retrieval at the Norwegian Meteorological Institute. DNMI Technical Rep. No. 124.
- Engen, G., H. Johnsen, H.E. Krogstad, S.F. Barstow, "Directional Wave Spectra by Inversion of ERS-1 Synthetic Aperture Radar Ocean Imagery", IEEE Trans. on Geoscience and Remote Sensing, Vol. 32, No. 2, March 1994.
- Krogstad, H.E., O. Samset and P. W. Vachon: "Generalizations of the Nonlinear Ocean-SAR Transformation and a Simplified SAR Inversion Algorithm", Atmosphere and Ocean, Vol. 32(1), pp 61-82, March 1994.
- Krogstad, H.E.: Ocean-SAR Inversion with ERS-1 Wave Mode product, Proc. 2nd ERS-1 Workshop, CERSAT/IFREMER. 15-17 March 1994 (To be published)
- Reistad,M, L.I.Eide, J.Guddal, and A.K.Magnusson: Wave model sensitivity study. DNMI 1988.
- The SWAMP Group, 1985: Ocean Wave Modelling, Plenum Press.



NUMERICAL ANALYSIS OF THE WIND-INDUCED CIRCULATION IN THE BRANSFIELD STRAIT (ANTARCTICA) USING ERS-1/WSC WINDS

Manuel Espino, Marc García, Joan Puigdefábregas, Julia Figa, Agustín S.-Arcilla

Laboratori d'Enginyeria Marítima
Universitat Politècnica de Catalunya
c/Gran Capitán s/n, mòdul D1
08034 Barcelona, Spain
phone: (+34) (3) 401 64 68, fax: (+34) (3) 401 73 57

ABSTRACT

One of the goals of the Pilot Project "Application of ERS-1 products to Geophysical Research in Antarctica" (PP2-E1) was to assess the characteristic wind-induced circulation patterns in the Bransfield Strait region during Austral summer.

From the WSC.FDC data set corresponding to the period December 1992 to April 1993 which was forwarded to us by ESA, we extracted 21 synoptic wind fields covering the study area. A simple method was established to interpolate the wind velocity and direction at error-flagged nodes and to reassess the wind direction where necessary.

The directional distribution of the computed WSC wind fields compares reasonably well with the few available local meteo statistics. On the other hand, the WSC winds exhibit a spatial variability which could not be resolved by the local observations.

Representative WSC wind fields have been selected and used to force a quasi-3D primitive equation finite element circulation model developed at LIM/UPC. A first numerical simulation using a "short-term climatological" average wind field is presented. Our results suggest that the circulation on the Antarctic Peninsula continental shelf may be significantly affected by the wind action, whereas the geostrophic current is the main contribution to the long-term averaged flow everywhere else.

1. INTRODUCTION

Within the framework of the Spanish National Programme on Antarctic Research, LIM/UPC is carrying out a three-year study of the dynamical oceanography of the Bransfield Strait during Austral summer. The Strait is a semi-enclosed sea of 50,000 km² extending between the South Shetland archipelago and the coast of the Antarctic Peninsula (see figure 1). About 50% of the existing Antarctic polar stations are located in this

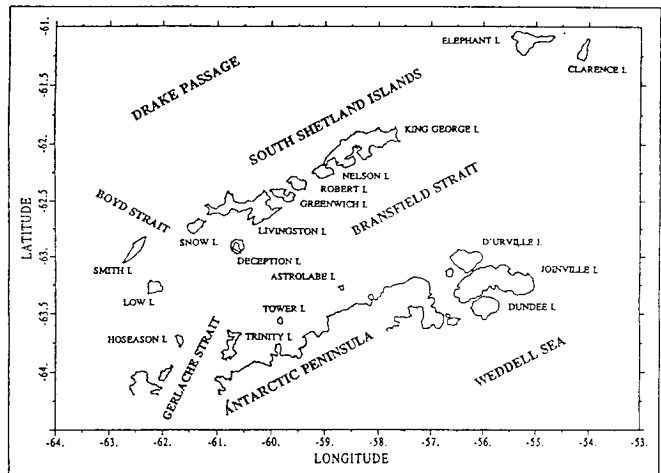


Fig. 1. Location of the Bransfield Strait

region. Shipping activities related both to logistic needs and to tourism have increased considerably in the area over the past few years. Whereas pollution risks due to accidental oil spills are now more than just a possibility, we still lack a comprehensive description of the local circulation at different time scales, which is required to predict the fate and trajectory of oil slicks.

Past research efforts in the study area concentrated on the water masses distribution and associated geostrophic circulation (see e.g. Refs. 1 and 2). The mesoscale structure of the geostrophic flow has been addressed only recently (Refs. 3 and 4). Very little is known about the tidal circulation (Ref. 5), and no results about the wind-induced currents have been published so far to our knowledge.

From this standpoint, ERS-1 WSC winds emerge as a unique tool to provide the wind stress distributions required as input for model studies of the local wind-induced currents. The interpolation of local wind observations is not feasible, as the distribution of the local meteo stations is extremely sparse.

2. METHODOLOGY

According to the goals of the PP2-E1 project "Application of ERS-1 products to Geophysical Research in Antarctica", ESA forwarded to us a number of WSC.FDC files corresponding to the period December 1992 to April 1993. 21 synoptic wind fields covering the study area were selected for further modelling purposes. A simple method, which is illustrated in figure 2, was established to file-by-file interpolate the wind velocity and direction at error-flagged nodes and to check the consistency of the direction ambiguity removal. First of all, WSC wind data corresponding to error codes were eliminated. At a second step, the filtered wind field was compared with a gradient wind estimate derived from contemporary meteo charts and the wind direction was inverted when the discrepancy in direction was more than 90° . Finally, the gaps were interpolated using a weighted least-square method.

The statistics of the wind velocity and direction computed on the basis of the WSC data set showed a reasonable agreement with the few available statistics derived from field observations, and a "short-term climatological" wind field was derived by vector-averaging the WSC nodal values. It was further used as input for preliminary model calculations of the local wind-induced currents (figure 3).

We made use of a quasi-3D primitive equation finite element model of the steady-state shallow water equations developed at LIM/UPC (Ref. 6). The model employs a mixed Q1/P0 discretization scheme in the horizontal and an expansion of the vertical variation of the dependent variables in terms of a set of orthogonal basis functions (even-numbered Legendre polynomials). The pressure field is solved using a penalty function method, which allows decoupling of the continuity and the momentum equations. The algorithm is of the generalized Uzawa type and includes a macroelement technique to stabilize the pressure solution. We used just two vertical degrees of freedom for these first model runs.

Figure 4 shows the computational mesh we used for the simulations covering the western and central basins of the Bransfield Strait. The lateral boundary conditions were defined so as to fit the geostrophic flow distribution hypothesized in Ref. 2. No-slip conditions were defined for the land contours.

3. RESULTS

Figure 5 shows the model results obtained for the vertically averaged velocity when no wind forcing is applied to the study area. The flow is essentially

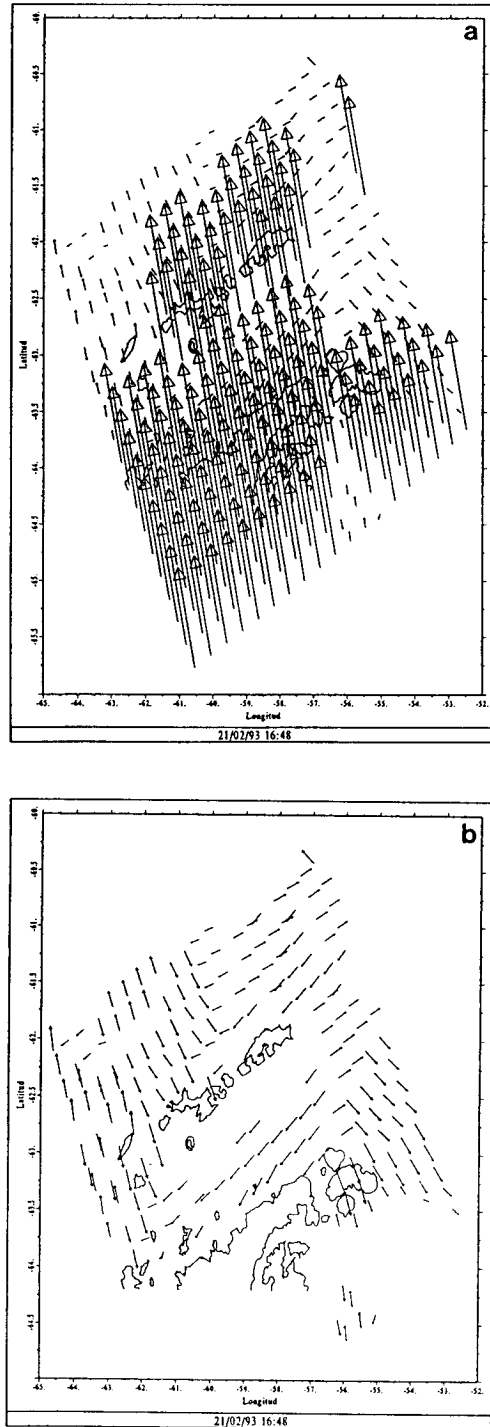


Fig. 2. Correction of WSC data. a) Raw file. b) After removal of error-flagged nodes.

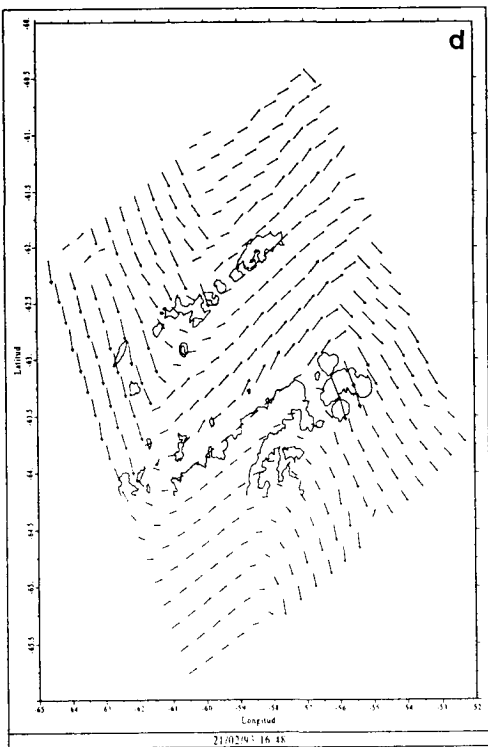
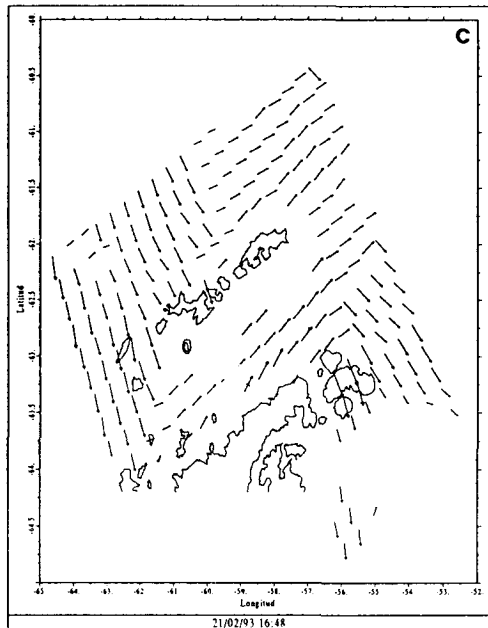


Fig. 2. (cont.) Correction of WSC data. c) Reassessed wind directions after check with a gradient wind estimate derived from meteo charts. d) Interpolation of gaps by means of a weighted least-square method.

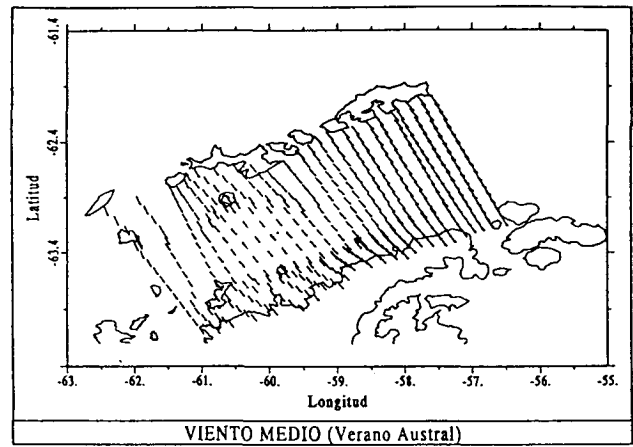


Fig. 3. "Short-term climatological" wind field representative of Austral summer 92/93. The wind velocities have been reinterpolated onto the computational mesh shown in figure 4.

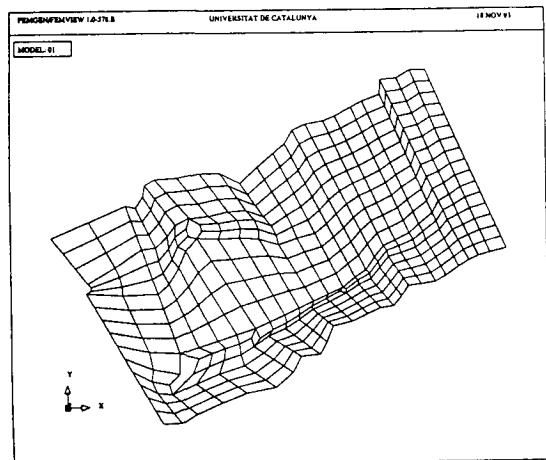


Fig. 4. Computational grid for the numerical simulation. The contours correspond to the coasts of the South Shetland Islands and of the Antarctic Peninsula. The islands included in the grid are Deception, Trinity, Tower and Astrolabe (see figure 1).

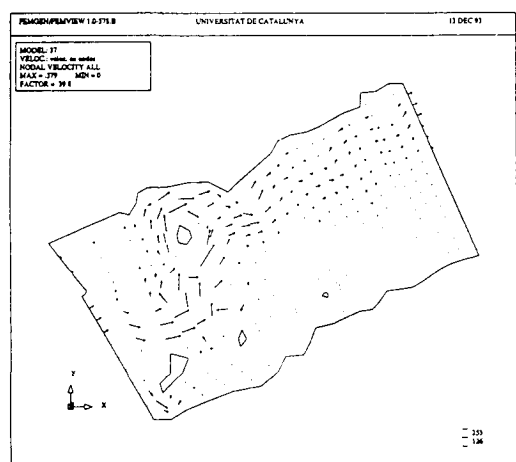


Fig. 5. Numerical solution for the vertically-averaged current velocity field with no wind forcing.

geostrophic and the current pattern shows a number of interesting features which could not be assessed just from field data (e.g. the split of the Bransfield Current into two branches around Deception Island).

Figure 6 shows the numerical solution for the vertically averaged flow when the wind distribution shown in figure 3 is used to force the model. We observe that the overall pattern remains the same but on the Antarctic Peninsula continental shelf where the current direction is observed to be to the NE, i.e. opposite to the (weak) geostrophic flow. Figure 7 shows that the difference may be even more remarkable for the surface current.

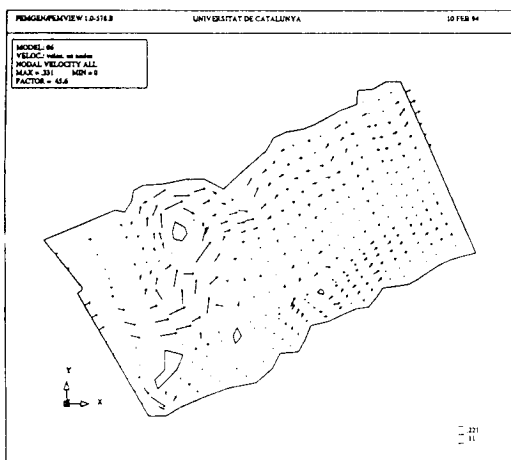


Fig. 6. Numerical solution for the vertically-averaged current velocity field when the model is forced with the wind distribution shown in figure 3.

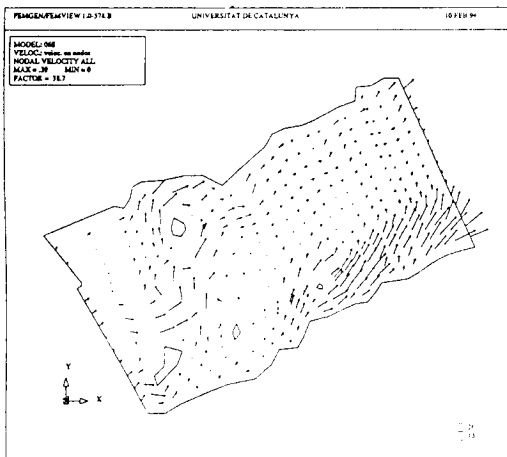


Fig. 7. Numerical solution for the surface current velocity field when the model is forced with distribution shown in figure 3.

4. CONCLUSIONS

Although the analysis of the wind-induced circulation in the Bransfield Strait requires further work, our first

model results suggest that the overall contribution of Austral summer winds to the residual flow in the study area may result in a significant modification of the current field on the Antarctic Peninsula continental shelf. For the rest of the considered domain, the geostrophic current seems to be the main contribution to the long-term averaged flow.

WSC data were the only source of information from which realistic local wind stress distributions including much of their detailed structure could be derived.

ACKNOWLEDGEMENTS

This study has been partially funded by the Comisión Interministerial de Ciencia y Tecnología (CICYT), grant no. ANT91-1279.

REFERENCES

1. Sievers H A 1982, Descripción de las condiciones oceanográficas físicas, como apoyo al estudio de la distribución y comportamiento del krill, INACH Serie Científica, 28, 87-136.
2. Grelowski A, A Majewicz, & M Pastuszak 1986, Mesoscale hydrodynamic processes in the region of Bransfield Strait and the southern part of Drake Passage during BIOMASS-SIBEX 1983/84, Polish Polar Research, 7, 356-369.
3. Niiler P P, A Amos & J H Hu 1991, Water masses and 200 m relative geostrophic circulation in the western Bransfield Strait region, Deep-Sea Research, 38, 943-959.
4. García M A, O López, J Sospedra, M Espino, V Gracia, G Morrison, P Rojas, J Figa, J Puigdefàbregas, & A S.-Arcilla 1994, Mesoscale variability in the Bransfield Strait region (Antarctica) during Austral summer, Annales Geophysicae (in press).
5. López O, M A García, A S.-Arcilla 1994, Tidal and Residual Currents in the Bransfield Strait, Antarctica, Annales Geophysicae (in press).
6. Espino M 1994, Estabilización de la superficie libre en la solución de ecuaciones shallow water por elementos finitos. Aplicaciones Oceanográfica, Doctoral Thesis, Universitat Politècnica de Catalunya, Barcelona, 443 pp.

USE OF ERS-1 DATA FOR WAVE MODELLING IN MEXICAN WATERS

Francisco J OCAMPO-TORRES, Roberto PADILLA HERNÁNDEZ

Departamento de Oceanografía Física,
C.I.C.E.S.E., Km. 107 Carret. Tijuana-Ensenada,
Ensenada, B.C., México. Fax: 52 (617) 44848, E-mail ocampo@cicese.mx

Ian S ROBINSON

Department of Oceanography, University of Southampton,
Southampton, S09 5NH, U. K.

ABSTRACT

The progress on wave modelling activities in Mexican waters is reported in this paper. A third generation numerical model (WAM Cycle 4) runs in a Cray YMP to simulate directional wave spectra in the Gulf of Tehuantepec region and the Pacific Ocean waters West of Central America. The area is practically exposed to swell generated almost anywhere within the vast Pacific Oceans. It is anticipated that an appropriate wave forecast (or hindcast) at a regional scale, must consider all those events capable of generating waves that might arrive in the area. Wave spectra is simulated for a coarse *oceanic* grid which provides boundary conditions for a fine *regional* grid in the area of interest. The usefulness of ERS-1 wave data (significant wave height from the altimeter) is demonstrated when compared with the modelled results. In addition, wind speed estimated from the same instrument is used to validate the wind fields used to force the model.

The area of study is of particular importance as strong northerly winds (*Tehuano*) are frequently present during the winter. These *Tehuano* events have a strong impact on the ocean dynamics and of course on the wave field, and all other related phenomena. A similar phenomenon is observed in the Gulf of Papagayo off the West Coast of Nicaragua. Wave and wind ERS-1 data represents a promising opportunity to contribute to the study wave development and the influence from incoming swell.

1. INTRODUCTION

The needs for properly hindcast and forecast waves in Mexican waters has been recognized for some time. There are specific regions where a better knowledge of ocean dynamics in general and ocean wave spectra in particular will have a beneficial impact on ship routing, offshore exploration, harbour manouevres, fisheries, etc. Unfortunately, there is no wave monitoring network in the Pacific Ocean off the coast of Mexico.

The Gulf of Tehuantepec is affected by strong and rather persistent northerly winds during the winter. A generally higher surface atmospheric pressure in the Gulf of Mexico results in a southward pressure gradient. Northerly winds are then forced through a low land region in the Sierra Madre mountain range. Similar phenomena occur in the Nicaragua region, where there are two other gaps in the mountain range near Gulf of Fonseca and Gulf of Papagayo. The wind events encountered show a rather persistent SW to W direction. Mixing of the upper ocean by these

wind fields induces a decrease in sea surface temperature that can be estimated by satellite radiometers [1]. Furthermore, we believe that meteorological and topographical conditions are appropriate for the region to be considered a unique area to study wave growth under fetch limited conditions.

The lack of data for southern oceans is a fact that has concerned oceanographers for years. This limitation is probably a reason for low quality wind data forcing a wave model, which in turns underestimates the significant wave height for southern latitudes [2]. It is our main interest to study the waves in this region and in particular in the region of the Gulf of Tehuantepec and Gulf of Papagayo. The model to be used therefore must cover practically the whole Pacific Ocean. Since data sources from the Southern Pacific Ocean are limited we demonstrate the usefulness of satellite data. ERS-1 altimeter wind and wave height information is being used to assess forcing winds quality and model performance respectively.

Further work along this line will deal with ERS-1 data assimilation into the model to improve wave forecast as one of the objectives of the Pilot Project (PP2 JP2 MXOT1361).

Table I. Grid characteristics and parameters used for WAM runs

Parameter	Description	Oceanic	Regional
LAT1 LAT2	Latitude limits	72°S 68°N	3°N 18°N
LON1 LON2	Longitude limits	120°E 69°W	105°W 85°W
NGX NGY	Grid points	172 141	241 181
Δx Δy	Spatial resolution	1° 1°	5' 5'
NFRC	Number of frequency bands	40	40
NDIR	Number of direction bands	36	36
IDELWI	Wind input time step	3600s	3600s
IDELPRO	Propagation time step	1800s	360s
IDELT	Integration time step	3600s	3600s
IDELWO	Wind output time step	3600s	3600s
IDELPRO	Results output time step	3600s	3600s

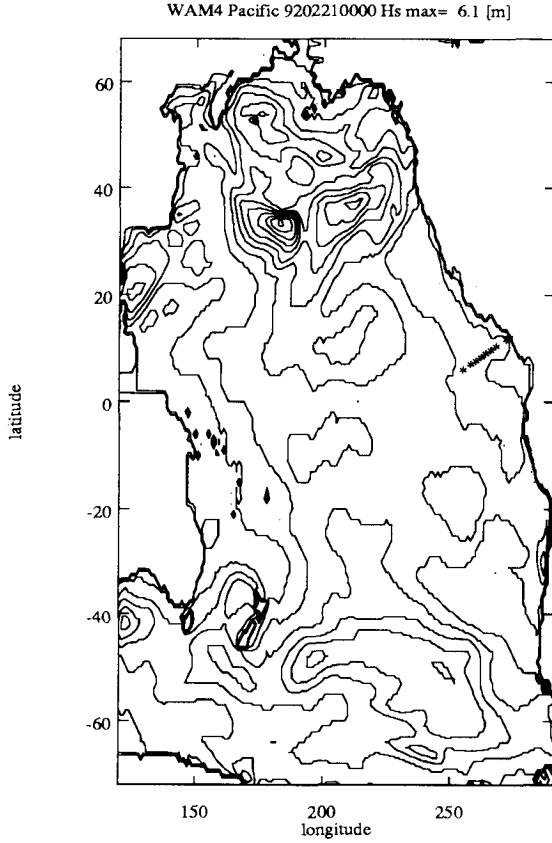


Figure 1: Map of significant wave height to show the oceanic grid domain. The resolution is 1° by 1° for this coarse grid. Some areas like the West of Japan, North of Australia, Gulf of Mexico and North East Atlantic are masked as land. Some grid points where directional wave spectrum information is obtained are represented by asterisks. The H_s contour interval is 0.5m.

2. THE MODEL

We run the so called *Cycle 4* of the WAM model [3], a third generation model which solves the wave transport equation explicitly without any *ad hoc* assumption on the shape of the spectrum. The evolution of the spectral energy density F is given by

$$\frac{\partial F}{\partial t} + \underline{C}_g \cdot \frac{\partial}{\partial \underline{x}} F = S_{in} + S_{nl} + S_{ds} \quad (1)$$

where $F = F(\omega, \theta, \underline{x}, t)$ is a function of wave frequency (ω) and direction (θ), position (\underline{x}), and time (t), and its variation is balanced by the source functions S_{in} which is associated to the wind input, S_{nl} related to the energy transfer due to the non-linear wave-wave interaction, and S_{ds} which describes the energy dissipation. The group velocity is denoted by \underline{C}_g .

The model has been implemented to run on two grids. A coarse grid covering most of the Pacific Ocean (oceanic grid) and a fine grid for the area of the Gulf of Tehuantepec and off Central America (regional grid).

The oceanic grid is shown in figure 1, where some land masked regions can be observed, like the West

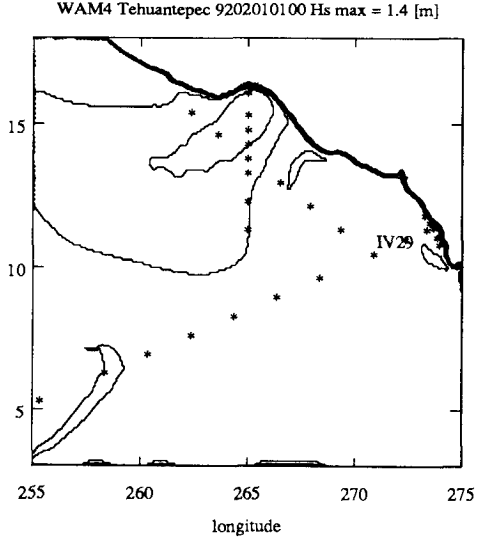


Figure 2: Map of significant wave height to show the regional grid domain. Grid resolution is $5'$ by $5'$. The H_s contour interval is 0.2m.

of Japan, North of Australia, Gulf of Mexico, and the North East Atlantic. A resolution of 1° by 1° results in a 172 by 141 grid points mesh from 120°E to 69°W and 72°S to 68°N . The grid points where directional spectra information is written are shown as asterisks.

The regional grid (see Figure 2) covers from 105°W to 85°W and from 3°N to 18°N with a resolution of $5'$ by $5'$ (241 by 181 grid points). The grid points to save wave spectra information from the model runs are also shown as asterisks.

Table I shows some of the important parameters used for the two different types of runs.

Preliminary results for runs on the oceanic grid are given in this work while further runs for the regional grid are being left for future work.

3. WIND FIELDS

Analysis wind fields have been provided by the United Kingdom Meteorological Office (UKMO), with a time step of 1h, and a spatial resolution $\Delta_{lat} = 0.0833^\circ$ and $\Delta_{lon} = 1.25^\circ$. Hindcast is performed for the time period 1 – 23 February 1992.

4. RESULTS

Figure 3 shows a comparison between the modelled significant wave height and that estimated from the ERS-1 altimeter for the Pacific Ocean. It seems that the ERS-1 radar altimeter tends to overestimate the significant wave height.

An obvious question is whether this is due to relatively high forcing winds. Figure 4 gives an idea of the comparison between the winds used to force the model with those inferred from the ERS-1 altimeter.

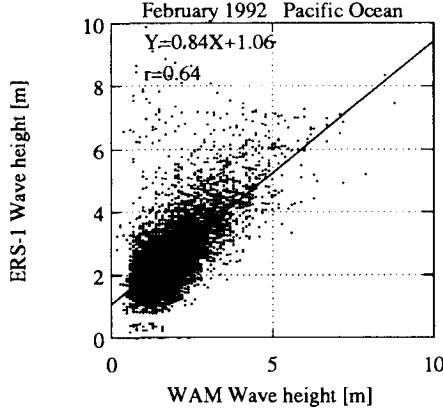


Figure 3: Comparison between significant wave height values estimated by the WAM model and those from the ERS-1 altimeter.

Apparently there is no obvious tendency to deviate from the 45° line, however some scatter can be noticed. The two different wind speed fields can be considered to be similar.

Some insight into surface wave dynamics can be obtained by analysing the directional wave spectra. Figure 5 shows an example of the model output at station IV29. A rather complex wave field can be observed. Of particular importance is the wind wave spectral peak nearly at the wind direction (asterisks at plot) which is rather persistent towards 250° approximately. The locally generated wave field shows a direction of propagation slightly deviated from the wind direction in some other cases (not shown). A case for offshore winds is presented. Time series for wind speed and direction and for significant wave height are shown in figure 6. Station IV29 is offshore Nicaragua, near to Gulf of Papagayo. Wind direction is rather persistent towards the end of the hindcast period, and in particular from 16 to 21 February, when the wind speed showed a slight increase which resulted in the highest significant wave simulated for this region.

5. DISCUSSION AND PLANS FOR FURTHER WORK

An attempt to discriminate any latitude related effect on the wind speed information used to force the model was made. Linear regression analysis showed practically no variation in the correlation coefficient between the altimeter winds and UKMO model wind speed for three different latitude sections. Only a slight increase in the correlation coefficient was observed for the analysis of winds between 40°N and 40°S , when compared to the values for northern and southern latitudes (higher than 40° N and S).

Slight deviation of locally generated waves with respect to wind direction might be due to the influence of incoming swell in nearly opposite direction. Further analysis is required to formally establish the effect of swell on wave development.

6. CONCLUDING REMARKS

Hindcast of waves over the Pacific Ocean is being done successfully through WAM model runs in a

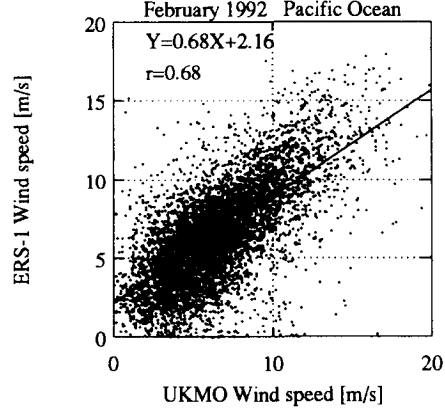


Figure 4: Comparison between wind speed from UKMO analysis used to force the wave model with those estimated from the ERS-1 altimeter.

CRAY YMP (UNAM, Mexico City). Analysis of wave fields is being done for the first time for the waters off the west and south of Mexico. Special cases are detected to further study the effect of swell on wave development.

The usefulness of ERS-1 data is proven by comparing the significant wave heights observed by the altimeter with those simulated by the wave model. Assessment of the model performance can be made for the area covered by an *oceanic grid* representing most of the Pacific Ocean, and for the area covered by a *regional grid* for southeast Mexico and west of Central America.

Validation of wind fields used to force the model is also being performed, demonstrating again the usefulness of ERS-1 data. Wind speed from the altimeter compare reasonably well with those used to force the model obtained from analysis of UKMO. Since the analysis performed by UKMO is independent of the satellite measurements, they are considered adequate measurements to validate forcing wind information.

ACKNOWLEDGEMENTS

Access to the Cray YMP has been granted by Supercomputo Academico UNAM. Wind fields have been provided by Martin Holt (UKMO). Thanks to Klaus and Susanne Hasselmann and the rest of the WAM group for providing *Cycle 4* of the WAM model. We acknowledge with gratitude the assistance of Julieta Castro on secretarial and word processing activities. ERS-1 data has been provided by ESA through Pilot Project PP2-JP2(MXOT1361).

REFERENCES

- [1] A. J. Clarke. Inertial wind path and sea surface temperature patterns near the Gulf of Tehuantepec and Gulf of Papagayo. *J. Geophys. Res.*, 93:15,491–15,501, 1988.
- [2] E. Bauer, S. Hasselmann, K. Hasselmann, and H. S. Gruber. Validation and assimilation of Seasat altimeter wave heights using the WAM wave model. *J. Geophys. Res.*, 97(C8):12,671–12,682, 1992.
- [3] WAMDI (The WAMDI Group). The WAM model - a third generation ocean wave prediction model. *J. Phys. Oceanogr.*, 18:1775–1810, 1988.

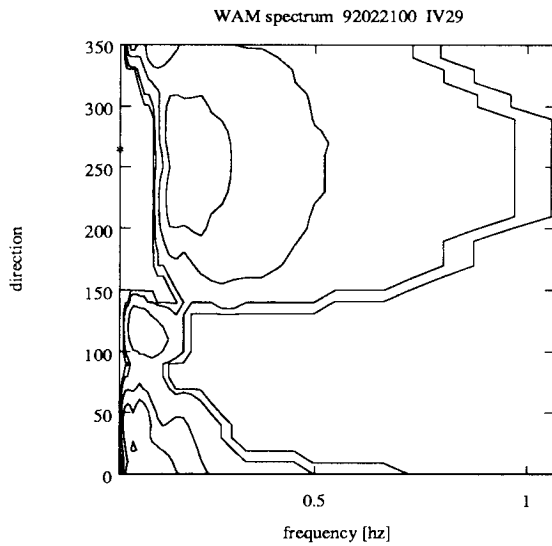


Figure 5: Directional wave spectrum at station IV29.
The contours are $0.001, 0.01, 0.1, 1$ and $10 \text{ m}^2 \text{rad}^{-1}\text{s}$.

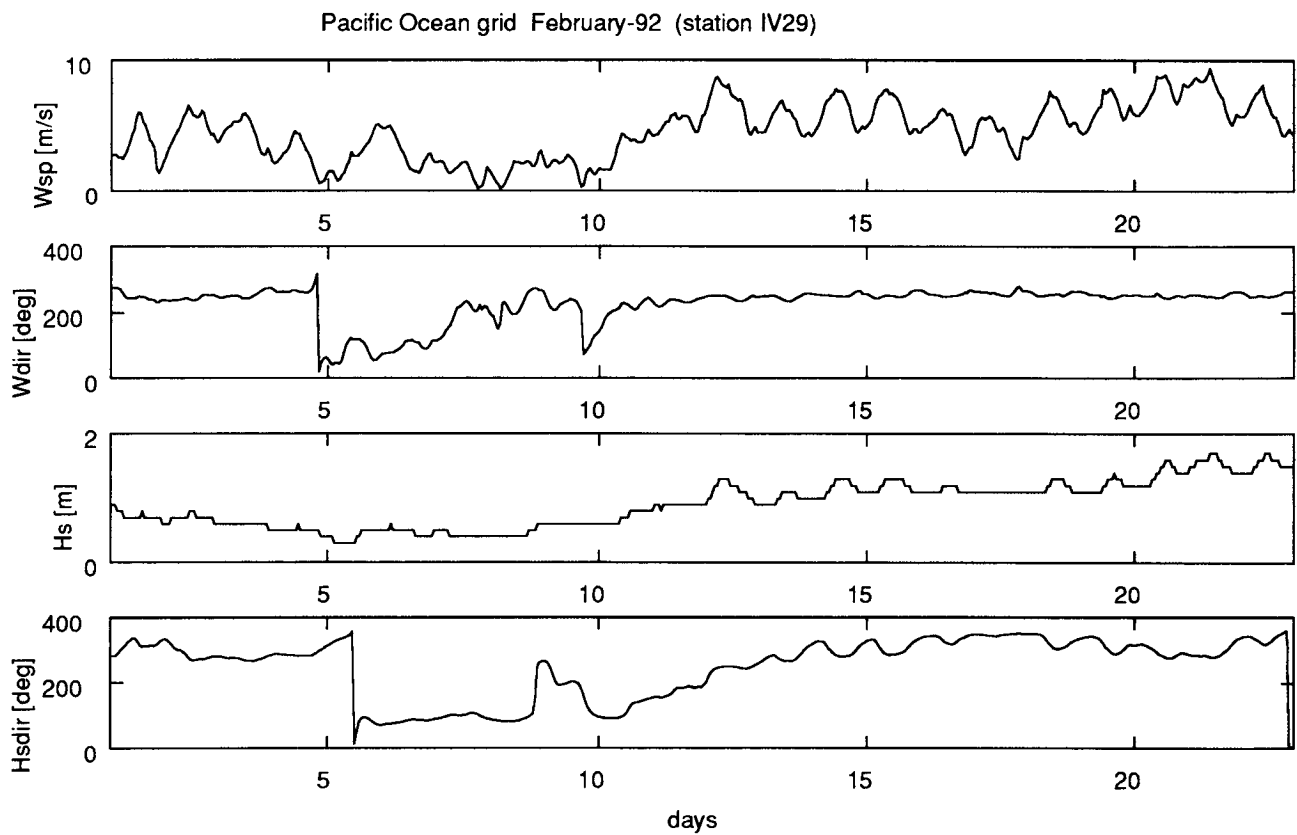


Figure 6: Time series of wind speed and direction at station IV29 as used to force the model, and significant wave height resulted from the WAM model.

Extraction of wave spectra from ERS-1 SAR wave mode spectra by an improved SAR inversion scheme

Claus Brüning¹ and Susanne Hasselmann²

¹Institut für Meereskunde, Universität Hamburg, Tropowitzstr. 7, D-22529 Hamburg, Germany

²Max-Planck Institut für Meteorologie, Hamburg, Bundesstr. 55, D-20146 Hamburg, Germany

ABSTRACT

An improved inversion scheme for SAR image spectra based on Hasselmann's closed integral transform is presented. The new algorithm uses an extended cost-function which in addition to the spectral SAR and wave terms minimizes the error of the motion induced azimuthal clutter cut off of the simulated and the observed SAR image spectra. Subsequent to the inversion of a SAR image spectrum the SAR inverted and the first-guess wave spectra are partitioned into their different sub-systems. The first guess wave systems are individually adjusted to agree in mean energy, wavelength and direction with the inverted systems. The spectra composed of the corrected wave systems are used as first guess spectra for a new SAR inversion procedure in an iterative retrieval algorithm. This scheme provides smooth wave spectra which are only weakly dependent on the first-guess spectra.

Keywords: SAR-ocean wave imaging, SAR inversion

1 INTRODUCTION

In wave mode the C-band synthetic aperture radar (SAR) included in the Active Microwave Instrument (AMI) aboard the First European Satellite (ERS-1) provides global information on two-dimensional wave spectra. Over the ocean small SAR images (imagettes) of 10 km x 5 km are acquired every 200 km along the satellite track. The power spectra of the imagettes computed at the ground stations are transformed into a reduced polar grid. The so-called ERS-1 SAR wave mode spectra are then distributed via the Global Telecommunication system (GTS) of the operational weather services for operational applications in near real time. These data can be used for global wave analysis and forecasting, provided the wave information can be extracted from the SAR image spectra.

Although the SAR-ocean wave imaging process is often highly nonlinear due to the orbital motion of ocean waves which distorts the Doppler history of the returned signal, the processes involved are basically understood (Ref. 1). Two models exist, which transform an ocean wave spectrum into a SAR image spectrum. Both models, the Monte Carlo method of Brüning et al. (Ref. 2) and the closed integral transform relation of Hasselmann and Hasselmann (Ref. 3), are based on the velocity bunching model. These algorithms have been carefully evaluated for buoy and wave model spectra by comparing model computed SAR image spectra with observed ones obtained during the Shuttle Imaging Radar B (SIR-B) experiment (Ref. 4) and the LEWEX experiment (Ref. 5). The

fast evaluation of the closed integral transform makes the inversion of the nonlinear mapping relation feasible within operational time constraints.

The SAR inversion scheme developed by Hasselmann and Hasselmann (Ref. 3) is based on the minimization of a cost-function which makes iterative use of the quasi linear mapping relation. This scheme was successfully applied in a pilot study analysing ERS-1 SAR wave mode spectra acquired over the Atlantic on three consecutive days in January 1992 (Ref. 6). The first guess wave spectra were computed with the WAM wave model (Ref. 7) which was driven by surface winds (u_{10}, v_{10}) from the atmospheric model of the European Centre for Medium Range Weather Forecasts (ECMWF). Even for complex sea states, the agreement between observed and simulated SAR spectra computed from SAR inverted wave spectra was in most cases remarkably good.

Nevertheless, the extensive analysis of the wave spectra retrieved globally from the ERS-1 SAR wave mode spectra also showed a few systematic shortcomings of the SAR-ocean wave inversion scheme:

- For high sea states the azimuthal cut off of the simulated SAR spectra computed from first-guess wave spectra is often much sharper than of the observed spectrum. This produced a very sharp peak in the retrieved spectrum.
- SAR inverted wave spectra often showed discontinuities in the transition region of the azimuthal cut off.
- SAR inverted wave spectra depend on the first guess wave spectra.

This paper presents an improved SAR inversion scheme (Ref. 8) based on the algorithms of Hasselmann and Hasselmann (Ref. 3) and Brüning et al. (Ref. 6), to remove these shortcomings.

In section 2 an extended cost-function is introduced. It minimizes the errors between the simulated and observed SAR image spectra and between the retrieved and the first guess wave spectrum as in the original scheme. However, before used in the cost-function the simulated SAR spectrum is smoothed to the coarse spectral grid of the ERS-1 fast delivery product (12x12 wave number-directional grid) and then interpolated back to the fine wave number grid. This yields a smoothing of the resulting wave spectrum across the azimuthal cut off region. In addition the error between the observed and simulated orbital motion induced azimuthal clutter cut off is

minimized by adjusting the latter one via an energy scaling parameter.

Finally, an extension of Gerling's partitioning scheme (Ref. 9) is presented in section 3 by which all wave systems of a SAR inverted and a first guess wave spectrum are decomposed into their individual wave systems. The first guess wave systems are adjusted to the characteristic parameters (significant wave height, mean wavelength and mean direction) of the SAR inverted wave systems which yields a new or second guess spectrum composed of the corrected systems for a new inversion cycle.

2 SAR IMAGING MODEL AND ITS INVERSION

Hasselmann and Hasselmann's closed integral transform (Ref. 3), which describes the mapping of an ocean wave spectrum $F(\mathbf{k})$ into a SAR image spectrum $P(\mathbf{k})$,

$$P(\mathbf{k}) = \sqrt{\pi} \exp(-k_x^2 \xi'^2) \sum_{n=1}^{\infty} \sum_{m=2n-2}^{2n} (k_x \beta)^m P_{nm}(\mathbf{k}) \quad (1)$$

can be rapidly evaluated by Fast Fourier Transforms. Here k_x denotes the azimuthal wave number component, β denotes the ratio of the slant range to the SAR platform velocity, and P_{nm} are higher order products of auto and covariance functions of the slant range component of the orbital velocity and real cross section modulation. The nonlinear exponential factor depends on the mean square azimuthal displacement ξ'^2 of a backscattering facet, given by

$$\xi'^2 = \beta^2 \langle u_r^2 \rangle = \beta^2 \int |T_k^r|^2 F(\mathbf{k}) d\mathbf{k} \quad (2)$$

where $\langle u_r^2 \rangle$ denotes the mean range component of the orbital velocity of the long ocean waves, and T_k^r is the range velocity transfer function.

The inversion scheme is based on a maximum likelihood method, where the error between the simulated and observed SAR spectra, represented by a cost-function, must be minimized. An additional penalizing term minimizes the error between the first guess and the retrieved wave spectrum to augment the spectrum at high wave numbers beyond the azimuthal cut off and to account for the 180° angular ambiguity in an observed SAR spectrum. An additional term of the cost-function minimizes the error between the simulated and observed azimuthal clutter cut off.

According to Alpers and Brüning (Ref. 10), the azimuthal clutter cut off wavelength λ_{cl} is proportional to the mean orbital velocity

$$\lambda_{cl} = c \beta \langle u_r^2 \rangle^{1/2} \quad (3)$$

where c is an arbitrary constant not relevant for this study. Following Hasselmann and Hasselmann (1991) and multiplying Eq. 2 by a mean energy scaling parameter α , Eq. 3 becomes

$$\lambda_{cl} = c \alpha^{1/2} \beta \langle u_r^2 \rangle^{1/2} \quad (4)$$

The mean cut off wavelength can be adjusted by varying the proportionality factor α and thus adjusting the spectral energy. Therefore the new cost function takes the form:

$$J = \int [P(\mathbf{k}) - \hat{P}(\mathbf{k})]^2 \hat{P}(\mathbf{k}) d\mathbf{k} + \mu \int \frac{[F(\mathbf{k}) - \hat{F}(\mathbf{k})]^2}{[B + \min\{F(\mathbf{k}), \hat{F}(\mathbf{k})\}]^2} d\mathbf{k} + \eta \frac{(\lambda_{cl}^2(\alpha) - \hat{\lambda}_{cl}^2)^2}{\max\{\lambda_{cl}^4(\alpha), \hat{\lambda}_{cl}^4\}} \quad (5)$$

where $\hat{F}(\mathbf{k})$ and $F(\mathbf{k})$ are the first-guess and best-fit wave spectra, and $P(\mathbf{k})$ and $\hat{P}(\mathbf{k})$ are the simulated and observed SAR spectra, respectively. The weight factor μ is taken sufficiently small ($\mu = 10^{-3} \hat{P}_{max}^3$) that the impact of the first-guess wave spectrum $\hat{F}(\mathbf{k})$ on the final solution is as small as possible. B is a small positive constant ($B = 10^{-4} \hat{F}_{max}$) introduced to prevent the denominator from becoming zero, and $\hat{\lambda}_{cl}$ and λ_{cl} are the mean clutter cut off wavelengths of the observed and simulated SAR image spectra, respectively. The weight $\eta = \frac{1}{2} 10^6 [\int \hat{P}(\mathbf{k}) d\mathbf{k}]^3$ is chosen such that the spectral SAR term and the clutter term of the cost-function are of the same order of magnitude.

In addition to a variation with respect to the SAR inverted wave spectrum in the present scheme the cost-function is also varied with respect to α . The minimization is carried out iteratively making use of the quasilinear relation between a wave spectrum and a SAR image spectrum obtained by truncating eq. 1 after the first term in analogy to Hasselmann and Hasselmann (Ref. 3, for details see Ref. 8).

The SAR inversion algorithm is carried out on a fine Carte-

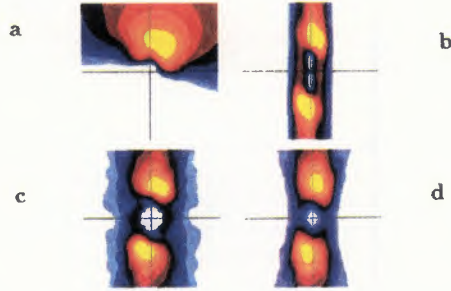


Figure 1: Panel a: First guess wave spectrum; Panel b: First guess SAR spectrum (present algorithm) computed from the wave spectrum of (a); Panel c: Observed SAR image spectrum; Panel d: SAR image spectrum computed from the wave spectrum of (a) smoothed in accordance with the observed SAR spectrum (c)

sian (k_x, k_y) wave number grid of 128x128 elements with a Nyquist wavenumber $k_x^{Nyq} = k_y^{Nyq} = 2\pi/32m^{-1}$. The ERS-1 SAR wave mode spectra (fast delivery products) are defined on a reduced polar grid of 12 logarithmically spaced wave number (between 100m - 1000m) and 12 directional bins. Interpolation of the observed spectra to the fine Cartesian wave number grid often caused distortions across the cut off region of the retrieved wave spectra. For numerical consistency the computed SAR spectra were smoothed to the coarse grid of the observations and then again interpolated to the fine wave number grid prior to the computation of the cost function. The actual improvement in the azimuthal clutter cut off for the simulated SAR spectrum can be seen in Fig.1. This yields inverted wave spectra which are smooth across the cut off region.

The SAR inversion scheme also yields calibrated SAR retrieved wave spectra. This is achieved by calibrating the observed SAR spectra by the SAR inherent clutter noise level superimposed on the SAR wave image spectra (Ref. 6). Subsequently the clutter noise is removed from the observed SAR spectra by subtraction. The clutter level is estimated as the average of the five lowest spectral values at the highest wavenumber ($k = 2\pi/100m$) bin of the ERS-1 SAR wave

mode image spectra.

3 AN ITERATIVE SAR RETRIEVAL SYSTEM.

Due to the second term in the cost function, Eq. 5, the retrieved spectrum is dependent on the first guess spectrum even if the weighting factor μ is taken small. Brüning et al. (Ref. 6) showed that in some cases an improved agreement between observed and simulated (computed from the retrieved wave spectra) SAR spectra could be obtained, if a coarse adjustment of the first guess spectra in mean direction, energy and wave number was carried out prior to the inversion for unimodal wave spectra. However, most wave spectra seen on the global oceans are extremely complex, containing a number of wave systems. Therefore, a scheme was developed, which decomposes wave spectra into their sub systems (Ref. 6, 8) by the simple rule, that a frequency - directional bin in a wave spectrum belongs to a certain system, if the neighbour of highest energy belongs to the same system. If all neighbours are smaller the bin is a peak itself. Systems are regarded as wind-sea, if the component of the phase velocity of the peak in the wind direction is less than 1.5 times the wind speed. Otherwise the systems are regarded as swell. Each wave system is characterized by mean spectral parameters: Significant wave height H_s , mean frequency \bar{f} , and mean direction $\bar{\phi}$. The present scheme first computes inverted SAR wave spectra. The first guess and inverted spectra are partitioned. SAR inverted and first guess wave systems are then crossassigned and the first guess wave systems transformed in mean energy, frequency and direction to agree with the characteristic parameters of the inverted systems. Spectra composed of the corrected wave systems can now be used as second guess spectra for a new inversion cycle (for details see Ref. 8). In many cases one inversion cycle was sufficient. However, often one or two wave systems needed a second inversion cycle to achieve good agreement between the simulated and the observed spectra.

Fig 2 shows two examples of the inversion cycle for spectra obtained on January 23, 1992 at 12:32 UTC, at 43 S, 318 E (PANEL A) and at 13:54 UTC, at 23 N, 310 E (PANEL B). It can nicely be seen how the wave systems are iteratively adjusted by the SAR retrieval algorithm. Panels (a) show the first guess spectra for the first inversion cycle (column 1 and 3) and the second inversion cycle (column 2 and 4). The simulated SAR image spectra of panels (b) are computed from the wave spectra of (a) by applying Hasselmann's closed integral transform. The SAR inverted wave spectra obtained after n-iteration steps are shown in panels (c). The corresponding best-fit simulated and observed SAR image spectra are shown in panels (d) and (e). The partitioning system described above is used to adjust and smooth the noisy SAR inverted wave spectra of (c) which yield the wave spectra of panels (f). The SAR retrieved wave spectra of column 1 (3), panel f are used as second guess for a new inversion cycle shown in column 2 (4). The SAR obviously tries to enhance the low frequency wave system and weakens the high frequency system of the bimodal wave spectrum of PANEL A. In the second example, PANEL B, the SAR reduces the trimodal wave spectrum to a bimodal wave spectrum but needs two inversion cycles to achieve this.

In Fig 3 the significant wave heights retrieved by the present

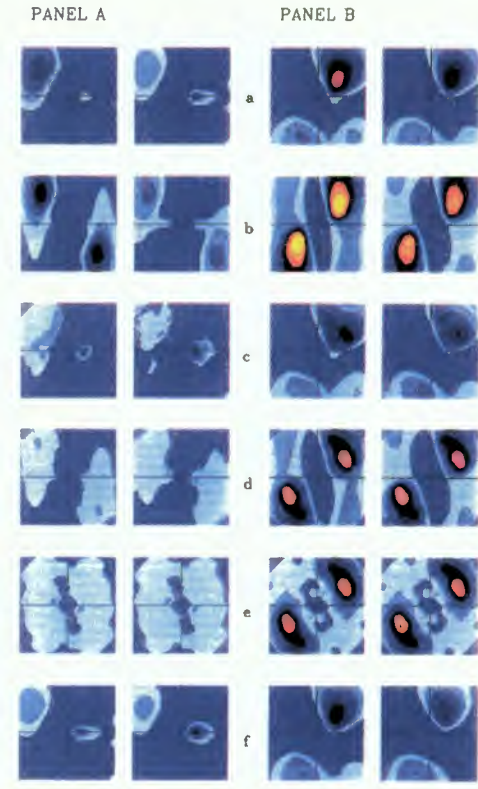


Figure 2: Two examples of an iterative retrieval of a wave spectrum from a SAR image spectrum: Panel A row (a) first guess wave spectrum from January 23, 1992 at 12:32 UTC (43 S, 318 E); Panel B row (a) first guess wave spectrum from January 23, 1992 at 13:54 UTC (23 N, 310 E) row (b) SAR spectra computed from the first guess wave spectra, (c) wave spectra inverted from the SAR image spectra, (d) best-fit SAR spectra, (e) observed SAR spectra, (f) SAR retrieved wave spectra. Columns 1 and 2 (3 and 4) show the first and second inversion cycles, respectively.

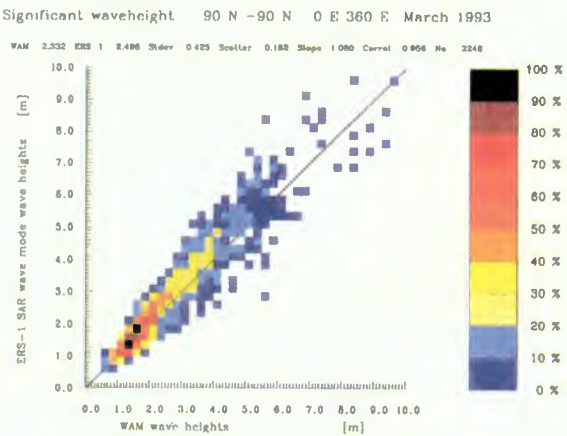


Figure 3: Comparison of WAM first guess and SAR inverted significant wave heights across the Atlantic area acquired between March 8-16, 1993

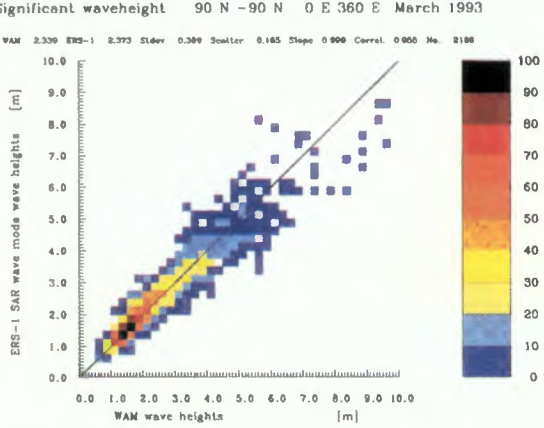


Figure 4: Same as Fig. 3, but for SAR inverted significant wave heights computed by the improved SAR inversion scheme

SAR inversion scheme (Ref. 6) shows a small positive bias for large wave heights and only small scatter. The positive wave height bias is reduced to 0.03 m by the extended SAR inversion scheme as shown in Fig 4. The slope regression line is 1.0, and the scatter index is 0.165.

The scatter of the wave height data retrieved by the present and the extended SAR inversion scheme is relatively small. However, the scatter is much increased if a second inversion cycle is applied using the SAR retrieved wave spectra of the first cycle as a second guess as shown in Fig 5. The SAR retrieved wave spectra of the combined two stage SAR inversion-partitioning scheme are much less dependent on the first guess wave spectra. The wave height bias computed is 0.11 m, the scatter index is 0.27, and the slope regression line is 1.035.

4 CONCLUSIONS

An extended SAR-ocean wave inversion scheme was presented to retrieve wave spectra from SAR image spectra. The scheme is based on an extented cost-function and an improved wave partitioning system. The total energy of a wave spectrum is controlled by minimizing the error between the simulated and observed azimuthal clutter cut-off via an energy scaling parameter. Wind sea and swell systems of the wave spectra are adjusted individually by the wave partitioning system which yields smooth retrieved wave spectra with little impact of the first guess spectra on the final result. The simulated and observed SAR image spectra correlate highly and show an excellent agreement also in the azimuthal cut off level. The algorithm yields not only a correction of the first guess wave spectra below the azimuthal cut off, but also adjusts the energy level in the high wave number domain of the spectrum. The positive bias of the wave height for large H_s , found by Brüning et al. (Ref. 6) is reduced by the extended SAR inversion scheme. A second SAR inversion cycle is often needed as indicated by the large scatter of the wave height data by which the SAR retrieved wave spectra become much less dependent of the first guess.

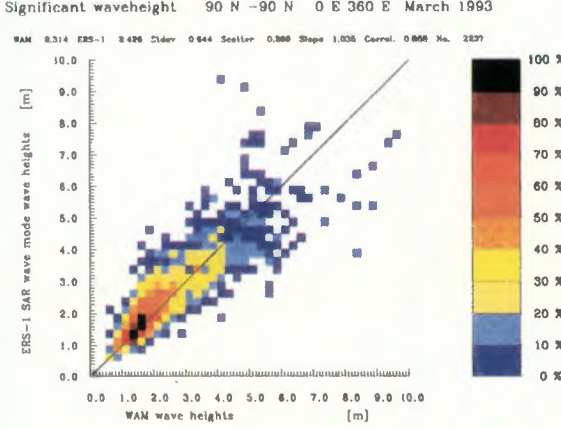


Figure 5: Same as Fig. 4, but for SAR retrieved significant wave heights computed by two cycles of the combined inversion-partitioning scheme

REFERENCES

- [1] Hasselmann, K., R.K. Raney, W.J. Plant, R.A. Shuchman, D.R. Lyzenga, C.L. Rufenach and M.J. Tucker, 1985. Theory of synthetic aperture radar ocean imaging. A MARSEN view. *J. Geophys. Res.* **C90**, 4659-4686.
- [2] Brüning, C., W. Alpers and K. Hasselmann, 1990. Monte Carlo simulation studies of the nonlinear imaging of a two-dimensional surface wave field by a synthetic radar. *Int. J. Remote Sensing*, **11**, 1695-1727.
- [3] Hasselmann, K. and S. Hasselmann, 1991. On the nonlinear mapping of an ocean wave spectrum into a SAR image spectrum and its inversion. *J. Geophys. Res.* **C96**, 10713-10729.
- [4] Brüning, C., W. Alpers, L.F. Zambresky, and D. G. Tilley, 1988. Validation of a synthetic aperture radar ocean wave imaging theory by the Shuttle Imaging Radar-B experiment over the North Sea. *J. Geophys. Res.*, **93**, 15403-15425.
- [5] Hasselmann,K., S. Hasselmann, C.Brüning, and A. Speidel, 1991: Interpretation and application of SAR wave image spectra in wave models. In *Directional Ocean Wave Spectra*, edited by R.C. Real, The Johns Hopkins University Press, pp 117-124.
- [6] Brüning, C., S. Hasselmann, K. Hasselmann, S. Lehner, T. Gerling, 1994. First evaluation of ERS-1 synthetic aperture radar wave mode data. In print in TAOS.
- [7] WAMDI group: S. Hasselmann, K. Hasselmann, E. Bauer, P.A.E.M. Janssen, G.J. Komen, L. Bertotti, P. Lionello, A. Guillaume, V.C. Cardone, J.A. Greenwood, M. Reistad, L. Zambresky and J.A. Ewing, 1988. The WAM model - a third generation ocean wave prediction model. *J. Phys. Oceanogr.* **18**, 1775-1810.
- [8] Hasselmann,S. and C. Brüning, 1994. An improved algorithm for the retrieval of ocean wave spectra from SAR image spectra. (In preparation)
- [9] Gerling, T.W., 1992. Partitioning sequences and arrays of directional wave spectra into component wave systems. *J. Atmos. Ocean. Techn.* **9**, 444-458.
- [10] Alpers, W., and C. Brüning, 1986. On the relative importance of motion-related contributions to the SAR imaging of ocean surface waves. *IEEE Trans. Geosci. Remote Sens.* **24**,873-885.

ON THE APPLICATION OF ERS-1 DATA FOR THIRD GENERATION WAVE MODELLING AND SHIPROUTEING

Susanne Lehner^{1*}, Susanne Hasselmann¹, Klaus Hasselmann¹, Pierro Lionello²

¹ Max-Planck Institut für Meteorologie
D – 20145 Hamburg

* presently at :
Deutsche Forschungsanstalt für Luft- und Raumfahrt
D – 82230 Weßling

² University of Padua
I – 35135 Padova

ABSTRACT

ERS-1 SAR wave mode spectra are assimilated into the third generation wave model WAM and the improved wave forecasts are then used for a new onboard shiprouteing system.

Although ERS-1 SAR images of the sea surface contain detailed information on the full two dimensional wave spectrum, the SAR spectra are distorted through nonlinear imaging effects caused by motions of the sea surface. Furthermore, the propagation direction of the waves can be determined only to within a 180 degree ambiguity. The nonlinearities and ambiguities are removed using a retrieval algorithm, based on a wave model spectrum as a first guess.

The retrieved spectra are assimilated into the WAM wave model using an optimal interpolation scheme for the characteristic parameters of the principal wave components of the partitioned two dimensional wave spectra. At the same time the wind field is corrected from the wave field. These corrected fields will then be used as an input to yield an improved ten day wind and wave forecast.

The forecast wave spectra are partitioned into their dominant windsea and swell components (significant wave heights, directions and periods). These parameters together with the wind fields are transmitted twelve hourly to the ship. A route optimization is performed onboard using a Bellmann algorithm.

Examples are given for a North Atlantic and Pacific crossing of a container ship.

1. INTRODUCTION

An essential progress in wave analysis and forecasting was achieved by the development of the third generation wave model WAM (WAMDI, 1989). However, results are still limited by the errors in the wind fields, because

of a lack of data for the data assimilation in atmospheric models.

Since the launch of ocean observing satellites a global coverage of wave data, like the significant wave height from the Altimeter and 2d wave spectra measured by the Synthetic Aperture Radar (SAR), has become available in real time. Therefore, wave modellers have become interested in data assimilation to improve model results and also correct the wind fields from wave field corrections. In a combined wind and wave data assimilation scheme these analysed winds can then be used as input into atmospheric models. Improved wave forecasting is of great value for coastal warning and shiprouteing systems as well as for off shore operations, while improved wave analysis yields improved wave statistics, which help to determine the wave forces for the design of ocean and coastal structures.

The two-dimensional instantaneous ocean-wave images of the SAR clearly contain valuable information for determining the full two-dimensional wave spectrum, which completely characterizes the local sea state.

However, because of nonlinear imaging effects due to motions of the sea surface the SAR spectra are distorted and the propagation direction of the waves can only be determined within 180 degree ambiguity (Hasselmann et al 1985).

A formula mapping wave spectra into SAR image spectra and its inversion has been developed, thus calculating ocean wave spectra from measured SAR spectra. The inversion algorithm is based on the minimization of a cost function, using a WAM wave model spectrum as a first guess (Hasselmann and Hasselmann 1991). It was extended to yield smooth, calibrated SAR retrieved spectra by Brüning et al. (1993) and Hasselmann and Brüning (1994).

In recent years several simple schemes have been devel-

oped to assimilate significant wave height data from the Altimeter into wave models (Thomas et al, 1988, Janssen et al, 1989, Lionello et al, 1990, Lionello et al 1994, Günther et al, 1992).

To correct the 2d wave spectrum from wave height information only, these schemes used either second generation wave models, which prescribe the shape of a wind-sea spectrum, or they had to introduce additional assumptions to adjust the energy level for a WAModel spectrum.

2. A SCHEME TO ASSIMILATE 2D WAVE SPECTRA INTO THE WAM

The scheme presented in this paper is based on a simple method developed by Lionello et al (1990, 1992), which assimilates ERS-1 Altimeter wave heights into the WAModel. The scheme is running operationally on a global scale at the European Center for Medium Range weather forecasting (ECMWF, Reading, UK).

From the data obtained at a number of data points a field is created at all model grid points by optimal interpolation. These analysed parameters are then used to adjust the two dimensional spectrum at all model grid points.

The scheme by Lionello et al adjusts the total energy and the frequency scale of the spectrum from the interpolated significant wave heights using fetch and duration laws for a wind-sea spectrum (direction of the highest peak lies within 15° of the wind direction and a peak frequency higher than the Pierson Moskowitz frequency). For swell spectra the adjustment is carried out under the side condition that the wave steepness is conserved.

However, most wave spectra seen on the globe contain several wave systems, which have to be adjusted separately (Hasselmann and Lionello, 1994). The algorithm presented in this paper therefore partitions all wave spectra into their different wave systems (Hasselmann et al, 1994, Hasselmann and Brüning, 1994) using the simple rule that each frequency-direction grid point of a spectrum is assigned to a wave system or a peak if the neighbour of highest ascent is assigned to the same system. If all neighbours are smaller the point is a peak itself. The algorithm also distinguishes wind-sea and swell systems. A wave system is regarded as wind-sea, if the component of the phase velocity of the peak in the wind direction is less than 1.3x the windspeed. Otherwise, a wave system is regarded as swell. For details see Hasselmann and Brüning, 1994.

From each of these spectral wave systems characteristic parameters (significant wave height, mean frequency and direction) are derived through suitably averaging over the spectral domain of the wave systems. This reduces the amount of data contained in a global 2d spectral set to a manageable data set.

In order to compute the error between characteristic parameters of wave systems, as needed for the optimal in-

terpolation, first guess wave systems and systems derived from data are cross assigned, if the dimensionless distance between them is less than 0.75. A distance is defined from the mean frequency and direction of a wave system in wave number space as:

$$\text{dist} = \frac{(\bar{k}_x^i - \bar{k}_x^j)^2 + (\bar{k}_y^i - \bar{k}_y^j)^2}{0.5 (\bar{k}_x^{i2} - \bar{k}_x^{j2}) + (\bar{k}_y^{i2} - \bar{k}_y^{j2})}$$

where \bar{k}_x, \bar{k}_y denote the mean wave number components.

With these tools the assimilation algorithm is carried out as follows: From the characteristic parameters of model first guess and SAR retrieved spectra an analysed field of characteristic parameters is computed by optimal interpolation (Hasselmann et al 1994). The wave systems in the model first guess spectra are then adjusted to agree with the analysed characteristic parameters at the equivalent model grid points. Combining these analysed wave systems yields an analysed wave spectrum at each model grid point.

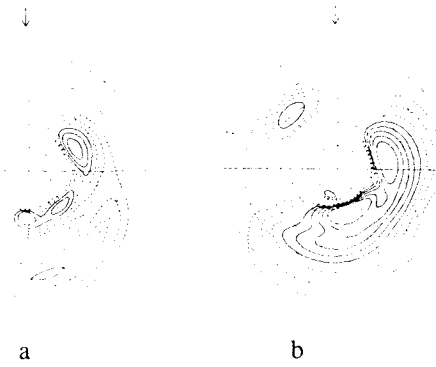


Figure 1: first guess(a) and analysed(b) wave spectrum

Figure 1 shows a first guess and an analysed wave spectrum taken at 56° S and 24° W on the 20.3.93 at 1:12. The arrow indicates the wind blowing from the north at 9 m/sec. The energy in all analysed wavesystems is enhanced. In particular the southward running windsea-system in the first guess spectrum has also been moved towards lower frequencies thus indicating an increase in the wind speed.

The correction of the local wind is carried out by applying relations between the wind speed and the total energy and mean frequency of a wave system, which were derived by Lionello et al, 1990.

3. OPTIMIZATION OF SHIP ROUTES

Shipbuilding institutes started to work on shiprouteing by optimization of fuel consumption during the oil crisis of 1972, a detailed discussion can be found in Soeding (1989).

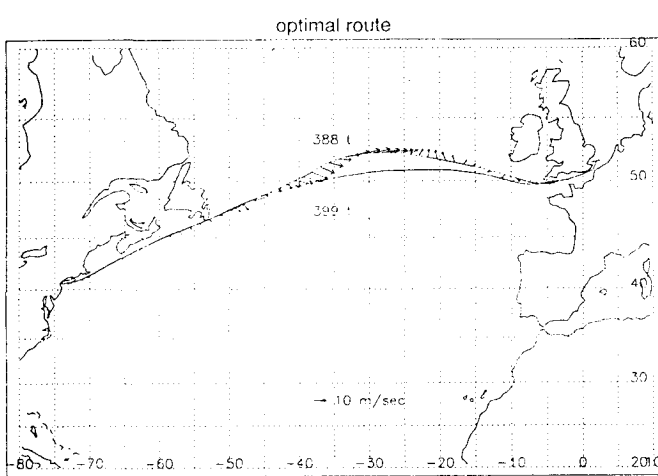


Figure 1 Shiprouting North Atlantic

Depending on given weather conditions a ship route of optimal fuel consumption is to be determined. In addition for untimely arrival of the ship a penalty cost function is to be taken into account. That is, the following functional is to be minimized:

$$J(\mathbf{x}, \mathbf{v}, t_a) = \int_{t_s}^{t_a} F_c(\mathbf{x}, \mathbf{v}, \text{par}) dt + \alpha_{\text{arr}} F_{\text{arr}}(T, t_a)$$

$$\mathbf{v}(t) = \frac{d\mathbf{x}}{dt} \quad \mathbf{v} \quad \text{ship velocity}$$

$$\mathbf{x}(t_s) = \mathbf{x}_s$$

$\mathbf{x}_s, \mathbf{x}_a$ coordinates of start, arrival

$$\mathbf{x}(t_a) = \mathbf{x}_a$$

T planned time of arrival

with $F_c(\mathbf{x}, \mathbf{v})$

cost function for fuel, engine damage and hazards

$F_{\text{arr}}(T, t_a)$ cost function for untimely arrival

The fuel cost function is evaluated modelling the ship by a Holtrop-Mennen algorithm (1982) and using tables of resistance depending on ship speed at given weather conditions from the Hamburger Schiffbau Versuchsanstalt (HSVA, Boese et al. 1974). To the fuel cost function penalty terms for possible engine damage and hazard areas are added with appropriate weights. The optimization problem is solved using a Bellman type optimization algorithm (Bellman 1967).

Up to now the algorithm has only been tested using the standard ECMWF 10 day wind and wave analysis on a three by three degree grid. Wind speed and direction and significant wave height, direction and period of a wind-sea and a swell peak are taken into account. Figure 1

shows an example of first guess and optimal route of a North Atlantic crossing from Thamesport to New York in 182 hours from the 24.3.94 to the 1.4.94 for the Container ship Bonn Express. The arrows along the optimal route indicate the wind conditions met during the crossing.

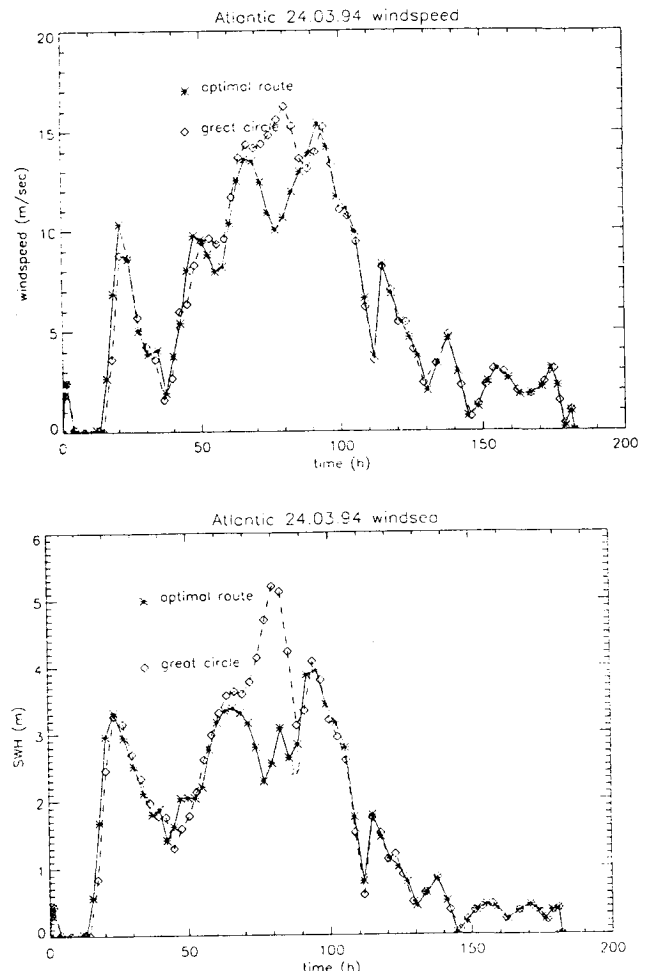


Figure 2 Conditions during the crossing.

On the optimal route the area of largest windspeed and wave height is avoided by sailing further north. At the same time the ship speed is accommodated to the weather conditions.

Figure 2 shows the windspeed and the significant wave height of the windsea met during a crossing on the first guess (shortest) and the optimal route.

For the first guess route 324 t of fuel are needed if weather is not taken into consideration, 399 t for the above weather conditions and 388 t when following the optimal route, saving about 3%. The accumulated fuel consumption is shown in figure 3.

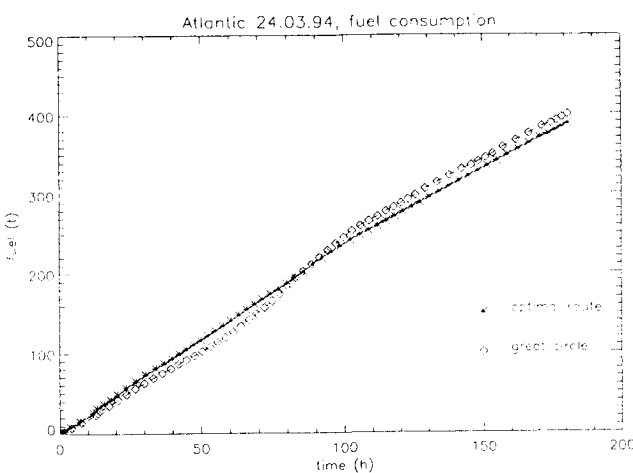


Figure 3 Accumulated fuel consumption

For the same weather period calculations of a 236 hour North Pacific crossing from Oakland to Yokohama were performed resulting in a southward route deviation and a fuel saving from 678t on the shortest route to 643t on the optimal route, a saving of 5.2%.

5. CONCLUSIONS AND OUTLOOK

A general assimilation scheme for improved wave and wind analysis and forecast using ERS data has been developed and tested. An optimization algorithm for ship routing was tested using standard ECMWF data. Future tasks will be to

- 1) Calculate optimal routes using standard and ERS assimilated wind and wave data in comparison.
- 2) Derive statistics for cost savings on ensembles of routes
- 3) Take the skill of the weather forecast into account.

6. REFERENCES

1. Bellman, R., 1967, Introduction to the Mathematical Theory of Control Processes Vol 1. Academic Press New York-London
2. Boese, P., P. Schenzle and P. Blume, 1974, Programm-system zur Berechnung der Schiffsgeschwindigkeit unter Dienstbedingungen, Inst für Schiffbau, Bericht Nr. 303.
3. Brüning, C., S. Hasselmann, K. Hasselmann, S. Lehner and T. Gerling, 1993, First evaluation of ERS-1 synthetic aperture radar wave mode data, TAOS 1,
4. Günther, H., Lionello, P. and P.A.E.M. Janssen, 1992, Assimilation of altimeter data in a global third generation wave model, *J. Geophys Res.*, 97, C9, 14453–14474.
5. Hasselmann, K., R. K. Raney, W.J. Plant, W. Alpers, R.A. Shuchman, D.R. Lyzenga, C.L. Rufenach, and M.J. Tucker, 1985, Theory of synthetic aperture radar ocean imaging: A MARSEN view, *J. Geophys Res.*, 90, 4659–4686.
6. Hasselmann, K. and S. Hasselmann, 1991, On the nonlinear mapping of an ocean wave spectrum into a SAR image spectrum and its inversion, *J. Geophys Res.*, C96, 10713–10729.
7. Hasselmann, S. and C. Brüning, 1994, An improved algorithm for the retrieval of ocean wave spectra from SAR image spectra, in preparation.
8. Hasselmann, S. et al 1994, Assimilation of wave observations. In: Dynamics and modelling of ocean waves, edited by G.Komen, Cambridge University Press.
9. Hasselmann, S. and P. Lionello, 1994, Assimilation of wave spectra retrieved from ERS-1 SAR wave mode image spectra in the WAModel, in preparation.
10. Holtrop, J. et G.G.J. Mennen, 1982, An Approximate power prediction method, International Shipbuilding Progress Nr. 7, 166–170
11. Janssen, P.A.E.M., P. Lionello, M. Reistad and A. Hollingsworth, 1989, Hindcasts and data assimilation studies with the WAModel during the Seasat period, *J. Geophys Res.*, C94, 973–993.
12. Lionello, P., H. Günther and P.A.E.M. Janssen, 1990, Assimilation of altimeter data in a global ocean wave model, in: Proc. of the second conference oceans from space, Venice.
13. Lionello, P., H. Günther and P.A.E.M. Janssen, 1994, A sequential assimilation scheme applied to global wave analysis and prediction. Accepted for publication in *Journal of Marine Systems*.
14. Thomas, J., 1988, Retrieval of energy spectra from measured data for assimilation into a wave model, *Q.J. Royal Meteorol. Soc.* 114, 781–800.
15. Soeding, H., 1989, Schiff im Seegang, in: Sicherheit und Wirtschaftlichkeit großer und schneller Handelsschiffe, edit. O. Geisler and H. Keil, VCH.
16. WAMDI group, Hasselmann, S et al., 1988, The WAM model – a third generation ocean wave prediction model, *J. Phys. Oceanogr.* 18, 1775–1810.

CHARACTERISATION AND ASSIMILATION OF ERS-1 SCATTEROMETER MEASUREMENTS

Ad Stoffelen^{*}, Dave Anderson, Catherine Gaffard
ECMWF, Shinfield Park, Reading, UK

^{*}KNMI, Postbus 201, 3730 AE de Bilt, The Netherlands
Phone: (+31) 30 206 585, Fax: (+31) 30 210 407
e-mail: stoffelen@knmi.nl

Calibration and validation activities at ECMWF have lead to the implementation of new transfer functions, giving an improved description of the relationship between backscattered radar power and the surface wind vector. We have shown that backscattered power can be interpreted by two geophysical parameters, and that these parameters are well represented by wind speed and wind direction. Scatterometer 10 m wind vectors have an accuracy that is higher than the accuracy of conventional surface wind data, such as from ships and buoys, as measured against the ECMWF analyses of surface wind. The retrieved scatterometer winds have been assimilated in statistical interpolation and variational data assimilation schemes at ECMWF. Four dimensional data assimilation techniques are best fit for the assimilation of surface wind data.

1. σ^0 MEASUREMENT SPACE

The ERS-1 scatterometer measures the normalised radar backscattered power, σ^0 , in three directions. Thus, each node on the Earth's surface is illuminated first by the fore beam, then by the mid and last by the mid beam. By plotting the three measurements in a 3D space the full characteristics of the ERS-1 scatterometer measurements can be observed. It was found that the measured σ^0 triplets lie close to a 2D cone-shaped surface (see Figs. 1 and 2). The extension of the cone in the 3D space corresponds to the sea surface roughness and by implication speed, whereas the opening of the cone is related to the anisotropy of backscattering which can be related to wind direction effects. Evaluation of the 3D space highlighted the necessity to change the formulation of the transfer function (CMOD2). It further reveals the close ambiguity of the two wind vector solutions, and by collocation to external data the dependency of backscattered power to geophysical parameters can be studied. The scatter of the σ^0 triplets normal to the cone surface is also easily evaluated in this 3D space, and was found to correspond to a few tenth of a m/s. A small amount of anomalous σ^0 triplets are rejected in a quality control procedure (see also Refs. 1-4).

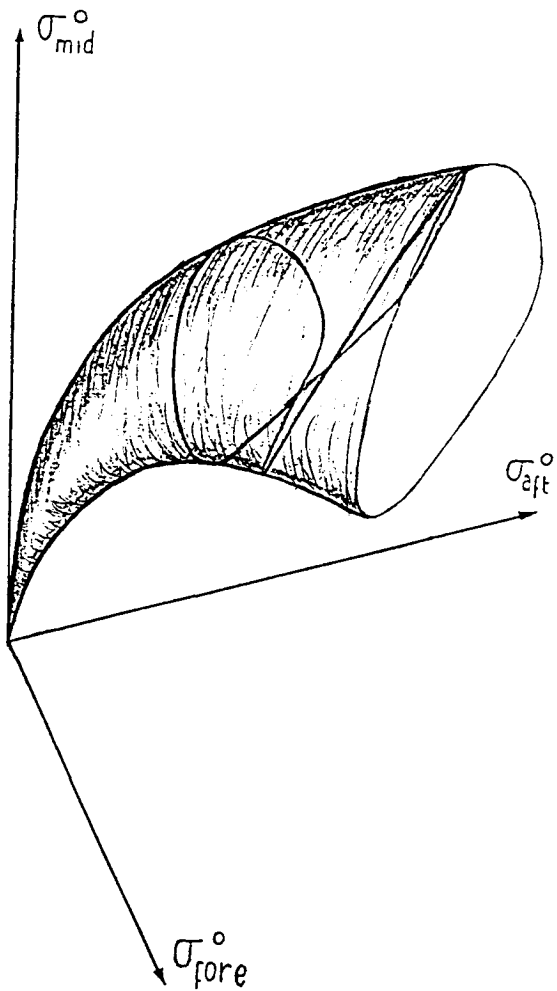


Fig. 1: 3D Measurement space. Triplets of measured backscattered power are expected to lie close to a cone-shaped surface.

2. INVERSION

Given a measured σ^0 triplet, the inversion problem can be reduced to the problem of finding the most probable "true" triplet on the cone surface. The cone surface is highly curved and by consequence the distribution of measured σ^0 triplets is not easy to

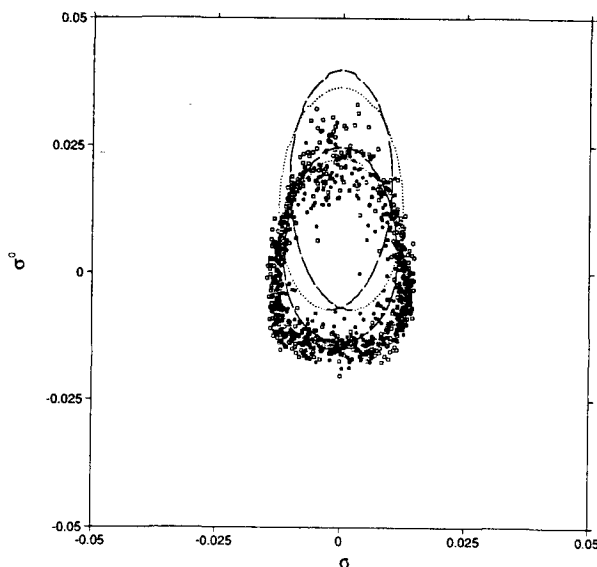


Fig. 2: Example of the distribution of measured triplets in a cross-section across the cone. The expected cone surface can easily be identified. The collocated analysis wind speed for the triplets plotted is roughly 8 m/s. ■ are "upwind" triplets, according to ECMWF analysis wind direction, and □ "downwind" triplets. The pre-launch transfer function (CMOD2) and the transfer function derived at ECMWF (CMOD4) are also shown (curves).

describe. Standard Maximum Likelihood Estimation (MLE) procedures use simple assumptions on the a priori expected distribution of measurements, and are therefore not valid for the scatterometer inversion problem. We used Bayes probability theorem to pose an optimal solution. For our assumptions it was essential that the measurement geometry of the scatterometer is symmetric. Therefore, for NSCAT for example (asymmetric geometry), it will be much more difficult to obtain an optimal solution (Ref. 6).

3. AMBIGUITY REMOVAL

Since two closely overlapping cones exist in the 3D σ^0 space, the inversion procedure will result in two, almost equally probable, σ^0 triplet solutions on the cone surface. By using the transfer function description of the cone surface, we can identify the two ambiguous wind vector solutions they represent. In the ambiguity removal of ERS-1 scatterometer winds it was found essential to use weather forecast information of the highest quality, i.e. with the shortest possible forecast lead. Taking the closest to a 3 to 9 hour surface wind forecast gives the correct solution in more than 95 % of the cases.

A filter developed at ECMWF, in a package called

PRESAT, that constrains wind vector consistency, further improves the ambiguity removal. Initially, the closest solution to the short term forecast is selected. If the vector RMS difference between this solution and the forecasted wind is large, then a low initial confidence is given to that solution. This is also done when the scatterometer wind direction accuracy is low. If at a particular node the alternative solution has a better wind vector consistency with its neighbours, weighted by the confidence in the neighbours, then this alternative solution is selected and the confidence increased. Thus, information in areas with high confidence is propagated to areas where the initial confidence is low. The scheme is able to correct phase errors in the short range forecast.

The ambiguity removal scheme used for the ESA Fast Delivery product relies less on forecast information, and uses forecast information with much lower quality. Only in 30 % of cases ambiguity removal is performed, and in another 5 % of cases the ambiguity removal fails. These cases tend to be in areas of meteorological instability, and therefore of great interest.

4. QUALITY OF PRESAT WINDS

PRESAT winds were verified against the ECMWF 3 to 9 hour forecasts. Similar verifications are done routinely for ship winds available from the GTS network. Surprisingly, we found that the scatterometer winds generally compare better to the ECMWF forecast than ship winds (see Table 1). One of the main reasons for this concerns the so-called representativeness error. The current ECMWF model represents spatial scales down to roughly 200 km. For the ERS-1 scatterometer, the corresponding scale is 50 km (footprint), but for conventional wind data this is less than one metre. The atmospheric turbulence on scales between one metre and 200 km (with a general wind vector variance of ~ 2 m/s) will make a substantial contribution to the difference between ship and forecast wind. It also follows from this that ship winds will report more often extreme conditions than the scatterometer or the ECMWF model will do.

	Standaard Deviation (m/s)	Correlation
Non-automatic ship	3.5	0.93
Automatic ship	2.8	0.95
Scatterometer (node 11)	2.2	0.97

Table 1: The standard deviation and correlation of the wind component departures for (non-)automatic ship winds and scatterometer winds (node 11) with the ECMWF forecast winds. ship data are for March 1993 and mainly in the Northern Hemisphere, and scatterometer data are global for the second half of March 1993.

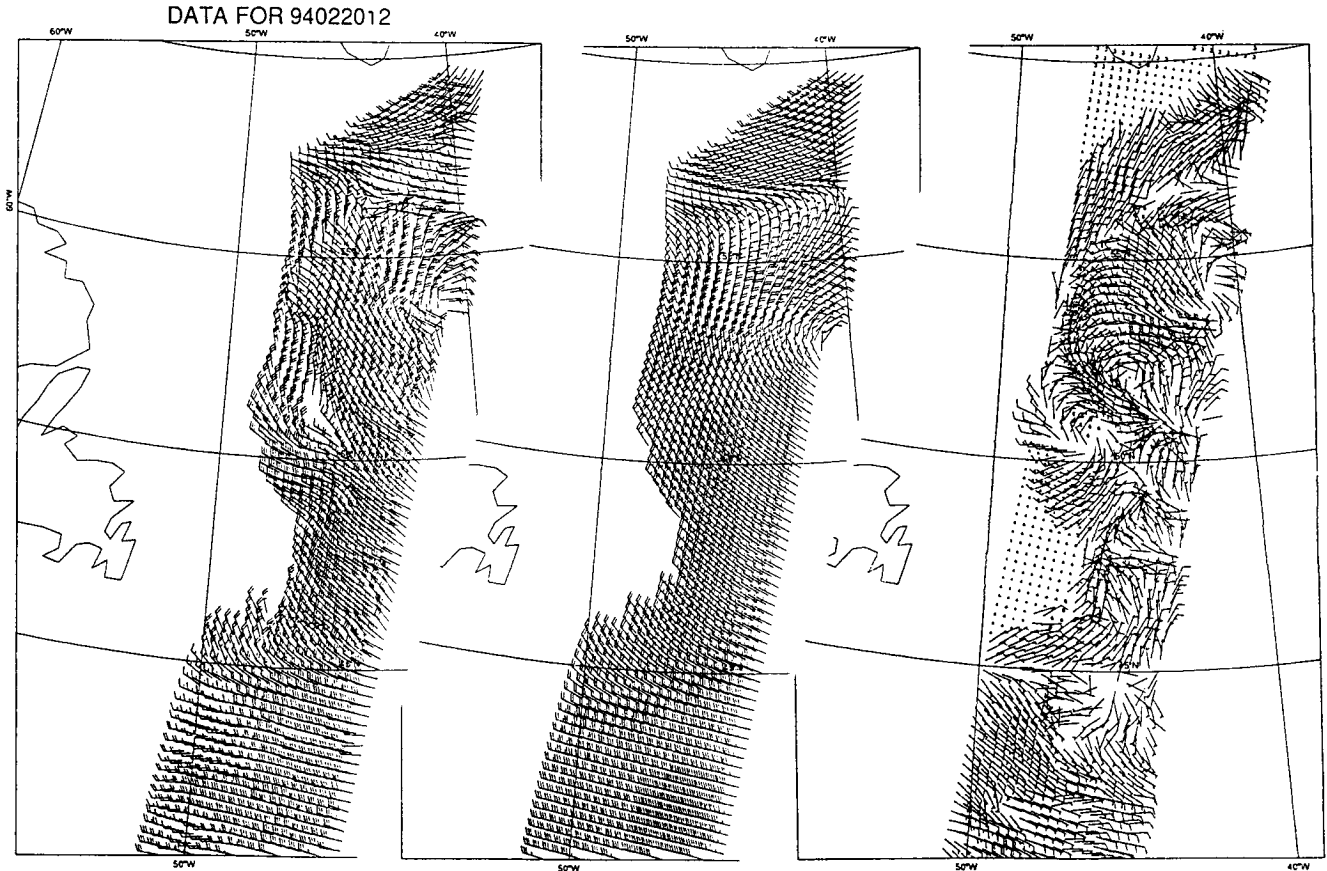


Fig. 3: a) ERS-1 scatterometer winds (PRESCAT) close to New Foundland, b) the ECMWF 6 hour forecast , and c) the difference of a) and (b). The scatterometer winds possess significant synoptic detail.

We further investigated the horizontal error correlation in PRESCAT winds. We found that for scales larger than 50 km no substantial error correlation is present (Ref. 7). As a consequence significant synoptic detail is present in the data, as illustrated in Figure 3.

Since 24 February 1993 the ESA FD product has stabilised (introduction of CMOD4), and we verified that the FD wind product is of similar quality than the PRESCAT product, but only when the cases of a failed ambiguity removal in the ESA product are ignored (see above).

5. SCATTEROMETER DATA ASSIMILATION

Given the quality of the PRESCAT scatterometer winds it seems worthwhile to assimilate them into the ECMWF model. The analysis is a compromise between a short range forecast (e.g. 6 hour forecast) and the observations received over the last few hours. We have explored both the assimilation into the current "optimal" interpolation (OI) analysis scheme, and into the 3D- and 4D- variational schemes (3D-

VAR and 4D-VAR).

5.1 OI

The assimilation of scatterometer winds in OI is similar to the assimilation of conventional surface wind data. However, a greater impact is expected since the scatterometer data are of better quality, more numerous and spatially consistent.

We did indeed find that the scatterometer has an impact on the analyses in the Southern Hemisphere. In the Northern Hemisphere however, the effect of the scatterometer on the weather analyses is less. The changes in the Southern Hemisphere were verified to be beneficial. Also the short range wind forecasts (up to 12 hours) throughout the troposphere were found to be improved (Ref. 6).

Scatterometer winds did not improve the medium range forecasts at ECMWF. In fact, they were found to be redundant with SATEM (satellite temperature soundings). In a data assimilation scheme, assumptions have to be made on the structure of error

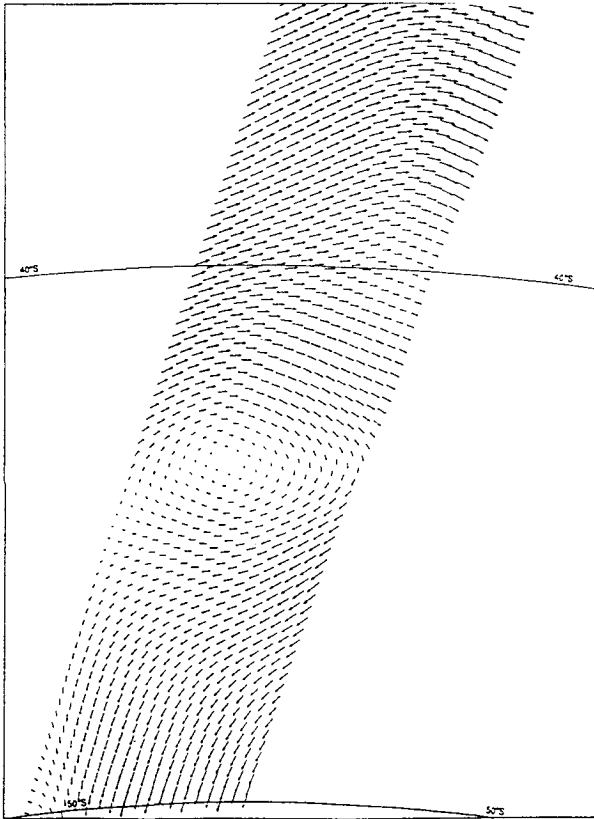
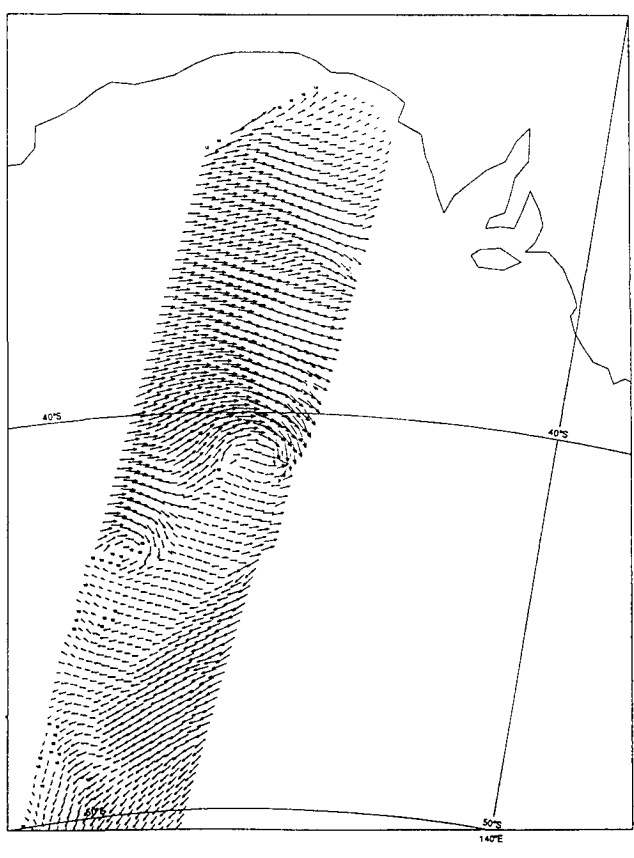
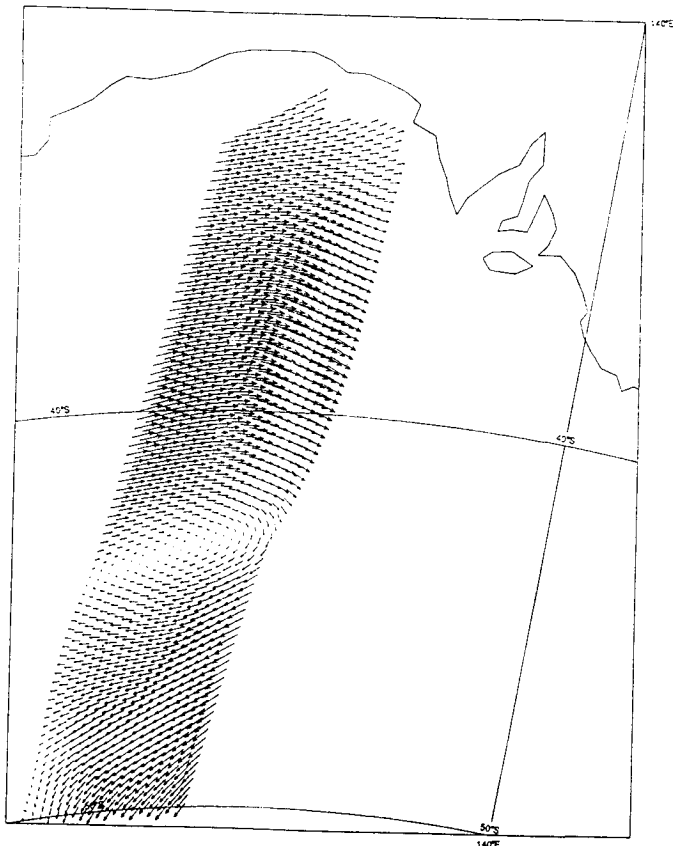


Fig 4: a) ERS-1 scatterometer winds (PRESCAT) for 93/03/26 0 UTC South of Australia, b) the ECMWF 6 hour forecast , and c) the 3D-VAR analysis using the information in a) and b), which is a reasonable large scale compromise. The horizontal resolution used in the experiment was at spectral truncation T106 (~ 125 km sampling).



of the forecast. This means for example that if the forecasted wind at a certain location is found to be wrong, then it is assumed that the forecasted wind, pressure and temperature are also wrong in an area above, below and around this location. So, when we have only SATEM data, then we will improve on the temperature fields of the forecast, and have an accurate temperature analysis. However, because of our assumptions on forecast error structure, we will also adapt the forecasted wind field. By verification of the operational surface wind analyses and forecasts with scatterometer winds, it was found that the changes to the forecasted surface wind field by upper air SATEM data are not always beneficial (Ref. 7). This implies that our assumptions on the structure of the forecast error are not adequate. The most limiting assumption is probably that the forecast error structure is assumed to be constant and independent of the meteorological conditions. This assumption is used in

most current data assimilation systems. In 4D-VAR experiments the weakness of this approximation has already been shown (Ref. 8). It offers an explanation for the neutral effect of the scatterometer winds on the medium range forecast skill and the redundancy between scatterometer and SATEM data.

5.2 3D- and 4D-VAR.

In a variational data assimilation scheme a penalty function is minimised. At the minimum the most likely "true" meteorological state of the atmosphere is found. This state will be a compromise between the short range forecast (6 hour forecast in case of 3D-VAR) and the observations. In order to compute this compromise properly we need to know what the probability of an observed wind vector is, given the "true" wind vector, in the case of a wind measurement. In the case of conventional wind data this probability simply depends on experience of how well the observational system fits the 6 hour forecast wind in general. Similarly, for scatterometer data it has also been found that the observation error can easily be described using the components of the wind. In terms of back-scattered power however the observation error structure is very complicated. This is due to the non-linear wind-to-radar relationship, embodied in the transfer function, and the relatively small detection error of the measured radar power. Therefore, also in 3D- and in 4D-VAR, scatterometer data are most easily treated like other surface wind data (Ref. 9).

By defining an observation cost function with two minima the ambiguity of scatterometer winds can be taken into account. The constraint of geostrophy on the resulting analysis will then be taken into account for the selection of the proper wind direction solution. This should result in a better ambiguity removal than the constraint of wind vector consistency currently used in PRESCAT. In this respect the first results from 3D-VAR look promising, as illustrated in Figure 4.

It is expected that the best use of surface wind data can be made within 4D-VAR. Scatterometer information will then effect the atmosphere in a dynamically consistent manner that depends on meteorological conditions.

6. CONCLUSIONS AND RECOMMENDATIONS

ERS-1 scatterometer winds as processed by PRESCAT are of high quality as compared to conventionally available surface wind data. The Fast Delivery ESA

product is of similar quality, except for the ambiguity removal problem. This can be solved by making two solutions accessible to the real-time users and provide them with the software for ambiguity removal.

The operational value of scatterometer measurements for Europe can be greatly enhanced by the provision of more frequent measurements. Especially for short range forecasting and in cases of extreme events this is important.

The assimilation of scatterometer data in the ECMWF global meteorological model has lead to noticeable improvements in the analyses and short term forecasts. A redundancy in the medium range forecasts was found between scatterometer data and satellite temperature soundings (from NOAA). The redundancy can be explained by the simplifying assumptions on the structure of the error in the forecast, as used in most current meteorological data assimilation schemes. It is expected that in a 4D-VAR assimilation scheme these assumptions are less of a problem.

In a variational assimilation system geostrophy is used to solve the ambiguity in scatterometer data. For users that do not possess a full 3D variational assimilation system, it may be useful to solve the ambiguity problem by a similar 2D variational system. We recommend this to be developed.

7. REFERENCES

1. A.C.M. Stoffelen and D.L.T. Anderson, "ERS-1 scatterometer calibration and validation activities at ECMWF: A. The quality and characteristics of the radar backscatter measurements", in Proc. European 'Int. Space Year' Conf., 30 March - 4 April 1992, Munich, Germany.
2. A.C.M. Stoffelen, D.L.T. Anderson, and P.M. Woiceshyn, "ERS-1 scatterometer calibration and validation activities at ECMWF: B. From radar backscatter characteristics to wind vector solutions", in Proc. European 'Int. Space Year' Conf., 30 March - 4 April 1992, Munich, Germany.
3. A. Stoffelen and D.L.T. Anderson, "Wind retrieval and ERS-1 radar backscatter measurements", Adv. Space Res. Vol. 13, No. 5, pp. (5)53-(5)60, 1993.
4. Ad Stoffelen, David L.T. Anderson, "ERS-1 scatterometer data characteristics and wind retrieval skill", presented at the First ERS 1 Symposium, 4-6 November 1992, Cannes, France.

5. Ad Stoffelen, David Anderson, "Characterisation of ERS-1 scatterometer measurements and wind retrieval", proceedings Second ERS-1 symposium - Space at the service of our environment, 11-14 October 1993, Hamburg, Germany, ESA SP-361, Januari 1994, published by ESTEC, Noordwijk, The Netherlands.
6. Ad Stoffelen, Catherine Gaffard, David Anderson, "ERS-1 scatterometer data assimilation", proceedings Second ERS-1 symposium - Space at the service of our environment, 11-14 October 1993, Hamburg, Germany, ESA SP-361, Januari 1994, published by ESTEC, Noordwijk, The Netherlands.
7. Ad Stoffelen, "ERS-1 scatterometer data assimilation", presented at workshop on "HIRLAM data assimilation - present techniques and future developments", Nörrkoping, Sweden, 23-24 February, 1994. Published by SMHI, Nörrkoping, Sweden.
8. J.-N. Thépaut, P. Courtier, R.N. Hoffman, "Use of dynamical information in a 4D variational assimilation", presented at the ECMWF workshop on variational assimilation with emphasis on 3 dimensional aspects, Reading, UK, 9-12 Nov. 1992. Published by ECMWF, Shinfield Park, Reading, UK.
9. Ad Stoffelen, "From measurement to model: ERS-1 scatterometer data assimilation", presented at ECMWF seminar "Developments in the use of satellite data in Numerical Weather Prediction", 6-10 September 1993, Reading, U.K..

Acknowledgements

The work reported here was done with ESA and ECMWF resources. The ERS-1 analysis team and ECMWF staff have contributed to useful discussions leading to the results reported here.

2. HYDROLOGY



THE USE OF ERS-1 DATA FOR SPATIAL SURFACE-MOISTURE DETERMINATION

W. Mauser, M. Rombach, H. Bach, R. Stolz,

A. Demircan, J. Kellndorfer

Institute for Geography

Chair for Geography and Geographical Remote Sensing

University of Munich

Luisenstr. 37, D-80333 Munich, Germany

Tel.: 0049-89-5203-320, Fax: 0049-89-5203-321

ABSTRACT

Within a project sponsored by DARA 28 ERS-1 SLC images of an agricultural area in the Upper Rhine Valley are integrated into a GIS structure after proper preprocessing. The GIS contains information on field-boundaries, land-use for each field, soils and the results of continuous soil-moisture and rainfall measurements on single fields in the test site (app. 50 km²). The GIS is used to establish relations between ERS-1 backscatter and measured surface soil-moisture for different land-uses. Since backscatter depends on soil- and surface properties statistical relations between temporal backscatter profiles of different soil-surface complexes are established. They allow to equalize the multitemporal ERS-1 images to a reference backscattering behavior of corn on loamy sand. Since surface soil-moisture has been measured for this soil-surface complex the ERS-1 images can be converted into reference surface-moisture images. These images are interpreted. Among others it is shown, that irrigated areas can be identified through their high reference surface moisture.

INTRODUCTION

Estimation of the spatial distribution of soil-moisture and surface cover is of central importance to at least three topics of land-surface process analysis:

- energy-balance and carbon-cycle studies of the land-surfaces in relation to climate research,
- more application oriented topics like water availability to plants for evapotranspiration and yield estimation studies,
- estimation and forecasting of floods and flood risks.

Because of this high scientific and application interest intensive theoretical and experimental studies have been undertaken to determine the sensitivity of microwave backscatter to the surface water content and surface cover (Ulaby(1978a,b), Bernard(1992), Wooding(1992)). The outcome of these studies showed, that at least in principle soil water content can be determined through microwave backscatter. The basic physical property, which is related to the changing backscatter of the surface is the dielectric constant of the soil-air-water complex. This signal though, is influenced by the chosen system parameters, like frequency, polarisation and incidence angle as well as surface features like roughness, cover and illumination geometry. For the system parameters of ERS-1 it was shown through simple model calculations (Bruckler(1988)), that this sensor is suitable for the determination of the water content of a relatively narrow top soil layer of 1-10 cm. The penetration depth is strongly depending on the actual soil water content. The water contained in this layer will be referred to as surface-moisture during the course of this paper. Although the relevant processes in the soil-plant-atmosphere interface, which is responsible for the above mentioned scientific and application topics occur in the root zone (top 1 m), the surface-moisture is the key parameter for infiltration of water into the soil and evapotranspiration from bare soils and grasses. The surface cover in principle changes the surface roughness and creates volume scattering, which at least adds a surface cover dependent signal to the scattering behavior of bare soil but can also totally mask the soil surface in case of dense forest. To be able to improve the existing approaches for flood-forecasts, energy balance calculations and yield estimation it is necessary to determine the spatial distribution of these parameters, which are used as input to appropriate models. This paper will show, how ERS-1 data in combination with GIS-tools can be used to determine these model parameters.

STUDY AREA AND GIS DATA BASE

STUDY AREA

The study area is situated in the Upper Rhine Valley near the City of Freiburg (Germany). The test-site covers an area of 6x8 km and shows a maximum elevation difference of a few meters. The climate in the region of the test-site is characterized through high temperatures and low precipitation (average: 650 mm p.a.). This creates periodic water stress mainly on light soils (sands, sandy loams) especially under forests and corn fields. The soils in the test-site are very inhomogeneous and consist of loamy to gravelly sands deposited by the river Rhine and silty and clay soils originated from the Loess soils in the hills surrounding the test site. Although the meteorological conditions in the test site can be considered constant this leads to a large spatial inhomogeneity of surface-moisture conditions.

The main crops in the test-site are corn (app. 30% of the agricultural land in 1991) and wheat. App. 25% of the test area are covered with mainly deciduous forests.

GIS DATA BASE

The GIS data base consists of the following spatial and point data:

- 28 ERS-1 single-look complex images of the period from Aug.17 to Oct.1, 1991, with a repeat cycle of 3 days. The data was taken during the Commissioning Phase of ERS-1. The data was calibrated using the ESA-supplied calibration factors and converted into power using:

$$\text{Eq.1: } P = \text{sprt}((10^*I + 10^*Q)^2)$$

I = amplitude component
Q = phase component

During the conversion a linear stretching factor of 10 was used to enhance contrast for the dark objects. Therefore corner reflectors, which are of no interest in this study were in saturation when using a 16-bit representation for the pixels. Further details can be found in Rombach et.al. (1993). After calibration a slant-to-ground range conversion was performed, which resampled the images to a pixel size of 4.1x7.9m. The different ERS-1 image were then registered onto each others using the nearest-neighbour criterion.

- a digital land use map of the test-site. It was constructed through digitizing the property boundaries of the 1:5000 topo maps of the test-site (pixel-size: 2m) and a field survey, which was conducted for each field in the test site.

After modification of the property boundaries according to the actual land-use boundaries and inclusion of the land use in the GIS two raster layers of the land-use data were created with the same geometry and pixel size as the ERS-1 data set:

- a) the land-cover in 21 categories
- b) the field map, which assigns each pixel the GIS-field number it belongs to. This enables an analysis of the ERS-1 data on a field-by-field basis.

The digital land use map is shown in Fig.1

- a digital soil map which was digitized from the Special German Soil Survey maps (pixel-size: 2m). The soil maps are derived from 1:5000 topo maps and are based on data, which was gathered on a 50m grid. It serves as the basis for the taxation of the German farmers. Among other data the soil type is given for each soil region. From the soil type of all agricultural areas in the test-site a raster layer was produced with the same geometry as the ERS-1 data set.

The digital soil map is shown in Fig.2.

- plant-parameter measurements on 4 fields in the test-site (ref. Demircan(1993)). On a weekly basis the following plant parameters were determined taking samples from the fields: - plant height [cm], - wet biomass [kg/m^2], - dry biomass [kg/m^2], - green leaf area index [m_2/m^2].

Fig.3 shows the development of the green LAI of the two corn fields, where soil-moisture was measured. As can be seen clearly the growing season of corn field 2 on silt soil is 2 weeks longer because of its superior water supply.

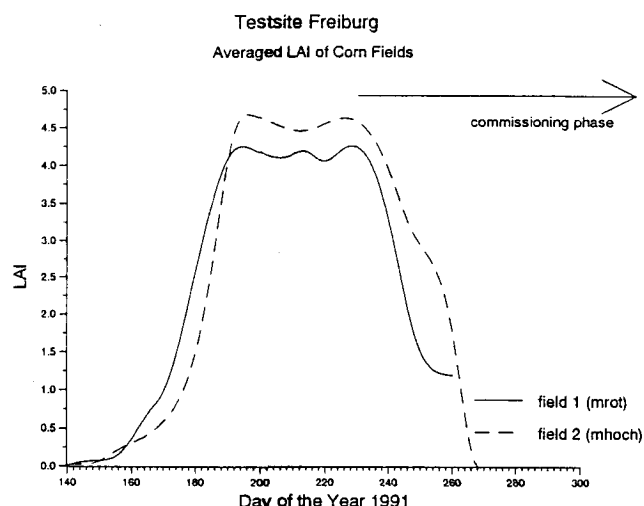


Fig.3: The course of the green leaf area index (LAI) of 2 corn fields in the test-site as determined through weekly measurements. Field 1 is on sandy loam, field 2 on silt soil.

- continuous soil-moisture measurements on 4 different fields in the test-site. The soil-moisture was measured hourly at 4 depths (2cm, 15 cm, 35 cm, 55 cm) using gypsum blocks and tensiometers. The soil suction curves and soil-physical parameters were determined in the laboratory. To cover a large variety of soil-plant parameter combination the soil-type and plant cover was chosen in the following way:

- field 1: corn on sandy loam
- field 2: corn on silt
- field 3: barley on sandy loam
- field 4: barley on loamy sand

Fig.4 shows the change in measured soil moisture at a depth of 2 cm and the backscattering signal determined from the multitemporal ERS-1 data set through calculation of the average power value of the corn field for each date. It can be seen, that there is a good agreement between the temporal change of the measured soil-moisture and the ERS-1 backscatter although the corn plants on the surface have changed from a height of 250 cm, a green LAI of app. 4 and a wet biomass of app. 4 kg/m² to zero for all parameters in October, as can be seen in Fig.3.

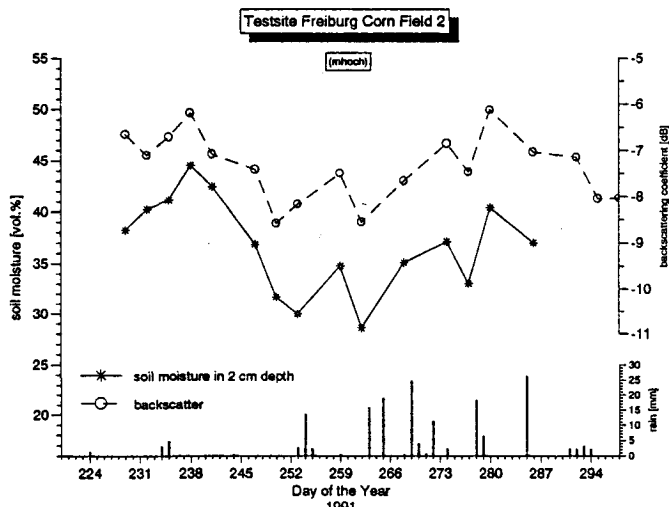


Fig.4: The course of the soil moisture at a depth of 2 cm under a corn field (loamy sand) in comparison to the temporal backscatter profile of ERS-1 for the same field and the measured rainfall.

Fig.5 shows the combined relation between the soil-moisture measured at a depth of 2 cm of all the 4 fields under investigation and the backscatter of ERS-1 for the measurement period from August to November 1991. As can be seen clearly a linear relation with a considerable correlation exists between the measured soil-moisture at a depth of 2 cm and the backscatter of ERS-1 even though one would assume, that the surface condition of the fields influence the backscattering signal (Rombach(1993)).

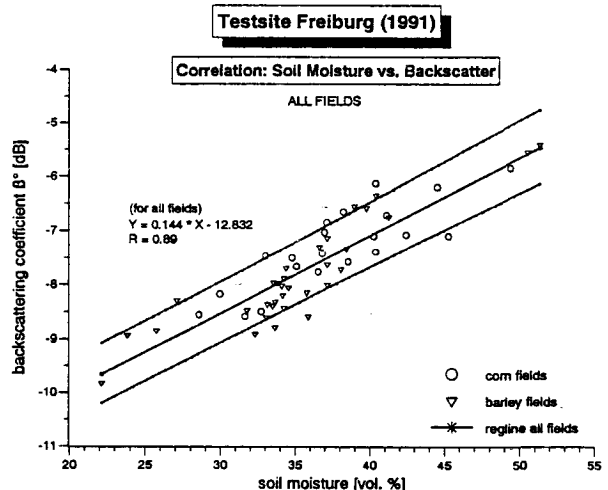


Fig.5: Relation between the measured soil-moisture on all fields (corn and barley) and the backscatter determined from multitemporal ERS-1 images.

SPATIAL DATA ANALYSIS

The aim if the analysis of the ERS-1 data set in combination with the additional GIS-based data on surface characteristics is to derive spatial and temporal patterns of surface-moisture for the test-site including the main influencing factors soils and land-use.

For this aim a segmentation of the entire ERS-1 image of the test-site on a field and even subfield basis is necessary to be able to distinguish different soil-surface complexes and to be able to study their backscattering behavior. At the present stage of research an automatic segmentation of ERS-1 images with regards to land-use does not lead to satisfactory results and cannot be conducted with regard to soils. Therefore the GIS-raster layers have been used as surrogate for information, which might be available in the future or through the use



Fig.1: Excerpt of digital land-use map of the test-site, produced on the basis of the 1:5000 topo maps of the test site and a field survey for each field (Landuses which were not analyzed in this paper are not included in this figure).

Testsite Freiburg (1991)

Digitized Soil Map

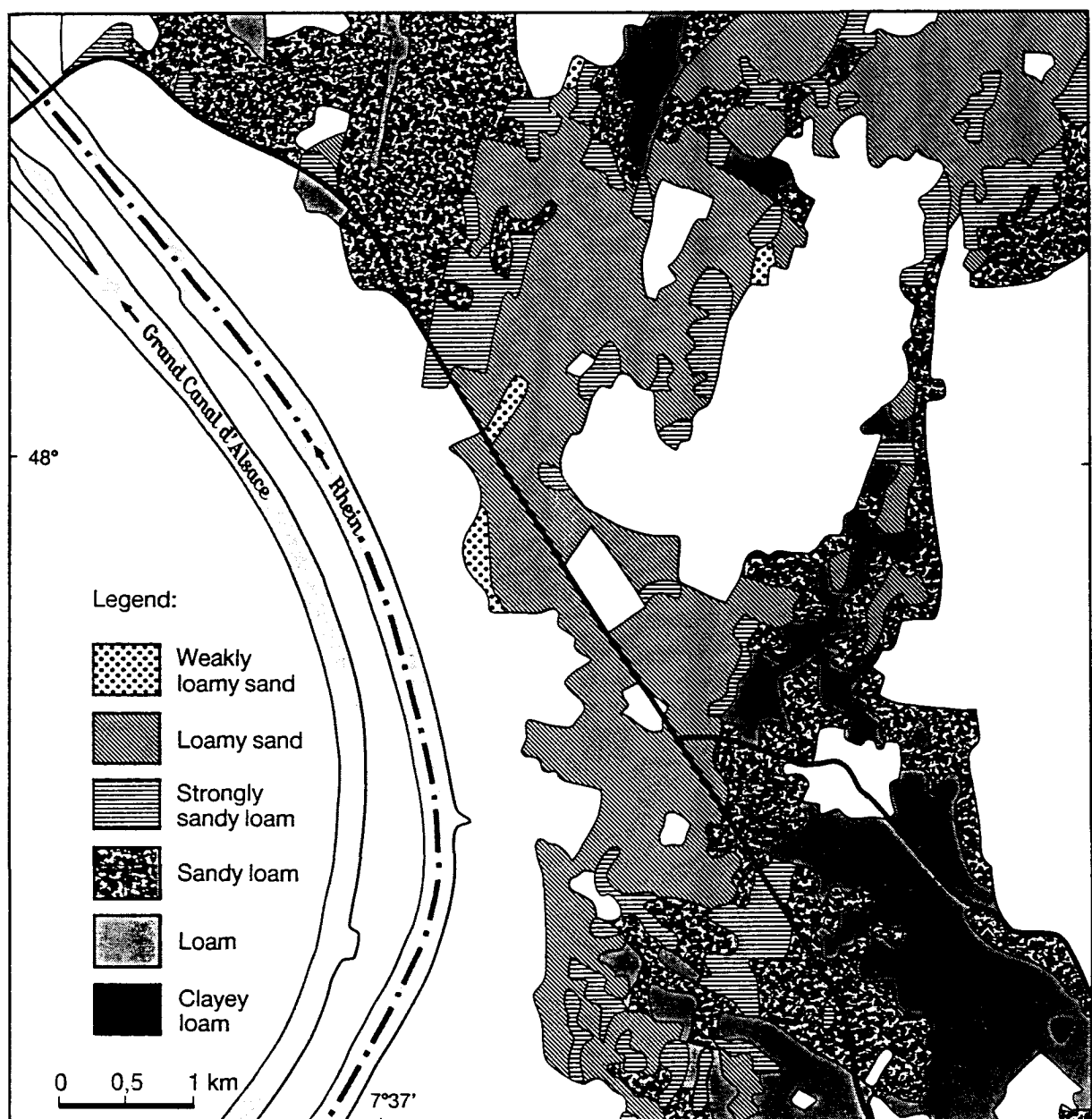


Fig. 2: Digital map of the soil-types in the test-site produced on the 1:5000 topo maps of the Special German Soil Survey.

of additional remote sensing data sources. The analysis of the data has been conducted using the FAP-software developed at the authors institute (Mauser et.a. (1993)).

HYPOTHESIS AND METHODOLOGY

Since the backscattering behavior of natural surfaces and the influences of the soil properties, soil roughness and surface covers on the backscatter are not yet understood to the point where a completely physically based model of backscattering can be applied a different approach based on statistical analysis has been chosen to determine the spatial distribution of surface moisture over an inhomogenous area. It is based in the relation between measured soil-moisture and the backscatter of ERS-1 data as shown in Fig.5. Although Fig.5 shows a considerable correlation between the two parameters the influence of surface roughness, plant geometry and temporal dynamics of the different soils due to different suction curves are included in Fig.5. To determine the relative influence of these parameters on the backscattering signal a statistical analysis has to be carried out based on the following hypotheses:

- the absolute value and the temporal behavior of backscatter is different for different land-uses and soil types due to the influencing factors mentioned above.
- one corn field on loamy sand, where soil moisture is measured is taken as a reference field to which all other soil-surface combinations will be compared and finally equalized.
- the meteorological conditions in the test-site are constant over space, which has been proven at least for the rainfall through the use of 20 raingauges.
- correlations between the backscatter of the reference field and all soil-surface complexes (which not necessarily have to be complete fields) are determined. As soil-surface complexes all combinations of the main land-uses and soil-types are taken. Assuming linear

relations between the backscatter on the reference corn field and the soil-surface complexes this leads to a 4x4 matrix of gain- and offset-values of corn, winter-barley, summer-barley, meadows on loamy sands, strongly loamy sands, sandy loams and loams respectively.

- the result of this analysis is a set of correction values to alter the backscattering coefficients for each soil-surface complex in the test-site to the behavior of corn on loamy sand and therefore to relative backscatter values for each of the

considered soil-surface complexes. These are the values, which they would show, if they were covered with corn and had a sandy loam soil.

- based on these relative backscatter values the reference surface-moisture can be derived from the relation underlying Fig.4 for each date of the ERS-1-time series.

To proof this approach first a comparison of the temporal backscatter profiles of different surface covers and different soils have been determined. Fig.6 shows the temporal backscatter profile together with the rainfall for all summer-barley fields in the test-site. The average power was determined for all summer-barley pixels in the test-site separating 3 groups according to the soil-type. The average power for each group was then converted into backscatter values. It can be seen, that the backscatter quite closely follows the

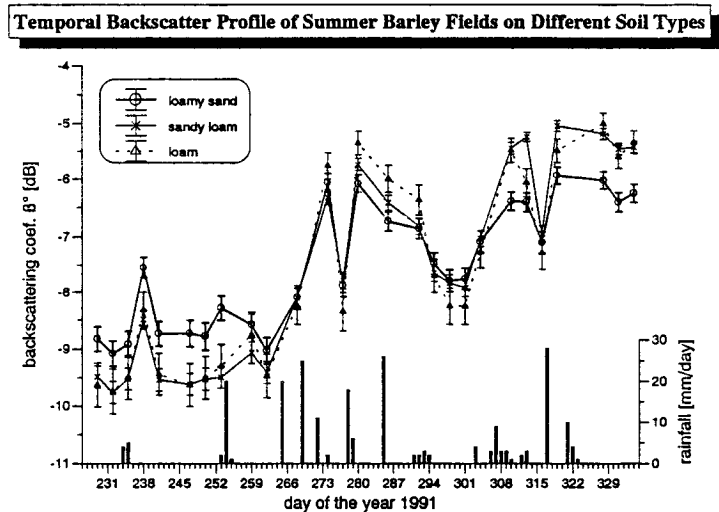


Fig.6: Temporal backscatter profile of all summer-barley fields on different soils in the test-site.

rainfall events for all fields in the area. It can also be seen, that summer-barley on sandy soils tends to show larger backscatter values at the beginning of the observation period and smaller backscatter values at the end of the observation period than summer-barley on the other soils. This clear behavior cannot be explained yet. Since all summer-barley fields were harvested when the observation began it cannot be caused by different growing conditions of barley on sandy soils. The high content of stones in the sandy soils might be responsible for the reduced sensitivity of

backscatter from the sandy soils to changes in surface-moisture. The reason might be, that stones are not included in the ground based measurements of soil-moisture but fully contribute to the average dielectric constant of the soil as seen by ERS-1.

Fig.7 shows the same analysis for the corn fields. Here the amplitude of the determined backscatter values of sandy soils is also smallest and the backscatter is much lower for sandy soils, than for all the other soils in the second half of the observation period.

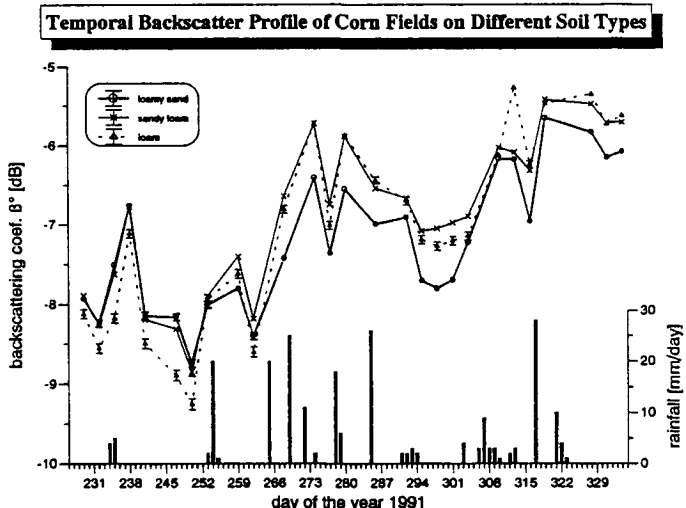


Fig.7: Temporal backscatter profiles of all corn fields on different soils in the test-site

As a next step a regression analysis between the backscatter value of the selected reference corn field on loamy sand (where actual soil-moisture measurements have taken place) and the backscatter values of the soil-surface complexes in the test-site, which are covered with corn was conducted including the 28 multitemporal ERS-1 images. The result can be seen in Fig.8. When looking at the black line, which would indicate perfect agreement between the backscatter of corn fields on different soils one can see a deviation, which might be caused by the influences of the different soils and their different soil-water dynamics. In general it can be said, that there is more dynamics in the backscattering values on strongly loamy sandy loam, sandy loam and loam than there is on loamy sand. Nevertheless the backscattering values are closely connected as might be expected for one species on different soils.

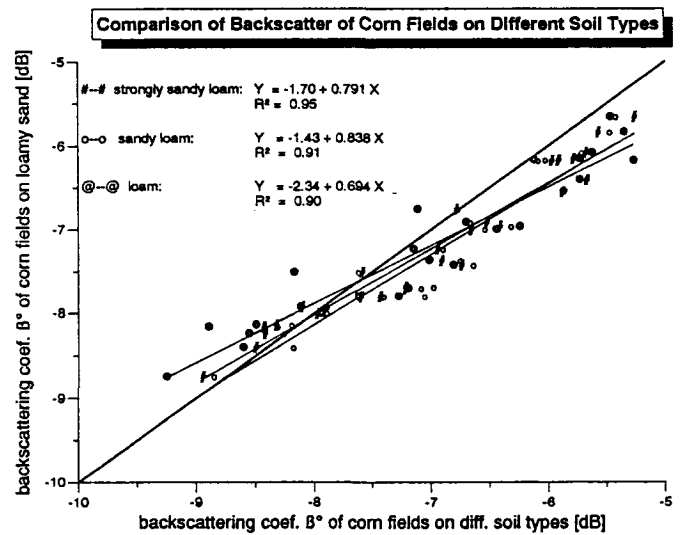


Fig.8: Comparison between the multitemporal backscatter of corn fields on different soils and the reference backscatter of corn on sandy loam.

In Fig.9 the results of the same analysis for summer-barley fields on different soils is shown. The black line again would indicate perfect agreement between the course of the backscattering

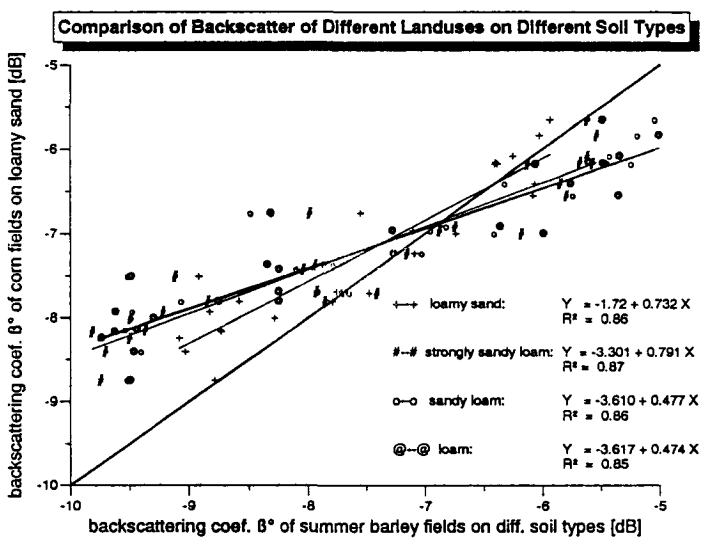


Fig.9: Comparison between the multitemporal backscatter of summer-barley fields on different soils and the reference backscatter of corn on sandy loam

of corn on sandy loam with the backscattering of summer-barley. The deviation of the backscattering behavior of summer-barley from that of corn on sandy loam is much more pronounced. It can be seen, that the barley fields show a much higher backscatter dynamic than the corn fields. Since the barley fields were already harvested this might be due to a shielding of the soil-surface by the biomass above it in case of the corn fields. This might cause the reduction in backscatter dynamics. In all examples shown here, the coefficient of determination R^2 is sufficiently high for statistically stable relationships.

The complete results of the statistical analysis for all examined combinations of land-cover and soil-type in the test-site are shown in Tab.1. Tab.1 includes the gains and offsets of the regression lines, the regression coefficient and the number of pixels included in the analysis for each combination of land-cover and soils. The values listed in these matrices serve as a basis to convert the backscatter of all pixels in the multitemporal ERS-1 data set according to their membership to one of the combinations listed in Tab.1. As a result they receive the reference backscatter value, that they would show, if they consisted of sandy loam and were covered with corn. The result is a set of

28 equalized ERS-1 backscatter images for the 28 dates under consideration. These images in turn can easily be transformed into reference surface-moisture images by applying the relation underlying Fig.4.

In Fig. 10, 11 and 12 three typical situations are shown for which the distribution of the reference surface moisture has been determined for the complete test-site. The first image shows the distribution on Aug. 23, 1991 (day 235). At this date the situation can be characterized by strong evapotranspiration and relatively dry surfaces. The image shows relatively low reference surface soil-moisture values throughout the test-site. The usual range lies between 20 and 35 Vol.% depending mostly on the plant cover. Corn fields tend to show larger soil-moisture values. This is in accordance to observation since the grown up corn plant does not extract water from the surface layer for transpiration and is a very efficient shield against surface evaporation. The only striking difference is in the center at the northern part of the image, where the corn fields have been irrigated because of the low water holding capacities of the underlying soils. There the reference surface-moisture is considerably higher and lies in the range between 35-45 Vol%.

OFFSET [dB]	Loamy Sand	Strongly Sandy Loam	Sandy Loam	Loam
Corn (Maize)	reference to	-1.697	-1.432	-2.335
Winter Barley	-2.798	-1.749	-3.532	-2.872
Summer Barley	-1.721	-3.301	-3.610	-3.617
Meadow	-1.556	-2.026	-1.847	-2.120
GAIN	Loamy Sand	Strongly Sandy Loam	Sandy Loam	Loam
Corn (Maize)	reference to	0.791	0.838	0.694
Winter Barley	0.588	0.703	0.527	0.583
Summer Barley	0.732	0.516	0.477	0.474
Meadow	0.656	0.574	0.776	0.609
Regression Coefficient [R^2]	Loamy Sand	Strongly Sandy Loam	Sandy Loam	Loam
Corn (Maize)	reference to	0.95	0.91	0.90
Winter Barley	0.83	0.81	0.77	0.79
Summer Barley	0.86	0.87	0.86	0.85
Meadow	0.77	0.76	0.86	0.82
Number of Pixel (statistical independent)	Loamy Sand	Strongly Sandy Loam	Sandy Loam	Loam
Corn (Maize)	30497	10069	23719	15991
Summer Barley	6572	2096	2181	1290
Meadow	1290	3146	946	1893

Tab.1: Results of the regression analysis of the multitemporal backscatter of different soil-surface complexes and the multitemporal reference backscatter behavior of corn on sandy loam.

23. August 1991 (day 235)

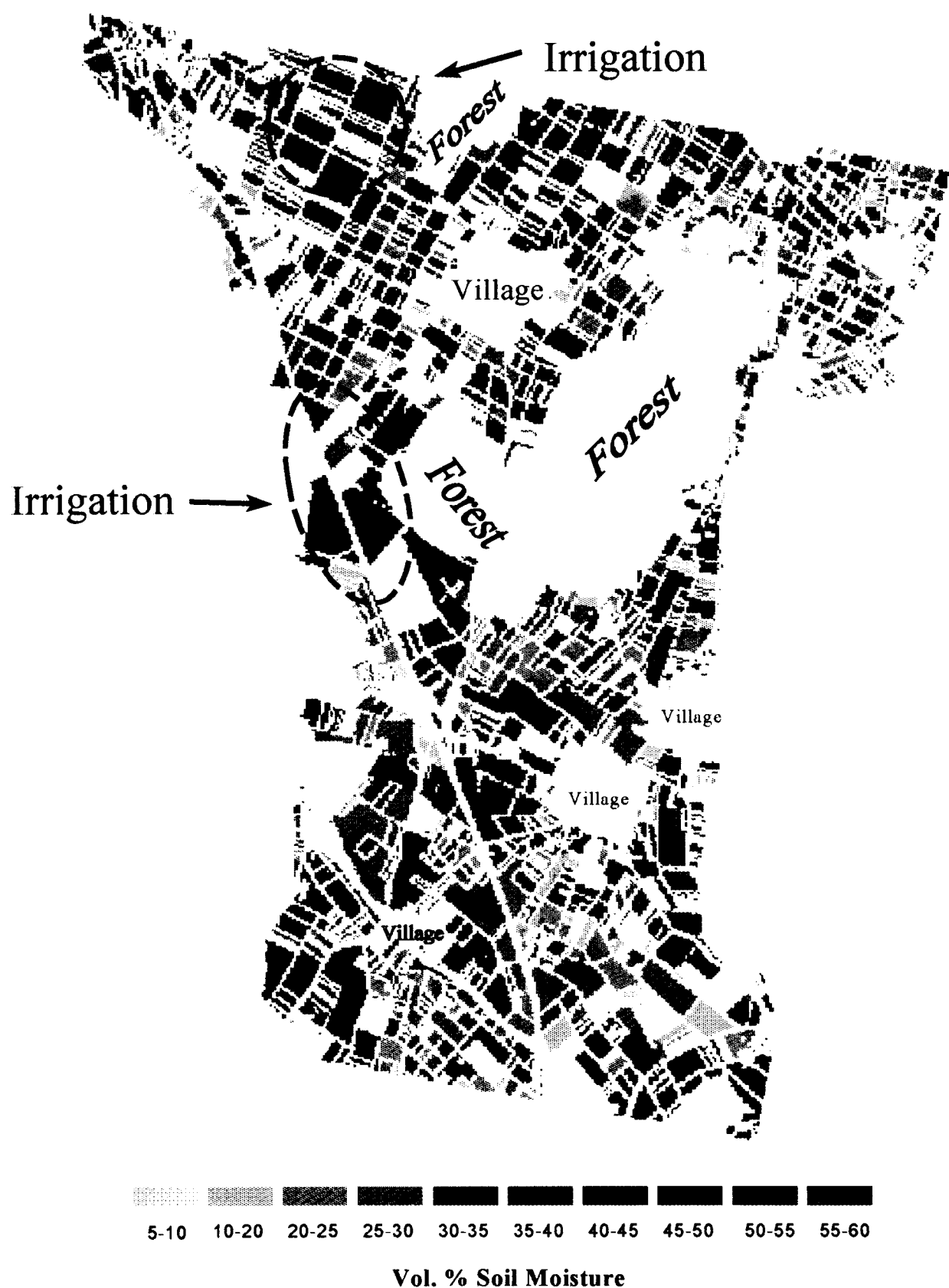


Fig.10: Distribution of reference surface-moisture for corn, winter-barley, summer-barley and meadows on different soils determined using ERS-1 backscatter values for Aug.23, 1991.

25. September 1991 (day 268)

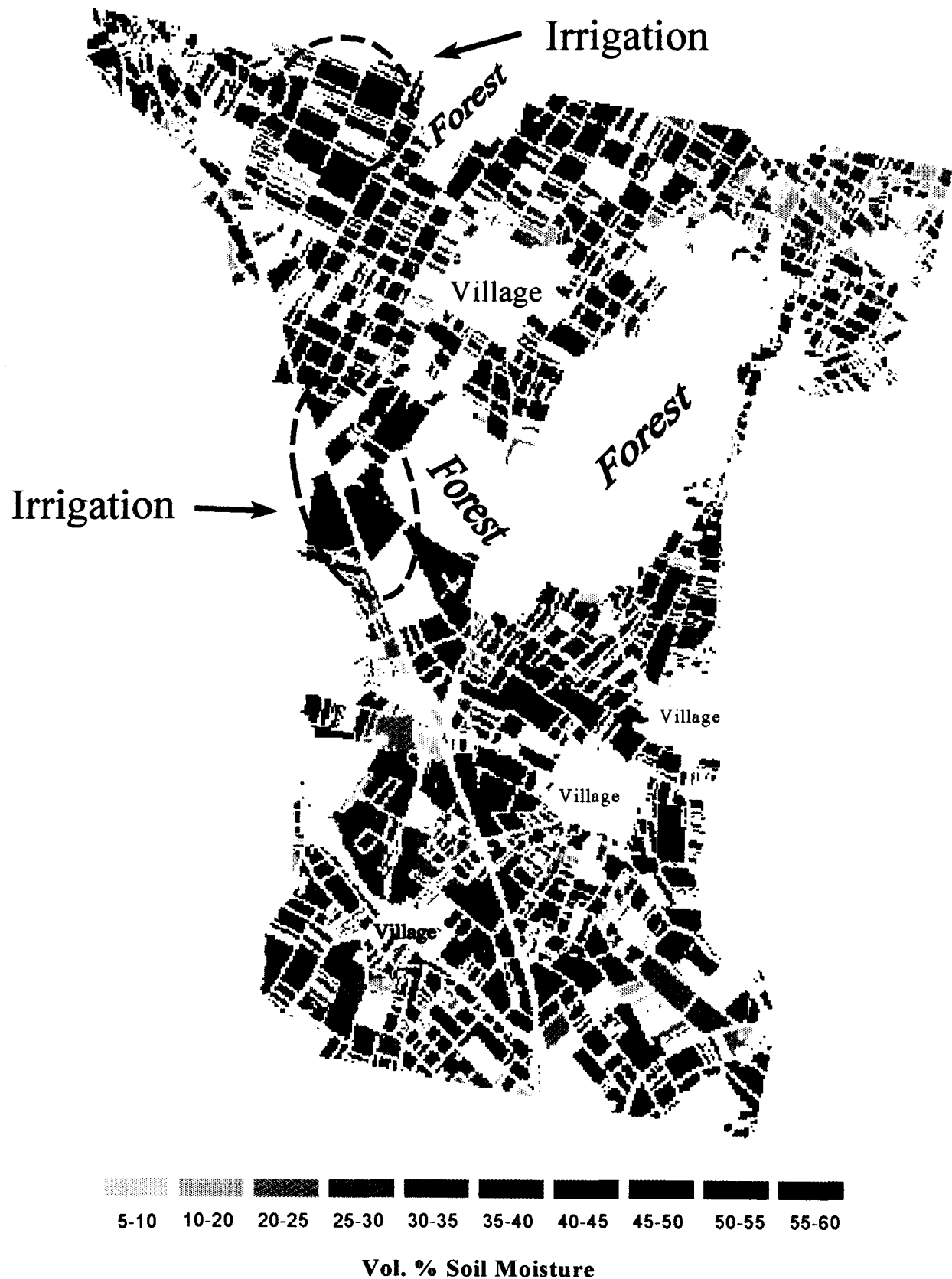


Fig.11: Distribution of reference surface-moisture for corn, winter-barley, summer-barley and meadows on different soils determined using ERS-1 backscatter values for Sept.25, 1991.

30. November 1991 (day 334)

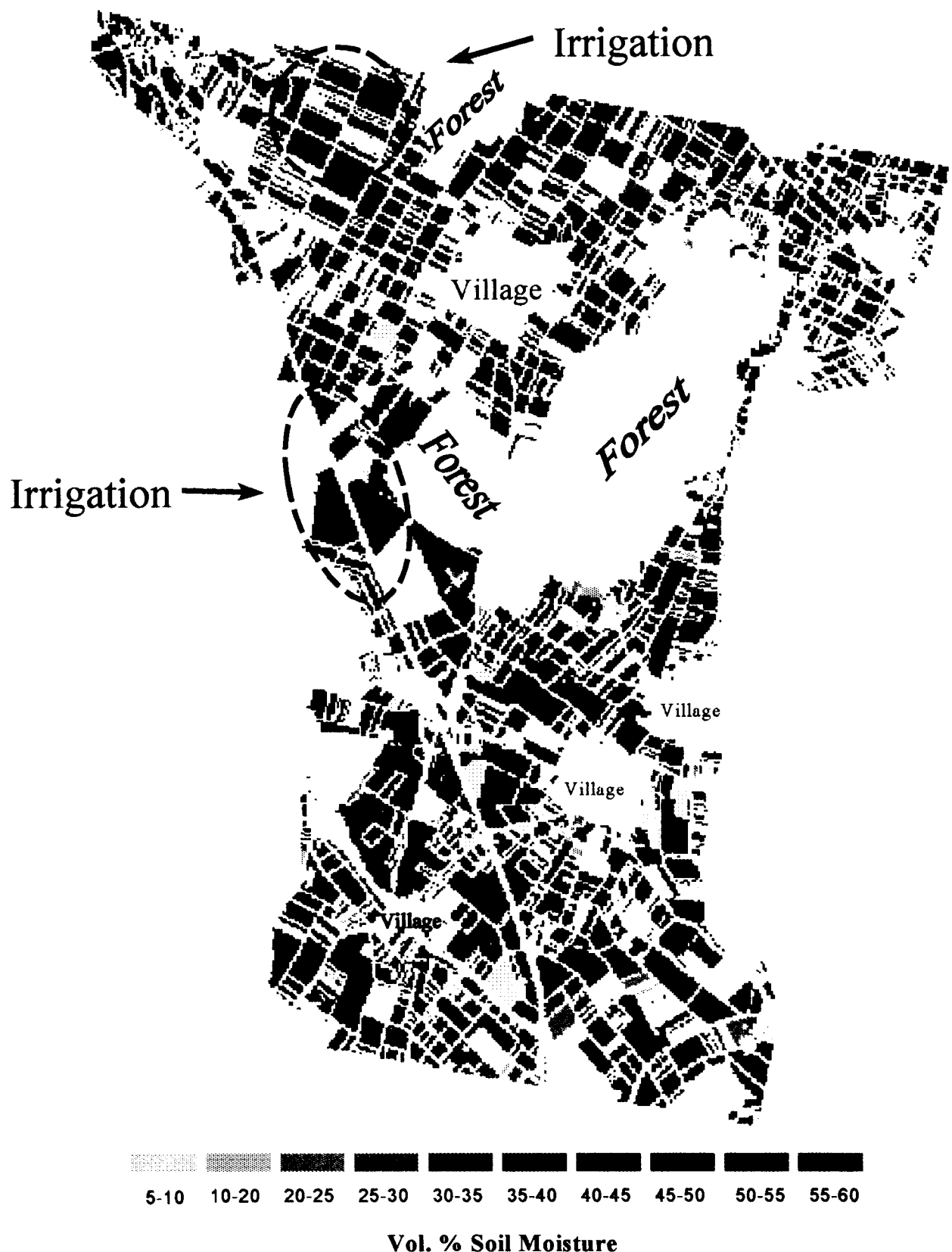


Fig.12: Distribution of reference surface-moisture for corn, winter-barley, summer-barley and meadows on different soils determined using ERS-1 backscatter values for Nov. 30, 1991.

In Fig.11 the reference surface-moisture distribution of Sept. 25, 1991 (day 268) is shown. The situation at this date is characterized through a strong rainfall event after a longer period of dry weather. The evapotranspiration capacity is strongly reduced at this time of the year due to mature corn plants and a lack of energy. Therefore a general increase in reference surface-moisture can be identified on almost all fields. Grassland, which is physiologically still able to transpire at the low temperatures encountered during this period shows the tendency to have lower reference surface-moisture values. The former irrigated fields, which at the date of this image have not been irrigated for at least 2 weeks still show more moisture but the effect is much less evident than in Fig.10. Fig.11 shows some similarity with the map of the soil types (Fig.2) in that fields with high reference surface-moisture tend to be located where the heavy soils (strongly sandy loam to loamy clay) are, whereas the low values of the reference surface-moisture can preferably be found on the light soils (sand to loamy sand). This might be due to differences in the soil permeability. The heavy soils have a lower permeability. This causes, that the water cannot be drained as quickly as in sandy soils and stays at the surface. The light soils drain the water much faster and leave a drier surface shortly after a rainfall event.

Fig.12 shows the distribution of the reference surface-moisture distribution on Nov. 30, 1991 (day 274) and can be considered the end-point of the spatial and temporal dynamics of the surface-moisture development of 1991. In October the available energy for transpiration has fallen to almost zero, the plant growth has almost stopped and the preceding rainfall events have filled the soil-moisture reservoirs. Therefore a homogenous distribution of the reference surface-moisture can be expected since the differences due to plant cover and soil-type have been equalized. The dominant reference surface soil-moisture lies between 40 and 50 Vol% and is therefore very close to saturation (for a sandy loam). Differences due to land-use and irrigation practices cannot be detected.

The interpretation of Fig.10 to 12 has shown, that the spatial distribution of the reference surface-moisture is in accordance with many features, which can be expected. The most striking effect is the detection of irrigated areas in August and a coincidence of soil features and surface-moisture in September. Nevertheless many features are difficult to interpret and evaluate since experience with such detailed surface-moisture distribution maps is very sparse.

CONCLUSIONS

The following conclusions can be drawn:

- it has been shown using a time-series of 28 ERS-1 images of the Commissioning Phase, that there is a strong dependency of ERS-1 backscatter on measured surface soil-moisture over different plants and soils.
- a statistical analysis of the influence of land-use and soil-type has shown, that there are distinct differences between the backscattering behavior of different plant canopies on different soils. The differences can be compensated linearly and have been quantified. They should be input to backscattering models, which should be used to physically explain the detected differences.
- A method has been demonstrated to statistically compensate the differences in backscatter of different fields due to land-use and soil-type using GIS-based analysis. The method determines a reference backscatter for each pixel, which is the original value equalized to the behavior of a corn field on sandy loam. This method in conjunction with soil-moisture measurements on the surface of one reference field allows to determine the spatial distribution of a reference surface-moisture.

The reference surface-moisture as defined in this paper is a value, which can be determined quite easily even on larger agricultural areas if the relations, which have been found in this study, prove to be stable. It is a parameter of potentially high practical value because it is closely related to the soil-suction in the top layer of the soil. The soil-suction is an even more important parameter than the soil-moisture since it determines the availability of water for the plant and to a large extent the actual infiltration capacity, which is one of the key parameters for a proper forecasting of floods. Although studies of this kind are quite laborious, continued effort should be put into stabilizing the relations, which have been found for different plants and soils and in modelling efforts to explain the differences in temporal backscattering signatures of different soil-surface complexes.

ACKNOWLEDGEMENT

The authors wish to thank the Deutsche Agentur für Raumfahrtangelegenheiten (DARA) for making this study possible through their funding of the project "Land-Use, Pedology and Soil Moisture from Multitemporal ERS-1 Data". The authors also wish to thank ESA for providing the necessary ERS-1 images through its PI-program.

REFERENCES

- Bernard, R., Martin, PH. (1982): C-Band Radar for Determining Surface Soil Moisture, *Remote Sensing Enviroment*, N° 12, 189-200.
- Bruckler, L., Witono, H., Stengel, P. (1988): Near Surface Soil Moisture Estimation from Microwave Measurements, *Remote Sensing Enviroment*, N° 26, 101-121.
- Demircan, A., Rombach, M., Mauser, W. (1993): Extraction of Plant- and Soil- Parameters from Multitemporal ERS-1 SLC-Data of the Freiburg Testsite, *Proceedings First ERS-1 Symposium Cannes 1992*, ESA SP-359, Vol. II 631-634.
- Mauser, W., Bach, H, (1993): FAP - Flächendaten Analyse Programm, Ver. 2, Institut für Geographie, Lehrstuhl für Geographie und geographische Fernerkundung, LMU München, 182p.
- Rombach, M., Kellndorfer, J., Mauser, W. (1993): Application ariented Requirements to SAR-Data Calibration - The Soil Moisture Case, *Sar Calibration Workshop Noordwijk 1993*, ESA WPP-048, 9-12.
- Rombach, M., Demircan, A., Mauser, W. (1994): Correlation between Soil Moisture and the Backscattering Coefficient of ERS-1 Data, *Proceedings Second ERS-1 Symposium Hamburg 1993*, ESA SP-361, Vol. II 861-864.
- Ulaby, F.T., Batlivala, P.A., Dobson, M.C. (1979): Microwave Backscattering Dependence on Surface Roughness, Soil Moisture and Soil Texture, Part I, Bare Soil; *IEEE Trans Geosci. Electron.*, GE-16, pp.286-295
- Ulaby, F.T., Bradley, G.A., Dobson, M.C. (1979): Microwave Backscatter Dependence on Surface Roughness, Soil Moisture and Soil Texture, Part II - Vegetation Covered Soil, *IEEE Trans Geosci. Electron.*, GE-17, pp.33-40
- Wooding, M.G., Griffiths, G.H., Evans, R. (1993): Temporal Monitoring of Soil Moisture Using ERS-1 Sar Data, *Proceedings First ERS-1 Symposium Cannes 1992*, ESA SP-359, Vol. II 641-648.



APPLICATION OF ERS-1 DATA FOR THE STUDY OF SOIL CONDITIONS IN SURINAME.

Viana A. Achthoven

Universiteit Gent
Laboratory for Regional Geography and Landscape Science
Krijgslaan 281 S8 A1 / 9000 Gent / Belgium / Tel.: +32 9 264709 / Fax.: +32 9 2644985
e-mail address : Viana.Achthoven@rug.ac.be

Abstract.

Poor drainage in most soils of the study area, delivers a major constraint for sustainable agricultural development. It's origin, macro drainage and even more important, as in this case, the on farm drainage. Hence the strongly heterogenous soil conditions and lack of a coherent, coordinated spatial data base, an on farm drainage is complicated. There is a need for proven land use planing. A clear insight of the drainage problem, an improvement and enhancement of the drainage can lead to a contribution to a sustainable land suitability. This will be performed in terms of a partial fulfillment of a land evaluation procedure for sustainable agriculture assessment in this area. The behaviour of soil moisture and the internal soil drainage can provide information about the strongly correlated soil conditions, liable to pedogenetic processes as well. Monitoring and identification of relevant features responsible for the internal soil drainage, water stagnation and vulnerabilities are therefore relevant. The approach and preliminary results of an ERS-1.SAR.GEC image, detailed observations in a sample strip of the study area and other available data sets, will be presented.

1 Introduction.

Soil moisture is the temporary subsurface storage of precipitation, often limited to the zone of aeration, that approximately coincides with the root zone. From the soil, the soil moisture will either be returned to the atmosphere, temporarily stored in surface vegetation, or will percolate to the phreatic (saturation) zone and eventually be transmitted to surface channels as streamflow. Soil moisture has a highly variable quantity often resulting from the inhomogeneity of soil properties, topography, land cover; and is difficult to measure in a way that is representative for a large area. ERS-1 SAR have great potentials to provide representative areal estimates rather than point measurements. The spatial and temporal information derived from the SAR images, coupled with direct measurements of hydrologic variables such as soil

moisture may lead to complete new model parameters or entirely new types of data.

2. Test site.

The area lies in the coastal plain of Suriname, with Greenwich geographic coordinates $5^{\circ}47'03''$ N - $5^{\circ}36'09''$ N, $55^{\circ}27'17''$ W - $55^{\circ}12'19''$ W. The test site is a gently undulating landscape, characterized by broad plains, also referred to as plates, low to moderate high ridges, depressions and filled up erosion gullies. It shows a remarkable feature within each landscape element or even - subelement, known as microrelief. Except the filled up erosion gullies, the profiles consist mainly of a varying thickness of very fine sand on loam on clay profiles. Especially in the long rainy season the poor drainage is expressed by flooded areas and extensive puddles. Monitoring of the soil moisture availability can be an short-time indicator of the origin of the problem encountered.

3. Approach.

The most important factors that determine the backscatter of soils are the geometric - (slope and surface roughness) and the electrical properties. The dielectric properties are defined by the dielectric constant, which has a strong influence on the backscatter. The dielectric constant, ϵ , is a complex parameter (also known as the complex permittivity) consisting of a real component, ϵ' , the permittivity of the material, and an imaginary part, $i\epsilon''$, the dielectric loss factor :

$$\epsilon = \epsilon' - i\epsilon''$$

The dielectric constant of a soil depends, among others on the soil moisture content. The complex dielectric constant increases with an increase of the moisture status of the soil. The theoretical basis of measuring soil moisture by microwave techniques is based on the large contrast between the dielectric properties of liquid

water and dry soil. The large dielectric constant for water results from the water molecule's alignment of the dielectric dipole in response to an applied electromagnetic field. The dielectric constant of water is 80 compared to that of dry soils, which is in the order of 3 to 5. As soil moisture increases, the dielectric constant can increase, even to a value of 20 or more, depending on the soil texture, amongst others. Figure 1. illustrates the change of the dielectric constant for several microwave frequencies.

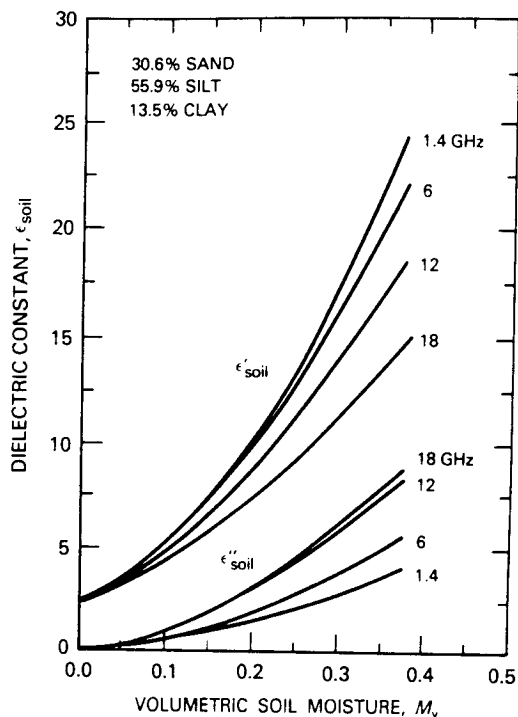


Figure 1. An illustration of the real and imaginary parts of the dielectric constant as a function of the volumetric moisture content for a loamy soil measured at four frequencies (after Ulaby et al., 1986)

The measured radar backscatter is made up of the backscatter of the vegetation, soil and attenuation, caused by the vegetation canopy. The backscatter of the soil is related to the surface roughness, the soil moisture sensitivity and the volumetric soil moisture. With change detection it is assumed that the only target change occurring; is the soil moisture, since it minimizes the impact of target variables such as soil texture. This means that with an ERS-1 multi-look dataset, which has a constant inclination angle of 23°, the backscatter relationship with the soil moisture is linear. Unknown parameters of the linear notation can be solved with linear regression. Striking is also that the changes in soil moisture are more important than the actual absolute value of soil moisture.

4. PREVISION, RESULTS AND DISCUSSION.

It is desired that at least two more covering ERS-1 scenes will be provided. By means of multi-look techniques it will be possible to obtain more information. Also colour composites will give interesting outputs.

Hereby all the objectives of the research can be reached.

Since the poor drainage of this area has a complex origin, the hypothetical approach towards this research is that the soil water management is determined by :

- The strongly correlated soil physical properties; the geogenetic and pedogenetic processes might have an impact on the water, especially in the rainy season.
- The topographic interrelation within the extremely variable landscape.
- The rainfall distribution and other climatic parameters.
- The human impact; i.e. inadequate removal of the stagnated water without taking the consequences into consideration.
- Other attributes, like civil engineering aspects, will not be considered or will be considered as having no limitation in this context of the study.

The area consists of a flat to almost flat very low land with Holocene marine and fluvio-marine fine -and coarse sediments of the young coastal plain and an almost flat low land with Pleistocene marine fine - and coarse sediments of the old coastal plain with erosion gullies, which are filled up with Holocene marine fine sediments. Derived from visual image interpretation and pixel information from the ERS-1 SAR image as well as the ground truth information, the following can be stated:

Different grey levels and random brightness can be observed and mostly, a micro texture. The structure of the roads can be distinguished, because of the light tone due to the strong radar backscatter signal of the roofs of the houses along the roads. The obvious dark tone of the Saramacca river and in the forested zones a slightly rougher texture can be observed, due to a combination of the radar illumination and the tree shadowing, a kind of spatial variability.

Areas that are very poorly to poorly drained, superficially to almost ripened mucky clay or - clay with a peat layer, shows a lighter tone (high intensity of the backscattered signal), have a thick diffuse double layer, a high water holding capacity and moisture content and a lower electrical conductivity. Striking is that from representative soil profile pits, the following can be interpreted from the laboratory analyses :

- The measured electric conductivity, Ec, is low (<=20) when the texture contains, proportionally, more silt and clay.
- If compared to the silt percentage, the amount of clay is higher, the Ec is less low than mentioned above.
- The Ec is even higher (>20), when the sand content is high (>60%). Mentionable is that within the soil profile the utmost upper surface soil has a higher Ec, because of the moisture status in the root zone, as well as the subsurface soil, close to the groundwater table.

The lighter tones (low backscatter signal return) can be found in depressions and filled up erosion gullies of the Leleydorp landscape, in the gullies and filled up creeks

of the river landscape, in the mara landscape and in the swampy plains, the basins and filled up river course of the abandoned river landscape.

Darker tones represents the waste area of the aluminium refinery and the old bauxite mine, swamps, puddles and fields suffering from stagnated water. It is obvious that in the gently undulating landscape with a sand to sandy upper soil, darker tones are visible, indicating stagnated water in the lower parts. Here the variable topography has a higher slope percentage of 2 - 8 %, which corresponds to an elevation variation of 1 to 6 m. Important to mention is the occurrence of orthstein layers (hard pans) in the subsurface, due to podzolisations, in the surroundings.

Zooming gives an even stronger speckle effect. Since the speckle effect probably contains valuable information, it is important to have descending as well as ascending scenes of different orbits. Speckle can be reduced and extra information can become noticeable.

The most important issue in this scope is to design a data base. The data base serves to process, analyse, interpret and capture the data, linking the microwave phenomena and classified units by means of a geographical information system (GIS).

By modelling with the GIS real time capabilities, different alternative drainage scenarios will be created. The best solution for the encountered problem will be given with recommendations, implementations and validations as well.



Figure 2. Descending scene of an ERS-1 SAR image, orbit 4764, frame 3483 / 3501, 13 June 1992.

5. Conclusion.

ERS-1 SAR, all weather, provide high resolution images that characterizes the physical properties (morphology, roughness, dielectric properties, geometric shapes,etc.) of the surface, its cover and near subsurface volume. SAR's ability to discriminate between wet -, water bodies and dry surfaces, its response to soil moisture, to plant canopy and geometric structure, leaf moisture content and leaf area index, especially it has the potential for providing micro to macro-scale information about areas of standing water, soil moisture, vegetation and topography. The above stated makes it a very suitable mean for hydrological applications i.e. study wet land conditions and soil moisture conditions.

References

- ESA, 1992. ERS-1 system, 87pgs., Pam Vass (EOS) & Bruce Battrick (ESA).
- ESA, ESRIN and Eurimage, 1994. Optical to ERS-1 SAR : a cross-over course at ESRIN, Frascati.
- FAO, 1993. Radar imagery : theory and interpretation, 103 pgs., Rome.
- Ulaby, F.T., Moore, R.K. and A.K. Fung. 1986 Microwave Remote sensing : Active and Passive, Vol III, Artec House, Inc, Dedham.



USE OF ERS-1 SAR DATA FOR SOIL MOISTURE ASSESSMENT

K.Dabrowska-Zielinska, M.Gruszczynska, M.Janowska,
K.Stankiewicz, Z.Bochenek

Institute of Geodesy and Cartography
Remote Sensing and Spatial Information Centre,
00-950 Warsaw, Jasna2/4, Poland

ABSTRACT

The project has been carried out for grassland and some agriculture crops. The selected test site is located in western Poland. The area which is investigated is covered by large grassland flooded in the spring surrounded by agricultural fields. During the ERS-1/SAR overpasses the measurements of soil/vegetation variables as soil moisture, vegetation moisture, wet biomass, dry biomass, LAI, height of the vegetation were carried out in the 15 grass and 15 crop ground points. For the vegetation growing seasons of 1992 and 1993 the data from ERS-1 SAR obtained from ESA, for Pilot Project PL-4 and NOAA/AVHRR data were examined. The different soil vegetation condition during these two periods have manifested itself in backscattering values. It was considered that the relationship between backscattering coefficient and soil moisture is strongly dependent on surface roughness which was characterized by leaf area index (LAI) or height of the vegetation values.

The possibility of applying backscattering coefficient averaged for different blocks of pixels for soil moisture estimates was examined. The data from AVHRR/NOAA and Landsat TM were merged with backscattering coefficient values calculated from ERS1/SAR in order to distinguish different vegetation features. The relation between backscatter and the soil moisture index introduced as the difference between surface temperature and air temperature was presented. The roughness of the surface was discriminated using AVHRR/NOAA which was essential for the soil moisture examination using backscattering coefficient, because even for the same grassland, the roughness condition changed during the year. Considering this, we have obtained much better results.

1. INTRODUCTION

The investigation of the application of satellite remote sensing data to assess and monitor soil and vegetation variables over large agricultural areas have been undertaken by the Remote Sensing and Spatial Information Centre (OPOLiS) of the Institute of Geodesy and Cartography (IGiK) since 1987. The work has

resulted in the establishment of several relationships between information derived from satellite images and the state of vegetation development. In order to derive and predict information about the yield of grassland or other crops, information about soil moisture is essential. The method developed by OPOLiS is based on the application of NOAA/AVHRR data. However, the operational use of this method is hampered by the presence of frequent cloud cover which makes it difficult to acquire routine AVHRR observations. The instruments on the board of the first European Remote Sensing satellite ERS-1 give the opportunity to make operational observations of the agricultural surfaces independently of weather conditions. AMI synthetic aperture radar (SAR) instrument is of particular interest to the required investigations of soil moisture.

In order to estimate the utility of the ERS-1 SAR data for soil moisture assessment the analysis of the crop and grass backscatter profiles simultaneously with the profiles of various ground truth variables throughout a growing season was examined to determine their impact on backscatter signatures. The backscatter - soil moisture relationships have been undertaken according to various vegetation surface roughness conditions closely connected with the vegetation development stage. The results and discussion are presented in this paper.

2. TEST SITE DESCRIPTION

The selected test site is located in Western Poland, in the Obra Valley approximately 80 km south-west of Poznan. The area is covered with large areas of grassland which are flooded during the early part of the growing season and by agricultural fields with the following dominant crops: wheat, rye, barley, oat, rape, maize, sugar beet and potatoes. The crop types varied from 1992 to 1993 with the exception of two sites where winter rye and spring wheat were planted in both years. The first ERS-1 SAR images for each year were acquired (towards the end of May) when winter crops were in their heading or flowering stage, spring crops were in their tillering or jointing stage, root crops and maize were in their emergence or germination stage and grass in the flowering stage before harvest. The predominate soil types for crops are sandy and sandy loam and for grassland peat and muck. The growing

season of 1992 was affected by drought. The area of the test site is flat with small parts of the upland areas covered with coniferous or mixed forest.

3. GROUND TRUTH DATA

Throughout the growing seasons of 1992 and 1993 and simultaneously to ERS-1 descending overpasses the measurements of soil and vegetation parameters were carried out at 30 points, 15 grassland and 15 cropland. The parameters measured were:

- volumetric soil moisture (0-10,10-20,20-30 cm) [%]
- soil water potential (pF) (0-10,10-20,20-30 cm)
- wet and dry biomass [g/m²]
- gravimetric vegetation moisture [%]
- leaf area index (LAI)
- height of the vegetation [m].

These measurements were based on samples taken at the sites which represent the whole field. Also, surveys were undertaken to record crop type with their actual development stage and grass growing condition.

4. ERS-1 SAR DATA

ERS-1 SAR.PRI data acquired during the 35-day repeat orbit were obtained from ESA for Pilot Project PL-4. Backscatter coefficients for each ground truth points were calculated and averaged for blocks of pixels ranging from 3 x 3 up to 11 x 11 pixels. The ground sample point was placed in the middle of each block. Extracted data were used to investigate the effect of pixel sample size on measurements accuracy of backscatter signature over ground measurement points. This preliminary work indicated that for the crop covered points the block of 6 x 6 pixels and for the grassland the block of 8 x 8 pixels are required to give the minimum variability. Such backscatter signature values have been included in the subsequent data analysis.

5. RESULTS AND DISCUSSION

With the data from two consecutive years 1992 and 1993 it was possible to examine the backscatter differences for the same sites and crop types due to soil moisture differences. For the growing season of 1992 which was affected by drought the backscatter values for crops and grassland were significantly lower than in 1993, (Fig.1). For the grassland the backscatter differences varied from 1 to 5 dB between these two years. The difference in soil moisture of 22% (point 11) yields in difference of backscatter of 2.5 dB.

BACKSCATTER FOR GRASS 1992 AND 1993

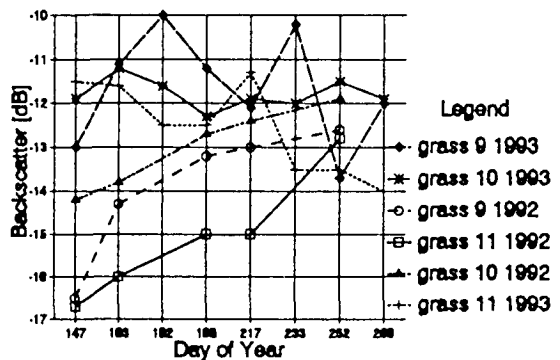


Fig. 1. Differences in backscatter for grass in the growing seasons of 1992 and 1993.

Figures 2,3,4 and 5 show the temporal profiles of backscatter and volumetric soil moisture for both growing seasons for winter rye and spring wheat. Because the crop type, soil type and site is the same, the lower values of backscatter signatures in 1992 were caused by lower values of soil moisture. Hot dry weather during the growing season of 1992 speeded up the crop development stages and ripeness of about two weeks which was confirmed by the displacements of the temporal profiles of backscatter for both years.(Fig.2 and Fig.4).

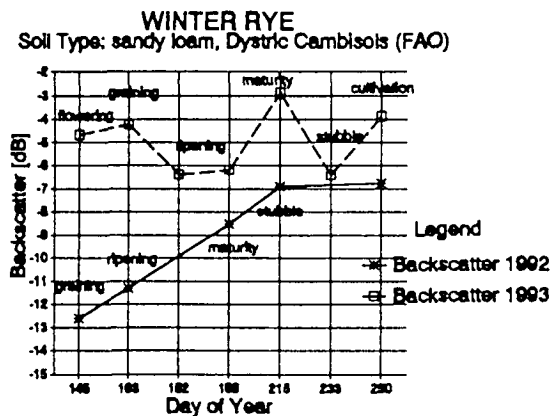


Fig. 2. Backscatter profiles for winter rye for 1992 and 1993.

During early stage of growing season (up to 163 Julian Day) root crops and maize showed a similar profiles of backscatter signatures mainly due to the influence of partially covered soil surface. During these early development stages backscatter decreased when soil moisture increased . For the winter crops and grassland the backscatter increased due to the increase of soil moisture (Fig.6). Two-way character of linear model of backscatter-soil moisture relationship was related to the differences in surface roughness.

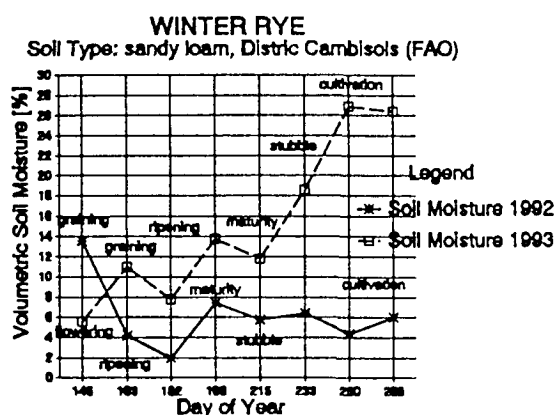


Fig. 3. Soil moisture profiles for winter rye for 1992 and 1993.

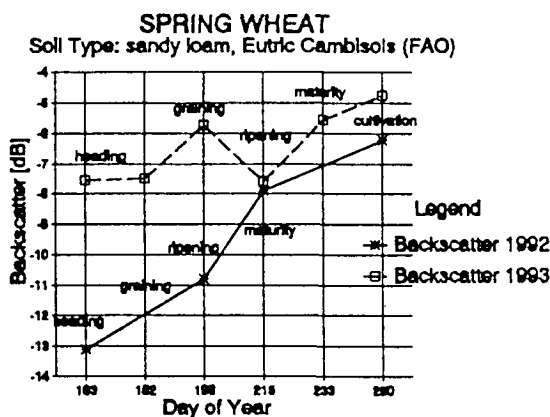


Fig. 4. Backscatter profiles for spring wheat for 1992 and 1993.

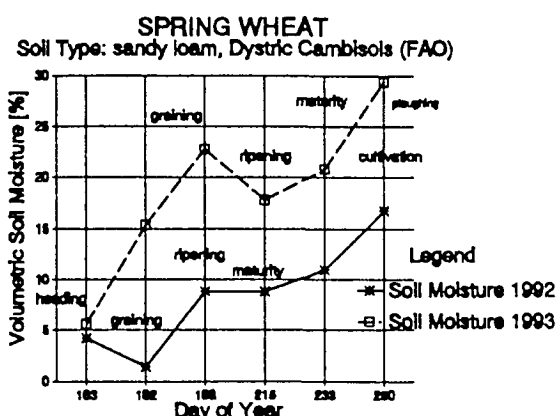


Fig. 5. Soil moisture profiles for spring wheat for 1992 and 1993.

BACKSCATTER FOR DIFFERENT CROPS 1993

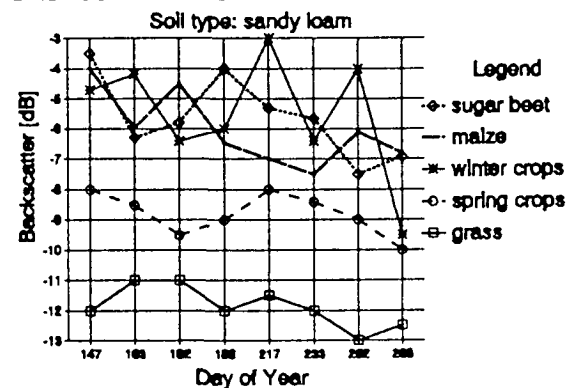


Fig. 6. Temporal backscatter profiles for different crops in 1993.

The grassland area was well distinguished on ERS-1 SAR image. The smooth surface of grass gave nearly the specular reflection and appeared in dark grey tone. The averaged backscattering coefficients values were from -11 up to -13 dB and differed from the other crops by 5-8 dB. The smallest differences in backscattering coefficient values appeared with spring wheat when the differences were c.a. 2-4 dB.

It was noticed that the relationship between backscattering coefficient and soil moisture is strongly dependent on the surface roughness. Even for the same type of vegetation the surface roughness was different. For the considered grassland the height of the grass varied from 0.10 to 0.80 m and LAI from 0.5 to 6.0. Also for the other type of vegetation like wheat the backscattering coefficient strongly depended on the crop growth stage which influenced different surface roughness. The similar results obtained Le Toan et al (1993). Therefore the relationship between backscattering coefficient and soil moisture (0-10 cm level) has been established within the values of LAI. Figure 7 presents the backscatter-soil moisture relationship for grass for the LAI values between 3 and 4. The backscattering coefficient ranged from -13 dB to -9.4 dB for soil moisture between 30 and 70%. For the increasing LAI values from 4.5 up to 6, higher values of soil moisture dominated. We found that the relationship for grassland was stronger for higher LAI values which corresponded to smoother surface. For the small values of LAI between 0.5 and 1.5 higher backscatter corresponded to smaller values of soil moisture (Fig.8). In this case the soil moisture was very small for this grassland area. The dominant role played vegetation moisture. Even for one date, i.e the 17th July 1992 the LAI values of the grass area varied from 0.4 to 3.0. The distribution of LAI values is presented on Map 1 of Landsat TM image. The Leaf Area Index corresponded to soil moisture conditions represented by surface temperature recorded by TM, channel 6. The lower soil moisture (17%) corresponded to the difference in surface and air

temperature of 6.9°C and backscatter of -14.3 dB , the smallest difference i.e. 2.4°C corresponded to -9.4 dB of 29% of the soil moisture. (Fig. 13)

The similar relationship was presented for backscattering coefficient and difference of surface temperature and air temperature for AVHRR/NOAA image. The backscattering coefficient was averaged for each NOAA pixel and related to the difference between surface temperature corrected for atmospheric water content and air temperature. Higher values of the difference corresponded to lower values of the backscattering coefficient, Fig.14. For each AVHRR pixel evapotranspiration was calculated using energy budget equation. Higher values of evapotranspiration represented area of higher moisture what gave higher values of backscattering , while lower values of evapotranspiration $70-110 \text{ W/m}^2$ corresponded to lower values of backscatter (-11.5 dB), Fig 15. The information about soil moisture using AVHRR surface temperature was much more efficient than the random soil moisture samples.

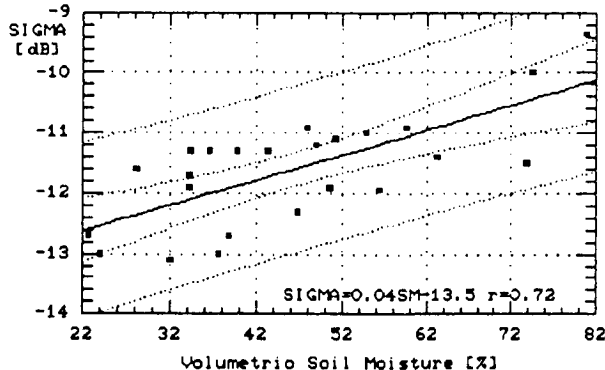


Fig. 7. Backscatter-soil moisture (0-10 cm) relationship for grass (LAI 3-4).

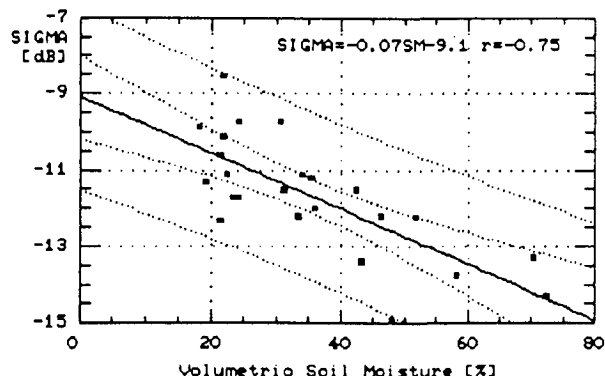


Fig. 8. Backscatter-soil moisture (0-10 cm) relationship for grass (LAI 0.5-1.5).

It is presented on Figure 9 that the spring wheat with the same LAI values as grass ie. 2.3 to 3.5 could also be considered for establishing the relationship between the backscatter and soil water potential together with the

grass. We applied soil water potential to eliminate the influence of soil type which varied for both plots.

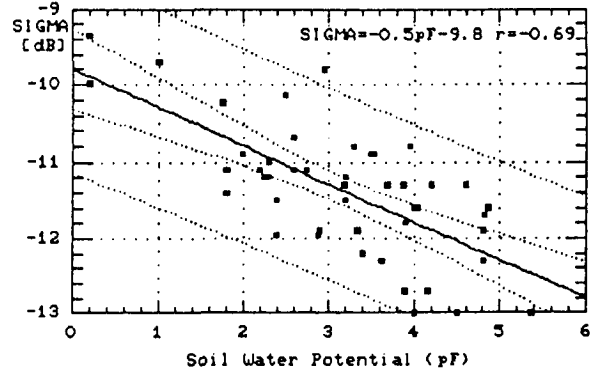


Fig. 9. Backscatter-soil moisture (0-10 cm) relationship for grass and spring wheat (LAI 2.3-3.5).

Figure 11 presents the information about backscatter, height of the grass, soil moisture and LAI for various points at the grassland. As it is shown the relationship between backscatter and soil moisture can be considered for the same roughness condition which is represented by different LAI and height values. For the point 5 and 7 when the height of the grass was the same i.e. 0.20 m the difference in soil moisture between these points corresponded to the difference in backscatter. While soil moisture values in points 2 and 7 was the same the backscatter differed due to the difference in LAI and the height of the grass.

Figure 10 represents the relationship between backscatter and soil moisture (0-10 cm) for spring wheat. During the time of ground measurements LAI values varied from 2.5 up to 3.5. With the increasing soil moisture values, the backscatter values increased which gave the good positive correlation.

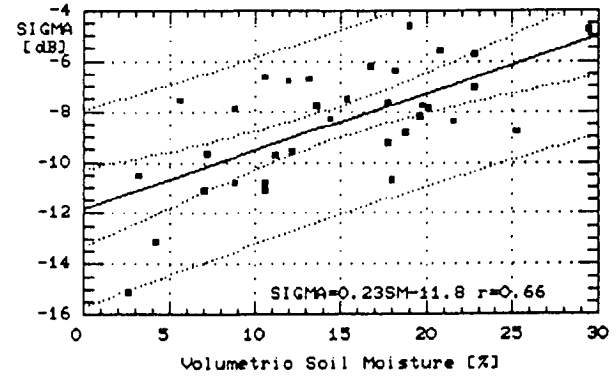


Fig. 10. Backscatter-soil moisture relationship for spring wheat.

Figure 12 presents the relationship between backscatter and soil moisture (0-10 cm) for the sugar beet. Backscatter values between -4 and -7 dB represented low values of the soil moisture i.e. 12%, while soil moisture between 18 and 23% has been represented by backscatter values from -14 to -16 dB . The

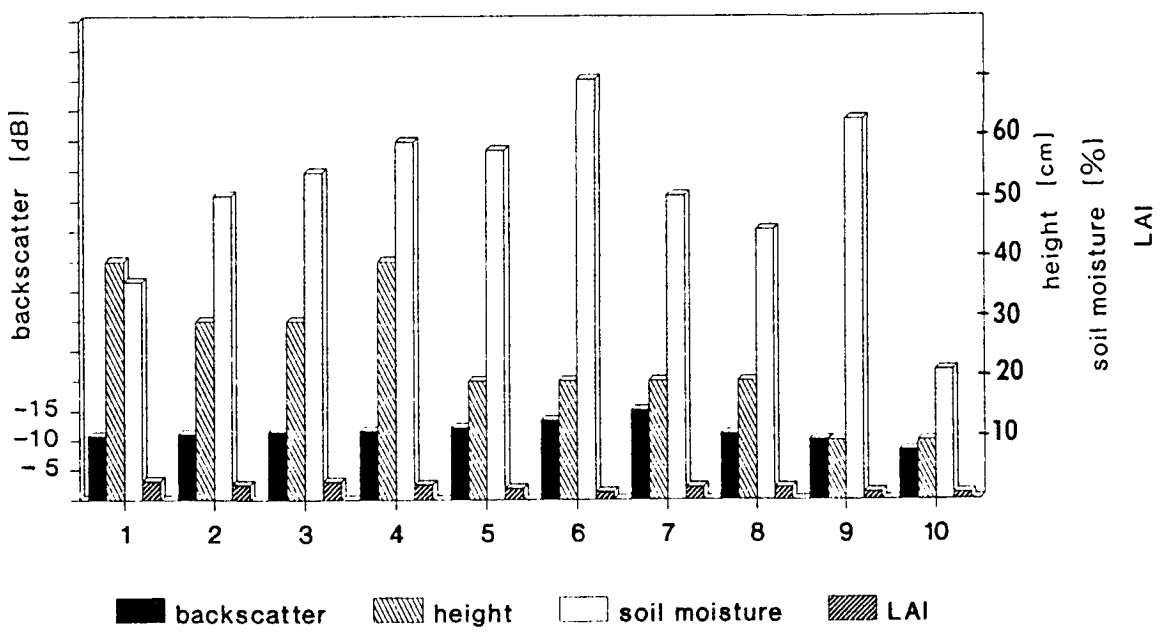


Fig. 11. Different grass condition.

measurements concerned the first and the last stages of sugar beet growth when the vegetation was sparse and the surface was rough and dry. Such condition gave good negative correlation.

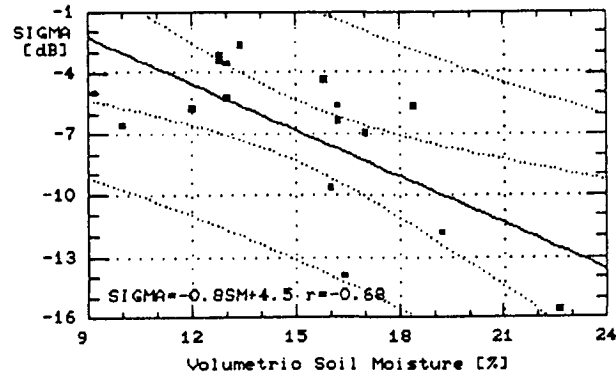


Fig. 12. Backscatter-soil moisture relationship for sugar beet.

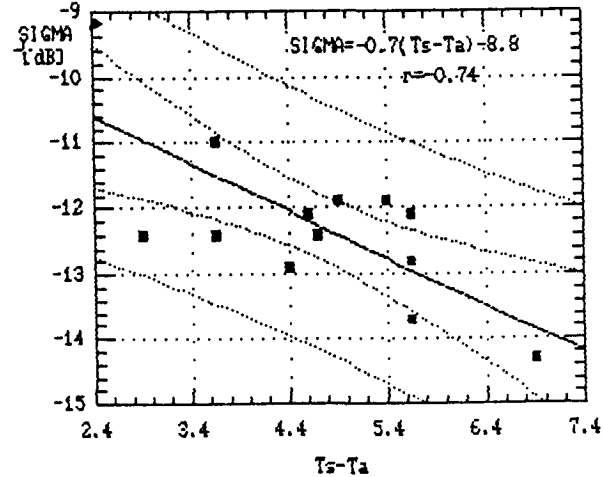


Fig. 13. The relation between $[Ts(TM) - Ta]$ and backscatter.

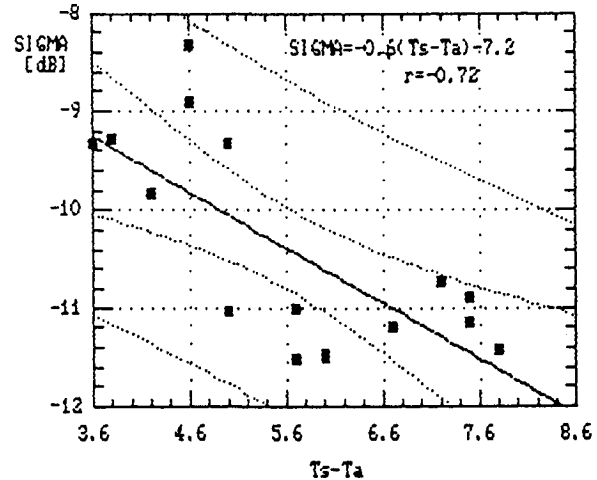


Fig 14. The relation between $[Ts(AVHRR) - Ta]$ and backscatter

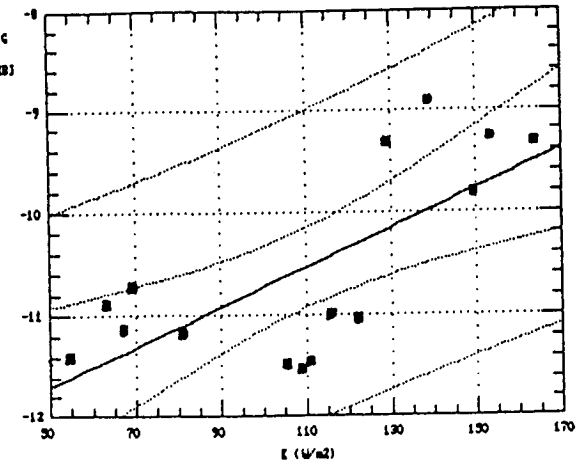


Fig 15. The relation between Evapotranspiration (AVHRR) and backscatter

6.CONCLUSIONS

The surface roughness and soil moisture influence the ERS-1 SAR backscatter signatures. When the soil was covered with vegetation leaf area index (LAI) could represent the surface roughness. For different vegetation roughness during crop developing stages there was not straight relationship between backscatter and soil moisture. The assessment of soil moisture in the depth of 0-10 cm can be considered from backscattering coefficients derived from SAR images for the distinguished vegetation roughness classes.

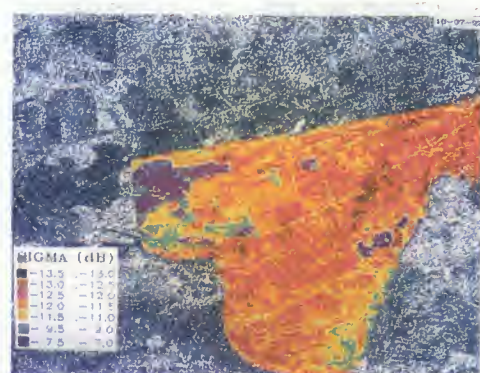
Also the relation was examined between backscatter and soil moisture indicator which was presented as the difference between surface temperature and air temperature and evapotranspiration derived from TM and AVHRR data. These soil moisture indicators were considered as better than random ground soil moisture measurements.

ACKNOWLEDGEMENTS

The authors want to acknowledge prof. A. Ciolkosz for the scientific discussion, our colleagues from the OPOLIS: St. Lewinski, I. Malek, Zb. Goliaszewski for the assistance and A. Kijowski who provided us with the soil parameters data.

REFERENCES

Le Toan, T., P.Smacchia, J.C. Souyris et al 1993. On the retrieval of soil moisture from ERS-1 SAR data, Proceedings of the Second ERS-1 Symposium, Hamburg, Germany:883-889.



**MULTI-TEMPORAL ERS-1 SAR DATA IN ENVIRONMENTAL STUDIES:
RESEARCHING A QUANTITATIVE APPROACH FOR SOIL MOISTURE
RETRIEVAL.**

**PILOT PROJECT : PP2-F4
SERTIT-STRASBOURG**

Kader Fellah*, Yves Besnus**, Stephen Clandillon*, Abdelkebir Ettajani*, Colette Meyer*, and Paul de Fraipont*.

* SERTIT, Boulevard Sébastien Brant, 67400 Illkirch, Tel : (33). 88.65.52.00, Fax : (33).88.65.51.99.
** LSIIT/GSTS, Boulevard Sébastien Brant, 67400 Illkirch, Tel : (33).88.65.50.44, Fax :(33).88.65.51.53.

ABSTRACT

Using a regional database, containing optical and ERS-1 SAR satellite imagery, plus data layers treating different aspects of the natural environment, this study involves evaluation studies on the potential of SAR data in the analysis, and in time the agro-environmental monitoring of rural areas. The study's application area, the Ried Centre Alsace, France, situated in the upper Rhine Valley, is heavily influenced by water. Following the analysis of temporal signal variations vis-à-vis their acquisition conditions and vegetal cover changes, the objective is to determine the relationship between the backscattering coefficient and volumetric soil moisture, while accounting for landuse differences. The results, as obtained, demonstrate that the possibility exists of isolating this fundamental parameter for use in natural area studies and, therefore, open a number of application domains to ERS-1 SAR data.

RESUME

A partir d'une base de données régionale comprenant des données satellitaires optiques et SAR ERS-1 ainsi que divers plans d'information sur le milieu naturel, cette étude s'intègre dans des travaux d'évaluation des potentialités des données SAR pour l'analyse et, à terme, le suivi agro-environnemental des milieux naturels. Elle s'applique à une région fortement influencée par l'eau, Le Ried Centre Alsace, situé dans le bassin du Rhin supérieur. Après l'analyse des variations temporelles du signal en fonction des conditions d'acquisition des images SAR et des évolutions temporelles du couvert végétal, l'objectif de ce travail est de déterminer en fonction des thèmes d'occupation du sol, les relations existantes entre le coefficient de rétrodiffusion et l'humidité des sols. Les résultats obtenus montrent la possibilité d'atteindre ce paramètre fondamental pour l'étude des milieux naturels et ouvrent des champs d'applications multiples pour les données du système SAR d'ERS-1.

Remerciements,

Ce programme a été mis en oeuvre et enrichi grâce au Conseil Régional d'Alsace, et au Centre National d'Étude Spatiale, qui contribuent à son financement, à l'Agence Spatiale Européenne qui procure toutes les facilités pour la fourniture des données SAR et grâce à la contribution de Méteo France, du Service des eaux et des milieux aquatiques d'Alsace et de l'Institut National de la Recherche Agronomique de Colmar, pour la fourniture de diverses informations nécessaires à la constitution de la base de données relative aux milieux naturels de la région étudiée.

The Study Area

The study area, the Ried Centre Alsace, is situated between Strasbourg and Colmar on the Alsace plain. It is strongly influenced by water, it being in the flood zone of the Ill, a Rhine tributary, and beneath it contains the largest fresh water aquifer in Europe. After canalisation of adjacent rivers, an intensification of agricultural practices has occurred that has led to environmental changes, changes that the authorities wish to evaluate and control (sensitive biotope protection measures, CAP, land set-aside).

This work lies within this context and is aimed at evaluating the potential use of these new satellite data in the understanding, management, and protection of this sensitive biotope.

The investigated parameter: Soil Moisture

The definition of soil moisture varies according to the spatio-temporal reference scale :

- instantaneous, volumetric, water content : a punctual physical measurement ;
- potential soil water retention : a local agronomical parameter ;
- hydrological moisture environment : a general environmental factor.

The aim of this study is to establish a quantitative relationship between the backscattering coefficient and instantaneous volumetric soil water content. In fact, the radar signal has the capacity to traverse vegetation cover and soil whereupon it is influenced by the soil's dielectric properties. It was demonstrated (Refs. 1, 2, 3, 4) that the soil layers close to the surface have the most effect and that a decimetric depth, adopted by researchers, seems to be a good compromise given differing moisture gradients.

1. DATA BASE

The programme's first stage involved the building of a large data base aimed at isolating information relating to soil moisture by dissociating and evaluating the importance of the parameters that affect radar signal return. The data base contains ERS-1 radar and optical satellite data, plus exogenous data.

1.1 ERS-1 data

Two constraining factors influenced the choice of ERS-1 data :

- synchronisation with optical satellite data, so as to avoid important landcover modifications between acquisition dates;
- variations in surface soil moisture in order to observe its effect on RADAR images.

Meteorological data were used in choosing ERS-1 scenes (see Table 1) enabling the differentiation between moisture due to rainfall and that caused by other factors (soil moisture retention, water table, etc....).

Table 1 : ERS-1 SAR DATA

DATE	ORBIT/FRAME
14/04/92	3910/963
17/04/92	3946/2637
22/05/92	4447/2636
04/09/92	5950/2637
09/10/92	6451/2637
18/04/93	9192/963
04/05/93	9421/963
07/05/93	9457/2637
04/09/91	714/963
04/09/91	707/2637
19/09/91	922/2637
22/09/91	965/2637
04/10/91	1144/963
28/10/91	1488/963
28/10/91	1481/2637
21/09/93	11425/963
26/10/93	11926/963
29/10/93	11962/2637

1.2 Optical satellite data

ERS-1 synchronous, SPOT XS data allowed the realisation of a precise landuse classification. Thematic masks were defined per class (water, forestry, grassland, crops, urban) permitting the segmentation of the radar data. These images were then analysed per landuse theme with the double objective of investigating variations between and within SPOT landcover classes.

1.3 Exogenous data

1.3.1 Digital Terrain Model

A DTM realised for SERTIT by ISTAR using July 1990 SPOT stereoscopic image pairs was integrated into the data base.

1.3.2 Piezometry

Precise piezometric data were obtained from the SEMA (Service des eaux et des milieux aquatiques d'Alsace), these being weekly recordings from 47 wells in the study area. The measurements were integrated with the aim of mapping water table depths synchronous to ERS-1 data capture.

1.3.3 Pedology and substrate deposits.

Two 1/250,000 surface soil maps (grain size, plus genesis and carbonatation) were digitized. These documents were elaborated and amiably donated by H. VOGT. The surface formations are comprised of recent detritic fluviaatile and aeolian deposits that form the substrate and, consequently, the water table reservoir.

Furthermore, links with INRA researchers give us access to complementary cartographic information on soil characteristics including an Agricultural Ministry 1/100,000 document that maps soil moisture retention properties and a 1/50,000 soil map that have been incorporated into the data base.

This information will be used in future phases of the programme. They should permit the study of the radar signal variability with respect to soil nature.

1.3.4 Airphoto and field data

Four field study campaigns were carried out the 24-25/04/93, 29/05/93, 21/09/93 and the 29/09/93. These were followed by four air surveys the 27/04/93, 08/06/93, 20/09/93, and the 10/11/93.

The aim of these sorties were to estimate the state of agricultural landcover during ERS-1 acquisitions. These observations were carried out on fifteen representative test sites including large parcels, cropland, grassland, and forestry.

The observations consisted of taking ground and air photographs plus the noting of diverse characteristics:

- landuse practises;
- surface rugosity (furrows, ploughing, harrowing, ..) their orientation and periodicity ;
- vegetal growth stage;
- qualitative estimation of soil moisture and composition.

1.3.5 Meteorological data.

The two principal stations, Meyenheim and Entzheim, to the south and the north of the study zone, permit the measurement of numerous meteorologic parameters (temperature, precipitation, wind, etc ...). Rainfall measurements are taken every six minutes. These information guided the choice of ERS-1 data.

METEO FRANCE equally have other stations between the principal centres being either "automatic" or "human operated" where daily rainfall measurements are taken. With these data rainfall events occurring before ERS-1 scene acquisitions were spatially mapped.

2. PRE-PROCESSING OF ERS-1 DATA

The SAR GEC processing level was chosen in order to avoid geometric and cartographic problems which do not come under the guise of this project. The study area was extracted from the selected ERS-1 images, followed by the projection of the subset images from the World Geodetic System 1984, UT 32, to Lambert 1, to allow image superposition with the rest of the data base. The ERS-1 scenes were fully calibrated, meaning they were corrected for in-flight SAR antenna pattern and compensated for range spreading loss. Laur's method (Ref. 5) was used to derive the backscattering coefficient for the images.

Temporal signal variation

The data base includes ERS-1 scenes acquired in descending and ascending orbits. In order to enable the comparison of backscattering coefficients obtained for all scenes, it is important firstly to ascertain the stability of the signal and the influence of the incidence angle per theme considered. This was performed in a study where the determination of the backscattering coefficient was carried out on a large number of sample pixels.

Table 2: Difference between descending and ascending acquisitions the 28/10/91.

Landuse	Number of pixels (N)	Orbit Difference desc-asc(dB)
water	80,153	0.24
forestry	584,486	0.05
grasslands	168,136	0.08
crops	805,187	0.15
urban	175,101	0.86

For this, the ERS-1 scenes, acquired the 28/10/91, are particularly well adapted. In fact, that day, there were two acquisitions within 12 hours and no precipitation was recorded between these acquisitions. Therefore, the differences in backscattering coefficient observed are related to signal stability and incidence angle effects.

The results (Figure 1, Table 2) show that there is little difference between themes and that urban demonstrates the greatest divergence (+0,86 dB). This phenomenon can be put down to urban interior geometry provoking multiple reflections. The wind variations during the course of the day are responsible for the fluctuations of water's backscattering coefficient. Otherwise, the grasslands, forestry, and crops themes are very stable (cropland variation, 0.15 dB). This variation value difference is well below ESA's tolerance threshold (+0,45 dB, Refs. 5, 6).

A deduction from this backscattering coefficient stability would be that it is possible to define thematic signatures for areas of low topographic relief independent of path and incident angle.

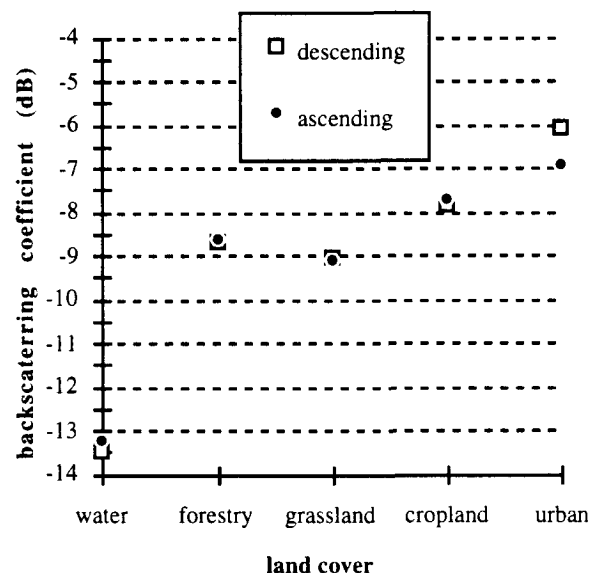


Figure 1: Backscattering coefficient per land cover at descending and ascending ERS-1 SAR Data acquisition the 28/10/91.

3. ANALYSIS

3.1 Analysis of the effect of landuse on the backscattering coefficient.

The SPOT derived landuse classification was used to segment the radar data with the theme by theme analysis being performed on the entire study area. The number of ERS-1 pixels per theme are shown in the table below.

Table 3: Number of ERS-1 pixels per land cover.

Land cover	N° of pixels
forestry	1,361,990
grassland	522,188
cropland	2,072,406

The aim of this analysis is to :

- calculate the differences between themes for the same acquisition;
- detect the variations of the coefficient at different temporal scales (seasonal, inter-seasonal, per year).

Figure 2 illustrates the backscattering coefficient's evolution with each acquisition.

To best explain the observed variations, an account must be taken of the pre-ERS-1 image acquisition meteorological data, as well as that of the state of vegetal growth.

The meteorological analysis was carried out in order to characterise soil wetness directly linked to antecedent precipitation.

The aerial observations permitted a precision on crop and grassland growth stages for each acquisition. Maize being the principal crop, it was, therefore, considered as the reference crop. Soil moisture conditions and crop evolutions are summarised in table 4.

Within each acquisition there is good discrimination seen between the different themes. The backscattering coefficient diverges more in autumn than spring for the themes grassland and cropland.

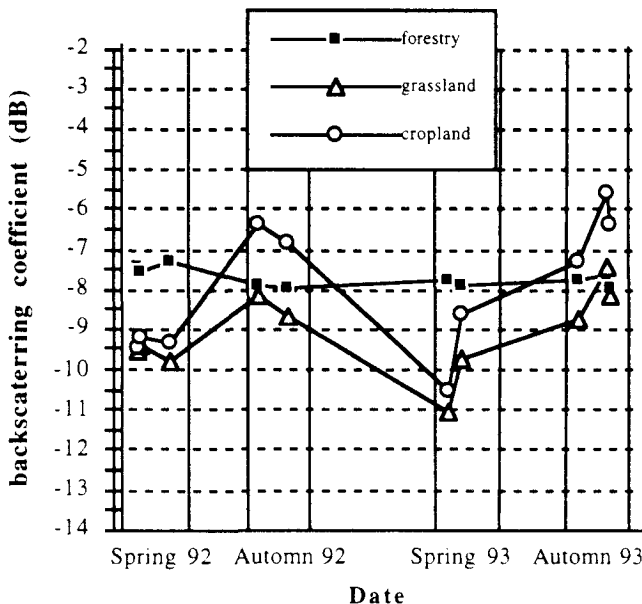


Figure 2 : Temporal backscattering coefficient variation with respect to landuse themes.

The backscattering coefficients for the cropland and grassland present the same temporal variations with the cropland variations being greater. Between spring and autumn, the backscattering coefficients for both grassland and cropland augment by 2dB and 3dB, respectively. In autumn, the cropland backscattering coefficient is greater than that of forestry. These variations are, in particular, explained by the evolution of the vegetal cover between spring and autumn. Forestry's backscattering coefficient remains quasi-constant, averaging -7,71 dB +0,22.

Equally, a backscattering coefficient variation for the grassland and cropland themes is observed in the case of temporally close acquisitions for which landuse would have no changed. The reason for these variations must be directly linked to soil moisture variations. This is the case in the following scene pairs: 14/04 and 17/04/92, 18/04 and 4/05/93, 26/10 and 29/10/93. This hypothesis is supported by the results shown in table 4.

The use of multitemporal ERS-1 data acquired at different stages of vegetal evolution allows a better discrimination between certain themes (Ref. 7). For example, the grassland and cropland themes are better differentiated in autumn than in spring. The good landuse discrimination evidenced by ERS-1 data shows that these data could be used to further complete and improve optical sensor, thematic classifications.

The effect that soil moisture has on the signal can be great and perhaps large enough to measure the variations in soil moisture.

Table 4: Moisture conditions and vegetal state before each ERS-1 acquisition.

Scenes ERS-1	Moisture Conditions	Vegetation state
14/04/92	homogeneously dry	- grass : 15-20 cm - cropland : baresoil
17/04/92	dry to moist, patchy	- grass : 15-20 cm - cropland : baresoil
22/05/92	dry with effects from showers	- grass : 40-50 cm - crops (maize: 30-45 cm)
4/09/92	slightly moist	- grass : 10-20 cm - crops (maize: 1.5-2.0m)
9/10/92	little moisture	- grass : 10-20 cm - crops (maize harvest)
18/04/93	dry to slightly moist	- grass : 15-20 cm - cropland : baresoil
4/05/93	moist, shower impact	- grass : 20-30 cm - cropland : baresoil
21/09/93	moist	- grass : 10-20 cm - crops (maize harvest)
26/10/93	very wet	- grass : 15-20 cm - crops (end of maize harvest)
29/10/93	moist	- grass : 15-20 cm - crops (end of maize harvest)

3.2 Analysis of the effect of a rainfall event on the backscattering coefficient.

According to WOODING (1994), BRISCO (1993) and TENG (1993), (Refs. 8, 9, 10) meteorological conditions affect the radar signal. The aim of this analysis is to pinpoint the sensibility of ERS-1 SAR image backscattering coefficients to the volumetric soil water content caused by a rainfall event. To accomplish this, the 14/04, 17/04 and 22/05/92 images were used. This completes the preliminary results obtained by FELLAH (1993) (Ref. 11).

3.2.1 Rainfall event mapping.

The 17/04/92 image was taken as a reference due to the abundance of rainfall preceding its acquisition and consequently the rainfall distribution was mapped with respect to the backscattering coefficient retaining the two themes grassland and cropland.

Twenty seven rainfall measurement stations were taken into account. In mapping rainfall occurrence before image acquisition, a summation of daily measurements, relating to the entirety of a preceding rain event, was calculated.

No rainfall occurred before the acquisition of the 14/04 scene. Conversely, three days of rainfall occurred before the 17/04 image was taken, principally concentrated in the preceding 48 hours. The rainfall sum before the 22/05 scene was negligible and occurred uniquely on the eve of acquisition.

Rainfall mapping was done through applying a fifth order interpolation polynomial (interval : 0.5 mm rainfall). It seemed reasonable to use a four zone regrouping for the reference date, the 17/04, in order to insure meaningful zonations. These zones were defined as follows:

- less than 6 mm rainfall : zone 1
- from 6.5 to 9 mm rainfall : zone 2
- from 9.5 to 12 mm rainfall : zone 3
- from 12.5 to 15 mm rainfall : zone 4

The average, precipitation per zone is shown in table 5.

3.2.2 Spatial analysis of the backscattering coefficient's distribution.

Firstly, the analysis was performed on the 17/04 scene, before which much rain fell, to allow a meaningful rainfall zonation to be established : this zonation was then used in the backscattering coefficient variation study. Secondly, the same analysis was carried out on the 14/04 and 22/05 images for which little rainfall was recorded beforehand.

Table 5: Average rainfall sum per zone occurring before each acquisition.

ZONES	Before the 14/04/92 (mm)	Before the 17/04/92 (mm)	Before the 22/05/92 (mm)
1	0,9	3,8	2,1
2	1,1	7,4	2,7
3	1,1	10,5	3,0
4	1,1	13,1	3,5

3.2.2.1 Analysis of the 17/04 ERS-1 scene

The backscattering coefficient was calculated for the grassland and cropland themes per rainfall zone.

Figure 3 demonstrates a regular rise in the backscattering coefficient comensurate with zones of increasing rainfall.

The cropland backscattering coefficient is slightly greater than that of the grassland theme by an average of 0.3 dB. The same type of variation is seen in both themes, noting here that at this time of year grass height is roughly 20 cm and that croplands are principally baresoil.

For an average rainfall sum of between 3.8 and 13.1 mm, the backscattering coefficient variation for cropland is very large (1.4 dB).

A very high correlation is seen between the backscattering coefficient and the average precipitation levels for the four zones.

In order to test for any rainfall independent, geographical effects, similar measurements were performed on the same zones taking in this case the 14/04 and the 22/05 images, which were unaffected by large preceding rainfall events.

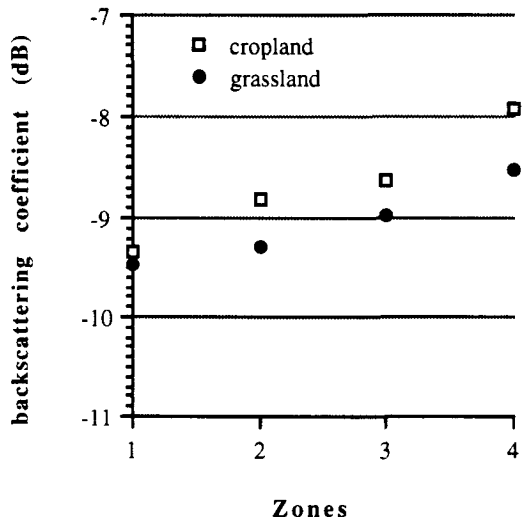


Figure 3 : 17/04/92 scene. Backscattering coefficient variation according to increasing rainfall for the grassland and cropland themes.

3.2.2.2 Analysis of the 14/04 ERS-1 scene

The analysis of the backscattered signal calculated for the same rainfall zones show no continuous, regular variation as seen for the 17/04 image (Fig. 3).

The backscattering coefficient varies little for the grassland and cropland themes and, furthermore, varies in like manner as the average of the summation of rainfalls.

As in the precedent analysis, the cropland backscattering coefficient variation is slightly larger than for grasslands.

Vis-à-vis the precedent analysis, the grassland and cropland back scattering coefficient variation is very slight. In zones 1 and 3, the grassland signature converges on that of croplands. Wetland grasslands are found within these zones, and it is thought that they could account for these slightly larger variations.

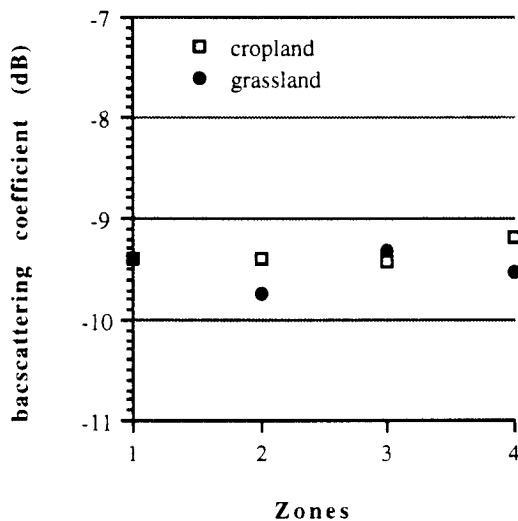


Figure 4 : ERS-1 scene of the 14/04/92. Backscattering coefficient variation per rainfall zone, taken from the 17/04 image, for the grassland and cropland themes.

3.2.2.3 Analysis of the 22/05 ERS-1 scene

The same zonal process of analysis was performed for the 22/05 image as for the 17/04 scene.

Except for an anomalous value in zone 1, the backscattering coefficient again, varies little and, as before, in the same manner as that of the average of summations of rainfalls (figure 5).

The zone 1 anomaly can be explained by a METEO FRANCE confirmed, very local rain event that does not appear on the rainfall mapping. The rain fell within zone 1 in an area of predominant cropland. This

explains the reason why only the cropland signal appears higher.

Contrary to the April images (14/04 et 17/04), it is noted that the grasslands have a slightly higher coefficient than that of the croplands. Between April and May the grass has grown from an average of 15-20 cm to 40-50 cm and the croplands have evolved from baresoil to a growing, and more abundant, vegetal cover (maize at between 20 and 40 cm). Therefore, it is thought that the change in vegetal state is the root cause of this difference.

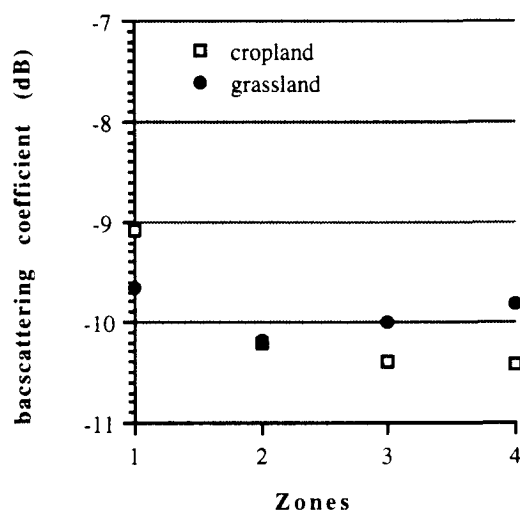


Figure 5 : 22/05/92 ERS-1 SAR scene. Backscattering coefficient variation per zone, as defined for the 17/04 image, for the grassland and cropland themes.

3.2.3 Synthesis

The analysis of the three ERS-1 scenes permits the observation of two kinds of phenomena from their backscattering coefficient's :

- The effects of antecedent precipitation amounts.

The 14/04 and the 17/04 scenes are sufficiently close that only rainfall events preceding the 17/04 image could account for the observed differences.

It is noted that, for the 17/04, the backscattering coefficient variations caused by soil moisture are large: 1.4 dB between zone 1 and zone 4 in figure 5.

In this scene, there is a strong correlation between the backscattering coefficient and the volumetric soil water content caused by precipitation.

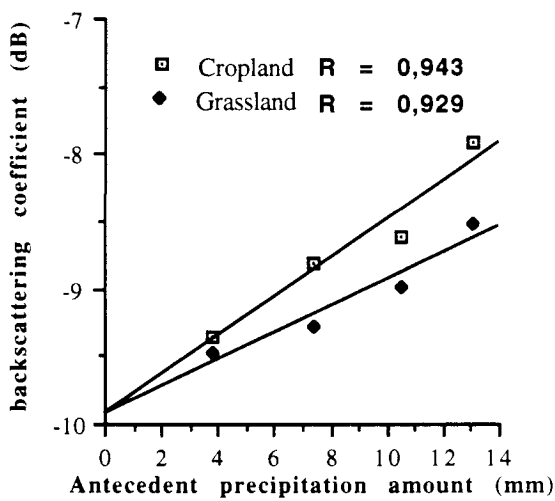


Figure 6: Correlation between backscattering coefficient and antecedent precipitation amount.

The linear correlation coefficients are 0.93 and 0.94, respectively, for the grassland and cropland themes. (Figure 6)

If, as shown by ULACY (1986) and BRUCKLER (1989) (Refs. 1, 2), a linear relationship is specified, two equation axis are found, $y=0.0997x-9.928$ for the grasslands and $y=0.1433x-9.923$ for the croplands.

However, it is noted, nevertheless, that a second order polynomial equation fits the point dispersion better than a linear axis. Consequently, it would be interesting to test for a non-linear link to rainfall in other case studies, and then define it.

- The effect of landcover.

For a given acquisition, a slight difference in the backscattering coefficient is observed for grassland and cropland themes, averaging 0.3 dB.

In the case of the April acquisitions, it is remarked that the cropland backscattering coefficient is marginally greater than that for grassland. Conversely, in May this pattern is reversed.

Between the 14/04 and the 22/05, a reduction in average backscattering coefficient is observed, being roughly -0.4 dB for grassland and -0.9 dB for cropland. The state and the evolution of the vegetal cover explains this phenomenon.

Given no rainfall event, the backscattering coefficient for a chosen theme is practically constant in the four zones. This leads to the deduction that the influence of vegetal cover is constant throughout the same scene.

This being so, it seems possible to decorrelate the signal from the landcover effect, meaning therefore the extraction of soil moisture related information.

CONCLUSION AND PERSPECTIVES

At this stage of the analysis three major results can be underlined :

- Owing to the overwhelming stability of the sensor, SAR data acquired under different conditions can be used in the determination of characteristic environmental signatures.

- The radar signal can be decorrelated from biophysical landuse effects.

- There is a strong correlation between the ERS-1 SAR backscattering coefficients calculated over large surfaces and volumetric soil moisture content linked to recent rainfall events.

A global approach to moisture was employed in this analysis. The backscattering coefficient's correlation to soil moisture, determined over large surfaces, is, statistically highly significant.

Therefore, it is concluded that the ERS-1 SAR backscattering coefficient is sensitive to the effects of antecedent precipitation on volumetric soil water content. The effect is so noticeable that a relationship can be established, independent of vegetal state, between the rainfall gradient and the backscattering coefficient.

Quantitative analysis will now follow on other ERS-1 scenes, for which the ground and weather conditions are defined by different controlling parameters. This being in order to facilitate the possibility of inverting the model and therefore, determining the possible fields of application in the study of natural terrestrial environments.

Several thematic applications are envisaged for the continuation of this study. They are resumed in table 6.

Table 6: Thematic applications to be tested in the continuing research programme.

Acquisition Frequency / Relevant Exogenous Data Layers	Meteorological Conditions.			
	No rainfall	Rainfall gradient	Homogeneous rainfall dispersion	Saturation on surface - flood
Single acquisitions	3	1	1	1 & 4
High frequency acquisitions Superficial formation maps	2 & 3	2	2	4
Low frequency acquisitions Piezometric Model.	3 & 4	4	4	4

Thematic Applications.				
------------------------	--	--	--	--

1 - Meteorological.

Amelioration of interpolation methods for ground based punctual climatic measurements.

2 - Agronomical.

Soil drainage rate monitoring, determination of soil hydrological constraints, evaluation of hydrological field water potential, field water requirements.

3 - Biophysical.

Landcover evolution and agricultural practice monitoring.

4 - Environmental.

Wetland landscapes, water table effects, flood event monitoring, flood extent, designation of flood risk areas.

The potential of hyperfrequency remote sensing in the domain of general moisture analysis seems promising. This is the reason why SERTIT wishes to follow through with this work. In this light, it has also responded to the CNES SIR-C research tender, and, furthermore, to that of ESA's ERS-1/ERS-2 pilot project programme.

REFERENCES

1. DOBSON M.C., ULABY F.T., 1986, Active Microwave soil moisture research., IEEE Transaction on Geoscience and Remote Sensing, Vol.24, N°1, 23-26.
2. BRUCKLER L., WITONO H., 1989, Use of Remotely Sensed Soil Moisture Content as Boundary Conditions in Soil-atmosphere Water Transport Modeling, 2. Estimating Soil Water Balance, Wat. Resour. 25, N°12, 2437-2447.
3. DABROWSKA-ZIEKINSKA K., GRUSZCZYNSKA M., JANOWSKA M., STANKIEWICZ K., 1994, Soil moisture based on ERS-1 SAR data for biomass assessment. Proceedings of the Second ERS-1 Symposium : Space at the service of our Environment, Hambourg, 11-14 Octobre 1993, ESA SP 361, 865-868.
4. MOHAN S., MEHTA N.S., MEHTA R.L., PATEL P., RAJAK D.R., SRIVASTAVA H.S., DAS D.K., SHARMLA S., SAXENA C.M., SUTRODHAR A.K., 1994, Soil moisture estimation using ERS-1 SAR data, Proceedings of the Second ERS-1 Symposium : Space at the service of our Environment, Hambourg, 11-14 Octobre 1993, ESA SP 361, 875-878.
5. LAUR H., 1992, ERS-1 SAR Calibration, Derivation of Backscattering Coefficient in ERS-1 SAR. PRI. products, Rapport de l'Agence Spatiale Européenne, N°1, 16 p.
6. LAUR H., MEADOWS P., SANCHEZ J.I., DWYER E., ERS-1 SAR Radiometric calibration, Proceedings of the CEOS SAR Calibration Workshop, ESA WPP-048., 21 p.
7. BOUMAN B.A.M., UENK D., 1992, Crop Classification Possibilities with Radar in ERS-1 and JERS-1 Configuration, Remote Sensing Environ. N°40, 1-13.
8. WOODING M.G., ZMUDA A.D., GRIFFITHS G.H., 1994, Crop discrimination using multi-temporal ERS-1 SAR Data, Proceedings of the Second ERS-1 Symposium : Space at the service of our Environment, Hambourg, 11-14 Octobre 1993, ESA SP 361, pp 51-56.
9. BRISCO B., BEDARD D., NAUNHEIMER J., BROWN, 1993, Environmental effects on radar data of agricultural areas. Actes du 18e Symposium canadien de Télédétection, Sherbrooke, Québec, 7-10 juin 1993, 283-288.
10. TENG W.L., WANG J.R. and DORAISWAMY, 1993 - Relationship between satellite microwave radiometric data, antecedent precipitation index and regional soil moisture. Int.J. Remote Sensing, 14, 13, 2483-2500.
11. FELLAH K., BESNUS Y., CLANDILLON S., FRAIPONT P., 1994, Multi-temporal ERS-1 SAR data in environmental studies: researching a moisture parameter measurement in the soils of Ried Centre Alsace, France. Proceedings of the Second ERS-1 Symposium : Space at the service of our Environment, Hambourg, 11-14 Octobre 1993, ESA SP 361, 869-874.

EVALUATION OF SOIL MOISTURE FOR THE AGRIMETEOROLOGICAL CONSULTING SERVICE USING ERS-1 DATA (PROJECT PP2-D15)

Andreas Weimann, Maria v. Schönermark, DLR - German Aerospace Research Establishment, Institute of Space Sensor Technology

Petra Jörn, Albrecht Schumann, German Weather Service,
Agrometeorological Consulting Service

Rudower Chaussee 5
D-12484 Berlin
Tel.: +49 (030) 69 545 648
Fax.: +49 (030) 69 545 642

This work is supported by the German Space Agency DARA GmbH

ABSTRACT

Soil moisture is one of the most important factors in nature and plays a decisive role in agriculture. For his work of estimating soil moisture, the Agrometeorological Consulting Service is interested in the use of SAR-data. Therefore ground truth and analyses of satellite images have been done for the loess districts of East Germany, which are characterised by extended agriculture land use. In order to define an inversion algorithm for determining soil moisture of bare soil with a defined roughness from ERS-1 data, a statistical approach is used. The results of our work from September until December 1993 are presented.

1. INTRODUCTION

In order to optimise the results, the Agrometeorological Consulting Service of German Weather Service gives special information about the weather conditions to the farmers. Punctual information based on the synoptic data of weather stations has been extrapolated in areas with help of models or comparative investigations. In the case of soil moisture such a conclusion from a point to an area results in inaccuracies because of the heterogeneous moisture distribution within fields and mesoscale areas too. Satellite data will overcome these difficulties. For using this advantage of satellite data we started the project PP2-D15 in the loess district of East Germany.

2. TEST SITES

The Consulting Service in Halle is giving advice for the districts of Saxony-Anhalt, Thuringia and Saxony in the south-east of Germany. The test sites are also in this region.

Two fields are in Bad Lauchstädt 30 km southwest of Halle/Saale and two fields in Großobringen 30 km north of Weimar. Each of the two fields in Bad Lauchstädt has a size of 30000 m² and each field in Großobringen 10000 m². All test sites did not have any vegetation during the period of measurement.

In the lee side of low range mountains at this area, the annual average of precipitation is about 500 mm. Compared to other regions in Germany with an average of 800 mm, this amount is very low. Soil moisture becomes the limiting factor for the plants of the district, the soil of which is mainly built in loess.

After the reparation of agricultural land under the former GDR government and agricultural large-scale production of co-operatives (LPG), the size of the fields is about 10000 m². These huge areas are particularly suitable for remote sensing from space, because the resolution of SAR is not high enough to recognise a field of low extension.

3. THE IMPORTANCE OF SOIL MOISTURE ON FALLOW FIELDS

At the present moment the problem of estimating soil moisture within vegetation by SAR is not yet solved. But also the knowledge of soil moisture at fallow fields is an essential tool for agrometeorological consultation.

Two time scales exist for the consulting service. The first is a direct one with only a very short time delay. It is a real time forecast. The second scale is without restriction to time.

3.1 CONSULTING BASED ON REAL-TIME DATA

This kind of consultation is the most important

one for the farmer, because most of the plants have a particular request to the soil moisture for optimal germination. The moment of sowing depends on the soil conditions and an appropriate time must be determined. Before and after sowing, fertilizer and herbicides must be spread onto the field. They can develop their full effects only under special conditions of soil moisture. If the soil is too wet, there is a great danger that these chemicals can not be absorbed but evaporate into the atmosphere.

Apart from that, numerical medium weather forecast is tied to a particular time. These estimations are based on models, in which the soil moisture has to be assimilated as a very important input parameter.

This real time information is distributed by Agrometeorological Weather Consulting Service through various media.

3.2 CONSULTING NOT BASED ON REAL-TIME DATA

This kind of information is suitable for monitoring of ecosystems.

Data on soil moisture are included in geographical information systems and is necessary for tasks of environmental planning.

A further example is the estimation of energy balance as well as the evaporation of large areas, which is needed for investigations of regional and global climate changes.

4. RESULTS OF THE PERIOD FROM SEPTEMBER TO DECEMBER 1993

4.1 GROUND TRUTH

In autumn 1993 the ground truth measurements have been taken on the four fields mentioned above. Three fields were harrowed to have nearly the same roughness. It is less than 5 cm on these fields. One field in Bad Lauchstädt was ploughed in order to have the possibility to compare the backscattered signal from similar soils but with different roughness.

The soil samples are taken from the upper 5 cm and also in a layer from 5 to 10 cm. The measure-

ment is taken with a time delay of less than 2 hours to the ERS-1 overflight during daytime and 4 hours during the night. Soil moisture is determined by standard gravimetric moisture sampling. In addition a time-domain-reflecting-probe is used for measuring the integral soil moisture of the upper 15 cm. Because of the homogeneous structure of the soil 9 samples are sufficiently representative of a field.

For compensation of random deviations of measurements, an average of the samples was made for each test site. This mean value can be compared with the satellite's pixel-mean of the same field.

Laboratory determination of cardinal values as field capacity and permanent wilting point was made. Based on this the soil moisture content is expressed in percent of usable field capacity for comparing different types of soil.

4.2 ANALYSES OF THE SATELLITE IMAGES

The first task was to locate the test sites in the image. The size of the test-sites is between 10.000 and 30.000 m². Unfortunately the ERS-1 ground resolution of 25-30 m is not high enough to determine the exact shape of the field directly from the image. Up to this time geocoded images of East-Germany did not exist. In order to identify our test sites we used aerial pictures with a scale of 1:12500. We digitalized them and set georeference points to compute the same sharpness of the aerial picture as the ERS-1 image. They were congruent and the test-sites were easily found.

For each field we calculated the mean of the grey level value and used the procedure of LAUR (1992) to derive a backscattering coefficient.

Finally, the dependency on the incident angle should be considered. An angle of 23° was chosen for standardisation. It is based on a diagram of ULABY & DOBSON (1989), which shows the dependence of the backscattering coefficient on the incident angle. For bare soil this dependency can be described as a linear function within the set of incident angles occurring in the ERS image.

4.3 RELATIONSHIP BETWEEN BACKSCATTERING COEFFICIENT AND SOIL MOISTURE

In the case of the harrowed field in Bad Lauchstädt, we did not find any relationship and for the ploughed field only a weak relationship for the upper layer. For the harrowed field we expect outliers and after eliminating them the relationship is stronger. This will be investigated further.

In the first and the second test site of Grossobringen there seems to be a relationship between the soil moisture and the backscattering coefficient. The correlation coefficient is 0.56 and 0.62 with a significance of 93 %. Because of equal soil properties we have put them together to get a larger sample (see Figure 1). For this case we get a correlation coefficient of 0.68 with a significance of 99.6 %.

Analysis of the usable field capacity includes all fields and shows a weaker correlation. But this is an effect of the bad relationship of the field in Bad Lauchstädt.

In order to make a more general statistical state-

ment we have to take a larger amount of experimental measurements. The work is still in progress this year. A new campaign with non vegetated fields has started in May.

5. CONCLUSION

Using ERS-1 data for the evaluation of soil moisture in the upper layer of single even though large fields, an exact analysis of the image data is necessary.

In order to derive an inversion algorithm for the special loess district of East Germany, regression analysis seems to be successful, but the available amount of measurements is not yet sufficient to give general statistical laws for the district.

6. REFERENCES

LAUR Henri (1992): Derivation of Backscattering Coefficient in ERS-1.SAR.PRI Products

ULABY Fawwaz T., DOBSON M. Craig (1989): Handbook of Radar Scattering Statistics for Terrain

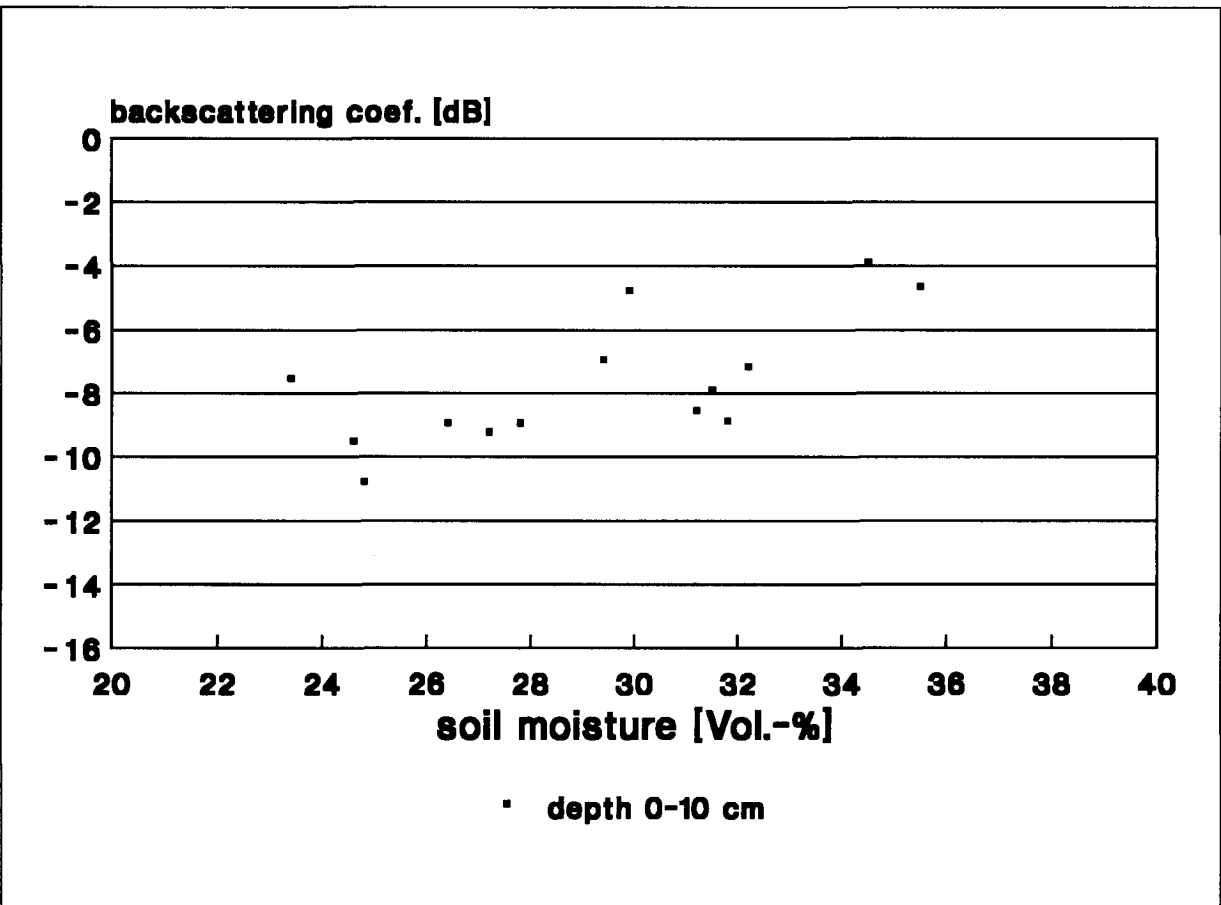


Fig. 1: Test site Großobringen (both fields)

ESTIMATION OF SURFACE SOIL MOISTURE FROM ERS.1/SAR DATA FOR HYDROLOGICAL MODELLING PURPOSES

**Michel NORMAND (1), Najiba CHKIR (1), Anne-Laure COGNARD (1),
Marie-Christine IMBERTI (2), Cécile LOUMAGNE (1), Catherine OTTLE (3)
Alain VIDAL (4), Daniel VIDAL-MADJAR (3)**

1 - CEMAGREF, Hydrologie, BP 121, 92185 Antony Cedex, France, Tél: (33) 1.40.96.60.54, Fax : (33) 1.40.96.61.99

2 - GEOSYS, Parc Technologique de Toulouse, 31526 Ramonville, France, Tél: (33) 61.75.12.10, Fax : (33) 61.75.87.22

3 - CETP, Centre Universitaire, 10/12 Avenue de l'Europe, 78140 Vélizy, France, Tél: (33) 1.39.25.49.12, Fax : (33) 1.39.25.49.22

4 - CEMAGREF, LCT, Domaine de Lavalette, 34033 Montpellier, France, Tél: (33) 67.04.63.36, Fax: (33) 67.63.57.95

ABSTRACT

This paper is concerned with the presentation of the first results of a project for using remotely sensed data in a hydrological model to improve the surface water resources monitoring. The general methodology to derive an index representative of the mean moisture state of agricultural basins from ERS.1/SAR data, jointly to visible and thermal infra-red data, is presented. The test site is located in the central part of Brittany, France. During the 1992/1993 period, extensive ground measurements and point automatic soil moisture measurements were carried out on the Naizin experimental catchment. Then, these data were compared with ERS.1/SAR data. On a basin scale, there is a clear correlation between the mean radar data and the soil moisture measurements during the period of low vegetation density. Moreover, the results are influenced by the vegetation cover during the summer months. On a field scale the relation depends on the type of culture. A comparison between the surface soil moisture simulated by the hydrological model and the mean radar data on a basin scale is presented. The results are in good agreement throughout almost the year 1992. These first results are very encouraging and open the possibility of using ERS.1/SAR data for hydrological applications. The next steps will be the correction of the vegetation effect on the radar signal on a basin scale and the assimilation of the remotely sensed data in the model.

RESUME

Cette communication présente les premiers résultats d'un projet d'utilisation de données de télédétection dans un modèle hydrologique afin d'améliorer la prévision des ressources en eau de surface. La méthodologie générale consiste à déduire des données du SAR d'ERS.1, conjointement à des données dans le visible et l'infra-rouge thermique, un indicateur représentatif de l'état hydrique moyen de bassins versants agricoles. Le site expérimental est situé dans la partie centrale de la Bretagne. Pendant la période 1992-1993 des mesures extensives au sol et des mesures automatiques d'humidité du sol ponctuelles ont été effectuées sur le bassin versant expérimental de Naizin. Ces données ont ensuite été comparées avec des

données du SAR d'ERS.1. A l'échelle du bassin versant, une étroite corrélation existe entre les valeurs moyennes du signal radar et les mesures d'humidité du sol pendant la période de faible densité de végétation. Cependant, les résultats sont influencés par le couvert végétal pendant les mois d'été. A l'échelle de la parcelle, la relation dépend du type de culture. On présente une comparaison entre l'humidité de surface du sol simulée par le modèle hydrologique et la moyenne du signal radar à l'échelle du bassin versant. On observe une bonne concordance entre les résultats obtenus, presque tout au long de l'année 1992. Ces premiers résultats sont très encourageants et ouvrent la possibilité d'utilisation des données du SAR d'ERS.1 pour des applications hydrologiques. Les prochaines étapes seront la correction de l'effet de la végétation sur le signal radar à l'échelle du bassin versant et l'assimilation des données de télédétection dans le modèle hydrologique.

1 - OBJECTIVES

This paper is prepared within the scope of an ESA pilot-project (PP2.F10) intitled "Estimation of the mean soil hydric state of small agricultural basins using remotely sensed data : Application to the calibration and the validation of a hydrological model".

The global objective of this project is the development of a methodology (figure 1), using spatial data from the Synthetic Aperture Radar (SAR) of the ERS.1 satellite, jointly with thermal infra-red data from NOAA/AVHRR and visible data from SPOT/HRV, to derive an index that could be representative of the mean moisture state of small agricultural catchments and that could be used to monitor its evolution throughout the year. Then, using a hydrological model able to assimilate these data, the final aim is to improve the surface water resources monitoring of gauged or ungauged basins (LOUMAGNE et al, 1994).

This paper is devoted first, to the presentation of the results obtained for the evaluation of the ERS.1/SAR capacity to estimate the surface soil moisture on a basin scale and on a field scale during the 1992/1993 period. Then, the results of a comparison between the evolution of the backscattered radar signal on a basin scale throughout

the year 1992 and the evolution of the surface soil moisture simulated by the model are presented. Finally, the next steps of the study are discussed.

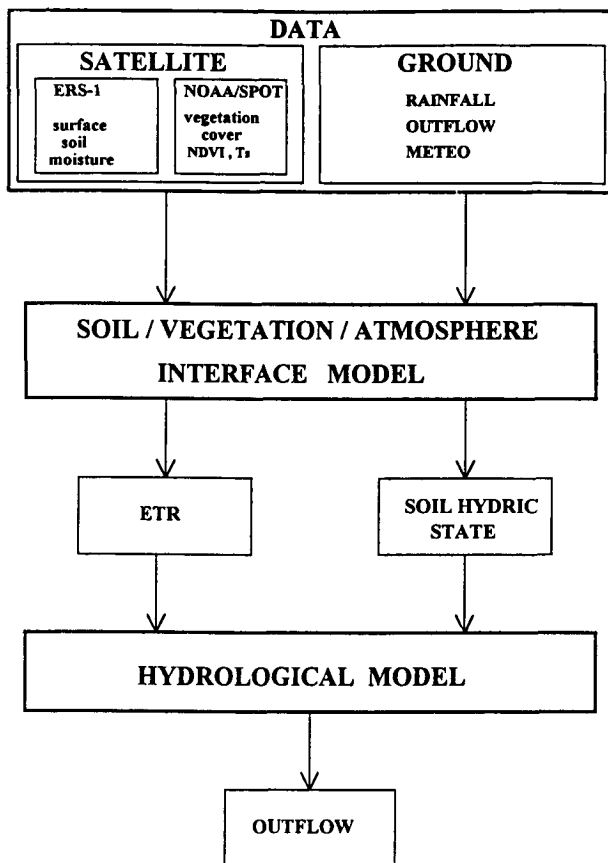


Fig.1 - General methodology of the project

2 - STUDY AREA DESCRIPTION

The study area is situated in central Brittany, France. The choice of this region is due to the possibility of obtaining ERS.1/SAR data during the three days phase, interesting for hydrological applications.

The Naizin experimental watershed is used first to calibrate the SAR data for the surface soil moisture estimation, and secondly, to calibrate the model able to assimilate the satellite data.

Then, about thirty watersheds will be used to validate the model and to effect the statistical verification of the results.

The Naizin watershed corresponds to the upper part of the Coët-Dan rivulet, tributary of the Evel river. It has a 12 km² surface and is 7 km long from North to South. Its altitude is comprised between 136 m in the North-Western part and 65 m at the outlet (figure 2). The relief is not greatly marked : a tableland forms the Northern part of the basin. In its middle and Southern parts, the drainage network is more deeply embanked, and then the relief becomes more undulating.

Soils are formed from clayey alterites expanded over the Brioverian schists bedrock. The top of the slopes are overlaid with acid brown soils. Gleys and semigleys cover low grounds.

The basin is characterized by intensive agriculture : 92% of the surface is occupied by croplands and grasslands. The principal crops are cereals, corn, peas, beans, and various vegetables. The remaining part is composed of woods (2%), buildings and roads (6%).

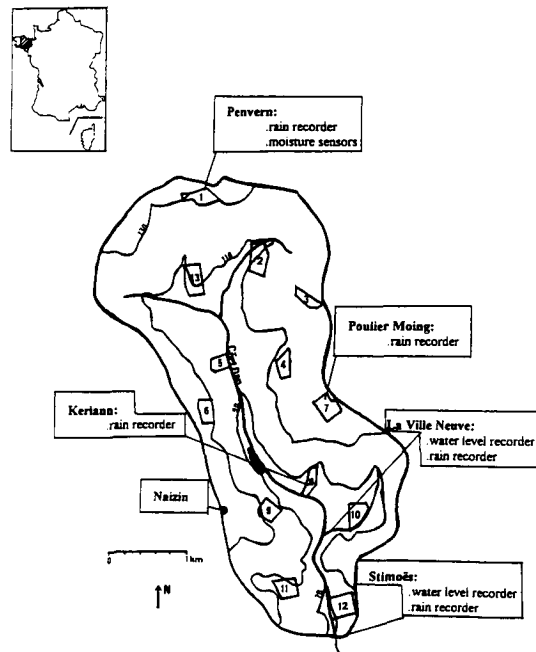


Fig.2 - The Naizin experimental catchment with the test fields and the location of the automatic soil moisture measurement station.

The mean annual rainfall over 22 years since 1971 is 711 mm ± 128 mm. The mean annual runoff during the same period is 303 mm ± 172 mm, and the mean annual actual evapotranspiration is about 330 mm. The major part of the rainfall occurs in autumn and winter. The summer period is relatively dry and the outlet flow disappears.

3 - THE DATA BASE

3.1 - Ground data

To assess the capacity of the ERS.1/SAR in evaluating the soil surface water content, ground truth measurements were carried out on the Naizin watershed. First, an automatic soil moisture recorder was set-up in the North of the basin. Secondly, several extensive field campaigns were conducted in coincidence with ERS.1 passes over the area.

At the automatic station, 8 capacitive sensors have been buried in the soil from 10 cm down to 90 cm. The data are recorded every 6 hours. They have been calibrated using gravimetric measurements taken at the same location. The site was already equipped with an automatically transmitting raingauge.

Thirteen test fields representative of the different agricultural practices and vegetation cover have been selected throughout the basin. During the 1992/1993 period 13 extensive campaigns were organized to estimate the soil moisture in the upper layer (0-5 cm) on a field basis, 4 in 1992, 9 in 1993. On each field 20 to 40 samples, depending on the field sizes (2 to 6 hectares) were taken for gravimetric soil moisture determination. The bulk density has been measured using a surface gamma neutron probe.

3.2 - SAR data

The images delivered by ESA are Precision Image Products (P.R.I.). These P.R.I. images are 3 looks georeference, digital images, corrected for antenna elevation gain pattern and range spreading loss. The pixel size is $12.5 \times 12.5 \text{ m}^2$ (OLIVIER and VIDAL-MADJAR, 1994). During the 1992 and 1993 period, almost all possible ERS.1 images for the selected basins were acquired for us by ESA from the overflight of 22 January 1992 (figure 3). From this first image to the end of March 1992, these images correspond to the phase B implemented to have a repetition period of 3 days. Since the end of March 1992 until the end of 1993, the ERS.1 orbits have been changed to have a repetition period of 35 days (phase C).

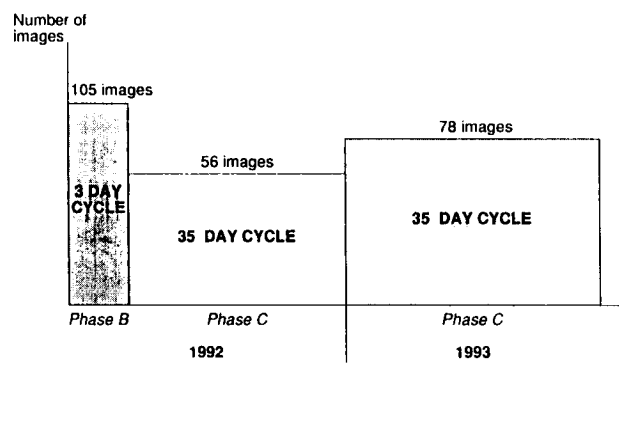


Fig.3 - Number of ERS.1/SAR images received for the phases B and C.

The superposition of the images on a map can be done locally easily using a simple transform based only on translation and rotation. This is due to the quality of PRI products and to the fact that the relief is quite gentle.

The backscattering coefficients for the images are derived according to the documents given by ESA (LAUR, 1992). They are calculated for the Naizin catchment and for its various test fields, and also for the other studied basins in Brittany.

4 - ERS.1/SAR calibration on surface soil moisture

The radar data were compared with ground truth on two different scales during the 1992/1993 period. The first one is the basin scale, suitable for hydrological global modelling. The second one is the field scale, useful for a more detailed analysis (LOUMAGNE et al, 1993).

4.1 - Analysis of the results on a basin scale

It has been proved using airborne experiments, that it is possible to link with a good degree of accuracy, the mean regional radar measurements to the mean soil moisture on the same scale (SOARES et al, 1988, BENALLEGUE et al, 1994). It was one of the objectives of this pilot-project to demonstrate that the same approach is possible from space. The figures 4 and 5 show the variations of the mean radar signal over the entire basin throughout the years 1992 and 1993, and the evolution of the in situ soil moisture measurements.

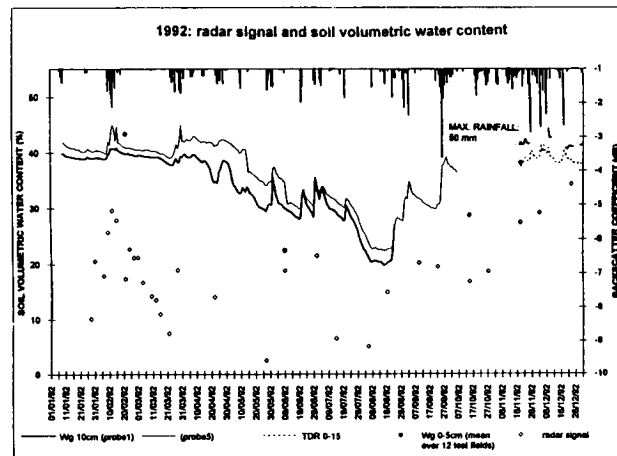


Fig.4 - Evolution of the mean radar signal over the Naizin basin for the year 1992 and results of the soil moisture measurements

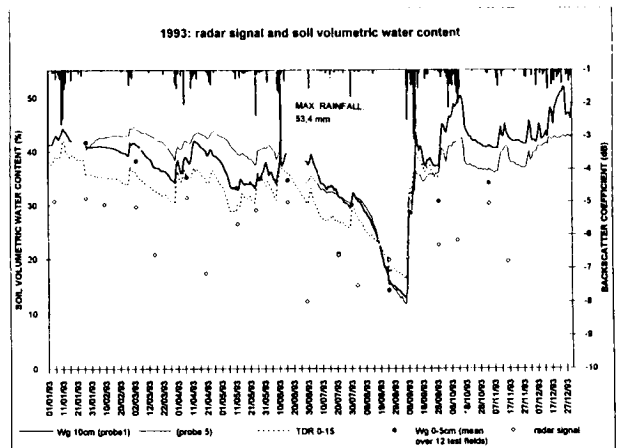


Fig.5 - Evolution of the mean radar signal over the Naizin basin for the year 1993 and results of the soil moisture measurements

Despite the fact that the point automatic measurements are taken at a very local scale and that the soil moisture is known to be a very heterogeneous parameter, it appears that it is possible to distinguish two periods. The first one corresponds to the period of low vegetation density, from January to May 1992 and from October 1992 to May 1993. During that period, both of the radar and soil moisture evolutions are in good agreement.

For the second period, from approximately June to September, the radar signal seems to be influenced by the high vegetation density. This influence is clearly visible specially in July and August 1993 on the figure 6 showing the radar signal evolution with the results of the mean surface soil moisture over the test fields (extensive campaigns).

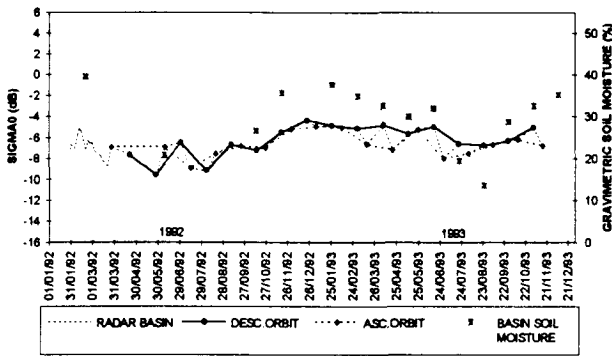


Fig.6 - Evolution of the mean radar signal over the Naizin basin for the 1992/1993 period with the results of the ground truth extensive campaigns

The figure 7 represents the correlation between the point soil moisture measurements and the mean radar signal, separately for the phase B with only winter data, and for the phase C including mixed data throughout the year.

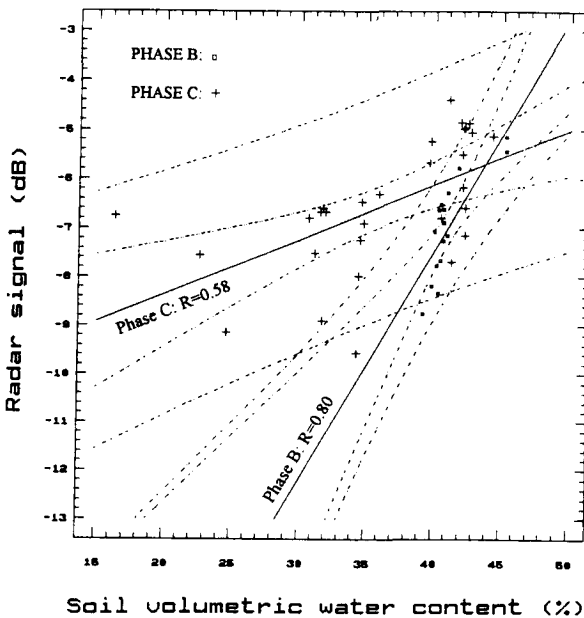


Fig.7 - Correlation between the mean radar signal over the Naizin basin and the point automatic soil moisture measurements separately for the phase B and the phase C.

The first phase is characterized by a high degree of correlation ($R = 0.8$) and by a good sensitivity of the radar to the soil moisture variations. Due to the summer data, the second phase is characterized by a reduction of the correlation coefficient ($R = 0.58$) with a diminution of the radar sensitivity to the soil moisture variations.

These observations show that it will be necessary to take into account the vegetation cover using NDVI estimation from optical images as those provided by NOAA satellites, to assess the surface soil moisture from ERS-1/SAR data with a good accuracy throughout the year.

4.2 - Analysis of the results on a field scale

The figures 8 and 9 show as an example the comparative evolutions of the mean radar signal and surface soil moisture (0 - 5 cm) for a wheat field and a grassland.

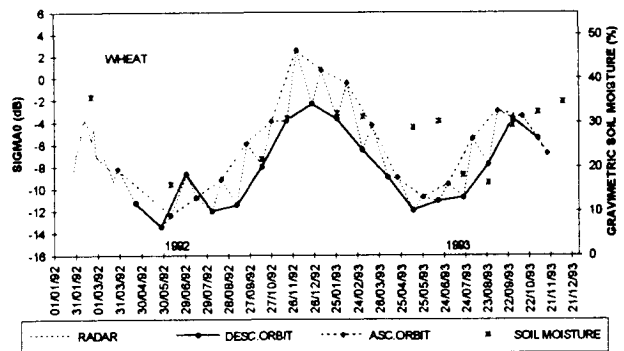


Fig.8 - Evolution of the mean radar signal on a wheat field for the 1992/1993 period with the results of the ground truth extensive campaigns.

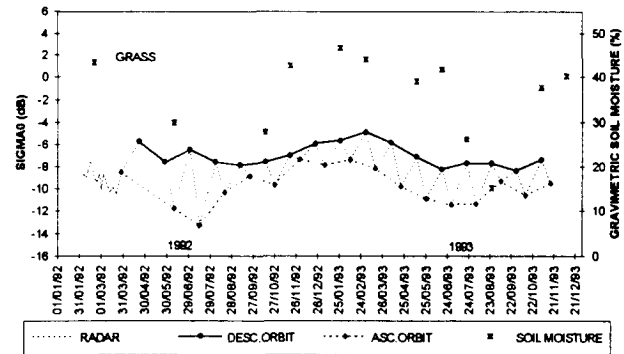


Fig.9 - Evolution of the mean radar signal on grassland for the 1992/1993 period with the results of the ground truth extensive campaigns

It can be noticed that both of the evolutions are similar except during the summer months. The variations of the radar signal are much larger for the wheat field than for the grassland, due to the respective influence of the vegetation density and of the agricultural practices.

The second observation is the systematic difference between the radar data for the ascending and descending orbits, and the inversion phenomenon between these fields, probably due to a relief effect.

These results show the difficulty in assessing the soil moisture variations on a field scale from the ERS.1/SAR data.

5 - RADAR SIGNAL EVOLUTION AND SURFACE SOIL MOISTURE SIMULATION

This section presents (figure 10) a comparison between the evolution of the mean radar signal on the Naizin catchment during the year 1992, and the results of a simulation of the surface soil moisture by the hydrological model, developed within the framework of this pilot-project, for the same period. This model is able to simulate the daily streamflows over small catchments by taking into account the average characteristics of the surface (soil and vegetation) for the calculation of actual evaporation and evapotranspiration. The model simulates also the daily evolution of soil moisture in two layers : the surface layer representing about the 10 first centimeters of soil, and the bulk layer representing the root zone (CHKIR, 1994, OTTLE and VIDAL-MADJAR, 1994).

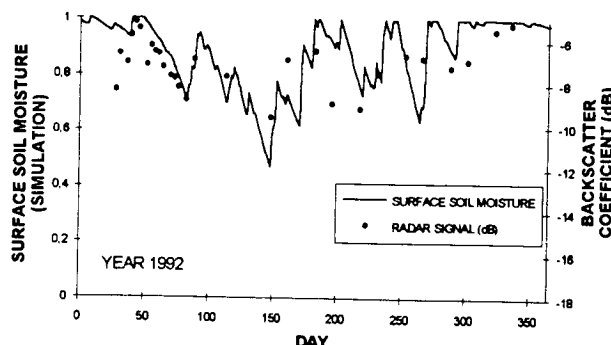


Fig.10 - Comparison between the mean radar signal over the Naizin basin and the simulated surface soil moisture for the year 1992

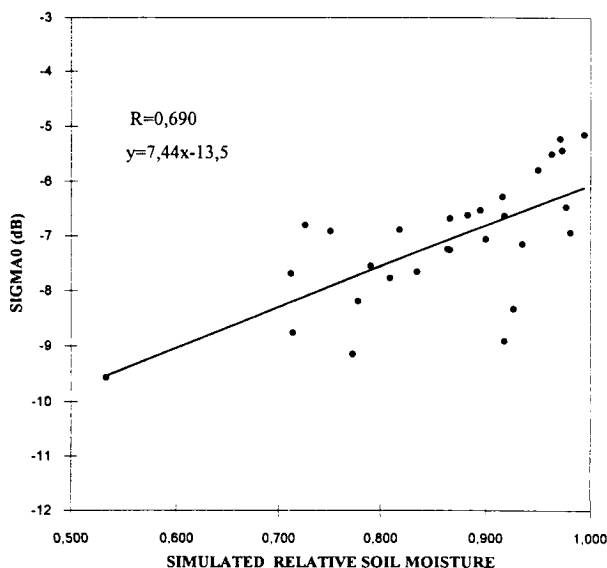


Fig.11 - Correlation between the mean radar signal over the Naizin basin and the simulated surface soil moisture for the year 1992

The radar data and the simulated relative surface soil moisture data show very similar evolutions, except for a few points, and the correlation between these data gives a rather good correlation coefficient ($R = 0.69$) (figure 11). These results are very interesting for the future applications of the ERS.1/SAR data in hydrological modelling.

6 - CONCLUSIONS

The work presented in this paper is the first step of a pilot-project to assess the usefulness of the ERS.1/SAR images to estimate the hydric state of small agricultural watersheds.

The comparisons between the radar data and the in situ soil moisture measurements were carried out on two different scale, the field scale and the basin scale.

On a field scale, the backscattering coefficient is different for the ascending and the descending orbits and the relationship between the radar data and the surface water content depends on the nature of the observed surface.

More interesting for hydrological applications is the comparison on a basin scale. It has been shown that during the fall, winter, and mid-spring periods, the evolutions of the basin mean radar signal and of the point surface soil moisture measurements are in good agreement. It may then be possible, as expected, to define a hydric state index from ERS.1/SAR data on a small agricultural basin at least during the period of low vegetation density. But, it would be better to take into account the influence of the vegetation using NDVI estimation, for a better assessment of the surface soil moisture by radar throughout the year. Nevertheless, the good agreement between the backscattering coefficient averaged over the whole experimental basin and the surface soil moisture simulated for the year 1992 by the new hydrological model developed in the scope of this pilot-project, is very encouraging for future hydrological applications of radar remote sensing.

The next steps of the project are, the inclusion of the results of the last ERS.1 three day phase (phase D) from January to the end of March 1994 (radar data and ground truth operations), the use of NDVI values to try to improve the surface soil moisture estimation from ERS.1 radar signal, the cartography of the surface soil moisture of the Breton basins, the integration of thermal Infra-Red data to derive the root zone soil moisture, and the assimilation of the remotely sensed data in the model.

The results obtained so far in the first step of the project, with regard to the surface soil moisture determination and the hydrological model are very promising. The figure 12 shows the scheme of the future operational system using remotely sensed data for hydrological modeling and outflow forecasting of gaged or ungaged basins in various climates and regions.

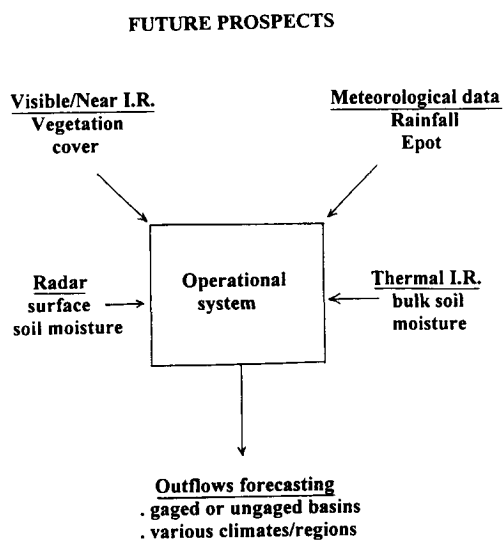


Fig.12 - Scheme of the operational system for outflow forecasting using remotely sensed data

LOUMAGNE C., NORMAND M., OLIVIER Ph., OTTLE C., VIDAL-MADJAR D., LOUAHALA S., VIDAL A. - 1993 - Evaluation of the ERS.1/SAR capacity to estimate surface soil moisture. First 1992 results over the Naizin watershed. Submitted to Remote Sensing of Environment.

OLIVIER Ph., VIDAL-MADJAR D., 1994 - Empirical estimation of the ERS.1/SAR radiometric resolution, to be published, IJRS.

OTTLE C., VIDAL-MADJAR D., 1994 - Assimilation of humidity inverted from infrared remote sensing in an hydrological model over the HAPEX/MOBILHY region, J. of Hydrology. 158 : 241-264.

SOARES J.V., BERNARD R., TACONET O., VIDAL-MADJAR D., WEILL A., 1988 - Estimation of a bare soil evaporation from airborne measurements, J. Hydrol., 99 : 281-296.

ACKNOWLEDGEMENTS

This work is supported by ESA who provides the ERS.1 images, by CNES, the French Space Agency, and by the French national remote sensing program (PNTS). Many thanks are going to our colleagues of CEMAGREF-RENNES who manage the Naizin experimental basin, to P. ANSART and other people from CEMAGREF for their precious help in conducting the fields measurements.

REFERENCES

BENALLEGUE M., NORMAND M., GALLE S., DECHAMBRE M., TACONET O., VIDAL-MADJAR D., PREVOT L. - 1994 - Soil moisture assessment at a basin scale using active microwave remote sensing : the AGRISCATT88 airborne campaign on the Orgeval watershed, Intern. J. Remote Sensing, 15,3,645-656..

CHKIR N., 1994 - Mise au point d'un modèle hydrologique conceptuel intégrant l'état hydrique du sol dans la modélisation pluie-débit. Thèse de l'Ecole Nationale des Ponts et Chaussées de Paris (France) "Sciences et Techniques de l'Environnement", CEMAGREF, mars 1994.

LAUR H., 1992 - Derivation of backscattering coefficient σ_0 in ERS.1/SAR. PRI Products, Doc. ESA, n°1, 16 p.

LOUMAGNE C., CHKIR N., NORMAND M., OTTLE C., VIDAL-MADJAR D., 1994 - Development of a conceptual rainfall-runoff model accounting for real soil hydric state. Part I : Introduction of the soil/vegetation/atmosphere continuum in the hydrological model, submitted to Water Resources Research.

**ERS-1 SAR IMAGERY APPLIED TO RURAL BASINS HYDROLOGICAL STUDIES.
II : GRASSLAND SOIL AND LOWLAND WETNESS CHARACTERIZATION**

S. Dautrebande, M. Badji, A. Dewez and A. Nonguierma

Faculté des Sciences Agronomiques de Gembloux
 Unité d'Hydraulique Agricole
 2, Passage des Déportés
 B-5030 Gembloux (Belgique/Belgium)
 Tel. + 32 (0)81 62 2187 or 2190; Fax. + 32 (0)81 62 2181

ABSTRACT

The Laboratory for Hydrology and Remote Sensing of the Land and Water Management Unit has undertaken a variety of information gathering activities on grassland productivity and impact on the hydrologic cycle. The study area is the agroecological zone of Famenne-Ardenne located in the Southern Region of Belgium (Wallonia), where grassland constitutes one of the major unit of the agricultural landscape. Grassland soil wetness characterization fits well in the framework of a research aimed to better understand the patterns of hydrological changes taking place in the area. Due to frequent cloud cover, it was decided to investigate the potential to use ERS-1 SAR imagery as a means to characterize grassland soil moisture, independently of weather conditions.

The Laboratory has also undertaken research activities in Burkina Faso (West Africa), in relation to lowland wetness characterization in Soudano-Sahelian environment. Conventional VIS/IR remote sensing applications to lowland wetness characterization is hindered by the cloud cover during the rainy season (from May-June to September-October). The fact that the radar (SAR) can provide constant monitoring, regardless of weather or time of day, has been used to investigate the feasibility of ERS-1 SAR imagery in characterizing wet lowlands extent as a function of time during the rainy season in the study site.

1. INTRODUCTION

Grasslands account for about 50% of cultivated land, covering some 650 000 ha in Belgium. Their dynamics is a complex result of the effects of climate, physiography and the interaction of man (anthropic activities) with the agricultural environment in response to a changing demand. Grassland soil wetness characterization research was carried out with the aim of better understanding the patterns of hydrological cycle changes in the agroecological zone of Famenne, located South of Belgium. Due to frequent cloud cover in the area, the potential to use ERS-1 SAR imagery as a means to characterize grassland soil

moisture, independently of weather conditions, was investigated.

The Soudano-Sahelian region has experienced a dramatic demographic pressure combined with a damaging drought during the years 1973 to 1983. This has induced a pressure on the lowlands. Lowland soils have high agricultural potential and have consequently become vital resources for Soudano-Sahelian farmers. However, this agricultural added-value is unsufficiently developed for many reasons. Among these reasons are the difficulty to apprehend the lowlands environment and the way their agricultural potential is being implemented. The use of

satellite remote sensing allows one today to relieve important constraints related to lowland use. Satellite remote sensing provides repetitive and spatial information required to meet the challenges of lowland soil and water management. During the rainy season the moisture regime of lowland in the Soudano-Saharan regions is particularly difficult to assess by conventional VIS/IR remote sensing due to cloud cover. The SAR instrument on board ERS-1 provided the opportunity to make operational observations of lowland surfaces independently of weather conditions.

2. MATERIAL AND METHODS

2.1. Material

In the framework of the two research studies following material is used :

- Phase C ERS-1 SAR.PRI images;
- An image processing software (PC-ERDAS 7.5);

The satellite ERS-1 records SAR signal returns from a track of 100 km wide. It looks at the Earth surface with a 23° incidence angle at mid-swath. A SAR.PRI image (PRI = Precision image) is corrected radiometrically. ERS-1 SAR operates in C-band (5.3 GHz) with vertical/vertical (VV) polarization . The general characteristics of ERS-1 SAR image are :

Pixel size	:	12.5 x 12.5 m
Image size	:	100 x 102 km
Coding	:	16 bits
Image volume	:	+ 131 Megabytes

Following images, provided by ESA, are used in the framework of grassland soil wetness characterization in the Famenne study site:

<u>Scene</u>	<u>Date</u>	<u>Orbit</u>
0999	01FEB92	2864
2601	12MAY92	4304
2601	16JUN92	4805
2601	25AUG92	5807
2601	29SEP92	6308
2601	08DEC92	7310
2601	12JAN93	7801

ESA has also provided, in relation to the study aimed at characterizing lowland wetness in Burkina Faso, following images:

<u>Scene</u>	<u>Date</u>	<u>Orbit</u>
3375	23APR92	4032
3375	28MAY92	4533
3375	06AUG92	5535
3375	10SEP92	6036
3375	15OCT92	6537
3375	19NOV92	7038
3375	24DEC92	7539
3375	28JAN93	8040
3375	08AVR93	9042

Among these images, we have selected three (23AVR92, 06AUG92 and 10SEP92) characterizing the lowlands area before, at mid- and at near end of the rainy season.

PC-ERDAS (Earth Resources Data Analysis Systems) software (version 7.5) enables one to perform radiometric and geometric corrections, image display enhancement (smoothing, contrasting, filtering, ...), information retrieval (ratioing, index calculation, ...); classification, georeferencing, etc...

2.2. Methods

The first step of the procedure used in the processing of ERS-1 SAR images in relation to

flood inundation mapping and monitoring (Dautrebande et al., 1994) is applied in relation to the two case studies. As a reminder, this consisted in ERS-1 SAR image pre-processing. ERS-1 image pre-processing is related to remapping 16-bit image data to an 8-bit gray scale representation and speckle reduction.

As regards soil moisture characterization under grass, the backscatter data, expressed in terms of digit numbers (DN), were compared to field observations.

The methodological approach used to characterize lowland wetness is similar to that utilized to identify and map flood inundated areas. It is termed here as wetness extent index and is expressed as follows :

$$\text{WEI} = (\text{DN}_2 - \text{DN}_1)/(\text{DN}_2 + \text{DN}_1)$$

where

WEI = wetness index

DN1 = digit number (return signal amplitude) at time 1

DN2 = digit number at time 2 consecutive to time 1

The study has benefited of information gathered in the area of interest during previous research programs related to lowland mapping with optical imagery. To recall, flood inundation mapping is based on the fact that large and still surface water body will normally appear black in a SAR image, i.e minimum radar echo.

3. RESULTS AND DISCUSSION

3.1. Grassland soil wetness characterization

1) Test site

Two zones located in Famenne, in South-Western Belgium, were selected for the study. They are characterized by soils with poor

natural drainage. Consequently, the areas frequently suffer of waterlogging responsible for a delay in vegetation development stage. These areas are also prone to drought in summer time. The first test site is located in a depression around the village of Focant and covers about 3 000 ha. Clay and silt is the dominant soil unit in the area. Grasslands account for more than 60 % of the cultivated area (Map 1). The second study site is located halfway between the cities of Philippeville in Belgium and Givet in France. The typical soils are silt with an important stone content, silt and clay on schist or calcareous substratum. They surround the village of Surice and cover an area of about 8000 ha. Permanent grass covers 30 % of the cultivated area (Map 2).

2) Field data

Measurement stations were established in both study zones. The station site was selected according to following criteria: (1) representativity as regards soil, topography and hydrology, (2) availability of antecedent data obtained from past research projects, land use and ease of access. Thirteen measurement stations were set in the area of Focant and ten in that of Surice.

Field data were collected the day before the pass or during the pass of ERS-1 satellite. The data consisted of : (1) near soil surface moisture, water table depth along transects and soil surface temperature. Complementary observations were made in relation to the actual farming practices, the state of the vegetation, the presence of dew and surface water.

Besides the field measurements and observations, the study has called on exogenous information such as digitized soil, digitized topographic (DTM), hydrologic, land consolidation and drainage maps. Climatic data relative to the study zones were gathered from the meteorological bulletins issued by the Belgian Royal Meteorological Institute.

3) Results and discussion

Polygons corresponding to the field measurement stations were digitized in order to retrieve the related backscatter coefficients expressed in terms of DN (digit numbers). Each polygon covers about 200 pixels (about 3 ha). The mean DN are then compared to the measured soil wetness.

Soil wetness can be expressed in many ways. We have adopted here the volumetric moisture content and the relative moisture content (in % of soil moisture content at field capacity). The mean soil bulk densities were 1.32 for clay, 1.42 for loam and 1.38 for loam containing stones.

An attempt was made to relate soil moisture content under grass, all major soil units included, and backscatter coefficient expressed in DN (Dewez, 1993). The soil moisture parameter was expressed in volumetric water content or in % of moisture content at field capacity. A linear relation relation was not obvious (Fig. 1). However, the general tendency was observed, that is an increase of return signal intensity with that of moisture content when the soil is not saturated, at least from a threshold value (about 30 %). A maximum of return signal intensity was observed when the soil moisture content is in the nearhood of saturation. For a moisture content greater than saturation, a decrease in return signal intensity is observed.

Effect of vegetation biomass, which can be related to the leaf area index or the degree of soil cover, in the assessment of cropped-soil near surface moisture is represented in Figure 2. The fields under concern were covered by green grass of 35 to 55 cm high. The return signal intensity tends to be higher when the grass cover has a height less or egal to 15 cm. This could be explained by the effect of soil roughness which is indeed relatively "better seen by the radar" in such a case. Figure 3

represents the possible effect of soil surface rugosity under crop cover.

Cropped-soil submersion (wetness greater than saturation) affects strongly the return signal intensity: the more important the submersion the lower the return signal intensity (Fig. 4).

3.2. Lowland wetness

The Laboratory for Hydrology and Remote Sensing of the Land and Water Management Unit has in the recent past carried out research aimed at characterizing the lowlands in Burkina Faso using images obtained from optical platforms (Landsat TM and Spot XS) (Mahamam, 1992; Vranckx, 1993). The general approach was based on two images taken before and after the rainy season respectively, when cloud cover is not important. An example of the results achieved in the framework of this research is given in Fig. 5., which is a map of main landscape units within the study area. It was very difficult to get an image of good quality during the raining period because of cloud cover. Thus our interest to investigate the capabilities of ERS-1 SAR imagery to provide an operational tool for a continuous mapping and monitoring of lowland, particularly its wetness. The application of ERS-1 SAR imagery calls on the principles used to delineate water bodies and the hydrographic network (Inhoff and al., 1987; Solomon, 1992; Dautrebande et al., 1994).

1) Test site

The study site is located in the North-West of Burkina Faso, within following geographic coordinates: Latitudes 11 and 12° N, Longitudes 4 and 5° O (Map 3). The climate presents two well contrasted seasons: a dry season (mid-October to mid-May) and a rainy season (mid-May to mid-October). The annual rainfall varies between 800 mm and 1100 mm. The area is drained by the Black Volta and its tributaries. The relief is gentle to hilly. The

soils are generally ferruginous. They are more or less leached on the slopes and hydromorphic, more or less gleyish in the floodplains or lowlands. The primary hydrographical network comprises some permanent streams. The secondary network consists of many swamps and temporary streams. The natural vegetation comprises bushy savannah on the slopes, temporary grassland and forestry spots in the humid areas. The floodplains and some depression areas constitute the main lowlands within the study zone.

2) Results and discussion

As regards hydrological concerns, there is not much to observe during the dry season in relation to lowland wetness in Soudano-Sahelian regions. This is shown by the ERS-1 SAR image of April 92 (Fig. 6). The upland soils, those located along the slopes and the lowlands are absolutely dry. The water table is deep. As a consequence, the return signal intensity is likely strongly affected by the surface roughness only.

The SAR images of August and September 1992 (Fig. 7 and Fig. 8) clearly show the wet lowlands. They were well covered with water on September. A humidity index considering two consecutive images was applied to refine the characterization of lowland wetness. From the results represented in Fig. 9, one can delineate detention spots (high wetness indices) and the areas flooded during the rainy season. The detention spots are those areas remaining wet long after the rainy season. These areas are of great importance for rice farming.

4. CONCLUSIVE REMARKS

From the research results, following remarks could be drawn :

- Theoretical relations between radar backscatter coefficient and near surface soil moisture

under grass could not be considered as obvious linear expressions. They are rather complex relations in concordance with the diversity of the parameters of influence which interact in natural considerations. In mapping near surface soil moisture under grass from ERS-1 SAR imagery, one must take into account the degree of soil cover, the presence of dew or surface water, etc... A proper guideline to achieve the goal of estimating cropped-soil near surface moisture from ERS-1 SAR imagery could be a holistic approach of the soil-crop-water system. In fact, radar backscatter is in theory a function of soil surface roughness, wetness, vegetation biomass and topography. Moreover, the return signal intensities observed in our study suggest that the crop cover components, its water content, its structure and organization are important factors to take into account for appropriate ERS SAR images interpretation as regards the soil moisture characteristics retrieval.

- It is possible, thanks to the specific radiometric characteristics of surface water, to monitor the extent of wet lowlands during the rainy season in Soudano-Sahelian areas. The methodology applied is simple and call on a wetness index based on two consecutive images. It could already allow one to refine, with an acceptable level of confidence, lowland development plans. Indeed, it has been shown that the water extent within a lowland can be easily monitored using ERS-1 SAR imagery. For a monitoring after the rainy season, ERS-1 SAR imagery or Landsat/Spot sole or in integration could be used.

- The results achieved so far point out the necessary integration of SAR images from ERS and geographic information systems as regards the characterization of agricultural land, namely grassland, soil and lowland wetness.

REFERENCES

Dautrebande, S., M. Badji, A-I Mokadem and A. Dewez. ERS-1 SAR imagery applied to rural basins hydrological studies. I: Flood inundation mapping and monitoring. Paper for presentation at the 1st ERS-1 Pilot Project Workshop, Toledo (Spain): 22-24 June 1994.

Dewez, A. 1993. "Hyperfréquences et humidité des sols. Rapport final. Services de Programmation de la Politique Scientifique, Programme National R-D, Etude des ressources terrestres et marines par satellite. Convention Telsat II/14, F.S.A.Gx (Unité d'Hydraulique Agricole)". pp 87.

Inhoff, M.L., C. Vermilion, M.H. Story, A.M. Choudhury, A. Gafor and F. Polcyn. 1987. Monsoon flood boundary delineation and damage assessment using space borne imaging radar and Landsat data. Photogrammetric Engineering and Remote Sensing, Vol.53 N°4, pp.405-413.

Mahamam, M., A-I. Mokadem, A. Nonguierma and S. Dautrebande. 1992. "Extrapolation spatiale de la méthode de caractérisation des zones humides au Sahel : Application à la région bioclimatique de Bobo-Dioulasso au Burkina Faso. Rapport scientifique, F.S.A.Gx, Unité d'Hydraulique Agricole". pp 54 and annex.

Solomon, I.S. 1992. Methodological consideration for use of ERS-1 imagery for the delineation of river networks in tropical forest areas. Proceedings of the First ERS-1 Symposium: Space at the Service of our Environment, 4-6 November 1992, pp.595-597.

Vranckx, V. 1993. "Contribution de l'imagerie satellitaire radar à l'identification des unités globales du paysage et en particulier à l'identification des zones inondées". Master thesis, F.S.A.Gx, Unité d'Hydraulique Agricole, Gembloux, Sept. 1993. pp 99.

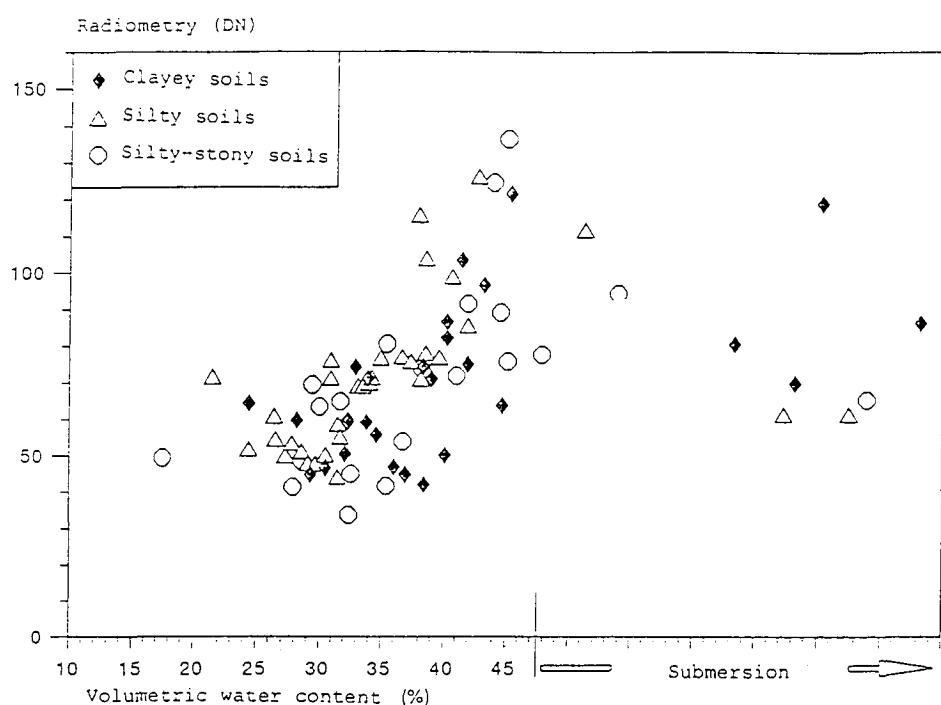


Figure 1. Radiometric response, expressed in DN, in relation to grassland soil wetness.

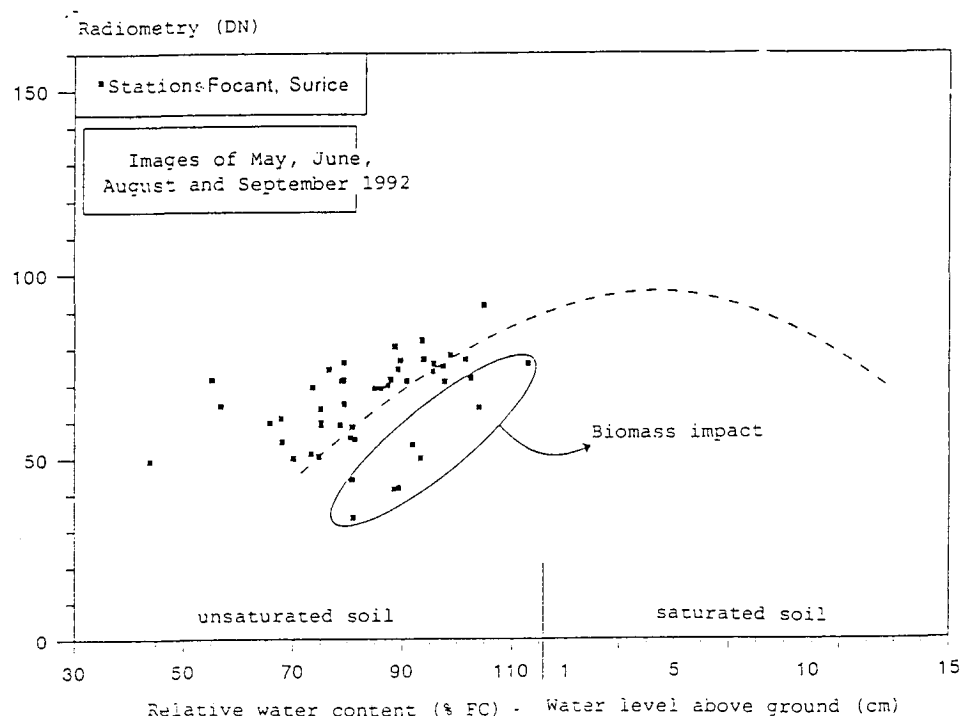


Figure 2. Radiometric response expressed in DN vs grassland soil wetness as possibly affected by biomass.

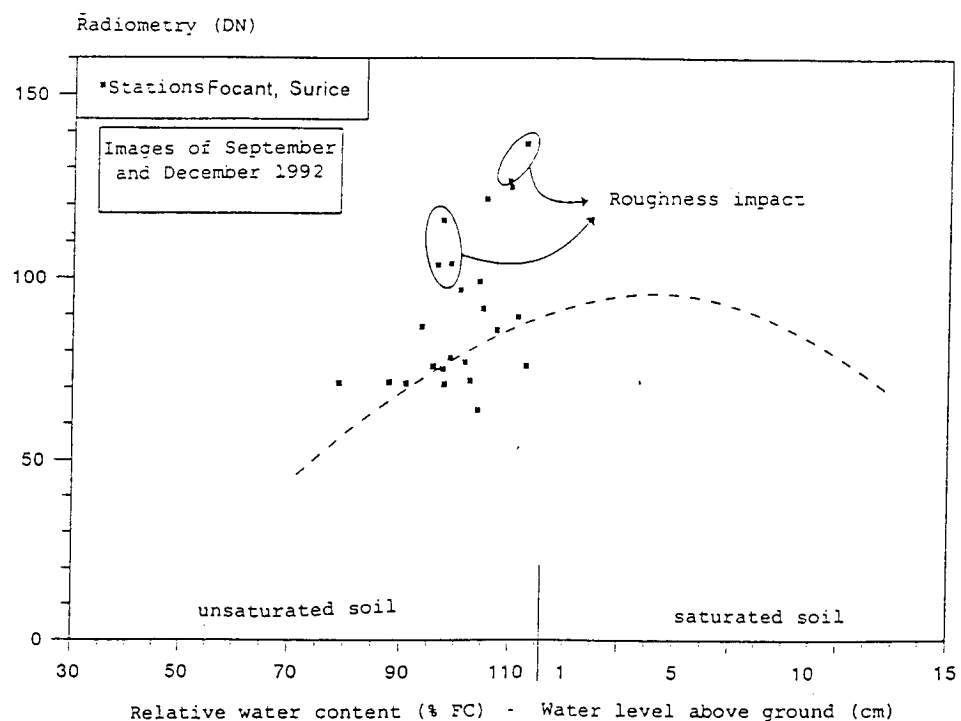


Figure 3. Radiometric response, expressed in DN, vs grassland soil wetness as possibly affected by biomass and soil surface roughness.

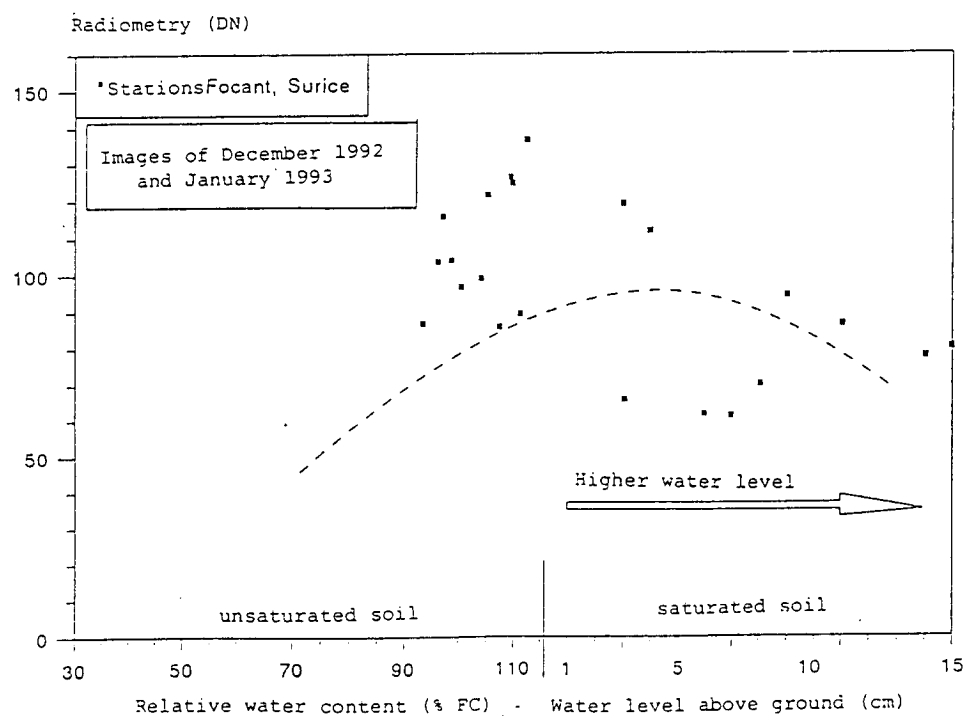
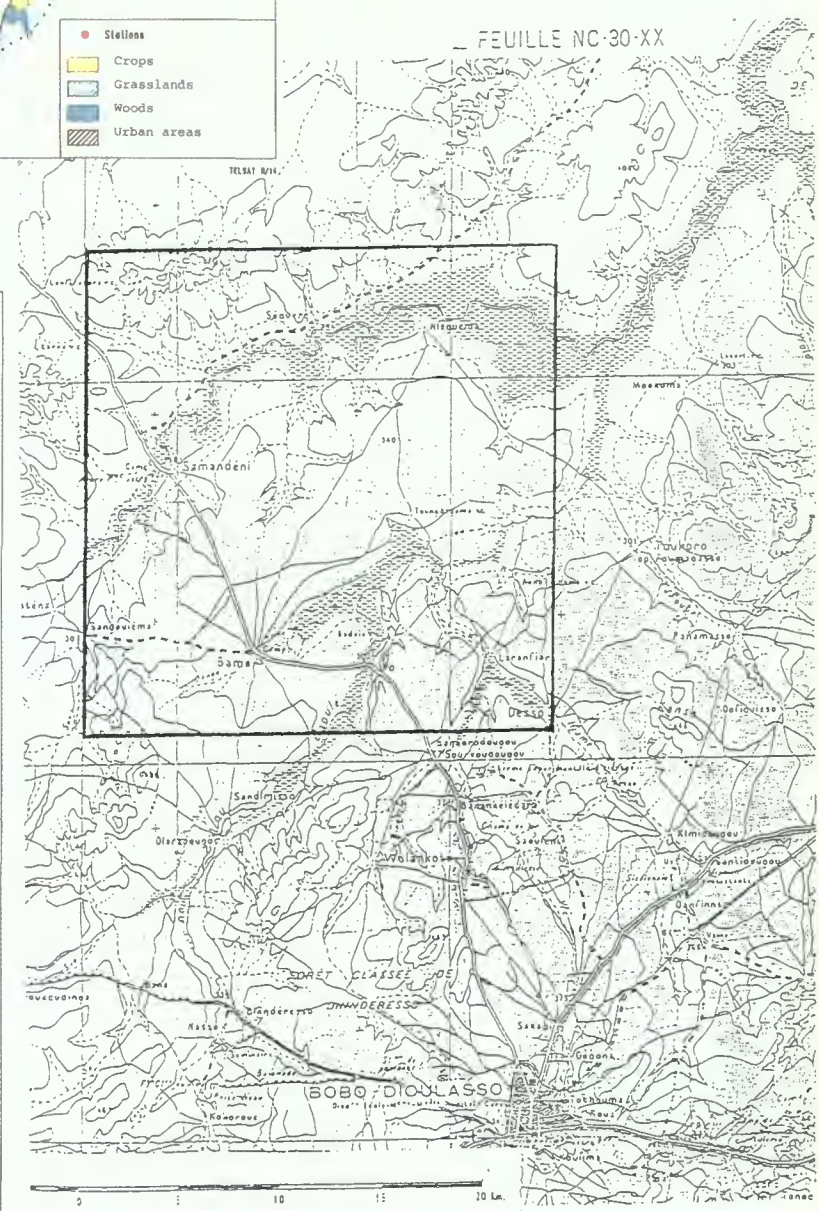
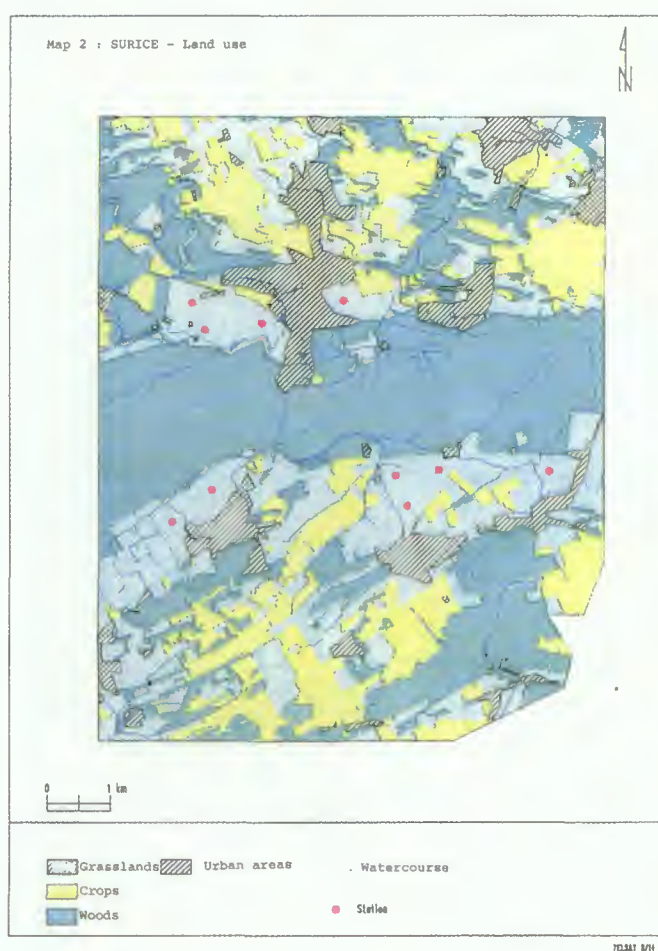
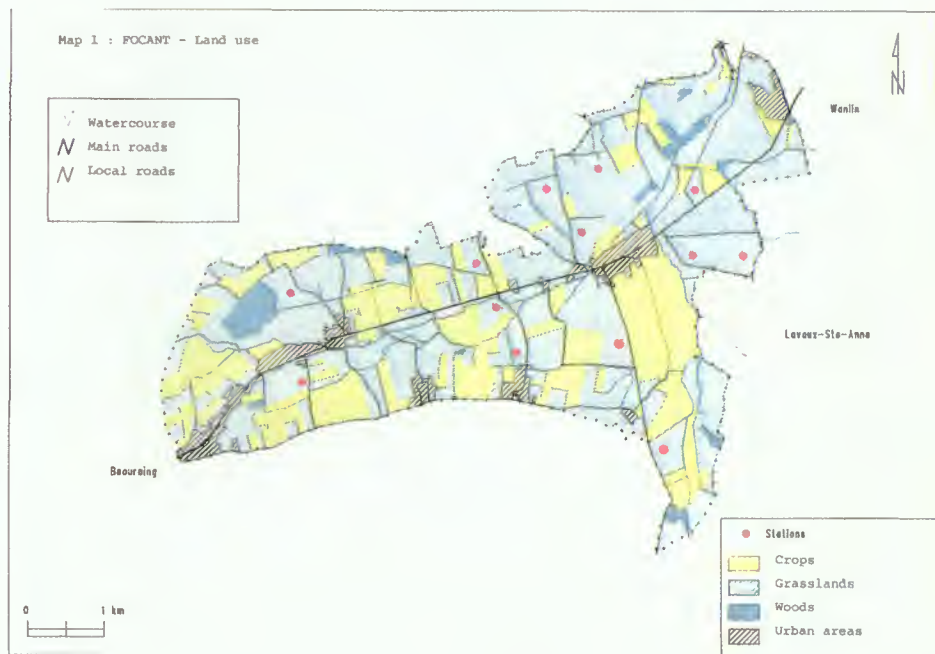


Figure 4. Effect of waterlogging within the grassland on ERS-1 SAR return signal intensity, expressed in DN.



Map 2. Surice - Land use

Map 3. Location map of the study area in Burkina Faso.

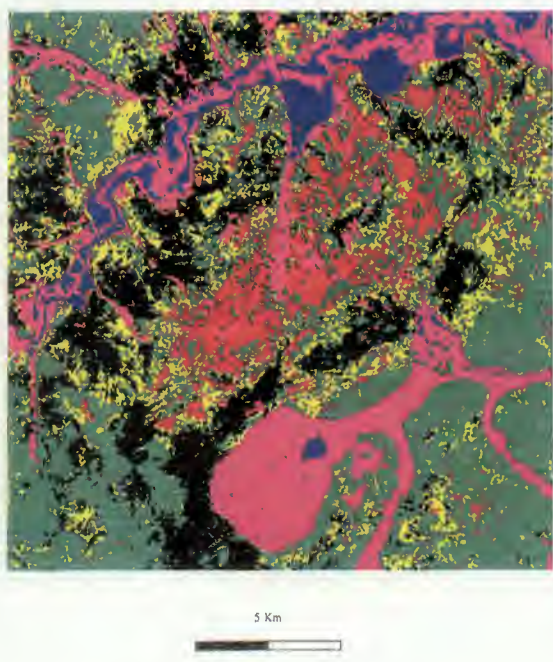


Figure 5. Main landscape units within the study area based on a classification made from Landsat TM imagery.

Figure 6. ERS-1 SAR image of the study area taken on April 1992 during the dry season.

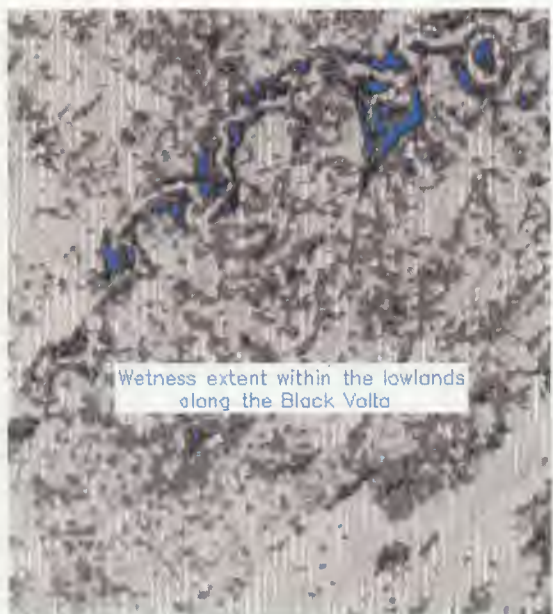
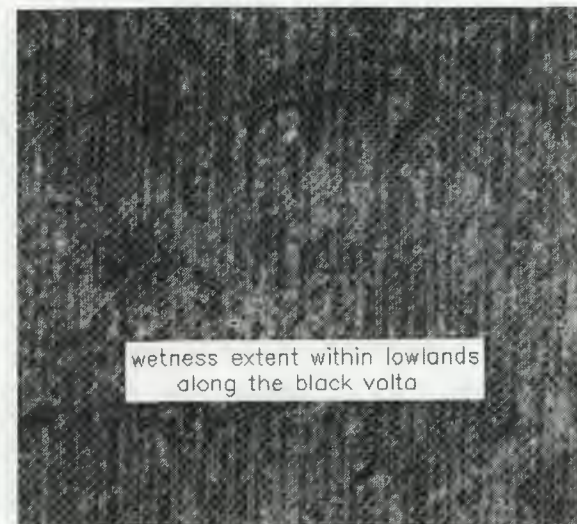


Figure 7. ERS-1 SAR image of the study area on August 1992.

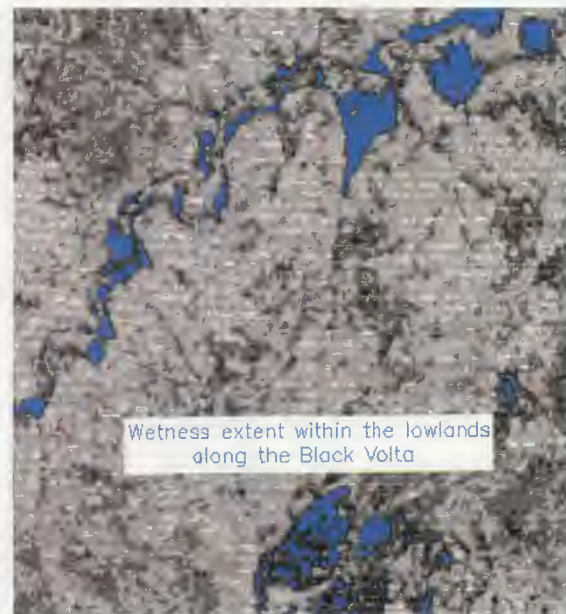


Figure 8. ERS-1 SAR image of the study area on September 1992.

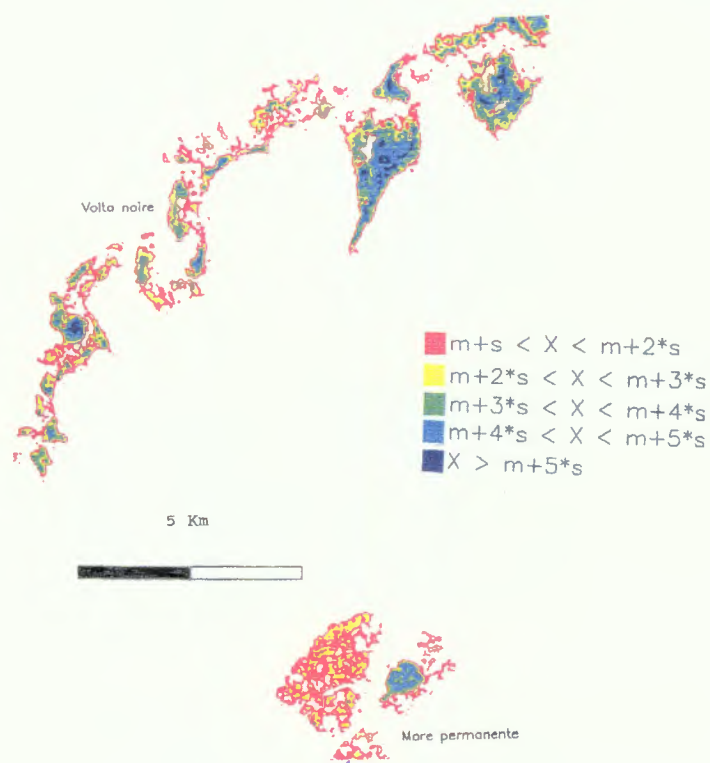


Figure 9. Result of a humidity extent index application for characterizing lowland wetness during the rainy season.



3. FLOODS



**ERS-1 SAR IMAGERY APPLIED TO RURAL BASINS HYDROLOGICAL STUDIES
I : FLOOD INUNDATION MAPPING AND MONITORING**

S. Dautrebande, M. Badji, A-I Mokadem and A. Dewez

Faculté des Sciences Agronomiques de Gembloux
Unité d'Hydraulique Agricole
2, Passage des Déportés
B-5030 Gembloux (Belgique/Belgium)
Tel. + 32 (0)81 62 2187 or 2190; Fax. + 32 (0)81 62 2181

ABSTRACT

In the Southern part of Belgium (Wallonia), particular rainfalls occurring during winter periods combined with conditions of saturated soils have often resulted in floods with damaging inundations.

The tools that are being actually used for the monitoring of moisture balance in watersheds are model-based. They integrated rainfall-runoff and discharge-flood relationships. Operability of these models is closely linked to the availability of spatial and multitemporal information like that provided by satellites. Applications of conventional satellite remote sensing (VIS/IR images) in a temperate humid climate characteristic of Belgium is strongly limited by cloud coverage and weather conditions. Because radar can provide images during the day or night, despite any presence of haze, light rain, snow, clouds or smoke, we have investigated the ability of ERS-1 SAR imagery to provide a proper tool for flood inundation mapping and monitoring in a humid temperate climatic environment. To this end, ERS-1 SAR (Synthetic Aperture Radar) images of December 1992, January and February 1993 were used in support to a study made along the river Lesse valley aimed at mapping and monitoring flood inundated areas. This period was selected because a pass of the satellite on January 12, 1993 has coincided with an extreme flood event which was responsible of inundations in the region. The results from the study have shown a real possibility to apply ERS-1 SAR imagery in flood inundation mapping and monitoring.

1. INTRODUCTION

This paper summarizes the studies that have been completed at the present time by the Laboratory for Hydrology and Remote Sensing of the Land and Water Management Unit in relation to flood inundation mapping and monitoring along the Lesse Valley, in the Southern Region of Belgium , Wallonia, using ERS-1 SAR imagery.

Despite the protection works along rivers and the better understanding of hydrology, extreme floods are still frequent in the Southern Region

of Belgium. These floods can result in severe damages. The Walloon authority, through its Service of Hydrologic Studies, is implementing a Geographic Information System for floodplains management. In this framework, our Laboratory has devoted specific effort to assess the feasibility of SAR (SAR = Synthetic Aperture Radar) imagery in flood inundation mapping and monitoring of areas of high risk.

The study area is located in the agro-ecological zone of Famenne-Ardenne along the Lesse river valley between the cities of Han-

sur-Lesse and Houyet. This river segment is often subjected to inundations which are more or less severe. The creeks composed of Biran, Wimbe, Lomme and Vachau constitute the main tributaries of the river in the study area. Frequent extreme flood events occurring in the region during winter time, have constituted a serious threat to tourism development and cities built in the river floodplain. Moreover cultivated crop damages are not negligible, especially when the soils are submitted to a submersion of long duration. Many protection dykes were built in the area during the last century. These structures did not prevent the floods of January and December 1993 to inundate the cities and villages of Han-sur-Lesse, Eprave, Focant, Balvaux... This paper is related to the flood inundation event of 12 January and 25 December 1993. It mainly synthetizes results published by the Laboratory elsewhere (Dewez, 1993; Mokadem and Dautrebande, 1994).

2. MATERIAL AND METHODS

2.1. Material

The material used in the framework of the study is constituted of SAR images from ERS-1 satellite and an image processing software, PC-ERDAS 7.5. Topographic, hydrographic network, soil and touristic maps were also used.

The satellite ERS-1 was launched in 1991. It has a heliosynchronous quasi-polar orbit at an altitude of about 785 km. The SAR images are obtained from the ESA Services. The images are relative to the 35-day cycle phase C (April 1992 - December 1993) of the satellite. The processed images are of C-band SAR.PRI (Precision Image) type. They were taken on 8 December 1992 and 12 January 1993. The pixel size in such an image is 12.5 x 12.5 m for a scene area of about 100 km.

Radar images have certain characteristics that are fundamentally different from images obtained using optical sensors such as Landsat and Spot. A radar image will present different grey levels related to the relative strength of the microwave energy backscattered by the landscape elements. The intensity of the backscattered signal varies according to roughness, dielectric properties and local slope. High intensity returns appear as light tones on a positive image, while low signal returns appear as dark tones on the imagery.

PC-ERDAS (Earth Resources Data Analysis Systems) software (version 7.5) is a tool enabling one to perform common image processing operations such as : radiometric and geometric corrections; image display enhancement (smoothing, contrasting, filtering, ...); information retrieval (ratioing, index calculation, ...); classification; georeferencing; ...

2.2. Methods

A three-step procedure was used in the processing of ERS-1 SAR images in relation to flood inundation mapping and monitoring. These steps are :

- (1) ERS-1 SAR image pre-processing;
- (2) identification an mapping of flood inundated areas; and
- (3) flood inundations monitoring.

ERS-1 SAR image pre-processing consists in the following :

- Remapping the 16-bit (2 bytes) image data to an 8-bit (1 byte) gray scale representation in order to ease processing with PC-ERDAS 7.5;
- Speckle reduction. ERS-1 SAR images are most often characterized by important grey level variations between adjacent resolution cells. This effect is caused by the coherent nature of the radiation used by the radar system and is called speckle. It happens

because each resolution cell associated with an extended target contains several scattering centers whose elementary returns, by positive or negative interference, originate light or dark image brightness. Speckle is a system phenomenon and is not a result of spatial variation of average reflectivity of the radar illuminated surface. It is important to treat speckle so as to improve the possibility of separation between different classes. Speckle reduction must be done with minimum loss of information. Speckle can be reduced by two methods (FAO/ESA, 1989): SAR image multi-look processing and filtering techniques. It is the latter method which has been used in the study in hand.

Flood inundation mapping is based on the fact that water will normally appear black in a SAR image, i.e minimum radar echo. This principle has provided the guidelines for mapping of inundated area.

Flood inundation monitoring will call on change detection based on temporal differences in radar backscatter. Differencing and ratioing are well-known techniques for change detection (Singh, 1989). In differencing, changes in radar backscatter are measured by subtracting the intensity values pixel per pixel between two dates. In ratioing, changes are measured by dividing the intensities values pixel per pixel and are conveniently expressed in dB (decibels) (that is taking ten times the logarithm in base ten of the ratio of the intensities). The approach used here for flood inundation change monitoring is the differencing method.

3. RESULTS AND DISCUSSION

3.1. ERS-1 SAR image pre-processing

ERS-1 SAR images are 16-bit coded. We have noticed that for the specific study area the image digit numbers (DN) are seldom greater than 1000. Moreover the image feature to be

identified, namely submerged soil, has most often shown DN less than 300. Consequently it was more interesting to remap the 16-bit (2 bytes) image data to an 8-bit (1 byte) gray scale representation. This is done in such a way to get a gray scale dynamics varying between 0 and 255. To this end, the algorithm proposed by Gillepsy (1993) can be used. However, this transformation, in our case, has been simply performed by dividing the 16-bit image data by 4. Any 16-bit image data greater than 1020 is reckoned to 255. By this any image value greater than 1020 is clipped to white. Our main reason to proceed so is that an 8-bit image representation is easier to process with PC-ERDAS 7.5 than a 16-bit image.

The second stage in ERS-1 SAR image processing is related to speckle reduction. The presence of speckle reduces the separability of the various geomorphologic and land use classes, based on radiometry and texture. It is thus important to treat speckle so as to improve the possibility of separation, but with minimum loss of information. To this end, many filters can be applied, depending on the objects to be classified, the image structure and computational aspects. In our case of study, application of complex filters is not justified. Indeed, submerged areas present low DN and a relative spatial homogeneity. Therefore, adjacent cell averaging has been applied successively on a moving window of 3 by 3 and 5 by 5 respectively.

The images obtained from this pre-processing are more homogeneous, with a significant reduction of the standard deviations. Table 1. gives the backscattering characteristics of image extracts including the study area (Lesse valley), before and after the pre-processing.

Table 1. Spectral characteristics of ERS-1 SAR image extracts of the study area (after Mokadem and Dautrebande, 1994).

Image	Before pre-processing				After pre-processing			
	Date	mean	s	min.	max.	mean	s	min.
08 Dec.1992	448.8	184.6	58	2830	111.8	28.3	38	248
12 jan.1993	427.4	231.1	60	6851	106.4	26.0	31	245

s = standard deviation min. = minimum DN max. = maximum DN

mean = mean calculated using a 12 x 12 moving window.

3.2. Identification and mapping of inundated areas

3.2.1. General principles

In using ERS-1 SAR imagery for flood inundation identification and mapping, the following should be considered :

- water will normally appear black, i.e minimum radar echo. This constitutes the basic principle of radar imagery interpretation to identify flood inundated areas.

However, this remark must be applied keeping in mind the following :

- wide area water bodies that display waves during the survey may present various reflectances depending upon the wave characteristics. However such areas can be delineated from other types of imagery, and therefore side situations are of no consequence for the problem at hand;
- other objects having smooth surface, e.g asphalt covered areas, will give low signal returns. These objects will also appear as dark tones. The shape and pattern of the objects should be considered to distinguish those likely to be flood inundated areas from others with similar low echo.

The same basic principle was applied by Solomon (1992) for river networks delineation

in tropical forest areas. Moreover they have been proved to be useful in monsoon flood boundary delineation and damage assessment (Inhoff and al., 1987).

3.2.2. Effective delineation of flood inundations

This is done by considering two different approaches. The first approach will utilise one image. The second one considers two subsequent images and applies a procedure similar to change detection algorithm based on normalized difference.

a) Approach based on one image. Its application requires the definition of a threshold corresponding to the radar echo for inundation still water. The processed images are that of 12 January and 25 December 1993, two dates corresponding to a flood inundation event. Images extract are shown in Figure 1a,b.

As regards the flooding that occurred on January 1993 inundated areas on a segment of the Lesse river, identified during field visit, are comprised in classes for which the DN are less than 80 for the image taken on January (Fig.1a). Extended submersion areas are indicated with an arrow on the image extract. To ease the feature location, the digitized river course is superimposed to the image. From the image extract, one can notice that inundations

did occur both along the Lesse river and some of its tributaries (Biran, Vachau, Wimbe, ...). One can also expect, considering the general principles of inundation mapping, that not only the inundated areas will show DN less than 80. The permanent water bodies and surfaces of low radar illumination will also present low DN. We can see in the image extract that the ponds, the E411 highway West banks and the natural slopes oriented to West could be confused with inundated areas. There is even a spatial continuity with actual inundation strips. As a consequence of this possible confusion, it is rather difficult to conceive a flood inundation mapping procedure based solely on one ERS-1 SAR image.

Concerning the image taken on 25 December (Fig.1b), inundation water has shown, in 8-bit representation, DN less than 40. The ERS-1 SAR image recorded the remaining flooding as it occurred on 25 December along the Sambre, a tributary of the river Meuse. ERS-1 SAR/Landsat TM overlay image was made and shown in Figure 2. We have believed that such an operation could provide important information for studying the effects of flood inundations in the region of concern.

The TM image is a multispectral sensor that collects data in seven bands, from the visible through the thermal infrared. These bands allow identification and classification of surface features with a high degree of accuracy. However, clouds, haze and rain can alterate the quality of Landsat TM image. Radar, as opposed to TM, is excellent for penetrating haze, light rain and clouds. However, the single-band nature of the data makes it difficult to identify and classify surface features.

The approach based on one image must call on the integration of DTM and maps of permanent water bodies to be actually operational. As regards image taken on 25 December, inundation water has shown, in 8-bit representation, DN less than 40.

b) Approach based on two images. The second method requires two different images of the same area. They must be selected to characterize the change in radar backscattering in relation to the dynamics of the flood inundation. The selection criterion for the two images is such that if there is any significant change between the two images it must be due to the presence or absence of the feature of interest, namely inundation water in this study case. As a consequence of this criterion, the two selected images must be taken in consecutive times. In consideration of this constraint, the images taken on 8 December 1992 and 12 January 1993 were chosen in applying the approach based on two images. These two images have, moreover, similar antecedent climatic conditions : humid and cold weather during the three days prior to image acquisition. The vegetation cover (grassland, forests, grain crops) has not significantly changed from December to January. Figure 3. represents an extract of the image taken on 8 December 1992, including the study area. The two images differ significantly only on the extent of inundated areas. In overlaying the two selected images, one can map actual inundated areas and clean the confusion features that would appear if the approach based on one image was applied.

3.3. Flood inundation monitoring

An index, based on the differencing approach for change detection, was implemented to detect temporal landscape changes. The related expression is as follows :

$$I = (DN_2 - DN_1) / (DN_2 + DN_1)$$

where

I = value of the derived image

DN₂ = digit number of image at time 2

DN₁ = digit number of image at time 1

If the two images are taken at a relatively short time interval so that the only possible significant change is due to the change in

inundated area extent. The index has proved to be an efficient tool for flood inundation monitoring. It was applied to derive an image from those of 12 January 1993 (DN1) and 8 December 1992 (DN2). The time interval between the first two images is 35 days (ERS-1 phase C cycle). The result of the derived image analysis is given in Figure 4.

This approach of flood inundation monitoring has also been applied to characterize the water detention areas along the Lesse river (Fig.5). Water detention areas are likely the locations where the water will remain for a certain time after the flood recession.

4. CONCLUSIVE REMARKS

ERS-1 SAR imagery was used to map and to monitor successfully inundated areas within the Lesse river watershed. These inundations have stemmed from extreme flood events that have occurred on January 12, and December 22-23, 1993.. The proposed methods are simple and easy to apply.

Because a still water body will normally appear black in a radar image, i.e minimum radar echo, this radiometric characteristics has provided the guidelines for mapping of inundated area with ERS-1 SAR imagery. The possible confusion with other elements giving low signal returns can be relieved through the integration of external information such as maps of wide area water bodies and other objects having smooth surface, e.g. asphalt covered areas, these objects appearing also as dark tones. The shape and pattern of the objects should be considered to distinguish those likely to be flood inundated areas from others with similar low echo.

Wide area water bodies that display waves during the survey may present various reflectances depending upon the wave characteristics. However such areas can be delineated from other types of imagery, and

therefore side situations are of no consequence for the problem at hand.

By using two images from two consecutive dates, it is possible to clean the confusion areas, included the effect of local slope.

It has been observed that ERS-1 SAR/Landsat TM overlay image could provide important information for studying the effects of flood inundations.

An index, based on the differencing approach for change detection, was applied to monitor the change in inundation extent as a function of time. The index has a mathematical expression similar to the well known normalized difference vegetation index. It was applied to map the flood water detention areas within the floodplain Lesse river.

REFERENCES

- Deweze, A. 1993. "Hyperfréquences et humidité des sols. Rapport final. Services de Programmation de la Politique Scientifique. Convention Telsat II/14". pp.87.
- FAO/ESA. 1989. Principles of radar imagery. FAO Remote Sensing Series No 46.
- Gillepsy, Th. 1993. Optimized algorithms for displaying 16-bit gray scale images on 8-bit computer graphic systems. Journal of Digital Imaging, Vol 6, N° 1 (February), 1993: pp.25-29.
- Inhoff, M.L., C. Vermilion, M.H. Story, A.M. Choudhury, A. Gafor and F. Polcyn. 1987. Monsoon flood boundary delineation and damage assessment using space borne imaging radar and Landsat data. Photogrammetric Engineering and Remote Sensing, Vol.53 N° 4, pp.405-413.
- Mokadem, A-I. and S. Dautrebande. 1994. "Télédétection des inondations par le satellite ERS-1". Tribune de l'Eau, Vol.47 N°567-1, 71-78.

Singh, A. 1989. Digital change detection techniques using remotely sensed data. Int. J. Remote Sensing, Vol 10(6):989-1003.

Solomon I.S. 1992. Methodological consideration for use of ERS-1 imagery for the delineation of river networks in tropical forest areas. Proceedings of the First ERS-1 Symposium: Space at the Service of our Environment, 4-6 November 1992, pp.595-597.

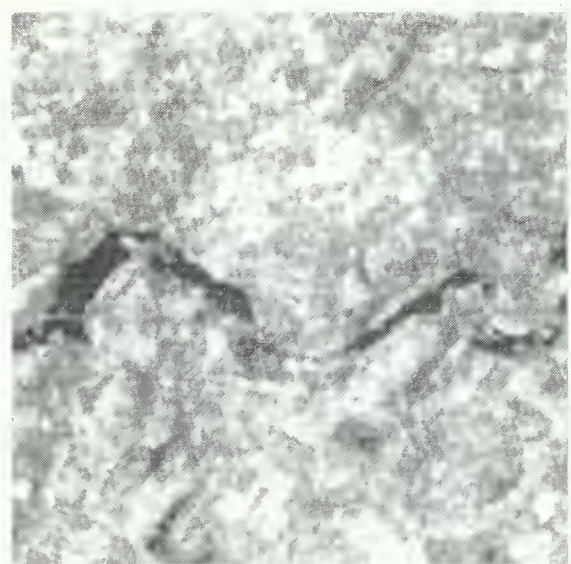
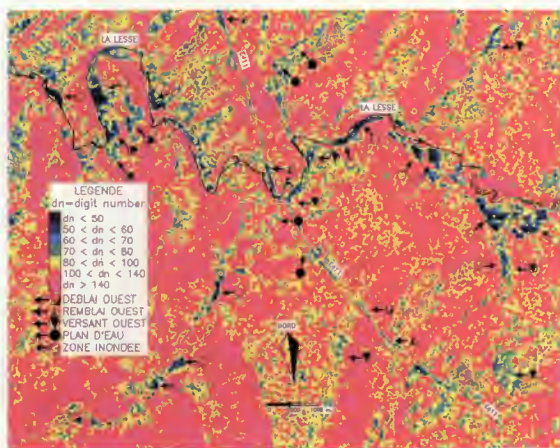


Figure 1a. Flooding along the Lesse river valley. ERS-1 SAR image of 12 January 1993.

Figure 1b. Remaining flooding on a segment of the Sambre catchment. ERS-1 SAR image of 25 December 1993.

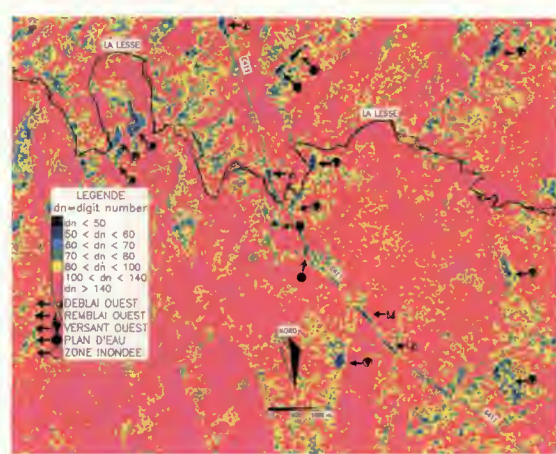
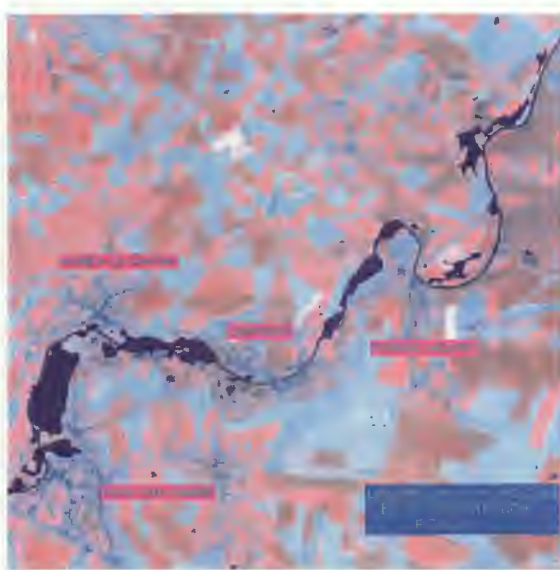


Figure 2. ERS-1 SAR/Landsat TM overlay image. The two images were overlaid to provide higher accuracy in determining landcover information to better assess what kind of areas are flooded.

Figure 3. ERS-1 SAR image of the studied area along the Lesse river valley taken on 8 December 1992.

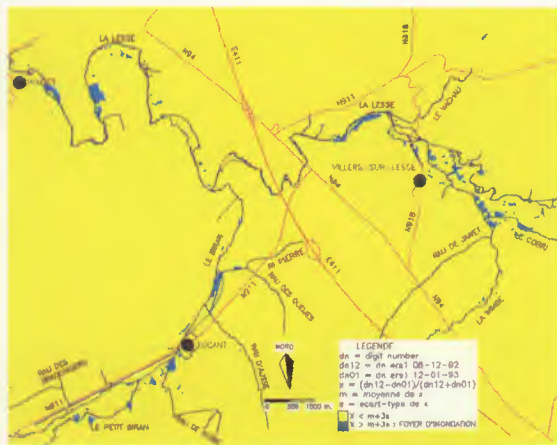


Figure 4. Result of index application for flood inundation monitoring along the Lesse river valley from multitemporal image analysis. The index is similar, in its mathematical expression, to the well known normalized difference vegetation index.

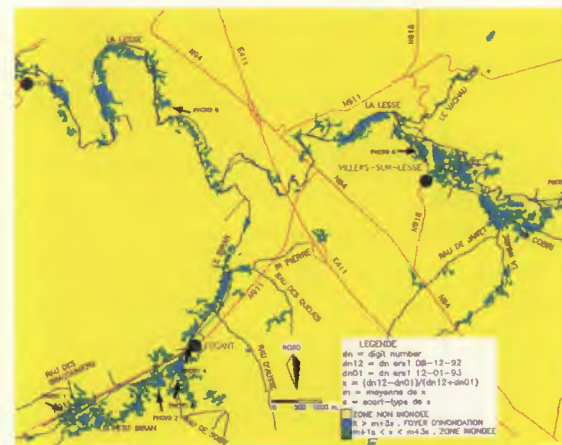


Figure 5. Characterization of flood inundation water detention areas. Water detention areas correspond to places where flooding water will likely remain for a certain time after the flood recession.

**A STUDY OF FLOODING ON LOUGH CORRIB, IRELAND DURING EARLY 1994
USING ERS-1 SAR DATA**

John Matthews and Sean Gaffney (PP2UK1)

School of Ocean Sciences
University of Wales, Menai Bridge
Gwynedd, LL59 5EY, Wales U.K.
phone: +44 248 382586, fax: +44 248 716367

ABSTRACT

ERS-1 SAR imagery is used to study the development and recovery of flooding on Lough Corrib, W. Ireland, following a period of high rainfall at the end of 1993. The SAR data provide a synoptic view of these events which would be very difficult to gain in any other way. The analysis is based on three SAR images from which we define lake boundaries corresponding to dry summer, flood and recovery phase levels. The largest changes in the overall shape of the lake take place on its eastern side with extensive flooding shown along the courses of the Clare and Cregg input rivers. The flood appears to wash a considerable amount of fresh surfactant material down into the lake which subsequently reduces the backscatter levels from the water surface recorded by the SAR.

1. INTRODUCTION AND OBJECTIVE

Passive remote sensing has been used to monitor lake water quality in Ireland for a number of years (McGarrigle, 1990). These techniques require largely cloud free atmospheric conditions which are often difficult to achieve and which inevitably bias data collection towards periods of fine weather in the summer months. The availability of ERS-1 SAR data on a more or less continual basis throughout the year opens up new possibilities for environmental monitoring, particularly for processes taking place in the winter months.

This study forms part of an ERS-1 Pilot Project (PP2UK1) aimed at oceanographic and hydrological applications of SAR imagery to the west coast regions of Britain and Ireland. Here, we use the fact that land and water surfaces generally have very different backscatter characteristics to monitor the spatio-temporal development of a winter flood event on the southern portion of Lough Corrib in the west of Ireland. The overall objective of the study is to demonstrate the feasibility of a more comprehensive flood research programme, based on ERS SAR, which could include other major Irish lakes and the Shannon river.

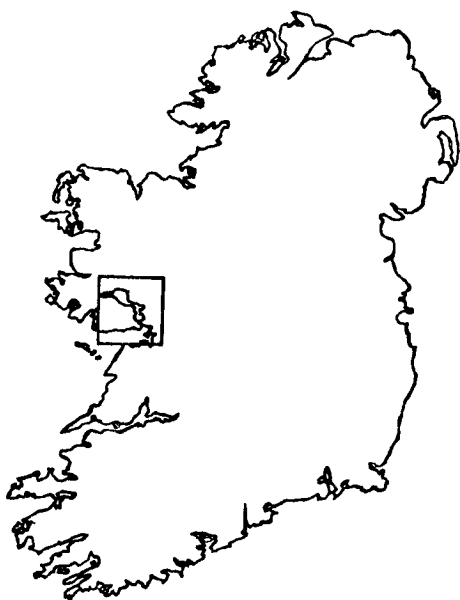


Figure 1 Map of Ireland (Lough Corrib inset).

2. DATA ANALYSIS

With an approximate area of 17,000 hectares, Lough Corrib is the second largest lake in Ireland (Figure 1) and lies roughly 5km to the north of Galway. The major riverine discharge from the lake is via the Corrib river which flows into Galway Bay, whereas water input is from a number of smaller rivers, including the Clare and Cregg rivers in the southeast and from underground links with Lough Mask in the north. The types of habitat around the lake shore include marsh, wood and pasture land. The climate is dominated by the frequent passage of low pressure systems from the Atlantic, so rainfall is spread throughout the year. The period of heavy rainfall considered in this study was in December 1993, when a relatively high monthly level above 240mm was recorded (Figure 2).

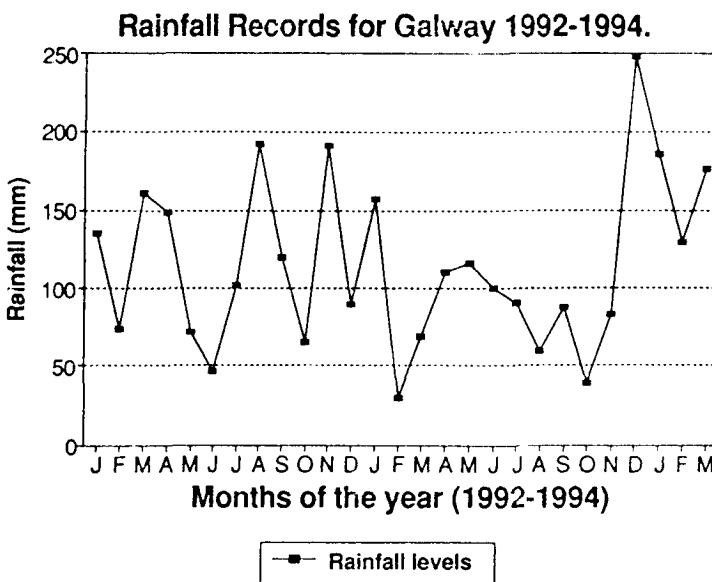


Figure 2 Monthly precipitation levels recorded at Galway, Ireland from January 1992 to March 1994.

The ERS-1 SAR image shown in Figure 3 was acquired on 7 July 1992 following a period of low rainfall of under 50mm in June of that year. For the present purpose, this image is taken to represent a nominal low water level for Lough Corrib. The distinction between open water (relatively low backscatter) and land is clearly visible in the image, as are the Corrib and Clare rivers to the south and east respectively. A series of striations, aligned roughly north-south can be seen on the lake. With light to moderate northerly winds present, these semi-regular bands probably indicate the presence of wind rows which can create linear slicks as a result of their rotary circulation patterns. The slicks are formed in the regions of dead water between adjacent rotation cells and contain detrital material and oils as decay products (e.g. Smith, 1975).

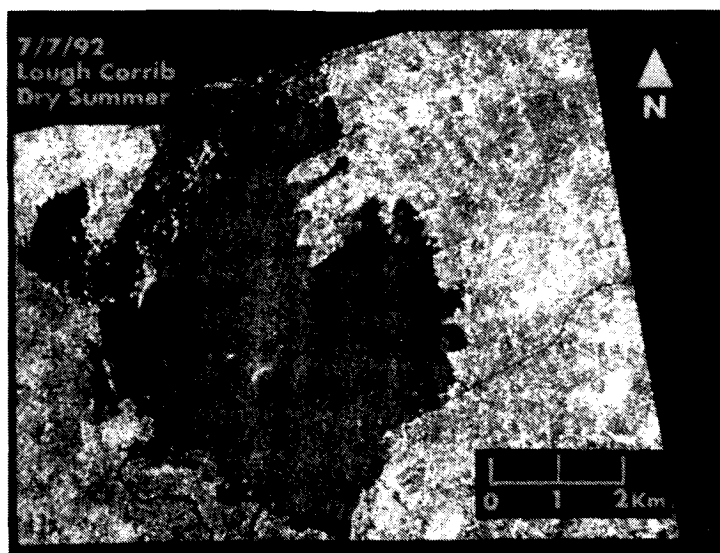


Figure 3 ERS-1 SAR image of Lough Corrib acquired on 7 July 1992 and corresponding to a dry summer lake level.

Figure 4 shows SAR imagery from 4 January 1994, following the heavy rainfall of the previous month. It is clear that large tracts of land have been submerged, particularly on the east side of the lake and going up the courses of the Clare and Cregg rivers. On this side of the lake, there is a complex pattern of interwoven slicks which does not appear further west. This suggests that fresh surfactant material is being washed into the lake from the newly flooded areas. To the south, the Corrib river is now spatially wider, indicating the anticipated enhanced discharge from the lake.

A close-up of the effect of the flooding along the Clare river is given in Figure 5 taken from the 4 January 1994 SAR image. Here the river banks are composed of waste material derived from dredging activities and, as these remain above water, they appear in the image as relatively bright lines in an otherwise dark(water) background. The region of flooding is sharply terminated some 5km upstream where the terrain rises.

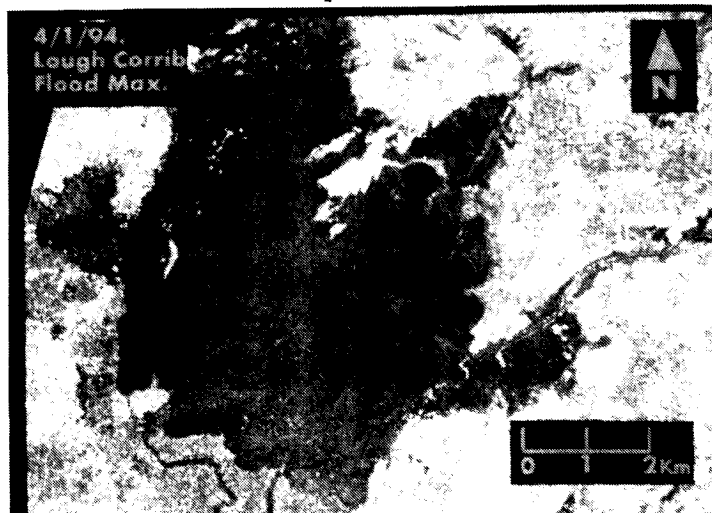


Figure 4 ERS-1 SAR image of Lough Corrib acquired on 4 January 1994 under flood conditions

The final image in the sequence is shown in Figure 6 and was acquired on 18 February 1994. Here the Lough Corrib water level corresponds to the recovery phase following the flood. It is perhaps surprising that in spite of continuing high rainfall of 130mm in January 1994, the lake boundaries defined here are close to those of Figure 3 following a relatively dry month with only 50mm of precipitation. This suggests that the time scales for the growth and decay of the inundation are fairly short (perhaps a few days) though a finer temporal resolution would be required in the data set to fully investigate this aspect.

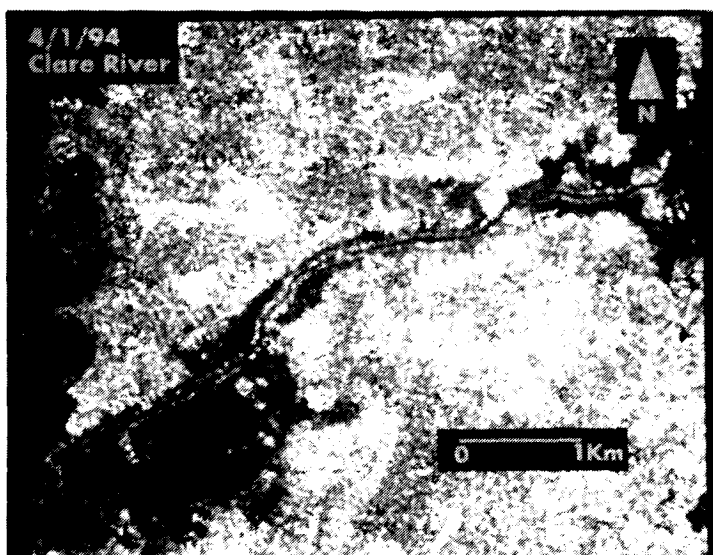


Figure 5 Close up of ERS-1 SAR image from 4 January 1994 showing flood development along the course of the Clare river

In Figure 6, an unusual and dramatic pattern of surface roughness variation can be seen in the eastern portion of the lake, where a wavy step-like change in backscatter strength develops. It is difficult to interpret this feature with any confidence, but evidence from the image shown in Figure 4 suggests a build up of surfactant films derived from flooded areas takes place in the east. In this, the recovery phase, the surface materials may have become consolidated into one large slick giving low SAR backscatter over a wide region in the east. Over the previous 24 hours, wind forcing has been moderate to strong and from a generally east-southeast direction, though at the time of the image, winds were decreasing to calm. Since strong backscatter is received on the west side of the lake (indicating higher waves) it is clear that wind forcing variations are also involved. The cause of the wave-like patterns formed along the boundary of the backscatter change is not yet known, though clearly this is a very perturbed and complex surface roughness scenario. In future work we will examine the fate of the surfactant input from the flood identified in Figure 4 (and possibly Figure 6) in terms of both decay and output from the Corrib river into Galway Bay.

As the boundary between land and water can usually be defined in the SAR images (since a large change in backscatter takes place there) the land-water transition for each of the three co-registered images discussed above was manually digitized and entered as an overlay plane in a flood GIS database. The result of this manipulation is shown in Figure 7. This figure provides a convenient summary of the development of the flood and clearly shows the submergence of low lying land along the Clare and Cregg river courses.

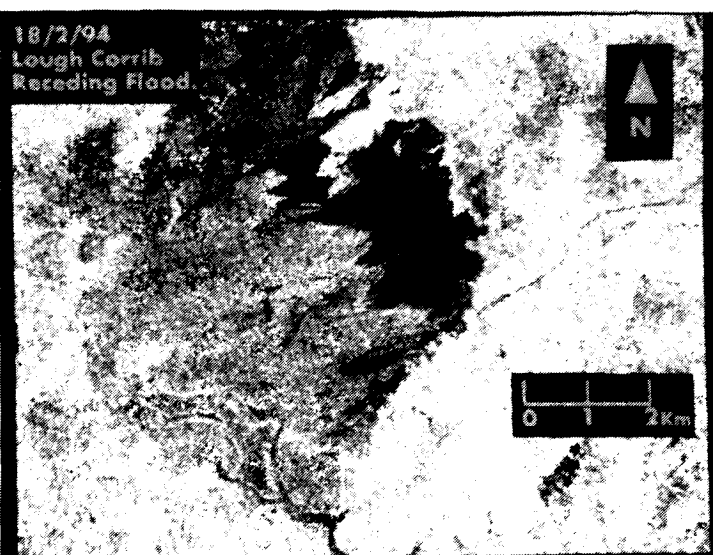


Figure 6 ERS-1 SAR image of Lough Corrib acquired on 18 February 1994 in the flood recovery phase

3. DISCUSSION

The pilot study reported here demonstrates the feasibility of using ERS-1 SAR data in flood studies in regions where frequent cloud cover hampers the application of passive optical and infrared techniques. But in spite of the obvious benefit of the greater availability of SAR data, there are a number of practical issues that need to be resolved before the technique of SAR flood mapping can be considered fully mature. Firstly, the process of defining a lake boundary through the large change in backscatter anticipated at a land/water interface begs the question of exactly what this boundary represents and how it might compare with a boundary drawn up from, say, passive infrared imagery.

In some cases the water edge defined from a SAR image could be incorrectly located, for example when, within the flooded region, a canopy of tall grass, bushes or trees dominates the backscatter or when strong wave activity on the lake smears out the border between land and water. An example of the latter problem can be seen in Figure 6 at the southern end of Lough Corrib where it is difficult to distinguish open water from the wetlands at the head of the Corrib river.

A second issue concerns the practical use of SAR data in flood warning and disaster management. From the discussion of flood timescales presented above, it is clear that a greater temporal resolution (less time between scenes) is required if SAR data are eventually to be used operationally. From this point of view, further dual operation of ERS-1 and ERS-2 is a significant advance.

ACKNOWLEDGEMENTS

The authors wish to thank M. McGarrigle for helpful advice and comments.

REFERENCES

McGarrigle, M.L., 1990, Satellite and low altitude remote sensing of lake chlorophyll in Ireland, Proceedings of the International Association for Theoretical and Applied Limnology, 24, 563-566, 1990.

Smith, I.R., 1975, Turbulence in Lakes and Rivers, Freshwater Biological Association U.K., pub. 29

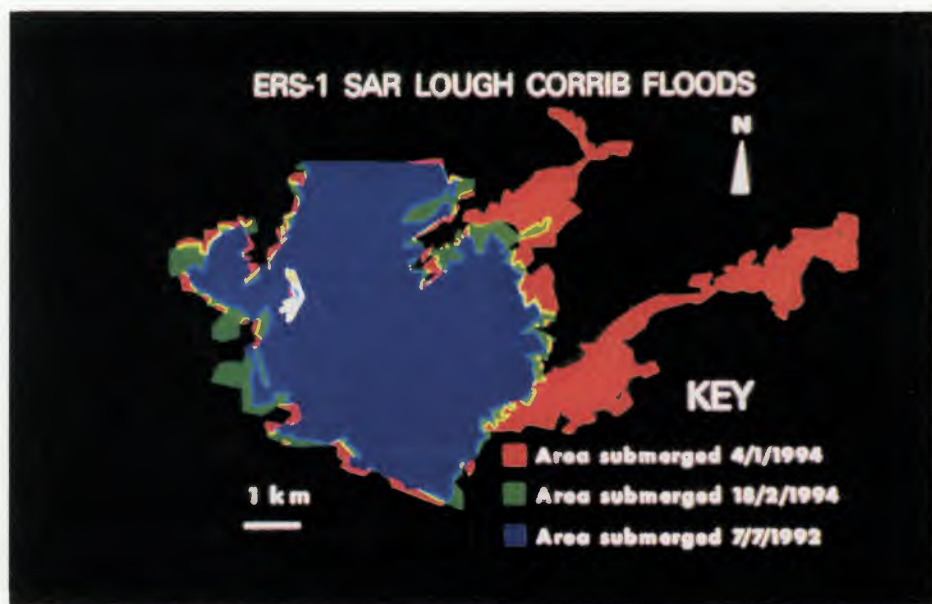


Figure 7 Overlay composite flood history derived from Figures 3,4 and 6

ASSESSMENT OF MULTI-TEMPORAL ERS-1 SAR AND LANDSAT TM DATA FOR MAPPING THE AMAZON RIVER FLOODPLAIN

Christoph Corves

Department of Geography
University of Edinburgh
Edinburgh EH8 9XP
Scotland, U.K.

Tel: + 44 - 31 - 650 2523

Fax: + 44 - 31 - 650 2524

E-mail: CORVES@GEOVAX.ED.AC.UK

Abstract

Multitemporal ERS-1 SAR data of the Amazon river floodplain have been assessed in terms of mapping the floodplain boundary, major vegetation formations, and floodplain inundation. Results derived from ERS-1 data have been compared with maps prepared from Landsat TM data and ground verification. The results indicate that the combination of two ERS-1 acquisition dates (high water season and low water season) allows to derive maps of the floodplain boundary and the major vegetation formations (woody vegetation, terrestrial herbaceous vegetation, floating aquatic grasses). Such maps would allow to scale point measurements of trace gas emissions, i.e. methane, up to regional estimates.

1. Tropical floodplains as source areas of atmospheric trace gases

Tropical ecosystems are important source regions of trace gases that can enhance the greenhouse effect. Global budget calculations indicate that tropical wetlands make a substantial contribution to tropospheric methane (see, for example, Bartlett et al., 1988; Bartlett et al., 1990; Devol et al., 1988). Bartlett et al. (1990) stratified flux measurements in the Amazon river floodplain according to three broad categories of land cover types: open water areas, mats of floating aquatic grasses ('floating meadows'), and flooded forests. Flux from floating meadows was higher than from flooded forest. Flux from both vegetation types was significantly higher than from open water. Calculations of the magnitude of regional or global fluxes from tropical wetlands have been difficult due to the temporal and spatial variability of the sources. Bartlett et al. state:

Accurate regional-scale flux estimates from large, heterogeneous areas such as the floodplains of the Amazon River are dependent on adequate characterisation of temporal and spatial variability in

emission rates and emission areas. This is particularly true in the case of the Amazon due to the controls on flux and emission area exerted by seasonal water level changes. ... The areas covered by the three broad categories of floodplain habitat are poorly known. ... Since habitat areas have been commonly expressed as percentages of the total floodplain, floodplain area is critical to regional extrapolation. This figure is not known with any certainty and estimates vary from $7 \cdot 10^4$ to $5 \cdot 10^5$ km². ... Assessment of temporal variability in the spatial extent of source areas remains fairly crude at this time and is probably the largest source of temporal error in regional extrapolation. (Bartlett et al. 1990).

Satellite based measurements of the following three parameters are key to improving current estimates of methane flux from tropical floodplains:

- (1) total extent of the floodplains
- (2) land cover of tropical floodplains (i.e. water, floating meadows, forest)
- (3) duration of inundation for different habitats and vegetation types of the floodplains

2. The project region

The Manaus region is situated in the central Brazilian Amazon basin. Geologically, it can be divided into Tertiary sedimentary plains ('terra firme') of varying levels of dissection (Barreiras Formation: heavily dissected; Solimoes Formation: low to intermediate level of dissection) and the floodplains. The floodplains are characterized by a complex mosaic of vegetation formations, ranging from floating aquatic grasses to dense forest. The annual fluctuation of water level in the main rivers varies between 9 and 15 metres with the high water period from May to August and the low water period from October to December (Figure 1). The floodplains along the sediment rich Amazon river are up to 70 km wide. A reconnaissance survey of vegetation and land use has been carried out concurrent with Landsat image acquisition in July-September 1991. The vegetation has been classified into formations based on geographical characteristics of the site (geology, geomorphology, soils, hydrology, etc.) and the structure of the vegetation (dominant life forms, canopy closure, canopy height, etc.).

3. Data

The study has used ERS-1 SAR data of 5/92, 6/92, 7/92, 11/92, 12/92, and Landsat TM data of 8/88 and 8/91. ERS-1 data were acquired in PRI format and Landsat TM data at 'system-corrected' level. The ERS-1 PRI data have been coregistered to the TM data using a 2nd order polynomial fit and cubic convolution resampling.

4. Mapping the extent of the floodplains

4.1. Existing Brazilian maps

Two map sources provide information on the extent of the flood plains in the Brazilian Amazon region: (a) 1:250,000 scale maps produced from the airborne radar survey of the Amazon executed under the Projeto Radam in the 1970s, and (b) 1:100,000 scale topographic maps produced from air photo surveys, also undertaken in the 1970s. Both map sources disagree widely on the extent of the area subject to inundation in the Manaus region.

4.2. Landsat data

Landsat TM data allow the visual interpretation of the floodplain / upland boundary. This can be achieved with relatively high accuracy where the floodplains cut through the strongly dissected sediments of the Barreiras Formation. The interpretation of floodplain limits is less reliable in areas where the floodplains cut through sediments of the much less dissected Solimoes Formation.

4.3. ERS-1 SAR data

Due to the inherent characteristics of side looking SAR and the high incidence angle of ERS-1 SAR, topographic elements such as hills and valleys are enhanced. Even in an area such as the Manaus region where topographic relief is not pronounced (the altitude varies between 30-150 metres), ERS-1 SAR data allow a more exact detection of flood plain boundaries than vertical view Landsat TM data. The first principal component band calculated from 5 dates of ERS-1 SAR data exhibited a greatly enhanced visibility of terrain features, much better representation of small scale detail, and reduced speckle. It was particularly suitable for the visual interpretation of the floodplain boundaries. The floodplain boundaries derived from ERS-1 SAR data agreed better with the 1:250,000 scale Projeto Radam maps than with the 1:100,000 scale topographic maps.

5. Mapping the vegetation of the floodplains

5.1. Landsat data

The vegetation in humid tropical regions tends to have high species diversity. Particularly in forests, individual tree species are rarely dominant to the extent that they determine the spectral response in visible / infrared spectrum (exceptions do exist, e.g. secondary forest dominated by Cecropia species). As a consequence, floristically quite distinct - but structurally similar - forest types on terra firme and

floodplains cannot be separated in TM spectral space. The analysis of TM spectral data has lead to the conclusion that TM data of the Manaus region primarily reflect vegetation structure (woody elements - herbaceous elements), soil, water or shadow (canopy shadow, topographic shadow). TM data allowed the differentiation of the following classes of floodplain vegetation:

1. Climax forest (closed canopy, emergents, short flooding)
2. Intermediate to late forest succession on levees (closed canopy, no emergents, short flooding)
3. Intermediate forest succession inn depressions (open canopy, no emergents, intermediate flooding)
4. Early succession on levees (dense shrubs and low trees, intermediate to short flooding)
5. Early succession in depressions (open shrubs and low trees, intermediate to long flooding)
6. Aningal (herbaceous aquatic vegetation with some shrubs or low trees, long flooding)
7. Floating meadows (floating herbaceous vegetation, mostly grasses, long flooding)
8. Grassland on high ground (grasses, some shrubs or weeds, short flooding)

5.2. ERS-1 SAR data

The variety of vegetation formations that can be mapped from TM data cannot be detected on monotemporal nor multitemporal ERS-1 data. However, during the inundated period, three vegetation formations can be distinguished in terms of backscatter intensity: (1) floating grass mats, (2) woody vegetation (including the entire spectrum from open shrub vegetation to closed forest), and (3) terrestrial grasses. During the low water season, only two distinct levels of backscatter exist: (1) terrestrial grasses and (2) woody vegetation (Figure 2). Visual interpretation of false colour composites of the July and November (or December) images allowed to map 4 classes: (1) water, (2) woody vegetation, (3) terrestrial grasses, and (4) floating meadows. A digital classification based on spectral properties has been carried out (speckle reduction; supervised training; maximum likelihood classification). It proved possible to separate the same four classes of land cover. Misclassification affected mainly water areas being classified as vegetation classes. This is due to the high variability (water currents, wind) of backscatter from large open water surfaces. The classification of the 1992 ERS-1 SAR data was compared with a classification of the 1991 TM data and with 1991 field observations. This showed a high level of agreement between the two maps for relatively large areas of homogenous vegetation type. Disagreement was concentrated in areas of small scale mosaic of land cover units. This is

probably due to the large kernel size of filters used in speckle reduction (9*9 pixels). The major grass species forming the floating meadows occur in habitats that may be flooded by many metres. There, dense mats of floating grasses form at rising water levels. The same grasses are also encountered on sites that only undergo short flooding. ERS-1 data appear to exhibit enhanced backscatter only in areas of truly floating grass mats. This may be due to the dense mats of roots and stems of floating meadows acting as strong scatterers in conjunction with the water surface. The thick layer of roots and stems does not develop on shortly flooded terrestrial sites.

6. Estimating the duration of flooding

6.1. Landsat data

Successional stage and vegetation structure are (among other factors) dependent on the duration of seasonal flooding (Junk, 1989). A map of structural vegetation units, therefore, provides some information on the duration of flooding. Flooding under closed vegetation canopies is, however, not directly reflected in TM data. The utility of TM data to monitor the extent of open water surfaces is limited by a high frequency of cloud cover from September to July.

6.2. ERS-1 SAR data

(a) Flooding in open terrain

Flooding in open terrain can be mapped by visual interpretation of ERS-1 SAR data. This allows to derive the extent of areas being permanently flooded.

(b) Flooding under vegetation cover

Synthetic aperture radar remote sensing has been used to detect flooding of forested floodplains (Hess et al., 1990). Successful applications have largely made use of L-band radar. C-band radar has a lower capacity to penetrate vegetation and radar backscatter from vegetated surfaces is less likely to be enhanced due to flooding. Data from the Manaus region suggest that a marginal enhancement of backscatter can be observed in areas of shrub vegetation of low to intermediate density. No enhancement of backscatter due to flooding has been observed under forest cover.

7. Conclusions

- * Floodplain boundaries can be mapped by visual interpretation of ERS-1 SAR data. The visibility of terrain features can be enhanced by principal components analysis of multitemporal data.
- * Mats of floating aquatic grasses exhibit high backscatter during the inundated period, while

the same areas have low backscatter during the dry period. This allows the differentiation of 3 classes of vegetation from two dates of ERS-1 SAR imagery (July, November): woody vegetation, terrestrial herbaceous vegetation, aquatic herbaceous vegetation forming dense floating mats.

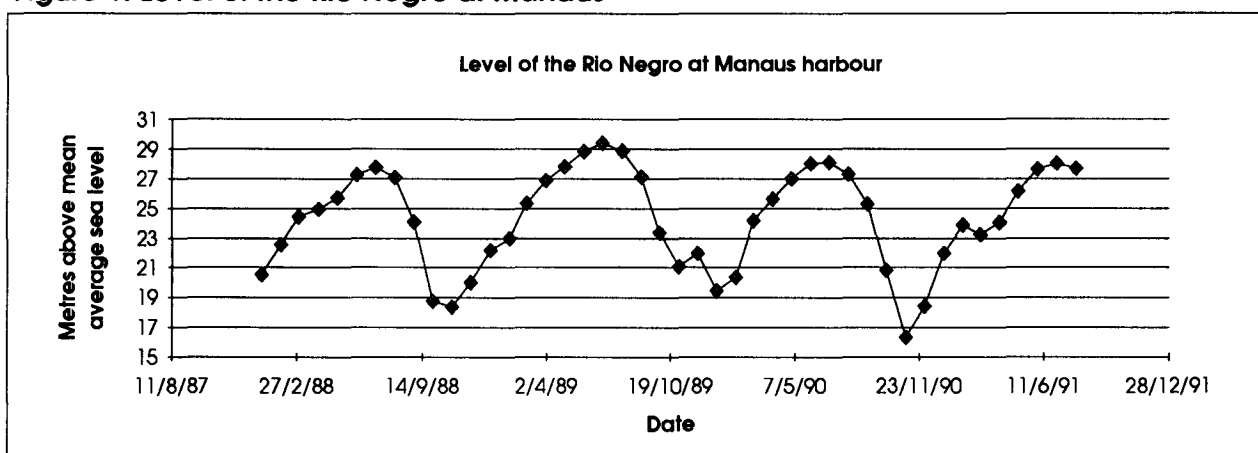
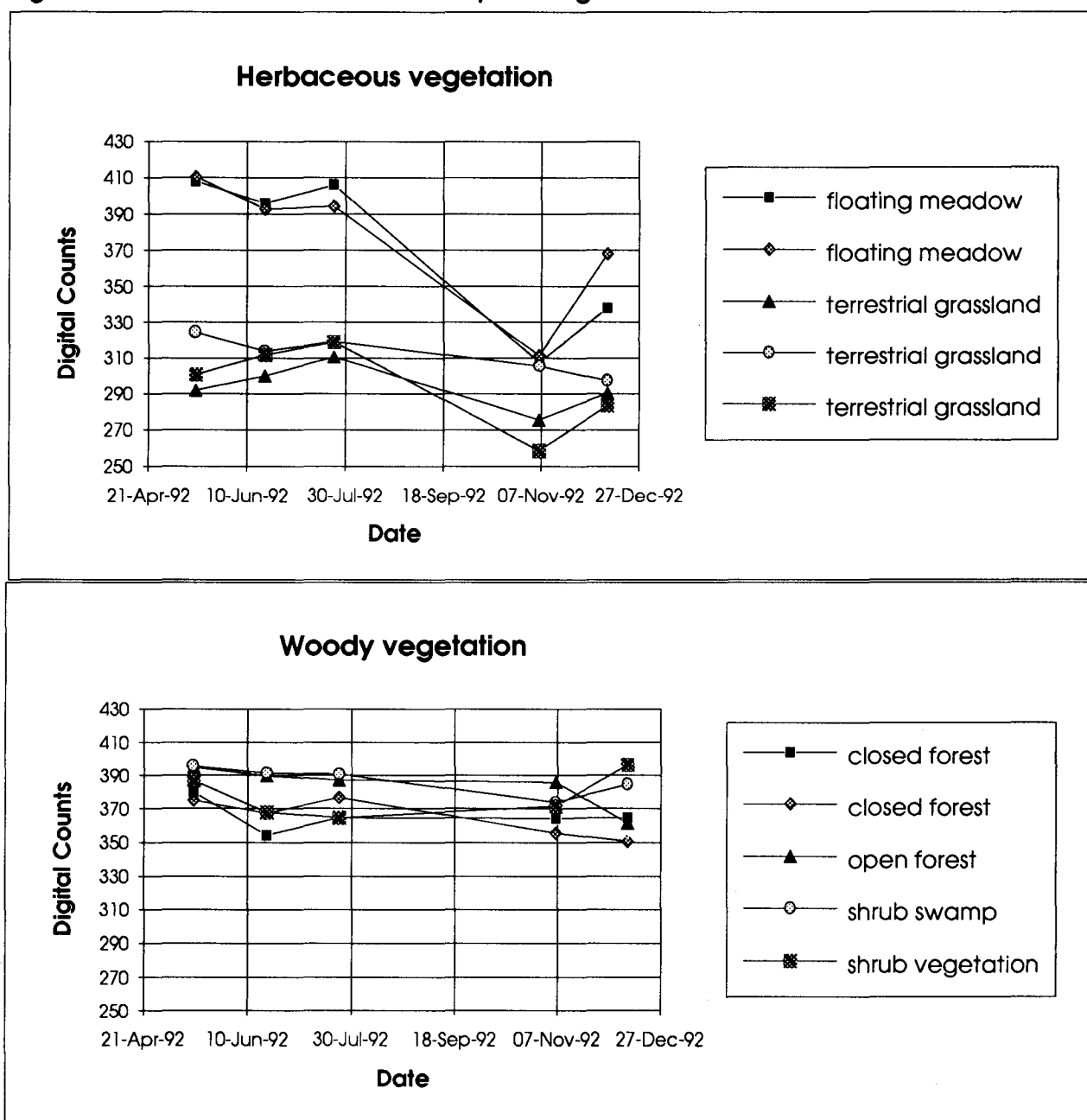
- * Multitemporal ERS-1 SAR data can be used to monitor the growth of floating meadows.
- * Backscatter from shrub vegetation is marginally enhanced due to flooding. No such increase in backscatter has been observed from forested areas. The magnitude of the effect appears too small as to be used for monitoring sub-canopy inundation.
- * ERS-1 SAR data appear to be as good as TM data or better for mapping the floodplain boundary. TM data are more suited than ERS-1 SAR data for mapping vegetation - if available. Under conditions of persistent cloud cover, multitemporal ERS-1 SAR data (representing the high and the low water season) allow to map basic vegetation formations.

8. Acknowledgements

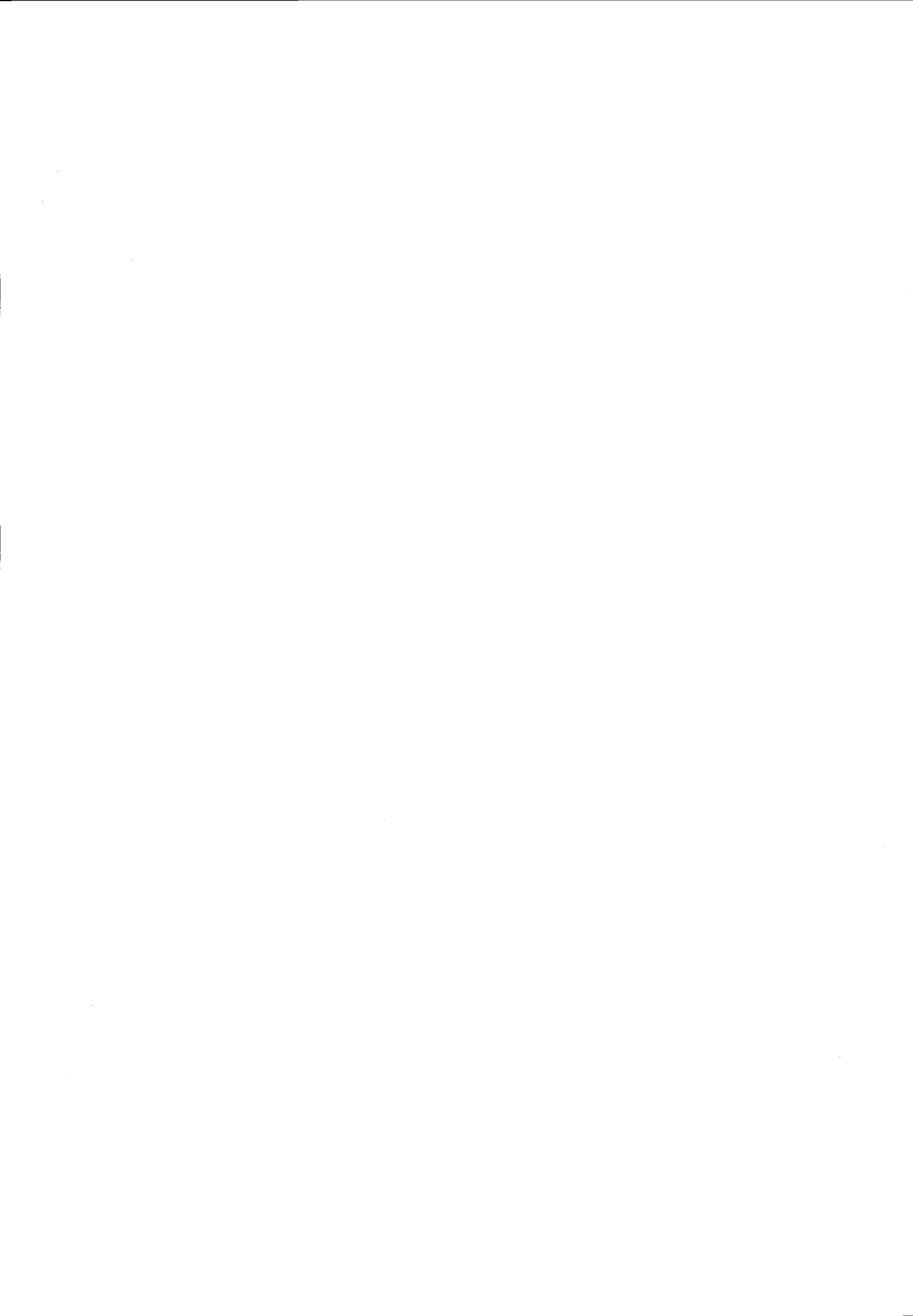
The work carried out for this project has been funded by the Commission of the European Communities under Contract No. ERBCHBICT930309. ERS-1 SAR data have been provided by the European Space Agency under pilot project agreement no. PP2-UK3.

9. Bibliography

- Bartlett, K.B., Crill, P.M., Bonassi, J.A., Richey, J.E., and Harriss, R.C. (1990): Methane flux from the Amazon river floodplain: emissions during rising water. *Journal of Geophysical Research*, Vol. 95, No. D10, pp. 16,773-16,788.
- Bartlett, K.B., P.M. Crill, D.I. Seebacher, R.C. Harriss, J.O. Wilson, and J.M. Melack (1988): Methane flux from the central Amazonian floodplain. *Journal of Geophysical Research*, Vol. 93, No. D2, pp. 1571-1582.
- Devol, A.H., J.E. Richey, W.A. Clark, S.L. King, and L.A. Martinelli (1988): Methane emissions to the troposphere from the Amazon floodplain. *Journal of Geophysical Research*, Vol. 93, No. D2, pp. 1583-1592.
- Junk, W.J. (1989): Flood tolerance and tree distribution in central Amazonian floodplains. In: Holm-Nielsen, L.B., J.C. Nielsen, and H. Balslev: *Tropical forests. Botanical dynamics, speciation and diversity*. Academic Press, London - San Diego - New York - Boston - Sydney - Tokyo - Toronto. 380 pp.

Figure 1: Level of the Rio Negro at Manaus**Figure 2: Radar backscatter from floodplain vegetation**

4. ICE



OPERATIONAL ICE MONITORING WITH ERS-1 SAR

Einar-Arne Herland

Space Technology

Technical Research Centre of Finland

Metallimiehenkuja 10, P.O.Box 13031 VTT

SF-02044 VTT, Finland

Tel. +358 0 4561, Telefax +358 0 456 4496

ABSTRACT

During the three last winters the Baltic Sea has been one of the application areas where ERS-1 SAR images have been used for real-time ice monitoring purposes. An image work station developed for the icebreaker crew has been extended to also allow the use of SAR images. Images are geometrically rectified and radiometrically modified before transmission to the icebreakers. Transmission of images to the icebreakers is done by means of the reporting system used by the icebreakers, which uses a file transfer protocol on the Nordic Mobile Telephone system (NMT). In order to reduce the amount of data to be transferred on the low-capacity telephone channel, image compression is applied before dissemination. Digital images are also made for the Ice Service to aid in the ice charting process. Telefax images are made for users without an image work station.

Keywords: SAR, sea ice, real-time

INTRODUCTION

The ice season in the northern Baltic Sea lasts for more than six months in the northernmost part during normal winters, with the maximum extent occurring in the period January to March. This severely affects marine traffic in the area, and the Finnish Board of Navigation operates nine icebreakers in the area throughout the winter. The Ice Service compiles ice charts daily during the ice season, and information on the ice condition is distributed to shipping and harbour authorities and to ships in the area. The Finnish Board of Navigation operates nine icebreakers in order to support marine traffic and keep important harbours open during the ice season. Since 1989 icebreakers have used an image workstation, developed by VTT (Technical Research Centre of Finland), for viewing NOAA images. This workstation has later been expanded to incorporate ERS-1 SAR images, too. The early phases are described in Kuitti-

nen(1989) and Mäkisara(1990). The Ice Service, belonging to the Finnish Institute of Marine Research, is an operational service, providing shipping authorities and vessels with ice information. This information is compiled in the form of ice charts on a daily basis during the ice season. The Ice Service has been using optical satellite images for a long time, but they are hampered with the fact that they can only be used in daylight and under cloudfree conditions. During 1993 and 1994 the Ice Service has received ERS-1 SAR images as an aid in their ice charting work.

IMAGE ACQUISITION

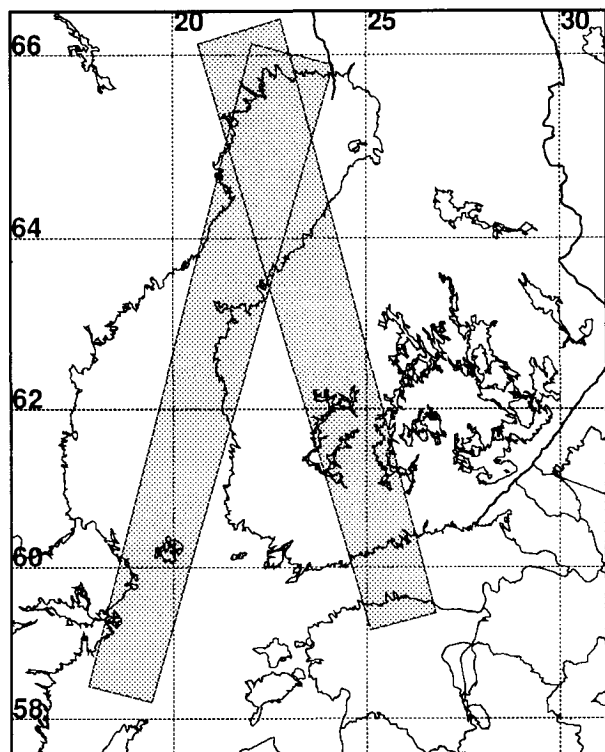


Figure 1. ERS-1 SAR coverage during the 3-day cycle orbit in 1992 and 1994.

The images used have been FD-images (fast delivery). Each image covers an area of 100 km by 100

km with 30 m resolution and are produced in near real time at the receiving stations in Kiruna, Sweden, and Fucino, Italy. The processing capacity is 3 images per orbit, and with the current processing policy, these images are always chosen from the just completed orbit. This imposes a limit of three consecutive images from a single pass if all images come from the same receiving station, and six images if the area is covered by both stations. The images are distributed via the Broadband Data Dissemination Network (BDDN) based on the EUTELSAT communication satellite (Garrido,1991), where it takes approximately 6 minutes to transfer a 63 megabyte FD-image.

During the winter 1994 the images used have been low resolution (100 m) images generated by lowpass filtering FD-images. These images have been obtained from Tromsø Satellite Station (TSS) in Norway, which also reads down ERS-1 SAR data. The processing capacity at TSS is 8 minutes per image, and images are transferred on Internet immediately after processing. With an image size of 2.5 megabytes, an image will typically be transferred in less than 10 minutes. It has thus been possible to receive up to 9 consecutive images, and the first image has under optimum conditions been at VTT about 40 minutes after the satellite overpass. ESA has also established a service whereby low resolution images can be obtained on the Internet, but the delay has typically been three hours, and the limitation of only three consecutive images still remains.

During the winters 1992 and 1994 ERS-1 was in the 3-day cycle orbit and in 1993 in the 35-day cycle orbit. The corresponding coverage over the Northern Baltic is shown in figures 1 and 2.

IMAGE PRODUCTS AND PROCESSING

Images are transmitted in digital form to the icebreakers, where the images are displayed on an image workstation (Herland et.al.,1992). In order to be able to combine different types of images, map information, and other information available to the icebreakers, all images are transformed to the Mercator projection before transmission to the icebreakers. For this purpose a special image format has been developed, which includes all necessary information on image aquisition time, sensor and geographical coordinates. Before transmission the images are also compressed with a lossy algorithm (Mäkisara,1991).

In addition to the digital images, telefax images are also generated directly from the FD-images, rasterized and transformed to fax format, and transmitted

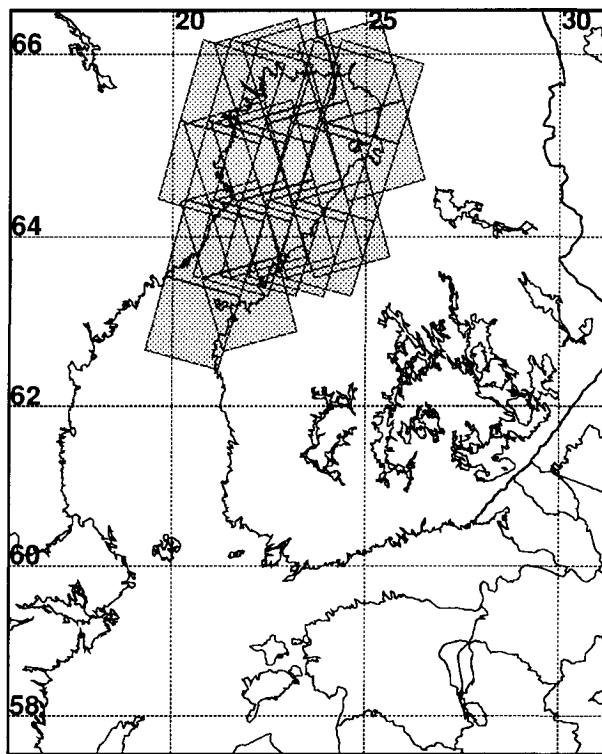


Figure 2. ERS-1 SAR coverage during the 35-day cycle orbit in 1993.

through a fax modem connected to the computer. This product is used for users without an image workstation.

FD-images are supplied in ground range projection, which means that the pixel spacing in range on the ground is constant. This is valid for both range and azimuth directions, but the pixel spacings are different for the two directions. The geographical coordinates of the four image corners are supplied in the image header. Since the system developed is meant for operational use, and the processing delay is an important factor, all processing is done automatically, as far as possible. This also means that the traditional method of picking ground control points manually for geometric rectification cannot be used. This would also be impossible for sea areas with no visible land contours. The supplied corner points are therefore used as tie points. Guignard(1991) describes a method for geolocalization of FD-images, where the corner coordinates are recalculated from the supplied equator crossing state vector by using an orbit propagator and the known imaging geometry. The resulting accuracy was better than 30 meters in range, and better than 200 meters in azimuth. The method described here uses the corner coordinates as they are, and measure-

ments have shown that the resulting accuracy is a few hundred meters. This is sufficient for the real-time applications considered.

Rectification to Mercator projection requires calculation of geographic coordinates for all pixels in the FD-image. A reasonable assumption is that individual pixel lines, in both directions, follow great circles on the earth. This is not strictly true for the azimuth direction, since the image azimuth direction is offset some 300 km from the nadir track great circle, but the resulting deviation is only a few meters. The output image pixel locations are calculated by first transforming the input image corner coordinates to the Universal Transverse Mercator projection (UTM). The output coordinates are then converted from Mercator to UTM, and the corresponding position in the input image is found by bilinear interpolation. When interpolating pixel values, the necessary lowpass filtering needed if the output resolution is lower than in the input image, is included in the interpolation.

The output image size, resolution and areal coverage can be chosen at will, and it is therefore possible to do a mosaic of several input images to the same output image.

For the digital images the grayscale is adjusted to fit into 8 bits, but no histogram optimization is done. This allows easy combination of different images, and when needed, the contrast can be enhanced in the ICEPLOTT application program in the image work station. For the telefax images, histogram equalization is done, and the images are then rasterized, typically to 10 levels of gray.

THE IRIS SYSTEM

The icebreakers are connected to a real-time Information and Reporting system Icebreaking Service (IRIS). The icebreakers report regularly on their activities through this system, and the images are also sent through the same system. IRIS is implemented through DECnet on the Nordic Mobile Telephone (NMT) system, and accordingly has relatively low capacity for image distribution. The compressed image size is therefore kept below approximately 100 kilobytes in order not to overload the system.

During the three winters SAR images have been transferred, the images have been distributed from VTT, which is not connected to the IRIS system. When the image distribution is connected to IRIS, it will be possible for the icebreakers to issue requests for images of specific areas, or the need can be judged from the current position and activity of each icebreaker. Ta-

ble 1 shows an excerpt from the reports regularly received from the icebreaker OTSO during a 3-day period. Each line constitutes one report, and gives the name of the icebreaker, the activity (ASS, FFL, etc.), date, time, nearest beacon and position relative to it, latitude, longitude, heading and speed. By tracking this information, as is done in the icebreaker image work station, images from areas around a given icebreaker can be sent.

CONCLUSION

The experiences from the last three winters have shown that it is technically feasible to use satellite SAR images for real-time ice monitoring. The main bottleneck has turned out to be time delay from satellite overpass until the user has the image. With the ERS-1 coverage, it is also not possible to cover all interesting areas in a timely fashion. With the planned systems, like RADARSAT and ENVISAT, the coverage problem will be alleviated, but large areal coverage will most likely require a satellite distribution channel even for 100 m resolution images. In order to allow near real time use of the images, this distribution must be done immediately after the processing at the ground station, and the processing capacity must be sufficient for the required areal coverage. The usefulness of the images has been clearly demonstrated, both for icebreaker operation and ice charting. If a recent satellite image is available, the icebreaker workstation lets the captain optimize the route for the icebreaker and advise ships by radio on how to find useful leads in the ice, thus minimizing the need for icebreaker assistance. For ice charting, SAR images offer a unique capability, especially during cloudy weather conditions.

ACKNOWLEDGEMENTS

The work reported on here has mainly been funded by the Technology Development Centre of Finland. Additional funding has been received from the European Space Agency through a series of studies on real-time use of ERS-1 SAR images.

REFERENCES

C.GARRIDO, 1991, "ERS-1 Broadband Data Dissemination Network, Receive station installation handbook", ER-TN-ESA-GS-0095, June 1991.

Table 1. IRIS reports from icebreaker OTSO from March 4-7, 1993.

OTS	FFL	93.03.04	23:27	KE1	220	05	65 19	23 58	180	16
OTS	ASS	93.03.05	02:25	NAH	342	05	64 41	23 50	090	08
OTS	STL	93.03.05	04:15	RAF	085	04	64 39	24 23	0	0
OTS	ASS	93.03.05	06:15	RAF	085	04	64 39	24 23	270	08
OTS	FFL	93.03.05	09:26	NAH	265	11	64 36	23 28	082	8
OTS	ASS	93.03.05	09:41	NAH	277	12	64 38	23 26	089	07
OTS	FFL	93.03.05	14:30	RAF	085	04	64 39	24 23	270	09
OTS	FFL	93.03.05	15:10	RAF	245	01	64 38	24 11	005	10
OTS	ASS	93.03.05	17:34	MAR	258	10	65 00	24 10	355	7
OTS	ASS	93.03.05	21:00	KE1	270	00	65 23	24 05	180	8
OTS	FFL	93.03.06	02:45	NAH	017	03	64 39	23 56	090	10
OTS	ASS	93.03.06	04:00	RAF	085	04	64 39	24 23	240	08
OTS	STL	93.03.06	07:20	NAH	360	11	64 47	23 53	0	0
OTS	FFL	93.03.06	17:38	NAH	350	09	64 45	23 50	016	14
OTS	ASS	93.03.06	19:10	MAR	280	14	65 05	24 01	190	10
OTS	STL	93.03.07	01:30	ULK	252	16	64 15	22 52	0	0
OTS	FFL	93.03.07	08:15	KOF	356	13	64 12	22 49	240	16
OTS	ASS	93.03.07	08:56	KOF	328	11	64 09	22 38	060	10

J.P.GUIGNARD, et.al., 1991., "ERS-1 SAR Fast Delivery Reference Image", ER-TN-JP-ESA-0009, November 1991.

R.KUITTINEN, et.al., 1989, "Real-time system for transmitting satellite data products to icebreakers", Advances in Space Research, Vol. 9, No. 7, pp. 209-212.

K.MAKISARA, 1990, et.al., "Satelliittikuvan digitallinen siirto jaanmurtajille", VTT Research Notes No. 1165, 1990, in Finnish.

K.MAKISARA, 1991, "Adaptive Laplacian pyramid compression of remote sensing images", 1991 International Symposium on Geoscience and Remote Sensing (IGARSS'91), June 3-6, 1991, Espoo, Finland.

E-A.HERLAND, et.al., 1992, "Demonstration of ERS-1 SAR sea ice mapping in the Baltic Sea", Proceedings of the Central Symposium of the International Space Year Conference, Munich, Germany, 30 March - 4 April, 1992, ESA SP-341, pp. 1009-1013.

E-A.HERLAND, 1993, "Real time ice monitoring demonstration in the Baltic Sea", Proceedings Second ERS-1 Symposium, Hamburg, Germany, 11-14 October, 1993, ESA SP-361, pp.681-685.

A.SEINA, et.al., 1993, "The operational mapping of ice conditions using ERS-1 images in the Baltic Sea", Proceedings Second ERS-1 Symposium, Hamburg, Germany, 11-14 October, 1993, ESA SP-361, pp.369-371.

K.STRUBING, et.al., 1991, "A feasibility study of an ISY real-time ice monitoring demonstration", ESA/ESTEC Contract No. 9115/90/NL/PP(SC).

J.P.SNYDER, 1982, "Map projections used by the U.S. Geological Survey", Geological Survey Bulletin No. 1532.

A PILOT ICE MONITORING SERVICE USING ERS-1 SAR IMAGES

Stein Sandven, Ola M. Johannessen, Lasse H. Pettersson, Martin W. Miles and Åsmund Drottning

Nansen Environmental and Remote Sensing Center
 Edvard Griegsvei 3a, N-5037 Solheimsvik, Norway
 phone: + 47 55 29 72 88, fax: + 47 55 20 00 50

ABSTRACT

In a series of demonstration projects during the last three years, Synthetic Aperture Radar (SAR) images from the ERS-1 satellite have been used pre-operationaly to monitor sea ice in selected areas. SAR is a favourable sensor for ice monitoring because it combines high spatial resolution with independence of weather and light conditions. By averaging full-resolution ERS-1 SAR scenes to images with 100 m pixel size, combining two or more adjacent images and applying a suitable grayscale function, a useful and convenient data set is obtained. Detailed ice maps are produced by interpreting the SAR images and using other data such as meteorological observations and SSM/I ice concentration maps. Satellite SAR systems are expected to develop from a research tool to an operational ice monitoring method in the 1990's.

1. BACKGROUND

The need for real-time sea ice monitoring in the European sector of the arctic is growing due to increased activities in fisheries, offshore oil exploitation, ship traffic, research and monitoring of pollution and the environment in arctic regions. In the Barents Sea and the region around Svalbard, a rich marine life is the base for extensive fisheries by several countries. Additionally, oil and gas production is moving farther north into the seasonal ice zone. The ship traffic in the Barents Sea and Kara Sea is expected to grow due to increased economic activity in Siberia. The sea ice conditions impose severe restrictions on these activites. Regular access to SAR imagery will improve the quality of the ice mapping and contribute to safer operations in the Arctic.

2. ERS-1 SAR DATA

The ERS-1, which was launched in July 1991, is the first satellite that has provided a large number of C-band SAR images of sea ice in both hemispheres. Although ERS-1 is a research satellite not intended to be operational, it has been operating with high regularity. In Norway the infrastructure to downlink, process and distribute SAR images in near real-time from the European sector of the arctic has been

developed. This infrastructure has enabled the Nansen Environmental and Remote Sensing Center to perform several pre-operational demonstrations where interpreted SAR images have been used to assist various types of arctic operations including research expeditions.

The interpretation of the SAR images is done in a fairly simple manner, without advanced computer-assisted classification techniques. This is because SAR ice classification remains an important research topic and there are not yet any standard classification algorithms suitable for operational use. However, some manual classification can be done with reasonable accuracy. Based on validation experiments (Ref. 1) it is clear that open ocean in ERS-1 SAR images can be well distinguished from any ice type in areas such as the Barents Sea. Also, new ice such as frazil ice and grease ice is clearly observed due to the very low backscatter. Gray ice and pancake ice has higher backscatter than most of the first-year ice. Multi-year ice has higher backscatter than most of the first-year ice, except during summer conditions. These characteristics are fairly general and can be applied for ice classification in other ice regions (Ref. 2). The main problem is to classify various stages and conditions of first-year ice based on tonal values only. Also, ice ridging and topography are not well captured by the ERS-1 SAR (Ref. 3) and floe identification remains problematic. However, these shortcomings do not preclude a manual classification of 2 - 3 ice types. Manually interpreted SAR ice images can be distributed to icebreakers, drilling ships, fishing vessels, oceanographical research vessels and other ships within 2 - 3 hours after the satellite overpass. The ERS-1 SAR coverage is limited to 100 km wide swaths and is therefore not feasible for large-scale monitoring.

3. THE PILOT ICE SERVICE

The purpose of the pilot ice service based on ERS-1 SAR images is to develop an operational ice monitoring and forecasting system based on data from future radar satellites. The pilot service can offer near real-time interpreted SAR ice images to customers during special campaigns and regular monitoring of smaller areas in the European sector of the arctic. Because the SAR coverage from ERS-1 is fairly limited, the service cannot offer regular mapping of larger areas. During

1994 the pilot service is therefore concentrated in the Svalbard area where the SAR coverage is good (Fig. 1)

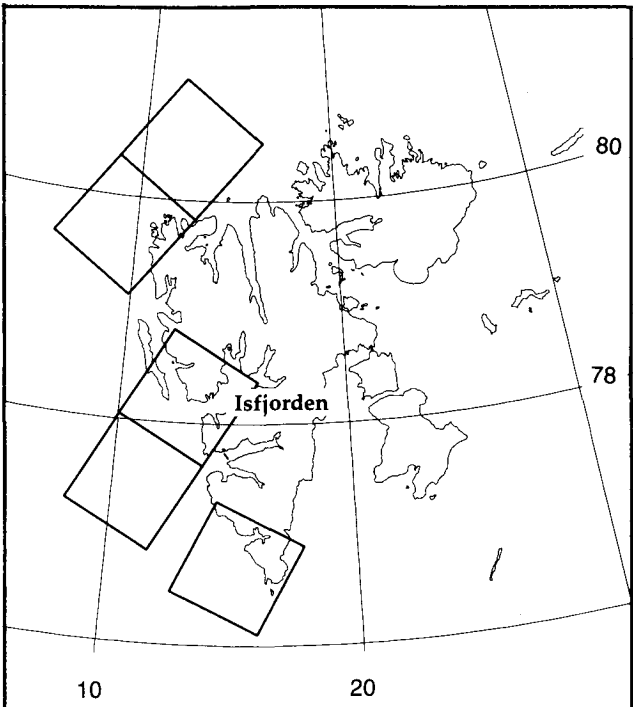


Figure 1. ERS-1 SAR coverage of the Svalbard coast from 19 to 24 April 1994 obtained in the Pilot Ice Service. The northern and western coasts are the most important area for ice mapping in the winter. During summer also the east coast is mapped.

and there is a year-round need for accurate ice information.

Fig. 2 shows a SAR scene from the west coast of Svalbard where the ice conditions in the Isfjorden area are clearly seen. The ice in this region is all first-year ice which is partly formed locally in the fjords and partly advected northwards along the coast. The land border is superimposed on the image to help distinguish sea ice from snow and ice on land. Histogram equalization has been applied to the image to enhance the contrast between open water (brightest signature) and the first-year ice (grayish and dark signature).

The receivers of the SAR ice images are the Weather Service in Svalbard, A/S Luftransport which operates the Coast Guard airplane in the Svalbard region, and the Governor of Svalbard. SAR ice maps have also been distributed to a fishing vessel in the ice edge region. The response from the customers on the pilot service has been generally good. Information on ice tongues and areas of open water inside the ice edge is important because this cannot be obtained from the large-scale ice maps.

4. OCEAN DRILLING PROGRAM

ERS-1 SAR imagery in combination with SSM/I data were used to map the ice conditions the Fram Strait region during the operations of the drill ship "JOIDES Resolution". This vessel, which is not ice-strengthened, operates worldwide for the international Ocean Drilling Program (ODP). In August and September 1993, Leg 151 of ODP was carried out in an area of difficult ice conditions where thick multi-year ice from the Arctic Ocean drifts southwards to the Greenland Sea. Near real-time ice monitoring based on satellite data as well as assistance from an icebreaker was of prime importance for planning and implementation of the drilling operations.

The ice service consisted of daily SSM/I-derived ice concentration maps which provided an overview of the Fram Strait area (Fig. 3). The contour line for 20 % ice concentration was used as definition of the ice edge. The drill sites as well as the SAR coverage for each day were also indicated on these maps. The SAR images provided detailed ice edge information, especially the location of ice tongues and eddies and the evolution of these features which is typical for the ice condition in this region (Ref. 4). These features are particularly important to monitor because ice can be advected 20 - 30 km out from the main ice edge in one day and be hazardous for operations such as the deep sea drilling. In most cases sea ice could easily be distinguished from open water in the SAR images (Fig. 4). Annotated images with geographical grid and adjusted grayscale to enhance the ice edge were produced. The most

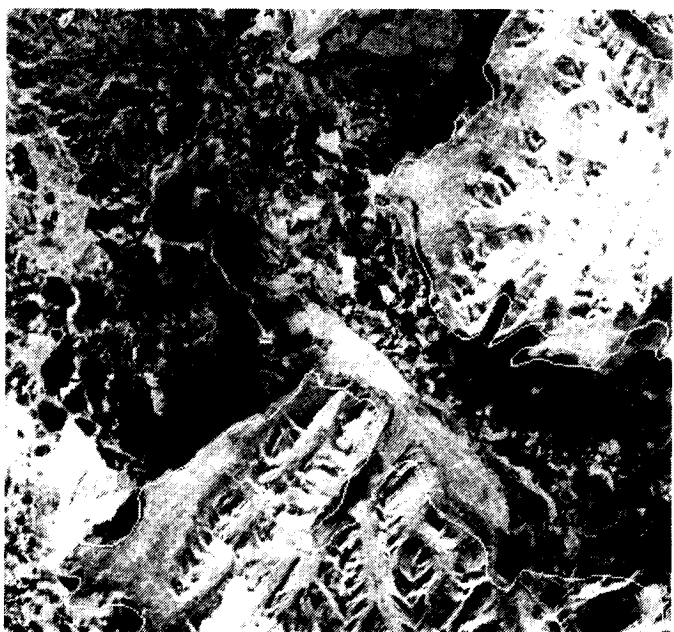


Figure 2. Example of a SAR scene of the Isfjorden area obtained on 24 April 1994. Original data © ESA/TSS 1994.

important information was the exact location of the ice edge and estimated displacement based on wind forecast. The ice images were sent out to the drill ship by telefax. Most of the time the ship was within the range of Inmarsat and telefax transmission was possible.

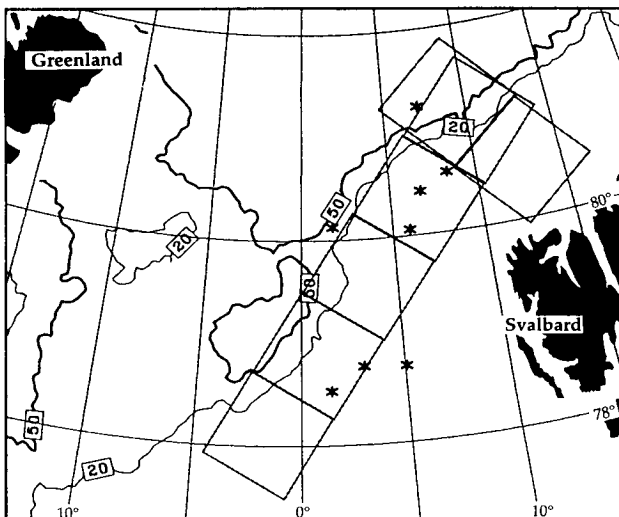


Figure 3. Ice concentration map in the Fram Strait region based on SSM/I data from August 22 1993. The isolines for 20, 50 and 80 % concentration are shown. The boxes mark the SAR coverage on the same day, and the asterisks show the northernmost drill sites during of ODP Leg 151.

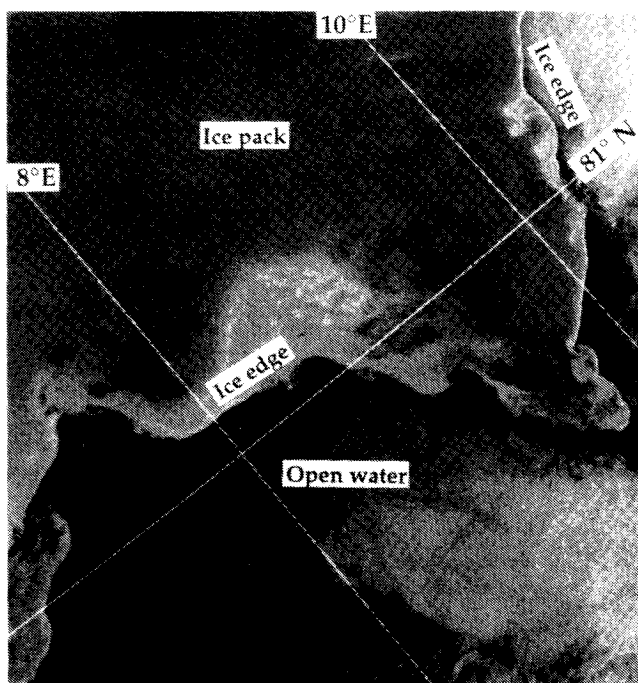


Figure 4. Subset of an ERS-1 SAR scene used to map the detailed ice edge on August 22 1993, covering an area of 70 by 70 km. Time series of SAR images were used to monitor the rapid changes of the ice conditions in the area. Original data © ESA/TSS 1993.

5. ICE NAVIGATION IN THE KARA SEA

The first demonstration of ERS-1 SAR images for ice navigation was during the "L'Astrolabe" expedition through the Northeast Passage in August 1991 (Ref. 5). Since then, the ice conditions, especially in the Kara Sea have been studied throughout the year using SAR data. In November 1993, a dedicated demonstration of near-real-time SAR ice monitoring was made onboard a Russian icebreaker (Ref. 6). This was also an important ice study and SAR ice validation experiment in an area where the ice conditions are different compared to other European regions such as the Greenland Sea and Barents Sea.

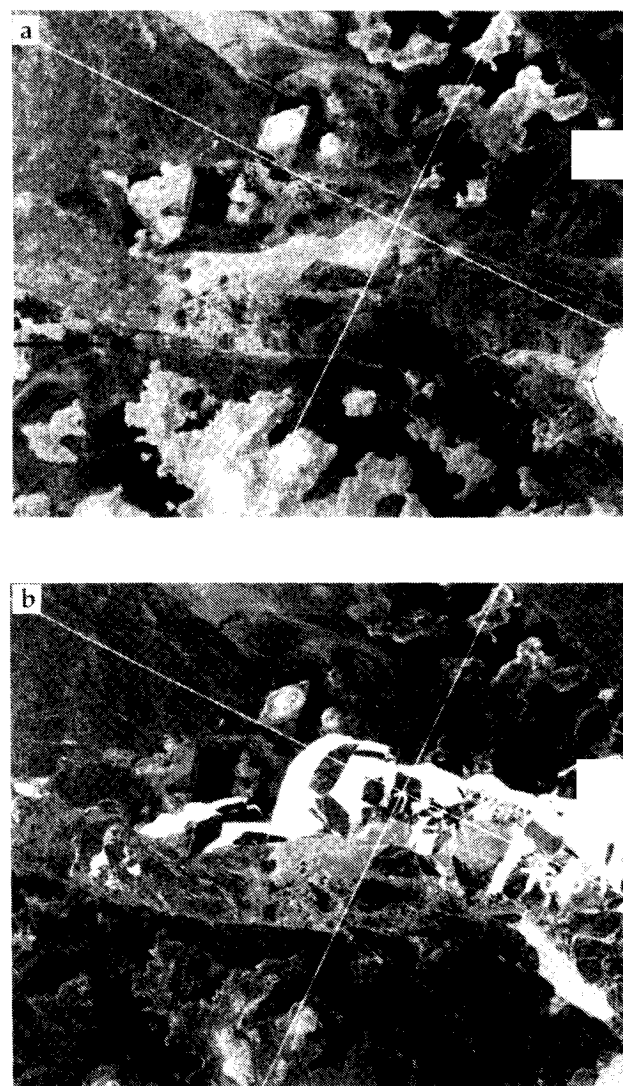


Figure 5. Two SAR images from the same area in the Nordenskjold Archipelago (Kara Sea) from November 28 (a) and December 1 1993 (b). Each image covers about 60 by 70 km. The bright areas in (b) is open water due to westerly winds which ahve broken up the ice in the sailing route. Original data © ESA/TSS 1993.

An example of a SAR image from the Nordenskjold Archipelago in the eastern Kara Sea is shown in Fig. 5. The ice between the islands are mostly landfast ice, refrozen leads and other types of first-year ice. Also the shear zones between the landfast ice and the moving pack ice are clearly seen in the image.

6. COMMUNICATION

A critical part of a near-real-time ice monitoring service is the transmission of the images or maps to the users onboard ships. Inmarsat-A stations with separate telephone and telefax lines onboard the receiving ships have been used in the demonstration projects. The transmission of a one-page SAR image normally takes 3 - 6 minutes. The relatively poor quality of the SAR images after telefax transmission reduced the possibility for interpretation onboard the icebreaker. Therefore, interpreted ice maps were also transmitted by telefax, but the fine image details were not included in these maps.

File transmission using modem with the Inmarsat telephone line was tested as an alternative method. The user onboard the ship calls the computer at NERSC, log in and transfers the image file using "ftp". The transferred image file is already reduced by compression techniques, so the size of one file is typically 100 - 200 kbyte. It is expected that marine communication, including data transmission, will improve and become less expensive in the next few years. Thus, the transmission of SAR images, preferably in compressed format, will become a routine operation.

7. CONCLUSION

Since August 1991 ERS-1 has provided a large number of SAR scenes covering sea ice areas. These data contain valuable information about ice types, ice edge processes, ice concentration, ice velocity, shear zones, leads and other ice phenomena. Although the SAR signatures of different ice types and ice conditions are not fully understood, the SAR has proved to be the most suitable sensor for detailed ice mapping (Ref. 4). The regularity of the ERS-1 SAR data has allowed the development of a pre-operational ice monitoring system which has been demonstrated to various users.

The high quality of the ice images, combined with interpretation by ice specialists, has been well received by the users so far. The ERS-1 SAR coverage is too sparse for large-scale regular monitoring. However, for special monitoring in smaller areas the ERS-1 has provided excellent data.

Future SAR coverage of larger areas will enable a more regular ice monitoring service. The goal is to use SAR,

other satellite data and meteorological data combined with coupled ice-ocean models in an operational ice monitoring and forecasting system.

7. ACKNOWLEDGEMENT

The SAR ice monitoring demonstrations have been supported by Norwegian Space Centre and the European Space Agency.

8. REFERENCES

1. Sandven, S., O. M. Johannessen, R. A. Shuchman, K. Kloster and M. Miles. "SIZEX 92 ERS-1 SAR ice validation experiment", in Proceedings of the Second ERS-1 Symposium Space at the Service of our Environment. 11 - 14 October 1993 Hamburg, Germany. ESA SP-361 1994, pp. 353 - 358.
2. Onstott, R. G. and R. A. Shuchman. "Arctic sea ice microwave signature and geophysical process study", in Proceedings of IGARSS 93, 1993, pp. 635 - 636.
3. Shokr, M., B. Ramsey and J. C. Falkingham. "Operational use of ERS-1 SAR data to monitor sea ice conditions in the Gulf of St. Lawrence", in Proceedings of the Second ERS-1 Symposium Space at the Service of our Environment. 11 - 14 October 1993 Hamburg, Germany. ESA SP-361 1994, pp. 663 - 668.
4. Johannessen, O. M., W. J. Campbell, R. Shuchman, S. Sandven, P. Gloersen, J. A. Johannessen, E. G. Josberger and P. M. Haugan. "Microwave study programs of air-ice-ocean interactive processes in the seasonal ice zone of the Greenland and Barents seas," in Microwave Remote Sensing of Sea Ice (Editor F. Carsey) AGU Geophysical Monograph 68, 1992, pp. 261 - 289.
5. Johannessen, O. M., S. Sandven, Ø. Skagseth, K. Kloster, Z. Kovacs, P. Sauvadet, L. Geli, W. Weeks and J. Louet. "ERS-1 SAR ice routing of L'Astrolabe through the Northeast Passage," in Proceedings of the Central Symposium of the 'International Space Year' Conference, Munich, Germany 30 March - 4 April 1992. ESA SP-341, 1992 , pp. 997 - 1002.
6. Johannessen, O. M., S. Sandven, L. H. Pettersson, K. Kloster, M. W. Miles and V.V. Melemyev. "ERS-1 ice monitoring of the Northern Sea Route" in Proceedings of the First ERS-1 Pilot Project Workshop, Toledo 22 - 24 June 1994.

ERS-1 ICE MONITORING OF THE NORTHERN SEA ROUTE

Ola M. Johannessen, Stein Sandven, Lasse H. Pettersson, Martin W. Miles, Kjell Kloster

Nansen Environmental and Remote Sensing Center
 Edvard Griegsvei 3a, N-5037 Solheimsvik, Norway
 phone: + 47 55 29 72 88, fax: + 47 55 20 00 50

Vladimir V. Melentyev

Nansen International Environmental and Remote Sensing Center
 Korpusnaya Str. 18, 197042 St. Petersburg, Russia
 phone: + 7 812 235 74 93, fax: + 7 812 235 43 61

ABSTRACT

The ice conditions off the Siberian coast, which has recently been opened for international ship traffic, impose severe restrictions on the navigation along the Northern Sea Route. The Russian icebreaker fleet, which is responsible for all sea transportation in the area, uses an extensive ice monitoring and forecasting service to assist in the navigation. Presently, this service does not utilize existing SAR data from satellite. In a pilot demonstration project ERS-1 SAR images have been used to monitor sea ice conditions in the Kara Sea at different times of the year. The SAR images have shown good capability to map drifting multiyear and firstyear ice, landfast ice, leads/polynyas and areas of thin ice. The results of the demonstration have been presented to the Russian Ice Service including some icebreakers. SAR images, which will cover larger areas and be available from several satellites from 1995, are expected to become an important component in the ice monitoring system for the Northern Sea Route.

1. INTRODUCTION

The possibility to monitor sea ice independent of daylight and cloud cover has improved considerably by the launch of the ERS-1 satellite in July 1991 [Ref. 1]. The ERS-1 has proved that SAR is an excellent instrument for detection, classification and monitoring of the sea ice distribution in many areas. The Nansen Environmental and Remote Sensing Center (NERSC) and the Tromsø Satellite Station (TSS) of the Norwegian Space Centre provide SAR data for real-time sea ice monitoring in European sector of the Arctic including the Kara Sea (Ref. 2). ERS-1 SAR images are down-linked and processed at TSS. Then the images are transmitted to NERSC for analysis, production of interpreted maps and distribution to end users [Ref. 3]. In addition, the SAR data can be coupled with passive microwave data from the Special Sensor Microwave Imager (SSM/I) of the Defense Meteorological Satellite Program to resolve the larger-scale ice coverage.

NERSC first demonstrated use of ERS-1 SAR data for near real-time ice mapping of the Northern Sea Route in August 1991, only a few weeks after the launch of the

ERS-1 satellite. SAR derived sea ice maps were then sent by telefax to the French polar vessel "L'Astrolabe" during her voyage through the Northeast Passage from Norway to Japan [Ref. 4]. This demonstration was evaluated as very interesting by the captains and sea ice experts onboard the Russian icebreakers which escorted L'Astrolabe through the ice-covered parts of the route. A second and more extensive demonstration was carried out in November 1993 using the icebreaker "Sovetsky Soyuz". In addition to the navigational aspects this experiment also had scientific objectives such as improved understanding of sea ice phenomena in the Kara Sea and their SAR signatures. The main results of the experiment are discussed in this paper.

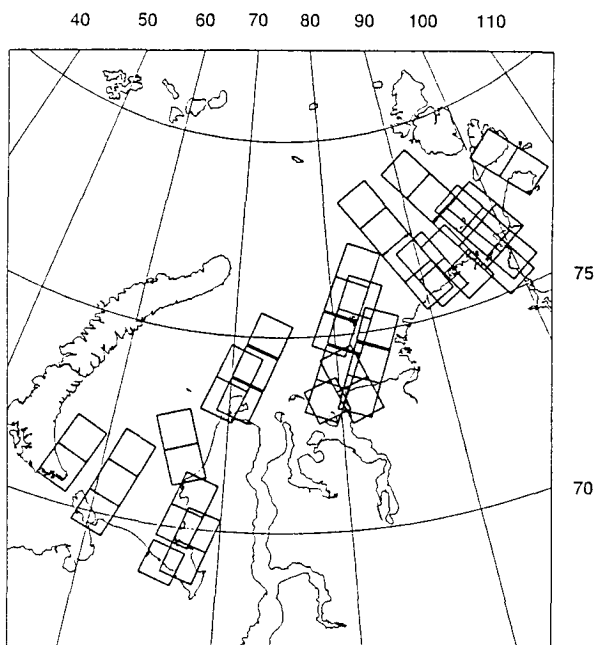


Figure 1. Map of the Kara Sea region showing coverage of ERS-1 SAR images in the period from October 30 to November 9 1993.

2. SAR IMAGE ACQUISITION AND PROCESSING

Through ESA's application oriented pilot project in the Kara Sea [Ref. 5] SAR data were obtained as shown in Fig. 1. The data needed in near real time were obtained

from TSS, whereas off-line data were obtained from the ESA archive. Both TSS and the ESA ground station in Kiruna can downlink and process SAR data from the Northern Sea Route west of Cape Chelyuskin. The data delivered from TSS were images with 100 m pixel size (LRI-images) which were readily transmitted by computer network to NERSC. The transmission time is about 8 minutes per scene. TSS can thus deliver up to 10 scenes within 1 hour of the ERS-1 overpass. At NERSC the following image analysis steps are carried out: 1) Reduction of data by averaging each scene to 8 bit and 200 m pixel size, 2) normalization of values across-track (correction of antenna-gain etc.), 3) two consecutive scenes are merged into one image, 4) marking of 0.5° lat. by 2° long. gridlines, 5) annotation of land/islands and interesting ice/ocean features, 6) histogram equalization of the image before a print to hardcopy in A4 format, 7) print of annotated ice map separated from the image, 8) production of a compressed image for file transmission, and 9) transmission of images and maps to the ship by telefax. This is the basic procedure necessary to enhance and compress the most important ice information in the SAR images, and sent it out to the icebreaker within 2 - 3 hours after the satellite overpass. Further interpretation and classification of the images were done onboard the icebreaker.

3. THE DEMONSTRATION CAMPAIGN

The demonstration project was carried out onboard the nuclear ice-breaker "Sovetsky Soyuz" during an expedition from Murmansk to the Chukchi Sea and back. "Sovetsky Soyuz" is one of the largest icebreakers of Murmansk Shipping Company, with 21.000 tons displacement and engine power of 75.000 horsepower. She is equipped with the modern satellite navigation and communication systems such as Inmarsat A station with telefax. Dr. Melentyev from NIERSC participated in the expedition as an ice scientist with special responsibility to interpret the SAR images sent to the ship and obtain accurate in situ observations of the ice conditions.

The acquisition of SAR data was coordinated day by day with the icebreaker's sailing schedule. Due to limited spatial and temporal coverage of SAR it was difficult to match the SAR images exactly to the icebreaker's position. However, in some cases near real time information of the ice conditions along the sailing route could be obtained from the SAR images. These cases are described in section 4.

The "Sovetsky Soyuz" departed from Murmansk on 30 October with the task to escort two cargo ships ("Mikhail Kutusov" and "Kapitan Kudlai") eastwards to the Chuckchi Sea where the eastern boundary of the drifting sea ice was located near 178°E. The icebreaker operated in the coverage area of TSS until 8 November when it passed eastward of Cape Chelyuskin. In the passage of Vilkitskogo Strait, where the ice conditions can be very difficult, the icebreaker "Yamal" also took part in the escort. "Yamal" received the same SAR images as "Sovetsky Soyuz" in this area. The SAR-images were also transmitted to the Western Arctic Marine Operations

Headquarters in Dikson, which is responsible for the operational ice monitoring and forecasting service west of Cape Chelyuskin. The demonstration project ended after "Sovetsky Soyuz" had returned to the Kara Sea region at the end of November.

As the SAR images were received onboard "Sovetsky Soyuz", the ice specialist who was responsible for analysis of the ice conditions, interpreted and evaluated the SAR images. The official Russian sea ice maps provided to the ship from the Marine Operation Headquarter were used as the basis for the navigation, and the detailed SAR images were used as a supplement.

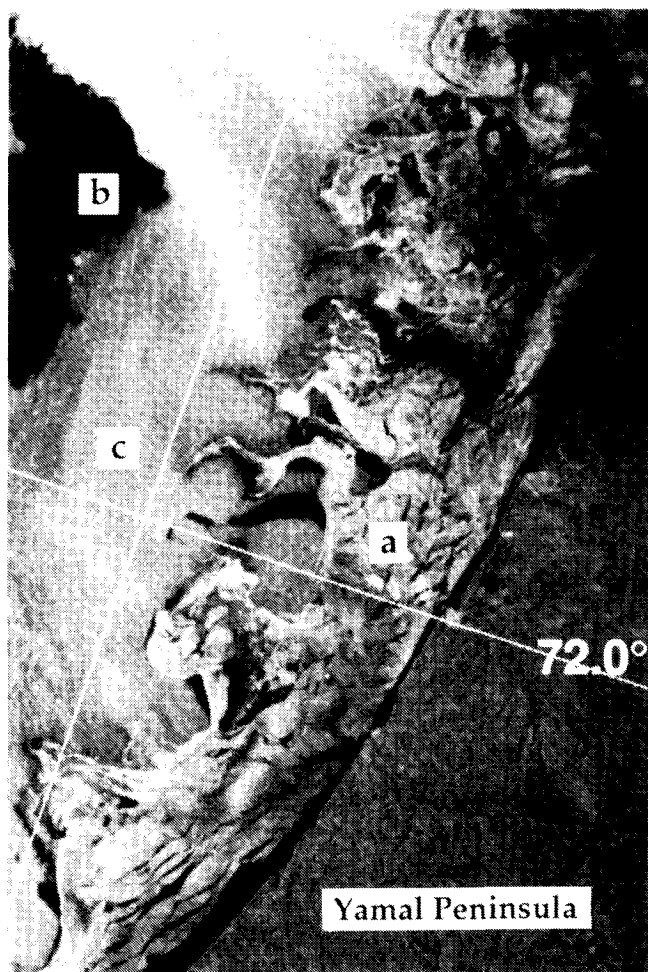


Figure 2. SAR image from October 29 1993 covering 50 by 75 km of the west coast of Yamal peninsula. a: nilas and gray ice less than 15 cm thick, b: grease ice and frazil ice, c: open water. Original data © ESA/TSS 1993.

4. CASE STUDIES OF SEA ICE CONDITIONS

4.1 The ice edge region during freeze-up

The usefulness of ERS-1 SAR for detection of ice edge features such as new ice formation was demonstrated as the icebreaker entered the icepack on its eastward voyage. The SAR image on October 29 (Fig. 2) was acquired during cloudy conditions when no other ice information

was available from this area. The region of open water is clearly resolved as a bright, fairly uniformly-white area in the SAR image. The first stage of new ice formation (grease ice or frazil ice) is shown as dark signatures in the image, whereas pancake ice or other gray ice which can be a few days old have a bright signature similar to open water. However, the image texture of the gray ice is clearly different from the of the open water, as is clearly seen along the Yamal coast where a meandering ice edge with several ice tongues were observed on October 29 1993 (Fig. 2). Such signatures have been well documented also in other regions [Ref. 1]. When *in situ* observations were made from the icebreaker good correspondence was found between the variations in the SAR backscatter and alternating areas of open water and new ice.

4.2 Residual ice in Vilkitskogo Strait

ERS-1 SAR images were also used to detect different ice types in the Vilkitskogo Strait which is a particularly difficult area for ice navigation. Thick residual floes (second - year ice) often occur in this region where differential ice motion causes heavy compression and ridging of the ice pack. The large thick floes, heavy ridges and as well as landfast ice make it difficult to navigate even for the most powerful icebreakers. The SAR image of 4 November 1993 shows examples of the ice types which often occurs in the the Vilkitskogo Strait (Fig. 3). For comparison the Russian ice map of the same area is shown in Fig. 4.

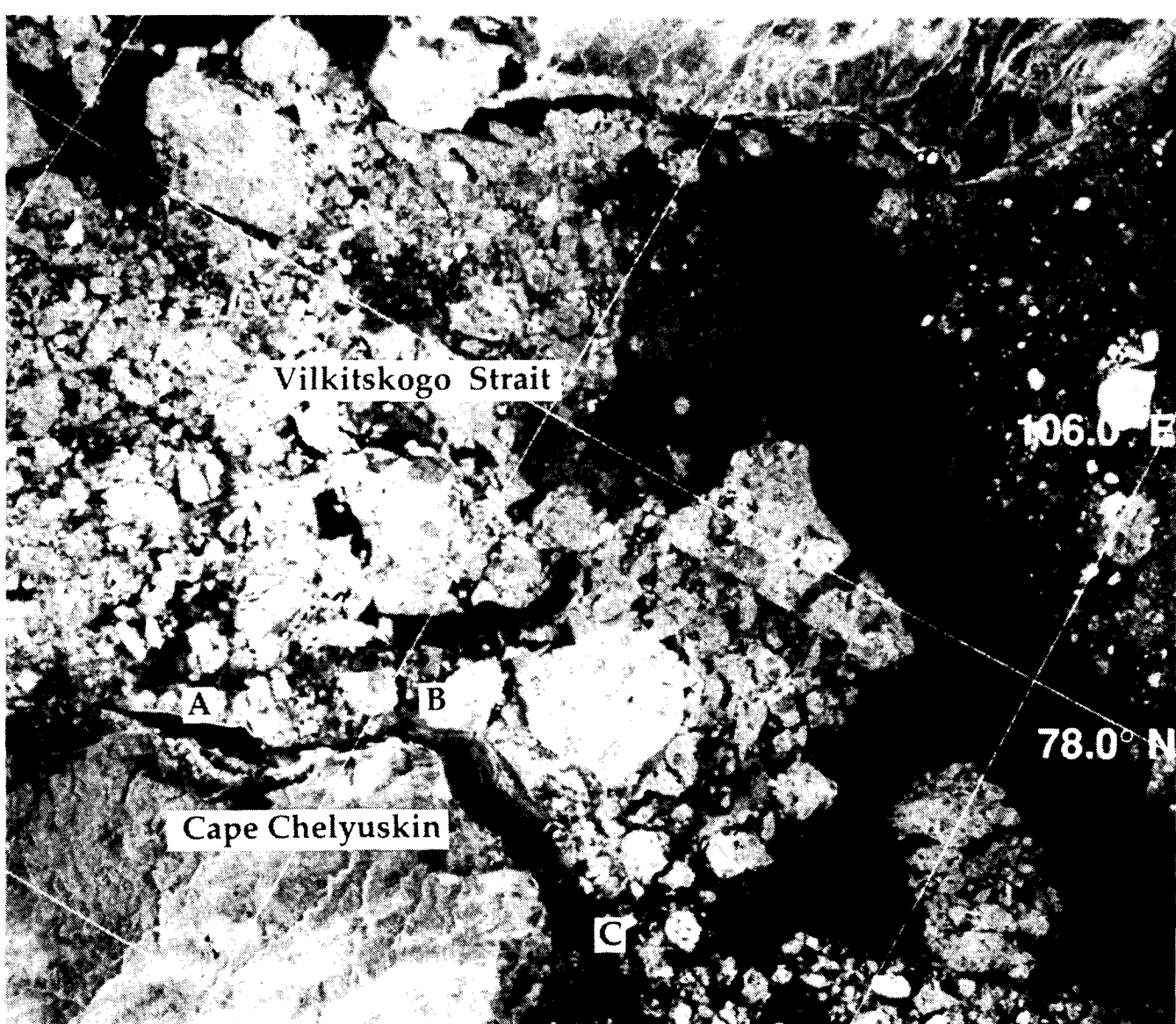


Figure 3. SAR image from November 4 1993 covering 100 by 100 km of the Vilkitskogo Strait. The icebreaker navigated along the flaw lead marked A - B - C. The bright floes are residual ice which can be more than 3 m thick, whereas the dark areas are first-year ice less than 50 cm thick. Original data © ESA/TSS 1993.

The "Sovetsky Soyuz" navigated along the Taimyr coast where three main ice types were found and recognized in the SAR image: (1) gray-white ice 15-30 cm thick, (2) thin first-year ice about 40 cm thick, and (3) residual ice about 3 m thick. Residual ice has a high backscatter, represented by a light-gray tone in the SAR image, in contrast to the darker young and thin white ice. The identification of residual ice from the SAR image is also possible by studying the flow shape; the older floes generally have a more rounded shape. For example, the residual floe marked B in Fig. 3 was documented by the icebreaker "Yamal". Mapping of residual ice is very important because navigation through such ice is difficult and should be avoided. The SAR image of 4 November provided useful information for the icebreakers to find the

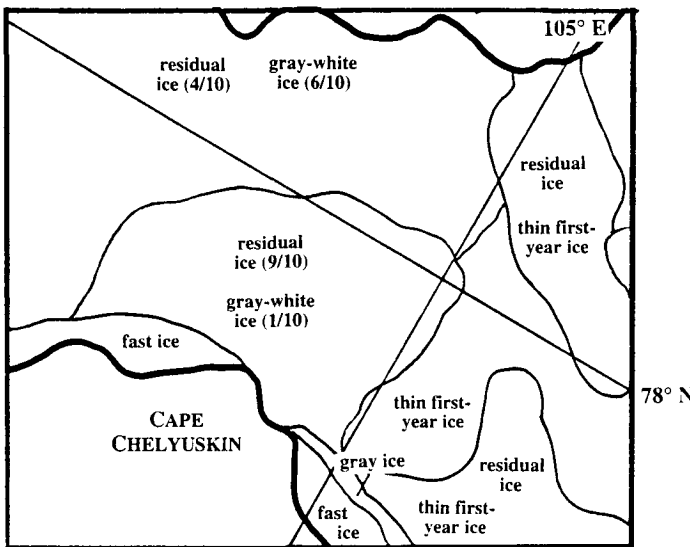


Figure 4. Russian ice map from the same area and period as the SAR image in Fig. 3. The ice concentration for each ice type is shown in tenths.

best sailing route. Navigation through the flaw lead along the Taimyr coast was much faster and less difficult and hazardous than through alternative routes, because the flaw lead was covered with thin new ice (dark SAR signature)

4.3 First-year ice types in the Nordenskjold Archipelago

Landfast ice, which is common around islands and along the margins of the Kara Sea, has variable thickness and can be heavily ridged. Icebreaker navigation in landfast ice such as in the Mathiessen Strait can therefore be difficult. The varied nature of the ice in this strait can be seen in the SAR image of 15 November (Fig. 5). This image was particularly useful because it was received and used by "Sovetsky Soyuz" during its westward return through this region. The ice near the west entrance to Mathiessen Strait (site A in Fig. 5) was observed to consist of:

- (1) Young ice 5 - 20 cm thick with dark SAR signature.
- (2) 1 - 2 km large mostly smooth, snow-free floes 30-40 cm thick observed near the fast ice boundary. The SAR image clearly reveals the location of the boundary and its extension around the small islands of the Nordenskjold Archipelago. At site A this border was crossed by the icebreaker.
- (3) Highly compressed and ridged first-year ice at site B. Further west (site C) the ice was fairly inhomogeneous with considerable ridging. The SAR signature of the ridged region is a mixture of brighter and darker patches. The navigation through this region was rather difficult.

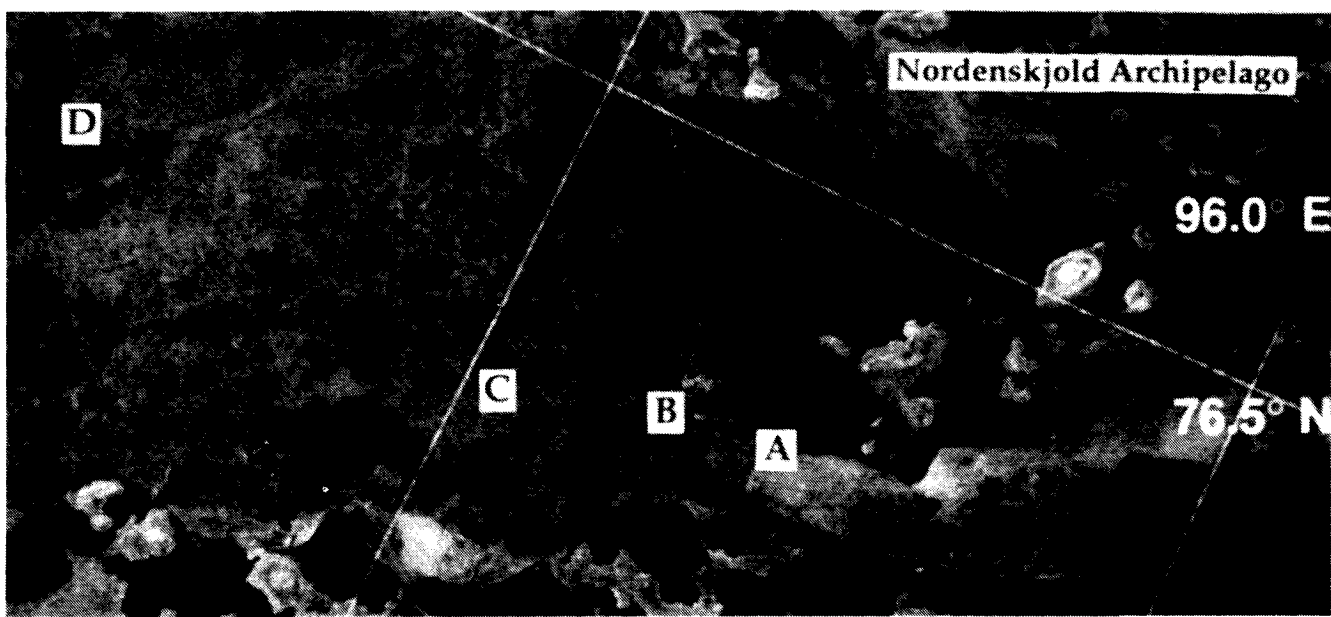


Figure 5. SAR image of the Mathiessen Strait in the Nordenskjold Archipelago from November 15 1993. Observations of ice conditions from the icebreaker were made along the route marked A - B - C - D. The image covers 100 by 50 km. Original data © ESA/TSS 1993.

The ice experts onboard "Sovetsky Soyuz" assumed that the relatively dark area in the western part of the image (site D) was smooth and fairly thin ice. Therefore, the captain changed the icebreaker route into this region. From site C to D the icebreaker penetrated ice of varying roughness, which was reflected by the variable SAR signature. At site D observations confirmed that the homogeneous dark SAR signature was 100 % thin ice.

Another ERS-1 SAR scene of the Mathiessen Strait area was obtained on 28 November and sent to "Sovetsky Soyuz" after the ship had passed through the area (Fig 6). In this period the region was cloud-covered, no other ships were present and no aircraft flights were made, so there was no updated ice information from the area. Therefore the SAR images were the only source of information which could be used by the icebreaker to update the ice maps and plan the sailing routes. The image interpretation done by the ice experts showed several ice types and dynamic features in the region: (1) The track of the "Sovetsky Soyuz" in the ice during its westward voyage two weeks earlier. (2) The boundary between thin first-year ice with different degrees of ridging (site A in Fig. 6) and the landfast ice around the islands of the Nordenskjold Archipelago. (3) A region of 90 - 100 % concentration of pancake ice causing high backscatter and bright signature in the SAR image (site B). (4) New landfast ice in bays, inlets and estuaries formed during calm weather. This ice is identified as dark homogeneous areas in the SAR image (site C).

5. CONCLUSION

The demonstration has shown that there are both advantages and disadvantages of using ERS-1 SAR images for ice navigation. The main advantages are: (1) SAR images can be used for detailed mapping of the ice edge and localize leads, thin ice types, landfast ice and thick multi-year ice, (2) SAR images are independent of cloud and light conditions, and (3) SAR images are available in near real-time. The disadvantages are: (1) the interpretation of the ice types can be difficult in some cases, (2) detection of ridges is generally not feasible, (3) the quality of the images are reduced by telefax transmission, and (4) the coverage is not sufficient for regular monitoring. However, the SAR coverage will be improved when RADARSAT is in operation in 1995. Up to 500 km wide swaths will be available, which means that most of the NSR will be covered every third day. The future plan is to make regular SAR ice monitoring from operational radar satellites available for the Russian ice service and thereby for all activities on the Siberian coast which need ice information.

6. ACKNOWLEDGEMENT

The project has been supported by European Space Agency, Norwegian Space Centre and Murmansk Shipping Company.

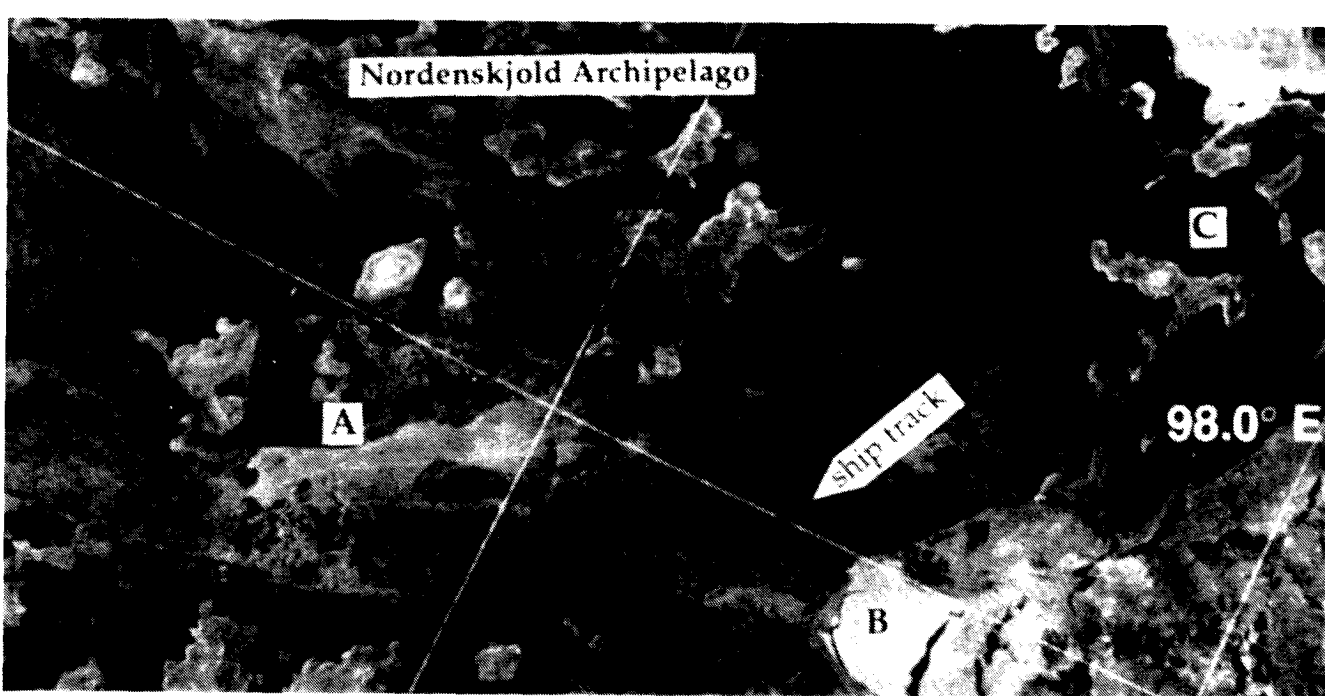


Figure 6. SAR image of the Mathiessen Strait from November 28 1993 after the "Sovetsky Soyuz" had passed through the area. The ship track in the ice can be seen in the image . A: boundary between landfast ice and drifting firstyear ice, B: pancake ice, C: new landfast ice. The image covers 100 by 50 km. Original data © ESA/TSS 1993.

7. REFERENCES

1. Sandven, S., O. M. Johannessen, R. A. Shuchman, K. Kloster and M. W. Miles. SIZEX 92 ERS-1 SAR ice validation experiment. Proceedings of Second ERS-1 Symposium - Space at the Service of our Environment, Hamburg, Germany, 11 - 14 October 1993, ESA SP-361 1994, pp. 353 - 358.
2. Sandven, S., O. M. Johannessen, L. H. Pettersson, M. W. Miles and Å. Drottning. A pilot ice monitoring service using ERS-1 SAR images. Proceedings of 1st ERS-1 Pilot Project Workshop, Toledo, Spain, 22 - 24 June 1994.
3. Sandven S., O. M. Johannessen and K. Kloster. Pre-operational use of Synthetic Aperture Radar (SAR) images from the ERS-1 satellite in sea ice monitoring. Proceedings of the International Symposium 'Operationalization of Remote Sensing' Enschede, The Netherlands, 19 - 23 April 1993, Vol. 5, pp. 125 - 136.
4. Johannessen, O. M., S. Sandven, Ø. Skagseth, K. Kloster, Z. Kovacs, P. Sauvadet, L. Geli, W. Weeks and J. Louet. ERS-1 SAR ice routing of L'Astrolabe" through the Northeast Passage. Proceedings of the Central Symposium of the 'International Space Year' Conference, Munich, Germany, 30 March - 4 April 1992. ESA SP-341 1992, pp. 997 - 1002.
5. Johannessen, O. M., and S. Sandven. Real time monitoring of sea ice in the Northeast Passage by ERS-1 SAR data. Accepted proposal to ESA's Second Call for Proposals for Application Oriented Pilot Projects based on the use of ERS-1 data. Bergen, September 1992, 12 pp.

THE OPERATIONAL SEA ICE CHARTING USING ERS-1 IMAGES IN THE BALTIC SEA

H. Grönvall and A. Seinä

Finnish Institute of Marine Research
P.O. Box 33, FIN-00931 Helsinki, Finland
Tel. +358 0 331044, Fax +358 0 331376, E-mail: hannu@ice.fmi.fi, ari@ice.fmi.fi

ABSTRACT

The Ice Service of the Finnish Institute of Marine Research received ERS-1 FD-SAR images numbering 141 between January and March 1994. The Gulf of Bothnia and the Gulf of Finland were selected as the experimental area for ERS-1 images. The images were used in routine ice service activities and some 30% of them were delivered to icebreakers. SAR images were combined with NOAA images and ground information from ice observation stations, ports, vessels and icebreakers. In this paper usefulness of the visually analysed ERS-1 SAR images is discussed from the point of view of routine ice service activities.

Keywords: Baltic Sea, sea ice, SAR, ERS-1, ice service

1. THE FINNISH ICE SERVICE

1.1 The Baltic Sea Ice Season

The ice conditions in the Baltic Sea have considerable variation. The maximum annual ice cover ranges from 52 000 km² to 420 000 km² (resp. 12-100 %) an average being 218 000 km² (Ref. 1). In the Bothnian Bay and in the eastern Gulf of Finland the probability for ice occurrence is 100 %, the 50 % probability lies in the northern Baltic Sea at around latitude 59° N, and 10 % covers the southern Baltic Sea. The maximum annual ice extent occurs between January and March (Ref. 2).

Ice formation begins in the northern Bothnian Bay in early November, in the Gulf of Finland in early December. The Bothnian Bay is covered with ice on an average in mid-January and the Sea of Bothnia in mid-February. The Gulf of Finland freezes completely on an average in late January, not freezing totally in mild winters. Predicting the severity of the winter in the beginning of the ice season is impossible - reasonable forecasts could only be given in the end of January. The normal breakup starts at April, by the beginning of May only remaining ice is situated in the Bothnian Bay, and the ice melts complete by the end of May - the beginning of June. The average duration varies from < 20 days in northern Baltic Sea Proper to 190 days in northern Bothnian Bay being in the northern archipelago of the Bothnian Bay of up to 7 months (Ref. 3).

The ice in the Baltic Sea occurs as fast ice and drift ice. The fast ice occurs along the coastal and archipelago areas where the depth is less than 15 meters. It develops during the early ice season remaining stationary to the melting period. The drift ice has a dynamic nature forced by the winds and currents.

The drift ice movements are large: during one day, in the storm conditions, the ice field can move 20-30 km. The motion results in uneven and broken ice field with distinct floes up to several kilometers in diameter, leads and cracks,

slush and brash ice barriers, rafted ice and ridges. The ridges and brash ice barriers are the most significant obstructions to navigation in the Baltic Sea. Powerful, ice strengthened vessels can break through up to 80 cm thick ice, but they are not capable to navigate through ridges and thick brash ice barriers without icebreaker assistant. The ice dynamics affects considerably navigation - high pressure in the ice field can be dangerous to the vessels and at least causes the vessels time delays from hours to days.

1.2 The Finnish Ice Service Activities

In Finland the sea ice observation network was set up in the 1800's, and during the World War I a real-time operational routine was started. The Finnish Institute of Marine Research was founded in 1918, and the operational Baltic Sea ice information service - shortly Ice Service - was organized to collect, combine, analyze and distribute sea ice information mainly to shipping authorities and to icebreakers. At first ice information was based on the information collected by telephone and mail from the observation stations and various vessels, but during the World War II aerial reconnaissance took place at large as a routine. Building of larger and more powerful icebreakers made possible, since 1971, to keep all the main harbours in Finland open all-year (Ref. 4).

Since the 1960's the Ice Service has used satellite images mapping the ice conditions, and since 1981, getting its own NOAA receiving station, the satellite images have been in real-time routine use. From 1992 digital NOAA imagery has been received from the Finnish Meteorological Institute via a telephone channel. Processed satellite images are sent to the icebreakers via an especially designed communication system (IRIS). The most important ground information sources are three times a day received icebreaker reports about the ice conditions of their operating areas, and reports of the fixed stations. The data is exchanged with other Ice Services. A numerical model has been used for ice forecasting since 1977.

In the winter 1993/94 the Ice Service has used a versatile image processing work-station, which enabled an effective working environment for the SAR -image analysis. The image processing software allows analysing satellite images (e.g. NOAA and ERS), and their processing together with older ice chart(s) to produce the new standard ice chart(s).

The information is collected from various sources: from NOAA-satellites several times a day, 2-3 times a day from icebreakers, 1-7 times a week from fixed stations and from aerial reconnaissance 1-2 times a week. In the international exchange the data is exchanged daily between the ice services. Airplane use has become rare because of intensive use of satellite images, the icebreaker based helicopters are used daily collecting ice data for navigation, and the reconnaissance charts are also sent to the Ice Service.

The data sources are highly weather dependent, and since rapid changes occur during cyclone activities the need of

weather independent methods are evident. Excluding the satellite images the data sources provide information only about small areas.

The Ice Service operates on a daily basis during the sea ice season. New ice reports, ice charts and ice forecasts are prepared daily ice cover characteristics changing with time. In highly dynamic cases the update of the ice information can be delayed even by one day information gap caused by cloudiness in satellite images and/or difficulties to maintain aerial reconnaissance.

Some major difficulties occur in constructing a real time ice chart using various data sources. The existence of discontinuities in ice properties creates interpolation problems, and objective analysis methods have not been developed for ice charting. Creating an analytic method using an advanced numerical sea ice model and attempts to create automatic algorithms to remote sensing have generally not been very successful. In all, the construction of a new ice chart and report is performed with manual and subjective methods using the previous ice charts provides a basis, which is updated using the new data.

Traditionally the main customers deal with shipping, fishing and military, and are listed: shipping, icebreakers, vessels in general, pilot and harbour authorities, navy and coast guard, weather services, fishermen and the great public via media. Most of the customers need ice information daily, some to their strategic planning on a longer time scale.

2. WINTER 1993/94

2.1 Weather

The winter 1993/94 started in October as a cold one. In November, December and January the air temperature was average or above average. February turned into the cold one having air temperatures 4.5 - 6.5°C under average. March was a normal one.

2.2 Sea Ice

The winter 1993/94 was an average one. As maximum the ice covered 49% of the Baltic Sea.

The freezing started in the northern Bothnian Bay in the end of October -approximately three weeks earlier than normal. The freezing continued in early-November: the ice was forming in all near-coast areas. In the mid-December started the third fast freezing period covering the outer islands of the Gulf of Finland; this was ca. 4 weeks under normal. During the Christmas started next freezing which under in December 29 the ice covered almost totally the Bothnian Bay, in the Bothnian Sea there was 15 nautical miles of ice and the Gulf of Finland was frozen from the east to the latitude of 25° 30' - ca. four weeks under average. In the end of January started a rapid freezing period covering the Gulf of Finland totally. In the February the rapid ice formation continued: the Bothnian Sea was frozen over at the 9th and the northern Baltic Sea Proper at the 18th. All this as an average. In the March 3 the maximum extent of ice cover of the ice-season was reached, 206 000 km², the ice covered the sea from the north to the latitude of ca. 59° N (Fig. 1).

Starting on March 6 the strong winds broke the ice fields drifting the ice northwards. In the mid-March half of the Bothnian Sea was open. In the beginning of April the ice in

the northern Baltic Sea Proper melted away. The Archipelago Sea was open on the end of April (5 days later than average) and in the eastern Gulf of Finland there was only rotting ice (-9 days). In the northern Bothnian Bay the ice was enough to the end of May, which is an average.

3. THE OPERATIONAL USE OF ERS-1 IMAGES

The ERS-1 images were delivered, numbering 141 between January 10 and March 28 1994, to the Ice Service of the Finnish Institute of Marine Research from Tromsø, Norway, via Instrument Laboratory of Technical Research Center of Finland after 1-5 hours of the receiving. In the Ice Service SAR images were used in the image processing workstation allowing satellite image processing together with ground information and chart handling combination. In practice the analysed ice charts were used as background and SAR images were analyzed on top of them. The analysing difficulties were solved using ground information from icebreakers and ice observation stations. As the scientists worked at the Ice Service the whole ice season the ice history was known.

As ice conditions in the Baltic Sea can change rapidly even in hours, the need of images much faster is great, and as the rapid changes of ice conditions are strongly connected to low pressure activities (and thick cloud cover) SAR images have larger serviceability than traditional NOAA images.

ERS-1 images were delivered with a resolution of 100 m, and a width of ca. 100 km. The cycles of 3 d were used during experiment 1994, which allowed two orbits: Helsinki - Bothnian Bay ("A"-orbit) and Bothnian Bay - Stockholm ("D"-orbit).

Analysing received ERS-1 images most of the problems in winter 1992/93 (Ref. 5.) were avoided. Winter 1993 was a mild one having high humidity areas, and the ice surface was wet. In 1994 the air temperature was mostly under freezing point the analysing problems were avoided. At the end of experiment the melted snow caused some analysing problems in the Gulf of Finland. The field experiment, however, going on the area solved the calibration. For the classification of ice and open water the two scales contextual classifier was used allowing classification in ten minutes (Ref. 6).

A field experiment was held March 14-28 in the Bothnian Bay, the Bothnian Sea, and the Gulf of Finland based on the research vessel *Aranda*. In the figures 2-4 are shown some examples of the analysed images. The images cover also the field experiment areas.

In the image of Bothnian Bay (Fig. 3) March 16 off the cities of Kokkola and Pietarsaari there is off the coast first ~70 cm thick fast ice, and then more grey area of ~40 cm thick ice with some ridges. The channels of the icebreakers are clearly visible. At the upper left corner there is more lighter area consisting 60-70 cm thick heavily ridged ice. The area was stationary for more than seven weeks. At the bottom of the area there is an area of more darker ice, which is 60-70 cm thick and relatively level.

In the image of Bothnian Sea (Fig. 4) March 23 off the city of Kaskinen there is off the coast first fast ice, 50-60 cm thick, and then 20-40 cm thick consolidated ice, at places ridged. At the ice edge there is very visible brash ice

barrier, very typical in the Baltic Sea. At the upper part of the image the belt of lighter area is a large heavily ridged area of 20-40 cm thick ice. The whole ridge was a new one, not frozen together. Irregular white area at the left is new ice and total bottom is open water.

In the image of the Gulf of Finland (Fig. 2) March 28 off the city of Helsinki there is at the top fast ice, 50-60 cm thick, with visible ship channels. More to the down there is a darker area representing thin ice covered lead with bright white areas of open water. At the middle of the image there is 40-50 cm thick consolidated ice in gigantic floes. The more lighter area on left is heavily ridged ice.

4. CONCLUSIONS

The Finnish Ice Service had valuable contribution of ERS FD-SAR images delivered from Tromsø, Norway. The images were delivered almost in real-time, which is very important considering the ice service activities of rapid ice information distribution to the end-users. In the winter 1993 the images were delivered in 24-48 hours, in the winter 1994 1-5 hours.

The analysis of the SAR images contains always some problems. However, the relatively stable air temperature and especially lack of high moisture prevented mostly the problems of 1993. Open water and ice discrimination classifier was tested successfully in real-time. The next classifier of ridges is under construction.

Analysing SAR images in the Baltic Sea area is more easier than in the Arctic and Antarctic areas having the possibility to use ground information widely.

References:

- Seinä, A. & Palosuo, E. 1993, Itämeren suurimpien vuotuisten jäätäpeitteiden laajuusien luokittelu 1720-1992 (Abstract: The classification of the maximum annual extent of ice cover in the Baltic Sea 1720-1992), *Meri* 20, 5-20.
- Leppäranta, M., Palosuo, E., Grönvall, H., Kalliosaari, S., Seinä, A. & Peltola, J., 1988, Phases of the ice season in the Baltic Sea, *Finnish Marine Research* 254, Supplement 2, 1-83.
- Seinä, A. & Peltola, J. 1991, Duration of the ice season and statistics of fast ice thickness along the Finnish Coast, *Finnish Marine Research* 258, 1-46.
- SMHI & Finnish Institute of Marine Research 1982, Climatological ice atlas for Baltic Sea, Kattegat, Skagerrak and Lake Vänern (1963-1979), Norrköping, 1-220.
- Grönvall, H. 1988, Finnish Ice Service, *Finnish Marine Research* 256, 95-110.
- Seinä, A. & Grönvall, H. 1994, The Operational Mapping of Ice Conditions Using ERS-1 Images in the Baltic Sea, *Proceedings Second ERS-1 Symposium - Space at the Service of our Environment*, Hamburg, Germany, 11-14 October 1993 ESA SP-361 (January 1994), 369-371.
- Herland, E.-A., Seinä, A. & Leppäranta, M. 1994, ISY Real Time Ice Monitoring Demonstration in the Baltic Sea, Final Report, May 1994, *ESA Contact Report*, ESA/ESTEC No 125475.
- Similä, M. 1994: Open water and Sea Ice Discrimination from ERS-1 Image by a Two Scale Contextual Classifier. To be published later.

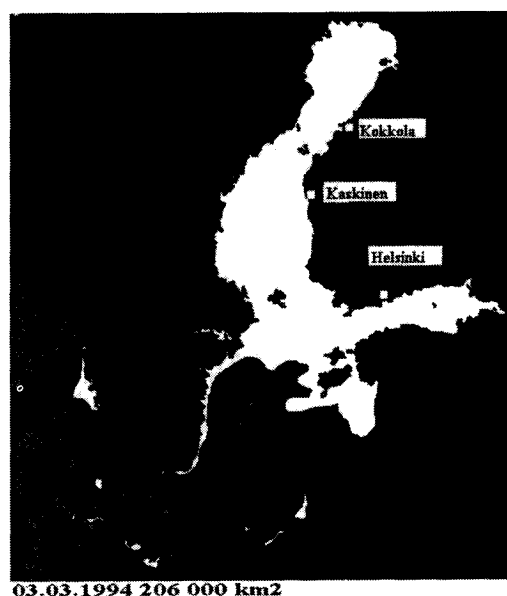


Figure 1. The maximum extent of ice cover in the winter 1994. The cities locate the images 2-4.

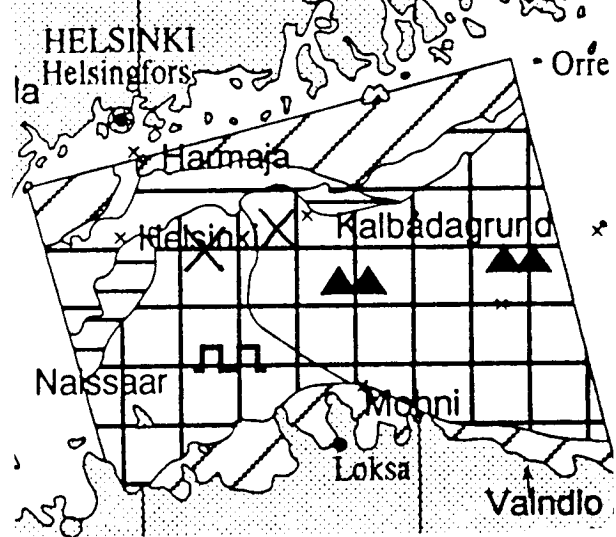
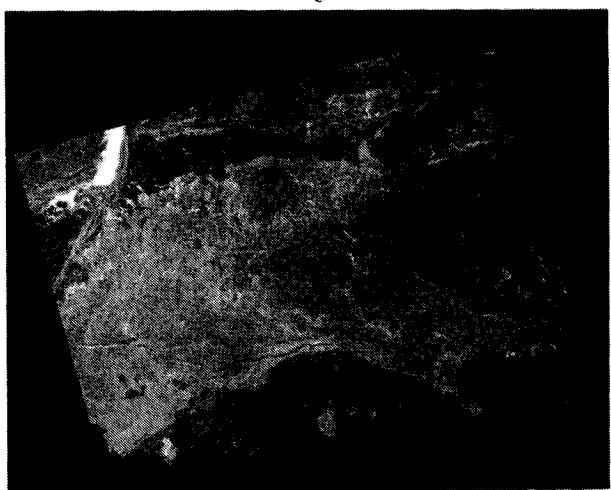


Figure 2. ERS-1 image March 28 at the Gulf of Finland off Helsinki (top) © ESA, processed by Tromsø sat. station, and analysis (bottom) © Finnish Institute of Marine Research X intensive research area.

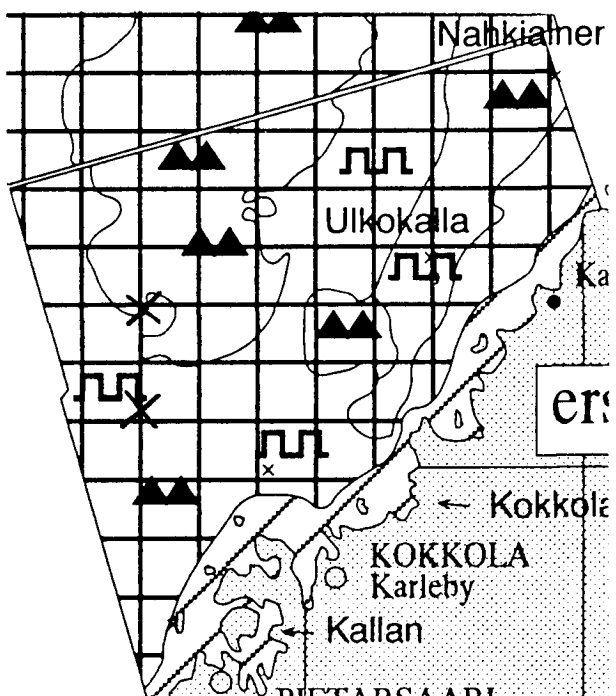
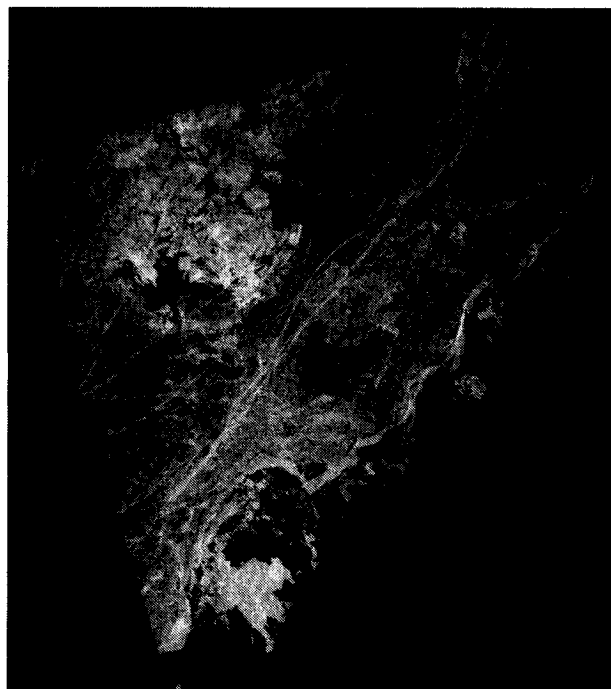


Figure 3. ERS-1 image March 16 at the Bothnian Bay off Kokkola and Pietarsaari (left) © ESA, processed by Tromsø sat. station, and analysis (right) © Finnish Institute of Marine Research. X intensive research area.

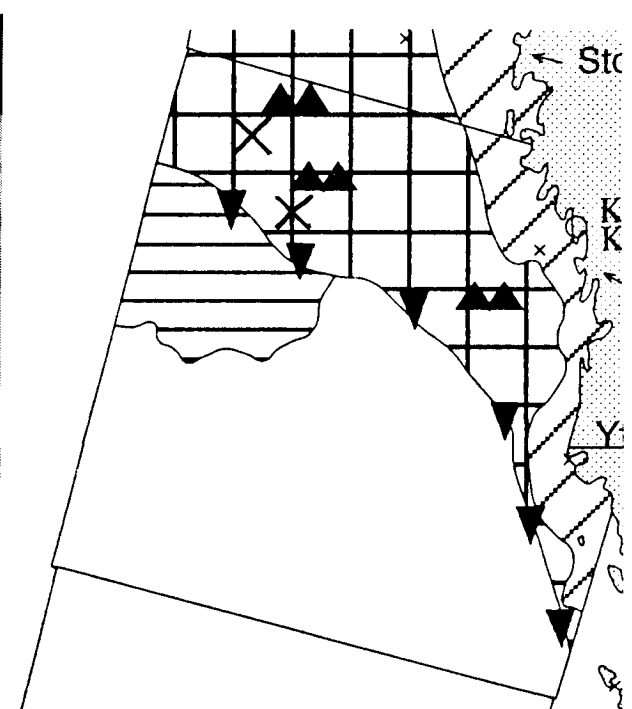
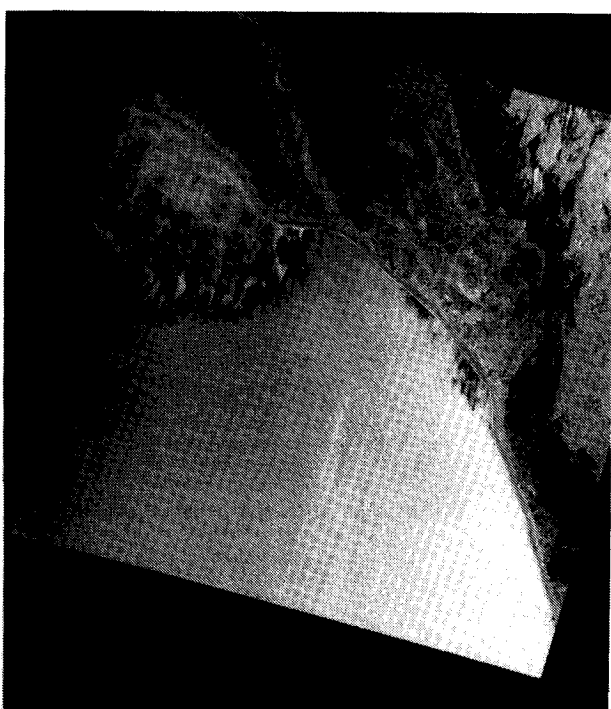


Figure 4. ERS-1 image March 23 at the Bothnian Sea off Kaskinen (left) © ESA, processed by Tromsø sat. station, and analysis (right) © Finnish Institute of Marine Research. X intensive research area.

EVALUATION OF REAL-TIME USE OF ERS-1 SAR IMAGERY FOR ICEBREAKING OPERATIONS IN THE BALTIC

B. G. Håkansson¹, M. Moberg¹, T. Thompson¹ and A. Backman²

¹Swedish Meteorological and Hydrological Institute, S-601 76 Norrköping
tel: * 46 11 15 80 00, fax: * 46 11 17 02 07, e-mail: bhakansson@smhi.se

²National Maritime Administration, S-601 78 Norrköping, Sweden.
tel: * 46 11 19 10 00, fax: * 46 11 10 19 49

ABSTRACT

Knowledge of present ice conditions is of vital interest for safe and efficient winter navigation. Since 1958 Swedish and Finnish ice services have established a successful cooperation and developed methods to provide icebreakers and icebreaking services with ice information. The main purpose of the icebreakers is to secure safe and regular winter navigation in the Baltic.

SMHI is engaged in ERS-1 validation/calibration and demonstration campaigns. An application programme for use of SAR imagery in sea ice mapping and icebreaker operations was realized during the ERS-1 ice-orbit (3-day orbit) i.e. January to April 1994. Low-resolution images from the Tromsø Telemetri Station in Norway were sent to SMHI, using the Internet facility, in order to get the data in near real-time. The overflight time for the northern Baltic was about 09.50 UTC. At SMHI the imagery was stretched to Mercator projection and linked to a software (Iceplot) which allows data to be overlaid with other types of information, like for example merchant vessel positions, whereafter the images were transmitted to the icebreakers using the Nordic Mobile Telephone net.

The usefulness of the data for ice mapping and icebreaking operations are presently under investigation using a questionnaire to obtain the users point of view. Officers in charge on icebreakers and staff responsible for the ice service are those who are answering the questionnaire. An important part of the work has also been to produce more accurate ice maps, using the SAR imagery.

1. INTRODUCTION

The Baltic Sea is located in northeastern Europe, bordering Sweden, Finland, Russia, Estonia, Latvia, Lithuania, Poland, Germany and Denmark. The population around the Baltic Sea is more than 70 million. The Baltic is a shallow and semi-enclosed sea with five subbasins; the Bothnian Bay (BB), the Bothnian Sea (BS), The Gulf of Finland (GF), the Gulf of Riga (GR), and the Baltic proper (Bp) (cf. Figure 1). It is one

of the largest brackish water bodies in the world with an area of 377 400 km² and a volume of 21 200 km³ (Sjöberg, 1992), and with an average surface salinity varying from almost 0 psu in the northern part of the Bothnian Bay to 8 psu in the southern Baltic proper.

Sea ice forms every year, but the extent of the icecover varies considerably between years (Figure 1) and, depending on location, the ice season typically lasts 3 to 6 months. Sea ice is formed in January in the Bothnian Bay and one month later in the Bothnian Sea on average, whereas break up occurs in May and April in the two subbasins. During strong winters the whole Baltic Sea is

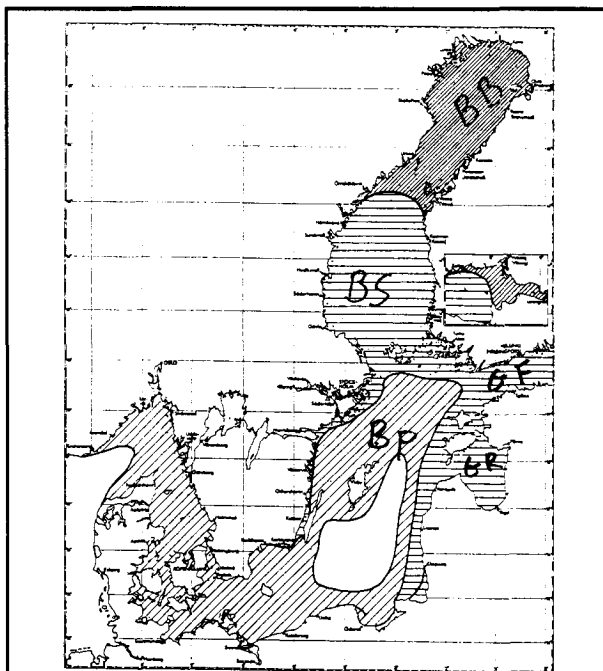


Figure 1: The typical ice cover during a mild (dense, slanting lines), normal (dense, slanting lines and horizontal lines) and severe (all area except the white ones) winter in the Baltic.

ice covered, but this takes place more or less ones per decade. Ice motions forced by winds and currents cause the drift ice to deform. In the open sea pressure induced ice ridges occurs frequently as well as shear induced ridged areas, and along the coastal zones in the Bothnian Bay hummocked ice areas can be formed. The thickness of

ridges vary, but can be as thick as 15 meters, whereas the level ice thickness is of the order of one meter.

All major ports in the Gulf of Bothnia have been open for sea-trade all around the year since 1970, and about one thousand icebreaker assistances are carried out each winter. This has been made possible by using modern powerful icebreakers to assist cargo vessels with high ice class and icegoing capabilities. Another reason to the success is that the icebreakers are provided with good ice information and forecasts. Almost all the Swedish and Finnish icebreakers are equipped to receive satellite images in digitized form.

In this study we present some results obtained during 1994 from the pre-operational use of SAR for winter navigation purposes. The aim of this experiment was to evaluate the use of SAR information focused on ice mapping in a real-time operational situation for the national ice service and for the icebreakers. Due to varying ice extent and ice dynamics such information should ideally be available once a day with a possibility to cover all areas of the Baltic Sea. The delay between registration and evaluation of the data should not exceed 3 hours for operational reasons. However, these prerequisites for operational use of SAR imagery were only partly achieved, taking into consideration the pre-operational nature of the ERS-1 orbit configuration, swath width and the data transmission system.

2. DATA PRESENTATION

The full-resolution data was received by the national BDDN-station, situated at SMHI in Norrköping, provided by the European Space Agency. The way of partition of

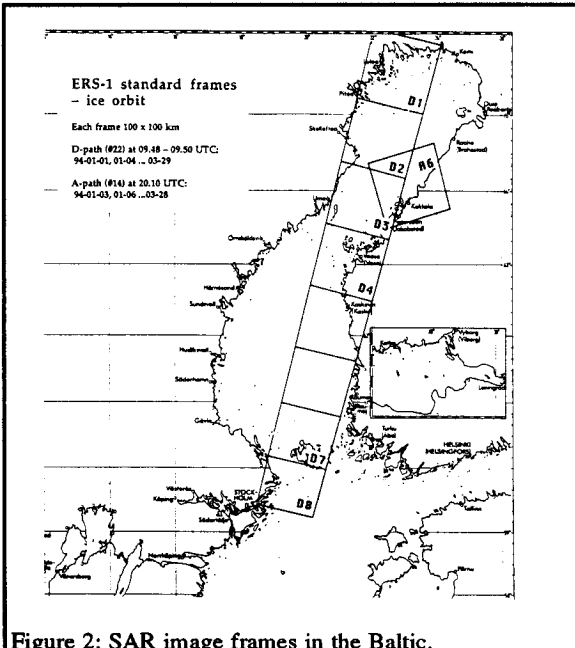


Figure 2: SAR image frames in the Baltic.

the transmission time slots between Kiruna and Fucino implied that data from frames D1 to D8 (descending orbit) could, as earliest, be transmitted during 1300 - 1330 UTC the same day when received by Kiruna, while data from frame A6 (ascending) could be transmitted as earliest the following day at 0800 - 0900 UTC. Radio horizon at Fucino permits a reception zone which covers frames D3 to D8 and A6 while the Kiruna reception zone covers all of the Baltic Sea. For various capacity reasons this scheme could not always be carried out. On the other hand low-resolution data, using a 5 by 5-averaging filter of the original received SAR data, were available at the Tromsö Satellite Station computer within an hour from acquisition time. Internet was used to transmit the data from TSS to SMHI. A Mercator transformation polynom was calculated, based on the header information of the geodetic latitudes and longitudes for 5 image points: the four corners and the center point. From this polynom an overview picture in Meractor projection and with a pixelsize of 200 m was generated. Using this overview picture any arbitrary sub-picture with full resolution (30 m for UT16 and 100 m for LRI) could be generated in Meractor projection, depending on the actual area of interest according to the ice conditions. These overview images and their derivatives were used at the ice service as information for the daily produced ice map. No calibration or classification was done but the images were manually interpreted, taking into account results and experiences from previous calibration and validation campaigns of ERS-1 in the Baltic (cf. Figure 3). In order to evaluate the benefit of the SAR information, separate

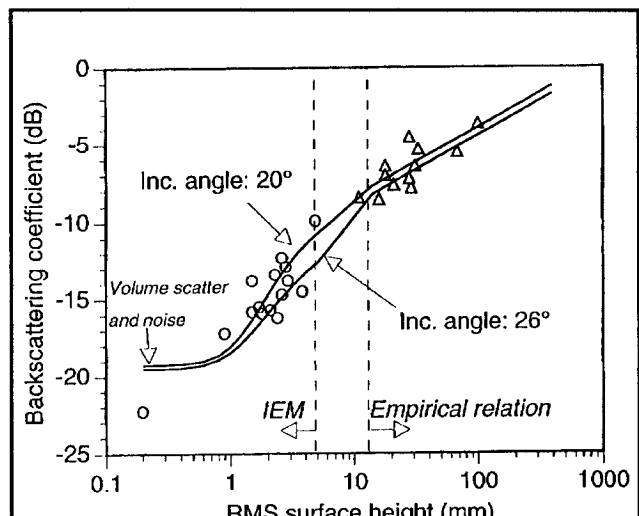


Figure 3: Analytical/empirical inversion model for SAR-Sea Ice interpretation by Carlström et al. (1994).

log files were used by the staff at the ice center and onboard some icebreakers.

For distribution and graphical presentation of maritime information, satellite images as well as weather and ice

forecasts on-board icebreakers the Iceplot software is used. This is an application developed jointly for the Swedish National Maritime Agency and the Finnish Board of Navigation. The software resides on Macintosh and PC compatible computers connected by a Novell network and using the Nordic Mobile Telephone System 450 MHz as the transmission method. The information are presented on Macintosh computers with large screens, situated at the icebreaker bridges. Positions of icebreakers, merchant ships and harbours are plotted on a graphic coordinate system showing the contour map of the Baltic Sea. When available, satellite images as AVHRR or SAR, are substituting the contour map, giving information of the ice conditions.

Low resolution images obtained from Tromsö was, on average, available at the SMHI computer 2 hours after satellite aquisition time. The various processing steps took in general another 1.5 hours before images were available at the ice service. Fast delivery (UI16) data received by BDDN were available at the local computer typically 19 hours after satellite aquisition time and the following processing took another 2 hours. The averaged transmission time between the ice service and the icebreakers, using the Iceplot system and the mobile telephone net, were 40 minutes for each frame.

3. EVALUATION OF SAR

As mentioned above five different icebreakers received SAR images. The limitations of the transmission system and the principle that only icebreakers with an activity in the current SAR frame should be furnished with SAR data had the consequence that in general two icebreakers had regular SAR imformation. All five icebreakers were answering questionnairs for each SAR they obtained, covering in total 34 frames. In addition to this information personal communication with several icebreaker officers took place during the evaluation period. In summary, we found that the following conclusions can be made:

- Interpretation of the imagery was not a problem.
- Information about ridges, an important ice feature in winter navigation, was quite well furnished by the SAR images.
- There were many occasions with operational use of the SAR information.

The interpretation of the images was evaluated, using a scale going from 1 (interpretation easy) to 5 (difficult). Icebreaker officers are used to sophisticated ship radars and seems to have no problem adopting to the SAR. The weather conditions also favoured the interpretation as air temperatures were mostly beneath 0°C, which kept the wetness in the snow low enough to give high contrast in the SAR images. Hence, the overall ranking turned out to be good and was on average two.

Quite often SAR information was reported to have had a direct influence on which way to go when assisting merchant ships in a convoy and for routing merchant ships going by there own. During the period January 19 to March 11 53 % of the images were used for vessel assistance and 37 % for ship routing. Note however, that these figures are to some extent preliminary in that the data material is not extensive enough for a statistical analysis, since only 30 questionnairs have been investigated. Nevertheless, the results broadly indicate the usefulness of this information and how the imagery were used onboard the icebreakers.

An interesting case was reported on January 19 from the icebreaker Ymer, heading north in the central part of the Bothnian Bay. Several hours earlier she assisted a merchant vessel, which was caught in an area of thick ice ridges outside the port she just left assisted by the local icebreaking tug. However, they did not have any information on the prevailing ice situation, so the merchant vessel was left in the drift ice, awaiting icebreaker assistance. As noted by the master onboard Ymer, he could have informed the local authorities of the harbour about the ice situation and told the tug to assist the merchant vessel some nautical miles further ahead, where there was only a thin ice cover which the vessel could manage by herself, had he had the SAR image a day before.

4. SUMMARY

There is no doubt about the operative usefulness of SAR imagery for sea ice purposes in the Baltic Sea. This winter experience demonstrate that the imagery were always used at the ice service and during icebreaking operations when the sea ice was deforming i.e. convergence/divergence of the ice field and ice drift or ice growth took place. The problems we faced and mentioned here has to do with the technical restrictions put on ERS-1 SAR image products, taking into account the high geometrical resolution but narrow swath width.

The image geometrical resolution of 200 meter pixel size gave interesting enough information for the icebreakers, although 100 meter would be prefered since small-scale information can be distinguished better. However, imagery with a pixel size less than 100 meters will limit the coverage too much, taking into account the present status of the technical equipment. From a operative point of view it is necessary to obtain SAR imagery on a daily basis with a larger spatial coverage of the Baltic Sea than is presently possible. On the other hand, this investigation has shown that the SAR imagery onboard the icebreakers were greatly appreciated and turned out to be very useful for ship routing and assistance. Routing cargo vessels with high ice class and icegoing capabilities is perhaps the most important operative application,

since it may save energy and time for the icebreakers.

Note also that the daily produced ice maps will be one of the most important data sets for improving the initialization process of both sea ice and weather models, in near future.

ACKNOWLEDGEMENT

Thanks to the Swedish Space Agency and the European Space Agency for financial and SAR imagery support as part of two AO projects.

REFERENCES

- Carlström A., L.M.H. Ulander and B.G. Håkansson (1994): Model for estimating surface roughness of level and ridged sea ice using ERS-1 SAR. Proceedings EarSeL 94, Göteborg, Sweden.
Sjöberg, B. (editor) 1992: Sea and coast. The National Atlas of Sweden. Almqvist & Wiksell International, Stockholm.

AUTOMATIC SATELLITE BASED SEA ICE MONITORING SYSTEM

Diane Boardman, David Darwin, Jolyon Martin, Neil McIntyre and Ken Sullivan

Earth Observation Sciences Ltd, Broadmede
 Farnham Business Park, Farnham, Surrey, UK
 phone: +44 (0) 252 721444 fax: +44 (0) 252 712552

ABSTRACT

Ship routing companies, resource exploration operations, weather forecasting agencies and glaciological research institutions are all interested in obtaining reliable sea ice information. Typically, this information is required for localised regions on short timescales.

To explore this market a prototype sea ice workstation (SIWS) has been developed. The workstation uses data from several current earth observation sensors, combining the advantages of regional survey, all weather capability and high resolution imagery. The output from the workstation is an integrated sea ice chart with the capability to display combinations of ice edge, ice type, ice concentrations, ice motion vectors and sea surface temperatures generated by the geophysical algorithms. A minimum of operator intervention is required to run the system.

During the course of its development significant new progress in automated ice classification has been achieved together with the enhancement of existing ice motion algorithms. The quality of the sea ice information from each of the geophysical algorithms was assessed through extensive validation.

1. INTRODUCTION

The user groups for sea ice information fall into three broad categories; research meteorological forecasting and off-shore operations. Although each of these groups has its own specialist requirements there are a number of basic sea ice parameters which are common. These include ice classification, ice concentration, ice motion and the positions of open water within pack ice. The most important ice classification is based on age, ice being classified as first-year or multi-year ice. This discrimination identifies thick (multi-year) ice which is a hazard to shipping and thin areas (first-year) which are important for ice advection and radiation transfer modelling. The extent of the ice and its motion provide safety limits for those concerned with ice avoidance. Areas of open water (polynyas and leads) and the ice concentration are important for navigation and modelling.

Current ice charting services, such as that provided by meteorological offices, are essentially tactical in nature,

producing regional ice surveys at intervals of between 1 and 7 days. Their ice charts show the ice edge, major ice characteristics and sometimes mean sea surface temperature isotherms. Generation of the charts is entirely manual, relying on expert interpretation of the imagery. The extent and information for the charts is fixed.

2. CONCEPT OF A SEA ICE WORKSTATION

In the context of the current and growing requirements for sea ice information in the polar regions the UK's Defence Research Agency (DRA) commissioned the development of a prototype sea ice workstation. The aims of the project were:

- (1) To demonstrate the feasibility of extracting sea ice information automatically from satellite data in a time period commensurate with the operational requirements.
- (2) To demonstrate the near real time integration of data from ERS-1 SAR, AVHRR and SSM/I data recognising that, in isolation, each of these sensors suffers from some weaknesses.
- (3) To demonstrate a high degree of automated operation.

The contract to develop the SIWS was won by a consortium lead by Earth Observation Sciences.

3. SIWS OPERATION

3.1 Overview

The SIWS system is operated through a graphical user interface which provides access to its five major subsystems; SAR swath prediction, data preparation, browse, geophysical processing and results display (see Figure 1). Modular design of the system makes its operation extremely flexible, allowing multiple paths and entry/exit points. During a single session the user can choose to create different forms of ice charts from previously saved analysis; run one algorithm repeatedly on a single dataset to investigate the effects of changing the algorithm control parameter settings; or ingest, pre-process and browse data, carry out automatic geophysical processing and produce standard ice charts in the fastest possible time.

The following sections describe the functionality of each of the SIWS sub-systems.

SAR swath prediction is a visualisation tool which calculates and displays the spatial coverage achievable from ERS-1 SAR for a given area and time period. It is used as an aid in planning future data requirements and selecting SAR ice motion pairs. Data preparation is the usual point of entry for users creating new charts. It provides the functionality for ingestion of data from a variety of media, the deletion of unwanted imagery and a variety of pre-processing tasks including the conversion of raw data to a standard form and the creation of geolocation information.

Browse allows the user to review the available pre-processed data for selection for geophysical processing. Spatial and temporal searches can be performed for each data type. The selection of pairs of SAR and AVHRR images is aided by drawing the outlines of SAR images onto AVHRR images and both outlines onto the map. SAR and AVHRR images may be displayed and inspected using image processing tools.

Control and access to the five geophysical processing algorithms is achieved through the geophysical processing sub-system. Each of the geophysical processing algorithms is controlled by a number of processing parameters. Algorithms can be operated automatically using their default settings or, alternatively, users may customise sets of their own control parameters which can be saved for later use. Details of the geophysical processing algorithms are given in section 3.2.

The display of the results of the geophysical processing and the generation of an integrated sea ice chart is achieved through the results display sub-system. It is possible to access and display any input data or geophysical product. The sea ice chart consists of foreground data derived from SAR and a context forming backdrop derived from lower resolution AVHRR or SSM/I. The chart can be customised by selecting its extent, projection, overlaying coastlines and latitude/longitude gridlines and user defined annotation. An example of a SIWS chart is shown in Figure 2.

3.2 Geophysical Processing

Sea ice information is currently extracted from AVHRR, ERS-1 SAR and SSM/I data although the system has been designed to allow other sources to be used at a future date. AVHRR data is widely used within the sea ice community; ice edge and ice types being derived manually from it. It does, however, suffer from the problems of clouds and for some channels darkness. SSM/I has the advantage of wide hemispheric coverage but its poor resolution (25km at best) makes it inadequate for small-scale ice applications. Both AVHRR and SSM/I have the advantage of having been operated almost continuously for several years. SAR which has been obtainable from ERS-1 since 1991 has the advantages of high resolution and all weather

operation, demonstrating the opportunity of navigation in ice infested waters. Currently, the main disadvantage of SAR is its limited spatial and temporal coverage, particularly given the dynamic nature of sea ice. By combining information derived from each of these sensors the SIWS can take advantage of the strengths of the individual sensors whilst overcoming the inherent weakness of being dependent on a single sensor.

Selection of the algorithms for inclusion into the SIWS was based on a review of user requirements and an understanding of what could currently be successfully achieved. A brief description of each of the geophysical processing algorithms is given below.

SAR Ice Concentration and Ice Edge

The key stage in calculating the ice concentration is the classification of each pixel within the SAR image into ice or water. This discrimination is complicated by factors such as fact that wind roughened and multi-year ice both appear bright in the image, the inherent speckle within the SAR image, and the multiplicity of surface types within a small area. This problem has stimulated many attempts at algorithms (e.g. Kwok et al, 1992, Drinkwater et al, 1992) but there is no accepted approach to the problem and it is still the subject of current research.

The SIWS algorithm was based on the result of new research undertaken for the project. The algorithm works in two stages. In the first stage texture measures are derived from small image blocks (i.e. small areas of the image). Cluster analysis using either a discrete or fuzzy approach, selected using the algorithm control parameters, is then applied to the derived texture measures. From the cluster analysis the water cluster is identified from its characteristic size and shape. The second stage projects the classified blocks onto the high resolution homogeneous regions in the image obtained from segmentation of the original image. In the case of fuzzy classification the final water class membership is controlled by a 'confidence threshold' which sets the minimum class membership value.

From the classified ice/water image ice concentrations can be calculated using spatial statistics and the ice edge derived from the user selected isoline.

SAR Ice Classification

The ice classification algorithm discriminates between first-year and multi-year ice within the overall ice cover. While there are large number of possible sub-classes of ice, the most important distinction is between first-year and multi-year ice since the hazard caused by the multi-year to shipping and off-shore installations is usually much greater.

The ice classification algorithm is an extension to the previously discussed ice concentration algorithm. Having classified the image into ice and water, ice pixels are sub-divided into multi-year and first-year ice on the basis of mean backscattering intensity; multi-year ice generally appearing much brighter in SAR

images because of its roughness.

Figure 2 shows the way in which the algorithm can discriminate water from ice even though some areas are relatively smooth. This is an ERS-1 SAR image of the area north west of Svalbard from March 1993.

SAR Ice Motion

Ice motion is obtained by determining the displacement between discernible ice floes in a pair of SAR images. The algorithm used is based on that of Fily and Rothrock, 1987. The algorithm works by matching features initially on a very low resolution image pair. The positions of the matches are refined in series of steps using data of successively higher resolution. Modifications to the algorithm for the SIWS have been based on the experience of the consortium members and include an option for matching features which have undergone rotation and a series of quality control measures to remove erroneous matches. The ice motion algorithm output are displacements per day on a 5 km grid.

SSM/I Ice Classification

This algorithm is based on the NASA Team Algorithm (Cavalieri, 1992). The percentages of open water, first-year and multi-year ice are calculated for each pixel in the SSM/I image from the 19 and 37 GHz channels. By assuming that the total surface component of the brightness temperature for each pixel is composed of contributions from each of the three pure surface types the relative contributions of each are determined.

AVHRR SST

The AVHRR SST algorithm processing is in two stages; image classification to detect cloudy pixels and exclude them from further processing followed by the calculation of sea surface temperature based on the brightness temperatures in channels 4 and 5. Pixel classification can be performed using either the method of Burns et al, 1992 or Muirhead, 1989. The calculation of sea surface temperature is based on a set of simple coefficients which are user selectable.

4. VALIDATION

Successful exploitation of the SIWS and similar systems can only be achieved by validating the results of the algorithms against independent data. The method adopted for validation of the individual algorithms was dependent on the algorithm heritage, more emphasis being placed on the new ice classification and ice edge algorithms as opposed to the widely used algorithms which have already undergone extensive validation. Assessment of the algorithms was carried out by members of the consortium not involved directly in the algorithm development and ranged from expert quantitative assessment to comparison with results obtained from other sources.

Independent datasets were available from a cruise of the German icebreaker Polarstern to the Greenland Sea in the spring of 1993. During the cruise helicopter photography of the ice and water conditions was collected. Detailed manual classification of the geolocated photography provided a good basis from which to compare the automatically classified images from the workstation. In addition the SAR images were also manually classified by expert glaciologists from SPRI. Using these two techniques a dataset of over 51,000 classified pixels was achieved from a wide range of locations and seasons. The comparisons with the results of the automatic algorithm were presented in the form of confusion matrices.

The overall conclusion of the ice classification validation was that the automatic algorithm does an excellent job when the ice cover is largely represented by interior pack ice and the ice edge is not heavily influenced by waves. The classification accuracy was found to vary between 90 and 70 %.

5. END USER EVALUATIONS

The development and results from the SIWS has successfully demonstrated the feasibility of extracting sea ice information automatically from satellite data. Further assessment of the workstation is currently being pursued in the form of a series of end user evaluations which aim to explore the value of the system for mapping and monitoring sea ice.

The main purpose of the end user evaluations will be to independently assess the workstation in a semi-operational situation. Algorithm validation will cover a wider geographical area and provide additional statistics with which to evaluate the workstation. Comments regarding the ease of use of the system and appropriateness of the chart in providing ice information will be collated and used to help provide direction for future developments and applications for the SIWS.

The end users have been carefully selected to provide a good cross section of potential customers, and include national meteorological services, live shipping services and research institutions.

5. ACKNOWLEDGEMENTS

The work reported in this paper stems from contributions by many individuals within the project consortium including Shaun de Witt, Yong Li, George Simpson, Trevor Smith, Jon Styles, Mark Suscens, Simon Tackley and others at EOS. Contributions were also received from Eileen Aldworth, James Brownhill, Ian Davy, Tom Hirose, Seymour Laxton and Peter Wadham.

The work has been directed by Lesley Murphy and Mike Boswell of the DRA, with inputs also being received from the BNSC.

6. REFERENCES

Burns B A, M. Schmidt-Grottrup, T. Viehoff, 1992, Methods of Digital Analysis of AVHRR Sea Ice Images. *IEEE Transactions on Geoscience and Remote Sensing*, 30, 589-602.

Cavalieri D, 1992, NASA Sea Ice Validation Program for the Defence Meteorological Satellite Program Special Sensor Microwave Imager: Final Report, NASA Technical Memorandum Number 104559.

Drinkwater M.R., R. Kwok, E. Rignot, H. Israelsson, R. Onstott and D.P. Winebrenner, 1992, Potential applications of polarimetry to the classification of sea ice. In Carsey, F. (ed) *Microwave Remote Sensing of Sea Ice*, Americal Geophysical Union Monograph 68, 419-430.

Fily M and D A Rothrock, 1987, Sea ice tracking by nested correlations. *IEEE Transactions on Geoscience and Remote Sensing*, 25, 570-580.

Kwock R, G Cunningham and B Holt, 1992, An approach to identification of sea ice types from spaceborne SAR data. In Carsey, F. (ed) *Microwave Remote Sensing of Sea Ice*, Americal Geophysical Union Monograph, 68, 355-360.

Muirhead K, 1989, Automatic classification of AVHRR images in 4th AVHRR User Meeting.

Steffan K and 11 co-authors, 1993, Snow and ice applications of AVHRR in polar regions: report of a workshop held in Boulder, Colarado, 20 May 1992. *Annals of Glaciology*, 17, 1-16.

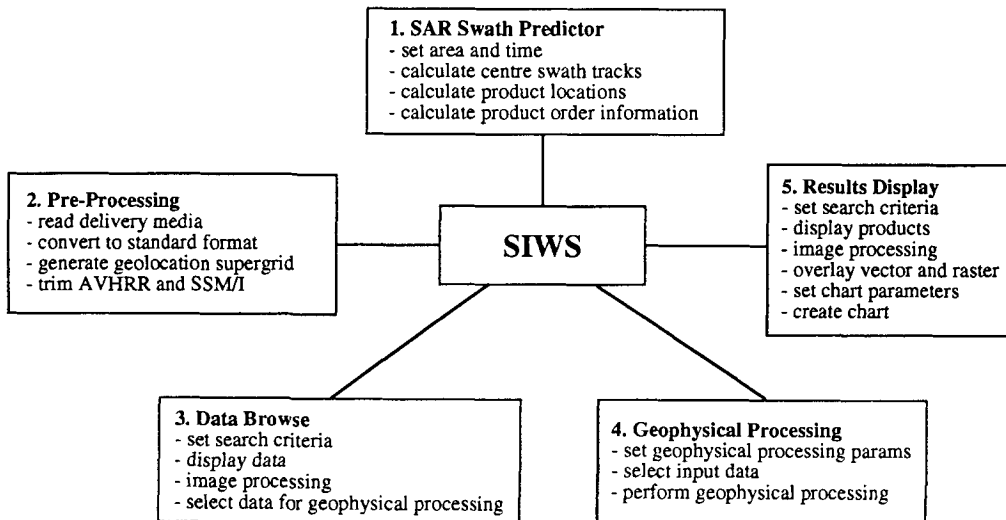


Figure 1: Functional Overview of SIWS

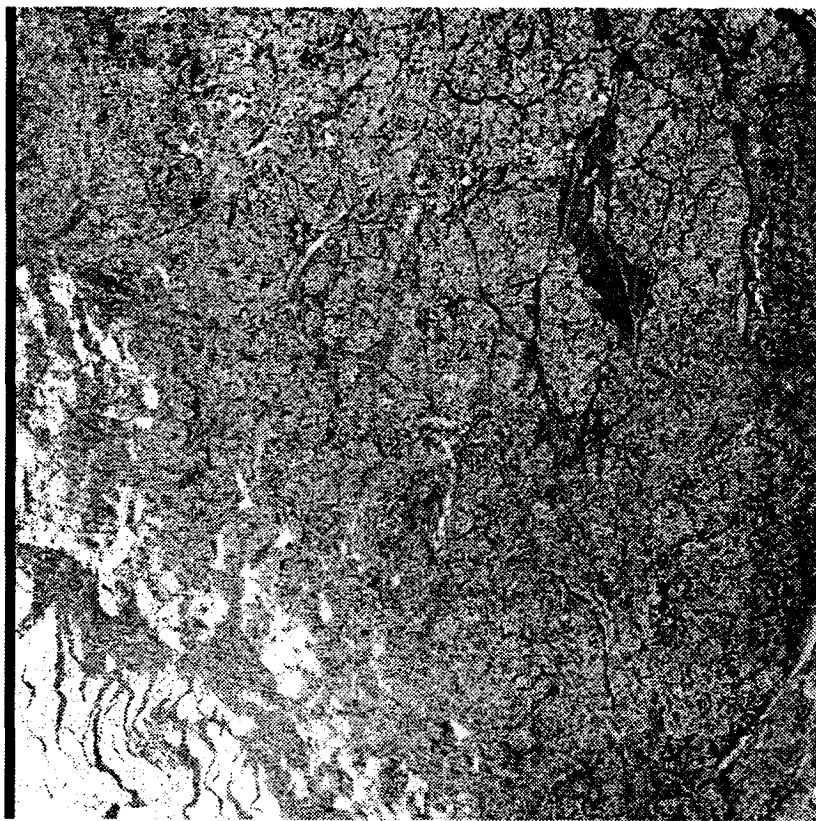


Figure 2a. ERS-1 SAR Image from NW Svalbard,
March 1993. Copyright ESA.

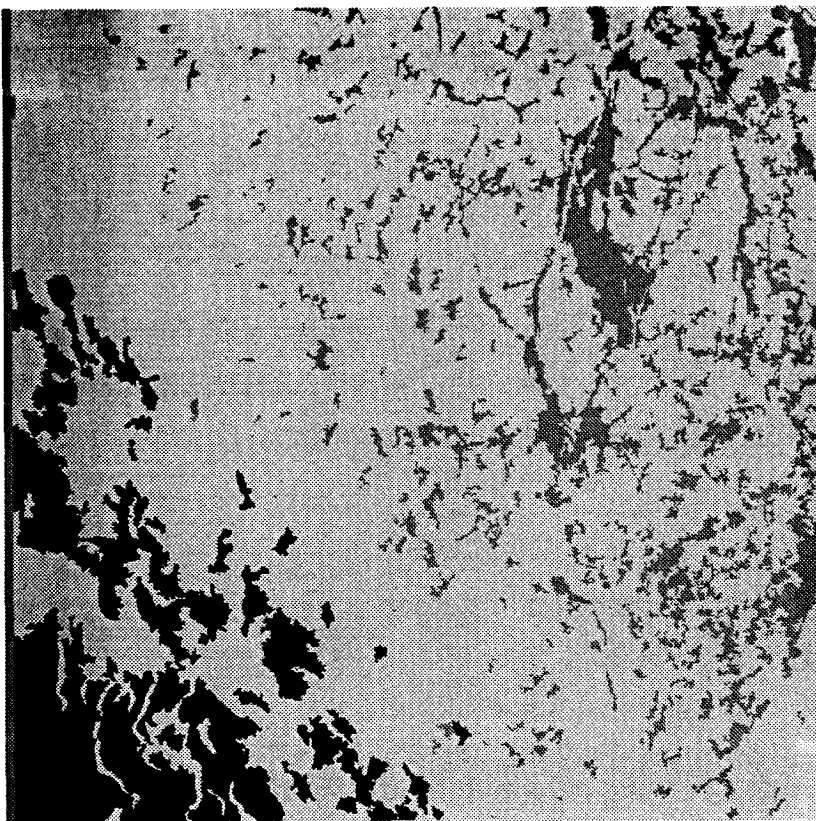


Figure 2b. Classified image in which black is water,
dark grey first-year ice and light grey multi-year ice.

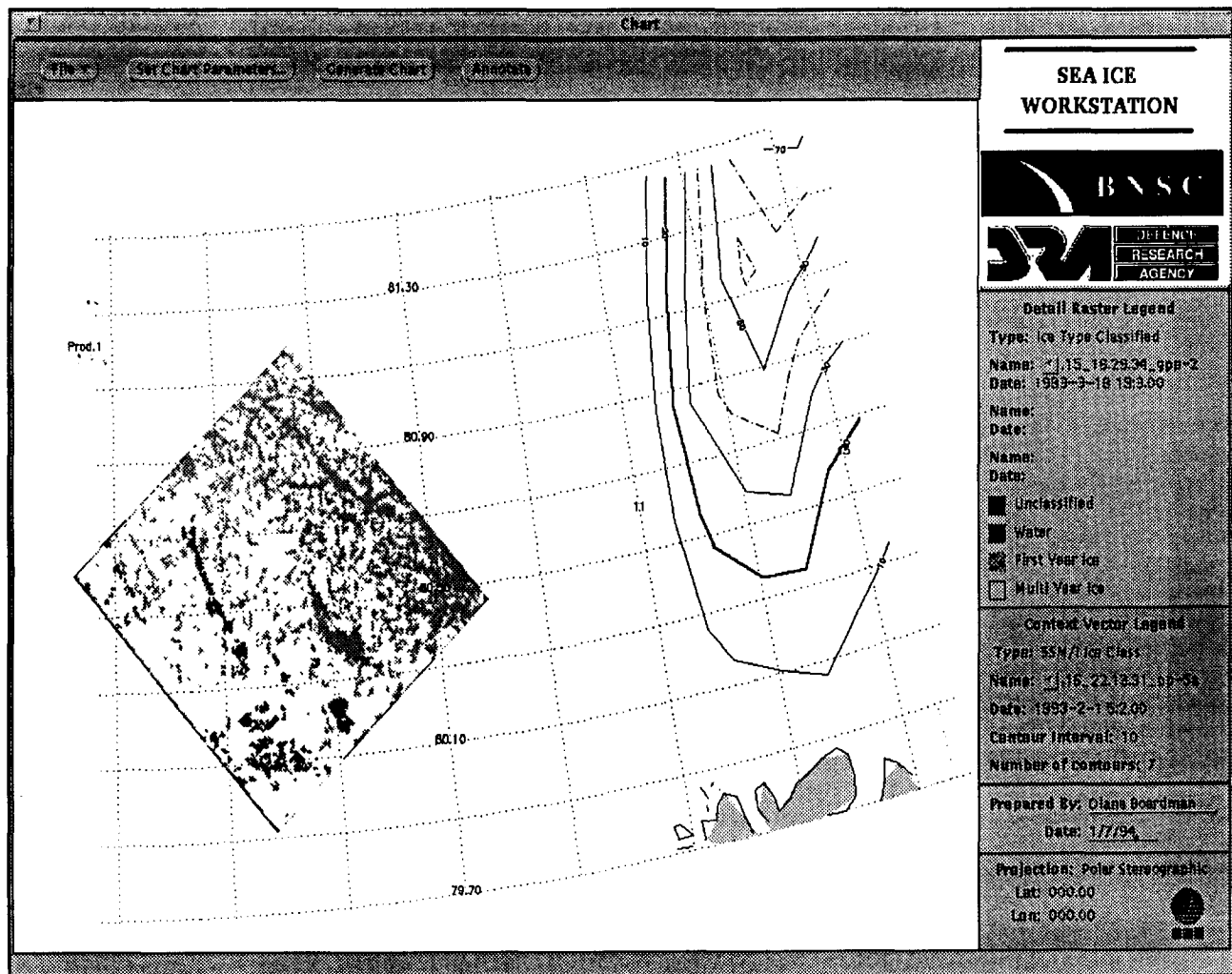


Figure 3. An example of an ice chart from the NW of Svalbard output by the SIWS. A raster plot for extracted parameters has been derived from a classified ERS-1 SAR scene in the central area and overlaid on a vector representation of ice concentration isolines derived from SSM/I data. The result is shown in Polar Stereographic projection with a legend.

TOWARDS A BETTER UTILIZATION OF SAR DATA IN SEA ICE MONITORING

Mohammed E. Shokr

Atmospheric Environment Service
4905 Dufferin Street
Downsview, Ontario, Canada
M3H 5T4
Tel: (416) 739 4906
Fax: (416) 739 4221

ABSTRACT

ERS-1 SAR images have been used to monitor sea ice in the Canadian east coast and the Gulf of St. Lawrence since December 1992. Based on visual image interpretation, ice parameters of operational relevance are determined. Some parameters are more viable to analysis than others. Examples are presented to demonstrate the strengths and weaknesses of SAR images in terms of their information contents and amenability to ice parameter retrieval. Limitations on data utilization are explained and related to sensor parameters. Recommendations to improve data utilization in operational programs are proposed.

Keywords: SAR, ERS-1, sea ice, ice monitoring.

1. INTRODUCTION

The Ice Centre Environment Canada undertakes a major operational program to provide information on sea ice, lake ice and icebergs in the Canadian navigable waters. The information is extracted from several remote sensing data sources including an airborne SAR (X-band HH polarization), an airborne SLAR (also X-band HH polarization), NOAA-AVHRR, and the passive microwave SSM/I. The information is compiled into a standard Ice Analysis Chart, which is a daily integrated view of synoptic scale ice conditions. Charts are transmitted by HF marine radio facsimile to clients such as the Canadian Coast Guard (CCG), commercial shipping, offshore oil and gas industry, and fishery ships. An overview of the program is included in Ref. 1.

Since December 1992, ERS-1 SAR images have been used as a supplementary data set to monitor ice conditions in Labrador Sea, Gulf of St. Lawrence and the Canadian Arctic region. Data reception, analysis, and products are described briefly in Ref. 2. SAR images are processed into Georeferenced Coarse Resolution images (8-bit, 100m ground resolution in both range and

azimuth, at 96 effective looks). The analysis is conducted visually by trained operators (ice analysts) to extract information on total ice concentration, ice types and concentration per type from delineated areas in the image.

In addition to the operational procedures, limited research activities were conducted to understand the data and to explore their limitations. The activities include: (1) comparison of images of the same scene acquired by ERS-1 and an airborne SAR operates in X-band HH polarization (for more details about that sensor see Ref. 1). (2) compilation of backscatter ice signature library, (3) validation of ice types and features in images through field observations, and (4) development of a techniques to evaluate the accuracy of manual estimates of ice types and concentrations. The operational procedures are addressed in Ref. 2, while results from the above-mentioned research activities are presented in this paper. An insight into data utilization and improvement as related to SAR parameters is also presented.

2. RESULTS AND DISCUSSIONS

The comparison between ERS-1 and STAR-2 images has provided clues on interpretation of ERS-1 images and on the nature of radar backscatter as related to ERS-1 SAR parameters. An example is shown in Fig. 1. The images were acquired on March 8, 1993 from the Gulf of St. Lawrence. Both images are resampled into 200m pixel spacing. Discrimination between rough water and new ice is more feasible in ERS-1 image as demonstrated in zone #1 where dark batches represent newly-formed ice. It is also evident from the ERS-1 image that zone #2 is mostly ice-covered; a conclusion which is not quite evident from the STAR-2 image. In fact, the relatively bright signature from that zone in the ERS-1 image indicates that the ice type is "grey", with thickness between 10 to 15 cm. An interesting observation is the suppression of small-scale floe structure in the ERS-1 image in zone 3. The apparent texture

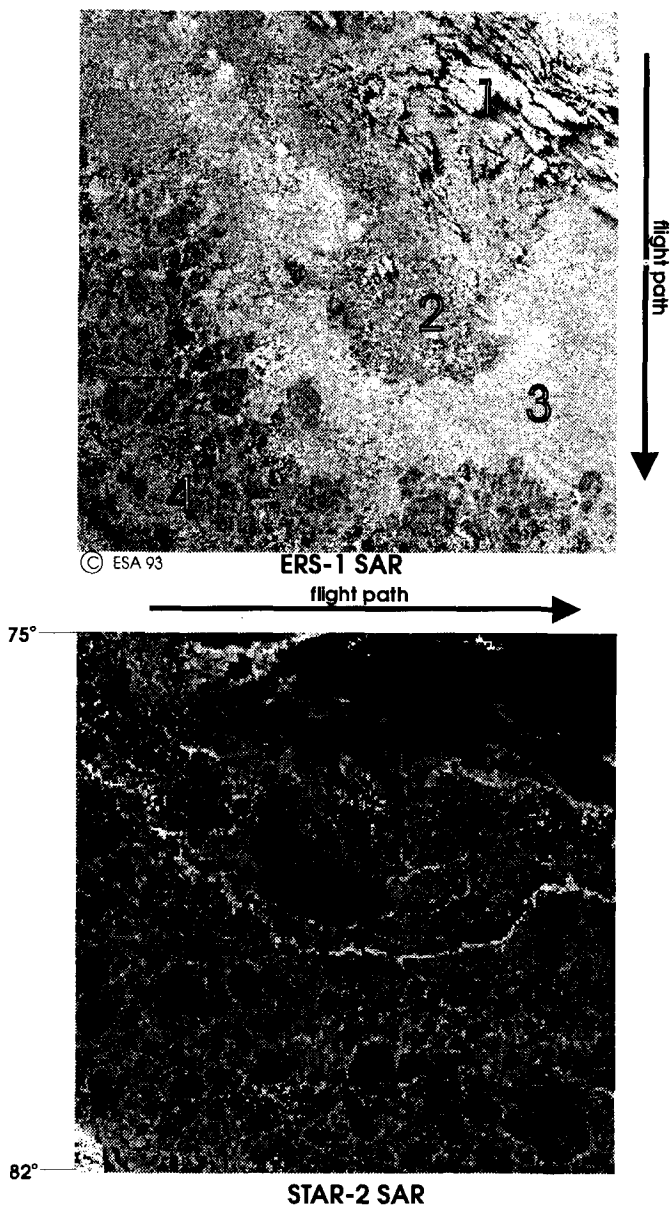


Fig. 1 Comparison between ERS-1 and STAR-2 images of a scene from the Gulf of St. Lawrence, acquired on March 8 1993.

in that zone in the STAR-2 image is replaced by a uniform bright tone in the ERS-1 image. The tone is most likely engendered by surface scattering. Only large-scale floes are identifiable in ERS-1 image (zone #4). Perhaps the most striking observation is the disappearance of the ridge (the bright line in the STAR-2 image) in ERS-1 image. Failure of ERS-1 SAR to capture surface structural features is generally true of all the images examined during this project.

Ice surface structure arises in radar images as a result of the contrast between low backscatter from smooth floes and relatively high backscatter from rough ice interspersed between floes. The steep incidence angle of ERS-1 SAR causes an increase in backscatter from smooth surfaces and

therefore abates that contrast. To the best of our knowledge, data on angular dependence of backscatter for various rough ice surfaces are not available in the literature. However, a qualitative illustration is shown in Fig. 2 (adopted from Ref. 3) to explain the above premise. At relatively small incidence angles, the backscatter is insensitive to the degree of roughness (the range where curves intersect in the figure). At higher incidence angles, a better discrimination between surfaces of different roughness can be achieved.

The 100km swath of ERS-1 SAR is too narrow to be operationally useful. In the 3-day repeat cycle orbit, the satellite coverage became very limited in the Gulf of St. Lawrence region as shown in Fig. 3. A minimum of 400km swath is required for daily coverage of the Gulf region. Daily coverage is crucial in dynamic ice fields such as marginal ice zones or ice production regions at southern latitudes. Figure 4 shows 2 images of the same area from the 3-day repeat cycle where conditions at the lee side of the shown island changed from open water on January 20 to young and first-year ice drifted from the main pack as a result of reversed wind on January 23, 1994. The openings in the ice pack (the bright features) which are visible in the January 20 image became frozen on January 23 due to a drop of atmospheric temperature to -8°C. The multi-temporal capability from the 3-day repeat orbit was not quite useful in this application. A maximum temporal resolution (repeat coverage) of 1 day is required.

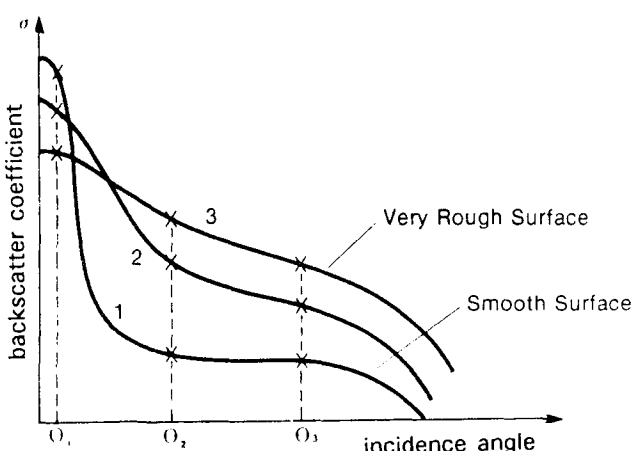


Fig. 2 A qualitative illustration of angular dependence of radar backscatter from surfaces of different roughness (adopted from Ref.4)

For the operational use, SAR images are analyzed manually by trained operators. The analysis aims at determining total ice concentration, classification, and concentration per type. A

quantitative technique has been developed to evaluate the accuracy of the manual estimates and to assess ice types in terms of their potentiality for successful identification. A very brief description of the technique is included in Ref. 4 (full description is the subject for a future publication). Preliminary results indicate that the New ice type, less than 10 cm thickness, is the most difficult ice to identify. The reason is the continuous growth of the surface layer, driven by atmospheric conditions, which gives rise to significant changes of ice physical and electrical properties that modulates the observed backscatter. Backscatter can be modulated in this case also by presence of frost flowers on ice surface. These factors result in a wide variety of signatures from New ice. The present observations agree with a conclusion in Ref. 5 that backscatter from thin ice forms is very complicated.

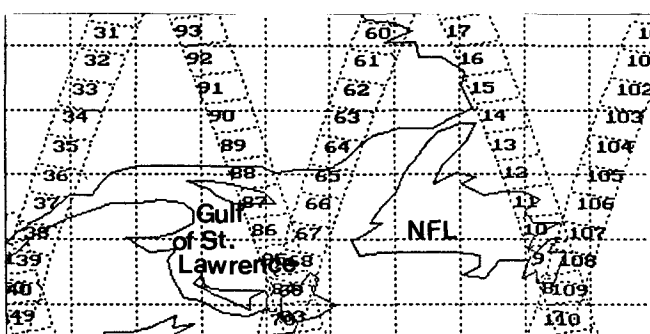


Fig. 3 ERS-1 SAR coverage of the Gulf of St. Lawrence during the second Ice Orbit, showing the limited areal coverage.

3. REFLECTIONS ON SAR USE FOR OPERATIONAL ICE MONITORING

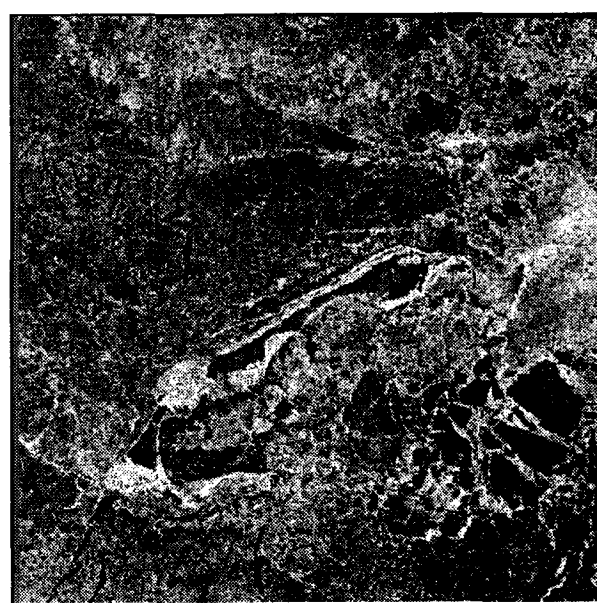
A single-channel SAR has traditionally been used in ice monitoring. From the airborne STAR-2 or the satellite-borne ERS-1 SAR, images are converted into a standard ice chart product which comprises information on ice types and concentrations in addition to gross description of surface topography (pancake, heavy ridges, .. etc.). However, from the marine operations' viewpoint, three ice parameters are essential: thickness, mechanical strength and degree of ridging. The feasibility of estimating these parameters from SAR depends on their role in determining the observed backscatter. Backscatter is mainly driven by surface roughness and electrical and physical properties of the sub-surface layer through which radar energy penetrates. Therefore, surface roughness (or ridging) is relatively easy to extract provided that appropriate incidence and viewing angles are used.

Ice thickness is not readily extractable but can be roughly estimated once ice type is identified. Ice type can be identified visually (by trained operators) using image attributes such as tone and texture in addition to ancillary information including contextual (e.g. new ice adjacent to water), historical (e.g. ice conditions detected in previous days), climatological (expected ice types according to historical records) and meteorological (wind and atmospheric temperature). Computer-



© ESA 94

Fig. 4 ERS-1 images from the Gulf of St. Lawrence showing the difference in ice conditions within a 3-day period. Images were acquired on Jan. 20, 94 (left) and Jan. 23, 94 (right).



© ESA 94

assisted techniques are also used to classify ice types based on empirical equations or look-up tables that relate ice types to backscatter or image tone. This approach, though pragmatic, has proven to be of limited use since the established empirical relationships do not define ice types uniquely especially in presence of wet snow and other ice-age-independent factors which contribute significantly to backscatter. Nevertheless, there is no alternative for using ice type as a proxy indicator for thickness since the penetration depth of microwave energy is limited to the first few centimetres in saline ice cover.

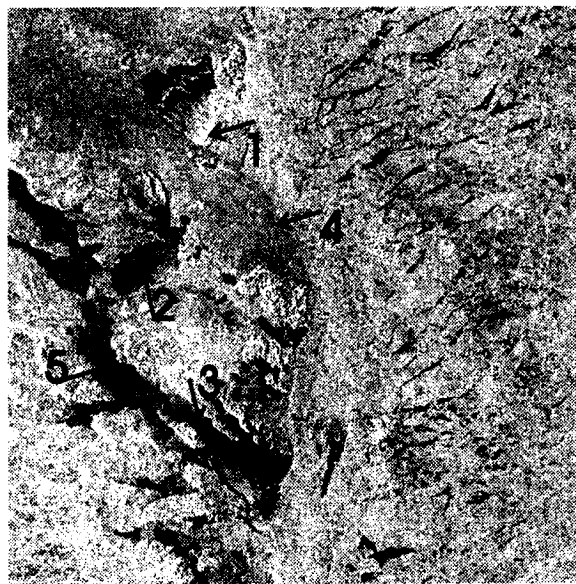
Retrieval of ice mechanical strength has not been fully investigated, perhaps because of its complexity. Mechanical strength is mainly a function of the bulk brine volume and the average size and spatial distribution of brine pockets within the ice thickness. Again, since microwave penetration is limited to the top few centimetres layer, mechanical strength can be retrieved only on the assumption that brine and crystalline ice properties in that layer are proxy indicators of corresponding properties throughout the ice thickness. The validity of this assumption is subject to study at this time. Unlike ice type, retrieval of mechanical strength requires a microwave scattering inverse modelling approach. Some images demonstrate well-delineated patterns of grey tone as shown in Fig. 5. At this time we cannot relate this information to ice properties, age or growth history. The apparent eddy-like pattern might be related to some sort of oceanic feature which determined ice boundaries



Fig. 5 A scene from Labrador Sea, acquired on Jan. 27, 94, showing eddy-like patterns of grey tone distribution. Can this information be interpreted in terms of ice properties or oceanic features?

during early ice growth. The challenging question is: what do grey tone represent in terms of surface roughness and/or volume properties? In other words, can we interpret the different tonal signatures as differences in dielectric constant, brine contents, and consequently ice mechanical strength? We are planning to use ERS-2 SAR data, among other approaches, to address this question.

The traditional use of single-channel SAR has limited the applications into extraction of gross information using field-established /or -verified empirical relationships. In order to convert SAR data into meaningful geophysical parameters, a microwave modelling approach which uses multi-channel data is required. With multi-channel SAR data, factors that contribute to the observed backscatter can be resolved. Examples showing effects of some of those factors are presented in Fig. 6. The image was acquired during a field experiment in Labrador Sea in March 94. The very bright tone in region #1 is caused by highly-structured pancake ice of approximately 12 cm thickness (i.e. grey ice type). This tone is not representative of that ice thickness and can be



© ESA 94

Fig. 6 A scene from Labrador Sea, acquired on March 7, 1994. Signatures in regions #1 and #2 are driven by highly-structured pancake and wet snow cover respectively. The boundary in region #3 separates fast ice (top) and new ice (bottom).

misinterpreted to represent very rough first-year ice or water. The tonal signature in region #2 was driven by wet snow of which a very high dielectric

The boundary marked with arrow #3 separates fast ice (grey signature in region #5) and new ice (dark signature at the bottom of the boundary). No apparent difference in surface roughness was observed between the two ice types. Hence the difference between the two signatures reflect a difference in volume properties. The boundary marked with arrow #4 divides two regions of first-year ice with different growth history: at the right side there is older ice with rougher surface and more fractures (re-frozen openings), and at the left side there is newer and smoother ice. These examples show the importance of using contextual information in image interpretation.

4. CONCLUSIONS AND RECOMMENDATIONS

ERS-1 SAR images have been used as an input in the Canadian sea ice monitoring program. Image interpretation has advanced and verified through comparison with coincident images acquired with an airborne X-band HH polarization SAR. Roles for interpretation have been developed. Detailed interpretation and conversion of image information into meaningful operational ice properties are still lagging.

Operational parameters are identified and related qualitatively to backscatter driving parameters in order to explore potentials and limitations of SAR data for operational use. Surface roughness is relatively easy to extract although the steep incidence angle of ERS-1 SAR has degraded the identification of ridges and floe boundaries. Ice type may be identified using the observed backscatter against an established empirical equation or a lookup table that relates backscatter to ice types. However, due to the diversity of the factors that affect microwave scattering, this approach may not lead to accurate ice type definition. Ancillary information on previous ice records, number of freezing days, atmospheric conditions, ..etc. is usually incorporated by ice analysts to support a decision on ice type. Ice thickness is usually inferred from ice type. An inverse microwave modelling approach, using multi-parameter SAR, should be used to convert

the observed backscatter into ice mechanical properties. Multi-parameter SAR will also be useful in resolving the factor(s) that dominates backscatter.

Analysis of ERS-1 SAR images have contributed to the long-term observation process needed to develop better use of SAR data. The next phase of investigation, using data from ERS-2 satellite and beyond, should be accompanied with more systematic and detailed *in-situ* measurements and a substantial microwave scattering modelling effort.

ACKNOWLEDGEMENT

The author wishes to acknowledge the contribution of Mr. Mike Manore of Canada Centre for Remote Sensing in interpreting SAR images acquired during the field experiment. Mr. Frankie Tsang prepared the images and graphs of this paper.

REFERENCES

1. Falkingham, J.C. 1991, Operational remote Sensing of sea ice, Arctic, Vol.14, pp. 29-31.
2. Ramsay,B.R. and J.C. Falkingham, 1994, Real-time use of ERS-1 SAR images in the Canadian Sea Ice Program: 3 years of experience, Procs. of the First ERS-1 Pilot Project Workshop, (this issue).
3. Elachi,C., 1988, Spaceborne radar remote sensing: applications and techniques, IEEE Press, New York, p.22
4. Shokr, M.E., B.R. Ramsay and J.C. Falkingham, 1994, Operational use of ERS-1 SAR data to monitor ice conditions in the Gulf of St. Lawrence, Procs. of the Second ERS-1 Symp., ESA SP-361, Vol.1, pp. 663-668.
5. Askne,J., L.M.H. Ulander, A. Carlstrom, Y. Sun and M. Patterson, 1994, Validation of ERS-1 SAR for Arctic ice properties from ARCTIC-91, Procs. of the Second ERS-1 Symp., ESA SP-361, Vol.1, pp. 257-262.



THE POTENTIAL ROLE OF ERS-1 SCATTEROMETER DATA IN SUPPORT OF ICE NAVIGATION

R. O. Ramseier¹, I. Arnon², R. Ezraty³, C. Garrity⁴, F. Gohin³, K. Strübing⁵

¹Atmospheric Environment Service, Ice Operations Research Group, P.O.Box 100, 195 Westbrook Road, Stittsville, Ontario K2S 1A2, Canada, Tel 1 613 832 0504, Fax 1 613 832 0505

²Atlantis Scientific Systems Group, 1827 Woodward Drive, Ottawa, Ontario K2C 0P9, Canada, Tel 1 613 727 1087, Fax 1 613 727 5853

³Institut Français de Recherche pour l'Exploitation de la Mer, B.P.70, 29280 Plouzané, France, Tel 33 98 22 42 99 ,Fax 33 98 22 45 33

⁴Microwave Group-Ottawa River, 3954 Armitage Ave., RR#1, Dunrobin, Ontario, K0A 1T0, Canada, Tel 1 613 832 0411, Fax 1 613 832 0505

⁵Bundesamt für Seeschiffahrt und Hydrographie, Bernhard-Nocht-Straße 78, Postfach 30 12 20, D-20305 Hamburg, Germany, Tel 49 40 3190 3220, Fax 49 40 3190 5032.

ABSTRACT

Ice information in support of navigation covers essentially any knowledge about ice conditions which might be useful to the master of the ship to decide which route to take and how to navigate around large ice floes. Satellite based sensors, primarily the ones operating in the microwave region of the frequency spectrum, can provide this information day and night and under most weather conditions. To date, passive microwave brightness temperature data originating from sensors such as the Special Sensor Microwave/Imager, are reasonably well understood, and can with suitable algorithms, be presented as useable ice information products, such as ice concentration and extent. The scatterometer backscatter coefficient σ^0 has the potential of being a useful parameter to describe the surface conditions of an ice cover, in particular to provide a roughness index. Combined with the passive microwave data, these two complementary data sets can contribute better information on ice type and surface conditions which in return permits a better basis for route selection. This paper focuses on the use of scatterometer and passive microwave data and surface measurements made with the German RV "Polarstern" during its winter cruise in the Weddell Sea, June-July 1992.

Keywords: Sea ice, ERS-1 Scatterometer, SSM/I, Ice navigation

1. INTRODUCTION

Ice information in support of navigation covers essentially any knowledge about ice conditions which might be useful to the master of the ship to decide which route to take and how to navigate around large ice floes. In general the route selection is based on a regional overview of ice edge position, ice concentration and types of ice present. Additional information on the state of the ice cover such as roughness, melt conditions, flooding at the snow-ice interface and amount of snow on the ice are also very useful in deciding which route to select. This type of ice information is known as strategic ice information. Often this type of ice information can also be used successfully in support of tactical decisions. Satellite based sensors, primarily the ones operating in the microwave region of the frequency spectrum, can provide this information day and night and under most weather conditions. Visible imagery, although very useful in support of navigation, is limited to nearly cloud free conditions. To date, passive microwave brightness temperature data originating from sensors such as the SSM/I (Special Sensor Microwave/Imager), are reasonably well understood, and can with suitable algorithms, be presented as useable ice information products, such as ice concentration and extent charts. The scatterometer backscatter coefficient σ^0 has the potential of being a useful parameter to describe the surface conditions of an ice cover, in particular to provide a roughness index. Combined with the passive microwave data, these two complementary data sets can contribute better information on ice type and surface conditions which in return permits an improved basis for route selection. This paper focuses on the use of scatterometer data in combination with SSM/I data and surface measurements made with the German RV

"Polarstern" during its winter cruise in the Weddell Sea, June-July 1992. First we will focus on the ability of the scatterometer to detect the ice edge. Secondly we will focus on the interpretation of the scatterometer data based on the ice type observations made from the RV "Polarstern" during its southward and initial westward legs. Finally a discussion on the ship performance as it relates to a number of geophysical parameters opens the way to further work and the desired new ice surface conditions "index" in support of ice navigation.

2. METHODOLOGY

2.1 Recent Studies using ERS-1 Scatterometer Data

The use of ERS-1 scatterometer data for ice research is a rather novel approach. The first group to explore the possibilities to map ice extent using the ERS-1 scatterometer data was done by A. Cavanac et al., (Ref.1) as presented during the Munich ISY European Conference in 1992. They showed that it was possible to map the ice boundary and that the backscatter coefficient σ^0 varied within the ice cover. Comparing the forward beam with the aft beam showed that the ice signatures were isotropic as compared to the ocean signatures. Intercomparison of the ice edge, as derived from scatterometer data and passive microwave data (SSM/I), showed a surprisingly good agreement for the eastern part of the Weddell Sea, the area of study in this paper (Garrity et al., (Ref.2). Drinkwater et al., (Ref.3) enhanced the resolution of the ERS-1 scatterometer data from 50 km to 14 km by using weekly averages. This provided again an ice edge and dynamic features of the ice which could be traced with time. However, this resolution enhancement comes at a price. One important assumption is that the radar and surface characteristic of the ice cover remain constant during this weekly interval. During the ice growth period this is not the case. This paper concentrates on a better understanding of the ice signatures as related to σ^0 derived from single orbits and three to seven day averages of σ^0 .

2.2 Approach

For the analysis of the satellite and ship data, the North-South leg of the RV "Polarstern" was selected because both SSM/I and the ERS-1 scatterometer data were available. This covers the period from 12 June 1992 when the RV "Polarstern" encountered the ice edge at $60^\circ 56'S$ along the 0 degree meridian until 20 June when the ship got stuck in front of the Neumayer station. The ship got again underway on 28 June. For the rest of the leg, during the month of July, the German Antarctic Research Station at O'Higgins was in operation, collecting a large number of SAR passes. Due to this activity the scatterometer data becomes a very sparse data set for the remainder of the trip.

The σ^0 curves shown in Figure 1 (AES) represent an average of the backscatter coefficient obtained over the time period 11-13 June over an areas consisting of 100% first year ice concentration based on the SSM/I data for 12 June and open ocean. To obtain a better understanding of the

backscatter from different ice types and conditions a correction for the incidence angle effect, as shown in Figure 1, needs to be made. The

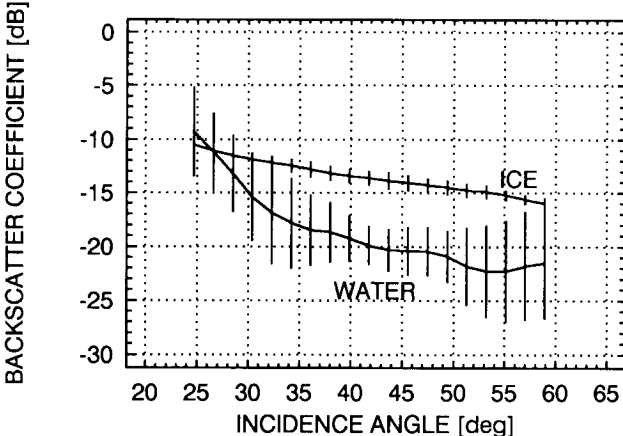


Figure 1. Scatterometer swath profile of fore beam antenna for ice and water from the Weddell Sea area.

difference of 5 dB from the near edge to the far edge of the 500 km swath shows a linear behaviour. The angle of normalization was chosen as cell one, or rather the incidence angle of the near edge swath which is about 25° for all fore and aft beam data.

The approach by IFREMER to correct for the incidence angle effect is somewhat different than the one by AES. IFREMER normalizes the level of backscatter at 50°. In addition, to derive a good discrimination between water and ice, the derivative (slope) of the backscatter water curve using a combination of all three beams at a normalized incidence angle of 28° is used (Ref.4). The result is a good definition of the ice edge as compared to the ice edge obtained through the use of the SSM/I data.

The IFREMER group data for the retrieval of actual incidence angles for different ice types and ice conditions were made as close as possible to the 0 meridian N-S line. The SSM/I data was processed as described by Ramseier et al..(Ref.5).

3. DATA SET

3.1 Ice Conditions Based on the SSM/I Ice Charts, Visual Observations and ERS-1 Scatterometer σ^0 Values

The SSM/I ice chart shown in Figure 2 is an example of the total ice concentration for June 12, 1992, 2023 UTC. The swath width of the SSM/I is about 1400 km with a resolution of about 33 km at 37 GHz and grid spacing of 25 km. The ship position at the time of crossing the ice edge is indicated on the ice chart. The RV "Polarstern" proceeded along the 0 degree meridian to about 69S where the ship started to head in a south-westerly direction towards Neumayer Station, located near 70.5S 8W. During this period (12 June-20June) the ice conditions changed significantly due to continuous new ice formation and growth. Of particular interest is the new ice formation in form of pancakes which commenced at the ice edge and were present until about 68S. From 68 to 69S the ice cover consisted primarily of first year (FY) ice followed by nilas and a FY ice mixture with the nilas being dominant.

Three examples are given in Figure 3. Figure 3a shows the backscatter for pancake ice (about -6.8 dB at 25 degree incidence angle) with some frazil ice mixed inbetween the pancakes for 12 June. Figure 3b shows the σ^0 for pancake ice inter-mixed with slush and some thin first year ice. Finally the pancake and frazil ice imaged on 12 June was again observed on 15 June as shown in Figure 3c.

3.2 Regional Overview Based on SSM/I and Scatterometer Data

Figure 4 provides a regional snapshot of SSM/I and ERS-1 scatterometer data along the ship track. The ice edge as retrieved from the SSM/I for 12 and 16 June are shown on the top of the figure. The black squares within the ice covered areas are due to resampling the data. The derived backscatter plots for the period 8-14 June and 15-21 June are based on the work by Gohin (Ref.4).

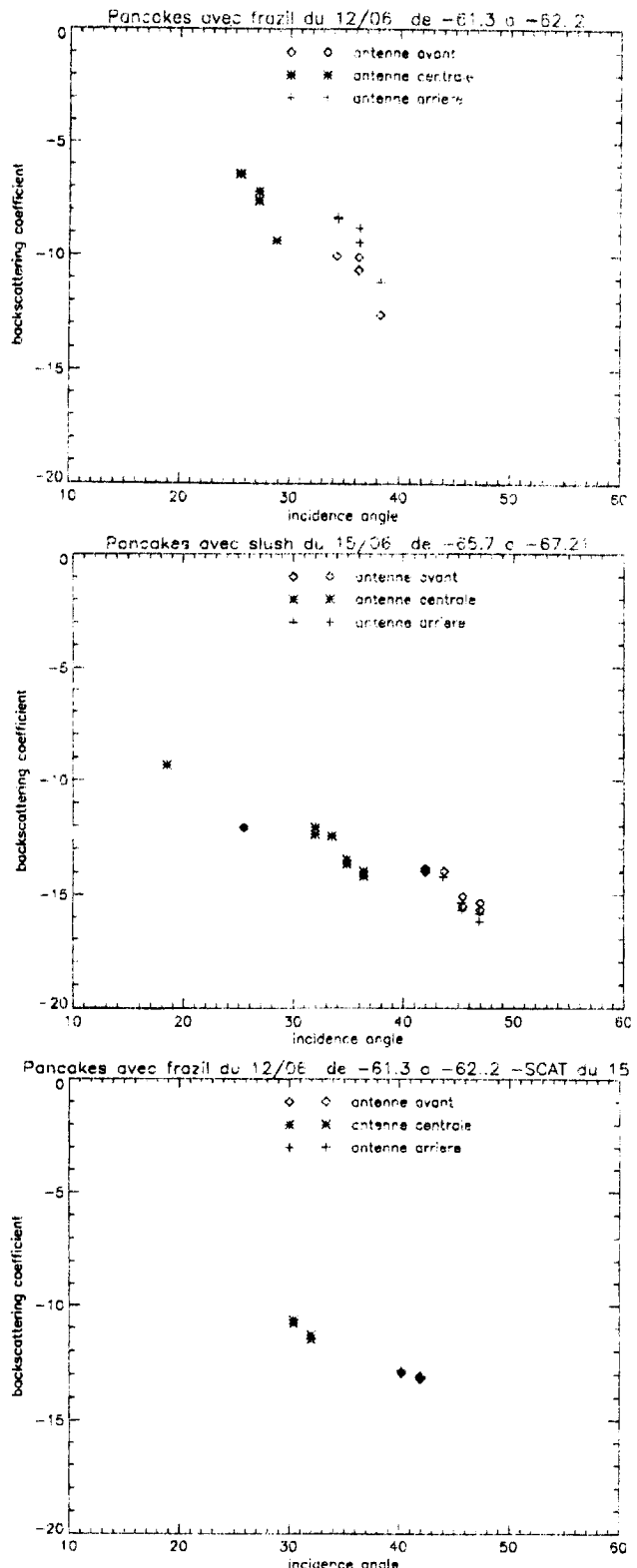


Figure 3. Scatterometer data for selected ice types along RV "Polarstern" route.

3.3 Profile Data Along the Ship Track

In Figure 5 all three plots show the ship speed and one specific parameter such as total ice concentration based on the SSM/I data, ice thickness as estimated visually from the bridge and the backscatter coefficient as a function of time in Julian days. Both the derived total ice concentration shows an inverse relationship, that is if the concentration increases the ship speed decreases and as the ice thickness increases so does the ship speed decrease. The correlation coefficient for total ice concentration based on the

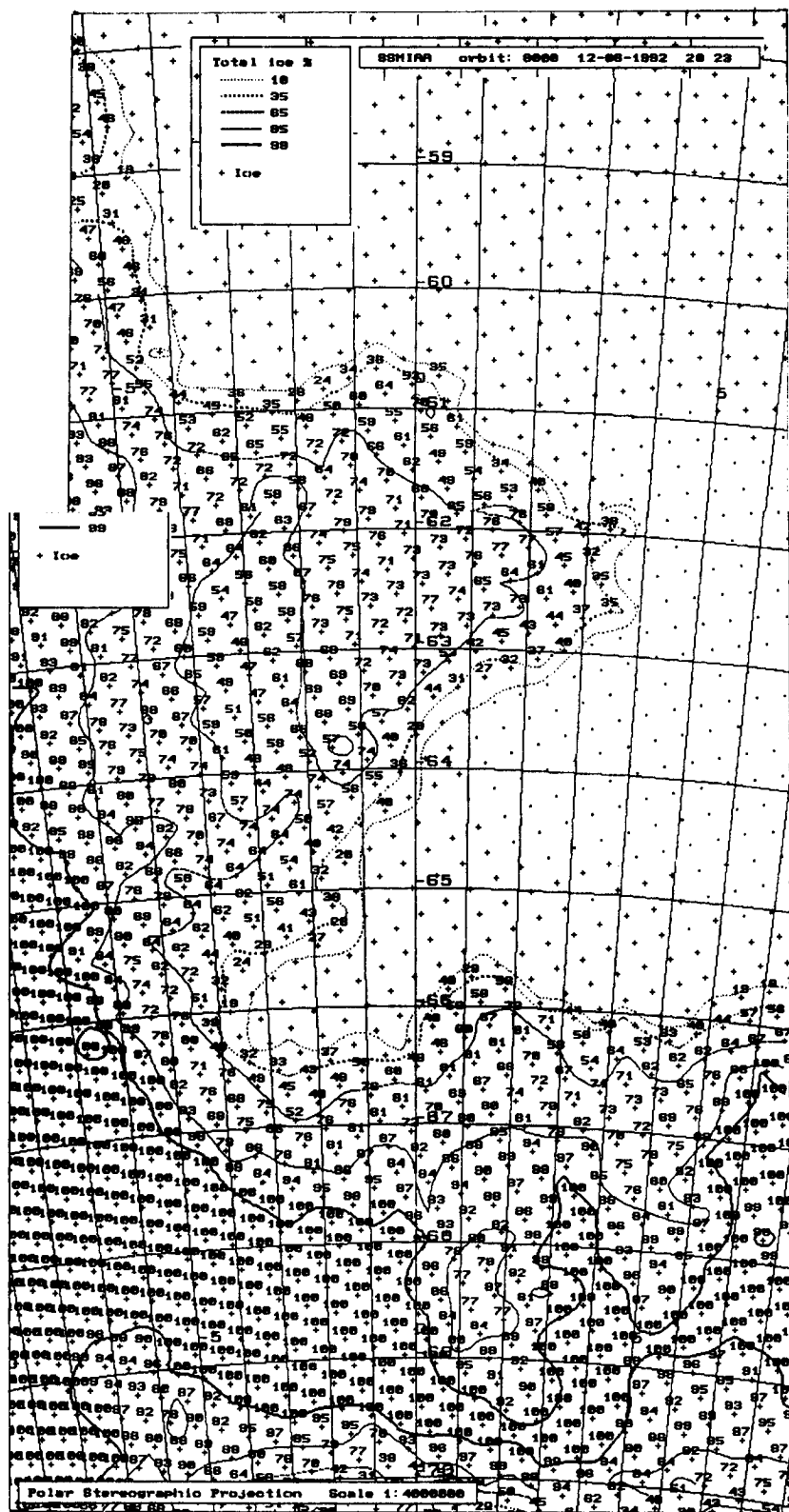


Figure 2. SSM/I derived ice information for orbit 8000, 12 June 1992, 2023 UTC, showing total ice concentration.

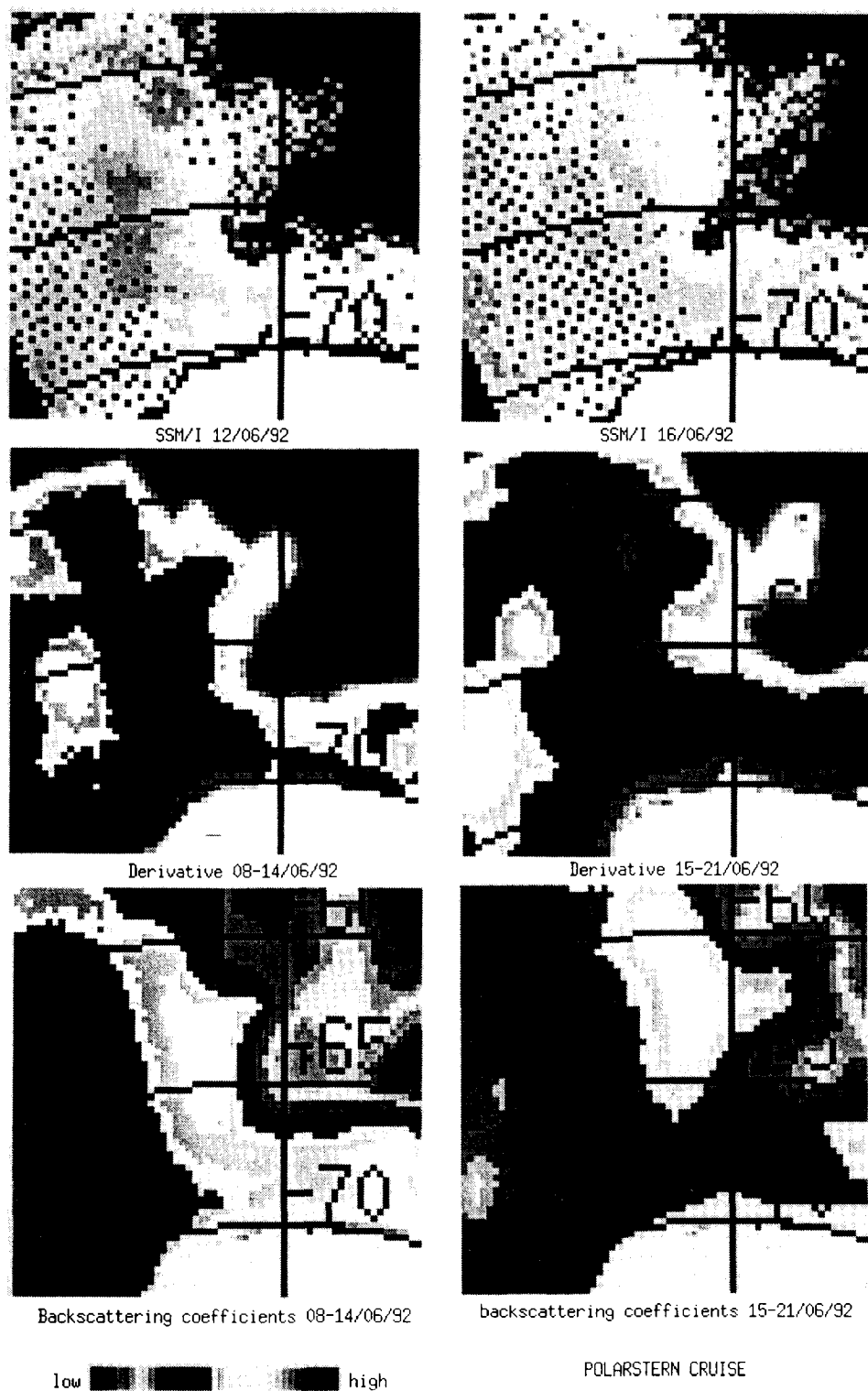


Figure 4. Regional snapshot of SSM/I and ERS-1 scatterometer data along ship track.

SSM/I data is -0.94 and for the ice thickness it is -0.91. The correlation coefficient for the backscatter is 0.21. These preliminary scatterometer results should be taken with some caution due to the fact that they represent two averages over several days.

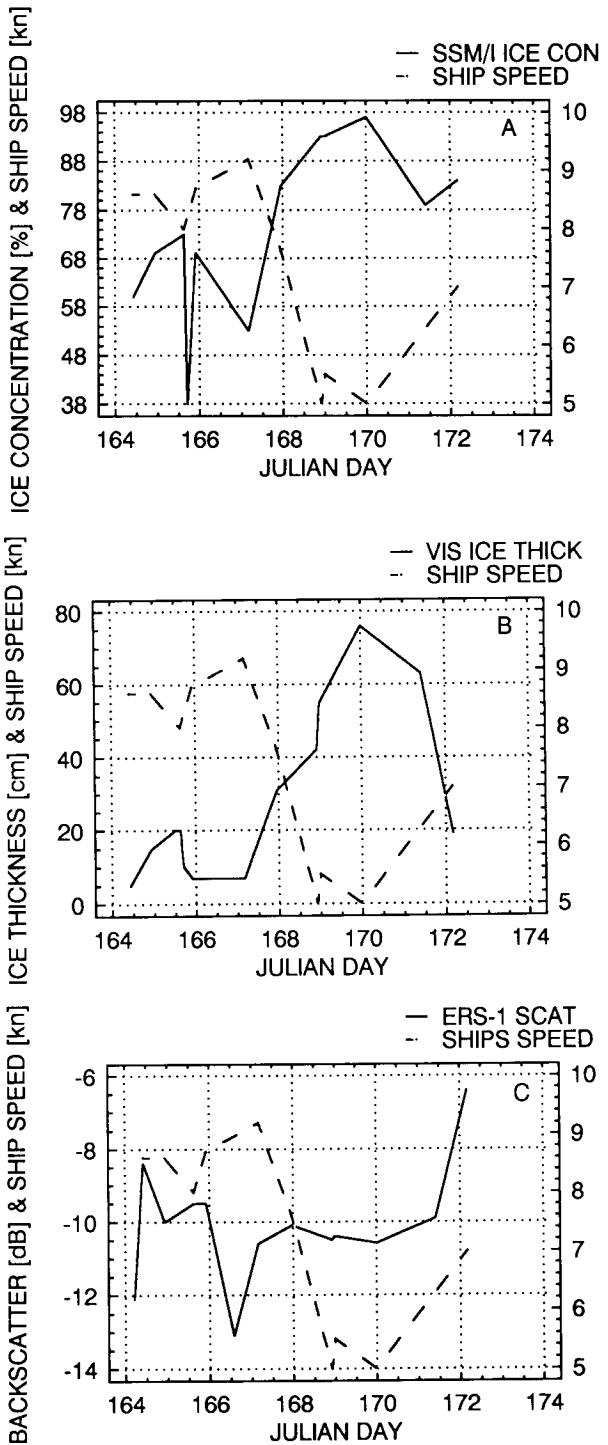


Figure 5. Ship speed as a function of a) total ice concentration, b) visual derived ice thickness, and c) ERS-1 scatterometer data normalized to an incidence angle of 25 degrees.

4. DISCUSSION OF RESULTS

4.1 Regional View

The SSM/I total ice concentration over the four day period as given in Figure 4 shows a significant increase in ice extent and concentration. This is possible due to the formation of new ice. The accuracy of the total ice concentration is of the order of 6% (Ref.6,7). It depends very much on ice type and algorithm used. The 6% value is consistent for first year ice while the new ice can have a negative bias for the total ice concentration of 5% (37GHz, vertical polarization). This was observed during this cruise by comparing ice concentrations derived from a ship mounted passive microwave radiometer for pancake ice and first year ice. For dark nilas this bias is 7%. A comparison between the Along Track Scanning Radiometer with Microwave Sounder (ATSR/M) data and the SSM/I data provide the same ice edge position as well as ice concentrations along the ATSR/M profile.

Comparisons of the ice edge position between the SSM/I derived ice edge and that of the scatterometer (Figure 4) provide good general agreement. For this study a complete set of SSM/I data were not available to provide a mean over the time period used for the scatterometer data. However, we feel that the results are very encouraging. For instance the development of the ice peninsula near the top center of the image is clearly observed for the passive microwave data over a four day interval. This is also reflected in the weekly average derivative images based on the ERS-1 scatterometer data. The bottom two images show the backscatter coefficients normalized to an incidence angle of 50 degrees. It is quite evident that the backscatter data alone does not provide a clear distinction between the ice edge and the open ocean. This can readily be understood by consulting Figure 1 which shows that the water backscatter curve crosses the ice curve. However one can observe significant changes in the backscatter values within the region of the ice peninsula as observed in Figure 4. The difficulty is to separate overlapping backscatter values associated with ice type, ice characteristics, and ice concentration effects as well as effects due to micro- and macro roughness.

4.2 Ship Track

The anisotropic behaviour of the pancake ice as observed in Figure 3a, that is, the difference in the backscatter between the fore and aft beams, is due to the presence of water. Over first year ice the backscatter values for the two beams are the same as seen in Figure 3b. Figure 3c shows the same area as Figure 4a, however the data is for 3 days later. It is interesting to note that in this case the difference in backscatter between the two beams has disappeared. Examining the SSM/I total ice concentrations indicate that for 12 June it was of the order of 72%, and on 14 June 86%. Visual observations (Ref.8) which provide a descriptions of the ice conditions indicate that the pancake ice was intermixed with frazil ice. Estimation of the total ice concentration, that is pancake ice and frazil ice, ranged between 75-100% with an average of 93%. Based on ship-board passive microwave measurements frazil ice has a very low brightness temperature and is very similar to water. They show about a 10 degree Kelvin increase above the water brightness temperature. Algorithms due not account for such small increases. Correcting the SSM/I data for the effect of the pancake ice would increase the total ice concentration to 77% and 91% (plus) respectively, leaving still 16% unaccounted for. One can assume that the 16% represents the frazil ice. One could argue that the visual ice concentration observations can not be correlated with the large coverage the SSM/I field of view provides. However, the great extend of new ice formation in this area of the Antarctic make this assumption invalid. This assumption seems to hold by examining the uniform distributions of ice concentration 65% contour line shown in Figure 2. This line extends along the 0 degree meridian from 61.6S to 63.3S. Taking the nearest neighbours of ice concentration values gives the 72% mentioned above. Two days later the concentration had increased to 91%. Adding the 5% for the bias of the pancake ice brings the total concentration to 96%. It is reasonable to assume that the concentration would have increased further on the third day. The frazil would have turned into slush with this increase in concentration. Therefore the results of the scatterometer backscatter values for 15 June (Figure 4c) showing no anisotropy are not surprising and the scatterometer data could provide a

possible link to determine ice concentration for a particular ice type (Ref.4).

In Figure 5 the major ice types are listed which were observed as the ship was travelling south. The order of ice type distribution are in decreasing order of fraction. The first group represent primarily pancake ice mixed with frazil with a relatively high ice concentration (72%) and a higher backscatter coefficient (-10dB) as compared to the second group which consists of pancake ice and slush with a somewhat lower concentration (50%) and lower backscatter coefficient (-11.7dB). The third group is a mixture of pancake ice, slush and first year ice. The ice concentration is higher (65%) while the backscatter coefficient is around -10.3dB. The fourth group consists mostly of first year ice with a very high ice concentration (90%) and a similar backscatter coefficient (-10.5dB) as the previous group. The last group is a mixture of nilas and first year ice and ice bergs. It is also closer to the continental shelf ice. The concentration is around 80% with a sharp increase in the backscatter coefficient to -7dB.

The small scale roughness sofar encountered should not really be an impediment to the ships nautical progress. One would expect that heavy ridging might be a more serious obstacle to the ships course progress than the relatively harmless pancake ice. Further analysis of the data will concentrate on daily averages to better correlate the scatterometer data with the ships data and will extent over the entire ships track through the Weddell Sea.

5. CONCLUSIONS AND FUTURE WORK

We were able to show backscattering results for different ice types due to the large distribution of pancake and first year ice.

There is a need to better understand the effect of backscatter as a function of ice concentration for a given ice type.

The use of the derivative of the water backscatter curve normalized to an incidence angle of 28 degrees is a key element for ice and water identification.

The backscatter values are consistent with values published in the literature.

The correlation of ship speed with ice thickness and concentration does not come as a surprise. However the high degree of correlation does, since we are using coarse resolution satellite data for the ice concentration.

The influence of the surface roughness on ship speed, as manifested through the backscatter coefficient, is not apparent with the limited data set used for this analysis.

This work is continuing with the analysis of the entire ship track through the Weddell Sea. Lack of ERS-1 scatterometer data due to the operation of O'Higgins ERS-1 SAR facility during the month of July, will severely limit the analysis.

The ERS-1 scatterometer geometry is compatible with the SSM/I.

6. ACKNOWLEDGEMENTS

The authors (CG and ROR) would like to acknowledge the invaluable support provided by the German RV "Polarstern", Alfred Wegener Institute for Polar and Marine Research, during its winter cruise of the Weddell Sea. The support given by B. Armour of Atlantis is well appreciated.

7. REFERENCES

1. Cavanie A., Gohin F. & Ezraty R. 1992, Ice Monitoring with ERS-1 Wind Scatterometer, Dept. d'Océanographie Spatiale IFREMER/Centre de Brest, France, Technical Note, pp. 10.
2. Ezraty R., Garrity C., Gohin F. & Ramseier R.O. 1992, personal communication.
3. Drinkwater, M.R., Long D.G. & Early D.S. 1993, Enhanced-Resolution ERS-1 Scatterometer Imaging of Southern Ocean Sea Ice, *ESA Journal*, Vol. 17, p. 307-322.
4. Gohin, F. 1994, personal communication.
5. Ramseier, R.O. Emmons A., Armour B. & Garrity C. 1994, Fusion of ERS-1 SAR and SSM/I Data, Proc. 2nd ERS-1 Symp.-Space at the Service of our Environment, Hamburg, Germany, 11-14 Oct 1992, *ESA SP-361*, p. 361-367.
6. Ramseier R.O. & al 1990, Canadian validation of the SSM/I and AES/YORK algorithms for sea ice parameters, Atmospheric Environment Service, Microwave Group, 168 p.
7. Steffen K. & al 1992, The estimation of geophysical parameters using passive microwave algorithms, Ed. F. Carsey, *Microwave Remote Sensing of Sea Ice*, Geophysical Monograph 68, American Geophysical Union.
8. Haas, C., T. Viohoff and H. Eicken 1992, Sea-ice conditions during the Winter-Weddell-Gyre-Study 1992 ANT X/4 with RV "Polarstern": Shipboard observations and AVHRR satellite imagery, *AWI Berichte aus dem Fachbereich Physik*, Report 34, Alfred Wegener Institut für Polarforschung und Meereskunde.

ERS-1 SAR IMAGES AND OPERATIONAL MAPPING OF SEA ICE IN THE GREENLAND WATERS, PRELIMINARY RESULTS OF A PILOT PROJECT..

Poul Nielsen, Frands Bromose Pedersen, Hans H. Valeur¹

Danish Meteorological Institute, Lyngbyvej 100, DK 2100 Copenhagen Ø,
Denmark, Phone: (45) 39157500, Fax: (45) 39157300.

INTRODUCTION

Since 1959 the **Danish Meteorological Institute (DMI)** has been responsible for the operational mapping of sea ice in the Greenland waters. Traditionally, the mapping has primarily been based on observations from aircraft and helicopters.

To an increasing extent it is being based on AVHRR images from NOAA satellites.

However, it is a well known fact that clouds often render the AVHRR satellite images useless. Therefore, we have a natural need to adopt cloud independent observation systems.

OBJECTIVES

The aim of the project **PP2-DK2** is to evaluate the usefulness of ERS-1 images for operational ice mapping in the Greenland waters:

- i Is the availability sufficient ?
- 2 Is the areal coverage sufficient ?
- 3 Is the frequency of coverage sufficient ?
- 4 What can be seen on the images ?
 and indeed:
- 5 What can not be seen on the images ?

MATERIAL AND METHODS

Several images have been used to support the AVHRR based ice mapping. However, we felt a strong need to ground truth material, either from ships or from air observations.

We estimated the ships 'Thetis', scheduled for seismic soundings for the 'KANUMAS' project in the Greenland Sea august-september '93, and 'Joides Resolution' scheduled for drilling operations off the Greenland east coast around 63° N for the scientific project 'Ocean Drilling Program' October '93.

Further we made several underflights off the Greenland west coast and around Cape Farewell, the southernmost tip of Greenland simultaneously with ERS-1 passes.

During the flights photographs were taken every minute; further the ice was mapped by visual observations and a 360° mapping radar.

We have received images from Kiruna and Tromsø telemetric stations and, eventually, from West Freugh as well, but not yet from Gatineau.

RESULTS

Greenland Sea:

Unfortunately, the 1993 seismic sounding project 'KANUMAS' was cancelled in the last moment - after deadline for ordering reception of ERS-1 images !

East coast around 63° N:

Ice mapping based on AVHRR imagery was performed for the Ocean Drilling Project through October, 1993. Yet, clouds permitted mapping on September 30, October 9, 10, 18 and 22, only.

ERS-1 SAR coverage could only be obtained on October 3, 19 and (partly) 16. Clearly this was not sufficient for daily mapping.

However, the images were used to support the AVHRR interpretation. There was a sharp boundary between water with (some ?) grease ice giving the sea surface a smoother appearance (dark on the images) and the warmer Atlantic water outside. The occurrence of grease ice was confirmed by the ship. When grease ice was present the polar ice, even as patches and strips of small floes, could easily be identified, and the interpretation was in agreement with that of the AVHRR images and with information from the ship. However, when the polar ice extended into the Atlantic water the strong signal from the capillary waves rendered much of the ice invisible.

Cape Farewell area:

Investigations from our main area (and the most dangerous area) the waters around Cape Farewell have just started; they had to await the possibilities of receiving ERS images in near real time. This has now been made possible by the courtesy of the DRA telemetric station at West Freugh in UK.

¹Project manager.

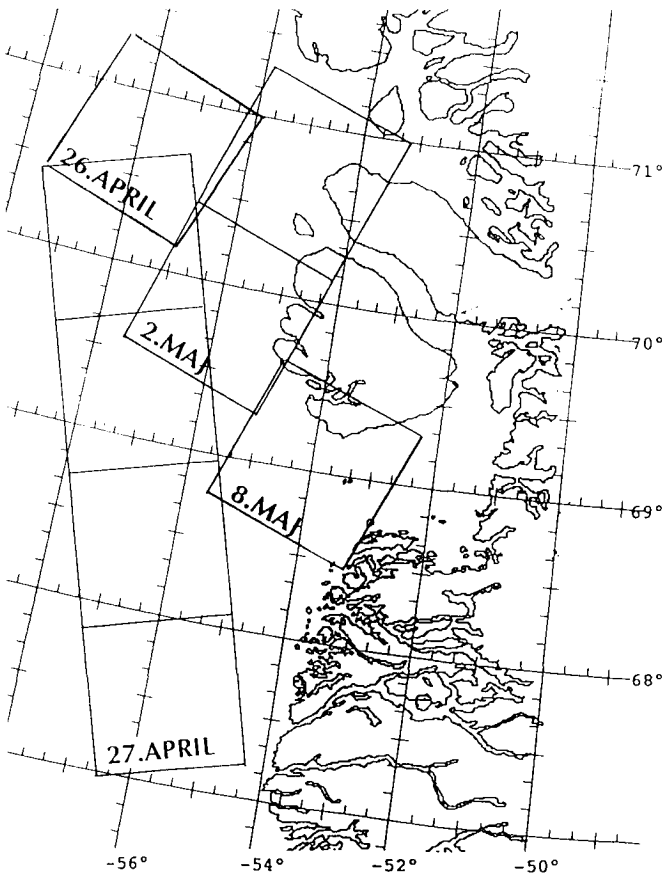


Fig. 1. Chart of investigated ERS-1 frames from Baffin Bay off the Greenland west coast.

Underflights were made on 30 May, 1,6,10 and 13 June. A preliminary investigation seems to indicate that considerable parts of the (polar) ice is invisible on the image due to capillary waves, but results are not yet ready.

Baffin Bay:

Underflights were made on 26 and 27 April and on 2 May as indicated on the map fig.1. Since the images of 27 April were outside the range of European telemetric stations, they had to be received by the Gatineau station, Canada, and were not yet available. Therefore only experiences from 26 April and 2 May will be treated in the present paper. The ice chart of 2 May from the Ice patrol (fig. 2.) gives an overall view of the ice conditions at break'up time in eastern Baffin Bay.

April 26 1994

Baffin Bay ice, in Greenland called 'West Ice' is first year ice. Towards the Greenland side of Baffin Bay the thickness of the west ice decreases, and being closer to the ice edge it is more subject to swell and breaks more frequently.

The image (fig. 3) shows very close or compact ice in the transition zone between a thicker (darker on image) ice about 60-70 cm thick with only few fractures to the west and a somewhat thinner ice (medium grey on the image) to the east. The lighter greytone of the latter is caused by several fractures and cracks.

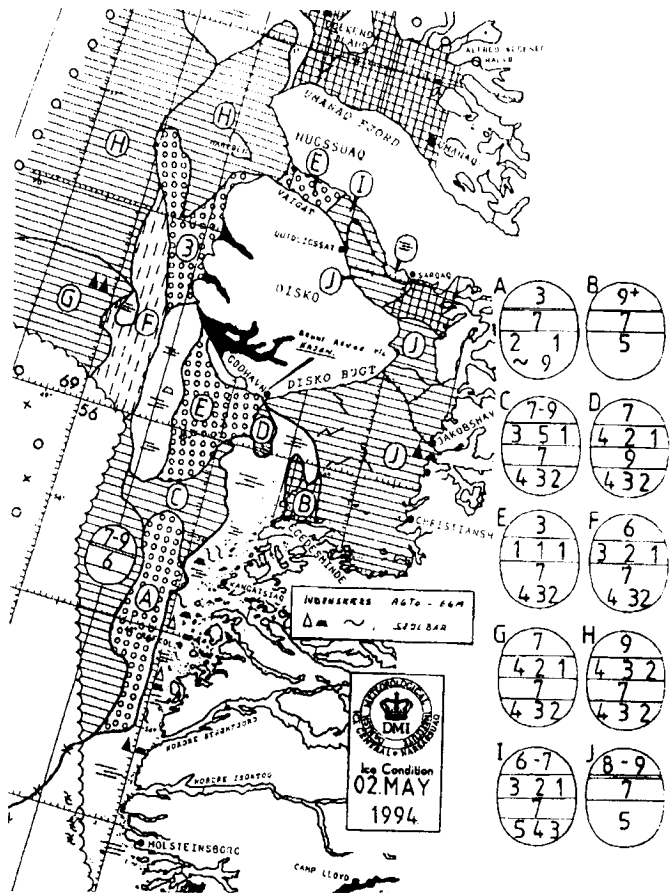


*Fig. 2. Ice chart from the ice patrol flight 2 May 1994.
(Fig. 3. is given on the next page).*



*Fig. 4. Port side 15:51:30 UTC (marked with an 'A' on fig. 3)
Part of a big ice floe (5 x 8 km) in the foreground, easily identifiable on the ERS image.
The fractures (light) are partly covered by light nilas (black)*

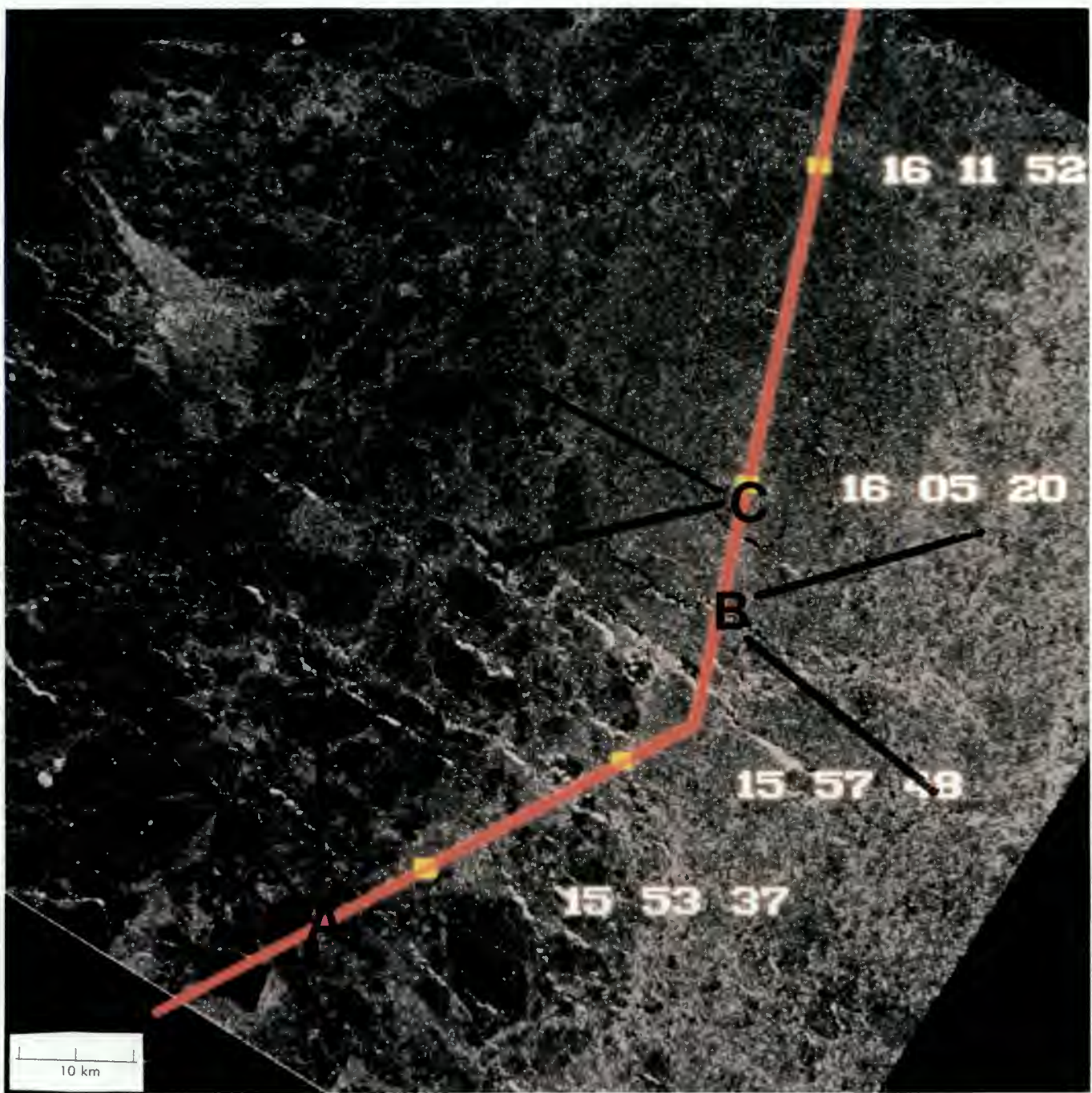


Fig. 3. ERS-1 SAR image (orb. nr. 14530 frame nr. 2169) from Baffin Bay 26 April 1994. All ERS images have been calibrated and resampled to Lambert conformal projection to fit operational charts.

The temperature was about -10° C and the wind about 10 knots from NW.

The lightest greytone is caused by the capillary waves on the water surface in the larger fractures. Some of the cracks are covered or partly covered by nilas, causing a very weak backscatter and thereby a black tone in the image.

Because of low clouds and poor visibility the aerial photographs had to be taken from a low altitude, ab. 300 m, and the ERS image clearly gives a lot more information than could be obtained by the visual observer on board the aircraft. The position of the photographs is marked with letters on the ERS image and the indicated horizontal viewing angle is 38° and 54° resp. for the quadratic and rectangular photographs. The width of the front end is 350 m and 700 m resp.

The line with time markings indicates the flight track of the Ice Patrol aircraft.

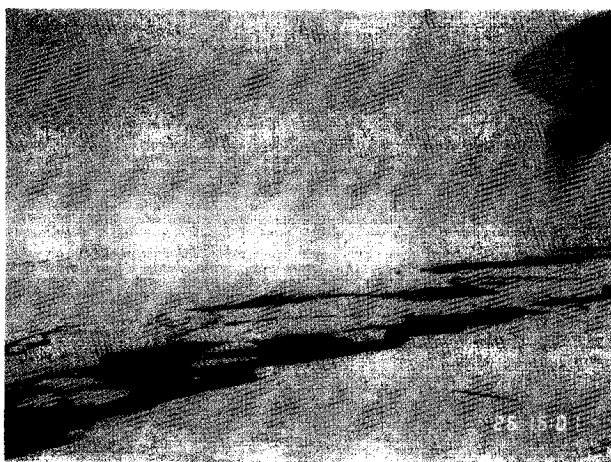


Fig. 5. Starboard 16:01:30 UTC (marked with a 'B' on fig. 3) A nilas covered large fracture appearing dark on the ERS image.

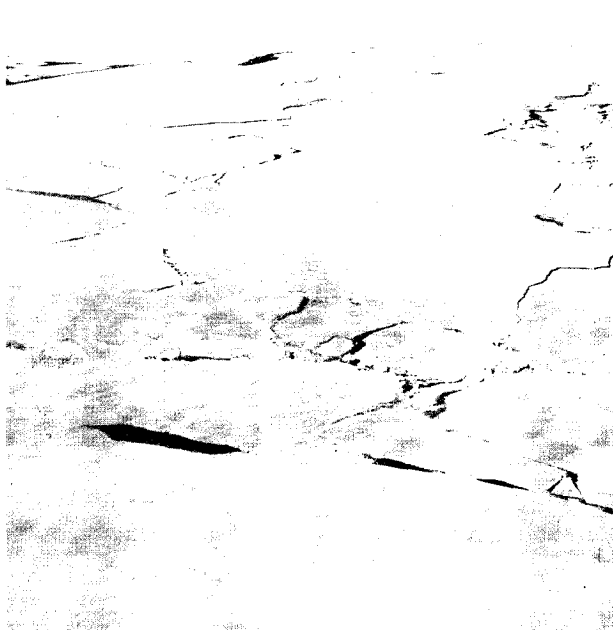


Fig. 6. Port side 16:05 UTC (marked with a 'C' on fig. 3) Compact, but heavily cracked 'west ice' gives a medium strong backscatter. The bigger nilas covered fractures can be seen on the ERS image as narrow black bands.

May 2 1994

The ERS_1 images of 2 May (fig. 7-8) are from the marginal zone near the Greenland west coast. The west ice is in a stage of breaking up and the ice concentration generally gets lower near the coast. There are still many big floes, although they are considerably smaller than those seen further to the west on the image of April 26.

The weather was nearly calm with temperatures slightly below freezing (ab. -2° C).

The visibility was fine, and the cloud level high, so the flight was performed at an altitude of 2.400 m adequate to visual observation and photographing.

The ERS images appear easy to interpret, but there are several pitfalls as the aerial photographs may illustrate. Occasional 'ground truth' information from e.g. ships or aircraft is most desirable.

Fig. 7. (next page): Part of the southernmost ERS image of 2 May (Orb.nr.14616, frame nr. 2187). For reason of layout the image is shown with north pointing to the left. The coast is visible in the top of the image.

Nilas covered open water stands out very clearly as dark areas due to the negligible backscatter. Uncovered open water has a light grey speckled appearance due to the capillary waves often hiding the ice floes.

The flight line with time markings is indicated and the position of the photographs is marked with letters on the ERS images and the indicated horizontal viewing angle is 38° and 54° resp. for the quadratic and rectangular photographs. The width of the front end is about 3 km and 6 km resp.

Fig. 8. (next page): Part of the northernmost ERS image of 2 May (Orb.nr. 14616, frame nr. 2169). The image is oriented in the usual way with north pointing upwards. The image appears light and has been enhanced to see the pattern in the darker areas.

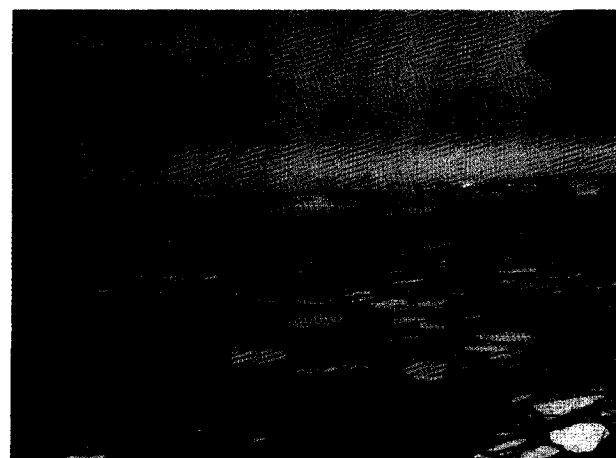


Fig. 9. Starboard 15:40 UTC (marked with an 'E' on fig. 7). Foreground: Icebelt with some big floes which are clearly identified as dark grey on the ERS images. The small floes and ice cakes in between and the open water to the left appear bright in the image.

Background: mainly nilas appearing black in the ERS image.

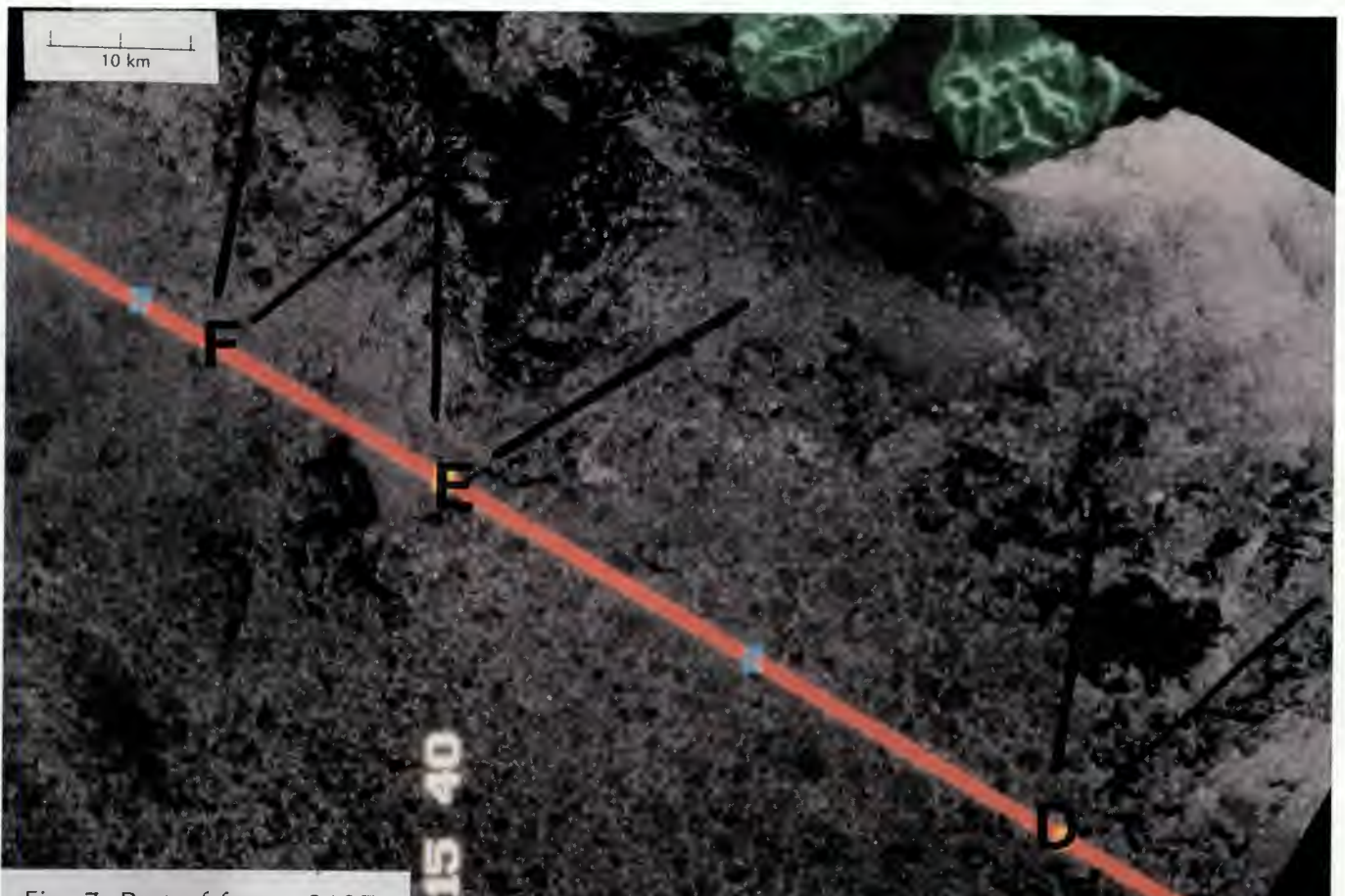


Fig. 7. Part of frame 2187

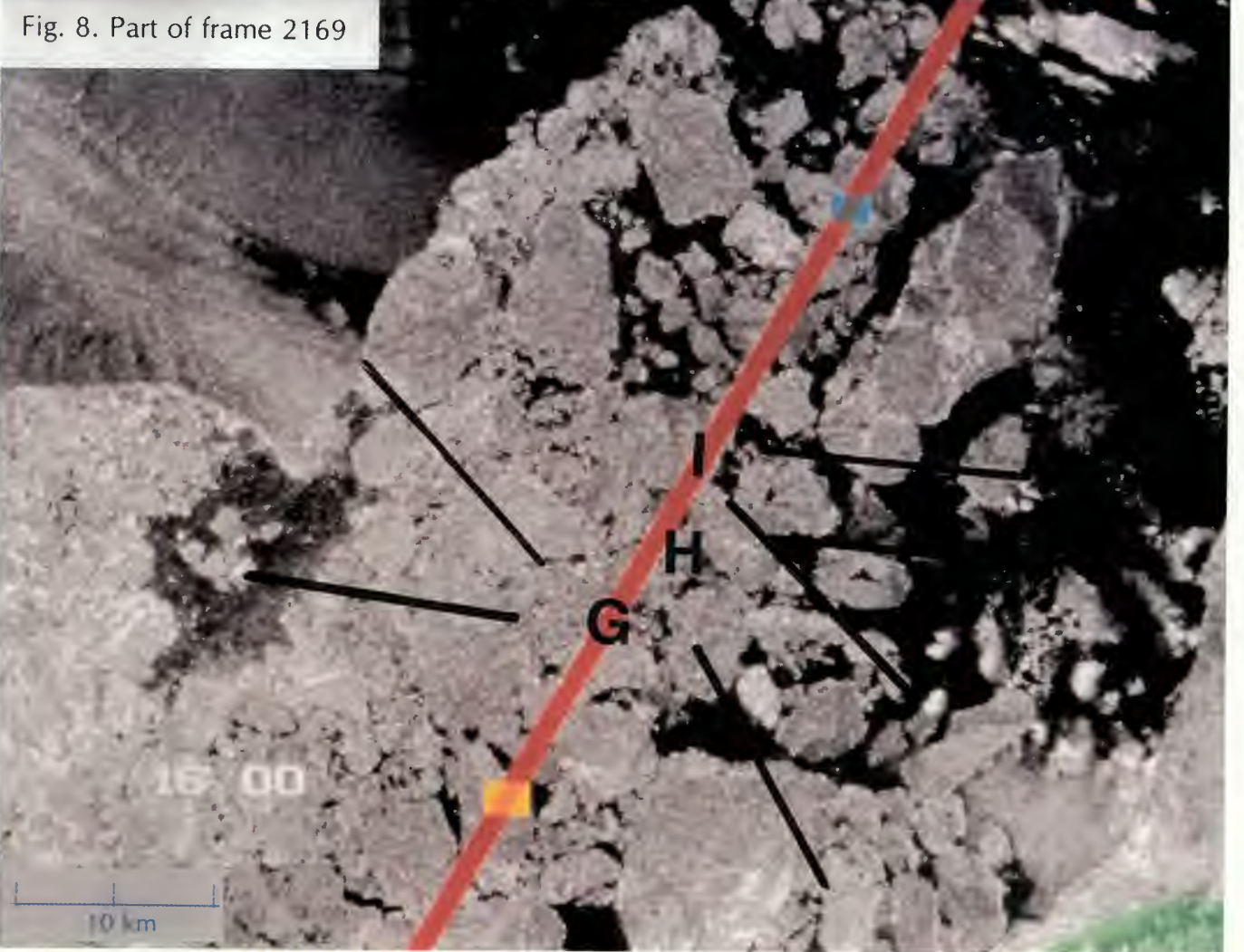


Fig. 8. Part of frame 2169



Fig. 10. Starboard 15:30:30 UTC (marked with a 'D' on fig. 7).

Big and medium floes in the foreground are clearly identified on the ERS image. So are the nilas covered water (and grease ice) in the middle ground and background, appearing dark on the ERS images.



Fig. 12. Port side 16:01:30 UTC (marked with a 'G' on fig. 8).
Breccia ice of west ice. In the middle ground to the left is seen a water area covered with light nilas (5-10 cm thick). To the right and in the background open water is seen, having a speckled light appearance on the image due to capillary waves.

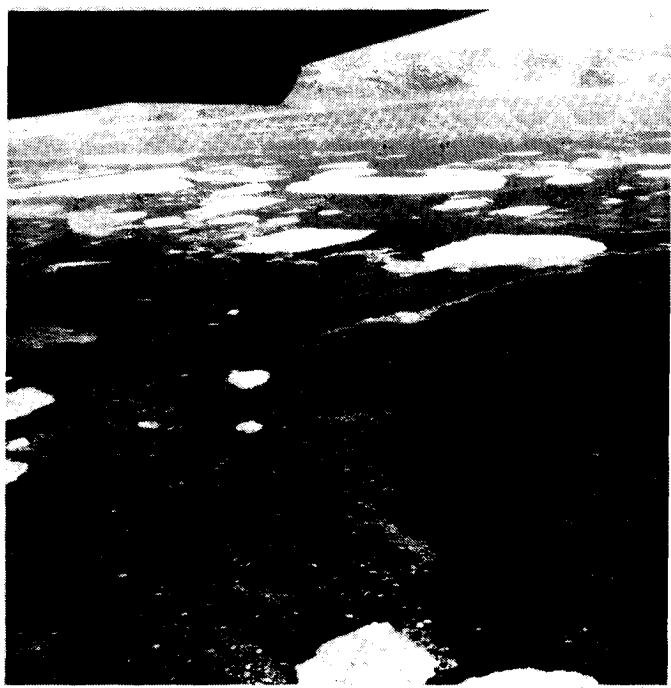


Fig. 11. Starboard 15:44 UTC (marked with an 'F' on fig. 7).

Foreground: Open water (specckled, light on the ERS image due to capillary waves). Middle ground: Big floes (1-2 km) appearing dark grey on the ERS image.
Backgr.: Strips of ice with nilas covered water in between. On the ERS image the strips appear light grey, the nilas black.



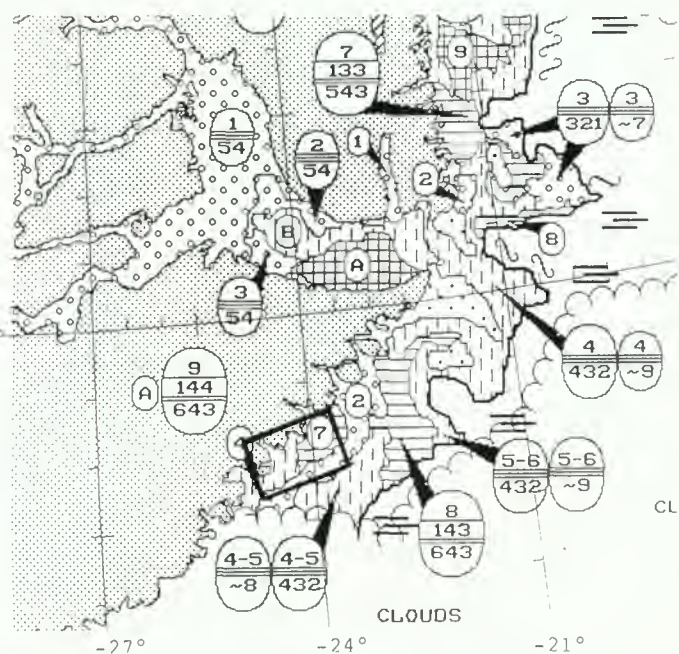
Fig. 13. Starboard 16:03:30 UTC (marked with 'I' on fig. 8).
Breccia ice, about $\frac{1}{2}$ m thick. The 2 groups of floes in the foreground each group having a center of nilas covered water can clearly be identified on the ERS image. The surrounding water containing sufficient amount of grease ice to smooth the

surface has a black appearance on the ERS image. In the utmost background the fast ice of Umanaq Bay is seen. The ice free water between the fast ice and the floe in the background to the right appear speckled light on the ERS image caused by pronounced capillary waves. The narrow wind belt causing the capillary waves can be followed towards NW on the other side of the ice belt. The colourphoto below to the left was taken ab. 1 minute before, and one of the ice floe groups with the triangular nilas covered centre can be identified on both photographs.



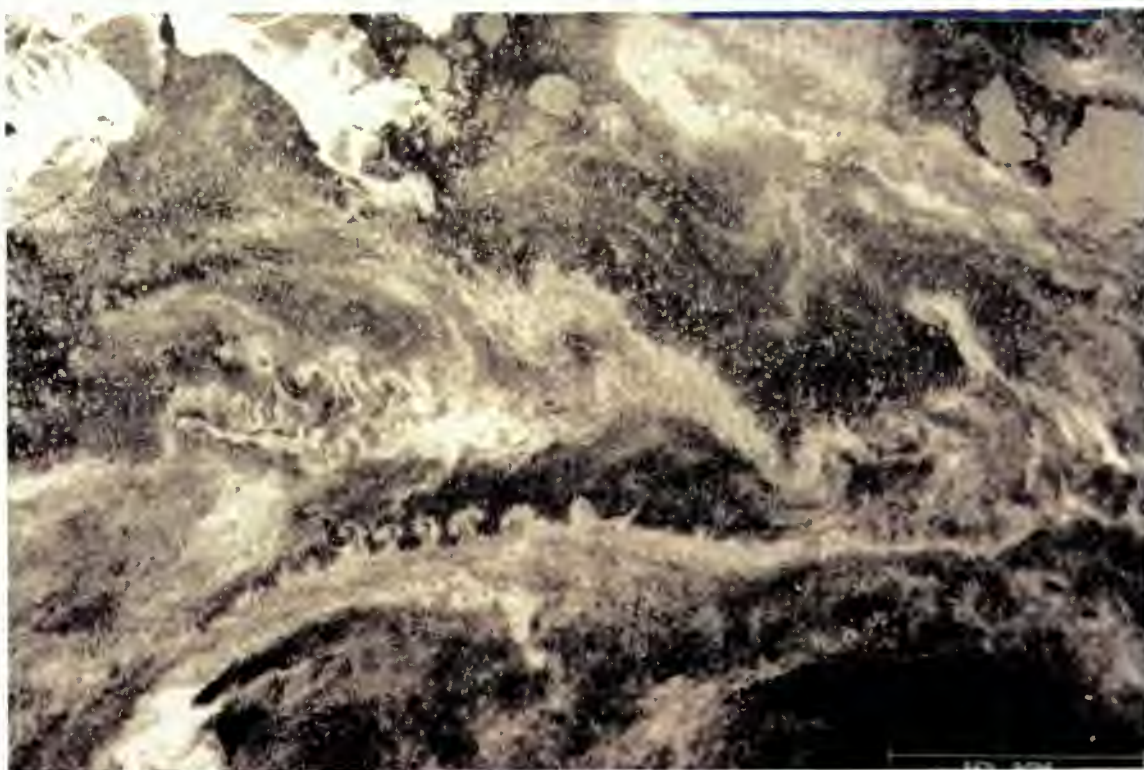
Fig. 14. Starboard 16:02 UTC (marked with a 'H' on fig. 8). (see text of fig. 13).

WHAT IS THAT ?
(below)



A section of an ERS image of 24 August 1993 near Scoresby Sound (below). It is indicated with a solid frame on the AVHRR icechart of August 23 above.

According to the interpreter there was between 2 and 7 tenths of ice in the area. The big floes can easily be distinguished and also a couple of small floes, but what causes the spectacular light grey eddies? Are they ice filled or does the change in greytone simply show a local change in the orientation of the capillary waves. Obviously, ground truth data are needed.



PRELIMINARY CONCLUSIONS

Based on low resolution images the following may be concluded:

1 Availability:

The acquisition time too long to fit navigational need. Since the estimated position of most ships in ice infested waters is not known till a few days before it is not possible to order the correct frames 5 weeks ahead unless an abundant number is ordered from which only a few per cent are actually being used. (= *navigational need 'unpredictable'*)

2-3 Areal coverage and frequency:

The coverage is not sufficient, since coverage is needed daily - or at least 2-3 times a week. Yet, combined with and as a support to interpretation from other (primary) sources the images can be very useful, even with the lower frequency.

The data must be timely.

4 What can be seen on the images ?

What ice information can be extracted ?

ERS-1 SAR images are generally good for monitoring:

Fast ice edges and nilas, yet background information is often needed to differentiate between level fast ice and nilas.

Vast and Giant floes (i.e. floes bigger than 2 km) can usually be identified in all concentrations

When the ice is close or compact (i.e. more than 7/10):

- Edges
- Leads (with/without Nilas)
- floesize distribution (for floes bigger than 400 m)
- Concentration
- (Thickness)

can be stated.

When no 'sea clutter' is present ERS-1 images are good for monitoring:

All concentrations of ice floes bigger than resolution cell (except nilas).

strips and patches of small floes

5

What can not be seen on the images ?

'Sea clutter' is extremely disturbing:

Masks normally out
small and medium floes (< 500 m)

When bad weather increases the need for SAR images the 'Sea clutter' (capillary waves) often renders the images useless.

In our most important
and navigationally most dangerous waters,
the waters around Cape Farewell
all ice is old ice or thick first year ice
as small or medium floes.

Needed information is:
ice edge, concentration and floe size.

Since nilas is normally not present
'sea clutter' is in all cases
obscuring the ice detection in this area..

RECOMMANDATION:

The influence of capillary waves
should be minimized.

By optional change of polarization

By suitable filtering of the high resolution images, if possible.

PARAMETERIZATION OF LEAD FORMATION IN THE WEDDELL SEA USING SAR-DERIVED ICE VELOCITY FIELDS

Marcus Thomas, Olaf Schulze, Rüdiger Brandt, Rainer Roth*

* Pilot Project Leader
Institut für Meteorologie und Klimatologie
Universität Hannover
Herrenhäuser Straße 2, D-30149 Hannover, Germany
phone: (+49) 511 762 4413, fax: (+49) 511 762 4418

ABSTRACT

The opening and closing of leads or polynyas in sea ice covered regions governs the heat exchange between the ocean and the atmosphere. One of the most important questions in modeling dynamical and thermodynamical processes of sea ice is the temporal and spatial variability of open water/thin ice areas. To investigate this question, ice velocity fields are calculated from ERS-1 SAR images with 100 m resolution along a transect at 67° southern latitude. The displacement vectors of significant ice structures are automatically generated by cross-correlations between pairs of SAR scenes from descending and ascending orbits. As an example the divergence of an ice velocity field from July 14th, 1992 is presented. Additionally, an ice classification approach based on radiometric and geometric properties and an estimation of sensible heat fluxes using additional meteorological data (synoptical analysis, ECMWF model) is shown. In free ice drift situations, the lead formation can be directly linked to the synoptic situation.

Keywords: ice classification, ice drift velocity fields, leads, heat exchange, Weddell Sea.

1. OBJECTIVES

As parameterization of heat exchange in the polar regions is difficult, climatological values are often used for an estimate. Due to investigations on dynamical and thermodynamical processes of the sea ice, it is a well-known fact that the opening and closing of leads or polynyas governs the heat exchange between the ocean and the atmosphere in ice covered regions. In those regions the formation of new ice is controlled by the energy balance at the surface and especially by the heat fluxes which are far more effective than radiation processes. While the ice cover acts as a heat resistance for the freezing beneath the ice, ice formation is most effective in open water areas. Leads or polynyas (open

water areas) arise from divergent ice motion driven by the wind.

Therefore, a detailed analysis of the temporal and spatial variability of open water/thin ice areas is necessary. The problem to be solved is the rapid change of the open water net area which is caused by changing wind fields in relation to the prevailing weather situation. In addition, high resolution ice motion trajectories are needed to calculate the divergence of the ice motion from an ice velocity field which otherwise cannot be derived from the trajectories of drifting buoys. However, buoy investigations show trajectories of the mean ice motion in the whole Weddell Sea for longer time scales (Ref. 1).

In-situ measurements in the Weddell Sea like the *Winter Weddell Sea Project 1986 (WWSP '86)*, the *Winter Weddell Gyre Studies 1989 and 1992 (WWGS '89, WWGS '92)* (Refs. 2, 3) are not suitable for investigating large scale sea ice dynamics whereas ice models (for instance Refs. 4-6) show these effects without spatial or temporal limits. To prove the modeling results, remote sensing is useful for spatial and temporal observations but there are some limitations on thermal infrared or optical sensors due to cloud cover restrictions (Ref. 7). Only the SAR allows an observation without this limitations and a detailed study of the ice drift in areas which are influenced by complex synoptic systems (mostly accompanied by compact cloud covers).

2. SEA ICE CHARACTERISTICS

For a demonstration of our analysis, we use a sea ice region of 50.4°-50.4 km² in size, its centre being located at 67.1° S, 43.2° W. (Fig. 1). This site is covered by the satellite track on July 14th, 1992 at 03:17 UTC and 11:27 UTC, the ERS-1 being in ascending and descending node, respectively (hereafter referred to as image 1 and image 2). The SAR-PRI scenes (Fig. 2)

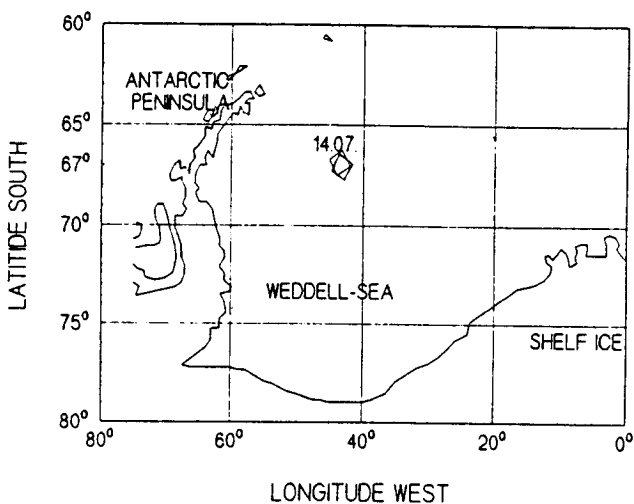


Fig. 1. Geographical position of the chosen pair of SAR images from July 14th, 1992 in the Weddell Sea.

were corrected for incidence angle variation with range and aligned to north. Due to the very large amount of SAR scenes which are interpreted and used for ice tracking, the images were reduced in geometric and radiometric resolution resulting in 100-m-pixel spacing and 8-bit pixel depth (Ref. 8).

The images show the typical characteristics of the sea ice in the central to western Weddell Sea in midwinter (Ref. 9). Large multiyear ice floes with high backscatter are dominant, but also regions with first-year ice floes (lower backscatter) are present. Yet, the most obvious features are the very bright regions which roughly align in the north-south direction; their eastern and western boundaries fit well to each other.

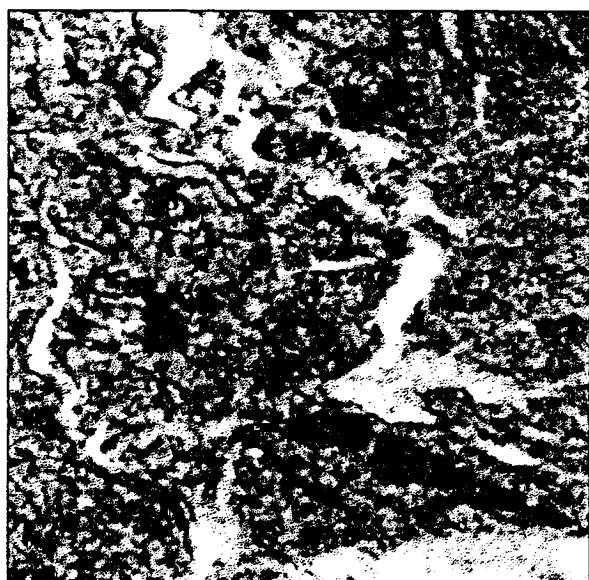


Fig. 2. SAR-PRI images taken on July 14th, 1992 in the central Weddell Sea. Image size: 50.4·50.4 km². Left : Orbit

After a close investigation using full-resolution images it is most likely that these are areas of former open water, which are completely covered by grease ice generated from new-formed frazil that accumulated at the (at that time) downwind edge of the lead.

A profile along the digital image 1 (Fig. 3) is used for an estimate of the backscatter coefficients σ_0 of the different structures. The σ_0 values have been derived after Ref. 10. Though the original images are to some extent smoothed by the downsizing (every 8·8-pixel-rectangle in the original PRI scene is represented by its mean value), a (5·5)-median-filter had to be applied in order to guarantee that the classification of the three most significant surface structures open water (OW), first-year ice (FY) and multi-year ice (MY) is not ambiguous due to overlapping σ_0 ranges. The filtering also decreases the geometric resolution; however, for investigating lead formation with respect to thermodynamical processes like heat exchange between ocean and the atmosphere the accuracy remains sufficient: The areas of open water and nilas govern the heat exchange in polar winter if they account for more than 1 percent of the considered region (Ref. 11). As the typical area of a SAR data analysis is 100·100 km², the surface cell size for an accuracy of 1 permill is 10 km² which leads to a condition for accuracy in linear dimension of approximately 3 km which is one order of magnitude larger than in the presented method.

The recognition of 3 most important "surface classes" open water, nilas (young, thin ice) and multi-year ice is essential for thermodynamical studies because the typical upward heat fluxes over those areas differ by an



5201, frame 5805 (ascending), Right: Orbit 5206, frame 4995 (descending). Note the dark leads in image 2.

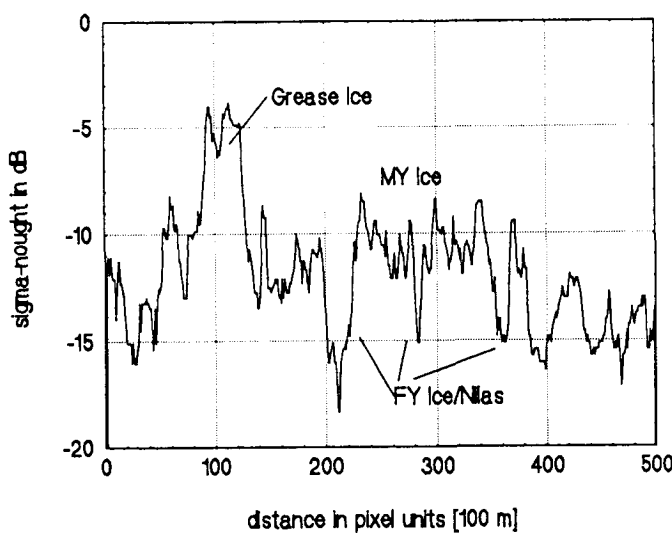


Fig. 3. Profile of σ_0 -values along the section indicated in image 1. The different surface structures are identified.

order of magnitude, respectively (Ref. 11). Consequently, we have to separate the images into this 3 surface classes to achieve a proper estimate of the total heat flux, and the discrimination open water/thin ice has to be taken care for most accurately. Regarding the two images shown, we derived the following threshold values based on σ_0 -profiles like in Fig. 3:

Surface Class	σ_0 -range
Firstyear Ice	$\sigma \leq -15$ dB
Open water	$-18 \text{ dB} \leq \sigma_0 \leq -14 \text{ dB}$
Multiyear Ice	$-13 \text{ dB} \leq \sigma_0 \leq -8 \text{ dB}$
Accum. frazil	$\sigma_0 \geq -8 \text{ dB}$.

Consequently, in this case (due to relative low wind speed in both SAR scenes) there is an ambiguity in discriminating FY from open water based on the average backscattering properties alone. However, the high spatial resolution of the SAR in connection with knowledge about ice formation processes and the geometric shape of the ice features allow us to overcome this problem.

First, FY (and MY as well) ice floes mostly show no variation in shape during the 8-hour-period between the consecutive satellite overpasses, while leads open or close more rapidly. Secondly, within leads there are often bright strips aligned in wind direction which are due to frazil ice, while ice-floes rather have irregular brighter linear features which are caused by ridging. Thirdly, if there is no possibility of open water formation by melting (like in our case studies during the austral winter), open water areas most probably will

have more linear shapes rather than circular or rectangular.

The atmospheric parameters which have great influence on the backscatter properties are the wind speed, which causes a variation of the waves and small ripples on the ocean surface, and the air temperature which is of particular importance if melting occurs. In the example shown, there is little change of the atmospheric conditions between the acquisition of the two images. According to ECMWF data and the weather charts produced onboard RV "Polarstern" during her cruise across the Weddell Sea in July 1992, the location was under the influence of a anticyclone with its center over the tip of the Antarctic Peninsula which weakened gradually. The air temperature, as interpolated using measurements from "Polarstern", drifting buoys, and weather stations on the Antarctic Peninsula, increased from -25°C to -22°C between 00 UTC and 12 UTC. The 10 m -wind speed u_{10} showed a slight decrease from 10 m/s to 7.0 m/s . Consequently, only little atmosphere-induced change in the backscatter of both open water and sea ice occurred.

In image 2, new-formed leads are visible which have a much lower backscatter than the surrounding pack ice. As the wind speed (7.2 m/s) is too low to generate a radiometric rough water surface, we assume that they consist of open water. Within those leads, brighter bands are visible which are aligned in wind direction (SSW). They belong to bands of new-formed frazil ice, which is driven downwind and accumulates at the NNE edges of the leads (see Fig. 4 for a blow up).

3. LEAD FORMATION IN DETAIL

The new formed leads in image 2 were analyzed in more detail using full resolution of the SAR image (pixel spacing: 12.5 m , ground resolution: 30 m). For reasons of space, the images in Fig. 4 are not aligned to north direction. It is obvious that leads have formed which have a width between 200 m and 500 m , covering areas of approximately 5 km^2 each. The flux of sensible heat to the atmosphere is 240 W/m^2 (Ref. 8). Due to their small size, their contribution to the total flux of sensible heat in this region is negligible, but their shape make them suitable for navigating.

The main axis of the leads are aligned nearly normal to the prevailing wind direction. At the downwind edges (upper right areas in Fig. 4) bright bands of accumulated frazil (grease ice) are clearly visible. The backscatter coefficient of these bands correspond well to those of the very bright, roughly north-to-south aligned wider leads mentioned above, thus giving further

indication that the latter are completely covered by accumulated grease ice.

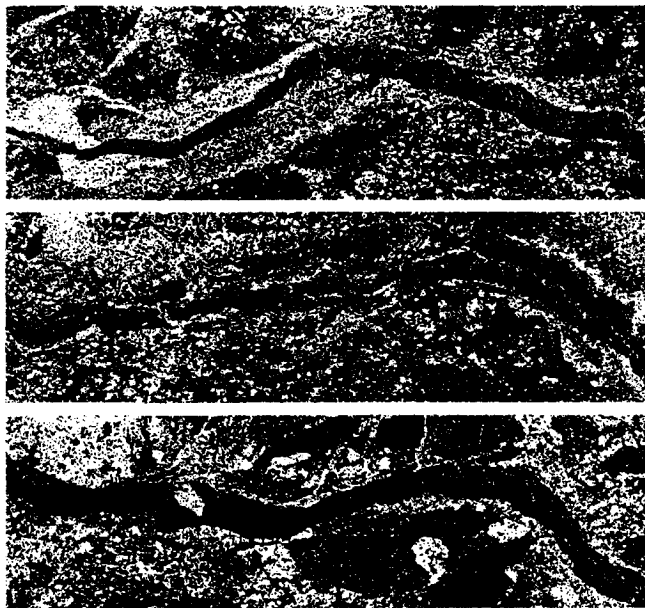


Fig. 4. Details of 3 partly new-formed leads in image 2. Size: 12.5·3.0 km². Note the bright edges of every lead in the upper right parts (=northeast boundaries).

The shape of the new-formed, radiometric "dark" leads as well as the bright ones are an indication for the main wind direction during their formation. The cause for lead formation in very compact ice like in this case study is caused by a differential drag on the ice floes. This can be due to a divergent wind field, or to minor extent to spatial variations of the drag coefficient c_D , or both. Having no direct measurements of c_D in the test area, we concentrate on the forcing wind field.

Approximately 3 hours before the acquisition of image 1 (00 UTC), the 10 m-wind field from the ECMWF analysis yields a wind speed $u_{10} = 10$ m/s, turning from WSW over SW at 06 UTC and decreasing to 7 m/s with direction S. The main axis of the new-formed leads are, as mentioned above, normal to the averaged wind direction, with a small deflection to the left, resulting from the leftward turning angle of ice drift with respect to the 10 m-wind vector. In absence of wind speed data with higher temporal resolution, the prevailing wind speed at 11:27 UTC (image 2) is interpolated to 7.2 m/s. Analyzing the wind field more in detail, one is able to recognize an increasing wind speed from the SW to the NE edge of the test site. This means that the ice is subjected a differential drag which is able to cause cracks at the weakest points of the ice structure. After having cracked, the lead will continue to open until the next crack is created elsewhere, thus decreasing the differential drag, or until obstacles like coastlines prevent further opening. To overcome the

boundary problem, we chose the central Weddell Sea for our pilot study of lead formation because the ice drift v_D there can approximately be described as free drift (Ref. 1).

Along the SW-NE direction, the wind speed increases 1.2 m/s per 115 km according to the ECMWF grid point values (approx. 0.01 m/s per km). Assuming a 10 m-wind factor $\beta = v_D/u_{10} = 0.02$ (Ref. 16), the width W_l of one single lead within a typical downwind distance of $x_0 = 50$ km after 8 hours can be estimated:

$$\begin{aligned} W_l &= x_0 \cdot \delta t \cdot \beta \cdot \delta u_{10}/\delta x \\ &= 50 \text{ km} \cdot 30000 \text{ s} \cdot 0.02 \cdot 0.01 \text{ ms}^{-1}/\text{km} \\ &= 300 \text{ m}. \end{aligned}$$

This fits well to the SAR observations. On the other hand, the closing time for a 500-m-wide lead due to frazil accumulation on the downwind lead edge is estimated to 12 hours (Ref. 13). Taking this into account, in the 8-hour-interval between image 1 and 2 two third of the lead would have to be covered by grease ice. This is obviously not the case, probably because the opening process is dominating the refreezing. To study this process more in detail, a higher temporal resolution of consecutive SAR scenes is needed (e.g. the optional tandem orbit of ERS-1/2).

4. SAR-DERIVED ICE-VELOCITY FIELDS

To investigate ice motions and divergence in the ice field in Antarctic winter time, until now 19 ice velocity fields were derived from ERS-1 SAR images. All examples are chosen from July 1992 because in-situ measurements are available from RV "Polarstern" in the same region and time.

The displacement vectors of significant ice structures are generated by cross-correlation (Ref. 14) between sections from pairs of SAR images from ascending and descending orbits which are showing almost exactly the same area. Due to orbit instabilities and the absence of geographical fixed pass points in the central Weddell Sea, the location error is approximately 300 m for each image giving a worst-case error for v_D of 0.02 m/s or 10 percent. However, differential quantities like divergence and rotation are not influenced by this errors.

As an example, the results from July 14th, 1992 are given in detail, using the pair of images described in section 2. Fig. 5 shows a field of displacement vectors which may be interpreted as mean ice motion within 8 hours. Each plotted vector is a mean representing 25 vectors around the start position of the plotted vector.

The mean ice drift is directed towards the northeast and the drift speed ranges from 22 cm/s to 27 cm/s with a mean value of 25 cm/s. Comparing the orientation of the ice motion and the geostrophic wind field which is calculated from the ECMWF surface pressure field (m.s.l.), the ice drift follows the wind with a mean turning angle of 35 degrees to the left from the geostrophic wind. This may be explained by the surface roughness which causes ageostrophic components and by the influence of the Coriolis force. Although the geostrophic wind velocity is 11 m/s, the turning angle in this example is greater than the deflection in other comparable examples (Refs. 15, 16). This may be due to the fact that the wind was decreasing as well as turning during the time between the image acquisition. Thus, the sea ice which has an reaction time due to its inertia of approximately 3 hours, had not reached its final drift vector according to the atmospheric conditions at the time of the second acquisition.

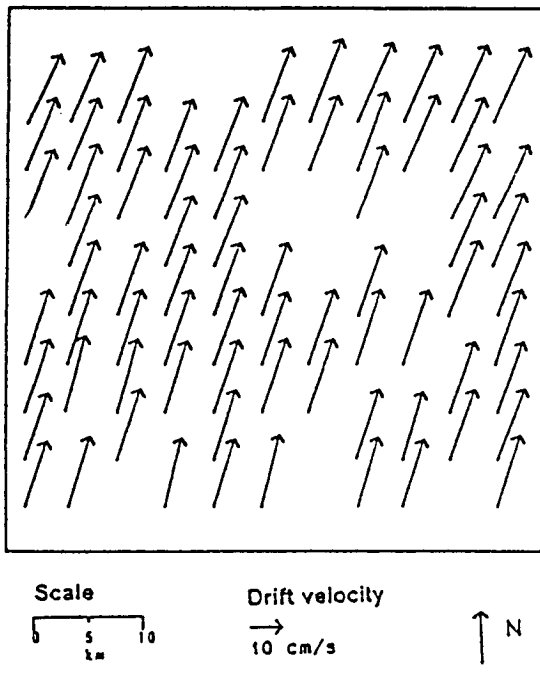


Fig. 5. SAR-derived ice velocity field from July 14th, 1992 showing the mean ice motion over 8 hours.

In addition, most of the vector fields show the signature of the prevailing weather situation, i.e., differential properties of the vector field can be related to synoptic systems in the considered regions.

In this example, the divergence and other differential properties of the sea ice motion are calculated from the SAR-derived ice velocity field. The divergence is illustrated in Fig. 6 using the displacement of a regular grid over 8 hours 12 min. The resolution of the regular grid is 1 km · 1 km in which each grid point is displaced with the corresponding displacement vector.

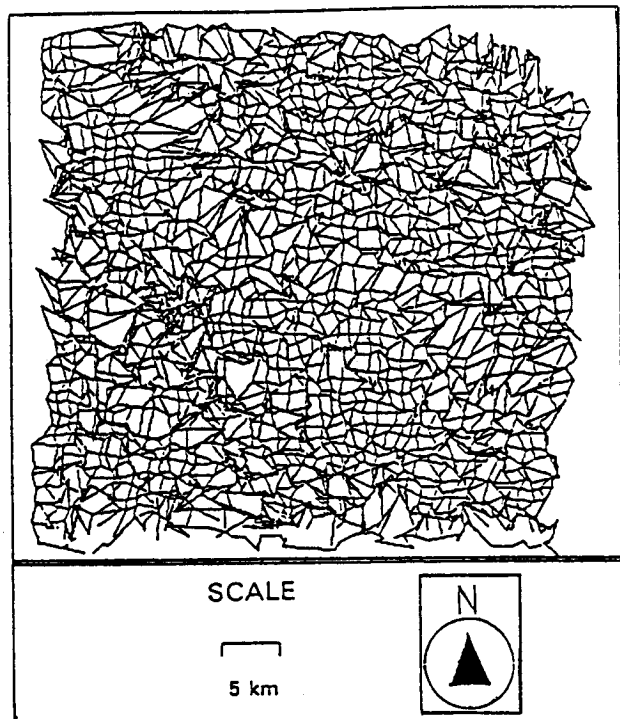


Fig. 6. Displacement of a regular grid over 8 hours (grid spacing is 1 km · 1 km) showing areas with divergent and convergent ice motion.

In zones with divergent or convergent ice motion the cells became deformed whereas the other cells are rigid. A region of divergence in the ice motion is aligned diagonally from northwest to southeast across the scene. A further one can be found in the northeast corner of the plot showing nearly the same orientation. The deformed grid cells can easily be connected to the opening of leads described above. This is the confirmation of the fact that these leads have opened due to divergent ice motion, and not due to melting, e.g. by upwelling of warmer water masses.

The calculated divergence of the ice drift ranges from $4.3 \cdot 10^{-8} \text{ s}^{-1}$ to $1.7 \cdot 10^{-6} \text{ s}^{-1}$. This means that over a period of 8 hours, leads as wide as 2500 m can open in the analysed area of $50 \cdot 50 \text{ km}^2$. These results are in good agreement with the analysis of the SAR images considering the fact that grease accumulation and refreezing prevent the formation of the maximum possible lead width.

5. CONCLUSIONS

It has been shown that SAR data, in combination with auxiliary meteorological information, can be used to monitor the opening of leads due to divergent ice motion. The main axis of the linear-shaped leads are aligned nearly perpendicular to the divergence in the

prevailing 10 m-wind field, with a slight turning angle to the left like the ice motion itself. This holds as long as there are no boundaries (coastlines) that prevent free ice drift. Because the ice motion is then nearly exclusively driven by the wind field, a forecast of the opening of leads (or for divergent ice motion in general) should be possible using only the wind field forecast in connection with the lead parameterization developed here. For practical purposes in more frequently used shipping routes as the North Atlantic or the Baltic, coastal boundaries have to be accounted for. However, this study proved that the SAR data have the capability for ice tracking that is far beyond that of other instruments, and that the often difficult classification of ice features can be made much more reliable when meteorological information is available. At present, this information, as well as the knowledge of the typical shape of ice features, has to be put into the classification process by the operator, but efforts are made to develop classification algorithms that, on a synergetic basis, will connect this information automatically.

6. ACKNOWLEDGEMENTS

The Pilot Project PP2-D8 is supported by the German Ministry for Research and Technology under grant 03PL504D. The authors would like to thank ESA and the D-PAF for their effort to supply lots of ERS-SAR images and the Alfred-Wegener-Institute for Polar and Marine Research for supplying meteorological and auxiliary remote sensing data.

7. REFERENCES

1. Kottmeier, C., J. Olf, W. Frieden, & R. Roth 1992, Wind forcing and ice motion in the Weddell Sea region, *J. Geophys. Res.*, 97, No D18, 20373-20383.
2. Augstein & al. 1991, Die Expedition ANTARKTIS-VIII/1-2 mit der Winter Weddell Gyre Study der Forschungsschiffe "Polarstern" und "Akademik Fedorov", *Ber. zur Polarforschung*, 39.
3. Engelbart, D. 1992, Thermodynamik und Dynamik von Küstenpolynien im Weddellmeer, *Ber. d. Inst. f. Meteorol. u. Klimatol. d. Univ. Hannover*, 40, 132pp.
4. Hibler, W.D., & S.F. Ackley 1983, Numerical simulations of the Weddell Sea pack ice. *J. Geophys. Res.*, 88, 2873-2887.
5. Lemke, P., W.B. Owens, & W.D. Hibler 1990, A coupled sea ice-mixed layer-pycnocline model for the Weddell Sea, *J. Geophys. Res.*, 95, No C6, 9513-9525.
6. Wefelmeier, C. 1992, Numerische Simulation mesoskaliger, dynamischer Wechselwirkungen zwischen Atmosphäre, Eis und Ozean, *Ber. d. Inst. f. Meteorol. u. Klimatol. d. Univ. Hannover*, 42, 141pp.
7. Lemke, P., & Th. Viehoff 1991, Anwendungen der Fernerkundung in der Meereisforschung, *Die Geowissenschaften*, 9, 266-271.
8. Roth, R., O. Schulze, M. Thomas, T. Rothe, & R. Brandt 1994, Sea-Ice and Climate-An Approach Using SAR Data, *Proc. 2nd ERS-1 Symposium, ESA SP-361*, 323-327.
9. Lange, M.A., & H. Eicken 1991, The Sea Ice Distribution in the Northwestern Weddell Sea, *J. Geophys. Res.*, 96, No. C3, 4821-4837.
10. Laur, H. 1992, Derivation of Backscattering Coefficient σ_0 in ERS-1.SAR.PRI products, Issue 1, Rev. 0, *ESA, Frascati*, 16p.
11. Badgely, F.I. 1966, Heat balance at the surface of the Arctic Ocean, in: *Energy Fluxes Over Polar Surfaces*, Geneva, 115-132.
12. Maykut, G.A. 1978, Energy Exchange Over Young Sea Ice in the Central Arctic, *J. Geophys. Res.*, 83, No. C7, 3646-3658.
13. Bauer, J., & M. Seelye 1983, A Model of Grease Ice Growth in Small Leads, *J. Geophys. Res.*, 88, No. C5, 2917-2925.
14. Fily, M., & D.A. Rothrock 1990, Sea ice tracking by nested correlation, *IEEE Trans. Geosci. Rem. Sensing*, 25, 570-580.
15. Martinson, D.G., & Ch. Wamser 1990, Ice drift and momentum exchange in winter antarctic pack ice, *J. Geophys. Res.*, 95, No C2, 1741-1755.
16. Thorndike, A.S., & R. Colony 1982, Sea ice motion in response to geostrophic winds, *J. Geophys. Res.*, 87, No C8, 5845-5852.

5. GEOLOGY



COASTAL AND RIVERS DYNAMICS STUDIES BY MEANS OF SPACE TECHNIQUES

G.Sylos Labini, R.Loizzo, C.Marzo, F.Vespe - ASI/CGS Loc.Terlecchia P.O.Box 11, 75100 Matera, Italy (tel.:+39.835.377237, fax:+39.835.339005)

G.Pasquarello, P.Blonda - IESI-CNR, Via Amendola 166/5, 70126 Bari, Italy (tel.:+39.80.5481612,fax:+39.80.5484311)
 P.Pieri, M.Pappalopore - Dep.Geology and Geophysic, Via Orabona 4, 70100 Bari, Italy (tel.:+39.80.242571,fax:+39.80.242625)
 M.Antoninetti - IRRS-CNR, Via Ampere 56, 20131 Milano, Italy (tel.+39.2.70643662, fax:+39.2.70643660)

ABSTRACT

This study proposes the use of different Earth Observations Systems in geologic applications. Over an area known as "Fossa Bradanica" (Southern Italy) an analysis with different techniques (Remote Sensing, Interferometry, Geodesy) is performed. Satellite sensed data will be used to provide geomorphological inspection, lithologic maps, lineament maps and land use maps. Interferometric SAR will be used to generate more accurate Digital Elevation Model for SAR data geocoding. Space precise positioning techniques (Very Long Baseline Interferometry, Satellite Laser Ranging, Global Positioning System), especially GPS, will be used in order to establish a dense fiduciary network in the area. This network will be used both to georeference the space sensed data and to link the local network to the global one. Last but not least this research will be devoted to state the operational applicability of advanced Image Processing and Pattern Recognition Techniques based on Neural Network Paradigms.

1.INTRODUCTION

The main objective of the work is to study the river and coastal dynamic in relation to the morphology and neotectonics of the study area. The specific research proposed has relevant impact also in hydrogeologic risk estimation and anthropic factor evaluation. The products of these activities will be useful also at planning purposes for local and national governments.

At this purpose remote sensing and space geodesy techniques are used. Remote sensed LANDSAT and SAR data are integrated in order to provide geo-morphological inspection, lithologic maps, lineament maps and land use maps of the area. The combined SAR - Landsat TM data are more useful than SAR or LANDSAT alone, because the information content of radar and optical imagery may be considered complementary. Visible and infrared sensing is mostly sensitive to chemical and thermal properties of the observed medium, while microwave sensing is mostly sensitive to the physical and dielectrical properties of the

surface. Moreover, SAR data are particularly interesting because of their extensive availability on regular basis, thanks to their weather independence characteristics. The radar backscattering dependence on soil moisture and roughness is fundamental for a better discrimination of different lithologic units. The main problem in integration of optical and SAR data is the image distortion due to side-looking radar that makes very difficult the registration with any other image. The accuracy of the registration depends on the goodness of SAR data geocoding. So the quality and even reliability of the registration is subordinated to the accuracy and availability of the DEM. The exploitation of INSAR (Interferometric SAR) and space geodesy techniques should be helpful to generate terrain elevation model used in geocoding SAR data.

The study will demonstrate the capabilities of integration of different space techniques and sensors. Moreover an assessment will be produced of the capabilities of microwaves versus optical remote sensing.

2.STUDY AREA AND DATA SET

The study area is located in the hinterland of the Gulf of Taranto (Southern Italy), where a series of the marine terraces outcrops along the Ionian coast, between the Apulia (Puglia) and the Apennines chain (fig.1).

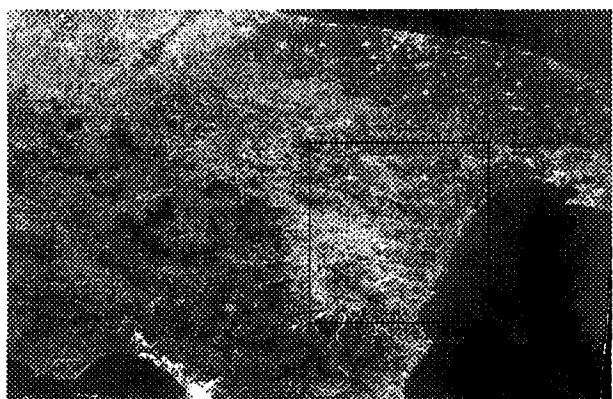


Fig.1 The Study Area

This area is known as "Fossa Bradanica". It is a NW-SE trending elongated basin and represents the southern part of the Apennines foredeep. The sedimentary sequence of the Bradanic trough consists of conglomeratic, sandy and clay deposits. The eastern margin of the Bradanic trough is represented by the Apulian foreland, the western one is formed by the thrust sheets of the Apennines chain. The area of the Bradanic trough, affected by a regional uplift, is crossed by several rivers debouching into the Ionian sea. The interference between tectonic uplift and glacio-eustatic fluctuations of sea level in the hinterland of the Gulf of Taranto (named Metaponto) resulted in the development of the above-named marine terraces (Ref.1).

The site is an agricultural area that presents a mosaic of croplands, vineyards, olives, orchards and a coastal pine forest.

In order to verify the complementarity of optical and SAR data in geomorphological inspection, lithologic maps, lineament maps, soil moisture evaluation and land use map, Landsat TM and ERS-1 data have been considered. The area is flat near the coast and slightly undulated in the internal region. Because of the terrain height variability within this region, ERS-1 Geocoded Terrain Corrected (ERS-1.GTC processed at I-PAF) data have been provided. A multitemporal set is created with the following ERS-1 images, acquired in descending orbit:

Band 1 24 Nov. 92

Band 2 18 May 93

Band 3 27 July 93

Landsat TM data are integrated in the following multitemporal set:

Landsat TM 2 Jan. 92

Landsat TM 28 May 93

Landsat TM 31 July 93

The georeferenced optical and microwave images are well registered and may be compared with any other geographical map. Over the study area ground truth geologic and thematic information are available on cartographic maps. These data are used to support satellite sensed data and to validate analysis and interpretation of the space data set.

3.IMAGE ANALYSIS AND RESULTS

In order to better manage all the information available on the study area, data acquired from remote sensing and from cartographic maps have been integrated in a unique data base. These information consist of thematic maps from cartography, land use map from classification of remote sensed data and lithologic map from photointerpretation of the images. Moreover visual lineaments detection on remote sensed images has been performed. In order to evaluate the differences between Landsat and SAR data, lineaments are mapped separately on the two data sets. The speckle of SAR images has been removed with a local statistic filter. Results show that the appropriately processed SAR data can significantly improve the detection of lineaments. In fact

lineaments detected on the SAR images have different orientation and length respect to the Landsat TM ones. The total number of lineaments is 147 for Landsat TM data (Fig.2) and 144 for ERS-1 data (Fig.3). The percentage of lineaments on the two images is approximately the same in North-North-East directions, while the main difference is in the percentage of lineaments in North-West and East-West directions. This result may be related to the different illumination direction of the two sensors. In fact while Landsat use an unstructured light source (i.e. sun light) the SAR provides a structured side illumination in the radar look direction.

These results show the complementarity of optical and SAR data. A future step of this work will be the analysis of ERS-1 data acquired in ascending orbit to investigate whether these data further improve the lineament detection. An analysis on multisensors and multitemporal images will be performed too. At this purpose Landsat TM data have been merged with SAR data to create a multisensor data with a multitemporal ERS-1 image.

4. NEURAL NETWORK ANALYSIS

An analysis of the multisource, multitemporal data set will be performed by a Multi Modular System, completely based on Neural Networks.

The ability to classify multispectral data correctly and quickly is very important especially as spatial and temporal resolution increase. Recently, several papers appeared about the applications of Neural Networks to remotely sensed data classification, prove that neural networks provide an interesting alternative to conventional statistical methodologies (Ref.2,Ref.3).

Neural Networks do not require explicit modelling of the data from each source and also avoid the problem in statistical multisource processing of specifying the influence of each data source in classification.

The Neural System proposed in this work consists of two modules (Ref.4). The first is an unsupervised architecture for data compression, called Linear Propagation Network (LPN), (Ref.5). It represents a neural approach to perform the Principal Components Analysis (PCA) of the input data, with no use of the covariance matrix. The inversion of the covariance matrix is a problem for the classical Karhunen-Loeve Transform in the case of high dimensional data involving limited training samples. The transformed bands obtained as LPN output will provide the input to the second Module. This is a Multilayer Perceptron (MLP), trained with the Backpropagation rule, for supervised feature recognition (Ref.6).

The main objective of the modularity is the reduction of the amount of computation required to train the supervised MLP, whose main limitation is the weakness of very slow convergence during the learning phase. This work will explore the feasibility of using the Modular Neural System for classification of the integrated images.

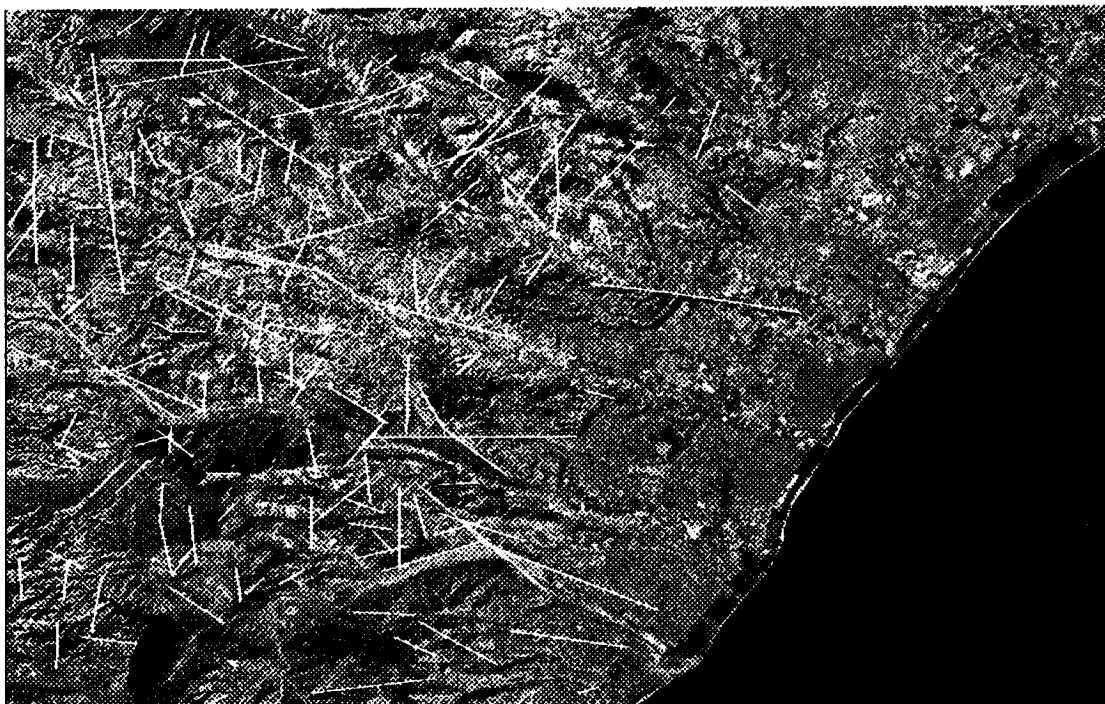


Fig.2 Landsat TM Lineaments Map

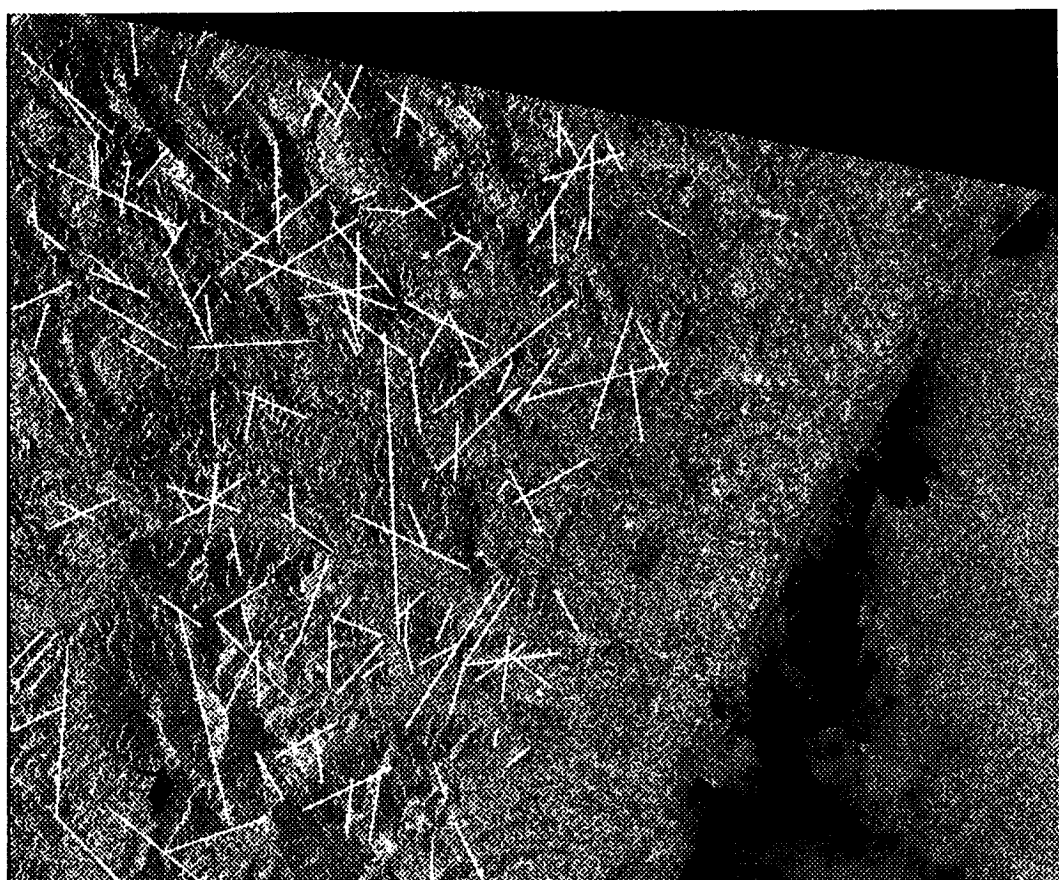


Fig.3 ERS-1 Lineaments Map

5.INTERFEROMETRY

The SAR Interferometric technique (INSAR) has been exploited in the past years taking advantages from the availability of reliable data. The ERS-1 FRINGE working group has demonstrated the feasibility of very accurate DEM's selecting as test areas to perform product validation Bonn (Germany), Matera (Italy) and Death Valley (USA) (ref.6).

The INSAR technique typically consists of two SAR antennae separated by a distance named Baseline. An interferogram is produced by interfering the back scattered microwave signal received from both antennae.

In the single antenna satellite, the Interferometric technique is "simulated" by using two images sensed in repeated pass over the same area. The altitude can be computed pixel by pixel by using phase unwrap techniques and satellite precise orbit parameters.

The ERS-1 SAR gives a unique opportunity to perform INSAR. Thanks to a very good orbit repetition, better than 1 Km, ERS-1 guarantees high quality interferograms.

In the framework of the interferometric activities and DEM generation we have planned to deploy a network of Corner Reflectors located with Differential GPS technique. Next we will be able to make a first correction to the available DEM acquired from the digital cartographic database (vector data) by IGMI (Istituto Geografico Militare Italiano) which is the most important source of precision DEM in Italy. After this "Ground Truth" initial phase, the interferograms produced starting from ERS-1 data, will be used to validate the INSAR technique and to produce new and more accurate DEM.

In order to produce high quality elevation data we have planned to integrate different methods:

- ERS-1 precise orbit will be processed at the CGS
- Multiple Interferograms will be used to avoid phase unwrap ambiguities and to improve the standard deviation of elevation
- Crossed Orbit Interferograms are planned to provide data where radar shadow and layover are present on images [2]
- Data set will be extended by using data coming from other missions (RADARSAT, JERS, etc.)

6.CONCLUSIONS

The activities until now performed demonstrate the successful use of ERS-1 data in benefit preoperational activities in sinergic use with others sensors.

Next step of the work will be the following:

- improve the data set with ERS-1 data from ascending pass
- geocode ERS-1 data using a more accurate Digital Elevation Model obtained from INSAR and GPS campaign
- geomorphological analysis of data set to study coastal and rivers dynamic.

7.REFERENCES

1. Ciaranfi N., Maggiore M., Pieri P., Rapisardi L., Ricchetti G., Walsh N. "Considerazioni sulla Neotettonica della Fossa Bradanica", CNR Pubbl. N.251 del Prog. Fin. Geodinamica, 1979; pp.73-95.
2. Benediktsson J.A. & al, "Conjugate-gradient neural networks in classification of multisource and very-high-dimensional remote sensing data", in Int. J. of Remote Sensing, 1993, vol.14,no. 15,2883-2903.
3. Hertz J., Krogh A., Palmer R.G., "Introduction to the Theory of Neural Computation", Redwood City, CA: Addison-Wesley, 1991.
4. Blonda P., La Forgia V., Pasquariello G., Satalino G., "A Modular Neural System for the classification of Remote Sensing Images", Proceed. of the Intern Conf. of Artificial Neural Networks, Sorrento, Italy, 26-29 May, 1994, 1173-117
5. Pasquariello G. Blonda P., "Multitemporal Remote Sensing Data Classification using Neural Network", in Proc XVIIth ISPRS Congress, Whashington, \$922--\$929\$, 1992.
6. Sanger T.D., "Optimal Unsupervised Learning in a Single Layer Feedforward Neural Networks", in Neural Networks, 2, \$459--\$473\$, 1989.
7. S.N.Coulson "SAR Interferometry with ERS-1", Earth Observation Quarterly n.40 ,April 1993 page 20-22
8. A.K.Gabriel R.M.Goldstein "Crossed orbit interferometry theory and experimental results from SIR-B", International Journal of Remote Sensing Vol.9 nr.5

CONTRIBUTION OF ERS-1 DATA TO GEOLOGICAL MAPPING IN DESERT AREAS ATACAMA REGION - CHILE

First results

G. Delpont*, J.F. Desprats*, E. Tidy, J.C. Prevot*, S. Chevrel*, C. King***

*** BRGM, BP 6009, 45060 Orléans Cedex 2, France**

**** CODELCO, Santiago, Chile**

ABSTRACT

The analysis of a radar ERS-1 image covering the desertic region of Atacama (North of Chile) leads to the following preliminary results, established in an operational technical context :

- two dimensional geometric processings carried out by a traditional way (ground control point, with reference to a topographic map) cannot solve the high geometric distorsions which affect the image,
- because of these distorsions the geological interpretation of areas with contrasted morphology is of poor benefit, especially when compared with interpretations coming from optical images like Landsat Thematic Mapper,
- among the filters used to eliminate the speckle effect, only the Frost one allowed to underline the major structures without too borrowing the details in the flat pediment surfaces,
- only the ERS-1 radar image revealed an original structural information in these surfaces : linear discontinuities appear at the surface of the pediment which correspond to important faulting affecting the bed-rock. The intense seismic activity could be the origin of these discontinuities.

1. INTRODUCTION

The more attractive results of radar imagery is known in equatorial and tropical climates, where the cloud cover precludes to the use of optical imagery. However specific interest of radar imagery on desertic climate areas appeared at several occasions and has been noticed by different teams (i.e. BLOM et DAILY 1983, REBILLARD et al. 1983, EVANS D.L. et al. 1992, CHOROWICZ et al. 1993, SCHABERT et al. 1993). One of the most famous example corresponds to the SIR-A image which allowed to catch a paleo-hydrographic pattern below sand cover in the Sahara desert of Algeria (MC CAULEY et al. 1986).

It seemed then to be interesting to search for the capability of the radar imagery to be used, in an operational approach, in such climatic conditions for geological purposes, such as mapping, lithological differentiation, structural setting, ... The two main objectives were to test the capability of radar for revealing lithologic features through sand cover sheet and its sensitivity to microtopographic surface variations related to structures and lithology

In the frame of this pilot project, the Atacama desert area (Chile) was chosen as a one of the test regions because of three simultaneous interests : various lithological and morphological contexts, important mining interest and active geodynamical context.

2. DESCRIPTION OF THE STUDY AREA

The study area, part of the Atacama region, is located in the north of Chile, at an altitude of 2500-4500m (fig. 1). It suffers a very dry climate characterized by an average precipitation of 70 mm/year.

The area is geologically constituted of volcano-sedimentary and sedimentary jurassic-cretaceous rocks intruded by recent granites and drowned by miopliocene pediment deposits, resulting from erosion-alteration processes.

Morphologically, the area consists roughly in north-south volcano-sedimentary rocky trends culminating up to 1000 m over the sub-horizontal surfaces of the pediments. These surfaces correspond to regs, notched by a recent regressive erosion.

It is to be noticed that this area as the whole Chile suffers frequent seismic movements due to the subduction mechanism of the Nazca Plate under the South American continent. This study will show its possible consequence on the radar perception of the structural elements.

Finally, the study area is characterized by a rich mining environment. As an example, can be cited the Chuquicamata copper mine, which is the biggest open-pit in the world, of which 700,000 metric tons of run of mine ore are extracted every day.

3. IMAGES AND PROCESSINGS

3.1. The Landsat Thematic Mapper (TM) image

The TM image is used there as a reference image for geological interpretation and ground localization because of its very good radiometric quality and the antiquity of the existant topographic maps.

The processings performed on this image consist in :

- a geometrical processing, using the topographic base maps of Chile (scale 1:50,000),
- a radiometric processing, to enhance the contrasts,
- a decorrelation stretching, calculated with the 5 first bands, especially to enhance the pediment surfaces and compare with the radar image.

3.2. The ERS-1 image

Only an original PRI descending image was used for the first step of this study because of the unavailability of the ascending one. The characteristics of the image are as follows : path 4478, row 4059, date 09 march 1993 (which corresponds to the end of the summer).

Various filtering processes were performed to reduce the speckle anomalies : Lee, Kuan, Map and Frost were successively tried and evaluated in a empirical approch. The Frost one, with a 9*9 window, gave the best results:

- on the areas caracterised by a contrasted morphology (mountaineous rocky trends), the Frost filter allows the best lithological differenciation, even if it remains very low, compared with the one of the TM image,
- on the areas caracterised by a non-contrasted morphology (pediment flat areas), the Frost filter allows to catch the main structures but all the details come out blurred.

The fine or low contrasted structures of these areas have been kept mixing the filtered image and the original image, the relative weight of 50%- 50% giving the best thematic result.

The image was then geometrically processed, with reference to the already processed TM image, because it was very difficult to catch the ground control points directly from the topographic base map and no DEM was available. The result is poor, particularly in hilly

and montaneous parts of the site due to the angle of incidence of the radar. For example in this case, a 2-4 pixels (25-50m) error were obtain for the lines and 13-16 pixels (160-190m) for the rows in the contrasted morphology areas.

Finally, a contrast enhancement was performed before the photo-laboratory processes.

4. IMAGE INTERPRETATION

The analysis and comparison between optical and radar images has been performed, before and after a ground survey focused on typical morphogeological targets, namely contrasted and non-contrasted morphology, where the results seem to have various levels of interest in term of geological mapping.

4.1 Areas with contrasted morphology

These areas correspond to the north-south rocky trends which are structuring the landscape. Because of the important geometric distorsions already mentioned, the following interpretation problems can be noticed :

- the homogenisation of the outcrop morphology makes the lithological differentiation difficult . All the mountain sides, lighted up by the satellite, are narrowed and bright, because of the high backscattering, while the opposite side is stretched, dark and seems to be constituted of chevron structures. Moreover, the hydrothermal altered areas, which are of major importance in mining research, are not distinguished of their environment.
- the trend of structures such as folds, faults and fractures, as interpreted from the image cannot be used directly because of the important geometric distorsions. A more accurate geometrical processing is needed before a thematic use and will require a DEM.

As a brief and severe conclusion, such an image does not present interest in arid climatic condition with contrasted morphology , compared with Landsat TM. This point has not been enough highlighted by previous works using SAR satellite data : without drastic geometric corrections, the images do not provide reliable structural information in contrasted morphology at medium and local scale (1:100,000; 1:50,000). However, the cost of such processings is not compatible with an operational approch.

4.2. Areas with non contrasted morphology

Theses areas correspond to the accumulations over the basement rocks of recent mio-pliocene pediment formations that preclude the perception of geological

information on the basement of this region. 2 main types of geomorphological features can be seen :

4.2.1. The surface units

On the surface of the pediments, the TM image shows different surface units characterized by different colours. They correspond to fans, the colours of which are depending on those of the original rock (sedimentary, volcanic, altered rocks, ...). The limits seen on the image are generally checked and well seen in the field.

On the same way, the ERS1 image shows different surface units characterized by different backscattering intensities, which evoke the same phenomenon. But the limits do not correspond systematically to those of TM image and moreover cannot be seen easily in the field. No visible variation in the distribution or stone size of the reg can justify these variations of backscattering. So, the explanation would require a fine textural and structural analysis of the pediment surface, requiring a dedicated and heavy investment, out of an operational work. Clear limits have been seen only once where the contrast of backscattering was strong.

4.2.2. The linear features

Numerous linear features, which have generally a very slight backscattering contrast and which for the geologist supposes they have a structural significance, can be seen on the image at the surface of the pediment (fig. 2):

- on the field nothing appears, at the surface of the pediments, that clearly justify the satellite information, except when cut gullies exist perpendicular or oblique to the lineament. Fractures can then be seen on the wall of the pediment formations. Some of them, the nearest of the surface, are materialized by cristalization of gypsum, due to the percolation caused by the superficial evaporation. Most of these fractures are similar in direction with the lineament trend, and their density tend to increase close to the lineament

- at depth, nearer the bed rock, faults, sometimes typical normal faults, can be seen, probable witnesses of a subsidting movement. In many cases, these faults cross the lithological limit between the bed-rock and the pediment formations.

In spite of these limited first results, the radar imagery brings an important contribution in the structural knowledge of the area, providing with additional informations where neither optical imagery nor field work can do.

5. HYPOTHESIS TO EXPLAIN THE RADAR OBSERVATIONS

Because of the seismic activity, which induces frequent movements of the existing faults in the bed-rock, the field observations lead to propose some hypothesis which remain to be established firmly during a next field work :

1. slight linear collapses can occur at the surface of the pediment, which could be magnified by the oblique illumination of the radar image,
2. the seismic effect could lead the natural evolution of the hydrographic network to an alignment of the water beds,
3. the seismic activity could have induced a progressive modification of the position of the reg stones,

These three possibilities, the effects of which can be cumulative, could induce a different backscattering and make the perception of the linear features possible .

6. CONCLUSIONS

In the region of Atacama (North of Chile), the preliminary study of a descending ERS1 image leads to the first following conclusions, relative to the interest of the radar image for geological purpose in desert climatic conditions, at a medium scale (1:100,000) :

- this interest seems to be very low in the case of a contrasted morphology, either for lithologic recognition or for structural interpretation, because of the high level of distortion of the image, processed with the software available at the moment, from an operational point of view,
- this interest seems to be low for contouring pediment units from the same point of view,
- this interest seems to be high or very high, in the case of a non contrasted morphology to reveal the bed-rock structural informations through the recent pediment formations, probably due to an important seismic activity.

7. NEXT STEPS AND PROSPECTS

The next step of this pilot project will be to try to elaborate optical andradar combined products in non contrasted morphology areas to be used for structural investigation

In the future, and to establish a more quantitative approach of the linear features highlighted only by the radar image, a second field work could be planned and combined with a structural geology study, because of the active geodynamic context.

ACKNOWLEDGEMENT

This article (scientific publication n° 94-041 of the BRGM) was prepared as a part of a scientific project financed by BRGM research funds and CNES SAR Aval program.

REFERENCES

- EVANS D.L., 1992. Current status and future developments in radar remote sensing. ISPRS Journal of Photo. and Remote Sensing, 47, 74-99.
- CHOROWICZ J., DEFFONTAINE B., HUAMAN D., PUBELLIER M., LUXEY P., RUDANT J.P.. Geomorphic objects detected by ERS1 SAR images in different geodynamic Contexts. 2nd ERS 1 Symp. Hambourg, Octobre 1993, 923-929.
- SCHABER G.G. and BREED C.S., 1993. Subsurface mapping with imaging radar in deserts of Africa and Arizona. In Thorweih and H. Schandeingeier (eds) Geoscientific Research in Northeast Africa, pp. 761-765.
- REBILLARD P. and EVANS D.L., 1983. Analysis of coregistered Landsat, Seasand ans Sir A images of varied terrain types. Geophys. Res. Lett., 10(4), 277-280.
- BLOM R. and DAILY M., 1982. Radar image processing for rock type discrimination. IEEE Trans. on Geosci. and Rem. Sens., GE-20, 343-351.
- MAC CAULEY J.F., BREED C.S., SCHABER G.G., MC HUGH W.P., ISSAWI, BAHAY, HAYNES C.V., GROLIER M.L. and ELKILANI, 1986. Paleodrainage of the Eastern Sahara : the radar rivers revisited. IEEE Trans. on Geosci. and Rem. Sens., GE24, 624-648.



Fig. 1 - Localisation of the study area



Fig. 2 - Chuquicamata Area Lineament only seen on ERS1 image (see arrows)

TECHNOLOGICAL RESEARCHES AND DEVELOPMENTS, REGARDING THE INTEGRATION OF SAR-ERS DATA WITH OTHER TYPES OF SATELLITE AND GROUND INFORMATION, AS WELL AS DETERMINING THEIR COMPLEMENTARITY, WITH APPLICATIONS OVER THE CONTINENTAL PLATFORM OF THE BLACK SEA, THE DANUBE DELTA AND THE SEISMIC ZONE VRANCEA; SOME CONTRIBUTIONS TO DATA CALIBRATION AND VALIDATION"

Nicolae OPRESCU (*), Florin SERBAN (**), Cora BRAESCU (**), Marius NECSOIU (**)

(*) Professor and Consultant, Technical University of Civil Engineering Bucharest - Remote Sensing Laboratory, B-dul Lacul Tei 124, sect.2, code 72302, Bucharest 38, phone/fax 0040/1-3128793, 40-0-3127780 and 40-1-6504222, E-Mail piso@roifa.bitnet .

(**) Drnd (doctoral stage) Eng. - Institute of Optoelectronics, Department of Remote Sensing, 76900, Bucharest, Magurele, phone/fax: 401-3124545, E-Mail fserban@roifa.bitnet .

ABSTRACT

The basic idea consists of intensive radiometric measurements, taken as system profiles over sample areas, with the Exotech 100AX radiometer (with Landsat MSS&TM filters) linked with a PC 486 computer with color display, for reducing to a minimum the number of satellite images needed; this aspect is of great importance for the East/European countries and, of course, for Romania also; that is, contributions to remote sensing technology, adapted to restricted means. The field and airborne radiometric profiles, taken at convenient times (seasonal data would be most convenient) must be positioned on airborne and satellite images (seasonal data base), using mainly differential GPS - kinematics mode; the data obtained on the profiles are extended over the area by using adequate algorithms and models.

The results obtained over the "great profile" over Danube Delta (fig. 3), covering characteristic ecosystems are very promising.

Focusing technological aims, referring to:

- Integration of the ERS-SAR data with other types of data, by registration and synergism and compatibilisation of these data;
- Assessment of the degree of complementarity between the whole of the data, together with the determining of the intrinsic dimensionality for different thematics;
- Drawing up and implementation of a specific LIS (Land Information System);

Are also presented: the complex radiometer, interfaced with the PC 486 and some results.

In fact, the present paper represents a part of the cooperation proposal with ESA, sent on 10.03.1994, in the frame of the ERS Announcement of Opportunity - Pilot Project Manager - Prof. N.Oprescu.

1. INTRODUCTION

We must mention that the present proposal is a rather ambitious programme for us, however it is based on rather well-grounded arguments:

- the Danube Delta and the coastal zone of the Black Sea, represent areas of high scientific interest; the Danube Delta represents the world's largest surface, compactly covered with rush; this interest grew because the Danube Delta was declared in 1990 a natural reservation of the biosphere;

- the hydrocarbons interests in the continental platform of the Black Sea are very high, these interests imply the intensive use of remote sensing, mainly based on SAR-ERS type recordings;

- we have a powerful hardware/software basis, as well as high qualified staff.

We must take into account all the remote sensing and conventional data, as well as the measurements made over the coastal zone of the Black Sea, the Danube Delta and the lower basin of the Danube, zone which became an extensive and partly intensive test-site (over 20 years of repetitive recordings - Landsat MSS and TM, SPOT recordings and also LFC and lately SAR-ERS-1 recordings; repetitive airborne recordings for over 40 years - in panchromatic, IR and colour, and colour IR; measurements with the Exotech 100AX radiometer); and also have in view the experience acquired in handling, processing and development of these data.

In fact, the present proposal, as a whole, is the continuation - on a new level and on a new basis - of the G-27940 agreement, concluded with NASA, on the theme: "Use of ERTS- LANDSAT data, for natural resources investigation in the lower basin of Danube and the Danube Delta/ Programme DaDelta/", which practically represented the beginning in remote sensing techniques for Romania /1/, in the '70 years, first by analogue means, next by hybrid means, and finally by digital means, including the establishment and functioning of a terrain remote sensing laboratory in the Danube Delta - 54 km, on the Sf.Gheorghe Danube branch.

2. AIMED OBJECTIVES AND EXPECTED RESULTS

- 2.1. New attempts for "speckle" type reduction (if not elimination);

- Further development of registration and synergism techniques and also for integration of the whole data and for compatibility;
- Further continuation of evaluation and development attempts for independent use of ERS data for land regions, by comparing the satellite data with "ground truth" data;
- Further attempts to estimate the complementarity of the ERS data provided by other satellites (SPOT, Landsat TM and MSS), airborne recordings in panchromatic, IR and colour IR, as usually, the ground truth comparison, by several different algorithms;
- The elaboration of the operational configuration between the radiometer Exotech 100AX, the portable PC and GPS plus air-photo or videography;
- Drawing up and implementation of a specific LIS and respectively the data base; LIS oriented towards the problematic of the continental platform of the Black Sea of the coastal zone, the Danube Delta and respectively towards the seismic zone - Vrancea;
- Per all the principal objective is the development of a pluri and interdisciplinary team, that will currently and constantly work for the proposed thematic.

2.2. The assimilation and development of specific principles and technologies for each of the proposed activities:
"Integration and technologies";
"Complementarity";
"Profiles";
"Danube Delta and the Black Sea".

- Contributions to the calibration/validation of the data obtained from the satellite and airborne recordings, and mainly from the ERS type recordings, by direct and also indirect methods.

3. TEST - AREA PRESENTATION

The area under investigation is very diversified: mountains, hills, plains, rich water network, lakes, delta, continental platform, marine zone, all having varied pedology and geology, respectively different ecosystems with different coverage: forest, pasture, land, crops, natural vegetation, and so on, including also the sensible

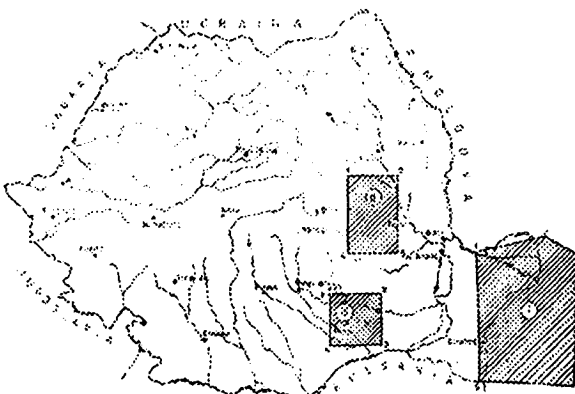


Fig.1 The selected test sites

seismic zone Vrancea (see fig. 1); there are also very large and homogeneous areas, as well as medium ones, which are very suited to be applied the segmentation process.

The test sites are named as follows:

Test site 1: Black Sea - Danube Delta

Test site 2: Vrancea - Bacau

Test site 3: Bucarest - Fundulea

4. DATA AND DEVICES USED

4.1. Airborne sequential recordings, taken over the last 40 years (in panchromatic, IR, colour and colour IR) as well as the airborne color IR images, which will be recorded in July - this year; these airborne recordings will be taken according to a well defined, systematic plan, thus each frame will cover a unit, at the 1:25000 scale;

4.2. Seasonal coverage by Landsat MSS and TM (for MSS beginning with the September 1972) - negative film and colour composite, as well as analogue and digital, periodical recordings, until 1981; also some SPOT and ERS recordings;

4.3. Radiometric measurements, take with the configuration of the system radiometer-the portable PC and GPS, shown in Fig.2 (airborne and field measurements), sys-

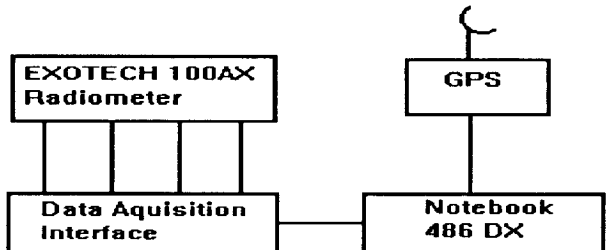


Fig.2 The link between the radiometer, PC&GPS

tem profiles;

The data acquisition interface has four analogue input channels which are linked with the four output channels of the Exotech radiometer. The radiometer channels correspond to the four MSS spectral bands and with appropriate filters could match the Landsat TM bands. The resolution of the analogue-digital converter is 8-12 bits and the sampling frequency is 20-100 kHz. The link with the PC is made by connecting the radiometer to one of the parallel interfaces, or to an extension of the data bus, same as for the GPS.

4.4. The satellite data used are:

Test site 1

Landsat MSS - 24/07/1975, Landsat TM - 20/08/1989,
 ERS-1 SAR - 27/04/1993 (PRI), ERS-1 SAR -
 06/07/1993 (PRI)

Test site 2

Landsat TM - 14/10/1989

Test site 3

Landsat TM - 29/03/1989, ERS-1 SAR - 30/03/1993,



Fig. 3 The test site 1 with the "great deltaic" profile

ERS-1 SAR - 09/06/1993, ERS-1 SAR - 13/08/1993

The ERS-1 SAR data used were Precision Image (PRI) processed to 3-looks and with a 12.5x12.5 m pixel size.

5. REGISTRATION - SYNERGISM

The registration and geocoding were first carried out between existing maps (topographic maps) and the Landsat TM data. It was produced by digitising (collect) ground control points - GCPs in the maps and in the TM data. 28 GCPs were used for the third order polynomial coefficient calculations, with cubic convolution as resampling method. The RMS error were 0.71 pixel. The relative accuracy of the geocoding was verified by scanning parts of the topographic maps and superimposing TM band 4 on them.

The geocoding of Landsat MSS data has been done in the same way, but with 16 ground control points and using second order polynomial coefficients. The RMS error was 0.91 pixel (30x30 m size).

The ERS-1 SAR PRI data registration was done in two steps. The image from the first date was chosen as reference. Due to the very good geometry, only translation in X and Y directions were necessary to achieve a satisfactory fit. Since the ERS-1 satellite has a very stable orbit, images from repetitive orbits can be registered with only few match points (e.g. strong scatterers such as single buildings).

Difficulties were encountered at the second step, during the ERS- SAR PRI data geocoding in identifying enough GCPs. For this reason, the topographic map/SAR image GCP collection was difficult despite of the topographic maps recently updated. Finally 18 GCPs were selected

with RMS error 0.73 pixel (second order polynomial coefficients).

6. DATA PREPROCESSING

Digital data were analysed in the Remote Sensing Laboratory of the Institute of Optoelectronics - Bucharest by using PCI software (EASI/PACE). The main aim of the digital processing was to produce enhanced optical data, SAR filtered data and optical/microwave combinations for visual interpretation.

6.1 SAR Filtering

The multiplicative noise (speckle) of a SAR image causes difficulties to visual perception and interpretation as well as in digital data analysis using established classification algorithms. Speckle is a system phenomenon and is the result of spatial variation of average reflectivity of the radar illuminated surface. For a high resolution radar, there may be useful scene texture which differs from the speckle. This is the case for example of forested zones in which the combined effects of radar illumination and tree shadowing create a rougher texture granularity than the speckle.

In a radar image we may find:

- zones where the only image texture is related to speckle that we may call regions "without texture" (extended homogeneous target);
- zones "with texture" that have spatial variations in scene reflectivity in addition to speckle.

Thus, in the case of "no texture" zones, it becomes possible to study the statistical distribution of the backscattered radar signal, which helps to estimate certain radar characteristics.

Generally, a homogeneous region with fully developed speckle is statistically described by only one parameter, its mean value, which is directly proportional to the backscatter coefficient sigma. However the image variation is also directly proportional to the backscatter coefficient.

Actually, the complex radar image of a homogeneous area can be represented by a narrow-band Gaussian process. The first order statistics of the received power are known to have an exponential probability density function. If noncoherent averaging is performed, then the probability density function for the power follows a gamma distribution [Frost, 1981]:

$$f_{P_r}(P_r(x_o, y_o)) = \frac{P_r^{N-1}(x_o, y_o) \exp\left[-\frac{P_r(x_o, y_o)}{\bar{P}_r/N}\right]}{(N-1)! \left(\frac{\bar{P}_r}{N}\right)^N}$$

with $P_r(x_o, y_o)$ = observed power at position x_o, y_o

$\bar{P}_r = E[P_r(x_o, y_o)]$ = the expected value of the observed power at position x_o, y_o

N = number of the independent images averaged by the sensor.

Conventional filters as mean, median, edge enhancement smoothing filters do not account for the scene

heterogeneity while adaptive filters (Frost, Lee, MAP) do. The results obtained using Frost filter on SAR image was considered satisfactory for the time being according with the aim of visual interpretation.

6.2. Visual interpretation of optical and microwave data.

The visual interpretation of the satellite data was performed using 1:100000 scale topographic maps. Complementary observations were done on digitally enhanced products.

The optical data (Landsat TM and MSS) were acquired during the dry season. For visual interpretation of vegetated areas were chosen different spectral bands combinations, as: TM 7/4/3 (RGB), which turned up to provide good information for visual classification. The 7/4/3 option shows water as blue to black, depending on its turbidity, predominantly green vegetation as green and rangeland as purple (pink), providing a more easily interpreted appearance.

Also satisfactory results were obtained from the Landsat TM 5/4/3 combination, especially for the moist zones delimitation and vegetation differentiation.

The ERS-1 images were acquired for the Test zone 1-one during a humid and the other during a dry season (27 April and 6 July). Visual interpretation of the raw data (with no filtering) gives very poor results, due to the "speckle" noise. On the filtered data (with a Frost adaptive filter of 7x7 pixels window) it is possible to delineate the humid and dry zones and also zones with high and low rugosity. The difference in spectral reflectance in the C band domain of the radar satellite ERS-1 helped us delineate reed and rush covered areas. In the April image there are only rush covered areas, and where reed grows, the soil is still bare, only with small roots. These bare areas give a high reflectance, appearing as light zones. In the July image the reed had grown and the respective areas will become darker than in the April image, but still lighter than the rush covered areas. The rush is humid and is darker than the reed in all periods.

6.3. Integration between optical and SAR data

Two methods of testing this complementary data sets were tested:

- in the first case a colour composite RGB as TM4/TM3/ERS-1-SAR or TM7/TM4/ERS-1-SAR was produced. The visual interpretation of the various colours enables a correlation between properties of the surface (roughness, moisture level) and its response on microwave/optical data.

- in the second case, the method for merging multisensor image data, using an Intensity/Hue/Saturation (IHS) transformation was applied. The TM 2/5/7 false colour composite was transformed from the RGB colour space into the IHS colour space, where the intensity component was substituted by the April SAR image data (Fig. 4). This new image was transformed back in the RGB colour space, for displaying. The main advantage of this method is that it combines radar backscattered values with spectral information contained in three optical bands. Classi-

cal image interpretation can be applied, e.g.: bright reddish colours correspond to high backscatter (rough surface) with dense vegetation, dark ones to low SAR backscatter (smooth surfaces), respectively.

7. Further developments

- to develop new methods and algorithms for speckle reduction;
- to develop inversion algorithms, this could be done using a combined experimental and theoretical approach:
 - > intercomparison of available data sets in order to determine statistical algorithms with their associated validity domains,
 - > development/improvement of theoretical models to interpret the increasing number of experimental data,
 - > developments of inversion models and algorithms which can be general, regional or even site and time dependent, according to the required uncertainties on the soil moisture content estimates;
- to define future instrument for soil moisture retrieval and monitoring with reduced effect of surface roughness and vegetation cover.

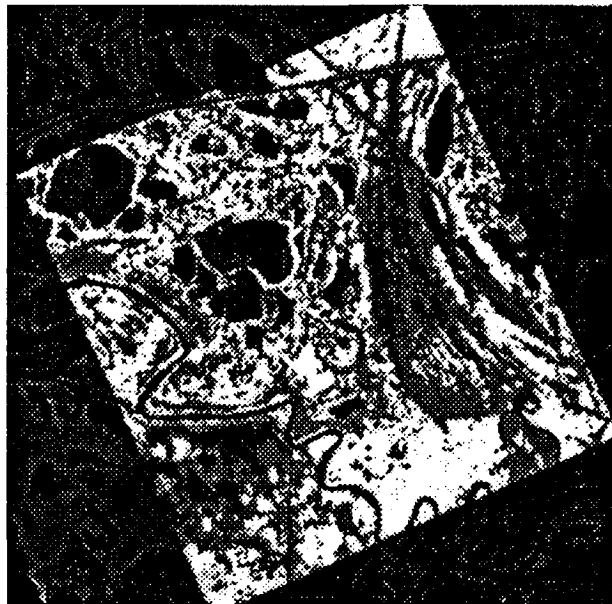


Fig.4 RGB-IHS-RGB Transform using TM 2,5,7 & ERS-1-SAR

8. References

/1/ "Use of the Landsat data for natural resources investigation in the lower basin of Danube and Danube Delta" Agreement SR Nr.27940 with NASA; principal investigator Prof. Nicolae Oprescu, Type III Report (Final Report, September 1977);

/2/ Oprescu, N. "Some results obtained in natural resources investigation in the lower basin of Danube and Danube Delta, using remote sensing technologies adapted to the case of restricted means", International

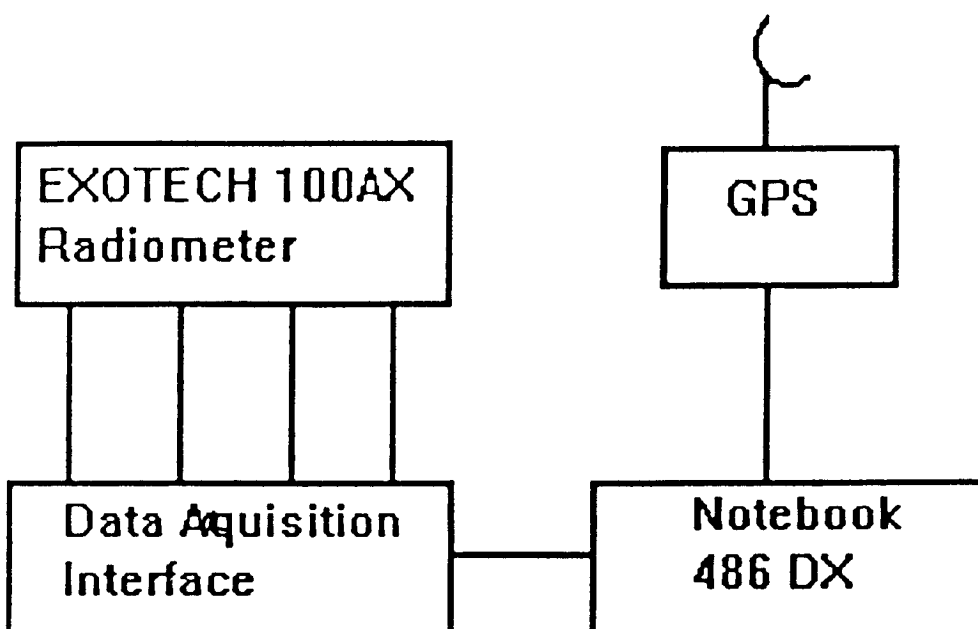
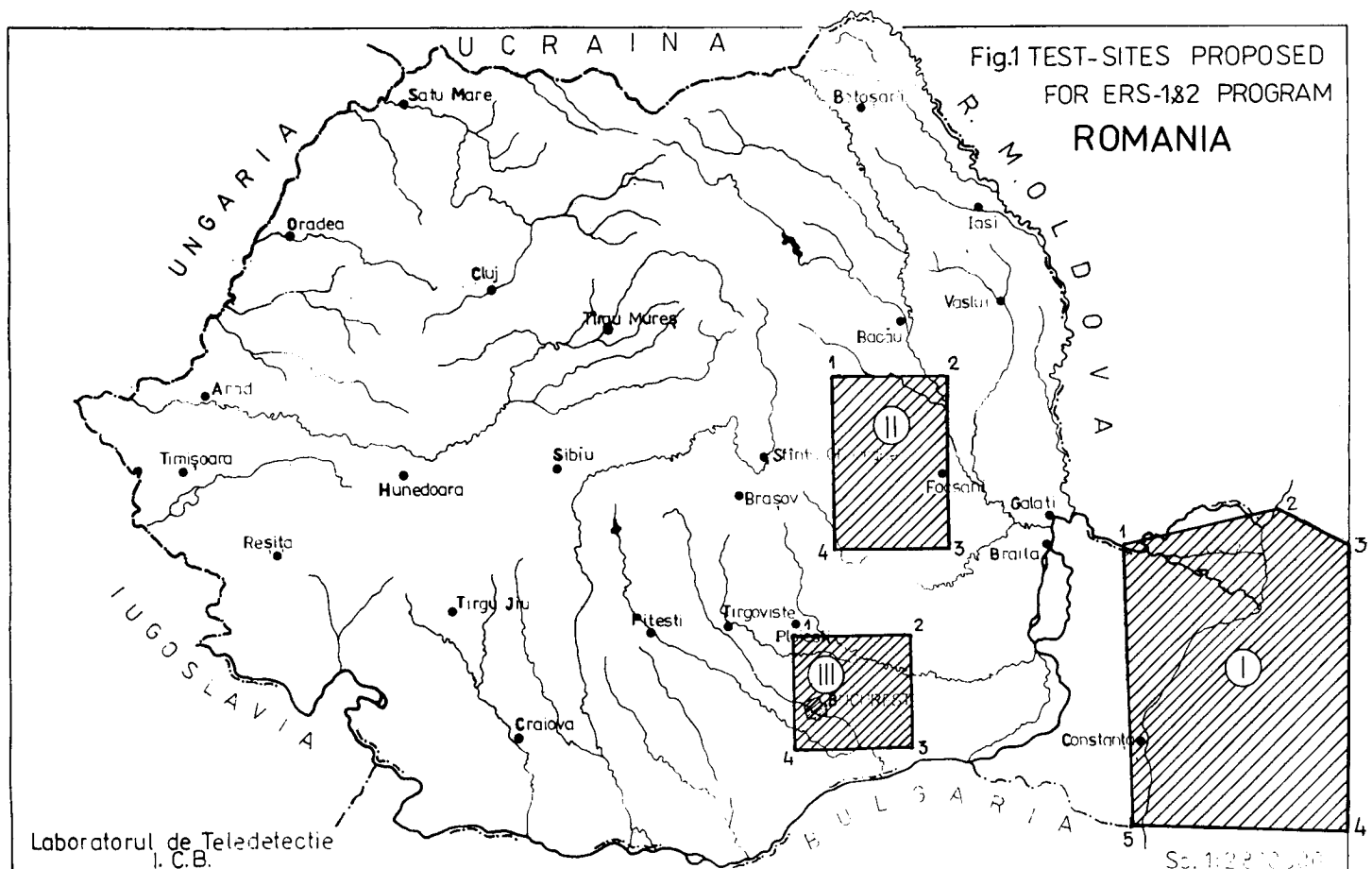
Conference "Earth observation from space and managements of planetary resources" - Toulouse, 6-11 March 1978;

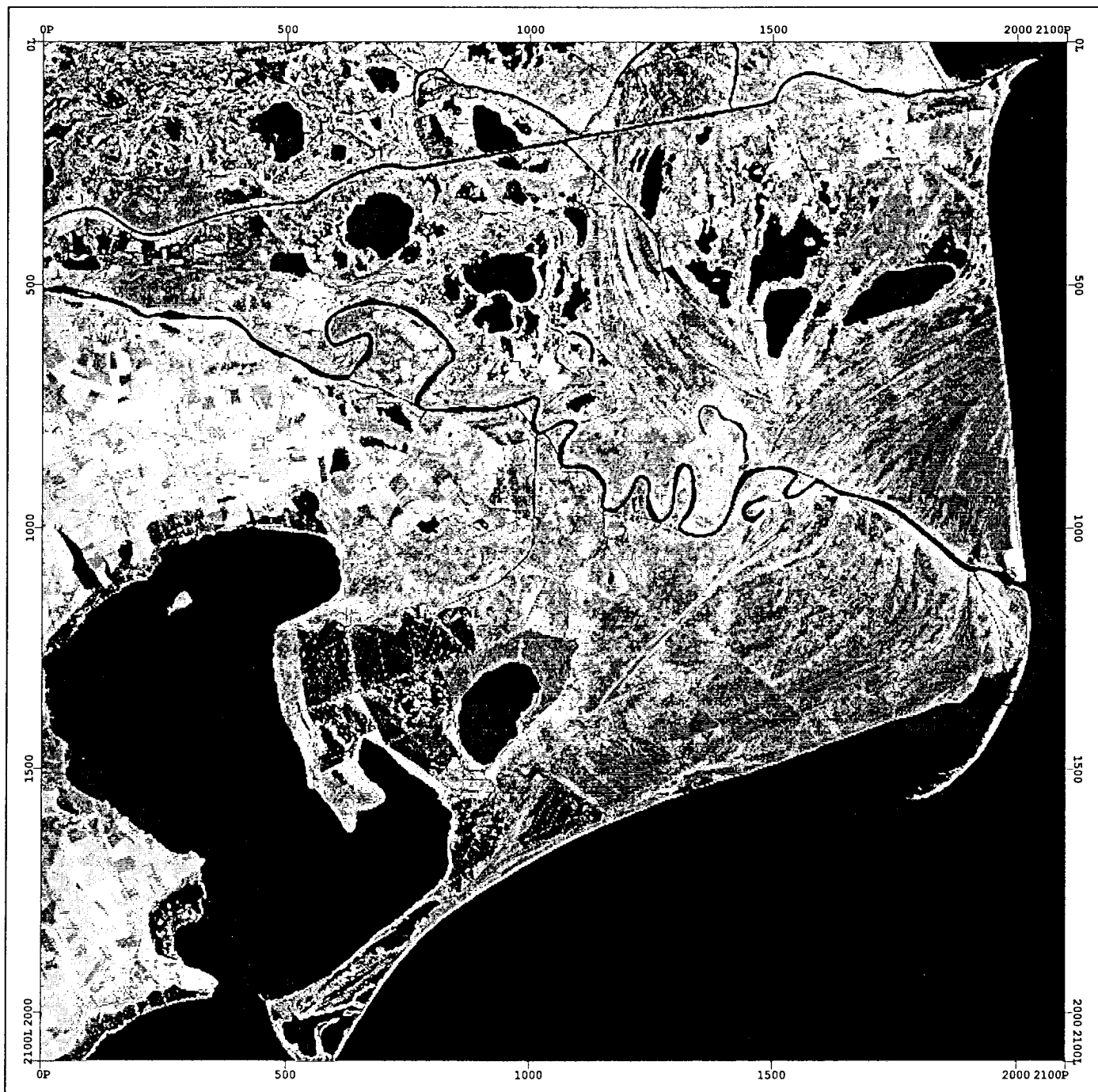
/3/ Oprescu, N.; Serban, Fl.; Badea, Al.; Craciun, M. "Romania case study: use of ERS-1 SAR data for land-use monitoring and for soil moisture assessment; contributions to monitor the privatisation process in territorial profile", ESA/FAO+EEC/Telespazio workshop "Use of ERS-1 SAR data for agriculture, forestry and environ-

ment applications in Central and Eastern Europe" - ES-RIN, Frascati, Italy, 8-12 November 1993;

/4/ J.F.Dallemand, J. Lichtenegger et al, ERS-1 SAR and optical data for land use/land cover mapping, Proceedings of the Second ERS-1 Symposium, 11-14 October 1993, Hamburg, Germany

/5/ Victor S. Frost, Josephine Abbott Stiles et al., A model of radar images and its application to digital filtering of multiplicative noise, IEEE Trans., 1982.





DANUBE DELTA AND RAZELM LAKE

b/w img.from TM7/4/3 combination (Aq. 20/08/89)

1:370 000 Scale

Pixels 500 0 500

PCI

NATURAL RISKS EVALUATION BY REMOTE SENSING : LINEAMENTS RESEARCH IN THE
PASTAZA BASIN (ECUADOR).

Pierre Ozer, Yves Cornet, *Alonso Moreno and André Ozer

Laboratoire de Géomorphologie et de Géologie du Quaternaire, Université de Liège,
Place du 20 Août, 7, B-4000 Liège (Belgique) Phone: +32 41 665335 Fax: +32 41 665722.

* INECEL-UMASE
Av. 6 de Diciembre 2427 y Av. Orellana - Casilla 565 - A y 9076 - Suc. 7 - Quito - Ecuador
Phone: +593 2 463947 ; Fax: +593 2 464058

Cette publication a été réalisée dans le cadre du "Programme de recherche scientifique dans le domaine de la télédétection spatiale - deuxième phase", pour le compte de l'Etat belge et de l'Agence Spatiale Européenne.

1. INTRODUCTION

This paper presents the preliminary results of the PP2B7 Pilot Project of the ESA which is supported by the SSTC-Belgium (Services fédéraux des affaires scientifiques, techniques et culturelles) and facilitated for the field checks in Ecuador by a convention with the INECEL (Instituto Ecuatoriano de Electrificación). The study of natural risks and especially the localisation of active faults in the Pastaza basin in Ecuador are data of the highest importance for the elaboration of the safety reports for two hydroelectric dams that have been built and a third that has been proposed. As researches by traditional optical remote sensing methods (like LANDSAT and SPOT) are difficult because of the intense cloud cover, SAR data's of ERS-1 entitle us to reach this goal. The image used is the December 15 1992 geocoded SAR of ERS-1, sensed in descending phase, which is the first -and so far the only one- satellite image of this sector of Ecuador without -of course- any cloud cover.

The other aim of this research is to make a comparative study using different scales which are:

- SAR of ERS-1 which gives a synoptic view of all the area,
- more detailed view using aerial photographs (1:60 000 scale),
- local in situ observations.

2. GEOLOGICAL AND STRUCTURAL BACKGROUND

The Ecuadorian territory is traditionally divided into three physiographical longitudinal zones as showed on Figure 1 [Ref. 1]:

- the Coastal plain,
- the Central Mountain Belt or Sierra,
- the Amazonian platform.

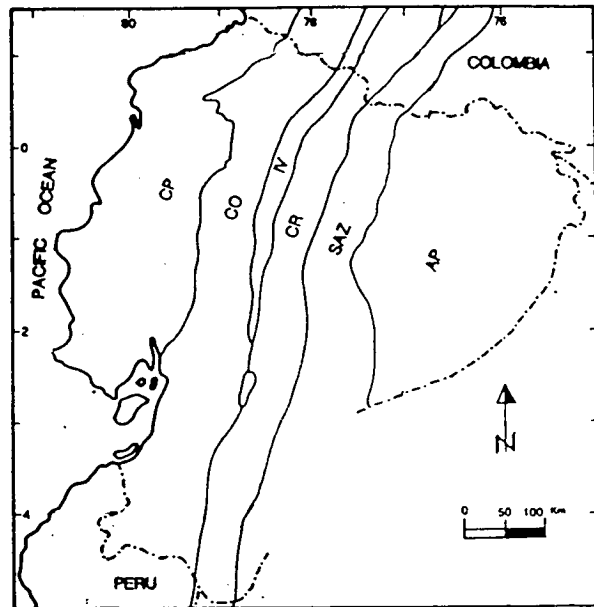


Figure 1: Physiographic map of Ecuador. CP: Coastal Plain; CO: Cordillera Occidental; IV: Iteranide Valley; CR: Cordillera Real; SAZ: Sub-Andean Zone (from Tibaldi A. and Ferrari L., 1991).

The Sierra, where this research is led [Figure 2], represents the Andean chain, due to the collision and subduction of the Nazca Plate under the South American one, characterised by two parallel ranges - the Cordillera Occidental and the Cordillera Real - divided by a depression known as the Inter Andean Valley.

The Cordillera Real is constituted by a magmatic and sedimentary metamorphosed rocks belt extending from Colombia to the Peru border. Those metamorphic rocks are considered to be Precambrian in age.

The Inter Andean Valley represents a zone of suture between the two cordilleras. Many Quaternary and still active (like the Tungurahua volcano which last eruption was in 1916) stratovolcanoes forming the highest peaks of the

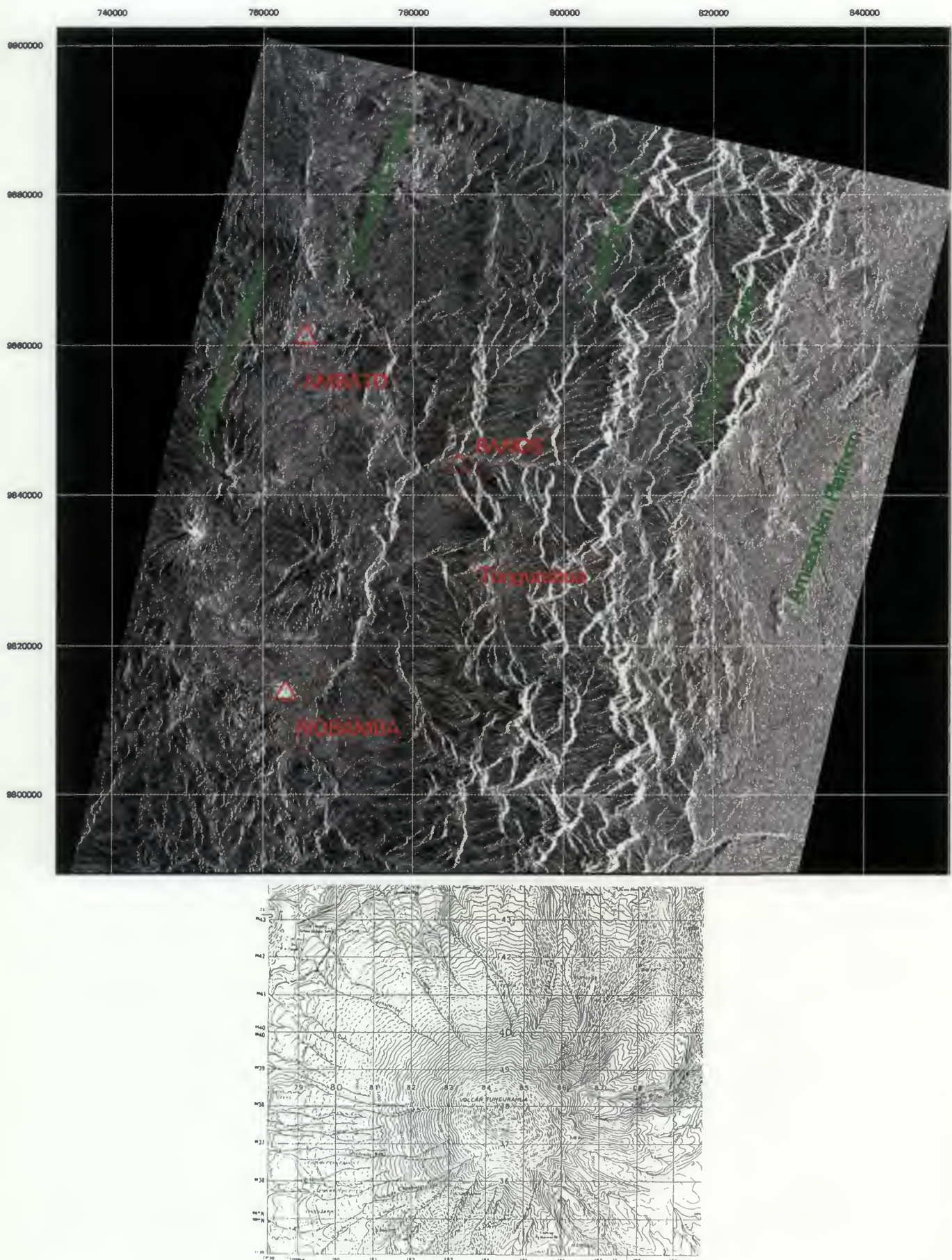


Figure 2: A.) SAR.ERS1.GEC image resulting of the stitching of two frames - DSC 7413/3627 and 3645 sensed the 15. december 1992 - and of a speckle reduction processing (application of a 5×5 sigma filter); location of the main physiographic zones. B.) Topographic map of the Tungurahua located south of Banos showing the geometric distortions on the SAR image (layover - foreshortening).

northern Andes are characterising this zone. They are responsible of the complex geological environment composed by undifferentiated basal, volcanic and volcano-sedimentary deposits filling the Valley [Ref. 2].

The principal stress direction for recent faults has been described as an East-West compressive system [Ref. 3 & 4]. In the Inter Andean Valley, N-S and NNE-SSW lineaments with normal oblique motions are widespread. The feature of the Cordillera Real is a marked family of lineaments with an overall trend of N 30°E [Ref. 1 & 4].

But this is just a basic information that we have to deal with, otherwise, it is important to mention that the major part of the territory studied does not have any topographical, geological or lithological map cover. The ERS-1 document thus allows us to detect a significant number of lineaments and so to complete the knowledge of the neotectonical context of this area at a regional scale.

3. METHODOLOGY.

The first step of the image processing methodology consisted in the stitching (mosaiking) of the two frames which cover the studied area. Unfortunately, the two GEC frames have been geocoded on the basis of different height's reference. The overlapping zone in which we choiced several ground control points gave us the opportunity to adjust a first order model. This model has permitted the georeferencing of the southern frame in the same reference systems than the northern one. After this first step, a sigma 3 x 3 filtering has been applied to get a better contrast, we faced huge distortion problems due to the steep slopes of the Andes. The best example would probably be the volcano Tungurahua's case [Figure 2] which is represented as a triangle with a curvilinear base on the SAR image when it is supposed to be a perfect circular volcano. On the image, the top of the volcano is displaced of 3,5 km east from its real position.



Figure 3: Example of the full resolution (1024 pixels x 1024 pixels) digitizing of lineaments on the SAR image in the zone of Baños using two different directional filters - compass north (red) and compass east (blue).

The second problem we had to resolve was the highlighting of the lineaments positioned on the SAR image. Some directions are favoured by the SAR system and others -perpendicular to the track- are much less visible. For example, in the Baños area, lineaments have been digitised considering strait lines -as done on optical

images- [Figure 3] and the graph representing the preferential directions of the lineations in relation to their length shows clearly two modes and a loss in the N 80-100°E direction [Figure 4]. Thus, this minimum has no geomorphological significance. So, a lineament will be defined on a SAR image

by some strait lines as well as by the succession of V shapes.

The lineament network drawn on the SAR image results of its analogical interpretation as well as on the aerial photographs. The methodology consists in digitizing the lineations on the SAR image and to see what they are corresponding to on the aerial photographs interpretation. Often, the lineaments detected on the SAR document are not known on the aerial photographs because of the scale difference. To separate active faults from other lineaments, field checks have been necessary. And this is not an easy thing to do because steep mountains, dense vegetation and bad climatic conditions make of

the Ecuadorian Andes a particularly inaccessible region.

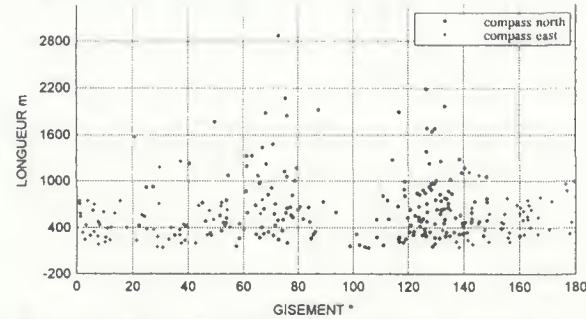


Figure 4: Scatterplot of the lineaments digitized on the SAR image in the zone of Baños (Figure 3) in function of their length and of their direction.

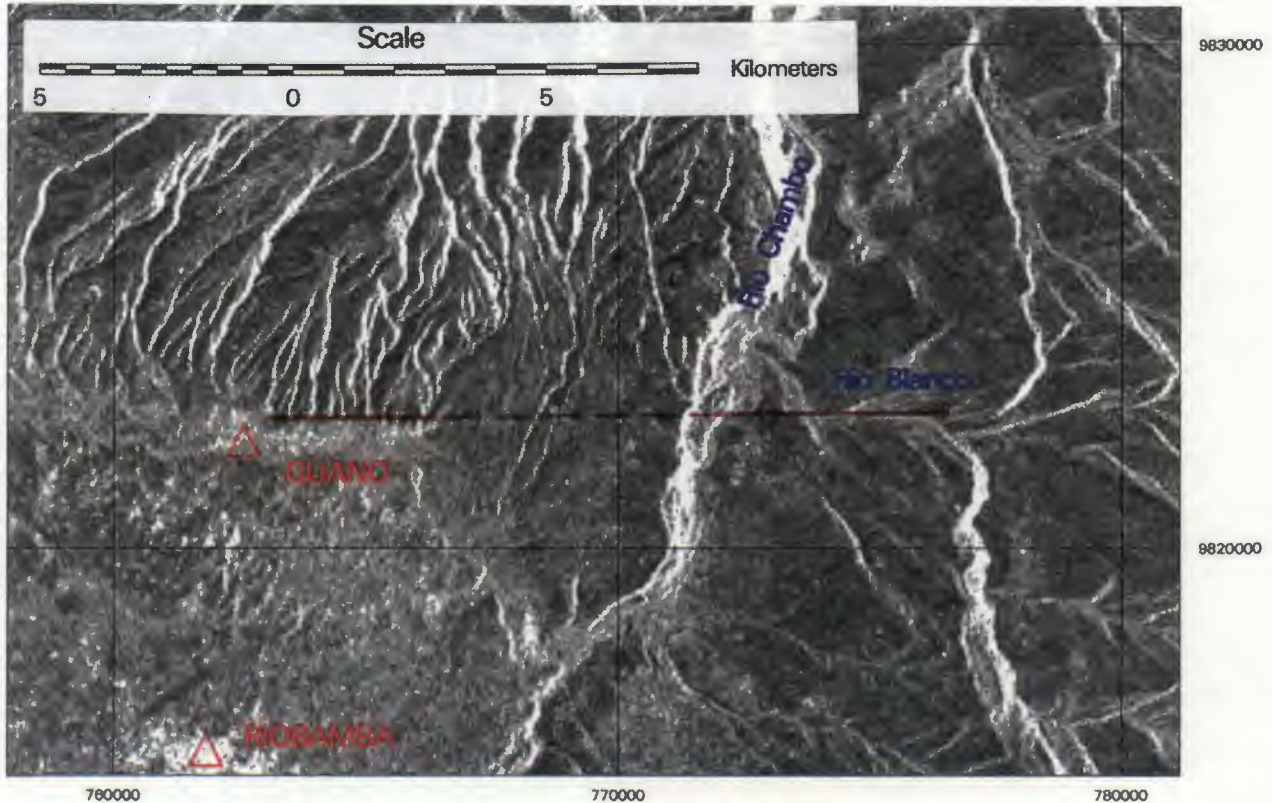


Figure 5: The extension (red) to the east (along the rio Blanco) of the lineament corresponding to the Guano fault is visible on the SAR image.

4. CASE STUDIES

4.1. Penipe's fault.

Studying the well known Guano's active fault on the SAR image of ERS-1, our attention has been directly focused on the east side of the Rio Chambo, where we suspected a very clear extention of that fault (Figure 5).

The field checks have confirmed that hypothesis and three outcrops along this lineament are proving that it behaved like an active fault during the Quaternary.

Figure 6 shows a clear fracture in some Holocene post-glacial deposits. This fracture has been filled up by fine sediments and its direction is clearly W-E. Many broken pebbles can be noticed in the same section, they are an other evidence of successive compressions.

Figure 7 shows another outcrop characterised by successive quaternary volcanic deposits that has been displaced of more than three meters. A close look on this section shows many other fracturations which could give evidence for other events of less importance.

Mesuring the fracturation plans of some metamorphic rocks, a W-E direction of the shiftings -as showed on figure 8- is clearly highlighted.

So, the ERS-1 information completed with field observations allows us to extent the Guano's fault of 15 Km further to the east.



Figure 6: Holocene post-glacial deposits containing broken pebbles and the fracture filled with fine sediments.



Figure 7: The evidence of a fault in quaternary volcanic deposits near Penipe.

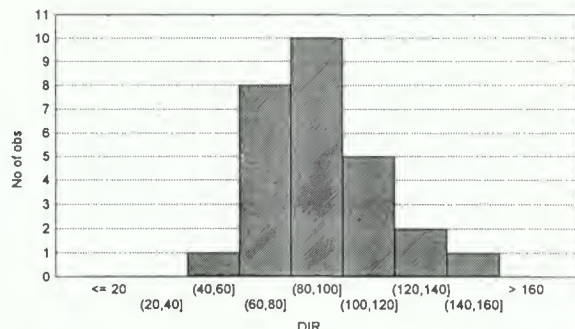


Figure 8: direction of the fracturation planes mesured in the metamorphic rocks.

4.2. The Baños's fault.

After ERS-1 investigations in the area of the Rio Pastaza, it was proposed that the valley of the river itself was underlining a huge lineament passing all the way through the Cordillera Real from west to

east. But, according to a tectonical study realised before the construction of the Agoyan dam for the INECEL [Ref. 4], this would not be an active fault and not even a lineament. Never the less, consulting data about earthquakes occurred in Ecuador during the last fifty years [Ref. 5], it is obvious that this zone has been moving many times along this lineament.

5. CONCLUSION

In conclusion, the SAR image of ERS-1 is, until now, the only way to realise a regional complete cartography of the lineaments and, after in situ surveys, active faults of this not well known area of Ecuador.

The results of this study will surely help to determine the best site for the dam that has been proposed.

6. REFERENCES

1. Tibaldi A & L Ferrari 1991, Multisource remotely sensed data, field checks and seismicity for the definition of active tectonics in Ecuadorian Andes, Int. J. remote sens., 12 (11), 2343-2358.
2. Barberi F, M Coltellini, G Ferrara, F Innocenti, J M Navarro & R Santacroce 1988, Plio-Quaternary volcanism in Ecuador, Geol. Mag., 125 (1), 1-14.
3. Ego F, M Sebrier, A Lavenu & A Eguez 1993, Quaternary state of stress in the northern Andes and the restraining bend model for the Ecuadorian Andes, Second ISAG, Oxford (UK), 21-23/9/1993, Ed. ORSTOM, Paris, 89-92.
4. Winter T 1990, Mécanismes des déformations récentes dans les andes équatorielles, Thèse, Université de Paris-Sud - Centre d'Orsay, 167 p.
5. Woodward and Clyde Consultant 1981, Investigaciones para los estudios del riesgo sísmico del sitio de la presa Agoyan, INECEL, Quito.
6. Ocola L 1984, Proyecto de sismicidad andina (SISAN). Catalogos sísmicos: República del Ecuador, Instituto geofísico del Perú - Geofísica aplicada, Lima, Perú, 152 p.



ERS SAR DATA AS A TOOL FOR LANDFORM & LINEAMENT IDENTIFICATION IN PREVIOUSLY GLACIATED AREAS

Chris D. Clark and Jane K. Knight

Department of Geography, & Sheffield Centre for Earth Observation Science,
The University of Sheffield, Sheffield, S10 2TN, United Kingdom.
phone: (+44) 742 824749, fax: (+44) 742 797912
phone: (+44) 114 282 4749, fax: (+44) 114 279 7912 after 16 April 1995

ABSTRACT

This paper describes the context, objectives and initial results of a project that aims to improve our ability to extract useful geomorphological information from ERS-1 SAR data. It focuses on previously glaciated areas covering a range of terrain types, some drift covered and some bedrock. The application realms that it seeks to address are: for reconstructing the behaviour of former ice sheets; lineament identification and mapping; and for mineral exploration.

Objectives of the project include investigation of geomorphological targets in relation to backscatter, and development of the optimal techniques for both photointerpretative and automated methods of information extraction. Performance of these SAR-based techniques will be assessed relative to methods utilising optical/IR imagery.

The imagery is proving excellent and beyond our expectations for identifying and mapping glacial landforms. We are able to identify individual drumlins and subtle patterns within the subglacial bedform suite and have already discovered hitherto unknown evidence of former ice flow.

1 INTRODUCTION

This paper describes the context, objectives and initial results of a project that aims to improve our ability to extract useful geomorphological information from ERS-1 SAR data. The European Space Agency have supplied the project [“ERS-1 SAR data; a tool for landform analysis in previously glaciated areas” PP2-UK8] with over 90 ERS-1 SAR images under their pilot project scheme. The location of images are documented in table 1.

Area	Latitudinal Range	Longitudinal Range
Ungava Peninsula	52° N to 62° 30' N	79° 30' W to 65° W
Baffin Island	62° N to 66° N	78° W to 65° 30' W
Ireland	53° 12' N to 55° 15' N	10° W to 5° 20' W
Finland	62° 50' N	30° 40' E
Athabasca, Canada	59° N	106° 54' W
Boyd Lake, Canada	61° 15' N	103° 42' W
Vatnajokull, Iceland	63° 50' N to 64° 25' N	17° 44' W to 15° 36' W
Settle/Sedburgh, England	54° 17' N	2° 39' W

Table 1: Table showing locations of ERS-1 SAR imagery

Approximately thirty per cent of the Earth's land surface has been previously glaciated, including most

of Canada and Scandinavia, and parts of northern Europe as well as many mountain ranges and their adjacent lowlands. Large parts of these areas, such as arctic and sub-arctic Canada and Eurasia, remain poorly explored and mapped. The project aims to investigate, develop and evaluate appropriate image processing methods for ERS-1 SAR data of such areas, and to develop and evaluate automated feature detection and photo-interpretative methods to facilitate the extraction of geomorphological information.

A major emphasis of the project is on lineament detection. Lineaments are defined here as terrestrial linear features of a geomorphological and geological nature. Bedrock geological structure such as faults, joints and fold patterns are included, and of especial interest are lineaments formed in drift (superficial sedimentary deposits). These latter features include landforms such as drumlins, flutes and mega-lineations formed by the activity of over-riding glacial ice in the last glaciation.

From a theoretical stand-point SAR should be the most promising form of remote sensing for the identification of lineaments as they are often expressed as subtle morphological forms. These should be better detected by slope and textural parameters, which radar backscatter is particularly sensitive to, rather than by spectral differentiation related to cover type which is the predominant means by which optical/IR sensing operates.

2 APPLICATION CONTEXT

There are three main application realms that this project addresses:

Reconstructing the complex dynamics of former ice sheets:

The last North American Ice Sheet covered most of Canada and part of the United States. Its dynamic behaviour is of great importance as it was a major component and modulator of long term climate change (10,000 to 100,000 years). The behaviour of this ice sheet (i.e. its flow directions, margin positions, changes in geometry etc.) is partially recorded in the glacial geomorphological evidence that remains scattered over the Canadian Shield. Identification and mapping of these landforms using SAR data can thus provide a methodology for reconstructing the ice sheet's dynamics.

Lineament identification and mapping:

Ground-based surveys find it hard to detect large-scale lineaments, whereas they are often readily visible on satellite imagery. In addition to the glaciological application outlined above, bedrock lineaments can be extremely important in determining the tectonic history of a region and in locating zones of mineralisation.

Mineral exploration:

When lineament detection and mapping by SAR is applied to glacial lineaments in drift, it can lead to a re-evaluation of ice flow history which has important implications for mineral prospecting. Erosion and transport of bedrock by the activities of former ice sheets has resulted in an extensive layer of sediment (drift) draped over the landscape. Tracer deposits of important minerals (uranium, gold, diamonds etc.) found in these sediments must have had a source rock in the up-ice direction, and so a knowledge of ice flow history should assist in identifying the source rocks.

3 POTENTIAL OF SAR AS A GLACIAL MAPPING TOOL

Traditional methods for mapping glacial landforms involve intensive fieldwork often combined with the use of aerial photography. More recently advances have been made using satellite imagery. A principal advantage is one of scale in that it is possible to map extremely large areas and to be able to interpret ice dynamics on the scale at which they operated (100-1000's km's). Using mainly Landsat imagery, Punkari [1] was able to reconstruct large-scale ice dynamics in Finland and an adjacent part of Russia, and following from Clark's mapping of ice flow landforms for most of the area of Canada [2], a radical re-interpretation of the dynamics of the former North American Ice Sheet was produced [3,4]. Remote sensing made these developments possible by means of the ability to map extremely large areas and obtain comprehensive coverage, and through the ability to observe and map hitherto undetected landform elements [5].

Landsat data however, whilst being relatively easy to process and interpret, is not the ideal medium for detecting and mapping glacial landforms. Ford [6] demonstrated that SEASAT imagery was far superior for detecting drumlins in Ireland and a range of other glacial landforms in Alaska. The Canadian Centre for Remote Sensing operated an airborne C-Band SAR imaging system to permit the development of image processing and analysis techniques in preparation for the launch of ERS-1 and Radarsat. Graham and Grant [7] used this imagery of an area of central Newfoundland for the purposes of geological reconnaissance. They reported excellent capabilities in identifying certain glacial landforms, in particular for hummocky and rogen moraine and ice flow lineaments. They regarded the imagery as providing a better tool for glacial mapping than aerial photography in spite of the inferior spatial resolution of the radar data. Visual tex-

ture analysis revealed that boulder fields and stony tills could be discriminated which permits identification of surface erratics, and thus has important implications for mineral exploration. The viewing geometry and advantage of imaging with two orthogonal illumination directions is different to that of ERS-1 data, but the potential of radar data is clearly indicated.

4 OBJECTIVES

The overall objective is develop an optimal methodology for the extraction of glacial geomorphological and lineament information from ERS-1 SAR data. To inform this approach requires an understanding of the properties of the geomorphological targets and how they give rise to the radar backscatter, and this is therefore an important part of the research.

The project runs in parallel with two application projects which utilise the results as a basis for reconstructing the dynamics of the Ungava sector of the last North American Ice Sheet, and selected sectors of the last British and Irish ice sheets.

5 OUTLINE OF METHODOLOGY

This can be divided into 6 sections which can be distinguished in terms of approach, although they are interdependent and lead to a common goal:

Properties of geomorphological targets.

The main interest is in understanding how slope changes that describe a landform are recorded in the backscatter signal, and in assessing how the along-range variation in incidence angle affects this. On relatively flat terrain simple relationships between texture and backscatter will be sought as a means of assessing the utility of using the SAR data for distinguishing between drift and bedrock and for delimiting the surface extent of glacial deposits.

Development of optimal methodology.

Using a number of test sites for which ancillary information is available in the form of aerial photographs, field maps, and Landsat data, the SAR images will be processed by a variety of methods to explore how their information content can be improved. Quantitative and visual qualitative assessments of their utility will be made. As feature extraction is to be achieved by both photo-interpretative and automated means it is anticipated that different processing methods will be necessary for each.

- a) optimal image enhancements; performance testing of speckle reduction and edge and texture filters to determine the best for visual interpretation (which will be scale dependent) and for automatic feature extraction. Assessment of optimum contrast stretching and resampling techniques.
- b) data fusion experiment; different methods of fusion of SAR and Landsat data will be explored to determine if extra utility is yielded by this approach.
- c) SLC versus PRI experiment; for a well known test site at which landforms are known to exist at and

beyond the resolving powers of ERS-1, single look complex data will be processed and analysed to ascertain the potential resolution benefit in comparison with a 4-look precision image.

Assessment of landform detectability and bias

Realistic limits of detectability of landforms and lineaments will be assessed in terms of scale/resolution and orientation/illumination direction. This is to include use of both ascending and descending path images of the same area.

Photointerpretation

Optimum methods for visual analysis and mapping will be assessed. Criteria for landform identification and a picture library will be assembled.

Image segmentation

Automated methods of image segmentation will be evaluated and developed with a particular focus on techniques for linear feature detection.

Relative performance of SAR against other data.

The relative merits of mapping from ERS-1 SAR data against Landsat MSS and TM, aerial photographs and field mapping will be assessed.

6 INITIAL RESULTS

SAR-Landsat comparison.

For test areas in northern England, Canada and Finland coincident SAR and Landsat TM and MSS images have been acquired in order to evaluate their relative performance and to assist in developing SAR-based interpretations. The northern England SAR image contains a wealth of glacial lineaments that are relatively easy to detect and map, which is in contrast to the

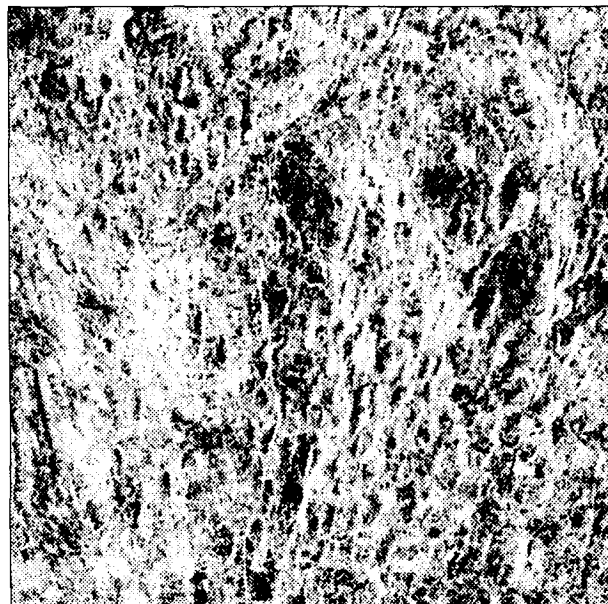


Figure 1: Subset of ERS-1 SAR image of northern England. The 'blister-like' manifestations visible in the image are drumlins formed by overriding ice flow from the north. Radar illumination from the right. Image is ca. 20 km wide.

TM image in which few of the landforms are visible. Figure 1 displays a SAR image of the same area as the TM image in figure 2, in which the difference in feature recognition is outstanding. It must be recognised however, that if TM images are acquired in winter when solar elevation is low, then the same kind of topographic enhancement is apparent. Greenbaum et al [8] demonstrate this capability for identifying glacial landforms using a TM image acquired in winter. The problems of acquiring cloud free winter TM images makes this an impractical solution for many areas. In addition the SAR imagery has the benefit of a choice of illumination directions.

Speckle reduction

A pilot study evaluating the relative performance of speckle reduction techniques has been conducted. For a small area of drumlinised terrain in northern England the following filters were applied using various iterations and kernel sizes: mean, median, local region [9], local statistics [10,11] and sigma [12]. Evaluation of the relative performance of these operations was conducted by visual qualitative assessment and by quantitative methods using measures of signal-to-noise ratio, edge strength and edge preservation [13,14]. For photo-interpretative use the local region filter was found to be the best as it was able to preserve edges whilst reducing speckle noise more effectively than the other filters tested. Further investigations of speckle reduction will include more filters and performance evaluation incorporating the use of segmentation algorithms as a measure of effectiveness.

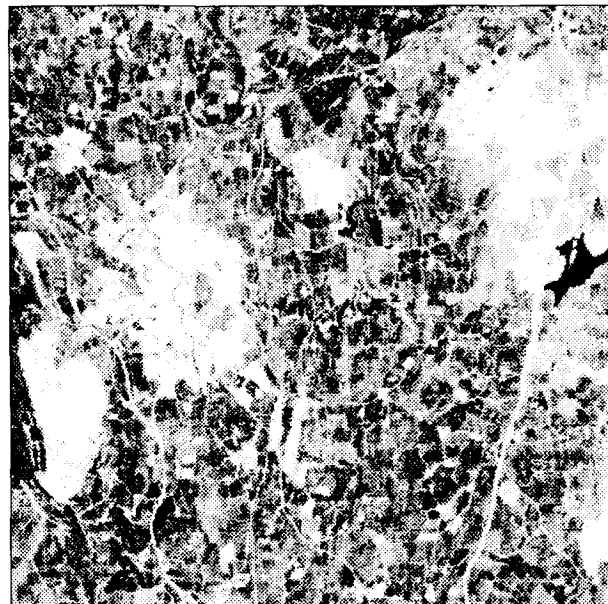


Figure 2: Subset of a Landsat TM image of the same area as in figure 1. The town of Kendal is visible in the mid-left portion of the image and the M6 motorway runs up the right hand side. Note that in comparison to the SAR image in figure 1 that none of the drumlins are visible.

Photo-interpretative mapping

The following approach for mapping glacial lineaments has been adopted. An initial visual segmentation of images into areas of drift and bedrock is first performed. The most salient visual cue to assist in this task is the directional 'strength' of the features. Both glacial and geological lineaments exist in a parallel fashion but the directional trend of glacial features is often more consistent and stronger across an image with the features displaying a mean orientation with low variance. Geological trends are often of more than one direction and may be curved. Differentiation is also enhanced by the texture of the image: drift areas appear 'smoother' and often 'smeared' unlike bedrock areas which appear more granular.

Once drift areas have been identified, the mapping of glacial geomorphological features is attempted. This is performed at a variety of scales with the effects of oblique radar illumination and the pattern of lake boundaries providing the main criteria for identification. Illumination from one direction results in a 'shadow effect' in the lee of the geomorphological features creating a sense of topography which assists in identifying such features as drumlins, eskers and subtle geomorphological patterns. Larger phenomena (e.g. mega lineations) are more readily identified by an often apparent linear lake pattern. Figure 3 shows a detailed interpretation of glacial lineaments of one SAR image in Ungava, Canada.

Field validation

Plans have been made to visit an important location in Arctic Canada (the Larch River area, northern Quebec) in August 1994 to validate some of the land-

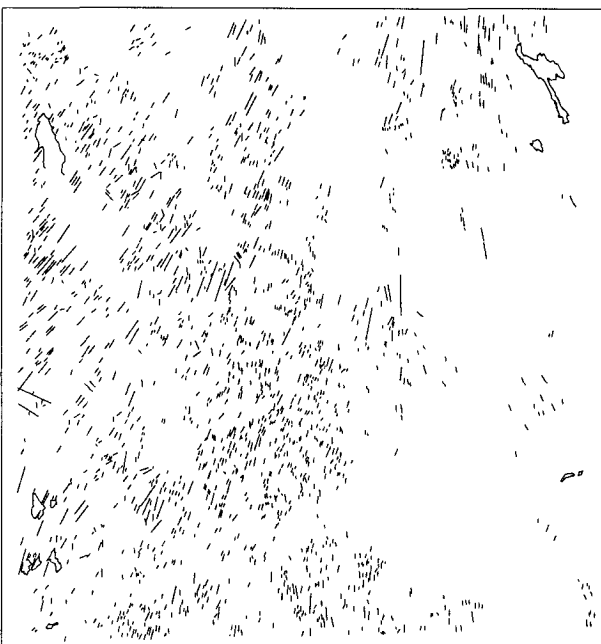


Figure 3: Interpretation of glacial lineaments in the Ungava region, Canada (orbit number 9861, frame number 2457). The interpreted lineaments display a diverging trend, and more than one direction of former ice flow is suggested.

form interpretations that have been made. A 300km traverse of this remote area, achieved by raft-descent of the river, will enable image-based interpretations of landform type and pattern to be checked and an initial assessment of the sensitivity of drift cover to backscatter variations to be performed.

Much of the SAR validation work will also be achieved using aerial photographs for lineament verification.

7 CONCLUSIONS

Good progress has been made in developing the necessary interpretative skills for identifying and mapping glacial landforms. The imagery is proving excellent and beyond our expectations for this task. We are able to identify individual drumlins and subtle patterns within the subglacial bedform suite and have already discovered hitherto unknown evidence of former ice flow.

ACKNOWLEDGEMENTS

The European Space Agency is gratefully acknowledged for the supply of data under its pilot project scheme, and the University of Sheffield for financial support and a scholarship supporting JKK. Dan Mathers is thanked for his contribution to the speckle reduction analysis.

BIBLIOGRAPHY

1. Punkari, M., 1982. Glacial geomorphology and dynamics in the Eastern parts of the Baltic Shield interpreted using Landsat Imagery. Photogrammetric Journal of Finland, V9, 1. 77-93
2. Clark, C.D., 1990. Remote sensing scales related to the frequency of natural variation; an example from palaeo-ice flow in Canada. IEEE Transactions on Geoscience and Remote Sensing, 28, No.4, 503-508
3. Boulton G.S. & Clark C.D., 1990. A highly mobile Laurentide Ice Sheet revealed by satellite images of glacial lineations, Nature, 346, 813-817.
4. Boulton G.S. & Clark, C.D., 1990. The Laurentide Ice Sheet through the last glacial cycle: the topology of drift lineations as a key to the dynamic behaviour of former ice sheets. Transactions of the Royal Society of Edinburgh: Earth Sciences, 81, 327-347.
5. Clark, C.D., 1993. Mega-scale glacial lineations and cross-cutting ice-flow landforms. Earth surface processes and landforms, 18, 1-31.
6. Ford, J.P., 1984 Mapping of glacial landforms from SEASAT radar images. Quaternary Research, 22, 314-327.
7. Graham, D.F. AND Grant, D.R., 1991. A test of airborne, side-looking synthetic aperture radar in Central Newfoundland for geological reconnaissance. Canadian Journal of Earth Science, 28, 257-265.
8. Greenbaum, D., Marsh, S. and Trageim, D. 1994. Landsat inputs to UK geological mapping. Geoscientist, 3, 4-6.

9. Nagao, M., and Matsuyama, T., 1979, Edge preserving smoothing, Computer graphics and image processing, 9, 394-407.
10. Lee, J., 1981, Speckle analysis and smoothing of synthetic aperture radar images, Computer Graphics and Image Processing, 17, 24-32.
11. Lee, J., 1986, Speckle suppression and analysis for synthetic aperture radar images, Optical Engineering, 25, 636-643.
12. Lee, J., 1983, Digital image smoothing and the sigma filter, Comput. Vision Graphics Image Process., 24, 255-269.
13. Paudyal, D.R., and Aschbacher, J., 1993, Evaluation and performance tests of selectd sar speckle filters, Proceedings Int. Symp. Operationalization of remote sensing,(ed. van genderen, van Zuidam and Pohl, ITC, Netherlands) 5, 89-96.
14. Abramson, S.B., and Schowengerdt, R.A., 1993, Evaluation of edge-preserving smoothing filters for digital image mapping, ISPRS, Journal of Photogrammetry and Remote Sensing, 48, 2-17.
15. Clark, C.D., and Fowajuh, C.G., 1993. Remote Sensing as a quantitative tool for examining glacially streamlined bedforms. In programme with abstracts, Third International Geomorphology Conference, 1993, McMaster University, Hamilton, Canada, p122.
16. Knight, J.K., and Clark, C.D., 1993. Reconstruction of former ice sheet dynamics utilising a geographical information system (GIS) approach. In programme with abstracts, Third International Geomorphology Conference, 1993, McMaster University, Hamilton, Canada. p171.
17. Mitchell, W.A., and Clark, C.D., 1994. The last ice sheet in Cumbria. In Walden and Boardman (eds), The Quaternary of the Lake District: Field Guide. Quaternary Research Association. England. in press.



6. FORESTS



TREES ERS-1 STUDY '94: ASSESSMENT OF THE USEFULNESS AND RELEVANCE OF ERS-1 FOR TREES

J-P. Malingreau, J. Aschbacher, F. Achard, J. Conway, F. De Grandi, M. Leysen

EC Joint Research Centre (JRC), IRSA-MTV-TREES, TP440, 21020 Ispra (VA), Italy
Tel: +39-332-78-9830, Fax: +39-332-78-9073

ABSTRACT

JRC and ESA have decided to initiate the *TREES ERS-1 STUDY '94* with the objective to assess the usefulness of ERS-1 SAR data for tropical forest studies under various ecological and environmental conditions, and on a global scale. Within this framework questions related to (i) the use of ERS-1 for AVHRR validation, (ii) the use of ERS-1 as gap filler in cloud-covered areas, and (iii) the usefulness of ERS-1 for operational deforestation monitoring are addressed.

On the technical side various analysis procedures are investigated such as speckle filtering, texture analysis, segmentation, classification, terrain geocoding, interferometry and backscattering modelling. A total of 21 study areas along the tropical belt are selected, representing different forest conditions in terms of *forest ecology, forest density, deforestation states* and *terrain characteristics*. The per-site investigations are jointly carried out by JRC and international institutions. Intermediate results of the JRC based studies are shown. Indicative results incorporating all 21 studies are expected before the end of 1994 and will provide the basis for further considerations regarding the use of ERS-1 for forestry, and in particular within the framework of TREES II (1995-98).

1. INTRODUCTION

Monitoring of tropical forests has become an increasingly important issue in the past decade. Environmental considerations related to global change of the Earth's climate have been the prime force behind the attempts to better understand changes in the tropical forest cover. Logging, burning, shifting cultivation and natural hazards are causes for deforestation, most of which are anthropogenic. Although remote sensing with spaceborne data has more than two decades of experience the extent of tropical forests and particularly its rapid decrease are still not precisely known at present. One obstacle in the use of optical remote sensing is frequent cloud coverage in tropical areas. Radar remote sensing instruments such as those onboard ERS-1 may provide a significant contribution towards an operational use of remote sensing data. Within the frame-

work of TREES II (1995-'98) such a global tropical forest monitoring system is developed based on the forest cover classification performed within TREES I (1991-'94) (Malingreau et al., 1993). In order to assess the potential of ERS-1 SAR data the *TREES ERS-1 STUDY '94* was initiated.

2. PRELIMINARY RESULTS OF PAST ERS-1 STUDIES WITHIN TREES

In the past few years the use of ERS-1 SAR data within the TREES Project was concentrating on the development of technical tools for SAR data analysis. Emphasis was put into terrain geocoding, speckle filtering, texture analysis, signal calibration and SAR processing. In addition, a few application oriented investigations

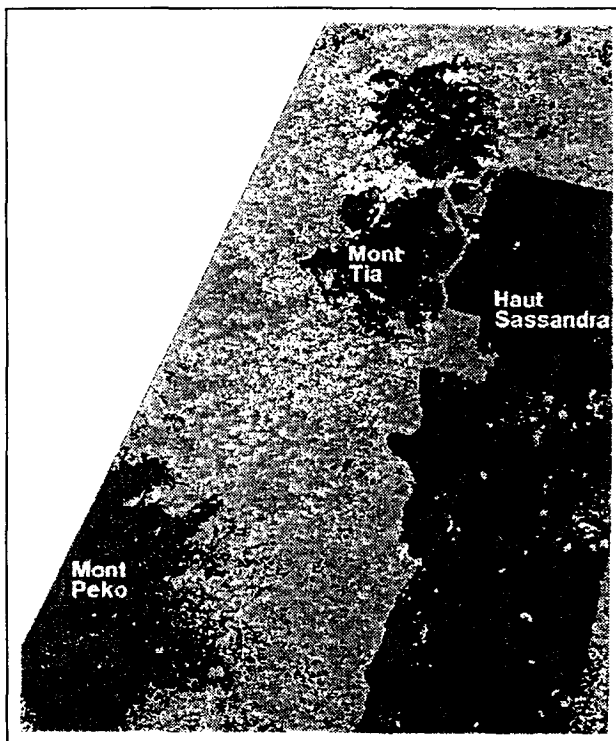


Figure 1: Coincidence map of ERS-1 SAR versus SPOT PAN classification. Colour code: light grey (non-forest in both), dark grey (forest in both), black (forest in SPOT, non-forest in ERS-1), white (forest in ERS-1, non-forest in SPOT).

have been carried out based on two sites, one in Ivory Coast (Sassandra) and one in Brazil (Acre). Preliminary results of these studies are shown in the following.

2.1. STUDY AREA: SASSANDRA (IVORY COAST)

The study site is located in the western part of Ivory Coast ($6^{\circ}50' - 7^{\circ}50' N$, $6^{\circ}50' - 7^{\circ}30' W$) within the natural zone of wet evergreen forests and close to the neighbouring savannah zone in the North. The area is characterised by moderately undulating terrain, a mean annual rainfall of about 1500 mm with a pronounced dry season from December to February.

Previous work concentrated on forest/non-forest discrimination (Leysen et al., 1993; Conway et al.; 1993) based on a time series of nine subsequent ERS-1 images between July 1992 and May 1993, in PRI format. A straight-forward supervised multi-date classification was carried out at different pixel spacings of 25 and 100 m, respectively. The results were compared with the classification of a mono-temporal SPOT Panchromatic image. The coincidence map shown in Fig. 1 shows that - apart from topographic effects in ERS-1 SAR data and atmospheric effects in SPOT data - a different sensitivity to fragmented forests is observed at the 100 m pixel spacing. The results obtained with 25 m pixel spacing, however, confirm the importance of multi-temporal versus single-date classifications and timing of the acquisition. The separability between major land cover classes is higher during the dry season.

Combination of dry and wet season data allows a more detailed classification based on the different seasonal behaviour of the observed vegetation types.

Based on the extensive field data collected during the last dry season the analysis is currently focusing on multi-temporal aspects, forest ecology, tree structures and the influence of rainfall during data acquisition. Terrain geocoding is performed for better interpretation. A short term objective is also to identify minimum/optimum number of

images and optimum acquisition timing.

2.2. STUDY AREA: ACRE (BRAZIL)

The test site is located at the border of the state of Acre, Brazil, covering part of the south-west Amazon valley. The test-site shows distinct deforestation patterns arising from cattle ranching activities. Within this area of the Amazon there is a specific dry season from June to September.

In this study four PRI images consisting of two consecutive frames from two consecutive orbits (acquired 30th May and 15th June, 1992) were used. The PRI images were filtered using the GMAP filter and block-averaged to achieve 100 m pixels in both, range and azimuth. A preliminary classification of the images was carried out for forest/non-forest discrimination using the supervised non-parametric K-K' Nearest Neighbour classifier using training areas selected with the aid of hard copy TM images of the area.

One of the original objectives for the use of ERS-1 SAR data within the TREES project is the validation of the low resolution 1 km AVHRR results. With this in

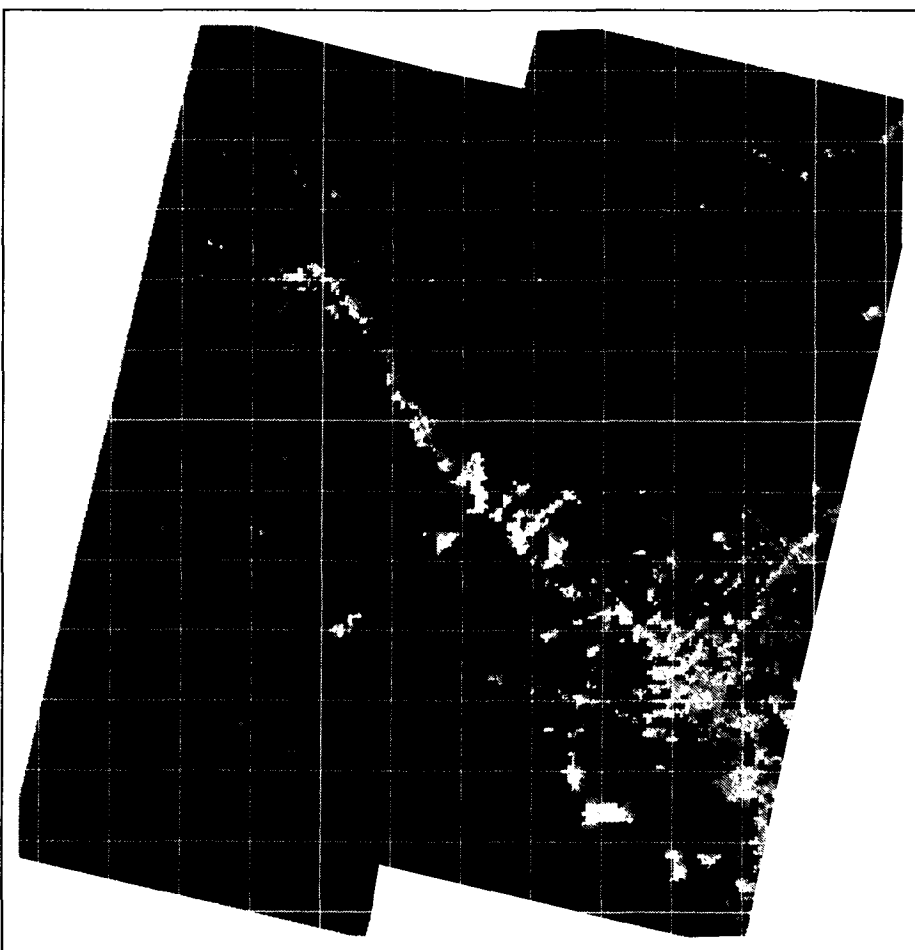


Figure 2: NOAA AVHRR - ERS-1 SAR Coincidence map (explanations see main text)

mind, the four intermediate resolution ERS-1 SAR classifications were then mosaicked to produce a single forest/non-forest map for comparison with the preliminary AVHRR derived classification. A quantitative comparison was made, after co-registering the two classifications on a block by block bases (to reduce mis-registration effects) the sources of disagreement between classifications were identified (Conway, 1993).

The results of the comparison can be visually seen in Fig. 2 which shows a coincidence map produced from both classifications, where the black indicates forest in both classifications, white indicates non-forest in both classifications, light grey indicates forest in ERS-1 SAR but non-forest in AVHRR, and dark grey indicates non-forest in the ERS-1 but forest in the AVHRR classification.

The results from this first analysis indicate that there was a good agreement (> 90%) between the AVHRR classification and the ERS-1 SAR classification for well defined non-forest areas with relatively homogeneous spatial structure (e.g. areas of large cattle ranches typical of the deforestation occurring in this area). However, for areas containing spatially heterogeneous deforestation, the AVHRR classification underestimated the forest percentage compared with the ERS-1 SAR derived classification. The AVHRR derived classifications also missed small scale non-forest features such as rivers and roads which were detected in the ERS-1 SAR derived classifications.

Efforts are continuing to improve the ERS-1 SAR classification (for example, firstly by using calibrated rather than digital values). The effects of using the digital counts of PRI products can be seen at the edges of the classified images where errors in the classification can be found.

3. OBJECTIVES

The major objective of the TREES ERS-1 STUDY '94 is to examine the potential of ERS-1 SAR data for tropical forest monitoring. The assessment will be geared towards an operational use of radar data. The principal goal is forest/non-forest discrimination. In addition, also questions related to (i) the use of ERS-1 for AVHRR validation, (ii) the use of ERS-1 as gap filler in cloud-covered areas, and (iii) the usefulness of ERS-1 for operational deforestation monitoring are addressed. State of the art analysis tools will be compared. Further, optimum timing and frequency of acquisitions, product types and analysis procedures will be recommended. The systematic assessment includes a great variety of ecological and environmental conditions.

4. STUDY AREAS

A total of 21 study areas along the tropical belt have been selected which represent different forest conditions in terms of *forest ecology*, *forest density*, *deforestation states* and *terrain characteristics*. The study areas, approx. 2 x 2 degrees lat. x long. in size, are located in Latin-America, Africa and Southeast-Asia, respectively. In order to benefit from already existing expertise study areas were selected at which radar and/or optical data have already been investigated in past or on-going studies. Examples of such activities are Wooging et al. (1993), Hoekman et al. (1993) or Aschbacher et al. (1994). Table 1 gives an overview of the study areas selected within this current project.

Table 1: Overview of TREES ERS-1 STUDY '94 study areas.

SOUTHEAST - ASIA		
SEA-1	China/Laos	21-23 N, 100-102 E
SEA-2	Thailand/Myanmar	14-16 N, 98-100 E
SEA-3	Thailand - Peninsular	7-9 N, 98-100 E
SEA-4	Sumatra - Central	0-2 S, 101-103 E
SEA-5	Sumatra - South	3-5 S, 103-105 E
SEA-6	Papua New Guinea	6-9 S, 141-143 E
SEA-7	Cambodia/Vietnam	12-14 N, 106-108 E
SEA-8	Indonesia - Kalimantan	1 N-2 S, 115-117 E

AFRICA		
AFR-1	Ivory Coast - Sassandra	6-8 N, 6.5-8 W
AFR-2	Equat. Guinea, Gabon	1-3 N, 9-11 E
AFR-3	Zaire/CAR	3-5 N, 22-24 E
AFR-4	Zaire - Central	3-5 S, 22-24 E
AFR-5	Zaire - West	0-2 N, 18-20 E

CENTRAL- & SOUTH-AMERICA		
LAM-1	Panama/Costa Rica	8-11 N, 81-84 W
LAM-2	Brazil - Acre	8-10 S, 67-70 W
LAM-3	Brazil - Manaus	2-4 S, 59-61 W
LAM-4	Brazil - Rondonia	10-12 S, 60-62 W
LAM-5	Brazil - Tapajos	2 - 4 S, 54 - 56 W
LAM-6	Colombia - Araracuara	0-1 S, 71-73 W
LAM-7	Guyana - Mabura	4-6 N, 58-60 W
LAM-8	Colombia - Guaviare	2-3 N, 72-73 W

5. SCIENTIFIC ISSUES TO BE TACKLED

There is a great number of technical issues that will be addressed during this study. An overview of these issues is given below:

Analysis techniques

- calibration
- speckle filtering
- texture analysis & image segmentation
- classification techniques
- optical/radar data fusion

Multi-temporal aspects

- influence of meteorological conditions during acquisition time (i.e. rainfall, plant moisture, etc.)
- minimum/optimum number of acquisitions (i.e. for seasonal versus evergreen forest)

Terrain geocoding

- terrain geocoding with DEM
- merging of ascending/descending paths

Towards operational applications

- data reduction & data handling
- optimum product types
- optimum acquisition timing
- production of a regional mosaic
- change detection (deforestation monitoring)
- optical - radar information compatibility

R & D issues

- potential of interferometry for forest/non-forest discrimination and the meaning of coherence information over tropical forests
- backscatter modelling
- potential of large scale radar altimeter data

Emphasis will be put into terrain geocoding considering that hilly and mountainous areas are mostly covered by forests in the Tropics. Also, the potential of interferometry will be investigated, in particular the usefulness of coherence information for forest/non-forest discrimination.

A selection of above issues will be made for each study area, depending on the respective site's characteristics.

6. TIME FRAME

The following time frame is envisaged for the scope of this project:

TIME	ACTIVITY
Nov '93	TREES ERS-1 STUDY '94 proposed jointly by JRC and ESA
Jan-Apr '94	Study strategy design
28-29 Apr	Brainstorming/kick-off meeting at ESA-HQ
Apr-Nov	ERS-1 data analysis work by JRC and international PIs
May	Final ERS-1 data requests to ESA
May - Nov	ERS-1 data delivery by ESA
Dec	TREES ERS-1 Study '94 Seminar
Dec '94	Statement by JRC-TREES regarding ERS-1 Study '94 results

The results of the current TREES ERS-1 Study '94 will be presented at the final results seminar scheduled for the end of 1994. The results are expected to be of interest for a wider forest and remote sensing user community.

7. OUTLOOK & FUTURE PLANS

Based on this systematic ERS-1 data assessment under various ecological, environmental and geographical conditions general recommendations will be formulated regarding the usefulness of ERS-1 for tropical forest studies. This assessment will, of course, also incorporate experience drawn from other studies outside this TREES ERS-1 STUDY '94, such as those obtained from the recently conducted SAREX92 campaign over tropical forests in Latin-America (ESA...., 1994).

In view of the expected operational use of ERS-1 data the possibility of creating an ERS-1 SAR mosaic over the Central African base is currently studied. For this purpose the acquisitions of the transportable station at Libreville, Gabon, will be merged to create a regional mosaic. Single-date as well as multi-temporal mosaicking will be investigated.

Further, the potential of newly emerging analysis techniques such as interferometry or new classification methods is investigated. The use of coherence information is expected to support thematic interpretation, particularly forest/non-forest discrimination. Also, the potential of information derived from radar altimeter data is assessed. The latter, however, addresses a different spatial scale caused by the instrument's resolution in the km-range.

The recommendations retrieved from this analysis will largely benefit any development of an operational tropical forest monitoring system, as it is envisaged within the TREES II project.

8. ACKNOWLEDGEMENTS

The authors are grateful to ESA for the support of this study through the provision of ERS-1 data. Special efforts have been made by ESA to provide the required data over tropical areas, where data availability is generally limited. Also, the authors wish to thank their colleagues at JRC-IRSA for many fruitful inputs to the design of this study.

9. REFERENCES

Aschbacher, J., C. P. Giri, R. S. Ofren, J-P. Delsol, T. B. Suselo, S. Vibulsresth, T. Charupat; 1994: *Tropical Mangrove Vegetation Mapping Using Advanced Remote Sensing And GIS Technology*; Final Project Report, Austrian Academy of Sciences; 73 pp.

Conway J. A.; 1993: *Tropical Forest Mapping using ERS-1 SAR Data over a test site in Brazil*, Proc. TREES Conference, Belgirate, Italy; (in press).

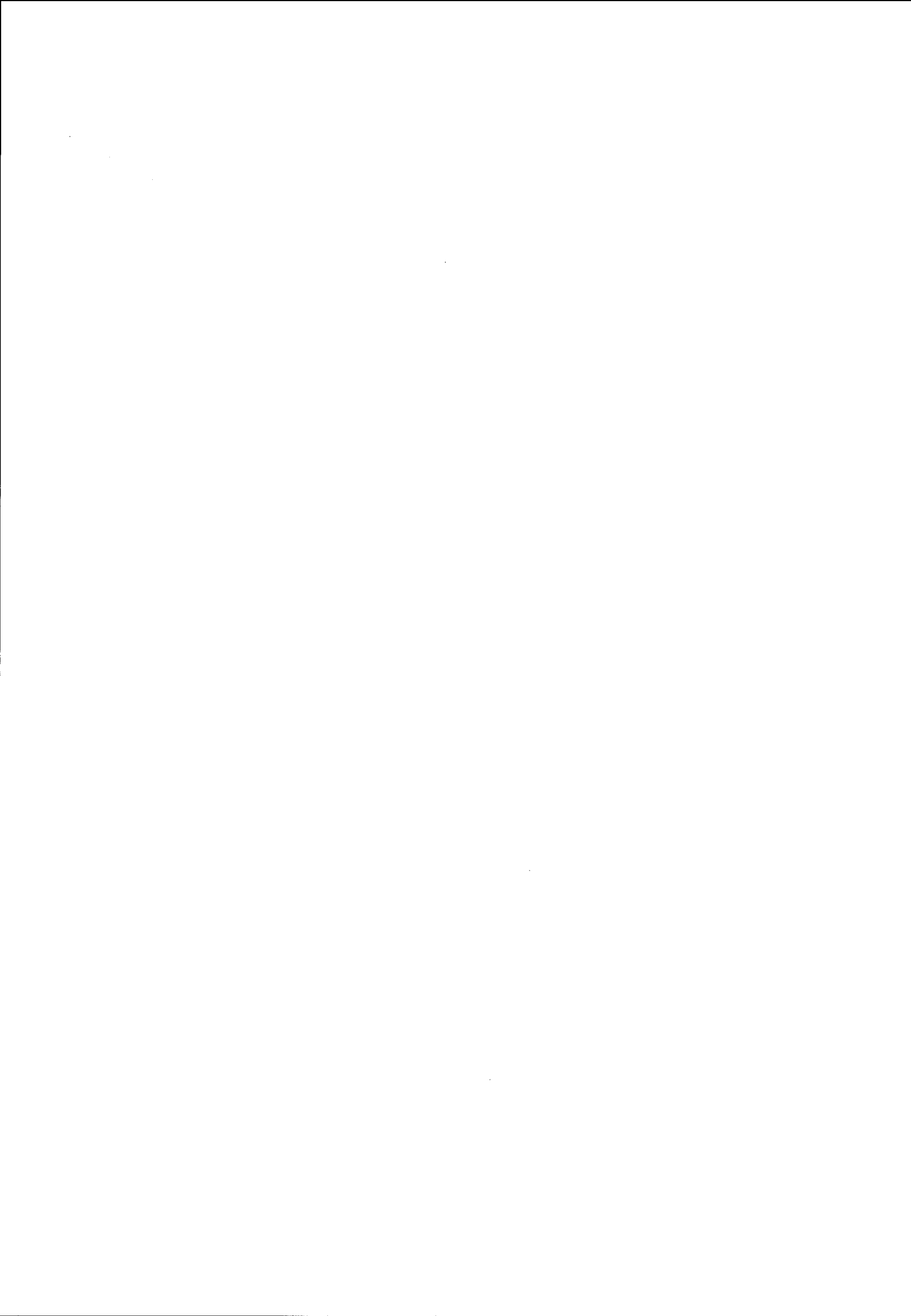
Conway, J. A., M. Leysen and A. J. Sieber; 1993: Evaluating Multi-temporal ERS-1 SAR Data for Tropical Forest Mapping: Data Selection, Processing and Target Identification; Proc. Second ERS-1 Symposium, Hamburg, Germany, 11-14 Oct '93 (ESA SP-361); p. 441-446.

Hoekman, D.H. and J.J. van der Sanden; 1993: Results of the SAREX-92 Campaign in Guyana and Colombia; Proc. SAREX-92 (ESA-WPP-76), pp. 157-166.

Leysen, M., J. A. Conway and A. J. Sieber; 1993: Evaluating Multi-temporal ERS-1 SAR Data for Tropical Forest Mapping: Regional Mapping and Change Detection Applications; Proc. Second ERS-1 Symposium, Hamburg, Germany, 11-14 Oct '93 (ESA SP-361); p. 447-452.

Malingreau, J.P., F. Achard, G. D'Souza, H.J. Stiebig; 1993: AVHRR for Global Tropical Forest Monitoring: The Lessons of the TREES Project; Proc. TREES Conference, Belgirate, Italy; (in press).

Wooding, M.G., A.D. Zmuda, E. Attema; 1993: An Overview of SAREX-92 Data Acquisition and Analysis of the Tropical Forest Environment; Proc. SAREX-92 (ESA-WPP-76), pp. 3-14.



APPLICATION OF THE ERS-1 IMAGES FOR ASSESSMENT OF DAMAGE TO CONIFEROUS FOREST IN POLAND

Tomasz ZAWILA-NIEDZWIECKI, Andrzej CIOLKOSZ, Zbigniew BOCHENEK

Remote Sensing and Spatial Information Centre-OPOLIS

Institute of Geodesy and Cartography

00-950 Warsaw, Poland; 2/4 Jasna St.

ABSTRACT

The multitemporal ERS-1 images of the Sudety Mts. as well as images of vast coniferous pine forest located in the Central Polish Lowlands affected by huge forest fire and pine stands being in good condition have been used for assessment of quality of forest. It has been found that images taken in microwave part of electromagnetic spectrum by SAR installed on the board of ERS-1 have rather limited application in detection of forest classes, they have almost no value in differentiation between different stages of damage to spruce trees, however, they may be used for assessment of extent of deforestation including burned areas within forest. The information provided by microwave images can be treated as auxiliary data which can support to some extent the data collected in optical spectrum.

Keywords: forest damage assessment, forest fire.

Since several years a number of investigations aiming at the assessment of the quality of forests in Poland have been undertaken. In some cases, especially where the threat to forest stands was serious or evident damage to forests occurred the remote sensing methods have been used. On the basis of aerial photographs as well as satellite images a number of maps showing the various stages of damage to pine and spruce forest have been elaborated. The method

of assessment of forest quality based on aerial and satellite images have been accepted by the Polish forest authorities.

The methods, however, has a serious limitation. Due to frequent cloudiness occurring in growing season taking of aerial photographs or satellite images is impede or very often quite impossible. Thus the methods based on remotely sensed data in optical spectrum can not be considered as a fully operational. That is why new investigations with application of microwave images taken by ERS-1 have been undertaken. In selection of test sites the quality of forest stands has been considered.

The first test site was located in the Sudety Mts., the western part of which has been recognised as a region of ecological disaster. A number of investigations have been done in this region to evaluate a quality of forests and to classify the damage to spruce stands. After several years of investigations a large volume of information from ground measurements and analysis of satellite images has been collected and stored in geographical information system. This data has facilitated the analysis of ERS-1 images.

The following parameters of forest stands, determined in the course of field works, were analysed and compared with those derived from microwave images: age, breast diameter, height of tree, height of crown base, crown diameter, crown length, canopy closure, number of trees per unit area, number of dead trees per unit area in the main stand and

number of trees in the secondary stand, defoliation, needle discoloration stand quality and slope. Defoliation and discoloration were evaluated according to ICP-Forest instructions (International Co-operative Programme on Assessment and Monitoring of Air Pollution Effects on Forests) and quality of trees was assessed on the basis of state of assimilatory apparatus, height increments and vigour of trees.

The results of examination have revealed that relationships between radar images of forests and their terrain parameters are not significant. When studying all spruce stands the highest correlation coefficient of 0.34 was obtained, expressing relationship between backscattering coefficient and crown diameter. In some cases correlation coefficients increase, when only forests on favourable aspects are considered. However these relations are distinct only for crown diameter and breast diameter ($r=0.76$), height of trees (0.72), age (0.61) and crown length (0.54), well, parameters having influence on roughness of upper surface of stands (Ciolkosz et al.).

Besides simple regression, multiple relations between stand parameters and SAR signals have been also searched. The highest correlations were reached for spruce stands with full canopy closure, covering slopes with NE, E and SE aspects; the regression equations are as follows:

$$(I) \quad \sigma^0 = 17.33 - 0.07 \text{ Age} + 0.34 \\ D_{1.3} + 0.75 O_K \quad R^2=0.83$$

$$(II) \quad \sigma^0 = 13.35 + 0.33 D_{1.3} - 0.07 \\ N + 0.71 NMG \quad R^2=0.64$$

$$(III) \quad \sigma^0 = 3.99 + 1.11 O_K - 0.09 N + \\ 7.6 Dm \quad R^2=0.62$$

So, variability of backscattering coefficient can be mostly explained by changes of stand age, breast diameter, crown diameter, number of trees per unit area, number of dead trees in the main stand and quality of trees characterised by index of damage (Ciolkosz et al.).

In the course of visual interpretation of radar satellite images it was found, that speckle characteristics for this kind of

images makes analysis of single images much difficult. Visual analysis of colour composites, formed from multiday images, gives more interesting information, which is not easy to derive from individual images. In order to create colour composite for the Sudety Mountains, three images collected on Sept. 24, 1992, Dec. 3, 1992 and April 6, 1993, were utilised. They were projected using green, blue and red beam respectively, which gave rendition of forests in different shades of green colour, facilitating interpretation.

Results of visual interpretation reveal, that the following forest classes can be distinguished on ERS-1 images; older stands, thickets, clear-cuts and stands with very loose canopy closure. The boundary between forest and arable land is clearly visible. On the other hand, delineation of species is not possible. Moreover, interpretation of dwarf mountain pine, high mountain grasses and bare rock, due to relief and high radar response from rocks and dwarf mountain pine, is much more difficult, being sometimes impossible.

In southern Poland, in Upper Silesian Industrial Region, enormous forest fire broke out in 1992. It devastated more than 9 000 ha of forestland. One could observe smokes and extension of burned area even on satellite images taken by AVHRR radiometer installed on the board of NOAA satellite. This area was also chosen as a test site to evaluate of usefulness of ERS-1 images in assessment of forest damage. SPOT XP and XS images were also used for detailed analysis of forest damage due to fire and results of this analysis were compared with information derived from ERS-1 images. Due to substantial changes in roughness of surface of the forest and burned areas the recognition of burned forest on microwave images is extremely easy. It has been found that the accuracy of delineation of burned areas on both types of satellite images is almost the same, however, on SPOT XS image one can distinguish survived clumps of deciduous forest which are not recognised on microwave images due to the speckles.

This test site was covered three times by ERS-1 in July, August and

September 1993. Colour composition formed from these images has provided information on extension of recultivation works.



Fig. 1. Burned areas within pine forest seen on ERS-1 images.

Third forest test site for our studies has been selected in Central Poland. It is located in lowland area, characterised by different forest sites and slightly undulating relief. Pine is predominant tree species here, although mixed and deciduous forests also appear in this region. This forest test site is not heavily affected with unfavourable environmental impacts, however, slight damages to pine stands appear within the area due to industrial pollution.

That study area has been covered by three ERS-1 scenes collected in January, February and March 1994. Colour composite was formed from these images in order to make thorough visual analysis of this forest test site. Results of interpretation revealed that general discrimination between coniferous stands and mixed or deciduous forest can be

done quite easily; these delineations correspond to changes of forest sites. Mixed stands located in marshy areas differ much from more dry sites.

Variability of radar response from coniferous stands is mainly dependent on forest canopy closure (caused by both number of stems on given area and lack of needles on the trees on images taken during winter) which expresses roughness of the surface. Forests with very loose canopy closure and especially clear-cuts can be clearly visible on multidate colour composites. Nevertheless it must be emphasised that evaluation of forest damages and delineation of tree species is not possible with the use of SAR images. These remarks are consistent with conclusions drawn from analysis of ERS-1 images covering mountainous test sites. (lit. Zawila-Niedzwiecki, 1993).

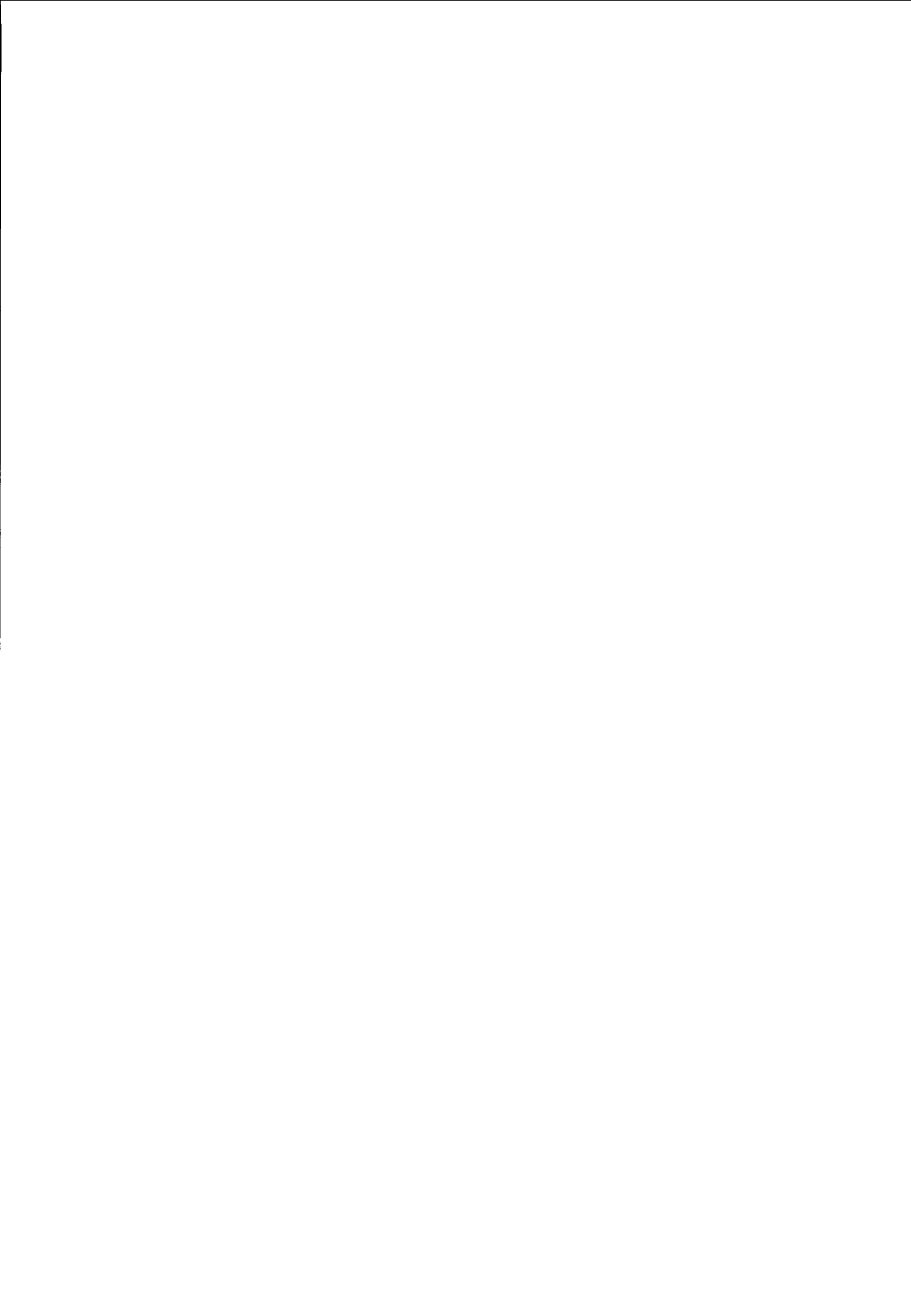
So, the general conclusions drawn after two years of application-oriented studies concerning the use of SAR ERS-1 images for the three forest test sites in Poland can be summarised as follows:

- assessment of forest quality, i.e. evaluation of damage is not possible;
- stratification of species composition is not possible; general discrimination between coniferous, deciduous and mixed stands can be done;
- detection of very loose canopy closure as well as delineation of openings (deforestations) is possible;
- large afforestations can be located on multidate images;
- inventory of burned forest areas can be done quite easily .

REFERENCES:

Ciolkosz A., Zawila-Niedzwiecki T., Bochenek Z., 1993: The application of ERS-1 images for forest damage assessment. *Proceedings of the Second ERS-1 Symposium "Space at the services of our environment"*. 11-14 October 1993, Hamburg, Germany.

Zawila-Niedzwiecki T., 1993: Use of satellite data and GIS technology for forest damage monitoring. *Final Report of the CEC-JRC Project No 2484*. Laboratory of Remote Sensing and Forest Management, University of Gent, Belgium.



SYNERGY OF REMOTELY SENSED DATA: a European scientific network in the field of remote sensing.

A.P. Cracknell
 Department of Applied Physics and Electronic and Manufacturing Engineering,
 University of Dundee
 Dundee, U.K.

Tel: +44-382-307549
 Fax: +44-382-202830

J.L. van Genderen
 (Network Coordinator)
 Dept. Earth Resources Surveys,
 I.T.C.,
 P.O. Box 6, 7500 AA
 Enschede, The Netherlands

Tel: +31-53-874254
 Fax: +31-53-874436

G. Konecny
 Institute for Photogrammetry and Engineering Surveys,
 Univ. of Hannover,
 Nienburgerstrasse 1,
 3000 Hannover,
 Germany

Tel: +49-511-7622482
 Fax: +49-511-7622483

A. Sieber
 Advanced Techniques Unit,
 Institute for Remote Sensing Applications,
 CEC-JRC-Ispra,
 Ispra, Varese 21020,
 Italy

Tel: +39-332-789089
 Fax: +39-332-785469

ABSTRACT

Under the CEC DG XII's Human Capital and Mobility Programme, the ITC has received an ECU 600,000 research grant to establish and develop a European scientific research network in the field "Synergy of Remotely Sensed Data", integrating various European approaches into a sustainable European remote sensing research environment. The first phase of the research will be for three years 1994-1996. There are eleven network members from Europe (Italy, Germany, U.K. and the Netherlands) at present, and several Central and Eastern European partners are expected to join the research network in the near future.

One of the objectives of the Research Network is to study the complementarity and additionality of optical (e.g. SPOT, Landsat TM), thermal (Landsat TM, NOAA-AVHRR) and microwave (ERS-1, JERS-1) data.

This presentation will concentrate on the microwave data and how this can best be integrated/combined with other data sets in order to increase the information extraction value of the fused data set. The paper describes the individual research contributions of each of the European research partners, and discusses the approach of the Network for "value-adding" by using a synergistic approach to data integration combining multisensor, multispectral, multiresolution and multitemporal data sets.

1. INTRODUCTION

Under the Commission of the European Communities, Directorate General XII for Science, Research and Development, the ITC has received an ECU 600,000 research grant to establish and develop a European scientific research network in the field of "Synergy of Remotely Sensed Data", integrating various European approaches into a sustainable European remote sensing research environment. The first phase of the research

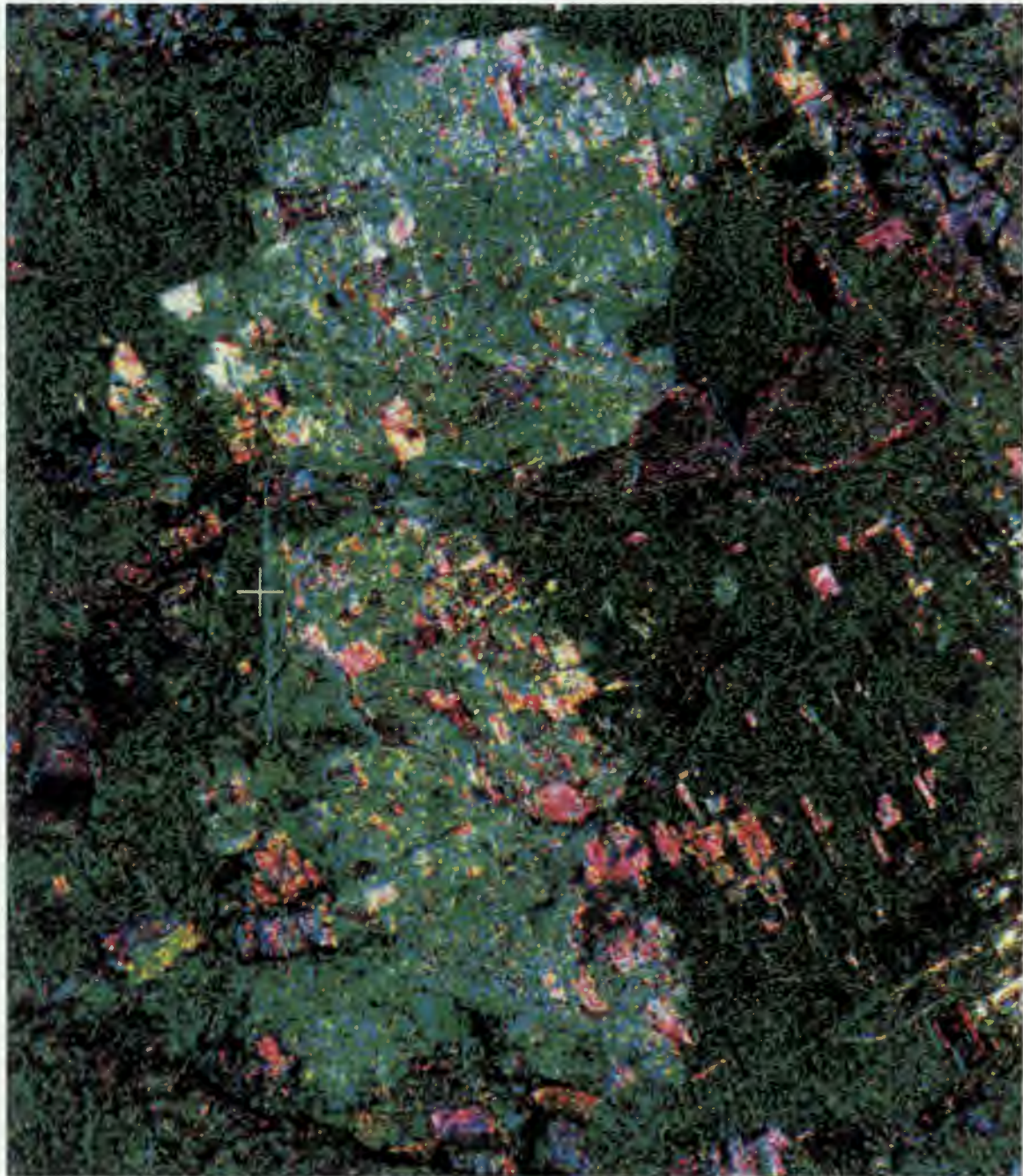
will be for three years 1994-1996. The following institutes are currently members of this research network:

- JRC-ISPRRA: Advanced Technologies Unit of the Institute for Remote Sensing Applications, Italy.
- ITC, The Netherlands.
- Albert Ludwigs Universität Freiburg: Institut für Forsteinrichtung und Forstliche Betriebswirtschaft, Abteilung Luftbildmessung und Fernerkundung, Germany.
- Wageningen Radar Surveys, The Netherlands.
- University of Hannover: Institute for Photogrammetry and Engineering Surveys, Germany.
- University of Dundee: Department of Applied Physics and Electronic and Manufacturing Engineering, United Kingdom.
- Ludwig Maximilian University of Munich: Department für Landnutzungsplanung und Naturschutz, Germany.
- Consorzio per la Ricerca e lo Sviluppo di Telesensori Avanzati, Naples, Italy.
- Albert Ludwigs Universität Freiburg: Institut für Physische Geographie, Germany.
- University of Munich: Arbeitsgruppe Fernerkundung am Institut für Allgemeine und Angewandte Geologie, Germany.
- Technische Universität Dresden: Institut für Waldbau und Forstschutz, Germany.

Many of these Network members are actively involved in ESA's ERS-1 programme as Principal Investigators or as Pilot Project Leaders. As no one member institute can cover all aspects of the synergistic use of ERS-1 data with other data types, the Network pools the resources of its members to achieve this objective.

At the request of the Commission, a proposal for expansion of the existing "Synergy" research network to institutes in Central and Eastern European countries and with the new independent states of the former Soviet

**APPLICATION OF ERS-1 IMAGES
FOR ASSESSMENT OF DAMAGE TO CONIFEROUS FOREST IN POLAND
PP PL-3**



ERS - 1 IMAGES OF THE SILESIAN BURNT FOREST
(28 AUGUST '93, 30 JULY '93, 3 SEPTEMBER '93 IN RED/GREEN/BLUE)

Union was recently submitted to the CEC. The following remote sensing centres in these countries are expected to join the network before the end of this year:

- Remote Sensing and Spatial Information Centre (OPOLIS), Poland.
- University of Mining and Metallurgy, Ostrava, Czech Republic.
- Aerospace Methods Lab, Moscow State University, Russia.
- Dept. of Geoinformatics, University of Forestry, Hungary.
- Inst. of Remote Sensing Methods for Geology (VNIKAM), Russia.
- Microwave Remote Sensing Lab., Inst. of Electronics, Bulgaria.
- Inst. for Geology, Geotechnics and Geophysics, Slovenia.
- Optical Radar Systems Lab., Academy of Technological Sciences, Ukraine.
- Polish Geological Institute, Poland.
- Solar-Terrestrial Influence Lab., Bulgaria.
- Dept. of Forest Management and Geodesy, Technical Univ. Zvolen, Slovakia.
- Inst. of Geodesy, Photogrammetry and Cartography, Romania.
- Dept. of Cybernetics and Artificial Intelligence, Technical Univ., Kosice, Slovakia.
- Image Processing Section, Space Research Institute, Bulgaria.
- Videosystems Dept. Space Research Institute, Bulgaria.
- Institute for Computers, Romania.

2. GOALS AND OBJECTIVES.

2.1 The scientific context

Current and future remote sensing programmes are based on a variety of imaging sensors that will provide timely and repetitive multisensor earth observation data on a global scale. Visible, infrared and microwave images of high spatial and spectral resolution will eventually be available for all parts of the earth.

This multisensor, multispectral, multiresolution, multitemporal and multiscale information presents a data processing challenge to the remote sensing society that has to be addressed. Integrated processing techniques have to fuse the multi image information to make it useful for a user community that is concerned with mapping, monitoring and modelling the earth's components. These present and future instruments will allow scientists to study the physical, chemical and electrical properties of the Earth's environment on a global scale and over an extended period of time. To derive geophysical parameters of interest for each of the planned science applications, the data collected by these

sensors must be combined and analyzed in a multidimensional manner. However, the sensors may be on different platforms and in different orbits, have different physical characteristics, viewing geometries and data collection and processing systems. Therefore it will be necessary to study in more detail the possible synergism between optical and microwave sensing techniques in terms of information content, combining not only data provided by the Western nations, but also the remote sensing data available from PECO countries (PECO = Cooperation in Science & Technology, with Central and Eastern European countries and with New Independent States of the former Soviet Union).

For research into the synergistic use of remotely sensed data, CEC and PECO collaboration between research groups is therefore not merely desirable, it is essential. There are three reasons for this: firstly, such research encompasses many different disciplines such as physics, mathematics, electronics, image processing, computer science, geology, soil science, forestry and terrestrial ecology. The need for new working links among them and the pooling of intellectual resources, transcends the existing structures for scientific contacts based on those traditional fields. Secondly, no single research institute can collect the many remote sensing datasets that are required for the synergy of earth observation; agreement has to be reached on sharing responsibilities for research at different locations, and, as far as possible, common methodologies to ensure the inter-comparability of results. Thirdly, there is an urgency to such work, set by the political implications of increasing environmental degradation and concern for sustainable development.

The existing CEC research network was established in 1993 to address these challenges on the potential of the synergy of remotely sensed data, recognizing that the complexity and importance of this topic required a European approach, with emphasis on a soundly based framework for research planning, implementation and synthesis.

This complex research theme needs a multidisciplinary research effort to tackle not only all the individual components, but integrate them into an overall concept/model for data integration. Hence this problem can only be tackled by a Network of research institutes with complementary capacity, pooling their individual scientific and technical expertise.

2.2 Overall objectives

The overall aim of the Network encompasses a wide spectrum of research activities. To provide coherence, effort is focused on the processes of remote sensing data integration that will most likely lead to practical capability of the synergy of remotely sensed data.

- To assess the possibility to remotely sense the biochemical and biophysical variability of a relatively homogeneous vegetated area using data from optical and microwave sensors.
- To study the complementarity of optical and microwave remote sensing data (to see which parameters can be observed by one of the sensors when the others are not available).
- To study the additionality of optical and microwave remote sensing data (to see to what extent the information furnished by one sensor is improved and enlarged when data from the other sensor is used).
- To study the synergy of remotely sensed data and auxiliary data, such as topography, phenology, etc.
- To develop an integrated operational methodology for merging different types of remote sensing data, including:
 - * multisensor data from cameras, scanners, antennas, spectrometers, etc.).
 - * multispectral (merging visible light with reflective and thermal infrared, radar, etc.).
 - * multiresolution (merging 10 metre SPOT data with 25 metre ERS-1 data, with 30 metre Landsat TM data, etc.).
 - * multitemporal (merging seasonal data for sequential monitoring (e.g. crops), multidate data for environmental change studies, using single or multiple data sources for integration).
 - * to establish a long-term Pan-European remote sensing research Network.
 - * to promote greater mobility and exchange of research results between researchers from CEC member states and PECO members.
 - * to integrate individual research results and coordinate research activities into an overall coherent research programme on data fusion and synergy of remotely sensed data.

3. RESEARCH CONTRIBUTION OF EACH NETWORK MEMBER

The following section describes the research activities being carried out as part of the "Synergy" network by each of the network members, in as far as these relate to ESA's ERS-1. It should be noted that many of the network members are either Principal Investigators or Pilot Project Leaders for ESA's ERS-1 programme, the network ensuring that their individual research results are integrated into an overall methodology for the synergistic use of optical and microwave data.

3.1 CEC-JRC-IRSA Advanced Techniques

The Unit for Advanced Techniques (AT) has many years of experience in the fields of signature research and advanced signal data analysis in the microwave part of the electromagnetic spectrum. Through various airborne campaigns, initiated by the JRC and in close collaboration with ESA and national agencies, IRSA-AT is making available to the network members large data sets from different European test sites. In addition, AT manages not only the unique experimental facility of the European Microwave Signature Laboratory (EMSC), but it has also built up and developed important SAR signal processing and analysis techniques, which it disseminates to the "Synergy" research network.

3.2 ITC, the Netherlands

In addition to acting as the Network Coordinator, ITC is carrying out research into the geometric aspects of image fusion (SPOT, LANDSAT-TM with ERS-1, JERS-1) for map updating in cloudy areas in Northern Europe and tropical developing countries (PP2-NL2).

3.3 Wageningen Radar Surveys, the Netherlands

This private company, dedicated to SAR processing and applications, is examining the synergistic use of ERS-1, JERS-1 and SIR-C/X-SAR for agricultural and forestry applications. It is particularly concerned with facilitating the operational implementation of successfully proven applications developed by the network members, in order to assist in their future commercial use.

3.4 University of Dundee, Scotland

The Department of Applied Physics and Electronic and Manufacturing Engineering is concentrating on the analysis of high spatial and spectral resolution imaging spectrometer data, to serve as inputs to the other network members concerned with data fusion and with those integrating spectrometer data with SAR data.

3.5 CO.RI.S.T.A., Italy

The Consorzio per la Ricerca e lo Sviluppo di Telesensori Avanzati, in Naples is providing inputs to the Network by means of their research in ERS-1 SAR interferometry. Based on their research experience with the SAR-580, JPL's TOPSAR and other SAR campaigns, a research worker from another network node, the University of Hannover, will work at CO.RI.S.T.A. on developing DTM's from ERS-1 interferometry, to be used for image mapping.

3.6 University of Hannover, Germany

The Institute for Photogrammetry and Engineering

Surveys at this University is developing a multisensor and multilevel digital geocoded data base as an input to the application oriented network members (forestry, geology). This data base will contain the raw data as well as the analyzed (e.g. filtered or geocoded) and classified data. An important research component here is the geocoding of ERS-1 SAR data. The Institute has been heavily involved in the "ERS-1 D-PAF geocoding" project as well as the "Radarmap Germany" project. They are also involved in ESA's ERS-1 programme (PP2.D8).

3.7 University Freiburg, Germany

The Institut für Forsteinrichtung und Forstliche Betriebswirtschaft abteilung Luftbildmessung und Fernerkundung of the Albert Ludwigs Universität in Freiburg's contribution to the network's research programme focuses on microwave and optical sensor data for forest biomass in environmental modelling and resources management.

Together with another network member (see 3.8 below), they are Principal Investigators for JERS-1 and PRIRODA data evaluation, as part of a research project entitled "ERS-1 für die Forstwirtschaft", concerning an assessment of ERS-1 and other SAR data for forest inventories and dynamic modelling.

3.8 Inst. of Physical Geography, University Freiburg, Germany

Their research experience in topo-climatology, meteorology, thermal modelling applied to landscape evaluation and environmental planning will provide inputs to network members concerned with the synergy of thermal infrared and SAR data.

3.9 Landnutzungsplanung und Naturschutz, Ludwig Maximilian Universität, Munich, Germany

Working in close cooperation with several other network members (see 3.10 and 3.11 below), this research group is collecting ground truth, using existing SAR data sets and creating an integrated digital data base. They are working towards the development of an expert system for the complementary and synergistic use of optical and SAR data for vegetation and land use purposes.

3.10 Arbeitsgruppe Fernerkundung, Institut für Allgemeine und Angewandte Geologie, University of Munich, Germany

Their main contribution to the network lies in their investigations to combine SAR and imaging spectrometry data sets towards the extraction of geophysical/chemical parameters relevant for geological/soil applications and environmental monitoring.

3.11 Institute of General Ecology and Environmental Protection, Technical University Dresden, Germany

They are collaborating with several other network members (notably 3.9 above) to collect and assess vegetation and soil parameters in the various test sites as input into the synergy models being developed by the Network.

4. INTENSIFYING EUROPEAN SCIENTIFIC COOPERATION

This network research programme on synergy of remotely sensed data benefits component national studies in the individual research institutes from CEC and PECO countries in many ways. The most important overall effect is to maximize scientific progress at minimum extra cost. Thus this coherent pan-European research framework provides "added-value" by increasing the productivity of each individual network member. The way in which this is achieved varies according to the scientific development within a particular Network Member, but the main benefits of this European research network in remote sensing are:

1. Assists the planning of European data fusion research programmes by providing a soundly-based intellectual and organizational framework for focused research, with clearly defined overall aims, priorities and implementation endorsed by the European remote sensing science community.
2. Adds to the scientific value of component synergy studies and provides complementary information, for example by widening the range of synergy topics addressed extending their temporal and spatial coverage and through inter-network comparison exercises, testing models and improving their predictive power.
3. Promotes the rapid communication of data fusion ideas and results at the frontier of scientific knowledge through the Networks' Workshops, Newsletter, meetings and publications and by encouraging interdisciplinary liaison at the pan-European level between individuals and all the network research groups.
4. Develops and tests the applicability of standard European methods and protocols for measuring key image fusion variables, thereby facilitating European quality control, intercalibration studies, and subsequent data exchange.
5. Assists in the cost effective deployment of major capital equipment and facilities (such as CEC-JRC-IRSA in Ispra and at ITC) by encouraging their collaborative use and efficient scheduling.
6. Promotes the transfer of technological expertise between members.

7. Makes available some of the largest remote sensing data sets to all network members and assists in developing common European/international data management strategies.
8. On a long-term basis, this research collaboration facilitates access by the Network members to other international, European and/or bilateral research programmes in Earth observation in which individual network members are already involved.

5. CONCLUSIONS

Although accuracy requirements have been well defined for single instruments such as ESA's ERS-1 SAR, little or no accuracy requirements have yet been clearly defined for multisensor registration by the scientific community. More research is needed in this area for each thematic science application such as mapping geology, forestry, land use, etc.

This European scientific network on "Synergy of remotely sensed data" involves many disciplines ranging from physics, photogrammetry, image processing through various application such as forestry, soils, land use and geology, and hence can tackle research aspects of image fusion not possible by an individual research member alone.

Although there was already existing research collaboration between sub-groups of this Network, by placing their research into an overall perspective, individual research workpackages are more focused and enable an overall coherent research strategy and methodology to be developed in Europe.

A highlight of this CEC initiative is the mobility of the many Ph.D. researchers involved in the networks activities. Young remote sensing research scientists from one member institute are carrying out their work in other network members' laboratories, thereby benefitting from a multidisciplinary approach, assisting them in obtaining advanced technical/scientific support to carry out their research, and obtaining other approaches to solving synergy issues to those employed in their home institute. Grouping these young researchers around a team of skilled experts at an international level is showing to be a very effective way to train young European scientists. Their participation in such a multinational research project strengthens the necessary information exchange between scientists of the different member states of the CEC and will create new competence to undertake multidisciplinary research activities at the European level.

6. ACKNOWLEDGEMENT

This research is being partially funded under the CEC's Human Capital and Mobility Programme to set up a European scientific network on "Synergy of Remotely Sensed Data" (Contract No.: CHRX-CT93-0310).

7. REFERENCES

1. Genderen, J.L. van and Pohl, C. (1993): "Geometric integration of multi-image information". (Proc. ESA ERS-1 Symp. on Space at the Service of our Environment, Hamburg, Germany).
2. Genderen, J.L. van, Zuidam, R.A. van and Pohl, C. (eds) (1993): Operationalization of remote sensing in Europe. (Proc. Int. Symp. on operationalization of Remote Sensing, Vol. 2, 236 pages).
3. Pohl, C. and Genderen, J.L. van (1994): Multisensor fusion: optimization and operationalization for mapping applications. (Proc. SPIE Conf. Orlando, USA on "Signal Processing, Sensor Fusion and Target Recognition III". April, 1994).
4. Lavalle, C., Grandi, G. de, Groof, H. de, and Sieber, A. (1992): Polarimetric SAR Calibration: the JRC approach. (Proc. Final Workshop of MAESTRO/AGRISCATT, ESTEC).
5. Visser, M.A.M. and Verhoeven, R. (1993): Radar mapping application in the rain forests and coastal plain of Guyana. (BCRS Report, Delft).
6. Moccia, A. and Vetrella, S. (1986): An integrated approach to geometric precision processing of spaceborne high resolution sensors. (Int. Journal R.S. Vol. 7 no. 3. pp. 349-359).
7. Schuhr, W. (1990): Geometrische Korrektur von Radargrößen (Festschrift Gottfried Konecny, Univ. Hannover, Heft 13).
8. Sasse, V. (1989): Correlation of SAR data with optical data and with simulated data. (Proc. 2nd Int. Workshop on Image Rectification Techniques for Spaceborne Synthetic Radar, Austria).
9. Oesten, G., Kuntz, S. and Gross, C.P. (eds) (1991): Fernerkundung in der Forstwirtschaft: Stand und Entwicklungen (Wiemann-Verlag, Karlsruhe).
10. Goosman, H. (1991): Die Nutzung Geographisches Informationssysteme in der Angewandten Klimatologie. (GIS. Vol. 4 No. 3, pp. 3-7).
11. Koch, B. and Forster, B. (1992): The use of polarimetric radar remote sensing data for applications in forestry. (Proc. ISY, Space in the Service of the Changing Earth, Munich).
12. Bodechtel, J., Sommer, S., Boch, H. and Mauser, W. (1992): Use of airborne imaging spectrometry to the definition of optimized specifications for land applications with future spaceborne imaging spectrometers (Proc. ISY. Conf., Munich).

**APPLICATION OF ERS-1 SAR -DATA
IN LARGE AREA FOREST INVENTORY**
Project PP2-SF1

Erkki Tomppo 1), Martti Hallikainen 2)
Petri Mikkeliä, Helena Henttonen, Matti Katila 1)
Jouni Pulliainen, Kari Heiska, Juha Hyypää, Teemu Tares 2)

1) Finnish Forest Research Institute
Unioninkatu 40 A, 00170 Helsinki, Finland, phone: 358-0-85705340, fax: 358-0-625308
2) Helsinki University of Technology, Laboratory of Space Technology
Otakaari 5 A, 02150 Espoo, Finland, phone: 358-0-4512378, fax: 358-0-460224

ABSTRACT

The main objectives of the study are to test the applicability of ERS-1 SAR images together with other information sources, in estimating forest resources in large areas, for instance at sub-national, national or larger level and, if possible, to develop an operative forest inventory system which utilizes SAR -data. Six test areas, three in Finland and one in each in Canada, China and Russia have been chosen for the study.

First results show that backscattering properties of boreal forests are affected heavily by seasonal changes as well as weather conditions before and during the imaging (moisture in needles and soil). This phenomenon can be utilized by means of multitemporal images, which might be the only possible way to have information for forestry purposes.

1. INTRODUCTION

The total land area of Finland is 30.5 million hectares and the forestry land area 26.4 million hectares, of which 20.1 million hectares are classed as productive forest land (the mean annual increment is at least 1 m³/ha). The total growing stock is 1900 million m³ and the annual increment 80 million m³. Private persons own 63 % of the forest area, the state 24 and companies 9 %, the rest belonging to municipalities, parishes etc. At the end of eighties, the annual removal, cuttings and natural mortality, was 54 million m³, while the gross stumpage earnings of timber sales amounted to 8000 million FIM and the total annual net sales of Finnish forest industries 50000 million FIM. The annual value of exports of forest industries products was 40000 millions FIM, corresponding to about 50 percent of the net income from foreign trade. Forestry and the forest industries thus form the most important single industrial sector in Finland.

The National Forest Inventory of Finland (NFI) has produced large-area forest resource information for over 70 years for management planning of finnish forestry and forest industries. The present operational method exploits satellite image data (Landsat TM), digital map data (e.g. arable land, built areas, roads, digital elevation model when relevant), in addition to ground measurements. The most serious problem in the application of the system are the clouds which often prevent from obtaining images from the growing season of ground measurements.

The Laboratory of Space Technology at the Helsinki University of Technology has developed a helicopter-borne scatterometer (HUTSCAT). It is a dual-frequency (5.4 and 9.8 GHz) FM-CW internally and externally calibrated radar designed for co- and cross-polarized backscattering measurements of natural targets such as forests. Due to the ranging capability, the HUTSCAT can probe the canopy from the top to the bottom with a range resolution of 65 cm (Ref. 2).

The feasibility of the HUTSCAT to estimate stand characteristics of sample plots was evaluated in earlier study (Ref. 3). It was shown that the radar-derived mean and dominant tree heights agree with field-measured mean heights with a standard error of 1.3 metres. The corresponding accuracy of radar-derived stem volume estimates at stand level were 31.3 m³/ha (20 %). The capability of profiling sensors to classify development class, land class, bog type and fertility class is demonstrated in Ref. 3. The percentage of correctly classified cases was surprisingly good (>70 %) for each above class.

2. OBJECTIVES OF THE STUDY

The objective of the study is to develop an operative method for utilizing ERS-1 SAR images in large area forest inventories, such as national forest inventories.

Answers to the following problems will be sought:
1) which variables can be estimated with SAR

data, e.g. land use, site fertility, tree species, stem volume, LAI, biomass, 2) what kind of changes can be estimated, e.g. clear cuttings, deforestation, afforestation, defoliation, 3) what is/are the optimum season(s). should single image or multitemporal images be used, 4) what is the reliability of the method in an area of the size a) 0.5 - 1 million hectares b) 50 000 hectares c) 10 - 100 hectares d) 0.5 - 5 hectares, (Note that the minimum area for which the results can be estimated reliably enough with field measurements only in NFI is of the size 300 000 and with field measurements and optical data about 1000 hectares.) 5) what are the optimal parameters of HUTSCAT-instrument for forest inventory, 6) is it possible to compensate a part of field measurements with HUTSCAT measurements?

A cost-benefit analysis of the method is an essential part of the project.

3. MATERIAL

3.1. Test sites

Six different test areas representing mainly boreal or subboreal forests have been chosen to the study. The size of each site is 100 km × 100 km. Table 1 gives the names, latitude and longitude of the sites.

TABLE 1. *Six test sites of the study.*

Name	Country	Latitude	Longitude
Porvoo	Finland	60° 48"	25° 30"
Teijo	Finland	60° 10"	23° 00"
Inari	Finland	69° 40"	27° 30"
Sortavala	Russia	61° 50"	31° 00"
Hebei	China	48° 50"	130° 10"
Whitecourt	Canada	54° 25"	244° 20"

From these sites, research has been carried out mainly with Porvoo site so far. In addition, a Sodankylä test site in North Finland from another project has been utilized.

3.2 Field measurements

The NFI sample plots are utilized as ground truth data and, to some extend, as a reference data, too. The plots used in this study were established and measured in 1986. The plots are located in L-shaped clusters, the distance between clusters being 8 km in the north-south direction and 7 km in the east-west direction. One cluster consists of 21 Bitterlich-type sample plots (relascope factor 2) with an interval of 200 m.

The sample plots which located at least 30 m apart from the closest stand boundary were remeasured in the summer and autumn 1993 for the study. Total number of these plots was 444. Plots were lo-

calized with GPS (Pathfinder Basic). Tree species, breast height diameter, crown storey and tree quality class were measured from tally trees. Each 7th tally tree was measured as sample tree, measurements involving increments, bucking, damages etc. Usual stand characteristics were measured from surrounding forest stands.

Standwise inventory data measured for operative forest management planning are utilized for reliability assessments. These reference data are based on visual ground estimation with relascope measurements and information from false colour aerial photographs.

Standwise data were located on three different blocks, 119 and 393 ha of spruce dominated forest and 142 ha pine dominated forest. Mean stem volumes were 121, 153 and 126 m³/ha respectively and total number of stands 358 on eight forest holdings. Field checks of stand data were carried out in 1992 and 1993.

3.3. Radar data

ERS-1 SAR.PRI -images from the summer and autumn 1993 have been received, rectified and processed, total number amounting to 19. Winter images have also been received but not processed yet.

A program named VIP is used for geometrical rectification. VIP is programmed in Technical Research Centre of Finland. It utilizes as input a digital elevation model (DEM) (pixel size 25 m, resolution 0.1 m), an ERS-1 SAR.PRI image and optionally a digitized map, from which ground control points can be picked up. Output consists of three channels: first is geometrically rectified image, second is the groundarea/pixel and third is the local incidence angle. Output pixel size is 25 meters.

HUTSCAT measurement will be conducted along NFI sample plot lines in late summer 1994. The pre-defined survey lines can be flown using the GPS-navigator.

3.4. Ancillary data

Digital map data are applied from separating forestry land from other land use classes. The applied themes are arable land, roads and other built areas. Digital swamp mask has also been tested but it is not reliable enough. Water areas are extracted from Landsat TM images.

The ground-reference data also includes the meteorological statistics including the daily precipitation information. These data were acquired from various meteorological stations on the test site for five month period from 1st on May to 1st on October. Data values include the sum of daily precipitation for every day in that time span. Using interpolation

methods the precipitation values for entire test site were calculated.

For the Porvoo test area, soil moisture measurements have been conducted simultaneously with the ERS-1 measurements for selected test areas, and in future, the soil moisture estimates for the whole Porvoo test area will be obtained. Thorough soil type measurements have also been carried out for moisture sample plots.

Numerical soil-class maps from Southern Finland were used as reference data for soil type classification. The scale of the maps is 1:100000 and the pixel size 25 meters. Soil classes were defined as: 1) open rocks, 2) eskers, 3) gravel and sand, 4) peat, 5) fine sand and 6) clay and silt, 7) till.

4. METHODS

Speckle Removal

Several methods for speckle removal have been tested. Principal component analysis (PCA) removes speckle from the first principal components. The method requires several images to work properly. Iterated Conditional Modes method (ICM) based on Gibbsian random field assumption is introduced in Ref 1. By applying the method on one image with a window size of 3×3 pixels about three times, regions approximately of the size of a typical stand can be recognized. Sigmafilter (Ref. 5) is an edge-preserving speckle removing filter. The method is simple and operates on one image at time. Simulated annealing method has also been tested. Its results were fairly realistically segmented images, but the size of the segments was too big to be of use in operative forest management.

Image analysis

A *k*-nearest neighbour classification has been applied on our test area in Porvoo, using seven images. Images covering all forest stands applied as test data were selected for analysis. Three of the images are from an ascending and four from a descending orbit.

The basic classification algorithm is as follows. The Euclidean distance, $d_{i,p}$, is computed in the feature space from the pixel p to be classified to each pixel i whose ground truth is known (sample plots). Take $d_{(1),p}, \dots, d_{(n),p}$, ($d_{(1),p} \leq \dots \leq d_{(n),p}$), $n \sim 5 - 10$ and define $w_{(i),p} = \frac{1}{d_{(i),p}^2} / \sum_{i=1}^n \frac{1}{d_{(i),p}^2}$. Define the estimate \hat{m}_p of the variable M for the pixel p

$$\hat{m}_p = \sum_{j=1}^n w_{(j),p} \cdot m_{(j),p}, \quad (1)$$

where $m_{(j),p}$, $j = 1, \dots, n$, are the values of the variable M in the n closest pixels in the spectral space to the pixel p (Ref. 7).

Three different optionally pre-processing meth-

ods for ERS-1 -images after rectification were used: 5×5 average, mode filtering and no filtering.

5. RESULTS

Comparisons with standwise field measurements

The performance of the classifications was judged by comparing the obtained standwise estimates with the corresponding standwise estimates of FBD data (totally 654 hectares). Correlation coefficients weighted by stand area, difference (BIAS) and root mean square error (RMSE) were calculated.

Twice mode-filtered ERS-1-images gave the best results in standwise comparisons though none of the pre-processed images gave statistically significant correlation coefficients for mean volume at stand level. The mean of the estimated stand volume was $159.8 \text{ m}^3/\text{ha}$, BIAS $-18.3 \text{ m}^3/\text{ha}$ and RMSE $104.6 \text{ m}^3/\text{ha}$. The same estimates by volume classes (VCL) are presented in table 2.

TABLE 2. The mean stem volume (V), BIAS and RMSE in the forest holdings.

VCL m^3/ha	stand area ha	V m^3/ha	BIAS m^3/ha	RMSE m^3/ha
0 - 49	0.1	45.0	-45.0	45.0
50 - 99	2.9	88.0	4.9	86.9
100 - 149	177.7	141.4	17.4	96.7
150 - 199	463.7	166.3	-31.2	107.7
200 - 299	10.7	206.8	-60.1	100.6

The classification was also studied at forest holding level. Eight forest holdings were composed from stands, size varying from 20 to 195 hectares. The best result was received with an unfiltered SAR image. Table 3 shows the areas, estimated mean volume and BIAS by forest holdings.

TABLE 3. The mean stem volume and BIAS by forest holdings.

area ha	V m^3/ha	BIAS m^3/ha
142.3	152.2	-26.4
19.2	147.8	41.5
21.7	154.4	-7.5
98.4	151.2	20.7
78.7	153.2	-56.0
193.7	156.7	-6.2
32.6	155.0	-11.1
68.5	148.2	-8.4

Comparison with Landsat TM classification

Because of lack of sufficient large field measured data, classification results were compared with that obtained with Landsat TM and field sample plots.

Eleven test squares each of 16 km^2 were placed inside the area of SAR images. These test squares were subdivided into squares of one km^2 .

Landsat TM image (date 25th May 1992) was classified using the k-nearest neighbours method. Five nearest neighbours were chosen and the ground truth data was the same updated NFI data as used in SAR classification total number of sample plots utilized being 382. Digital map data was utilized in order to separate forest and non-forest areas.

The means of the estimated variables were calculated for each test square. The performance of the SAR classification was judged by comparing the differences of the estimates and calculating the correlation coefficients.

The correlation coefficient between mean stem volume estimates in one km^2 test square (176 observations) was 0.22. The estimated (SAR) mean volume, difference BIAS and RMSE for one km^2 and 16 km^2 test squares are shown in Table 4. One reason for the large BIAS may be that the ground truth for the TM image covers larger area than the SAR images. Anyway, the BIAS and RMSE seem to decrease when the area increases from 1 km^2 to 16 km^2 .

TABLE 4. The SAR mean stem volume (V), BIAS and RMSE in the test squares of one and 16 km^2 .

	V m^3/ha	BIAS m^3/ha	RMSE 1 km^2		RMSE 16 km^2	
			176 squares		11 squares	
			m^3/ha	%	m^3/ha	%
all tree species	154.5	-18.4	28.0	18.1	20.8	13.5
pine	28.2	5.2	8.6	30.5	7.1	25.2
spruce	97.4	-16.4	24.7	25.4	18.3	18.8
birch	25.8	-6.4	7.2	28.3	6.7	26.0
broad leaved trees	3.0	-0.7	1.0	33.8	0.8	27.2

Effect of soil moisture to the backscattering coefficient

ERS-1 SAR images from the dates 24th of July, 28th of August, 2nd of October and 6th of November were applied for analyzing the co-effect of soil type and moisture variation on backscattering coefficients. SAR images were compared pixelwise with the soil map. SAR images were geocoded using the terrain elevation model. Mean values of the backscattering coefficient for different soil-classes are presented in Table 5.

TABLE 5. Mean values of σ^0 for the soil classes

Date	Open rocks	Moraine	Moraine ridges	Eskers	Clay and silt	Peat	Gravel, sand, fine sand
24.7.93	-9.87	-7.79	-8.99	-9.27	-10.00	-7.72	-8.80
28.8.93	-9.02	-10.26	-7.85	-8.75	-9.02	-9.79	-7.83
2.10.93	-9.07	-9.29	-10.26	-7.66	-8.49	-8.83	-10.17
11.6.93	-7.68	-8.64	-8.99	-10.01	-7.72	-8.75	-8.92

High values of fine sand and clay classes are mainly caused by high moisture content of those soil types. There was a strong rain during the SAR data acquisition on the 24th July.

Statistical inversion approach and a developed semi-empirical model (Ref. 6) can be employed to estimate forest parameters (e.g. stem volume) from multi-temporal images. Field-measured reference sample plots are necessary as a priori data for inversion.

The comparisons have been conducted using ERS-1 SAR data corresponding the NFI sample plots from the Porvoo test area. The semi-empirical backscattering model has been fitted into the sample plotwise SAR results using two free parameters which correspond to (1) volumetric soil moisture and (2) volumetric forest canopy moisture. Only the sample plots on mineral soil forest or scrub land are applied (85 % of the plots). Table 6 shows the environmental conditions during ERS-1 SAR images acquisitions.

TABLE 6. Environmental conditions for ERS-1 images employed.

Porvoo area conditions in summer and autumn 1993 during the ERS-1 data acquisition.							
Date	Precipitation(mm)(days prior to image acquisition)				T (°C)	snow water equivalent (mm)	
30 June	0	0	0.6	0.8	0	15.0	No snow
24 July	0	4.7	0	0.1	7.9	15.8	No snow
4 Aug.	0	5.6	0	0	0	17.6	No snow
28 Aug.	11.8	0	0	0.8	1.2	12.1	No snow
2 Oct.	0	0	0	0	0	7.1	No snow
13 Oct.	0	11.3	3.4	15.1	0.7	9.9	No snow
6 Nov.	0	0	0	0	0.3	No snow	

Figure 1 presents the model fittings obtained for summer and autumn 1993 for the Porvoo test area ERS-1 SAR images. The highest positive correlations are obtained in cases where a long non-rainy period (over one week) has occurred before the SAR image acquisition (6 November and 2 October). Hence, the soil moisture has evidently had low values compared e.g. with the results for 13 October when a substantial rain occurred a day before the image ac-

quisition (Table 6). The comparison of results of Figure 1 with the weather statistics given in Table 6 indicates a logical behaviour: the higher the rain rate has been, the higher is the level of backscatter from ground (since the soil moisture is evidently higher). The variation of the backscattering coefficient appears to be higher for unforested areas ($V = 0 \text{ m}^3/\text{ha}$) than for heavily forested areas. This indicates that the changes in forest canopy moisture are lower than those at forest floor. The model fittings propose the average soil moisture to vary from 9.5 % (6 November) to 15.5 % (13 October). The anomalous behaviour in the results for 24 July is probably due to the heavy precipitation during the image acquisition.

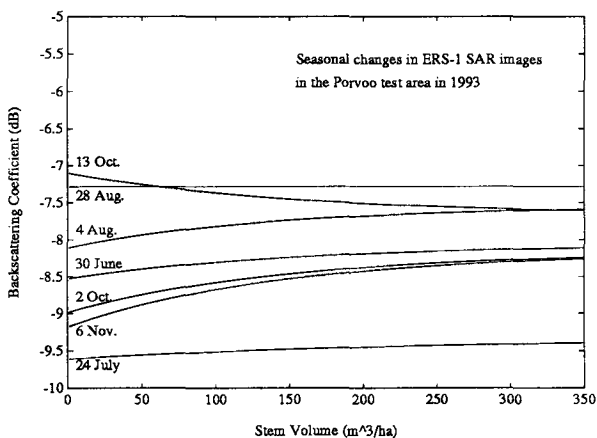


FIGURE 1: The observed average behaviour of ERS-1 SAR-based backscattering coefficient as a function of forest stem volume in the Porvoo test area in the summer and autumn of 1993.

The analysis of winter time images in Sodankylä test area show that the response to forest stem volume is at its highest level with the presence of wet snow-cover (Ref. 4). This phenomenon occurs probably either (1) due to the high signal attenuation caused by the wet snow or/and (2) due to the low level of backscatter from the (smooth) air-snow boundary.

The modelled response of the backscattering coefficient to soil moisture is depicted in Figure 2. The results are shown for VV polarization but the magnitude of the soil moisture effect is similar for the other polarizations. The results show that the effect of soil moisture is higher than that of the stem volume on the backscattering coefficient. The volumetric soil moisture typically ranges from 5 to 15 % on moraine lands (the most usual soil type in Finland). Higher moisture values for moraine lands are possible in the snow melting period and after heavy rain. For spruce and pine mires (peat soils), and for clay soil, higher soil moisture values are evident.

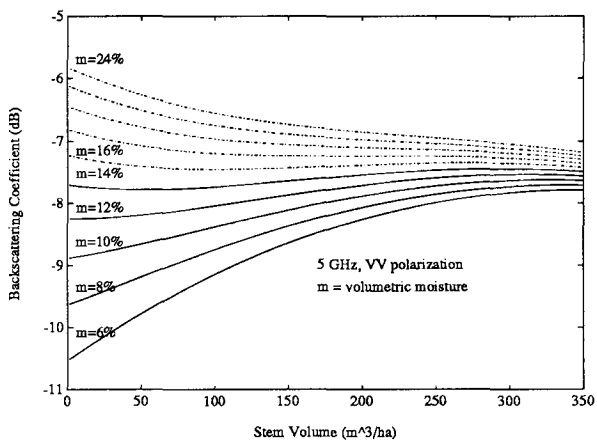


FIGURE 2: Behaviour of the backscattering coefficient at 5 GHz, VV polarization as a function of stem volume with a varying volumetric soil moisture value (2 %-unit intervals).

6. CONCLUSIONS

The method for utilizing ERS-1 SAR images in large area forest inventory are under development. The behaviour of backscattering properties of boreal forests are investigated. The following conclusions were drawn so far.

The correlation of the backscattering coefficient to forest biomass can change from positive to negative depending on weather and seasonal conditions. The highest positive correlations can be observed in cases where the ground is either very dry or covered by wet snow. The highest negative correlations are evident after heavy rain when the soil is still wet, but the forest canopy is back to its normal moisture value.

The estimation of stem volume using ERS-1 SAR data requires data representing at least two cases: the one with a positive and the other with a negative correlation of the backscattering coefficient to stem volume. When multi-temporal data are employed, the radar speckle evident in a single image can be reduced using principal component analysis or filtering methods.

Experiments show that multitemporal ERS-1 SAR data could be of use in operative large area inventories. Methodology development for these applications will continue.

Stand profiles obtained with the airborne ranging radar may provide valuable reference data for national forest inventories. Additionally, radar-derived stand profiles can be used to estimate standwise stand characteristics such as mean and dominant height, stem volume, development class, land class, bog type and site fertility.

7. REFERENCES

1. Besag, J.E. 1986. On the statistical analysis of dirty pictures (with Discussion). *J.R.Statist.Soc.* B, 48, 259-302.
2. Hallikainen, M., Hyppä, J., Haapanen, J., Tares, T., Ahola, P., Pulliainen, J. and Toikka, M., 1993. A helicopter-borne 8-channel ranging scatterometer for remote sensing, Part I: system description, *IEEE Transactions on Geoscience and Remote Sensing*, Vol. 31, No. 1, 161-169.
3. Hyppä, J. 1993. Development and feasibility of airborne ranging radar for forest assessment. Helsinki University of Technology, Laboratory of Space Technology, Report, 112 p.
4. Hyppä, J., Pulliainen, J., Hallikainen, M., Koskinen, J., Heiska, K., Tomppo, E., Mikkel, P., Henttonen, H., Katila, M. 1994 Radar-aided forest inventory. To appear in: Proceedings of Piers-symposium.
5. Lee, J.S. 1983. "Digital Image Smoothing and the Sigma Filter", *Computer Vision, Graphics and Image Processing*, nr. 24, 255-269
6. Pulliainen, J. 1994. Investigation in the backscattering properties of Finnish boreal forests at C- and X-band: a semi-empirical modeling approach. Laboratory of Space Technology, Helsinki University of Technology. Report 19, 121 p.
7. Tomppo, E. 1991. Satellite Image-Based National Forest Inventory of Finland. International Archives of Photogrammetry and Remote Sensing, Vol 28, Part 7-1, 419-424.

APPLICABILITY OF ERS-1 SAR IMAGERY IN MAPPING FOREST REGENERATION IN BURNT AREAS SUBJECT TO DESERTIFICATION

C. Banninger, H. Gallaun, K. Granica, L. Kenyi, H. Raggam

Institute for Digital Image Processing, JOANNEUM RESEARCH
Wastiengasse 6, A-8010 Graz, Austria
Tel: (+43) 316 876 735 Fax: (+43) 316 876 720

ABSTRACT

ERS-1 SAR imagery acquired from burnt forested sites in southern Greece proved only moderately successful in determining plant species, density and height associated with their natural regeneration. Speckle-filtered images provided better discrimination of these plant variables than did the corresponding non-filtered images, as did descending scenes compared to ascending scenes, although the latter is likely only a function of the position of the burnt areas relative to the radar look direction. The presence of a terrain component in the backscatter signal received from the burnt sites complicates the interpretation of the relationships derived between the SAR data and ground features measured, and needs to be removed before a proper assessment of these relationships can be made.

1. INTRODUCTION

The capacity of satellite remote sensing data to provide information on surface features and conditions contributing to the onset and progression of desertification in semi-arid regions of the Mediterranean is being investigated at the Institute for Digital Image Processing within the framework of an EU-sponsored study to develop a GIS-based decision support system for assessing the likelihood of land degradation leading to desertification triggered by forest fires. Both multitemporal optical (Landsat Thematic Mapper and SPOT) and different look-direction radar (ERS-1 SAR) images are being utilised within the study in combination with map and ground-collected data, to evaluate the thematic information provided by each sensor and combination of sensors. Such an approach necessitates a high level of image processing to be able to merge the different remote sensing and ground data sets to extract the pertinent thematic information (e.g., plant species, density, biomass) from the imagery. This would allow the degree and extent of plant regeneration in burnt areas to be determined and hence a measure of the level of recovery of an area.

The Mediterranean region is plagued by fires that yearly destroy vast tracts of forests. Because of the fragile nature of the environment in this region, land degradation can develop rapidly if the burnt

areas do not swiftly recover and soil erosion is able to proceed unchecked by plant regrowth.

SAR data are able to provide information on plant variables that can be used to assess plant regeneration in burnt areas. However, because of terrain-induced distortions and coherency-related noise in the SAR data, these need to be removed before the data can be used for this purpose. The extent to which ERS-1 data are able to provide information on plant regrowth in burnt areas is examined and their usefulness evaluated for fire-related land degradation assessment in semi-arid environment. The Greek forestry service selected four forested areas for detailed study in the Attica region of southern Greece that had suffered extensive fire damage in the early 1980's. Within these four burnt areas, they defined 39 test sites for extensive ground survey for use in the evaluation of the remote sensing data acquired from the sites.

2. TEST AREA DESCRIPTION

The four test areas and their 39 test sites are situated in a mountainous region that extends to the west and east of the city of Athens. The test sites, each measure several 100 meters on their sides and represent various stages of regeneration, ranging from scarce to almost complete plant cover. Aleppo pine, maquis, and phrygana comprise the principal vegetation types at the sites, whereas rocks, stones, and bare soil the non-vegetation cover. Most plant growth is at an early stage of recovery, with plant heights rarely exceeding 1.0-1.5 metres.

Test site variables measured by the forestry service at each site include plant species, per cent cover of each species, and their average height, and the per cent cover for rocks and stones, plus bare soil.

3. ERS-1 SAR DATA

Five ERS-1 SAR scenes, comprising two descending June 1993, one descending July 1993, and two ascending June 1993 images, cover the four test areas examined in the study (Figure 1).

ERS-1 data contain a considerable amount of „noise“ in the form of speckle, which degrades the interpretability of the images. Although speckle is the result of coherent scattering from different ground features, it is treated as noise and needs to

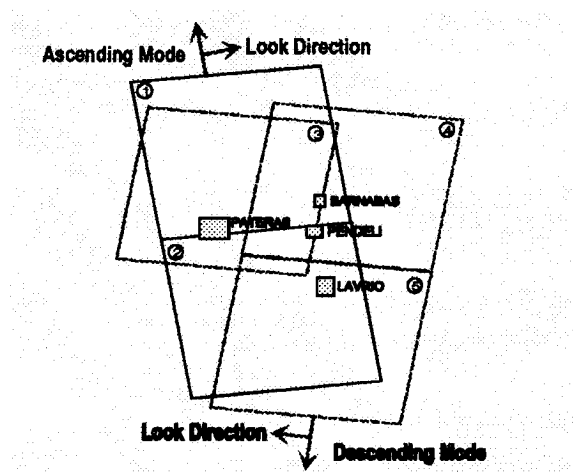


Figure 1: ERS Coverage of Test Areas

be either removed or reduced before data analysis is undertaken. This can be achieved by the use of the Minimum Mean Square Error (MMSE) estimation or Frost filter with the formula:

$$e^2 = E \{ [X - I \cdot M]^2 \}$$

where
 I=original image intensity (16 bit)
 X=filtered image
 e = quantity to be minimised
 M=expected filter response

Using a 3x3 pixel window, the Frost filter reduced the amount of speckle in the images while at the same time keeping smearing to a low level. This resulted in the smoothing of homogeneous areas, whilst preserving fine details in the image, with a minimum loss in textural information. As images from different dates, orbits, and look directions are employed in the study, and the region under investigation comprises mountainous terrain, a precise registration amongst the various SAR and ground data sets is required for a proper analysis of the ERS-1 imagery. This is particularly important for SAR imagery acquired from high relief areas, where the viewing geometry can result in displacements of 500 m at 250 m elevation and 3000 m at 1000 m elevation.

The geometric rectification of the SAR data entailed a parametric restitution of the images to the Greek Geodetic Coordinate System (EGSA87), by means of ERS-1 orbit parameters and Digital Elevation Models (DEM's) of the four test areas. Despite difficulties encountered with errors in the orbit parameters and the DEM's, and the identification, distribution, and digitisation of ground control points (GCP's) in the imagery and topographic sheets, an approximate 1 pixel (± 20 m) registration accuracy was achieved for the five ERS-1 scenes.

4. DATA ANALYSIS AND RESULTS

The thematic aspect of the study involve the development of algorithms that relate the ERS-1 SAR data to ground features and variables of interest within the burnt forest test sites. A statistical approach is being used that involves regressing SAR intensity values against the test site variables of rocks+stones, bare soil, rocks+stones+bare soil, maquis, phrygana, maquis+phrygana, Aleppo pine, and maquis+phrygana+Aleppo pine per cent cover, plus a bioheight index, defined by:

$$\text{Bioheight Index} = (\text{maquis+phrygana} \times \text{average height maquis+phrygana}) + (\text{Aleppo pine} \times \text{average height Aleppo pine})$$

at each of the 39 test sites. The highest correlation coefficients (r values) and coefficients of determination (r^2 values) derived from the regression of the June ascending and June and July descending ERS-1 data against each of the nine ground variables are given in Table 1.

Test Site Variable	SAR Images	No. of Test Sites	Original SAR Image		Filter SAR Image	
			r	r^2	r	r^2
Rocks+Stones	Dsc	9	0.42	0.18	0.72	0.52
	June		-	-	0.32	0.10
Bare Soil	Dsc	9	-	-	-	-
	June		-	-	-	-
Rocks+Stones +Bare Soil	Dsc	9	0.30	0.09	0.65	0.43
	June		-	-	-	-
Maquis	-	-	-	-	-	-
	Phrygana	26	-0.48	0.23	-0.48	0.23
Phrygana	Asc	9	-0.22	0.05	0.66	0.44
	June		-	-	-	-
Maquis+Phrygana	Dsc	9	-0.43	0.18	0.61	0.37
	June		-	-	-	-
Aleppo Pine	Dsc	9	0.31	0.09	0.32	0.11
	June		-	-	-	-
Maquis+Phrygana+A. Pine	Dsc	9	-0.30	0.09	-0.27	0.08
	June		-	-	-	-
Bioheight	Asc	26	-0.45	0.21	-0.45	0.20
	June		-	-	-	-
Bioheight	Dsc	12	0.64	0.40	0.65	0.42
	July		-	-	-	-

Table 1: Coverage of Test Areas

Because of the presence of radar shadow and topographic layover in the SAR scenes acquired from the four test areas, complete coverage of all 39 test areas was not obtained for either the set of ascending or descending SAR images, as shown in Table 1.

A high standard error of estimate (SEE) is associated with all the r and r^2 values listed in Table 1 and indicates a large variance between the data sets employed in the regression analysis.

5. CONCLUSIONS

The descending ERS-1 SAR images from June 1993 consistently produced the highest correlations with respect to the test site variables, with one exception. The use of filtered images in the analysis markedly improved the regression statistics over that obtained with the original images and confirmed the necessity to perform this enhancement to the SAR data prior to image analysis. These results, however, are tempered by the small sample size employed ($n=9$) and the large standard error of estimate associated with the regression analysis.

The positive correlations obtained for non-vegetative features (rocks, stones, bare soil) and the negative correlations for the vegetation component (maquis, phrygana, Aleppo pine) may be related to the volume scatter of the radar signal within the plant canopy compared to the surface scattering related to the solid materials. As vegetation density increases, volume scattering becomes more dominant, with a resultant decrease in the strength of the radar return signal.

The results obtained between the ascending SAR June imagery (negative correlation) and the descending SAR July image (positive correlation) for the bioheight index are unexplained, that may be due to a significant contribution of the terrain to the backscatter signal from the sites, which would speak strongly for its removal prior to any analysis.

The merging of ascending and descending scenes of the same ground area would prove to be useful in removing image layovers and shadow related to topography that resulted in a loss of scene information.

6. REFERENCES

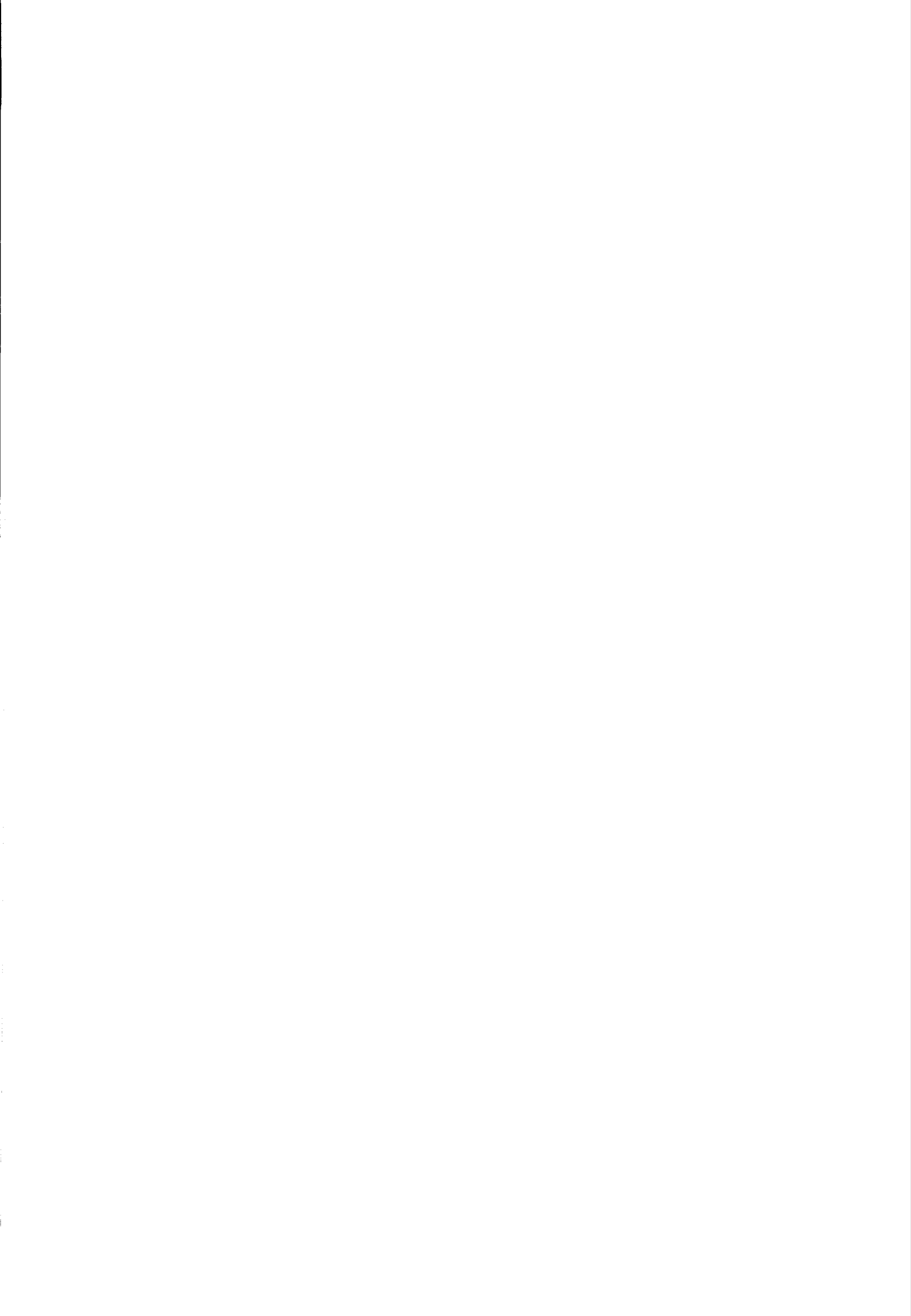
Almer A., Raggam J. & Strobl D. (1991): High-Precision Geocoding of Spaceborne Remote Sensing Data of High-Relief Terrain. *Proc. ACSM/ASPRS/Auto Carto Annual Convention, Baltimore, Maryland, March 25-29, 1991.*

Frost V.S., Stiles J.A., Shanmugan K.S. & Holtzman J.C. (1982): A Model for Radar Images and its Application to Adaptive Digital Filtering of Multiplicative Noise, *IEEE Trans. on Pattern Analysis and Machine Intelligence, Vol. PAMI-4, No.2, March 1982, pp. 157-166*

Holecz F., Meier E. & Nüesch D. (1993): Postprocessing of Relief Induced Radiometric Distorted Spaceborne SAR Imagery, in: *SAR Geocoding: Data and Systems, ed. Schreier G., pp. 299-352, Wichmann Verlag*

JOANNEUM RESEARCH (1994): Remote Sensing Software Package Graz. Software User Manual. Institute for Digital Image Processing, Graz.

Raggam J., Almer A. & Strobl D. (1992): Multisensor Mapping Using SAR in Conjunction with Optical Data, *Int. Archives of Photogrammetry and Remote Sensing, Vol. 29, Part B4, Commission II, pp. 556-563, 17th ISPRS Congress, Washington D.C., 1992*



TROPICAL RAINFOREST INVESTIGATION IN BRAZIL USING ERS-1 SAR DATA

Dominic R. Scales, Manfred Keil, Rudolf Winter

German Remote Sensing Data Center (DFD), German Aerospace Research Establishment (DLR),
D-82234 Oberpfaffenhofen, Germany

ABSTRACT

Multitemporal ERS-1 SAR data of a testsite north of Rio Branco, state of Acre, Brazil, are investigated in combination with Landsat TM data for monitoring of tropical rainforest cover and land use change detection. These studies within an ERS-1 pilot project started in May 1993 and are funded by DARA. They are integrated in a cooperation with the Brazilian National Institute of Space Research (INPE) and continue studies on TM data. The results are going to be included within the TREES programme.

Five ERS-1 datatakes between April and December 1992 were available as geocoded ERS-1 products. Multitemporal ERS-1 products and combinations with TM products are discussed for forest / nonforest separation. Promising results for classification have been acquired by the EBIS classifier ("Evidence based Interpretation of Satellite Images", Lohmann, 1991). Monotemporal as well as multiseasonal ERS-1 datasets were used for classification.

Keywords: Rainforest, monitoring, ERS-1 SAR data, supervised classification.

1. INTRODUCTION AND OBJECTIVES

High resolution satellite imagery is a very valuable base for monitoring of tropical rainforest regions. In 1989, a cooperation between the German Aerospace Research Establishment (DLR) and the National Brazilian Institute of Space Research (INPE) was started. The aim is to study the abilities of remote sensing for monitoring the environmental impact of deforestation in the Amazon region and for mapping of rainforest formations and anthropogenic land use. The study site was defined in the southwestern part of the Amazon basin near Rio Branco/Acre. Mainly Landsat MSS and TM data of the period between 1975 and 1990 were used besides microwave data of the RADAM campaign (Ref. 1). Based on these studies and within this cooperation, an ERS-1 pilot project (PP2-D3) started in May 1993, funded by DARA, in order to test C-band SAR data for forest monitoring purposes in areas of frequent cloud

cover.

Objective of the project is to identify the potential value of ERS-1 SAR data for monitoring rainforest regions and to detect changes due to human activities (e.g. deforestation by logging and burning). Various tools are to be developed and tested especially for the differentiation between forest and nonforest areas and for different regrowth and land use states. The information content of ERS-1 SAR data is also to be investigated for differentiation of forest types (dense and open rainforest), the influence of seasonal changes and the dependence on surface topography. The use of combined TM and ERS-1 SAR products is to be demonstrated, e.g. in the context of biomass loss estimations for climatic research (Ref. 2) and also for regional planning purposes.

The study site Sena Madureira/Rio Branco has recently been covered by the first SIR-C/X-SAR shuttle mission, the area, a backup super testsite for ecology, will be investigated by a PI project led by DLR/DFD.

2. STUDY SITE

The study site covers an area in the southwestern part of the Amazon basin, in the bordering region of the states of Amazonas and Acre. The area includes a part of the Trans-Amazon, the main road BR-364, between Rio Branco, the capital of Acre, and the town of Sena Madureira northwest of it (see Fig. 1). The study site is covered by different primary and secondary rainforest formations and, along the BR-364 and around Sena Madureira, nonforest areas mainly used as pastures. The geomorphology is characterized by the plateaus of tertiary sediments (cut by the drainage system), hilly zones and the flat river bed parts of Rio Purus (Ref. 1).

Mainly cattle farmers have pushed the deforestation, which lead to large deforestation patterns along the main road BR-364 between Sena Madureira and Rio Branco. The cultivation of pastures, the progress in burning and logging as well as the actual regeneration of deforested land are an important factor to the equilibrium of the ecosystem. In the Acre testsite, the dry period starts about

end of May and continues up to the mid of September. Withinin that period, annual burning of pasture land alters the seasonal vegetation cover. The most homogeneous aspect is shown during the end of the dry season.

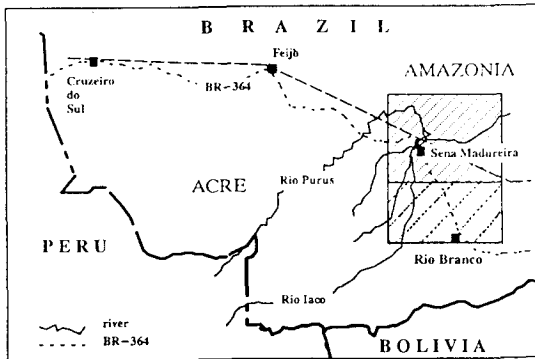


Figure 1. Location of the testsite Sena Madureira / Rio Branco.

3. DATA

3.1 ERS-1 SAR data

ERS-1 SAR datasets have been ordered for two to three times a year in order to detect seasonal differences and to perform change detection. Up to now, data of five acquisition dates from 1992 are available as GEC products (Geocoded Ellipsoid Corrected):

- April-26, May-30 and Dec-26 from descending orbits,
- May-15 and June-19 from ascending orbits.

3.2 Reference data

A Thematic Mapper scene from September 1990 was the main base for reference studies. In several subscenes around Sena Madureira, TM classifications of rainforest formations and nonforest areas were available (Ref. 1) based on this scene. A floating TM scene from August 1992 has been ordered to reference 1992 data, covering Sena Madureira and the continuation towards Rio Branco.

4. METHODS

4.1 Georeferencing

The ERS-1 SAR scenes were used as GEC datasets. The reference TM scene from 1990 was co-registered to the

ERS-1 scene from May 30, using 15 control points. The GEC products of different acquisition dates were mismatching between 1 and 6 pixels of 12.5 m by 12.5 m. In order to perform a multitemporal ERS-1 SAR evaluation, a simple improvement of geo-referencing could be accomplished by linear shifting of SAR scenes along lines and columns. This gave satisfying results for GEC products of the same orbit direction. Using a rough mean for the four pixels concerned, a resampling to 25 m proved to be more adequate for the SAR pixel resolution.

4.2 Data combinations and visual interpretations

For the area around Sena Madureira, TM data of 1990 were used for comparison. A TM based classification of deforested land along the BR-364 was available, covering an area of mainly pasture land of 30 km by 30 km (Ref. 1). The deforestation was also extracted by a TM classification for an area of 60 km by 60 km. The border line of this forest / nonforest classification was superimposed on monoseasonal and multitemporal ERS-1 SAR datasets for visual interpretations and classification checks.

4.3 Classification

For classification purposes, several methods such as thresholding and maximum likelihood classification were tested, also for filtered data (e.g. Frost filter). A special investigation covered the EBIS classifier by Lohmann ("Evidence based interpretation of satellite data", Ref 3). In contrast to maximum likelihood method, EBIS enables the definition of each object class by several different descriptors. Besides Gaussian distribution, also multinomial distributions for local histograms within choosable window environments around the central pixel are supported. The method proved to be suited to classify heterogeneous rainforest stands by TM data (Ref. 1) and seems to be also suitable for SAR patterns, as the speckle and textural information in a pixel environment is taken into account.

5. PRESENT RESULTS

5.1 Visual interpretation

Within the rainforest areas, the dominant ERS-1 SAR information is given by the relief. The plateaus of tertiary sediments, cut by the drainage systems, can clearly be separated against the river basins and the hilly zones.

The deforested areas can be separated because of the lower backscatter compared to rainforest areas (Fig. 2). The contrast was found higher in the later May and June scenes, further within the dry season. The December scene shows less homogenous contrast. Different backscatter levels in the rainy season seem to point out different development of vegetation cover which has to be studied by sampling ground check information. Partly backscatter reaches higher levels in the deforested areas. Thus the December scene gives a bad base for monotemporal investigations but can give interesting additional information in a multitemporal overlay.

Also the deforested areas are partly strongly influenced by relief, especially in a region half way between Sena Madureira and Rio Branco (lower right part of Fig. 2). Backscatter values overlap for illuminated deforested areas and more shadowed rainforest areas.

In parts of the deforested areas, the ERS scenes of May and June show nearly the same backscatter levels as in rainforest areas. Thus, an area used as pasture in 1990 could not be separated in the ERS-1 SAR scenes of the beginning dry season of 1992 (Ref. 4). A higher amount of shrub vegetation seems to have developed in the two-years period (to be checked at the planned field survey in June/July 1994) leading to similar backscatter behaviour as over rainforest cover. By integrating the wet season data of December, the separability is improved.

5.2 Results of classification

For separation of forest / nonforest, both thresholding and maximum likelihood classification gave no satisfying results. Promising results were reached using the EBIS classifier. A search window of 7x7 was found to be more adequate than a 5x5 window.

The result of monotemporal SAR classification in the subarea around Sena Madureira, covering an area of 60 km by 50 km, is shown in Fig. 3. In order to enable comparisons with TM based classification, the border line of this forest / nonforest classification is superimposed again. As EBIS uses local histogram descriptors for classification, there was no large difference between original data or Frost filtered data as input. Especially because of the relief influences a larger amount of misclassification remains which can be reduced by post-classification filters.

Comparisons between TM and ERS-1 based classification in two subareas gave following results

(without post-processing by filtering):

In a subarea South of Sena Madureira, 92.8% of rainforest areas by TM classification were hit by ERS-1 (30-May-92) and 61.6% of nonforest areas. In a more hilly subscene along BR-364, the corresponding values were 91.6% and 59.4%. Misclassifications were found in possible regeneration areas and areas of higher relief.

Multitemporal classification improved results in parts of the regeneration areas.

6. CONCLUSIONS AND FUTURE WORK

Due to the present results, ERS-1 SAR data have a high information content for discrimination between forest and nonforest areas in the Acre testsite. A partial overlap of rainforest and bushy regeneration areas remains. By data acquisition during the late dry season an improved forest / nonforest separation is expected. As the relief gives the main contribution to the signal within the rainforest, the differentiation of rainforest formations seems to be difficult, but correlations seem to exist. Promising results for classification were reached with the EBIS classifier. A better assessment of classification success will be possible after integrating the field campaign data of June/July 1994. A new EBIS version is under development which will allow to integrate texture measures into the classification process.

The classification approach is planned to be extended to the North (smaller deforestation patterns along Rio Purus) and to the Southeast (environs of Rio Branco). Large-area use of forest/nonforest classification will be especially interesting when ERS-1 datasets of different years are available for change detection. Interesting supplementary results are expected by the SIR-C/X-SAR missions of 1994, when L-band and X-band data will be available in subregions of Sena Madureira.

7. REFERENCES

1. Hönsch, H. 1993, "Erfassung und Klassifizierung von tropischen Regenwaldinformationen und anthropogenen Nutzungen anhand von multisensoralen Satellitenbilddaten am Beispiel Brasiliens", Dissertation Universität Trier, *DLR-FB 93-15*, Oberpfaffenhofen.
2. Hönsch, H. 1992, Remote Sensing Satellite Data as an Instrument to Verify a Greenhouse Gas Convention – A

Case Study in the Brazilian Amazon. – Di Primio, J.C., and Stein, G.(eds.): A Regime to Control Greenhouse Gases. – *KFA-Proc. Band 10*, 12.–14.6.1991, Bad Neuenahr, p. 155–166.

3. Lohmann, G., 1991, "An Evidential Reasoning Approach to the Classification of Satellite Images", Doctoral thesis Technische Universität München,

DLR-FB 91-29, Oberpfaffenhofen.

4. M. Keil, H. Hönsch, R. Winter 1993, Tropical Rainforest Investigation in Brazil using ERS-1 SAR Data, *Proceedings of the 2nd ERS-1 Symposium, 1–14 October 1993, Hamburg*, I, 481–484.

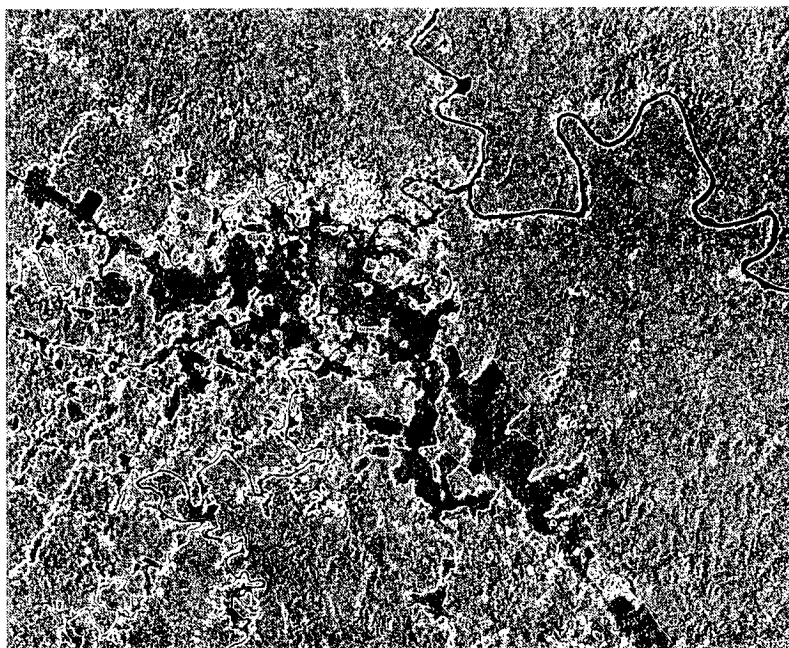


Figure 2. ERS-1 SAR subscene of 60 km by 50 km (30–May–1992). From Sena Madureira in the northwest part of the subscene, the road BR-364 leads southeast towards Rio Branco, accompanied by large deforested areas. Superimposed is the border line of forest/nonforest extracted by an EBIS classification of the TM scene of 1990.

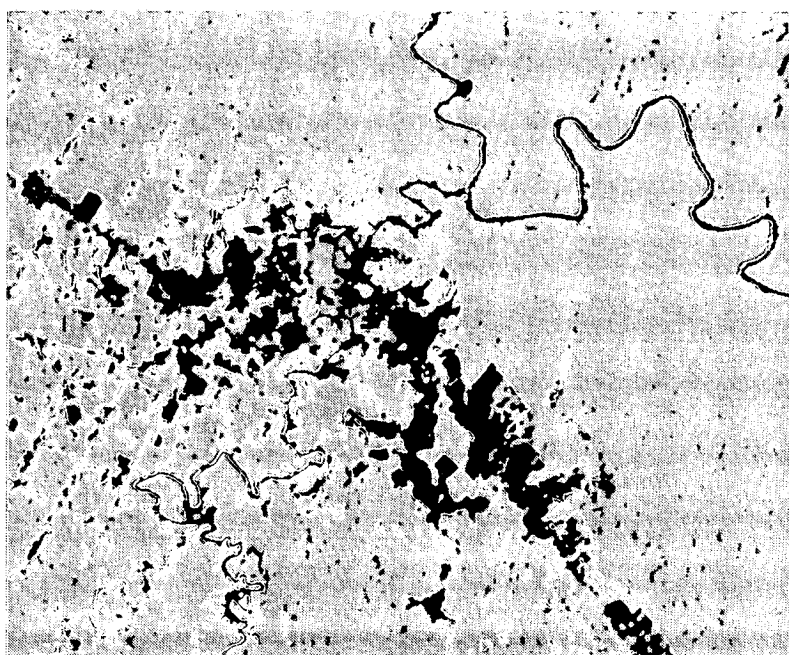


Figure 3. Result of a monotemporal EBIS classification of the ERS-1 SAR subscene of 30–May–1992. For comparison, the border line of forest/nonforest extracted by the TM classification is superimposed again.

THE USE OF ERS-1 SAR DATA AS A MEANS OF ASSESSMENT FOR DEGRADED AREAS AND POTENTIAL AID FOR AGRICULTURAL AND SILVICULTURAL DEVELOPMENT IN THE AMAZON FOREST REGION (PP2-I03)

F. Lucarelli¹, R. Somma²
 P. Neri³, P. De Stefano¹, P. Murino¹, D. Oricchio^{2,4}, G. Pasquali^{3,4}, F. Alfieri³

1. University of Naples (Italy)
 Phone: (+39).81.675097/7682351 - Fax: (+39).81.675094

2. Alenia Spazio S.p.A.
 Via Saccomuro, 24 - 00131 Rome (Italy)
 Phone (+39).6.41512014 - Fax (+39).6.4191391

3. Tesis S.p.A.
 Via S. Bargellini, 4 - 00157 Rome (Italy)
 Phone: (+39).6.4393485 - Fax: (+39).6.4396685

4. Consorzio Spazio Ambiente
 Via Saccomuro, 24 - 00131 Rome (Italy)
 Phone (+39).6.41514125 - Fax (+39).6.4190675

ABSTRACT

In the framework of a co-operation between an Italian scientific and industrial team, with the support of the Brazilian Institute of Amazon Research (INPA), an ERS-1 Pilot Project has been proposed aimed at investigating, from one side the socio-economical aspects related to the exploitation of forest products, from the other side, SAR data interpretation techniques for monitoring Amazon areas and detecting changes due to human activities. ESA approved as PP2-I03.

An attempt to provide a classification, based on ERS-1 SAR images, has been carried out and a comparison with a Landsat TM-based classification has been performed.

In the future, being one of the test areas, also a super testsite of the SIR-C/X-SAR shuttle mission, operated in April 94, it could be desirable to go on in the research also by using multifrequency and multipolarization SAR data.

1. INTRODUCTION

The Amazon region has been subjected, in recent years, to a great immigration process, which has caused a rapid expansion of the agriculture.

The exploitation of some areas of the Amazon Region has been varied passing from traditional agricultural systems (shifting cultivation) to the utilisation of areas for cattle pasture and cutting the trees for generating power.

The deforested areas can be exposed to a dynamic process, the result of which could be either the environmental regeneration or degradation; in the first case the area regeneration favours the formation of secondary vegetation, while in the second case the low biological productivity of the soil does not allow any agricultural exploitation, leading to a complete degradation of the area.

The above transformation process concerns large areas of the Amazon forest zone and then, to investigate it, it is mandatory to refer to a technology based on space remote sensing techniques, particularly adequate to monitor the dynamic variations of the land use for a large territory.

Beginning with this information, it is expected that it will be possible to suggest a better exploitation for some Amazon zones in order to recover the degraded areas.

For this reason a co-operation between an Italian scientific team (University of Naples) and an industrial team (Alenia Spazio, Consorzio Spazio Ambiente, Tesis) has been established in order to undertake, with the support of the Brazilian Institute of Amazon Research (INPA), an ERS-1 Pilot Project aimed at investigating about the potential value of the ERS-1 SAR data (and SAR/optical data fusion) for monitoring Amazon areas with fast agricultural development and high anthropic pressure.

2. STUDY OBJECTIVES

It is well known that optical remote sensing techniques are today well consolidated as far as forestry applications are concerned.

The problem of optical remote sensing in the Amazon Region is the cloud cover.

As an example in 1992, among the available Landsat images over one of the selected test sites (Iranduba):

- 46% of the images present a total cloud-cover
- 34% of the images present a cover greater than 40%
- just one image is completely cloud-free.

In 1993 (up to June), over the same test site:

- 90% of the images present a total cloud-cover
- the best available image presents a 30% cloud-cover

This means that a regular monitoring of the Amazon region can be assured only by SAR data, able to provide systematic and reliable all-weather information.

Objective of PP2-I03 is to investigate SAR data interpretation techniques (visual interpretation, texture analysis, interferometric analysis, multitemporal analysis, classification methods) in order to assess the potential of SAR data in the identification of thematic classes (primary and secondary forest, deforested areas, cultivated areas, pastures, degraded areas, areas of great anthropic pressure, flooded areas etc.) and the control of their changes (deforestation rate, urbanisation and degraded areas expansion etc.)

The SAR interpretation techniques are applied over areas for which other reference data (cartographic data, optical images) are available and correlation analysis can be performed. In a second phase ground truth data will be collected in a field campaign to assess the validity of the methodology.

3. STUDY TEST SITES

Three test sites have been selected in the frame of PP2-I03, taking into consideration these main criteria:

- areas in which socio-economic problems are present and that have already been studied by INPA during previous researches
- areas that provide sufficient warranty that the study results and the used processing methodology, could be extended to other equivalent areas

These are:

Iranduba Municipality (3°10'S, 60°15'W)

This area presents a particularity due to the intersection of two rivers, the Rio Negro and the Rio Solimoes. The Municipality has a high concentration of deforested areas, which reached in 1989 a percentage of 13.9%. This process is also caused by the presence, in the area, of industrial activities (brick-kiln, tile-kiln) using trees as combustible.

Itacoatiara Municipality: Fazenda Aruana (3°S, 58°50'W)

This area has been selected as an example of applied ecology. Placed approximately 180 Km from Manaus, it is a large area of agricultural development within an area of formerly degraded pasture, in which a reforestation system has been introduced for the reproduction of the Pará chestnut, culture particularly productive and highly paying from an economic point of view. The peculiarity of the plantation system based on biodiversity principle, is represented by alternate zones of primary vegetation (5 Km by 0.5 Km) with strip lines of secondary vegetation and others without vegetation (for cattle pasture). This system allowed to limit, to a great extent, the attack of parasites.

Manaus Municipality: Reserva Florestal Ducke (3°S, 60°W):

This area (10 Km x 10 Km) is a natural reserve created in November 1962 and managed by INPA for their scientific activities and represents the most important area of primary forest at the border of Manaus. Today, due to the increased anthropic pressure in direction of the border of this forest reserve, large areas of forest are being cut.

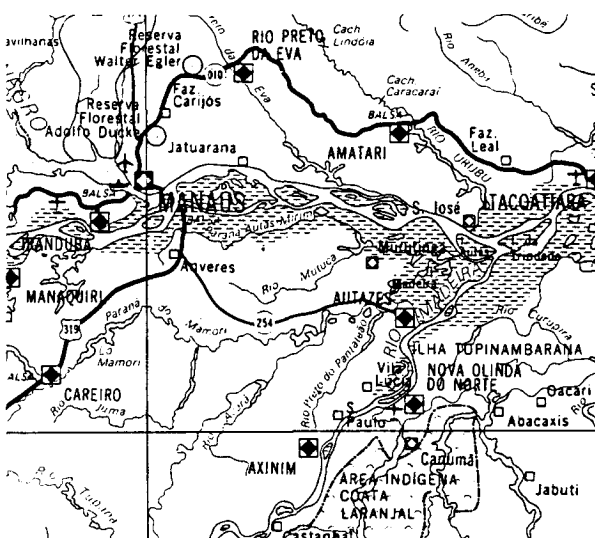


Fig. 1: Location of the test sites - Iranduba, Fazenda Aruana (Itacoatiara), Reserva Florestal Ducke

4. MAN AND FOREST PRODUCTS IN AMAZONIA: A MULTIDISCIPLINARY APPROACH OF EXTRACTIVISM

For the purpose of our research, we have defined extractivism as: the systems of exploitation of forest products, which are intended for sale on the regional, national or international markets.

Extractivism is often thought of as obsolete, a reminder of Brazil's numerous economic cycles. Both the recent political activities of the seringueiros trade-unions and the growing public awareness of ecological problems, have served to propel this aged practice of forest resources management into the centre of the debate on forest ecosystems survival.

The low returns, the precarious balance of resources, the narrow scope of the markets, the competition from industrialised plantations and the growing marginalization of the actors, all compound to condemn extractivism as a valuable model of exploitation of Amazonian ecosystems. From collecting the products in the forest to marketing them, the actors of extractivism are many and are linked by social relations of production and power whose diversity depends on the resources, market accessibility and local history.

The factories for transforming the products are all characterised by decayed machinery, often installed between the two world wars, the paternalistic labour relations and the familial aspect of the firm which gives it its social cohesion. They look as if no investment or policy of modernisation and improvement of labour conditions have ever been attempted, not even during the more dynamic periods. The staff, mostly women, work year after year although they may be laid off during times of shortage of products. Consequently the staff turnover is very low. The attachment of the manpower to the firm and its owners is linked to the huge paternalistic character of the work relationships, and one may wonder whether it is the reciprocal obligations or the economical value of the production which maintains the continuation of the activity.

For a long time, the main wholesalers families have diversified their activities in the trade and into the factories in the Free Zone of Manaus and left the management of the sector of extractivism in the hands of some of their elders. Though becoming negligible if compared to the fabulous incomes they created in the past, these activities still give rise to benefits according to the low level of investments. Their main interest, however, seems to be found in the permanency of an old and complex network of social relationships which permit these families to maintain their political influence and their glamorous lifestyle. For those last "barons" of extractivism, the decline of the activity is mostly due to external factors. They claim that the financial support of the State to the Free Zone and the taxes levied on marketing of the natural resources has blocked the development of an economy based on the forest management and penalised the caboclo, the man from the forest.

Extractivism can be considered as an economic management of the forest ecosystem whilst allowing ecological sustainability.

In its current form, extractivism does not represent a satisfactory alternative for the long term future. The low income that it creates and the socio-economic structures that it contributes to maintain devalue the perception of this activity. It is currently replaced by subsistence

agriculture in the remote regions or commercial agriculture in the places that are near an urban centre.

But set of techniques are available to enrich the forest in valuable species such as planting in forest trails, enriching gaps, selective felling of old individuals and cutting vines in order to increase the amount of light and reduce the competition. As yet we have not been able to observe any of these practices other than that of enriching the fallow in fruit species in order to complete the basic household consumption. The forest is usually minded as a place for natural harvesting and which does not need to be managed. In carrying out any improvement experiments within a community, it has to be borne in mind that the collectors need prior information to convince them of the value of changing practices in order to increase the productivity of the natural stock.

Those considerations demonstrate that with some improvements, the extractive activities associated with other production activities, could be integrated in development scenarios.

5. STUDY METHODOLOGY

While for the optical images consolidated classification techniques already exist, this is not true for the SAR images. Scope of this phase is then to investigate interpretation and classification technique based on SAR images, by using correlation analysis, i.e. a comparison of the SAR images properly filtered and processed (by analysing intensity, texture, interferometry) together with the optical images and the actual thematic cartography over known test area.

Multitemporal analysis has also been performed in order to detect thematic changes such as deforestation urbanisation expansion and so on.

5.1 Input data

SAR data

Multidate ERS-1 SAR data (19 June 92 and 6 November 92) have been provided by ESA: geocoded (GEC) data, RAW data to be used in order to test SAR processor facilities, and Single Look Complex (SLC) data to be used in the interferometric analysis.

Reference data

- cartographic data (1:50.000 scale)
- two multispectral Landsat-TM images: 8 August 91 (3 bands) and 23 June 92 (7 bands)
- aerial and in situ photographic campaign.

5.2 Input data acquisition and preprocessing

The first phase has been aimed at collecting input data (SAR and optical images, cartography) and processing them in order to produce a data base containing all the information, on the selected test areas, useful for the subsequent analysis and interpretation phases.

The following data processing procedures have been applied:

- Topographic data digitizing and production of digital base maps and DTM
- SAR RAW data processing
- SAR images mosaicing
- Landsat-TM images geocoding on SAR images

5.3 Visual Interpretation

A visual analysis of the geocoded SAR images for the Itacoatiara and Iranduba areas has been performed: image processing tools (Lee filtering for speckle noise reduction, subsampling, operations of contrast stretching, histogram normalization, filtering, false colour display etc.) have been used in this phase and comparisons of the images with an overlayed vector digitized cartography have been done for changes detection purposes (Fig. 2).

The intensity and the texture of the images enable to discriminate the following thematic aspects:

- dense forest
- deforested areas
- water (normally appearing as dark tones)
- urban areas, settlements, fazendas and man made structures (appearing as bright tones).

The drainage pattern and the morphological structure of the areas are clearly visible, while roads are not easy to distinguish depending on their size and their orientation w.r.t. the satellite flight direction (Fig. 3).

Within the deforested areas, in general, it is very difficult to distinguish among bare soil, crops, degraded areas and pastures; very clear have appeared the plantations of Parà chestnut, in the Itacoatiara region, due to their particular texture (parallel adjacent stripes, Fig. 4).

Quite difficult is the differentiation between primary and secondary forest usually possible with TM data.

The overlaying of the vector digitized cartography on the images has evidenced new deforested areas, new roads and the expansion of the urban areas.

5.4 Multitemporal Analysis

Up to now only visual inspection of multitemporal images have been performed; the dates of the acquired images are relevant to the periods of the year where, respectively, the maximum (June) and the minimum (November) extension of the flooded areas are expected.

The multitemporal comparison performed for the Iranduba site has highlighted these flooded areas, differences in some deforested areas (probably due to the different soil moisture content) and some differences related to the presence of man made structures (Fig. 5).

Multitemporal images, in the classification procedure, will be used as soon as significant multitemporal data sets will be received.

5.5 Interferometric Analysis

SLC SAR data have been requested in order to test the usefulness of interferometric processing techniques (developed for topographic purposes) applied over forested terrain in order to map clear cuts and to discriminate primary and secondary forest [1].

This should be possible, by analysing the interferometric phase and the degree of coherence, due to the different heights and densities of the trees in the two types of forests.

All the algorithms for the interferometric analysis have been implemented, but unfortunately, due to the high temporal distance between the two SLC images received up to now (about 5 months), the measured degree of coherence was too low to allow this type of discrimination. Further investigations in this field are foreseen in the future.

5.6 Classification

A classification attempt of the Iranduba monotemporal SAR image (19 June 92) has been performed with conventional algorithms by integrating the SAR intensity data with different texture features that have been extracted by using the co-occurrence matrices [2], [3].

The SAR images to be classified have been subsampled by averaging groups of four adjacent pixels, in order to reduce the computational burden needed to process the data.

Since the area of interest was contained in two different ERS-1 frames, a mosaic of two SAR images has been done. From this image four different texture images have been extracted and used as "spectral" bands :

- Angular Second Moment
- Contrast
- Entropy
- Inverse Difference Moment

Each texture image has been obtained by replacing the pixel (i,j) with the relevant texture measure computed in a window of 7x7 pixels centred on it.

A first classification procedure has been carried out without using ground data references; in this case, by visual inspection of the original SAR image, just four homogeneous subareas, relevant to well defined thematic classes have been identified: 1) Primary Forest; 2) Deforested Areas (including bare soil, crops, degraded areas, pastures); 3) Water; 4) Urban Areas.

For each class, the "spectral" signatures have been extracted, both from the original image and from the texture images and used in the classification procedure.

The visual analysis of the classified SAR image shows a bad separability between the spectral signature of the water and that of the deforested areas (Fig. 6).

For this reason SAR + Texture data have been re-classified neglecting the water by masking the relevant areas.

The classification procedure has been also carried out by using bands 3,4,5 of Landsat TM image of the same area of interest in order to obtain a reference thematic map.

The visual inspection of the image allows the identification of at least 7 thematic classes: 1) Primary Forest; 2) Secondary Forest; 3) Deforested Areas (including bare soil, crops, degraded areas, pastures); 4) Dark Water (water of the Rio Negro); 5) Muddy Water (water of the Rio Solimoes); 6) Flooded Areas; 7) Urban Areas.

An attempt to classify the SAR image by using the 7 spectral signatures, whose training areas have been identified on the TM image, has shown that monotemporal SAR intensity + texture features are inadequate to allow a good discrimination among these classes.

An integration of optical and SAR data has also been done; a colour composite Red/Green/Blue of TM4/TM3/SAR images was produced and a classification based on both SAR and TM data has been carried out using the 7 spectral signatures, that shows, by visual inspection, an improvement in the class separability (Fig. 7).

A quantitative estimate of the classification accuracy, not possible at the moment for unavailability of ground truth data, has to be done in the future; in Fig. 8 a comparison between the SAR based and TM based classifications, over four thematic classes, is shown, representing in yellow the pixels classified as deforested areas both in the SAR based and in the TM based classifications, in green the pixels classified as deforested areas only in the SAR based classification and in red the pixels classified as deforested areas only in the TM based classification.

The obtained results are from a preliminary analysis based on the use of unsophisticated image processing techniques applied over monotemporal SAR images; the use of multitemporal SAR images and the integration, within the classification procedure, of the interferometric analysis are expected to provide better results.

6 CONCLUSIONS

The aim of PP2-I03 was to investigate on the applicability of SAR images to earth surface classification purposes.

The research has been applied, up to now, on monotemporal SAR imagery.

The study has demonstrated the possibility of classifying at least 4 thematic classes, primary forest, deforested areas, water and urban areas if texture information are used in the classification procedure together with intensity information.

As expected, monofrequency SAR images allows the identification of a number of classes lower than what can be obtained by using multispectral optical images and the integration of SAR and optical data allows to increase the number of different classes.

Nevertheless it has appeared very evident that the use of SAR is mandatory over areas affected by extensive (in space and time) cloud cover (as in the case of Amazon Region); in particular the peculiarity of SAR to detect, in all weather conditions, new deforested areas, must be appreciated.

It is expected that the use of multitemporal images and interferometric analysis, applied on proper couples of SLC data, could improve the classification accuracy in significant way.

7 ACKNOWLEDGEMENTS

The authors would like to thank all the people who have contributed to the results of this research: R. Bertoni, O. Bombaci, V. Panaccia of Alenia Spazio, F. Alliney of Consorzio Spazio Ambiente, A. Maraziti, D. Micarelli of Tesis, L. Castellano, A. Siciliano of University of Naples, A. Carneiro Filho, F. Dionizia de Almeida and J. Ferraz of INPA.

8 REFERENCES

- [1] Ulander L.M.H., Hagberg J.O., Askne J., ERS-1 SAR Interferometry over forested terrain, Proceedings Second ERS-1 Symposium - Space at the Service of our Environment, Hamburg, Germany, 1993, pp.475-480
- [2] Marceau D., Howarth P., Dubois J.M., Gratton D.J., Evaluation of the grey level co-occurrence matrix method for land cover classification using SPOT imagery, IEEE Transaction on Geoscience and Remote Sensing, Vol. 28, n. 4, July 1990, pp. 513-519
- [3] Saurer H., Triebfurst B., Texture analysis as an aid for the evaluation of ERS-1 SAR data from a part of the Antarctic peninsula, Proceedings Second ERS-1 Symposium - Space at the Service of our Environment, Hamburg, Germany, 1993, pp.297-302

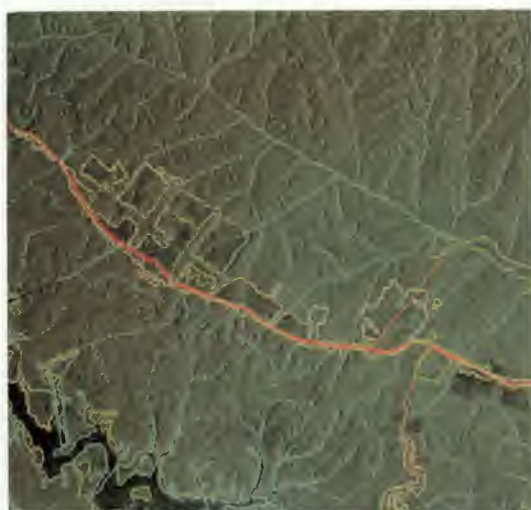


Fig. 2: Itacoatiara test site: on the left comparison between the SAR image and an overlayed digitized cartography;



on the right new deforested areas and new roads are highlighted in red colour.



Fig. 3: Itacoatiara test site: full resolution SAR image showing, on the bottom right, new deforested areas; the Mil Madeireiras fazenda is clearly detectable, as bright tones, in the centre of the image. Roads are not easy to distinguish depending on their size and their orientation w.r.t. the satellite flight direction.



Fig. 4: Itacoatiara test site: plantations of Pará chestnut appearing very clear due to their particular texture (parallel adjacent stripes).



Fig. 5: Iranduba test site: multitemporal comparison of two SAR images, dated respectively November 1992 (left) and June 1992 (right), where respectively, the minimum and the maximum of the floods are present.

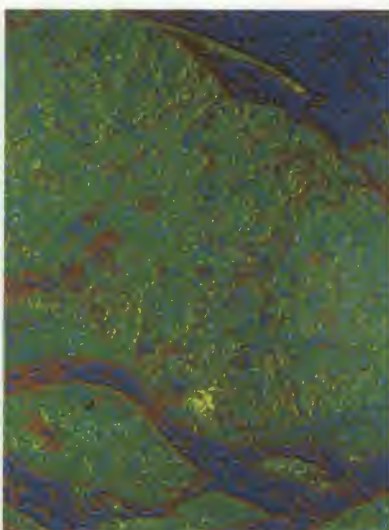
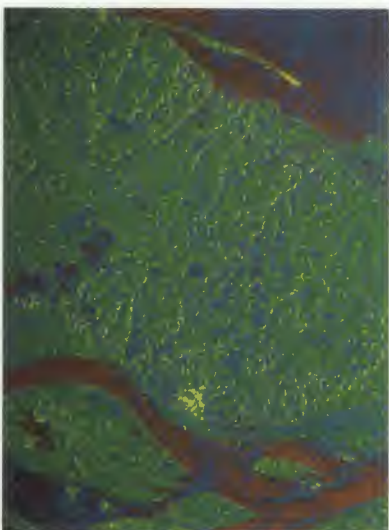


Fig. 6: Iranduba test site: comparison of two classification attempts, respectively based on SAR intensity only (left) and on SAR intensity + texture (right); in green primary forest, in brown deforested areas, in blue water and in yellow urbanized areas.

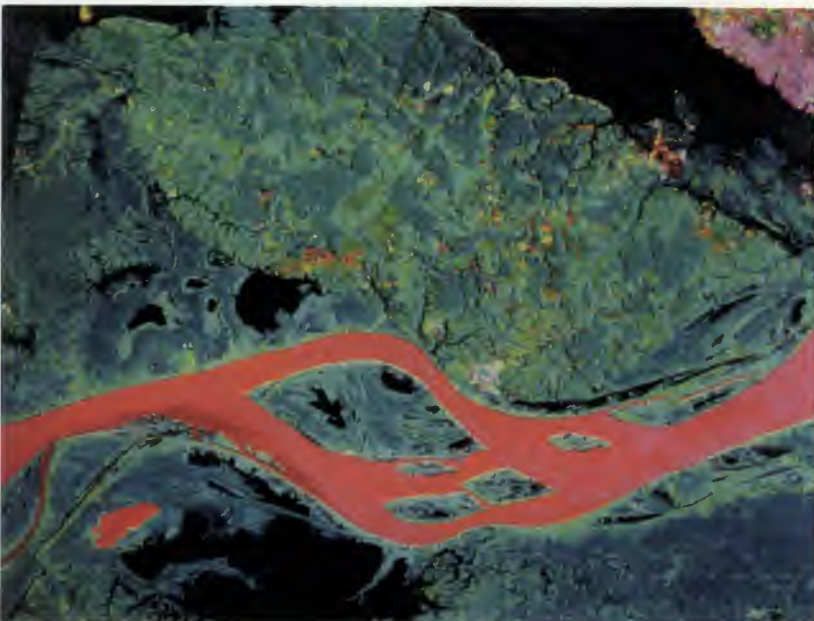


Fig. 7: integration of optical and SAR data: colour composite Red/Green/Blue of TM4/TM3/SAR images

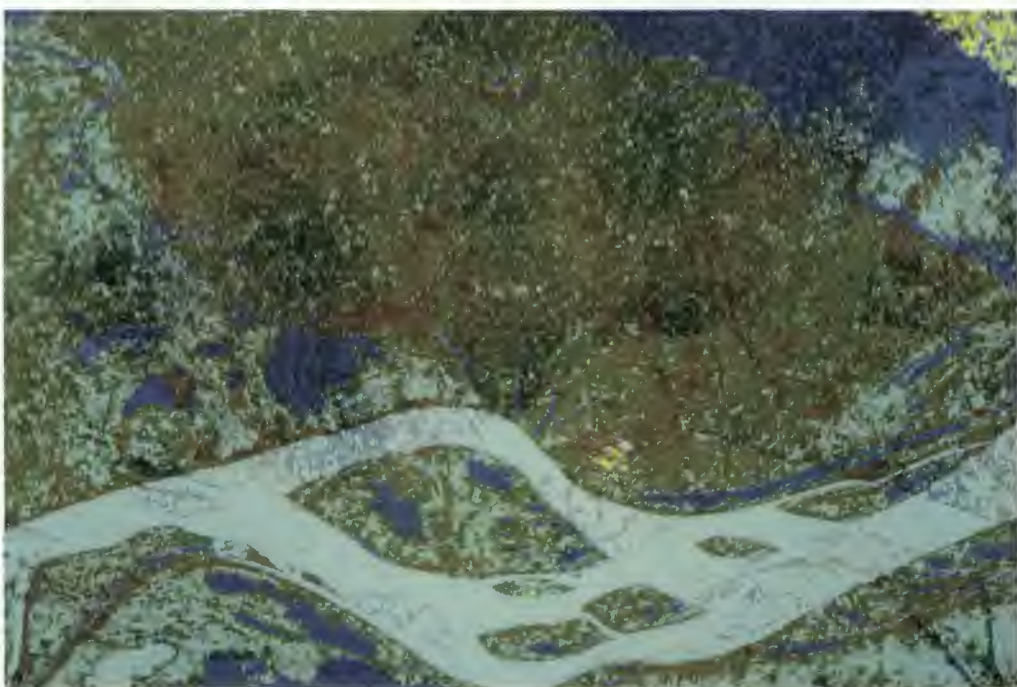


Fig. 8: integration of optical and SAR data; the classification based on SAR+TM data allows an improvement in the class separability;

in green primary forest, in light brown secondary forest, in brown deforested areas, in light green flooded areas, in blue water, in yellow urbanized areas.

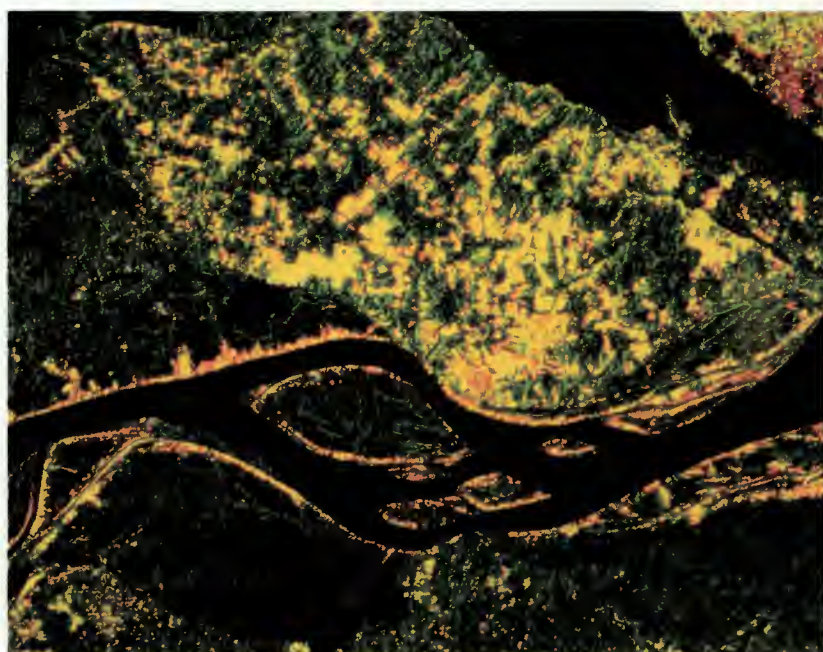


Fig. 9: comparison between the SAR based and TM based classifications, over four thematic classes; in yellow pixels classified as deforested areas both in the SAR based and in

the TM based classifications, in green pixels classified as deforested areas only in the SAR based classification and in red pixels classified as deforested areas only in the TM based classification



Fig. 10: Iranduba; multispectral LANDSAT-TM reference data, dated August, 1991

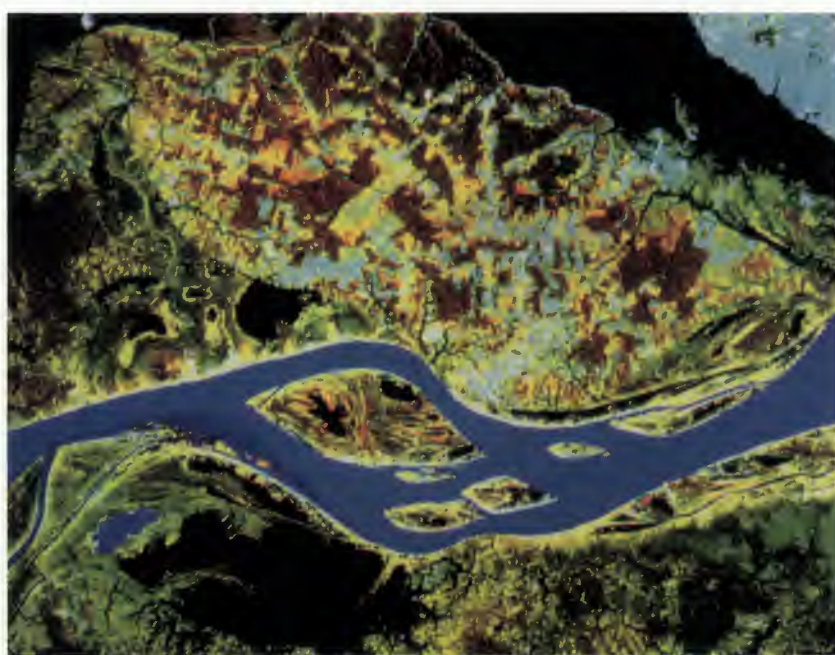


Fig. 11 : Iranduba ; multispectral LANDSAT-TM reference data, dated June, 1992

OBSERVATION OF THE TROPICAL FOREST WITH THE SYNTHETIC APERTURE RADAR OF ERS-1

Christophe Ponsard*, Patrick Kremer^o, Albert Guissard*, Jules Wilmet^o

*Catholic University of Louvain
 Laboratory of Telecommunications and Remote Sensing
 Place du Levant, 2 — B-1348 Louvain-la-Neuve — Belgium
 Tel: ++32-10/472300 — Fax: ++32-10/472089
 E-mail: ponsard@tele.ucl.ac.be — guissard@telec.ucl.ac.be

^oCatholic University of Louvain
 Laboratory of Remote Sensing and Regional Analysis
 Place Louis Pasteur, 3 — B-1348 Louvain-la-Neuve — Belgium
 Tel: ++32-10/472870 — Fax: ++32-10/472877
 E-mail: kremer@geog.ucl.ac.be — wilmet@geog.ucl.ac.be

ABSTRACT

Due to its all weather capability and its high spatial resolution, the ERS-1 synthetic aperture radar seems to be a very interesting tool for many applications in tropical environment. As a particular case, our study is related to the monitoring of tropical forests and the understanding of their degradation.

As part of the evaluation of the potentialities of the ERS-1 SAR for tropical forests monitoring, we attempt to obtain a correct discrimination of some forest types or degradation levels. An area located in Ivory Coast (West Africa) serves as a test site.

Starting this study, we first processed SAR data by using simple techniques. The aim is mainly to attenuate the speckle and to yield a first classification. We point out a number of problems and propose ways for further improvements.

1. INTRODUCTION

This ESA Pilot Project study (PP2-B10) is financially supported by the Belgian Government's "Services Fédéraux des Affaires Scientifiques Techniques et Culturelles" as a part of TELSAT research program (T3/10/017). It started in October 1993, and is jointly conducted by an electrical engineer and a geographer. As a result of such a collaboration, we attempt to get a better understanding of both the electromagnetic point of view (tool level) and the geographic point of view (thematic level).

The satellite data provided by ESA for this study consist of a multitemporal set of 18 ERS-1 SAR .PRI images (C-band, pixel size of 12.5 times 12.5 meters, ground resolution of about 30 times 30 meters),

acquired every 35 days within the period from April 14th, 1992, to November 30th, 1993. Three .SLC images are also to be used.

Our study zone (see figure 1) is located in the central-west part of Côte-d'Ivoire (West Africa). Two major forested blocks are situated within this area, and are relatively densely covered. These are the Mont Tia and Haut Sassandra forests; both are nationally protected areas. The surroundings of these two blocks are also to be categorized as "forest", although they are densely cultivated and very degraded. Some fields are spatially well-discernable in the ERS-1 SAR images. Small patches of savanna, generally sparsely wooded, constitute the last type of vegetation cover in the study zone. This is also characterized by a heavy relief in the north-western part, another mountain (the Mont Tia) and some hills everywhere. This area is densely populated, so there are many villages and their inhabitants are the main forests products users.



FIGURE 1. Localisation of the test site.

In February 1994, we staged in Côte-d'Ivoire for a two weeks recognition mission. We wanted to identify the main features that we noticed on the images, to check the accessibility of various locations for a

future mission and to collect ancillary data about the study zone, such as maps, aerial photographs and meteorological data. More field work is scheduled within the next few months.

For the following developments, please refer to the flow chart presented on figure 2. It summarises the project in its present status.

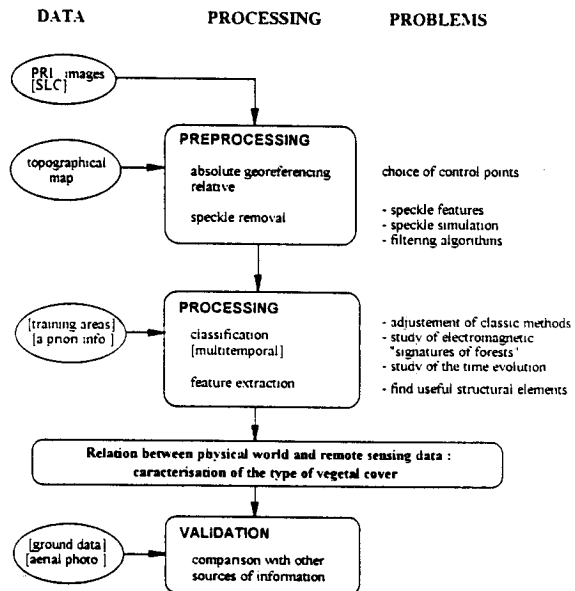


FIGURE 2. Data processing flow chart.

2. PREPROCESSING

2.1. Georeferencing

Due to the geometry of SAR images in heavy relief areas, it is difficult to reference them in relation to a map or a satellite image in the visible range of the electromagnetic field. As we don't need an absolute georeferencing of the SAR images in the first stages of this study, we restricted our geometric correction to a coregistration between the different SAR images. One image, that is visually better than the others (February 1993, Ref. 1), was chosen as the reference image (Ref.3).

The ground control points that one could recognize in several images of a same area are of different types. It is important to understand that the quality of these control points is variable, depending on the point of view. The best control points consist on huts with corrugated iron roofs. They are visible in one particular image and it is possible to define their location precisely (often less than one pixel). The third characteristic is also essential: they are generally easily recognisable in several images.

Others elements often have only two of the three above-mentioned characteristics. So they can sometimes constitute good control points, but have to be used carefully. They can be constituted of other huts,

or some trees, for instance. The relief elements can easily be seen in all the images, but their high intensity zone is more diffuse, so the localisation accuracy is not very high. We avoided to use such kind of elements as ground control points.

Let us consider the role of the speckle on the referencing operations... Some elements are highly influenced by this phenomenon. The trees, for instance, but also the huts without iron roof, are particularly concerned. The general texture is so heavily affected by the speckle that it is often impossible to identify a single element in it. This is a real inconvenience for georeferencing operations, especially in forested areas where there are so few iron roofs.

2.2. Speckle analysis

A second classical preprocessing for SAR images is speckle removal. The speckle is basically due to the interference of a lot of scattering elements within the resolution cell. With some simple assumptions it can be shown that this results in a multiplicative noise which is uniformly-distributed in phase and Rayleigh-distributed in amplitude or exponentially-distributed in power. For multilook images (with independent looks), the resulting distribution in power is a gamma law. We have calculated the distribution of a set of homogeneous forest pixels and we have found a distribution corresponding to an equivalent number of looks (ratio of the square mean to the variance) near 0.8 for .SLC data set (figure 3.a) and near 2.3 for .PRI data set (figure 3.b).

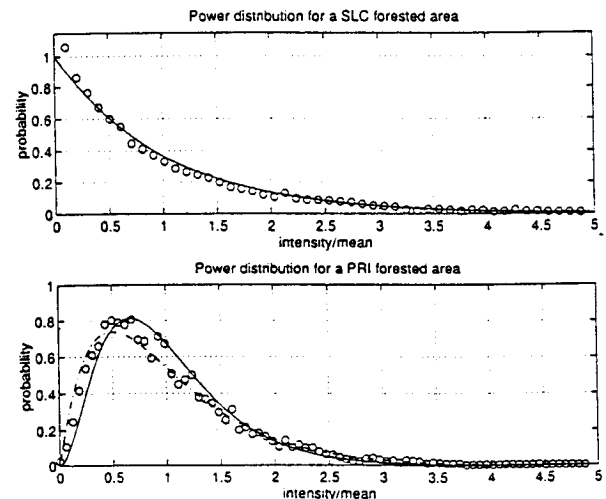


FIGURE 3. Power distribution for a homogeneous forested area.
 (a) .SLC image (— exponential distribution; ○○○ data)
 (b) .PRI image (gamma distribution for 2 (--) and 3 (—) looks; ○○○ data)

We have already tested some simple and well known speckle removal filters: the average, median, sigma and geometric filters (Réf. 4, 2). We are now trying more adaptive filters such as Frost, Lee, or MAP filters.

3. FIRST ATTEMPT FOR A CLASSIFICATION

We proceeded to a first trial for classifying the ERS-1 SAR data, in order to get a better insight into what are the problems we have to deal with. This

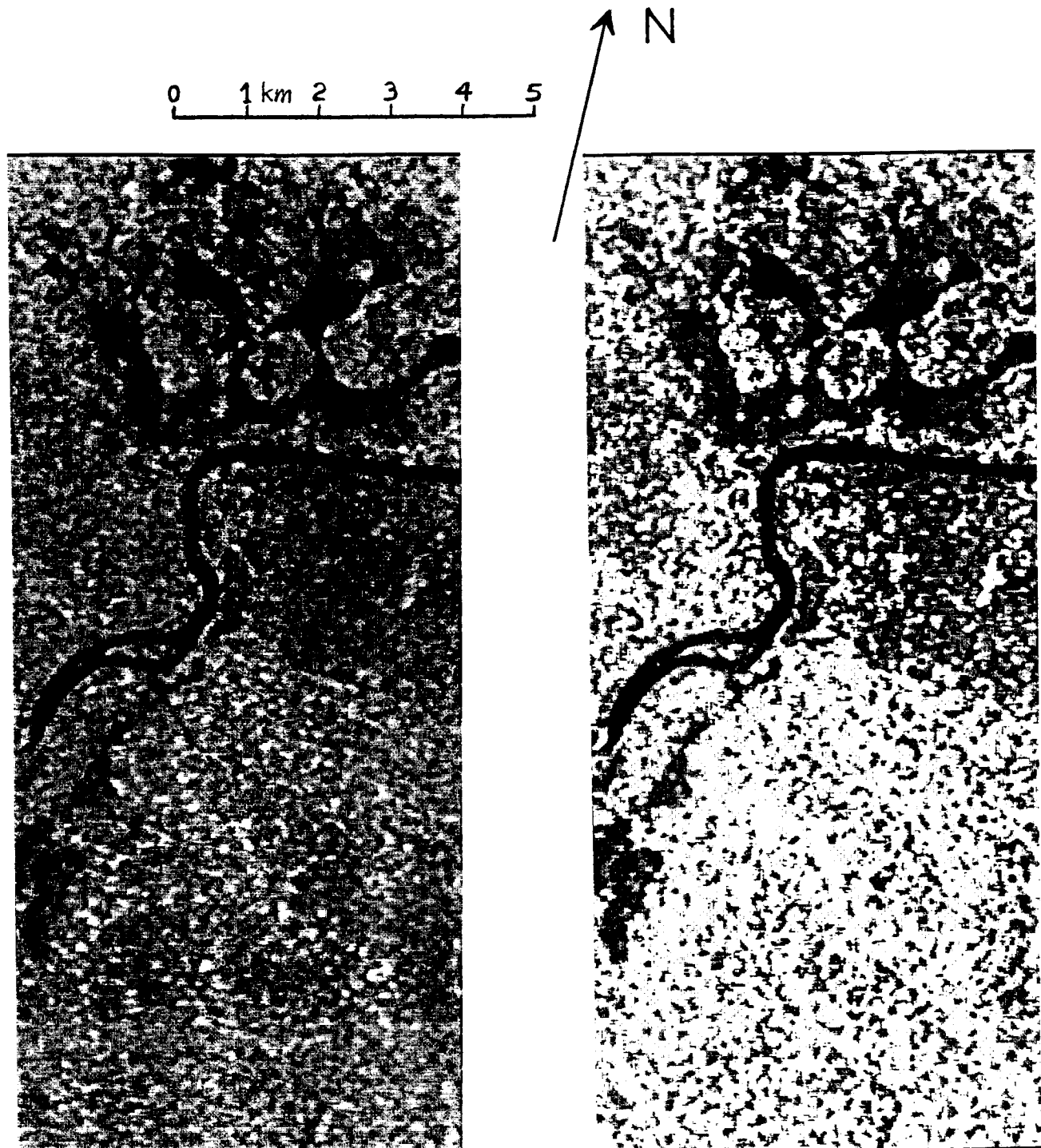


FIGURE 4. Subzone of the test area with the various types of vegetation cover (.PRI image)
 Left: median filtered image. Right: classification result for classes water, savanna, cultivated forest, dense forest on eastern slope, subhorizontal terrain, and western slopes, in increasing grey values.

classification has been made on a 150 km² area where elements corresponding to various land cover types are present. We chose to use only one .PRI image (February 23d, 1993). The zone is presented on figure 4 (left).

We applied a simple and well known procedure (Maximum Likelihood), although we are aware that this is probably not best adapted to radar data characteristics. The data were first filtered, by means of a median filter applied in a 7x7 pixels moving window. The distribution function of the values in the filtered image is approaching a normal distribution, much more than the one for the raw image (see figure 5). So the Maximum Likelihood classifier can be used. A peak in the lower values corresponds to the water pixels.

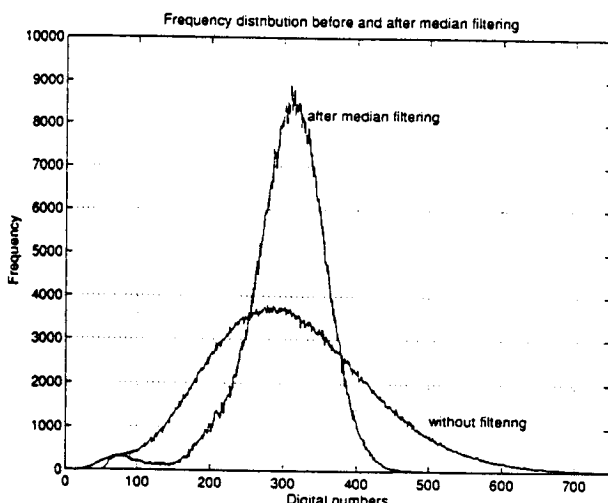


FIGURE 5. Frequency distribution before and after median filtering.

Six classes have been selected:

- water
- savanna
- forest that is heavily cultivated
- dense forest on eastern slopes and some other forests that are slightly cultivated
- dense forest on subhorizontal terrain
- dense forest on western slopes (regarding the antenna)

The result is globally satisfactory (see figure 4, right) although some confusions appear at a more detailed scale. Our aim to reveal problems is well achieved. Here are some considerations we made on this basis.

Border effects

These are mainly due to the filtering procedure we chose to use. Other techniques (i.e. adaptive ones) can considerably reduce these effects.

Orientation effects

The geometry of the SAR images implies that significant variations will occur between backscattering intensities for elements of a same taxon that are located on slopes with different values and orientations. We had to face this problem in our classification and we tried to solve it by defining classes corresponding to different orientations of the same taxon ("forest"). This effect is confirmed by the result of the classification procedure. Unfortunately, the backscattering signal of the dense forest on eastern slopes and of the slightly cultivated forest are very close to each other, so we had to put these two. The ideal solution would be to correct the relief by using a digital elevation model but this is more difficult to achieve, and time consuming as the model do not already exist.

Texture

The texture is not considered in the present classification procedure. We also did not calculate any texture parameter for including it as an extra-channel in the classification process. But it is important, especially in forested areas. In addition the speckle, disturbs the texture. Unless a classification algorithm is used that could cope with the speckle, it has to be reduced while preserving the texture.

4. CONCLUSIONS AND PROSPECTS

We succeeded in the coregistration of a set of images with an accuracy of the order of the pixel. Some simple speckle filters have been tested. A first classification pointed out the main problems to solve.

In order to further improve the classification results, we need to implement more efficient speckle filters and use texture-derived information. We also would like to look into some structure features. This could be useful from a thematic point of view.

5. REFERENCES

- Conway J.A., M. Leysen, A.J. Sieber, 1994, «Evaluating multi-temporal ERS-1 SAR data for tropical forest mapping. Data selection, processing and target identification». *Proceedings Second ERS-1 Symposium in Hamburg*, 441-446.

2. Crimmins T.R., 1985, «Geometric filter for speckle reduction». *Applied Optics*, 24, 1438-1443.
3. Fog B., Poulsen J.N., Sandholt I., Skriver H., Stjernholm M., 1993, «Monitoring land-cover and crop types in Denmark using ERS-1 SAR and optical satellite images». *Proc. Symp. "From optics to radar, SPOT and ERS applications" in Paris*, 71-78.
4. Lee J.S., 1983, «A simple speckle smoothing algorithm for SAR images». *IEEE Trans on Systems, Man, and Cybernetics*, Vol.13, n°1, 85-89.



EVALUATION OF ERS-1 SAR DATA FOR FOREST MONITORING IN INDONESIA (Tropical Rainforest and Use of Land Investigation, TRULI)

Steffen Kuntz (*), Florian Siegert (**)

(*) Steffen Kuntz, Kayser-Threde GmbH, Wolfratshauserstr. 48, 81379 München,
Tel: (+49)-89-72495-119, Fax: (+49)-89-72495-291

(**) Florian Siegert, Zoologisches Institut der Ludwig-Maximilians-Universität, Luisenstr. 14, 80333 München,
Tel: (+49)-89-5902442, Fax: (+49)-89-5902450

ABSTRACT

The potential value of ERS-1 SAR data as a tool for monitoring rainforest conversion and land use planning was investigated. Of highest priority was to develop an easy to use system which is operational under conditions found in many countries of the tropical belt. Therefore only commercial software and established procedures were used for the analysis. Russian MIR KFA1000 images with a high ground resolution and data acquired during an extensive ground truth campaign served as a reference. The analysis shows that major land use classes and different forest types can be identified in a single ERS-1 SAR scene in tropical rain forest environment. Texture analysis using simple image processing means allows to discriminate 1.) undisturbed forest 2.) logged forest 3.) clearings by fire and clear-cutting 4.) roads and 5.) different forest types. The results obtained so far give reason to establish the use ERS-1 data as a tool to monitor deforestation processes and landuse in the tropics.

1. OBJECTIVES

This paper is the first status report concerning the ESA proposal Tropical Rainforest and Use of Land Investigation (TRULI, PP2-D11, started in 7/93), which is funded by the German Space Organization (DARA) and supported in Indonesia by the German Society for Technical Cooperation (GTZ) as well as national institutions as the National Land Planning and Mapping Board (Badan Pertanahan Nasional, BPN) (1).

Tropical rain forests as a natural resource with still not well documented potentials as well as an important regulative of global climatic processes have to be considered as ecosystems which preservation must be of highest interest to everybody. However, the utilisation and conversion of tropical rain forest proceeds mostly uncontrolled and with increasing rate. In the past mainly optical satellite images and aerial photos were evaluated based on experience gathered on visual interpretation or computer-aided classification approaches, respectively. However, major disadvantage of optical images for operational monitoring is the frequent cloud coverage in tropical regions. The all-

weather-capacity of SAR is the major advantage for land surface monitoring under these conditions (2).

The aims of the pilot project TRULI are therefore 1.) to analyse radar backscatter of tropical environments in single and multitemporal data sets, 2.) to develop a monitoring system which will allow to record long-term changes in tropical rain forests due to human activities, and 3.) to assess the usefulness of these data as a tool for land use planning activities. Data evaluation is executed using simple means only based on commercial image processing software because *operationality* of data evaluation procedures as well as *know-how transfer* to Indonesia are strongly emphasized.

2. THE TEST AREA

The test area is located in Indonesia on the island of Borneo. It lies at the middle reaches of the Mahakam river in the province Kalimantan Timur. The vegetation is dominated by lowland *Dipterocarp* forests. The center of the test site is located at 0°15'S, 115°45'E. **Figure 1** shows the geographic location as well as available ERS-1 descending paths and MIR image swath. The test area was chosen in coordination with the GTZ and the Indonesian Organisation "Badan Pertanahan Nasional, (BPN)" and overlaps in part with the project area of the bilateral "Land Use Planning and Mapping (LUPAM)" project. The test area includes examples of many different problems relevant to the protection and management of tropical forests.

3. DATA ACQUISITION

Although the project started in July 1993 we only had two scenes available in our laboratory to work with (*ERS-1 scene No.: 10397/3591; 07.12.93* and *No.: 11399/3609; 09.20.93*). Ten more scenes were acquired but until now not delivered. The situation concerning support of ERS-data from foreign receiving stations especially in tropical regions is still far from an operational status.

In fall 1993 a 5 week ground truth campaign was conducted in Kalimantan. Major aim of this field campaign was to inspect three different regions within the project area in order to establish an interpretation key for the visual interpretation of our MIR space photographs and the

processed ERS-1 SAR images. Due to the fact that there is only little knowledge available concerning topography as well as landuse, logging activities, infrastructure etc.. The Russian MIR space photographs with a ground resolution of 7m turned out to provide better geographic and thematic information, than the best maps available (see Fig 2A). Based on this field trip and the interpretation of the MIR photographs, we have now exact ground truth data for a large area covering approx. 2500km² of tropical rain forest and converted land. Information was gathered about surface relief, forest types, intensities of selective logging, infrastructure, human settlements and agricultural activities and transferred towards a GIS system. The information derived from the MIR-images and ground truth can be compared directly with the ERS-1 SAR data for detailed analysis and identification of objects. Without this additional information from the test site it would rather be impossible to achieve the results presented in this report.

4. ERS-1 SAR DATA EVALUATION

Due to the restriction on using commercial software only to meet operational requirements in the TRULI-Project, ERS-1.SAR.GEC data have been used. Because the maps available from our test area showed bad geometric accuracy no further geocoding was applied. The first step of image enhancement was contrast stretching. The original data - and the filtered images as well - have been stretched with a standard deviation of 1.5. By this we obtained best results for visual interpretation. Speckle noise was reduced with two filters, a Lee Sigma Filter, and a Median Filter (kernel-size 7x7 pixel; (3)). Next we performed a texture analysis. Radar backscatter is mostly influenced by the geometry of an object (roughness) and it's humidity (ϵ' dielectrics constant). Different surface roughness has certain impacts to the backscatter characteristics and therefore to image texture. At first look the "raw" data set shows topographic information and major water bodies only. Without texture analysis it is difficult to classify even such simple features like forest - nonforest in our test site with good accuracy. To enhance the texture information of the image we used the Variance formula (variance = $f(SD)^2$) with variable kernel-sizes provided by the ERDAS radar module. With kernel-size of 15x15 and 31x31, respectively we obtained best results. Other algorithms like (e.g. Skewness, Kurtosis) couldn't improve the results.

To combine the advantages of the different filter products, a RGB - image for visual interpretation was created (Fig 2B). The channel-assignments of the color composite are red= Variance - Filter 15x15 (texture); green= Combined Sigma + Median - Filter (speckle reduction) and blue= Variance - Filter 31x31 (texture). This RGB - Image is a modification of the three-layer variance image (15x15, 31x31, 61x61),

described by Ref (4). The speckle reduced image (Combined Sigma + Median Filter) was assigned to the green layer because this band is least affected by filtering operations and contains the most of the information of the original image. Furthermore smooth surfaces as undisturbed forest are only little affected by texture enhancement and occur in a homogenous green. Thereby the image looks more similar to a map and all colors different from green which origin from differences of texture will become enhanced.

5. VISUAL INTERPRETATION

The first step of any visual interpretation of remotely sensed data in general is the development of an interpretation key. In the TRULI project the russian KFA-1000 space photographs from MIR served as "ground truth" to facilitate the interpretation of the ERS-1 data and the development of a SAR-interpretation key for our test area. Because no SAR data were available in the first months after the kick-off of TRULI the first ground truth campaign was basically aimed to develop an interpretation key for the KFA-1000 images.

5.1. Land Use Patterns

Figure 2 shows a comparison of the MIR photograph (A) and the processed ERS-1 image (B). The photographs show approximately the same area of 45x30km. The ERS-1 image must be rotated by about 45° to the right in order to overlap properly. The MIR photograph demonstrates that the whole area is covered by tropical rainforest. Clouds cover nearly half of the image. Logging roads appearing white, brown or green in the MIR photograph cover the whole visible area. Shifting cultivation activities can be seen all along the Mahakam river. Active selective logging is visible to the extreme upper right in Fig 2A. Carefull inspection of the processed ERS-1 image showed that five different classes of land use can be detected. The location of each land use class is indicated by equal numbers in both the MIR photograph and the ERS-1 image (Fig 2). 1.) Old secondary forest (not disturbed), and 2.) new secondary forest showing a patchwork of magenta/white spots within the green colours. Both classes appear mainly near to the Mahakam river. The canopy of secondary forest is disturbed by small agricultural areas and newly grown vegetation. 3.) Selectively logged forest. Small gaps in the forests which origin from selective logging activities can be seen as white spots. 4.) Even minor settlements can be detected easily, since the backscatter of metal roofed houses (corner reflection) is high. 5.) Clearcuttings. These clearcuttings were newly made in the years 1992/93 in order to establish plantations for paper pulp production. They are not visible in the MIR image, since it was acquired before 1992. The location of the ground truth photograph in Fig 4C, showing

a recently clearcutted area prepared for timber plantation, is indicated by an arrow in **Fig 2B**. Based on the enhanced SAR-image and the aid of the interpretation key described above a preliminary landuse "map" from the northern part of the TRULI test area was created by visual delination of detectable features.

5.2. Natural Forest Types and selective logging

In order to demonstrate the capabilities of ERS-1 in a tropical environment more clearly **Figure 3** shows an enlargement of the area in the upper right corner of **Fig 2**. Both, the MIR and ERS-1 image cover an area of approximately 18x12km and are oriented equally. In **Fig 3A** a logging road reaches from left to the center of the photograph and branches where active logging takes place. The ground truth campaign showed, that the wedge-shaped structure extending from the left to the center of **Fig. 3A** is virgin *heath* forest, not yet disturbed by human activities (with exception of the logging road near the tip of the wedge). The forest which surrounds the wedge belongs to the lowland *Dipterocarp* forest type. Both natural forest types can be clearly identified in the enhanced ERS-1 image (note the wedge in **Fig 3B**). *Heath* forest grows on poor siliceous soil and it's canopy shows a much more regular and smoother structure compared to *Dipterocarp* forest (5). This smoothness is assumed to be the reason, why backscatter of this forest type can be clearly distinguished from lowland *Dipterocarp* forest. The ground truth photographs in **Fig 4B+D** show typical views of *Dipterocarp* (**B**) and *heath* (**D**) forest. The location of the ground truth photographs is indicated. The mountain slopes on the right in **Fig 3B** show a similar backscatter. From ground truth it is known, that this area is also covered by *heath* forest. However, under mountainous conditions interpretation is much more difficult and should be done carefully, since topography may influence the signal and ambiguities between other classes have to be expected. The forest surrounding the wedge was already selectively logged. The branched logging roads and the brown colored spots, which disturb the dark green canopy near the roads, indicate active logging operation (**Fig 3A**). The ground truth photograph in **Fig 4A** shows a typical view towards the sky in this area. In virgin forest the canopy is completely closed. However, in this heavily logged forest more than half of the view is open sky. Forest below the wedge was logged 5 years earlier. These activities are still visible as light green spots which interrupt the canopy (**Fig 3A**). The area indicated by arrows (upper arrows in **3A+B**) represents undisturbed forest, which appears uniformly dark green. **Fig 3B** demonstrates that undisturbed and exploited forest areas can be distinguished in ERS-1 SAR images. Disturbances of the forest canopy due to selective logging (gaps between trees) are visible as magenta/white spots and a rougher

texture. This is even true if logging was stopped several years ago. On the contrary undisturbed forest appears uniformly green in the ERS-1 image and shows less texture. Since no multitemporal data was available until now it is not yet clear if it is possible to assess different logging intensities. The logging roads and the small river (red in the MIR photograph) demonstrate the spatial resolution of the ERS-1 data. The road, clearly visible in the MIR photograph is approximately 15m wide. In ERS-1 images roads are visible if they are oriented at an angle towards the radar beam, but invisible if they are oriented straight towards the beam. The location where the logging road crosses the tip of the wedge is indicated by an arrow (lower arrows in **3A+B**). The river is between 15-30m wide. It can be detected quite clearly in the ERS-1 image.

6. DISCUSSION

The lack of multitemporal coverage of ERS-1 SAR data of our test site finally turned out to be a minor problem to achieve the anticipated results of the TRULI test phase. The constraint to investigate intensively a single ERS-1 image lead to results that were much better than expected before. Based on the ground truth collected in Kalimantan special attention was paid on the extraction of certain features within the test site known in advance, which probably would create some impacts to radar backscatter. To visualise those features various filter operations offered by the commercial ERDAS software package were applied on raw ERS-GEC data. A combination of different filters for speckle reduction and texture enhancement, respectively, was selected after subjective weighting of the resulted filtered bands. The final selection of filter combinations was based on the investigators experience and on the ground truth collected from the test site.

The available image processing means provided good results. The possibility to separate different forest types as well as logged forest and several land use activities using texture information derived from one single ERS-1 scene are supposed to origin from differences in roughness of the forest canopies (**Fig. 5**). Undisturbed *Dipterocarp* forest has a high stocking density and a great variety in tree height (from 30 to 50 m) and species diversity resulting in a medium backscatter signal without or only few high signal peaks from single trees. In the contrary undisturbed *heath* forest shows a smooth and homogenous canopy surface; due to a different species distribution and a reduced average height of 20 m resulting in low backscatter. This clear difference in the backscatter signal opens up the possibility to use ERS-1 SAR data for land use planning tasks in rainforests, since *heath* forests are characterized by very poor soils which are completely unsuitable for agriculture. In selectively logged lowland *Dipterocarp* forest usually all

valuable timber with a diameter > 40 cm is logged and removed. Huge old trees, living or dead, with low timber quality and remain in place. Therefore canopy surface roughness is especially high with corner reflection on single trees resulting in high peaks and a large variety of dB-values. In addition reflection of the unvegetated surface which provides information about micro-relief is added to the signal.

Based on our experience gained so far on the evaluation of an enhanced ERS-1 SAR image over the TRULI test area, it seems to be possible monitor land use, and logging activities in forested areas in the tropics in single scenes. However, several ambiguities between landuse classes and forest types even in the enhanced SAR-images can be found. Therefore the interpretation process itself needs skilled personnel which is able to integrate *a-priori* expert knowledge of landuse activities in a specific area into the interpretation process. For example, the differences between agricultural activities and selectively logged forest can be very small. However, it is known that agricultural activities of the local population are normally within a small distance to the rivers while selectively logged forests are more inland and are opened up by roads. Linear structures normally indicate roads and one can interpret logging operations with a high probability.

The results obtained so far give reason to establish the use of ERS-1 data as a "quick and dirty" tool to monitor deforestation processes and landuse in the tropics. In the framework of a multistage monitoring system to be developed, it is expected, that ERS-1 SAR data can be utilized to stratify or monitor areas. These areas then can be examined in more detail using conventional survey methodology like high resolution optical data from space, aerial photography, ground survey etc.. Such a procedure would allow to reduce time and money for survey, looking only on regions where unwanted changes could be detected. It must be mentioned that these results could be obtained only in flat areas. The northern part of the ERS-scene which was not evaluated, is mountainous and the extraction of information under these circumstances is much more complicated or even impossible. However, major logging activities in the tropics are primarily concentrated on more or less flat areas. Under these circumstances ERS-1 SAR images can provide essential information for forest monitoring and land use assessment in the most endangered and inaccessible regions.

Further investigations in the second phase of the TRULI project will have to provide security on the results found so far. A map was drawn from our test area by analysing stereo pairs of MIR images. After that the map and all available ground truth data was fed into a GIS system. The data of the

GIS will serve in second phase of TRULI to analyse the ERS-data more accurately. Furthermore it is expected that multitemporal analysis will increase ERS-1 data information content (6). The results found so far as well as new findings will be checked during a second ground truth campaign in order to test mapping accuracy and data reliability. It is planned to test the interpretation keys in a new area, from which no information is available *a priori*. This will show whether or not this approach is feasible in previously unknown terrain. Finally transfer of methods and results to the indonesian partner organisations is central part of the final phase of the TRULI project.

Literature

1. Kuntz S., Siegert F. & Fritz R., (1994). Tropical rainforest and Use of Land Investigation (TRULI). 1. Progress Report
2. Hildebrandt, G. (1991): On the use of high resolution satellite data for forest mapping and monitoring in developing countries, FAO-contract 729811. Sayn-Wittgenstein, L. (1991): The contribution of radar to forest inventories in Developing Countries, in: Oesten, G., Kuntz, S. & Gross, C.P. (Hrsg.) 1991: Wichmann Verlag, Karlsruhe
3. Lee, Y.S. (1986): "speckle suppression and analysis for SAR Images". Optical Engineering, Vol.25, No.5 ref.: KNIPP, ISPRS Workshop and conferences, p. 177
4. Blom, R.G. and Daily, M. (1982): Radar Image Processing for Rock-Type Discrimination, IEEE Transactions on Geoscience and Remote Sensing, Vol GE, No.3, July 1982
5. Whitmore T.C., (1984). Tropical rain forests of the far east. Clarendon Press, Oxford
6. Kattenborn, G., Nezry, E., De Grandi, G. & Sieber, A.J. (1993): High resolution detection and monitoring of changes using ERS-1 time series, Proc., 2nd ERS-1 Symp., 11-14 Oct. 1993, Hamburg, pp. 635-642. Leysen, M., Conway, J.A. & Sieber, A. (1993): Evaluating Multi-temporal ERS-1 data for Tropical Forest Mapping: Regional Mapping and Change Detection Applications, in: Proc., 2nd ERS-1 Symp., 11-14 Oct. 1993, Hamburg, pp.

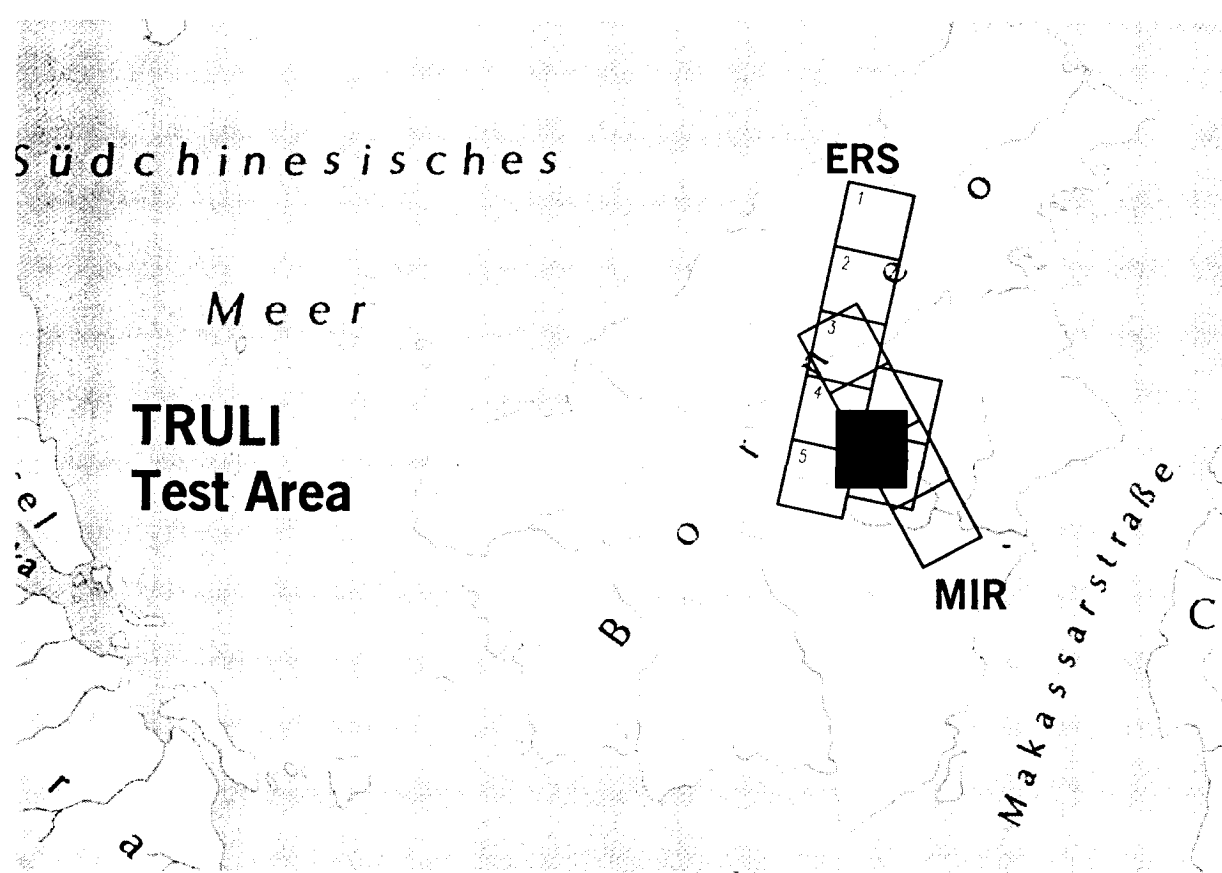


Figure 1.

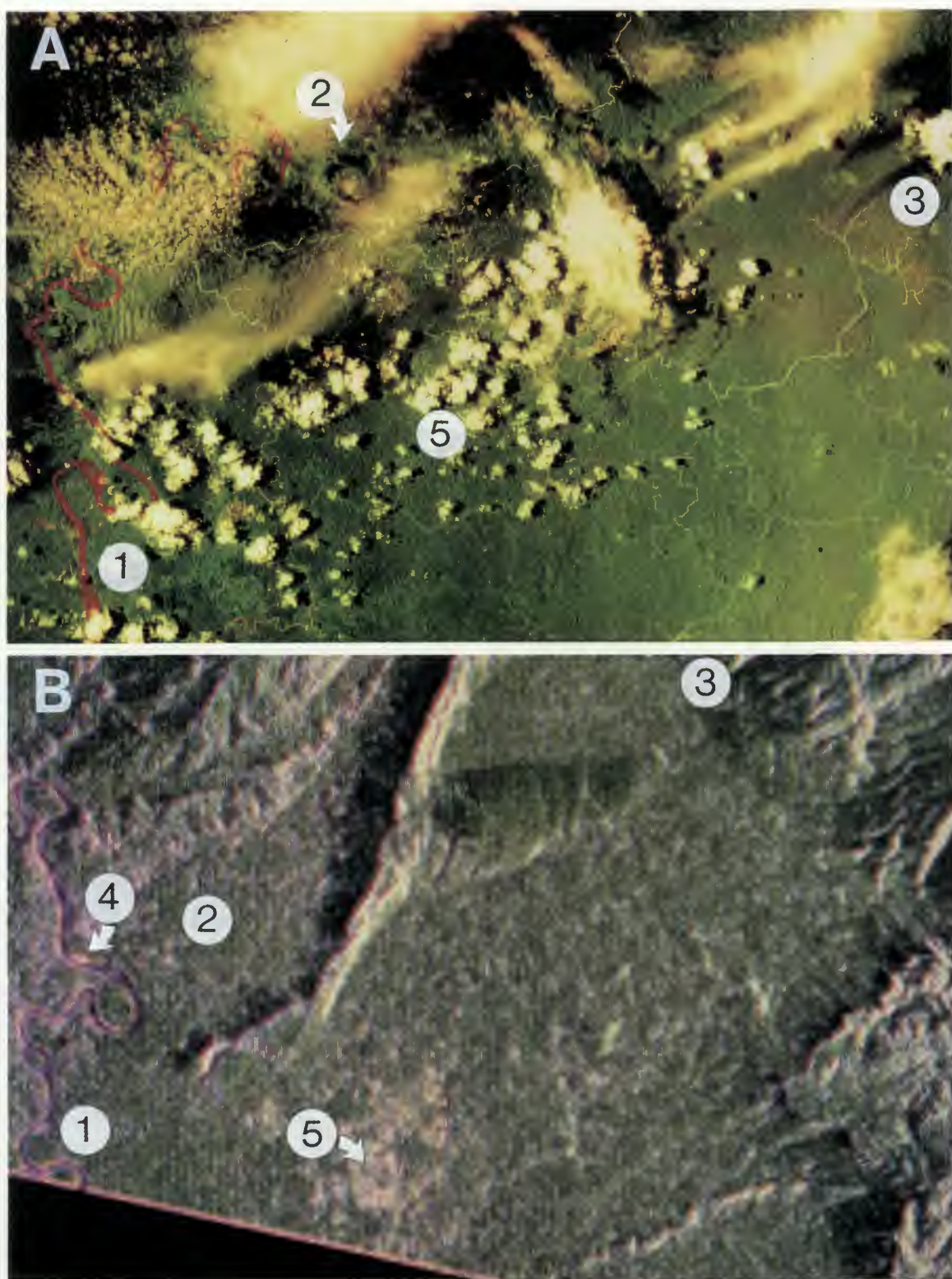


Figure 2.

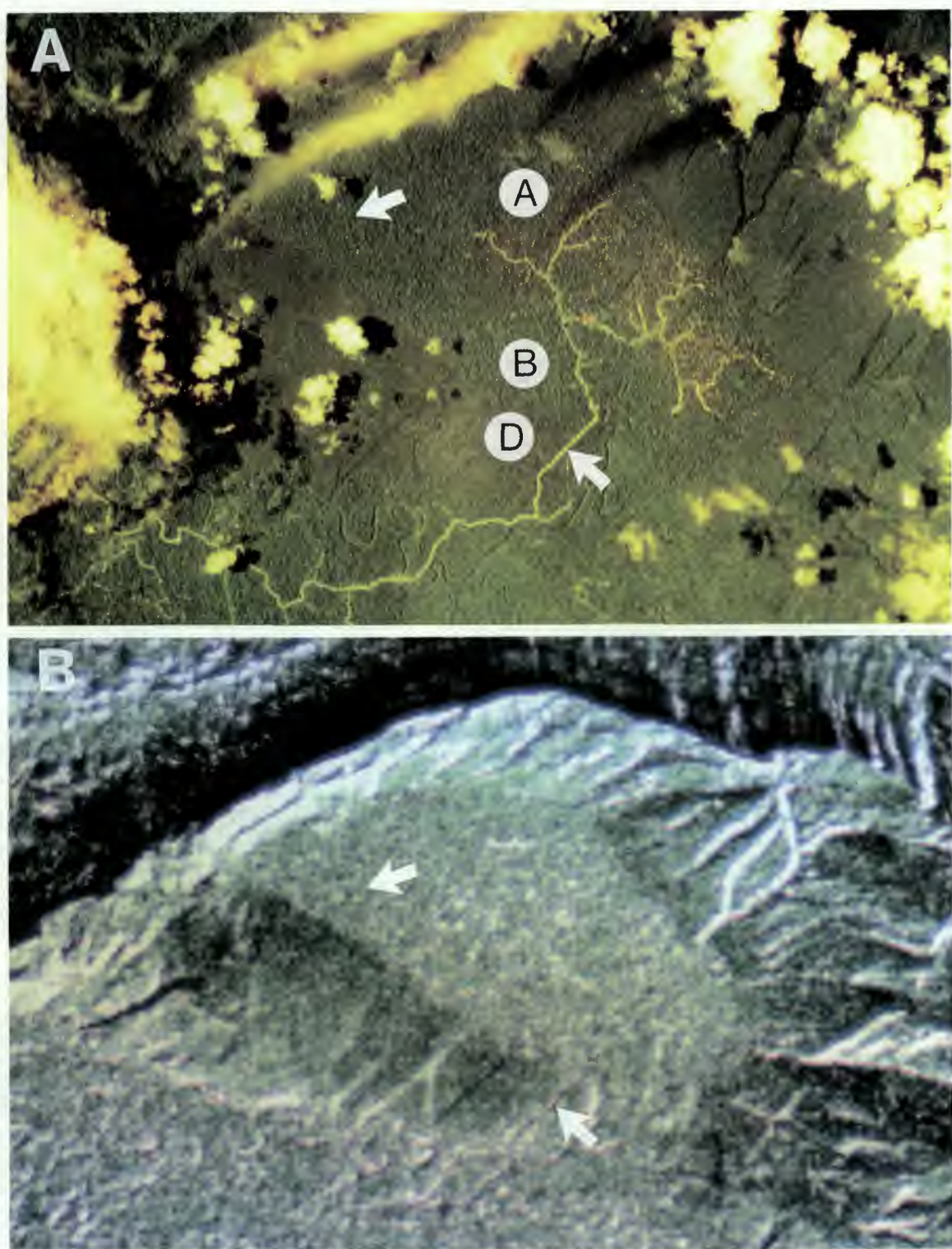


Figure 3.

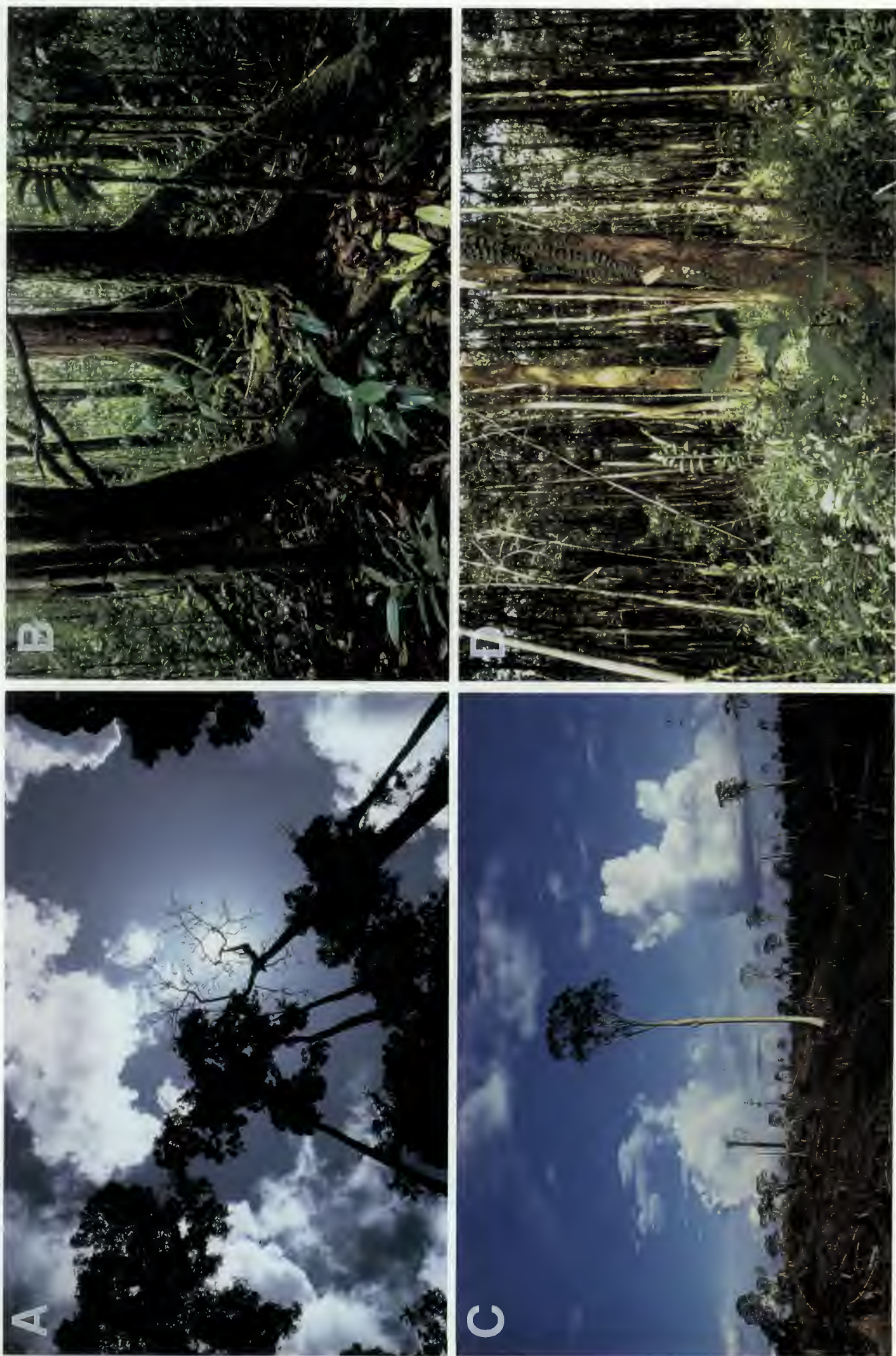


Figure 4.

height in m

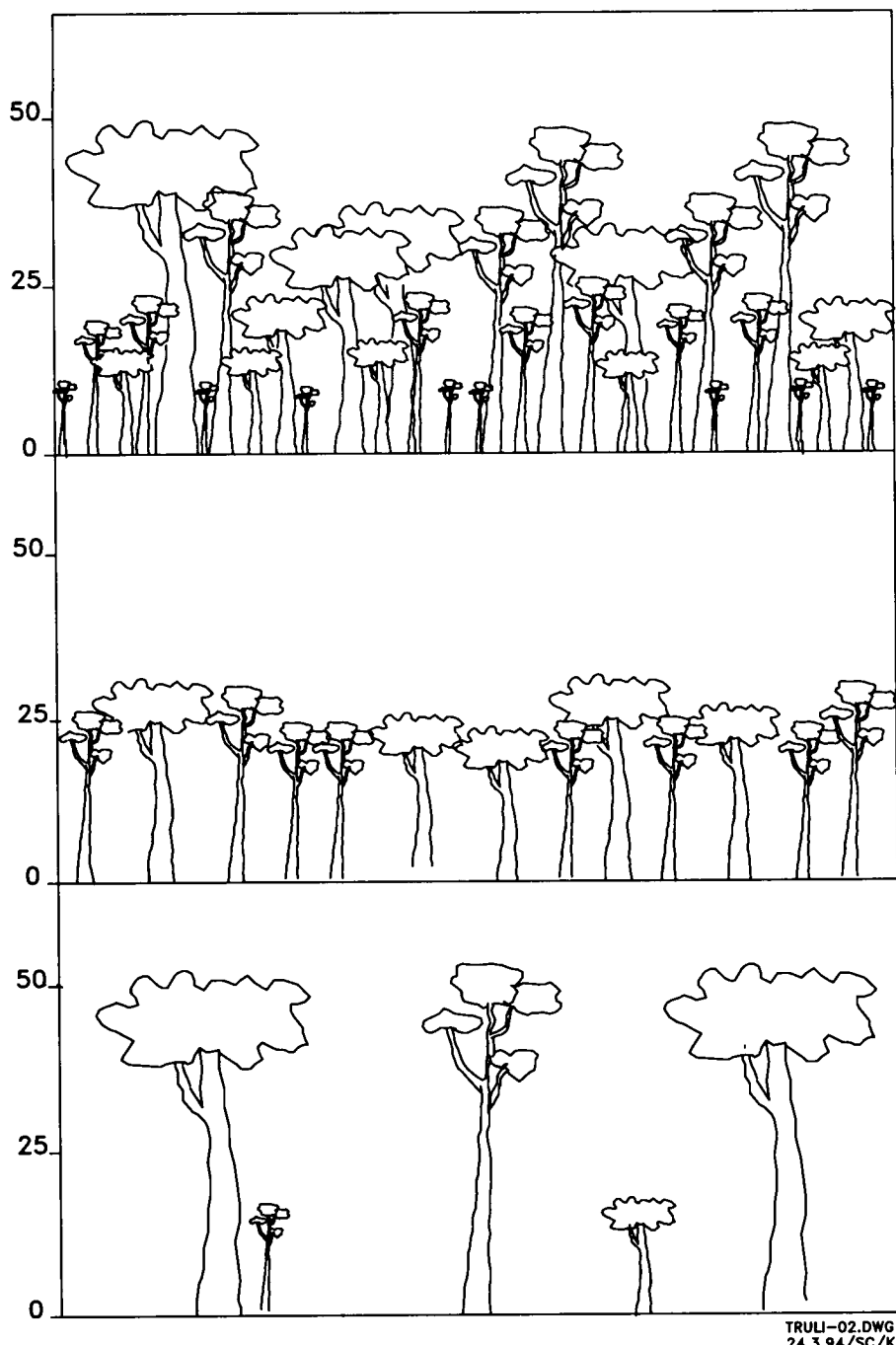


Figure 5.



ASSESSMENT OF THE POTENTIAL OF ERS-1 DATA FOR MAPPING AND MONITORING A MANGROVE ECOSYSTEM

Isabelle.PONS¹ and Thuy LE TOAN ²

1. Société GEOSYS, Toulouse, France. Tel (33) 61 75 12 10, Fax (33) 61 75 87 22
2. Centre d'Etude Spatiale des Rayonnements CNRS, université Paul Sabatier, Toulouse, France. Tel(33) 61 55 66 71, Fax (33) 615567101

ABSTRACT

The objective of this ERS-1 pilot project study is to assess the capabilities of ERS-1 data to map and monitor a mangrove ecosystem.

The studied area, located North of Conakry, Guinea, has been chosen according to an existing management project conducted by experts and local teams who provide to the study detailed inventory of the mangrove including maps and field investigation results. ERS-1 data has been acquired from May to September 93 in both ascending and descending passes.

Photo-interpretation and digital analysis of the data have been performed on different combinations. Backscattering coefficients have been analyzed as a function of the ground information (mangrove type, species, density, tide).

The results show that , at high tide, mangrove forest appear as a single class whereas at low tide, different mangrove types (high, low and heterogeneous covers) could be distinguished. Classification

algorithms have been applied to provide maps of mangrove types together with other land use/cover classes including ricefields, mudbanks and cut mangrove.

The results demonstrated the usefulness and the limitations of ERS-1 data for Mangrove monitoring and showed that methodology developed can be further investigated for operational use.

keywords : ERS-1, SAR, Mangrove, Guinea.

1 - INTRODUCTION

Mangroves are precariously balanced ecosystems. Due to numerous natural resources they provide, the mangroves are particularly exposed to an over exploitation which can cause irremediable damages.

Monitoring of the mangrove areas in the world is thus an urgent and important task. In the past, optical remote sensing has been used to map and monitor several mangrove areas. however, many of them are located in regions of important cloud coverage, where

the acquisition of SPOT and Landsat data is almost hazardous.

The first interest in using the all weather SAR systems to observe mangrove areas appears therefore obvious. It remains to determine the information content of SAR data to discriminate among different mangrove types and species, and monitor their temporal evolution.

The objective of the present study is
a/ to analyze ERS-1 SAR data acquired over
a mangrove site in guinea
b/ to interpret the results and
c/ to discuss about methodology which can
be used to map and monitor mangrove
areas.

2 - DESCRIPTION OF THE SITE AND STUDY CONTEXT

Fig.1 shows the location of the site, located in the north of Conakry in the bay of Sangareya. In this region, the mangrove ecosystem covers about 45 000 ha and includes woody areas and degraded terrain due to natural or anthropogenic effect.

- The mangrove stands are mainly of two species, *Avicennia* and *Rhizophora*, in a diversity of height density. Five different types have been mapped :

- closed high stands, mainly constituted of *Rhizophora*
 - closed mixed stands of dense and rather low *Avicennia* and rather high *Rhizophora*
 - closed low stands of monospecific and low trees (mainly *Avicennia*)
 - open low stands, mainly of low *Avicennia*

- mosaic of small dimension stands and ricefields.
 - the bare areas result from a natural or anthropogenic degradation
 - the ricefields installed on exploited mangrove areas.

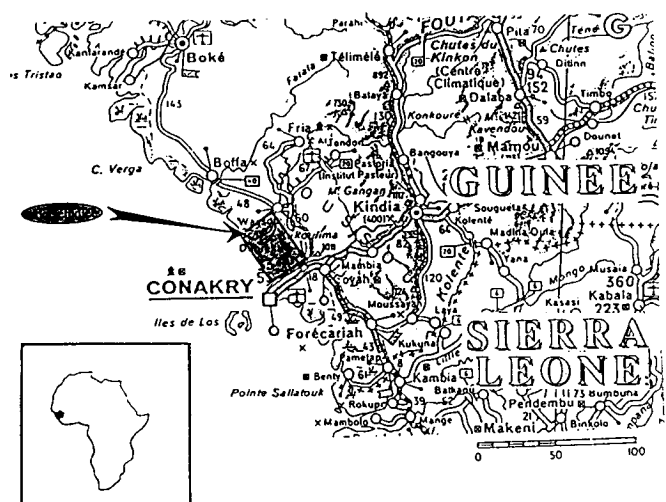


Figure 1 : site localisation

The resources of this mangrove ecosystem include the following :

- forest exploitation which supplies the wood for domestic need to the neighboring cities and villages
 - ricefields which supply rice for an important part of the Guinea.
 - salt extraction
 - fishing.

To facilitate a well controlled exploitation of the resources of this area, EEC project has been achieved. The project aimed at determining a directive scheme for the management of the Mangrove (SDAM : Schema directeur d'aménagement de la Mangrove). The first part of the project has

resulted in a detail mapping and an in depth inventory of the available resources in several regions including the bay of Sangareya.

The ERS-1 pilot project benefits from a collaboration with the SDAM project which makes available the following documents :

- vegetation map at the scale of 1/100 000
- forest maps at the scale of 1/20 000

3 - ERS-1 DATA

Table 1 summarizes the ERS-1 data acquired for the project. The first 2 SLC images in 1992 were purchased in the first phase. Then the data acquisition has been requested to ESA for the period from May to September 93. In total, 6 images as been used, 3 in ascending pass and 3 in descending pass.

Table 1 : ERS-1 data acquired

acquisition DATE	TYPE	REFERENCE orbit/frame*
15-06-92	SLC	4791 / 3411
28-09-92	SLC	6294 / 3411
15-05-93	PRI	9572 / 3411
16-05-93	PRI	9594 /189
31-05-93	PRI	9801 / 3411
20-06-93	PRI	10095 / 189
05-07-93	PRI	10302 / 3411
25-07-93	PRI	10596 /189
09-08-93	PRI	10803 / 3411

* 3411 : descending (day)

189 : ascending (night)

The image on 15-05-93 cover only a small part of the area and is not used for this study.

4 - SAR DATA ANALYSIS

• 16 to 8 bits conversion :

A resampling method was chosen to preserve most dynamic range of the Mangrove area. The mean and standard deviation are estimated for each image and a linear function centered on the mean with a range of 3 standard deviation was applied. The saturation was observed only on pixel related to built up areas.

• geographical correction :

the data were geographically corrected using the four corners coordinates given in the header file. The images are now projected along the north-south direction.

• data coregistration :

multidate images are coregistered to provide multidate combination. For the data of the same frame (ascending or descending mode) the coregistration was realized using a coordinates translation. For the different frames, because of the different look angle, a correction with control points is necessary. As the study area is relatively flat, a linear deformation was sufficient to obtain a good superposition. however, in spite of the correction, some offsets are observed in the multitemporal combinations of the 6 frames, in particular at the border of some waterways

5 - PHOTointerpretation

Photointerpration was performed on the colorprint of the two frame combinations realized at 1/100 000 scale. For photointerpreters who are not familiar to these SAR images, the interpretation

consisted mostly in relating image characteristics with ground features provided by the maps - Fig 2 shows an extract of the interpretation of ERS-1 multidate SAR images.



Figure 2 : extract of the photo interpretation

Five different land use/land cover were identified

- free water, with strongly variable tone according to the acquisition date (see figure

3)

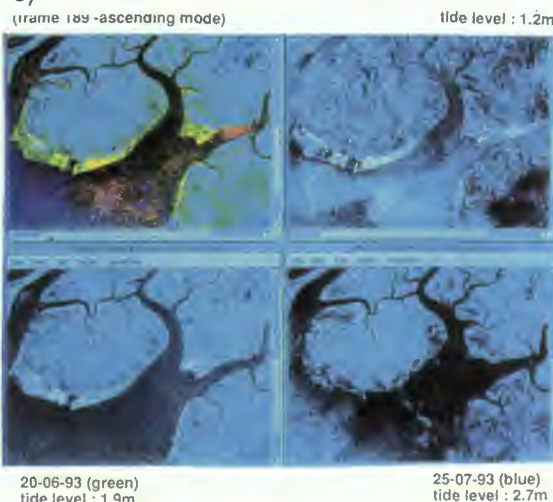


Figure 3 : multidate combination and associated ERS-1 images

- mud bank, non visible at high tide, bright area at low tide
- non wooded area which can be bare area or ricefield
- wooded area
- outside Mangrove (no change between different date).

CLASSIFICATION FINALE



Figure 4 : multidate classification results

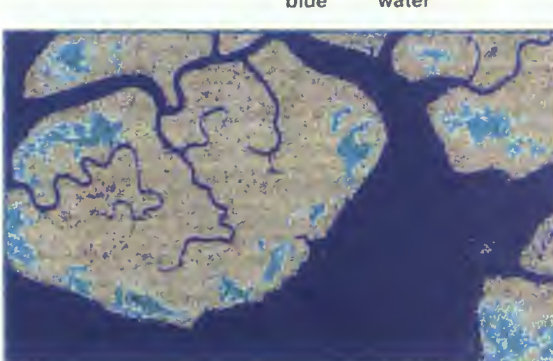


Figure 5 : random markov field results

At low tide, a distinction between 3 different types of wooded area is possible. Using the forest inventory result, the three types correspond to the following units:

- high (12-25m) and dense formation with characterized by high backscatter pixels.
- low (<12m) and dense stands, partially degraded of *avicennia*, characterized by a more uniformed pixel intensity distribution.
- heterogeneous open stand with different height (5-25m) of *avicennia* and *rhizophora*.

6 - CLASSIFICATION

Training samples have been selected based on the photo-interpretation result. Table 2 shows 13 training areas mean and standard deviation retrieved from 3 dates selected as follow :

- May 16 93 for the discrimination between mangrove stands,

- May 31 93 corresponding to the largest dynamic range for other land use / land cover classes

- July 05 93 for the specific responses of open ricefields.

A mean filter (7*7) was first applied to reduce speckle effect.

The classification results appear in good agreement with the existing map but the boundaries between classes appear noisy (Figure 4).

Table 3 shows statistics of the land use classes to be validated by further investigations.

The classification can be improved by the use of a better filter (like MAP, LEE) and by a more appropriate classification algorithm.

table 2 : mean and backscatter values of training samples

	size	5/16/93		5/31/93		7/5/93	
		mean	backscat	mean	backscat	mean	backscat
1	mangrov1	10434	138.3	-6.33	135.0	-5.74	141.5
2	mangrov2	12272	122.9	-7.73	118.4	-7.25	136.9
3	rice-bare1	1508	104.2	-9.92	90.6	-10.42	122.7
4	rice-bare2	7368	122.6	-7.86	106.3	-8.48	101.6
5	rice-bare3	4955	111.2	-9.00	107.3	-8.45	110.6
6	mudbank1	14904	154.3	-5.06	135.2	-5.79	105.1
7	mudbank2	18076	137.7	-6.24	138.8	-5.61	110.1
8	rice	2172	110.7	-8.90	99.2	-9.57	114.5
9	water+sedi	14919	156.9	-4.67	85.0	-11.57	95.6
10	water	36960	106.3	-9.48	87.2	-11.12	103.8
11	rice-sup	13070	136.5	-6.35	123.1	-6.74	84.3
12	outside1	123380	125.1	-7.35	99.2	-9.40	120.3
13	outside2	101372	126.0	-7.39	103.3	-8.73	124.7

Table 3 : Land use/cover statistics obtained by classifications results

Land use Type (mangrove)	surface (ha)	% surf tot
Mangrov1	9909	26,77
Mangrov2	15281	41,28
rice-bare	5728	15,47
mudbank	4541	12,27
rice sup	1559	4,21
TOTAL	37018	

To evaluate a new approach, we have also processed a classification by markov field, developed specifically for classify SLC data without pre filtering. This algorithm is based on speckle distribution at a low level (4 neighbours in the image) and considers region (4 classified pixel) of the result in a recursively process. As no filtering is applied before classification, the speckle distribution is preserved during the classification process. The consideration of 4 neighbours in a recursively process until the stability leads to a relatively smooth results on noisy (SLC) data.

With the two SLC images of 1992, corresponding to low tide (conditions where different mangrove stands cannot be distinguished) the result shows the potentiality of this approach (see Figure 5)

7 - BACKSCATTER ANALYSIS

The backscattering coefficient of each training area has been calculated from the original 16 bit data using the calibration formula given by ESA.

7-1 Dynamic range of σ_0

The dynamic range of different mangrove stands is only about 1.5dB. The range observed on mangrove area (mud-bank and rice-growing excluded) is about 3dB which is relatively low.

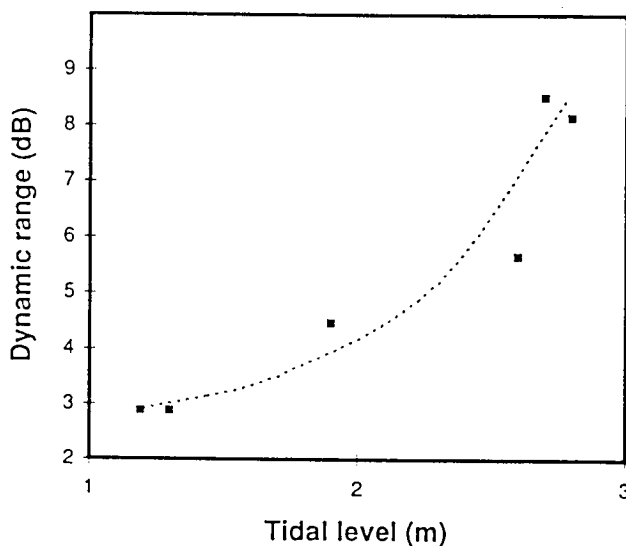
For the entire region, the dynamic range is more important at high tide, providing easier discrimination for different broad land use classes (figure 6)

7-2 Backscatter coefficients of mangrove

The distinction in the backscattering coefficients (0.4 versus 1dB) between high stands and low stands is observed at low tide (see figure 7).

An explanation can be given using sketch shown in figure 8. At low tide, the radar backscatter from the two types of stands (high, rizophora ant low, avicennia) results from the volume scattering which differ from one canopy to the other. At high tide, the double reflection tree trunk / water surface is dominant and differ not significantly from each other. This explanation has to be confirmed by more quantitative interpretation e.g. by modeling, based on quantitative measurement of the canopy parameters.

Figure 6 : Dynamic Range of backscatter



7-3 Backscatter coefficients of ricefields and land use

- **mudbank** : low backscatter coefficient is observed at high tide due to the water surface that covers the mudbank. At high tide, bright return by rough periodic mud surface, especially when the direction of the roughness is perpendicular to the radar look direction

- **ricefields** :

open ricefields have low radar backscatter at high tide (water surface) and high backscatter at low tide. Closed ricefields correspond to low backscatter and are not related to the tide level.

8 - CONCLUSIONS

Following the preliminary results obtained in this project, the use of ERS-1 SAR data to observe mangrove ecosystem can be done :

Mapping

With multitemporal data (3 dates), the discrimination between free-water, non wooded area (ricefield, bare terrain), mudbank and 2 types of wooded stands is possible by visual interpretation or by supervised classification. Because of the speckle effect on the 3 look PRI image, the appropriate scale for the resulting cartography is 1/100000.

However, it appears that the use of ERS-1 data to cartography mangrove types is restrictive and less performing than the use of optical data.

Monitoring

Two important phenomena of the Mangrove ecosystem is characteristic on SAR data :

- Bare terrain are visible on the 3 dates combination and confirmed by ground survey,
- Coastal dynamic accessible by the accurate delimitation of the sea and the characteristic signature of sediment transportation in the water.

This two points are very important for the balance of the Mangrove ecosystem and are more visible in SAR images than in optical images. ERS-1 as an all weather system, can provide regular monitoring of the phenomena.

Figure 7 : backscatter coefficient of different types of Mangrove

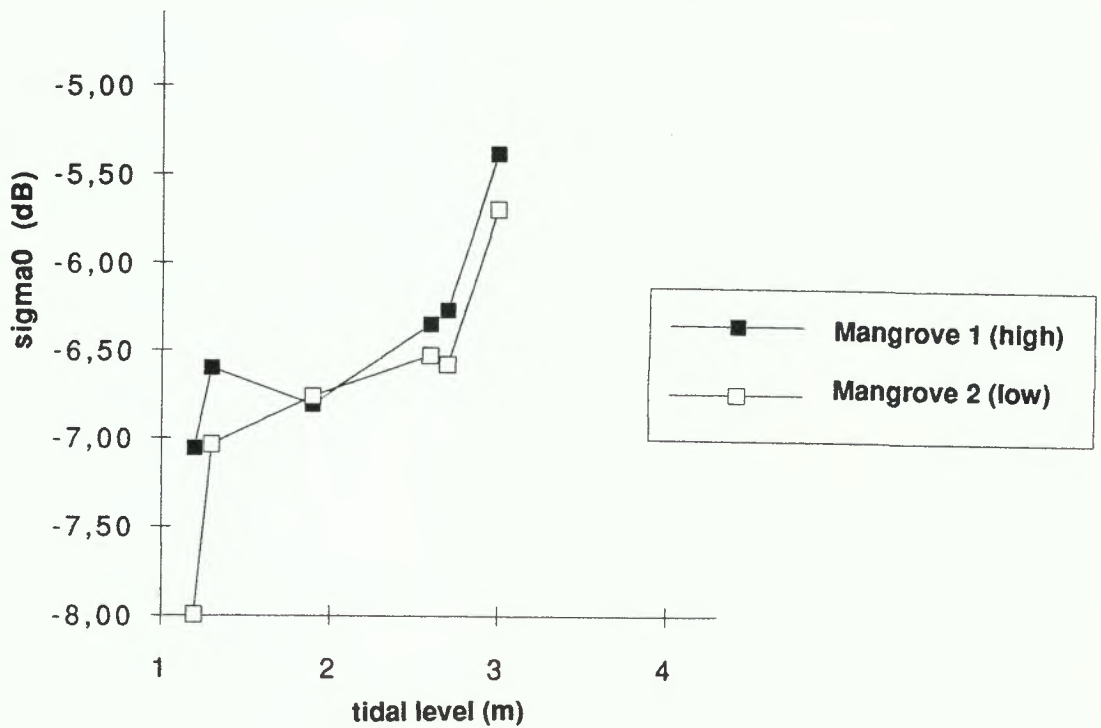
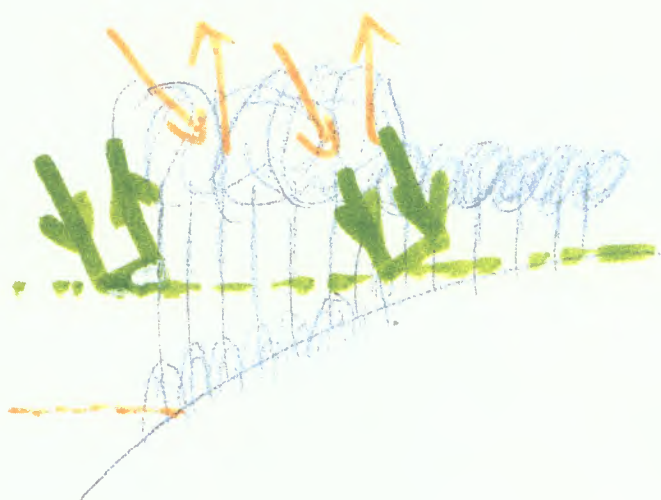


Figure 8 : explanation proposed



high tide :
multiple scattering
trunk/water dominant
 $\sigma_0 \text{ rhiz.} \approx \sigma_0 \text{ avi.}$

low tide :
volume scattering
dominant
 $\sigma_0 \text{ rhiz.} > \sigma_0 \text{ avi.}$

The use of multi-temporal set of ERS-1 data is necessary to have interesting information.

The link between tide and discrimination among the mangrove types, noticed in our data set, lead us to propose low tide acquisition for the mangrove observations.

The first conclusions are to be validated and completed by other specific studies of this area or similar area with more appropriate and simultaneous ground survey.

9 - ACKNOWLEDGMENTS

This study is supported by the CNES and ESA provides the ERS-1 data.

We thank the DNFC (direction national des forets et chasse) in Guinea for their collaboration (ground survey, maps) and the intervention of A. YANSANE, forestry engineer, during data exploitation and ground survey.

We also thank M SABATIER, which had realized the photo-interpretation of ERS-1 data with his experience (He already participated to the cartography of this area based on aerial photography).

RETRIEVAL AND ANALYSIS OF TEMPERATE FOREST BACKSCATTER SIGNATURES FROM MULTITEMPORAL ERS-1 DATA ACQUIRED OVER HILLY TERRAIN

A. Beaudoin¹, M. Deshayes¹, L. Piet¹, N. Stussi², T. Le Toan³

¹ Laboratoire Commun de Télédétection LCT CEMAGREF-ENGREF
648 rue J.F. Breton, B.P. 5093, 34033 Montpellier cédex, France / Tel: (33) 67.04.71.14 fax: (33) 67.04.71.01

² Ecole pour les Etudes et la Recherche en Informatique et Electronique (EERIE)
Parc Scientifique Georges Besse, 30000 Nîmes, France / tel:(33) 66.38.70.00 fax: (33) 66.84.05.06

³ Centre d'Etude Spatiale des Rayonnements (CESR/CNRS)
9, Ave Colonel Roche, B.P. 4346, 31029 Toulouse cédex, France
tel: (33) 61.55.66.71 fax: (33) 61.55.67.01

ABSTRACT

This paper presents the first results of a study aimed to assess the use of multidate ERS-1 SAR data for temperate forest applications over hilly terrain. The study was conducted over a mountainous French forest test-site. We first present a new radiometric correction method using SAR image simulation and a DEM to calibrate the data corrupted by ground area variability within pixels (up to 10 dB) and correct the data for σ^0 angular response (up to 1.5 dB). Both corrections are included in a SAR post-processing chain necessary to obtain optimized geocoded multitemporal σ^0 images.

Preliminary results showed that uncorrected data over hilly terrain are useless for discrimination purposes. After the validation of the radiometric correction, corrected backscatter, having a low range as a function of season and forest type, was found to be mainly sensitive to forest density and ground/canopy moisture state linked to environmental conditions (rainfall & temperature). Discrimination was possible at few dates (April, June) between crops/grassland, sparse and dense forests.

1. INTRODUCTION

Forest applications from spaceborne SAR data is a subject of on-going research, as a result of the sensitivity of the radar backscattering coefficient σ^0 to canopy geometric and hydric properties (biomass, LAI, water content...) and the increasing availability of spaceborne SAR data such as ERS-1. Possible forest applications using C-band SAR data are clear-cut mapping, forest type discrimination, regeneration follow-up and mapping of burned areas [1- 4].

To this aim, recent studies have stressed the need for multitemporal SAR data, taking advantage of seasonal σ^0 cover changes [1,2,3,11]; related methodologies are currently under development [7]. In addition, there is a need for a SAR post-processing chain to correct specific geometric and radiometric distortions over moutainous areas [4,5,10], where forests are often found in temperate regions. These distortions usually exceed the underlying SAR information pertaining to surface properties of interest. Few integrated correction schemes exist and R&D efforts, especially for the calibration aspect [5,10] are necessary for the quantitative use of SAR data over hilly terrain.

The main goal of this project is to contribute to the assessment of multitemporal spaceborne SAR data for forest applications in a temperate forest context over hilly terrain. This paper, related to results obtained in the first half of this project, mainly deals with a new relative calibration procedure using a DEM (Digital Elevation Model) and image simulation, to properly retrieve σ^0 of forests over hilly terrain. Then, some preliminary results are presented, concerning 1) the calibration assessment and 2) the general angular and temporal σ^0 behavior of forest covers over hilly terrain.

2. TEST-SITE AND ERS-1 SAR DATA

The forest test-site is situated in the Monts de Lacaune in the Tarn *département* in south-western France. It is a 20x20km area of moderate mountains with altitude ranging from 300 to 1200 m and maximum slopes of around 30°. Forest covers are composed of high forests (oak, beech and other hardwoods), plantations of coniferous species under 40 yr-old (silver fir, Douglas fir and other softwoods), sparse and dense stands of other coniferous and deciduous species, and mixed woods. Non-forest covers include crops, grasslands and villages. Available ground data consist of a digital French forest inventory at scale 1:25000 from a 1988 aerial IRC photo survey, produced by IFN (*Inventaire Forestier National*). Table 1 contains 15 cover classes derived from the 29 original IFN classes, with related area coverage (%). In addition, a DEM presented in a Lambert III map projection with 40m grid size was acquired from IGN (*Institut Géographique National*).

Class	Species	Structure	% area
1	oak	high forest	2.32
2	beech	high forest	6.26
3	poplar	high forest	0.02
4	other hardwoods	dense stand	5.83
5	other hardwoods	sparse stand	18.30
6	silver fir	strip planted	0.57
7	silver fir	plantation	12.96
8	Douglas fir	strip planted	0.05
9	Douglas fir	dense stand	2.91
10	other softwoods	sparse stand	0.55
11	other softwoods	strip planted	0.26
12	other softwoods	plantation	7.07
13	mixed woods	dense stand	1.08
14	crops, grasslands	-----	41.35
15	wildland	-----	0.46

Table 1: 15 cover types of the forest test-site

9 Multitemporal ERS-1 SAR.PRI amplitude images (16 bits) were acquired over the area between March and November 93. 4 images were obtained in the ascending mode (Frame 2727: April-30, June-04, July-09, August-13) and 5 in the descending one (Frame 873: March-23, April-27, June-01, July- 06 and Nov.-11). Fig. 2 summarizes multiday data acquisition along with daily rainfall events. A simple geometric correction (i.e. without resampling) was applied to overlay multitemporal data using relative translations, with RMS error better than one pixel.

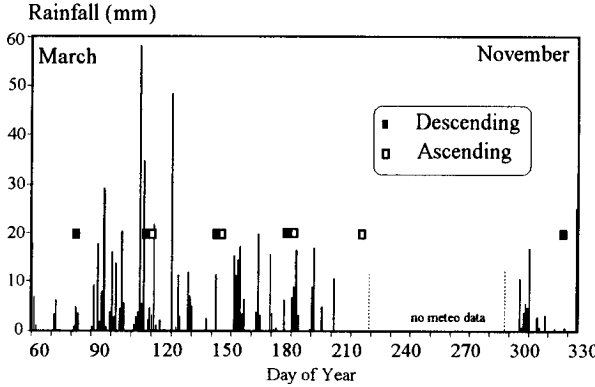


Figure 1: ERS-1 SAR data acquisition over the test-site, along with rainfall events

3. σ^0 RETRIEVAL OVER HILLY TERRAIN

Strong geometric and radiometric distortions are easily observed in SAR images acquired over hilly terrain, as seen in Fig. 5a. Removal of these distortions is necessary for σ^0 retrieval and thus, the quantitative use of SAR data. The correction scheme should rely on simple yet robust geometric and radiometric image model, as described in the following.

3.1 Geometric model

Severe geometric distortions of SAR images compared to terrain originate from slant range imaging mode and foreshortening/layover over hilly terrain. As a consequence, pixel location and size relative to the ground is highly variable. An image-to-map transform model is necessary to project the SAR data into a cartographic projection. In addition, this model is useful for radiometric corrections through SAR image simulation. Fig.2 presents a model for both tasks that will be illustrated in part 3.3.

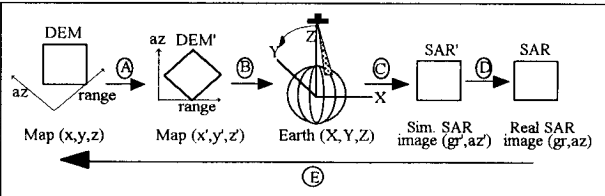


Figure 2: Direct and reverse map-to-image geometric model

3.2 Radiometric model

Relief-induced radiometric distortions are mainly due to 1) the ground area responsible for scattering within the pixel and 2) local incidence angle affecting the backscatter behavior [9]. To account for these distortions, we adopt the

following image radiometric model including speckle noise, system and topographic effects. Image pixel intensity I can be expressed as:

$$I = \bar{I} \cdot S \quad (1)$$

where \bar{I} is the mean radar reflectivity of extended surfaces over hilly terrain and S is the multiplicative speckle noise. In the case of ERS-1 and neglecting thermal noise, \bar{I} is proportional to backscattering coefficient σ^0 through the usual radar equation in its area-extensive form:

$$\bar{I} = G_p \bar{P}_r = K \int \frac{G^2(\theta) \sigma^0(\eta) dA}{R^3} \quad (2)$$

where \bar{P}_r is the mean received power from an extended target, G_p the processor gain, K is the absolute calibration factor including constant system parameters, η the SAR local incidence angle over terrain and dA a differential scattering area. Van Zyl et al. [10] showed that θ variations within a pixel can be neglected. Furthermore, $\delta r \ll R$ and $\sigma^0(\eta)$ is assumed to be constant within the scattering area. Therefore, G , σ^0 and R terms can be removed from the integral. In addition, ERS-1 data have been corrected for G and R . Eq. 1 can be simplified as:

$$\bar{I} = K \sigma^0(\eta) \int dA \quad (3)$$

with

$$K = \frac{K_{esa}}{A_{ref}}, \quad A_{ref} = \frac{\delta a \delta r}{\sin \alpha} \approx 400 m^2 \quad (4)$$

where K_{esa} is the ESA calibration constant estimated at reference incidence angle $\alpha = 23^\circ$ over flat terrain, giving a pixel area A_{ref} that must be removed. Combining eq.1,3 and 4, ERS-1 image radiometric model over hilly terrain is given by:

$$I = (K_{esa} \sigma^0 C_\eta C_a) S \quad (5)$$

with $C_\eta = f(\eta)$, $C_a = \frac{\int dA}{A_{ref}}$

where C_η and C_a are relief-induced terms accounting respectively for the relative angular backscatter behavior and variable pixel area. The only difficulty in using eq. 5 is to estimate the local incidence angle and pixel ground area of each pixel. This problem has been addressed by very few authors [4,5,10]. To this aim, knowledge of the terrain altitude along with slope components in the azimuth and range directions are necessary and can be obtained by linking the SAR viewing geometry to a DEM.

3.3 Pseudo-SAR image simulation

In the following, we present a new method we called Terrain Facet Integration (TFI) for ground area and incidence angle estimation. Estimates are made directly in the SAR image space, using pseudo-SAR image simulation based on the DEM replaced in an Earth cartesian projection. This is possible using the map-to-image transform of Fig. 2:

A) The DEM in the cartographic space is rotated in a new pseudo-cartographic space with y axis parallel to the satellite

track. The DEM is resampled to the grid size of ERS-1 images (12.5x12.5 m) using bilinear interpolation.

B) The modified DEM along with a local spherical Earth and satellite position are projected in an Earth-centered cartesian projection, to reproduce the SAR viewing geometry of the terrain. At this point, we obtain the configuration in Fig. 3, where a SAR azimuth line intercepts the terrain between 2 DEM lines azimuthally separated by δ_a , while a slant range SAR pixel variably intercepts the DEM from X_{\min} to X_{\max} (foreshortening).

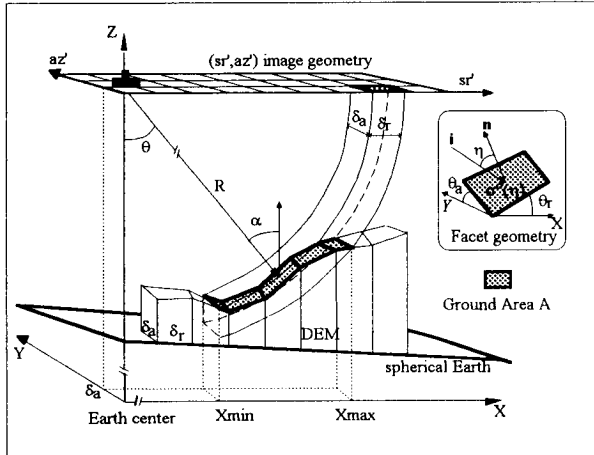


Figure 3: Configuration for image simulation and estimate of pixel ground area and local incidence angle over hilly terrain

C) Using this configuration, a pseudo-SAR image in slant range/azimuth coordinates (sr', az') can be simulated using an iterative procedure in the azimuth and range directions. The projection of the output grid (sr', az') in the (X,Y,Z) projection allows to find pixel intercepts with the terrain and therefore, the terrain facets associated to this pixel. Then, we use the Terrain Facet Integration method to compute ground area and local incidence angle of each simulated pixel.

Ground area and local incidence angle

Each terrain facet has mean slope components θ_{ri} and θ_{ai} , and basal area $\delta_a \delta_r$, as seen in Fig. 3. Then, each facet elementary area ΔA_i is approximated by:

$$\Delta A_i = \frac{\delta_r}{\cos(\theta_{ri})} \frac{\delta_a}{\cos(\theta_{ai})} \quad (6)$$

Local incidence angle η_i of each facet is defined in Fig. 3 as the angle between the normal vector n and the SAR incidence vector i :

$$\eta_i = \arccos \frac{n \cdot i}{|n||i|} = \arccos \frac{\sin \alpha + \cos \alpha}{\sqrt{\tan^2 \theta_{ri} + \tan^2 \theta_{ai} + 1}} \quad (7)$$

As each pixel X-intercepts with the DEM are known, the area integral in eq.5 is approximated by a discrete summation of N elementary facet areas ΔA_i found within the pixel:

$$A = \sum_{i=1}^N F_i \Delta A_i \quad (8)$$

Similarly, the pixel mean local incidence angle is computed using:

$$\bar{\eta} = \frac{1}{N} \sum_{i=1}^N F_i \eta_i \quad (9)$$

where F_i is the facet fraction included in the pixel area. Other products are derived from the simulation: shadow and layover bitmaps, and radial ambiguity image. All simulated images are then projected in a (gr', az') geometry using linear resampling in the range direction with 12.5m ground spacing.

D) Finally, simulated (gr', az') images are tied down to the real SAR (gr, az) images by 1st-order polynomial transform using bilinear interpolation, to correct for residual errors in the SAR image simulation [4].

3.3 Post-processing chain

Fig.4 shows a SAR post-processing chain including radiometric and geometric corrections, similar to the one proposed by Holecz et al. [5].

3.3.1 Radiometric correction

The different radiometric correction steps involved in eq. 5 to retrieve σ^0 can now be applied, as all terms are known for each pixel from simulation step: 1) relative calibration consists in removing Ca term; 2) data can be filtered for image σ^0 local estimate. Notice that filtering can be the first step applied, but it is expected that filtering should be eased after removal of image structure (bright ridges) due to relief-induced radiometric distortions. However, σ^0 values here will be estimated by pixel spatial averaging $\langle \sigma^0 \rangle$ for analysis purposes.

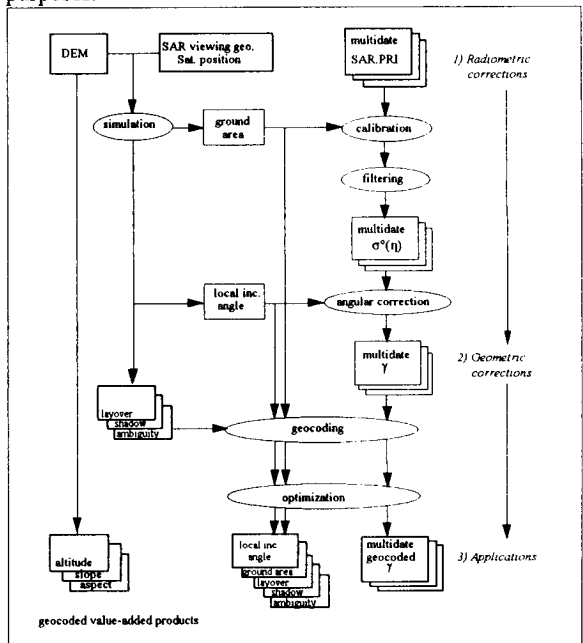


Figure 4: Post-processing chain for spaceborne SAR data acquired over hilly terrain

3) Angular correction is performed using appropriate empirical or theoretical angular backscatter model. For the angular correction, we propose a simple cosine law correction $C_\eta = \cos(\eta)$, where η is the local incidence angle. The validity of this correction for forest covers will be shown later. 4) Finally, absolute calibration allows to obtain σ^0 values. Notice that for temporal analysis, K_{esa} was found to have high stability of 0.43 dB [6] and will be considered constant for all images.

3.3.2 Geometric corrections

Geometric corrections consist in two steps: geocoding and resolution optimization. 1) The development stage of the proposed post-processing chain does not authorize geocoding (phase E in Fig. 2). Therefore, geocoding was performed using the analytic method described in [6] which is implemented in a commercial software. Both ascending (4) and descending (5) multitemporal σ^0 images in (gr,az) geometry were projected in the original Lambert III cartographic projection along with ground area and local incidence angle images. In addition, other value-added products derived from the geocoding process, such as shadow and layover bitmaps, were added to the geocoded SAR data set, which are useful for further analysis [4,5].

2) The following resolution optimization scheme was applied, to improve the ground resolution in areas of foreshortening/layover [5]. 3 pairs of geocoded ascending and descending images (April, June and July) acquired at 3-day interval were available. For each pair, relief is viewed with opposed SAR look directions, so range compression of terrain slopes is smaller in one of the two images. Therefore, an optimized image was created by selecting for each output pixel, the pixel from the ascending or descending image offering the smaller ground area, by comparing their geocoded A values. Related optimized ground area and local incidence angle images were also produced.

4. DATA ANALYSIS

From the post-processing chain, geocoded SAR data available for data analysis are 1) 1 optimized data set (3 dates) and 2) 1 ascending and 1 descending data set (4 and 5 dates). For each data set, images are available at different steps of the radiometric correction: uncorrected data, relatively calibrated σ^0 images and γ images.

Preliminary data analysis was performed with respect to general backscatter angular and temporal behavior, for different cover types. To this aim, the forest inventory map with 15 classes was stratified with the geocoded local incidence map, presented in 5 classes from 0° to 50° with $\Delta\eta = 10^\circ$. Then, only forest stands with at least 200 pixels were retained to obtain a good confidence level on σ^0 estimate through pixel averaging. Statistics were then extracted from post-processed images for more than 2000 polygons, at the stand and forest class levels.

4.1 Calibration assessment

The calibration must be assessed prior to data analysis. Fig. 5a and 5b include a sub-area (700 x 500) of an ascending ERS-1 SAR amplitude image (June), respectively before and after relative calibration using eq. 5. From bottom to top, this area includes a lake, grasslands surrounded by forests (mountainous area) and crop area (gently rolling terrain). Fig. 5c contains the simulated image of ground area A, with values ranging from 160 m² (slopes opposed to the radar) to 2500 m² (slopes facing the radar). This strong ground area variation is mainly due to its variable range component (12.5m to 200m) resulting from range compression.

Globally, image tones of a given surface type are homogenized due to the elimination of relief-induced distortions. In Fig. 5a, bright ridges, related to compressed slopes facing the radar, disappear in fig 5b, while terrain slopes opposed to the radar see their tone values increase. As a consequence, the visual distinction between surface types is much easier (for example, grassland surrounded by forest in the center of image center in Fig. 5b).

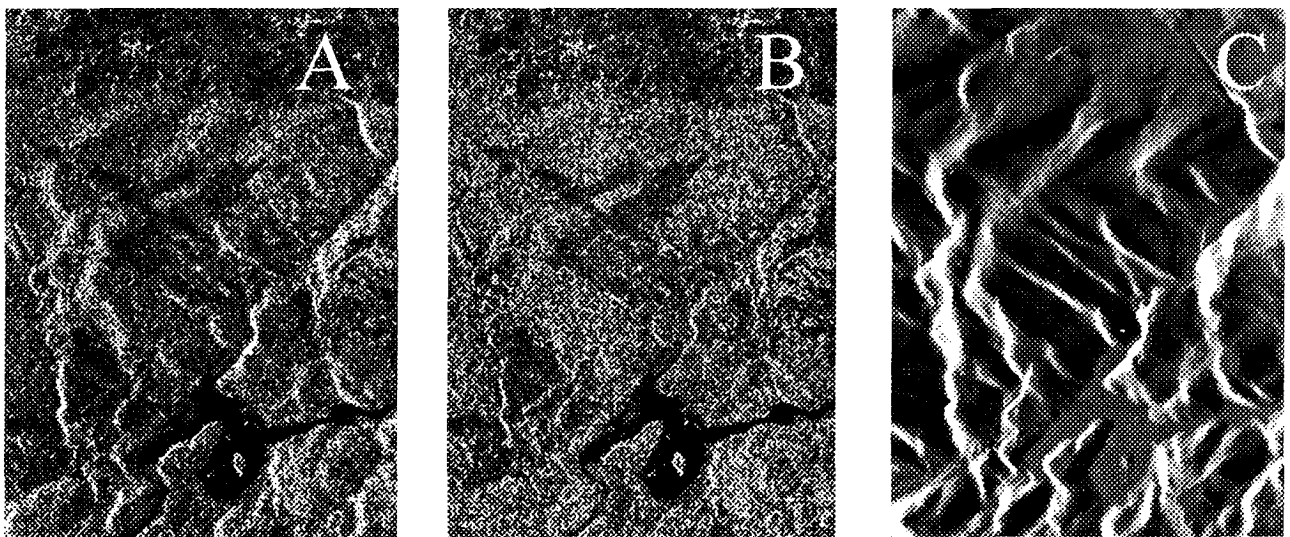


Figure 5: Sub-area (700 x 500) of an ascending SAR.PRI image in ground-range/azimuth geometry with illumination from the left, A) before correction, B) σ^0 image after calibration and C) simulated ground area image used for calibration

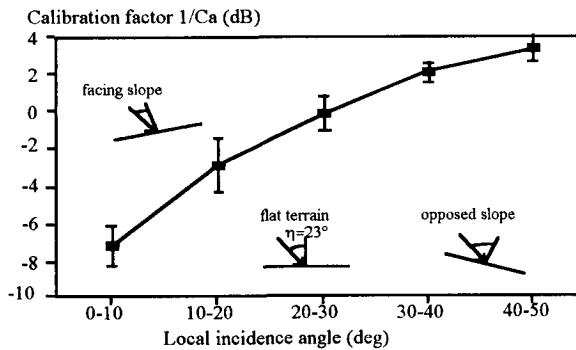


Figure 6: Correction factor for the removal of relief-induced radiometric distortions, as a function of local incidence angle classes, for ascending data set

To quantify the calibration error due to relief-induced distortions, Fig. 6 shows the measured relative calibration factor equal to $1/C_a$ as a function of η classes. As high as +7 dB calibration error occurs for slopes facing the radar, then the error decreases towards 0 dB as η approaches 23° (local flat terrain) and finally can reach -3 dB for slopes opposed to the radar. This is in accordance with results from Van Zyl et al. [10]. The calibration error is mainly dependant on θ_r , which in turn greatly affects the local incidence angle η .

Quantitative assessment of the calibration procedure is difficult to achieve. The accuracy of the area estimates depends on the accuracy of the DEM, the SAR viewing parameters and the overall coordinate transform model. As a preliminary assessment, for the geometric aspect, a positional RMS error of only 0.8 pixel (≈ 10 m) in gr and az was found between the simulated ground area image and the real SAR image. For the radiometric aspect, the analysis of σ^0 angular response can be used for calibration assessment, as some vegetation covers have relatively well-known angular behavior.

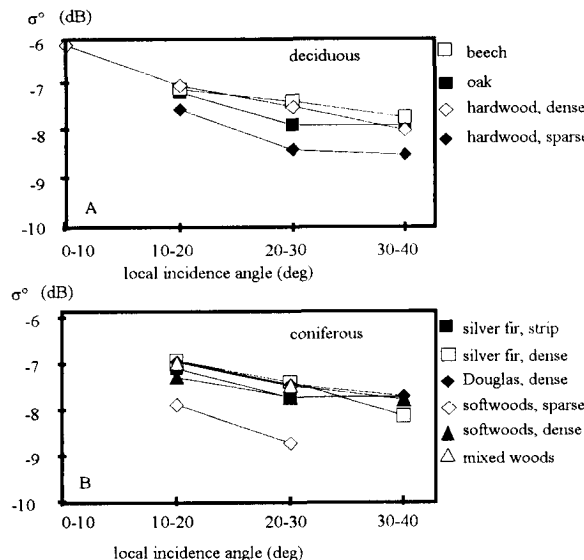


Figure 7: Mean σ^0 as a function of the local incidence angle η , for different forest species: A) deciduous and B) coniferous species

4.2 Angular backscatter response

Even calibrated, σ^0 can still be affected by the relief, through the dependence of scattering mechanisms to the local incidence angle [9]. Fig. 7 shows mean σ^0 angular response for various cover types, as a function of the local incidence angle. All covers show a slow angular decrease of about 1 dB from 10° to 40° ; a RMS value of 0.28 dB was found relative to a cosine law. For deciduous trees at C-band, this expected behavior is typical of volume scattering originating from uniformly oriented foliage within a dense canopy [8].

In addition, coniferous forests show a similar behavior with higher RMS of 0.43 dB, probably due to the less isotropic character of coniferous foliage. Therefore, we can conclude that 1) the calibration is satisfactory as expected backscatter behavior is retrieved for deciduous trees and 2) in a first approximation, the transform $\gamma = \sigma^0 / \cos(\eta)$ is an appropriate forest angular backscatter model in the post-processing chain, to reduce residual σ^0 variability due to the relief and improve the cover type separability.

4.3 Backscatter temporal behavior

Fig. 8 contains the temporal evolution of mean gamma value γ for non-forest and forest areas, A) before and B) after calibration and angular correction. In Fig. 8a, the mean γ for both cover types is undifferentiated, while standard deviation is very high. In Fig. 8b, the mean is now differentiated while at the same time standard deviation has decreased dramatically, down to about 1.5 dB. This illustrates the strong radiometric distortions due to relief and the great benefit of the radiometric correction for discrimination purposes.

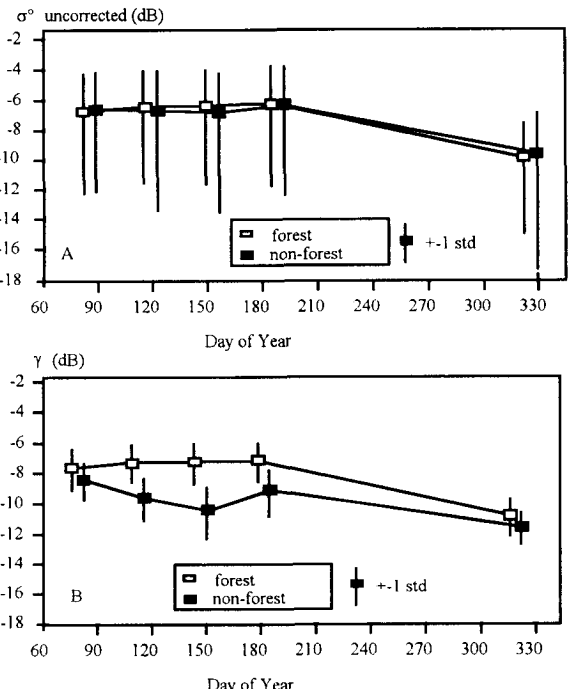


Figure 8: Temporal mean backscatter behavior of forest and non-forest areas (descending set) for A) uncorrected original data and B) gamma γ values (fully corrected data)

However, Fig. 8b already points out the limits of C-band SAR data for even simple discrimination purposes, considering 1) the general confusion between forest and non-forest except at 2 dates (June and April) and 2) the low forest γ range of about 3-4 dB. Therefore, the only straightforward forest application using a single ERS-1 image is probably forest/non-forest mapping and largely depends on the acquisition date, in relation with cover and environmental conditions [1,2, 11].

γ temporal behavior can be exploited to widen discrimination possibilities. For example, crops (Fig. 8b) show higher mean γ variability than forest for the first 4 dates, due to faster changes in dielectric and geometric properties of agricultural and grassland areas compared to forest. In addition, a strong γ decrease appears for both covers in November. This last change can be explained by a freeze event that occurred in the preceding night, causing a general decrease of the dielectric constant.

Temporal change detection is best achieved using backscatter ratio as described in [7]. In our case, ratioing was performed on optimized γ images. We present some results using two dates where all trees have their leaves on (June & April), with $\Delta\gamma = \gamma_{\text{June}}/\gamma_{\text{April}}$. Fig. 9 presents mean values of $\Delta\gamma$ plotted against γ (June), for respectively A) deciduous and B) coniferous stands with various structure types.

In both cases, the backscatter range is low, from -9 to -6 dB, and γ increases from low to high biomass covers: crops/grasslands, wildlands, sparse stands to dense stands. However, dense covers with high biomass levels are undifferentiated with γ saturation around -6.7 dB, except for plantations of Douglas fir (strip planted), probably due to its particular structure. Therefore, species discrimination of high forests can not be achieved using γ in this particular case, despite the species difference in foliar structure.

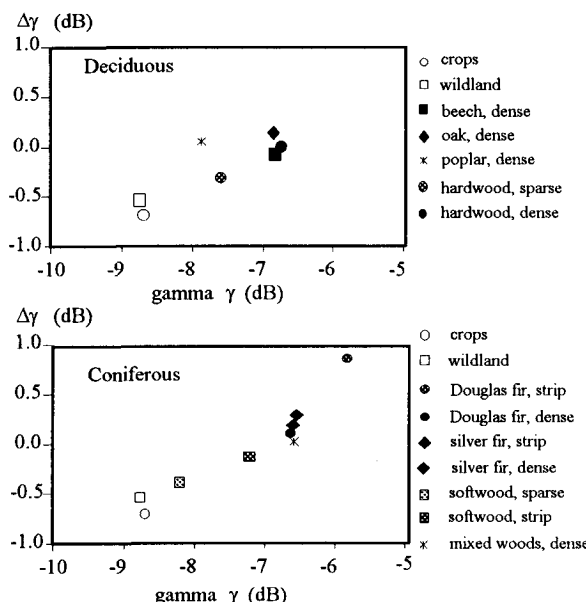


Figure 9: Mean gamma γ (June) and gamma ratio $\Delta\gamma$ (June/April) for A) deciduous stands and B) coniferous stands, along with non-forest covers (crops, wildland)

Mean backscatter change $\Delta\gamma$ has a range of about 1 dB and varies from about 0.2 to -0.8 dB from high to low biomass covers (dense, sparse stands, wildland to crops/grasslands). This may be explained by the fact that backscatter from low woody biomass covers (wildland and sparse covers) should have a significant contribution from the ground, with higher moisture variations compared to canopy moisture. In this case, higher soil moisture content in April compared to June, due to higher rainfalls in April (Fig.1), could explain the temporal backscatter decrease for low biomass covers, which is not observed for dense cover (no ground contribution). The highest γ changes for crops are easily understood since these covers exhibit high temporal changes of vegetation type, growth stage, soil moisture and roughness state.

5. CONCLUSION & FUTURE WORK

The reported work was intended to assess the potential of multitemporal spaceborne SAR data for forest applications. For this purpose, a new calibration method, integrated in a SAR post-processing chain, was developed and promising results were obtained as most topographic effects disappeared after correction. This improvement was confirmed in forest backscatter angular response, in agreement with a cosine law. However, the method has to be assessed in more detail including the impact of the DEM on both the radiometric and geometric accuracy of the method. It should be compared to the results obtained using other methods such as the local tangent plan approximation [10]. In addition, the cosine law correction proved to be useful to remove forest backscatter variability due to terrain.

Concerning the data analysis for cover type discrimination, preliminary results showed that 1) dense forests have a low backscatter range at C-band with higher temporal stability than low biomass covers, 2) forest backscatter mainly scales with cover density (except for dense forests) while species discrimination is difficult, 3) forest backscatter change seems to scale also with cover density due to variable environmental impact (rainfalls) on backscatter through the ground scattering contribution. However, these first interpretations from preliminary results must be refined and confirmed.

At this stage, considering the low backscatter range and small backscatter temporal changes of forests (except for freeze events), it is expected that possible forest applications in our particular case will be forest/non-forest discrimination, clear-cut mapping and discrimination between dense and sparse forest covers. These applications will have to rely on careful segmentation applied to optimally filtered SAR geocoded images.

Further work will include detailed analysis for all forest stands using geocoded temporal backscatter for all available dates. In particular, change detection will be applied for two dates (1 in Summer + November) with and without leaves for deciduous species, for possible deciduous/coniferous discrimination.

ACKNOWLEDGEMENTS

We would like to thank ESA for providing the ERS-1 data within pilot project PP2-F22. Also special thanks to Sylvain Labb  , Fran  oise Axes and Sylvie Durrieu, all from LCT, for their help and useful comments concerning the DEM, GIS and forest aspects of the work.

REFERENCES

- [1] Ahern, F.J., D.J. Leckie and J.A. Drieman 1993, "Seasonal changes in relative C-band backscatter of northern forest cover types", *IEEE Trans. on Geoscience and Remote Sensing*, Vol. 31, No.3, May 1993, pp. 668-680.
- [2] Ahern, F.J., D.G. Leckie and D. Werle 1993, Applications of RADARSAT SAR data in forested environments, *Can. Journal of Remote Sensing*, Vol. 19, No. 4, pp. 330- 336.
- [3] Dobson, M.C., L. Pierce, K. Sarabandi, F.T. Ulaby and T. Sharik 1992, Preliminary results of ERS-1 SAR for forest ecosystem studies, *IEEE Trans. on Geoscience and Remote Sensing*, Vol. 30, No.2, march 1992, pp. 203-211.
- [4] Guindon, B. and M. Adair 1992, Analytic formulation of spaceborne SAR image geocoding and "value-added" product generation procedures using digital elevation data, *Can. Journal of Remote Sensing*, Vol. 18 No 1, janvier 1992, pp. 2-12.
- [5] Holecz, F., E. Meier and D. N  lesh 1993, "Post-processing of relief induced radiometric distorted spaceborne SAR imagery", Ch. 14 in *SAR Geocoding: data and systems*, Gunter Shreier Editor, pp. 298-352.
- [6] Laur, H., P. Meadows, J.J. Sanchez and E. Dwyer 1993, ERS-1 SAR radiometric calibration, CEOS Calibration Workshop, ESA/ESTEC, October 93.
- [7] Rignot, E. and J.J Van Zyl 1993, Change detection techniques for ERS-1 SAR data, *IEEE Trans. on Geoscience and Remote Sensing*, Vol. 31, No.4, July 1993, pp. 896-906.
- [8] Ulaby, F.T., K. Moore and A.K. Fung 1986, Microwave remote sensing, Vol. III, Ch. 21, Artech House, Norwood, MA.
- [9] Van Zyl, J.J. 1993, The effect of topography on radar scattering from vegetated areas, *IEEE Trans. on Geoscience and Remote Sensing*, Vol. 31, No.1, January 1993, pp. 153- 160.
- [10] Van Zyl, J.J., B.D. Chapman, P. Dubois and J. Shi 1993, The effect of topography on SAR calibration, *IEEE Trans. on Geoscience and Remote Sensing*, Vol. 31, No.5, Sept. 1993, pp. 1036-1043.
- [11] Villasenor, J.D., D.R. Fatland and L.D. Hinzman 1993, Change detection on Alaska's North slope using repeat-pass ERS-1 SAR images, *IEEE Trans. on Geoscience and Remote Sensing*, Vol. 31, No.1, January 1993, pp. 227- 236.



MONITORING FUNGI DISEASES IN PINE FORESTS USING ERS-1 SAR DATA

Yrjö Rauste and Einar-Arne Herland

Space Technology

Technical Research Centre of Finland

Metallimiehenkuja 10, P.O.Box 13031 VTT

SF-02044 VTT, Finland

Tel. +358 0 4561, Telefax +358 0 456 4496

ABSTRACT

The possibility to map fungi diseases and other forest damage using ERS-1 SAR was studied. A multitemporal geo-coded data set of ERS-1 SAR images was created. Colour composites of winter-time images were studied to identify areas affected by fungi diseases or other forest damage. Four such test points were inspected on the ground. All of these test points suffered from some kind of stress (fungi diseases, elk damage, drying, or use as pasture land). The test points on peat land suffered from fungi diseases despite increasing backscatter.

The C-band SAR of ERS-1 seems to have potential for mapping forest damage on mineral soil.

Keywords: SAR, forest damage, coniferous forest

INTRODUCTION

Boreal forests form an important carbon source and sink in the global carbon cycle. When the temporal variation in carbon balance is studied, the role of fungi diseases and other types of forest damage becomes more and more important with the expected spreading of these diseases in connection of global warming.

SAR data has been studied for clear-cut mapping (e.g. Drieman 1987, Ahern and Drieman 1988, Till *et al.* 1988, and Drieman 1994). Very few studies have been published on the use of SAR for forest damage mapping (e.g. Lahti *et al.* 1993).

The *Gremmeniella Abietina* fungus is an example of fungi diseases that occur in Boreal forests (Salemaa *et al.* 1991). This disease causes defoliation of trees, starting in the lower branches. Defoliation of spruce is detectable using an X-band radar with a wavelength of 3 cm (Pulliainen *et al.* 1992). The *Gremmeniella Abietina* fungus mainly affects pine. The needles of a pine are approximately twice as long as those of a

spruce. The C-band radar of ERS-1 (wavelength 6 cm) is expected to be efficient in detecting pine forest diseases where the symptoms are drying and loss of needles. The change in microwave backscatter due to fungi diseases is very small. When multitemporal images are used so that images from the same season of different years can be compared to each other, the minor changes in microwave backscatter due to fungi diseases may be detected. Winter images where a smooth snow surface forms an absorbing background to trees and where most of the backscatter comes directly from the needles and smaller branches, are expected to facilitate detection of fungi diseases.

TEST SITE AND SAR DATA

The study site (centre: 61°26' N, 28°42' E) is in South-Eastern Finland close to the towns of Imatra and Lappeenranta (figure 1). The main tree species in the study area is Scots pine (*Pinus sylvestris*). The area is relatively flat. The elevation ranges between 66 and 171 metres above mean sea level.

The SAR data were acquired by the AMI (Active Microwave Instrumentation) sensor aboard the ERS-1 satellite (Vass and Battrick, 1992). SAR data from 13 days (table 1) were available during the writing of this paper. The data was in the form of precision images, which implies that the data were calibrated with respect to antenna pattern and range-spreading effects (Battrick 1993).

IMAGE PROCESSING

Multitemporal analysis of remote sensing data requires that the image data are geo-coded or resampled to the same, preferably geo-referenced grid. The SAR images were geo-coded using a digital elevation model (DEM). The DEM, based on the contours from the topographical maps in scale 1:20 000, was obtained from the National Board of Survey.

Table 1. Weather conditions on image acquisition days in Lappeenranta.

Acquisition date	Previous day			Acquisition day		
	Cloudiness	T (°C)	Snow (cm)	Cloudiness	T (°C)	Snow (cm)
1993-01-24						
1993-02-28						
1993-04-04						
1993-05-09				clear	+22	
1993-06-13	cloudy	+10		cloudy	+14	
1993-07-18	partly cloudy	+23		cloudy	+21	
1993-08-22	cloudy	+13		cloudy	+17	
1993-09-26	partly cloudy	+6		clear	+6	
1993-10-31	cloudy	+3		cloudy	+4	patches
1993-12-05				cloudy	+1	20
1994-01-08						
1994-02-13	clear	-18	56	clear	-11	56
1994-03-21	cloudy, snow	-3	59	partly cloudy	-3	58

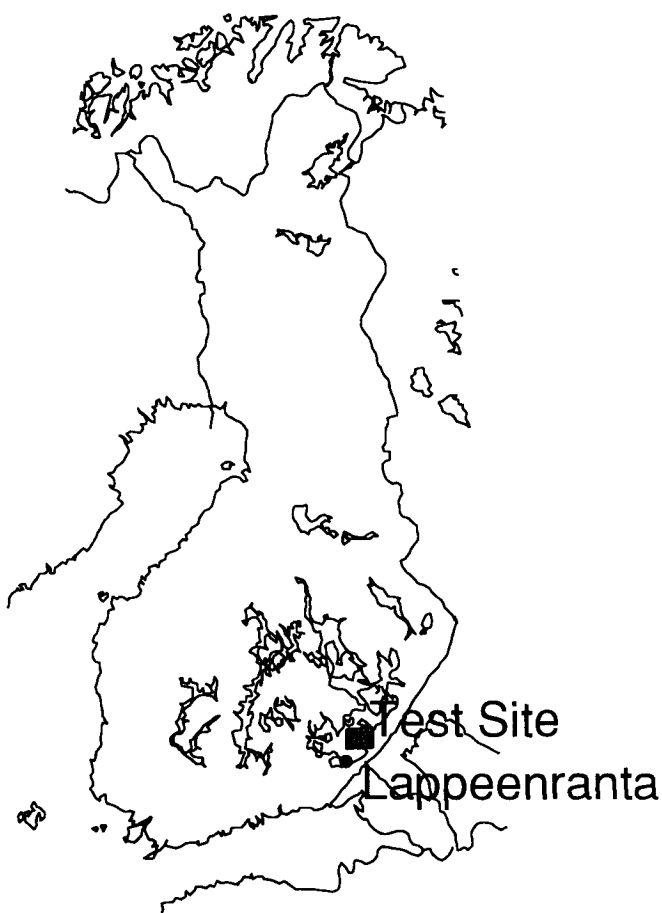


Figure 1. Location of the study site.

The geo-coding was done using an adaptive polynomial rectification method. Ground control points (GCPs) were measured from topographical maps in scale 1:20 000. The root mean square error (RMSE) in GCPs varied from 15 to 20 metres. The geo-coding accuracy indicated by RMSE was verified by visual comparison between the geo-coded images and the topographical map.

In the resampling process, bilinear interpolation of pixel values was used. Bi-linear interpolation produces some speckle reduction in the geo-coding process. Further speckle-reduction was achieved by using Gaussian averaging of the geo-coded image data. A pixel size of 25 m by 25 m was used in the geo-coding. The resolution was degraded to 50-m-by-50-m pixel size in the Gaussian averaging.

The topographical effects on image radiometry were reduced in connection of geo-coding. The variation of the size of a resolution cell due to topography was taken into account.

Search of areas affected by fungi diseases or other damaging agents was based on visual interpretation of winter-time images. Three-channel colour composites were produced. Decorrelation stretch was used to enhance anomalous pixels in 3-channel colour composite images. ERS-1 SAR images of winter season are highly correlated. In such cases the decorrelation stretching exaggerates colour saturation independent of lightness and leaves the distribution of hues substantially unmodified (Gillespie 1992). After the decorrelation stretch, the images of different dates are no longer comparable to each other in terms of calibration.

Two different colour composites were used in visual interpretation:

	Composite 1	Composite 2
Red	930228	930228
Green	930404	940108
Blue	940108	940213

The pixels where the backscatter has decreased are shown in shades of red. The pixels where the backscatter has increased are shown in shades of green-blue. For both of the data sets, a colour composite image was generated separately for forests on mineral soil and for forested peatland. Waters, agricultural areas, and the opposite soil type (peat or mineral soil) were masked out from the colour composite images before visual analysis.

RESULTS

Anomalous areas were identified in the colour composite images. As large patches as possible were aimed at. In total 11 points were chosen for ground checking. Eight of the points were on mineral soil. In four of these, the backscatter had decreased suggesting a damage. In four points, the backscatter had increased. Three of the points were on peatland. Figure 2 shows the behaviour of the backscatter in the ground-checked points. Data in figure 2 are from the original geo-coded images and should be comparable between dates. The terms "increasing" and "decreasing" refer to the decorrelation-stretched images where scenes of different dates were normalized to have the same mean and variance. The left-most date (January 1993) was not used in selection of test points.

Table 2 lists the possible reasons for the change in backscatter for the test points.

DISCUSSION

It was assumed that *Gremmeniella Abietina* fungus and many other types of forest damage that decrease the needle mass of conifers would lower the (winter-time) C-band backscatter of affected areas. The ground-inspection of eight test points on mineral soil support this assumption. In the two test points located on peat land, the backscatter had increased despite the presence of *Gremmeniella Abietina* fungus. This is contrary to the assumption. One possible explanation is that the *Gremmeniella Abietina* epidemics may have been worse in the previous year, and that the trees are now recovering from it. Addition of January-February scenes of 1995 to the data set could confirm this.

The small number of test points makes it difficult to draw firm conclusions. The preliminary results suggest that the C-band SAR aboard ERS-1 satellite has potential in mapping forest damage, at least in forests on mineral soil.

ACKNOWLEDGEMENTS

The authors would like to thank the Finnish Academy for funding this study (as a part of the Finnish research programme on climate change, SILMU) and Enso Gutzeit Ltd. for providing ground data and assisting in field work.

REFERENCES

- Ahern, F., and Drieman, J. 1988. Assessment of clearcut mapping accuracy with C-band SAR. Proceedings of IGARSS'88 Symposium, Edinburgh, Scotland, 13-16 September 1988, ESA SP-284 (IEEE 88CH2497-6), p. 1335-1338.
- Battrick, B. (editor) 1993. ERS user handbook. ESA SP-1148, Revision 1, European Space Agency, Noordwijk, The Netherlands, 1993, 129 p.
- Drieman, J. 1987. Evaluation of SIR-B imagery for monitoring forest depletion and regeneration in Western Alberta. Canadian Journal of Remote Sensing, Vol. 13, No. 1, July 1987, p. 19-25.
- Drieman, J. 1994. Forest cover typing and clearcut mapping in Newfoundland with C-band SAR. Canadian Journal of Remote Sensing, Vol. 20, No. 1, January 1994, p. 11-16.
- Gillespie, A. 1992. Enhancement of multispectral thermal infrared images: Decorrelation contrast stretching. Remote Sensing of Environment, Vol. 42, p. 147-155.
- Lahti, K., Rauste, Y., and Holm, M. 1993. Relationship between C-, L-, and P-band SAR data and forest damages, 12th EARSeL Symposium for monitoring the changing environment of Europe, Eger, Hungary, 8-11 September 1992, Publisher: A.A. Balkema, Rotterdam, 1993, p. 61-67.
- Pulliainen, J., Heiska, K., Hyppä, J., and Hallikainen, M. 1992. Laboratory and tower-based microwave measurements of spruce defoliation, Proceedings of the International Geoscience and Remote Sensing Symposium IGARSS'92, Houston, Texas, May 26-29, 1992, Vol. II, p. 1177-1180.

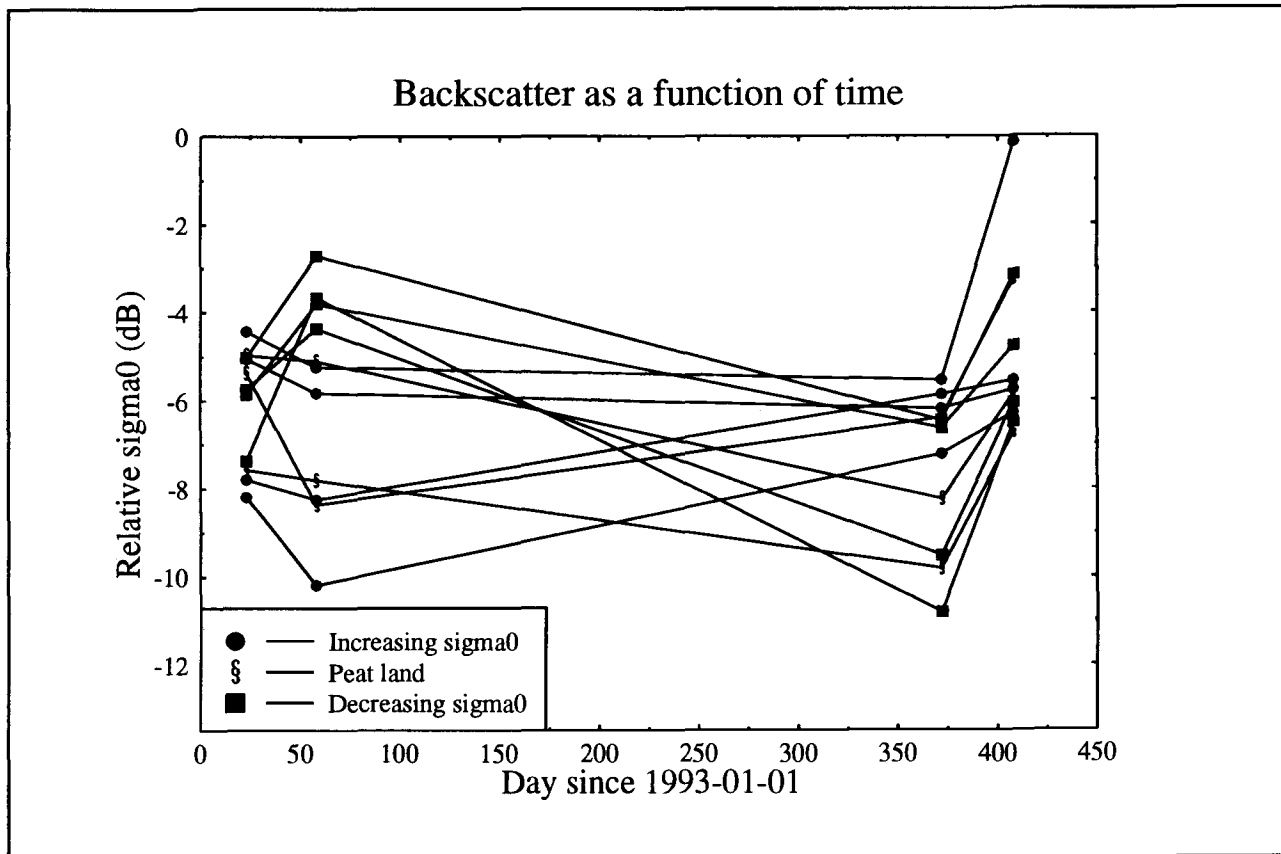


Figure 2. C-band backscatter in winter images (January-February) of the ground-checked points.

Salemaa, M., Jukola-Sulonen, E., and Lindgren, M. 1991. Forest condition in Finland, 1986-1990. *Silva Fennica*, Vol. 25, No. 3, p. 147-175.

Till, S., Gray, A., and Ahern, F. 1988. Remote sensing for forest resource management: CCRS advances in electro-optical and radar imaging systems. 16th Congress of the International Society for Photogram-

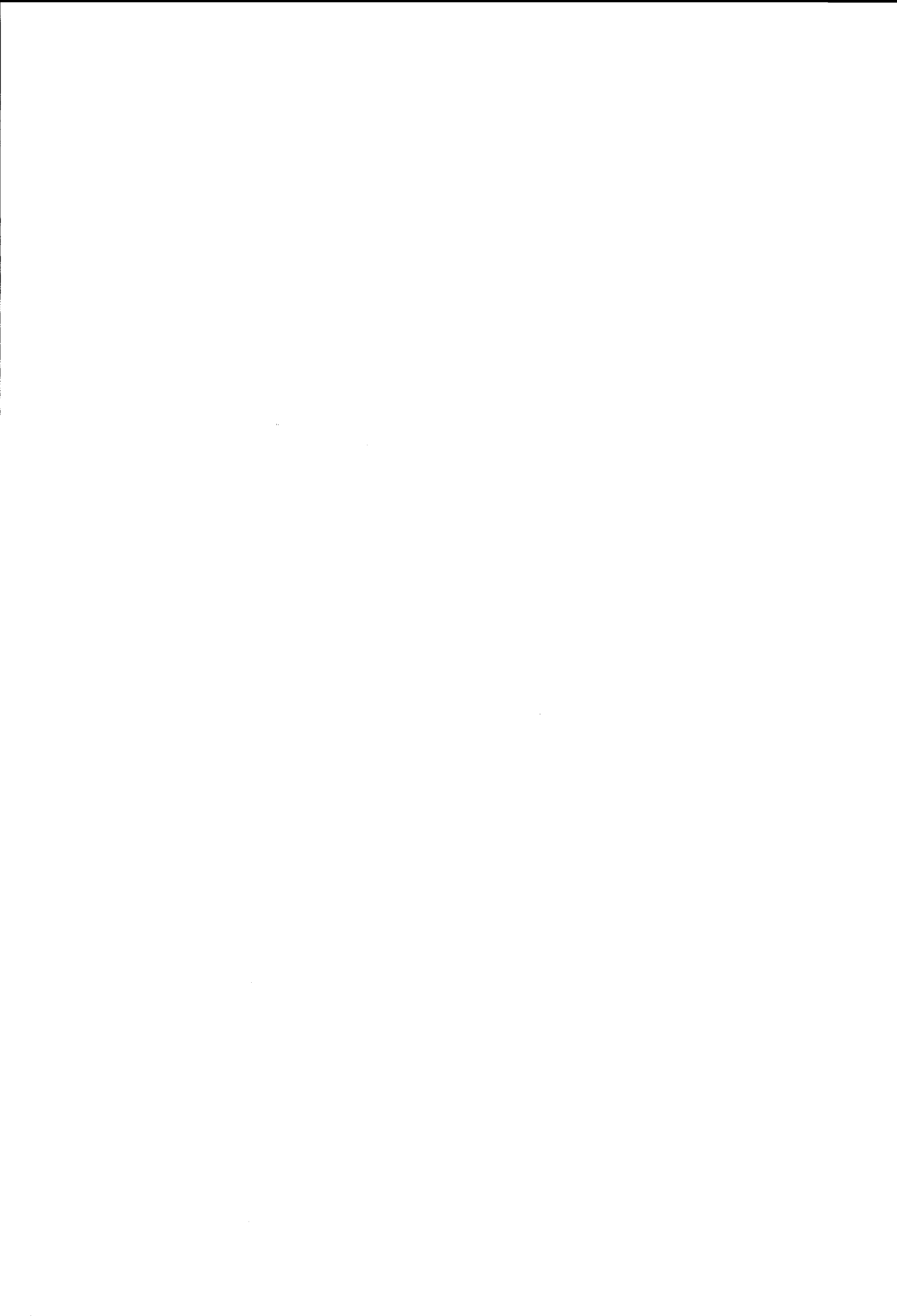
metry and Remote Sensing, Kyoto, Japan, 1988, International Archives of Photogrammetry and Remote Sensing, Vol. 27, Part B9, p. VII-232-239.

Vass, P. and Battick, B. (editors) 1992. ERS-1 system. ESA SP-1146, European Space Agency, Noordwijk, The Netherlands, 1992, 87 p.

Table 2. Anomalous points checked on the ground.

Direction of back-scatter change	Soil type	Possible reason for the backscatter change
Decreasing	mineral	Bushes (appr. 5-m high) suffering from use as pasture
Decreasing	mineral	Trees (appr. 20-m high pines) suffering from root rot caused by <i>Heterobasidion annosum</i> fungi and the connected loss of needles
Decreasing	mineral	Trees (appr. 20-m high spruce) suffering from drying on the border of a clear-cut area
Decreasing	mineral	Trees (appr. 8-m high pines) suffering from an elk damage
Increasing	mineral	Trees (appr. 15-m high spruce) recovering from a thinning cutting 2-3 years earlier
Increasing	mineral	Pine plants (appr. 120 cm high) emerging from under the snow cover between winters 1993 and 1994
Increasing	mineral	Trees (appr. 15-m high, mixed) recovering from an earlier damage and an old (over 5 years ago) thinning cutting
Increasing	mineral	No obvious reason for increase in backscatter, possibly the joint effect of relatively pronounced topography and minor errors in geo-coding
Increasing	peat (2 points)	No obvious reason for increase in backscatter, forested (appr. 10-m high pines) swamp suffering from <i>Gremmeniella Abietina</i> fungus
Increasing	peat	No obvious reason for increase in backscatter, open bog

7. TOPOGRAPHY/GEODESY



THE CONTRIBUTION OF ERS1 AND SPOT DATA IN THE MORPHOLOGIC AND BATHYMETRIC STUDY OF THE NORTH SEA AND THE SCHELDT ESTUARY

Anne Lise COMHAIRE - André OZER - Annick JASPAR.

Université de Liège
 Laboratoire de Géomorphologie et de Géologie du Quaternaire
 Phone : (+ 32) 41.66.53.35 - Fax: (+32) 41.66.57.22.

Cette publication a été réalisée pour le compte du SSTC (Etat belge) - contrat Telsat III.

ABSTRACT

The objectives of this project are mainly to develop a methodology which uses satellite and particularly ERS1 imagery to create topographic maps of the sea bed, to understand local factors responsible for visible surface phenomena seen on radar and to use the tide level to cartography some flooded zones.

The first one is situated in North Sea between Zeebrugge (Belgium) and Walcheren peninsula (the Netherland) where we want to extract information about sea floor morphology. The image chosen are the one with the best contrast which seems to be the one sensed one or two hours before or after tide. After different processing we did a classification which gives a very good information for the Vlakte van de Raan and the Spleet bankje where there are high currents. In the areas where the depth is higher than 15 meters it seems difficult to get information.

The second area is the Scheldt estuary where we studied the location and the extention of some islands in function of the tide. The tidal flat area of Saaftinge was examined too to follow the evolution of this zone

1. Location and interests.

As part of this research programme, we examined two zones situated to the North of Belgium, on the Belgian continental shelf submitted to regular tides and currents (Fig.1).

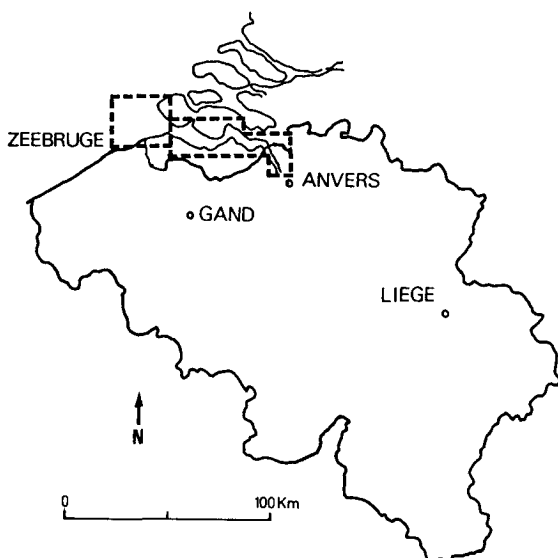


Fig. 1. Location of the areas of interest in Northern Belgium.

The first one extends (Fig 2) from the port of Zeebrugge (Belgium) to Walcheren peninsula (The Netherlands). In this zone, the depth varies from 0 to 25 meters. Looking at the deep areas, we find the navigation channel called the Scheur channel (up to 15 meters depth) extending from the port of Zeebrugge to the Scheldt estuary and the area along the western coast of Walcheren peninsula (up to 25 m depth).

The shallows are represented by the Vlakte van de Raan, a large sand bank of triangular form with its south border parallel to the Scheur channel and its east border parallel to the Spleet bankje (shallower zone: 0,9 m) and the Zoutelande bankje (shallower zone: 0,5 m) the nearest to the coast.

These last banks are long and thin banks oriented to the NNW-SSE and located between the Vlakte van de Raan and Walcheren peninsula.

The second zone is the Scheldt estuary from the mouth of the river to the port of Antwerp. This river is a tidal river and one have to be sensible to the fact that the tide level is not the same in the whole estuary.

The depths, in this area are approximatively the same as in the first area. There is a succession of islands which are changing in location and area and this information is very important for navigation. The tidal flats and marshes areas of Saaftinge situated near to the port of Antwerp have also been observed.

The objectives of this research are:

- 1) to develop a methodology which uses satellite images to create topographic maps of the sea bed.
- 2) to understand local factors responsible for visible surface phenomena seen on radar.
- 3) to show the relations between sea floor topography and surface phenomena such as sea currents and waves.
- 4) in the Scheldt estuary zone, to realize cartographic representations of the flooded zones as a function of tidal high.

The benefits will be the following : get a detailed knowledge of shallow coastal water zones and dynamic of the sea bed, this is of particular interest in the understanding of a natural ecosystem where man is increasingly active; get information for problems concerning sedimentation and erosion of the beaches as well as access channels to ports and identify sedimentary structures and their mobility.

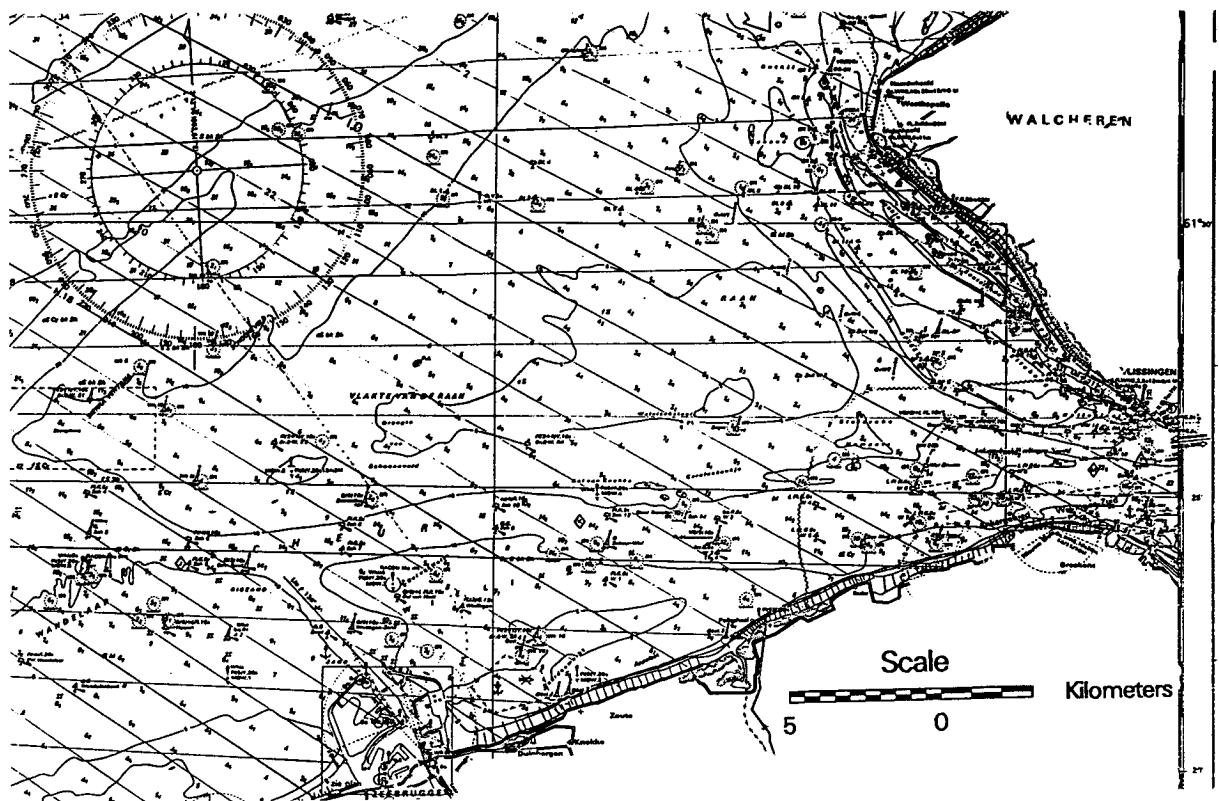


Fig. 2. Bathymetric map of the area (source: Hydrografische Dienst der Kusthavens Oostende, 1992).

2. From Zeebrugge to Walcheren peninsula.

2.1. Classification by multitemporal composition

Among the fifteen SAR-PRI images of the zone we get, we have chosen the three images the most interesting by their high contrasts to realize a multitemporal composition followed by a classification. The images are:

- 4848 - 2565 from the 19/06/92 at 10:40:49
(1h28 after low tide at Zeebrugge).
- 3996 - 1034 from the 20/04/92 at 21:48:21
(0h58 after low tide at Zeebrugge).
- 11361 - 2565 from the 17/09/93 at 23:49:10
(1h27 before high tide at Zeebrugge).

The images with the best contrast appear to be those which are taken one or two hours before or after the tide just when tidal currents are at the strongest. This point seems to be fundamental for bathymetric studies by SAR images and the study will go on with a comparative study in this domain.

The image processing was approximatively the same for the different points of interest of this paper. It will be described here.

Rectification :

A Spot image was first rectified by reference to the topographic map by facility. The three radar images

were rectified using first the four coordinates given in the header and further by reference to the Spot image.

Masking :

Using SPOT XS3 a mask was performed to extract only the sea and it has been applied to each ERS1 image.

Filtering:

Each image was then submitted to a median filter, just as efficient over the sea as statistical filter, to reduce irregularities.

Transformation into 8 bits images :

This is due to the weak power of our workstation which makes impossible the work on multitemporal compositions on 16 bits images.

Multitemporal composition:

It was done by superimposing the three bands.

Supervised classification:

Some visually homogeneous areas selected manually on the multitemporal composition were used to help the classification. The result contains 5 classes.

Filtering:

A 5 x 5 majority filter, which eliminated isolated pixels from classification was applied.

Result of the classification see fig.3

Class	% of points	Depth
1	2,76	0 - 2 m
2	19,2	2 - 4 m
3	8,12	No indication
4	16,59	4 - 6 m
5	53,33	6 - 18 m

-Class 1 includes the zones from 0 to 2 meters deep. We find a good correspondance at the Spleet Bankje. This class appears too at the south west border of the Vlakte van de Raan which is not explain.

-Class 2 includes the zones from 2 to 4 meters deep. We find it at the Spleet Bankje, the Vlakte van de Raan and the Zoutelande Bankje where we have a good correspondance.

-Class 3 is difficult to interpret since its origin is due to an artefact on the image 4848-2565 (extremely dark area but due to a decreasing of the roughness not yet explained). This is present at the river mouth (13 to 18 meters)

and to the east of the port of Zeebrugge (2 to 4 meters). This fact is an illustration to show how prudence is important to interpret SAR images.

- Class 4 represents depth from 4 to 6 meters. This class is present in the western border of Vlakte van de Raan as well as to the area situated between the precedent sand bank and the Spleet bankje.
- Class 5 concerns the remaining pixels. It doesn't give any indication.

The radar has detected the three sand banks of our zone but there are parasit areas of the class 2 in the open sea and the extension of these banks is not exactly the same than on the numerical terrain model.

By now, no difference has been detected for the depth higher than 15 meters.

Another classification was done from a multitemporal composition of two SPOT band and one SAR image. The result get approximatively the same limits for the banks but in the Vlakte van de Raan we get 2 classes and the higher depth appears better. The results have to be confirmed.

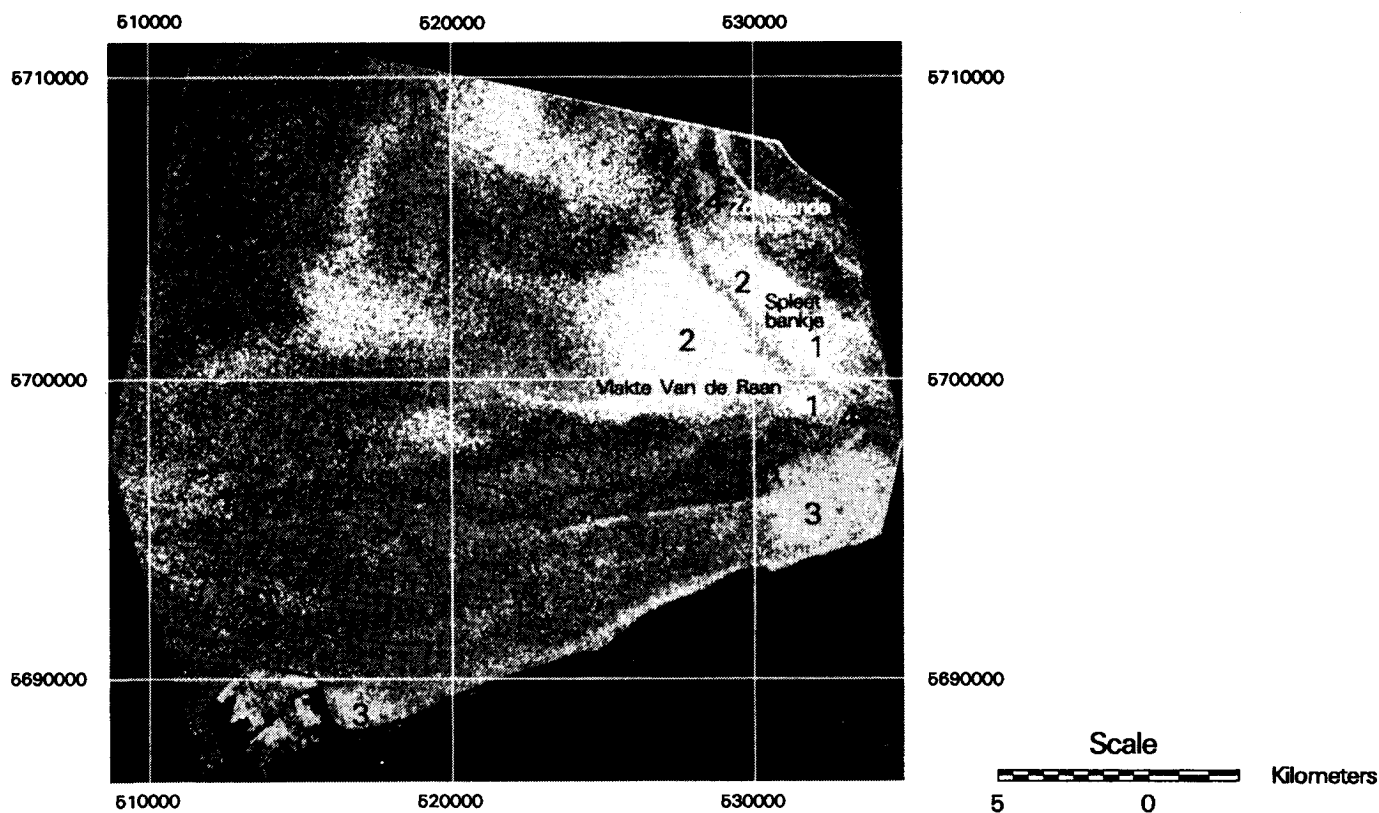


Fig. 3. Result of a classification realized by supervised classification on a multitemporal image.

2.2 Area of the Vlakte van de Raan

When we look at the limits of the Vlakte Van de Raan on ERS1 and SPOT data, we notice that on satellite imagery it has an extension to the SSW not present on the numerical terrain model (Fig 4). This information must be controlled now by "in situ" measurements.

*Remark:*we get different informations for the SAR images: on one image the Vlakte Van de Raan appears very contrasted, on another one, we can't see anything at this place. This is a problem of correlation between the sea surface morphology due to the meteo-marine conditions and the ERS1 SAR images.

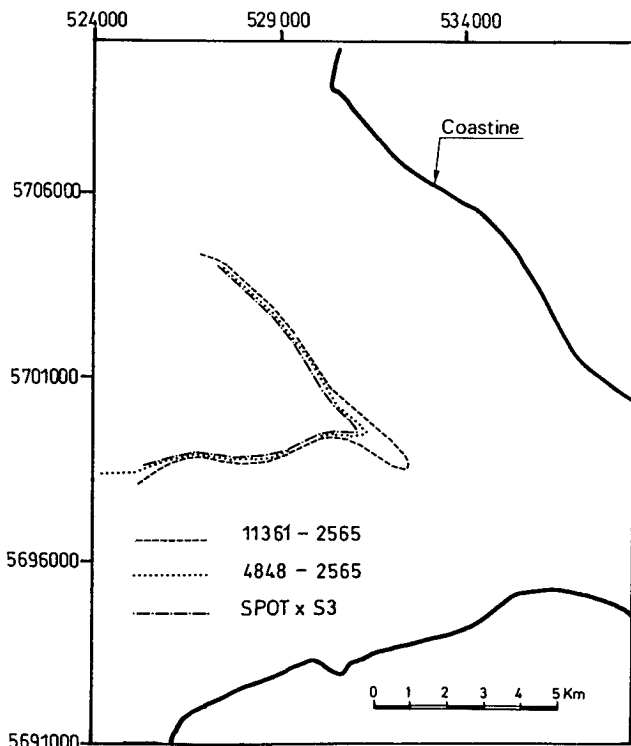


Fig. 4. Location and extension on satellite images (ERS1 and SPOT) of the Vlakte van de Raan. An extension to the SSE is visible which is not present on the map.

2.4. Conclusion

The classification done on the three ERS1 images give a general information concerning the morphology of the area but sometimes not very precise. Opposite to this, the position of the crests give a very precise information concerning the limits of the bank showing that tides and currents take a place of first importance for detecting submarine topography.

The two methods are complementary to give information concerning the sea bed and its evolution.

The morphology near Walcheren appears better than the one near Zeebrugge and Vlissingen probably because of the higher strength of the current force at these places

2.3. Area of the Spleet and the Zoutelande bankje

Some crests appears on differents ERS1 images (Fig.5). These crests where located on the map and we can see that one is situated just above the south border of the Spleet bankje and the other one is just above the south border of the Zoutelande bankje. This phenomena is due to currents which create a different roughness on the 2 sides of a sandbank. A more thorough study on the currents direction and intensity is underway in our laboratory.

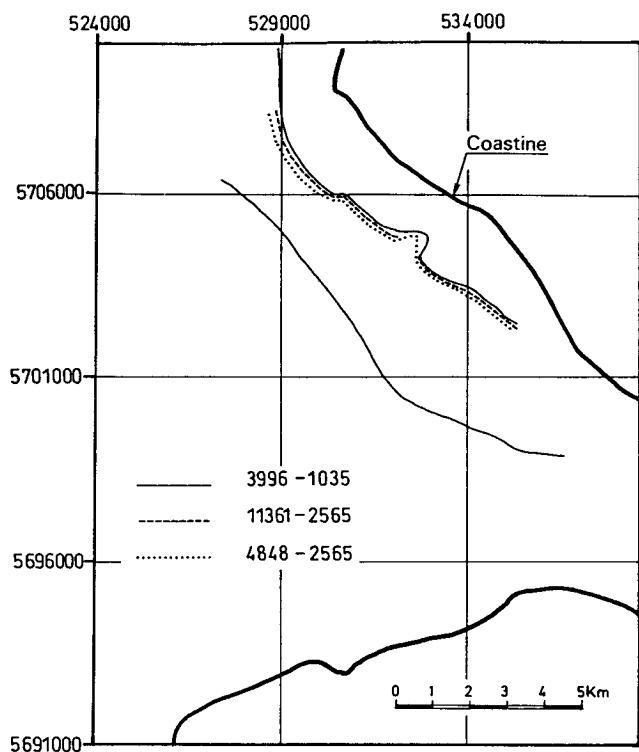


Fig. 5. Location of crests seen on radar which appears to be just above the south border of the Spleet bankje and the Zoutelande bankje .

(other images in study). In zones without tides and currents, it seems improbable that ERS1 could give sea floor information. What we can see depends very strongly of the current model of the area.

3 From Vlissingen to Antwerp

We selected the three images we get which contain this area :

- 4848 - 2565 / 19.06.92 at 10:40:49
(1h05 before low tide in Antwerp- high : 1,13 m)
- 11361 - 2565 / 17.09.93 at 23:49:10
(1h33 after low tide in Antwerp- high : 0,83m)
- 7854 - 2565 / 15.01.93 at 15:28:29
(1h12 after low tide in Antwerp - high: 0, 38m).

The tide levels were calculated for Antwerp. We project to calculate the tide level for each station in the Scheldt estuary. We had the chance to get three images near low tide, that makes them in fact more interesting for us.

3.1. Precise location and extension of islands discovered at low tides.

With the three images, we did a multitemporal composition. We could locate the actual position and extension of the islands and observe that their form has changed and that they have drifted (Fig 6).

These result must be confirm by other images because of the possible interference of the wind which can create a very important roughness when it meets an island and a very small one behind it. The effect of the wind increase then artificially the extension of the island by creating the same signature then the island behind it

where in fact we have only water.

For example, the Platen van Valkenisse has moved to the NW and its shape has changed. Monitor the evolution of these islands is by itself an interest of ERS1 SAR.

3.2. The extension of an island as a function of the tides is a relevant information for cartography.

We concentrated our mind on one island located nearly in front of Saaftinge. With the help of the different images we can map this island at different moments of the tide. This allow us to get an evolution of the emerged areas when the tide goes down. The method enables to draw some contour lines and then to realize a partial topography of these zones by an indirect method (Fig. 7).

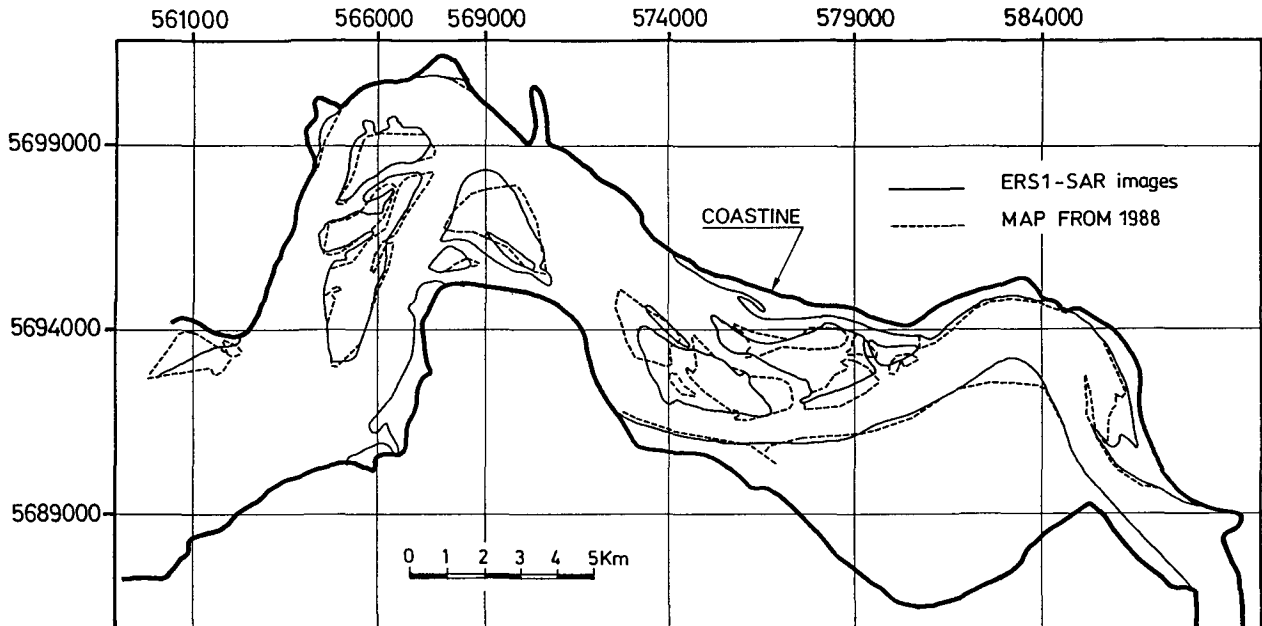


Fig. 6. Extension of the islands of the Scheldt estuary observed on multitemporal composition of three ERS1 images and comparison with the topographic map of the area of 1988. The shape and the extension of some islands seem to have change.

3.3. Visualisation of the Scheldt estuary channel on an image

Only on a part on one of the three images, can be seen the navigation channel of the Scheldt estuary. This is a future point of investigation to see if a monitoring of this channel can be done.

3.4. Tidal flat and marshe zones of Saaftinge.

On the same multitemporal composition, the tidal flat area of Saaftinge was examined (fig. 8). The superposition allow us to observe the nearly maximal extension of the tidal flat zone. When it is comparated to the actual map of the same place we observe a very

good correspondance for nearly every tidal-creek. In these areas, we can find very different kinds of signatures: a very bright one when the tide is low and that the tidal zone has been dried and where we usually find ripple marks, and a very dark one when the tide has just left or is just coming, when there is a thin water film on the surface of the area. We plan to do *in situ* measurements when ERS1 will sense the zone and hope to be able to give reliable informations concerning the dominant factors which influence radar in this area.

A classification on the multitemporal composition was done showing the different phases of the retreat of the tide.

4. Conclusion

4.1. Scheldt zone

ERS1-SAR, extremely sensible to water, can use the information given by the movement of the tide, it allows to map intertidal zones, and eventually later to create a DEM of the area. Further, a monitoring of these zones by comparing two situations is possible. This area of study belongs to a recent interest of us which has been confirm by our results. Deeper investigation will follow to understand the real factors which have a primordial importance in these kind of areas. When they will be elucidated, they will be usable in other places without any need of anterior map which is not the case for the morphological map of the North sea.

Then we can say that for the study and the mapping of areas submitted to regular flood, radar give impressive results at a scale of 1:50000.

4.2. The North sea zone

The study of the currents, their orientation and their strength, especially in North sea but also in the Scheldt estuary is of great importance to understand what we observe in the shallow zones (up to 15 meters) in the radar images.

Due to different factors, the quality of the images is very variable. Determine the best conditions for observing a maximum of phenomena will be studied on the different images we have. Classifications will be done on the best contrasted one eventually on smaller areas then what we did yet.

In the future, we hope that this methodology will be used in regions difficult to access like in Hai Phong bay (Vietnam). A project to apply it there with ERS2 has been proposed.

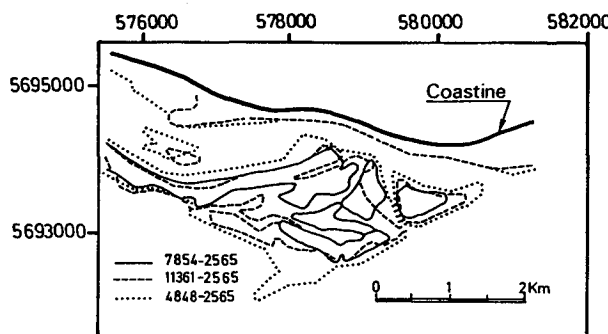


Fig. 7. Evolution of the extension of an island with the retreat of the tide by means of three ERS1-SAR images taken at different moments.

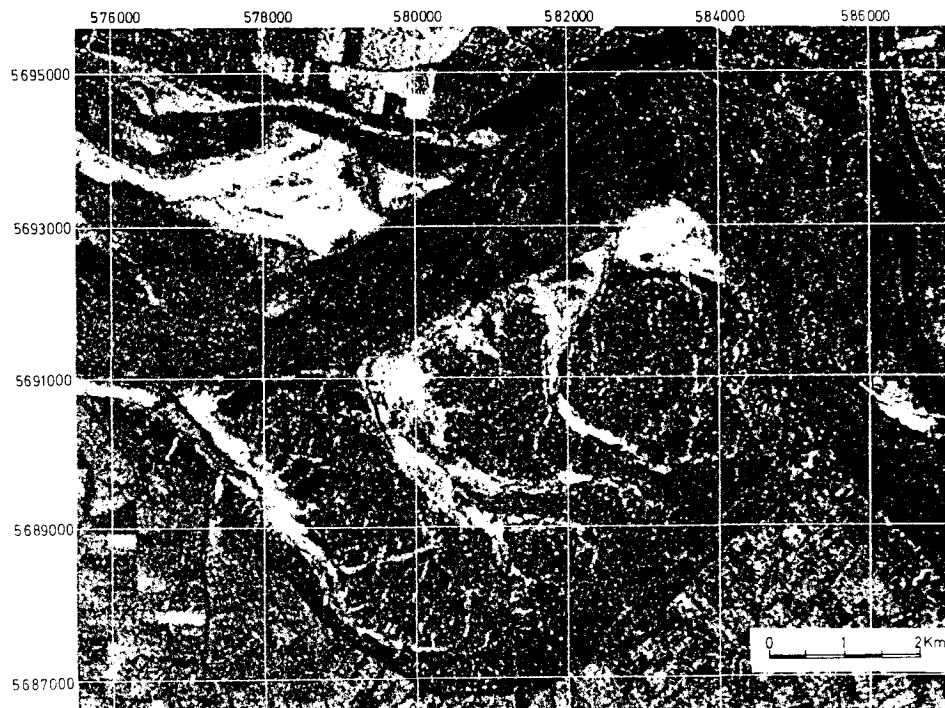


Fig. 8. Multitemporal composition of three ERS1 images taken near low tide showing nearly the maximal extension of the tidal flat area in Saaftinge (situated in the Scheldt estuary).

DETECTION OF SEA-BOTTOM TOPOGRAPHY WITH ERS-1 SAR.PRI IMAGES ON THE BELGIAN CONTINENTAL PLATFORM.

Linde Vande Velde, Carlos Vernemmen, Guy De Moor, Annick Jaspar

Departement of Geography, Research Unit Marine and Coastal Geomorphology, Krijgslaan 281/S8, 9000 Gent, Belgium.

phone: (32) 9 2644636, fax: (32) 9 2644970

ABSTRACT

Visual comparison of ERS-1 SAR.PRI sea surface images with bathymetric maps suggests a certain correspondence with the sea bottom topography in the area of the Kwintebank and Middelkerke Bank (Continental Platform of the Southern Bight). The sea bottom topography has been deduced from existing nautical maps and from graphic representations of new depth data acquired at sea during the satellite passage. The matching suggests a slight translation between map and image positions. Possible links between simultaneously acquired field data on sea water temperature at a few meters depth and on the bathymetry have been studied. In a perspective of optical image analysis such information could be useful for further sea bottom detection.

1. OBJECTIVES

This research is part of the Belgian Telsat-III program. Its final objectives are: (1) to deduce the sea bottom topography from the characteristics of ERS 1-SAR images; (2) to obtain information about sediment transportation by using sequential radar images; (3) to use these radar images for studying possible relationship between sea bottom topography and oceanographic characteristics such as temperature, salinity and chlorophyl-a content.

This paper reports on bathymetric, oceanographic and meteorological data acquisition on board of the oceanographic vessel Belgica in the research area during passages of the ERS-1-satellite in september 1993 and in november 1993. It deals as well with the results of a visual comparison of the radar images with such mapped data, especially with different types of bathymetric maps. It also reports on a matching of sea water temperature data with depth data.

2. RESEARCH AREA

The research area covers the Flemish banks, offshore the Belgian coast and, more specifically the Middelkerke Bank and the Kwintebank (total area approximately 12 x 12 km) (figure 1).

The Flemish banks are a group of parallel sandbanks stretching in a SW-NE direction, slightly oblique to the sandy macrotidal coast. The banks are separated by swales dipping to the NE. The swales generally are not deeper than 30 m below mean spring low water level. The banks are about 20-30 km long, 10-20 m high and 1-2 km wide. In some parts of the banks the crest zone rises to less than 4 m

below spring low water level. The flanks and the summits of the banks are covered with various types of bedforms especially at their northern edges, where large dunes reach heights up to 8 m and where the energy of the waves is higher. Upslope the flanks large and small dunes gradually become parallel to the crest line of the banks (De Moor, 1985).

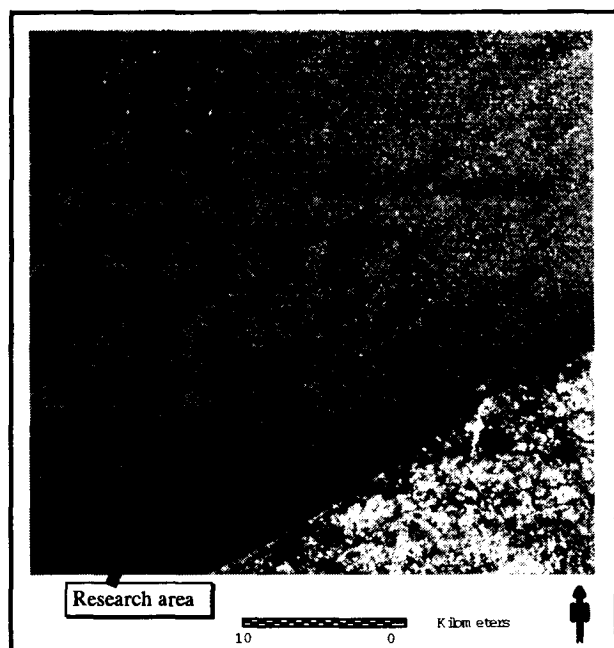


Figure 1 : Research area (150 km²)

3. DATA ACQUISITION AND PROCESSING

3.1. Oceanographic terrain data

3.1.1. Data acquisition

Table 2 shows the oceanographic data acquired at sea during the Belgica campaigns of 13-18 September 1993 and of 8-10 November 1993.

data	equipment	freq. of acquisition
position	Syledis	2 Hz
bathymetry	Echosounder	2 Hz
wave height	TSS	2 Hz
sea temperature	Sea-bird	1/12 Hz
salinity	Sea-bird	1/12 Hz
chlorophyl-a	Fluorometer	1/12 Hz
meteo-data	Friedrichs	0,03 Hz

Table 1: The recorded oceanographic data

The meteo-data are wind speed, wind direction, air temperature, atmospheric pressure and humidity. These data were acquired along fixed tracks with a length of 2 km and an equidistance of 1.4 km sailed perpendicularly to the elongation of the sandbanks.

3.1.2. Processing

Data about bathymetry, temperature, salinity, and chlorophyll-a, have been mapped. These maps form the basic documents for the comparison with the ERS-1 SAR images. Matching of the maps allows to analyse the relationship between different oceanographic data and the bathymetry. Analysis of sequential isobathic maps yields maps of equal height difference and an evaluation of erosion and deposition. Results of such matching however have to be interpreted very carefully because of the acquisition method of the depth data and of the Kriging interpolation method ("Surfer") used for mapping.

Moreover it is well known that meteo-marine conditions have an influence on radar images (Ulaby, 1981). Therefore current velocity and direction as well as wave characteristics have to be known at the moment of the satellite passage to allow the interpretation of patterns recognised on the radar image. Tide also conditions the image. During low water, the sandbanks are approximately 4 m nearer to the sea surface than during high water. Therefore banks are marked by higher rugosity and scattering on images taken during low tide than during high tide. That is still more the case if wind triggers the wave activity. Weather conditions provoke still other sea surface phenomena which influence the images. Under optimal meteo-marine conditions (low wind velocity and a minimal wave activity) long superficial foam and debris lines can be detected on the sea surface. They run parallel to the crest of the Kwintebank and of the Middelkerke bank and at their west side, over a distance of several hundreds of meters. On the bank side of these foamlines the sea surface is smoother while towards the channel axis the sea surface is rougher. These characteristics have a fundamental signification for the analysis of the ERS-1 SAR images.

3.1.3 Preliminary results

During the Belgica campaign of september, 13-18, 1993 sea water temperature at 4 m depth has been recorded continuously along the tracks. Mapping of the data (figure 2) shows that in the vicinity of the Kwintebank and of the Middelkerke bank there was a weak thermal gradient perpendicular to the bank crest: 0.05°C difference isotherms run slightly winding parallel to the bank crest.

Impact of the tidal current is very debatable as current directions show a 12 hour inversive cycle while the isothermic map represents data acquired over a 24 hour period.

Displacements of the banks during the period between september 1993 and november 1993 have been analysed by matching the corresponding bathymetric maps.

Figure 3 shows the position of the isobaths on both dates.

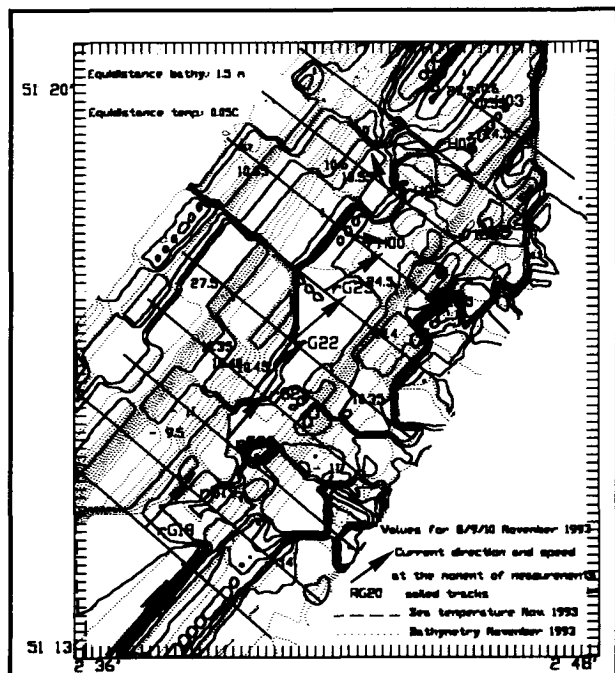


Figure 2: sea temperature and bathymetry
(17 september 1993)

That comparison suggests that the general bathymetric pattern remains constant but that locally some displacement of isobaths occurs.

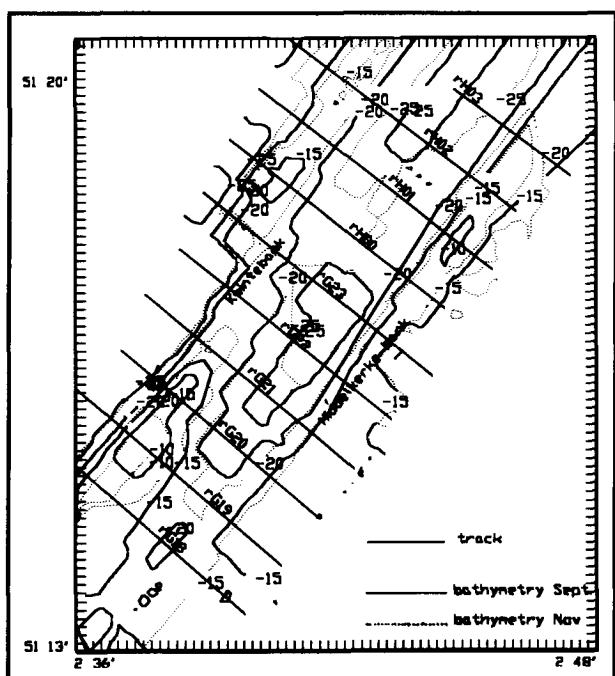


Figure 3: Multitemporal bathymetric map

Current direction and velocity are deduced from the current atlas (Stroomatlas, 1991) for twenty stations within the area covered by the satellite image. These data correspond to mean values for a longer period. They don't however account for the meteo-marine conditions at the very date of passage. Actual wind direction and velocity at the moment of the

satellite passage are measured on board of the Belgica. Registration of the wind parameters begins from five hours before the satellite passage because of the inertia of the sea surface. Wind vectors are calculated for this period and superimposed over the radar image.

3.2 Analysis of the ERS-1 SAR images

3.2.1 Image acquisition

An ERS-1 image was available for the 17th september 1993 at 12h40. Unfortunately that image didn't cover the Kwintebank and Middelkerke Bank area. A second image was available for the 10th of november 1993 at 11h43 (figure 1). That image covered the research area. Campaigns for terrain data collection were organized on these data in order to validate the interpretation of the features detected on the radar images.

3.2.2 Processing of the images.

3.2.2.1. Geocoding

Processing starts with the geocoding of the ERS-1 SAR.PRI images. A first geocoding could be performed using the coordinates of the corner points and the center of the image as indicated by the header file of the ERS-1 SAR image. A control by means of known coordinates of coastline locations showed a twenty to thirty meters displacement of the coastline towards the south on the image. A second rectification was performed by means of location comparison of road crossings, river confluences and some isolated buildings along the coastline. In spite of that second rectification, the precision over the sea remained insufficient. Zooming in on buoys with known coordinates (Akkaert buoy, Bol van Heist, A2 buoy) wasn't succesful. Further rectification couldn't be performed.

For more precision over the sea area, corner reflectors should be installed on the buoys.

3.2.2.2. Speckle reduction

Radar images are influenced by destructive and constructive interferences between echos of individual surface scatters within a resolution cell (Leberl, 1989).

After the rectification, a reduction of that speckle effect has to be carried out. Several filters available on the radar module of the ERDAS "imagine" software have been essayed.

Best visualization of the structures on the ERS-1 image has been obtained with the median (7x7) filter. That filtering process showed clearly that the influence of the meteorological conditions at the moment of the image shooting is of fundamental importance for the quality of the ERS-1 image. The meteorological conditions at the moment of the satellite passage are given in table 2.

Date	Tide	Wind Velocity	Wind Direction
17/09/93	1 h before HW	3.2 m/s	SSW
10/11/93	2 h after HW	13.4 m/s	S

Table 2 : Meteo-marine conditions during campaigns

The filtered image of september (figure 4) taken at low wind velocity (3.2 m/s) has a better visual quality than the filtered image of november (figure 4), taken at a higher wind velocity (13.4 m/s). For further quality improvement, a combination of the median (7x7) filter and the sigma filter was applied on the radar image of november. Despite poorer quality of the november image such filtering improved the visibility of structures (figure 1).

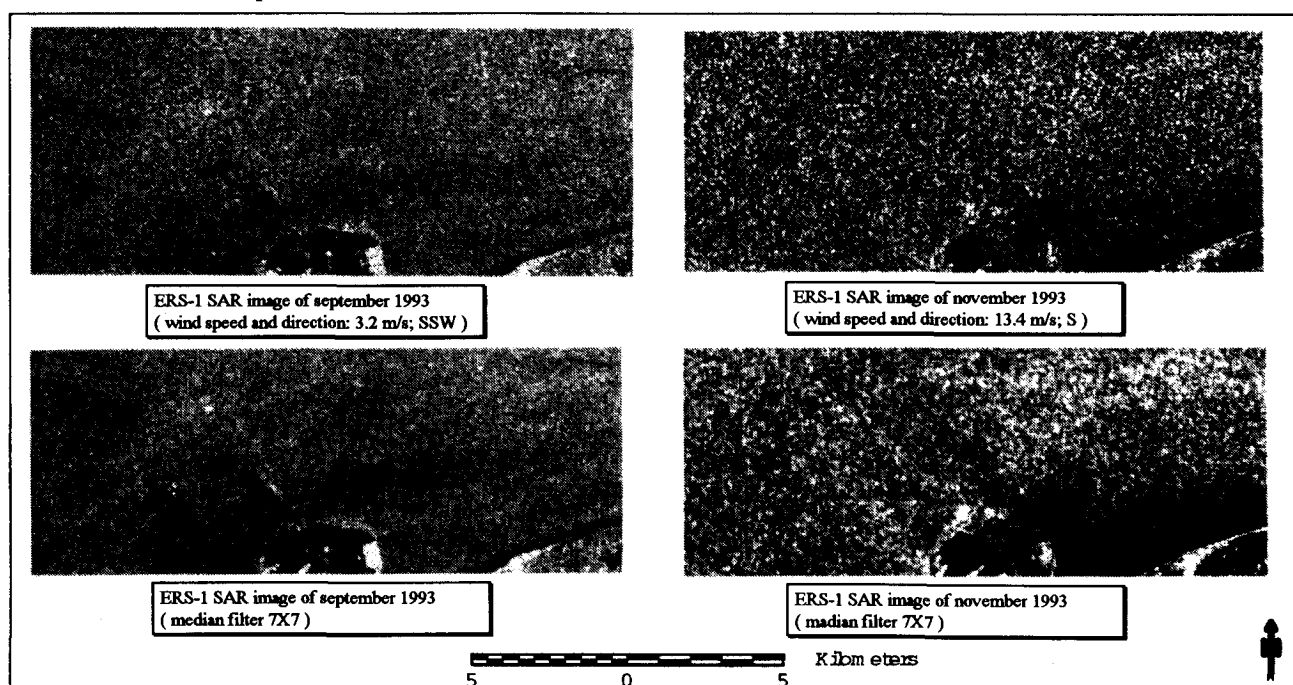


Figure 4: Images before and after filtering

A first visual interpretation of the image suggests alternating black and white patterns aligned parallel to the elongation of the sandbanks (SW-NE). For objectivity's sake these alternating black and white structures were digitized by a person unfamiliar with the bathymetry.

3.2.2.3. Multitemporal imaging

In a single ERS-1 image a rough sea surface is due to a high backscattering of the sea surface and results in white pixels on the ERS-1 image, while a smooth sea surface is due to a low backscattering of the sea surface and results in black pixels on the ERS-1 image.

A multitemporal image is created by superposition of successive images. Due to the variability of the targets, the stability or changes of superficial characteristics can be detected on the multitemporal image.

Because there was no covering of the research area by both images (september 1993 and november 1993), multitemporal imaging was applied to the area of Zeebrugge, the common part of both images. Despite the fact that there are no real sandbanks in this area multitemporal imaging (MTI) was tested for visualization and detection of sea bottom features. Both images were put in different colour channels (I colour); september in red, november in green.

	I colour	r/s	r/s	r/s	r/s
sept. 93	red	rough	rough	smooth	smooth
nov. 93	green	rough	smooth	smooth	rough
MTI colour		yellow	red	blue	green

Table 3: Interpretation of multitemporal images.

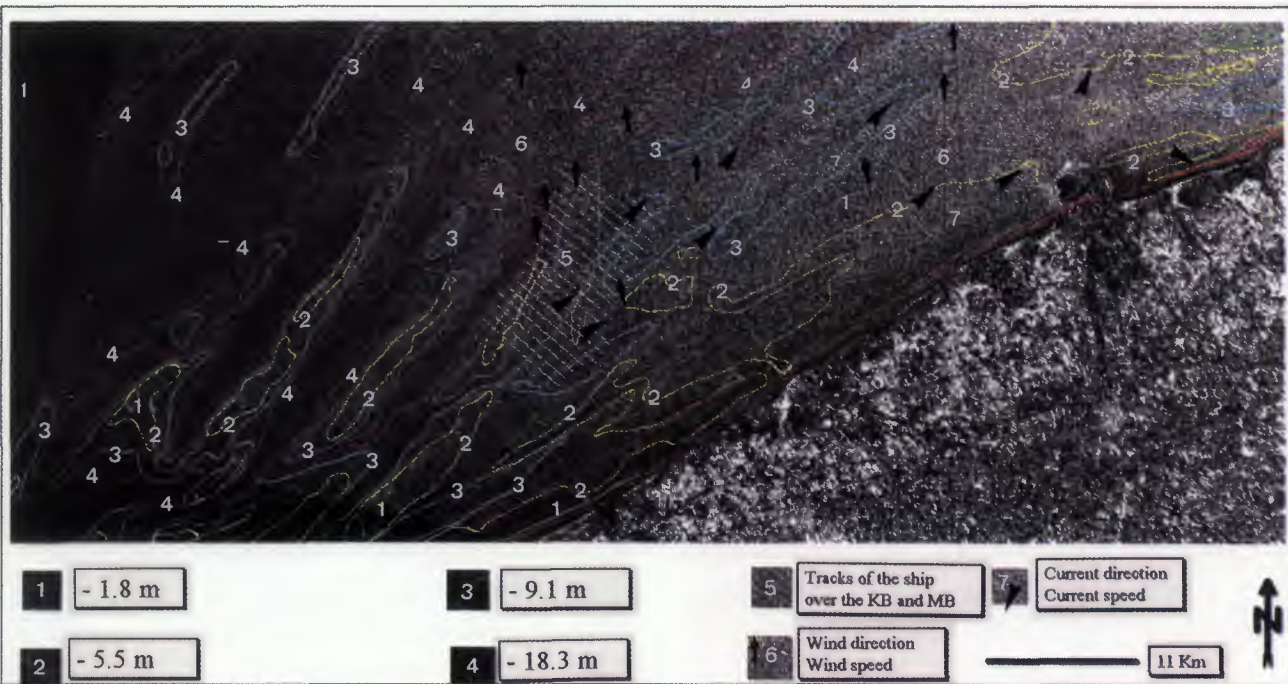


Figure 5: Superposition of the small scale bathymetric map and the ERS-1 image

Yellow colours on a multitemporal image are considered as indicators for a rough surface in both months (Cross-over course, Frascati, 1993).

This would mean that the sea surface is rough in september and in november. In the Zeebrugge area a yellow patch characterizes the Scheur channel that connects the Schelde mouth with the open sea at a mean depth of - 15 m.

Red colours on a MTI are considered as indicators for a rough surface in september and a smooth in november.

Yellow and red patches appear at the western harbour breakwater and also along the eastern harbour breakwater. These red patches probably are caused by the roughness of the breakwater construction.

Blue colours on a MTI are considered to indicate a smooth surface during both months. No blue appears on the sea surface itself. The high beach is characterised by this blue colour. It probably indicates a beach without important bedforms at that moment. The water surface in the inner part of the harbour of Zeebrugge as well appears in blue on the MTI. Here it could be explained by the continuous smoothness of the water surface due to the protection of the harbour breakwaters.

On multitemporal images green colour characterizes areas where the sea surface was smooth in september and rough in november 1993

The strong winds during the november 1993 recording (13.4 m/s) increased the wave activity, which results in a higher backscattering in comparison with the low winds during the september recording (3.2 m/s) where the sea surface remains smoother and results in a lower backscattering.

3.3 Matching of ERS-1 SAR images with bathymetric data.

Different types of depth maps have been used for matching with the ERS-1 SAR image. The result depends on the scale.

3.3.1 Small scale comparison

Micro-scale comparison comprises matching of the digitized bathymetric map "Dover and Calais" (1/250.000, 1983) with the total radar image on the same scale (figure 5).

Visual analysis of the ERS-1 SAR image shows a difference on between the easterly part of the image with a strong backscatter (white pixels) and its westerly part with very little or no backscatter (black pixels). This difference can be due to the incidence angle on the descending image of november. In the coming research, the image will be corrected for this incidence angle.

Lack of backscattering characterizes the Negenvaam swale, situated between the two banks, and the Kwindegeul swale, NW of the Kwindebank. This could indicate a smoother sea surface above the gullies due to less wave breaking than above the nearby bank crests. No wave data however are available.

3.3.2 Large scale comparison

Macro-scale comparison comprises matching of the bathymetric map drawn by means of the *in situ* depth measurements of november 1993 with the radar image on the same scale and acquired at the same date. That depth map, based on bathymetric recordings along fixed tracks at sea during the november 1993 campaign, has been drawn in the same coordinate system (UTM, zone 31) as the rectified radar image of november 1993.

Comparison of the *in situ* measured bathymetry and the ERS-1 SAR structures on a macro-scale shows patterns on the ERS-1 image parallel to the elongation of the sandbanks (SW -NE) marked on the bathymetric map.

Matching the radar image of november 1993 with the bathymetric map it appears that large parts of the banks in its western part are characterized by strong backscattering (white pixels) (figure 6). This suggests that differences in surface rugosity indicated by the backscattering coincide with differences in the underlying bottom topography. The surface rugosity looks somewhat shifted in the direction of the superficial currents what could be caused by ENE direction of the currents over the sandbank at that moment, or to the inaccuracy of the rectification due to the scarcity of ground control points in the research area.

3.3.3. Other indicators

A remarkable superficial feature, consisting of a foam and debris line situated in the swales at some distance west of the bank crests has been observed during vessel campaigns under calm conditions and smooth sea surface, and especially during the september 1993 campaign (photo 1).

The sea surface on both sides of the foam and debris line has different rugosities. At the side of the foam line where the

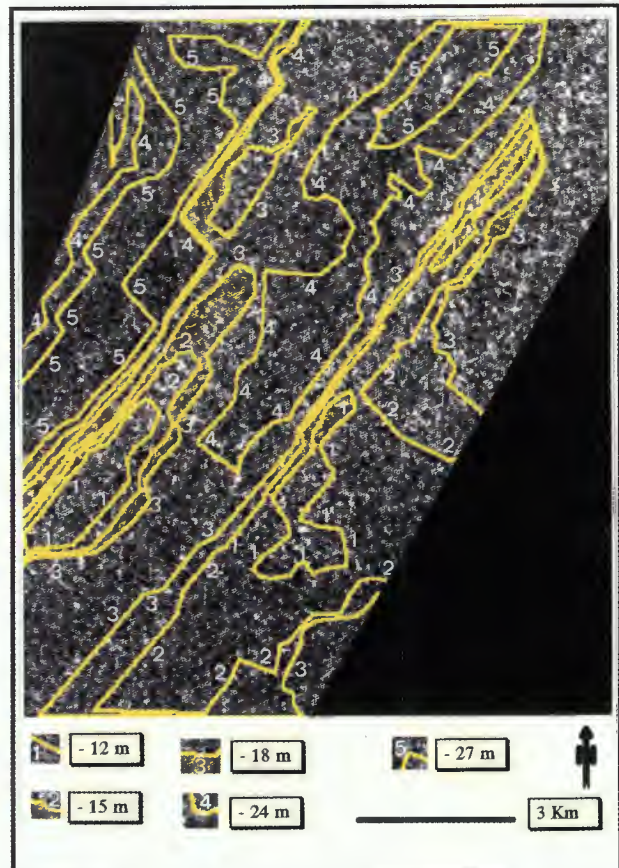


Figure 6: Large scale terrain bathymetry superposed on the ERS-1 image of november 1993



Photo 1 : Foam and debris line parallel with the crestline of the Kwindebank.

current is coming from, the sea surface is rough, while at the side the current is flowing to, the sea surface is smooth. According to De Moor (pers. communication in accordance with Bastin, 1977) it could be due to an upwelling of water at the west side of the bank during flood conditions when the current is hitting the bank's steep side obliquely.

No such local sea surface roughness differences have been observed on the november radar image, probably because of the large overall roughness of the sea due to the high wind velocity at that moment.

3.3.4. Image classification

The bathymetric measurements performed simultaneously with the acquisition of the ERS-1 SAR image in november 1993, are used as a basic tool for classification. Small polygons, corresponding with a certain measured bathymetric value are created and used as signatures for classification. The classification is done on both the macro-scale and micro-scale. Despite the fact that 5 classes have been introduced, the classification merely results in a visual distinction of banks and gullies at macro-scale inspection. The classification method on the micro-scale is the same as for the macro-scale. It results in a distinction between gullies and sandbanks but merely on the west side of the classified image, because its east side is deformed by the incidence angle.

4. CONCLUSIONS

After a preliminary analysis on the superficial characteristics of the sea surface recorded on the ERS-1 SAR images, some conclusions could be drawn about the possibilities to deduce underlying bottom features from the radar image. It has to be stressed that until now the results are based on visual interpretations. These interpretations show certain correspondences between the sea surface characteristics and the underlying sea bottom features. They are dependent on the momentaneous current direction. The next phase of the research will focus on the digital analysis of the pixel values in order to obtain more detailed information about the relations between the image characteristics and oceanographic parameters, especially sea floor topography.

5. ACKNOWLEDGEMENTS

This research was carried out in the framework of the "Telsat- III Program", funded by the Belgian Ministry for Science Policy. The help of the Management Unit Mathematical Model North Sea providing the opportunity for observations at sea has greatly been appreciated.

6. REFERENCES

- DE MOOR, G., 1985. Shelf bank morphology off the Belgian coast. Recent methodological and scientific developments. In: Recent trends in physical geography. Liber Amicorum L. Peeters (M. Van Molle, ed.), Brussels, VUB Study Series, 20, p. 47 - 90.
- DE MOOR, G., 1992. A quantitative evaluation of erosive and accretional sections along the Belgian coast in the period 1978 - 1990. *Tijdschrift van de Belg. Ver. Aardr. Studies - BEVAS*, 92-2, p. 413 - 424, 7 fig.
- LEBERL, F.W., 1989. Radargrammetric Image Processing, Artech House, Norwood, pp. 595.
- ULABY, F.T., MOORE, K.R., FUNG, A.K., 1981. *Microwave remote sensing : active and passive*, Artech House, Norwood, pp. 2162.
- VOGELZANG, J., WENSINCK, J., VAN DER KOIJ, M. and VAN DER BURG, G., 1981. Seabottom topography with X-band Slar, Netherlands Remote Sensing Board Report BCRS 89-25, Delft, Netherlands, pp. 84.
- CROSS-OVER COURSE AT ESRIN, ESA, Frascati, Decembre 1993.

PEGASE PROJECT : MID-1994 STATUS
OR
ON THE USE OF ERS-1 ALTIMETER DATA IN THE ARCTIC OCEAN

Frédérique Blanc¹, Louis Géli², Philippe Gaspar¹

¹ CLS Argos, Space Oceanography Group, 18 av. E. Belin, 31055 Toulouse Cedex, France

(Ph: 33 / 61-39-47-68 , Fax: 33 / 61-75-10-14, E-mail: blanc@atlas.cnes.fr)

² IFREMER, Marine Geosciences Department, B.P. 70, 29280 Plouzane Cedex, France

(Ph: 33 / 98-22-42-27 , Fax: 33 / 98-22-45-49, E-mail: geli@ifremer.fr)

ABSTRACT

The major goal of the PEGASE pilot project is a precise determination of the geoid and free-air gravity anomalies over the Arctic ocean using ERS-1 altimeter data and its interpretation in terms of the geology and geophysics. The unique ERS-1 contribution comes from its high latitude coverage, its high spatial density (except for the 3-day repeat cycle) and from its multiple repeat orbits.

The project is split into three phases. Phase 1 focuses on the altimeter data processing which is no easy task for latitudes polewards of 60°N - because of sea-ice -, and allows preliminary computations of the gridded geoid and the gravity anomaly fields. This paper presents the first phase results. Phase 1 started in June 1993 based on April 1992 - January 1993 altimeter ocean products (cycles 1 to 8 of the 35-day repeat orbit, ALT-OPR 02 in version 2).

We developed and simultaneously validated techniques to filter the data (i.e. to validate them and discriminate between open-ocean and sea-ice data), to correct the data for environment errors (available with the products), to reduce the orbit error (constrained sinusoidal crossover adjustment) and to compute the mean sea or geoid profiles (collinear-track method and specific gridding technique) then derive the free-air gravity anomalies.

North of 72°N, the solution reveals contours of sedimentary basins in the Kara and Barents seas.

Keywords: Altimetry - Arctic ocean - Geoid - Mean Sea Surface - Gravity Anomalies

1. OBJECTIVES

The continental shelf in the Arctic ocean, North of Russia consists in a series of epicontinental seas, which are the offshore continuation of potentially oil and gas rich basins on land (the deeper the sedimentary basins, the stronger the potentiality). The geology of all these epicontinental seas is -however- still poorly known, due to the remoteness, the inhuman climatic conditions and the huge costs associated with seismic exploration. Remote sensing satellites thus provide a great opportunity to observe these inhospitable regions and altimeter sensors a unique tool for studying the geological structures off the coast.

Within this context, the PEGASE project was proposed as a pilot project for the use of altimeter data of the European Remote Sensing satellite ERS-1 for petroleum exploration. It results from an active collaboration between 3 French groups: the CLS Space Oceanography Group (Toulouse), the Marine Geosciences Department of IFREMER (Brest), and the "Groupe de Recherche en Géodésie Spatiale (GRGS)"

(Toulouse). Its major goals are a precise determination of the geoid and free-air gravity anomaly field over the Arctic ocean using the ERS-1 altimeter data and the interpretation of geoid variations in terms of the geology and geophysics (e.g. boundaries and thicknesses of the sedimentary basins).

The unique ERS-1 contribution comes from its high latitude coverage (81.5° South and North) and its space and time density. Launched in July 1991, it was set onto its 35-day repeat orbit in April 1992, offering an along-track resolution of 6.5 km, and a cross-track resolution ranging from 40 km at 60°N to 14 km at 80°N .

Project was agreed by ESA in March 1993 (ref. PP2-F14, category A), approved and funded by CNES since October 1992 (ref 92/CNES/0382 - AVAL SAR).

It is split into three phases. Phase 1 focuses on the data processing to achieve high quality/high precision geoid with ERS-1 altimeter data, phase 2 on the methods to derive the gravity anomaly fields, phase 3 on the methods to interpret the gravity signal in terms of geology and geophysics. This paper presents the first phase results.

2. DATA FILTERING

Altimeter data are altimeter ocean products i.e. data processed using a tracker model designed for open ocean conditions [Brown, 1977]. Products contain altimeter measurements recorded on a geophysical data record format (GDR). A GDR gives information on UTC time measurement, latitude, longitude, orbit height, one second altimeter height average, geophysical corrections (atmospheric effects, tides, etc.), and other quantities derived from the altimetric observations (e.g. significant wave height, wind speed). The orbit height was computed using a precise but non-definitive orbit.

We worked on cycles 1 to 8 data (no cycle 3) of the 35-day repeat orbit (ALT-OPR 02, versions 2.6 and 2.7) which covers the period April 1992 to January 1993. We re-organized the data sets into half-revolution products and harmonized them to the last product version. As most of the existing validation processes have never been tested at such high latitudes, special attention is required and we closely analysed the data to determine how to process them best. For instance, looking at the distribution in space of the altimeter data, from summer to winter, data sets are clearly contaminated by sea-ice. We defined a set of criteria to retain only valid altimetric observations over open ocean (see table 1). Each criterion tests a GDR parameter by comparison with thresholds or an invalidity value (unavailable parameter). A criterion may depend on latitude.

Main reasons to reject data are a parameter value is missing - or part of the necessary information was not available while processing the data - or a measurement is thought to be over sea-ice:

a) Missing parameters.

Most of these points are near land and are due to the fact that the altimeter measurement has no associated radiometer measurements. Other points are located in the open-seas, especially in the North Atlantic ocean, and are due to problems in the telemetry acquisition or missing parameters such as the ocean tide, the standard deviation of measured altitude, or the backscattering coefficient. 30% of the North polar measurements are "missing" (unavailable).

b) Sea-ice measurements.

The ice affects the shape of the altimeter return pulse (7-km footprint) and the brightness temperatures measured by the radiometer (20-km footprint). It therefore affects GDR products such as the number of

GDR parameter	Unit	Outliers	Invalidity value
FOR ALL LATITUDES			
1 Number of 20 elementary measurements	/	< 10	/
2 Standard deviation on altitude	cm	< 0 , > 40	< - 3270 , > 3270
3 Backscattering coefficient	dB	< 6 , > 30	-327
4 Significant wave height	m	< 0 , > 15	/
5 Electromagnetic bias	cm	< -50 , > 0	/
6 Dry tropospheric correction	m	< -2.5 , > -1.9	32.76
7 Radiometer wet tropospheric correction	cm	< -60 , ≥ 0	0 and 3276
8 Ionospheric correction	cm	< -40 , ≥ 0	0
9 Ocean tide	m	< -5 , > 5	32.76
10 Body tide	m	< -1 , > 1	32.76
11 Loading tide	m	< -5 , > 5	32.76
12 Sea surface height	m	< -130 , > 100	/
ABOVE 60° NORTH OR SOUTH			
1 Number of 20 elementary measurements	/	< 17	/
2 Standard deviation on altitude	cm	< 5	/
3 Backscattering coefficient	dB	> 20	/
4 Significant wave height	m	≤ 0	/
5 Electromagnetic bias	cm	≥ 0	/
7 Radiometer wet tropospheric correction	cm	< -20	/
12 Sea surface height	m	< -100	/

Table 1 : Data discrimination criteria

elementary measurements used to compute the one second measurement (20 Hz), the standard deviation on altitude and the radiometer wet tropospheric correction. Indeed, the best GDR parameters* to filter out data over sea-ice are the number of elementary measurements (lower threshold 17 or the maximum reached during calibration) and the radiometer wet tropospheric corrections (lower threshold -20 cm). From summer to winter, 13 to 51% of the North polar measurements are thus eliminated, that is because of the presence of sea-ice.

The number of validated data ranges from 34 000 to 58 000, depending on the cycle (25% more during summer). And the altimeter data distribution is now

consistent with the sea-ice extent, precisely revealing its limits (see figure 1).

3. DATA PROCESSING

Once validated and filtered, data need corrections for all type of errors (measurement errors, atmospheric range delay, tide, etc.). A data or sea surface height measurement is the orbit height minus the altimeter height. For ALT.OPR 02, it is referred to the ellipsoid ($a=6378.1364$ km, $f=1/298.2564$). Corrections are available in the GDRs. They are :

- dry tropospheric correction and inverse barometer effect, (from French Meteorological Office model, computed according to Saastamoinen [1972]);
- radiometer wet tropospheric correction;
- ionospheric correction, [Llewellyn and Bent, 1973];
- oceanic tide, (enhanced Schwiderski model, [Schwiderski, 1980, Le Provost et al, 1991]);

* The best parameter to check if the returned waveform fits into the model, is not in the GDR products. It is the peakiness of the data : the better the fit the lower the peakiness and the more reliable the measurement.

- loading tide, [Francis et Mazzega, 1990];
- body tide, (MERIT standard);
- electromagnetic bias, [Barrick and Lipa, 1985].

We reduced orbit error using a constrained sinusoidal crossover adjustment [Tai, 1988]. The orbit error is due to the inaccuracy in the computed radial position of the satellite. The orbit error is known to be at large scales with a dominant component at one cycle per revolution. It is modelled for each revolution as a constant plus a one-cycle-per-revolution sine wave. A revolution starts and ends at South pole. Sine waves are fitted together by minimizing the crossover differences over each global cycle (about 40 000 crossovers per cycle). We checked the continuity of adjustments from a revolution to the next. For each cycle, the adjustment reduces the crossover rms from 60-70 cm to 20 cm (20 cm and 15 cm respectively with the definitive orbit). The residual

is mainly due to ocean level variability caused by surface currents.

Data set is now filtered and corrected. To retrieve the geoid signal, we developed techniques based on the collinear-track method that is using the fact that the satellite is on a repeat-orbit. Profiles with less than 15 measurements are rejected. All other profiles are resampled every 7 kilometers along-track using a cubic spline to provide constant, regular sampling in latitude, (cycle-independent). Interpolation is done only for points surrounded by two valid one-per-second raw altimeter heights; for other points, the interpolation point is considered as non-valid and flagged. We numbered all valid, collocated points from April 1992 to January 1993 and averaged the sea surface height measurements. The number of cycles used for averaging is plotted on figure 1.

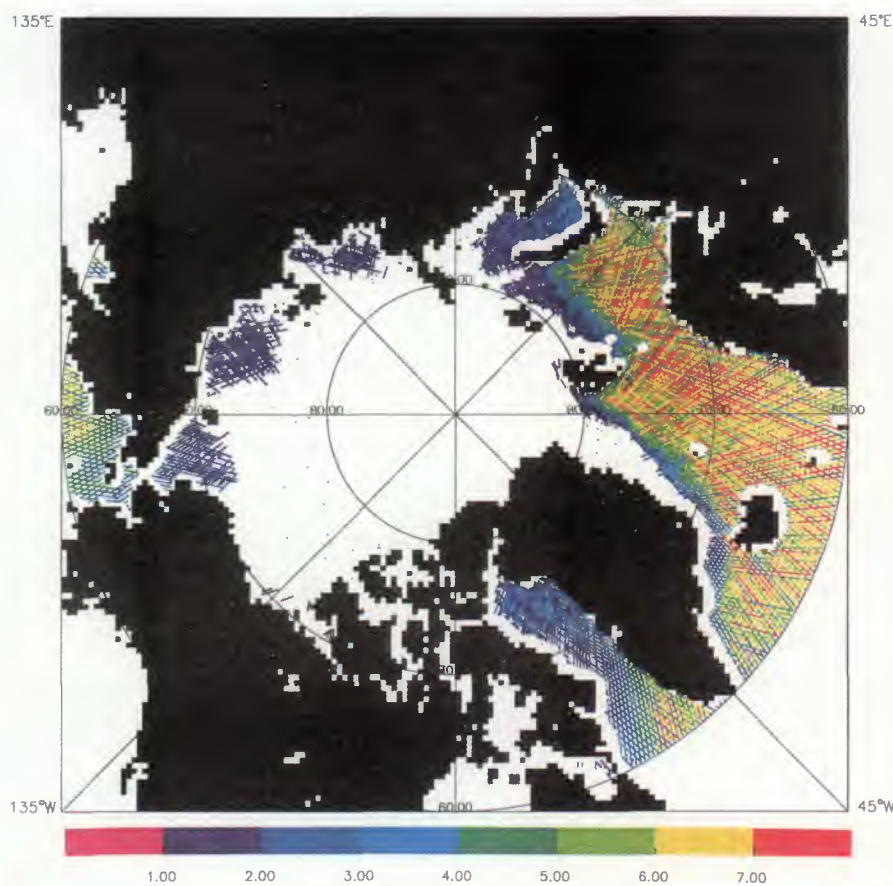


Figure 1 : Number of cycles available per location (cycles 1 to 8)

4. DATA COVERAGE

We analysed the distribution in space and time of actual data series to determine if enough geographical coverage of the Arctic ocean, and especially of the Siberian shelf or above the continental shelf, can be obtained.

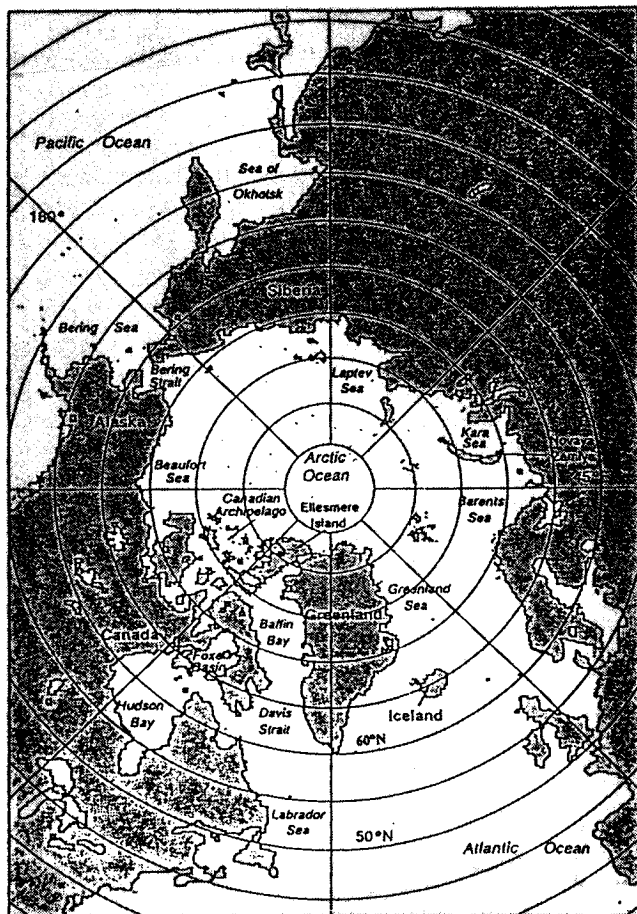


Figure 2 : Ocean and seas of the North polar area
 (central Arctic ocean, Baffin bay, Greenland sea,
 Barents sea, Kara sea, Laptev sea, East Siberian sea,
 Chukchi sea, Bering sea and Beaufort sea)

By means of figure 1, we evidenced the open-sea / sea-ice fluctuations areas : dark colors are representative of 2 to 3 cycles available per measurement. We reported in table 2 time periods for which the different Arctic ocean and seas (see figure 2) are pure ocean, i.e. not ice covered.

During winter, the ice extent is maximum, covering the

central Arctic ocean, Kara sea, Laptev sea, East Siberian sea, Chukchi sea and the Beaufort sea and being extensive for large portions of the other surrounding seas and bays, in particular the Bering sea, Baffin bay, Davis strait, Greenland sea and Barents sea. During the melting and freezing seasons, rapid changes occur in the surface condition and extent of the ice (e.g. ice floes). The springtime retreat of the ice edge tends to begin first in the Davis strait and in the Greenland sea, and last in the Bering sea, then affects portions of the Greenland sea, Kara sea, Laptev sea, East Siberian sea and Chukchi sea. At the time of minimum ice extent, during summer, the pack-ice is mostly confined to the central Arctic ocean, reaching the North coast of Greenland and many of the Canadian islands, but not to the coast along much of the Alaskan, Siberian and European coastlines. Essentially, no ice remains in Baffin bay, the Barents sea and the Bering sea : most of the continental shelf is ice-free. Recalling the decadal fluctuations in regional ice extent, mainly due to salinity anomalies (e.g. the "icy" 1968 year), 1992 year is favourable indeed for observing the Arctic ocean and seas, especially the Greenland and Kara seas (during summer).

Baffin bay	Aug-Oct	3 cycles (4-6)
Greenland sea	Apr-Dec	7 cycles (1-8)
Barents sea	Apr-Dec	7 cycles (1-8)
Kara sea	Aug-Oct	3 cycles (4-6)
Laptev sea	Aug-Sept	2 cycles (4-5)
East Siberian sea	Aug-Sept	2 cycles (4-5)
Chukchi sea	Aug-Oct	3 cycles (4-6)
Beaufort sea	---	---
Central Arctic ocean	---	---
Bering sea	Jun-Dec	6 cycles (2-8)

Table 2 : Arctic ocean areas (ice-free) and time period
 as observed by ERS-1 altimetry for year 1992

5. DATA QUALITY

We first checked on the data quality already achieved by comparing altimeter profiles of a same track. Depending on the track, we observe biases which will affect the geoid computation - tracks visible when mapping the geoid -. An explanation is in the orbit error (residuals). The data quality and/or data processing are still not sufficient. Note also that the ERS-1 altimeter tracker bias on the sea surface height measurements is estimated at $-41.5 \text{ cm} \pm 5.2 \text{ cm}$ [Francis, 1992]. Using version 3 altimeter ocean products, we expect a significant improvement of the data quality (i.e. using the precise and definitive orbit). We will also enhance the data quality through the data processing. We will get a new tidal model better suited to the Arctic ocean and use Topex/Poseidon data as a constraint in the orbit reduction procedure.

6. GRIDDING THE GEOID

Altimeter data give access to the mean sea surface which is the geoid plus the sea level signal associated with the permanent ocean circulation (also called mean dynamic topography). Except in the most energetic regions of the world ocean (Gulf Stream, Kurushio, Etc.), the permanent sea level signal is weak* and the mean sea surface is a fair approximation of the geoid. Prior to gridding and transforming the geoid into gravity anomalies, we referred it to a (cosine-tapered) low order geoid model (JGM2 [Nerem et al., 1993]). At the end of the process, the low-order geoid model will be added back to the residual gravity anomaly grid. The gridding of the residual geoid heights is a delicate operation because 1- the data sampling is not isotropically distributed and 2- even after correction, it remains errors

leading to significant biases between profiles (e.g. residual orbit error). We thus compared two methods. First, we tested a method which computes a spline surface with continuous curvature and eventually interior and boundary tension factors [Smith and Wessel, 1990]. As recommended in Olgiatti et al. [1994] and because of data gaps, we set the interior tension factor to zero, added some zero-points and a tension factor along the edge. As unfortunately expected, the mapping reveals tracks or stripes (see section 5).

In the second method, we used geostatistical techniques [Dubrule, 1981]. We performed a detailed variogram analysis of the data, modelling the natural variogram using polynomial, exponential or spherical theoretical functions. The contouring process is better using the spherical model. The geostatistical approach improves the results compared to the first method. It strongly attenuates shifts between profiles (see figure 3). The short wavelength patterns of the geoid clearly correlate with major geological structures, i.e. the ocean bottom topography. Because of the dense pattern of the ERS-1 satellite ground tracks the spatial resolution of the sea height is very high and many features are really distinguishable.

7. GRAVITY ANOMALIES

Finally and for preliminary results, we converted the grid of geoid anomalies restricted to the Barents and Kara sea to the Fourier domain, multiplied by $(i.kz)$, and transferred to the spatial domain through an inverse Fourier transform. The main drawback of this straightforward method is that it requires to adjust shifts between profiles. We adjusted again the data using a local crossover adjustment and tested the method on the Barents and Kara seas. The mapping (shown on figure 4) clearly reveals the major structural elements and the contours of the sedimentary basins. For instance, we

* The Barents sea is the more energetic part of the Arctic ocean, with more or less permanent currents lower than 25 cm/s. The permanent circulation of the Kara, Laptev and East Siberian seas is lower than 10 cm/s.

can identify the Hammerfest, Nordkapp, Olga and Sorkapp basins of the Barents sea [Johansen et al., 1993]; detailed features appear within the north and south basins. In the Kara sea, we observe a series of gravity lows which do not show up in recent compilation maps of sedimentary thicknesses [Jackson and Oakey , 1988 and Gramberg and Puscharovski , 1989]. In phase 2 of PEGASE project, we will use a more sophisticated method to compute the gravity anomalies (Sandwell 1992, Mc Adoo and Marks, 1992) Detailed discussion and a full analysis of the gravity fields are forthcoming with the third phase.

8. SUMMARY AND FOLLOW ON

Based on the first ERS-1 altimeter data of the 35-day repeat cycle (ALT.OPR 02 in version 2) of the North polar area, we defined criteria to filter out bad data from valid data, sea-ice data from open-sea data. We computed the sea surface heights, corrected for geophysical errors (available in the GDRs) and reduced orbit error (using a constrained sinusoidal crossover adjustment).

We then analysed the data coverage. ERS-1 altimeter is highly valuable for delineating the sea-ice extent in polar areas. The ice extent is best computed using the number of elementary measurements and the radiometer wet tropospheric correction. We could deduce monthly climatology of sea-ice cover. Recalling the decadal fluctuations in regional ice extent, 1992 is optimum indeed in terms of observing the Arctic ocean.

We checked on the data quality already achieved by comparing individual profiles. Comparison is not as good as expected, biases remain between profiles. The quality of the ALT.OPR 02 data we used is not sufficient for our purpose. We think it is mainly due to the product version (2). Nevertheless we used this data

set to develop processing techniques and algorithms which are the goal of the first phase of the PEGASE project.

To check on the data processing and the methodology applied, we computed a preliminary geoid from above corrected altimeter measurements based on the collinear-track method and geostatistical techniques for the gridding procedure. We ignore the mean dynamic topography induced by the permanent ocean circulation and assimilate the mean sea surface to the geoid. The mapping is satisfying although satellite tracks are visible. We then continued the geoid anomaly onto the Fourier domain and derived gravity anomalies. They clearly reveals familiar features of the marine geoid and confort us on the use of ERS-1 altimetry in the Artic ocean and in the data processing. But efforts must be pursued to improve the quality.

Further investigation will focus on :

- Achieving a high quality/high precision geoid with ERS-1 altimeter data.
i.e. to use the two years of the 35-day new ALT.OPR - version 3 - as well as the forthcoming six months of the 168-day repeat cycle - early 1994-, to correct the data for tide effects using the best model today available, to enhance the data quality with Topex/Poseidon data.
- Improved the geoid gridding and along-track geoid derivation.
i.e. to compute the mean profile, to study the ocean variability for its impact evaluation when assimilating the mean sea surface to the geoid, to retrieve the gravity anomaly fields.

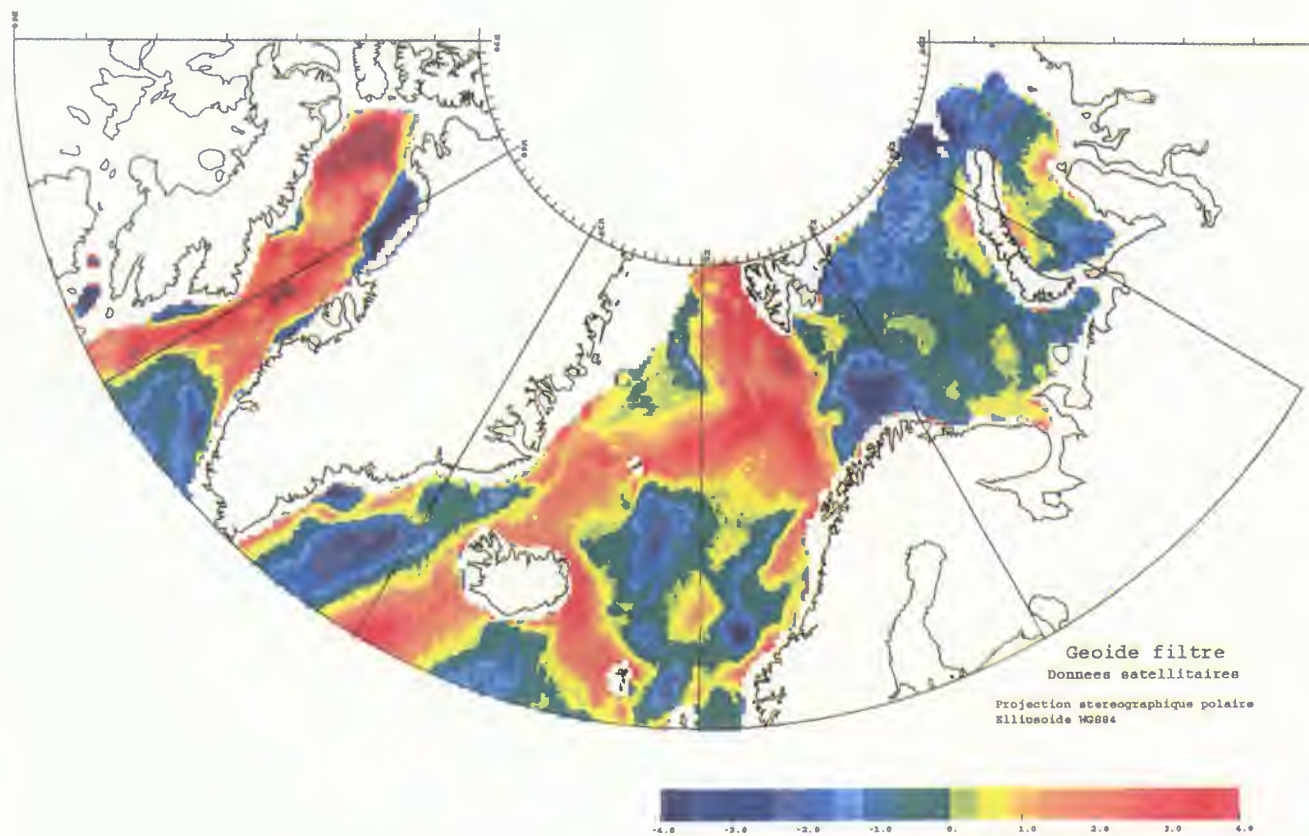


Figure 3. Pegase – First geoid gravity anomalies.

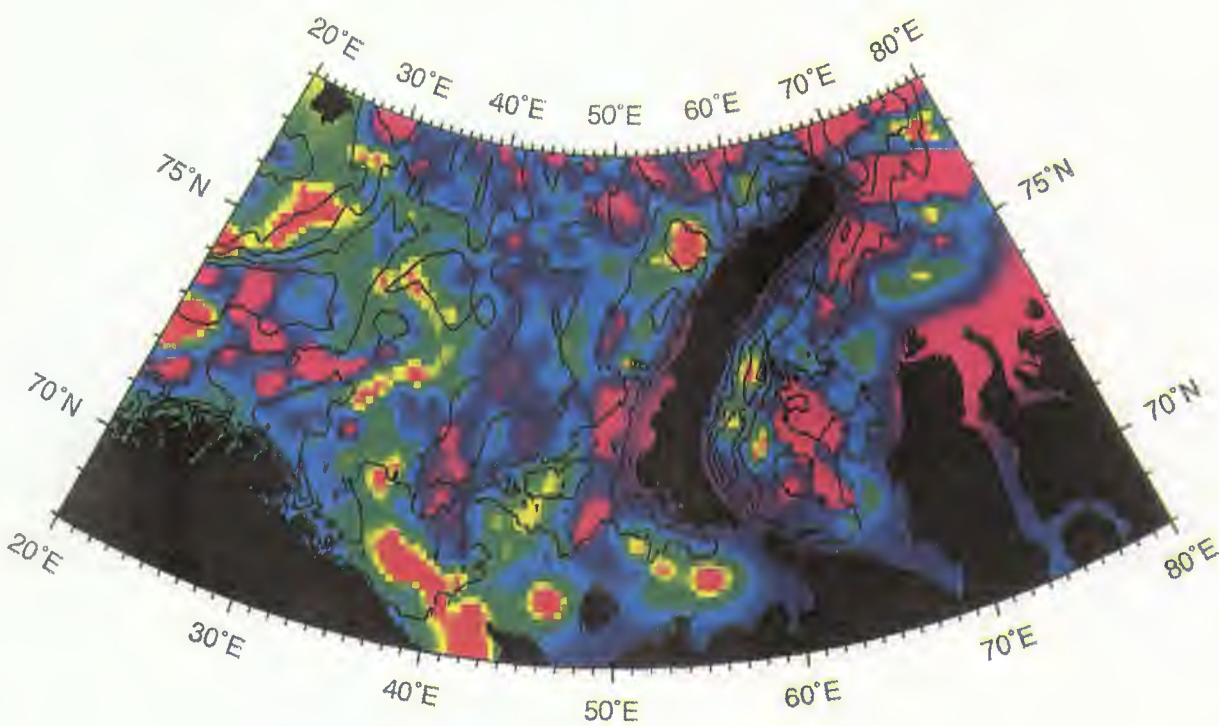


Figure 4. Pegase – Preliminary gravity anomaly fields.

9. REFERENCES

- Barrick D. E., B. J. Lipa, 1985, Advances in geophysics, *Satellite Oceanic Remote Sensing*, **27**, 86-93.
- Brown G. S., 1977, The average impulse response of a rough surface and its application, *IEEE Trans. Anten. Prop.*, AP-25, 67-73.
- Dubrule O., 1981, Krigeage et splines en cartographie, *Ph. D Thesis*, Ecole Nat. Sup. Mines de Paris.
- Francis O., P. Mazzega, 1990, Global charts of ocean tide loading effects, *Journal of Geophysical Research*, **95**, 11411-11424.
- Francis R., 1993, The calibration of the ERS-1 radar altimeter, the Venice calibration campaign, *ESA report*, ER-RP-ESA-RA-0257.
- Gramberg I. S., J. M. Puscharovski, 1989, Map of the relief of the heterogeneous basement of the Arctic region and adjacent areas, 1:10 000 000, compiled and translated by JEBCO Seismic Limited, *JEBCO House*, 22 Armoury way, London SW18 1EZ.
- Jackson H. R., G. N. Oakey, 1988, Sedimentary thickness map of the Arctic ocean, vol L, the Decade of North American geology, Geological Soc. Am.
- Johansen S. E., B. K. Ostisty, O. Birkeland, Y. F. Fedorovsky, V. N. Marirosjan, O. B. Christensen, S. I. Cheredeev, A. Ignatenko, L. S. Margulis, 1993, Hydrocarbon potential in the Barents sea : play distribution and potential, *Arctic geology and petroleum potential*, T. O. Vorren et al., Editors, Elsevier Publisher.
- Le Provost C., F. Lyard, J. M. Molines, 1991, Improving ocean tide prediction by increasing the number of semi-diurnal constituents, *Geophysical Research Letters*, **18**, 845-848.
- Llewellyn S. K., R. B. Bent, 1973, Documentation and description of the Bent ionospheric model, AFCRL-TR-73-0657.
- Mc Adoo D. C., K. M. Marks, Gravity fields of the southern ocean from Geosat data, *Journal of Geophysical Research*, **97**, 3247-3260.
- Nerem R. S., F. J. Lerch, J. A. Marshall, E. C. Pavlis, B. H. Putney, B. D. Tapley, R. J. Eanes, J. C. Ries, B. E. Schutz, C. K. Shum, M. M. Watkins, J. C. Chan, S. M. Klosko, S. B. Luthcke, G. B. Patel, N. K. Pavlis, R. G. Williamson, R. H. Rapp, R. Biancale, F. Nouel, 1994, Gravity model development for Topex/Poseidon, Joint Gravity Models 1 and 2, *Journal of Geophysical Research*, *Topex/Poseidon special issue*, in press.
- Olgiatti A., G. Balmino, M. Sarraih, 1994, Gravity anomalies from satellite altimetry : comparison between computation via geoid heights and via deflections of the vertical, *submitted to Manuscripta Geodaetica*.
- Saastamoinen J., 1972, Atmospheric correction for the troposphere and stratosphere in radioranging of satellites, *Geophys. Monogr.*, **15**, American Geophysical Union, Washington DC.
- Sandwell D. T., 1992, Antarctic marine gravity field from high density satellite altimetry, *Geophys. J. Int.*, **109**, 437-448.
- Schwiderski E. W., 1980, On charting global tides, *Rev. of Geophys. and Space Phys.*, **18**, 243-268.
- Smith W. H. F., P. Wessel, 1990, gridding with continuous curvature splines in tension, *Geophysics*, **55**, 293-305.
- Tai C. K., 1988, Geosat crossover analysis in the Tropical Pacific: 1. Constrained sinusoidal crossover adjustment, *Journal of Geophysical Research*, **93**, 10621-10629.



**MEAN SEA LEVEL DETERMINATION IN THE
SEAS SURROUNDING
GREECE**

T. Engelis,
G. Veis,
K. Katsambalos,
D. Paradissis

Objectives

- Pilot project in the frame of a Cooperation Agreement between ESA and Greece.
- First analysis of ERS-1 35 day repeat arcs to obtain estimates of the mean sea surface and its time variations in the Eastern Mediterranean Sea.
- Follow the 'non sophisticated user' approach, ie. a simplistic processing scheme of the ERS-1 altimeter data, without any consideration of orbit error removal techniques.
- Evaluate results against GPS/tide gauge measurements to assess accuracy of the data and validity of approach.

- Data selection has been made according to the following criteria

valid only data
 $>17/s$ obs
 $\sigma < 30$ cm
 $SWH < 10$ m
 $0.05 < \sigma_{SWH} < 3$ m
windspeed < 10 m/s
All corrections available
 $|ssh - N| < 4$ m

- Corrections applied to data

- All valid corrections were applied
- E-bias correction replaced with $0.052*SWH$
- Inverse barometric correction applied, consistent with the TOPEX/POSEIDON correction.

Overview

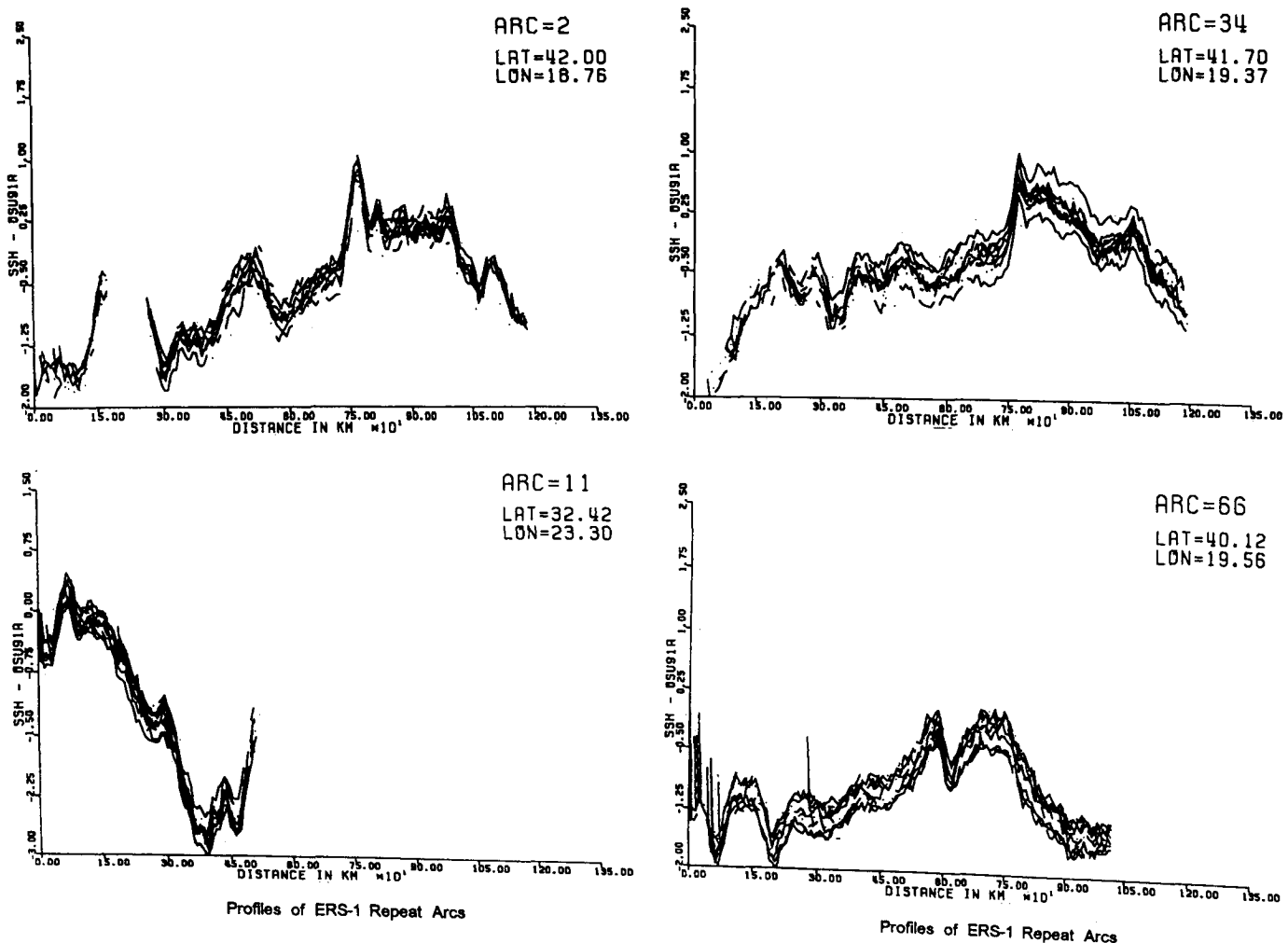
Statistics of 35 day repeat arcs

- First preprocessing and selection of data. Computation of statistics regarding data availability and variability.
- Repeat arcs and crossover discrepancies computation to assess precision and repeatability of the data.
- Prediction of gridded mean sea surface for the time span of the data, as well as its time variations.
- Prediction of sea level at 22 sites with M.S.L. estimates implied by GPS measurements

Arc	Total obs	Select. obs	RMS (cm)	Mean (cm)	Rel. mean
1	8902	3529	98	-68	-10
2	7871	2776	91	-57	-1
3	7337	2602	89	-52	6
4	8765	3191	84	-49	9
5					
6	9127	3852	84	-45	13
7	9175	4811	89	-50	8
8					
9	10611	4564	102	-65	-7
10	8800	4176	99	-69	-11
11	8779	3284	93	-66	-8
12	8835	2903	95	-66	-8
13	9168	3434	100	-69	-11
14	9172	3558	91	-57	1
15	8972	3392	85	-50	8
16	8663	3222	83	-46	12
Total		49295	92	-58	

Data preprocessing

- Altimeter data have been received from ESRIN in CCTs, exabytes and CDs.
- Data include all 35 day repeat arcs from 1 to 16 with the exception of 5 and 8.
- The corresponding time coverage is from May 1992 to October 1993.
- The areal coverage of interest to this work is between $30 < \phi < 42$ and $15 < \lambda < 35$.



**RMS of Crossover Discrepancies
between Repeat 35 Day Arcs
In cm**

	1	2	3	4	5	6	7	8	9	10	11	12	13	14	15	16
1	19	21	20	24	0	23	22	0	21	23	21	24	23	22	25	27
2	22	21	22	20	0	21	21	0	24	26	21	22	21	19	23	22
3	24	21	17	22	0	20	22	0	26	27	23	23	21	21	20	23
4	25	21	22	20	0	22	21	0	26	26	23	23	22	20	21	21
5	0	0	0	0	0	0	0	0	0	0	0	0	0	0	0	0
6	26	23	21	19	0	21	20	0	28	28	22	24	20	22	21	21
7	27	23	21	19	0	20	22	0	26	27	25	24	24	20	21	19
8	0	0	0	0	0	0	0	0	0	0	0	0	0	0	0	0
9	20	19	20	23	0	21	23	0	21	21	21	22	19	22	23	24
10	21	23	20	22	0	22	23	0	22	23	21	24	20	21	24	22
11	19	21	20	24	0	24	23	0	21	26	23	22	20	22	24	24
12	23	21	22	24	0	21	23	0	23	26	19	21	21	24	21	25
13	22	20	20	23	0	22	21	0	23	23	21	21	20	17	23	23
14	27	18	17	21	0	20	22	0	25	24	22	21	18	18	19	20
15	26	22	20	20	0	20	21	0	26	27	24	25	24	21	20	20
16	27	22	23	21	0	21	21	0	27	27	24	22	23	21	21	22

Total RMS 23 cm

**Number of Crossover Discrepancies
between Repeat 35 day Arcs**

	1	2	3	4	5	6	7	8	9	10	11	12	13	14	15	16
1	105	85	73	76	0	112	109	0	112	105	98	93	105	101	88	82
2	79	72	65	70	0	88	87	0	86	86	80	69	85	82	78	67
3	72	64	57	62	0	80	84	0	73	72	71	61	78	81	71	63
4	87	83	83	82	0	111	114	0	99	98	87	90	96	113	100	85
5	0	0	0	0	0	0	0	0	0	0	0	0	0	0	0	0
6	91	86	81	94	0	112	116	0	94	95	87	93	101	115	102	87
7	104	98	88	98	0	126	121	0	102	99	103	94	112	126	111	97
8	0	0	0	0	0	0	0	0	0	0	0	0	0	0	0	0
9	108	94	80	89	0	114	122	0	119	109	102	105	114	115	99	86
10	107	94	88	92	0	110	117	0	115	113	101	108	111	113	93	87
11	95	86	76	76	0	99	104	0	101	96	89	83	97	101	81	76
12	95	81	80	84	0	105	107	0	101	98	94	92	96	104	84	75
13	93	78	68	76	0	100	105	0	96	91	85	85	96	96	89	77
14	94	87	79	85	0	108	110	0	102	92	92	89	98	102	95	80
15	82	85	75	82	0	103	108	0	89	87	88	85	90	101	94	76
16	91	87	92	89	0	113	118	0	95	93	90	91	111	117	108	83

All Discrepancies greater than 50 cm are excluded

Total Crossovers 18220

**Mean Value of Crossover Discrepancies
between Repeat 35 Day Arcs
In cm**

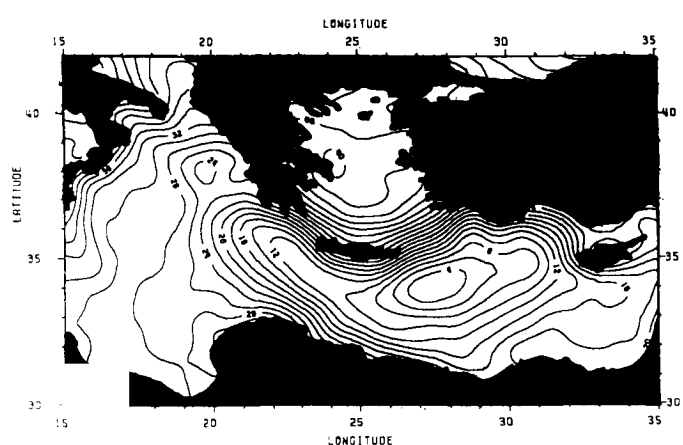
	1	2	3	4	5	6	7	8	9	10	11	12	13	14	15	16
1	-1	9	7	15	0	12	13	0	-3	-2	2	4	8	12	16	17
2	-9	3	4	6	0	9	5	0	-11	-7	-4	-1	0	4	10	10
3	13	-7	-2	3	0	5	0	0	-15	-15	-10	-6	-6	-1	2	7
4	-15	-7	-4	1	0	-1	0	0	-16	-16	-12	-11	-10	-1	0	0
5	0	0	0	0	0	0	0	0	0	0	0	0	0	0	0	0
6	-19	-11	-7	0	0	-5	-5	0	-20	-15	-11	-10	-10	-3	-2	-3
7	-19	-11	-7	0	0	-2	-2	0	-17	-14	-16	-11	-10	-2	0	2
8	0	0	0	0	0	0	0	0	0	0	0	0	0	0	0	0
9	-5	1	7	10	0	8	11	0	-9	-6	0	1	3	8	11	12
10	-6	4	8	9	0	9	7	0	-8	-5	-1	0	4	8	11	10
11	-7	3	7	11	0	11	8	0	-5	-6	-4	0	2	9	14	11
12	-9	1	3	8	0	4	6	0	-8	-9	-1	0	0	5	11	15
13	-9	-2	5	9	0	8	7	0	-9	-6	-7	0	3	2	11	11
14	-18	-5	0	2	0	2	0	0	-15	-14	-9	-8	-7	0	5	4
15	-17	-10	-2	2	0	-2	-4	0	-17	-14	-12	-11	-14	-4	0	3
16	-19	-10	-8	-2	0	-4	-3	0	-20	-17	-15	-13	-9	-5	-2	-4

Crossover discrepancies computed as : $\text{ssh}(t_2) - \text{ssh}(t_1)$, with $t_2 > t_1$

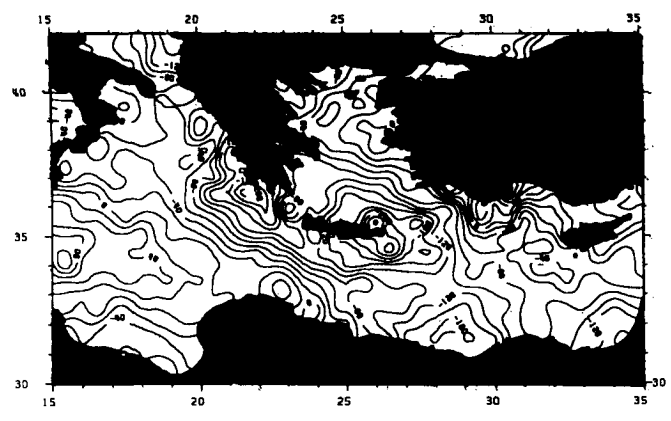
**Mean Value of Crossover Discrepancies
between Repeat 35 Day Arcs
In cm**

	1	2	3	4	5	6	7	8	9	10	11	12	13	14	15	16
1	-3	0	1	4	0	0	1	0	-8	-7	-6	-3	1	3	0	-2
2	-7	-1	-3	3	0	3	2	0	-10	-13	-10	-8	-7	-3	-7	-8
3	-8	0	0	0	0	1	-1	0	-15	-12	-10	-10	-6	-5	-3	-5
4	-13	-5	-6	-6	0	-6	-8	0	-11	-10	-11	-10	-9	-7	-7	-7
5	0	0	0	0	0	0	0	0	0	0	0	0	0	0	0	0
6	-7	-5	-2	-1	0	-5	-8	0	-8	-10	-8	-7	-5	-8	-6	-5
7	-9	13	-6	-5	0	-7	-12	0	-8	-11	-13	-12	-13	-9	-8	-6
8	0	0	0	0	0	0	0	0	0	0	0	0	0	0	0	0
9	-7	-8	0	1	0	-2	-5	0	-12	-13	-11	-7	-4	-3	-4	-1
10	-12	-2	-3	0	-7	-5	0	-10	-15	-13	-10	-6	-6	-8	-4	-4
11	-3	-10	-4	-4	0	-6	-6	0	-12	-17	-13	-8	-8	-6	-5	-8
12	-5	-2	0	0	-2	-3	0	-11	-12	-7	-8	-5	-2	0	-2	-2
13	-4	-8	-2	1	0	-4	-5	0	-10	-12	-9	-6	-4	-2	-2	-2
14	-5	-5	0	-1	0	-3	-8	0	-9	-9	-11	-7	-4	-4	-3	-4
15	-4	-7	-7	-4	0	-9	-9	0	-9	-11	-11	-9	-9	-7	-8	-8
16	-2	-7	-3	-5	0	-6	-5	0	-5	-9	-11	-3	-3	-5	-5	-8

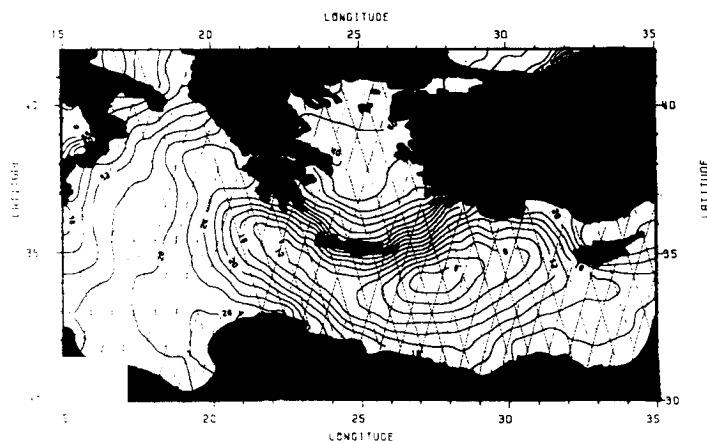
Crossover discrepancies computed as : $\text{ssh}(\text{asc}) - \text{ssh}(\text{desc})$



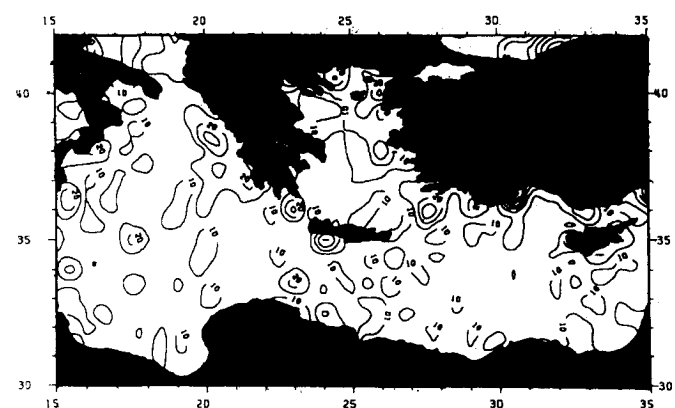
OSU91A geoid of the East Mediterranean Sea C.I.=2m



Differences between the ERS1 implied mean sea surface and the OSU91A geoid. C.I.=20cm

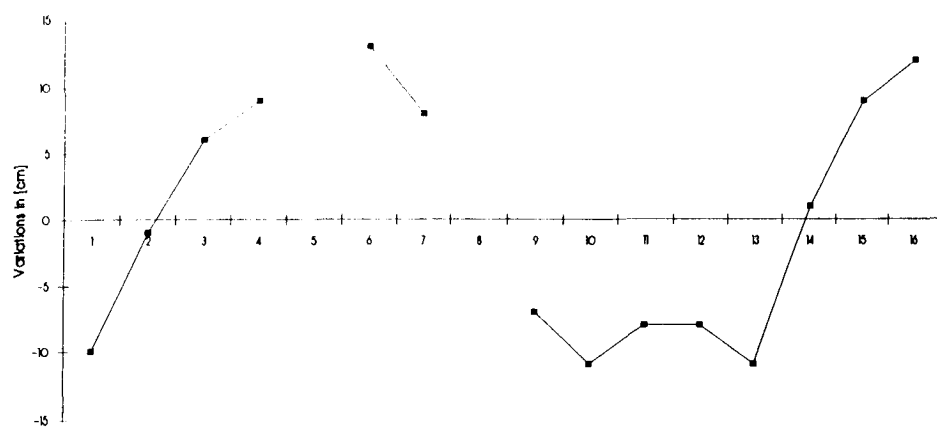


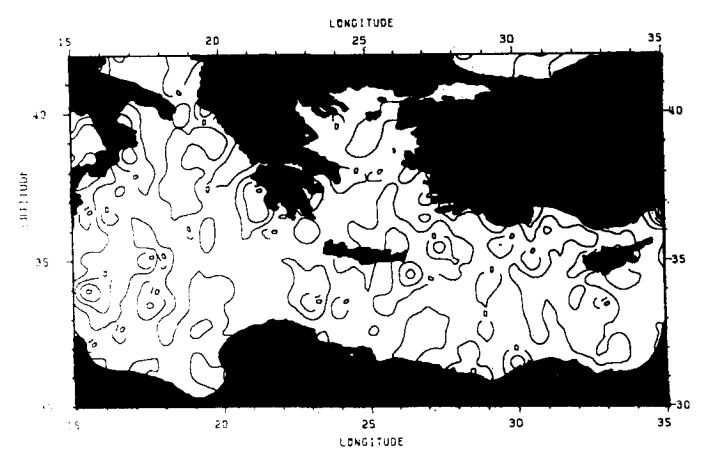
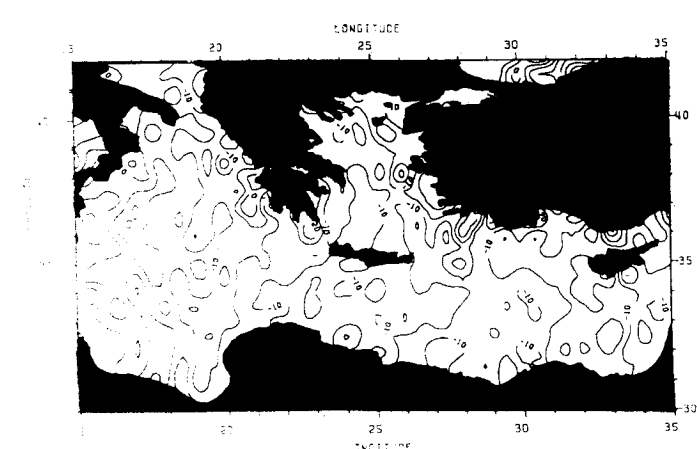
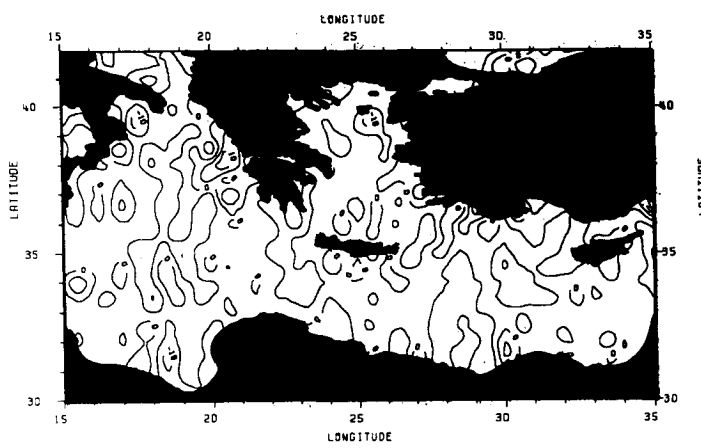
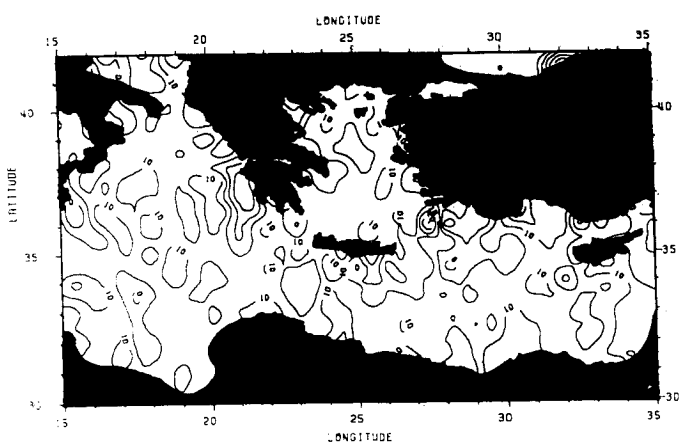
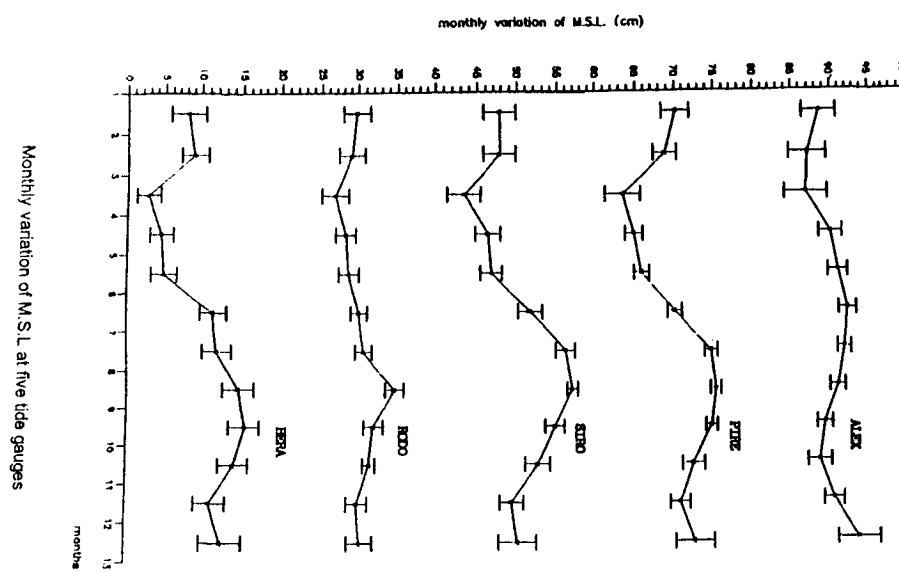
Mean Sea Surface of the East Mediterranean Sea implied by 14 repeat 35 day arcs of ERS1. C.I.=2m

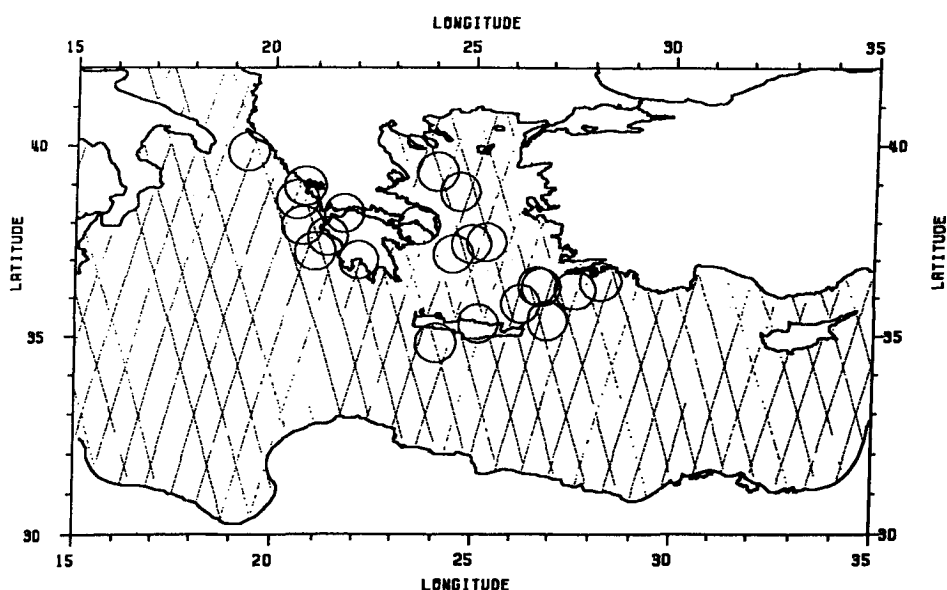


RMS variation of 14 repeat 35 day arcs with respect to mean sea surface implied by ERS1. C.I.=10cm

Mean variations of 35 day repeat arcs w.r.t MSL







Location of 22 GPS sites.

**Comparison of ERS1 observations with
GPS implied sea level**

Site	ϕ	λ	GPS	GPS-N	GPS-SSH
PIREAS*	37.933	23.625	37.73	-136	-40
PATRA*	38.247	21.728	26.36	-139	5
PREVEZA*	38.959	20.755	26.93	-132	-32
KALAMATA*	37.024	22.116	25.65	-149	17
SIROS*	37.441	24.946	38.58	-103	-30
RODOS*	36.446	28.230	20.85	-18	3
HERAKLION*	35.344	25.136	24.94	-155	7
STROFADES	37.250	21.016	22.93	-114	-1
K.PANAGIA	39.327	24.079	39.23	-59	-26
GAVDOS	34.837	24.074	15.35	-74	44
SKINARI	37.929	20.704	25.18	-117	-32
SERIFOS	37.173	24.487	37.57	-110	-16
D.SKIROU	38.808	24.643	39.58	-13	6
KATAKOLO*	37.644	21.319	23.50	-235	-82
OTHONI	39.856	19.379	31.86	-124	-74
MYKONOS	37.487	25.333	38.05	-121	-73
ALATSOG	36.337	26.663	31.67	-7	89
STEFANIA	36.300	26.760	30.85	1	97
GALANOU	35.415	26.918	17.37	-54	106
MYLOS	36.217	27.612	25.12	60	115
HAMILI	35.864	26.229	28.17	-21	131
VASILIKI	38.607	20.573	30.80	480	559

* Tied to tide gauges

MONITORING LAKES IN KENYA USING ERS-1 ALTIMETER DATA

Diane Boardman, Earth Observation Sciences Ltd, Broadmede
 Farnham Business Park, Farnham, Surrey, UK
 phone: +44 (0) 252 721444 fax: +44 (0) 252 712552

Wyn Cudlip and Jeff Ridley, Mullard Space Science Laboratory, UK

Martin Chodota, RCSSMRS, Kenya

ABSTRACT

As part of a larger study project to develop a methodology to model and monitor lake level changes in three Rift Valley lakes in Kenya (Naivasha, Nakuru and Elementeita) the feasibility of monitoring lake levels using ERS-1 altimeter data has been investigated.

As none of the altimeter tracks directly crosses any of the three lakes a return echo modelling technique was used to extract the lake level. This method modelled the expected response of the altimeter to a given lake outline passing through the altimeter footprint. By matching the modelled waveforms to the observed data the off-ranging correction to be applied to the retrieved height was derived. Atmospheric, instrument biases, geoid and tidal corrections were calculated. A full analysis of all the errors contributing to the final lake height was undertaken.

The conclusions of the study were that through the use of modelling, lake height measurements of off-nadir lakes can be obtained. The best estimate of the lake level obtained was consistent with the in-situ measurements to within 10 cm, although the error associated with the measurement was 80cm.

For lakes crossed at nadir the measurement of the variation of the lake level to an accuracy of 10 to 15 cm is possible, the error increasing rapidly with off-nadir distance. The usefulness of the technique for any given application must therefore be considered on a case by case basis.

1. INTRODUCTION

Lakes Nakuru, Elementeita and Naivasha in the Central Kenyan rift valley are all subject to changing lake levels, but this phenomenon is yet to be studied in any systematic way. Changes in the water levels for these particular lakes may have significant consequences for Kenya as it could affect fisheries, tourism and agriculture. In the case of Elementeita and Nakuru, the environmental consequences could be potentially severe as the lakes support a unique ecology of flora and fauna which reflects their unusual alkali environment.

To understand the hydrological processes operating on these lakes, and thereby understand and predict lake level changes a hydrological model is being developed. Lake level data is an essential component for calibrating such a hydrological model. Although some in-situ lake level data is available locally, the routine supply of this information is sporadic and the prospect of routinely monitoring lake levels remotely is therefore attractive.

Following the launch of ERS-1 and Topex-Poseidon and the proposed mission of ERS-2 and Envisat, there is now the prospect of a continuous source of satellite altimetry data extending well into the foreseeable future. This opens up the possibility of continuous monitoring of lake levels by satellite altimetry.

2. METHOD

One of the difficulties of obtaining lake heights using satellite altimetry is that because altimeters were designed primarily to track over the relatively flat surfaces of the oceans, loss of lock (or the inability to follow the undulations of the surface), if often experienced over land surfaces. In this study this problem was overcome by scheduling the ERS-1 altimeter to be in preset tracking with a fixed range window over the lakes.

2.1 Waveform Modelling

From the shape of the waveform data received, the position of the leading edge of the waveform corresponding to the mean surface was located using the standard Offset Centre of Gravity (Wingham, 1986) technique. Because none of the lakes were crossed directly by the satellite track, the range measurement corresponding to the leading edge cannot be directly converted into a surface height. Thus, an off-ranging correction is required to extract the lake levels.

The off-ranging correction was determined by modelling the expected response of the altimeter to the given lake coastline and matching the results with the observed return echo waveforms. The modelling technique used was the terrain facet model (Guzkowska et al, 1990).

This technique generates a sequence of waveforms from a 3 dimensional surface with a specific pre-defined

distribution of scattering areas. The waveform generator calculates the delay time to, and the backscattered power from, each facet or scattering area in the 3 dimensional surface. Model waveforms are produced by integrating the power returned for a series of satellite positions along the track. The geometry of the model is shown in Figure 1.

The 3 dimensional surface used in the modelling corresponded to a 100m grid centered on the sub-satellite track in which each of the grid cells was labelled as either lake (1) or land (0). The grid was generated from the sub-satellite track and the digitised outlines of the lakes. Further details can be found in Boardman et al, 1994.

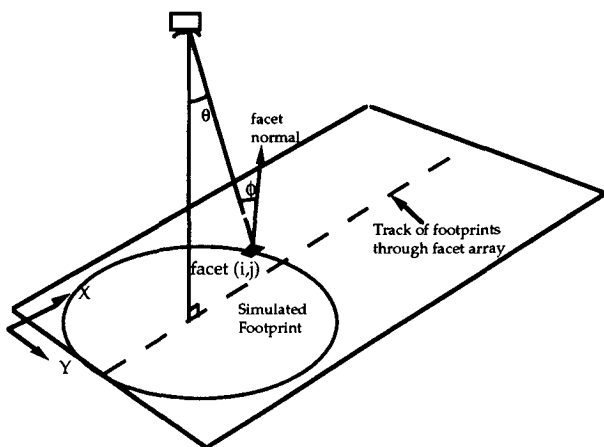


FIGURE 1. The geometry used for the Facet Model. Each triangular facet is characterised by its slope, elevation, backscatter coefficient and polar response.

2.2 Atmospheric Corrections

The atmospheric corrections account for the reduction of the speed of light in the troposphere and ionosphere. The tropospheric corrections depend on the air pressure (dry tropospheric correction) and the water vapour content (wet tropospheric component) and the total liquid water content (liquid water correction).

Atmospheric corrections for the wet and dry tropospheric corrections were calculated from the pressure, temperature and total integrated water vapour available from global forecast analysis data using the methods described in Cudlip et al, 1994. For comparison the corrections were also calculated from radiosonde ascents from Nairobi. No corrections were made for the total liquid water content.

The ionospheric corrections were calculated by T. Robinson from the University of Leicester using the methods described in Leigh et al, 1988.

2.3 Other Corrections

In addition geoid, tidal and instrument bias corrections

made, for further details see Boardman et al, 1994.

3. RESULTS

3.1 Preliminary

Before lake levels were extracted from the altimeter data a number of investigations were performed to determine the effect of a number of parameters on the modelling accuracy.

One of the inputs to the waveform modelling is the polar response of the surface which will change with the wind speed conditions. Since the wind speed conditions may change from pass to pass this might create uncertainties for change detection. The magnitude of this error was investigated by running the model for the two extremes of an ocean-like surface and with a very narrow polar response simulating very calm conditions. The resulting parabolic responses for Lake Nakuru are shown in Figure 2. The two lake conditions gave a difference 90 cm in the derived lake height which corresponds to the worst case error.

The effect of an uncertainty in the satellite track was also investigated by "moving" the lake 1 km closer to the track, this gave a difference of 8 m in the height of the parabola emphasising the fact that the satellite ground track must be known accurately if its uncertainty is not going to introduce significant error into the retrieval of the lake level. The modelled parabolic response is shown in Figure 2.

During the preliminary investigation it was also noticed that the leading edge of the observed waveforms were significantly broader than those for the modelled waveforms. Examining maps of the area showed that the shores of Nakuru were swampy. This is consistent with the observed broadening since the swampy areas would introduce additional reflecting areas at a smaller range than the lake itself resulting in a broadening of the leading edge of the waveform.

3.2 Final Results

From the preliminary investigation it was known that the ground track location must be determined accurately. Consequently, the analysis was limited to those overpasses for which precise orbit data was available. This section presents the results from the ascending passes between February and April 1993.

The ascending tracks pass between 1.5 and 2.7 km from the eastern shore of Lake Nakuru and about 8 km from the western shore of Lake Elementeita. The retracked height profiles together with the modelled profiles are shown in Figure 3.

The retracked height profiles shown in Figure 2 are quite complicated in shape because for the first half of the overpass the altimeter receives echoes from both lake Nakuru and Elementeita. The observed response for lake Elementeita can be seen to be quite variable, with a dip

for the 7th March data around the point of closest approach. Analysis of the backscatter profiles for the three tracks showed that while the profiles for the 11th April and 16th May were modelled quite well the pass of the 7th March showed a quite different profile to the other two. The most likely explanation for this is unusual wind conditions on that day, although, unfortunately, in situ-data to support this hypothesis is not currently available.

The results of the analysis for the three ascending tracks are presented in Table 1 along with the corrections applied and the error estimates. The root sum square for the current error budget for the 11th April is 80 cm. The error for the other two passes is larger since for the 7th March track there was significant backscatter variation and precise orbit data was not available for the 16th May.

4. CONCLUSIONS

Lake height estimates have been obtained for three ascending and three descending passes between April and May 1993. The best estimate of the water level from Lake Nakuru obtained from the ascending track on the 11th April was 1761.02 ± 0.8 m which is consistent with the in-situ level measurements of 1761.00 ± 0.1 m obtained a few months later.

The current overall error budget for the ascending track analysis of 80 cm is dominated by the error in the off-ranging correction derived by modelling. This error could probably be reduced to 50 cm with an improved modelling technique through a better understanding of the backscatter behaviour and a better fitting technique to obtain the perceived height. However, since the annual variation in the lake heights of the lakes is of the order of 60 cm, this, in theory doesn't seem adequate. In practice, however, this figure represents a worse case, since some of the error contribution from the modelling and geoid act as a bias and would not contribute to the uncertainty once the constant offset was determined.

Results of other work (Cudlip, 1993) show that for lakes crossed directly, rms lake level errors of the order of ± 15 cm are achievable, the main contributions being ± 10 cm from the orbit error and ± 10 cm from the retracking uncertainty. Thus if the lakes in this study were crossed directly this technique would be adequate for routinely monitoring them.

This study shows that it is possible to obtain lake heights from lakes off-nadir using modelling techniques, although the error increases rapidly with off-nadir distance. Whether this technique is useful for any given lake will therefore be dependent on the magnitude of the change to be detected and the off-nadir distance of the lake in question.

5. ACKNOWLEDGEMENTS

The EOS Kenya Lakes project team would like to thank Dr T. Robinson from the University of Leicester for supplying the ionospheric corrections and Ross Reynolds of the University of Reading for calculating height measurements from the radiosonde data. We would also like to thank ESA for providing data and especially Richard Francis and Berthyl Duesmann for operating the altimeter in preset tracking of the lakes.

This project was funded by the European Commission's Directorate General XII for Science, Research and Development; under the programme in Life Sciences and Technologies for developing countries.

6. REFERENCES

Boardman, D, W Cudlip, J Ridley, 1994, Monitoring Lakes in Kenya: An Environmental Analysis for Developing Countries Altimetry Report, EOS Ref: EOS-92/-93/TR-004, Earth Observation Sciences, Broadmeade, Farnham Business Park, Farnham, Surrey, UK.

Cudlip W, D R Mantrip, C L Wrench, H D Griffiths, D V Sheehan, M Lester, R P Leigh, and T R Robinson, 1994, Corrections for altimeter low level processing at the Earth Observation Data Centre. *International Journal of Remote Sensing*, 15, 4, 889-914.

Cudlip W, M Wolf, J Ridley, F Strawbridge, and J Bray, 1994, ERS-1 Performance Assessment, DRA Contract No. FRN1B/179. Space Department, DRA, Farnborough, Hants, UK.

Guzkowska, MAJ, C G Rapley, J K Ridley, W Cudlip, C M Birkett, and R F Scott, 1990, Developments in Inland Water and Land Altimetry, ESA Contract Report 7839/88/F/FL.

Leigh R P, T R Robinson and M Lester, Proceedings of IGARSS'88 Symposium. Ref ESA SP-284 (IEE 88CH2497-6).

Wingham D J , C G Rapley, and H D Griffiths, 1986, New Techniques in Satellite Altimeter Tracking Systems, Proc. IGARSS Symposium, Zurich, 8-11 September 1986. T D Guyenne and J J Hunt (eds), European Space Agency SP-254, 1339-1344.

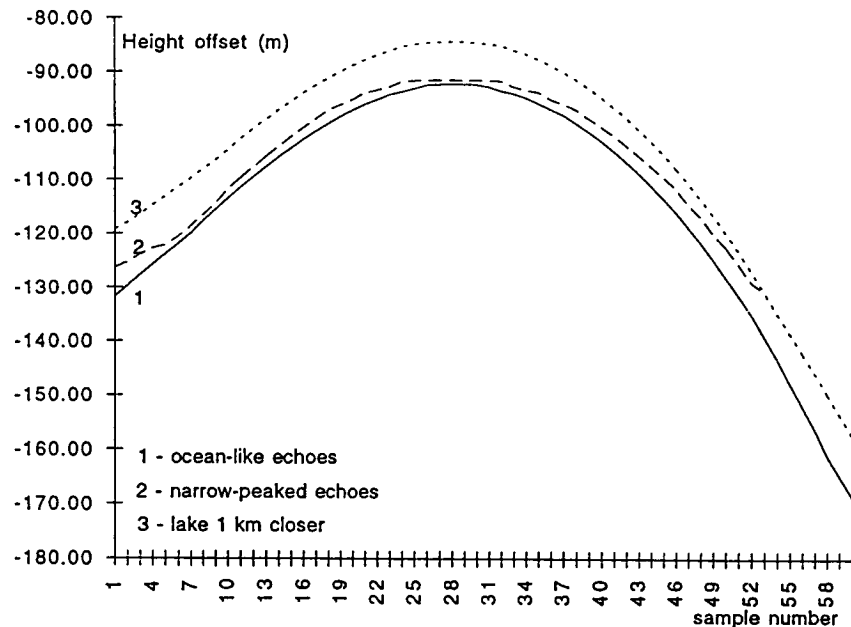


Figure 2. Modelled parabolic response for Lake Nakuru.

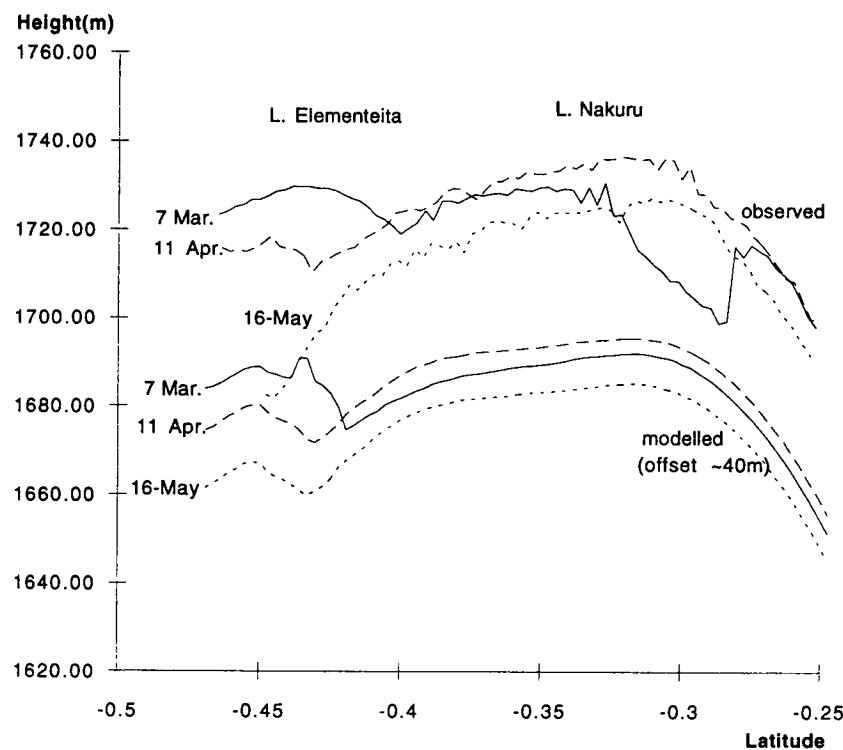


Figure 3. Retracked height profiles for the three ascending tracks past Lake Elementeita and Lake Nakuru together with the corresponding profiles (offset by 40m for clarity) generated by the MSSL return-echo modelling software. The lake level is estimated by shifting the modelled profile vertically to give the best fit to the observed profile.

Pass Date	7th Mar	11th Apr	16th May	Error Budget		Notes
				curr	poss	
Lake Distance	2.7 km	1.7 km	1.5 km			
Mean Backscatter (uncalibrated)	23 dB	24 dB	25 dB			
Off-ranging correction	8.05	4.60	3.87	0.50	0.30	1
height from fit	1740.00	1740.80	1730.00	0.50	0.30	2
orbit bias			11.0	0.20	0.10	3
dry tropo (model)	1.87	1.90	1.88	0.04	0.02	4
wet tropo (model)	0.09	0.13	0.10	0.06	0.02	4
<i>dry tropo (radiosonde)</i>	<i>1.87</i>	<i>1.88</i>		<i>0.04</i>	<i>0.02</i>	
<i>wet tropo (radiosonde)</i>	<i>0.10</i>	<i>0.12</i>		<i>0.06</i>	<i>0.02</i>	
ionospheric	0.08	0.08	0.08	0.03	0.03	
solid earth	-0.26	0.09		0.02	0.02	
ocean loading	-0.01	-0.01		0.01	0.01	
C of G correction	-0.85	-0.05	-0.85	0.01	0.01	
external cal correction	-0.42	-0.42	-0.42	0.05	0.05	
geoid	-19.50	-19.50	-19.50	0.30	0.30	
lake level (model)	1760.00m	1761.21m	1761.29m	0.80m	0.53m	
lake level (radiosonde)	1760.01m	1761.18m				
in-situ level	1761.09 (on the 23rd July, 1993)					
	1760.96 (on the 2nd October, 1993)					

Notes

- 1 Value at point of closest approach. Possible improvement though improved backscatter modelling.
- 2 Improvement possible though fitting routine
- 3 Improved orbit data will become available
- 4 Could be improved though use of in-situ atmospheric data

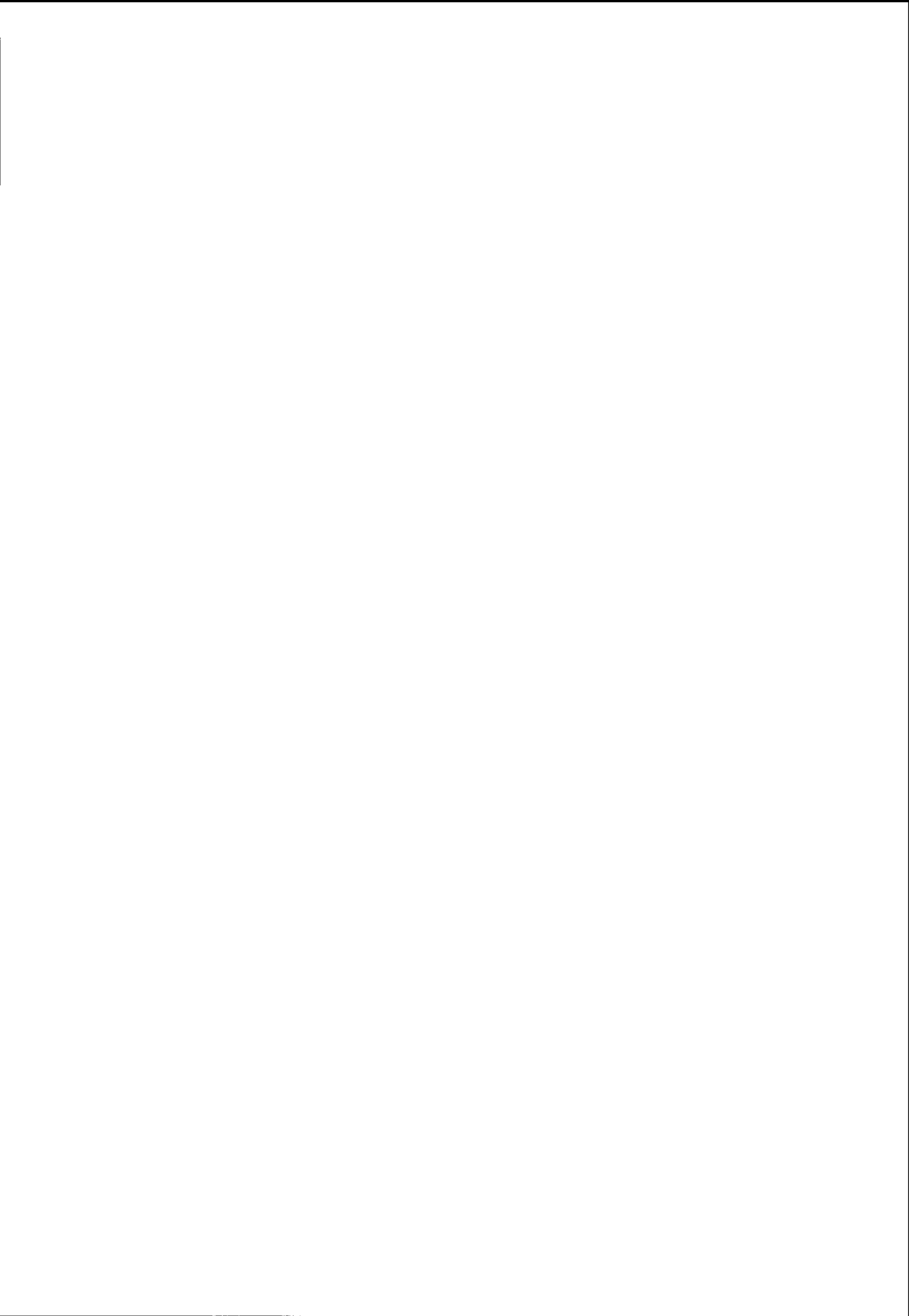
Table 1. Nakuru lake level calculation for ascending tracks.

Table 3.2 Nakuru lake level calculation - ascending tracks

Pass Date	7th Mar	11th Apr	16th May	Error Budget		Notes
				curr	poss	
Lake Distance	2.7 km	1.7 km	1.5 km			
Mean Backscatter (uncalibrated)	23 dB	24 dB	25 dB			
Off-ranging correction	8.05	4.60	3.87	0.50	0.30	1
height from fit	1740.00	1740.80	1730.00	0.50	0.30	2
orbit bias			11.0	0.20	0.10	3
dry tropo (model)	1.87	1.90	1.88	0.04	0.02	4
wet tropo (model)	0.09	0.13	0.10	0.06	0.02	4
<i>dry tropo (radiosonde)</i>	<i>1.87</i>	<i>1.88</i>		<i>0.04</i>	<i>0.02</i>	
<i>wet tropo (radiosonde)</i>	<i>0.10</i>	<i>0.12</i>		<i>0.06</i>	<i>0.02</i>	
ionospheric	0.08	0.08	0.08	0.03	0.03	
solid earth	-0.26	0.09		0.02	0.02	
ocean loading	-0.01	-0.01		0.01	0.01	
C of G correction	-0.85	-0.05	-0.85	0.01	0.01	
external cal correction	-0.42	-0.42	-0.42	0.05	0.05	
geoid	-19.50	-19.50	-19.50	0.30	0.30	
lake level (model)	1760.00m	1761.21m	1761.29m	0.80m	0.53m	
lake level (radiosonde)	1760.01m	1761.18m				
in-situ level	1761.09 (on the 23rd July, 1993)					
	1760.96 (on the 2nd October, 1993)					

Notes

- 1 Value at point of closest approach. Possible improvement though improved backscatter modelling.
- 2 Improvement possible though fitting routine
- 3 Improved orbit data will become available
- 4 Could be improved though use of in-situ atmospheric data



PRODUCTION OF SPOT/ERS1 IMAGE MAPS

Frédéric Perlant*, Jean-Paul Sempère**, Louis-François Guerre***

* ISTAR, Parc du Canal, Campus II Bat C, 3 av. de l'Europe, F-31400 TOULOUSE, FRANCE.
Phone (+33) 62 19 19 25, Fax (+33) 61 73 81 81

**IGN ESPACE, Parc technologique du Canal, 24 rue Hermès, F-31527 RAMONVILLE, FRANCE.
Phone (+33) 62 19 18 18, Fax (+33) 61 75 03 17
***SPOT IMAGE, B.P. 4359, F-31030 TOULOUSE, FRANCE.
Phone (+33) 62 19 40 88, Fax (+33) 62 19 40 53

ABSTRACT

To compare and merge informations given by two different sensors, one must have perfect geometric correspondence. The Pilot Project we present tries to take advantages of two sensors: SPOT and ERS-1. ISTAR, IGN ESPACE and SPOT IMAGE associated on this project. We show the different steps necessary to generate image maps. Using DTM and geometric modelisation, we describe how SPOT and ERS images can be geocoded in a selected cartographic reference and what are the characteristics of the products. Through the range of SPOT/ERS image maps generated during this Pilot Project, a cartographic analysis has been conveyed. Results and preliminary conclusions are presented on the potential and the limitations of the ERS-1 image maps. Finally, user needs are analysed to evaluate the suitability of the SPOT and ERS-1 image maps.

1. INTRODUCTION

After several experiments with various success (SEASAT, SIRA, SIRB), large number of SAR satellite data are commercially available (ERS-1). These remote sensed data different from what we are used to (LANDSAT, SPOT), reinforce the need for studies in sensor fusion. For many applications one need to register data from different sensors to be able to compare and analyse their diverse informational content. By analysing SAR data such as the one provided by ERS-1 it is obvious that SAR imagery presents particularities that we have to take into account when comparing with optical data. There is a big interest in merging or comparing SAR with optical data although this has to go through necessary processing steps. To take advantages of two sensors, ISTAR, IGN ESPACE and SPOT IMAGE associated to propose an ESA Pilot project and AVAL-SAR CNES program to produce SPOT/ERS-1 image maps. The main interest of this study is to guarantee up-to-date image maps even in cloudy areas. ISTAR is performing the geometric rectification (Terrain

geocoded product). IGN ESPACE is in charge of the image map generation (radiometry, cutting & dressing) and the cartographic analysis whereas SPOT IMAGE is responsible for the final restitution and the user needs analysis for the products.

Using DTM and geometric modelisation, we describe how SPOT and ERS images can be geocoded in a selected cartographic reference. This terrain geocoding makes the data providing from the two different sensors superposable for comparison, analysis or merging. The specificity of SAR data will be stressed to explain the technical difficulties and the solutions developed to generate geocoded product in the context of the Pilot Project. The different geometric and radiometric problems will be discussed. In particular radiometric (speckle noise) and the interpolation problems caused by overlays, foreshortening and shadows. Then we will present some of the limitations we have foreseen so far. From the range of products generated during this pilot project the potential use of such images maps will be discussed: in particular aspects such as the optimal scale, some complementarities between SPOT and ERS-1 or the possible ways to combine SPOT and ERS-1 data from a cartographic point of view. Finally we identify user needs in terms of image maps and present preliminary conclusions.

2. TERRAIN GEOCODED PRODUCT GENERATION

2.1 Generalities

ERS-1 image data are different from the optical images obtained by LANDSAT or SPOT.

The SPOT optical sensor is a passive sensor which gets earth radiometry in the visible and near infrared domain. Images correspond to lines successions and can be modelled by knowing the position vector, speed vector and attitude vector of the satellite. Depending on the earth radiometry, SPOT cannot acquire images

at night and presents major problems with clouds and high latitudes areas.

The SAR ERS-1 sensor is an active sensor which gets the intensity and polarisation of the Electromagnetic wave reflected or backscattered by ground cells. From raw data, signal processing techniques allow to form an image of the earth surface or sub-surface (Ref. 1). The image generated corresponds to a range-time array (in Slant Range geometry). Since the sensor has a side looking viewing perpendicular to the satellite speed vector only the position and speed vector of the satellite are necessary to model the image. Carrying it's «own illumination source», the SAR can get imagery at night, whatever the latitude and through clouds.

2.2 ERS-1 image characteristics

However SAR imagery presents some particularities that we have to take into account in comparing with optical data. ERS-1 images are generally 16 bits per pixel to accommodate the dynamic range of towns, bridges, railways tracks, and in our case we used SLC complex data that are 32 bits per pixel. It makes the data volumes to handle quite large.

In terms of radiometry it is important to point out “speckle noise” that makes difficult the interpretation as well as the necessary interpolations for the geometric transformations. Furthermore, people used to optical radiometric informations have to get acquainted with the radar retrodiffusion information. For instance bridges, and metallic objects can be seen as strong signal whereas other structures such as lakes, fields or roads disappear, in specific conditions.

Finally, and this point will be detailed later on, SAR geometry is very specific. The images we used, are in the Slant Range Geometry.

One interesting remark is that looking on the side (23 degrees angle for ERS-1), the images are geometrically similar to what we would get using an optical sensor with a very large side looking angle (here 67 degrees). The strong geometric deformations due to the relief generate overlays, shadows (occlusions) as well as geometric compressions and dilatations.

2.3 Products generation

For each site, we used ERS-1 images, SPOT P and/or SPOT XS images and a DEM corresponding to the area. One can point out that the DEMs used have been obtained using digital SPOT stereogrammetry (except for the Guyana area), but could be generated from

other techniques in cloudy areas (radargrammetry or interferometry for instance (Ref. 2), or map scanned contour lines). To generate the image maps one has to perform two distinct tasks : image geocoding to obtain terrain geocoded products, also called orthoimage, and map production. We present here ERS-1 terrain geocoding, its difficulties and how it can be specifically solved for the particular purpose of image map generation.

To generate orthoimage (or terrain geocoded products) one must use a DEM, ancillary data (orbitography) and geometric modelisation. Thus SPOT and ERS-1 images can be geocoded in a selected cartographic reference (UTM, Lambert...).

Modelization consists of setting up a function that gives for each point (X,Y,Z) on the ground (in a geocentric coordinate system for instance) the corresponding image coordinates (x,y) in image rows and columns. This transformation is optimized or calibrated for each image (SPOT and ERS-1) using ground control points. Thus, for each point of the resampled DEM to the final orthoimage format, we get the corresponding decimal (x,y) positions in the ERS image. We then interpolate from the ERS radiometry given for the neighboring integer image positions to obtain the radiometry corresponding to the (x,y) location in the terrain geocoded result image.

Image map is a map with an orthoimage as information layer and cutting and dressing like a classical map. In the case of ERS-1 image map, extra dressing and informations may be necessary such as satellite heading direction, side-looking angle and direction, to help in the interpretation of the scene.

2.4 Characteristics of the ERS-1 orthoimage

There are several limitations to ERS-1 geocoding. Because of the side looking angle (23 degrees for ERS) there are frequent overlays or compressions in mountainous areas (bright values). Tops and bottoms of the hills can't be seen correctly. Data providing from different geographic locations are mixed and difficult to interpret and interpolate. Figures 1 and 2 describe these difficulties. Figure 1 gives an idea, on a simplified geometry, of the ambiguity areas for which several distinct points on the ground give a single pixel in the SAR image. It presents also the overlay areas as well as the shadows. It is apparent that the larger the look angle the more shadows but the less overlays. Furthermore, because of ambiguities the interpolated ridge or valley bottom can be displaced. That is to say that unless we use the DEM to redistribute the backscattered energy, the border between bright and dark areas (on top of the hills or at the bottom of the

valleys) will be displaced, and the corresponding radiometry will come from the sum of various ground points responses.

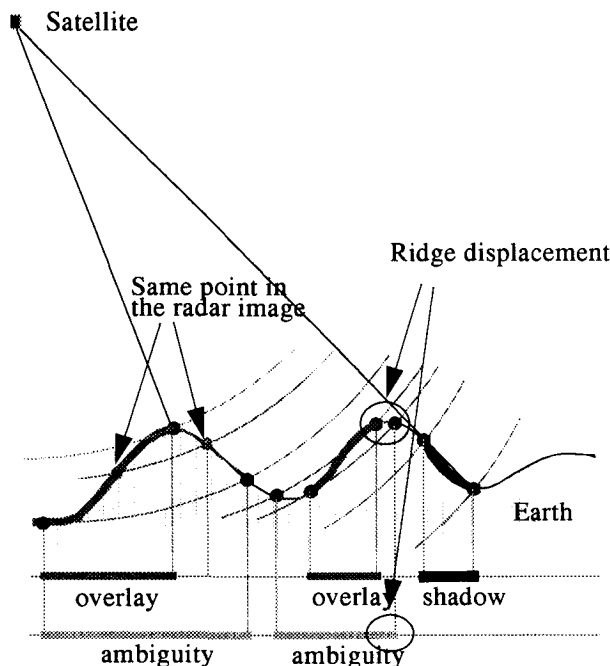


Fig. 1 : Radar geometrical problems

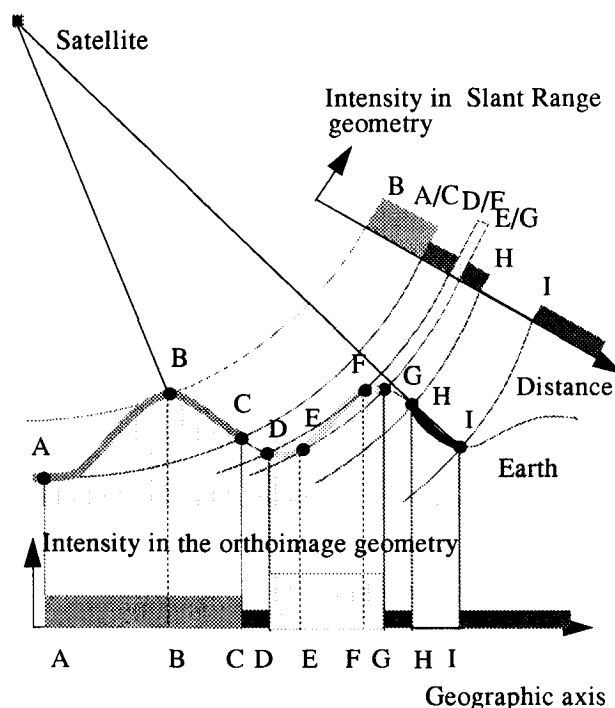


Fig. 2 : Radar geometrical problems

Figure 2 illustrates the interpolation process to obtain the radiometry for the geocoded product. Only the CD, GH and HI segments are unambiguous in this example. AB and EF are inverted (overlays). This diagram explains why the overall intensity in our geocoded product is not preserved. Redistributing energy is not that easy and several solutions can be right in some places and wrong in others. Choices depending on the particular use of the radiometry in different applications will have to be made.

In our case where a simple paper image has to be generated, the visual rendering is the most important aspect and is the main reason for our interpolation and radiometry transformations: bright areas (induced by the relief) are dilated in the final result. It has also to be considered that the photo-product being encoded on 8 bits we have to apply a radiometric transformation to the 16 bits ERS orthoimage generated.

Without filtering speckle noise effect persists in the SAR orthoimage. Filtering to reduce noise in homogeneous areas while preserving structure details is a real challenge (Ref. 3) and we are still looking for an efficient solution.

3. DESCRIPTION AND ANALYSIS OF THE PRODUCTS

3.1 Image maps produced

A total of twelve maps at various scales have been produced on three sites. For each site we produced SPOT and ERS-1 image maps.

The first site over FREJUS in the south of France, presents a variety of land cover, many infrastructures, a coastal zone and a moderate relief with high slopes. We generated five products at the scale 1/50,000: one SPOT P (pixel size 10 m), one SPOT XS (pixel size 20 m), one ERS-1 (pixel size 20 m), one SPOT P mixed with ERS-1 (pixel size 10 m), and one SPOT XS mixed with ERS-1 (pixel size 20 m). In the mixed products, the clouds in the selected SPOT images have been replaced by ERS-1 data. These products are actually SPOT products with ERS-1 patches.

The second site over SOUTHAMPTON (south of England) corresponds to an important urban area with a port and a coastal zone and an important agriculture area with large fields over low relief. Two products, a SPOT P (pixel size 10 m) and an ERS-1 (pixel size 10 m), have been generated at the scale 1/50,000, and two other products, a SPOT P (pixel size 10 m) and an ERS-1 (pixel size 20 m), have been generated with the same initial images at the scale 1/100,000.

Finally over French GUYANA, an area almost entirely covered with tropical forest, moderate relief and very few agriculture patterns, we have produced three image maps: one SPOT XS (pixel size 20 m) and one «3 dates ERS-1 color composite» (pixel size 40 m) at the scale 1/100,000 and one ERS-1 (pixel size 40 m) at the scale 1/200,000.

The different ERS images have been rectified at various pixel sizes to evaluate the effect on geometry and planimetry.

3.2 Production line

The image maps have been produced using the IGN ESPACE industrial production line, with existing operational tools originally developed for optical images. The production involved five steps.

We start with a radiometric enhancement (SPOT only) consisting in a local linear stretching (64x64 pixels), a global linear stretching and a texturation (edge enhancement).

Then we define the map extent and the subsequent extraction. We perform cloud cover delineation and image patch (SPOT mixed with ERS-1, Frejus site only), we generate geographic and cartographic coordinates overlay, we produce image layer film (Vizir) (figure 3 and 4), and finally marginal information, toponyms and map layout are gathered into a second film (layout in vector mode).



Fig. 3: Image layer of Southampton area with geographic and cartographic coordinates, scale of 1/100,000.

The production of the image film (Vizir) as well as the films combination and photographic enlargement have been carried out by SPOT IMAGE.



Fig. 4: Image layer of Guyana area with geographic and cartographic coordinates, scale 1/200,000.

3.3 Cartographic evaluation

a) ERS image maps evaluation

The advantages and limitations of image maps from optical sensors are well defined by now, the question mark then lies on the quality of the ERS products. For a topographic map, the quality involves a geometric (where is my object) as well as a planimetric aspect (what is my object) to be evaluated.

GEOMETRY

Evaluation of the generated products gives a relative location precision between SPOT and ERS-1 better than one pixel (when using SPOT DEMs). The absolute location precision depends on the quality of existing cartographic documents and DEM. For the Frejus and Southampton areas it lies between 10 to 20 m. For the French Guyana it ranges from 20 to 100 m due to the poor quality of the DEM (10 to 50 meters accuracy).

PLANIMETRY

For the Frejus (figure 5) and Southampton sites there are major discrepancies between existing map contents, SPOT capabilities and ERS-1 capabilities. ERS-1 shows a consistent lack of roads exhaustivity.

The major criteria for road recognition with ERS is orientation, as compared to size for SPOT, hence the unreliability.

One can mention a disturbing lack of planimetric homogeneity in the ERS-1 data, because of the influence of relief lightening direction.

Some interesting features (relief, hydrography) can be interpreted in the ERS-1 image map on the French Guyana site as can be seen on figure 6. Some equipment features are clearly visible in the Southampton docks.

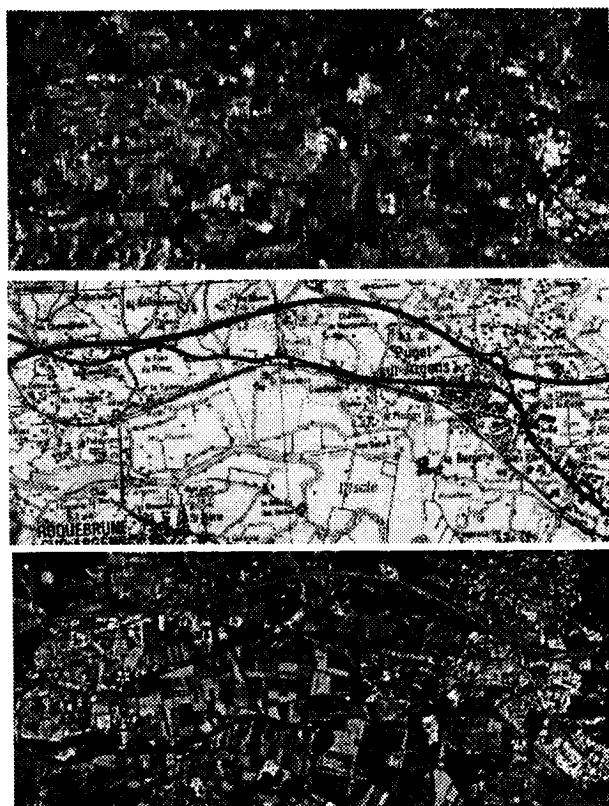


Fig. 5: Comparison of the cartographic potential of ERS-1 and SPOT images. 8km x 3.5km site west of Fréjus. Map at scale 1/50,000 ©IGN.

ERS-1 images have therefore a definite potential for some thematic visual interpretation, the limite being again exhaustivity and homogeneity (and the objective means to measure them).

b) ERS image map, an operational product?

The conclusion on the feasibility side is that although ERS-1 image map production is an operational process, the possible scales and uses of the products have to be clearly defined and understood on a case by case basis.

The planimetric content is suitable for medium to small scale cartographic coverage (1/100,000 to 1/1,00,000).

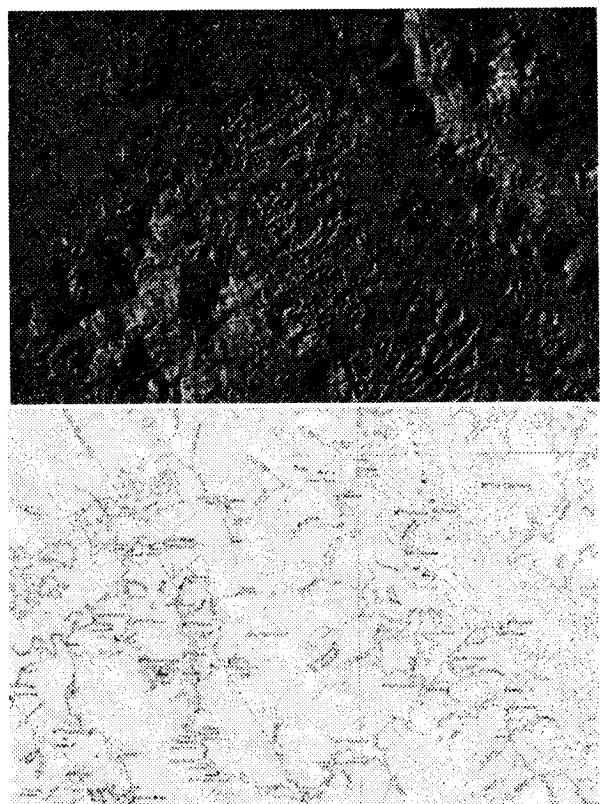


Fig. 6: Cartographic potential of ERS in tropical forested areas. 30km x 22km site south of Cayenne (French Guyana). Old map at scale 1/100,000 ©IGN.

The geometric precision is entirely dependent on the precision of the DEM, requiring a two steps process in most tropical areas with no cartographic data and heavy cloud cover. A DEM with interferometry for instance has to be generated to produce the ERS image maps.

With these limitations in mind, ERS-1 image maps compare favourably with old small scale cartographic documents over tropical forested areas.

4. ERS-1 IMAGE MAPS USER NEEDS

4.1 User demand on image maps

Users need geographic information and not Remote Sensing data. The Earth Observation Satellite Imagery provide effective and appropriate information and particularly for cartographic uses. Users have seen interests in using image maps for their activities, in particular in forestry, territory planning, environmental

studies, defence activities and cadastral projects and there is a strong demand for such products.

Market for image maps is growing and more and more users are integrating them in their management systems; the needs are now fulfilled by optical Earth Observation Satellites (SPOT, LANDSAT,...) when cloud free images can be acquired.

4.2 ERS-1 and SPOT image maps

With the arrival of ERS-1, new possibilities are now offered in terms of information and image acquisition. Therefore, three main questions have to be asked: Is it possible to offer ERS image maps to users? What kind of products could be interesting to users? How ERS-1 image maps and SPOT image maps are complementary?

The different products we generated for this pilot project tried to answer these questions.

4.3 Suitability of ERS-1 image maps

Many questions have been raised by this project:

Information contents of the ERS-1 image maps have to be balanced with interest of users for this information. The level of complementarity for SPOT and ERS-1 image maps is not constant. It is a function of the landscape and the end user requirements. Scale of edition of the ERS image maps regarding user needs and ERS information contents is a very important factor to take into account. Finally, which processing (particularly processing for visual edition) for which thematic uses do we have to perform?

Some answers could be given but more tests and products have to be made. Users have to be surveyed to know their interest in ERS image maps and the use of combined SPOT and ERS image maps. ERS-1 images are more adapted for image maps at 1/100.000 scale or smaller, due to their resolution. Identification of land cover and infrastructures is more effective and detailed on SPOT image maps; by comparison, interpretation of ERS-1 image maps is not so accurate except for specific targets. For geomorphology with vegetation ERS-1 image maps are very interesting on a tropical landscape; many information can be seen and particularly information of geomorphology and relief for areas covered by forest. ERS-1 image maps are of course of great interest for users interested in tropical areas or for countries frequently covered by clouds.

Some activities like geology, forestry, cartography could benefit from using optical (even partially

cloudy) and radar image maps on tropical areas as there are complementary in term of information.

5. CONCLUSION

Terrain geocoding is a necessity when we want to compare or use the complementarity of data from different sensors. For SAR imagery, depending on the area, different problems may arise in generating SAR geocoded data. On a specific case with a lot of constraints we showed a processing chain to generate image maps products. Although the preliminary conclusions, based on the generated products, express the limitations of the ERS-1 products, there seem to be potential use of such products. It is time to survey the final users and answer the many questions raised by this study, in terms of scale, merging and additional processings. Nevertheless, the SPOT/ERS1 image map application presented, opens the challenge to merge SAR data with other non-SAR imagery as a preprocessing stage for data analysis. The combined potential of the different data is not yet evaluated, but with the large number of SAR satellites such as J-ERS, ERS-1/2, ALMAZ or RADARSAT, this challenge is important to take up if we want to gain from the multiplicity of orbiting remote sensing platforms.

6. BIBLIOGRAPHY

- 1- John C. Curlander, Robert N. McDonough, "Synthetic Aperture Radar ; systems & Signal Processing". A Wiley-Interscience publication 1991.
- 2- Qian Lin , John F. Vesely and Howard A. Zebker, Topography estimation with interferometric synthetic aperture radar using fringe detection". *IEEE Trans. Geoscience and Remote Sensing* , 1991.
- 3- A. Lopes, E. Nezry, R. Touzi, H. Laur, "Maximum A Posteriori Speckle Filtering and First Order Texture Models in SAR Images". Proceedings of IGARSS'90, Vol.III, p. 2409-2412, Washington D.C., May 1990.

DEVELOPMENT OF AN INTER-TIDAL DIGITAL ELEVATION MODEL FOR THE U.K. LAND-OCEAN INTERACTION STUDY USING ERS-1 SAR DATA.

David Mason¹, Ian Davenport¹, Roger Flather², Brian McCartney² and Gary Robinson¹.

1. Natural Environment Research Council Unit for Thematic Information Systems (NUTIS), Dept. of Geography, University of Reading, Reading RG6 2AB, U.K. (Tel: (+44)-734-318743 Fax: (+44)-734-755865).
2. Proudman Oceanographic Laboratory (POL), Natural Environment Research Council (NERC), Bidston Observatory, Birkenhead, Merseyside L43 7RA, U. K. (Tel: (+44)-51-653-8633 Fax:(+44)-51-653-6269).

ABSTRACT

Progress towards the development of a method for constructing a Digital Elevation Model (DEM) of an inter-tidal zone using remote sensing and hydrodynamic modelling is described. The method should allow the construction of an inter-tidal DEM over large areas relatively quickly and cheaply, and is particularly suited to SAR satellite data because the all-weather day-night capability of SAR allows a much higher image acquisition rate than that achievable using visible-band satellite sensors. The resulting DEM could be used for the development of improved hydrodynamic models, and for studying sediment mass transport in the inter-tidal zone.

1. INTRODUCTION

This project, ERS-1 Pilot Project PP2-UK6, is also part of the U.K. Land-Ocean Interaction Study (LOIS). LOIS is a U.K. Community Research Programme which is being undertaken by scientists from the Natural Environment Research Council and Higher Education Institutions. It will provide an integrated holistic view of how coastal ecosystems work, and how they are likely to respond to future environmental changes.

The provision of accurate topography and bathymetry in the coastal zone is an important underpinning activity in LOIS, as many of the process studies require such data to be available. As part of this activity, this project is developing a method for constructing an accurate Digital Elevation Model (DEM) in the inter-tidal zone in the main LOIS study area between the Humber and the Wash on the U.K. East Coast, using a combination of remote sensing and hydrodynamic modelling techniques. The methodology developed should be sufficiently general to be applicable in other areas also.

The method (Figure 1) involves determining the horizontal position of the land-sea boundary from a remotely sensed image using image processing techniques, then superimposing on this boundary the heights relative to mean sea level obtained with a knowledge of the total tide plus surge water level from a hydrodynamic model run for this area with the atmospheric conditions pertaining at the time of

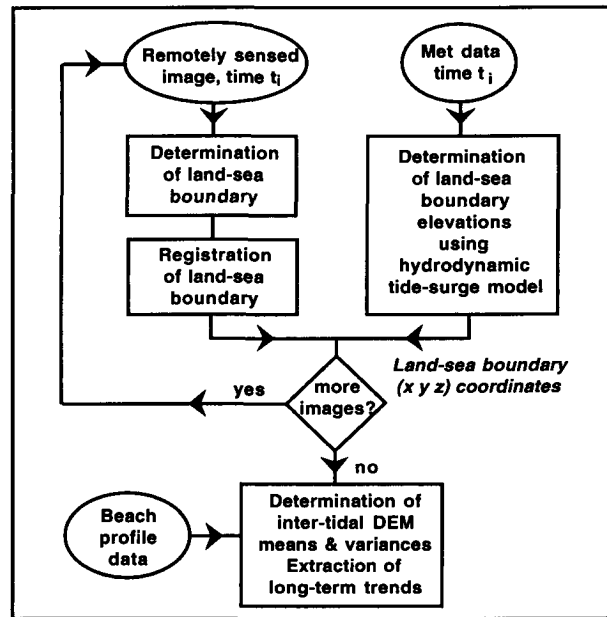


Figure 1. System flow diagram.

image acquisition. From multiple images obtained over a range of tide and surge elevations, a set of heighted land-sea boundaries within the inter-tidal zone can be constructed, and from this a gridded DEM may be interpolated. In effect, the sea is being used as an altimeter (Refs. 1,2).

The ability to construct an accurate inter-tidal DEM over large areas relatively rapidly would have two main uses. Firstly, it would lead to the production of improved tide-surge models. Short-term changes in sea-level are predominantly due to the tides, and to the effects of storms. Winds associated with a storm can raise or lower sea level by several metres in a matter of hours, producing a storm surge. These are superimposed on the normal astronomical tides, and may cause flooding of coastal areas if the peak surge occurs at the time of high tide. Forecasts of sea levels are commonly made using numerical models. Hydrodynamic tide-surge models solve the set of partial differential equations expressing the conservation of mass and the conservation of momentum for the sea (Ref. 3). Because both the

resistance term and the wind stress forcing term (which generates storm surges) in the hydrodynamic equation of motion are inversely proportional to water depth, an accurate knowledge of bathymetry is essential for the correct modelling of the tide and surge, particularly in shallow water. In addition, improved results for estuaries and shallow embayments can be achieved by appropriate treatment of sub-grid scale features, for example by estimating the fraction of each model grid cell which is covered by water at each time step in the model calculation (Ref. 4). Both these aspects can be addressed using the improved inter-tidal topography generated by the method. Better knowledge of bathymetry would thus lead to more accurate prediction of flooding.

Secondly, it would be possible to detect changes in the DEM as a function of time in order to measure sediment mass transfer within the inter-tidal zone. This might occur as a result of a major storm season, or more slowly due to sea-level rise caused by global warming. It would allow the calculation of changes in volumes of banks and salt marshes, and the display of areas of sedimentation and erosion, for comparison with the predictions of sediment transport models.

An example of erosion in the LOIS study area is that occurring along the Holderness Coast. This section of coastline between Flamborough Head and Spurn Head is backed by glacial till cliffs which are renowned for their very rapid rate of erosion of on average 1.7 m/year. The resulting annual supply of one million cubic tons of sediment to the North Sea represents the largest single coastal source. It has been observed that the most rapid rate of erosion occurs at the positions of low sections of beach which form irregularly-spaced rhythmic features along the coast known as 'ords' (Ref. 5). The ords migrate southwards at a rate of over 0.5 km/year, moving their associated zones of rapid cliff erosion with them.

Considering changes occurring over a longer timescale, sea-level rises due to global warming in the coming century are predicted to be substantially larger than those experienced during the present century, with a mean predicted rise of about 50cm per 100 years (Ref. 6). Rising sea levels generally lead not only to shoreline retreat but also to beach erosion. If these predicted rises do indeed materialise, the implications for coastal geomorphology will be profound. An example is the likely impact on coastal salt marshes, which are important not only ecologically but also from a socio-economic standpoint. They can provide coastal communities with protection from storm surges, as the presence of vegetation mitigates flood levels and flood velocities. If marsh accretion is less than sea level rise, soil waterlogging may prevent adequate nitrogen uptake by plants and the marsh may be lost. This may necessitate the building of an expensive sea wall.

If it proves possible to use satellite imagery to build an accurate inter-tidal DEM, this would give the great advantage of being able to construct a DEM over large areas relatively rapidly and cheaply. One feature of the method to be investigated in the project is its accuracy. There should be a height uncertainty of a few centimetres or so due to the hydrodynamic model, providing the weather is reasonably calm. There is also likely to be an uncertainty of about a pixel in the land-sea boundary positions. The tidal range in the LOIS area is about 5m, with an average beach width of say 250m, giving an average beach slope of 1 in 50. For ERS-1 SAR data this translates to a height uncertainty of about 25cm, so that the dominant error should be due to the satellite resolution. On a flatter beach (1:500 slope) this height uncertainty would be only 3cm.

In contrast, the conventional method of surveying the inter-tidal zone by geodetic levelling is accurate to about 1cm in height (though this level of accuracy is probably unnecessary due to natural short-term variations in beach level (see below)). This method is expensive, and large areas can be sampled only sparsely and relatively infrequently. The proposed method could complement such conventional surveying. Considering other satellite-based methods giving high spatial resolution, DEMs produced from SPOT stereo image pairs have a height accuracy of ~5m. It appears difficult to construct a DEM using SAR interferometry in an inter-tidal region. Assuming that two images taken at low tide are used to construct the interferogram, there is often loss of coherence between corresponding pixels due to different beach drying conditions and to the low radiometric response of wet sand in SAR images (Ref. 7). It is possible to obtain height resolution of ~1cm using aircraft altimetry though this would be expensive for large areas. Photogrammetric techniques using aerial stereo photography could also approach this accuracy, but would again be expensive.

One of the problems of developing an inter-tidal DEM is that the inter-tidal region is a highly dynamic area. A single large storm can alter beach levels significantly, and several months may be required for a beach to recover from such an event. This leads to the need for a statistical approach to the analysis of inter-tidal heights. Ideally at each point a mean beach height and its variation as a function of time is required, in order for long-term trends to be determined (Ref. 8). This statistical approach requires many more satellite images than would be necessary if the beach was a static entity. The all-weather day-night capability of SAR allows a much higher image acquisition rate than that achievable using visible-band remote sensors, even though the multi-spectral capability of the latter may make detection of the land-sea boundary easier. A data set of about 50 ERS-1 SAR scenes of the LOIS area has been built up covering a 2-year period.

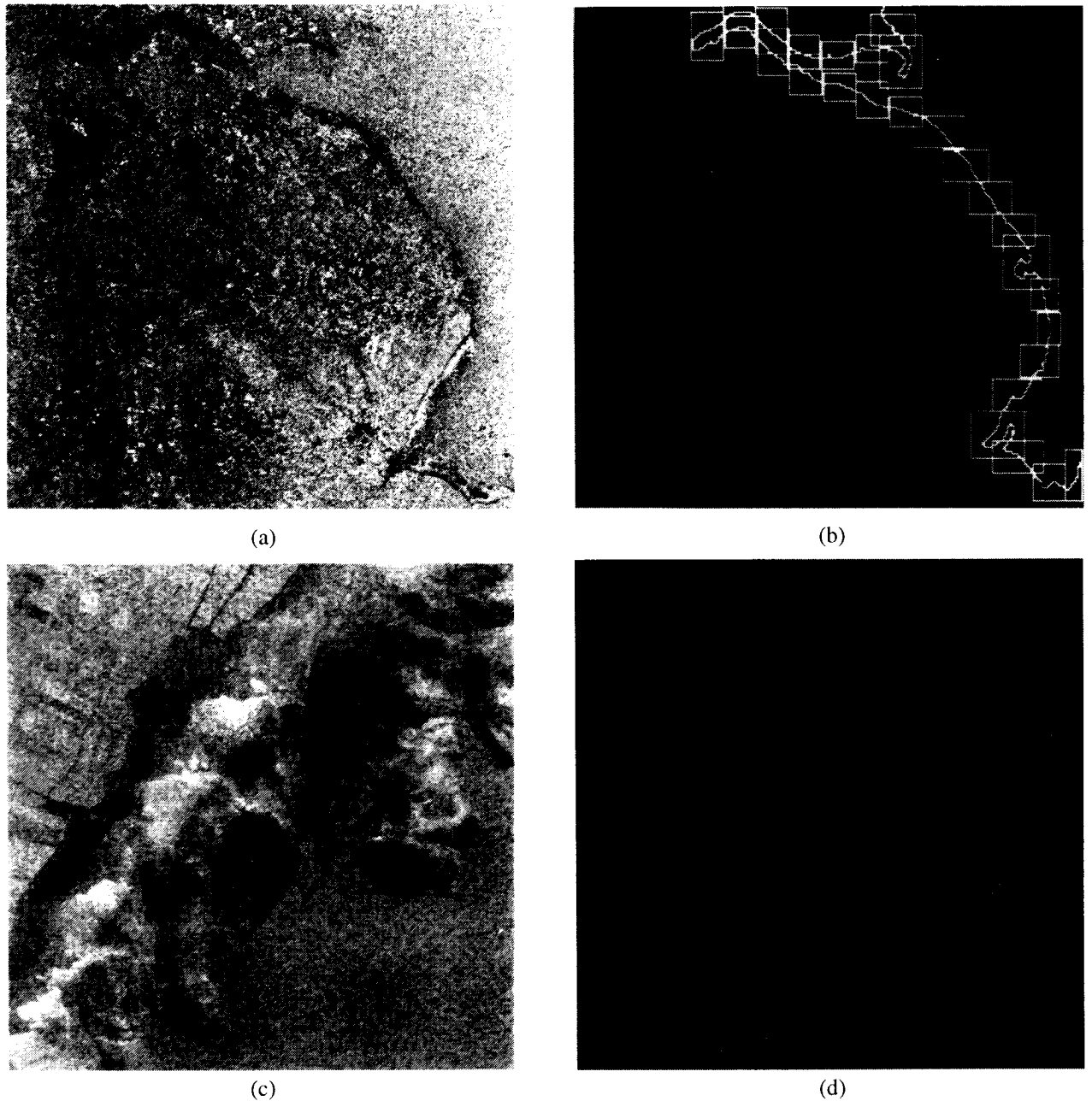


Figure 2. Semi-automatic delineation of the land-sea boundary. (a) ERS-1 SAR scene of U.K. Humber/Wash area, (b) set of rectangles generated along land-sea boundary, (c) 512 x 512-pixel sub-image at full resolution, (d) land-sea boundary segments from Figure 2(c).

2. METHODOLOGY

2.1 Semi-automatic delineation of the land-sea boundary

Due to the substantial effort and subjectivity involved in manual delineation of ~100km of land-sea boundary in each SAR image, a semi-automatic method of delineation is under development. Previous work on this problem is described in Ref. 9. The method attempts to improve on the positional accuracy achieved there without necessarily extracting a continuous land-sea boundary. Whilst examination of

the SAR images confirms the feasibility of determining the land-sea boundary by eye over large stretches of the imagery (see *e.g.* Figure 2c), in some areas this becomes very difficult. This is generally due to variations in the radiometric response of different points on the beach, but may occasionally occur because at low wind speeds both sea and beach may be too dark to differentiate. As a result, the method attempts to determine just those segments of boundary in which it has high confidence, rather than distinguishing long continuous boundaries stopping only at the image edges. It is also designed to process complete SAR images efficiently.

The procedure comprises a sequence of algorithms which execute within the MuSIP image-processing system (Ref. 10), which is capable of dealing with complete SAR images and their vector segmentations in tiled form in an integrated fashion. It begins by finding a rough division between land and sea working on a complete ERS-1 SAR PRI scene at low resolution, and then applies high resolution processing in the neighbourhood of the land-sea boundaries. Whilst a complete scene contains about 8000x8000 pixels, the inter-tidal zone is a strip about 500 pixels wide only, so that by limiting high resolution processing to this strip a saving of ~ 16 in computation time can be made.

The low resolution processing involves smoothing the original image (Figure 2a) using non-overlapping averaging to obtain an image of reduced size and substantially reduced speckle. In the reduced image the sea can be differentiated from the land because it is much smoother. The method assumes that sea occupies a substantial percentage (>20%) of the image. Edges are detected in the reduced image, and an image of edge strength per unit area (a measure of texture) is constructed. A texture segmentation of this image is made, and regions of sea are selected as large connected regions of low texture contrast which coincide with the image frame. Boundaries of these regions which do not coincide with the image frame are extracted, and a set of rectangles is generated along these boundaries within which to perform high resolution processing (Figure 2b).

Further processing at full resolution is then applied within each rectangle (*e.g.* Figure 2c). Edges are detected using the contrast ratio edge detector (Ref. 11), which has a constant false alarm rate in the multiplicative noise found in SAR imagery. An edge refinement stage using non-maxima suppression, hysteresis thresholding, edge thinning and edge linking follows. The region most likely to be sea is selected as the connected region touching the image frame which best exhibits the combined attributes of large size, low edge density and a centroid position similar to that of the sea region predicted for this sub-image from the low resolution processing stage. Land-sea boundary segments are then extracted as connected edge segments bounding this region which have high edge strength, do not intersect the image frame, exceed a certain length, and have a similar mean intensity half the contrast ratio edge detector window width away on their seaward side as that of the sea region they bound (Figure 2d). The vector land-sea boundary segments may be edited manually to correct any errors introduced in the automatic delineation process, before being registered to ground coordinates.

To confirm the accuracy of the land-sea boundary positions estimated from the imagery, ground measurements have been made at time of satellite overpass during two field visits. The land-sea boundary positions determined from the images have been found to agree with the measured ground

positions to within a pixel or so. Due to the numerous ways in which Doppler ambiguities in the SAR processing can lead to errors in the positions of nearshore waves, it is not obvious that edge positions deduced from the image will correspond to true ground positions (Ref. 12). One difficulty experienced with the method is in deciding the position of the true land-sea boundary in the vicinity of stream networks entering the sea from the beach.

2.2 Development of the hydrodynamic model

A fine resolution (1.2km grid) hydrodynamic model for the U.K. East Coast between Whitby and Cromer is under development. The model links to a 12km resolution shelf model developed by POL and used to provide operational flood warnings in the U.K.. The East Coast model is driven by tidal input consisting of 26 harmonic constituents and a storm surge component on its open boundaries, interpolated from shelf model solutions, and by meteorological forcing derived from assimilation runs of the U.K. Meteorological Office's "limited area" atmospheric model. The model has been run to simulate the tides

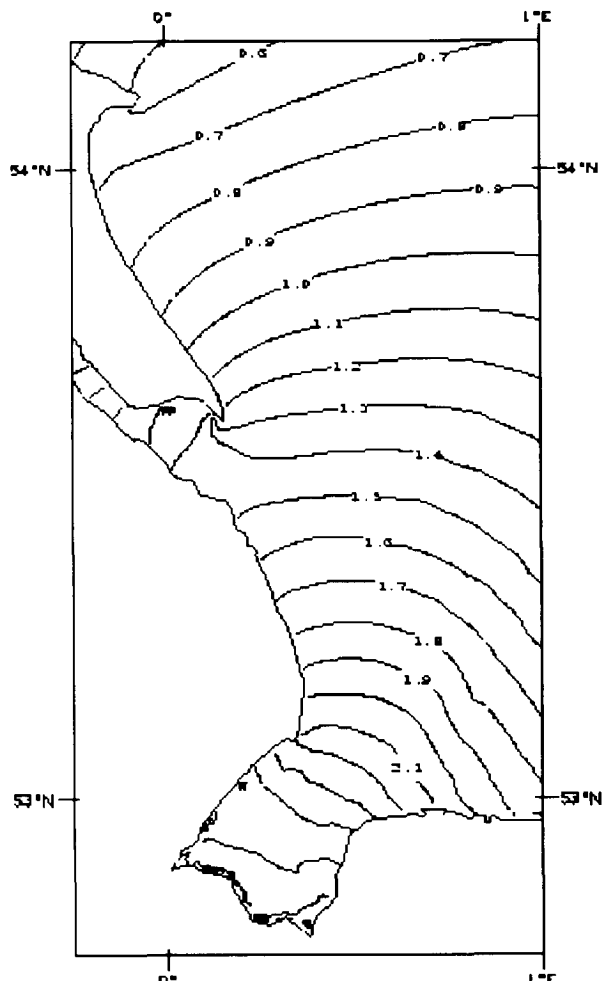


Figure 3. Hydrodynamic model output.

for 6-month periods and tidal analyses of hourly output arrays carried out. Comparisons with harmonic constants from tide gauges provided a check on the model accuracy and have allowed some optimisation of open boundary forcing and dissipation to be made. The model tidal predictions are generally of good accuracy, though errors increase in the upper part of the Humber estuary. This is thought to be due to the neglect of river flow, which will be taken into account in future versions of the model.

Model runs, including tide and storm surge components, have also been carried out for periods of two months during the winter of 1993-94 and comparisons of the surge component with values extracted from tide gauge measurements carried out. Comparisons of model water levels and ground measurements have also been made to validate the model heights. For the two field visits made so far, the ground measurements and model heights agreed to within a few centimetres. Figure 3 shows an example of the model output with contours of water level in metres relative to the model datum at ERS-1 morning overpass time on 5th December 1993.

Future work will include the development of local refinements with resolution ~100m or less to provide details of small scale variations in the coastal zone. These will be developed in an iterative procedure in which model water levels provide heights for the construction of an initial DEM, which in turn will provide improved bathymetry to refine and improve the model solutions. Waves are not taken into account at present, and, to minimise elevation errors *e.g.* due to wave setup (Ref. 13), only images acquired during periods of low wave activity are currently used to construct the DEM. It is intended to incorporate the effect of waves in the near future by making use of coupled wave - tide - surge models being developed at POL.

2.3 A preliminary DEM

A preliminary gridded DEM has been constructed from a set of six 512x512 pixel sub-images of the Wrangle Flats area. These span the complete tidal range, and were obtained mainly during the First Ice Phase (3-day repeat cycle) of ERS-1 between January and March 1992. The land-sea boundaries (Figure 4a) were converted to a Triangulated Irregular Network (TIN) (Figure 4b) using Arc/INFO, and a gridded DEM was generated from this (Figure 4c). Heights are relative to the model datum. The DEM is preliminary as the boundary heights estimated from the hydrodynamic model contained no surge component, and also because it was assumed that no change in the topography of the inter-tidal zone occurred within this period.

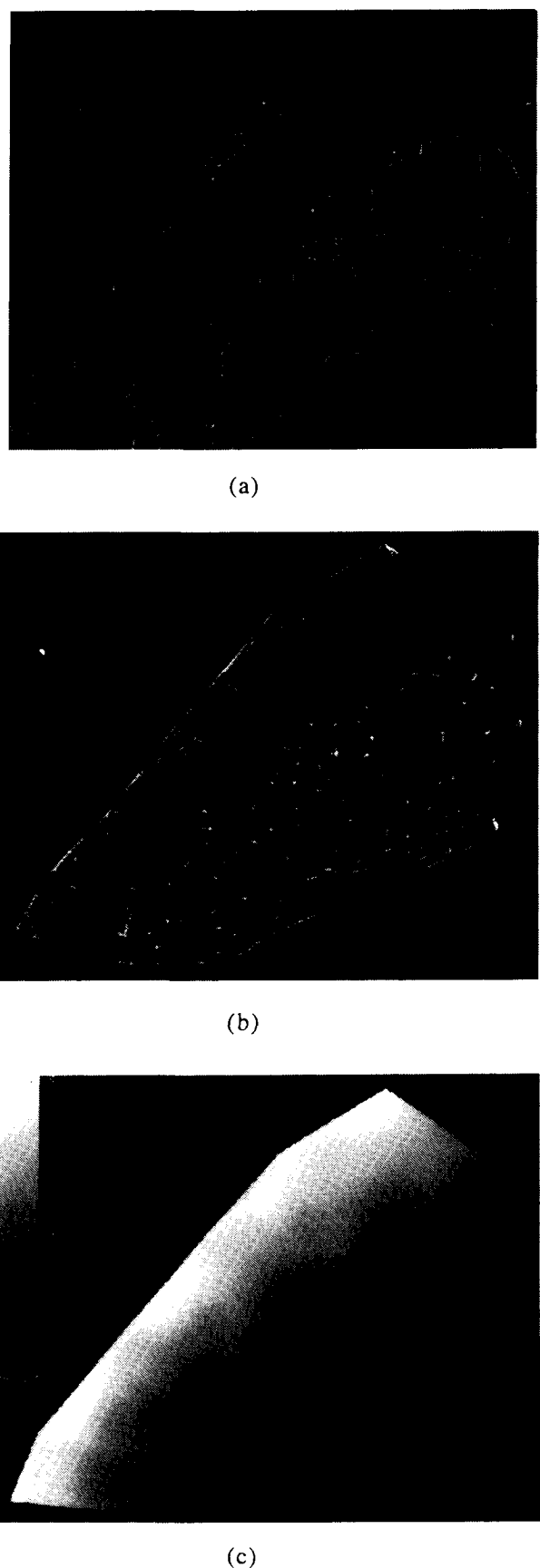


Figure 4. Preliminary DEM. (a) Land-sea boundaries, (b) TIN generated from these, (c) gridded DEM interpolated from TIN.

3. FUTURE WORK

Further development of the semi-automatic land-sea boundary detection technique and the hydrodynamic model will occur, together with extensive further ground-referencing. A method for constructing a statistical DEM from a set of land-sea boundary segments obtained over a range of times and tidal/meteorological states, together with contemporaneous ground survey data, will also be developed.

4. ACKNOWLEDGEMENTS

This work was funded partly under NERC contracts F60/G6/12 and GST/02/777.

5. REFERENCES

1. Koopmans, B. N. and Yiman, W. (1992). ERS-1 imaging radar over the Waddensea-N, Netherlands. Proc. First ERS-1 Symp., Cannes, France, 4-6 Nov. 1992. 861-865.
2. Jensen, J. R., Cowen, D. J., Althausen, J. D., Narumalani, S. and Weatherbee, O. (1993). The detection and prediction of sea level changes on coastal wetlands using satellite imagery and a geographic information system. Geocarto International (4) 87-98.
3. Flather R. A., Proctor R. and Wolf J. (1991). Oceanographic forecast models, in Computer Modelling in the Environmental Sciences (Eds. Farmer D. G. and Rycroft M. J.). Oxford University Press. 15-30.
4. Flather, R. A. and Hubbert, K. P. (1989). Tide and surge models for shallow water - Morecambe Bay revisited, in Modeling Marine Systems (Ed. Davies, A. M.). CRC Press, Boca Raton, Florida. Volume 1, 136-166.
5. Pringle, A. W. (1985). Holderness Coast erosion and the significance of Ords. Earth Surface Processes and Landforms 10, 107-124.
6. Stewart R. W., Kjerfve B. and Dwivedi S. N. (1990). Relative sea-level change: a critical evaluation. UNESCO reports in Marine Science, 54, 1-21.
7. Rossi, M. (1994). Private communication.
8. Brampton, A. H. (1990). Coastline monitoring. Report IT 345, February 1990, Hydraulics Research, Wallingford, U.K.
9. Lee, J-S. and Jurkevich, I. (1990). Coastline detection and tracing in SAR images. IEEE Trans. Geoscience and Remote Sensing, 28(2), 662-8.
10. Mason D. C., Hindley N., Johnson D. G., Jones-Parry I. H., Oddy C. J., Pike T. K., Plassard T., Rye A., de Salabert A., Sawyer G., Serpico B. and Wielogorski A. (1992). The MuSIP multi-sensor image processing system. ITC Journal 1992-1 73-86.
11. Touzi, R., Lopes, A. and Bousquet, P. (1988). A statistical and geometrical edge detector for SAR images. IEEE Trans. Geoscience and Remote Sensing, 26(6), 764-773.
12. Ulaby, F. T., Moore, R. K. and Fung, A. K. (1986). Microwave remote sensing (Volume 3). Artech House, Inc. MA, USA. 1722-1726.
13. King, B. A. (1990). Observations of wave-induced set-up on a natural beach. J. Geophysical Research 95(C12), 22289-22297.

TOPOGRAPHIC AND ENVIRONMENTAL MAPPING OF TIDAL FLATS USING ERS-1 SAR IMAGERY

Fergus Kennedy and John Matthews

School of Ocean Sciences, Menai Bridge, Anglesey,
Gwynedd LL59 5EY, U.K.
phone 0248 382586, fax 0248 716367

ABSTRACT

Mapping the subtle topography of tidal flat regions can be a laborious and even dangerous task. However, baseline information on tidal flat topography for immediate use in coastal zone management can be derived from ERS-1 SAR imagery. In general, the signature of a tidal flat region in these data varies from light (dry, exposed and rippled sand) to dark grey (flats covered by a surface water film) and then disappears (merges with open sea signature) as the flats are submerged. For regions of high tidal range, intertidal topography can therefore be mapped by observing the change in location of the land/ sea interface over the tidal cycle. In this study, a sequence of 4 SAR images of Traeth Lafan sands (N.Wales) from different tidal states was used to construct a contour overlay by digitizing the boundary of the exposed sand on each image. The SAR topographic map was consistent with earlier knowledge of the area and showed that the highest regions ($> \sim 3.9\text{m}$ above chart datum) lie in the central portion of the landward fringe, with projections of high sand running out to the west and north. Combining the topographic data with a knowledge of the locations and paths of sewage slicks defined in ERS-1 SAR imagery enable us to identify those areas of the Traeth Lafan sands most vulnerable to contamination. Since commercial cockle dredging and other fishing activities take place on Traeth Lafan such information is of great value.

1. INTRODUCTION

The topography of tidal flats is known to have an important influence on the distribution of intertidal organisms since it affects the duration of tidal exposure (Eagle et al. 1974, Yates et al. 1993). Information on topography, when combined with data on effluent discharge, sediment type and a variety of other environmental variables, can form an integral part of a predictive model for tidal habitats. In this study we show how ERS-1 is used to provide baseline information on topography for practical application in coastal zone management.

Traeth Lafan sand flats in North Wales were the

focus of the study (See fig. 1 for map). The area is a statutory Site of Special Scientific Interest (SSSI), a local nature reserve and a Special Protection Area (SPA) under the European Community Conservation of Wild Birds Directive. Commercial exploitation of cockles and mussels takes place in certain parts of the sand flats and concern has been expressed over possible detrimental impacts on invertebrate stocks and the bird populations which feed on them as a result of these activities. In addition, several domestic sewage outfalls discharge untreated sewage into the sea on or close to Traeth Lafan. The wide variety of potentially conflicting usages of this region contribute to a complex resource management problem and make the need for accurate and timely geographical and environmental information more pressing than ever.



Figure 1. Map showing the location of Traeth Lafan sands

Early ERS-1 publicity material released by ESA demonstrated clearly the ability of SAR to provide information on the extent of exposed tidal flats. By

combining information from a number of SAR images taken over a range of tidal heights, a topographic map of an area of tidal flats can be constructed. Note that our approach is not concerned with the generation of a rigorously accurate map (in terms of height contours). Rather, we aim to show that even the basic information derived from a simple approach can have an immediate application in coastal zone management.

2. METHOD

Four SAR images and one Landsat image representing a range of tidal states over Traeth Lafan were obtained (Table 1). Image subsets were made to cover the study area and these were rectified and georeferenced to the Ordnance Survey map projection.

Table 1

IMAGES USED IN THE CONSTRUCTION OF THE TOPOGRAPHIC MAP

Image	Orbit No.	Frame No.	Date	Overpass Time	Tidal Height	Flood/Ebb	Up/Down Pass
SAR	5108	2529	07/07/92	11:14 GMT	1.9m	Flood	D
Landsat	204*	23**	22/07/84	10:30 GMT	2.5m	Ebb	-
SAR	11225	1071	07/09/93	22:18 GMT	3.0m	Flood	U
SAR	4104	2529	28/04/92	11:14 GMT	3.9m	Ebb	D
SAR	9815	2529	18/05/93	11:14 GMT	4.6m	Ebb	D

*Path Number **Row Number

From each image an overlay plane was then created by digitizing the sand/ sea and the land/ sea boundary (largest change in backscatter consistent with the context) to form a polygon representing the extent of the tidal flats at the time of image acquisition. These overlay planes could then be colour coded and combined to produce a map. Estimates of tidal heights at the time of image acquisition were obtained using tide tables produced by the Unit for Coastal and Estuarine Studies in Menai Bridge and gave predictions of tidal height on an hourly basis for the local area. The tidal height estimates were included in the map as a key to the overlay planes.

3. RESULTS

The four rectified and georeferenced SAR images of Traeth Lafan at different tidal heights are shown in figure 2. Note that in images C and D the surface of the sand flats is darker in colour than in A or B. This is probably due to the fact that C and D were acquired on ebb tides and A and B on flood tides. Thus the surface of the sand is well drained in the latter two cases, whereas extensive layers of surface water are present in C and D.

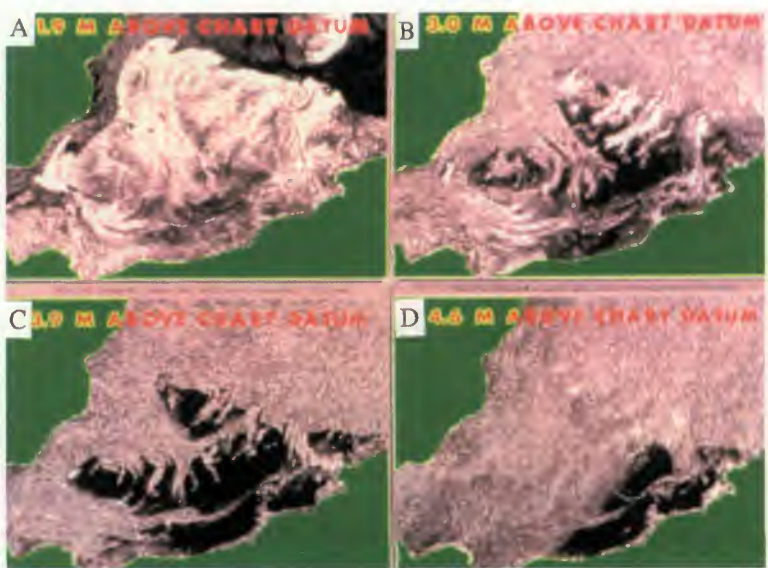


Figure 2. SAR images used in the construction of the topographic map: A 1.9m above chart datum (ACD), B 3.0m ACD, C 3.9m ACD, D 4.6m ACD.

Figure 3 shows the topographic map produced by combining the overlay planes derived from the four SAR images and one Landsat image. Generally the highest parts of the sand flats (> 4.6m above chart datum) are in the central portion of the landward fringe and show the position of a drainage channel which cuts across this higher region. Projections of high sand higher than 3.9m above chart datum run out to the north and west from the central landward portion. The similarity in extent of the images 2.5m and 1.9m above chart datum indicates that the gradient of the sand flat steepens close to the seaward fringe. The overall accuracy of the map can be improved in future by considering factors such as pressure and wind influences on tides and by using images over shorter time periods.

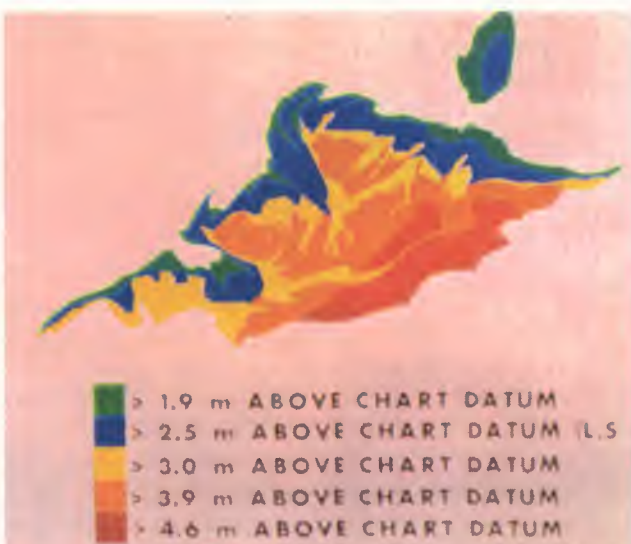


Figure 3. Topographic map of Traeth Lafan.

4. DISCUSSION

The topographic map obtained by the combination of satellite images corresponds well with existing knowledge and observations of Traeth Lafan. Topographic information derived by this method becomes particularly useful in a coastal zone management context when combined with information on other themes and from other sources. In this instance information is available (from ERS-1 SAR) concerning the path of sewage plumes close to the sand flats and (from Landsat) the distribution of sediment types on the study area.

Figure 4 shows an ERS-1 SAR image from 7th July 1992. The extent of the exposed tidal flat is visible. The locations and approximate discharge rates of known domestic sewage outfalls has been included as an overlay plane. Sea surface slicks can clearly be seen in the vicinity of the Bangor, Beaumaris, Llanfaes and Llangoed sewage outfalls. The freshwater/ surfactant input from the effluent alters the surface properties of the water in such a way that it is less prone to wind rippling and remains smooth, giving it a dark radar signature. The surface component of the sewage plume is then mapped under the particular conditions prevalent and the moment of image acquisition. By combining this information on the fate of sewage after leaving the outfalls with topographic information derived from the SAR data we can identify those areas of the sand flats which will be exposed to the effluent for the longest periods. In this case, the lowest lying areas on the far left of figure 3 (>1.9m above chart datum) would be exposed to relatively high concentrations of effluent from the Bangor outfall under the flood tide conditions prevalent in figure 4. This is indeed an area where small scale mussel harvesting takes place.

5. ACKNOWLEDGEMENTS

The authors wish to thank T. Sherwin of the Unit for Coastal and Estuarine Studies (UCES), Menai Bridge for making information on tidal height available and E.I.S. Rees of School of Ocean Sciences, Menai Bridge for his valuable advice throughout this study. We also thank staff of the ERS-1 Helpdesk at ESRIN.

6. REFERENCES

1. Eagle, R.A., Hartley, J.R., Rees, E.I.S., Rees, L.J. & Walker, A.J.M.. 1974. Ecological survey of the Lavan Sands: Invertebrate macrofauna. *University of Wales Marine Science Laboratories Benthos Research Report 74-3*.
2. Yates, M.G., Jones, A.R., Mc Grorty, S. and Goss-Custard, J.D. 1993. The use of satellite imagery to determine the distribution of intertidal surface sediments of the Wash, England. *Estuarine, Coastal and Shelf Sciences* 36, 333-344.



Figure 4. SAR image from 7th July 1992, showing locations of sewage outfalls and sea surface slicks.



Application/Utilization of Data Sets Obtained by the Combination of ERS-1 and MS Satellite Data for Monitoring of the Wadden Sea

Oliver Krämer, Peter Lohmann, Volker Sasse

Geoscan GmbH Deutsche Gesellschaft für Fernerkundung und Umweltanalytik, Gelber Stern 1,
31134 Hildesheim

Abstract

The aim of this Pilot Project PP2-D19, sponsored by DARA GmbH, was to investigate ERS-1 images in regard to an operational Wadden Sea monitoring System. Within this project time parallel ground truth data, airborne and satellite multispectral scanner data and ERS-1 radar data had been acquired. By means of remote sensing important ecosystem parameters should be visualized and analysed.

1. Geographical Description of the Investigated Area

The investigated area of Spiekeroog belongs to the backbarrier tidal areas of the German Wadden Sea and is part of an old barrier island chain. The whole Wadden Sea covers nearly 10.000 km² (FLEMMING & DAVIS 1992). The German Bight can be divided into three characteristic tidal types (REINECK 1982):

- open tidal areas
- bight or estuary tidal areas
- backbarrier tidal areas.

The investigated area can be divided into a western part and into an eastern part by the tidal flat watershed leading from Harlesiel to the island of Spiekeroog. The mean tidal range in the western part is about 2.6 m, in the eastern part 2.8 m (FLEMMING & DAVIS 1992).

Since 1000 p.d. the seaward moving dyke line causes changes in the energy level of the backbarrier deposition system. The result is a continuous shifting to coarser grain sizes (sand fractions) especially along the dyke line. The remaining mud fractions can lead back on the existence of organic layers almost the whole year long.

The existence of the large organic layers find the explanation in the high fertilizer input of the intensive agriculture along the Harlinger Land in the southern region. The fertilizer input runs to 120 kg/ha+a (HERR 1992).

These basic geographical informations are essential by interpreting (visual or automatic) the acquired data sets within this Pilot Project. As important ecosystem Parameters to monitor we chose the following:

- Hydrography (flow structures, dynamics)
- Phytobenthos Communities

- Sedimentology (grain sizes, morphodynamics).

2. Remote Sensing Data Sets

In this study we used satellite and airborne multispectral data. In 1993 we could only acquire 1 TM scene of the backbarrier tidal area, that was the reason why we used our Daedalus AMS in the winter campaign 1994. So we could ensure that the scanner data would represent exactly the situation during an ERS-1 overpass. In contrast to terrestrial surfaces the tidal surfaces are part of a high dynamic and sensible ecosystem. Object boundaries, such as field parcels, remain very constant over one period. Object boundaries in the tidal area, such as organic layers or areas of the same surface roughness, show a high dynamic within some days or weeks of monitoring (own observation during the two field campaigns).

Using the actual CIR aerial photographs a orthophotomap had been composed. That orthophotomap established the base for a DEM and for geocoding the scanner/radar data sets within one campaign.

The following list gives a short overview over the used data sets:

Field Campaign Summer 1993:

Date	Data Set
11.05.1993	TM
14.06.1993	ERS-1
10.07.1993	Daedalus (TIR)
19.08.1993	Daedalus, CIR
23.08.1993	ERS-1

Field Campaign Winter 1994

Date	Data Set
21.01.1994	ERS-1
20.02.1994	ERS-1
04.03.1994	ERS-1
	Daedalus
	b/w IR photos
	TM (possible)
22.03.1994	ERS-1

3. Ground Truth Sampling and Basic Maps

The ground truth sampling was carried out by the Senckenberg Research Institute in Wilhelmshaven. The sampling on tidal flats

had to be determined within only four hours, because of the difficult accessibility in the backbarrier tidal area and the incoming flood. The tidal dynamic causes changes in the surface roughness from tide to tide. The following sediment parameters had been investigated:

- sediment grain size (in phi units)
- sediment temperature
- sediment moisture content
- sediment surface roughness.

The results of the first campaign with 41 locations showed very clearly, that we had to overwork our locations in regard to more homogeneous sampling locations. We decided to enlarge our samples to 200 locations in the second campaign.

Although we received a high amount of existing maps in a scale of 1:25.000 such as:

- morphologic maps
- benthos communities
- sediment distribution
- organic layers (mostly green algae).

These maps were totally obsoleted (even those from 1992) and had to be replaced by new maps. The new maps had been composed by our remote sensing data sets. In contrast to the organic layer maps used before by visual delineation during an overflight, we could locate and quantify the organic layers much more precise with the scanner data.

4. Multispectral Scanner Data Sets

In combination with the CIR aerial photographs, the scanner data had been used to get updated quantitative and qualitative information of the objects within the investigated area, such as organic layers, sediment distribution and sediment moisture content.

We chose the following steps producing a sediment distribution map in accordance with the works of DOERFFER & MURPHY (1988).

1. extracting the terrestrial surfaces by delineating with polygons

2. unsupervised clustering with three classes to remove water bodies and organic layers.

As result of these steps only uncovered sediment surfaces had been displayed. So we could minimize misclassification between terrestrial surfaces and sediment surfaces. The additional removing of organic layers had been necessary, because organic layers mask the information about sediment grain sizes in multispectral scanner data. Using the sediment distribution maps of Senckenberg we could find a visual correlation between organic layers and occurrence of sediments in the mud fraction. At least the sediment classification was carried out by a supervised MLH classification, using channels of red and

NIR (COLEMAN & MONTGOMERY 1987; CONDIT 1970; DAVIS et al. 1979; GERBERMANN & NEHER 1979). In contrast to the work of DOERFFER & MURPHY (1988) a PCA brought no optimization in regard to, our work. The following grain size classes had been calculated (mean grain size of the frequent sand fraction):

- | | |
|-------------------|---------------|
| - medium sand | <2.0 phi |
| - fine sand | 2.0 - 3.0 phi |
| - very fine sand | 3.0 - 4.0 phi |
| - mytilus, shell. | |

5. First Visual Interpretation of ERS-1 Data

A short description of visual interpretation of ERS-1 data concerning our investigated area should be very useful to understand, what we can monitor with radar data in the backbarrier tidal area. In fact, the object backscattering differs completely from the known on terrestrial surfaces. Most parts of the area are covered with sandy tidal flats and rippled marks with a wavelength of 6-7 cm and a height of 0.5-1 cm. Applying the BRAGG backscattering model with regard to the rippled orientation (mostly from SW to NE) we found out, that the above mentioned rippled marks fall exactly in the highest sensitivity range of the ERS-1 C-band radar. So BRAGG reflexion occurs and the signal will contain a no quantifiable moisture information from the sediment.

Generally sandy tidal areas appear in medium-high returns, according to their rippled marks. Mud flats (very coarse silt) appear dark with low-no returns, according to their smooth surface. A smoothing of the surface is also caused by bulky organic layers and increasing tide. The increasing tide covers more and more sediment surfaces with water, so specular reflexion will occur. Because of the influence of surface roughness on backscattering an automatic separation (edge enhancement, filtering, automatic classification) (WELCH & EHLERS 1988) between water and tidal flats is at the moment not possible. Only in the scenes of January and February a separation between tidal areas and water was possible, because the tidal flats were covered with snow (it causes no return by volume scattering within the moist snow body). On the other side the snow gives no information about the sediment characteristics. The 'snow scenes' had no importance to our work. The water mask obtained from the scanner data could not be applied to the radar because of the changing tide from scene to scene.

An combination of ERS-1 data and scanner data by means of IHS or PCA showed no better results for interactive visual or automatic interpretation/classification

(HAYDN et al. 1982).

6. Hydrography

The interpretation of the flow events is done by counting mean value images of different weather periods. During a summer period without storms, changes are very unlikely. After the stormy winter period changes may be very likely. The used mean value images have the following characteristics:

- reducing the specke without filtering
- continous flow structures will be enhanced and are easy to delineate.

By overlaying the different mean value images in a RGB-colorspace morphological dynamics or sediment transportation are detectable as obvious colored areas on the screen.

7. Organic Layers

As mentioned before organic layers smooth the tidal surface and so lead to low return values in the different images. But actually is not clear if the signal comes from the bulky organic layers or indeed from the muddy sediment. The organic layers are mainly located on certain positions in the backbarrier tidal area. These areas are those of low flow velocity located near the dyke line and on inner tidal flats. At the beginning of one weather period (January or February) an initial state will be defined by an organic layer classification with scanner data. That initial organic layer coverage will be updated by the following ERS-1 scenes with a high repetition-rate. As output of the end of one year multitemporal organic layer coverages are present, which will give some important information to the scientists.

8. Object-based Sediment Classification

To achieve valuable information about the sediment characteristics, we applied the principle of an object-based filtering (MÜLLER et al. 1993). Because there should be an correlation between sediment grain size, moisture content, we used the vectorized sediment distribution map as boundary input for the filtering. But the boundaries of the filtered objects showed less correlation with the original object boundaries. So we vectorized interactively the object boundaries for every single original image. On terrestrial surfaces the object boundaries can easily be achieved by segmentation on base of TM or SPOT data, because the field parcels remain almost the same over one crop period. A multitemporal image, composed of different

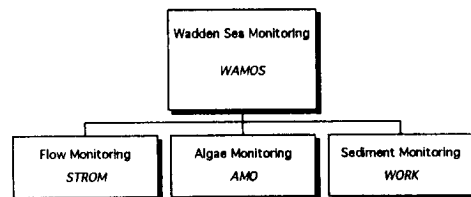
filtered radar images should show good results in regard of an backbarrier tidal flat classification.

9. Conclusion

During the summer campaign of 1994 we hope to get more detailed information about the sediment surface roughness to simulate the influence of moisture and roughness on the backscattering signal.

In the actual state of research we can say, that the parameters hydrography and organic layers are operational to monitor by applying interactive processes of visual interpretation. At the end of this Pilot Project we plan to establish an Wadden Sea Monitoring System WAMOS with the following modules:

- | | |
|---------------------------|-------|
| - Hydrography | STROM |
| - Algae Monitoring | AMO |
| - Sediment Classification | WORK. |



Literature:

COLEMAN,T.L.;MONTGOMERY,O.L. (1987): Soil Moisture, Organic Matter and Iron Content Effect on the Spectral Characteristics of Selected Vertisols and Alfisols in Alabama.- PE & RS, Vol.53, No.12, 1659-1663

CONDIT,H.R. (1970): The Spectral Reflectance of American Soils.- PE & RS, Vol.36, No.9, 955-966

DAVIS,C.F. et al. : The Use of Remote Sensing in the Determination of Beach Sand Parameters.- o.a.

DOERFFER,R.;MURPHY,D. (1988): Factor Analysis and Classification of Remotely Sensed Data for Monitoring Tidal Flats.- Helgoländer Meeresuntersuchungen, 43(1989), 275-293

FLEMMING,B.W.;DAVIS,R.A. (1992): Holocene Evolution, Morphodynamics and Sedimentology of the Spiekeroog Barrier Island System (Southern North Sea).-

GERBERMANN,A.H.;NEHER,D.D. (1979): Reflectance of Varying Mixtures of Clay Soil and Sand.- PE & RS, Vo.45, No.8, 1145-1151

HAYDN,R. et al. (1982): Application of IHS Color Transform to the Processing of Multisensor Data and Image Enhancement.- Proc. of the Int. Symp. on Remote Sensing of Arid and Semi-arid Lands, Cairo, 599-616

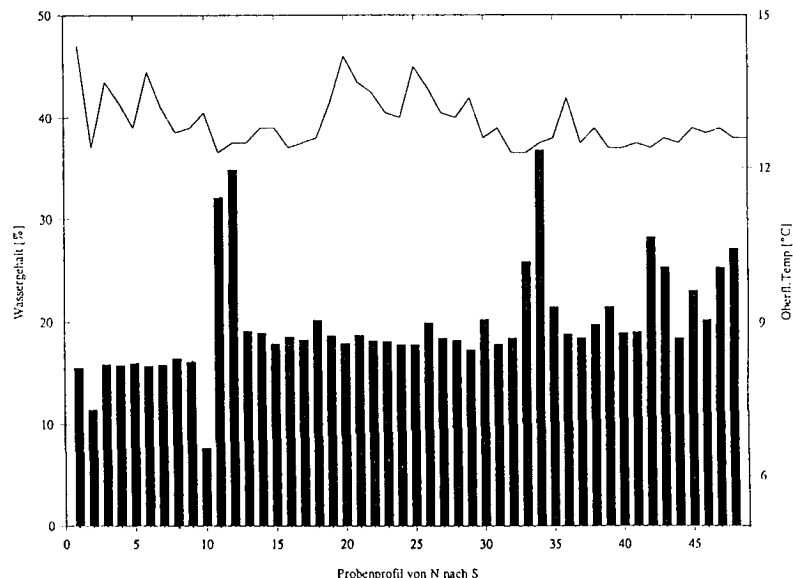
HERR,E.W. (1992): Die Bedeutung der Marschgewässer für den Naturschutz.- Mitt. aus der NNA, 3.Jhrg., Heft2, 3-12

MÜLLER,U. et al. (1993): Suitability of ERS-1 SAR PRI-Data for Multitemporal Agricultural land-use Mapping.- Proc. of the Second ERS-1 Symposium 11-14 October, Hamburg

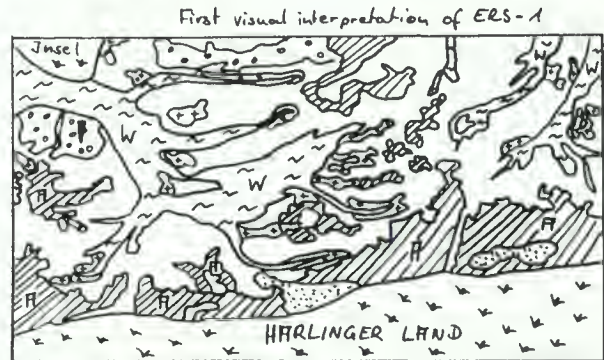
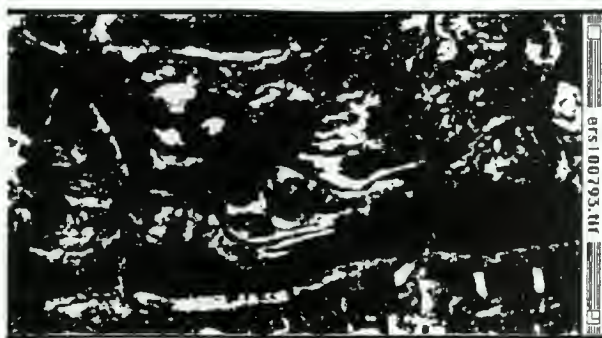
REINECK,H.-E.(1978): Das Watt, Ablagerungs- und Lebensraum.- 2.Auflage, Frankfurt/Main

WELCH,R.;EHLERS,M. (1988): Cartographic Extraction with Integrated SIR-B and Landsat TM Images.- Int.J.Remote Sensing, Vol.9, No.5, 873-889

Sediment parameters of the first summer campaign 1993:

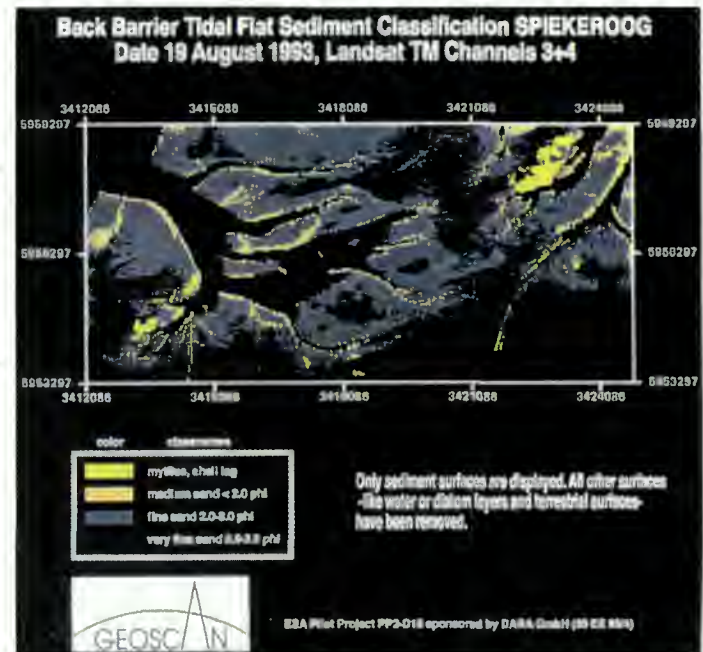
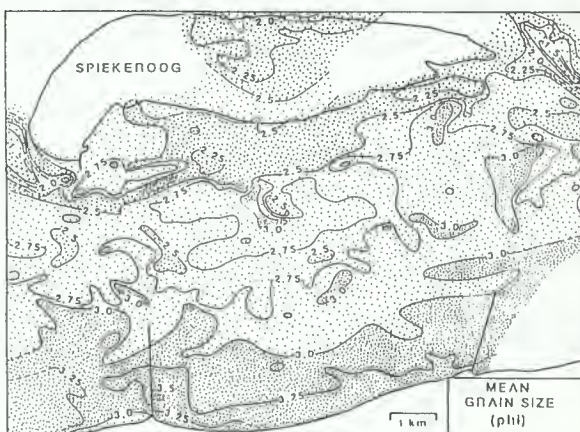


The way from a first visual interpretation to an object-based filtered radar image of the backbarrier tidal area of Spiekeroog.



Legend:

- [Water]
- [organic layer]
- [rough tidal flats of finer grain sizes]
- [BRAGI and corner reflection of coarser grain sizes (sand fraction)]
- [smooth sandy sediment surfaces]
- [unsolved phenomena, coarse grain size no organic layer but no return]
- [sandy tidal flats of mean grain sizes]





8. LAND USE – INTERFEROMETRY



ERS-1 FOR LAND USE MONITORING IN COSTA RICA: FIRST RESULTS

Verbist B. & De Roover B.

Laboratory of Remote Sensing and Forest Management, University of Gent

Coupage 653, B-9000 Gent, Belgium

Phone: (+32) 9 264 61 09 Fax:(+32) 9 264 62 40

E-mail: Bruno.Verbist@rug.ac.be

Boudewijn.DeRoover@rug.ac.be

ABSTRACT

ERS-1.SAR.PRI images were acquired over the Central Pacific in Costa Rica. The area consists of a coastal plain and a mountainous region with slopes of 30° and 40°. Strong layover effects and radar shadow are present in the data and reduce the potential of radar data for land use monitoring in mountainous regions substantially. No digital elevation model was available in the presented study. Flat areas were selected accordingly for the study, which covers three different topics.

Mangroves form a rich but fragile ecosystem in the (sub)tropics. Two mangrove reserves have been established in the Central Pacific in Costa Rica in order to conserve this ecosystem. Detailed maps however are lacking. A field campaign was conducted to evaluate the potential of ERS-1 SAR data for the discrimination of types of *mangrove*. No discrimination was possible; the spatial resolution of ERS-1 SAR appears to be an important limiting factor. The data set (all images from the rainy season) did not allow a discrimination between mangrove forest and seasonal dry tropical forest. It is concluded that SAR data from dry and wet season are needed for a further investigation.

The potential of ERS-1 SAR for *land use change monitoring* was evaluated for a test site containing palm plantations, rice fields and pasture land as major land use classes, in the area of Parrita and Tarcoles. Only the results for the oil palm plantation are presented. This plantation can be discriminated from the neighbouring rice fields and pastures. For a discrimination of different age classes of the palm plantation two factors are of main interest: tree height and canopy closure. The height differences do not produce differences in backscatter level nor in texture in ERS-1.SAR.PRI data. Only one very recently replanted plot of the palm plantation could be clearly discriminated, probably because of a very open canopy and the soil effect in the backscattering.

The potential of ERS-1 data for *monitoring of the urban encroachment* was evaluated for a small study area near Parrita. Amongst the studied factors which influence potentially the detectability of man-made constructions in ERS-1.SAR.PRI data, only the size of the construction appears to be important.

Keywords: ERS-1.SAR.PRI, texture, mangrove, land use, urban encroachment, monitoring

1. INTRODUCTION

The monitoring of the natural resources by satellite is one of the objectives in an ongoing EC-project in Costa Rica. From the beginning it was realized that problems arise in the elaboration of a monitoring system based on optical high resolution data due to frequent cloud coverage. A study was therefore started to assess the capabilities of the ERS-1 SAR which is a weather independent system.

The backscatter in SAR images is basically related to the geometry and dielectric properties of the objects in the landscape. The scattering mechanisms can range from specular reflection (surface scattering) to complex multi-layer interactions (volume scattering)(Curlander, 1991). Data acquired over mountainous regions suffer from layover and shadowing effects. These effects introduce the necessity respectively of specific georectification procedures and of data acquisition under different viewing geometries (Colwell, 1983).

Man-made constructions are mainly simple rectangular geometries composed of elements with smooth surfaces and often act as corner reflectors. They can therefore appear in the radar image as bright spots, depending on, amongst other factors, the orientation, size, type of material and surrounding landscape.

The urban encroachment is a fastly evolving feature in the test area due to strong tourism development. Meanwhile a modest pressure exists due to the population increase. From visual analysis it was concluded that optical satellite systems can only provide partial information on the urban encroachment. The basic difficulties are the spectral overlap in the signatures and the scarcely available data over regions with frequent cloud cover. ERS-1 SAR data could therefore be an interesting data source, in an independent way or in combination with optical data.

The natural environment displays a much more complex pattern. Vegetation structure, surface roughness and/or soil moisture play a dominant role in the backscattering of microwaves at 5.3 GHz (C-band). The opportunity was taken to analyse the influence of specific stand parameters upon the backscatter, as excellent field data on oil palm plantations in the study area were available. The mono-species stand can be regarded as a simple object: only tree height and canopy closure vary with age. The ability to discriminate the major

age classes by using ERS-1 SAR would encourage further research on other types of plantations. Capabilities to monitor this type of land use would be interesting for control purposes at the management level, e.g. in reforestation programs based on subsidies.

Finally, the capability of monitoring of the land use in general by using ERS-1 SAR data, whether or not in combination with optical satellite data, is of high interest for global and regional programs focussing on environmental and socio-economical issues; specifically for regions where detailed maps are lacking.

2. OBJECTIVES

The objectives was to contribute in the assessment of the capabilities of ERS-1 SAR data for:

- a/. tropical forest classification whereby the main emphasis was put on the discrimination of mangrove areas and seasonal forest;
- b/. the monitoring of land use change in a region wherein the major land uses are oil palm plantations, grasslands with different types ranging from intensive use to almost abandoned, and rice cultivation;
- c/. monitoring of urban encroachment: the study was focussed on the small villages and isolated farm constructions in a rural area under high pressure by the tourism industry.

3. METHODOLOGY

The following methodology consisting of five steps was applied:

- a/. collection of field data, independently of the SAR data
- b/. entry of the field data in a database and GIS
- c/. SAR image calibration & georeferencing
- d/. visual interpretation of the SAR-data with respect to the discrimination of mangroves, monitoring of land use and detectability of man-made constructions in ERS-1 SAR images
- e/. analysis wherein texture analysis, filtering or principal component transformation of the data were included.

4. DESCRIPTION OF THE STUDY SITE

The study site overlaps with the region selected for the ongoing EC-project Forest monitoring by satellite and integrated watershed management in Costa Rica' which improved the availability of reference data. The study site covers the Central Pacific in Costa Rica, situated between following coordinates: 9° 20' -10°N and 84° - 84°45' W. Core zone is the 10.000 ha of the Carara Biological Reserve and the neighbouring Turrubares zone, both mountainous areas covered with tropical forest with a high biodiversity (five different Holdridge Life Zones are discriminated).

Different types of mangrove were studied in the Gulf of Nicoya. The mangrove of Guacallillo at the mouth of river

Tarcoles is mainly dominated by Rhizophora mangle and much less by Avicennia germinans. In Tivives at the mouth of river Jesus Maria dominance of Rhizophora mangle is less explicit and there is a mixture with Avicennia germinans, Laguncularia racemosa en Conocarpus erecta.

The mangroves form part of a conservation area and are rather inaccessible. Some small scale logging however takes place, because of the scarcity of sawnwood in the region. No detailed maps exist for the reserve, neither for the bordering conservation area which consists mainly of seasonal dry tropical forest and extensive grasslands.

In the southern coastal plain of Parrita oil palm plantations covering about 12.000 ha were studied. The same region features large irrigated and dry rice fields as annual crop. Grasslands constitute the third major land use class, present under different forms varying from rotation crop (in combination with rice) to very extensively used permanent prairies, which are frequently burned in order to suppress the regrowth of natural vegetation..

The region of Parrita includes finally a coastal area which is in rapid development. Hotels and beach ressorts are constructed in order to boost the economical development of the area, based mainly on tourism.

The climate is humid with a dry season from december till april. Annual rainfall varies between 3000 and 4000 mm.

5. REMOTE SENSING DATA

Three ERS-1.SAR. PRI images were made available by ESA, acquired in descending mode on 4/9/1993, 9/10/1993 and 13/11/1993. All data were thus acquired during the wet season. Cotopaxi was the captation station.

Optical satellite data were made available by the EC-project: two SPOT XS-images (path/row: 622/330, 623/330 recorded on 22/3/1991 and 21/1/1993). One TM-image (path/row: 15/53 recorded on 6/2/1986) was provided by the TeleSig laboratory in Costa Rica..

All optical images are partially covered with clouds and date from the dry season. The SPOT-images do not completely cover the plain of Parrita.

A set of black and white aerial photographs from 1984 with a scale of 1/30.000 covering the mangroves and a set of 1992 with a scale of 1/60.00 partly covering the palm plantation was also available.

6. ANALYSIS OF ERS-1 SAR DATA

6.1. SAR IMAGE CALIBRATION & GEOREFERENCING

The ERS-1 SAR images were geometrically corrected using the topographic map as reference, with cross-roads and bridges as control points. Difficulties were experienced in finding appropriate control points for the following reasons: (1) rivers (normally interpreted with ease) changed their

course, (2) no reference points were available along the coast side, and (3) the topographical maps dated from 15 years ago.

All ERS-1 images were calibrated using the formulas described by Laur (1992) after retrieval of the values for zero-Doppler range time t1, incidence angle at range pixel 1 and geodetic latitude in the header files. As the three ERS images were acquired on the same frame, the values did not differ for the three data sets.

The calibrated images (σ^0 in dB) were linearly rescaled to 8-bit for ease of further processing; care was taken to cover the total range of data values. The inverse relationship was used to recalculate the backscattering coefficient σ^0 where appropriate.

6.2. DISCRIMINATION OF MANGROVE

6.2.1. COLLECTION OF FIELD DATA

Field work was executed from 20 till 23 of April. A rough plan with description and situation of the different species, including the height of the stand, was drawn at different locations whereof the coordinates were acquired with a GPS. The field observations confirmed the visually observable differences on the aerial photograph and the SPOT-imagery: a low (< 5m) scrubby form of Rhizophora mangle in the muddy flood zone along the rivers can clearly be discriminated from higher (> 20 m) stands in the less wet areas.

6.2.2. ENTRY OF THE FIELD DATA IN A DATABASE AND GIS

Both the aerial photograph and the SPOT-imagery were used as reference document to delineate polygons with the different vegetation- and terrainclasses for a later statistical approach.

6.2.3. VISUAL INTERPRETATION

The mangrove can clearly be discriminated on the SPOT-image from the neighbouring dry open seasonal forest, agriculture and water (fig.1). Two different types of mangrove related with the height of the stand can be discriminated.

On the ERS-1 image however, no difference in structure of mangrove could be found. ERS-1 SAR images from the wet season alone do not allow a clear discrimination of the different terrain or mangrove classes (fig.2). A discrimination could be made by visual interpretation between agriculture and mangrove but not between dry open seasonal forest and mangrove. Relief, though moderate, is introducing large variation in the backscattering coefficient of the dry forest. Hence confusion with other classes occurs.

The visual interpretation was carried out on the monitemporal ERS-images and on the RGB-combination. In order to reduce the speckle two approaches were adopted: smoothing with the Lee-filter and multitemporally averaging. The former is a conditional and statistical filter, typically elaborated for radar imagery. It was preferred over classical smoothing filters (e.g. median filter).

Multitemporal averaging narrows the spectral resolution and produces therefore enhanced images. Care has to be taken however when image data acquired during a long time span as this approach is in fact only applicable for objects which remain stable in time, as is the case for the mangrove.

Despite the higher image quality for visual interpretation, no amelioration was obtained with regard to the discrimination of types in the mangrove.

6.2.4. ANALYSIS AND CONCLUSIONS

The results of the visual interpretation have been confirmed in the digital analysis of the backscattering coefficient.

Images of forests often display texture. A texture transform was therefore applied in order to detect textural differences in the mangrove, if present. The images have been transformed using the coefficient of variation which is a first order texture measure. It was used successfully in airborne radar data for forest type discrimination (Grover, 1993).

Analysis of the texture signature (Fig.3) obtained over window sizes of 3x3, 5x5 and 7x7 pixels, revealed that no further discrimination was possible in the mangrove forest. Classes related with tree height could thus not be discriminated with ERS-1.SAR.PRI data. Main texture differences appeared to originate from the relief effect in the dry seasonal forest.

Pons (1994) could discriminate two vegetation classes in the mangroves of Guinée Conakry. Separation was based on differences in tidal level (up to 3-4 m) in a multitemporal image of three following months.

As differences in tidal level in the mangroves of Guacalillo and Tivives are less (about 1.5 m), a discrimination based on this phenomenon could not be performed.

It would be interesting to investigate if a series of multitemporal images, covering both wet and dry season helps to discriminate mangrove from the neighbouring, dry seasonal open forest. It is assumed that during the dry season the soil will have a major effect on the backscatter value of the dry seasonal forest.

6.3. LAND USE CHANGE MONITORING

6.3.1. COLLECTION OF FIELD DATA

A collection of ground truth was executed in the summer of 1993 in the framework of the ongoing EC-project Forest monitoring by satellite and integrated watershed management in Costa Rica' using the aerial photograph and SPOT-imagery. Field work in the palm plantation was executed from 17 till 20 of April 1994. An age class map and data of rainfall were obtained from the company Palma Tica. Because the age class map was only obtained the last day, it was only superficially appraised on the terrain. Differentiating parameters of the different plots were investigated. The same triangular plant configuration (planting distance of nine meters) was applied over the entire plantation area. According to the FAO soil map, the area is homogeneous with regard to the soil. Differences in stand structure are tree height and for the very young plantations the canopy closure.

The possible use of ERS-1 SAR to discriminate these stand development classes was examined.

6.3.2. ENTRY OF THE FIELD DATA IN A DATABASE AND GIS

An age class map (scale: 1/20.000) of the plots of the oil palm plantation 'Palma Tica' was digitized. This map was drawn with the topographic map of 1976 as a reference, which was based on aerial photographs of 1957 and 1974. An overlay of this map with more recent images of TM and ERS-1 SAR showed that some new villages were built and that most meandering rivers changed their course. All parcels bordering a river had to be corrected using the image data. For this purpose the SPOT and TM images proved to be superior than the SAR-image. Only if the road and grass verge separating two blocks were wider than about 50 m, the inner parcel boundaries in the oil palm plantation could be discriminated on the ERS-1 images. Generally the outer boundaries were easier to discriminate. Inner parcel boundaries could be distinguished on the optical imagery only if the distance between two neighbouring blocks was more than 30 m.

6.3.3. VISUAL INTERPRETATION

A histogram stretch of the ERS-1 image allowed to clearly discriminate a one year old plot with a very low backscatter. A lower backscatter corresponds with the oldest and the youngest plots. On the TM-image the younger plantations appear brighter than the older ones. Unfortunately no data with 1986 as base are available. Part of the data can be extrapolated from the age class map of 1993.

6.3.4. ANALYSIS AND CONCLUSIONS

A mean backscattering coefficient by plot varied from -8 to -6 dB and variance varied from 2.6 to 3.0 dB.

To reduce the high variance of the mean backscatter by plot, a multitemporally averaged SAR image of the three available ERS-1 images was produced. As could be expected, this time averaged image is very much correlated with the individual images, more than 95%. Variance is lowered to 1.7 dB. A Lee-filtering of each individual image lowers the variance slightly more to 1.6 dB. All these images are very much correlated as table 1 shows.

A general trend in the relationship between the backscattering coefficient and the age of the stand can be observed in Figures 5 and 7: the backscatter increases with age until the age of about 8 whereafter it decreases. The youngest and oldest plantations can not be distinguished unfortunately.

An *Analysis of Variance* (table 2) shows that no statistical relationship exists between the mean backscattering coefficient of the time averaged image and the age of the stand. With a probability of 95% backscatter values and age data are significantly different series. This suggests that age class, and thus tree height, is not a detectable factor with ERS-1 and confirms the results obtained in the mangrove area.

Differences in annual rainfall (3000-4000 mm) exist between regions in the plantation area which result in significantly differing levels of productivity, according to the plantation manager. The annual amount of rainfall was the only figure available to be included in the analysis. It does not seem to be a factor of influence (fig. 6). This result was expected as it is very unlikely that hydrological differences exist at the time of data acquisition: all soils should be water saturated at the end of the wet season (Palma Tica, 1994). An *Analysis of Variance* (table 3) shows that no statistical relationship exists between the mean backscattering coefficient of the time averaged image and the annual rainfall. With a probability of 95% backscatter values and annual rainfall are significantly different series.

One of the seven one year-planted plots displays a remarkable low backscatter in the three ERS-1 images. This deviating behavior is probably related with a particular treatment (e.g. replanting after failure, soil conditioning) but this should be verified in the field.

A *Principal Component (PC) Transformation* was executed separately on the ERS-1 data set and on the Landsat-TM image. Samples were selected exclusively in oil palm stands. A clear distinction of age classes could only be extracted from the TM-image.

The first principal component of the ERS-1 images and the first four components of the TM-data were used for a second PC-transformation. Most of the oil palm plots of 4, 5 and 6 year old could be discriminated using components 3 and 4 (fig. 8). These age classes correspond with the oldest palm plantations in 1986 which appear quite dark on the TM-image. The 4-6 year old plots which cannot be discriminated appear brighter on the TM-image. Probably these plots were younger and had a disease or lowering production when they were cut and replanted. This fusion of the components of ERS-1 and TM does not provide any extra information in comparison with the original components.

A *texture analysis* using coefficients of variation for window sizes of 3x3, 5x5 and 7x7 was executed. The coefficient of variation is presented in function of year of planting in Fig. 9. A zone of 3 pixels (37.5 m) along the boundary of each plot was not involved in the calculation of the coefficient of variation in order to avoid border effects.

Over different neighbourhood sizes, a high correlation was found between the coefficients of variation obtained. No correlation could be found between the coefficients of variation and annual rainfall or year of planting (Table 4; five sets of rainfall data were only available for 59 plots). This could be expected from the results of the higher mentioned analysis of variance.

After inspection of the texturally transformed images it was concluded that the main texture differences originate from the relief effect. In conclusion: oil palm stands appear to be structurally homogeneous for the ERS-SAR, independently of age. With the size of the neighbourhood used in the textural

transformation the coefficient of variation increases (Fig. 9) and tends to a more normal distribution with a reduced spread of values (Grover, 1992). Visible differences in mean values are more apparent at the larger window size (Grover, 1992). However, the use of larger windows is limited by the size and form of the plots.

6.4. MONITORING OF THE URBAN ENCROACHMENT

6.4.1. COLLECTION OF FIELD DATA

An inventory of constructions in the test area was conducted in the period of 10-17th of April 1994. For practical reasons, related with the accessibility of constructions, the inventory was limited to those situated along roads.

Tracks along roads with different orientations were fully inventoried, taking into account the following parameters: localisation, orientation, size, type of material, slope and shape. Constructions with common walls have been considered as an entity for which measurements per constituting element had to be carried out. Very complex and large constructions (e.g. a rice processing plant) were inventoried only superficially.

The localisation, determined by latitude and longitude, was obtained for reference points, near to one or more constructions. A global positioning system (GPS) was used, without base station. The position of each house relative to the reference points was estimated by using a metric tape or by calibrated step-counting.

Orientation and slope were estimated for each element of the construction using a compass and a clinometer. The respective instrument accuracies are 2° and 1°.

Special features, such as swimming pools, additional floors, large TV antennas or iron fences were recorded where appropriate. Trees were recorded if the distance to the wall was less than or equal to the height of the tree. Other special features included in the inventory were the presence of electrical poles and their distribution.

6.4.2. ENTRY OF FIELD DATA IN GIS

The GPS data, totalling 95 way points, were entered in the GIS in order to visualise the position of each entity, on top of the displayed satellite images.

Difficulties were experienced in the overlaying of way points due to errors from different sources:

- a. errors in the GPS measurements: those errors are linked to the lack of a differential mode and to the dependence upon the satellite configuration and signal mode.
- b. errors in the topographic maps, which were old and at a scale of 1:50000.
- c. residual errors after rectification of the SAR images.

The way points have been corrected in order to obtain a maximum fitting with the image. This process was executed only on groups of way points, using linear features (roads) as well as bright points with evidence of correlation with large constructions in the image. The translation distances varied between 100 m and 300 m.

Field data were entered in a database for some 170 entities (groups of connected constructions), corresponding with 290 basic elements (construction compartments).

Some parameters were deducted from the input data: the effective surface area for each roof side was calculated using the slope of the roof and the length and width of the construction element, together with the information on the shape of the roof. Most roofs had only one ridge, of the same length as the compartment. The orientation angle of the SAR has been derived from the topographic map, using reference points located in the same line in the PRI product.

6.4.3. RADAR DATA INTERPRETATION

A quantitative approach has been excluded as it became clear from a preliminary analysis that the ERS-1SAR ground resolution in PRI images is too coarse (22m by 25m) in combination with the speckle. Construction elements can not be assessed individually on their possible radar backscatter. A visual approach has therefore been adopted. Three classes have been distinguished on the SAR image, according to the presence of relatively bright spots:

- Class 1. 'undetectable': no bright spot present where it could be expected according the localisation
- Class 2. 'detected': a relatively bright spot undoubtedly present and related to one or more neighbouring elements
- Class 3. 'ambiguous case': ambiguity due to the low contrast or high uncertainty in localisation.

The classification has been carried out on the multitemporally averaged image (Sep-Oct-Nov1993), as well as on the separate Lee-filtered images. A histogram stretch was applied on the images in order to enhance the contrast.

The classification results have been added to the database: e.g. a code "y" was given to each element of a construction or group of neighbouring constructions for which the detection was positive.

6.4.4. ANALYSIS RESULTS AND CONCLUSIONS

Most of the roofs consist of sheets of corrugated iron with a 'wavelength' of 8 cm; a contribution in the backscatter of a resolution cell can therefore be expected under different viewing geometries. Less effect can be expected from the changing geometry during the travelling of the object through the synthetic aperture.

The analysis on factors with significant influence on the detectability of constructions in ERS-PRI data is much hampered by the lack of precision in spatial localisation of the construction elements: many elements are present in one and the same resolution cell. The number of individual observations is not sufficient to perform a statistical multivariate analysis. The results are therefore presented in raw form with comment.

a. Backscatter values of the constructions

Figure 10 depicts a double scattergram for the acquisition dates September and October respectively November, and after applying the Lee-filter. Displayed are the maximum

backscatter values in very small subareas in the image which could be positively associated with constructions. The form of the bright spot was changing from image to image, possibly due to the speckle phenomenon.

It can be observed in Figure 10 that the change over time in backscatter can be relatively large (2 to 5 dB's). Some constructions are therefore only visible in one of the three images. Possible reasons are 1- the drop in contrast with the neighbouring pixels and associated changes in the phenology of the crops, 2- small differences in viewing geometry at the different acquisition dates, and 3- different meteorological conditions (wind, rain).

From Figure 10 it can be concluded that the September image is best suited for detection of constructions as it provides most contrast. Figure 11 displays the backscatter values (maxima) for the constructions in the September image. The baseline is the sigma naught value for palm plantation, plus or minus one standard deviation. Palms are amongst the landscape elements with relatively high backscatter values and thus well suited to provide a base line for contrast.

b. Influence of the type of roof material

More than 80% of the roofs in the field survey are made of iron or eternite material.

Figure 12 shows that, with regard to the type of roof material, 'iron' or 'not iron' does not play an important role in the detectability. The reason is that other factors are governing the detectability: the coarse resolution of the SAR, the imprecision of the GPS, the presence of trees around the houses. For the subtypes of 'not iron' no conclusions are possible as the number of observations is insufficient.

c. Influence of the type of wall material

Most houses in the field survey are build up with walls in concrete or wood (Figure 13). However, there is no strong evidence that the type of wall material does play a dominant role in the detectability of the construction. Wooden constructions are less detectable while the reverse is true for iron constructions.

d. Influence of the roof slope, roof exposition and roof element size

Figures 14 and 15 display the distribution of three factors which could be strongly associated with the detection of constructions: size (white dots), slope and exposition (both black dots). In abscissa are indicated the observations according to the detectability: no or yes when the detection was unambiguous, possible when not.

The data of the Figures 14 and 15 have been sorted according to the slope and exposition angle respectively. It can be seen that no correlation exists between each factor and the size of the construction element (R varying between -0.166 and -0.015). Figure 16 indicates that no correlation exists between slope and exposition angle ($R=-0.049$ and $R=-0.219$ for respectively 'not detected' and 'detected' series).

Roof slope neither roof exposition appear to influence significantly the detectability of constructions. The detectability appears to be linked with the size of the roof

element: the higher the size, the better the chance to be detected. However, detection is not guaranteed as can be deduced from the 'not detected' cases, unless the size is larger than some 400 m^2 .

Detailed analysis of the list of detected elements (i.e. most right side in the graph) indicated that:

- 34 constructions were detected, which could be decomposed in 63 elements; of these, 23 constructions consist of at least one element with an exposition between -26° and 26° , while 11 constructions consist of elements with an exposition outside the given range;

- all the construction elements with an exposition angle lower than -174° are part of a construction with at least one element facing the SAR, and consist of flat roofs. The average size of all remaining elements is 129 m^2 , while an average of 54 m^2 is obtained for all 'not detected' elements.

In conclusion, only large constructions can be detected consistently: factories (with complex forms), large farm buildings, open hangars for cattle or agricultural machinery and hotels. Two small villages, consisting of separate houses build around a soccer field, could not be detected. Single houses can not be identified consistently.

e. Miscellaneous

The major villages (e.g. Parrita: diameter 1 km) are easily identified, as far as the centre (contiguous zone of constructions) is considered. From the observations made above one can deduce that the periphery with individual houses can not be delineated correctly.

Poles of the electrical network were not visible in the image. Only lines of secondary order were present in the study area. Poles were made of wood or concrete; the net consisted of four electrical wires.

7. CONCLUSIONS AND RECOMMENDATIONS

7.1. MANGROVES AND LAND USE

1. The mangrove can clearly be discriminated on the SPOT-image from the neighbouring dry open seasonal forest, agriculture and water. Two different types of mangrove related with the height of the stand can be discriminated. ERS-1 SAR images from the wet season alone do not allow a clear discrimination of the different terrain or mangrove classes. A multitemporal series covering dry and wet season might help to discriminate mangrove from dry seasonal forest.

2. An *Analysis of Variance* shows that no statistical relationship exists between the mean backscattering coefficient and the age and thus the tree height of the stand. A clear distinction of age classes could only be extracted from the TM-image. No statistical relationship could be found either between the mean backscattering and the mean annual rainfall.

A fusion of the *Principal Components* of ERS-1 and TM does not provide extra information in comparison with the original components with regard to the detection of age classes.

3. Oil palm stands appear to be structurally homogeneous in the ERS-1.SAR.PRI, independently of age, and thus tree height. Main texture differences originate from the relief effect.

7.2. URBAN ENCROACHMENT

1. Strong backscatterers are obviously present in the ERS-1 SAR image data as bright spots. The backscattering coefficient is not stable, probably due to changing geometry and meteorological conditions: the difference from image to image ranges between 0 and 5 dB. The form of the spots varies as well.

2. The visual analysis of a flat study area indicates that those bright spots correspond with construction elements. Surprisingly, the size appears to be the only factor of influence on the detectability of man-made constructions in ERS-1.SAR.PRI data. Other factors analysed were: type of material for the walls and roof, slope and exposition of the roof. The availability of data from descending and ascending orbits would provide more insight, specifically with respect to the influence of the exposition on the detectability.

3. Individual houses in the study region are too small to be detected. Larger constructions (hotels, farms, etc) can be detected more reliably provided that some elements are oriented towards the radar. Monitoring by ERS-1 SAR of the urban encroachment, e.g. in touristic regions with rapid development, could be envisaged.

4. As information on urban encroachment can be derived only partially from ERS-1.SAR.PRI, a comparative analysis on optical satellite data is desirable in order to assess the complementarity of both types of sensors with regard to monitoring of urban encroachment in tropical regions.

8. REFERENCES

- Colwell, R. (1983). Ed.:Manual of remote Sensing, ASP
- Curlander, J. & McDonough R., (1991). Synthetic Aperture Radar: systems and signal processing. Wiley & Sons, Inc..
- Grover, K.D. & Quegan, S. (1992). Image quality, statistical and textural properties of SAREX data from the Tapajos test site. University of Sheffield, UK, & P. Tissi & A. Hiroshi Alves, National Institute for Space Research (INPE), Brazil.
- Laur, H. (1992). Derivation of backscattering coefficient σ^0 in ERS-1. SAR.PRI products. ESA/ESRIN.

Metternicht, G. (1994). A comparative study on the performance of spatial filters for speckle reduction in ERS-1 SAR data. EARSEL symposium, Dundee.

Palma Tica (1994). Informacion meteorologica de suelos y de produccion de palma aceitera en la division de Quepos, Palma Tica.

Pons, I. et Le Toan, T. (1994). The potential of ERS-1 data for cartography and monitoring mangrove ecosystem. Abstract. First ERS-1 Pilot Project Workshop. Toledo, Spain.

Solarzano, R. et al.. (1991). La depreciacion de los Recursos Naturales en Costa Rica y su relacion con el Sistema de Cuentas Nacionales p97-115

ACKNOWLEDGEMENTS

The paper is prepared in the scope of the PP2 - B6 agreement with ESA. We express our gratitude towards the Belgian National Science Policy Office for funding the study. We further gratefully acknowledge the Palma Tica company for providing us detailed reference data on the plantations and the TeleSig laboratory at the Universidad Nacional in Costa Rica for providing TM-data.

APPENDIX

Table 1. Correlation of average backscatter (dB) plots between Lee-filtered image, original bands and timeaveraged image

	Lee9	Lee10	Lee11	dB9	dB10	dB11	dBTime
Lee9	1						
Lee10	0.890	1					
Lee11	0.894	0.915	1				
dB9	0.999	0.891	0.898	1			
dB10	0.886	0.999	0.914	0.889	1		
dB11	0.893	0.913	0.999	0.897	0.912	1	
dBTime	0.957	0.967	0.971	0.960	0.966	0.971	1

Table 2. Analysis of variance between the mean backscattering coefficient σ^0 of the time averaged image and the rainfall.

Anova: Single-Factor annual rainfall and mean backscattering coefficient of time averaged image						
Groups	Count	Sum	Average	Variance		
annual rainfall	62	202581.3	3267.44	118935.2		
σ^0 time av. (dB)	62	-414.984	-6.6933	0.165647		
Source of Variation	SS	df	MS	F	P-value	F crit
Between Groups	3.32E+08	1	3.32E+08	5588.218	9.4E-104	3.918814
Within Groups	7255059	122	59467.7			
Total	3.4E+08	123				

Table 3. Analysis of variance between the mean backscattering coefficient σ^0 of the time averaged image and the age of the stand.

Anova: Single-Factor year of planting and mean backscattering coefficient of time averaged image						
Groups	Count	Sum	Average	Variance		
age	62	122834	1981.194	64.0275		
σ^0 time av. (dB)	62	-414.984	-6.6933	0.165647		
Source of Variation	SS	df	MS	F	P-value	F crit
Between Groups	1.23E+08	1	1.23E+08	3816685	4.4E-276	3.918814
Within Groups	3915.782	122	32.09657			
Total	1.23E+08	123				

Table 4. Correlation between the coefficients of variation of the different window sizes and the year of planting

	Covar3	Covar5	Covar7	year	based on 71 plots
Covar3	1				
Covar5	0.966	1			
Covar7	0.929	0.987	1		
year of pl.	-0.171	-0.219	-0.237	1	
	Covar3	Covar5	Covar7	year	annual rainfall based on 59 plots
Covar3	1				
Covar5	0.968	1			
Covar7	0.942	0.990	1		
year of pl.	-0.256	-0.304	-0.308	1	
an. rainfall	0.153	0.227	0.257	-0.099	1

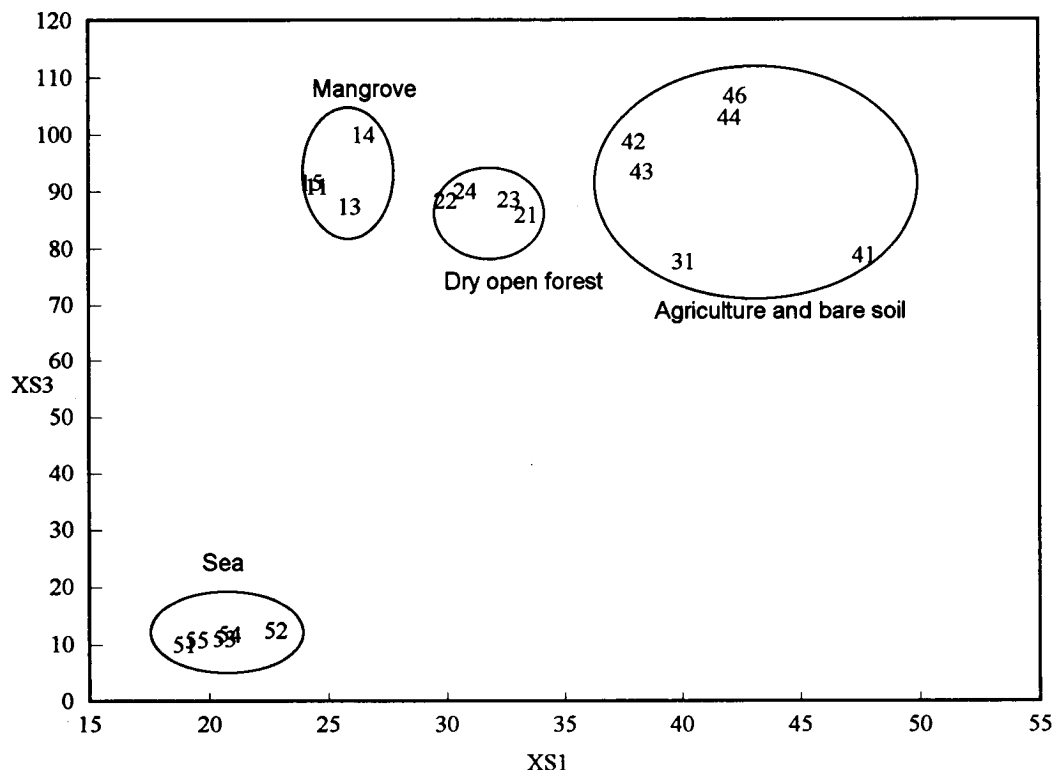


Fig. 1 Scattergram of digital values for different terrain classes in the studied mangrove area for bands XS1 and XS3 of the SPOT image of January 1993.

Legend for the mangrove area:

- Labels 11-15: mangrove
- 21-24: dry open forest
- 31 : bare soil
- 41-46: agriculture
- 51-55: sea

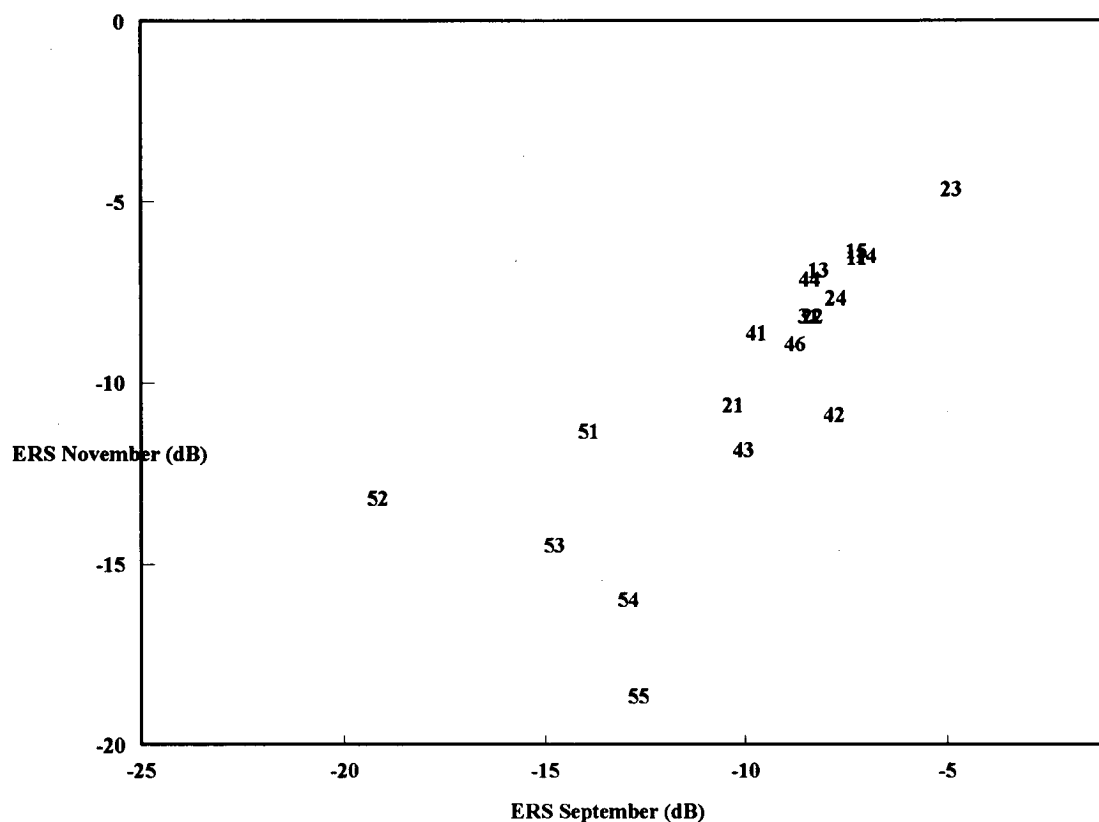


Fig. 2 Scattergram of backscattering coefficients σ^0 (in dB) for the mangrove area of the ERS-1 SAR images of September and November.

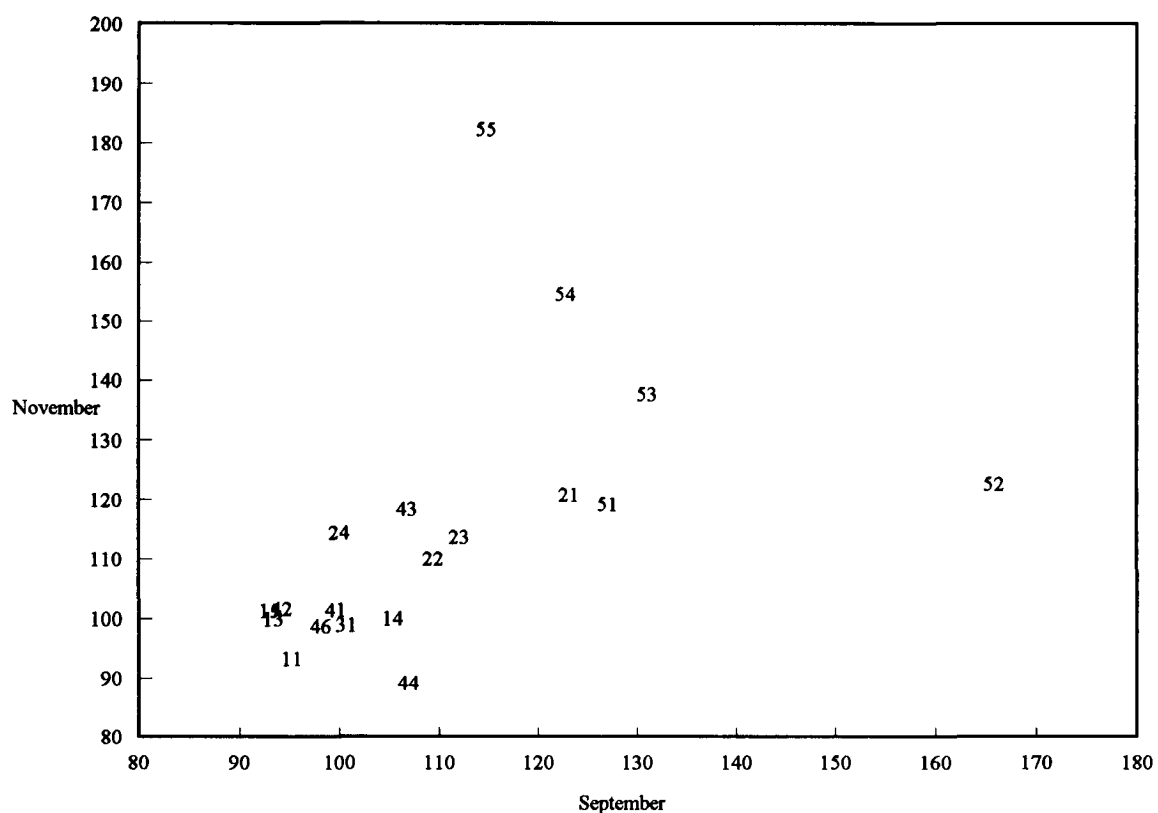


Fig. 3 Scattergram of coefficients of variation (x 1000) of a 7 X 7 window for the mangrove area of the ERS-1 SAR images of September and November Components of a PC-transformation of the 3 ERS-1 images.

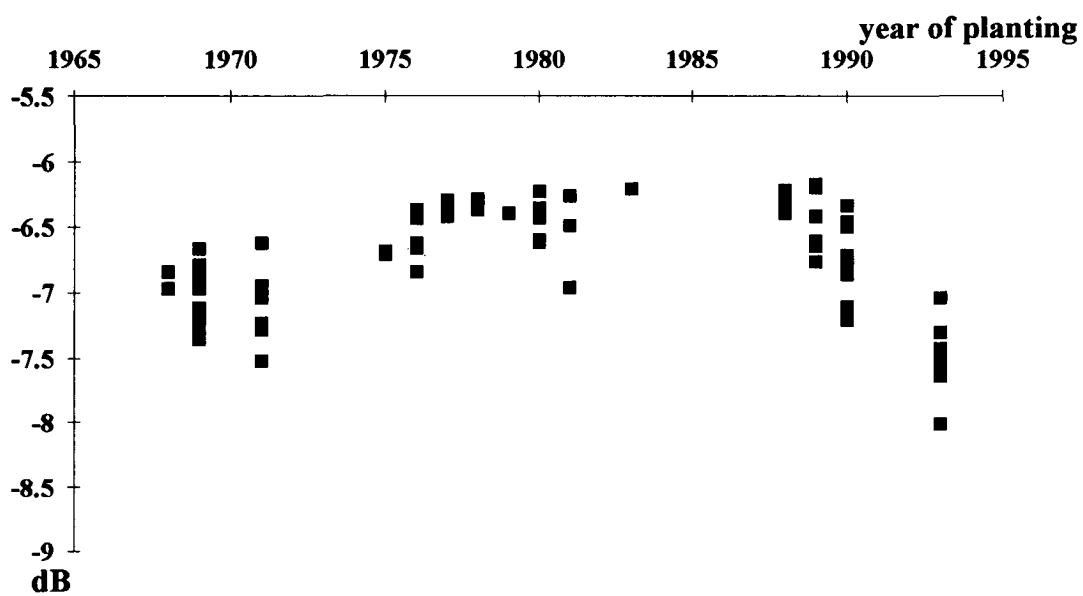


Fig. 4 Backscattering coefficients σ^0 (in dB) for the plots in function of the year of planting for the time averaged ERS-1 SAR image.

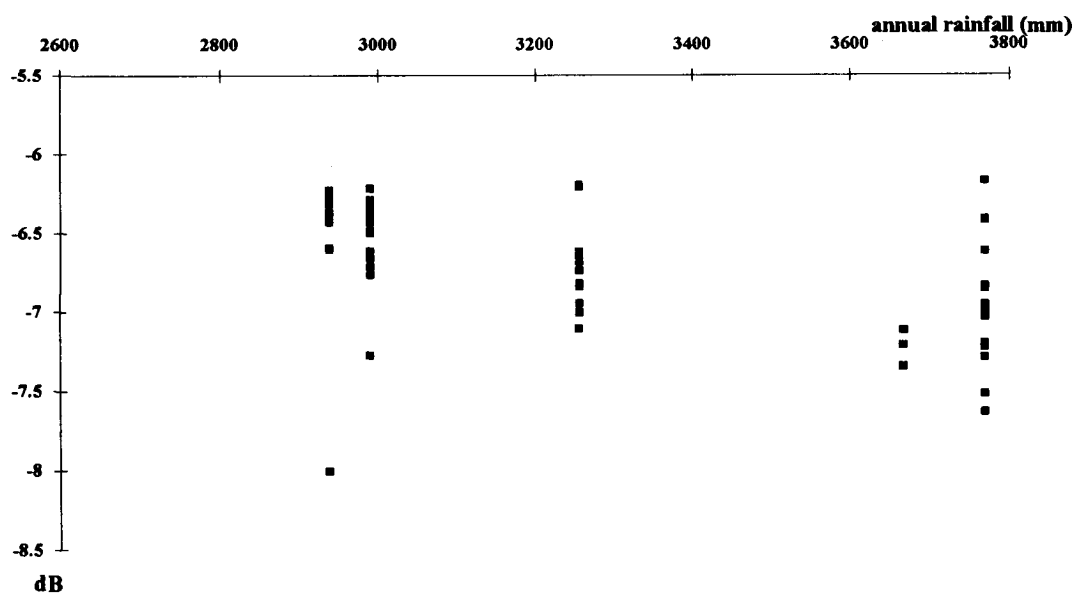


Fig. 5 Backscattering coefficients σ^0 (in dB) for the plots in function of rainfall for the time averaged ERS-1 SAR image.

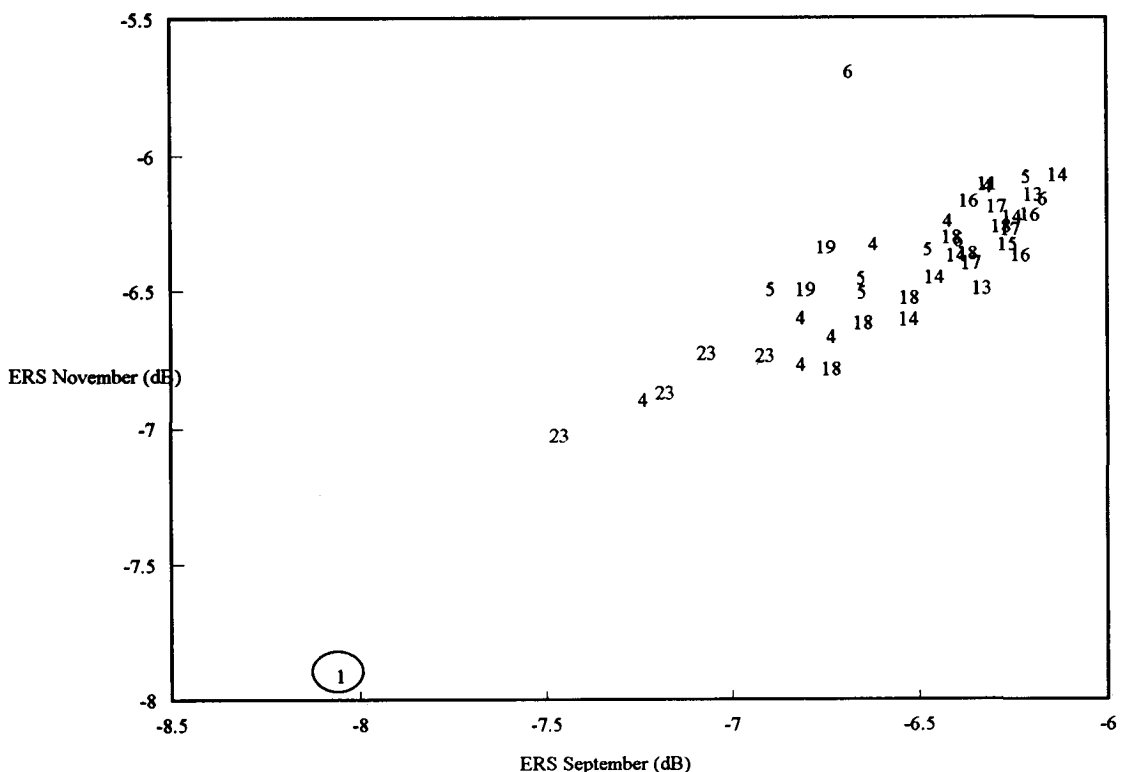


Fig. 6 Scattergram of backscattering coefficients σ^0 (in dB) for the palm plantation area for the ERS-1 SAR images of September and November. The labels symbolize the age of the planted plot. Note the encircled one year old plot.

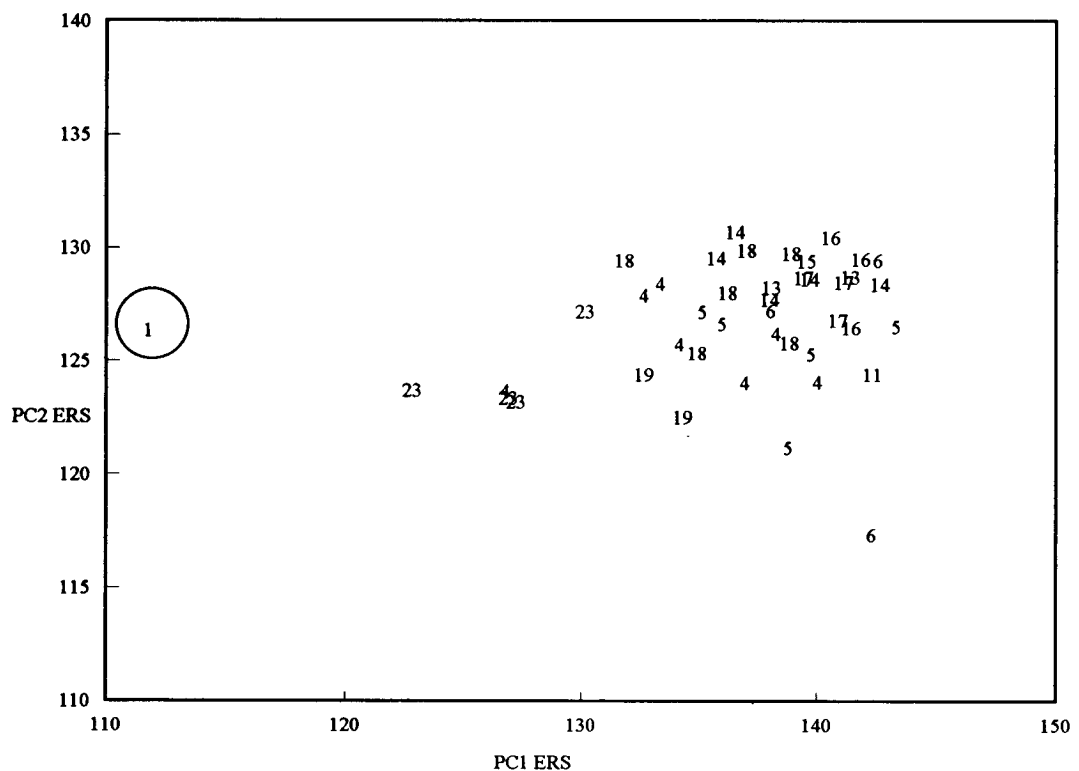


Fig. 7 Scattergram of the first 2 Principal Components of a PC-transformation of the 3 ERS-1 images with statistics based on the palm plantation. The labels symbolize the age of the planted plot.

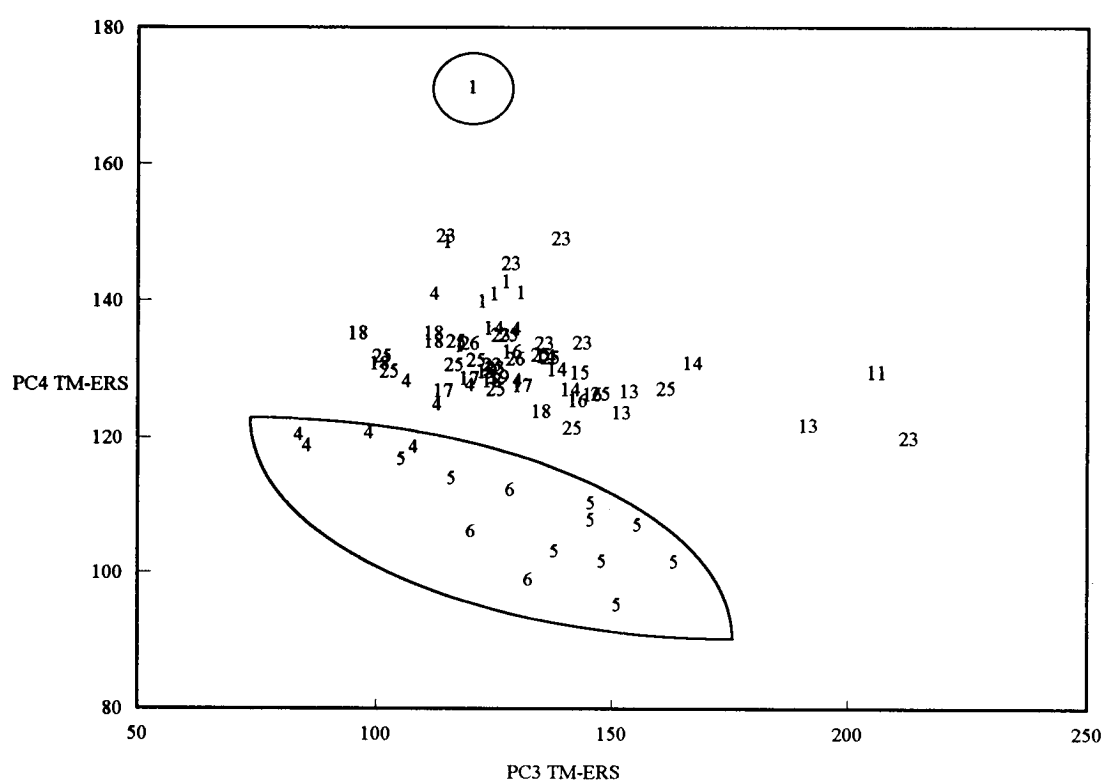


Fig. 8 Components 3 and 4 of a PC-transformation of the Principal Component of the 3 ERS-1 PC's and the first 4 PC's of 6 TM PC's. The labels symbolize the age of the planted plot.

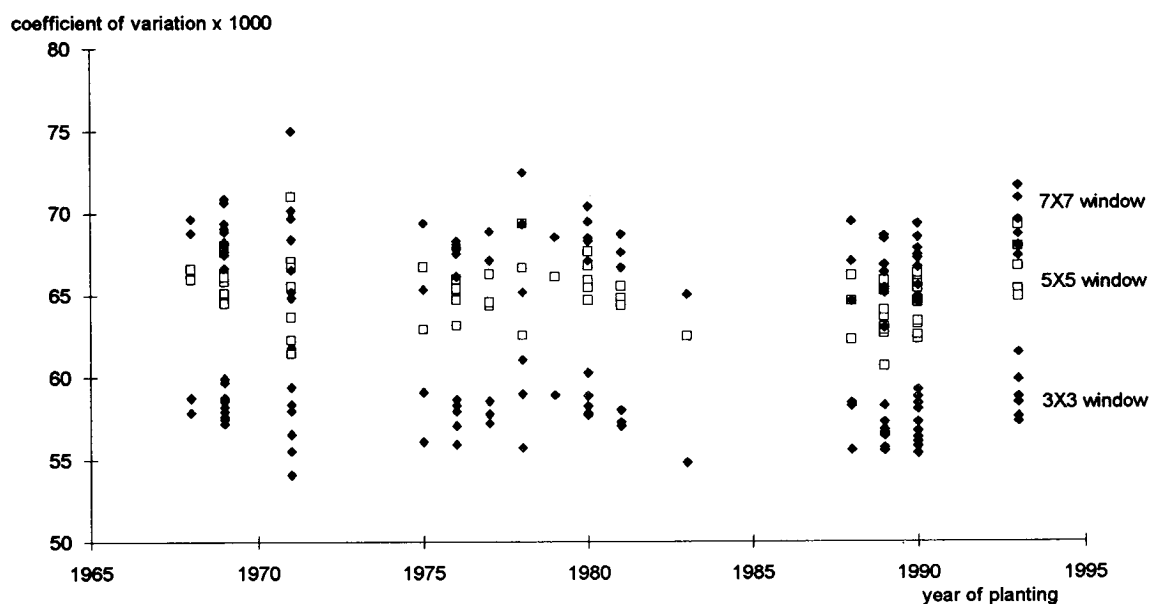


Fig. 9 Coefficients of variation of 3X3, 5X5 and 7X7 windows in function of the year of planting.

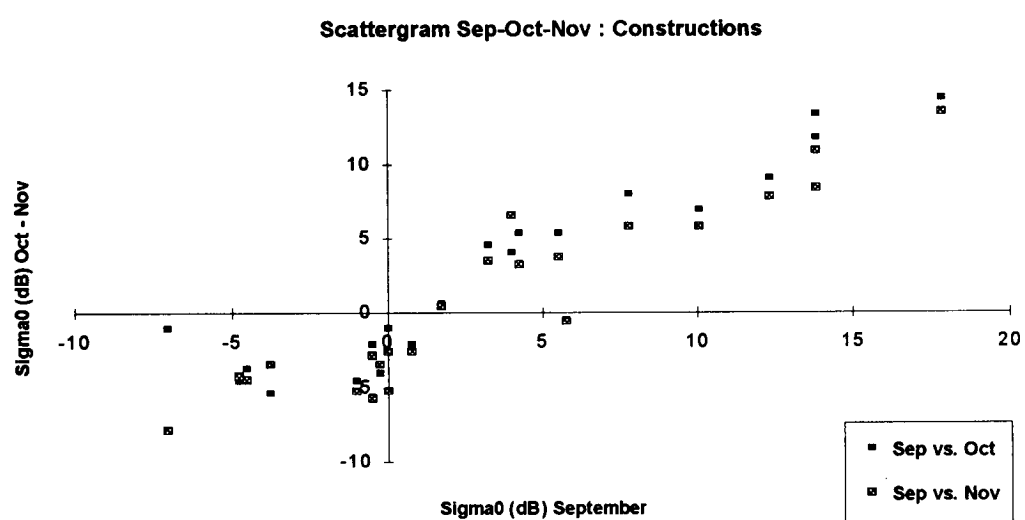


Figure 10: Scattergram of ERS1.SAR.PRI data of September versus October and November, respectively in dark and white dots.

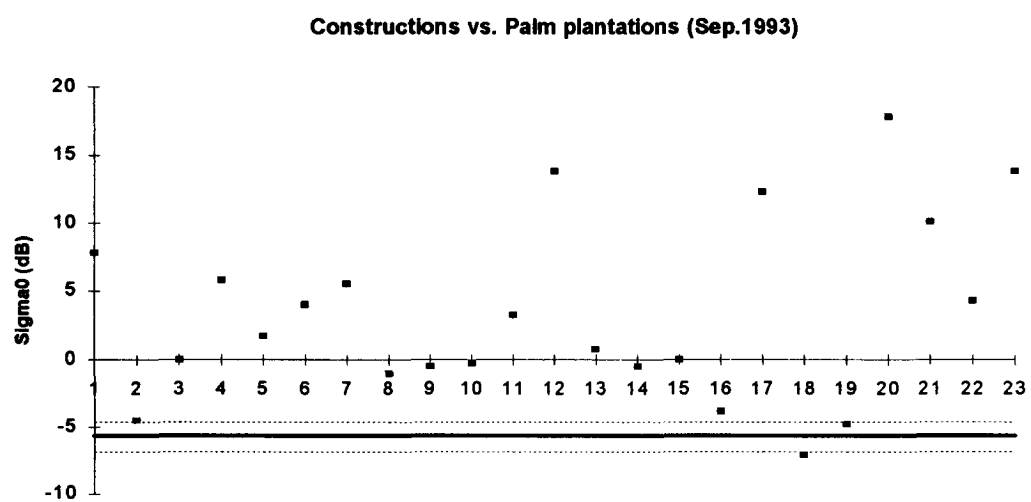


Figure 11: Backscattering coefficient of constructions (maxima); the base line represents the average backscattering coefficient of oil palm plantations.

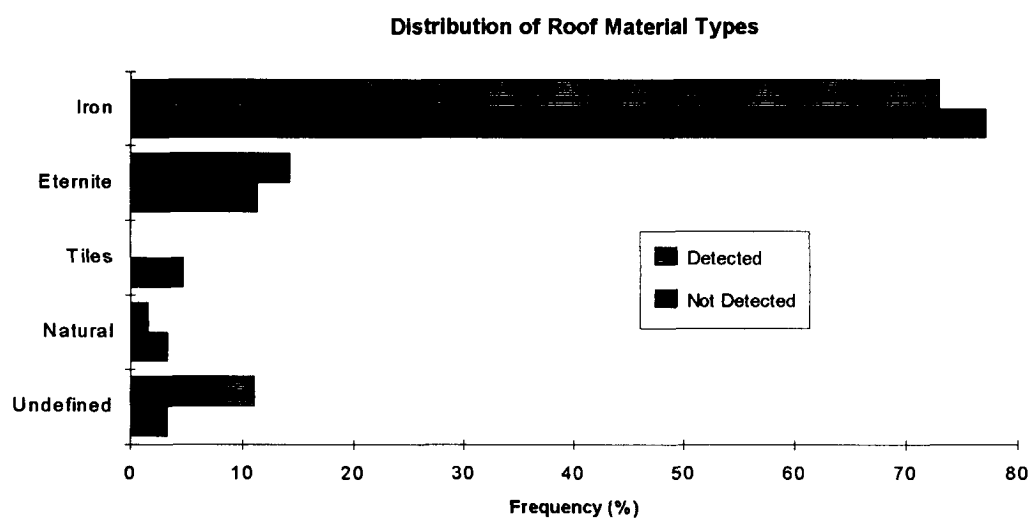


Figure 12: Distribution of the types of roof material for the detected and undetected constructions.

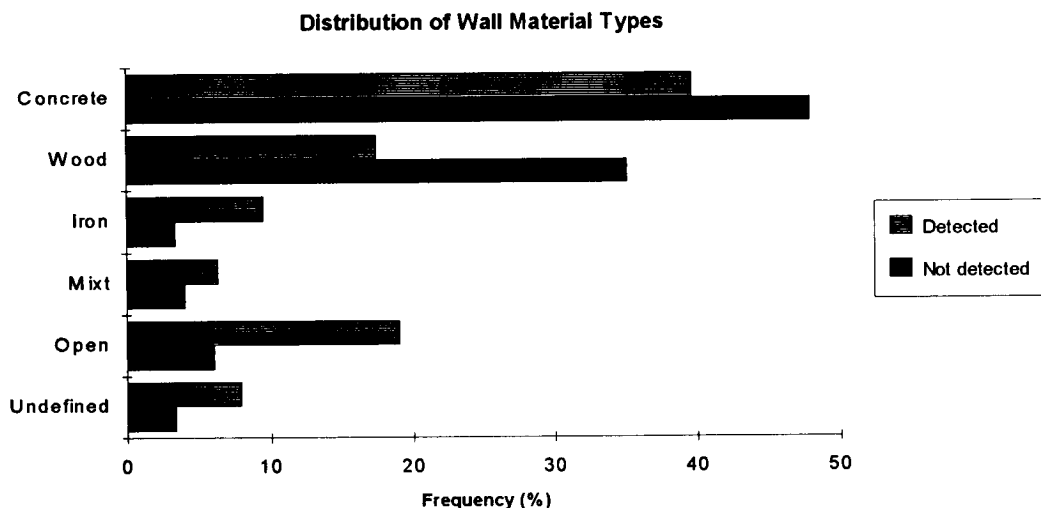


Figure 13: Distribution of the types of wall material for the detected and undetected constructions.

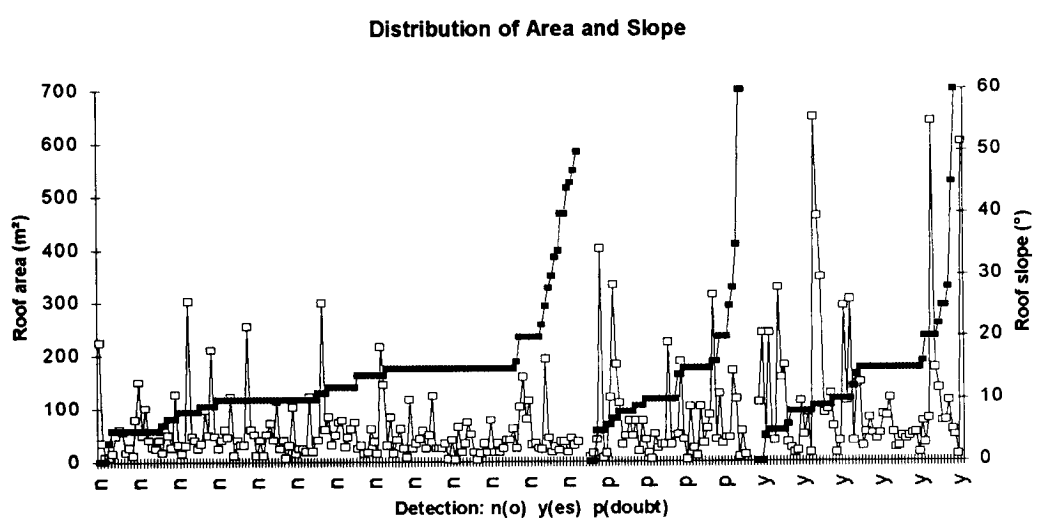


Figure 14: Distribution of the size of constructions (white dots) and of the slope of the roof (dark dots). Data sorted for slope angle.

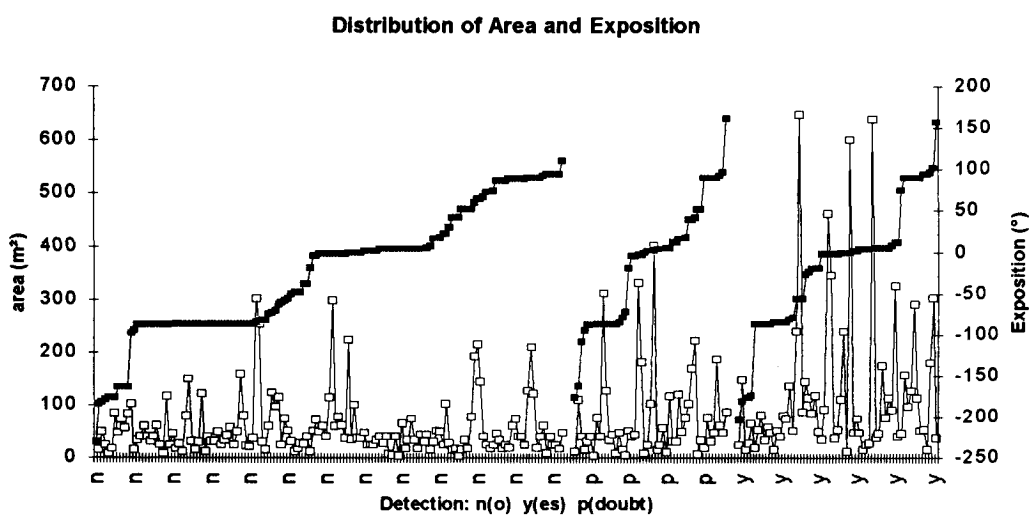


Figure 15: Distribution of the size of constructions (white dots) and of the exposition of the roof relative to the ERS-SAR (dark dots). Data sorted for exposition angle.

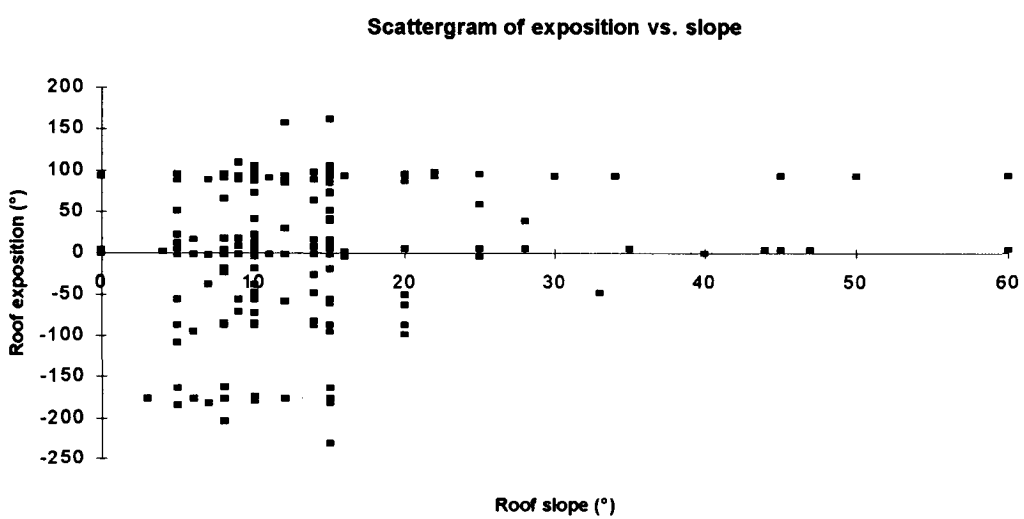


Figure 16: Scattergram of the angles of slope (abscissa) and exposition relative to the ERS-SAR.

POSSIBILITES CARTOGRAPHIQUES OFFERTES PAR ERS1 EN CONTEXTE TROPICAL HUMIDE (Projet PPF12).

Exemples en Guyane Française:
**(Bathymétrie, Formations de la plaine côtière, Géologie,
Hydrologie, Urbanisme, Iconocartes)**
Apports spécifiques des séquences multitemporelles.

Rudant J.P. (1), Baltzer F.(2), LCL Czerwinski G.(3), Deroin J.P.(4),
Lointier M.(5),Maitre H.(6), Pénicand C (7), Prost M.T.(8), Sabatier D.(5).

- 1-Université Pierre et Marie Curie, LGGST, Tour 26, 4 place Jussieu, Paris**
Tél: 33 1 44 27 50 87, Fax: 33 1 44 27 50 85, Email: jpr@lgs.jussieu.fr
- 2-Université Paris XI, Laboratoire de Sédimentologie, Bat 504, 91 Orsay**
- 3-Armée de Terre**
- 4-B R G M, Direction de la Recherche, BP 6009, 45060 Orléans**
- 5-O R S T O M, 911 ave Agropolis, BP 5045, 34032 Montpellier**
- 6-Télécom Paris, Laboratoire Images, 75013 Paris**
- 7-DGA / CEGN 16 bis ave Prieur de la Côte d'Or, 94114 Arcueil**
- 8-Musée Goeldi, Département Écologie, CP 399 Bélem, 66040 Pará, Brésil**

Résumé

Nous présentons ci dessous les principaux résultats obtenus sur la Guyane Française dans le cadre du projet PPF12. Différents domaines d'applications thématiques ont été abordés : dynamique littorale, hydrologie, topographie, géologie, structures anthropiques et cartographie opérationnelle.

Une couverture totale du pays, constituée d'images radar du satellite ERS1 a pu être obtenue entre avril et décembre 1992. Une mosaïque numérique a été effectuée, permettant ainsi la première vision globale de l'ensemble du territoire. Ce produit n'est pas géoréférencé avec précision mais l'intérêt de la vision synoptique apparaît néanmoins très clairement; ce qui devrait susciter de nouvelles applications basées sur l'imagerie SAR ERS1.

Parallèlement des iconocartes à l'échelle du 1 / 100 000 ont été réalisées sur les régions de Cayenne et Kourou. Accompagnées d'interprétations thématiques en marge, destinées à faciliter leur emploi par des utilisateurs novices en la matière. Ces spaciocartes constituent également les premiers documents de ce type établis pour un département français d'outre mer.

I-Introduction

L'objectif général du projet "Apport des données hyperfréquences à la connaissance de l'environnement guyanais" était de valider l'imagerie radar pour des études d'environnement et de cartographie dans le contexte tropical humide de la Guyane française en profitant, en particulier, de son insensibilité au couvert nuageux. La Guyane est située sur le littoral Nord-Est de l'amérique du Sud à 500 km de l'embouchure de l'Amazone.

II- La réalisation d'iconocartes

II-1 Mosaïque globale non géoréférencée :

Une mosaïque (Rosaz, Maitre, Rudant) regroupant 18 images ERS1 a été établie à partir d'une couverture totale du territoire obtenue entre avril et décembre 1992 et constituée de 5 orbites (d'Est en Ouest les orbites 7412 du 15 décembre, 4177 du 3 mai, 4449 du 22 mai, 4721 du 10 juin, 3991 du 20 avril). Le traitement a consisté en des corrections géométriques (translation et rotation) et radiométriques visant à annuler sur la forêt les effets de la variation d'incidence (19° à 26°) à l'intérieur d'une trace (Travaux effectués au Laboratoire Images de l'ENST et à l'UPMC). Le coefficient de rétrodiffusion variant plus rapidement avec l'incidence en mer que sur la forêt, des discontinuités radiométriques persistent donc entre traces sur l'océan, au nord de la scène. Des contrastes de radiométrie sont également visibles à terre entre orbites acquises à des dates différentes; ces contrastes correspondent alors à des évolutions temporelles naturelles des milieux rétrodiffusants.

La vision synoptique facilite la perception du réseau hydrographique et de la géomorphologie à l'échelle régionale,

même si pour des raisons liées aux techniques de restitution, la résolution initiale des images a dû être dégradée. La mosaïque numérique a été établie avec un pixel de 40 m, correspondant à une résolution voisine de 100 m, alors que les images d'origine ont une résolution de 30 m pour un pixel de 12,5 m.

Pour le moment, l'utilisation systématique de cette mosaïque comme fond de carte est handicapée par le fait qu'elle n'est pas géoréférencée mais nous prévoyons d'effectuer une nouvelle réalisation dans la référence UTM/WGS84. Les coordonnées d'un certain nombre de points d'amer ont déjà été mesurées dans ce but sur le terrain en utilisant un système de positionnement différentiel (Système GPS). La disponibilité d'une deuxième couverture complète nous permettra d'améliorer la résolution effective des images en réduisant l'aléa dû au "speckle" par fusion multidates et le document final pourrait alors être disponible à l'échelle du 200000 ème.

II-2 Iconocartes au 1 / 100000 sur les régions de Cayenne et Kourou (Figure 1).

(Les travaux présentés ci dessous ont été effectués dans le cadre d'un partenariat avec l'Armée de Terre et la Cellule d'Etudes en Géographie Numérique de la DGA)

La combinaison d'images acquises à des dates différentes sur une même zone permet la réduction de la part aléatoire du signal due au speckle sans augmenter la taille du pixel. Cette pratique mise à profit sur les régions de Cayenne et Kourou (Pénicand et al.) nous a permis l'établissement d'iconocartes au 1/100000 ième à partir de 3 images (Région de Cayenne: Images des 3 mai (marée basse, début de saison humide), 7 juin (saison humide) et 29 novembre 1992 (fin de saison sèche). Région de Kourou: Images des 17 avril (marée basse, début de saison humide), 22 mai (saison humide) et 18 décembre 1992 (fin de saison sèche)). L'efficacité du procédé en terme de filtrage est dû à la décorrélation du speckle obtenu entre images successives sur les zones homogènes. Avec 3 images, le "nombre de vues" mesuré à partir du coefficient de variation est voisin de 9. L'amélioration de la résolution effective des images est particulièrement nette dans les zones où les variations temporelles propres au paysage imposé sont réduites.

Ces produits cartographiques représentent un redécoupage d'une zone couverte par trois scènes ERS1 différentes correspondant à deux orbites adjacentes et donc à 6 dates d'acquisition. La fusion d'images en provenance de dates différentes n'a pas posé de problème dans le choix du mode de représentation colorée car, d'une part, nous disposions pour chaque scène de deux acquisitions en saison humide (périodes de avril-juin 1992) et de une à la fin de la saison sèche (1992 a été une année particulièrement déficitaire sur le plan de la pluviométrie) et que, d'autre part, chaque zone a bénéficié d'une image acquise à marée basse en saison humide. Cette distribution permet d'obtenir une représentation colorée unique pour

les deux orbites adjacentes, cohérente pour les bancs de vase et les zones de la plaine littorale qui sont inondées en saison des pluies

Des points d'appui, dispersés sur la zone à traiter et repérés au préalable sur les images, ont été localisés à l'aide d'un système de positionnement différentiel par le service géographique de l'Armée de Terre de Joigny. La rectification géométrique a été effectuée en utilisant un modèle polynomial basé sur tous les points d'appui disponibles. Etant donné la topographie globalement très plate de la région traitée, l'assemblage a pu être réalisé à partir des données brutes. Aucun traitement spécifique n'a été effectué pour tenir compte des reliefs, qui existent néanmoins de manière localisée, et l'erreur de positionnement en résultant pour un point donné devrait être proportionnelle à la différence entre l'altitude du point et l'altitude moyenne des points de contrôle. Il n'a pas encore été possible d'évaluer la précision des iconocartes obtenues à l'aide de contrôles supplémentaires réalisés *in situ*.

Remarquons que l'échelle pratique de restitution de tels documents est fonction du nombre d'images utilisées pour une même scène (puisque augmenter ce nombre revient à diminuer le chatoiement), et que la disponibilité de nouvelles données permettrait d'améliorer encore les possibilités cartographiques offertes par les images. Par ailleurs la modélisation physique du capteur associée à une connaissance de la topographie autoriserait l'élaboration d'iconocartes sans rendre obligatoire la prise de points d'appui sur le terrain, étant entendu que la disponibilité de ceux-ci améliorerait sensiblement la qualité des géocodages effectués.

III- L'information thématique

Les enseignements généraux qui suivent renvoient pour la plupart à des publications déjà effectuées et fournies en référence (Baltzer et al., Deroïn et al., Héry et al., Lointier et al., Mougin et al., Prost et al., Rudant et al., Tonon et al.). Les travaux les plus récents correspondent à des interprétations thématiques détaillées et 3 d'entre elles sont proposées ci-dessous (route de l'Anse (bathymétrie), de Crique Fouillée (mangroves et marais) et de la piste de Saint Elie (activité anthropique)). Elles ont été effectuées sur des zones test choisies à l'intérieur des aires couvertes par les iconocartes et elles exploitent d'une manière systématique l'apport des séquences diachroniques d'images. Ces interprétations se retrouvent en marge des spatiocartes (présentées au II-2) afin de faciliter leur utilisation.

III-1 Le littoral

III-1-a La bathymétrie

Trois images disponibles sur le nord-est de Sinnamary les 17 avril, 22 mai et 18 décembre 1992 permettent de préciser l'extension du banc de vase présent sur la côte, au nord-est de Sinnamary.

La vase molle, extrêmement lisse, joue le rôle d'un miroir pour les ondes électromagnétiques de la bande C de ERS1 (longueur d'onde 6 cm) et l'énergie rétrodiffusée par ce type de cible est quasiment nulle. Le niveau radiométrique est alors celui du bruit de fond thermique du capteur, très faible, et de ce fait les bancs apparaissent en noir sur les images considérées séparément. La valeur élevée du contraste radiométrique existant entre la vase lisse et son environnement marin et terrestre permet d'en tracer les limites sans difficulté.

Une composition colorée multitudes (Figure 2) restitue alors les limites bathymétriques correspondant aux hauteurs d'eau existant aux heures de passage du satellite (10h30' solaire, c. à d. 11h local). Ces niveaux sont: 0,65m (17 avril), 2,25m (22 mai), 2,65m (18 dec)

Ces bancs s'étendent ainsi vers le large avec une pente très douce et nous observons ainsi une extension de plusieurs km (entre 1 et 3,5 selon la direction retenue) pour un dénivelé de 1,65m entre le 17 avril et le 22 mai. Ce résultat simple montre que l'extension immergée des bancs est déca kilométrique et l'observation globale du domaine côtier indique que 5 bancs existent actuellement, répartis à peu près régulièrement de l'est à l'ouest de la Guyane.

Une observation attentive permet d'observer des intersections entre les diverses limites de bancs obtenues pour des hauteurs d'eau différentes. Cette complication tient à la dynamique du système étudié car des transformations importantes peuvent intervenir entre deux dates de prise de vues. Dans ce contexte, les plus probables sont: soit des mouvements de bancs (qui pourraient

être de plusieurs centaines de mètres), soit des évolutions d'états de surface dues, par exemple, à la colonisation de la vase par de la mangrove pionnière. En effet, dans ce contexte de très haut contraste radiométrique dû à la réflexion spéculaire des ondes sur la vase lisse, l'apparition d'une légère couverture végétale augmente significativement la rétrodiffusion et la radiométrie de la partie correspondante de l'image.

Signalons que nous n'avons pas pu obtenir directement de résultats concernant la bathymétrie des fonds immédiatement en permanence à partir de la radiométrie enregistrée. L'analyse des images que nous recevrons pour l'année 93 nous permettra de préciser ce point.

III-1-b L'étude des zones de mangroves et de marais

En bordure de l'océan, la cartographie des forêts de mangrove est possible car leur faciès image est caractérisé par une texture image spécifique, très fine. Des étendues marécageuses et de savanes séparent les mangroves de la forêt sur socle. La limite entre la plaine littorale et la forêt intérieure est perçue pour des raisons texturales et radiométriques; les étendues de savanes et de marais correspondant à des zones de textures fines et de radiométries contrastées alors que la forêt est associée à une texture plus grossière et une radiométrie plus uniforme.

L'analyse de la zone de l'embouchure de la rivière de Cayenne et du marais Leblond (Figure 3) fournit les résultats suivants:

La région à l'Ouest-Nord Ouest de Cayenne se caractérise par une zone de marais en bordure de la rive externe du dernier méandre de la rivière de Cayenne.

La branche SE-NW de la crique Fouillée est très visible en raison des contrastes de rétrodiffusion dus à cette saignée ouverte dans la forêt. La petite zone de marais centrée autour de la crique permet de distinguer trois zones: une bande relativement étroite en bordure d'estuaire correspond à une génération récente de palétuviers, formant une forêt dense et relativement basse (de l'ordre de 10 m). Une bande claire marque la limite avec les mangroves de 20 m de haut en moyenne situées plus à l'intérieur des terres. Le passage de la zone basse à la zone haute forme une marche clairement soulignée par la rétrodiffusion. Les mangroves plus anciennes de l'intérieur donnent un grain relativement grossier et un gris moyen tacheté de taches plus claires. Ce grain grossier, comparé à la texture fine que l'on rencontre en général pour les forêts de mangrove adulte non altérée traduit un début de senescence. La zone représentant les mangroves est marquée sur la composition colorée multitudes par un semis de taches colorées qui traduisent là encore l'inhomogénéité du couvert.

Les marais de la crique Fouillée présentent des surfaces de savane inondables, dans lesquelles le sol est alternativement recouvert de quelques décimètres d'eau en fin de saison des pluies ou asséché et éventuellement affecté par des fentes de dessiccation en fin de saison sèche. La radiométrie de cette zone est plus basse que celle des mangroves voisines et l'effet de la dessiccation apparaît lors de la saison sèche.

III-2 Hydrologie (Figure 4):

L'intérêt des images ERS1 dans le domaine de l'hydrologie peut être analysé à diverses échelles. Nous distinguons ci-dessous petite échelle (vision synoptique) et grande échelle (analyse détaillée).

A petite échelle, la vision globale permet de préciser la morphologie des grands bassins versants couvrant l'ensemble du pays. Les cours d'eau apparaissent sous forme d'une bande ou d'un liseré noir lorsque la largeur d'eau libre représente plusieurs fois la taille d'un pixel. D'une manière générale, le réseau hydrographique est facilement perceptible pour deux raisons; d'une part la radiométrie de l'image est modulée par la morphologie des bassins versants et d'autre part les zones de bas fonds inondables produisent une rétrodiffusion légèrement supérieure au milieu environnant et une texture d'image très lisse (par exemple au Sud Ouest de Cayenne la plaine inondable de la rivière Comté).

A grande échelle, l'apport concerne plus particulièrement les petits bassins versants de la plaine littorale. Aucune image de télédétection haute résolution exploitable n'avait pu être acquise jusqu'à présent pendant la saison des pluies sur la Guyane. Les

images ERS1 obtenues en mai et juin 1992, période pluvieuse et très nuageuse, constituent donc un apport particulièrement intéressant pour l'étude des bassins du domaine littoral. Dans la région du bassin versant de la Karouabo, de superficie 83 km², il est maintenant possible de comprendre l'évolution annuelle des principales zones de stockage des eaux. Cette possibilité permet de mieux comprendre le fonctionnement hydrologique de la basse plaine côtière, qui joue un rôle important en regard de l'influence océanique par ses effets "tampons" sur les écoulements naturels (Lointier et al.).

Cette approche dynamique des mécanismes de circulation sur le site test de Karouabo permet de préciser jusqu'à la mer le schéma de fonctionnement particulier du bassin versant (**Figures 4**). Deux familles de milieux peuvent être distinguées:

- Les zones d'accumulation d'eau
- Les zones de circulation

Les premières sont constituées de marais assurant un stockage permanent (n°1), ou temporaire (n° 2, 3). Les données multitemporelles obtenues avec ERS1, assurent d'une bonne définition pour traiter l'aspect dynamique des eaux de surface. On observe que les zones codées 1, sont des plans d'eau permanents, non recouverts de végétation.

A l'inverse, les zones n°2, qui appartiennent au système de plans d'eau se distinguent, en décembre, par une forte augmentation de la rétrodiffusion car une végétation importante semble se développer pendant la saison sèche. Ces zones seront classées à inondation temporaire, à l'échelle mensuelle.

La zone n°3, circonscrite à l'aval de la crique Karouabo, s'individualise le 17 avril, à la suite d'une crue survenue deux jours auparavant. Cette observation est importante car elle confirme la présence de possibilités de stockage de l'eau, en aval, sur une période de quelques jours seulement. Il semble réaliste dans ce cas, d'évoquer un phénomène "d'amortissement" par ces milieux, soit des crues, avant qu'elles n'arrivent en mer, soit des remontées salines biquotidiennes. On explique ainsi l'absence des remontées salines à la station de jaugeage, mais aussi certaines anomalies hydrauliques observées pendant les crues.

Enfin, le milieu n°4, qui contient les zones précédentes, est caractérisé par la présence de multiples cheniers, recouverts de végétation. Ceux-ci font en grande partie obstacle aux écoulements, mais laissent également circuler l'eau à des endroits bien localisés. C'est une zone à double fonction, de circulation et de stockage pendant la saison sèche.

La seconde grande catégorie que nous avons identifiée est celle des zones de circulation (n° 5 à 10). L'analyse multitemporelle met nettement en évidence deux types de milieu de savane, l'un dont la rétrodiffusion est élevée et constante aux trois acquisitions (n°8), l'autre dont la rétrodiffusion est nettement plus basse en décembre (n°7). L'interprétation en terme de dynamique de circulation est plus délicate puisqu'il s'agit d'interpréter des variations dans le couvert végétal. Néanmoins, à l'échelle de temps à laquelle nous décrivons les phénomènes détectés par ERS1, nous pouvons faire l'hypothèse d'une inondabilité faible ou nulle pour le milieu n°8, où aucun changement n'est observé, et une inondabilité temporaire, modifiant la croissance de la végétation pour le type de savanes basses et argileuses n°7.

Les autres domaines ont un fort couvert végétal, dont la nature et la structure dépendent de leur distance à la mer. Aucune différence de rétrodiffusion n'est observable aux trois dates, au cœur même de ces milieux. En termes de dynamique de circulation de l'eau au sol, il n'est pas possible d'obtenir une information pertinente au sol, puisque le domaine d'investigation des micro-ondes en bande C pour un couvert dense, ne concerne que le toit de la végétation. La rétrodiffusion enregistrée permet, en regard des données de terrain, une localisation de ces milieux :

-la zone de mangrove de front de mer (n°5), où les effets de marée sont importants, et où les eaux marines recouvrent la surface vaseuse à marée haute.

-la zone de forêt galerie dans laquelle circulent les eaux de crique (n°6)

- la zone mixte de savane et de forêt (n°9)
- la zone de forêt dense sur socle (n°10)

Pour conclure ce paragraphe consacré à l'hydrologie, insistons sur le fait que l'approche dynamique des mécanismes de circulation des eaux en milieu côtier est considérablement enrichie par l'interprétation des données de ERS1 acquises à quelques mois

d'intervalle. La possibilité d'observer ces écosystèmes durant la saison des pluies permet de distinguer deux types de milieux, les uns propices au stockage, les autres à la circulation. Leur localisation précise est rendue possible, tout comme une évaluation des volumes stockés, par la mesure des surfaces en eau. La confrontation avec les données hydrologiques permet également d'apprecier la durée de ces stockages, annuel, mensuel ou hebdomadaire.

III-3 Topographie et géologie

Des résultats relatifs à la topographie et la géologie sont présentés dans les publications suivantes : Tonon et al. . Deroïn et al, Rudant et al.

III- 4 Activités anthropiques

Nous présenterons dans ce paragraphe quelques aspects liés à la perception des zones urbaines ainsi qu'à la détection des zones de savanes et de prairie (naturelle ou artificielle) et des pistes.

Les structures urbaines: le site du Centre Spatial Guyanais

Comme pour les autres applications , la composition d'images successives permet de réduire le bruit de speckle sans augmenter la taille du pixel et ainsi d'améliorer la résolution effective des images.

Pour les pixels correspondant à des cibles ponctuelles, c'est à dire pour lesquels un très fort réflecteur domine (coin d'immeuble, structure métallique), la radiométrie peut être considérée comme déterministe car l'aléa dû au speckle n'existe plus. Les bâtiments isolés apparaissent toujours sous forme de points brillants dans un environnement ou le "speckle (chatoiement)" est présent. L'exemple traité sur la base de Kourou montre que l'élimination progressive du "speckle" (par composition des scènes disponibles), permet d'isoler nettement les bâtiments et les autres structures (réseau routier par exemple) et de différencier les sols selon leur couvert végétal. L'échelle de restitution semble pouvoir atteindre le 50000ème lorsque l'on utilise plus de 6 images de la même zone. Dans ce dernier cas, le "nombre de vues" calculé sur les zones homogènes à partir du coefficient de variation est de l'ordre de 18. Des tests sont actuellement effectués sur cette zone test pour optimiser le traitement de 6 images obtenues sur le site (3 images par orbite dans une zone de recouvrement de 2 orbites adjacentes).

Notons que l'amélioration de la résolution spatiale permise par l'exploitation des séquences d'images est particulièrement net dans ce domaine d'application .

Site piste de St. Elie - Sinnamary: (Figure 5)

Sur le site de la Piste de St. Elie, on trouve un contact forêt-savane. Ces savanes occupent des sols podzolisés, inondables en saison pluvieuse (Décembre à Juin). Les marges forêt-savane sont généralement abruptes - témoignage du passage régulier du feu en saison sèche (Août-Novembre.). Ces savanes se différencient aisément de la forêt constituée d'un peuplement dense (voûte fermée à 30-35 m. du sol) riche en espèces arborescentes. La rétrodiffusion correspondant à ces zones est plus faible que celle de la forêt environnante. Leur inondation partielle ou totale en saison des pluies fait que leur localisation est plus aisée sur les images acquises en ces saisons car la présence d'eau libre conduit à une rétrodiffusion encore plus faible, alors que le comportement radiométrique de la forêt reste beaucoup plus stable. La savane occupe les sédiments de la plaine côtière ancienne au Nord, et la forêt se trouve sur le socle cristallin au Sud. De larges zones ont été transformées en pâturages et ne subissent plus ces variations saisonnières. Une piste d'orientation générale Nord-Sud, dite piste de St. Elie, pénètre en zone forestière sur une vingtaine de km. Son tracé sinuex date de 1973. Large de 6-7m, elle est bordée de part et d'autre, sur une vingtaine de mètres, d'une végétation pionnière arborée très différente, par sa composition et sa faible hauteur, du peuplement forestier voisin. Une piste latérale d'orientation générale Est-Ouest et au tracé rectiligne se connecte à la piste de St. Elie dès sa pénétration en zone forestière. Cette dernière piste est d'ouverture récente (1991); ses bas-côtés ont été défrichés et remaniés sur une vingtaine de mètres. Le remaniement du sol limite pour l'instant fortement l'installation d'une végétation pionnière.

De part et d'autre de la piste de St. Elie, sur les cinq premiers kilomètres de sa pénétration en zone forestière, se sont installées des cultures par défrichement et brûlis (abattis) de 1 à 5-6 ha., sans parcellaire précis. Certains de ces abattis transformés en pâturages

ou en vergers perdurent depuis une dizaine d'années; cependant, la plupart sont abandonnés et reconquis par la végétation pionnière après 3-4 ans d'exploitation. Chaque année, de nouvelles parcelles de forêt sont défrichées.

L'image radar permet de différencier ces différents faciès lorsque leurs surfaces et contrastes sont suffisants (1 hectare minimum et des abattis d'âges inférieurs à 5 ans). Pour des abattis plus anciens, la recrue est importante et la différenciation radiométrique devient difficile voire impossible. Les zones deforestées apparaissent également dans l'image lorsque l'on peut repérer le contact de la frange forestière de grande hauteur avec une végétation plus basse. La limite est perçue différemment selon que l'on trouve dans le sens du faisceau radar la succession (végétation basse- végétation élevée) marquée par un trait clair ou la succession (forêt- végétation basse) marquée alors par une bande noire due à l'ombre.

Les pâturages entretenus, caractérisés par une rétrodiffusion faible, sont, à surface égale, plus facilement repérables que les abattis.

Le repérage de la piste est rendu nettement plus commode par l'usage de la séquence multitemporelle. Lorsque la piste est parallèle au faisceau (branche latérale), celle-ci est suffisamment large pour concerter 2 pixels et la rétrodiffusion est plus faible car le sol est moins rugueux. De plus, le tracé rectiligne de cette branche facilite son repérage car l'œil est très sensible aux structures rectilignes malgré la présence de bruit résiduel dans l'image. La branche N-S de la piste plus sinuose et de largeur plus faible ne peut être repérée que grâce à des effets de lisière évoqués précédemment à condition toutefois que la largeur ne soit pas trop faible. Notons ici que la faible incidence du faisceau facilite sa pénétration jusqu'au sol entre les deux franges forestières et qu'une incidence plus élevée, à longueur d'onde égale, aurait rendu sa localisation plus difficile. Une longueur d'onde plus grande aurait pour sa part facilité la pénétration de l'onde dans la végétation et probablement conduit à de meilleurs contrastes.

IV- conclusion et travaux futurs

L'imagerie radar ERS1 ouvre donc un champ d'applications très variées en pays tropical humide. Les différents domaines thématiques évoqués ci dessus montrent que ce type d'imagerie est particulièrement bien adaptée à l'étude de l'environnement Guyanais et à celle des transformations que lui font subir divers phénomènes dynamiques, à différentes échelles d'espace et de temps.

Avantage considérable par rapport à l'imagerie "optique", l'insensibilité des ondes centimétriques au couvert nuageux permet d'intégrer des informations de télédétection satellitaire acquises en saison humide dans les études réalisées.

La résolution spatiale des images actuellement disponibles ne permet pas d'aborder avec la même aisance tous les domaines thématiques (en particulier, la cartographie des phénomènes liés aux activités anthropiques) car la précision souhaitée diffère pour chacun d'entre eux. Ce défaut n'est pas intrinsèquement lié au mode d'imagerie considéré; il est associé aux caractéristiques techniques du système spatial actuellement disponible. L'exploitation d'images aéroportées de meilleure résolution sur des sites test ainsi que l'amélioration du rapport signal/bruit par superposition d'images ERS1 successives nous a montré que la résolution était l'un des facteurs essentiels dont dépendait la lisibilité des images. Dans le cas de ERS1, l'échelle pratique d'utilisation varie entre le 200 000 ème (lorsque que l'on dispose d'une image) et le 100 000 ème ou le 50 000 ème lorsque l'on superpose plusieurs images de la même zone.

Nous prévoyons de compléter les travaux présentés dans ce rapport en abordant de nouvelles questions ayant trait à l'écologie et à l'aménagement. La mosaïque réalisée doit servir de fond de carte pour diverses explorations , en particulier pour des prospections géologiques et la préparation des plans d'aménagement du futur parc naturel au sud de la Guyane. Nous espérons également pouvoir suivre fin 1994 l'évolution de l'environnement autour du barrage de Petit Saut et surveiller ensuite l'évolution des végétations aquatiques qui risquent de se développer à la surface du lac artificiel.

La prochaine disponibilités d'images acquises en 1993 nous permettra de préciser l'intérêt des séquences d'images multitemporelles. Par ailleurs, l'extension prévue du domaine géographique de l'étude aux littoraux voisins des états de l'Amapá et du Pará (au Brésil) et du Surinam doit nous permettre de valoriser l'expérience menée en Guyane Française dans un contexte régional en collaboration avec nos collègues brésiliens et surinamiens.

Remerciements: Les travaux présentés ci dessus ont bénéficié de multiples aides et supports techniques. Le Projet Pilote ERS1 "Environnement Littoral et Fluvial Guyanais" , projet commun BRGM-ORSTOM-UPMC a été également mené en collaboration avec les organismes suivants: ADAT, Armée de Terre, CESR, CNES, CRPE, DGA/CEGN, ENST, GDTA, JRC/IRSA, Ministère de l'Environnement, MRT, Université de Paris XI-Orsay. Nous remercions particulièrement le COMSUP Guyane pour nous avoir permis des contrôles de terrain dans des zones très difficiles d'accès.

Références

- Baltzer F., Plaziat JC., Prost MT., Rudant JP., Dechambre M. Use of SAREX, ERS and Erasme data for a comparison between geochemical measurements on interstitial waters and vegetation distribution in equatorial littoral swamp sediments: an example from Marais Leblond, French Guyana. Final Results Workshop, SAREX 92 sous presse
- Deroïn JP., Braux C., Cautru JP., Rudant JP., Toux L. ERS1 SAR: an aid for geological mapping and mineral exploration in rain forest areas. Symposium ERS1 Hamburg pp 897-902
- Héry P., Ducrot-Gambart D., Lopes A., Mougin E., marty G., Fromard F., Blasco F., Rudant J.P., Lointier M., Prost M.T. Cartographie de la végétation tropicale et suivi de la dynamique des mangroves de Guyane par SPOT et ERS1, Colloque SPOT ERS, Paris, Mai 1994.
- Lointier M., Rudant JP., Sabatier D., Prost MT., Nezry E., Degrandi G., Conway J., Sieber AJ. Contribution of ERS1 SAR data to hydrologic approach in tropical area: example in French Guyana. Symposium, ERS1 Hamburg pp 1267-1272
- Mougin E., Lopes A., Héry P., Marty G., Le Toan T., Fromard F., Rudant J.P Multifrequency and multipolarisation observations on mangrove forests of French Guyana during SAREX-92 experiment. Preliminary results.Final Results Workshop, SAREX .sous presse
- Pénicand C., Champseix N., Ledez C., Lentz C., Rudant J.P. Utilisation de l'imagerie satellitaire radar pour la cartographie de base en milieu tropical, Fifth European Conférence EGIS , Paris 29 mars -1 avril 94.
- Prost MT., Baltzer F., Rudant JP., Dechambre M. Using SAREX and ERASME imagery for coastal studies in French Guyana: example of the Kaw swamp.Final Results Workshop, SAREX 92, ---
- Rosaz JM., Maitre H., Rudant JP. Mosaicking ERS1 images: difficulties, solutions and results on the French Guyana.Proceedings Symposium Hamburg pp 1221-1226
- Rudant J.P., Cautru J. P., Lointier M., Charron C., Dechambre.M., Deffontaines B., Deroïn J.P., Prost M.T., Raymond D., Vanderhaeghe O.First results of ERS1 SAR data analysis, pilot project PPF12: Coastal and fluvial environment in French Guiana, Proceedings Symposium Cannes pp 835-845
- Rudant J.P., Lointier M., Prost MT., Cautru JP., Deroïn JP., Sabatier D., Girault D., Tonon M., Nezry.E., Degrandi G., Sieber A.J.. ERS1 SAR dat analysis of the French Guyana coastal plain: some thematic aspects. Proceedings Symposium Hamburg pp 953-960
- Rudant J.P. "La Guyane a travers les nuages, première couverture satellitaire globale", Revue ESA "Observation de la terre" , Juin 1994 ,sous presse
- Tonon M., Rudant J.P., Sabatier D., Nezry E., Degrandi G., Sieber A. Relief Estimation in Tropical context (French Guyana) with SAR-ERS1 imagery Proceedings Symposium, ERS1 Hamburg pp 1261-1268

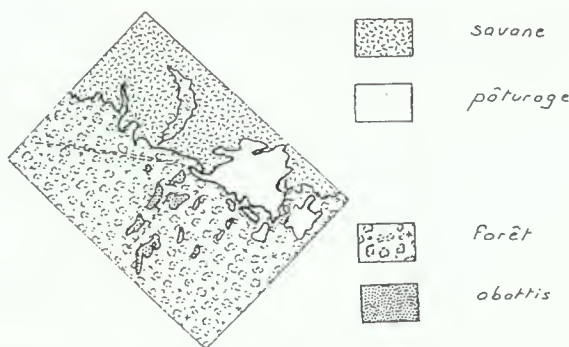
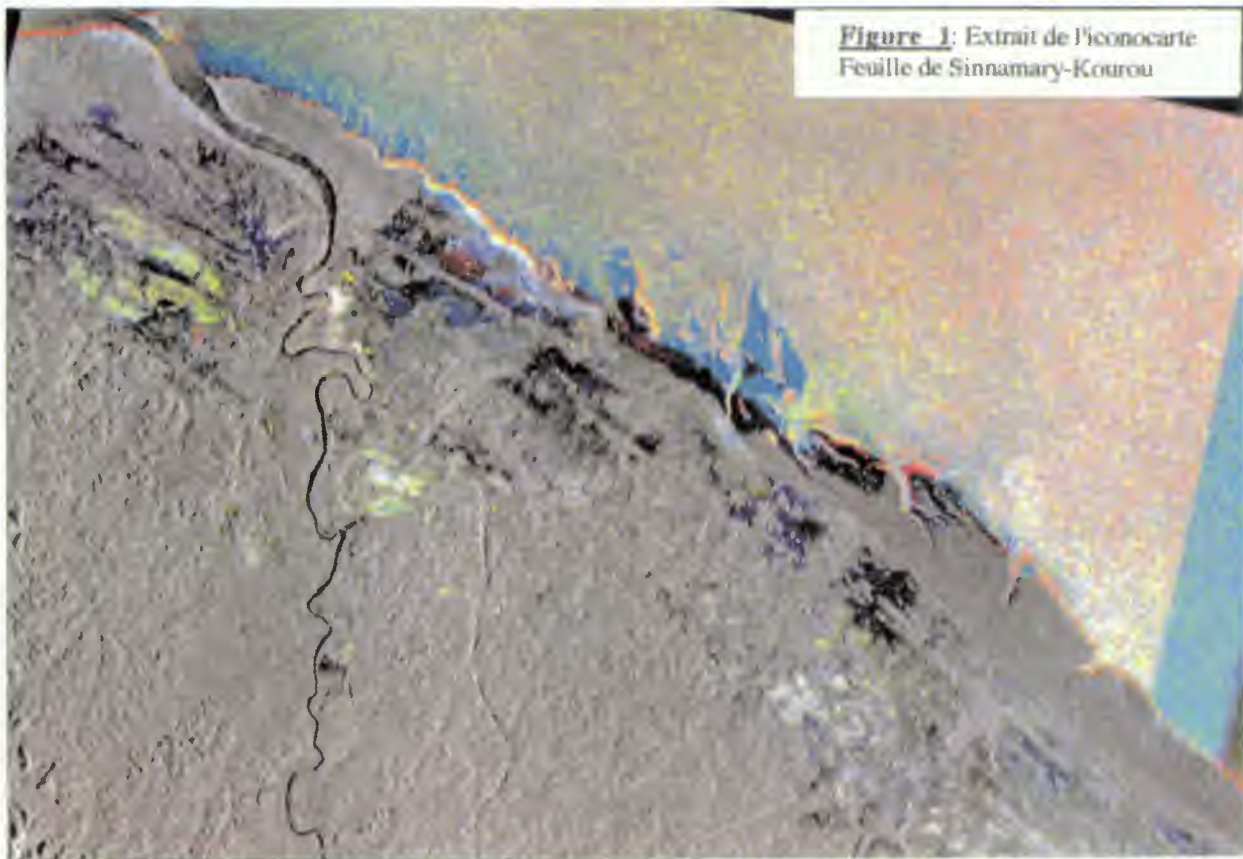


Figure 5: Le voisinage de la Piste de St Elie

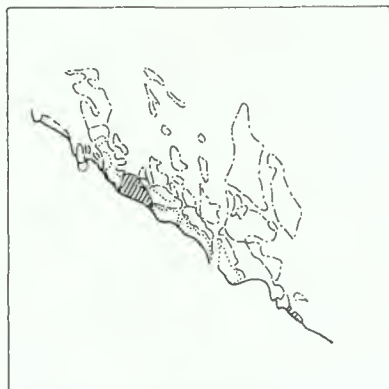


Figure 2: Limites bathymétriques

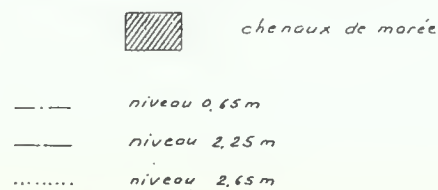
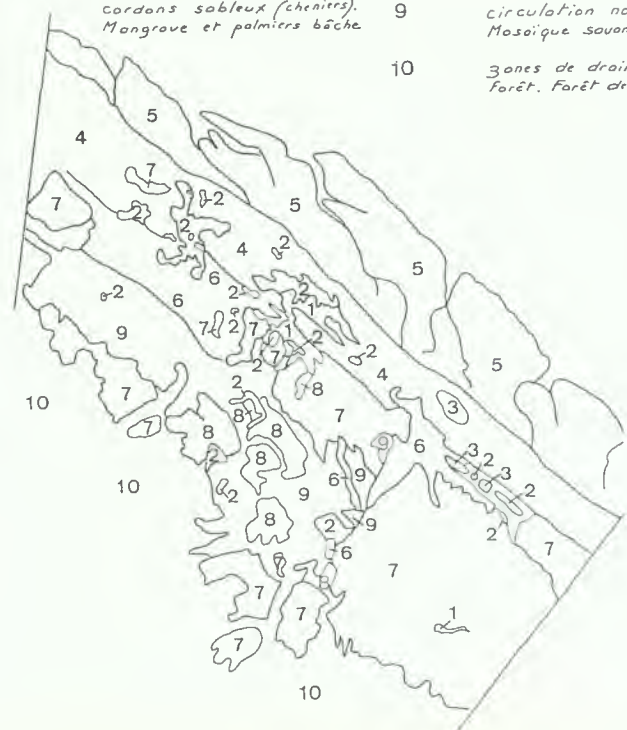
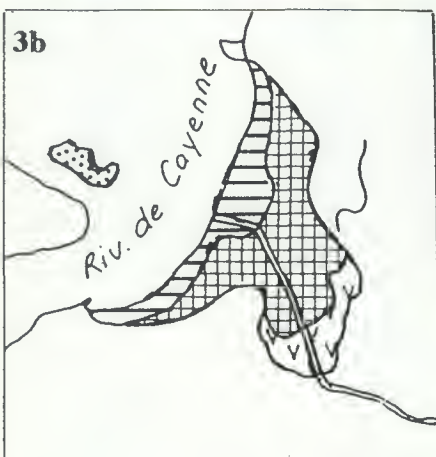
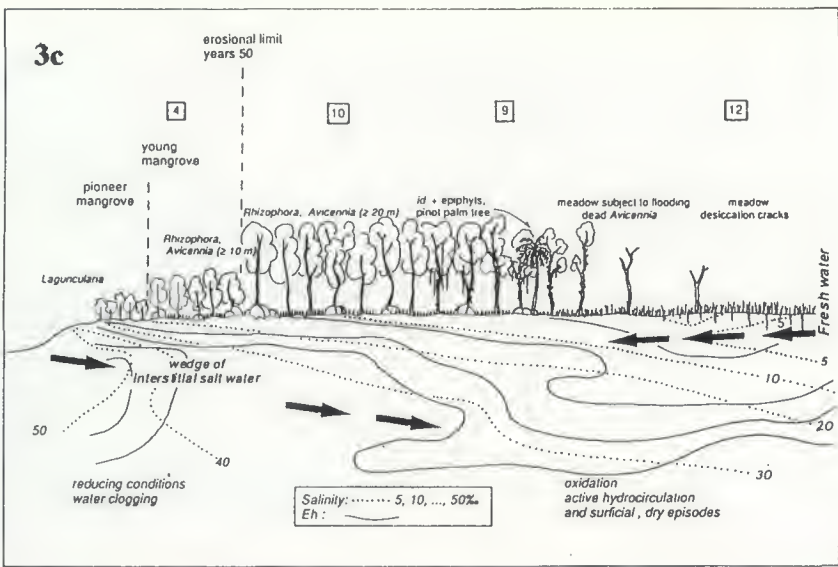
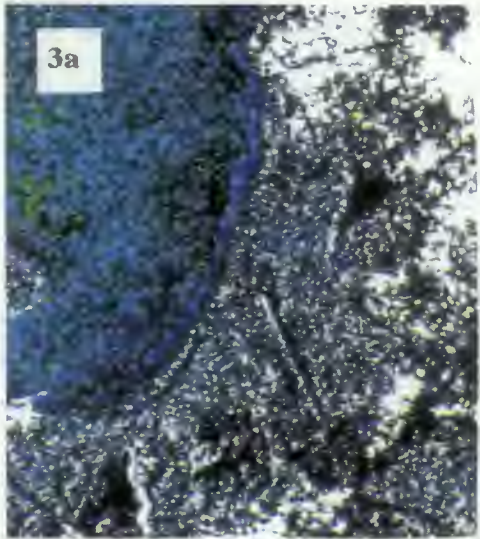


Figure 4: Crique Karouabo:
Zones de stockage et d'écoulement des eaux

- | | | | |
|--|--|---|--|
| | Savane
pâturoge
Forêt
obattis | 1 stockage permanent. Eau libre des marais côtiers
2 stockage temporaire à l'échelle du mois. Marais côtier à développement de végétation en saison sèche
3 stockage temporaire à l'échelle de la journée (une crue)
4 zone de stockage potentiel et de circulation entre cordons sablo-sableux (cheniers). Mangrove et palmiers bâche | 5 circulation avec effets de la marée. Mangrove de front de mer
6 circulation importante sans effets de marée (crique). Présence d'un lit marqué. Forêt galerie |
| | | 7 savane basse orgueilleuse inondable temporairement (à l'échelle du mois) | 8 savane non inondable
9 circulation non observée. Mosoïque savane-forêt |
| | | 10 zones de drainage sous Forêt. Forêt dense sur socle | |





mangrove basse dense



mangrove haute



savane inondable

Figure**3: Zone de Crique Fouillé****3a**-Image ERS1**3b**-Interprétation**3c**-Interprétation géochimique de l'évolution des sédiments et des végétations associées. d'après Baltzer et al.**3d**-Vue aérienne.De l'extérieur vers l'intérieur,
jeune mangrove dense
et mangrove adulte haute**3e**-Fentes de dessiccation en saison sèche zone de savanes inondables

THE USE OF ERS-1 DATA FOR THE DETECTION OF URBAN AREAS

Maylis Galaup, Jochen Harms, Philippe Puyou-Lacassies, Thierry Rabaute

SCOT CONSEIL

1 rue Hermès, Parc Technologique du Canal, 31526 Ramonville Saint Agne, France
phone: (+33) 61 39 46 00, fax: (+33) 39 46 10

ABSTRACT

The goal of this study is to investigate the potential of ERS-1 data and data from other radar satellites for the detection of urban areas and to develop adequate interpretation tools. For this purpose, the test site Barcelona has been chosen. With the help of visual interpretations, the different radar sources were evaluated. Following this, automatic classifications by a pixel classifier approach and a segmentation based field classifier approach were applied to the ERS-1 data. The results show the potential using ERS-1 data specifically within a complementary approach with optical data. The single use of radar data is less important compared to results to be potentially achieved with optical data, taking the higher spatial resolution of this data type into account. Although certain limitations could be shown for the use of ERS-1 data for the detection of urban areas, its usefulness to obtain less precise information in the tropical belt with almost permanent cloud cover should not be underestimated.

1. INTRODUCTION AND OBJECTIVE

Within the past few years the status and evolution of urban areas started to become a study object for the application of remote sensing tools. Optical high resolution data were successfully used to define borders of urban areas. Different urban classes could be identified. In the future, these remote sensing techniques will help the urban planners to investigate for example the urban growth or to evaluate sealed surface. The capabilities of radar data for this purpose have not been investigated yet. Therefore, the major purpose of this study is to evaluate the potential of ERS-1 data for urban application.

2. TEST AREAS

First experience of using ERS-1 data for urban applications could be gained over the MARS Action IV test site Seville and in a cooperation project with the CNT of Tunisia. Following this, a urban radar project has been started to evaluate the capacities of this data type over Barcelona using ERS-1, SEASAT and SPOT data.

3. METHODOLOGY

In a first step visual interpretations of mono- and multitemporal ERS-1 data sets have been performed in order to get accustomed with the radar features. SPOT data and maps of Barcelona were used as a *a-priori* knowledge replacing the ground check. In a second step, automatic unsupervised classifications of the multitemporal ERS-1 data were made. ERS-1 images were compared with the SEASAT image.

4. RESULTS

The results of the visual computer-aided interpretation indicate that within the monotemporal radar data it is very difficult to distinguish some urban areas from other land covers. More particularly, the influence of relief on the differentiation between urban and non-urban areas was clearly shown. However, the different structures corresponding to several districts of the town could be identified. The multi-temporal data sets slightly improve the interpretation quality. On the other hand, some buildings, clearly to identify in the first ERS-1 image are not visible in the second. In order to better understand these phenomena, meteorological (rain, wind) data have been used to avoid misinterpretations. In a further step, a field trip to Barcelona has been organized to compare the radar signal with the reality. This allowed to check the results of visual interpretation and to explain the changes discovered in the multi-temporal data set.

6. NEXT STEPS

As for other applications, the complementarity of radar and optical data can be of major importance for urban investigations. Therefore, the understanding of these effects and the potential for operational applications will be a central point of investigation in the next step.



GIVING AN OPERATIONAL STATUS TO SAR INTERFEROMETRY

Didier Massonnet
CNES French Space Agency
 18, Avenue Edouard Belin 31055 TOULOUSE Cedex
 Tel : (33) 61 27 34 18 - fax (33) 61 27 31 67

SAR interferometry has been confirmed as a very promising technique by the amount and quality of the data provided by ERS1. CNES engaged itself in an effort to give interferometry an industrial and operational status which requires a lot of activity along two axes:

- the development of an industrial network capable of turning raw interferometric products into value added products
- the precise understanding and quantification of the phenomena involved in the interferometric measurement
- the assessment of the extent and the gravity of coherence losses, which is critical for interferometric market share assessment and scene selection

We decided to promote the first point by organising a commercial distribution of selected interferometric product through Spot Image which extends the ERS1 data distribution activity of this company. The three available products will be described. The first point has also been promoted by specific actions, such as an interferometric DEM feasibility study conducted by ISTAR under CNES contract.

The second point can only be made by an in-depth analysis of a large amount of data. This in turn demand the availability of an almost fully operational interferometric processing chain which will be described. Such a tool has been developed at CNES and processed more than one million square kilometres of interferograms with time separation ranging from three days to eighteen months and orbital separations ranging from two meters to eleven hundred meters. The sites we used will be presented as well as the interesting phenomena we spotted, such as landslide, earthquake, water withdrawal or atmospheric propagation errors.

The third point is now better understood as well. We observed a clear case of coherence rebuilding with time, indicating that coherence may be lost temporarily. A tentative explanation of such a phenomena could be found in moisture changes. This situation could be corrected by being more demanding in orbit selection in such areas, at the cost of DEM accuracy.

These activities allow us to have a much clearer view of the potential interferometric market and of the technical features of a future SAR mission which would allow even better performances.

BACKGROUND

SAR interferometry has demonstrated its capability to produce large scale digital elevation models or to detect small moves of various origins, such as surface deformation produced by a large earthquake, a landslide, smaller earthquakes or fault slip as small as 2 cm. More studies detected tidal moves on glaciers or phase surface changes.

At CNES we developed an intermediate product, the interferometric product, which allows the building of topographic models with dedicated industrialists as well as new scientific developments in cooperation with field specialists.

The success of this initial phase urged us to go beyond the conventional uses of interferometry and differential interferometry. Conventional DEM

computation deal with typical scene size of less than 100 km. Conventional moves detection amounts to 10 cm to several meters and develop on at least one square kilometer. We tried to go further with the study of the Landers earthquake, were the large extension of the site (300 km) required very accurate orbit modeling. However, the amount of moves to be measured was still very large. New applications may be much more demanding in terms of scene length and calibration accuracy.

An example where interferometry would be pushed forward in terms of performance is the measurement of local tidal loads on Earth's crust, caused by ocean tides. We plan to study the effect of such a loading on the Cotentin (Normandie, France) in cooperation with GRGS. For this purpose we should be able to study a 600 km long scene for the detection of centimeter sized phenomena.

This urges us to place a high priority on the study of the specific artifacts which could make such applications difficult.

Name of site	Cooperation	Coverage in 1000 sq. km.	# of scenes	Application	Result	COMPLETED STUDIES
Ukraine	ISTAR	14	2	DEM	good	
Ukraine	internal CNES	315	50	System stability	good	Surface : 616000 sq. km.
Ukraine	SOOT	14	2	Phasimetry	promising	
Ukraine	internal CNES	10	4	submetric DEM	good	Number of scenes : 143
Flevoland	ESA - MCS	2.5	2	Processor validation	good	
Sardinia	ESA - ISTAR	5	2	DEM ERS1 versus SPOT	good	
.....	14	2	underground nuclear tests	average	
Landers I	GRGS	3.5	18	earthquakes	good	
Landers II	internal CNES	2.5	4	earthquakes	poor	
Joshua tree	internal CNES	14	4	earthquakes	average	
Northridge	GRGS	20	3	earthquakes	poor	
St Etienne Tinde	ESA - IPGP or BRGM	5	6	Landslide	good	
Papua New Guinea	SPOTIMAGE	40	8	DEM	poor	
Nice	ISTAR	1.4	6	DEM	average	
Berne	ISTAR	1.4	2	DEM	average	
Utah drum Mt	ISTAR	1.4	4	DEM	good	
Utah Irish Cany.	ISTAR	1.4	4	DEM	good	
Pic St Loup	ISTAR	1.4	4	DEM	average	
Spitsberg	ISTAR	1.4	3	DEM	average	
Khyatum	SICORP for US Defence	1.4	2	submetric DEM	poor	
Mount Etna	ESA - IPGP	5	21	volcanic crisis	good	

Name of site	Cooperation	Coverage in 1000 sq. km.	# of scenes	Application	ON GOING STUDIES
Awaji shima	NASDA	5	3	J-ERS1 investigation	Surface : 212000 sq. km.
Northern Hokai.	NASDA	2	4	J-ERS1 investigation	Number of scenes : 76
Sevilla	SOOT	1.4	3	Phasimetry	
Iceland	GRGS + ibd	1.4	2	Rift expansion	
Turkey	ESA - IPG	2.5	6	Fault slip	
Washington	NPOM	2	2	interferometry with ALMAZ	
Siberia	NPOM	2	2	interferometry with ALMAZ	
Le Bouc	BRGM - ESA	2.5	10	Landslide	
Pottstown	GRGS	1.4	3	earthquake	
Eureka	GRGS	1.4	2	earthquake	
Gardanne	BRGM	2.5	6	subsidence from mining	
Spitsberg	Norsk polar institutt	1.4	12	continental glacier flows	
Bretagne	IGN	1.4	10	DEM	
Caucasus	CNRS montpellier	1.4	2	DEM	
Thassos	LTIS	1.4	3	DEM unwrapping	
Bretagne	LGST	1.4	6	Phasimetry	

Name of site	Cooperation	Coverage in 1000 sq. km.	# of scenes	Application	FUTURE STUDIES
Ito Peninsula	NTED	1.4	2	Tectonic uplift	Surface : 907000 sq. km.
Merapi	LGST GRGS	2.5	4	Volcanic crisis	
Atacama	IPGP	2.5	4	earthquake	Number of scenes : 560
Latur	ESA	2.5	14	earthquake	
Cotentin	GRGS	8.0	12	Tidal loads	
Larzac	LTIS	1.4	3	DEM unwrapping	
Colmar	UPMC	1.4	6	Subsidence	
Guyana	UPMC	2.5	6	Equatorial forest	
.....	ISTAR	80	100	DEM	
Western US	French Def. ESA investigation	560	409	atmospheric propagation, clock stability, geophysics	

SCIENTIFIC AND INDUSTRIAL PROGRAM AT CNES

The procedure we used to promote SAR interferometry is clearly explained by figures 1a), 1b) and 1c), which list, respectively, the sites where the investigations are over, the ones where it is on-going and our future plans. The number of scenes involved and the surface of each site is given. The cooperations we built are also indicated with the expected application.

This program is itself a way to ease the access to interferometry for a large number of people. It was completed by the availability of commercial interferometry, now distributed by SPOTIMAGE.

The three proposed products are:

- co-registered single look complex data
- phase, coherence and amplitude of a given pair in slant range
- differential interferogram in map coordinates

The French company ISTAR demonstrated the feasibility of turning interferometric products into digital elevation models, under CNES contract.

AUTOMATIC PROCESSING METHOD

It is clear that a proper development of radar interferometry depends on the existence of a software package capable of dealing with the data automatically. This requirement is already obvious at the scientific investigation level, due to the large number of potential applications and also to the large number of unknown factors, such as the list of artifacts or the success rate in terms of quality. It becomes even more obvious when talking of offering an industrial service.

We developed such a software package based on the method we proposed for dealing with differential interferometry: the digital elevation model elimination method (DEME). This package has been successfully used with ERS1 as well as J-ERS1 data.

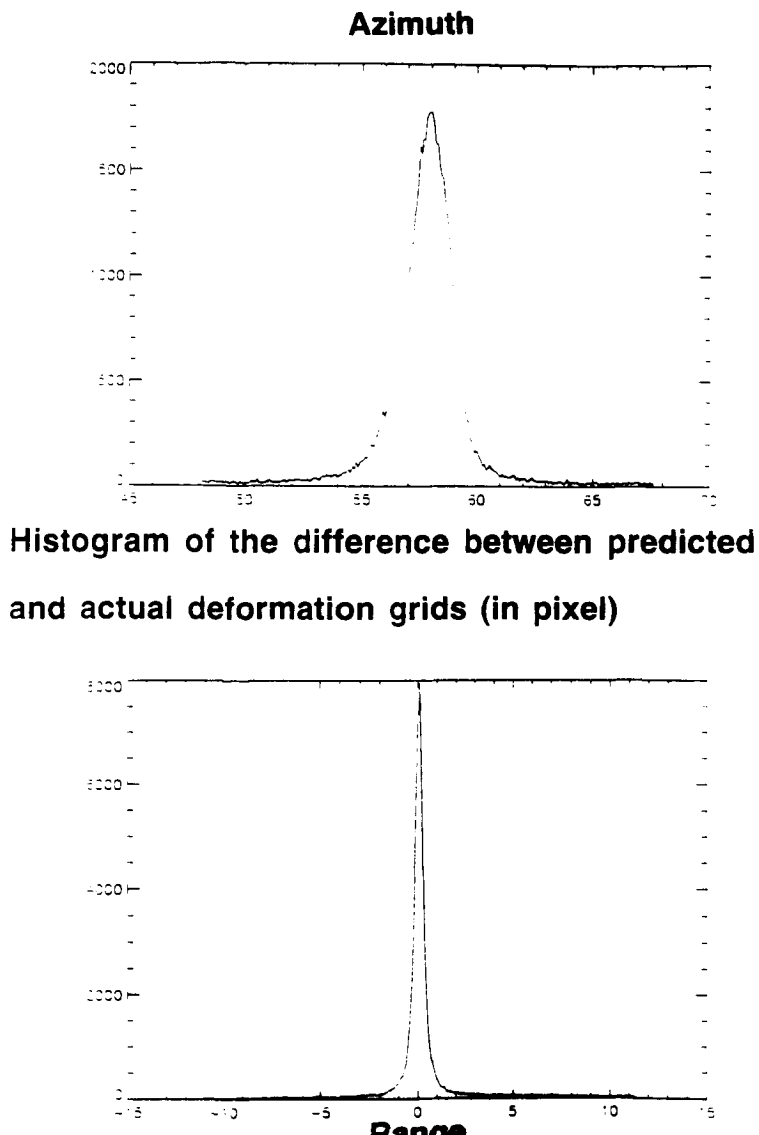
This method consists in simulating and subtracting the topographic fringes from the interferogram in order to extract any motion experienced by the ground between the data takes or to extract any topographic error from the DEM injected in the process.

The method contrasts with the one used by JPL, the double difference method (DD), in differential interferometry. The reason of our choice results of the respective advantages and disadvantages of the two methods.

A clear disadvantage of the DEME is the need for a DEM, which does not exist everywhere. However, we feel that this disadvantage is attenuated by the fact that the heavy geometric distortion of a radar image will require a DEM anyway, for proper geometric correction and data analysis. Furthermore, a DEM can be obtained by a variety of methods: map digitization, optical stereoscopy, and, of course, radar interferometry, but using a pair which has not to be related with the pair of interest. For instance it could be an ascending pair versus a descending pair, a pair from another orbital cycle. The time of orbital difference of the "DEM pair" versus the "motion pair" could be just anything. At worse, if a triplet is available, one could build a DEM from one pair, provided it is motionless, and use the method with the other pair. On this regard, the DD method is the worst case of the DEME method.

We find several advantages to the DEME method. First; the quality of the interferogram is improved, since the data fusion process is improved by slope dependant finite impulse response filters (such filters were optimized

on large quantity of data and their impulse response is based on five points). Second; most of the unwrapping is eliminated since the only remaining fringes come from the moves or the errors in the DEM. Even the roughest DEM, that is a DEM obtained from 1/1000000 scale map digitization, for a cost similar to the one of the ERS1 raw data of the site, will leave only a few remaining fringes. Third; the probability of finding two adequate scenes on a given site, complying to the orbital and surface preservation conditions, is much higher than the probability of finding three such scenes. Four; however rough, a DEM is generally unbiased regarding the long spatial periods. It allows an easy detection of artefacts such as propagation problems or unsuspected moves. These artefacts, if on the "DEM pair" of the DD method, would be modified by equations which apply only to topographic features, which could make the final result very difficult to interpret. Finally, the DEM method proved to be very easy to automatize, even a very rough DEM helps the prediction of the deformation between the images of the pair. The results of local correlations are corrected from the topography and give an indication of the error along the orbit and the error in range with a single voice, as if the image were in the same geometry. Using this, a conventional correlation give a performance in co-registration reaching a few hundredth of a pixel, both in range and azimuth. Figure 2 shows the kind of error detected by these simple correlations, collaborating on the global surface of the image.



The co-registration is obtained not only between the images of the pair, but also between the images and the DEM, which acts as a very large collection of poor ground control points, with an excellent final result.

Figure 3 depicts the interferometric software package. The inputs are the raw data, the orbit estimates and whatever DEM is available. If no DEM is available, the ellipsoid or the geode can be substituted. Five different map conventions are accepted by the software, covering the most common map conventions in the world.

Low resolution images are produced using the zero doppler geometry and are subsequently compared by local correlations to a predicted deformation grid. The difference between the grids can be reduced to two constant numbers since the effect of topography has been taken into account (this effect is quite small, it never reaches one pixel). These constant numbers are used to better the orbits and the near-range.

Using this result, it is possible to process the raw data with one scene following the zero doppler convention and the other being slaved to the first one in terms of geometry, using the deformation prediction which is now very precise with the correct orbit. Our focussing software, called PRISM, allows such a change of geometry during the processing into single look complex data. It is also possible to use the geometry correction software described in the next paragraph.

Once the data have been produced on the high resolution complex format with the same geometry, they are merged, using the above mentioned filters, and produce the three components of the interferometric product : phase, coherence and combined amplitude, with the choice of a slant range or a map geometry.

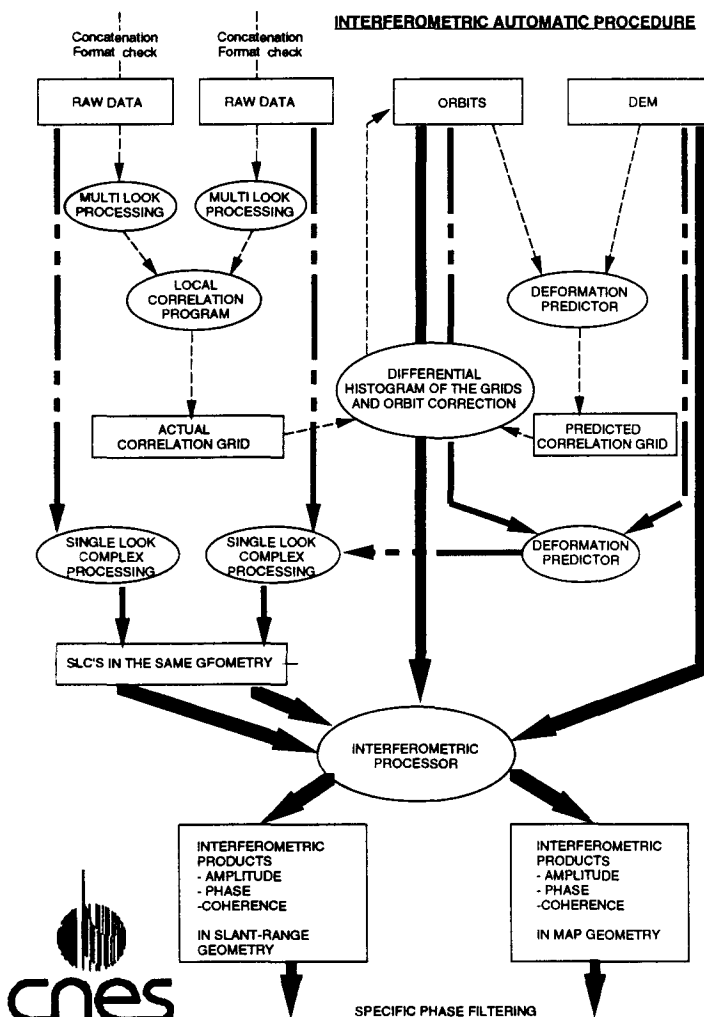
Several mechanisms of lesser importance are not described in figure 3. In particular, it is possible to create a fake amplitude image from the DEM and to use part of figure 3 procedure to coregister the DEM and one of the radar images. Its orbit is then corrected accordingly, which gives the absolute position of the scene. It is also possible to work with single look complex data, using a piece of software which turn them into low resolution images in order to use the co-registration mechanism, and another piece of software which can turn any radar geometry into any other, using FFT based oversampling.

MAJOR HURDLES

The availability of large quantities of high quality interferograms is of little help if we cannot define precisely what is measured. We recently documented clock instabilities using a very long interferometric strip, acquired during orbits 1014 and 1100 (six days apart : 25th of September and 1st of October 1991, 1 A.M. local time), when ERS1 was in commissioning phase. We modelled the clock instabilities and internal studies were conducted in CNES in order to define new clock specifications. The modifications are feasible and not very costly. However, we will have to live with the possibility of clock instabilities with ERS1 and ERS2 and we should be prepared to model such errors and to retrieve them. This is part of an ERS2 investigation which we recently proposed.

More important are the artefacts due to changes in the propagation conditions in the atmosphere. They present a very different signature than topographic or instrumental artifacts. The scene where the problem occurred is identified because all the interferometric pairs to which it participated are affected by the artifact with a constant level, unlike the inaccuracies in the DEM which are weighted by the baseline of each pair. In this, it is similar to the instrumental clock artifact, but unlike the latter, it is not linked to the pulse lines and its amplitude is unlikely to reach more than a few fringes. Once the faulty image has been identified, one can check, knowing the very minute of the data take, the meteorological conditions at that time.

An image over Southern California, taken on August 27 1993, 18:28 UT, shows several 5 to 10 km wide irregular, circular patterns, amounting to up to three fringes (fig. 4), which are clearly identified as



propagation problems using the above logic. The meteorological image of 19:31 shows a chain of small circular clouds which are not yet formed in the 17:01 image (fig.5). This indicates that the fringes are due to tropospheric turbulence, possibly linked to the formation of thunderstorm clouds.

A critical knowledge for the future of SAR interferometry is the behavior of the coherence, which measures the quality of phase preservation, with time and surface types. Generally accepted models assume a linear loss of coherence with time with a slope depending on surface type. Although it is clear that the general trend of coherence versus time could only be a decrease, we observed clear examples of coherence rebuilding with time.

We have no clue as to what could cause a reversible surface state, but soil moisture appears to be a very likely candidate, as it can be restored in its initial value. The coherence of a pair could also be spoiled by bad conditions (for instance high winds) applied to one of the images of the pair.

Another important point in coherence assessment is the major impact of volume scattering. In Southern California, we observed more severe coherence losses on forested areas, as compared to areas where the terrain slopes were similar. However, the situation is not hopeless, as data acquired much later, but with a better orbital configuration, showed an almost complete recovery of the coherence losses. This suggests that targets showing volume scattering are more demanding in terms of orbital repetition than surface targets. As a consequence, the filters we use for interferometric scene matching, which were empirically optimized for surface targets using only the local terrain slope as input, could be optimized with a target dependence. Early results are promising. However, one could question the ability of SAR interferometry to remain operational status and automated if target dependent filtering is required.

9. SLICKS



ERS-1 SYNTHETIC APERTURE RADAR IMAGERY OF THE RHINE-MEUSE DISCHARGE FRONT - PRELIMINARY RESULTS

Jean-Bernard Moens and Kevin Ruddick

Management Unit of the Mathematical Models of
the North Sea and the Scheldt Estuary (MUMM) ,
100 Gilledelle, B-1200 Brussels, Belgium.

Tel : ++ 32 2 773 21 31 ; Fax : ++ 32 2 770 69 72 ; E-mail : mastkr@camme.ac.be

Abstract

Since fronts have often been observed on airborne and satellite radar images, ERS-1 may be useful for studying and monitoring the dispersion at sea of nutrient- and pollutant-rich freshwater from river discharges. The aim of this study is to evaluate the usefulness of ERS-1 SAR for complementing *in situ* measurement campaigns and 3D hydrodynamic modelling of the Rhine-Meuse discharge. Analysis of 16 ERS-1 SAR images suggests that the discharge front is visible as a "step" change in backscatter (σ_0) at low wind speed ($U < 3ms^{-1}$), and as a line of high σ_0 at intermediate wind speed ($U < 10ms^{-1}$). In high winds ($U > 10ms^{-1}$) frontal features are masked by the high ambient sea clutter. The "step" fronts are thought to arise from sea surface temperature (and, hence, air-sea interface stability) discontinuity. The "line" fronts may result from wave-current interaction at the strong surface current convergence, though this hypothesis is only tentative.

1 INTRODUCTION

As the largest river discharging into the North Sea, the Rhine (and its tributaries, including the Meuse) has an important influence on the ecosystem of the Southern Bight via dissolved and sediment-bound nutrients and pollutants. To understand and to quantify better the effect of the Rhine-Meuse discharge on the North Sea, a series of measurement campaigns are being conducted [16] in the Dutch coastal zone and mathematical models are being developed to simulate the hydrodynamics of the region and the influence of hydrodynamics on biological activity and sediment transport. Since frontal structures, separating regions of fresh Rhine water from surrounding North Sea water, may be detected from their surface roughness signature, ERS-1 SAR has been identified as a potential source of data to help understand plume dynamics and to validate models, complementing *in situ* measurements by providing synoptic coverage. The aims of this study are to answer the following three questions :

- Can the Rhine-Meuse discharge front be detected by ERS-1 SAR ?
- What is the front's SAR signature ?
- What is the physical process responsible for this signature ?

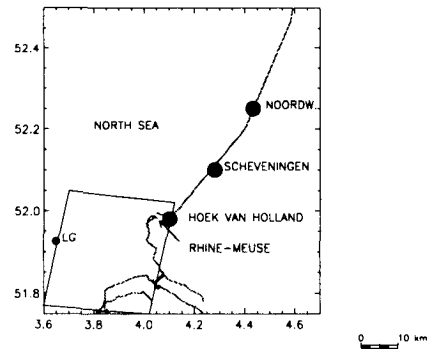


Figure 1: The Dutch coastal zone showing the Rhine-Meuse discharge point (arrow) the zone (box) covered by the ERS-1 SAR sub-image in Figures 2 and 4, major towns and the platform Lichteiland Goeree (LG).

The front formed where Rhine water discharges from the Rotterdam waterway was first observed in the early seventies by Dutch scientists using Side-Looking Airborne Radar (SLAR) [3, 5]. A feasibility study [15] conducted using real aperture X-band SLAR confirmed that the line of high radar backscatter corresponds to the foam line and water colour discontinuity observed at this front. Visual observations of water colour suggest that the cross-front length scale is small ($\sim 10m$).

The variety of radar signatures for fronts found in other regions indicate that frontal discontinuities of current (and, hence, wave-current interaction), surface temperature (and, hence, air-sea interface stability) and/or surface films (and, hence, Bragg wave damping) may influence backscatter [13]. For example, intensive study of the Norwegian coastal zone using airborne, SEASAT and ERS-1 SAR has shown linear high [9] and high-and-low [10] backscatter fronts thought to be caused by wave-current interaction at eddy boundaries, step changes in backscatter at wind fronts and low backscatter filaments arising from surface slicks at mesoscale eddy convergence zones [8]. A combined ship/helicopter/aircraft campaign in the far-field of the Rhine plume [12] showed low backscatter at a front where surfactants caused damping of capillary waves. Surface slicks following eddy stream-

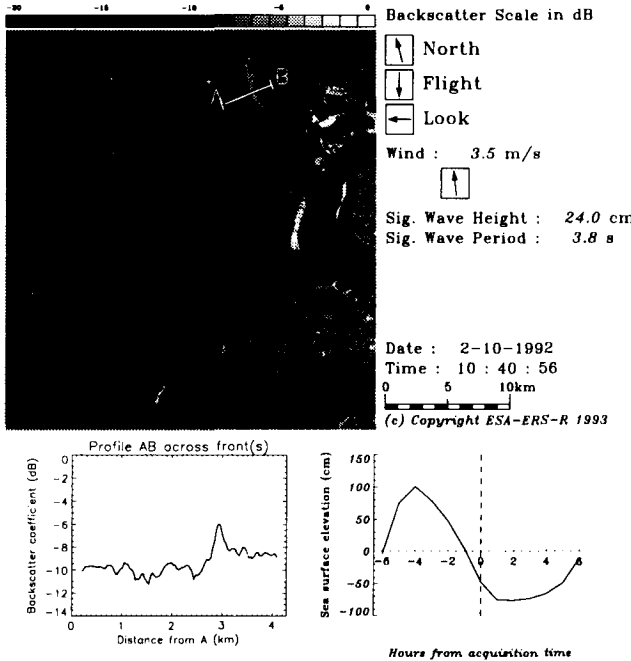


Figure 2: ERS-1 SAR image with front as a bright line of high σ_0 , halfway along the cut marked between the labels A and B. The profile of σ_0 along AB shows a peak about 4dB higher at the front. The water level time series indicates that the image was taken 4 hours after high water at LG, suggesting a weak tidal current to the North-East, just before current reversal [6].

lines were found on ERS-1 SAR images near Vancouver island [7]. Gulf stream fronts may appear as a step change in backscatter, attributed to sea surface temperature change [2], or high or low linear features, for which accumulation of surfactants or wave-current interaction are given as possible explanations [4].

2 SAR IMAGES OF THE DISCHARGE FRONT

All 16 ERS-1 SAR images of the discharge zone from June-December 1992 have been processed and annotated with the prevailing wind, wave and tide data at Lichteiland Goeree (LG), supplied by Rijkswaterstaat. Two types of front were observed in the discharge zone :

- Lines of high σ_0 (9/16 images), e.g. Figures 2 and 3. Typically at the front σ_0 was $\sim -5\text{dB}$, a few dB higher than the surroundings, though there was considerable variation between images.
- Step changes in σ_0 with $\Delta\sigma_0 \sim 15\text{dB}$ (2/16 images), e.g. Figure 4, and higher σ_0 on the (warmer) Rhine side of the front.

The location of these fronts corresponds qualitatively with hydrodynamic model results [14]: freshwater spreads to the South-West with a sharp front on the North-East plume boundary when current is from the North-East (roughly when the tidal elevation is above

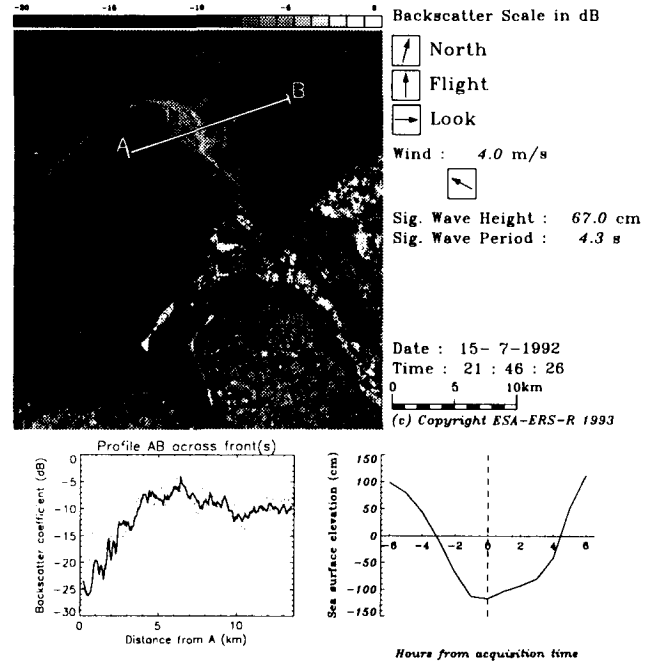


Figure 3: ERS-1 SAR image with front as a bright curved line of high σ_0 , halfway along the cut marked between the labels A and B. The profile of σ_0 along AB shows a 2km band about 3dB higher at the front. The image was taken at low water at LG, suggesting a tidal current to the South-West [6]. The light and dark patches correspond to wind stress variations.

mean sea level), and spreads to the North-East with a sharp front on the South-West plume boundary when current reverses.

Appearance of the radar fronts is strongly linked to wind speed, U (or equivalently, significant wave height H_s). As a rough guide,

- for low winds ($U < 3\text{ms}^{-1}$, $H_s < 0.3\text{m}$) "step" fronts are seen
- for intermediate winds ($3\text{ms}^{-1} < U < 10\text{ms}^{-1}$, $0.3\text{m} < H_s < 1.5\text{m}$) "line" fronts are observed
- at high wind speeds ($U > 10\text{ms}^{-1}$, $H_s > 1.5\text{m}$) the ambient sea clutter is so strong that no frontal features can be detected.

No clear correlation was apparent between the strength of the high σ_0 "line" fronts and neither the phase of the tide (\Rightarrow strength of the surface current convergence), nor wind-look directions. Interestingly though, in contrast to shear-dominated fronts observed elsewhere [10], the "line" fronts never appeared as low σ_0 features.

3 CONCLUSIONS

The strong fronts occurring where the Rhine discharge jet meets the alongshore tidal current (a few kilometers offshore of Hook van Holland) have been observed for many years as lines of high backscatter on X-band SLAR images. Numerical modelling of the hydrodynamics in this region have shown that there is a very strong surface

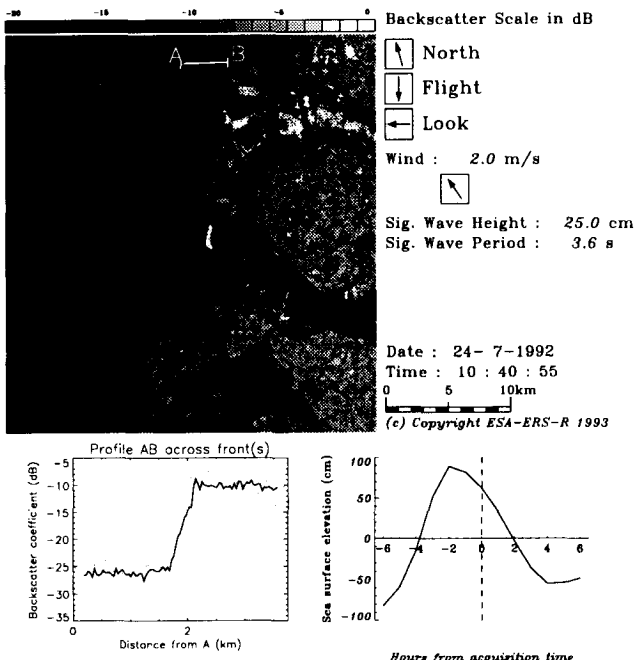


Figure 4: ERS-1 SAR image with front as a step change in σ_0 , separating the high σ_0 Rhine plume water (B) from the low σ_0 ambient water (A). The image was taken 2 hours after high water, suggesting a tidal current to the North-East [6].

current convergence here; this is supported by visible observations of a frontal accumulation of foam and floating debris.

Analysis of ERS-1 SAR images suggest that at

- a) low wind, $U < 3 \text{ ms}^{-1}$

The front appears as a step change in σ_0 with $\Delta\sigma_0 \sim 15 \text{ dB}$.

- b) intermediate wind, $U < 10 \text{ ms}^{-1}$

The front appears as a line of high σ_0 , typically a few dB higher than the surrounding water.

- c) high wind, $U > 10 \text{ ms}^{-1}$

No frontal features are discernible from the high ambient sea clutter.

The “step” fronts probably arise from the difference in sea surface temperature and, hence, air-sea interface stability, across the front. That such fronts are only visible at low wind speed, though then with a very strong backscatter modulation, is consistent with such a hypothesis [2].

The explanation for the “line” fronts is rather more elusive. Wave-current interaction, and possibly wave-breaking, at the strong frontal surface current convergence may explain this. The theoretical basis for wave-current interaction and the subsequent radar backscatter modulation is a subject of ongoing research, though there is hope that analytical or numerical solution of the wave action transport equation, e.g. [1, 17, 11], may provide a quantification of σ_0 modulation by current convergence and shear and thus facilitate testing of such a hypothesis.

4 ACKNOWLEDGEMENTS

This study was funded by the TELSAT programme T3/58/020 managed by the Belgian Science Policy Office. ERS1 data was supplied under Pilot Project PP2-B5. The authors are grateful to J.A. Johannessen, J.P. Matthews, and J. Vogelzang for discussions on SAR imagery of fronts at the ERS-1 symposium in Hamburg. D. Van den Eynde is thanked for advice on wave refraction by currents. The CAMME team, and J.P. Malisse in particular, are acknowledged for providing valuable computing support.

References

- [1] W. Alpers and I. Hennings. A theory of the imaging mechanism of underwater bottom topography by real and synthetic aperture radar. *Journal of Geophysical Research*, C89:10529–10546, 1984.
- [2] F. Askari, G. L. Geernaert, and W. C. Keller. Radar imaging of thermal fronts. *International Journal of Remote Sensing*, 14(2):275–294, 1993.
- [3] E. P. W. Attema and P. Hoogeboom. Microwave measurements over sea in the Netherlands. In T. Lund, editor, *Surveillance of environmental pollution and resources by electromagnetic waves*, pages 291–298. D. Reidel, 1978.
- [4] R. Beal, V. Kudryavtsev, D. Thompson, S. Grodsky, D. Tilley, and V. Dulov. Large and small scale circulation signatures of the ERS-1 SAR over the Gulf Stream. In *Space at the service of our environment*, Proceedings of the second ERS-1 symposium, pages 547–552. European Space Agency, 1994.
- [5] G. P. de Loor. The observation of tidal patterns, currents, and bathymetry with SLAR imagery of the sea. *IEEE Journal of Oceanic Engineering*, OE-6(4):123–129, 1981.
- [6] Dienst Der Hydrografie van de Koninklijke Marine. *Stroomatlas HP16*. Uitgegeven door de Chef der Hydrografie, 1992.
- [7] J. F. R. Gower. Mapping coastal currents with SAR, using naturally-occurring surface slick patterns. In *Space at the service of our environment*, Proceedings of the second ERS-1 symposium, pages 415–418. European Space Agency, 1994.
- [8] J. A. Johannessen, L. P. Røed, and T. Wahl. Eddies detected in ERS-1 SAR images and simulated in reduced gravity model. *International Journal of Remote Sensing*, 14(11):2203–2213, 1993.
- [9] J. A. Johannessen, R. A. Schuchman, O. M. Johannessen, K. L. Davidson, and D. R. Lyzenga. Synthetic Aperture Radar imaging of upper ocean circulation features and wind fronts. *Journal of Geophysical Research*, 96(C6):10411–10422, 1991.
- [10] J. A. Johannessen, R. A. Schuchman, C. Wackerman, G. Digranes, D. Lyzenga, and O. M. Johannessen. Detection of surface current features with ERS-1 SAR. In *Space at the service of our environment*, Proceedings of the second ERS-1 symposium, pages 565–569. European Space Agency, 1994.

- [11] D. R. Lyzenga. Interaction of short surface and electromagnetic waves with ocean fronts. *Journal of Geophysical Research*, 96(C6):10765–10772, 1991.
- [12] J. P. Matthews, V. R. Wisman, K. Lwiza, R. Romeiser, I. Hennings, and G. P. de Loor. High spatial resolution observations of the surface roughness characteristics of Rhine plume frontal boundaries by sunglint and multi-frequency radar techniques. submitted to *Journal of Geophysical Research*, 1992.
- [13] I. S. Robinson. *Satellite oceanography*. Ellis Horwood, 1985.
- [14] K. G. Ruddick, E. Deleersnijder, T. De Mulder, and P. Luyten. A model study of the Rhine discharge front and downwelling circulation. *Tellus*, 46A:149–159, 1994.
- [15] K. G. Ruddick, L. Lahousse, and E. Donnay. Location of the Rhine plume front by airborne remote sensing. *Continental Shelf Research*, 14(4):325–332, 1994.
- [16] J. H. Simpson, W. G. Bos, F. Schirmer, A. J. Souza, T. P. Rippeth, S. E. Jones, and D. Hydes. Periodic stratification in the Rhine ROFI in the North Sea. *Oceanologica Acta*, 16(1):23–32, January 1993.
- [17] J. Vogelzang. The mapping of bottom topography with imaging radar : a comparison of the hydrodynamic modulation in some existing models. *International Journal of Remote Sensing*, 10(9):1503–1518, 1989.

POLLUTION MONITORING USING ERS-1 SAR IMAGES

Terje Wahl (*), Åge Skølv (*), Jørn Harald S. Andersen (**), Guro Dahle Strøm (***)¹, Tom Anderssen (****)

(*) Norwegian Defence Research Establishment (NDRE), P O Box 25, N-2007 Kjeller, Norway.
Phone: +47 63 80 70 00. Fax: +47 63 80 72 12.

(**) Norwegian State Pollution Control Authority (SFT), Oil Pollution Control Department
P O Box 125, N-3191 Horten, Norway.
Phone: +47 33 04 41 61. Fax: +47 33 04 42 57.

(***) Norwegian Space Centre (NSC), P O Box 85 Smestad, N-0309 Oslo, Norway.
Phone: +47 22 53 38 00. Fax: +47 22 52 23 97.

(****) Tromsø Satellite Station (TSS), N-9005 Tromsø, Norway.
Phone: +47 77 68 48 17. Fax: +47 77 65 78 68.

ABSTRACT

Extensive near real-time use was made of ERS-1 SAR images for pollution monitoring in Norwegian waters throughout 1993. This paper presents four rather different events which demonstrate the slick detection capability of ERS-1 under favourable wind conditions. The detected pollutants were: 1) A mixture of fish oil and diesel, 2) Run-off water from an open depository, 3) A controlled chemical spill, and 4) Drilling fluid from an oil rig. In all four cases direct action was taken to clarify the nature of the ERS-1 slick observations. However, no clean-up operations were required. The transfer of the daily ERS-1 pollution monitoring operations from the research lab to more operational entities has been initiated.

INTRODUCTION

Side-looking airborne radar (SLAR) has since 1981 been used operationally by the Norwegian State Pollution Control Authority (SFT) for pollution monitoring in North Sea waters because of the radar's ability to detect dampening of short surface waves. The ERS-1 synthetic aperture radar (SAR) is also very sensitive to changes in the capillary/short gravity wave field on the ocean surface. At low to moderate wind speeds this means that surface slicks of various types can be detected in the SAR images as dark areas against a brighter surrounding sea surface. The temporal and spatial coverage of ERS-1 (and its successor ERS-2) makes it reasonable to use the satellite primarily for early warning, while other assets such as surveillance aircraft are more suited for being brought into action to identify the polluter and estimate the amount of oil when a first alarm has been sounded. This is the basic philosophy underlying the radar satellite oil spill detection project currently being

pursued in Norway. The major milestones in this project have been the following:

- A dedicated ERS-1 oil spill experiment on Haltenbanken outside Central Norway in July/August 1991, where 3 x 20 tons of crude oil were released (Ref. 1).
- An experiment phase in June 1992 - Jan 1993 with near real-time analysis at NDRE of 175 ERS-1 SAR images from the coast of Norway, to explore on-line operations and the problems of false alarms due to slicks of natural origin (Ref. 2).
- A Pilot Operation Phase in April 1993 - Dec 1993, with extensive SAR coverage of Norwegian waters and close cooperation between NDRE and SFT (Ref. 3).

This paper describes four interesting slick detection events that occurred during the Pilot Operation Phase in 1993. The four cases have the following in common:

- Direct action was taken, mainly by SFT, based on near real time analysis of ERS-1 SAR images at NDRE.
- The pollutants causing the detected slicks mostly were of a rather "light" type, thus giving strong evidence of the ERS-1 surface slick detection capability.
- Weather conditions were favourable for slick detection.

The four cases discussed here also show that very different kinds of pollution can cause slicks that are detectable in ERS-1 SAR images. However, a SAR sensor alone is currently not capable of distinguishing between the different pollutants or identify polluters unless the spill is caused by e.g. an oil rig with a fixed position.

INFRASTRUCTURE

The pre-operational chain utilized in Norway for radar satellite detection of marine pollution consists of the following elements (see Figure 1):

- The ERS-1 satellite.
- Tromsø Satellite Station (TSS), a national ERS-1 receiving station located close to 70°N.
- A fast SAR processor at TSS (8 minutes per 100km x 100km SAR scene).
- 2 Mbit/s and 64 kbit/s links from TSS to NDRE for SAR image transfer.
- Operators and workstations at NDRE for fast visual image analysis
- A Fairchild Merlin 3B surveillance aircraft with SLAR, video, IR and UV instruments; contracted and operated by SFT.

Most of the time the project has made use of the 100 m resolution SAR images processed at TSS. This product has a very high radiometric quality (reduced speckle noise), and is very well suited for detection of slicks. During the Pilot Operation Phase, analysis of images from descending ERS-1 passes was usually completed at NDRE within 2 hours after ERS-1 had passed over the area (images from ascending passes were usually analysed the next morning).

SAR images were generally ordered by NDRE 2 days in advance. Meteorological predictions were received on a daily basis at NDRE, making it possible to predict whether one could expect favourable conditions for slick detection. In cases where the long-term weather forecast predicted strong winds, no SAR images would be ordered.

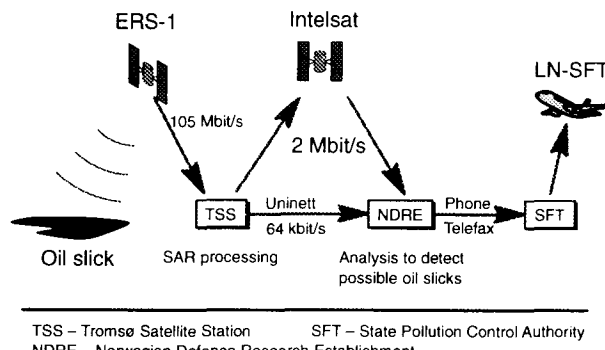


Figure 1.
Infrastructure for oil spill detection using ERS-1.

PILOT OPERATION PHASE

The Pilot Operation Phase lasted from 1 April to 15 December 1993. A total of 255 ERS-1 SAR images, mainly from Norwegian waters, were analysed in near real time during this phase. In the following we present four different cases which show how radar satellite data can be used for pollution monitoring purposes.

Case 1: Fish oil spill, Western Norway, 6 May 1993

This is a typical example of how a satellite observation can be used to trigger aircraft operations. A 4 km² large slick was detected in a position 8 km from the coast (see Figure 2). The situation evolved as follows:

- 10:49 UTC: Descending ERS-1 pass along western cost of Norway.
- 11:50 UTC: Digital images are received at NDRE.
- 12:00 UTC: Image analysis is completed at NDRE. Slick detected. Alarm sounded to SFT.
- 12:10 UTC: Surveillance aircraft directed to the site by SFT.
- 13:25 UTC: Aircraft arrives at indicated position, confirms the presence of oil, and makes estimates of type and quantity.

Wind conditions were very light, there was just enough wind to ripple the sea surface in the area. The aircraft observations revealed that the pollutant was mainly fish oil (probably caused by cleaning of a trawler) mixed with some diesel oil. The size and the position of the slick reported from the aircraft agreed well with the satellite measurements. An interesting fact is that the estimated oil content in the fish waste mixture was very small, only 40 litres. The amount and the type of oil made further action unnecessary, and the case was closed by SFT.

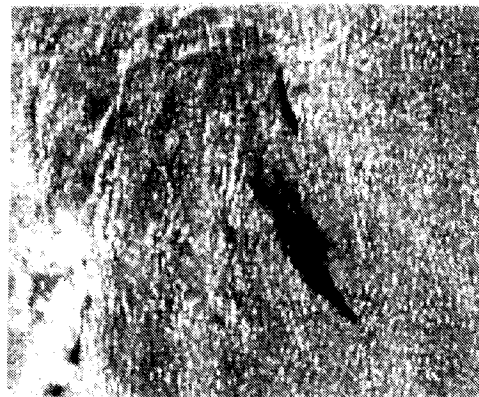


Figure 2.
Oil slick (fish oil and diesel), 6 May 1993. Backscatter change: -8 dB. ERS-1 SAR image: (c) ESA/TSS.

Case 2: Chemical spill, Vestfjorden, 5 July 1993

This was a rather different situation, where a non-toxic chemical (EMKAROX) was deliberately spilled from a research vessel for testing the dampening of short surface waves. However, this controlled release of a slick-forming chemical was not known in advance by the person doing the SAR image analysis at NDRE. Thus it constituted a good test of the detection chain. The events proceeded as follows:

- 19:50 - 20:30 UTC: 20 litres of EMKAROX is released by a foreign research vessel prior to ERS-1 overflight.
- 20:53 UTC: ERS-1 pass over the area.
- 22:00 UTC: Images are received at NDRE.
- 23:00 UTC: Image analysis is completed at NDRE. Several ships are detected, one of them only a few kilometers away from features looking like oil slicks (see Figure 3).
- 04:49 UTC: The foreign research vessel reports to NDRE its position and the observed wind conditions by the time of ERS-1 overflight. The position information confirms that the research vessel was the ship observed close to the detected slicks.

A request from NDRE then followed, asking whether any oil had been spilled from the ship during the last hour before the ERS-1 pass. The answer was that three controlled releases of EMKAROX had been made (for which permission had been granted in advance). A total of 20 litres had been spilled. Wind speed measured on board the ship at ERS-1 overflight was 6 m/s. EMKAROX is a substance which is known to be very effective in forming slicks that affect capillary and short gravity waves (J.C. Scott, pers. comm.).

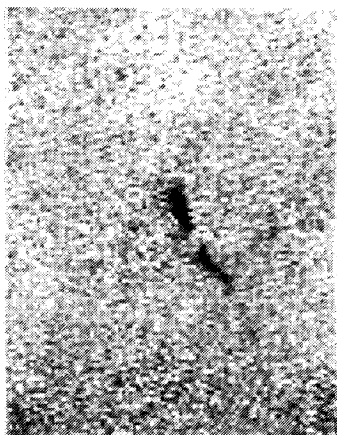


Figure 3.

Chemical slicks, 5 July 1993. Backscatter change: -4 dB. SAR image: (c) ESA/TSS.

Case 3: Run-off from a depository, Oslofjorden, 21 August 1993

This is another interesting case, although the near real time aspect was not as crucial this time. The event occurred after several days of rainfall in the area, and the rain in fact turned out to be a key factor in resolving the case. The following happened:

- 21:14 UTC: ERS-1 descending pass over Oslofjorden, light winds.
- 22:30 UTC: SAR images are received at NDRE.
- 08:30 UTC: First analysis shows no signs of slicks in the open water part of the fjord.
- 10:00 UTC: Further analysis reveals a 6 km thin streak close to land (see Figure 4).
- 11:30 UTC: It is realized that the stripe apparently starts from a place very near an old oil refinery.

SFT was then informed by NDRE about the observation. A paper copy of the SAR image was sent from NDRE to SFT on 24 August for official use.

27 Aug: SFT sends a letter to the refinery, presenting the ERS-1 SAR image and asking for a possible explanation.

1 Sept: A written response is received from the refinery, stating that no oil had been spilled. However, due to heavy rain earlier in the week, run-off water from an old open depository nearby had flowed into the fjord, causing a thin microlayer on the sea surface.

This run-off phenomenon has long been known to occur after rainfall, and is considered to be of no serious harm. The case was then closed by SFT. The phenomenon has later been observed in other ERS-1 SAR images as well as from the SFT surveillance aircraft.

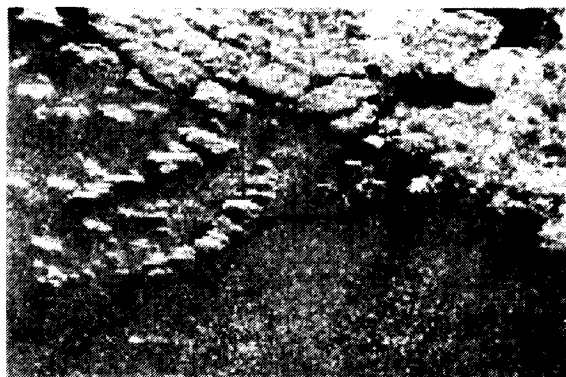


Figure 4.

Run-off water slick, 21 Aug 1993. Backscatter change: -5 dB. SAR image: (c) ESA/TSS.

Case 4: Drilling fluid at oil field, 9 Oct 1993

This is another situation where a signature was found which at first was believed to be oil, but later turned out to have a different, however still very interesting, explanation. On 9 Oct 1993 (a Saturday) the ERS-1 SAR imaged areas some 175 km off the coast of Norway, covering areas where some oil and gas exploration is taking place. The following happened:

10:45 UTC: A descending ERS-1 pass over the Norwegian Sea.

12:30 UTC: Five SAR images are received at NDRE.

15:30 UTC: A 1.1 km² slick is detected at the Heidrun oil field. The source seems to be a rig.

16:30 UTC: Oil spill alarm to SFT from NDRE.

Because of the limited size of the slick and its position far from land, no immediate clean-up operation by the responsible oil company or SFT was required. However, the case needed to be investigated, and SFT requested a copy of the ERS-1 SAR image from NDRE for official use (see Figure 5). A formal letter was later sent from SFT to the oil company responsible for the drilling, referring to the SAR image and requesting an explanation. It turned out that no oil had been spilled from the rig, but during the last 24 hours before the ERS-1 pass a total of 274 m³ of drilling fluid had been released. Some remnants of this fluid was obviously causing the slick. Drilling fluid usually contains baryte, gypsum, and PAC.

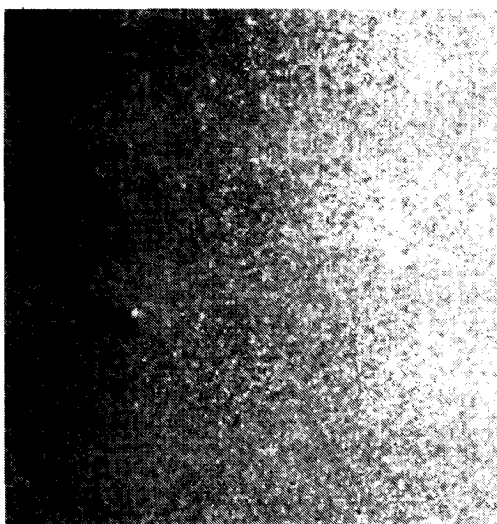


Figure 5.
Drilling fluid slick, 9 Oct 1993. Backscatter change: -4 dB. SAR image: (c) ESA/TSS.

DISCUSSION

The four cases presented in this paper show several aspects of the use of radar satellites for practical pollution monitoring:

- A significant early warning capability
- The ability to detect even very light spills under suitable weather conditions.
- The problem of discriminating between different sorts of pollution.
- Various ways of responding to radar satellite observations, notably
 - * Redirecting patrol aircraft for short-range observations.
 - * Requesting further information from ships.
 - * Formal written requests to refineries, industrial plants, or rig operators.

It is worth mentioning that although no major clean-up operation or legal actions were deemed necessary in these cases, the contribution from ERS-1 was still of high value. Cases 1, 3, and 4 represented real-life situations which would probably have gone undetected without the use of the satellite. It is an important goal of the Norwegian State Pollution Control Authority to have as precise knowledge as possible about spills (not only oil) in the Norwegian waters, although clean-up operations or legal actions will only be initiated in some of the cases. It is believed that the presence of radar satellites such as ERS-1 promote the willingness of the off-shore industry and ships to report pollution incidents according to governmental regulations. However, it must be stressed that ERS-1 data alone is not sufficient for evidence to court documentation.

ERS-1 monitoring of Norwegian waters has continued at NDRE during the first half of 1994. In addition, operators at TSS have undergone training in order to discriminate between pollution signatures and natural slicks. Thus, work has been initiated to ensure a successful transition of the ERS-1 pollution detection service from a research laboratory (NDRE) to a more operational entity (TSS).

CONCLUSIONS

Near real time use of radar satellites in pollution monitoring has recently been demonstrated in Norwegian waters. Four events that occurred in 1993 have been described in this paper. In all four cases ERS-1 SAR images were instrumental in detecting and locating the spills. In three of the cases, the information from the SAR images was forwarded to the Norwegian State Pollution Control Authority, and led to further action being taken. However, it must be stressed that ERS-1 detection of spills like those presented in this

paper is very dependent on wind speed. A wind speed of 3-4 m/s is ideal for imaging of such slicks.

Despite problems with strong winds, ERS-1 and ERS-2 will be important sources of information about pollution on the ocean surface in the years to come. The Norwegian ERS-1 oil spill detection pilot project has reached the point where Norwegian research labs can now focus on new challenges (RADARSAT, SEASTAR, ENVISAT,...) while the daily ERS operations are being taken over by more operational entities.

REFERENCES

1. Bern, T.I., Wahl, T., Anderssen, T., Olsen, R., Oil Spill Detection Using Satellite Based SAR; Experience from a Field Experiment. *Photogrammetric Engineering & Remote Sensing*, Vol 59 (1993), pp 423-428.
2. Wahl, T., Anderssen, T., Eldhuset, K., Skøelv, Å., Ship Traffic Monitoring and Oil Spill Detection Using the ERS-1 SAR", in Proceedings, International Symposium "Operationalization of Remote Sensing, ITC Enschede, the Netherlands, 1993, pp 151-160.
3. Wahl, T., Anderssen, T., Skøelv, Å, Oil Spill Detection Using Satellite Based SAR: Pilot Operation Phase, Final Report. NDRE, January 1994.

Acknowledgements

The Norwegian ERS-1 oil spill detection project is coordinated by Norwegian Space Centre (NSC) on behalf of a Steering Committee with representatives from NSC, SFT, European Space Agency, Marine Spill Response Corporation, Esso Norge A.S., and Statoil, all of which have made valuable contributions to the project.

The authors wish to express their gratitude to Dr John C. Scott of Defence Research Agency, Portland, UK, for details about the controlled chemical slick experiment in Vestfjorden in July 1993. Also, fruitful contributions from the following persons are gratefully acknowledged:

T. I. Bern, OCEANOR A.S.
 H. A. Hovland and G. Digranes, NERSC.
 J. A. Johannessen, NERSC (now at ESA/ESTEC).
 P. Bos, Rijkswaterstaat, the Netherlands.

AUTOMATIC SATELLITE BASED OIL SLICKS DETECTION AND MONITORING SYSTEM

Dr David R. Sloggett, Mr Ian S. Jory

Earth Observation Sciences Ltd, Broadmeade
Farnham Business Park, Farnham, Surrey, UK
phone: +44 (0) 252 721444 fax: +44 (0) 252 712552

ABSTRACT

Environmental agencies, conservation groups and coastguard authorities are all interested in obtaining reliable information on the scale of coastal pollution. Research carried out in Europe, Japan and the United States has demonstrated the potential of the Synthetic Aperture Radar (SAR) on the ERS-1 satellite to detect oil slicks on the surface of the water. However many oceanographic phenomena cause similar effects to oil. If the research carried out thus far is to be used in an operational way these potential sources of false alarms must be removed and the real slicks reliably identified. This is the subject of the research reported within this paper.

The approach discussed is based upon evidential reasoning. This shows that many natural phenomena can be discriminated using reasoning techniques. The paper concludes with a vision of an operational network in Europe linking ERS-1 ground stations, modelling centres and end user agencies.

1. INTRODUCTION

Lean and Hinrichsen (1992) have shown that illegal discharges from tankers accounts for 22% of the oil that exists on the world's oceans. Other sources include municipal waste sites and natural seepage from oil deposits on the ocean floor. Research reported by many European scientists such as Bern et al (1992), Wismann (1993), and Pellemans (1993) has shown that oil slicks can be detected using the Synthetic Aperture Radar (SAR) system on ESA's ERS-1 satellite. In ERS-1 SAR images oil slicks are seen as dark areas where the radar cross section is heavily attenuated. These arise due to the damping of capillary waves when oil lies on the surface.

Research, such as that described by Wismann (1993), has shown that the detection of oil slicks is hampered in three ways. In conditions where the surface of the ocean is totally calm oil slicks will remain undetected as they will merge into the image background. In extreme weather conditions, where the wind speed is very high and the sea surface is well developed, research has shown that the oil slicks become increasingly difficult to detect. Often they break up rapidly and disperse. The second problem arises due to the presence of other features in ERS-1 imagery of oceans and coastal regions arising from natural phenomena, such as other types of surface slicks - such as those arising from dense patches of algal blooms, effects that arise due to being in the lee of coastal features, and several other sources. Several of these effects are now illustrated.

Figure 1 shows an image taken in the Dover Straits on the 16th of June 1994. The weather conditions were excellent and the sea was flat calm, with no wind. This image illustrates shows several vessels moving in the area. It also shows how difficult it is to detect oil slicks in totally calm weather conditions. Figure 2 shows the image published by Bern et al (1992). This shows an oil slick on the ocean with many other natural phenomena that have reduced radar cross sections. Figure 3 shows an image of the North Sea taken on the 20th of June 1994 with an oil slick on the left hand side of the image and several other natural phenomena with characteristics similar to slicks. These last two images highlight the problems faced by research groups whose interest is in the operational exploitation of oil slick information. The key issue here is to reliably detect the single spill in both images whilst removing the false alarms that arise from other natural phenomena who create reduced radar cross section segments within the scene. This is the focus of the research reported in this paper.

2. POTENTIAL USER AGENCIES AND THEIR INFORMATION REQUIREMENTS

Operational use of ERS-1 SAR data for monitoring oil spills has already been pioneered in Norway and The Netherlands. The work reported by Wahl et al (1992), and Pellemans (1993) has been based upon manual interpretation of ERS-1 imagery. Recently, Sloggett and Jory (1994) have suggested that it may be possible to envisage an operational network, operated throughout Europe, based upon information automatically derived from ERS-1 SAR imagery. In Europe there are several potential agencies that would be interested in information on the location and size of oil slicks. They would also be interested in a simple assessment of the type of the slick if that could be derived. Coastguard agencies throughout Europe operate aircraft based sensor systems and ships to monitor these illegal discharges of oil. Their search areas and time on station are limited by the duration of the aircraft or the speed of the ships and the area they can cover in a set period of time. Operations are often limited to daylight hours where a visual identification of the slick can be made. Budgetary constraints also serve to reduce the number of hours that aircraft can patrol. Given all of these constraints the issue is one of using limited resources in the most effective way possible to deter the potential polluters. This is where satellites may have a role to play.

The information derived from ERS-1 data could be integrated within an overall oil spill monitoring and nowcasting based service. This service would use information derived from the ERS-1 ground stations to supply reports on the location, size and type of slicks to local nowcasting centres based in each Member State. This would use local knowledge of coastal currents, tidal patterns, bathymetry and meteorological conditions to provide a nowcasting service to the coastguard authorities on the development of the spills. An important feature of the modelling facilities would be the integration of facilities to simulate the dispersal of the slick. This is where an assessment of the type of oil on the surface would be very important.

The nowcasting service could be used by the agencies concerned to carry out an assessment of the threat posed by the spill to a number of important assets, such as marine aquaculture, coastal resorts, environmentally sensitive areas and harbour facilities. This concept is illustrated in Figure 4. Given the results of this threat assessment the agencies concerned, such as conservation groups, fisheries managers and local authorities, can then make an informed decision as to how to respond most effectively to the spill. The key point here is to select the most cost effective response to the incident.

Another agency that will be interested is the European Environmental Agency (EEA). One task of this organisation will be to collect information on the environment to provide accurate assessments to the European Parliament. They require quantified assessments of many environmental variables in order to select the most appropriate policy response from one of a number of options. The key issue being the development of sustainable economic policies which take account of the environmental impact of each potential approach.

Before conducting socio-economic studies, policy makers require accurate assessments of the nature of the oil spill problems in their regions in order to draft legislation that will be effective. The satellite based system outlined in this paper could provide one element of a system designed initially to collect the statistics that illustrate the nature of the problem and then monitor the effectiveness of any policy that was subsequently implemented.

3. THE RESULTS OF THE PILOT PROGRAMME

3.1 Details of the Research Programme

Research at Earth Observation Sciences Ltd (EOSL) in the United Kingdom has been sponsored by a number of agencies. These are: the British National Space Centre

(BNSC); the Defence Research Agency (DRA); and the Advanced Techniques group of the Institute of Remote Sensing Applications (IRSA) of the Joint Research Centre at Ispra. This research has resulted in the development of a pre-operational capability to automatically detect oil slicks on the surface of the ocean which has recently been installed at the DRA West Freugh ground station. The research programme has focused upon a test area in the North Sea. The test area is shown in Figure 5, where the overpasses in this area for a period in early June is illustrated.

3.2 The Processing Chain

The pre-operational version of the automated algorithm is currently undergoing validation with a number of collaborators in Europe. This algorithm, illustrated in Figure 6, shows that the image is subjected to a number of processing stages. The first of these reduces the resolution of the image prior to it being processed using an edge detection filter. The segmentation process then results in a set of initial regions in the image which are then contrasted with the background. A series of potential oil spills is then identified, called targets, and these are individually processed to derive a series of features that can be used to discriminate natural targets from oil spills. Evidence is built up from each of the potential discriminants as to the probability that this is a slick before a final target region identification algorithm produces a definitive list of likely objects in the image that have characteristics close to a spill.

3.3 Results of the Research

Images collected at West Freugh have been processed and oil spills detected at the ground station have been reported, within a matter of hours, to the United Kingdom (UK) Marine Pollution Control Unit (MPCU) at Southampton who operate the oil spill detection service for the UK Department of Transport. In the period from the 14th of June when the West Freugh ground station started its pre-operational service 5 slicks were detected in the first two weeks of operation in the test area. The first of these was detected on the 20th of June off the coast of the Humber estuary. The slick is shown in Figure 7. It was detected and classified by the automated facility and the report was passed onto the MPCU. In another case, on the 27th of June, a slick was detected by the satellite after a midday pass over the Straits of Dover. The presence of the slick was reported and validated by the UK MPCU within hours of the overpass. The slick detected off the coast of Eastbourne is shown in Figure 8. This had been reported slightly earlier by a ship operating in the area. At this time the wind was blowing south-westerly and it was 2-3 hours before high water on a spring tide which was heading south-westerly at 2.6 knots. The dispersal pattern of the slick appears to support the inference that it developed from the top right hand side of the image with a

combination of wind and tide spreading the slick in a south-westerly direction (towards the bottom left).

This research has provided some preliminary indications that it is possible to derive an automated approach to the detection of oil slicks. The key features identified in the images collected thus far are the fractal characteristics of the edges of the slick, its shape and overall dimensions. Whilst these measures are important false alarms can still occur. Rejection of these is a key aspect of the ongoing research programme to ensure that an operational service is able to provide reliable information on the location and extent of slicks.

The ongoing research programme is focusing upon the integration of more complex evidential reasoning techniques into the automated processor. The second generation of the processor is divided into three elements (Figure 9). The first element - the direct processing chain - is used to derive many parameters directly from the image and a segmented version of the image which is derived from a combination of an edge detection algorithm and a sigma-mu filter. The direct parameters, which are derived on a segmented basis, include statistical assessments of the radar backscatter, measures of the fractal nature of the edges, texture, shape and measures of the size of the slick. Assessments are also carried out over the whole scene to derive background statistics and analysis of the wave spectra. These background measures allow the derivation of an assessment of effect of potential slicks on the underlying wave structure. This is potentially important for trying to classify the type of the slick.

The second processing element is the contextual processing chain. This element brings to the overall reasoning process information on the location of coastlines, meteorological data, tide and current movements and bathymetric data. These sources of information can be used in the reasoning process and in the third element of the oil slicks processor the indirect element. This element uses information from the contextual element to produce inferences about what should be derived from the direct processing element. An example will illustrate this process. The indirect element can use models of the dispersal of a slick to forecast its development from a number of ways in which the slick is originated. Using a combination of wind, wave, tide and current information the shape of the slick can be inferred given a few assumptions about the type of oil present on the surface. The indirect processing chain can deduce several hypothesis about the likely dispersal pattern given that the oil is heavy crude, light crude, or any one of a number of other types of pollutant. This can then be correlated with the actual shapes derived from the image to determine which

most closely match those derived as potential slicks.

The outputs from the three processing chains are brought together using a combination process based upon evidential reasoning. The outputs from the indirect processing element are compared with those derived from the direct processing element to see which of the inferences is most likely. In this combination process the contextual element provides the background to the reasoning to set the reasoning in context. The reasoning process seeks to weigh the evidence to support or refute one of several potential hypothesis as to the likely nature of the object detected in the water. These could be dark ship wakes, sewage outfalls, oceanographic features, wind effects, a algal bloom or a real slick. The evidence is weighed in the reasoning process to determine which of the possible solutions is most likely. If two outcomes are seen to be too close then the process is repeated with slightly different weighting applied to the reasoning to see if a clearer distinction emerges between the likely outcomes.

4. CONCLUSIONS

This research is showing some encouraging results in finding ways in increasing the reliability of detecting oil slicks in ERS-1 imagery and in reducing the probability of false alarms that originate from a variety of different sources. The research has shown that it is possible to provide an automated information service to end user agencies on the location and size of oil spills and slicks in the North Sea. The automated process is based upon the use of evidential reasoning techniques where parameters are derived directly, indirectly (through the use of models) and contextually. The research is still in the pre-operational service stage as we are continuing the validation of the existing processing system and considering improvements that will improve the quality of the information generated. In time we hope to demonstrate that it may be possible to make some form of simplistic assessment of the type of the oil on the surface as a result of analysis of the texture within a slick. This information is of particular interest to the user community as they plan their response to specific oil related incidents.

5. ACKNOWLEDGEMENTS

EOSL would like to acknowledge the support it has received from BNSC, DRA and, more recently, the Advanced Techniques Group of the Institute for Remote Sensing Applications (IRSA) at the Joint Research Centre (JRC) Ispra in carrying out this research activity. Dr Sloggett would like to also acknowledge the

contribution made by Dr Alois Sieber, Mr Mike Boswell, Professor Werner Alpers, Dr Volkmar Vissman and Dr Eric Halsema in the course of this programme.

6. References

Bern, T., Wahl, T, Anderssen, T, Olsen, R. (1992): Oil Spill Detection using Satellite Based SAR: Experience from a field experiment. Proc. First ERS-1 Symposium - Space at the Service of our Environment, Cannes, France, ESA SP-359.

Pellemans, A., Bos, W.G., Van Swol, R.W., Tacoma, A., Konings, H. (1993): Operational use of real-time ERS-1 SAR data for oil spill detection on the North Sea. First Results. Proc. Second ERS-1 Symposium - Space at the Service of our Environment, Hamburg, Germany, ESA SP-361.

Sloggett, D.R., Jory, I. (1994): Oil slicks detection and information dissemination. Proc. 14th EARSeL Conference, Goteborg, Sweden.

Wisemann, V. (1993): Oil spill detection and monitoring with the ERS-1 SAR. Proc. Second ERS-1 Symposium - Space at the Service of our Environment, Hamburg, Germany, ESA SP-361.



Figure 1 Dover Straits Image 10.06.94



Figure 2 North Sea Test Slick Pre-processed Image

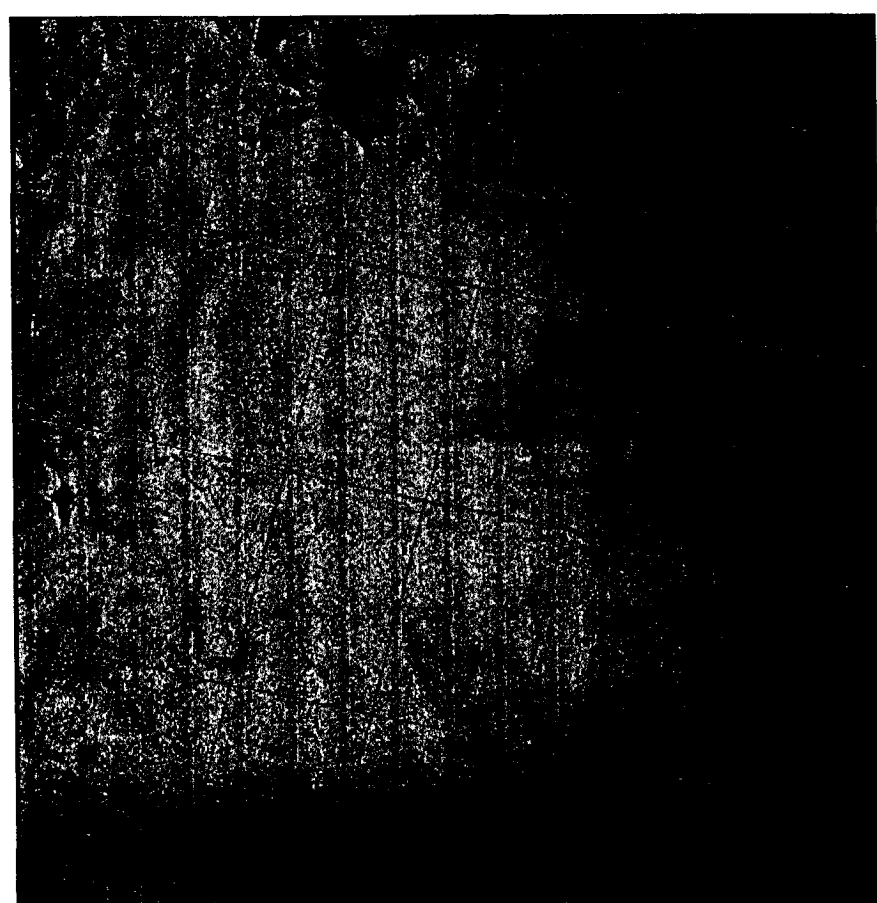


Figure 3 North Sea Image 20.06.94

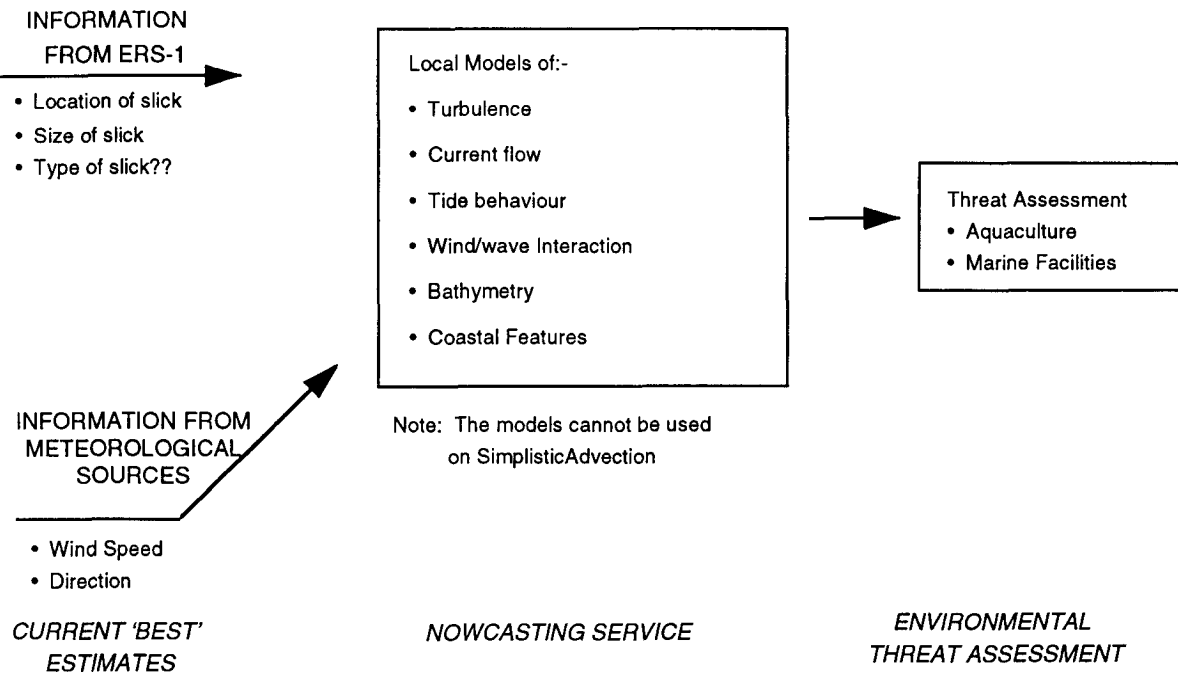


Figure 4 Nowcasting Concept

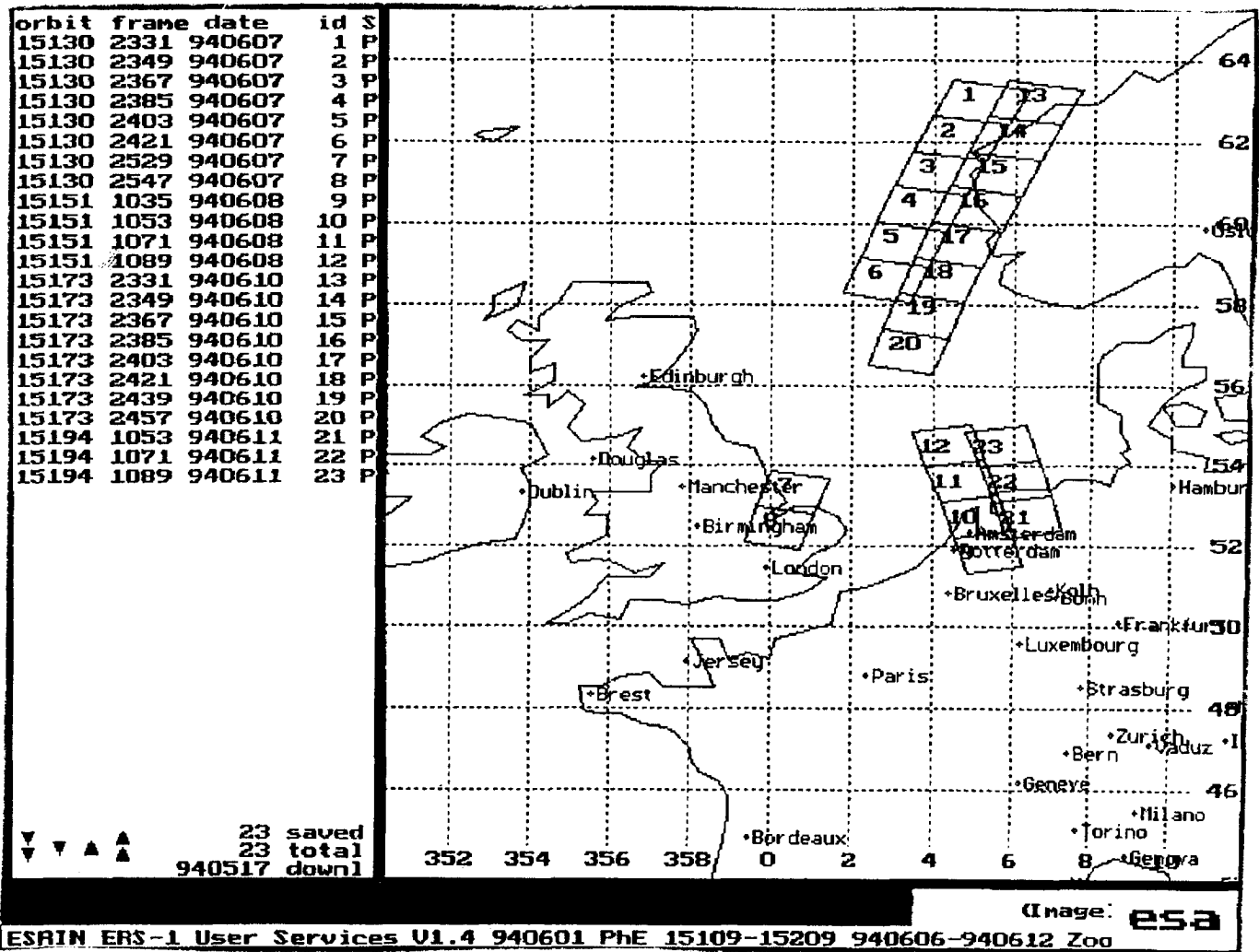


Figure 5 June Test Area

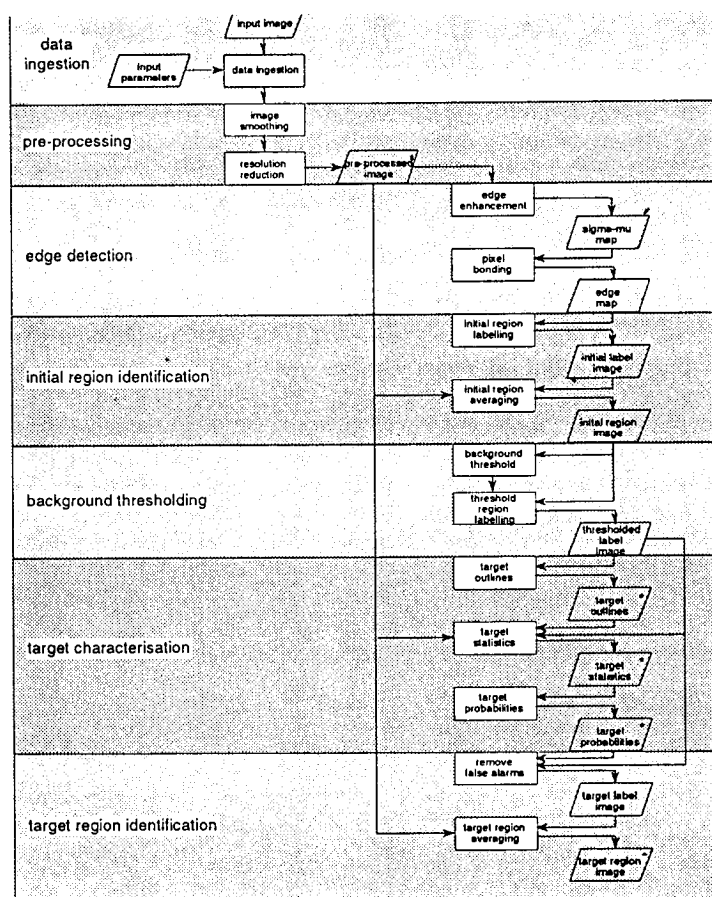


Figure 6 Algorithm Chain

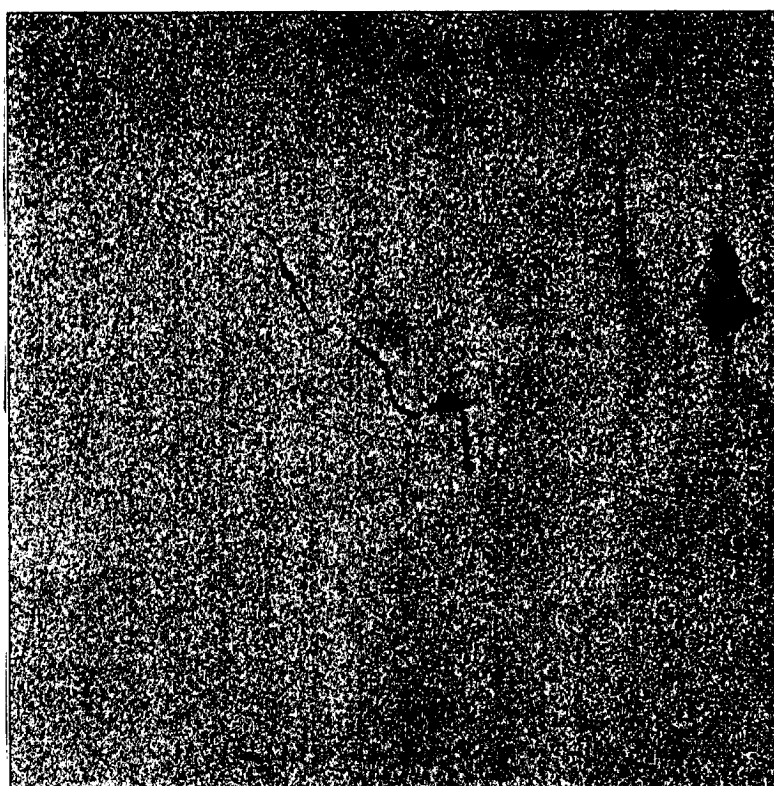


Figure 7 Humber Site

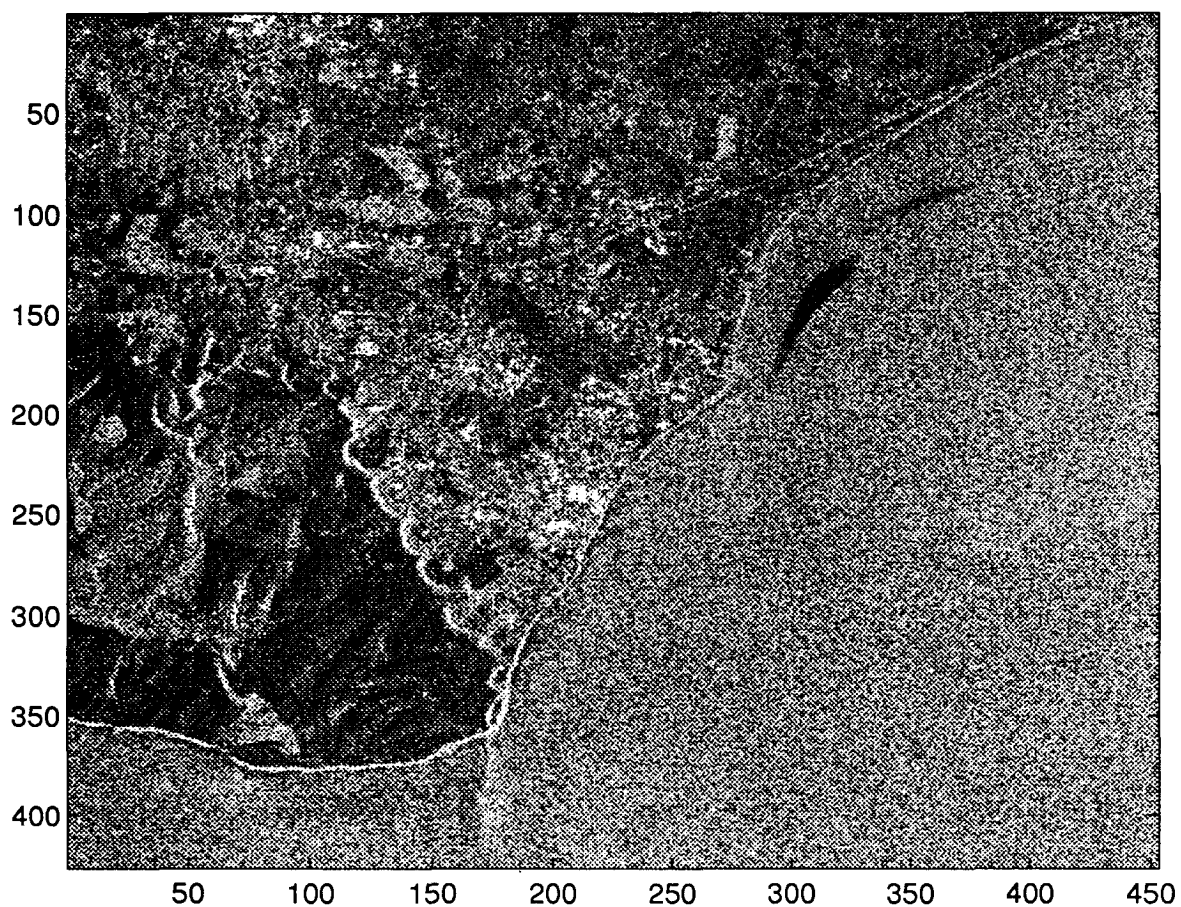


Figure 8 Eastbourne Image

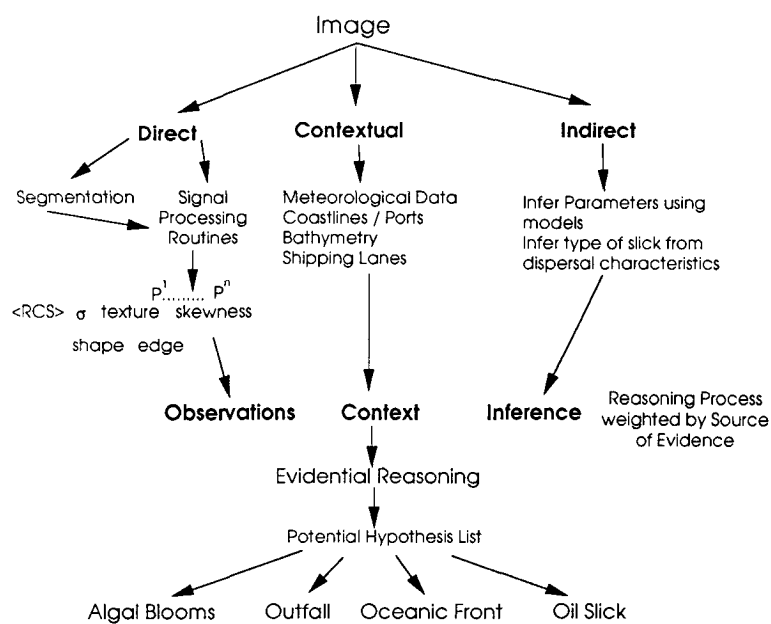


Figure 9 Reasoning Process

OPERATIONAL SYSTEM FOR 'REAL-TIME' OIL SLICK DETECTION BASED ON ERS-1 SAR DATA

A.H.J.M. Pellemans¹, H. Konings², W.G. Bos², R.W. van Swol³

¹Survey Department Rijkswaterstaat
P.O. Box 5023, 2600 GA Delft, The Netherlands
phone: (+31) 15 691362, fax: (+31) 15 618962
email: pellemans@mdi.rws.minvenw.minvenw.400net.nl

²North Sea Directorate Rijkswaterstaat - The Netherlands
³National Aerospace Laboratory NLR - The Netherlands

ABSTRACT

During the multi-disciplinary phase of the ERS-1 in 1993 a pilot project on the usefulness of ERS-1 SAR data for 'near real time' oil slick detection was carried out. In this pilot study both the researchers and the potential end user work closely together. Big advantages of this co-operation are that the information needs, the know how and the equipment of the responsible authorities are available to the researchers and that the end users are acquainted with inside information like intermediate results, the possibilities and the problems. During the pilot project ERS-1 data and simultaneously acquired airborne remote sensing data and environmental information, are gathered and brought together to give insight in the conditions under which ERS-1 can add information to the existing warning systems. A relatively large number of oil slicks were detected by both ERS-1 and the airborne SLAR system. This significant data set gives good insight in the application of ERS-1 data for oil slick detection. Although not all processes of radar remote sensing of the sea surface are known yet, the surplus value of ERS-1 SAR data for oil slick detection can give sufficient ground to establish a ground station and interpretation system for operational oil slick detection.

On the other hand the user requirements are as important as the technical capabilities. The user requirements are also presented in this paper.

1. INTRODUCTION

Airborne imaging radar systems are used for oil spill detection on an operational basis for 10 or 15 years. Recent studies [Bern et al. 1992a,b; Okamoto et al. 1992; Wahl et al 1993] showed that also ERS-1, equipped with a synthetic aperture radar (SAR), can be used for oil slick detection purposes. In 1993 a pilot study was carried out. The objectives, which were discussed in detail in [Pellemans et al. 1993a,1993b], of this pilot are :

- to demonstrate the operational capabilities of ERS-1 FD SAR imagery for oil spill detection.

- to determine the value of the ERS-1 SAR imagery for oil slick detection.
- to propose an operational system for oil slick detection by means of the ERS-1 FD SAR.

Both ERS-1 FD SAR and airborne SLAR information were collected and compared. The work has been done in close cooperation between the research group of Rijkswaterstaat (Survey Department), the North Sea authorities (North Sea Directorate of Rijkswaterstaat) and the Netherlands National Aerospace Laboratory NLR for specific knowledge on ERS-1 and the BDDN network receiving station. The preliminary results of the pilot are presented in this paper.

2. RESULTS

Amount of data.

During the period between 1-jun-93 and 31-dec-93 from the total of 191 assigned ERS-1 SAR FD images, 171 were received and processed (almost 90 percent). Four causes can be identified for an image not to be processed :

- not acquired by ERS-1
- not pre-processed at ground stations
- not transmitted by BDDN
- wrong header information

Due to malfunction of the down link of the ERS-1 during december 1993, and the reconfiguration of the orbit from the 35 days orbits into the ice orbits, in december many images were not acquired. Incidentally an image was not scheduled for Fast Delivery. Also problems had occurred with the SAR processor. A few images (less than 5) had wrong header information. As the header is used for automatic geocoding the images could not be processed.

On 12 days the aircraft has been scheduled to fly simultaneous with the ERS-1. The aircraft has been able to fulfil ten of the twelve planned mission, one mission was carried out by the English colleagues.

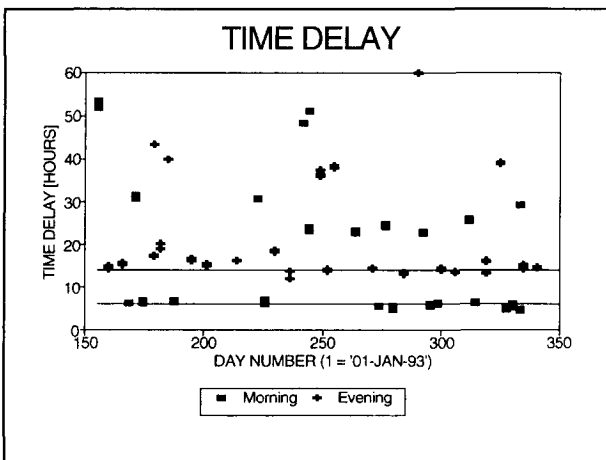
Time delay.

The time delay between actually acquiring and processing of the images is made visible in figure 1 in

date	mission	remarks
04/06	yes	
23/06	yes	
09/07	yes	
28/07	no	technical problems a/c
13/08	yes	
01/09	yes	
17/09	yes	
06/10	yes	no total coverage
22/10	yes	
10/11	yes	
26/11	no	no mission due to fog
15/12	yes	mission carried out by U.K.

Table 1. Aircraft missions.

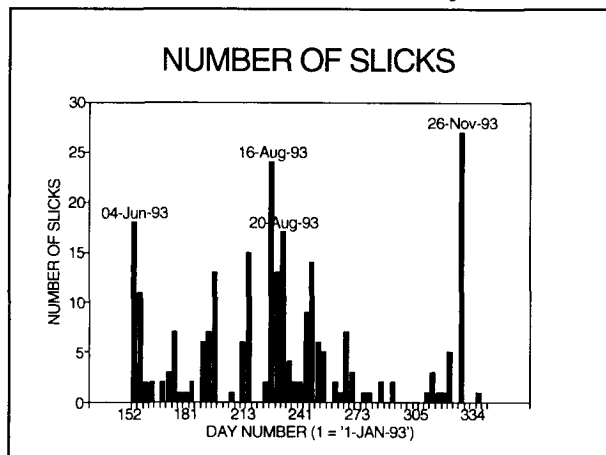
which the time delay in hours is plotted against the day number (day 1 = '1-jan-93'). Due to the fact that the participating institutes do not provide operational services, many of the time delays are large (larger than 20 hour). It is expected that in operational mode these time delay will not appear any more. The interesting part of the figure are the short time delays (shorter than 20 hours). In the figure two levels, marked with two solid horizontal lines, are visible; one at 6 hours and one at 14 hours.

**Figure 1.** Time delay for the ERS-1 SAR images between acquisition and interpretation.

These levels are the best reachable delay time using the BDDN network with the time slots. The level of 6 hours are the morning images that were transmitted in the afternoon slot of BDDN. The second level are the evening images that were transmitted in the time slot of the next morning. These time delays can not be improved unless the time slots of the BDDN network are broadened, or the BDDN network is by-passed.

Number of slicks.

In the processed 171 images a number of 255 slicks were detected what is equal to an average of 1½ per frame. In figure 2 the number of slicks are plotted against the day number. The identified slicks are not all fully investigated, frankly put, it is quite unclear whether or not the slicks represent oil. The slicks were initially only identified by remote sensing specialists, in a later stage all slicks have been checked with the aid of the North Sea Directorate where a lot of experience is available in interpreting radar imagery. This resulted in 48 new slicks and 64 rejected slicks.

**Figure 2.** Number of detected slicks.

The size distribution of the slicks, given in table 2, shows that most slicks are quite small. The small slicks, however, represent only a relative small part of the total covered area. The average slick covers an area of about 2 km².

area class	number of slicks	total area of class [km ²]
< 1 km ²	131	58
1 - 2 km ²	62	92
2 - 5 km ²	36	115
5 - 10 km ²	18	116
≥ 10 km ²	8	151
Total	255	532

Table 2. Size distribution of detected slicks.

Environmental conditions.

The best conditions for detecting oil slicks are not yet fully investigated. But a few preliminary results can be identified. Plotting the number of slicks in one frame against the wind speed at acquisition time a typical pattern becomes visible (figure 1).

The pattern suggests that there is a limit (solid line) above which no sample points exists. It suggests that the probability of detecting oil slicks decreases with increasing wind speed which corresponds well with the results from [Bern et al., 1992b]. For a firm

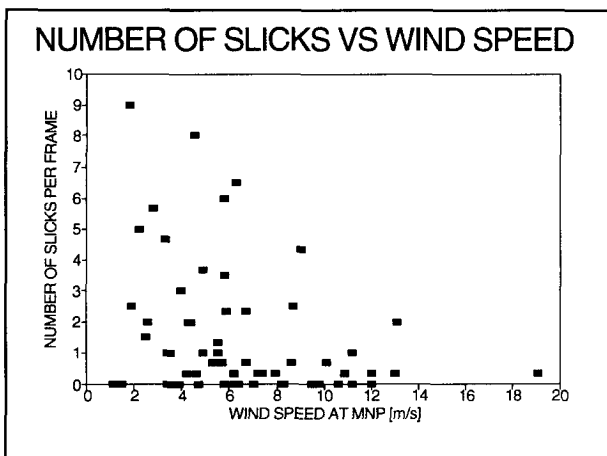


Figure 3. The number of slicks as function of the wind speed.

conclusion more data is needed.

As the radar back scatter depends on the look direction in relation to the wind direction, also the oil slick detection capabilities could show this dependency. Figure 3 shows a random cloud of samples in which no correlation is visible. The suggested relation, however, is not present in the data set. It should be noted here that in figure 3 and 4 the number of slicks is divided by the number of frames on that day (normalised).

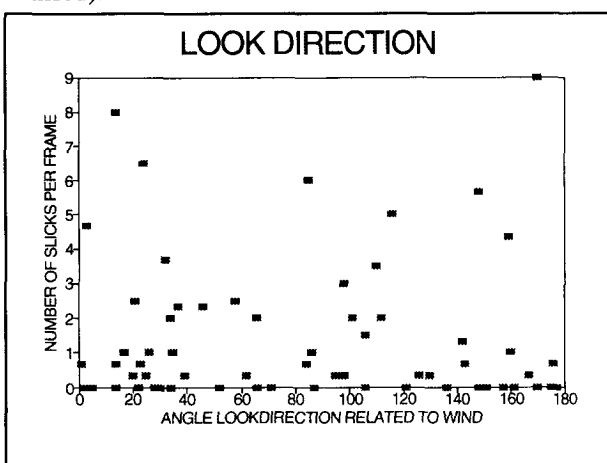


Figure 4. Number of detected slicks in relation to the look direction and the wind direction.

Comparison ERS-1 results and airborne results.

Several slicks are detected by the ERS-1 and the aircraft simultaneously. Plate 1 gives an overview of five of these slicks. The first column are the slicks in full resolution (SAR FD image), the second column shows the same slick after the low resolution processing and the geometric processing. See [Pellemans et al., 1993a, 1993b] for more details. The interpretation is done using low resolution (LR) imagery. The third column are acquired with the remote sensing aircraft of the North Sea Directorate. The instrument used was

an X-band SLAR system with a geometric resolution of 37.5 meters. Notice the agreement of the shape of the slicks. One could easily conclude that the operating frequency of the radar (X-band for SLAR and C-band for SAR), or the incident angle is not relevant for oil slick detection. However, in plate 1 only the slicks which were seen by both instruments are published; most slicks are only seen by just one of the instruments. For a better understanding of the relation between the SLAR and the SAR recent work from [Wismann et al., 1993] has to be incorporated.

date	number of slicks aircraft	number of slicks ERS-1	number of slicks both
04/06	21	18	7
23/06	4	7	1
09/07	5	6	2
28/07	N/A	0	N/A
13/08	1	2	0
01/09	3	9	0
17/09	4	2	0
06/10	1	1	0
22/10	2	2	0
10/11	0	3	0
26/11	N/A	27	N/A
15/12	0	N/A	N/A
SUM	41	77	10

Table 3. Detected slicks from aircraft and ERS-1.

3. USER REQUIREMENTS

Whether a spaceborne SAR system will contribute to the needs of an operational marine organization or not, is depending on several factors. First of all one has to know what kind of information is required. Some general questions concerning long term policy of the organization, budget, required manpower and alternatives have to be answered. More detailed questions like the amount of data, frequency, delivering speed, format, etc. will come up in a later stage.

The North Sea Directorate of Rijkswaterstaat, Directorate-General for Public Works and Water Management, is responsible for the quality of the water in the Dutch part of the North Sea. This area, the Netherlands part of the Continental Shelf, is about 57,000 square km. In order to obtain a rapid and regular overview of the situation at sea, the use of Remote Sensing techniques are considered indispensable.

The organization in which a spaceborne SAR system could be implemented is the section Operational af-

fairs of the North Sea Directorate. The main objectives of this section are:

- Oil pollution combat,
- aerial surveillance, and
- enforcement of marine laws and regulations

Reflecting those objectives to the kind of information a spaceborne SAR system may offer, three categories of pollutions can be distinguished:

1. Large, and therefore most likely combatable spills.
2. Relatively small spills, used for statistics.
3. Operational/accidental discharges by ships or offshore installations.

It is emphasized that the information obtained from a spaceborne SAR alone, is not sufficient to qualify a slick in terms of type and amount; the image will show differences in reflections of the open sea and:

- a. Any substance; mineral- or vegetable oil, natural slicks, chemicals etc.,
- b. geological circumstances; sandbanks, shallow waters etc.,
- c. oceanographic influences; tidal streams, wave patterns etc., or
- d. meteorological influences; wind fields, rain etc.

The requirements of an operational spaceborne SAR system for an operational marine organization are depending on the kind of information in relation to the above mentioned items. Disregarding costs and manpower, time delay of the system (time delay between recording, transmission and receiving of the spaceborne SAR data), frequency and amount of data are the three main questions for the North Sea Directorate. Each of these topics are of different importance to the three objectives of the Department (combat, statistics and operational/accidental discharges):

Requirements for oil combat:

Time delay: Maximum 1 hour.

It is evident that the factor time is crucial in counter pollution strategy. Before any combat vessels is sent out for a combatting action, an aircraft has to verify the spaceborne SAR report in order to advise 'headquarters' what action is feasible. Therefore, the spaceborne SAR data must be available as soon as possible.

Frequency: Every 12 hours.

A serious spill can occur any time, anywhere. It is obvious that an operational organization requires relevant information concerning a major pollution as soon as possible in order to take adequate measures. Combatable slicks will, in general, last more than 12

hours. To get an update of the actual situation, headquarters requires a new situation report at least every 12 hours.

Amount of data/covered area: The entire coastal zone up to 100 miles out.

One image of the ERS-1 covers an area of 10,000 square km. Three adjacent images of an orbit close to the shoreline will cover the most sensitive area.

Requirements for statistical information:

Time delay: A few days.

Statistical information is not depending on recently recorded data. For this reason a time delay of a few days is acceptable.

Frequency: Every 12 hours.

Statistics become more accurate when increasing the number of observations.

Amount of data: See 'frequency'.

Requirements for operational/accidental discharges:

Time delay: No time to waste.

After detection of a pollution by a spaceborne SAR system, an aircraft has to verify the slick, estimate the quantity and identify the source. It is almost impossible to catch the offender 'red handed' due the loss of time (about 1 hour notification of the aircraft and the ferrytime to the slick). Therefore a minimum time-delay is a must.

Frequency: Continuously.

An operational/accidental discharge may happen any time. The chance to catch discharging vessels red handed increases with the increase of observations.

Amount of data: Same as frequency.

The chance to detect an offender increases with the increase of the inspected area. Nevertheless, most traffic sails according several Traffic Separation Schemes relatively near to the Netherlands coast. An orbit covering these Separation Schemes will be most effective, all the more since the main offshore fields on the Netherlands Part of the Continental Shelf are located in between two Separation Schemes.

4. OPERATIONAL USE OF THE ESA MISSIONS

Repeat coverage.

The repeat coverage presented in the earlier mentioned user requirements of 12 hours will not be possible with the present and next generation of radar remote sensing satellites. Although, there are no technical constraints. An orbit like the meteorological NOAA satellites combined with a swath width which is sig-

nificant larger than that of the ERS-1 and 2 could be a solution. The future mission of the Envisat will have an advanced SAR (ASAR) on board. This instrument can be switched in a mode with a larger swath width. This opens the opportunity for acquiring imagery on a higher frequency.

The presented repeat cycle of ERS-2, 35 days, produces subcycles of three days in which 20 to 30 percent of the Netherlands Continental Shelf will be covered. On a yearly basis a maximum of about 400 to 500 images can be acquired. Both satellites operational at the same time will double this amount; then it gets really interesting.

Time delay.

The user requires a time delay of maximum one hour between acquisition and the actual oil slick alarm for oil recovery purposes. During the pilot phase of the project the shortest time between acquisition and oil slick alarm was in the order of 5 hours. This is by far not sufficient for operational use. The most important time delay factor, the transmission, has to be reduced. The BDDN network, which operates for only two hours a day, has to be improved or by-passed. The latter possibility can be achieved by using the Tromsø Satellite Station (TSS) where the SAR processing and the LR processing (low resolution) can be done instantaneous and transmission can be accomplished by using land lines. The second important factor for time delay is the priority scheduling for the SAR processor. In Fucino and Kiruna only three images in a row can be processed. No figures of the processing capacity at TSS are available. For the Netherlands part of the North Sea one track produces a maximum of five images on a row. A new problem will be borne the moment all countries bordering the North Sea will join in. A structural solution will probably have the longest breath.

Amount of data.

As the purpose of the oil slick detection is to monitor the whole area of interest as often as possible in a time as short as possible, it may be clear that the amount of data must be as large as possible. This means the ERS-1 and the ERS-2, but also Radarsat and Envisat, will have to be switched in the AMI Image mode every time when crossing the North Sea. All SAR data has to be made available as FD product, preferably as LR reduced data.

5. CONCLUSIONS

Oil slick detection based on the ESA SAR satellites generation is not far from operational use. The ESA will have to meet the constraints on amount of data made available, the orbits in which a complete coverage is needed and the delivery time, in which

images will be made available, will have to be at maximum one hour after acquisition.

North Sea Directorate would be supporting strongly in their task of operational oil slick detection when space borne SAR systems like ERS-1, ERS-1, Envisat and Radarsat are frequently available at low costs and with short time delay. Where the technical design meets the user requirements there is an opportunity for a useful system.

6. REFERENCES

- [1] Bern, T.I., Wahl, T., Anderssen T., Olsen, R. (1992a): "Oil spill detection using satellite based SAR: experience from a field experiment". *First Thematic Conference on Remote Sensing for Marine and Coastal Environments*, New Orleans, Louisiana, USA, 15-17 June 1992.
- [2] Bern, T.I., Wahl, T., Anderssen, T., Olsen, R. (1992b): "Oil spill detection using satellite based SAR: Experience from a field experiment", *First ESA ERS-1 symposium Cannes*, France, 4-6 November 1992.
- [3] Okamoto K., Shimada M., Nakai M., Shibata A. (1992): "Artificial oil pollution detection and wave observation in the sea adjacent to Japan by ERS-1 SAR", *First ESA ERS-1 symposium Cannes*, France, 4-6 November 1992.
- [4] Pellemans, A.H.J.M., Swol R.W. van, Konings H. (1993), Operational application of 'Real Time' ERS-1 SAR data for oil spill detection. *Proceeding of the International symposium Operationalization of Remote Sensing*, 19-23 April 1993, ITC Enschede, The Netherlands.
- [5] Pellemans, A.H.J.M., Bos, W.G., Swol, R.W. van, Tacoma A., Konings H., (1993), Operational use of 'real-time' ERS-1 SAR data for oil spill detection on the North Sea, *Second ERS-1 symposium "Space at the service of our environment"*, Hamburg, Germany, 11-14 October 1993.
- [6] Wismann V., M. Gade, W. Alpers, H. Huhnerfuss (1993). Radar signatures of mineral oil spill measured by an airborne multi-frequency multi-polarisation microwave scatterometer. *Proceedings of the OCEANS'93 conference*, Victoria, Canada. October 18-21, 1993.
- [7] Wahl T, Eldhuset K, Skoelv A (1993): Ship traffic Monitoring and Oil spill detection using ERS-1. *Proceeding of the International symposium Operationalization of Remote Sensing*, 19-23 April 1993, ITC Enschede, The Netherlands.

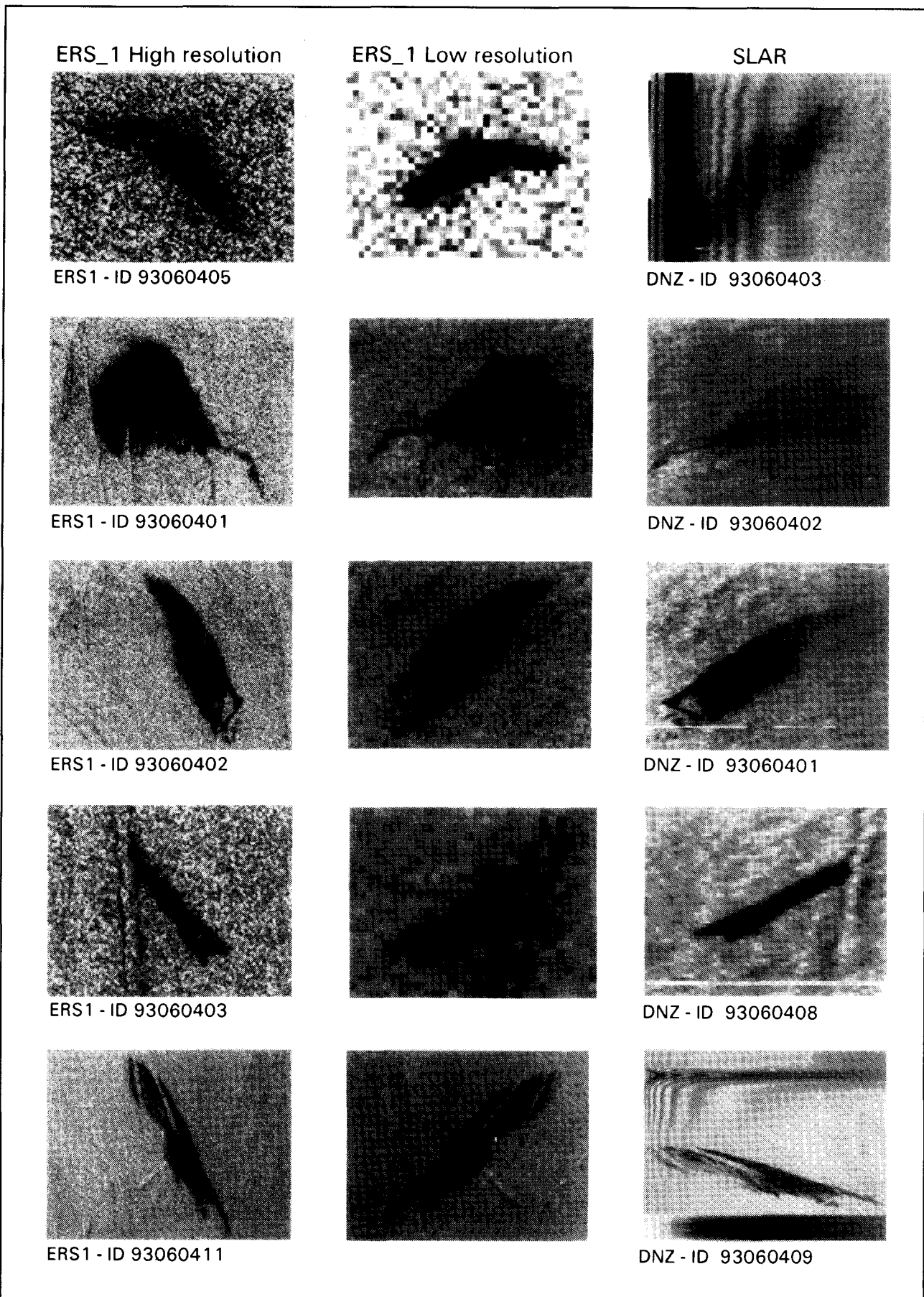


Plate 1. Five oil slicks in original SAR FD image, in Low Resolution image and seen by the airborne SLAR.

Oil Spill Detection and Monitoring with ERS-1 in the "Aegean Sea" Disaster of La Coruña (Dec. 3, 1992)

Antonio de la Cruz, INFOCARTO S.A.
Nuñez de Balboa 115 -2ºJ; 28006, Madrid (Spain)
Phone. 341-5641356; Fax 341-5631147

ABSTRACT

SAR images from ERS-1 have allowed to monitor the accidental oil spill caused by the "Aegean Sea" in the proximity of La Coruña, which on the 13 of December 1992 (ten days after the accident), the ERS-1 SAR image indicated a spilled area of approximately 1000 square Km.

Winds and marine currents pushed the spill from La Coruña to Malpica in the southwest and to the Cape of Estaca de Bares and Ria de Vivero to the northeast. There is some evidence in the SAR images that the oil spill moved further offshore in some areas (Malpica, Estaca de Bares).

Although the wind speed was within the proper range for detection, the strong wave refraction pattern visible in the SAR image of 17 of January, precluded the identification of the spill on this date. After two months of the accident, the SAR image of 8 of February, still showed a clear indication of a considerable oil spill around the area of the accident. Nevertheless, recent examination of SAR images after this date, not included in this study, indicate that the oil spill could have stayed longer on the sea surface around La Coruña Bay.

SAR images show that approximately 200 km of coastline was affected by the spill.

Wind data from the observatory of La Coruña, at the time when the ERS-1 images were obtained, remained within the acceptable range for oil spill identification.

1. INTRODUCTION

On December 3, 1992, the oil tanker "Aegean Sea" carrying 80.000 tons of Brent crude oil run aground due to bad weather conditions when trying to reach the entrance of the harbor of La Coruña. As a result of the accident, some explosions took place and a fire developed that burnt some of the oil but most of it stayed at sea drifting with the winds and polluting the coastline and marine ecosystems.

2. OBJECTIVES

The present project was undertaken by INFOCARTO S.A under contract with the spanish Dirección General de Política Ambiental (Ministerio de Obras Publicas, Transportes y Medio Ambiente) to identify and monitor the extension and duration of the spill with satellite images from LANDSAT, NOAA and ERS-1. Due to the cloudy conditions of this part of Spain, LANDSAT and

NOAA data were of little use. Therefore, most of the study was made with SAR images of ERS-1 obtained in the following dates: **4 October 92**. This image obtained 2 months before the accident was important to compare the effects "before and after"; **13 December 92; 1st. January 93; 17 January 93** and **8 February 93**. However, the fire and associated plume of smoke of large dimension was identified by LANDSAT TM on a pass which coincided with the date of the accident.

The SAR images of ERS-1 were processed with the Radar Module of ERDAS -IMAGINE V.8.1. by Julio de la Cruz

3. OIL SPILL DETECTION BY RADAR

Detection of oil spills by radar is a mature application in which many good results have been obtained and there are already a number of operational projects providing reliable services in oil spill surveillance. However, since this is the first application case that this technology was attempted in Spain, there were some misconceptions that have to be addressed by educating and training the potential users. As the area was frequently surveyed by flights during the clean up operations, there were many comparisons between the spilled areas identified by radar and from the airplanes. Many observers from the air thinking that the spilled areas indicated by radar far exceed those identified from the airplanes. Their maps of polluted areas, obtained from daily flights, showing rather small and scattered spills, reflect this belief. It was explained to them that from experimental projects in which a controlled amount of oil is dumped into the sea (Galli de Paratesi, 1992), it is well

DETECCION DE VERTIDOS POR RADAR

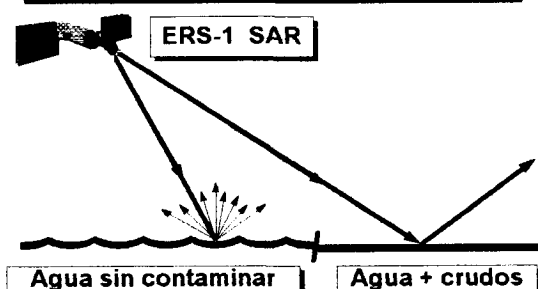


Figure 1. Backscatter difference in clean and polluted waters

known that a very thin layer of oil of a few um (a millionth of a meter !) is enough to damp and eliminate the capillary waves that causes the roughness and therefore the wide backscattering that is typical of clean non-polluted waters in the images of radar of ERS-1.(Fig. 1).

It is also known from experimental projects (Sorensen, 1993) that by damping 60 litre of oil into the sea -the volume equivalent of the petrol tank of a car- the effects of this spill would be identified by radar sensors in airplanes and satellites (Fig. 2). It should also be considered that aerial surveys in that part of Spain are restricted by cloud cover. Therefore, if 80,000 tons of crude oil are released into the sea, we are likely to see a lot of it and during a long time in the images of radar.

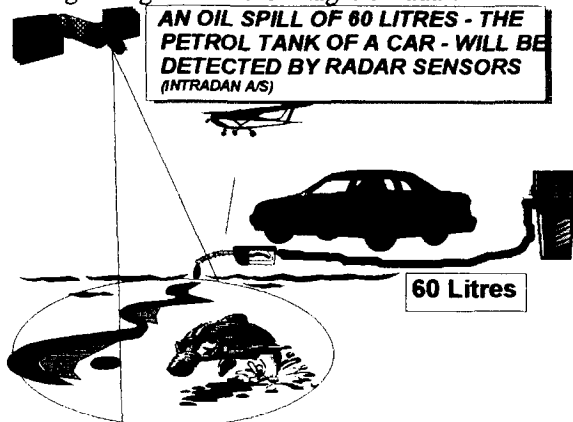


Figure 2. Sensitivity of radar sensors to oil spills

The backscattered signal measured by the SAR sensor is directly related with the surface roughness. The state of open waters could be anything from calm to extremely rough. The rougher the water, the greater the amount of backscattered energy and vice versa. Oil floats on water due to its viscosity and minor density. This floating oil produces a dampening effect on the water in comparison with the surrounding areas (Fig. 3). For effective oil monitoring by SAR images, this dampening effect, should produce less backscatter than the surrounded areas.



Figure 3. Capillary waves are associated with clean waters and absent in spilled areas

As shown in figure 4, oil spill detection by radar is restricted by environmental factors such as wind speed. Optimal results are obtained in the window between 3 and 9 m/s. Below this range, spill areas can not be differentiated from calm areas in the dark zones registered by the images of radar. Above this range, oil interacts with water constantly and detection has not been observed in the SAR images which present light zones due to intense backscattering. This was the case after the accident of the "Braer" oil tanker that took place in the Shetland Islands one month after the accident of the "Aegean Sea.

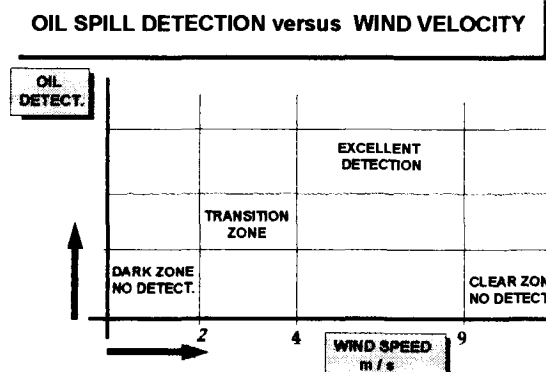


Figure 4. Influence of wind speed on oil spill detection

4. IDENTIFICATION AND MONITORING

In this section the SAR images from ascending and descending passes that were selected to follow the development of the oil spill will be described and interpreted in chronological order.

4.1. ERS-1 SAR image of 4 October 1992.

This image (Fig. 5) obtained almost two months before the accident was selected to compare in the SAR images the effects of the spill "before and after" the accident. This image is very "clean" indicating the absence of low wind speed areas or other oceanographic phenomena that could have produced dark zones. This circumstance made comparisons before and after the accident even more dramatic. The only dark areas, which are very small, are restricted to some of the "rias" and have been caused by the sheltering effects of the coast. Wind speed data from the Observatory of La Coruña registered a range between 3 and 6 m/s for this date which is favourable for the interpretation.

This image has a westerly look direction subperpendicular to the wave direction which is an excellent situation for SAR identification.

4.2. ERS-1 SAR image of 13 December 1992.

This is the first image obtained by ERS-1 after ten days of the accident of the "Aegean Sea" and clearly indicates the extension of the spill of approximately 1000 square km. (Fig. 6). The dark zone of the spill is not uniform and several tones of grey to black can be observed. Although SAR images can not measure thickness, they can provide a rough estimation as to where the heavy concentration of pollution could be situated. By comparisons with aircraft observations it is concluded that the very dark area is heavily polluted while the lighter grey tones correspond with more dispersed oil (Lichtenegger, 1994.) This image has also a westerly look direction which is subperpendicular to the few wave directions observed in the image. This was an optimal set up to identify the oil spill clearly.

On this date, wind speed was 3 m/s and above.

4.3. ERS-1 SAR image of 1st January 1993.

By comparison with the previous image of 13 December 92, this image (Fig. 7) shows the oil spill migrated to the west under the influence of winds and appears fragmented in several smaller zones. One of these zones is polluting an area that affects Punta de las Olas, Punta de San Adrian, Islas Sisargas and Malpica. There is another zone that remained in Bahia de La Coruña and toward the north affecting Ria de La Coruña and Ria de Betanzos. The image also shows other zones further offshore that seems to suggest that part of the spill migrated to deep seas in agreement with aircraft observations.

Wind speed data on this date ranged between 2,3 and 4.2 m/s.

4.4. ERS-1 SAR image of 17 January 1993.

The most outstanding feature in this image (Fig. 8) is the fine detail in the waves that reflects a well developed refraction pattern that affects even the inside of several rias. This phenomena has been caused by a high swell associated with a distant storm. Some shear currents are perfectly visible at the entrance of Ria de Ferrol and Ria de Betanzos. The local wind speed which is not related with the conditions of the distant storm, was between 3 and 6 m/s. It is interesting to observe that in spite of the acceptable wind speed, the oil spill was not identified on this date probably because of the roughness caused by the intense backscattering on the swell even from polluted areas. This is another environmental restriction for oil spill identification that should be taken in consideration in any future oil spill surveillance.

4.5. ERS-1 SAR image of 8 February 1993

The SAR image (Fig. 9) has identified clearly the location of the polluted areas on this date. They are affecting Cabo Prior, Punta Rasa, Ria de La Coruña, Punta del Salto y Punta de las Olas. The shape of these polluted areas is basically the same. They are wider in the proximity of the coast and thin out further offshore branching off in numerous tails with more grey tones where oil is probably more dispersed and thinner. The image shows a very well developed wave pattern in the non-polluted areas which is absent in the areas affected by the spill probably because the oil has eliminated the capillary waves and therefore there is not backscattering coming from these polluted areas.

As opposed to the previous dates, this image has an easterly look direction. This circumstance has been positive for the identification of the spill as the near edge of the radar beam, which has a higher depression angle, is closer to the spilled areas (Fig. 10). Other favourable factor for identification is that wave direction is subperpendicular to the radar beam.

Wind speed data on this date ranged between 2 and 4,5 m/s

There were other SAR images considered in this study that are not presented now due to lack of space. One such image corresponds to the area of Estaca de Bares-Ria de Vivero on 29 December 1992 which shows the the spill affected this area on this date.

The SAR image of 8 February 1993 was the last one that our budget for the study could afford. However, together with ESA/ESRIN, we are examining SAR images after this date, not included in this study, which seems to indicate that the oil spill could have stayed longer on the sea surface around La Coruña Bay.

A multitemporal image of 13 December 1992 and 8 February 1993 is presented in figure 11

Considering the continuous threat of accidental and intentional oil pollution in spanish waters INFOCARTO S.A. has submitted the project OILWATCH to the E.U. to design a geographical information system that could act as a decision system to combat oil pollution. In such a system radar data from ERS-1/2 and other radar platforms including airborne radar sensors would play an important role.

5. CONCLUSIONS

SAR images from ERS-1 have provided a very good coverage of data to identify and monitor the accidental oil spill caused by the Aegean Sea in a region such as Galicia where other remote sensing data are normally impaired by clouds.

The following conclusions can be drawn from the study:

A.- The extension of the coastline affected by the spill was approximately 200 Km stretching from the area of Malpica (SW of the location of the accident) to the Cape of Estaca de Bares-Ria de Vivero to the NE. The original spill reached a rounded shape of 1000 square km from which it was separated in smaller areas drifting with winds.

B.- The span of time in which the spill was identified in the SAR images goes to 8 of February 1993. However, new data now been examined could probably extend the duration of the spill after this date.

C.- It is well known that oil spill identification with radar sensors is influenced by environmental factors, such as wind speed. Other environmental factors, derived from this study, that could impair identification, even if wind speed is right for detection, are wave refraction patterns derived from high swell. These patterns could hide the presence of spills.

D.- In this study of the identification and monitoring of the oil spill of La Coruña, the optimal conditions for detection were as follows:

1.- Radar beam is subperpendicular to the direction of the waves.

2.-The spill is closer to the near edge of the beam (higher depression angle)

6 REFERENCES

ERDAS, 1992, ERDAS Radar Module; IMAGINE v. 8.0.1. 50 pags. Atlanta. GA.

ESA SP - 1148, 1992. ERS-1 User Handbook. European Space Agency, Paris.

Galli de Paratesi, S.R. 1992. Remote Sensing for Surveillance of Oil Spills in European Marine Environments. Geo Observateur-Marisy 92- Rabat. pp 229-240. Royal Center for Remote Sensing. Rabat.

Lichtenegger, J. 1994. Using ERS-1 SAR images for oil spill surveillance. Earth Observation Quaterly pp. 7-10 No. 44; June 1994.

Sorensen, B.M. 1993. The European Operational Airborne Oil Pollution Surveillance Scenario. First Thematic Conf. on Remote Sensing for Marine and Coastal Environments, New Orleans.



Figure 5. ERS-1 SAR image of 4 October 1992.

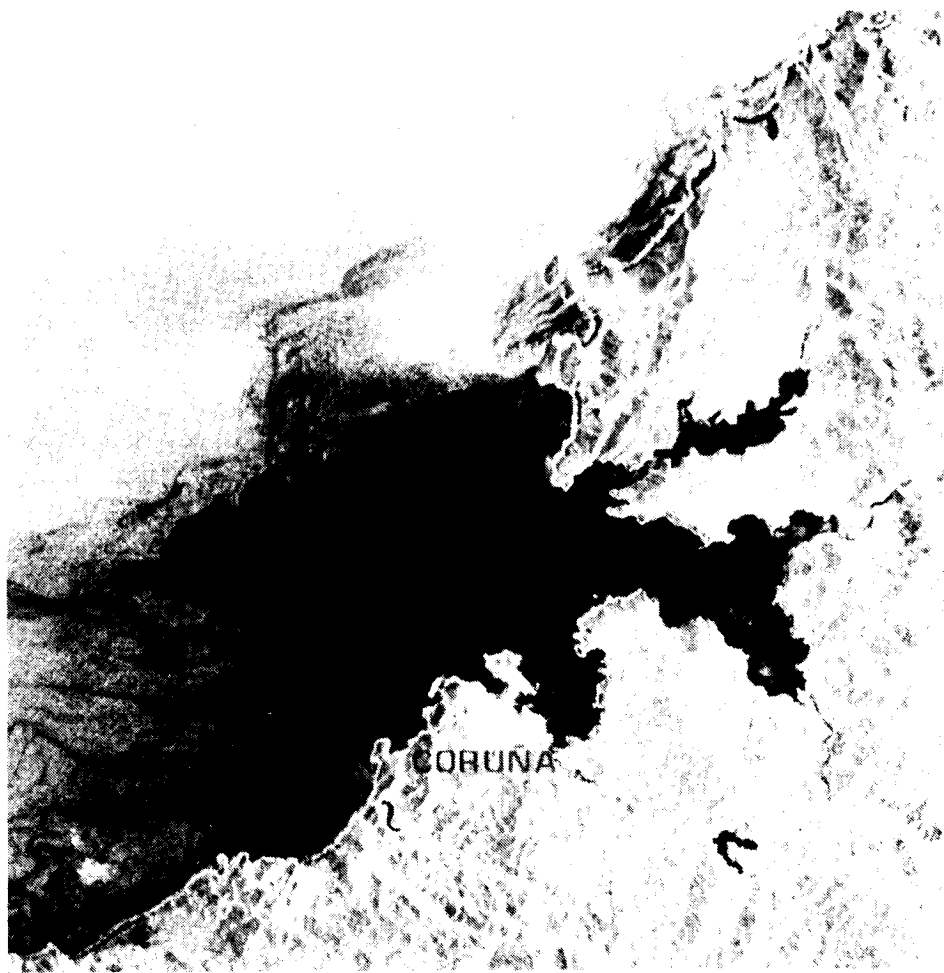


Figure 6. ERS-1 SAR image of 13 December 1992.

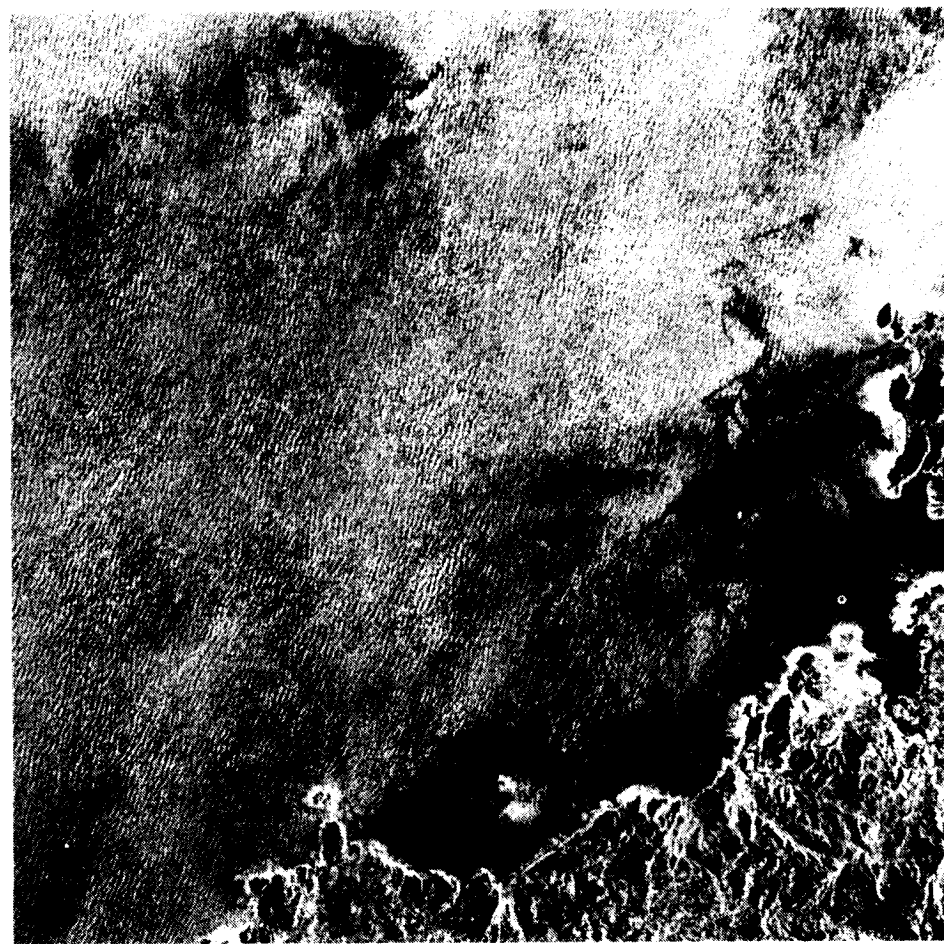


Figure 7. ERS-1 SAR image of 1st January 1993.

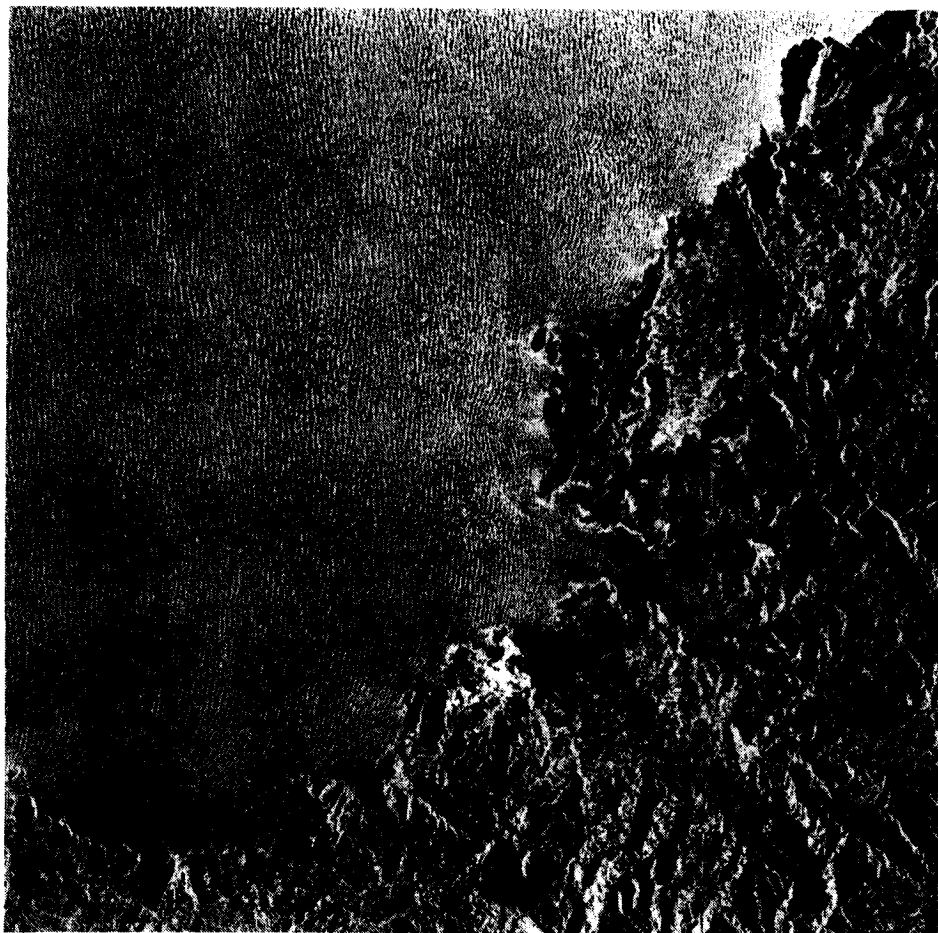


Figure 8. ERS-1 SAR image of 17 January 1993.

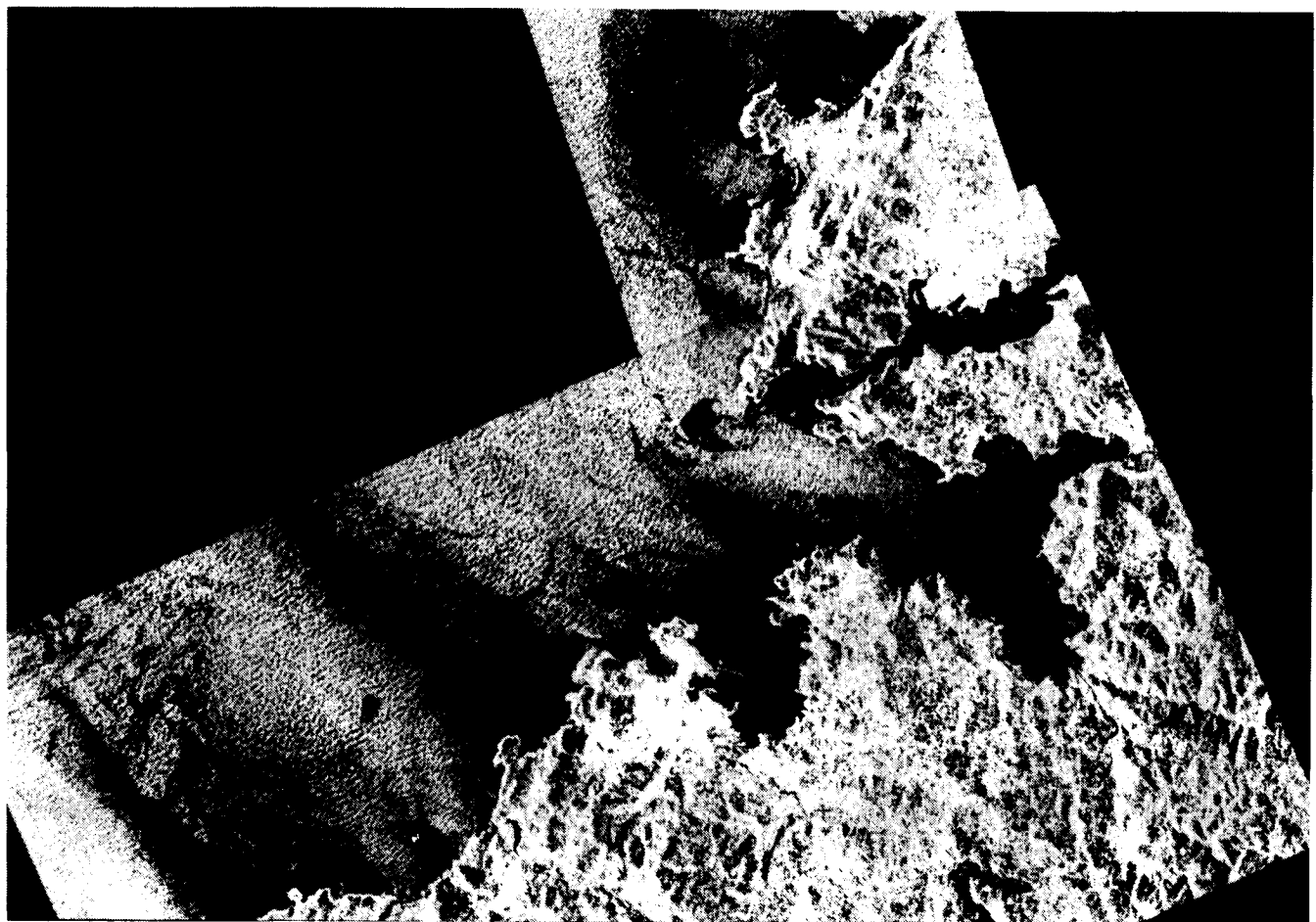
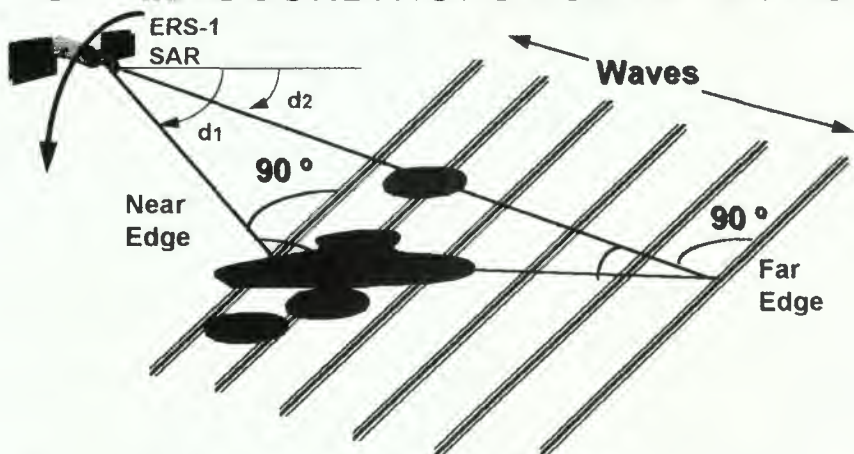


Figure 9. ERS-1 SAR image of 8 February 1993

OPTIMAL CONDITIONS FOR DETECTION



- The radar beam is subperpendicular to the waves
- The spill is closer to the near edge of the beam (higher depression angle ; $d_1 > d_2$)
- Wind speed 3 - 9 m/s

Figure 10. Optimal conditions for oil spill detection

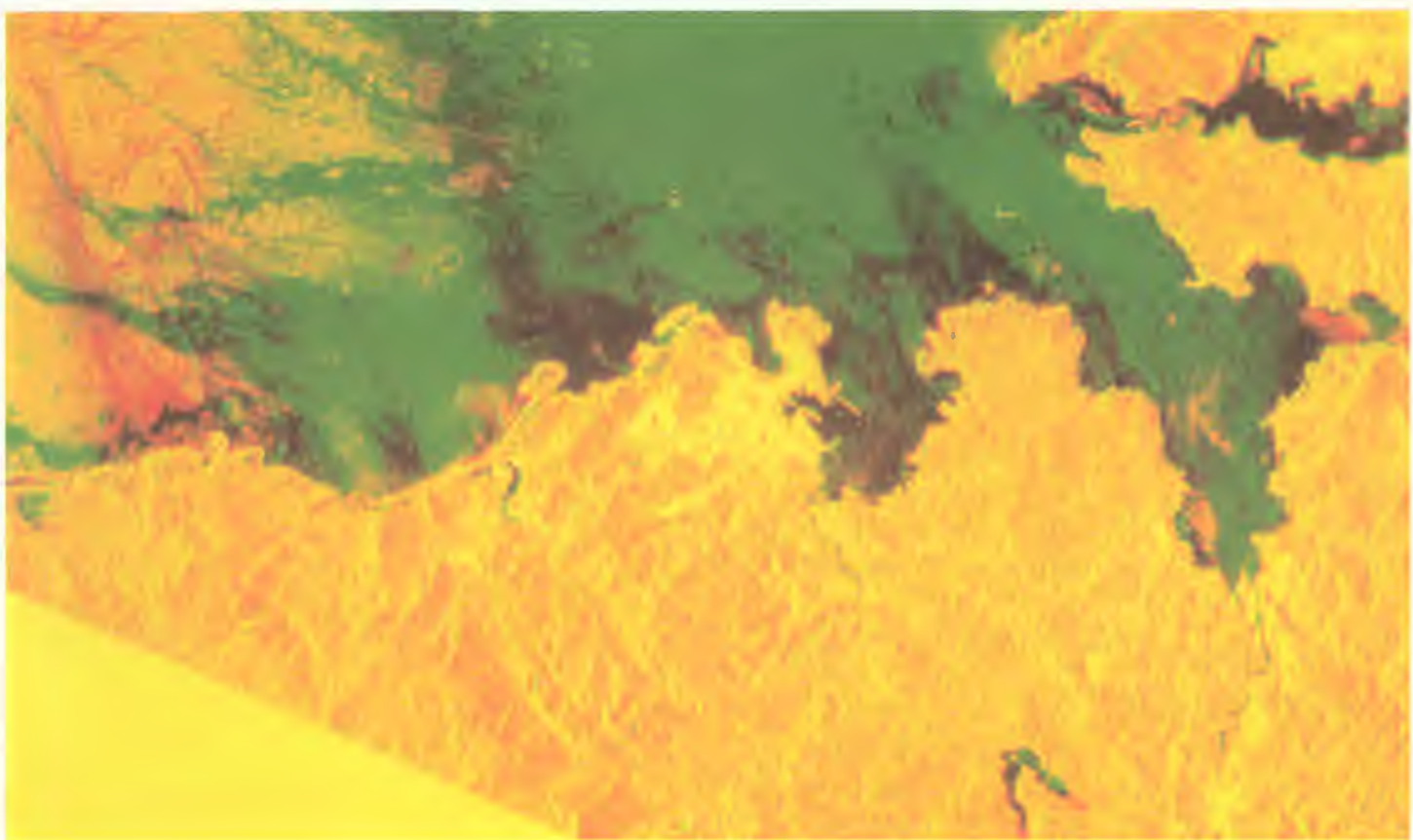


*Figure 11. Multitemporal image
13 December 1992 (GREEN); 8 February 1993 (BLACK)
Spill area outside the zone polluted in the two dates (RED)*

GOSAP**PP.USA-1****GULF OFFSHORE SATELLITE APPLICATIONS PROJECT**

Dr. E.K. Biegert (Director, Project GOSAP, The Geosat Committee, Inc),
 Dr. R.N. Baker (AMOCO), Dr. R.V. Sailor (TASC), Dr. K.E. Schaudt (MARATHON),
 Dr. I.R. MacDonald (Texas A&M University), Dr. B. Tapley and Dr. C.K. Shum (University of Texas),
 Mr. John Amos (Earth Satellite Corporation), Mr. J.L. Berry (Pecten International Company),
 and Mr. A.T. Herring (EDCON, Inc.)

Pecten International Company, 200 North Dairy Ashford, Houston, Texas 77079 U.S.A.
 Telephone: (+1)713-544-4690; Fax:(+1)713-544-4873; email: biegert@shell.com

Abstract

Project GOSAP is a multi-organizational effort to determine how best to use remote sensing technology, and ERS-1 data in particular, to address offshore problems and operations faced by the exploration and marine engineering industries. Remotely sensed data integrated with "sea truth" are used to quantify meteorologic and oceanographic events, to detect and track ocean currents and gyres, to image the sea floor, map subsurface geology, or detect oil seeps from orbital altitudes. GOSAP participants are evaluating the potential for satellite-based offshore exploration, ocean engineering, and environmental applications using combined satellite and airborne measurements constrained by real time "sea truth."

Overview

In the Fall of 1992 and Spring 1993 the European Space Agency acquired SAR imagery for GOSAP from the ERS-1 satellite over the Santa Barbara and Gulf of Mexico test sites. In coordination with the Gulf of Mexico overflights, a very comprehensive program of sea truth was conducted by various agencies, ranging from sea bottom submarine observations, sea surface sampling from ships and platforms, aircraft overflights, and imagery from several satellites.

Initial processing of the SAR, Landsat, and SPOT data by GOSAP members has resulted in excellent images of surface oil slicks in both the Santa Barbara and Gulf of Mexico sites. Progress is being made in correlating sea, air, and spaceborne measurements to determine optimum procedures for detecting and monitoring oil in marine environments.

We present results of experiments to compare observations of natural oil slicks and related phenomena from ERS-1 SAR data and other satellite imagery to water-column, sea-surface, and sea-floor measurements collected from

fixed and mobile platforms in the Gulf of Mexico. ERS-1 SAR data were used in a "near real-time" mode by Earthsat to detect surface oil slicks and to direct previously deployed sea-truthing teams to the location. Comparison of oil slicks detected using the ERS-1 data with previously collected TM, AVHRR, SPOT, and space shuttle imagery showed excellent agreement for locations of over 30 active seeps. Theoretical models developed by Texas A&M University describing the behavior of oil rising through the water column and dispersing on the sea surface constrain the image signatures of oil slicks detected by satellite and airborne remote sensing. This investigation of remote detection of natural seepage extends the probable range of chemosynthetic communities dependent on hydrocarbon seepage in the Gulf of Mexico to the 750-1000 m depth range. It demonstrates that natural oil seepage is current and ongoing at many sites and provides specimens and observations from communities at intermediate depths.

Comparisons of ERS-1, Landsat TM, Landsat MSS, SPOT, Seasat, SIR-A, and Almaz imagery over the Santa Barbara Channel by Earthsat and other GOSAP participants demonstrate the repeatability and reliability of satellite-based marine oil slick detection and suggest a set of satellite viewing conditions for image selection.

The utility of ERS-1 altimeter data for observing the gravity field, eddies, and ocean currents in the Gulf of Mexico is being demonstrated by GOSAP participants. TASC computed the noise levels and resolution capability of ERS-1 data, finding it comparable to that of the Geosat altimeter. Other GOSAP investigators, including the MOBIL, the University of Texas, Scripps, and Ohio State University have computed gravity and geoid maps of the Gulf using ERS-1 and other data. Comparisons are in progress between the ERS-1 altimeter data and EDCON's high resolution marine gravity data. The ultimate goal of the gravity work is to be able to observe the small, short-wavelength signature of a salt dome, but present indications are that it will be difficult to improve the

along-track resolution to better than about 20 km.

GOSAP participants are determining if ERS-1 satellite imagery and altimetry can be used to properly define eddy current regimes in a real time cost-effective basis and are developing a method to disseminate data products. The Gulf of Mexico has unique current regimes: the Loop Current and eddies that spin off from the Loop Current. Precise definition of spatial extent and current magnitudes of eddies is lacking, but satellites have the potential to resolve these issues. ERS-1 and TM imagery are combined with infra-red satellite data (limited by cloud cover and seasonal water surface temperature differences), deployment of current measurement devices, shipboard Acoustic Doppler Current Profiler, and underwater cables.

Participants

Formed in 1990, GOSAP is being undertaken under the auspices of the Geosat Committee, Inc. by members of the petroleum, marine, and environmental industries representing about 30 companies, government agencies, and universities. Participants range from individuals to large corporations and form a productive mix of sophisticated users, value-added companies, data suppliers, and research organizations and universities. Although nominal annual participation fees are collected, members contribute staff time, data, and equipment in a cooperative research endeavor. Participants include: Amoco, Arco, Chevron, Enserch, EDCON, Mobil, Marathon, Shell, Texaco, Unocal, Petroscan, Earthsat, Erim, Eosat, Radarsat, Intera, SPOT, TASC, BHP, Loral Aerosys, TerraMar, MacDonald-Dettweiler Associates, The Office of Naval Research, The U.S. Coast Guard, NOAA/NOARL, LaMont-Doherty Earth Observatory, Minerals Management Service, Texas A&M University, The University of Texas at Austin, Louisiana State University, the University of Southern Mississippi, Scripps Institute of Oceanography, and Ohio State University.

Activities

Participants are comparing sea surface spectra from satellites (ERS-1, Radarsat, SIR, Seasat, Landsat, SPOT, and others) with water column, sea surface and sea floor measurements from instrumented fixed and mobile platforms in the Gulf of Mexico. These comparisons will yield methods aimed at establishing repeatable correlations between sea surface, sea floor, subsurface and general geology. Techniques developed to process the data sets will be applied to exploration, engineering and environmental problems encountered by Geosat member companies.

Data are being evaluated over two test sites: the Santa

Barbara area offshore southern California and in the Gulf of Mexico. Both sites contain a number of known active oil seeps, have extensive existing marine gravity surveys, and contain numerous instrumented offshore platforms. Extensive measurements are being made above, at, and below the sea surface.

The correlation of satellite-collected sea surface signatures, oil seeps, subsurface and general geology enables explorationists to extrapolate these techniques into less fully understood test sites and eventually into unexplored frontier areas world-wide. Petroleum exploration in little known regions requires synoptic wide area coverage both onshore and offshore. While onshore petroleum exploration using remote sensing techniques has become nearly routine, many of the remaining oil provinces within reach of present drilling technology lie offshore at shallow to moderate water depths; thus it is useful to develop remote sensing methods which extend land-based interpretations into the shallow offshore.

The use of satellites to obtain area wide meteorological and oceanographic data enables industry to have a more complete picture of oceanographic events that are occurring at or near an area of activity. Non-satellite techniques provide only sparse "snapshot" data of these events.

The GOSAP project involves cooperation between organizations who each contribute to the data collection, image processing, interpretation, and report writing phases. Most participating organizations have several people assigned to one or more of the five GOSAP working groups discussed below.

Sea-Truth Activities. In conjunction with acquisition of the ERS-1 satellite data over the Gulf of Mexico test site, GOSAP is fielding several teams to collect simultaneous sea-truth data:

ERS-1 SAR Imagery	European Space Agency
ERS-1 Altimetry Data	European Space Agency
ERS-1 Scatterometer Data	European Space Agency
SPOT Imagery	SPOT Image Corp.
Landsat Imagery	processed by Earthsat
Submarine NR-1	Texas A&M (GERG)
NASA ER-2 (U-2) Aircraft	MSRC
ALF Survey	World Geoscience
AVHRR	LATEX / USM / SAIC
Aerial Photography	LATEX / USM / SAIC
High Altitude Remote Sensing	Office Naval Research
Instrumented Oil Rigs	Shell
Instrumented Buoys	Marathon

The goal of one particular set of observations is to verify

the presence of slicks detected in the satellite imagery in a water depth range of 750-1000 meters, a previously undocumented regime. Because seep activity is sporadic in time, we performed near real-time interpretation of the ERS-1 imagery to locate active seeps and to direct a special deep-diving submarine to visit the most active seep sites and pinpoint seepage locations on the seafloor. We worked closely with ESA officials, the ERS-1 Order Desk, the Canadian Center for Remote Sensing, Radarsat International, and GOSAP participants to achieve a quick release of ERS-1. Earthsat analyzed the satellite images, located the slick sources, and directed the submarine to the seep sources. At the seafloor seep locations, benthic communities were observed, geochemical samples were acquired, oceanographical measurements were made, and seep rates were determined by placing special collecting devices over the active seeps.

In early June, an ER-2 flew over portions of the continental slope between the 500 and 2000 m isobaths collecting imagery on two flight patterns: a four-spoked star pattern centered on the sun-glint when the sun-glint is in the vicinity of GC234/371 and along-isobath (East-West) flight-lines between the Green Canyon and Garden Banks lease areas. The ER-2 carried a down-looking Daedalus Airborne Ocean Color Imager (AOCI) and a forward-looking electronic still camera with multiple polarizing filters. This exercise provided additional imagery of slicks from different sensor types and further documented the characteristics of surface slicks formed by natural seepage. The AOCl provided information on the primary productivity in the vicinity of the slicks; the polarizing camera produced high-resolution images of the slicks that will provide information on the heterogeneity of slick thickness.

High quality aerial photographs were acquired from an aircraft underflying the ERS-1 over areas of known coastal bathymetry, an eddy, and storm fronts. These data will be used to test methodologies and technologies to observe and follow energetic ocean features such as fronts and eddies, to use ocean wave refractions to determine coastal bathymetry and energetic fronts, and to determine the effects of weather and sea-surface conditions on the SAR imagery.

Gravity. Satellite altimeter data yields the possibility of direct determination of the ocean surface, i.e., the height of the instantaneous sea surface above a reference ellipsoid. For geodetic purposes the analyses of altimeter data provides information about the shape of the mean sea surface, normally called the geoid, from which geopotential or gravity information can be derived.

In ocean areas where water depth information is sparse, a number of studies of altimeter data have identified hitherto unknown seamounts, fracture zones and subduction zones. In offshore areas where reliable water depth information is separately available, elimination of the sea bottom topography yields geopotential maps or gravity maps giving information about significant density contrasts within the earth's crust and sedimentary column.

GOSAP investigators are producing a number of geopotential and/or gravity maps over the Gulf of Mexico and the Santa Barbara test areas from altimeter data and will evaluate derived gravity maps with existing shipborne gravity measurements, correlate and demonstrate the ability of remote sensing in exploration by detecting geologic and geophysical anomalies over areas where extensive seismic surveying and drilling have provided adequate geologic control, and explore methods for characterizing major structural features (e.g. sedimentary basin, salt domes, structural highs).

Several GOSAP participants have been actively investigating the issues of processing satellite altimetry to derive an estimate of the marine gravity field and then to measure the accuracy and resolution of the gravity data. The University of Texas and several companies, including Petroscan, TASC, Mobil, Shell, and Texaco have been developing procedures and comparing existing satellite gravity with shipborne gravity. Petroscan has published a comparison of the resolution of several satellite gravity determinations and estimated the improvement when the ERS-1 data will be added.

TASC has used the 1-second average sea surface heights from the 3-day ERS-1 repeat cycle to compute mean height profiles and to evaluate the noise levels and gravity field resolution capability of the OPR-02 altimeter product. Preliminary results indicate that the performance of ERS-1 is comparable to that of the Geosat altimeter. Deflections of the vertical should be recoverable (for wavelengths longer than about 35 km) to an accuracy of about 1 arcsecond, except near land. Since the quality of the 1-second average sea surface heights provided in the OPR-02 product is highly variable, it is necessary to work with the 10 sample/second heights and to carefully edit these to obtain the best possible profiles (20 sample/sec data would be even better). It is expected that careful data processing, along with averaging of at least 20 repeat tracks, should reduce the errors in recovered gravity anomalies to the level of about 3 or 4 mGal.

Oil Slick Detection. The ability to detect both natural or man-made oil slicks in coastal waters by spaceborne

synthetic aperture radars (SAR) has been demonstrated in the Seasat and Shuttle imaging radar (SIR A & B) programs. Several data passes over the test site reveal the persistent or ephemeral nature of the slicks, suggesting a natural or man made origin (long term seep versus oil spill or pipeline leak).

As an exploration tool, the remote identification of hydrocarbon seeps is particularly useful to geologists responsible for large or frontier regions. General models which describe seepage from source to surface must consider mechanisms for migration, geometry and density of migration channels (faults, fractures, preferential directions of porosity and permeability) barriers to migration, either physical or chemical (oxidation/reduction barriers), and ultimate expulsion at the sea floor or land surface, followed by degradation or dispersion.

GOSAP investigators are attempting to determine optimum parameters for detection of oil slicks (spectral bands, image processing techniques, data synergism, volume and film thickness of oil, etc.) and to discriminate between natural and man-made slicks - temporally, spatially, and/or spectrally. Earth Satellite Corporation has processed a suite of satellite imagery of oil seeps in the Santa Barbara Channel to determine best parameters to detect oil in the marine environment. Seeps enhancement work has been done on spills in the Arabian Gulf (AVHRR, TM) and Santa Barbara Channel (MSS, TM, ALMAZ preliminary).

A SPOT XS image of a major oil slick in the Gulf of Mexico from the Tanker Mega Borg was processed by Amoco's Remote Sensing Group to develop operational image processing techniques. Additional work is ongoing in the Middle East (Landsat TM) and the Santa Barbara Channel (TM, MSS).

Remote detection of natural seepage can be used to extend the probable range of chemosynthetic communities dependent on hydrocarbon seepage in the Gulf of Mexico. Conversely, presence of the communities documents that natural seepage is a ongoing in a particular location and that it has persisted during recent time. The goal of the sea floor observations is to document a previously undocumented seep features, preferably in 750-1000 m depth range, based on remotely sensed slicks. Accomplishing this will demonstrate that natural oil seepage is current and ongoing at the site and provide specimens and observations from communities at intermediate depths. Based on Thematic Mapper imagery and on photographs taken from the space shuttle, communities in the 900 m depth range are believed to be located in GC321 and GC287. These sites have not previously been explored by submarine although

chemosynthetic fauna were recovered by trawling in GC278.

Current Monitoring. The Gulf of Mexico has unique current regimes: the Loop Current and eddies that spin off from the Loop Current. Precise definition of spatial extent and current magnitudes of eddies is lacking. Satellites have the potential to resolve these issues. Present monitoring techniques include: infra-red satellite data limited by cloud cover and seasonal water surface temperature differences, deployment of current measurement devices, shipboard Acoustic Doppler Current Profiler, and underwater cables.

GOSAP participants are determining if eddy current regimes can be properly defined in real time and on a cost-effective basis and are developing a method to disseminate data products.

Expendable bathythermograph (XBT) measurements were made on several cruises at approximately 10 nautical mile spacing. A number of current measurement were also made using acoustic Doppler current profilers (ADCPs) and expendable current profilers (XCPs). The measurements showed that Eddy Triton was only separated from the Loop Current during the second cruise. On the other two cruises a connection between the two features existed at the southeastern corner of the cruise track. On all the cruises, an anticyclonic center of circulation existed near the center of the cruise track. Dynamic heights relative to 700 m have been calculated for each of the XBT profiles using a standard temperature-salinity curve for Loop Current water. The relief at the center of circulation is on the order of 0.65 m.

Wind and Wave Measurements. Several Gulf of Mexico oil platforms are instrumented with wind and wave measurement devices that transmit routinely to the National Weather Service; these data are combined with the wind and wave data collected from the NWS buoys deployed in the Gulf. Verification that satellite data can quantify wind and wave data will lead to improved weather forecasting and provide an enhanced data base which could lead to improved structure design criteria.

Database and Archive. The diverse computing environments spread throughout North America of the companies, universities, and government organizations participating in GOSAP creates a unique set of problems for data distribution, sharing, and archiving. In addition to ERS-1 data products, GOSAP members are contributing and sharing other data, such as satellite imagery, gravity data, weather information, well logs, bathymetry, and oceanographic data. These and other data are being

archived and distributed by the Database and Archive group. This group is also implementing an electronic catalogue (index) for all the GOSAP data products that can be browsed by GOSAP members.

Summary

Members of Project GOSAP are undertaking a comprehensive data collection program in the Gulf of Mexico to evaluate commercial and scientific applications of satellite data in the areas of ocean engineering, offshore exploration, and environmental applications. Instrumented offshore oil platforms provide a stable, valuable source of data for calibrating airborne and satellite remotely sensed data. Improved understanding of these new technologies with enhanced image processing and analysis techniques is stimulating additional research within the participating organizations.

Acknowledgments

We give special thanks to Lisa MacArthur, Geosat Administrator and to F.B. Henderson III, former President of Geosat who initiated GOSAP. The European Space Agency provided ERS-1 data. Use of the submarine Johnson *Sea-Link* was partially funded by the University of North Carolina at Wilmington National Undersea Research Center. This work was partially funded by NASA EOCAP Program contract number NAS13-444 to Earth Satellite Corporation.

Coauthors

This project would not have been successful without the contributions from all of its participants. We especially want to thank GOSAP participants and coauthors: David Sandwell (Scripps Institute of Oceanography), Richard Rapp (Ohio State University), John Everett (Earth Satellite Corp.), David Sheres (University of Southern Mississippi), Peter Price (Marathon), D.C. Rodenberger (Pecten International Company), G.Z. Forristall (Shell), Donn Walklett (TerraNova), Jim Brooks (Texas A&M University), Dave Buthman (Unocal), Scott Hill (Chevron), John McKeon (Arco), Roger Mitchell (Earthsat), Thomas Parr (TASC), Jonathan Pershouse (Mobil), Jim Reilly (Enserch), D. Smith (ONR), Bob Borger (Mobil), Bill Haxby (LaMont-Doherty), Ron Phair (Texaco), Doug Biggs (Texas A&M University), Jared Black (Unocal), Mavis Driscoll (TASC), Thomas Mitchell (Texaco), and Jim White (TASC).

Some GOSAP Publications

Natural Oil Slicks in the Gulf of Mexico Visible from Space, I.R. MacDonald, N.L. Guinasso, Jr., S.G. Ackleson, J.F. Amos, R. Duckworth, R. Sassen, and J.M. Brooks, *Journal of Geophysical Research*, Vol. 98, No. C9, pages 16351-16363, September 15, 1993.

Verification of GEOSAT Data for Operational Use in the Gulf of Mexico, G.Z. Forristall, K.J. Schaudt, and J. Calman, *Journal of Geophysical Research*, Vol. 95, pp 2985-2989, 1990.

Verification of TOPEX Altimetry in the Gulf of Mexico, R.R. Leben, G.H. Born, D.C. Biggs, D.R. Johnson, N.D. Walker, *TOPEX/POSEIDON Research News*, pp. 3-6, September 1993.

Gulf Offshore Satellite Applications Project, F.B. Henderson III, E.K. Biegert, R.V. Sailor, R.N. Baker, K. Schaudt, *MTS Journal*, Vol. 27, No. 2, pp 87-90, 1993.

Ship, Aircraft, and Satellite Observations of Loop Current Eddies "U" and "W" and their Interaction with the Continental Margin of the Western Gulf of Mexico, D. Biggs, G. Fargion, P. Hamilton, K. Schaudt, J. Feeney, R. Leben, L. Rouse, and N. Walker, *EOS Transactions of the AGU*, Supplement to Vol. 75(16), p 212, 19 April 1994.



The Geosat Committee, Inc. Sponsor for GOSAP

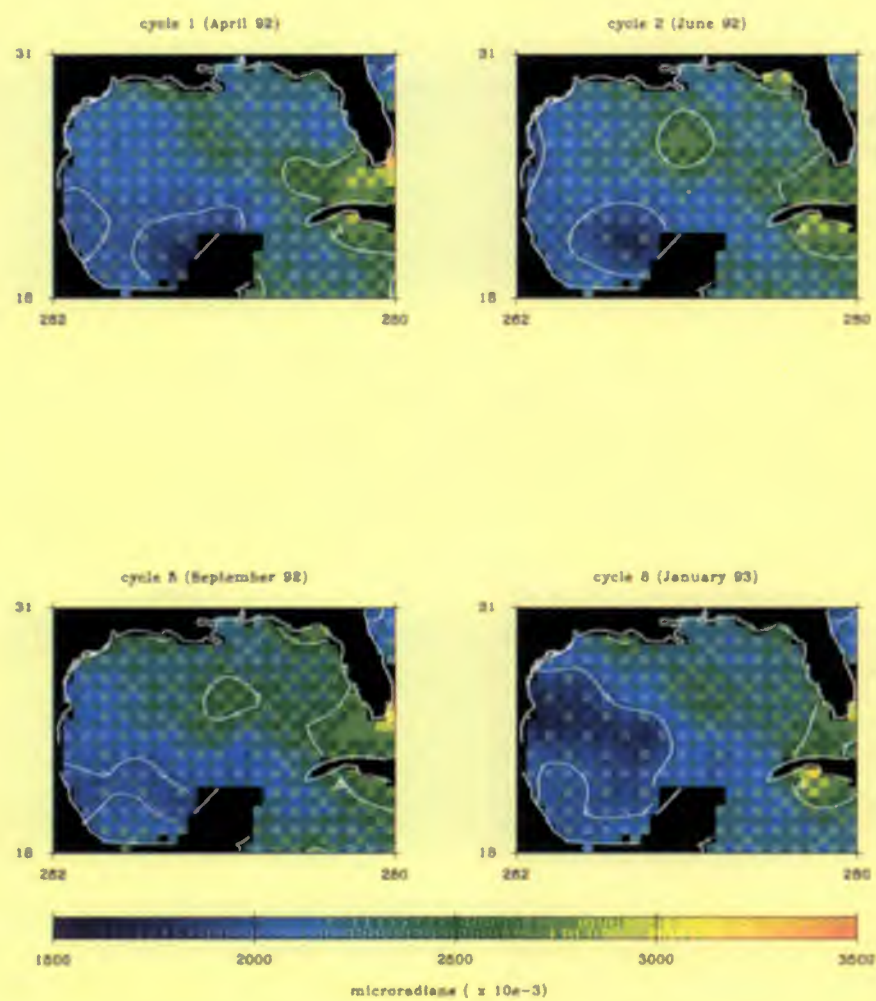
"The voice of the Remote Sensing Community since 1976"

The Geosat Committee provides a unique forum and network contacts within the commercial sector of the remote sensing user industry. It conducts special cooperative research projects among members and with government and academic institutions when advantageous to the membership.

The Geosat Committee facilitates access and availability of aerospace and airborne earth observation data for members worldwide.

The Geosat Committee provides a collective voice on members' developing needs to suppliers of aerospace satellites, airborne earth observation data, and related technologies so that the suppliers may provide data and services appropriate to members' requirements.

ERS-1 Mesoscale Variability – Annual Change in Gulf of Mexico
G.E. Peterson, C.K. Shum, B.D. Tapley

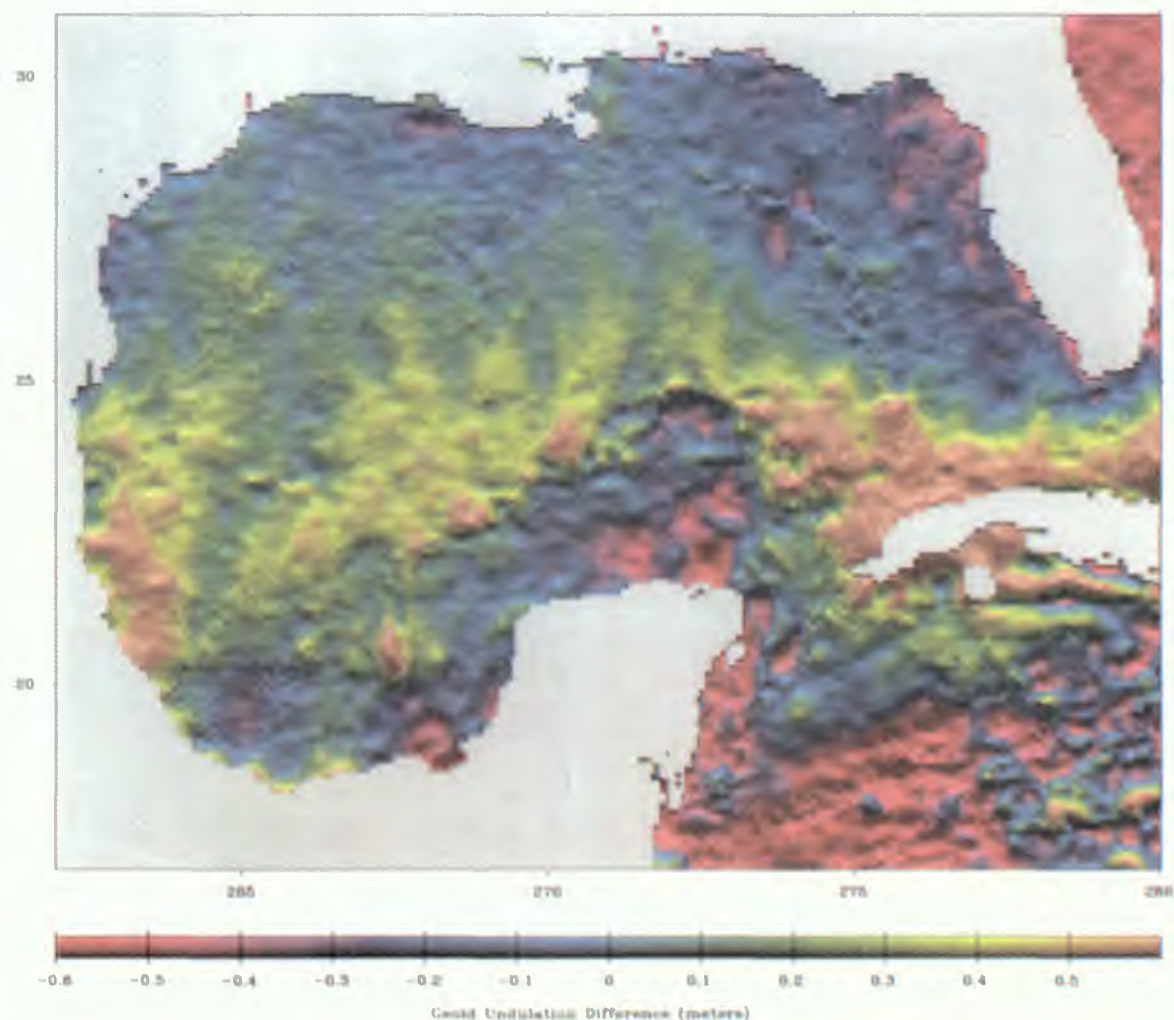


Center for Space Research

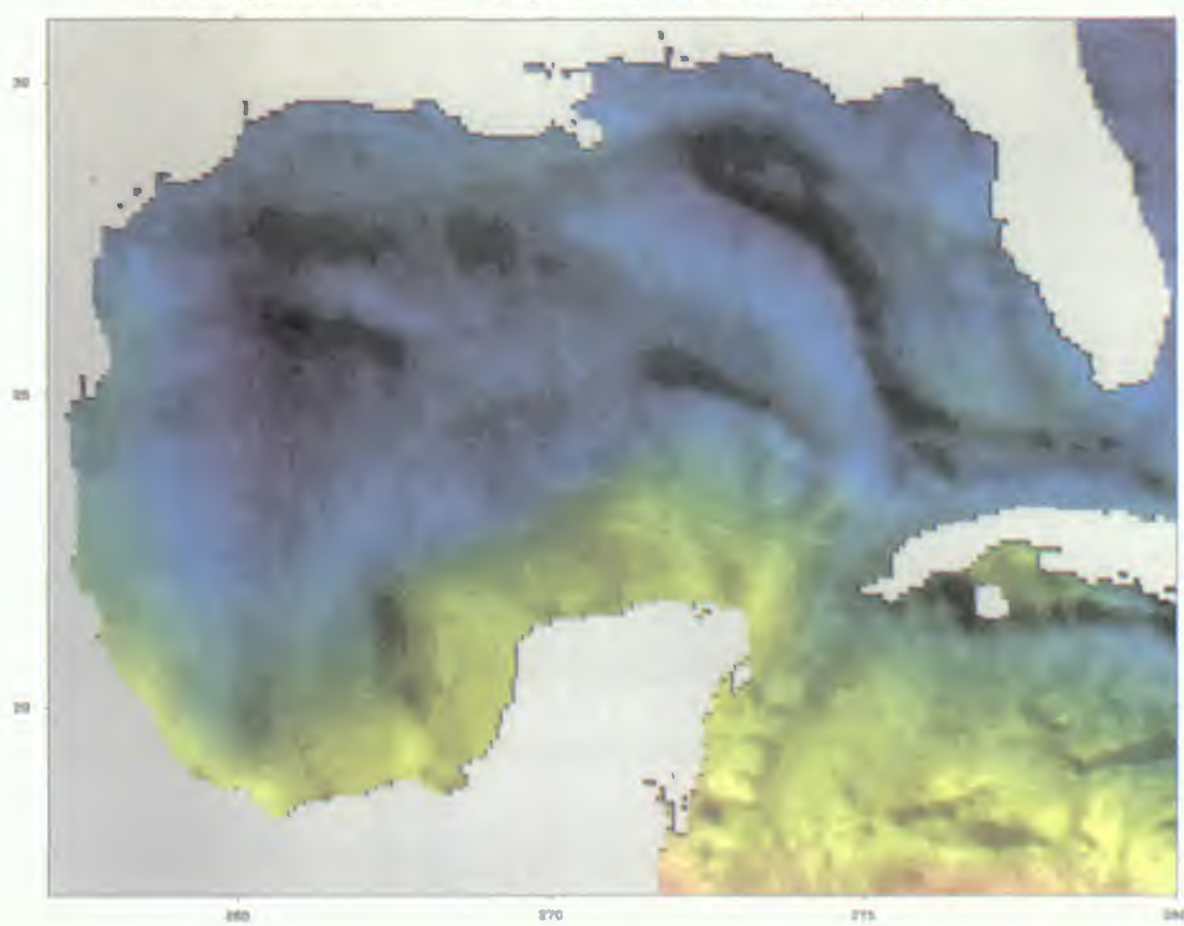
The University of Texas at Austin

Difference Between the UT/CSR and OSU Models (RMS=30.8 cm).

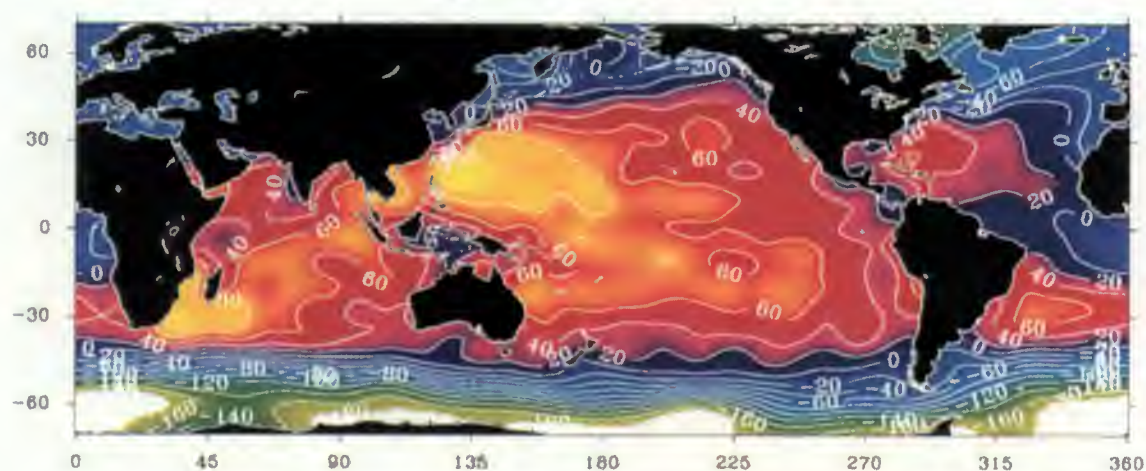
423



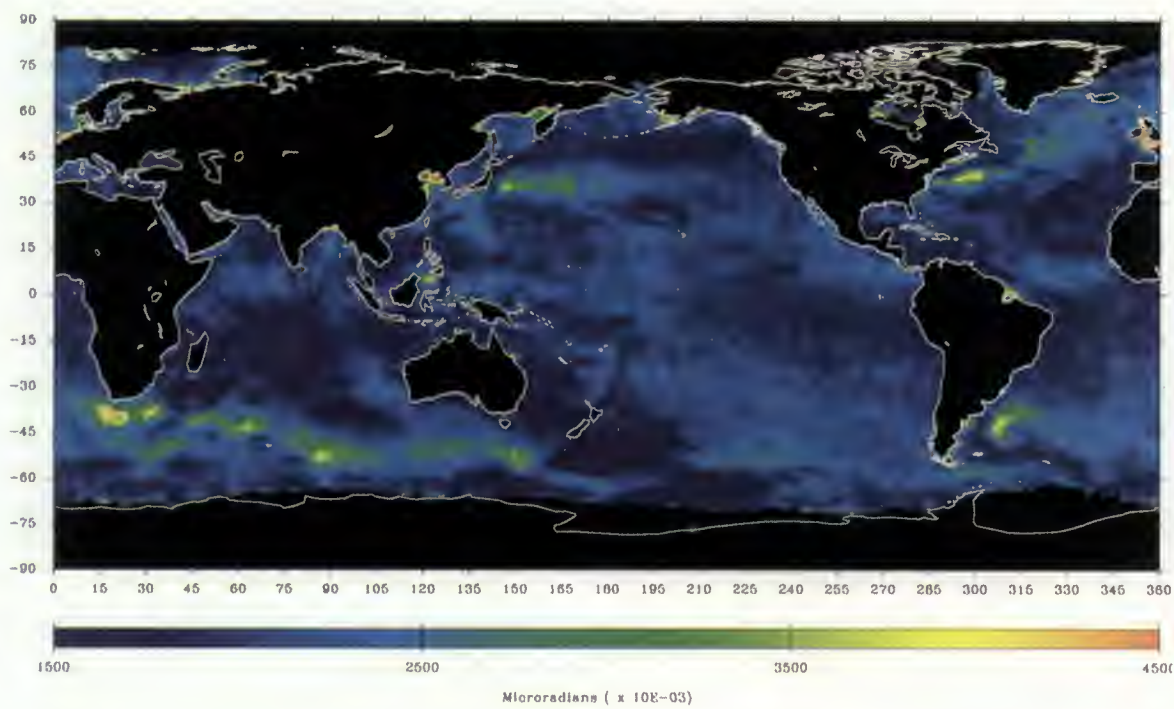
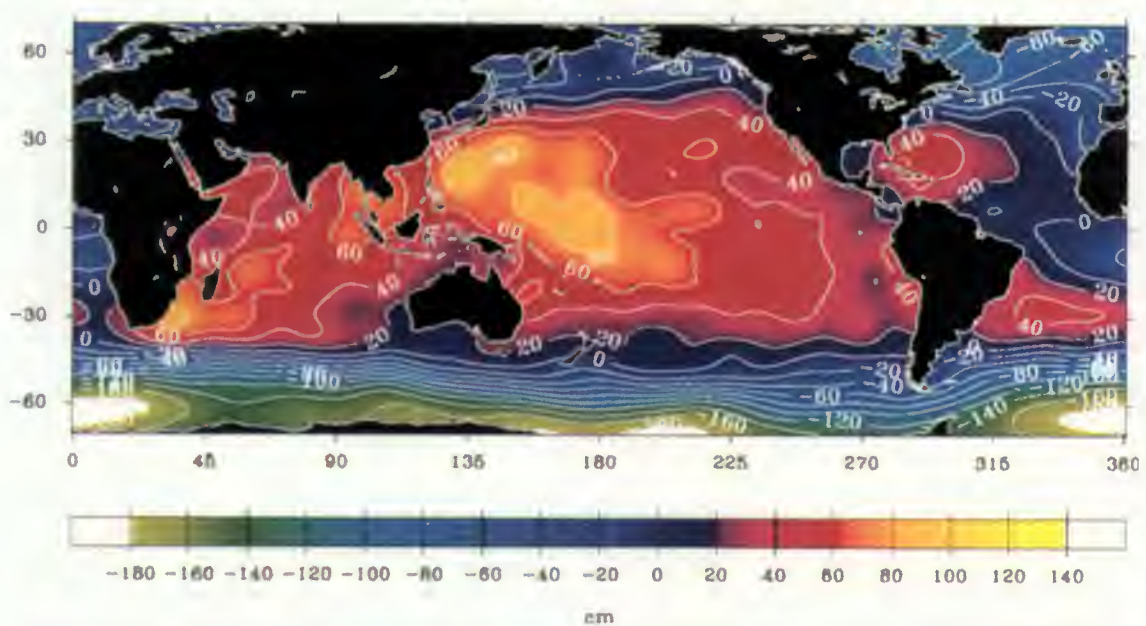
Gulf of Mexico Marine Geoid Determined from Seasat, Geosat, ERS-1 and Topex/Poseidon Altimetry (CSR Model).



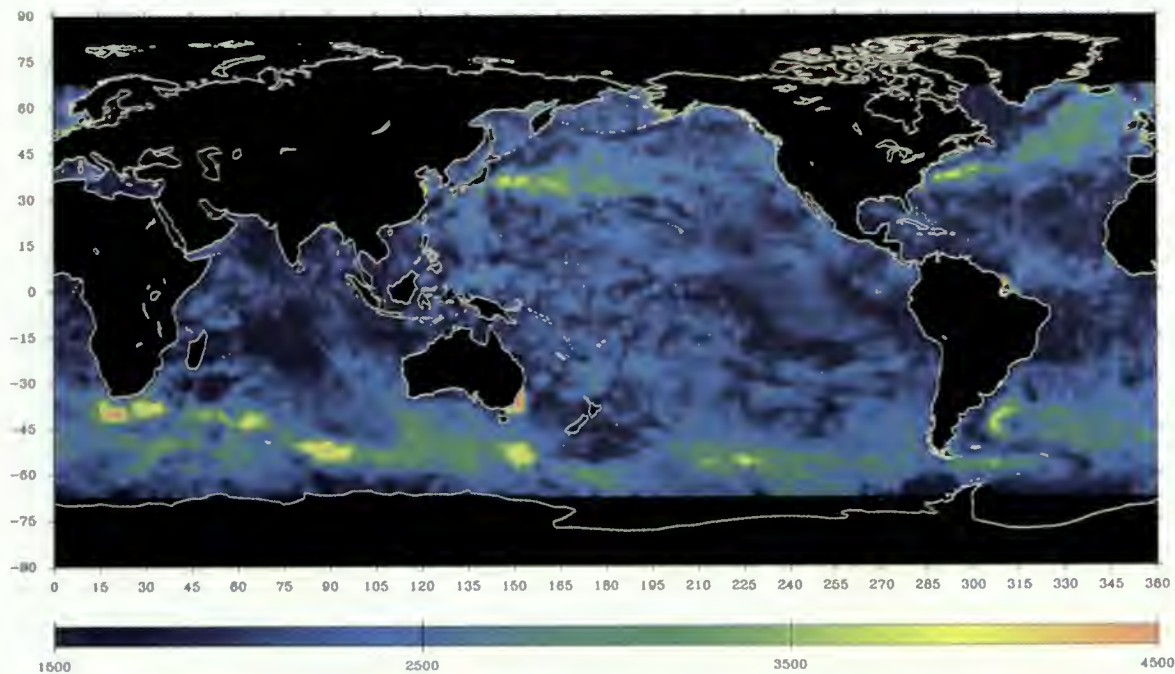
data spanning 5/22/92 to 8/13/92



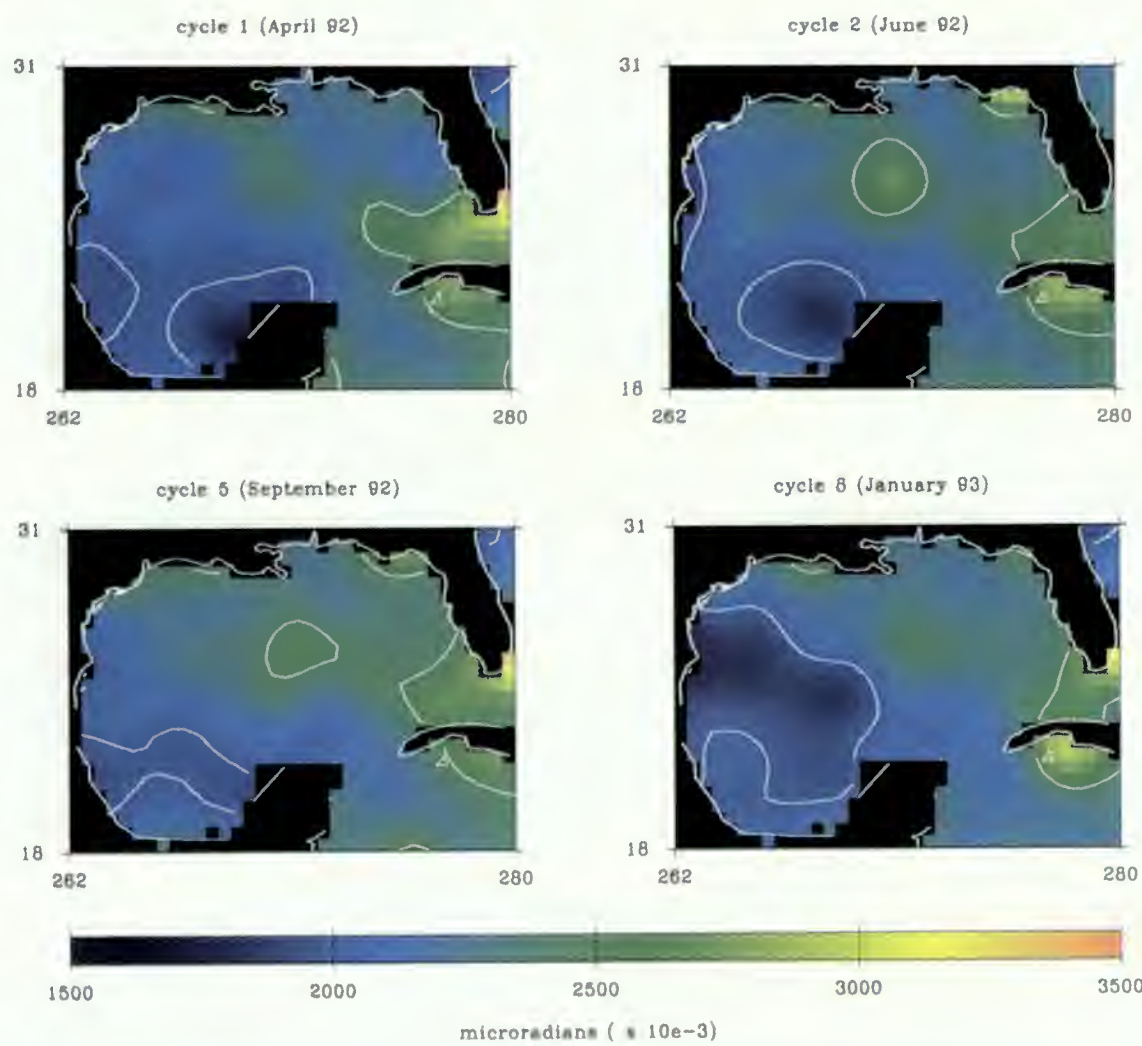
data spanning 10/1/92 to 11/6/92



ERS1 Global Mesoscale Slope Variability

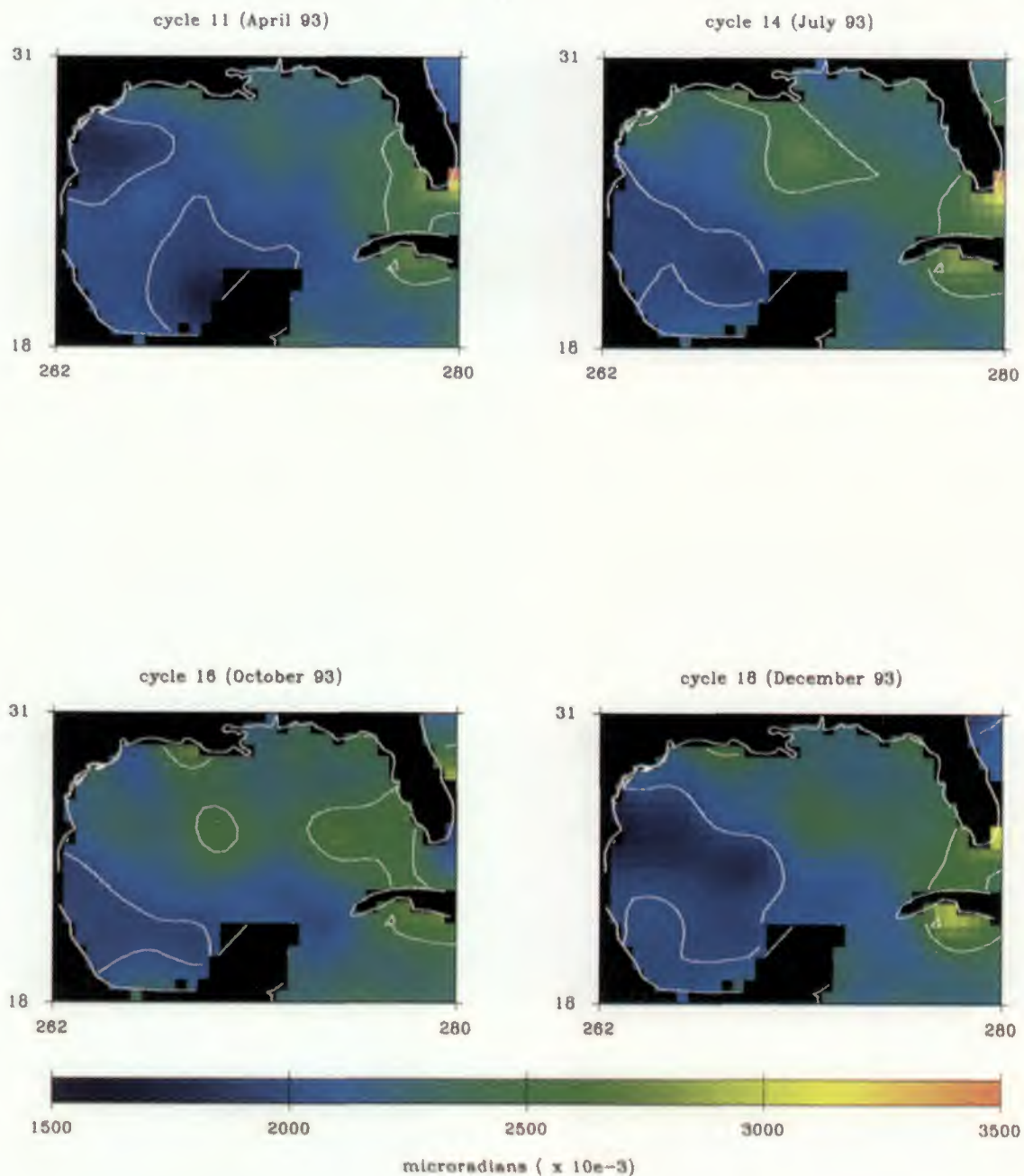


TOPEX/POSEIDON Global Mesoscale Variability

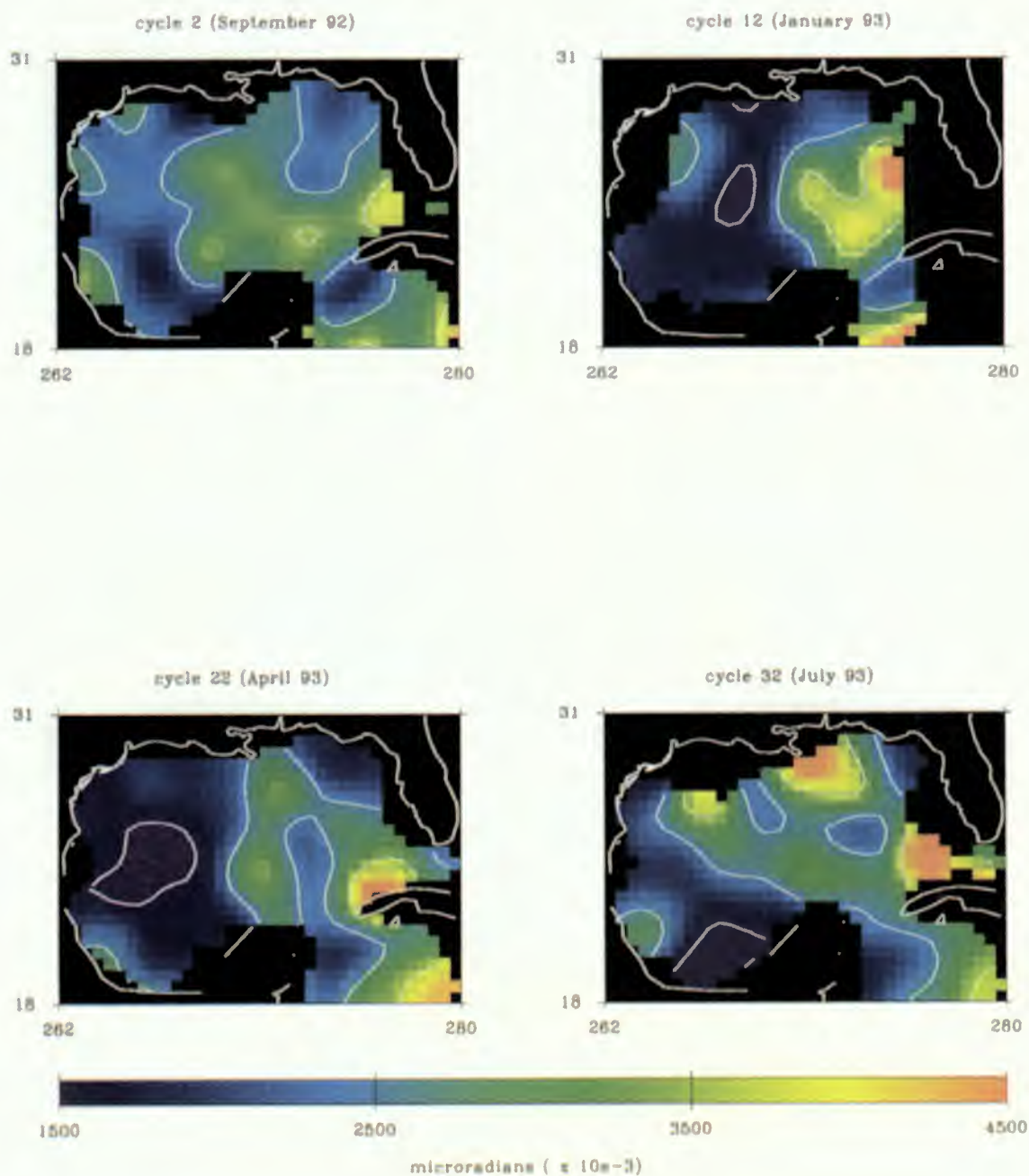


ERS-1 Mesoscale Variability – Annual Change in Gulf of Mexico

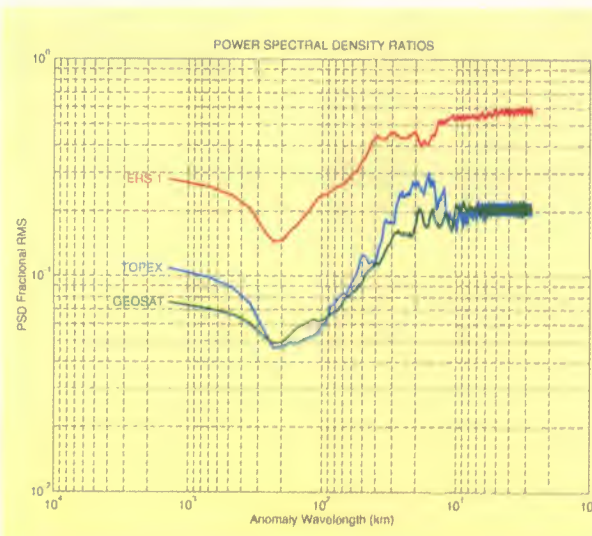
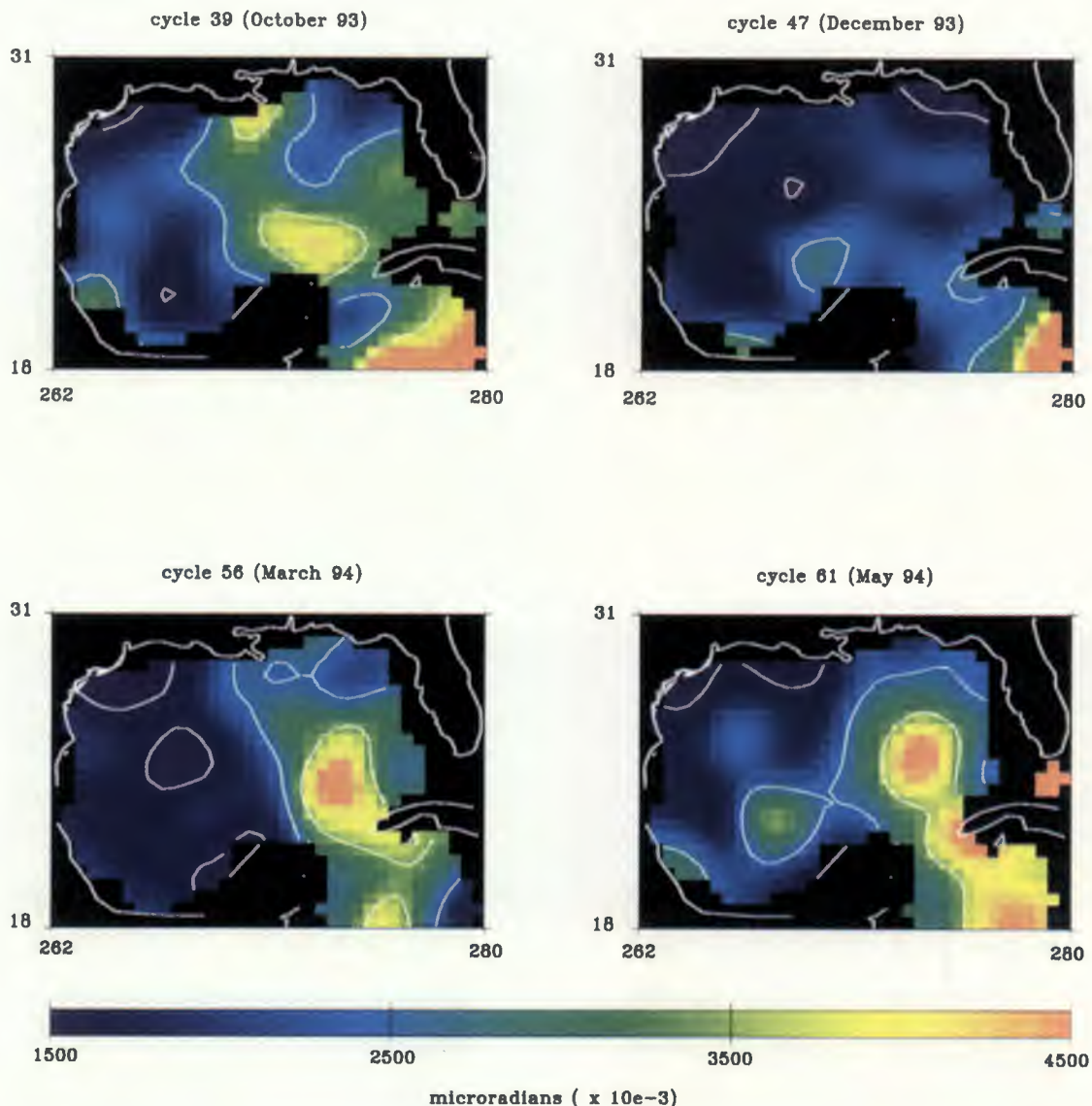
ERS-1 Mesoscale Variability – Annual Change in Gulf of Mexico
G.E. Peterson, C.K. Shum, B.D. Tapley

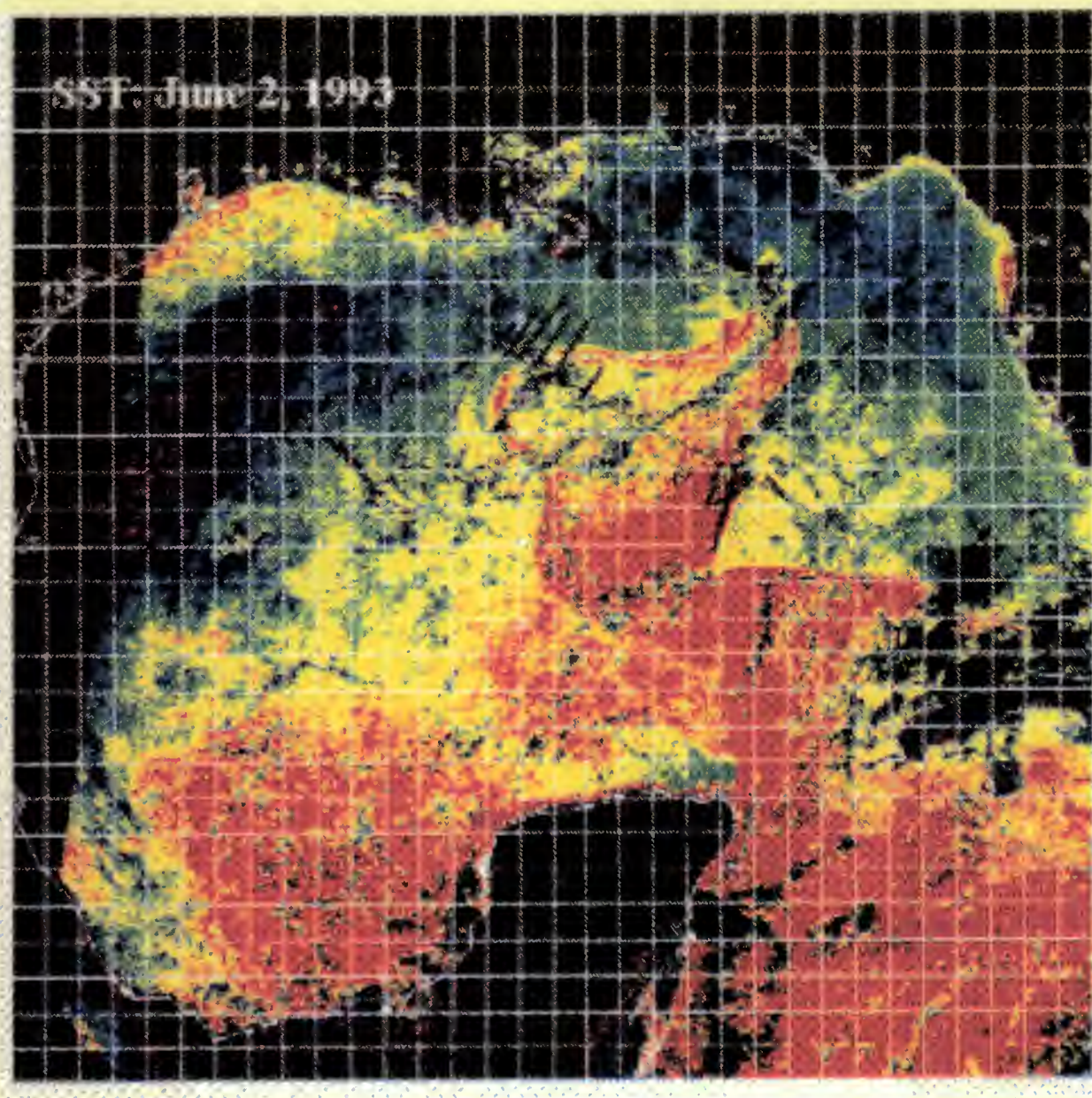


TOPEX Mesoscale Slope Variability – Annual Change in Gulf of Mexico
G.E. Peterson, C.K. Shum, B.D. Tapley



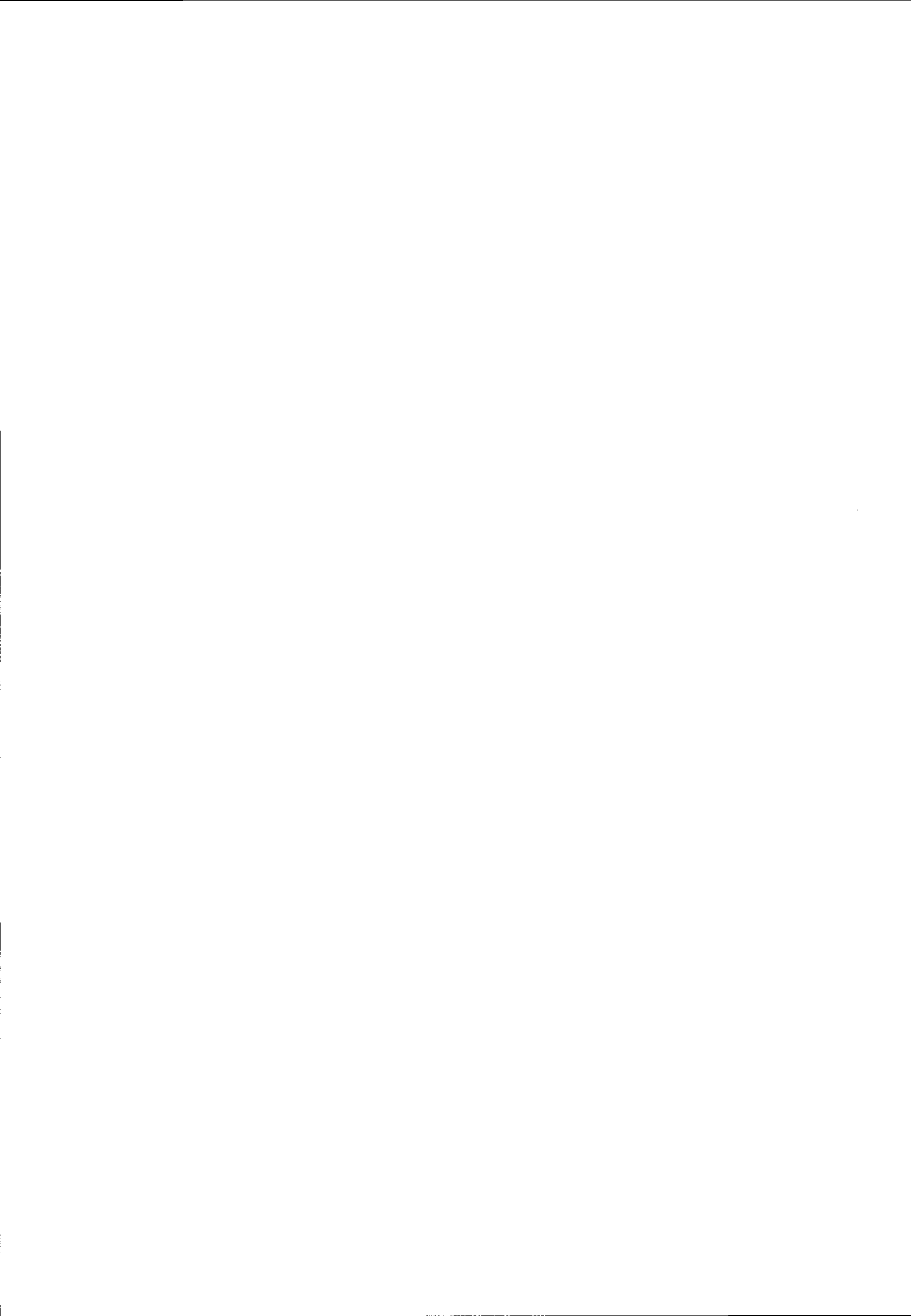
TOPEX Mesoscale Slope Variability – Annual Change in Gulf of Mexico
 G.E. Peterson, C.K. Shum, B.D. Tapley





AVHRR data supplied by M. Roffers Fish Forecasting.

Imagery processed by Peter Price, Marathon.



10. AGRICULTURE



**TOWARDS THE INTEGRATION OF ERS SAR DATA
IN AN OPERATIONAL SYSTEM
FOR
THE RAPID ESTIMATE OF CROP ACREAGE AT THE LEVEL OF THE
EUROPEAN UNION**

**Hans-Günter KOHL, Edmond NEZRY,
Marek MRÓZ*, Hugo DE GROOT**

Joint Research Centre of the European Communities (JRC)
Institute for Remote Sensing Applications (IRSA)
Agriculture Information System (AIS)
TP441, I - 21020 Ispra (VA) - Italy
Phone : +39-332-785449, Fax : +39-332-789074
e_mail: hans.kohl@cen.jrc.it

*Akademia Rolniczo-Techniczna, Olsztyn - Poland
In training at GDTA, 17 Av. E. Belin, Toulouse - France.
Detached to JRC/IRSA/AIS, Ispra - Italy

ABSTRACT

In previous studies conducted at AIS [1], it was shown that the combination of ERS-1-FD and SPOT imagery improves significantly the classification accuracy of agricultural crops, if compared to a single SPOT-XS scene. More recently, the work has been directed towards the independent analysis of high dimensional, multi-date ERS-1 SAR PRI data sets. 9 images of the agricultural season 1992-1993 over the Seville (Spain) site of the MARS project were analyzed and compared to the results obtained with multi-date SPOT imagery. In addition, 2 PRI images over Olsztyn (Poland) were analyzed in the framework of a JRC/GDTA collaboration. The preprocessing methods used were based on an enhanced structure retaining Gamma-Gamma MAP speckle filter [2] taking now into account also second order statistics (Sum average or autocorrelation functions) [3]. The thematic analysis has been improved by the use of historical land-use information (occurrence masks), giving *a priori* probabilities for certain crop aggregations likely to occur.

A first evaluation of crop area estimates derived from SAR data only, on subareas of the Seville site, gave accurate results for rice, cotton, wheat and sunflower. On the Polish test-site (Olsztyn), the additional SAR channels did not improve the accuracy of the SPOT based land-use classification, but contained additional information useful for the mapping of wetlands.

1. INTRODUCTION

The MARS- (Monitoring Agriculture by Remote Sensing) project includes a specific action aimed at crop acreage estimation based on satellite imagery. For 53 European sites, SPOT or TM imagery is nominally acquired four times during the growing season. Due to unfavourable weather conditions, it proved difficult to get a sufficient number of images on the sites in northern Europe. The weather constraints, as well as the potential already demonstrated by ERS-1 data analysis [1], emphasize the interest to introduce ERS SAR data into the MARS-project.

The current research work is oriented towards the following directions:

- Enhancement of pre-processing methods (calibration, resampling, filtering).
- Introduction of geographical knowledge in the data analysis process (occurrence masks).

This research is conducted with the support of a limited number of contractors in Europe.

Emphasis is also put on the assessment of synergism between ERS SAR and SPOT data and its temporal and/or spectral complementary [1]. An important aspect of complementarity of ERS SAR and SPOT data is, for example, the expected possibility to produce early area estimates of certain agricultural crops using SAR data only. Another important item is the cost-effectiveness of SAR data compared to SPOT imagery.

The JRC/IRSA/AIS unit conducts an experiment on the Seville site of the Rapid Estimates project. The current experiment is aimed at the above mentioned short- and medium-term research goals.

The longer-term goal is to integrate ERS SAR data into the operational system by developing and implementing backscattering and agrometeorological models. This should finally lead to a better understanding of the underlying physical phenomena.

2. OBJECTIVES OF CURRENT INVESTIGATION

The general work objective is to integrate agricultural management practices, historic agricultural land-use information, meteorological data, and finally SPOT and ERS SAR derived information, in a simple knowledge based system. This database is and will be used:

- For the construction of "occurrence masks", allowing to indicate a level of *a priori* likelihood for crops to appear in specific landscape units.
- To estimate with ERS SAR data already early in the year (at bare soil conditions), the acreage of a limited number of economically important agricultural crops.
- To improve crop discrimination during the growing season, taking profit of the complementary information content of ERS SAR and SPOT data.

The main conclusions of the studies conducted up to now, either by IRSA/AIS, or by other research groups, can be summarized as follows:

- Similar crops show similar distinctive temporal backscatter profiles (but not similar backscatter level) whatever the soil type. Thus, the use of temporal backscatter profiles matching techniques seems a promising method for crops identification.
- The backscatter of crops is highly variable at early growth stages.
- Effects of meteorological parameters need to be more deeply investigated, but could be considered as discriminant factors for statistical analysis of ERS time series, and identification of economically important crops.
- Some level of ERS SAR data pre-processing is needed, in order to retrieve ERS SAR information (speckle filtering, discriminant

analysis of time series, mutual information between acquisitions, mutual information between ERS SAR and SPOT/TM data, etc...).

According to the current status of operation oriented research, the following items of immediate interest have been identified.

2.1 Enhancement and operational use of ERS SAR preprocessing

In the case of SAR data, the first step in low-level processing, consists of image adaptive speckle filtering, in order to reduce problem complexity by enhancing all desirable image properties as, for instance, signal to noise ratio, backscattering coefficient, edges and structural features, textural properties. These methods have been enhanced and transformed into operational tools, optimized for both, higher level processing and photo-interpretation.

With reference to the above mentioned topics, work has been concentrated on:

- The restoration of ERS SAR reflectivity and texture, by enhancing the performance of a structure retaining adaptive speckle filter. This filter, already successful for radar reflectivity restoration, has been optimized for a better preservation of ERS PRI image texture in the presence of correlated speckle [3]. In this way, texture becomes readily available as an additional discriminator.
- The extraction of field boundaries from SPOT-Panchro or Russian KFA-1000 imagery, to perform high-level processing on a per field basis. Nevertheless, due to the limitations in SPOT/TM data availability, direct ERS SAR image segmentation methods are under development [5].

2.2 Early acreage estimation of agricultural crops using ERS SAR

Conventional agricultural inventory and monitoring systems using optical spaceborne data are based on image acquisition and analysis during the growing season. The satellite data is acquired in time-windows from March until October. However, rapid estimates of crop surfaces early in the season are often hampered by the lack of suitable spaceborne remote sensing data due to cloud cover. Optical remote sensing imagery of late fall and winter periods is excluded from the analysis not only for cloud cover, but as well

for the lack of an agricultural vegetation cover which would result in characteristic reflectance values.

Although the vegetative cycle comes to a halt during the winter period, the land preparation and agricultural practices during this period modify often the characteristics of the agricultural landscape. Different crops require different field preparation, which is guided by environmental conditions such as temperature, rainfall, soil composition, and common management practices such as crop rotation schemes.

As the SAR is sensitive to the geometrical characteristics of the soil surface layer, commonly referred to as the soil "roughness" and to the soil humidity, the analysis of winter SAR imagery can probably provide information on the spatial crop distribution.

Another important reason to incorporate ERS SAR data in an early estimation system is the advanced stage of microwave backscatter modelling theory for bare surfaces. Backscattering of bare soil surfaces is relatively well understood and its computer implementation rather straightforward. Feeding these models with both, environmental parameters and surface characteristics will allow the development of a backscatter database with characteristic values for various types of land preparation.

In this way a relation between the observed backscatter values and those resulting from the backscatter models can be established. This will allow the identification of the crop type already at this very early stage.

2.3 Analysis of ERS time series for the monitoring of land use changes in agriculture

An expert workshop [7] took place in February 1994 in JRC/IRSA/AIS Ispra, in order to collect ideas and expertise, especially in the fields of general SAR image understanding, modelling, segmentation, and interpretation. The recommendations lead to the following orientations of the research work.

In the high-level processing, meaningful descriptions of the physical objects observed by the ERS SAR sensors include the geographical identification of changing areas (since agriculture involves seasonal changes), as well as the type of change. This implies the use of multiple source data, i.e. the following approaches are already under investigation:

- The use of physical backscattering models can help to reach some level of backscatter prediction. This needs more investigation of the relationships between:

- i) C-band, 23 degrees ERS backscatter,
 - ii) soil moisture content,
 - iii) soil composition,
 - iv) soil roughness,
 - and v) crops evolution (type, phenology, height).
- As an example,

correlation between ERS backscatter and rainfall (responsible for soil moisture) has been already experimentally investigated. This research imposes to use ERS fully calibrated PRI images.

- On the other hand, one can consider soil moisture, dielectric properties of soils, texture, etc... as instantaneous parameters. For instance, soil moisture (i.e. dielectric constant), a predominant parameter influencing the mean backscatter of agricultural surfaces during the growing season, is often considered as a measurement disturbance. In this case, a fully statistical approach involving analysis of mutual information between ERS acquisitions through maximum entropy and/or standardized principal component analysis is expected to provide good crops classification. This point does not exclude the previous one (backscatter models), since both approaches could provide complementary results.

- Change detection techniques will also be investigated and improved in order to provide a dynamic image of the agricultural landscape. This research will also use ERS PRI images.

- Integration of the change detection and classification results (ERS SAR time series) into the GIS used by the Agriculture Information System, which will provide the ancillary data (soil maps, topographic maps, data from meteorological networks, previous years classifications, etc...) needed for their final interpretation, in terms of physical and thematic meaning.

- We will try to establish an interactive and comprehensive link between the parameters introduced in the predictive agrometeorological models used by the Agriculture Information System and the ERS SAR change detection results, to make easier change interpretation and adjustment of the model's parameters possible.

2.4 ERS SAR and SPOT data complementarity and data fusion

This is a field in which the Agriculture Unit (AIS) has already a some experience. Additional efforts to relate changes occurring in ERS time series to optical data are undertaken to establish further strategies for the complementary use of both sensors, with the scope

to improve the efficiency of remote sensing applied to agriculture:

- Analysis of the crop information content of ERS SAR data in comparison to SPOT/TM imagery will concentrate on crop types for which SPOT/TM data does not provide clear separability.

- On the other hand, when based SPOT/TM based crop separability is satisfactory, ERS SAR data together with agrometeorological and backscatter models, can be used to give quantitative results on crop growth, even if neither radiometric nor textural separability between these crops is achieved by the radar itself.

3. EXPERIMENTAL PLAN

Ground truth collection on the test sites will be ensured, either by JRC/IRSA/AIS, or through contracts with the University of Stuttgart (Institute for Navigation), and the Instituto Nacional de Investigaciones Agrarias, Madrid. The later will provide us with ground information on 250 segments, sampled 7 times a year. In order to get a more complete knowledge on land cultivation practices, crop rotation, etc..., ground truth has been collected, from 1988 up to now.

A Pilot Project proposal has been submitted to ESA. The proposal intends to evaluate standard ERS SAR image (PRI) products for their integration in the context of AIS.

Experimental studies already began on the sites of Seville (Andalusia, Spain) and Great Driffield (UK), as well as on an additional test site in Poland (Olsztyn).

4. FIRST RESULTS

4.1 Seville site

The spatial extent of available information (ground truth, DTM, ERS-1 frame 2853 coverage) made it possible to extend our Seville test site [1] from 40x40 km to 62.5x75 km. 4 SPOT-XS, 9 ERS-1 and the ground segments from 1991/1992 have been georeferenced to a panchromatic SPOT orthoimage. Raster and vector information have been integrated in a database.

A pre-processing chain for ERS-1 PRI images has been implemented, consisting in full image calibration, image resampling to 20x20 meters (linear weighted intensity method), and adaptive structure retaining filter [2, 3].

In order to address image segmentation, a KFA-1000 (5m resolution) frame of the Seville test-site has also been evaluated. This evaluation is still under way, and seems to be promising.

	RICE	COTTON	WATER	OTHER
SPOT (AIS)	31.8	16.1	3.5	48.6
SPOT (S)	29.8	17.9	7.3	45.0
ERS-1	24.8	14.6	5.5	55.1

SPOT (AIS) : 4-date, performed by AIS
 SPOT (S) : 4-date, performed by contractor
 ERS-1 : 4-date, performed by AIS

Table 1 Classification results, percent of total area

Based on available crop calendars [8], appropriate dates of SPOT and ERS-1 acquisitions have been selected. Figure 1 shows the results of 4-date SPOT classification, and of a 4-date ERS-1 classification, directed towards the identification of rice and cotton fields in an area south of Seville. In addition the figure shows also the classification results obtained in the operational framework of the Rapid Estimates Project. These three classifications are consistent, and show only minor differences. This is confirmed by the acreage estimates presented in Table 1. Figure 2 and table 2 show the results of a sunflower and wheat classification in an area north-west of Seville.

Figure 3 gives a visual impression of the quality of the ERS-SAR processing level. The geometric resolution of the SAR image is comparable to SPOT .

	WHEAT	SUNFLOWER	OTHER
SPOT (AIS)	34.8	34.3	30.9
SPOT (S)	37.7	32.0	30.3
ERS-1	39.1	39.3	21.6

SPOT (AIS) : 4-date, performed by AIS
 SPOT (S) : 4-date, performed by contractor
 ERS-1 : 3-date, performed by AIS

Table 2 Classification results, percent of total area

4.2 Olsztyn test site

In the perspective of the extension of the EC-MARS Project to Eastern Europe, a pathfinder study has been conducted at JRC/IRSA/AIS in the framework of the GDTA training program (CETEL). The study was oriented towards the use of optical and SAR data for land-use mapping of the Olsztyn (Mazuria, Poland) area. Two ERS-1 PRI (April & May 1992) and one SPOT-XS (April 1992) were combined. The main results obtained on this test-site [9] with regard to ERS-1 can be qualitatively summarized as follows:

- ERS-1 data allow for accurate discrimination (better than SPOT) between built-up and natural (forest, agriculture) vegetated surfaces,
- Discrimination between the principal land-use components, bare soil/grasslands versus agricultural crops and forested areas can also be successfully achieved by ERS-1.

In Figure 4, the radar signal has been combined with SPOT-XS using an IHS transform. This kind of product has demonstrated its usefulness for the mapping of areas with high water or soil moisture content.

5. PERSPECTIVES AND CONCLUSION

The integration of the ERS SAR PRI data into the MARS project will have the following useful aspects:

- Spectral complementarity to SPOT/TM optical data: the expected advantages are better discrimination of target crops using ERS/optical data and derived higher level products.
- Temporal complementarity to SPOT/TM optical data: early detection/classification of crops appears possible using ERS SAR PRI data, and will therefore be assessed.
- Eventual substitution of ERS SAR PRI data to optical remote sensing data in the case of SPOT/TM missing sites.
- Pricing and rapid delivery by ESA should prove valuable arguments for operational use of ERS SAR PRI data. Reduction of the overall agriculture monitoring costs can also be reasonably foreseen at longer term.

H. Laur from ESA/ESRIN, for the rapid data delivery and related general assistance. A debt of gratitude is due to the participants to the Expert Workshop held at JRC/IRSA/AIS on 16-17 February 1994 [7], whose recommendations have been considered in the present paper.

REFERENCES

- [1] H.G. Kohl, C. King, H. De Groof, 1993: "Agricultural Statistics : Comparison of ERS-1 and SPOT for the Crop Acreage Estimation of the MARS Project", Proceedings of the 2nd ERS-1 Symposium, ESA SP-361, Vol.1, pp.87-92, Hamburg (Germany), 11-14 October 1993.
- [2] A. Lopes, E. Nezry, R. Touzi, H. Laur, 1993: "Structure detection and statistical adaptive speckle filtering in SAR images", Int. J. Remote Sensing, Vol.14, n°9, pp.1735-1758.
- [3] E. Nezry, H.G. Kohl, H. De Groof, 1994: "Restoration of textural properties in SAR images using second order statistics", to be published in the Proceedings of IGARSS'94, Pasadena (CA), 8-12 August 1994.
- [4] G. Kattenborn, E. Nezry, G. De Grandi, A. Sieber, 1994: "high resolution detection and monitoring of changes using ERS-1 time series", Proceedings of the 2nd ERS-1 Symposium, ESA SP-361, Vol.1, pp.635-642, Hamburg (Germany), 11-14 October 1993.
- [5] R.P.H.M. Schoenmakers, H.J.C. Van Leeuwen, G.G. Lemoine, E. Nezry, 1994: "Segmentation of combined high resolution optical and radar imagery for the determination of field inhomogeneities", to be published in the Proceedings of IGARSS'94, Pasadena (CA), 8-12 August 1994.
- [6] M.A. Karam, A.K. Fung, R.H. Lang, N.S. Chauhan, 1992: "A microwave scattering model for layered vegetation", IEEE Transactions of GRS, Vol.30, n°4, pp.767-784, July 1992.
- [7] "Integration of ERS-1/2 SAR's in the Advanced Agriculture Information System", Expert Workshop, held at JRC/IRSA/AIS, Ispra (Italy), 16-17 February 1994.
- [8] J.M. Moreira Madueño, 1991: "Capacidad de uso y erosión de suelos. Una aproximación a la evaluación de tierras en Andalucía", Junta de Andalucía, Consejería de Cultura y Medio Ambiente, Agencia de Medio Ambiente.
- [9] M. Mróz, 1994: "L'utilisation des images ERS-1 (SAR) et SPOT XS pour l'étude d'occupation des sols dans le nord-est de la Pologne", Rapport de stage CETEL 1993/ 1994, GDTA Toulouse.

ACKNOWLEDGMENTS

The authors would like to thank the European Space Agency, and especially Dr. G. Kohlhammer and Dr.



Figure 1 Classification results (rice and cotton)



Figure 2

Classification results (wheat and sunflower)



Figure 3 Comparison SPOT versus ERS-1 PRI

**Figure 4**

Olsztyn (Poland). IHS transform of filtered PRI image, SPOT-XS and topographic map. Dark tones indicate areas with potential water accumulation.



UTILIZATION OF SAR FOR CROP STUDIES IN THE EASTERN SEABOARD, THAILAND

Thailand Remote Sensing Center,*
National Research Council, Thailand

1. Introduction

The development of Synthetic Aperture Radar (SAR) system for all weather, all season has lead to increase interest in remote sensing applications. It is known that specific algorithms for SAR data classification have not yet sufficiently developed. The combination of other optical data such as Landsat with SAR data as well as the combination of ERS-1 SAR multitemporal data are suggested for surface changes especially crop types identification. The objectives of the study is to evaluate ERS-1 SAR data for tropical crop identification and to develop methods for using ERS-1 SAR data in a complementary mode with optical remotely sensed data for crop monitoring.

1.1 Study area (Figure 1)

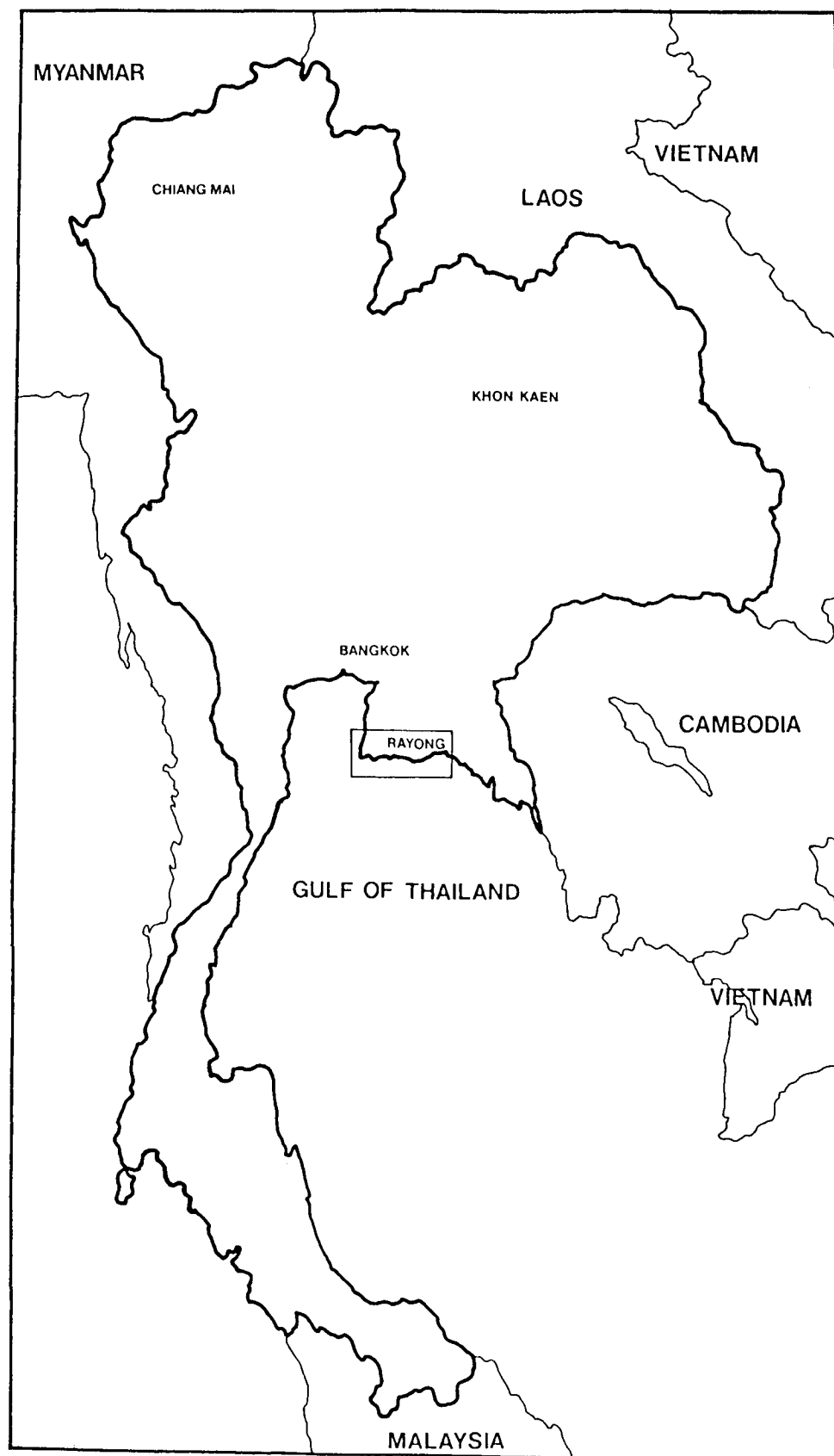
The study area is in the Eastern Seaboard of Thailand. The area is located in Rayong province between latitude $12^{\circ} 20'$ - $13^{\circ} 10'$ N and longitude $101^{\circ} 10'$ - $101^{\circ} 45'$ E. Topography of the area is ranging from riverine terrace, undulating and mountainous features. The major cultivations in this area are rubber plantation, mixed orchards, paddy and field crops including pineapple, cassava and sugar cane.

2. Data Acquisition

2.1 Satellite data

The satellite data used in this study were obtained from Thailand Ground Receiving Station. The data are in the form of CCT and the acquired dates of images are as follows.

* S. Vibulsresth, D. Dowreang, T. Rangsikanbhumi, J. Pornprasertchai, S. Polngam



STUDY AREA

Satellite	Sensor	Data	Stage of crop plant
ERS-1 SAR	Microwave	July 29, 1993	Rainfed Paddy is in harvested season, off season Paddy is in vegetative stage.
ERS-1 SAR	Microwave	September 02, 1993	Rainfed Paddy is in vegetative stage.
ERS-1 SAR	Microwave	April 18, 1994	Rainfed and off season paddy are in harvested stage.

2.2 Ground truth information

Ground information for this area were collected from direct field observation and also personal interviews with local farmers.

2.3 Topographic Maps

Topographic maps at a scale 1:250,000 and 1:50,000 were used.

3. Methodology

Image analysis was performed on a Meridian package software available at the Thailand Remote Sensing Center.

Using the Meridian system, an image compression is the first step to be done in which each digital values are transformed from 16 bits to 8 bits image and can be run on the system.

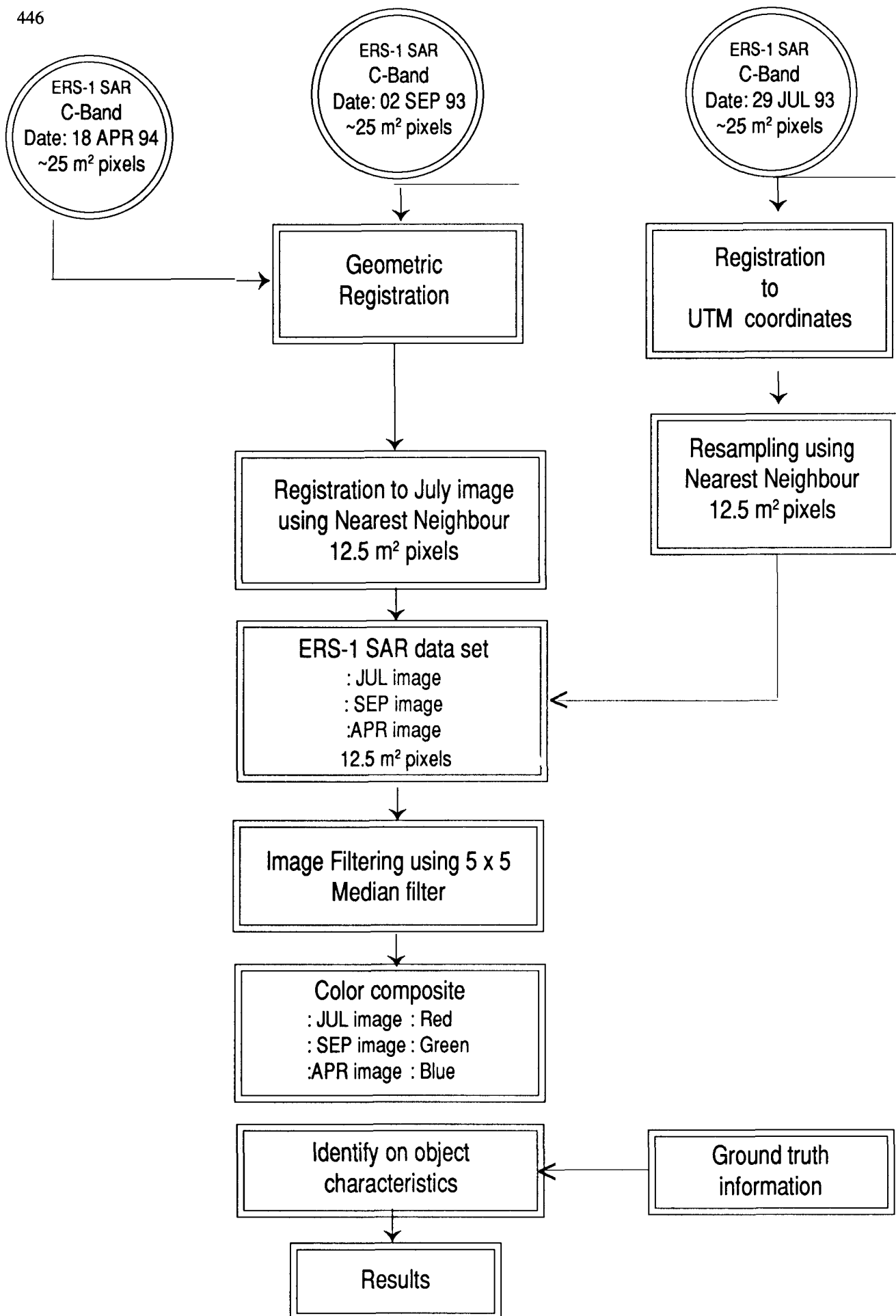


Figure 1 Processing chart of ERS-1 SAR multitemporal study

Geometric correction was applied to the July images for registering to a Universal Transverse Mercator (UTM) projection and resampling using Nearest Neighbour technique to 12.5 m square pixels (see detail in figure 2) and then use this image as a reference image to which all data were registered.

Data analysis was conducted visually based on ERS-1 SAR multi temporal data. It should be noted that ERS-1 SAR data have speckle noise which masks fine details on the image. Therefore, a standards filtering technique, the Median filter with 5 x 5 window was applied to remove such a noise.

ERS-1 SAR has a single wavelength. In this case, image analysis is a difficult task for identification of crop types, different surface types will look similar on SAR image. So, image combinations were done following the two approaches mentioned earlier.

4. Results

The data set of SAR with 12.5 meters square pixels size was devided into sub areas where it is ranging from flat to gently sloping terrain. Some areas in the mountainous zone were cut off due to a geometrical mismatch between different date of ERS-1 SAR data since SAR data were not terrain corrected (DTM software is unavailable on the Meridian). Color composite of ERS-1 SAR July 1993 image, September 1993 image and April 1994 image were displayed in Red, Green and Blue respectively (see figure 2). A satisfactory results were obtained with regard to the identification of color, pattern and texture. Table 1 shows a correlation between SAR characteristics and crop types.

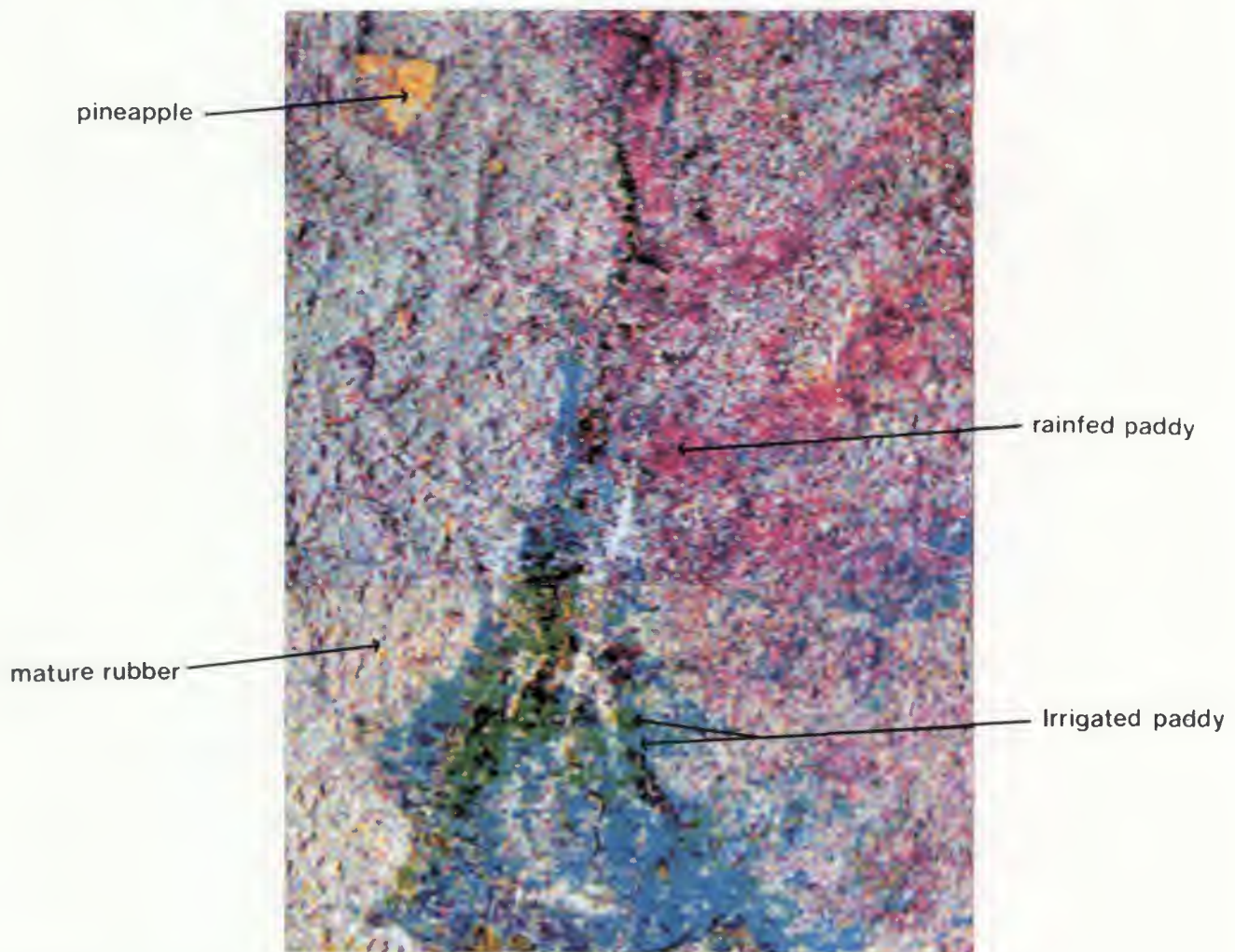


Figure 2 Color composite of ERS-1 SAR July 1993 image, September 1993 image and April 1994 image which were given in Red, Green and Blue, Rayong area.

No	Description	color	Texture/Patter	Remark
1	Rainfed Paddy	green	regular pattern with fine texture	The September image is in a vegetative stage of paddy plant. On the image appear bright (high backscatter)
2	Off-season Paddy	Magenta and Red	regular pattern with fine texture	The July image image is in a vegetative stage of paddy plant.
3	Pineapple	yellow and Purplish and blue	regular pattern fine texture	The images taken in July and September are in a vegetative stage of plant
4	Rubber	yellowish tone	regular pattern with coarse texture	An unchange areas are display in Black and volute colors such as Urban area, Dam and forest area
5	Young Rubber	green	rectangular pattern	The begining stage of rubber tree

Table 2 The correlation between color and crop types based on color composite of ERS-1 SAR multitemporal in figure 3

5. Future Work

- 1) A digital analysis of ERS-1 SAR 3 dates will be done and then compare the results to the classification of Landsat TM and ERS-1 SAR data .
- 2) For agricultural crop identification, ERS-1 SAR data taken on a timely basis of crop information since a percent of vegetation covered, row direction or row spacing are influencing to the return signals, will be carried out and merged to the data set.

6. Conclusion

This paper describes how SAR data could be used for identifying crops types in Rayong area. Color composite of ERS-1 SAR multitemporal combination have been analyzed with expectation of greater advantages in the identification of crop types than use a single wavelength image. In mountainous zone, a Digital Terrain Model is necessary for SAR geocoding. It was evident that field size of respective crop is important as well as coincident ground truth information should be collected during a satellite pass.

In order to improve the analysis on SAR data, an operational tool must be further developed.

7. References

1. DAVID S. SIMONETT, Manual of Remote Sensing, Second edition, Volume I, p. 1144-1158
2. ROB SCHUMANN, SAR data for Cartographic Application paper submit to training course on ERS-1 & SPOT : A Complementary tool for Natural Resources Management, August 19-26, Bangkok, Thailand
3. ROBERT A. SCHOWENGERDT, Techniques for Image Processing and Classification in Remote Sensing p. 110-116
4. THOMAS M. LILLESANO, RALPH W. KIEFER, Transmission Characteristics of Radar Signals, Remote Sensing and Image Interpretation, p. 492-503

THE USE OF ERS-1 DATA FOR RICE MONITORING THE EXAMPLES OF SEVILLE, EBRO DELTA, INDONESIA

Jochen Harms

SCOT CONSEIL

1 rue Hermès, Parc Technologique du Canal, 31526 Ramonville Saint Agne, France
phone: (+33) 61 39 46 00, fax: (+33) 39 46 10

ABSTRACT

The goal of the different projects has been to establish the feasibility to monitor rice with ERS-1 data and to subsequently develop an operational monitoring system for Indonesia. For this purpose, two test sites in Europe have been chosen to better understand the phenomena and to start to test different classification approaches. The results show the usefulness of the segmentation based field classifiers. Applied to multitemporal datasets, the rice surface can be estimated to a very high degree of accuracy. Further information on the crop status can equally be found within the data. Following this preparation phase, two test sites in Indonesia have been chosen, in order to apply the defined method to a different geographic location and to further extent the feasibility. The further improvement of the method will be the basis for the later operational system to be almost entirely based on the use of radar data.

1. INTRODUCTION

Rice is the major food supply for the world population. Its monitoring and assessment can be seen as one of the most important tasks. Remote sensing and specifically radar might help to reach the goal of monitoring the world wide growth conditions of rice in a cost-effective and operational way. Within a number of ERS-1 pilot projects the use of radar data for the operational monitoring of rice has been investigated.

2. TEST SITES AND IMAGES

Sevilla in Spain is one of the official Action IV test sites of the MARS project (Monitoring Agriculture with Remote Sensing). About 15 ERS-1 images from 1991 to 1993 have been used in order to investigate the potential of radar for monitoring agriculture. One major crop on the test site is rice.

The Ebro delta is one of the major rice cropping areas of Spain. In total, 12 ERS-1 scenes have been utilized in order to investigate the use of radar data for detecting changes in land use pattern on regional level.

For Indonesia, the supply of rice is of major importance. A first feasibility study has been carried out. For this purpose, one ERS-1 image of November 1993 of a site

close to Jakarta has been successfully acquired and shipped to SCOT CONSEIL, four other images, acquired over a different site during the 3-day-cycle, are underway.

3. METHODOLOGY

In a first step, investigations, mainly over the test site of Sevilla, focused on the visual detection of rice in mono- and multitemporal ERS-1 scenes. Following this, traditional classification technics (supervised classification) have been compared with the new approach of segmentation based per field classifier. Segmentation were obtained from SPOT. The interpretation results of the ERS-1 images were compared with the classifications of optical data. Furthermore, complementary analysis of SPOT/ERS-1 have been performed. Over the test site Ebro delta, mainly automatic technics have been applied to the radar data and optical data. A new tool, the direct segmentation of mono- and multitemporal ERS-1 scenes could be successfully applied to the radar data. Results were compared with classifications of optical data and ancillary information. With the help of one ERS-1 images over Indonesia, it has been possible to study the capabilities of radar to monitor the irrigation pattern by visual interpretation. Automatic technics will be applied to the data acquired over the second test site in Indonesia.

4. RESULTS AND CONCLUSIONS

Within the two projects performed over Sevilla and the Ebro delta, it could be shown that the visual interpretation of ERS-1 data and the distinction of rice from other crops is possible. The radar signal enables the interpreter of the image to differentiate different growth phases of the rice crops. Specifically, the period of May and June allows to distinct rice from other crops. The influence of the wind on fields under water has to be taken into account. Over both sites, the automatic technics of segmentation and field-based classification could be successfully applied to the radar data. The multi-temporal approach should be applied when possible, in order to avoid confusion with other water covered surfaces. Advantages of this approach could also be identified for the classification itself.

Over the Indonesian test site, it has been possible to identify different irrigation phases within one ERS-1 image. The problem of confusions between urban areas and rice fields could be solved with the multi-temporal approach.

The capacity of using of radar and optical data in a complementary approach could be identified. Major impacts are seen in the segmentation process as radar tools still need some improvements. Further developments are also necessary in the field of speckle reduction (filtering of ERS-1 data).

6. RECOMMENDATIONS AND NEXT STEPS

Within the different rice related projects, it could be clearly shown that radar data are a very suitable tool to monitor this crop from space in a cost-effective and operational way. Therefore, operational applications in this field can be strongly recommended. Specifically in Asia, where the cloud cover hinders the use of optical data, the ERS-1 radar and its successor instruments on-board of ERS-2 and ENVISAT will allow to start operational activities of monitoring the growth conditions and the irrigation control of rice.

Use of ERS-1 SAR Imagery for crop monitoring.

JM. Roques*, T. Rabaute**, C. Demailly*, J. Harms**, A. Carrou*

* CISI, Direction Observation de la Terre, 13, rue Villet 31400 Toulouse, France

** SCOT Conseil, 1, rue Hermès, Parc Technologique du Canal 31526 Ramonville St Agne France

ABSTRACT

The aim of this study is to investigate the potential of SAR data for crop identification and to define a methodology toward an operational monitoring of agriculture resources based on radar imagery.

Four sites of the Action IV test sites of the MARS project have been selected, presenting varied agricultural and climatic types. PRI mode images are used.

Two approaches are examined. The first one focuses on speckle filtering, followed by a classification process. This method tends to be similar to those usually applied to optical data.

The second approach uses the total radar information without speckle filtering, and aims at defining relevant classifying parameters for non filtered radar images. This part of the study is mostly dedicated to the statistical analysis done to select those parameters.

Results of both approaches are shown and the use of multi temporal data is discussed.

1– Introduction

The aim of this study is to assess the feasibility of using SAR Data in an operational system of crop monitoring, as a complement of optical imagery already in use within the MARS Action IV project.

This study was conducted jointly by Cisi and Scot Conseil in Toulouse.

Both companies have worked actively on this subject for several years using both Spot and LANSAT images. The acquired experience helped the analysis of the subject on two axes :

a– How radar data can complete optical ones when crop determination is problematic.

This case often occurs in various rural sites where numerous annual cultures show development cycles very close in time to each other, that make them difficult to discriminate. This is particularly true with corn and sunflower or cereal and meadows (grasslands) in Northern Europe, or vineyards and orchards.

Owing to their independence from sun light and cloud cover, SAR images should help complement optical images.

b– Eventually replacing optic imagery by SAR when the cultural system is simple enough.

The economic issues are of importance, as SAR imagery could be introduced within remote sensing applications,

and notably European projects which are presently in a definition or preoperation phase with the following objectives :

- to allow a better discrimination of annual and perennial cultures, and consequently produce better statistics,
- to obtain desired information earlier.

Two different approaches are examined to fulfil crop discrimination.

The first one (called hereafter "optical way") is to adapt the methodology already in use with optical sensor images :

SAR images must consequently be pre-treated before entering a classification process.

The second one ("radar way") relies more specifically on the analysis of the radar signal information (structures, textures, ...) to find relevant discriminant parameters.

Both approaches aim toward image classification after a whole treatment chain. The design of the whole chain makes up part of the study.

2– Retained Areas

Four agricultural areas were chosen for this work : Arles and Bourges in France, Albacete in Spain and Great Driffield in the UK.

These areas are already being studied within the Mars Action IV European Project, which notably simplifies the validation aspect of our study. For each site, we had a history of field enquiries (for 1992), and we were able to use the previous interpretation work which had been done with visible imagery. These images in the visible domain were still at our disposal.

These sites were also chosen, because they showed zones with small relief variations, in order to eliminate geometric and radiometric rectification problems that would have arisen on non flat areas.

As a consequence, we were able to reproject Spot images on ERS-1 ones with a simple technique of polynomial deformation computed from a set of corresponding points.

3– The optical way

3.1– Method description

In this approach, traditional methods generally used for processing visible sensor images are preferentially adopted, as they have been validated operationally with Spot and Landsat images. Moreover image interpreters are nowadays well trained with these methods.

To run with optical sensor oriented designed techniques, radar images have to be pre-processed so as to filter the speckle, arising from radar signal coherence. Speckle effect dramatically prevents optical techniques of segmentation and classification to work on SAR images. Moreover, optical images, used in classification processes are multi-channelled, which multiplies the information, and helps the discrimination of the plant cover, while ERS-1 provides single frequency, fixed polarisation images. As such, to obtain as much information as the optical images do, we need to work on several views shot on different orbital paths, that is to say, working on a multi temporal basis.

The chain process is made up of the following steps :

- specific filtering of speckle for ERS-1 images,
- SAR and Optic image superposition,
- Spot and ERS-1 image classification,
- classification comparison.

3.2– Speckle Filtering

As the first step, a bibliographic search for efficient algorithms was made :

Five different classes of algorithms have been considered :

- Statistical filters (most often encountered).
- Geometric filters (based on mathematical morphology).
- Multi temporal filters (use of multi temporal information instead of spatial as in statistical filters).
- Filters applying an improved diffusion equation on initial image data.
- Wavelet analysis based filters.

For the most promising ones, we implemented them, or, in some cases, we asked the authors to proceed to some tests on our images.

The filters which have been retained within this study, are statistical and geometric ones.

Later on, we were able to test improved diffusion filters and wavelet analysis, but outside of the general scope of this study.

3.2.1– Statistical Filters

The principle of the following filters is to minimise the quadratic mean between the speckled image and the estimated corrected image.

In this family, the best known techniques are the FROST, LEE, KUAN filters.

Other statistical methods based on different principles gave SIGMA, MAP or adaptive filters.

Best results for final usability are obtained with the Frost and Lee filters. However, the Frost technique is very time consuming and is not better than Lee's. Others filters give rise to texture artefacts or to some loss of contrast.

3.2.2– Geometrical Filters

Filtering is done by a combination of algebraic operations (erosion/ dilatation & opening and closure) based on multi directional structuring elements.

We chose to implement two filters described in [SAFA-89]. Both filters rely on Alternated Sequential Filtering (ASF) theory.

Multi directional ASF :

Structuring elements are line pieces of changing directions with a cleaning process following each couple of opening/closure. The cleaning process consists of an opening/closure done with a square of the same dimension as the line pieces used before.

Comparative ASF :

Structuring elements are made of increasing concentric circles.

The techniques of implementation are slightly different from the bare opening/closure processes.

For both filters, we showed an increase of the signal/noise ratio of 3 to 6 for the first one and 5 to 8 for the second.

3.3– Radar and Optic images superimposition

To validate results in order to compare Spot classification and ERS-1, we needed to superimpose ERS-1 and Spot images on each of the chosen scenes. ERS-1 images are PRI one (12.5×12.5 m), in the sensor geometry, already resampled to form square pixels.

Our concern being radar signal, we chose to reproject Spot images on ERS-1 to avoid a second resampling, which would have changed the statistical properties of the images.

Reprojection is done by constructing a simple polynomial deformation model from corresponding point positions on both images.

Two problems arose :

- the first one is due to relief. We avoided it by selecting flat areas within the retained sites,
- the second one is linked to the deformation between Spot and ERS-1 which is more important when SAR acquisition is done during an ascending orbit. This particular effect increases with latitude, which explains the lesser quality of the rectification obtained at the Great Driffield site (1.9 pixels rms for the registration error).

3.4- Filter evaluation and selection

The evaluation process on filters is made from the comparison of segmentation results between Spot and ERS-1 images. The segmentation software used here is based on the watershed line algorithm and is already operational on Spot images.

The evaluation was done exhaustively on every image of the Great Driffield and Bourges sites and for every preselected filtering technique. Results were then verified on the two other sites.

We finally estimated that the most efficient filters within our scope (ERS-1 PRI images) were :

- an adapted LEE filter applied using a 5 pixel window,
- both SAFA ASF filters with a level 1 iteration followed by a level 2 iteration,
- Sigma modified filter applied on a 5 pixel window.

3.5- Segmentation of ERS-1 images

As already mentioned, the image segmentation is done using a software which uses the watershed line algorithm applied to the gradient of the input image. This algorithm makes use of a regulation parameter for the segmentation which acts as a smoothing effect on the image and may be considered as an admissible signal variation within a single segment. This parameter must be higher for noisy images than for smoother ones.

To obtain classified parcels equivalent in shape and size, this parameter varies from 20 to 40 depending on the chosen filters.

The best filters for mono temporal segmentation purposes are Lee's modified and ASF comparative.

We then tried to confirm our choice of filters and integrate several shots of the same site in the case of multi temporal segmentation.

Various strategies were relevant for our purpose, depending on the order of the proceedings. We can for instance :

- filter first each image, then compute the average, and the gradient on the averaged image (first choice) or,
- compute the temporal average on the images, then filter the resulting image and compute the gradient (second choice) or,
- filter first, compute the gradient on each image, then compute the averaged gradient (third choice).

Each choice was tested on three, then seven, images on two sites with the two selected filters. We came to the following conclusions :

- the first and third strategies are better than the second, the third one giving slightly better results,
- 3 images give better segmentation, the use of 7 images diminishes the contrast too much during the average computing phase,
- LEE's modified filter is definitively better,
- the segmentation parameter stays nearly the same as compared with mono temporal computations.

Thus we retained the following steps for a multi temporal processing of classification by parcels :

- filter selected radar images with LEE's adapted filter with a 5 pixel window,
- compute mono temporal gradient on each of the filtered images,
- compute the multi temporal average of the gradient images,
- go through the segmentation process with the averaged gradient image.

3.6- ERS-1 Image classification

The last step of the "optical way" is to realise a cultural thematic classification on our images.

For optical images in operational systems there are two ways of doing so :

- pixel classification,
- parcel classification.

3.6.1- Pixel classification

As could be expected, pixel classification does not work with mono temporal images, even though on the Bourges site, large cereal fields, showing a good homogeneity, are rather well separated.

For multi temporal images, the result is slightly better, but the pixel variability from one shot to another still disturbs the classification process.

3.6.2– Parcel classification

We selected the following discriminant parameters for the classification process :

- the mean,
- the mean deviation,
- the standard deviation,
- the coefficient of skewness,
- the coefficient of kurtosis,
- the number of pixels within a segment.

3.6.2.1– Mono temporal classification

With mono temporal data, the result of the segmentation/classification is poor.

The variety of discriminant parameters is of no use, as the best results were obtained on the Bourges site using only the mean.

Using a segmentation already computed (on a multi temporal basis), the classification process is clearly improved : on the Bourges site, 70% of the cereal cover is separated on a single scene. This result is much less encouraging on the Great Driffield data.

3.6.2.2– Multi temporal classification

With multi temporal data, results vary along with the site, and the dates of the image acquisition. Some of the results are shown on figures 1, 2, 3 and 4.

For the Bourges site, most of the cover can be identified while using three dates. However, some confusion arises between wood parcels and corn where the speckle effect seems higher. Using 7 dates eliminates most of this confusion, but other ones appear elsewhere (colza and cereals).

On the Great Driffield site, results are less encouraging. Using three dates, the separation between meadows and cereals is poor, even though the segmentation is rather good. Using seven dates does not improve the classification.

At the Arles and Albacete sites we had few workable images as most of their acquisition was not made during 1992 where we had validation data.

The main reasons of this relative failure may be :

- a majority of small sized parcels in the surveyed areas,
- a lack of images at convenient dates,
- too few or inadapted discriminant parameters.

3.7– Conclusion on the Optical way

The implementation of this approach helped to show limits of such an approach, but also future possibilities.

A general orientation was brought up, as for the hierarchy of treatments and their linking, though without defining a truly operational methodology.

Additional research is necessary on the one hand, to improve the filtering step while adding to it a multi temporal notion, and on the other hand, to take into account new statistical parameters, which is the subject of the second approach.

4– The Radar way

We use the hypothesis that the whole radar data are significant, and that even the speckle noise contains some information that should not be removed

Going along with the first approach, we already tried some statistical parameters to compute multi temporal classifications after the segmentation step. The results were rather promising, yet not good enough for our purpose.

Our vision of an operational system of crop monitoring using SAR images supposes, first of all, that we are able to segment the images into parcels, then to classify them with relevant discriminant parameters. This procedure must be reliable for all kinds of observed zones with various culture covers.

The cover discrimination is, in our opinion, the most critical step. For that reason, our work concentrated on the determination of relevant discriminant parameters. Our study, on that matter, consisted in :

- a critical bibliographic search of quoted parameters,
- a discriminant analysis of the selected ones with sampled observations on radar images in a mono or multi temporal mode,
- a validation of the discriminant analysis.

4.1– Discriminant parameters

Our choice of image discriminators was mainly based on [Laur-89] and [Beupere-92].

The ERS-1 sensor does not allow for incidence, frequency or polarisation variations. Consequently, all of the parameters that can be used are related to the tone and texture characterisation, along with temporal variation.

Tone parameter :

This parameter is computed as the local mean of intensity computed on the parcel.

Texture parameters :

Many parameters contain textural information in one way or another ; they are, without being exhaustive :

- the coefficient of variation,
- the coefficient of skewness,
- the coefficient of kurtosis,
- the auto correlation function,
- its Fourier Transform (Power spectrum density),
- the co-occurrence matrix coefficients.

We limited our choice to the first four of this list.

The auto-correlation function is calculated in four directions (Vertical, Horizontal, + 45°, -45°),, and for distances between pixels from one to 6. This makes 24 additional parameters for this last function only.

4.2– Methodological description

In order to realise the discriminant analysis, we need to compute the various selected parameters on sampled areas of known culture cover in the images.

On the selected zones of observation, we obtained results of image interpretation for the year 1992 made within the MARS Action IV Project using Spot and Landsat images, and validated by in situ surveys. The result of the interpretation is provided on classified Spot images.

We proceeded the following way :

a– First, we had to superimpose Spot classified segmentation data over ERS-1 images. The invert approach (SAR data over Spot) was unacceptable as it imposed a resampling of SAR data and consequently a numerical diffusion of the initial information. The test zones were chosen in order to avoid the relief problem in the superimposition process.

b– Then, the validated classified Spot images, once registered on Radar images, allowed us to sample various rectangular zones with known cover, and this, for each of the cultures of interest.

One sample of one class of culture cover is made of several observations on a single site. Around twenty observations at least, for each culture of interest, on each surveyed zone, are necessary to obtain significant results, which means that about one hundred of rectangles have been selected on each of the four zones.

c– Next, for each single observation, the various preselected parameters are computed. This gives us tables of parameter values for each observation of the class samples which are entered into a statistical analysis software that helped us realise the discriminant and classifying analysis on our selected observations.

4.3– Discriminant analysis procedure and results

The first step of the discriminant analysis, is to reduce the set of the discriminant parameters involved in the analysis.

To achieve this, we applied statistical tests on each of the discriminant parameters using Fisher's ratio within an analysis of variance (one way anova). The hypothesis tested is the equality of the mean of each class observation related to the specific parameter.

A factorial discriminant analysis restricted to the selected parameters is then performed on the sampled observations.

The case study was realised on the four sites.

The Bourges site was first given a marked preference, because its parcels were larger, which helped the rectangular observation samplings, its cover less complex, and the radiometric quality of the images seemed better.

We first started with mono temporal data, with six parameters, then moved on to multi temporal data with fewer parameters. The results were encouraging, but their extrapolation on other sites did not work as well. So, we tried to improve the discrimination, adding some more parameters in the analysis. Excellent results were obtained with multi temporal data.

The problematic cases of separation of cultures that occur when working with optical data was also studied. Improvement of discrimination using SAR data is clearly shown in this particular case.

4.3.1– First tests with simple parameters

a– Bourges Mono temporal

The discrimination analysis was done on five covers : Cereals, Colza, Corn, Sunflower and Woods. Six discriminant parameters with equal weight were used : the mean, the mean deviation, the standard deviation, the coefficient of variation, the coefficient of skewness and the coefficient of kurtosis.

On the five dates the global results vary from 47% (10/92) to 74% (07/92) of successful parcels reaffectation.

The best discrimination is obtained in July. The group visualisation diagram and the confusion matrix are shown on figure 5. One can note that sunflowers are discriminated 100% (this is supposedly due to the flower presence at this time) but that corn is confused for 25% with woods.

b- Bourges multi temporal

The multi temporal discriminant analysis is somewhat different than the mono temporal one : we decided to keep only the most discriminant parameters within the previous set which are by far the mean and the coefficient of variation. Instead of working with the bare values of the parameters at several dates, we chose to work with their variations between two consecutive dates, and with their averaged values on the different dates.

The multi temporal analysis was conducted on three, four and five consecutive dates.

The global results are : 92% of successful reaffection with 3 dates, 93% with 4 dates and 96% with 5 dates.

On that particular site, the multi temporal discrimination shows much better results than the mono temporal one. Three dates, well adapted to the growing cycles of the cultures, are sufficient to obtain good results. More dates do not significantly improve the discrimination. In some cases, late dates may even alter the result.

The group visualisation diagram and the confusion matrix are shown on figure 6 for the three date analysis.

c- Albacete

Only one date (22 June 1992) is usable.

The analysis with six parameters gives 63% of parcel recognition.

d- Arles

Both mono and multi temporal analysis were achieved on the Arles images using the same processes as with Bourges, with the four dates available during year 1992. The mono temporal results, this time, were not as good (40% of successful reaffection at the maximum).

With multi temporal data (four dates) we obtained 60% of good classification.

These poor results may be explained by the fact that we used winter dates to proceed to the analysis. Some covers are satisfactorily separated, such as rice (70%) or water zones (100%). Woods, moors, vineyards and orchards are hardly distinguishable. Another point may be that the radiometry of the images used seemed of poor quality.

e- Great Driffield

The same processes were applied to the Great Driffield images with data from April to September.

The mono temporal analysis gave 63% of successful reaffection at the maximum (31/05/92).

The multi temporal analysis, including four dates, brought 77% of successful reaffection.

Here again, we can invoke contrast problems on some of the images used, to explain the relative poorness of the results.

4.3.2-Improvements with more parameters

We chose the Great Driffield site first, to test the analysis with additional parameters. This site contains hard-to-discriminate covers, and a complete serie of dates was available on it.

We started with mono temporal analysis and made use of the whole set of parameters, that is to say that we added the values of the auto correlation function computed on 1 to 6 pixels in four directions. This gave 30 parameters as input for the analysis.

The results reached a substantial improvement (88% at maximum). However, it may be noticed that we used more parameters than we had observations in the single groups. Their number is, in every case, too important for an operational application.

So, this set of parameters was reduced to twelve by a preselection test for the multi temporal analysis : we only kept the mean, the variation coefficient, and some coefficients of the auto correlation function in a favoured direction.

Using the three first dates (April to July) we reached 100% of success in reaffection. The group diagram and the confusion matrix are shown hereafter (figure 7). It may be noticed, on the group diagram, that most of the classes are well separated, except for winter cereals and meadows which are still close together.

After such a success, we applied the same set of parameters on the Bourges and Arles sites in multi temporal analysis :

On the Bourges site we again reached 100% of reassignment.

On the Arles site, with winter dates, we identified 86% of observations within their classes, with 100% for water, woods, moors and vineyards. Other covers (corn, sunflowers, rice, and orchard) would certainly have been more distinguishable, should we have used spring and summer data.

4.3.3- Specific discrimination of cultures

Some problems of distinction between specific covers exist when using optic data. We tried to test the radar images to see whether the use of one ERS-1 image could help in these specific cases.

4.3.3.1– Corn vs Sunflower discrimination

This problem was investigated on the Bourges and Albacete sites. Five parameters were retained for the analysis.

On the Bourges image acquired on July 24th, Corn is identified 100% while Sunflower is identified for 95%. On the 19th of June image, the proportions are 94% for Corn and 90% for Sunflower.

On this site, it appears that Corn and Sunflower may be discriminated earlier than when using optic images with which one has to wait until September to be able to separate these two covers with the same accuracy.

On the Albacete image shot on June 20th, using the same parameters, Corn is identified with 70% success only, while Sunflower is at 68%. The parameters that were efficient on the Bourges site do not seem to be as well adapted to the Albacete image.

4.3.3.2– Vineyards vs Orchards discrimination

On the Arles site, we defined a new class, grouping moors and woods. This new class was compared to the vineyard class and the orchard class at different dates. The analysis was made using 15 parameters.

Best results were obtained in winter (January 2nd) and a 95% global success was encountered. Vineyards, notably, were 100% successfully recognised.

4.3.3.3– Meadows vs Cereals discrimination

The analysis was conducted on the Great Driffield site with the May 3rd image. 10 parameters were used in the analysis to obtain a satisfactory separability.

The global score was 85%, with meadows and winter cereals being confused only 5%. However, Spring cereals are confused with meadows and winter cereals for 15%.

4.4– Conclusion on the radar data analysis

This case study, based on factorial discriminant analysis using texture and tone parameters on the SAR ERS-1 images, shows that crop discrimination is quite feasible with these images and that radar data contain the information needed.

Use of multi temporal data, with at least three dates, seems highly recommended to obtain reliable separation. Nevertheless, we must remember that the choice of discriminant parameters has been modulated from one image to another, and that we avoid small-sized parcels to compute them.

Moreover, the validation step of the analysis was made with the same samples as those used to make up the statistical model.

So, in order to validate this "radar only" approach, more work needs to be done : a fine selection of the discriminant parameters, on a whole set of different covers at various sites and dates is necessary. Other texture–displaying techniques can also be thought of : directional wavelet analysis, coupled with statistical parameters, may be a promising way.

5– Conclusion and future prospects

This work showed that the use of ERS-1 PRI type images may be considered in future operational systems for crop monitoring.

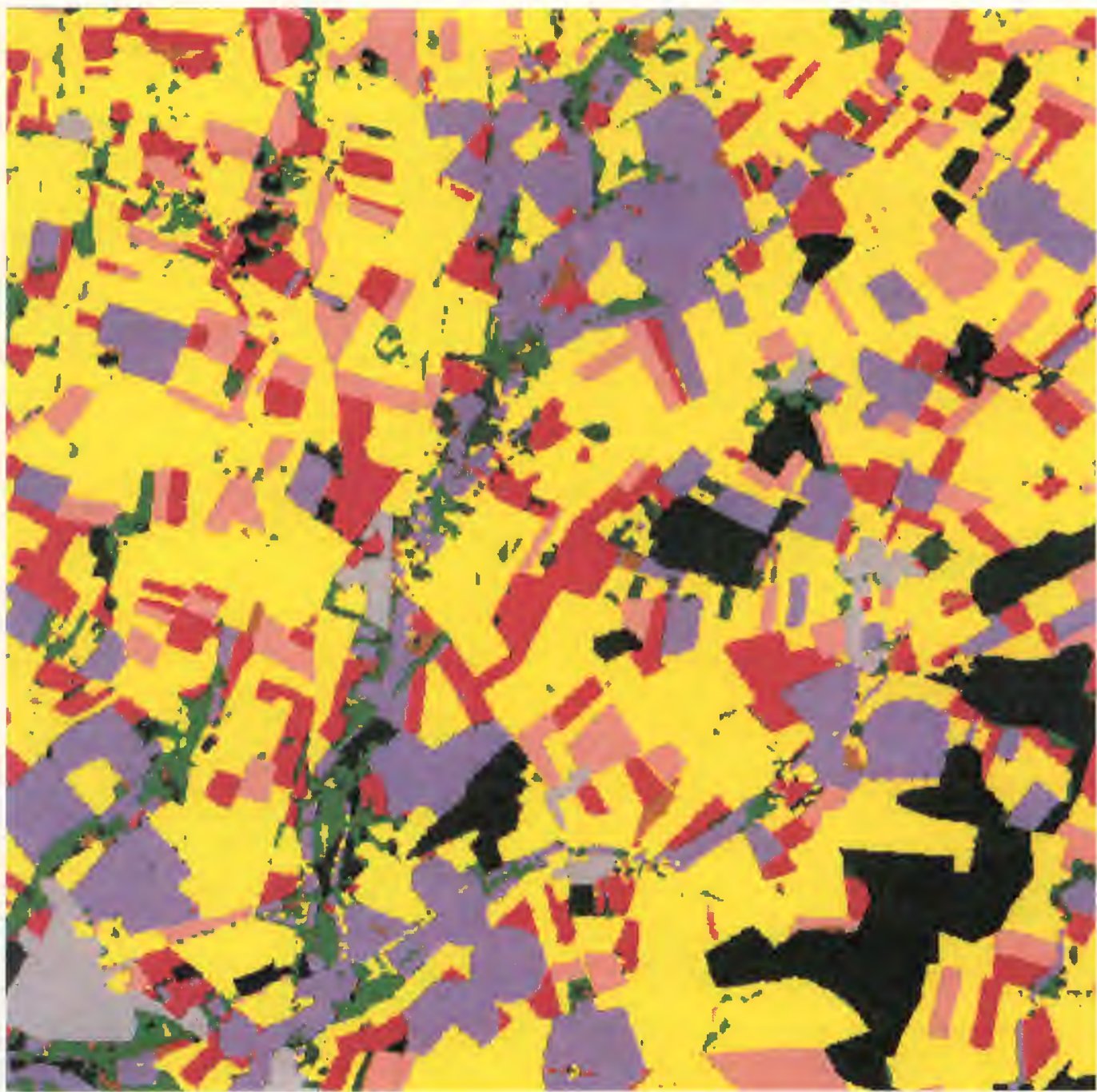
However, a crude adaptation of the already existing chain of treatment which is used with optical imagery will not be efficient enough.

The first approach of our work tried to find the necessary modifications to bring to such a chain : even if some good results were obtained with multi temporal data, the segmentation process based on gradient technique after a filtering step may be the weak link of the chain. The classification process, by parcel and using multi temporal data, should take into account some specific discriminant parameters computed without preliminary filtering and their evolution through time.

The second part of our study showed that radar data, when not filtered, contained richer information than we first thought. Tone and texture parameters can be input of statistical models toward accurate cover recognition. Best results are obtained with multi temporal data. However, there is a strong variability, from one site to another, of the best parameter choice, and we were not able to find some temporal signature of specific covers that could be validated through various sites.

So, this study should be pursued in two directions :

- First, we should try to define and validate general models using specific parameters that would apply with the same cultures on different sites on a multi temporal basis. To achieve this, we need data on more sites and through several month sequences.
- Second, new techniques of segmentation must be investigated. One of them may be the use of wavelet analysis that would provide a multichannel textural input to gradient or region growing type algorithms.



Legend :	yellow	cereals	pale pink	colza
	pink	sunflower	blue grey	corn
	middle green	fodder, STH	dark green	woods
	brown	moors, fallow fields	red	soy
	dark blue	water	grey	urban zones

Figure 1 : BOURGES Site – Reference classification from SPOT Data

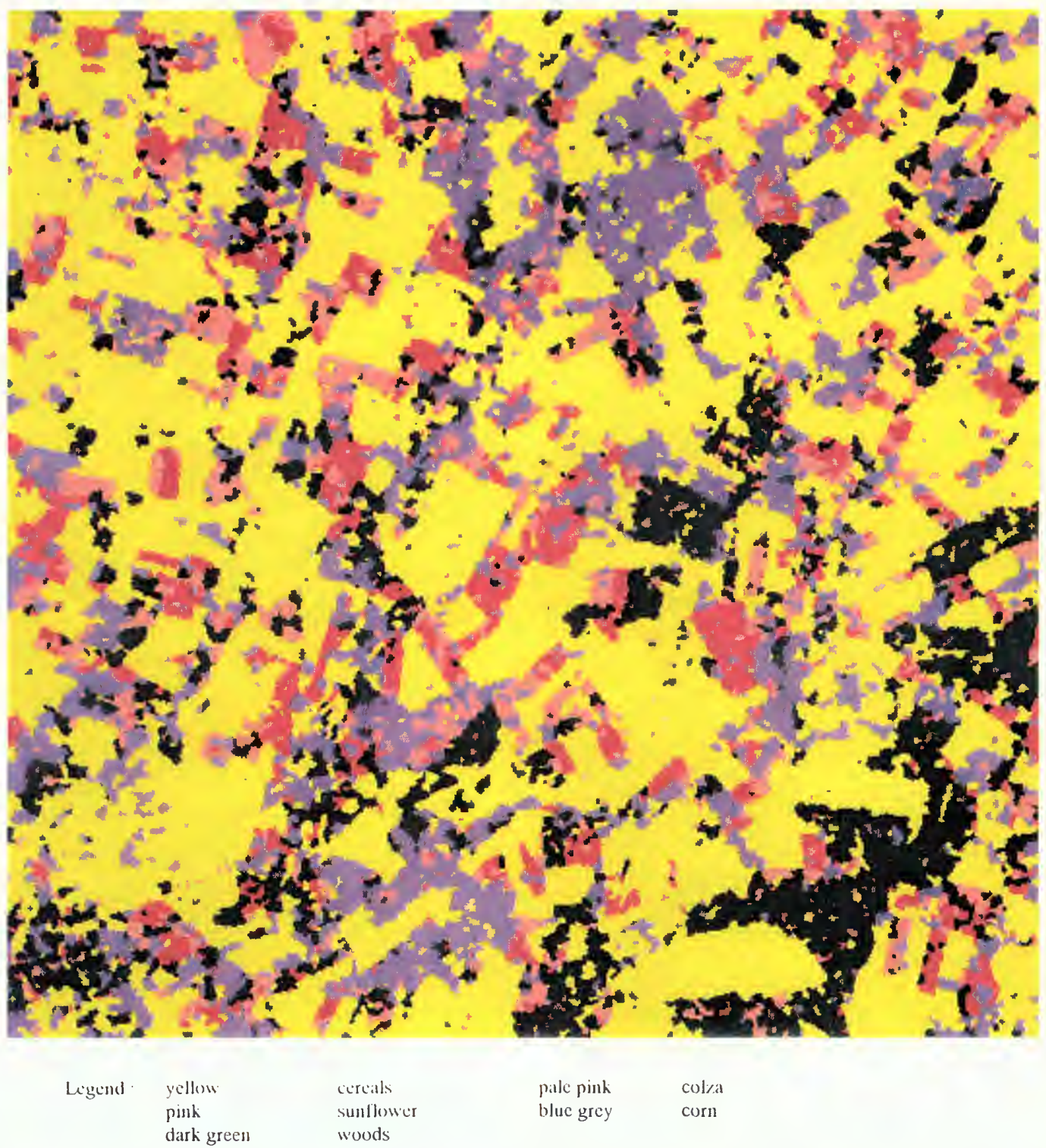
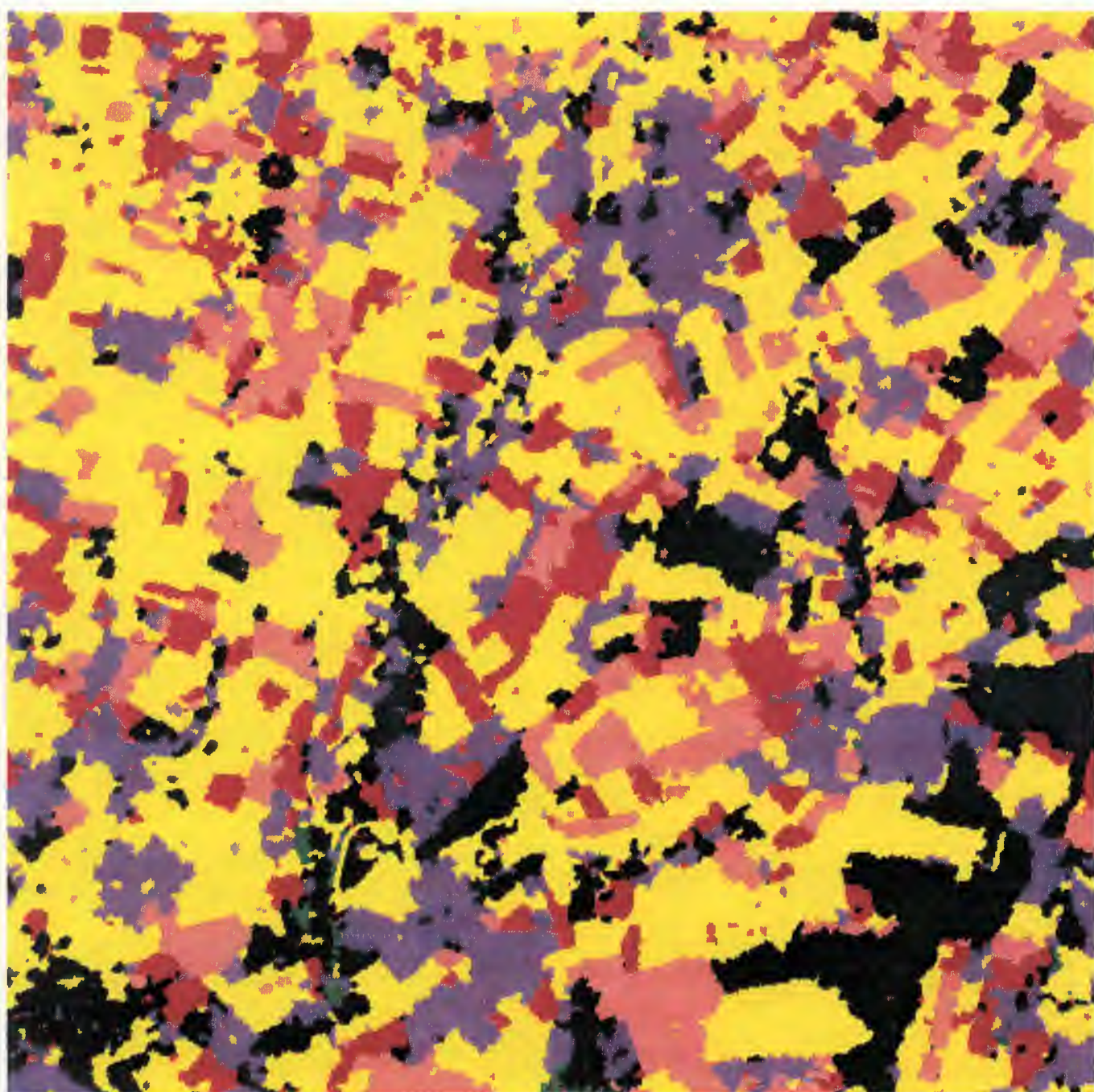
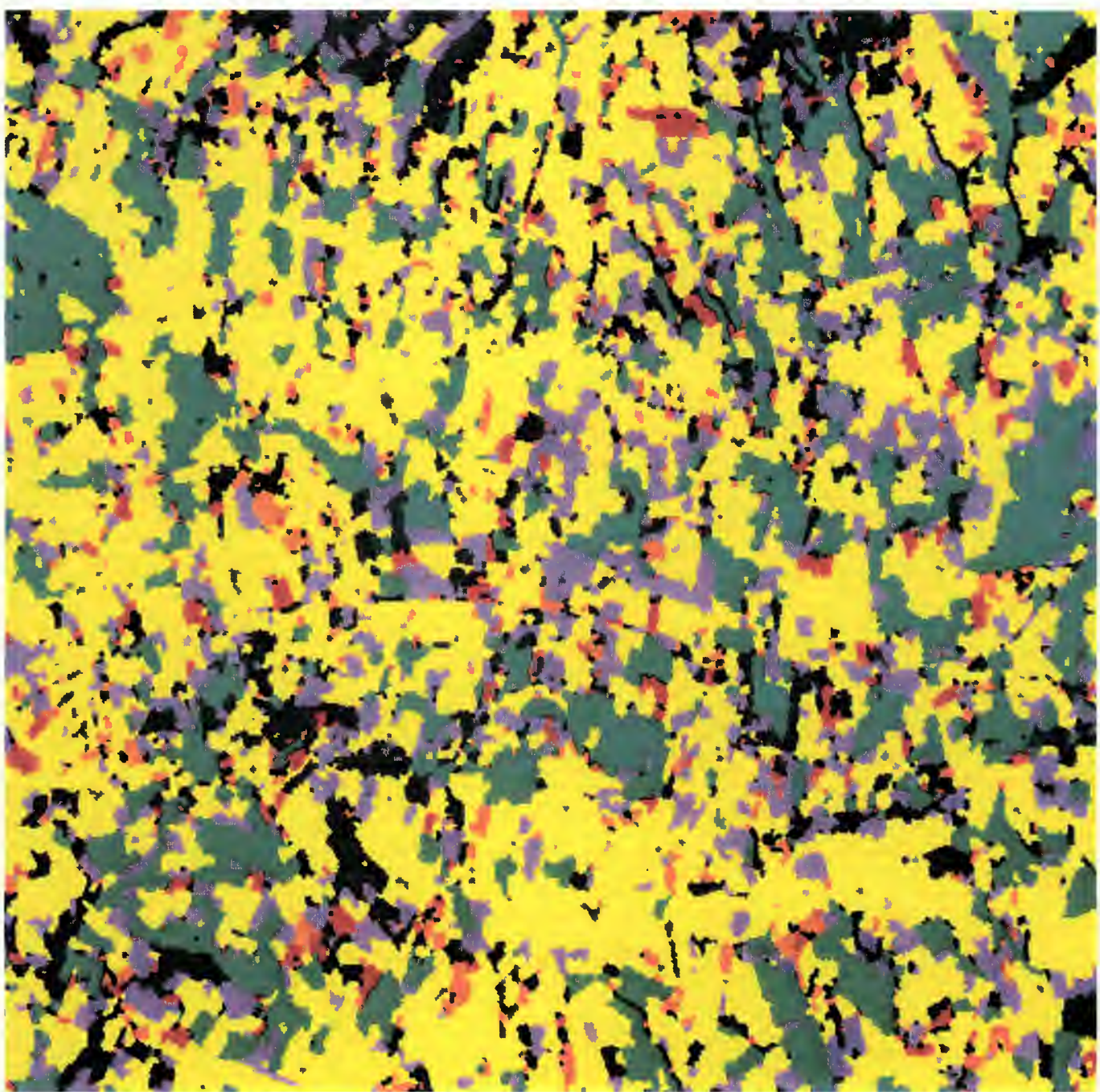


Figure 2 : BOURGES Site – By parcel classification results ; multitemporal mode (3 dates integration in segmentation and classification processes)



**Figure 3 : BOURGES Site – By parcel classification results ; multitemporal mode
(7 dates integration in segmentation and classification processes)**



Legend : yellow winter cereals orange spring cereals
 red colza blue grey summer cultures
 medium green meadows dark green woods

Figure 4 : GREAT DRIFFIELD Site – By parcel classification results ; multitemporal mode (3 dates integration in segmentation and classification processes)

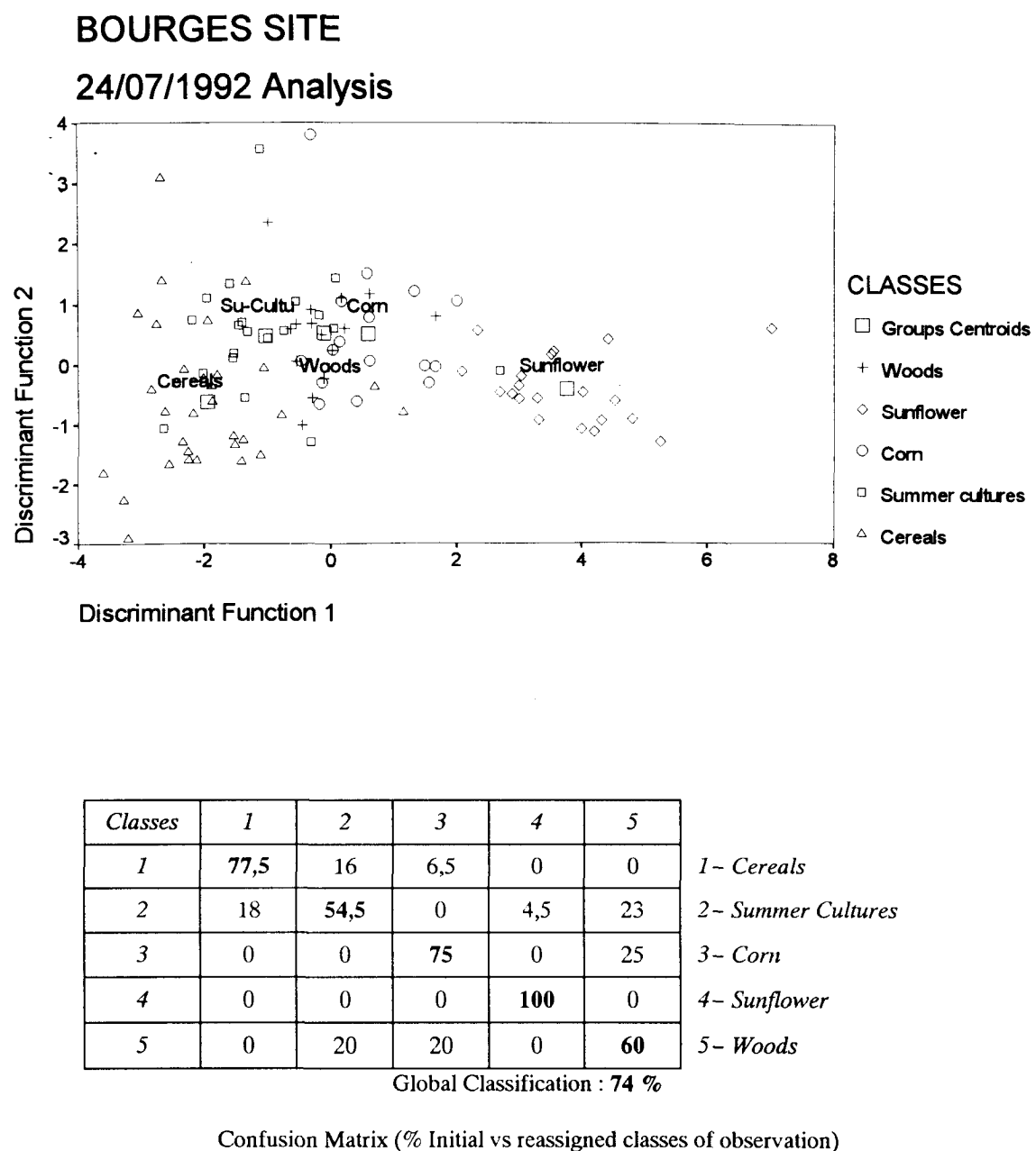
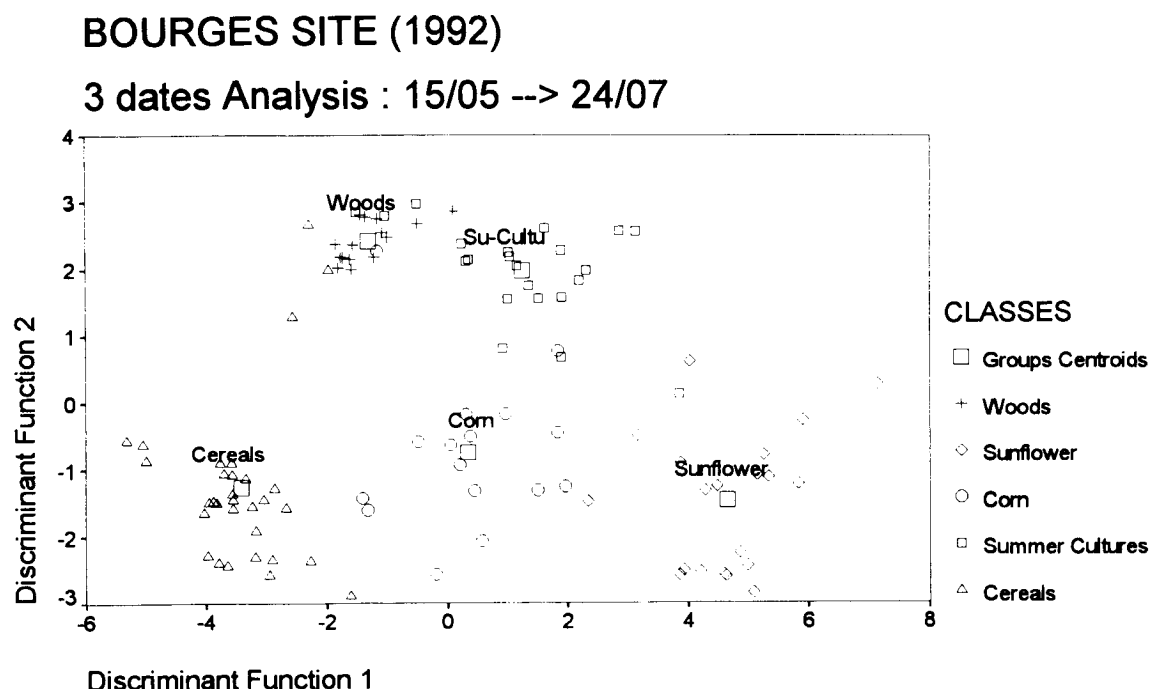


Figure 5 : Statistical analysis on the BOURGES Site – 1 date (24.07.92) – 6 parameters



Classes	1	2	3	4	5	
1	90,5	0	0	0	9,5	1 - Cereals
2	0	91	0	4,5	4,5	2 - Summer Culture
3	0	12,5	81,5	0	6	3 - Corn
4	0	0	0	100	0	4 - Sunflower
5	0	0	0	0	100	5 - Woods

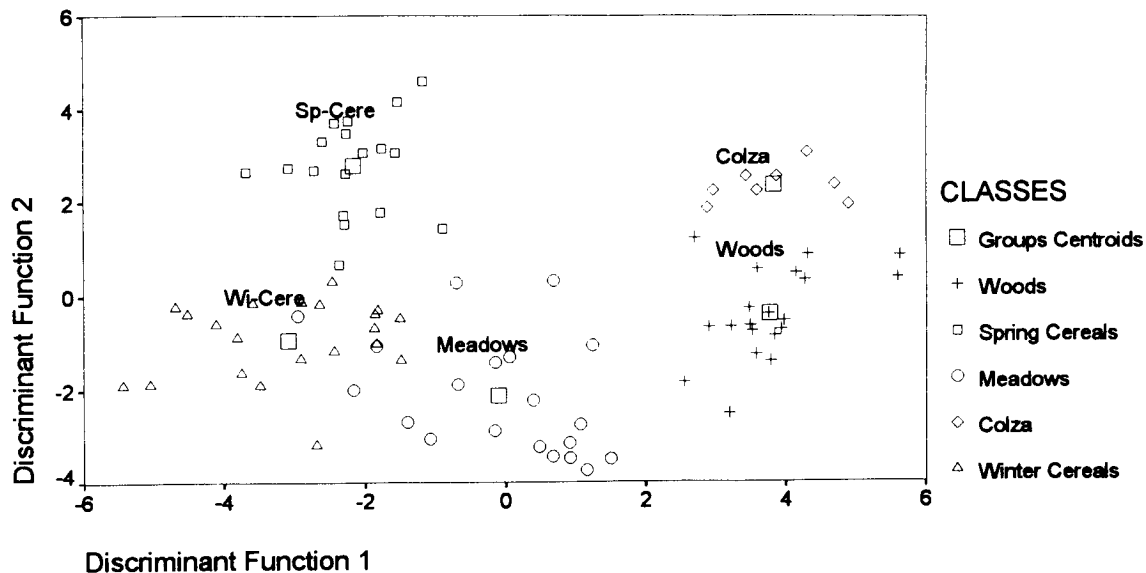
Global Classification : **92 %**

Confusion Matrix (% Initial vs reassigned classes of observation)

Figure 6 : Statistical analysis on the BOURGES Site – 3 dates (15.05, 19.06 et 24.07.92) – 2 parameters

GREAT-DRIFFIELD SITE (1992)

3 dates analysis : 31/05 --> 13/09



Classes	1	2	3	4	5	6	7	8	9
1	90	0	0	5	0	0	5	0	0
2	0	100	0	0	0	0	0	0	0
3	0	0	71,5	7	0	7	14,5	0	0
4	11	0	11	78	0	0	0	0	0
5	0	0	0	0	100	0	0	0	0
6	0	0	0	0	0	100	0	0	0
7	15	0	0	10	0	0	75	0	0
8	0	0	6	12	0	0	6	76	0
9	0	0	0	0	0	0	0	0	100

1 - W Cereals
2 - Water
3 - Corn
4 - Sunflower
5 - Woods
6 - Moors
7 - Rice
8 - Orchards
9 - Vineyards

Global Classification : 86 %

Confusion Matrix (% Initial vs reassigned classes of observation)
ARLES Site – 4 date analysis (02.01 à 20.04.92) – 12 parameters

Figure 7 : Results of statistical analysis with multitemporal data – 12 parameters
GREAT DRIFFIED and ARLES Sites

BIBLIOGRAPHY

- [BEAUPERE-92] A. BEAUPERE
 "Classification d'images de radar par mesures de texture"
Thèse de Doctorat, Université Paris VI, Juin 1992.
- [DURAND-87] J.M. DURAND, B.J. GIMONET &
 J.R. PERBOS
 "SAR Data Filtering for Classification",
IEEE Transactions on Geo. & Remote Sensing, Sept.
1987.
- [FROST-82] V.S. FROST, J.A. STILES, K.S.
 SHANMUGAN & J.C. HOLTZMAN
 "A Model for Radar Images and its Application to
 Adaptive Digital Filtering of Multiplicative Noise",
IEEE Trans on Pattern Analysis and Machine Int., Mar.
1982.
- [LAUR-89] H. LAUR
 "Analyse d'images radar en télédétection :
 discriminateurs radiométriques et texturaux",
Thèse de Doctorat, Université P. Sabatier, Mar. 1989.
- [LEE-80] J.S. LEE
 "Speckle Analysis and Smoothing of Synthetic Aperture
 Radar Images",
Computer Graphics and Image Processing, Dec. 1980.
- [LOPES-92] A. LOPES, E. NEZRY, R. TOUZI,
 H. LAUR
 "Structure Detection and Statistical Adaptive Filtering in
 SAR Images",
 Accepté pour publication dans *International Journal of
 Remote Sensing, 1992.*
- [SAFA-89] F. SAFA
 "Le speckle en imagerie cohérente : propriétés
 statistiques, relation entre l'image cohérente et l'image
 incohérente ; essai de filtrage morphologique",
Thèse de Doctorat, Université P. Sabatier, Mai 1989.



DEVELOPMENT OF NEURAL NETWORK TECHNIQUES FOR THE CLASSIFICATION OF MULTI-TEMPORAL ERS-1 SAR IMAGERY WITH RESPECT TO AGRICULTURAL APPLICATIONS

Martin Davison

VEGA Space Systems Engineering Limited
Arden Grove
Harpden
Herts, AL5 4SJ
United Kingdom

e-mail : mdavison@vegauk.co.uk

Tel: +44 (0)582 461678
Fax: +44 (0)582 461773

ABSTRACT

This paper describes a range of neural computing activities which have been performed as part of an investigation into the use of a multi-temporal sequence of ERS-1 SAR images for agricultural applications. The neural classification techniques applied are discussed and preliminary results presented.

1. INTRODUCTION

The aim of this work was both to examine the potential of ERS-1 SAR data to supplement existing data sources for agricultural inventory and monitoring, and evaluate the potential of neural network techniques for land-use classification applications. This work therefore supports the objectives of programmes such as the CEC's "Monitoring Agriculture with Remote Sensing" (MARS) project, which estimates crop cover and yield from optical and infra-red data acquired by Landsat Thematic Mapper, SPOT High Resolution Visible Imager and NOAA AVHRR instruments. Since these instruments require cloudless skies for efficient monitoring, it is hypothesised that ERS-1 SAR images may be able to bridge any gaps in these data sets.

Neural computing techniques are being increasingly applied to a wide variety of classification applications, and are particularly effective at solving problems whose solutions are difficult, if not impossible to define. This opens up whole new application areas which could not be described by conventional means. Neural computers are able to cope well with incomplete, contradictory, or "noisy" data as well as previously unspecified or unencountered situations, and are very flexible in the way they are able to adapt their behaviour to new and changing environments. Neural computing therefore offers considerable potential to the classification of multi-temporal SAR imagery, where the nature of the source data is "noisy" and the exact relationship between the seasonal variation of image pixels and specific land-use classes is not well understood.

The objectives of this work were threefold :

- To select appropriate imagery from data collected throughout the growing season that would maximise crop discrimination.
- To develop simple tools to register and visualise the sequence of images to enable further investigations to be performed.
- To develop neural network techniques to derive a classification directly from the multi-temporal input data.

These investigations have been carried out using data acquired over the CEC/JRC MARS project's test site in Great Driffield, UK. Thus, ground truth data for the area has been used in order to train and test the accuracy of the classification technique.

2. SAR DATA SELECTION

Careful data selection is paramount in order to maximise the discrimination between different crop types during classification. The MARS ground truth data was collected in May 1992, and so is applicable for the duration of the 1992 crop growing season. With this in mind a search of all ERS-1 SAR imagery collected over the Great Driffield test site between April and September 1992 was performed, from which three specific frames were selected. Two are taken from ascending passes and the other from a descending pass, thus offering a variation in frame orientation and test site incidence angle, which may provide additional information to the neural network (ref. Table 2.1). The selected frames cover most of the fifteen Agriculture Project sample test locations. Using site information provided by JRC, each of the test sites visible in all three frames were located and assessed.

The selected imagery are of Precision (PRI) product type, offering multi-look (noise reduced) ground range

pixels (12.5m by 12.5 m). Precision products are not terrain corrected and the landscape across much of the test area consists of gently rolling hills, consequently differential relief distortion was evident in places due to the combination of ascending and descending passes.

Type	Site	Date	Orbit
Precision	Driffield	26-04-92	Ascending
Precision	Driffield	01-07-92	Descending
Precision	Driffield	13-09-92	Ascending

Table 2.1 : Selected SAR Products

It was anticipated that the choice of imagery from April, July and September would serve to maximise crop discrimination by recording the changing ground backscatter characteristics between early crop growth, maturity and harvesting.

3. REGISTRATION AND VISUALISATION

Segment Number	Ground Cover
1	Winter Wheat
2	Sugar Beet
3	Temporary Pasture
4	Winter Wheat
5	Winter Wheat
6	Sugar Beet
7	Sugar Beet
8	Winter Wheat
9	Spring Barley
10	Spring Wheat
11	Potatoes
12	Spring Wheat
13	Winter Wheat
14	Winter Barley
15	Sugar Beet
16	Winter Wheat
17	Winter Wheat
18	Urban - House
19	Broad Leafed Forest
20	Temporary Pasture
21	Winter Wheat
22	Winter Wheat

Table 3.1 : Ground Truth Data for Sample Site 4

A series of tools were developed using "C" and the IDL visualisation package. These enabled the following operations to be performed :

- Extraction of 1024 x 1024 image segments from a full ERS-1 scene.
- Image segment registration, mapping the second and third images onto the first.

- Colour composite display of three multi-temporal image segments.

Figure 3 shows the composite image for Driffield test site 4, while the corresponding ground truth data is shown on the overlaid field boundaries. The ground cover found in each of the numbered segments on the overlay are specified in Table 3.1.

4. NEURAL NETWORK ARCHITECTURE

In order to test this technique we constructed a standard fully connected, multi-layer, feed-forward neural net, applying the back-propagation training algorithm. This network was implemented in software ("C") on a Sun SparcStation. The design of the neural network required a lot of preliminary study to decide upon the number of input image pixels to be applied, the number of hidden layers, the number of nodes in each hidden layer and the size and form of the training parameters. This was achieved through a process of trial and error.

4.1 INPUT LAYER

The first priority was to assess the prototype's ability to absorb and classify a "noisy" single SAR scene, for which the area surrounding sample site 11 was extracted for evaluation purposes. The image was displayed using a colour table that highlighted four broad divisions in pixel intensity, and 200 samples extracted from each region applying a 3 by 3 window as the basis for neural input. The neural net was trained and then passed over the complete image. The results were patchy, with poor class distinction, and it was concluded that a 3 by 3 input array was insufficient to overcome the speckle inherent in all SAR imagery. The window was then increased to a 5 by 5 array, which gave a much smoother classification (as given in figure 1), and so a 5 by 5 input array was applied for all future classification operations.

To test the ability of the neural net to absorb information from the three multi-temporal SAR scenes, a preliminary analysis was performed. Six dominant classes were evident in the colour coded multi-temporal display of the three images over Driffield test site 4. Test data was collected over each dominant class (green, purple, cyan, yellow, white, blue) by sampling each region and extracting a column of three 5 by 5 pixels, giving a total of 75 input nodes. The results are given in figure 2, and were generally found to be good, although there is some confusion between certain closely related classes, which can be attributed to the arbitrary divisions applied in collecting the training data. Of particular note is the region marked "a" in figure 2, which is barely visible in the original image, but is revealed as a single distinctive field by the neural net classifier.

4.2 HIDDEN LAYERS

A multi-layer neural network may have one or many internal, or "hidden" layers, passing connections from the input to output layers. All preliminary work was performed using two hidden layers, and this was justified by some experimentation. Three hybrids of the same network were produced, one with a single layer, the second with two and a third with three hidden layers. As a neural network learns and holds information through the interconnections between nodes, the number of connections was maintained the same in each model. Each network was trained on the same data, and comparison of the resulting training profiles confirmed a two layer network as the optimum configuration.

It was found that the minimum necessary number of nodes in each hidden layer depended on the complexity of each classification, such as the variability of the inputs and the number of classes to be extracted. However, if a network was oversized, then the number of passes the network required to train would in fact be less than that for optimum sizing, but with a greater overhead incurred during the classification pass of the imagery because of the effectively redundant connections. Thus, for the purposes of evaluation, an oversized network was configured, with two hidden layers of 16 nodes on each layer, ensuring a sufficient number of connections for all classification purposes.

4.3 OUTPUT LAYER

Of all the layers in a neural network, this is the easiest to configure since the number of output nodes simply represent the number of classes to be recognised.

4.4 TRAINING PARAMETERS

During training, the corrections to the connections between nodes are multiplied by a scale factor or step size, which requires tuning to obtain optimum results. If the step size is too big, then the network will not converge, and if too small, the network will not converge in a reasonable time. The step size is application dependent, and must be determined by a process of trial and error. Also, in certain instances, application of a single step size alone can result in oscillations which prevent improvements in the training cycle. This can be prevented by applying a secondary momentum factor which controls the rate of change in the size of the corrections applied, acting as a damping influence. Experiment showed that a combination of different step size and momentum factors gave the best results.

For all classification networks, little improvement in training performance was realised after 2000 iterations,

on average achieving a 97% recognition rate of the training data.

5. NEURAL NET LAND-USE CLASSIFICATION

All twelve of the MARS Project 700 m by 700 m Driffield sample sites covered by the multi-temporal imagery were registered and all useful ground truth extracted, to be used as the basis for crop classification.

5.1 TWO CROP-TYPE CLASSIFICATION

Winter wheat and winter barley are by far the most predominant crop types in the area, and so provide the greatest volume of ground data with which to train the classifier network. The range of crops evident across all usable test sites was quite varied, with fifteen different crop types available, but sometimes only a single field represented a complete crop type, which was not sufficient for training purposes. Also, during training data collection, the variability of SAR intensity due to terrain was quite apparent, and the wheat and barley training set was collected from a range of fields with differing slope characteristics.

Thus, as a first stage to crop type classification, the network was trained to recognise winter wheat and winter barley, using test data from all sites with the exception of site 4. The trained network was then passed across the imagery for Driffield test site 4. This provides an independent test, since the network has to recognise patterns to which it has not been exposed.

The resulting classification indicated that areas which are not either winter wheat or barley had been clearly identified, and wheat fields 4, 5, 10, 13, 16, 17 and 21 had been correctly classified. However, field 8 was classed as winter wheat by the ground survey, and appeared (largely) as winter barley in the neural classification. Reference to the raw spectral characteristics in the composite image of figure 3 shows that those of field 8 are very different to those of the surrounding wheat fields, and so may be attributed to a local anomaly. Overall, the areal classification accuracy was 84%.

5.2 FIVE CROP-TYPE CLASSIFICATION

The final classification applied training data extracted from winter wheat, winter barley, permanent pasture, sugar beet and potato fields. This demonstrates the neural network's ability to absorb and classify a range of different crop types. The results are given in figure 4, with an extract of the local Ordnance Survey 1:25,000 map superimposed.

Once again, reference to table 3.1 indicates that the network has successfully identified the wheat and sugar

beet fields (the most prevalent), but has mis-classified fields 8, 11, 20 and cannot resolve field 9 into a single class. The mis-classification of field 11 (classed as sugar beet rather than potatoes) can be attributed to the similarity between the characteristics of the two broad leaved crops in the selected imagery. Other factors contributing to mis-classification include variability of terrain in the training data, local drainage conditions, and local anomalies, where specific fields are just atypical of the area as a whole. However, the neural classifier still maintains a success rate of over 70% of the ground area correctly classified.

The classification of figure 4 shows a remarkable correspondence to the superimposed field boundaries outside of the test site survey. We have no information on the contents of these fields, but the match to field boundaries is encouraging, particularly as the network has not been trained to recognise discontinuities between different crop types.

6. CONCLUSIONS

In applying SAR imagery from the MARS Great Driffield region, we are attempting to classify areas in a "real" location, combining both flat and undulating terrain. Accurate SAR-based land classifications have been successfully employed before, but have been limited to local regions extracted from extensive sea-level plains, such as small areas of Flevoland or East Anglia. The SAR backscatter coefficient varies with incidence angle across the swath, slope gradient and slope orientation to the satellite, in addition to surface roughness and dielectric constant. Therefore to accurately model variation in image intensity through the growing season, we need to characterise such variation under all conditions of image geometry and terrain with known ground truth. Essentially, we currently have too many variables and too little ground truth to accurately model specific crop growth through the growing season. However, preliminary crop classification results do indicate the potential of applying SAR for land-use classification.

The analysis of the results also demonstrates the power of neural computing techniques for the extraction of land classification information from SAR imagery. A neural net acts as a "black box", whereby it is able to absorb information through exposure to test data and act on relationships between input and output that are not necessarily well defined. In our example, with 5 by 5 pixel inputs from each of our three multi-temporal images, the network is probably recognising both image texture and intensity to perform a classification. More conventional image segmentation techniques rely on forming similar regions prior to classification, thus effectively throwing away some of the information that could otherwise be used for crop classification.

Early results indicate the sensitivity of SAR to image geometry and terrain, factors which need to be incorporated into the classification process if the results are to be optimised. With a neural network this would appear to be a relatively straight-forward operation, whereby additional input nodes are incorporated to describe local incidence angle (derived from a terrain model and heading information). Given that the network is trained on a suitable range of ground truth, the network is able to absorb variation in SAR radiometry due to terrain, and extract classes solely on seasonal variation in surface roughness. Incorporation of such terrain information into conventional classification techniques is not so simple.

The preliminary results of this study have provided pointers to the complexity of using SAR imagery for SAR land-use classification, based on the limited ground truth provided by the MARS Great Driffield test site. Much work has yet to be done, but the potential for routine land-use classification derived from multi-temporal SAR imagery is apparent.

7. ACKNOWLEDGEMENTS

Many thanks to the CEC/JRC MARS Project, and Hans Kohl in particular, for the provision of ground truth data. The ERS-1 PRI SAR imagery applied in this study was purchased through the UK-PAF. Map overlay reproduced from the 1981 Ordnance Survey 1:25,000 Pathfinder map with the permission of the Controller of Her Majesty's Stationery Office. (c) Crown copyright.

8. REFERENCES

1. Dayhoff, J.E., 1990, Neural Network Architectures, Van Nostrand Reinhold.
2. Freeman, J.A., Skapura, D.M., 1992, Neural Networks, Addison-Wesley.
3. Hinton, G.E., 1989, Connectionist Learning Procedures, Artificial Intelligence, 40, 1-3, 185-234.
4. Hinton, G.E., 1992, How Neural Networks Learn from Experience, Scientific American, 267, 3 105-109.
5. McClelland, J.L., Rumelhart, D.E., 1988, Explorations in Parallel Distributed Processing, The MIT Press.
6. Rumelhart, D.E., McClelland, J.L., 1986, Parallel Distributed Processing, Volume 1 : Foundations, The MIT Press.

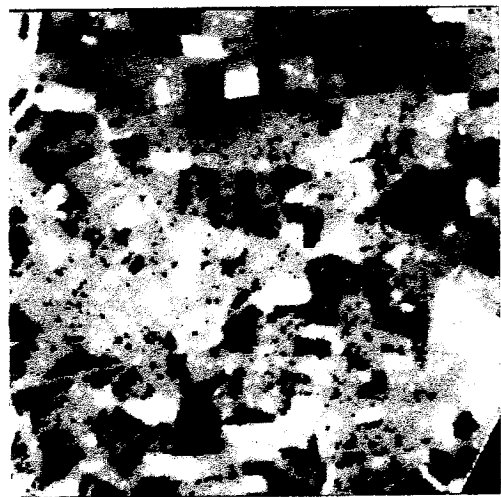


Figure 1 : 5 by 5 Pixel Single Image Classification

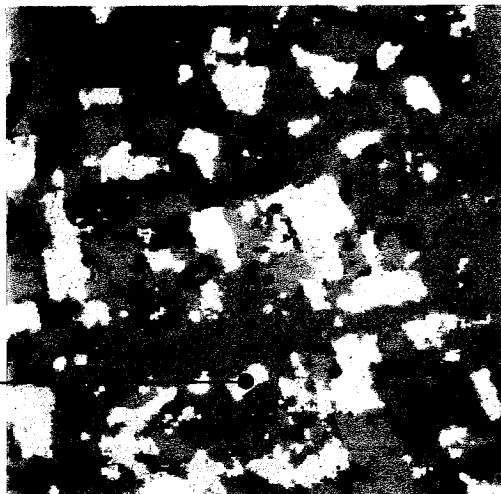


Figure 2 : Multi-Temporal 5x5x3 Classifier

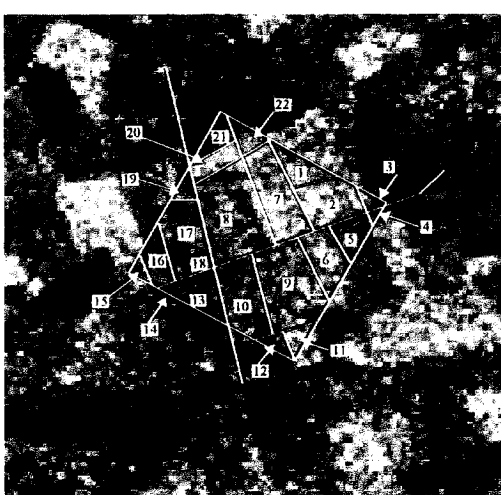


Figure 3 : SAR Multi-Temporal Composite

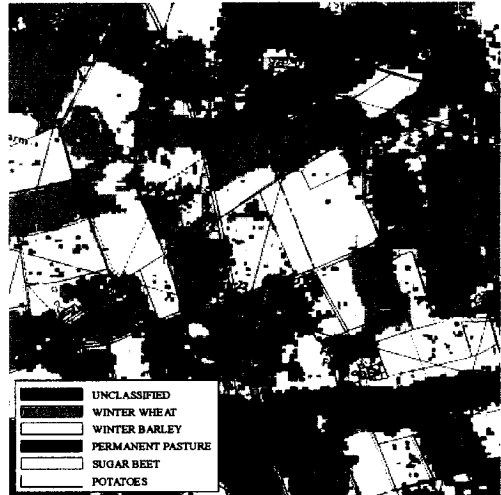
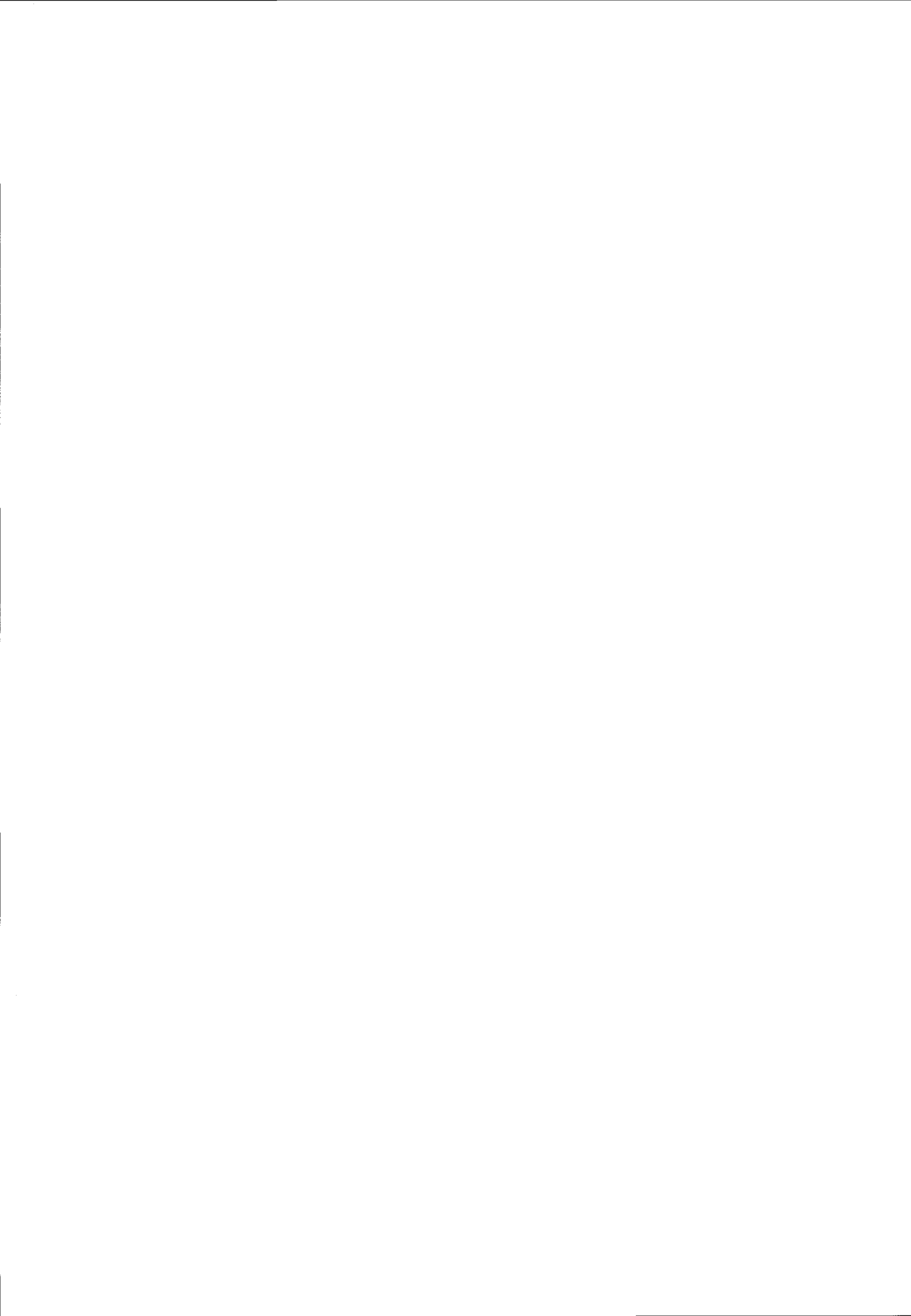


Figure 4 : Multi-Crop Classification



11. POSTER SESSION



LANDUSE CLASSIFICATION BASED ON SIGNATURE ANALYSIS AND TEXTURE ORIENTED NEURAL NETWORK APPROACH

Sebastian Carl¹, Andreas Gebhardt², Andreas Kannen², Roland Kraft¹

- 1** Technische Universität München-Weihenstephan, Abteilung Mathematik und Statistik,
Datenverarbeitungsstelle Weihenstephan; Hohenbachernstr. 2, D-85350 Freising, Germany
phone (+ 49) 8161 71-4040, fax (+ 49) 8161 71-4409
- 2** Deutsche Projekt Union GmbH Berlin-Brandenburg,
Technologie- und Gewerbepark, Haus 24; D-16225 Eberswalde, Germany
phone (+ 49) 3334 59-245/253, fax (+ 49) 3334 59-245

ABSTRACT

Analysis of ERS1-SAR.PRI data for agricultural crop monitoring is performed, including data calibration and data processing as well as derivation of backscatter values and signature analysis for different agricultural crops.

For landuse classification of mono- and multitemporal ERS1-SAR.PRI scenes a texture based Neural Network approach seems to be very promising. A processing pipeline of a Kohonen Feature Map and a Backpropagation Net was developed for this purpose.

First results of the classification are encouraging and demonstrate the possibility to discriminate several landuse units in multitemporal unfiltered ERS1 multilook data.

1 INTRODUCTION

Satellite data can be used for monitoring and control of areas that benefit from hectare payments financed by the European Community. In this context the task of processing and interpreting satellite data is to verify both area and crop type of a declared agricultural field.

Thus, regarding an operational use of ERS1-SAR data, classification of agricultural crops belongs to the most interesting applications. Especially for agricultural monitoring the all-weather capability of SAR-data is a major advantage.

Investigations of Pilot Project D12 concentrate on landuse classification in an area located in Brandenburg, East Germany, which is from social, economical and ecological point of view characterized by intensive agriculture. Specific objective of this study is the analysis of early detection capabilities of ERS1-SAR data for

agricultural monitoring. Thus, investigations focused on data from may and june.

2 DATA SET

The data used for signature analysis and classification are 16 bit ERS1 precision products (code: ERS1.SAR.PRI). Acquisition dates of the classified ERS1 scenes are 13.05.1992 and 17.06.1992. The test area is near Prenzlau in Brandenburg, Germany.

All ERS1-data were image to image rectified, which can be easily done by translation in x- and y-direction. For visualization purposes they were also referenced to a geocoded SPOT PAN scene using a 5th-order transformation.

Information about field boundaries in the test area have been updated using ground truth data as well as information derived from data merge of LANDSAT-TM and SPOT-PAN images. Ground truth mapping allows an overview about the main crops and land use units in the test area which are winter-wheat, winter-barley, rape, oat, summer barley, sugar-beet, maize, clover, lucerne and grassland areas.

Finally the following data set formed the basis for analysis:

- ERS1-SAR.PRI data sets from 13.05. and 17.06.1992
- SPOT-PAN from 23.05.1992
- LANDSAT-TM data from 28.05. and 29.06.1992
- Digitized Data Set containing FIELD BOUNDARIES and AGRICULTURAL CROPS of the investigation area.

3 SIGNATURE ANALYSIS

Signature analysis is based on derivation of mean intensities and mean backscatter values (σ_0) for digitized fields from ERS1-sub-scenes of the test area.

In order to avoid radiometric inconsistency between Far Range and Near Range of the images as well as inconsistencies between images processed by different PAF's, calibration of ERS1 data is required. Calibration of the ERS1 data set and derivation of backscatter values followed the method described by LAUR [1992] and was performed with software developed by ZALF (Centre for Agricultural Landscape and Land Use Research) in Eberswalde.

According to the objective of early stage detection, analysis concentrated on data from May and June which offer the best opportunities for agricultural applications.

Monotemporal analysis of backscatter values does not allow detailed distinction of agricultural crops. Anyhow, some tendencies can be seen. For example, winter-barley can be identified by very low mean backscatter (σ_0 range -14 to -16dB) in May. But values between -7 and -9dB can be found in fields of oat, summer-barley, winter-wheat, clover, rape and in some forested areas. Highest backscatter values (-4dB up to +9dB) in both ERS1-images can be interpreted as urban areas or (agro)-industrial sites. Exception in the image of May are three fields of sugar-beet which show positive backscatter values and where the signal has to be related to mostly bare soil.

In June three groups can be distinguished, represented by high σ_0 -values for rape and sugar beet, low ones for oat and summer barley and a third group in between, which includes all other crop units.

Research has shown that the backscatter signal is affected by surface moisture and surface roughness of the scattering object [e.g. WOODING et al. 1993]. As roughness of crops is highly dependent of their development stage, their backscattering differs in time. Thus multitemporal analysis of at least two acquisition dates improves crop differentiation.

A comparison of σ_0 for May and June shows that most crops build groups with characteristic multitemporal backscattering behaviour (Fig.1). A distinction between summer- and winter grain can be made and also between winter-barley and winter-wheat/winter-rye. Rape, clover/lucerne and grassland areas can be separated, too.

Forest areas (and urban areas) can have different mean backscatter values, but they do not show any significant temporal variations in mean backscatter and mean greylevels between May and June. This characteristic feature should be used as an important information for classification. It could be seen from monotemporal classification with a neural network that forest areas were mostly classified in one of the other land use classes, which did not happen when using both images for classification. Beneath using multitemporal images, classification results could possibly further improved by including textural information.

4 NEURAL NETWORK CLASSIFICATION APPROACH

In general there are three possibilities for classification of ERS1-SAR images.

A PIXEL BASED classification of SAR precision images can hardly be performed successfully unless the data are heavily smoothed. The occurrent "speckle noise" in radar images is a result of the interaction of the coherent electromagnetic wave with a surface. Basically it is the interference pattern resulting from the various returns from different scatterers on the illuminated surface [SCHREIER 1993].

Thus others than pixel based approaches must be considered if artificial effects according to any filtermethod shall be avoided.

An OBJECT ORIENTED classification should be appropriate if the boundaries of the objects are known and remain equally. If this conditions do not come true, a TEXTURE BASED approach is preferable.

A recent method to carry out a texture based classification is to use a NEURAL NETWORK like a Backpropagation Net or a self-organizing Kohonen Feature Map. This approach was tested on unfiltered mono- and multitemporal ERS1.SAR.PRI data

Like traditional classification approaches neural nets can be divided into supervised and nonsupervised learning networks. Supervised learning refers to classification, and nonsupervised learning to cluster analysis. Backpropagation Nets, representing the first group, obtain their information from training data sets that contain example vectors for each destination class. After the training phase, where the net learned to distinguish between different clusters, it should be well adapted to the given feature space. In the reclassification phase, where the training samples or even

better a different vector set with known destination class are presented, the overall reclassification error of the net can be determined. During the following classification phase the net assigns each presented vector to one of the given classes in generalizing its behavior [GROSS 1993].

A Backpropagation Net consists of several n-dimensional layers. Each layer is composed of neurons. The input layer fixes the dimension of the presented vectors. It is fully or partially (receptive fields) connected with at least one hidden layer. The number of neurons in the following output layer corresponds to the number of destination classes. Connections of the neurons are only permitted unidirectional between two layers. The learning algorithm is backpropagating [RUMELHART et al. 1986]. It should be noted, that the used gradient learning method must not lead to global minimum configurations.

Self-organizing networks like a Kohonen Feature Map however organize the data to be presented during the learning phase, where the result of the mapping is not required. In the first place the Kohonen map is used to perform a cluster analysis or a dimension reduction [GROSS 1993].

The Kohonen Map consists of two layers. The input layer which determines the dimension of the input vectors is completely connected with each neuron of the competitive layer. The weights associated with the connections are adjusted during the training according to given rules. Only one neuron of the competitive layer can be activated by an input vector at one time. This neuron represents the cluster which the data set belongs to. Due to the learning rules the spatial distance between two neurons reacting on two different input pattern represents the similarity of the two patterns [KOHONEN 1990].

Applying the dimensions x,y,z of the competitive layer to the RGB color space, the different appearing colors for each presented input vector can be used to determine suitable training samples for a following supervised classification.

The software to simulate the Kohonen Feature Map and the Backpropagation Net was developed in cooperation with ZGDV, Darmstadt (Computer Graphics Center) and GAF mbH, Munich (Company for applied Remote Sensing).

CLUSTER ANALYSIS:

To determine separable destination classes for the Backpropagation Net the textural feature space has to be analyzed by a Kohonen Map for

different sized neighbourhoods. Thus the dimension of the input layer of The Feature Map changes from 3x3 to 7x7.

Analysing the resulting RGB output of the monotemporal ERS1 data, it can be realized that only three main colors are apparent. Applying this to the feature space means that three different cluster can be distinguished clearly by their textural quality.

Looking at the RGB results of the multitemporal data set shows much more colored pictures. At least 6 to 7 different clusters are separable. Inside the agricultural field boundaries the appearing colors are more or less unique and clusters can be derived, distinguishing different crop types on the basis of their textural qualities.

CLASSIFICATION:

The following supervised classification with a Backpropagation Net requests a set of training samples.

Based on the performed cluster analysis of the feature space and available ground truth data, representative training sets can easily be defined.

The separation of the classes is a complex problem and requires a fully connected four layer net with two hidden layers. The input layer should have the same dimension as the corresponding input layer of the Kohonen Map. The number of neurons in the output layer matches with the number of destination classes. The optimal extent of the hidden layers can only be determined by comparing the reclassification errors of different attempts. However, if enough neurons are available to solve the problem, the extent of the hidden layers is in principle a function of processing time and accuracy. The following net topology is for example used to classify the multitemporal ERS1 data set:

input layer: 5 x 5 x 3
 hidden layer 1: 9 x 7 x 5
 hidden layer 2: 8 x 4 x 2
 output layer: 6 x 1 x 1

The reclassification error based on the training samples is less than 5%.

The classification of the agricultural fields fits quite well to the ground truth data. Though further investigations have to be performed to make an accuracy assessment.

5 CONCLUSION

This paper has shown that, according to multitemporal signature analysis, ERS1.SAR.PRI data should allow the distinction of different agricultural crops when performing a land use classification. A new technique for textural classification of mono- and multitemporal unfiltered ERS1 precision products is introduced. Especially the multitemporal approach on detection of agricultural crop types is very encouraging. This approach is only a basic attempt and should be seen as a first step to an operational classification method.

REFERENCES

- GROSS, M.:
Visualization of multidimensional image data sets using neural network,
Springer-Verlag, The Visual Computer, Vol.10,
10/1993, 145-159
- KOHONEN, T.:
The Self-Organizing Map,
Proceedings of the IEEE, Vol. 78, No. 9,
9/1990

LAUR, H.:
Derivation of Backscattering coefficient in ERS-1.SAR.PRI Products
ESA-ESRIN 17-10-1992

RUMELHART, D.E., HINTON, G.E., WILLIAMS, R.J.:
Learning internal representation by error propagation,
MIT-Press, Cambridge Massachusetts 1986

SCHREIER, G.:
SAR Geocoding: Data and System,
Wichmann-Verlag, Karlsruhe 1993

WOODING, M.G., ZMUDA, A.D., GRIFFITHS, G.H.: Crop discrimination using multi-temporal ERS-1 SAR data
Proc. Second ERS-1 Symposium, Hamburg 1993

ACKNOWLEDGEMENT

This work was supported by the German Space Agency (DARA)

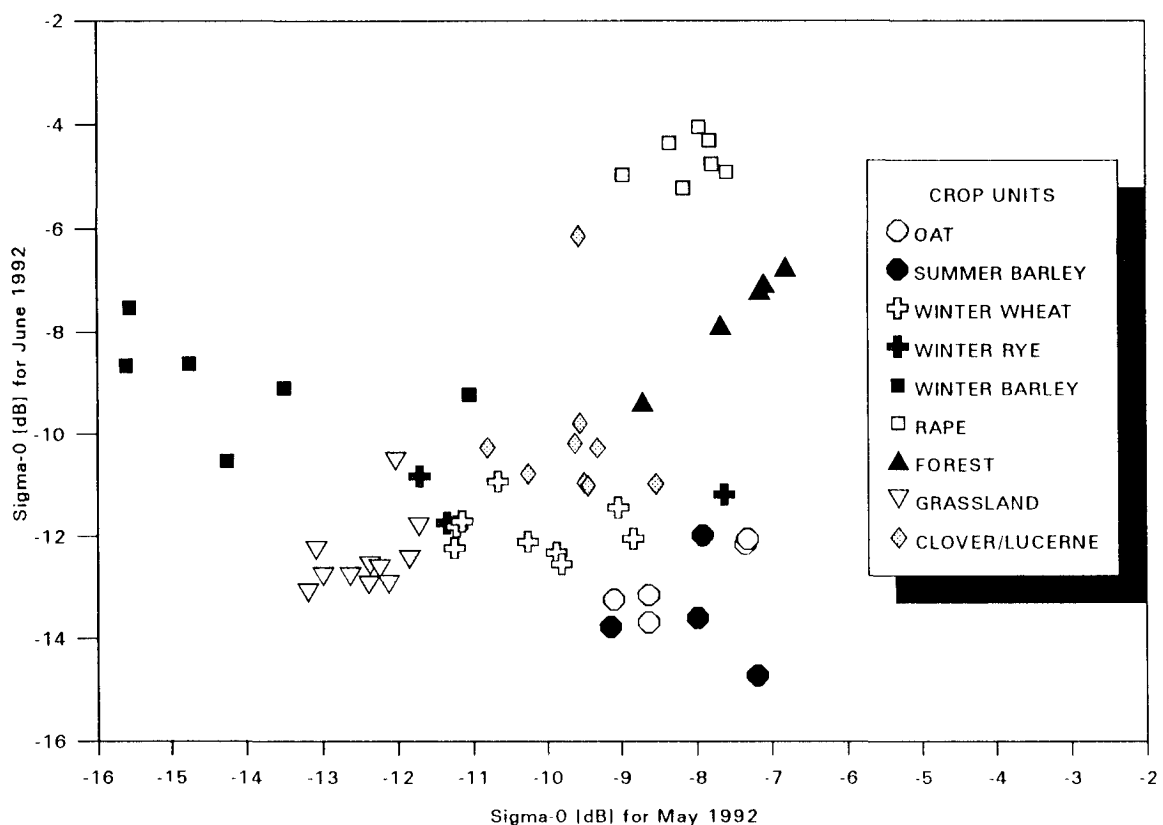


Fig.1: Comparison of sigma-0 from May and June for different crops

SOME RESULTS OF THE PASTA PROJECT CONCERNING AGRICULTURAL CLASSIFICATION

Philipp Hartl
Hans-Georg Klaedtke

University Stuttgart
Institute of Navigation (INS)
Keplerstr. 11
D-70174 Stuttgart
Phone: ++49-121-3400
Fax: ++49-121-2755

1. Introduction

The PASTA project investigates the application of ERS-1 multitemporal SAR data to the needs for agricultural statistics and inspection of land use. Large regions of Baden-Württemberg and of Thuringia are investigated. There exist considerable differences within and between these regions concerning land cover/ land use, topography, climate, and field sizes etc. We have, in any case, to investigate and apply multitemporal and multisensoral methods and combine them with GIS information. Reasons will be explained in the presentation.

Different classification methods have been applied. Our experiences concerning the different approaches will be reviewed. In accordance with our workplan we have concentrated, so far, our activities geographically to a few test sites, from which we know very well the required ground truth data.

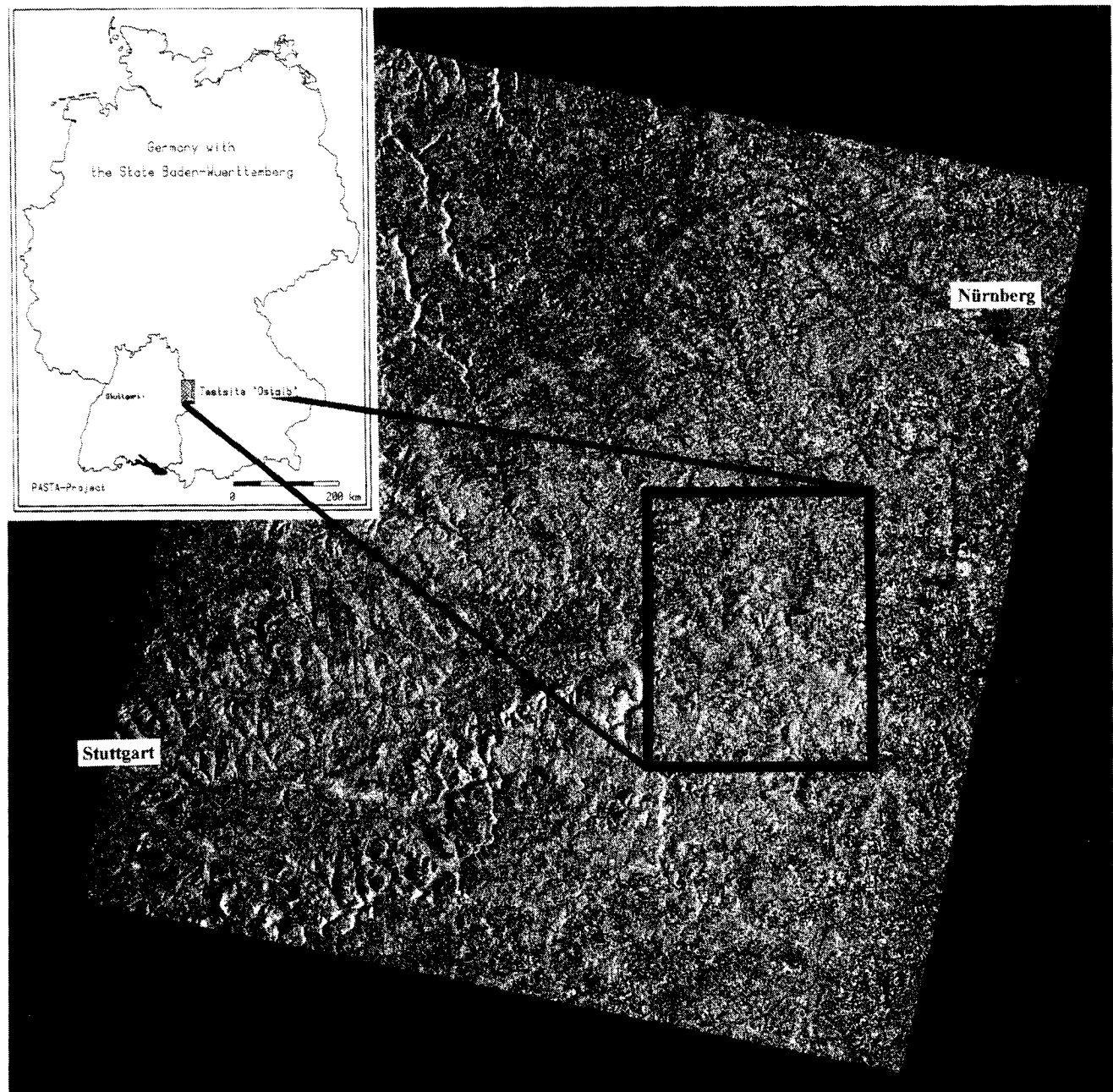
Close co-operation is needed and assured in our project with the administrative (State Ministries of Agriculture, Statistical Offices), and the industrial partners (DASA-Dornier and DASA-Jeno Optronik). This close co-operation supports our efforts to identify and to concentrate to the information which is really needed by the administration for the practical use. We benefit from the large amount of a priori knowledge existing in the State offices, and which have been acquired by means of the conventional techniques. We can use this information to mask irrelevant areas and to improve classification by expert knowledge.

Aims and Objectives:

Application of radar remote sensing data (ERS-1-type SAR data) in conjunction with optical remote sensing data and GIS-data (available digital data of a geoinformation system) for the tasks of agricultural administrators of CEC and national authorities for large areas.

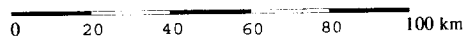
Aims for 1993/1994:

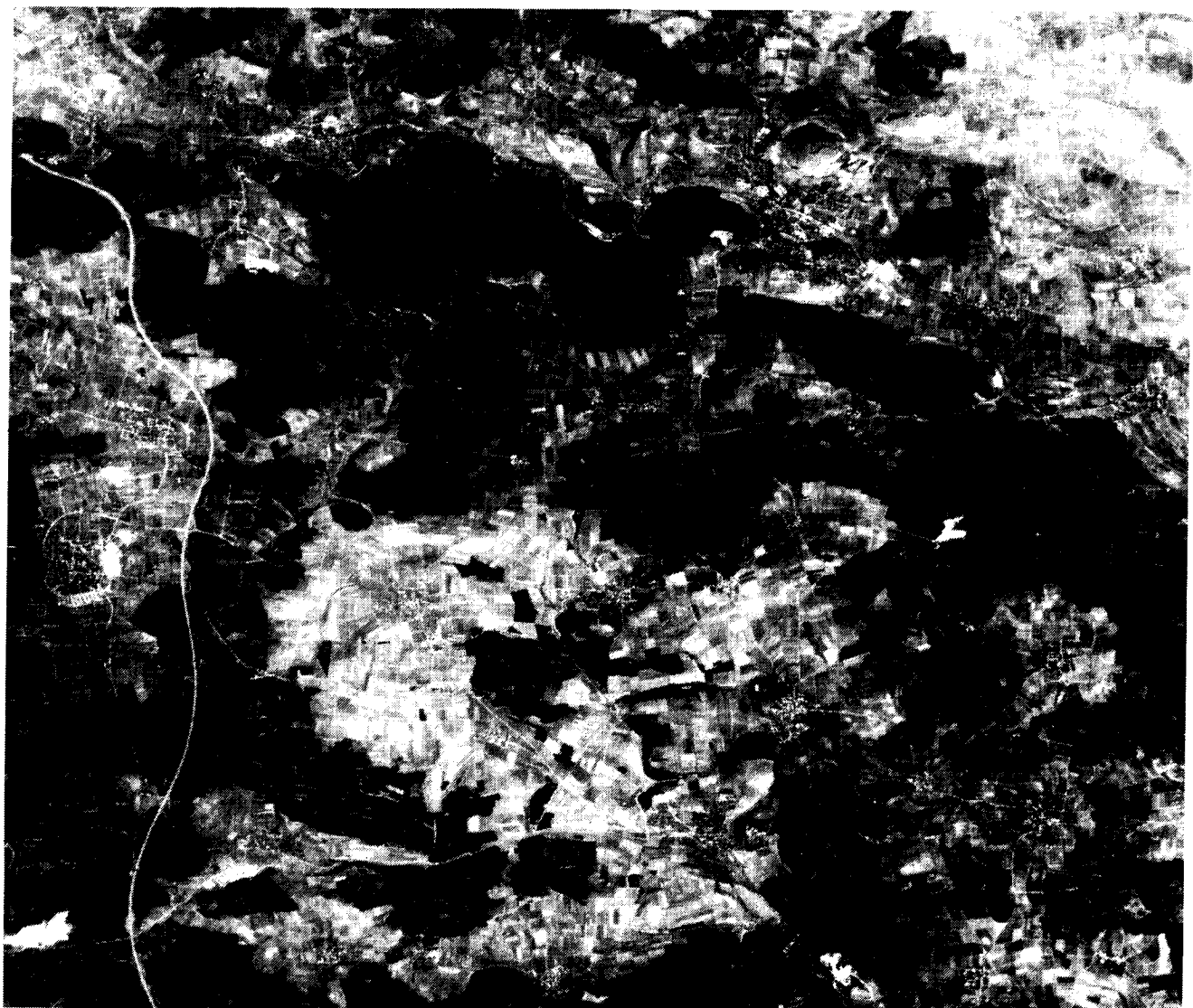
- > Analysis of radar data for smaller areas (testsite: Ostalb)
 - * Setup of GIS and implementation of data
 - * Provide mask for the non agricultural areas
 - * Acquisition/separation of main agricultural land use areas by land-use classification making use of multitemporal ERS-1 SAR data:
 - cereals (winter wheat, winter barley, summer barley, rye, oats and maize)
 - sugarbeets, potatoes
 - oilseeds (rape, sunflower)
- > Development of classification methods for the application of multitemporal SAR-data making use of a priori knowledge (GIS)



Baden-Württemberg Testsite 1993/94 Ostalb

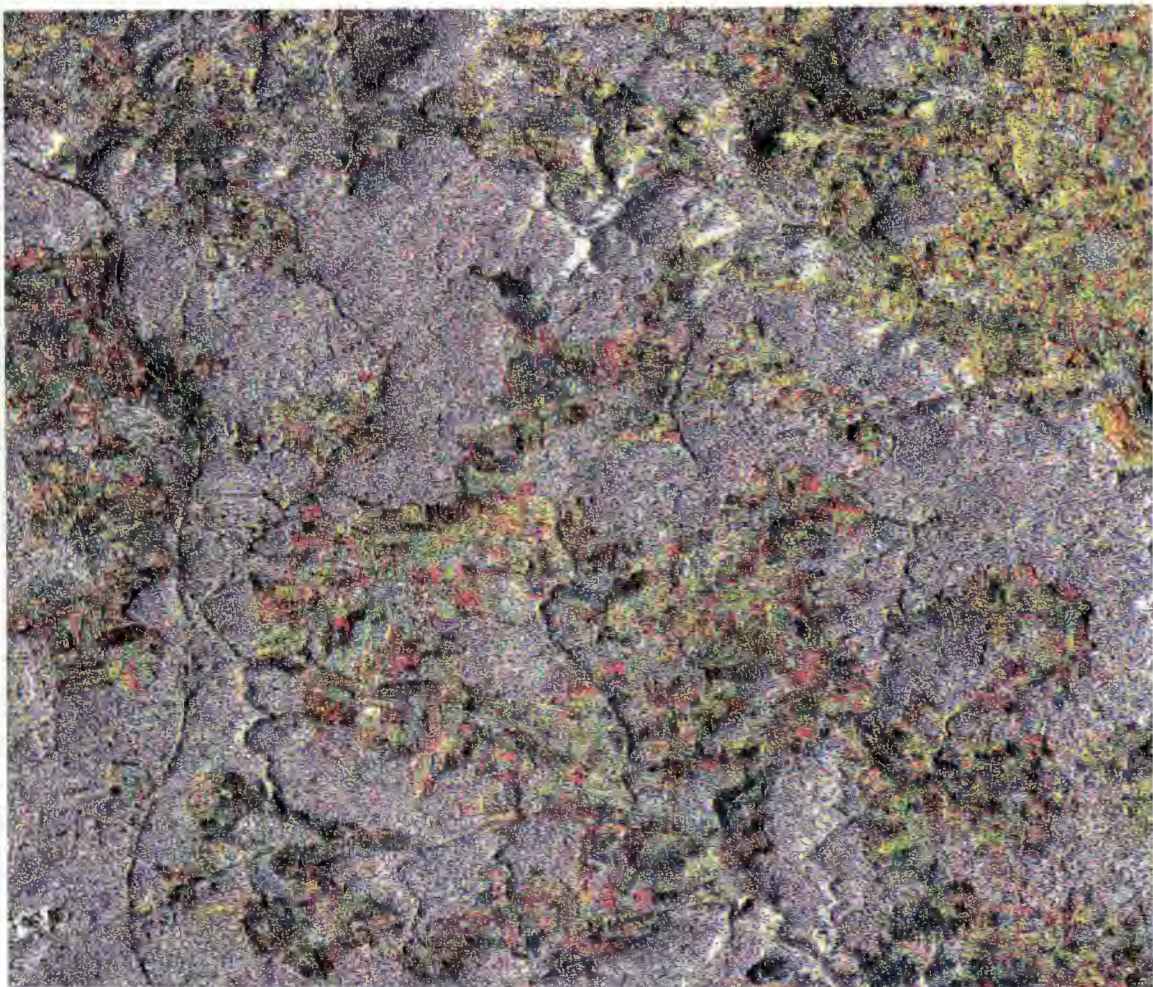
ERS-1 SAR image; date: 24/06/93; orbit: 10144; frame: 2619; type: GTC; D-PAF





Baden-Württemberg Testsite 1993/94 Ostalb
SPOT HRV 1 PAN 056-251 image; date 01/04/1993

0 2 4 6 8 km



Baden-Württemberg Testsite 1993/94 Ostalb

False color composite: ERS-1 SAR multitemporal-image
red = 20/05/93; green = 24/06/93; blue = 29/07/93

0 — 2 — 4 — 6 — 8 km

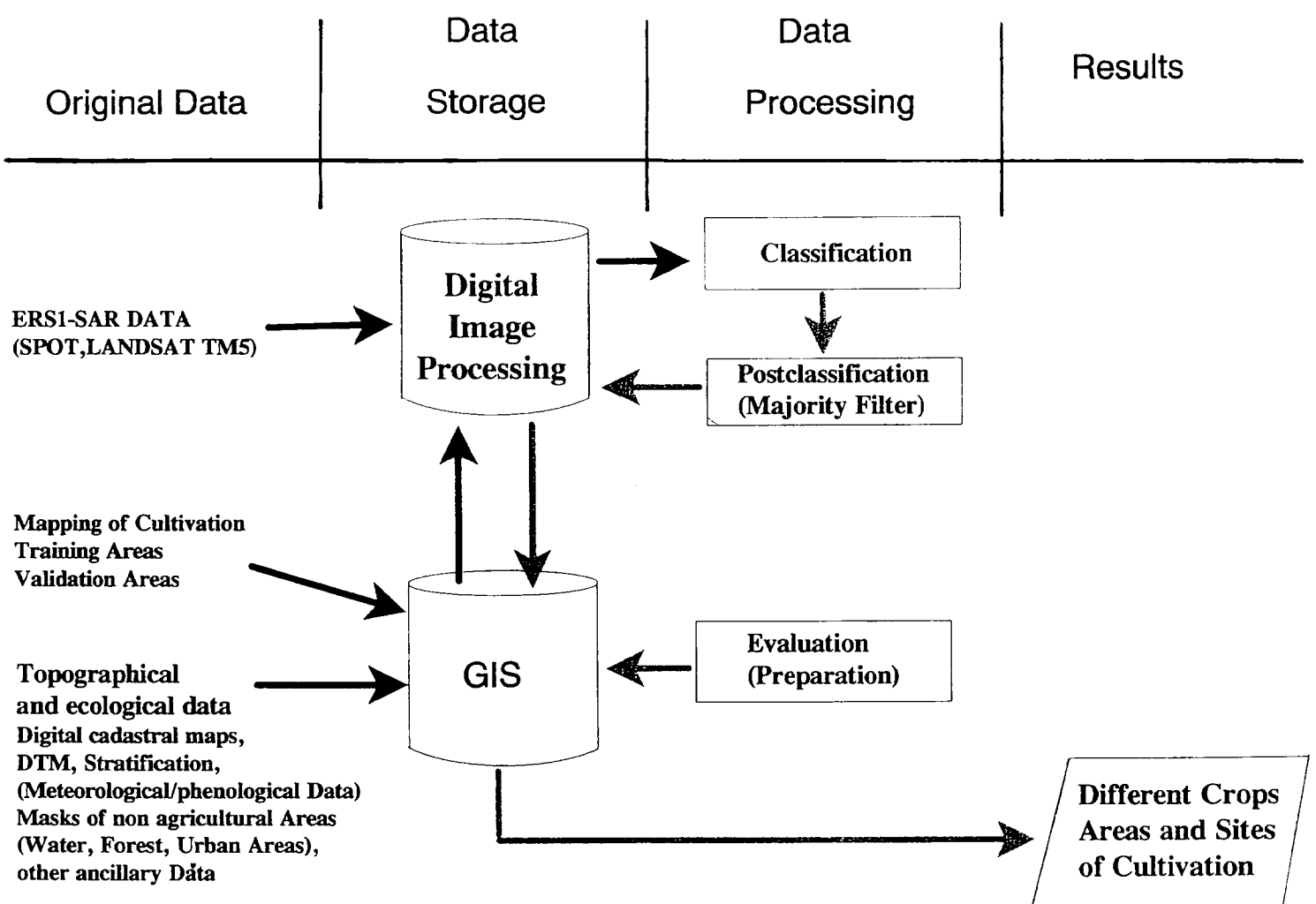


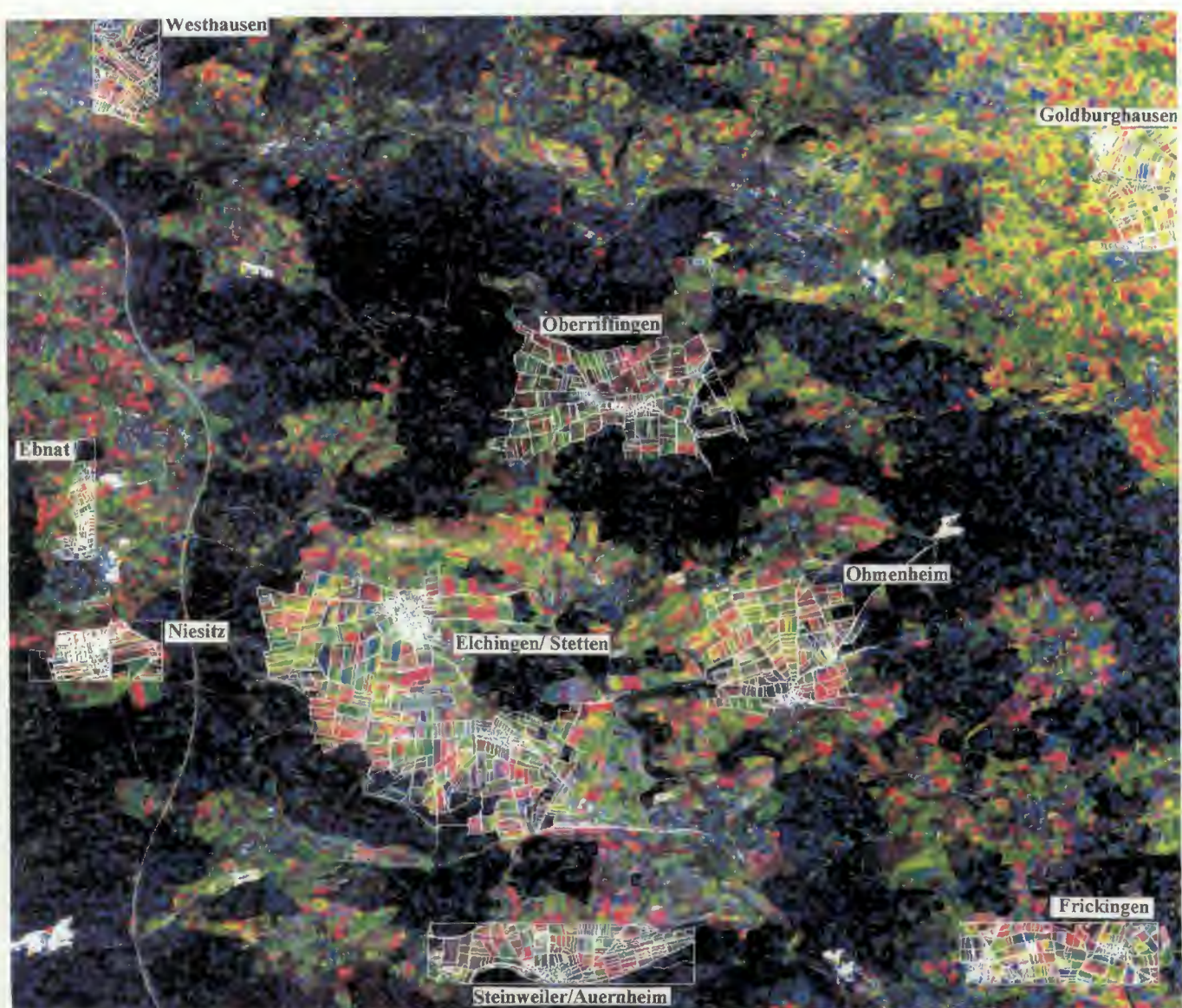
Baden-Württemberg Testsite 1993/94 Ostalb

Forest mask derived from Topographical Map 1:50 000; Baden-Württemberg

0 — 2 — 4 — 6 — 8 km

Integrated approach:



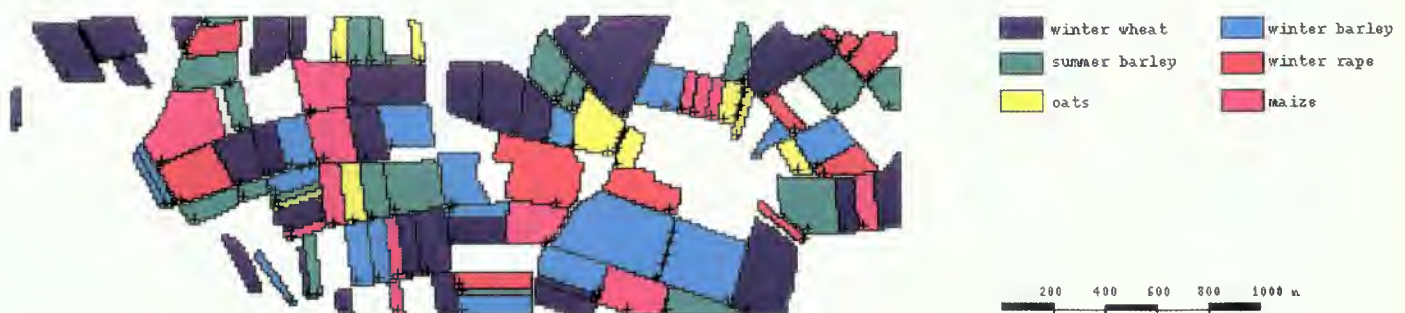


Baden-Württemberg Testsite 1993/94 Ostalb
IHS color composite: ERS-1 SAR multitemporal-image (20/05/93; 24/06/93; 29/07/93)
and SPOT PAN (01/04/93)

0 2 4 6 8 km

Validation area: Frickingen/Ostalb

Ground truth



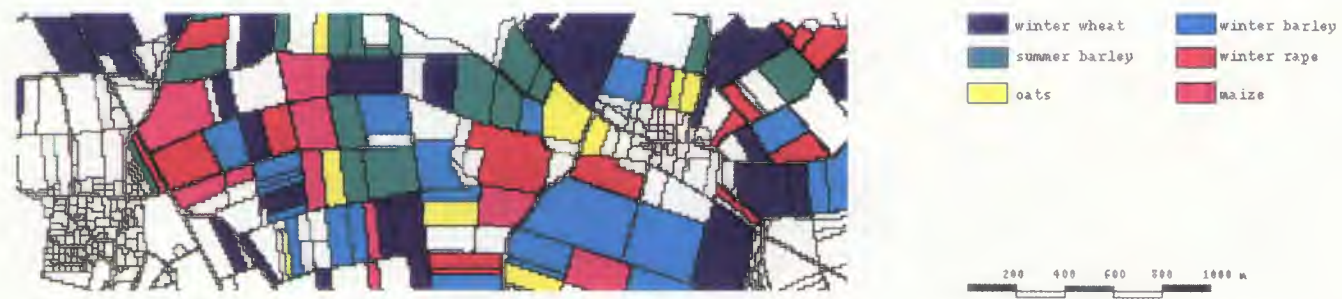
Area	Winter crops 147 ha			Summer crops 75 ha			Total
	Winter wheat	Winter barley	Winter rape	Summer barley	Oats	Maize	
Hectares	74	48	25	34	11	28	222
%	33	22	11	15	5	13	100

Classification result using Maximum Likelihood-Algorithm



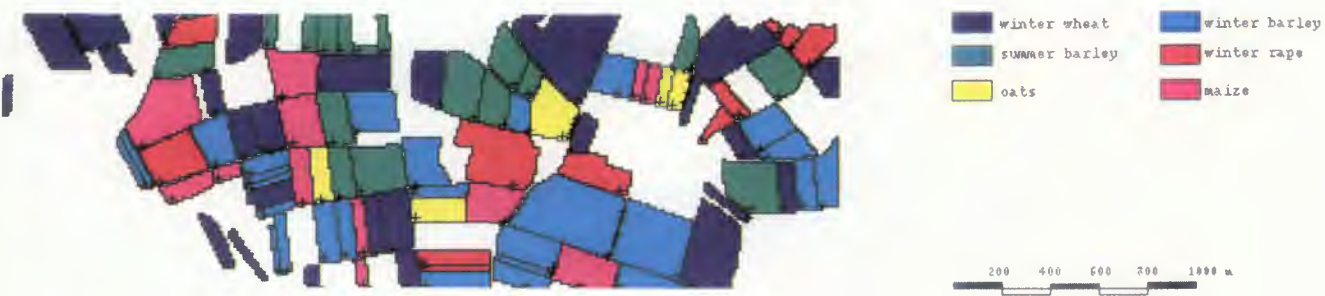
Crop	Hectares	undef.	Classification (%)					
			W.-wheat	W.-barley	W.-rape	S.- barley	Oats	Maize
Winter wheat	74	3,1	45,4	14,6	3,6	18,6	11,8	2,9
Winter barley	48	0,5	12,4	64,2	6,7	5,1	5,3	5,8
Winter rape	25	0,0	1,4	11,3	78,8	4,7	1,5	2,3
Summer barley	34	0,0	21,0	10,2	5,5	50,8	8,6	3,9
Oats	11	0,3	26,2	8,9	1,2	11,0	51,1	1,3
Maize	28	0,9	6,6	24,0	4,7	0,9	5,6	57,2
			Winter crops total					
				74,8				
Winter crops	147	1,7						
Summer crops	75	0,4						
			Summer crops total					
							23,5	
							63,5	

Post Classification Method: Majority Filter



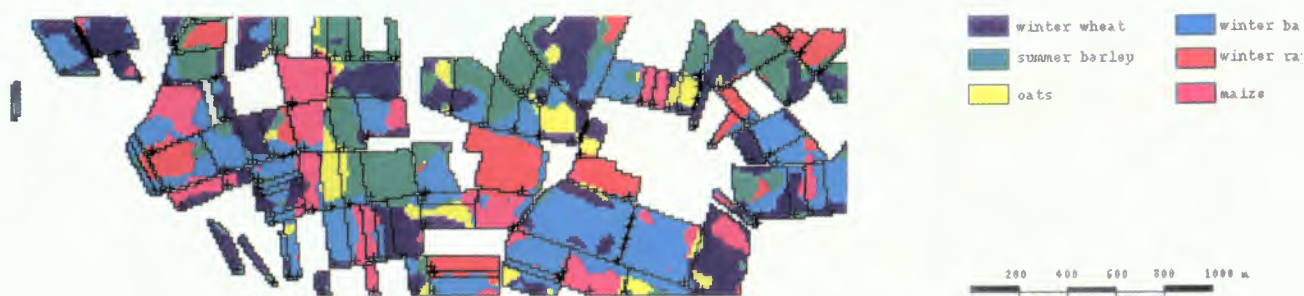
Crop	Hectares	undef.	Classification (%)						
			W.-wheat	W.-barley	W.- rape	S.- barley	Oats	Maize	
Winter wheat	74	3,8	43,2	11,3	0,9	37,0	3,8	0,0	
Winter barley	48	0,0	0,0	71,0	14,4	4,5	0,0	10,1	
Winter rape	25	0,0	2,9	7,3	89,8	0,0	0,0	0,0	
Summer barley	34	0,0	2,8	3,2	14,8	67,6	11,7	0,0	
Oats	11	0,0	44,9	0,0	0,0	21,6	33,5	0,0	
Maize	28	0,0	0,0	2,1	0,0	0,0	2,7	95,2	
		Winter crops total						Summer crops total	
Winter crops	147	1,9	72,8			25,3			
Summer crops	75	0	17,5			82,5			

Classification result using Maximum Likelihood-Algorithm (Context-Intensity-Window)



Crop	Hectares	W.-wheat	Classification (%)						
			W.-barley	W.- rape	S.- barley	Oats	Maize		
Winter wheat	74	50,2	18,4	1,6	20,4	5,7	3,7		
Winter barley	48	9,9	71,4	3,9	5,4	1,7	7,7		
Winter rape	25	1,4	16,9	71,3	6,5	0,6	3,4		
Summer barley	34	18,1	13,6	3,0	56,0	4,8	4,5		
Oats	11	33,0	11,0	1,1	12,5	40,9	1,6		
Maize	28	3,5	20,9	3,4	1,0	3,3	68,0		
		Winter crops total						Summer crops total	
Winter crops	147	78,4			21,6				
Summer crops	75	33,7			66,3				

Post Classification Method: Majority Filter



Crop	Hectares	Classification (%)					
		W.-wheat	W.-barley	W.- rape	S.-barley	Oats	Maize
Winter wheat	74	73,2	10,7	0,0	13,0	3,0	0,0
Winter barley	48	6,4	91,7	1,8	0,0	0,0	0,0
Winter rape	25	2,9	7,3	89,8	0,0	0,0	0,0
Summer barley	34	8,1	10,4	2,1	72,4	0,0	7,0
Oats	11	25,7	4,9	0,0	15,0	54,4	0,0
Maize	28	0,0	8,0	0,0	0,0	2,7	89,3
		Winter crops total			Summer crops total		
Winter crops	147	91,8			8,1		
Summer crops	75	17,4			82,6		



MULTITEMPORAL AND SINGLE IMAGE FEATURES EXTRACTION, FROM ERS-1 SAR IMAGE DATA, WITH WAVELET TRANSFORMS AND UNSUPERVISED NEURAL NETWORKS¹.

Marcello Melis², Andrea Lazzari

Space Engineering S.r.l.

Via dei Berio, 91, 00155 - Rome ITALY

Phone: +39-6-22595227; Fax: +39-6-2280739

Abstract

SAR images are potentially of great interest for activities as Land Survey because they are generated by an active microwave sensor, working in a range of frequencies where the clouds are transparent. This gives the investigators the maximum freedom in scheduling their monitoring activities living out the weather condition and sun position. On the other hand SAR images are affected by a multiplicative noise that creates strong irregularities and seriously limits the automatic interpretation of the data. As a consequence traditional segmentation and classification algorithms, usually applied to multi-spectral remotely sensed images (Landsat / Thematic Mapper, SPOT, etc.), have small applicability to the ERS-1 SAR data.

In this paper we propose a multistep methodology to process both Single Frequency - Single Polarization, and Multitemporal SAR images coming from ERS-1 satellite.

In the first step the original image is processed with Wavelet Transforms, Low-pass Filtering and Local Standard Deviation. Each transformation extracts a characteristic component from the image that will be used as a pseudo-band, so that each pixel will be characterized by a pseudo spectral signature, as it came from a multispectral sensor. In a second step the data obtained are used to feed a Self Organizing Neural Network in an unsupervised way, e.g. without the need to give an a-priori labeled training set concerning the area covered by the image. The Neural Network receives for each pixel its vector of components, clustering them into homogeneous classes. The results show the capability of the method to deal with noisy single SAR images without the supervision of a trained operator, giving a degree of class discrimination of practical use.

When Multitemporal sequences are available, the first step of the procedure is applied to each image of the sequence, but now the target is to reduce the local noise of the data and also to get a set of images whose characteristics have been enhanced. Now the Neural Network performs the classification using as input each pseudo-band obtained with the preprocessing of each image. The use of multitemporal data increases the discrimination of the classes, and, with a suitable number of multitemporal sequences, it is possible to consolidate a database of Multitemporal Signatures.

Furthermore, crossing over images coming from the ascending and the descending orbits, it is possible to afford the problem of the backscatter of fields, that is affected from the azimuth angle of incidence.

Future planned investigation will include a preprocessing of images based on the Markov Random Fields, that will provide the first or the second step, depending on the kind of classification required, with improved edge determination and reduced noise level.

1. Introduction

The ERS-1 carries a number of Active Microwave Instruments and one of them is the Synthetic Aperture Radar (SAR) that could operate in Image Mode, in Wave Mode or in Wind Mode. The main parameters of this sensor, when it operates in Image Mode, are the following:

SAR antenna size	10 m long, 1 m wide
Frequency	5.3 GHz (C band) ± 0.2 MHz
Bandwidth	15.55±0.01MHz
Polarization	linear vertical
Incidence angle	23° at mid-swath
Spatial resolution	30 m
Swath	100 Km
Data rate to Ground Stations	105 Mbps

The SAR sensor produces data that are processed at several levels depending on the target end-user. The SAR products delivered from ESA /ESRIN range from raw data scene to precision geocoded images. The delivery time of a product is proportional to amount of processing needed to obtain it. We used the Fast Delivery Image product, that is available ~24 hours after the data acquisition. The data coming from this level of processing are affected by a little error in the pixel position, but, for monitoring purposes, this drawback is acceptable, compared to the advantage of timely data availability. To test the classification capabilities of the Neural Network we used also three Precision Images, filtered with a Gamma/MAP 5x5 filter (courtesy of the Agriculture Information System - Joint Research Center CEC).

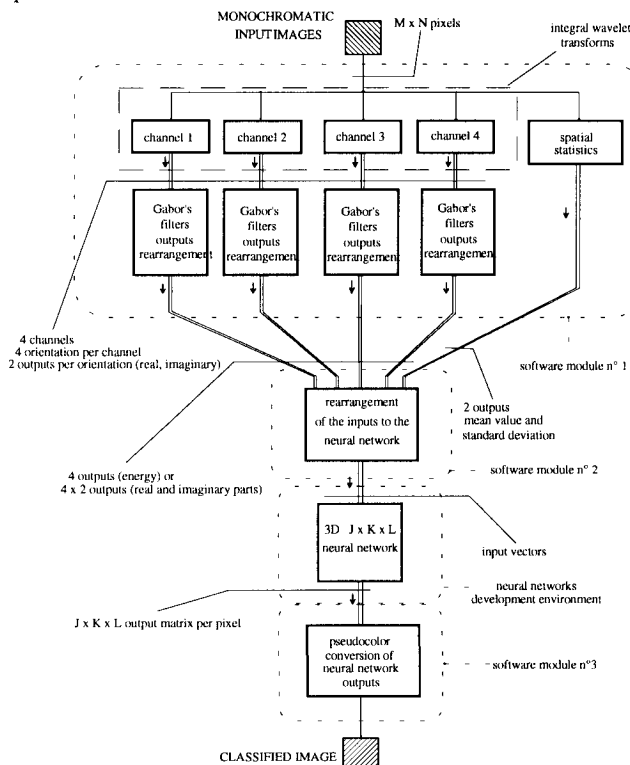
The following table summarizes the SAR Image Mode products with a summary of their characteristics.

¹ Pilot Project PP.ESRIN.11
² Principal Investigator

Product (data volume)	Size (samples)	Coverage (Km) Grid resolution (m)
Annotated Raw Data (300 Mbytes)	5616 x 27000	100 x 110 7.9 x 3.9 (nominal)
Fast Delivery Image (63 Mbytes)	5000 x 6300	100 x 100 20 x 15.8
Single Look Complex Image (150.2 Mbytes)	2500 x 15000	variable <10 x <10
Precision Image (131.3 Mbytes)	8000 x 8200	100 x 102.5 12.5 x 12.5
Ellipsoid Geocoded Image (165.2 to 288.2 Mbytes)	9100 x 9100 to 12000 x 12000	100 x 100 rotated to map grid 12.5 x 12.5
Terrain Geocoded Image (165.2 to 288.2 Mbytes)	9100 x 9100 to 12000 x 12000	100 x 100 rotated to map grid 12.5 x 12.5

The Fast Delivery images come with a Relative Radiometric Calibration (gain normalization), no Absolute Calibration and a Radiometric Resolution of 3dB. Each pixel is 16 bits deep (65536 levels), the pixels' values show a Rayleigh distribution with a mean value ranging about 2000 to 6000.

The first part of this work aims to transform single or multitemporal SAR images into multispectral ones, where each pseudo-band comes from the extraction of spatial-frequency and statistics characteristics. The second part of the work concern the application of an unsupervised classification method, based on the Kohonen's Self Organizing Maps, that using as input these pseudo-bands, produces a thematic version of the input images, partitioned into homogeneous classes. The next figure shows the block diagram of the whole process.



2. First step: SAR data preprocessing

The SAR sensor produces a huge amount of data and, in principle, it is possible to extract a lot of information from it. But realistically, in order to automatically manage these images, it needs to process them lowering the level of noise and splitting the image into several components with spatial-frequency filtering.

In literature a number of noise reduction methods are suggested for SAR images, like the Frost, Lee or MAP filters, that belong to the class of adaptive filters, and the Median filter. Each of them shows a noise reduction and a side effect that reduces the intrinsic image information. We walked through a different approach, looking for a transformation method able to preserve the geometric information of our interest via a flexible tuning of the transformation's parameters. The transformation adopted is the Integral Wavelet Transform with Gabor's functions used to generate the family of base functions. In general, given a wavelet function $\psi(x)$, we can define a family of related functions obtained by shifting and stretching by this one: $\psi_{\gamma,k}(x) = \sqrt{\gamma}\psi(\gamma x - k)$.

Starting from this base wavelet $\psi(x)$ and the generated functions' family, we can define an integral transform W_ψ of the generic function f belonging to $L^2(IR)$ as in the following:

$$(W_\psi f)(b, a, \alpha) =$$

$$\int \int f(x, y) f_\psi * [\alpha^\beta (x - x_1, y - y_1)] dx_1 dy_1$$

To transform a bi-dimensional signal as an image we can use the general form of a Gabor's function:

$$f_g(x, y, x_o, y_o) =$$

$$\exp \left[-\left(\frac{x^2}{2\sigma_x^2} + \frac{y^2}{2\sigma_y^2} \right) + i2\pi(u_o x + v_o y) \right]$$

that corresponds to a complex carrier modulated by a gaussian signal. Its Fourier transform is

$$G(u, v, u_o, v_o) = 2\pi\sigma_x\sigma_y \cdot$$

$$\exp \left\{ -2\pi^2 [\sigma_x^2(u - u_o)^2 + \sigma_y^2(v - v_o)^2] \right\}$$

This is a bidimensional gaussian centered in (u_o, v_o) with standard deviation

$$\sigma_u = (2\pi\sigma_x)^{-1} \text{ e } \sigma_v = (2\pi\sigma_y)^{-1}.$$

The final gabor's function family we have chosen for the Wavelet transforms is:

$$g_{\lambda_x, \lambda_y}(x, y, \theta) = \exp \left\{ -\left[\frac{x'^2}{\lambda_x^2} + \frac{y'^2}{\lambda_y^2} \right] + i2\pi x' \right\}$$

$$\text{with } x' = x \cos \theta + y \sin \theta$$

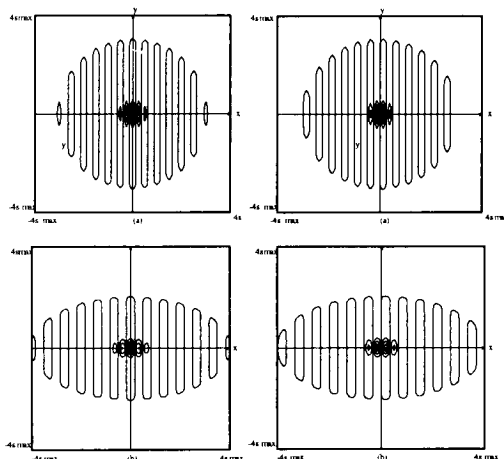
$$y' = -x \sin \theta + y \cos \theta$$

$$\text{and } \sigma_x^2 = \lambda_x^2 / 2 ; \quad \sigma_y^2 = \lambda_y^2 / 2 \\ u_o = \cos \theta ; \quad v_o = \sin \theta$$

It can be proofed that an integral wavelet transform with Gabor's functions of a function $f(x,y)$ is equivalent to a linear filtering of the $f(x,y)$ with filters who's impulsive responses are the Gabor's functions itself, and this transform can be implemented with a bidimensional convolution algorithm.

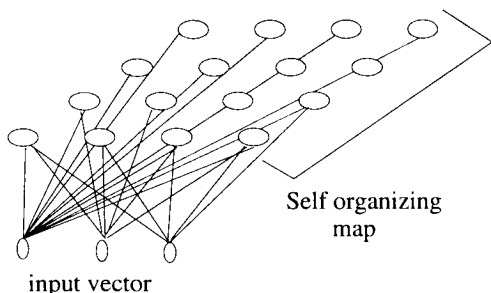
The statistic parameters associated to each pixel are evaluated as the mean value and standard deviation of the neighboring pixel, weighted with a bidimensional gaussian. The standard deviations of this gaussian along the x and y axis determine the amount of blurring allowed (or the cutoff spatial frequency of the low-pass filter).

Next figure shows two Gabor's functions with different eccentricity (left: real part, right: imaginary part).



3. Second step: Unsupervised Neural Network Classification

Once the original image has been transformed in its characteristic components, and statistic parameters have been extracted, we get a pseudo spectral signature associated to each pixel. Now a classification based on the information of the single pixel is viable. To perform an unsupervised classification it is adopted a neural network capable to cluster the pixels on the basis of their statistic distribution. The Kohonen's maps result the best trade-off between ease of implementation, efficiency and flexibility. The general form of this Self Organizing Maps is the following



(2D map example is shown):

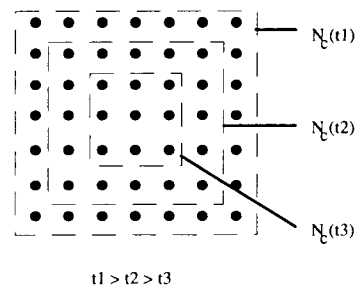
Each component of the input vector feeds all the neurons via a weighted connection. During the learning phase the weights of the connection changes accordingly with the probability distribution of the input training set. It is possible to configure the network positioning the neurons into a space with N dimensions. In our processing we adopted 2D, 3D and 4D Kohonen's maps.

Let $X = (x_1, \dots, x_m)$ be the generic input vector and $W_i = (w_{i1}, \dots, w_{im})$ the weight vector of the i -th neuron. The distance between them is defined as

$$D_i = \|X - W_i\| = \sqrt{(x_1 - w_{i1})^2 + \dots + (x_m - w_{im})^2}.$$

During the learning phase the winning neuron c satisfy the equation $\|x - m_c\| = \min_i \{\|x - m_i\|\}$ where i is the generic neuron of the network.

The relationship between the neurons is determined by the neighborhood topologic function:



At each learning cycle the weights are updated with the following law:

$$\begin{cases} w_{ij}(t+1) = \\ = w_{ij}(t) + \alpha(t)[x_j - w_{ij}] & \text{per } i \in N_c \\ = w_{ij}(t) & \text{per } i \notin N_c \end{cases}$$

Once the network is trained, the whole multispectral image is given to the network and for each pixel is identified the neuron that represents the closest point in the original space of bands. The class associated to the current pixel depends on the position of the winning neuron.

For multispectral classification the input vector is composed with a number of features coming from each one of the input images (low-pass channels, some of wavelet transforms channels).

To summarize. Each neuron of the network has a "double-face" character: 1) its position inside the topology of the network, needed to determine the neighborhood function, 2) the position that it represents inside the space of the input vectors (the centroid coordinates).

During the learning phase the second one changes to best fit the input vectors distribution, i.e. to seek the centroids of a classes.

During the classification phase each input vector is compared with the centroids represented by the neurons and it is associated to the closest centroid (Euclidean distance).

Three representations are available for the classified pixel:

- 1) a single number identifying the belonging class; the original image is transformed into a monochromatic one, where each class has a different gray level;
- 2) the coordinates of the closest centroid; the original image is represented in the same space, but now the number of 'colors' is reduced to the number of classes (neurons);
- 3) the topological coordinates of the neuron in the network; original image is now represented in the space of the neural network (especially useful with 3D Kohonen's maps).

4. Results

The method has shown good results in classifying single images of the class of the ERS-1 Fast Delivery Image, that are usually very noisy and difficult to process. Better results, of course, come from the multitemporal classification, and in this case the method was able to correctly segment the data into homogeneous clusters with a resolution in the order of the single pixel.

The result of the whole process depends on a number of parameters:

- in the first phase the center frequencies of the Gabor's functions, their orientation and the standard deviation of the modulating gaussian;
- in the second phase the number of dimensions of the Self Organizing Map (usually 2, 3 or 4), the number of levels per dimension, and the way of combining of the channels coming from the first step.

The Wavelet transforms, due to their ability to perform a selective analysis of the images, allow a classification focused only on the features of interest, masking the undesired components of the images. For examples it possible to eliminate from an image all the structures with specific spatial frequency and orientation, with a minimum loss of resolution, like roads, urban areas, rivers or geological structures, and to pass to the classifier only the information concerning cultivated fields, or it is possible exactly the vice-versa, focusing the analysis on the artificial structures (buildings, highways etc.).

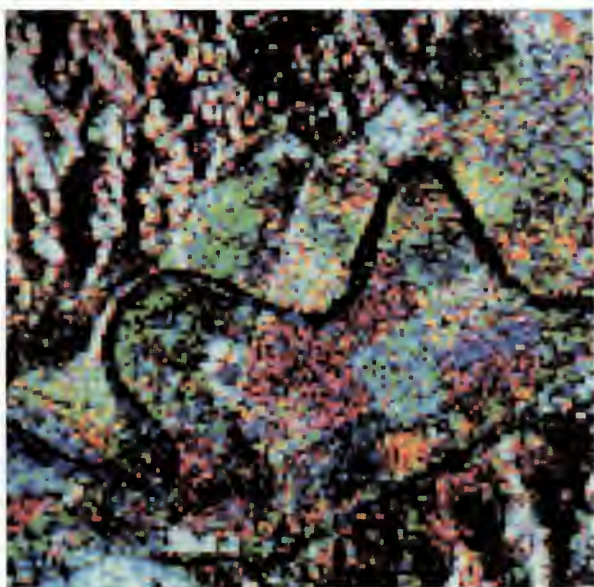
The classification based on the Kohonen's maps is able to recover the loss of resolution due to the noise filtering of the first phase. This is shown in the first sequence of photos (Fast delivery images of the Tiber

Valley - north of Rome, Italy) where a strong low-pass filtering was applied to the original images. The classification resulted segments the field with a transition not bigger than a couple of pixels.

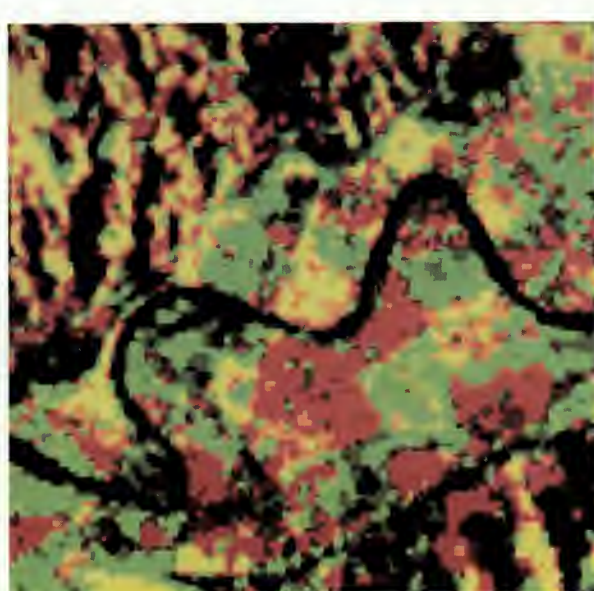
The second sequence of photos (PRI sampled 1 pixel over 2 - area of Toledo, Spain) shows two classifications: the first one focused on the identification of fields, and the second one focused on the morphology of the structures present in the images. The third sequence (PRI filtered with Gamma/MAP 5x5 filter - area of Seville, Spain) Shows a classification with a 3D Neural Network and 64 classes. A further result, when the input vectors are substituted with the closest centroids, is a compression of the original data, with a negligible loss of readability. For examples the RGB image (8+8+8 bits) of this sequence is classified and transformed with a 3D Kohonen's map of 4x4x4 neurons (2+2+2 bits) with a compression factor of 4:1. In this case the average error introduced in the level of each band is ~10 over a dynamic of 256 levels (~4%). On the other hand there is the benefit of an increased uniformity inside noisy areas that could improve the photointerpretation.

5. References

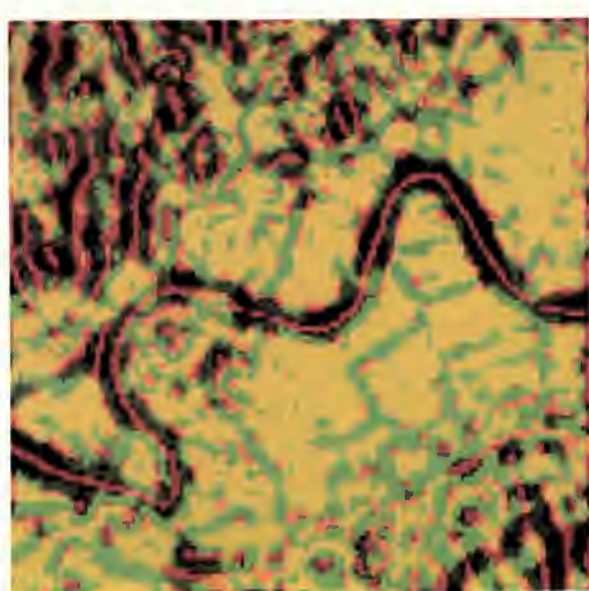
- W.G. Rees : "Phisycal principles of remote sensing" , 1990 Cambridge University Press.
- "ERS-1 system" , ESA sp-1146, September 1992.
- "ESA ERS-1 product specification" , ESA sp-1149, Issue 3.0, June 1992.
- C.K. Chui : "Wavelets analysis and its applications - Volume 1: An introduction to wavelets" , 1992 Academic Press.
- A.C. Bovik, M. Clark, W.L. Geisler : "Multichannel texture analysis using localized spatial filters" , IEEE Transaction on pattern analysis and machine intelligence, vol. 12, no. 1, January 1990.
- M.R. Turner : "Texture discrimination by Gabor functions" , Biological Cybernetics, vol. 55, pp. 71-82, 1986.
- R.P. Lippmann : "An introduction to computing with neural nets" , IEEE ASSP MAGAZINE, pp. 4-22, April 1987.
- P. Ciaccia, D. Maio : "Reti neuronali: proprietà e problematiche aperte", Alta Frequenza - Rivista di Elettronica, vol. 1, no. 3, Lug.-Set. 1989.
- T.K. Kohonen : "The self-organizing map" , Proceedings of the IEEE, vol. 78, no. 9, September 1990.
- J.A. Kangas, T.K. Kohonen, J.T. Laaksonen : "Variants of self-organizing maps" , IEEE TRANSACTIONS ON NEURAL NETWORKS, vol. 1, no. 1, March 1990.
- B.S. Manjunath, R. Chellappa : "A unified approach to boundary perception: edges, textures, and illusory contours" , IEEE TRANSACTIONS ON NEURAL NETWORKS, vol. 4, no. 1, January 1993.
- M.M. Van Hulle, T. Tollenaere : "A modular artificial neural network for texture processing" , Neural Networks, vol. 6, pp. 7-32, 1993.
- R. Chellappa, R.S. Manjunath, T. Simchony : "Neural networks for signal processing; cap. 2: texture segmentation with neural networks" , ed. B. Kosko, Prentice-Hall International Edition .



Multitemporal image of Toledo
(PRI 2:1 Pixel = 25 m)



Classification of fields (2-D NN)

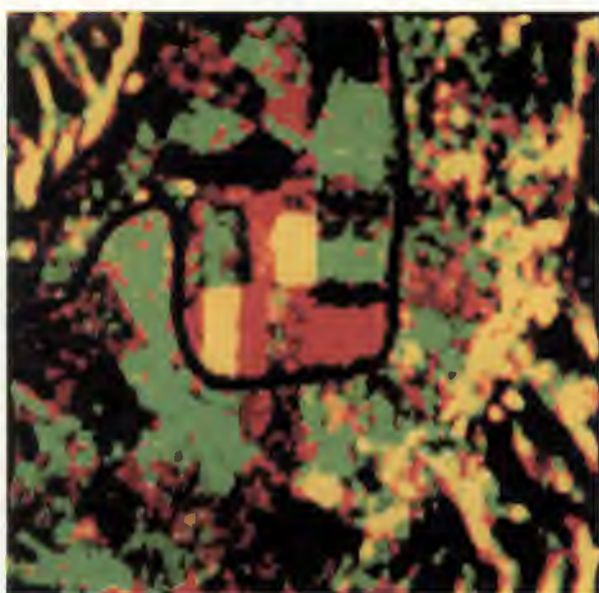


Classification of edges (2-D NN)

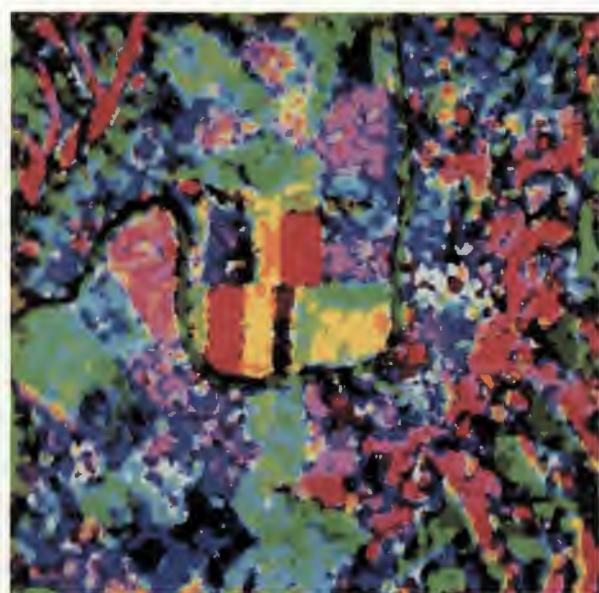


Mutitemporal image of Tiber Valley, Rome (FDI)

Classification with 2-D neural network



Classification with 3-D neural network



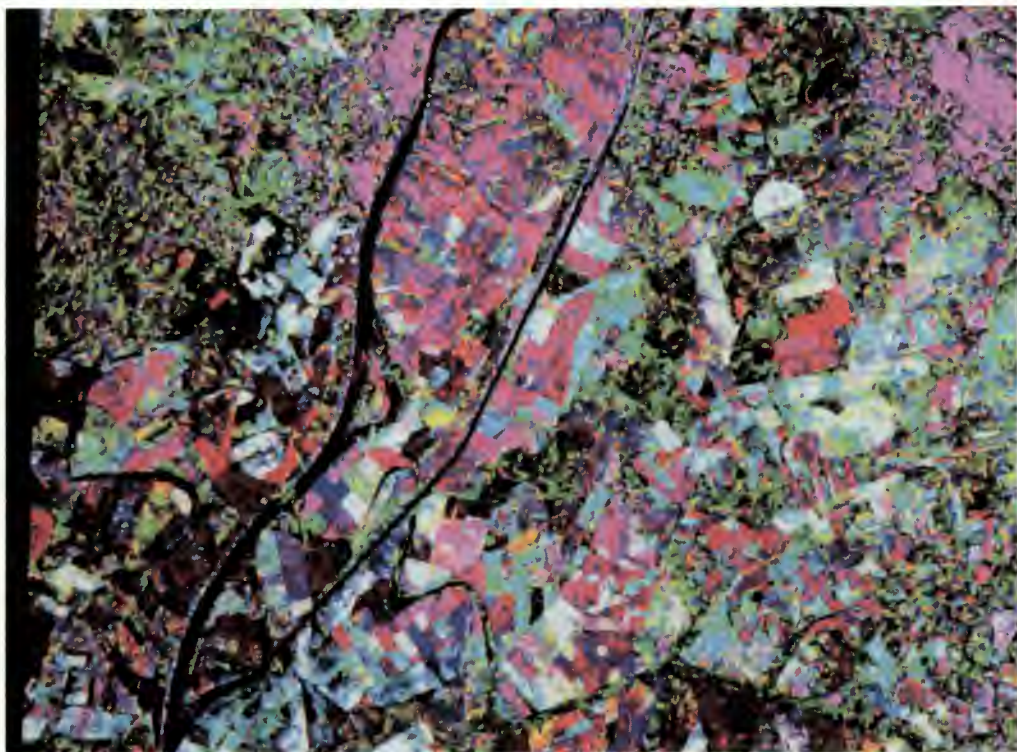


Image classified with 64 classes in a 3-D neural network ($4 \times 4 \times 4$ neurons). Colours rendered on the basis of the neural network topology (1 pixel: 6 bits).

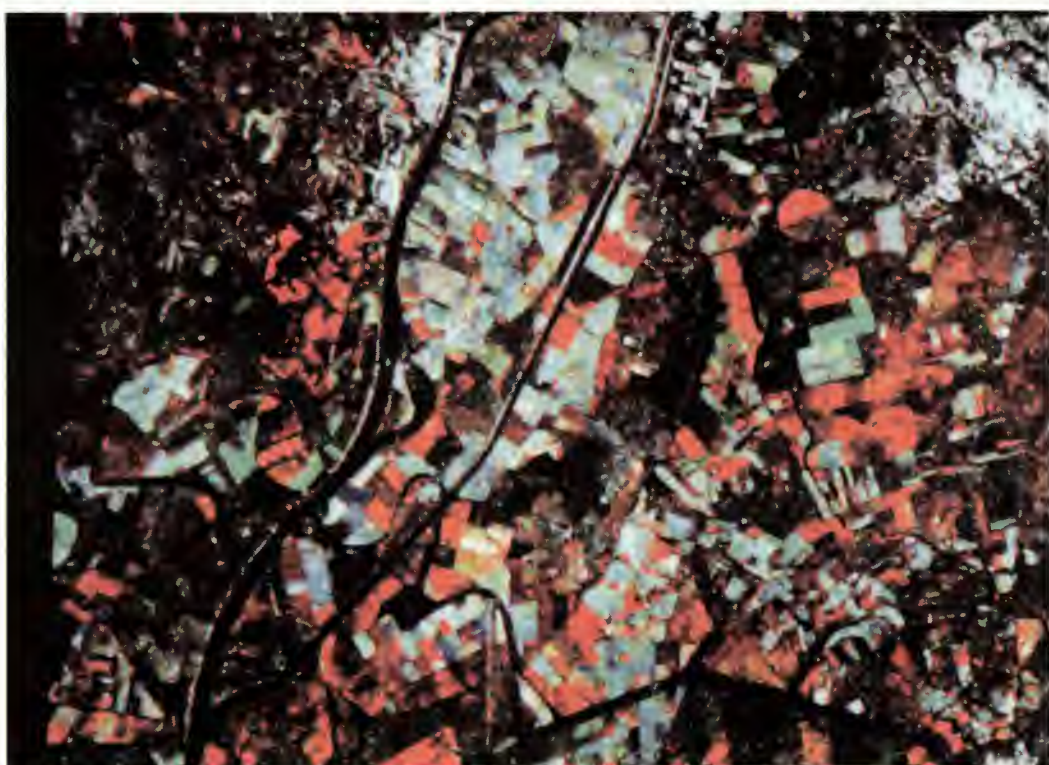
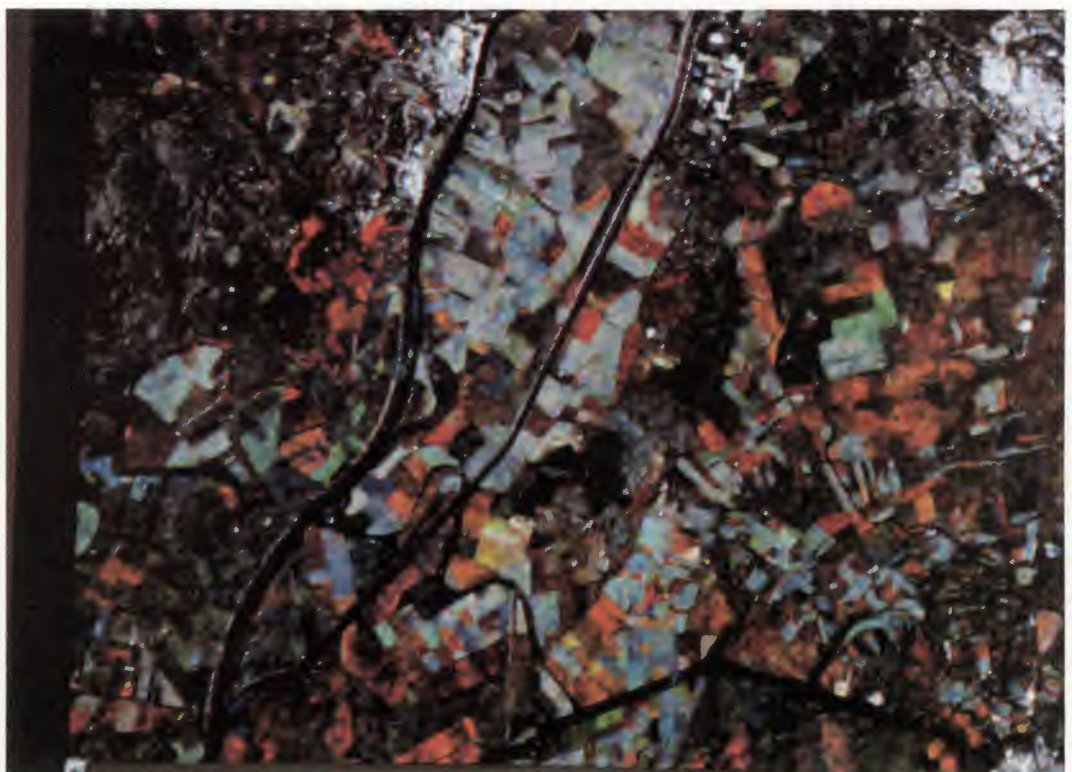


Image classified as above, coloured with the closest original colours (1 pixel: 6 bits).



*PRI multitemporal image of Sevilla (noise filtering courtesy of JRC-AIS, Ispra, VA).
(1 pixel: 24 bits).*

SAR IMAGERY SEGMENTATION AND SPECKLE REDUCTION IN THE EBRO DELTA AREA, SPAIN. (PP2
- E02).

O. Chic and L. Solé Sugrañes

Institute of Earth Sciences "Jaume Almera", C.S.I.C.
c/ Solé Sabarís s/n. 08028 Barcelona. SPAIN
phone (+34) 3-330 38 00. fax (+34) 3-411 00 12
Email: lsole@u.ija.csic.es

ABSTRACT

ERS1 SAR.PRI images of the Ebro Delta (Spain) have been used to test the behaviour of several filters to reduce the speckle effects. The SNR is too low in SAR images and it makes difficult the use of most popular textural segmentation algorithms. An acceptable segmentation of homogeneous land covers have been achieved using a recursive Lee's filter with an Edge Preserving Smoothing algorithm and edge detection by zero crossing techniques.

1. INTRODUCTION

ESA processed SAR.PRI ERS-1 images are obtained by convolution of three single consecutive looks. However, the signal-to-noise ratio (SNR) is still too low to benefit from the full spatial resolution of these images despite the use of three looks (compare figs. 1 and 2). The

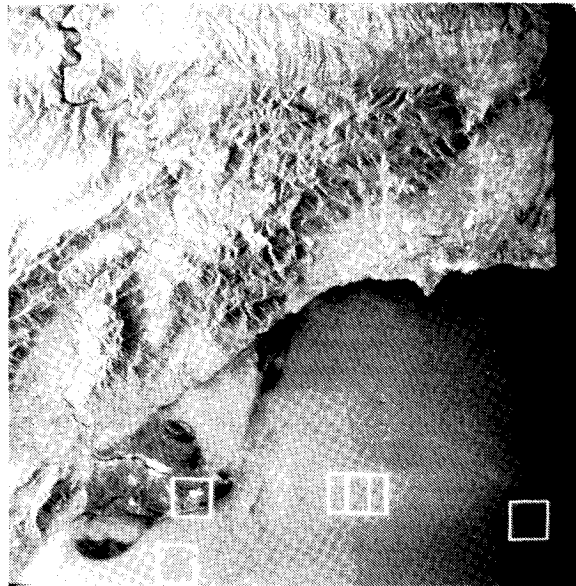


Fig. 1.- ERS 1 SAR.PRI scene of August 3 1991. Squares indicate the location of test site areas.

most part of noise in SAR images is due to speckle

which results from multipath interferences of multiple reflectors within the resolution field. The speckle dramatically increases the variance of radar images and makes it difficult to use grey level slicing classification techniques and the most popular textural segmentation algorithms.

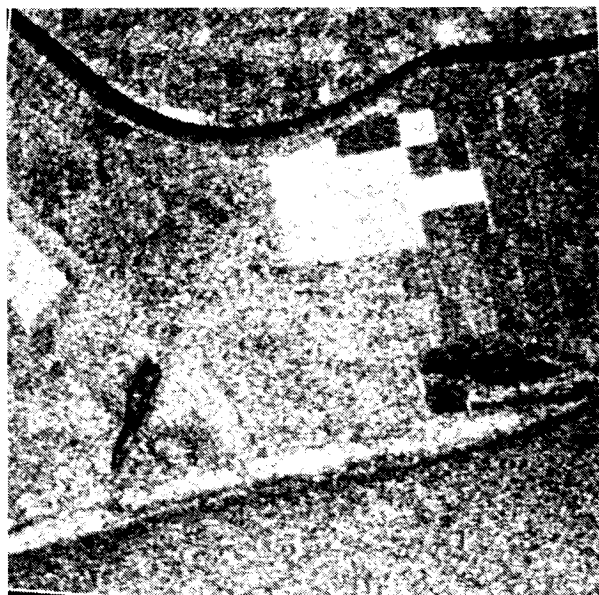


Fig. 2.- Original image of the test site 1 in the Ebro Delta at full resolution.

To minimize the speckle effect we have studied its frequency distribution in SAR.PRI images. Knowledge of speckle distribution provides a good basis to evaluate the effect of several filters on speckle reduction and textural image segmentation. The filter tests have been carried out in the Ebro Delta using an ERS-1 SAR.PRI scene of August 3, 1991 (fig. 1). The Ebro Delta is a well known and controlled area to evaluate the improvement of any classification technique. There is a very flat surface where several land cover classes like sea, river and lagoon waters, rice and oat crops and lacustrine and salt marsh vegetation coexist in a small deltaic area of less than 36 square kilometers. Fig. 1 shows the emplacement of the test site and fig. 2 is the image of

the test site scene at full spatial resolution without any kind of filtering or image enhancement except a 16 to 8 bit transformation.

2. SPECKLE CHARACTERISTICS

From the light coherency theory, the probability density function (pdf) of an image of pure speckle is an exponentially decreasing function (Ref. 10). The mean (μ) and the standard deviation (σ) of this pdf are identical and thus the coefficient of variation $C_v = \sigma/\mu$ is equal to unity. C_v represents a certain measure of the image homogeneity and can be used as a textural index. However, the convolution of single looks (three looks in SAR.PRI) changes the exponentially decreasing pdf to a Gamma function (Ref. 14)(see fig. 3). According to

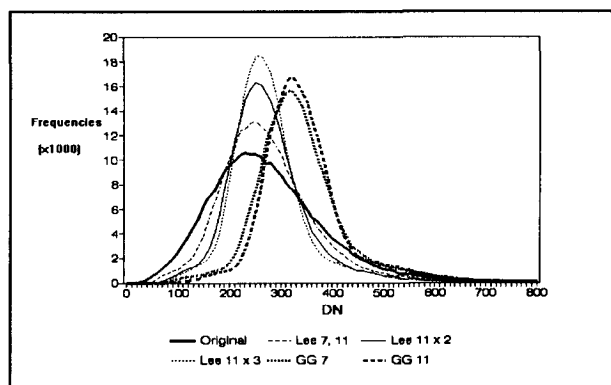


Fig. 3.- The effect of filtering on the PDF of test site 1 image.

Loudon's definition (Ref. 10) a multiplicative speckle model is assumed. Although strictly speaking it is only valid in "flat" areas with variations of the phase lower than 2π where small reflectors are not individualized by radar resolution (Ref. 13). The resampling method used causes a slight correlation between neighbor pixels. Thus, the noise of one pixel is not independent from that of its neighbors and then the speckle is a nonwhite noise (Ref. 7). However, Pearson correlation coefficient values greater than 0.5 only occur between the nearest neighbors. The process of forming the three look images can explain greater correlation values in the cross-track than in the long-track direction.

3. SOME METHODS TO REDUCE SPECKLE

The speckle is a random variable that modulates textural and structural information of radar images (Ref. 5). From the probability theory the sum of M identically distributed uncorrelated random variables has a mean value that is M times the mean of one component and a standard deviation that is \sqrt{M} times the standard deviation of one component (Ref. 3). Thus, an incoherent or intensity based average of M radar images redu-

ces C_v in a \sqrt{M} factor and so the speckle effect. Nevertheless this averaging method can only be used when several images of the same scene are available (i.e. in a multitemporal image composition). However very often it is necessary to process a unique scene image and then only digital filters can be used to improve SNR and reduce the speckle effect. The unknowning of frequency distribution are a hindrance to use Fourier techniques, tough some intents have been carried out assuming a low noise level (Ref. 1). In the direct space lowpass, median, adaptive filters (Lee, Frost, Kuan, Li, GGMAP) and geometric filters (Crimmins) are some digital filters used. Fig.4 compares the original image with the results of median 3x3, Lee's 11x11 and GGMAP 7x7 filters.

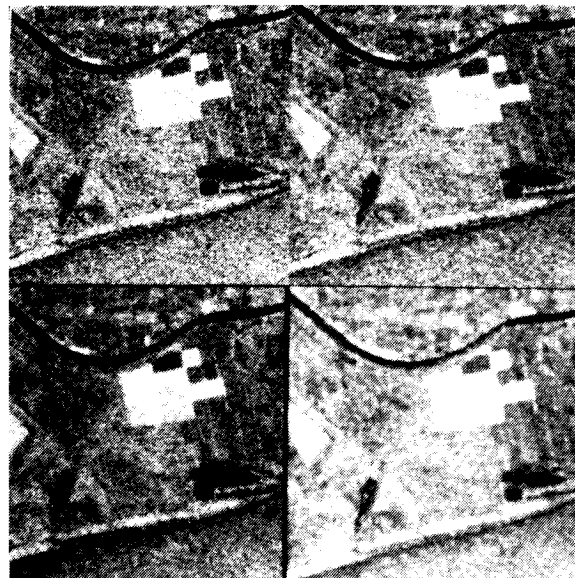


Fig. 4.- A: original image; B: efect of the median filter with a window size 3x3 pixels; C: efect of Lee's filter (11x11); D: efect of GGMAP filter (7x7).

4. BRIEF DESCRIPTION OF THE TESTED FILTERS

The **median filter** (Ref. 12) replaces the central pixel of a convolution matrix with the median value of the pixels inside this matrix. It is a nonlinear filter that cannot be implemented in the Fourier space and therefore it is difficult to be analyzed in the sense of how affects the frequency spectrum. However, there is known that preserve edges and removes impulsion noise. Convolution windows greater than 5 by 5 pixels produce a blurred effect and must be avoided.

The **Lee's filter** (Ref. 6) is an adaptive linear filter based on a zero mean additive uncorrelated noise model. Given an observed signal I , the estimated of the original sig-

nal O must minimize the mean square error. Lee's filter can be described as a weighted sum of the observed and the mean neighborhood pixel values.

$$O = I \cdot W + \bar{I} \cdot (1-W)$$

being

$$W = 1 - \frac{C_n^2}{C_i^2}$$

The weight (W) is very sensitive to the ratio between the variation coefficients of the speckle (C_n) and the intensity (C_i). C_n can be estimated from textureless "flat" zones or analytically computed (Ref. 15).

GGMAP (Ref. 9) is a maximum *a posteriori* filter (Ref. 4) based on a Gamma pdf for both reflectance and speckle. It maximizes the pdf to obtain an estimate output O reflectance given an observed intensity I.

$$O_{map} = \frac{(\alpha - L - 1)\bar{I} + \sqrt{(\bar{I}^2(\alpha - L - 1)^2 + 4\alpha L\bar{I})}}{2\alpha}$$

where $\alpha : 1/C_i^2$ and L : number of looks. Fig. 5 shows the effect of different window sizes of GGMAP filter and how brightness areas are slightly enlarged.

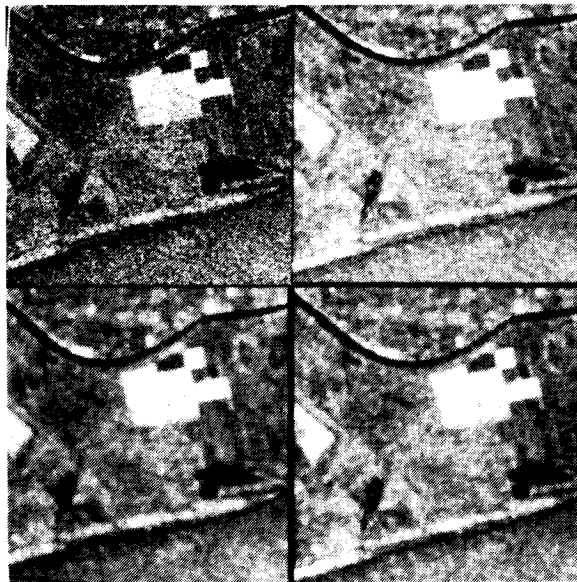


Fig. 5.- The effect of several window sizes for the GGMAP filter. A:original image; B: 7x7; C: 11x11; D: 9x9 pixels.

Crimmins' filter (Ref. 2) is a geometric filter based on the "eight hull algorithm" originally used to enhance

binary images. The objective of this filter is to iteratively smooth the peak signal of any object in the image.

5. WINDOW SIZE ESTIMATE

When applying filters by convolution like Lee's filter it is very important to estimate the best window convolution size, tough occasionally variable window sizes have been used adapted to image variability (Ref. 7).

The study of first order statistics can help to find the

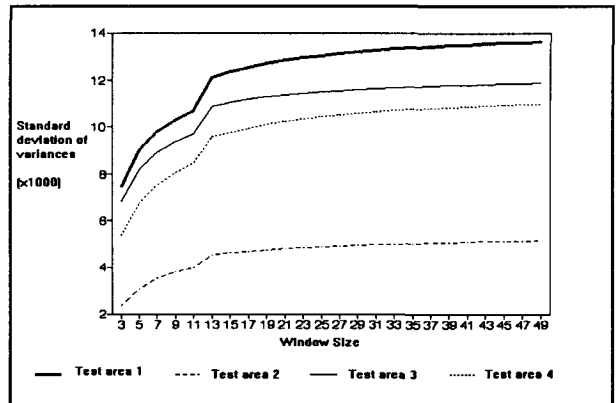


Fig. 6.- Standard deviation of variances in flat areas plotted against window size.

ideal window size related to the speckle correlation width. Four sea test sites have been selected as an approximation to near flat areas. The variances of 121 homogeneously distributed windows have been calculated with window sizes ranging from 3x3 to 49x49 pixels. Fig. 6 shows the standard deviation of variances against the window size. A discontinuity step clearly divides these curves into two zones. The left one can be considered as the noise dominated area (between 3-11) while the right one will be the textural information dominated segment (above 13). This agrees with Lopes (Ref. 9) bearing in mind the slight correlation between nearest neighbors. Fig. 7 is an example of the effect of different window size of Lee's filter.

6. QUALITATIVE SNR ESTIMATORS

The unknowing of frequency distribution makes difficult to find mathematical expression that can quantify the SNR and the success in filtering the speckle. However some qualitative estimators of goodness filtering have been defined and we have tested four of them.

1. **Coefficient of variation** can be used for local and global estimating the speckle reduction. Fig. 8 shows as the C_v decreases for window sizes above 13x13 pixels in Lee and GGMAP filtered images.

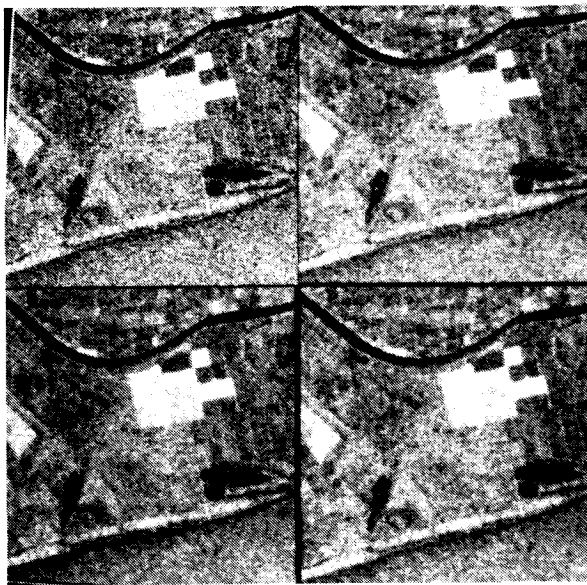


Fig. 7.- The effect of Lee's filter using different window sizes (original, 7x7, 11x11, 9x9).

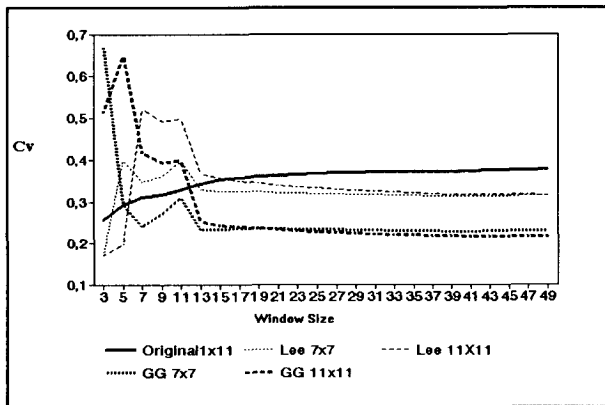


Fig. 8.- Coefficient of variation values against the window size for different filters.

2. The random nature of the speckle will increase the local variance of the original profiles. A comparative **profile analysis** between the filtered and the original images must show a slight modification of the local minimum/maximum preserving the shape of the original profile. Figs. 9 and 10 show an original profile and the effect of GGMAP (7x7) filter.

3. It's well known that when increases the number of looks decreases the speckle noise. Similarly, the same result can be obtained averaging several images of the same scene. Thus it is expected that the improvement of SNR will cause a shift from the original Gamma pdf

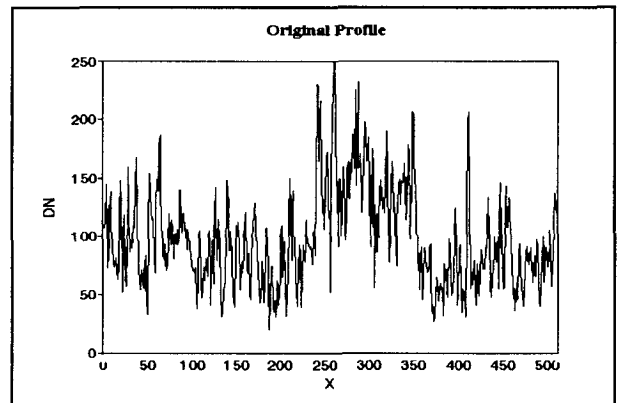


Fig. 9.- Original profile test site 1 (row 200)

to a Gaussian pdf. This **postfiltered pdf gaussianity** can be observed in fig 3 and can be used as an estimator of filtering goodness.

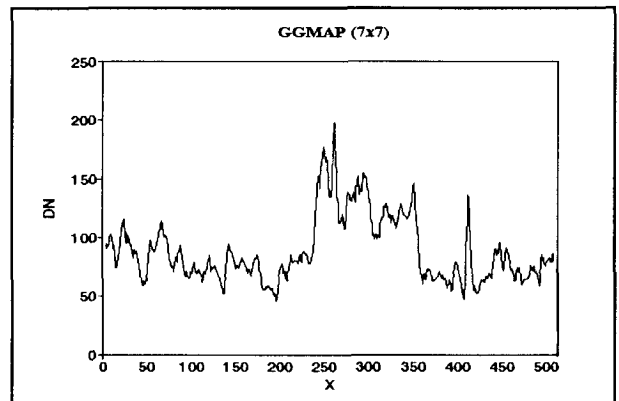


Fig. 10.- The same profile of fig. 9, after image filtering with GGMAP (7x7).

4. Also the effect of noise reduction must be detected when using any **edge detector** algorithm over a filtered image.

7. SEGMENTATION

The previous results suggest that Lee's filter may be one of the best for the speckle reduction. The linearity of the filter allows recursive iterations, but more than threeiterations can result in lost of the fine structural details (fig. 11). However, despite the goodness of these processes the SNR is still too low and segmentation is not yet a straightforward process as in optical images.

An **edge preserving smoothing** algorithm has been tested on the filtered images, but the algorithm after

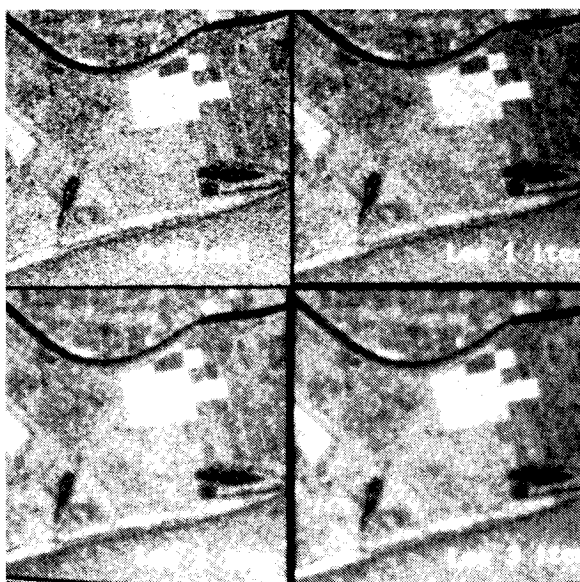


Fig. 11.- The effect of different iterations of the Lee's filter.

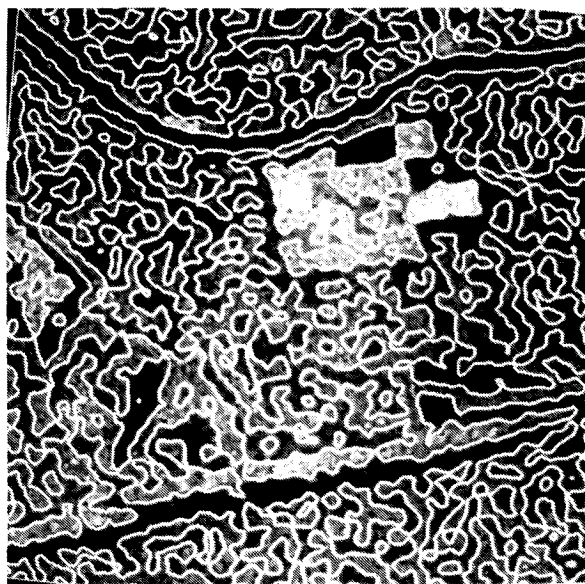


Fig. 12.- The effect of segmentation of SAR image of test site 1.

recursive iterations does not rise to steady state and the image is progressively degraded. Thus we have used the EPS algorithm only with three or five iterations and then the images have been processed with edge detector to individualize homogeneous patches.

The EPS filter calculates the minimum variance around a given pixel in eight directions. The pixel value is substituted by the mean value of the pixels in the direction of the minimum variance (Ref. 11).

A zero crossing algorithm has been used as an edge detector after smoothing. This algorithm is based on the second derivative application. A pixel is marked as an edge when a change of the sign of the second derivative occurs (fig. 15). It can be carried out using Fourier transform and therefore its efficiency is increased.

8. CONCLUSION

The unknowing of frequency distribution spectrum makes difficult the SNR optimization of SAR ERS-1 images and therefore textural segmentation. For these reasons we are working on optics simulation of the process of image formation. It will bring insight on the definition of SNR and the speckle spectrum frequency. That will allow to quantify the effects of different filters.

REFERENCES

1. Andrews H C & Hunt B R 1977, Digital Image Restoration. Englewood Cliffs, New Jersey: Prentice Hall.
2. Crimmins T R 1985, Geometric filter for speckle reduction, *Applied Optics*, 24, 10, 1438-1443.
3. Goodman J W 1976, Some fundamental properties of speckle, *J.O.S.A.*, 66,1145-1150.
4. Hunt B R 1977, Bayesian methods in nonlinear digital image restoration, *IEEE Transactions on Computers*, C-26,219-229.
5. Leberl F W 1990, Radargrammetric image processing, Artech House.
6. Lee J S 1981, Refined filtering of image noise using local statistics, *Comput. Graph. Image Proc.*,15, 380-389.
7. Li Ch 1988, Two adaptive filters for speckle reduction in SAR images by using the variance ratio, *Int. J. Remote Sensing*, 9, 641-653.
8. Lopes A , Touzi R & Nezry E 1990, Adaptive speckle filters and scene heterogeneity *IEEE Transactions on Geoscience and remote sensing*, 28, 992-1000.
9. Lopes A, Nezry E, Touzi R & Laur H 1993, Structure detection and statistical adaptive speckle filtering in SAR images, *Int. J. Remote Sensing*, 14, 1735-1758.

10. Loudon R 1973, The quantum theory of light, *Clarendon Press. Oxford University Press*. Oxford, 82-119.
11. Nagao M & Matsuyama T 1979, Edge Preserving Smoothing, *Comp. Graph. Image Proc.*, 15.
12. Scollar I et al. 1984, Image enhancement using the median and interquartile distance, *Comp. Graph. Image Proc.*, 25.
13. Tur M, Chin K C & Goodman J W 1982, When is speckle noise multiplicative?, *Applied Optics*, 21, 1157-1159.
14. Ulaby F T, Kouyate F, Brisco B & Lee Williams T H 1986, Textural information in SAR images, *IEEE Transactions on Geoscience and remote sensing*, GE, 24, 235-245.
15. Zelenka J 1976, Comparision of continuous and discrete mixed-integrator processors, *Journal of Optical Society America*, A, 66, 1295-1304.

PARTICIPANTS



LIST OF PARTICIPANTS

509

ACHTHOVEN Viana
LABORATORIUM VOOR REGIONALE GEOGRAFIE
EN LANDSCHAPSKUNDE
KRIJGSLAAN 281 S 8 A1
B-9000
GENT
BELGIUM

Tél:32 92 64 47 09
Fax:32 92 64 49 85

ALBANI M.
ESRIN/DEX
VIA GALILEO GALILEI
C.P. 64
I-00044
FRASCATI
ITALY

Tél:39 694 180 415
Fax:39 694 180 655

ALLAN T.D.
SATELLITE OBSERVING SYSTEMS
15 CHURCH STREET

GU7 1EL SURREY
GODALMING
U.K.

Tél:44 483 421 213
Fax:44 483 428 691

ALLEYN S.
ESRIN/DEX
VIA GALILEO GALILEI
C.P. 64
I-00044
FRASCATI
ITALY

Tél:39 694 180 1
Fax:39 694 180 361

ALLINEY F.
CONSORZIO SPAZIO AMBIENTE

VIA SACCOMURO 24
I-00131
ROMA
ITALY

Tél:39 6 41 51 41 25
Fax:39 6 41 91 76 5-

ALTIERI F.
TESIS S.P.A.
VIA S. BARGELLINI, 4

ROMA
ITALY

Tél:39 6 43 93 485
Fax:39 6 43 96 685

AMOR J-M.
MINAS DE ALMADEN Y ARRAYANES, S.A.
DPTO. DE GEOLOGIA Y TELEDETECCION
CERCDO DE SAN TEODORO S/N
E-13400
ALMADEN
SPAIN

Tél:34 26 71 04 00
Fax:34 26 71 04 37

ARGENTIERI A.
ESRIN/DEX
VIA GALILEO GALILEI
C.P. 64
I-00044
FRASCATI
ITALY

Tél:39 694 180 1
Fax:39 694 180 361

ASCHBACHER J.
JRC
IRSA-MTV
TP.440
I-21020 (VA)
ISPRRA
ITALY

Tél:39 332 785 545
Fax:39 332 789 073

ATTEMA E.
ESTEC
OEE/NWA
POSTBUS 299
NL-2200 AG
NOORDWIJK
NETHERLANDS

Tél:31 17 19 844 61
Fax:31 17 19 174 00

BADJI M.
FACULTE DES SCIENCES AGRONOMIQUES
UNITE D'HYDRAULIQUE AGRICOLE
2, PASSAGE DES DEPORTES
B-5030
GEMBLOUX
BELGIUM

Tél:(32) 81 622 190
Fax:(32) 81 622 181

BANNINGER C.
JOANNEUM RESEARCH
INST. FOR DIGITAL IMAGE PROCESSING
WASTIANGASSE 6
A-8010
GRAZ
AUSTRIA

Tél:43 316 8020 735
Fax:43 316 8020 720

BARCO R.
INISEL ESPACIO
S. OBSERVACIONALES
AVDA. BURGOS, 8 bis 3, APDO. 2144
E-28036
MADRID
SPAIN

Tél:34 13 96 33 11
Fax:34 13 96 32 22

BEAUDOIN A.
CEMAGREF-ENGREF
LABORATOIRE COMMUN DE TELEDETECTION
B.P. 5095
34033
MONTPELLIER Cedex 1
FRANCE

Tél:67 04 71 14
Fax:67 04 71 01

BIASUTTI R.
EURIMAGE
TECHNICAL DEVELOPMENT
VIA GALILEO GALILEI, 5
I-00044
FRASCATI
ITALY

Tél:39 694 180 657
Fax:39 694 180 510

BIDLOT J.R.
M.U.M.M
100 GULLEDELLE
B-1200
BRUXELLES
BELGIUM

Tél:32 2 773 21 31
Fax:32 2 770 69 72

BIEGERT E.K.
PECTEN INTERNATIONAL CO.
WOODCREEK 1328
200 NORTH DAIRY ASHFORD
TX. 77079
HOUSTON
USA

Tél:713 544 4690
Fax:713 544 4873

BLANC F.
CLS SERVICE ARGOS
SPACE OCEANOGRAPHY GROUP
4, AV. EDOUARD BELIN
31055
TOULOUSE CEDEX
FRANCE

Tél:33 61 39 47 81
Fax:33 61 75 10 14

BOALCH C.
BNSC
BRIDGE PLACE
88/89 ECCLESTON SQUARE
SW1V 1PT
LONDON
U.K.

Tél:44 71 215 0810
Fax:44 71 821 5387

BOSWELL M.
DEFENCE RESEARCH AGENCY
R16 BUILDING
HANTS.
GU14 6TD
FARNBOROUGH
U.K.

Tél:44 252 393 900
Fax:44 252 515 518

BROOKER G.
ESTEC
OEE/NWO
POSTBUS 299
NL-2200 AG
NOORDWIJK
NETHERLANDS

Tél:31 17 19 83 611
Fax:31 17 19 17 400

BRUENING C.
UNIVERSITY OF HAMBURG
INSTITUTE OF OCEANOGRAPHY
TROPLowitzSTR. 7
D-22529
HAMBURG
GERMANY

Tél:49 40 41 23 54 36
Fax:49 40 41 23 57 13

BRUZZI S.
EUROPEAN SPACE AGENCY
D/OEE
8-10 RUE MARIO NIKIS
F-75738 CEDEX-
PARIS
FRANCE

Tél:42 73 72 81
Fax:42 73 77 74

BUCKLEY C.
EURIMAGE
PUBLIC RELATIONS MANAGER
VIA D'ONOFRIO 212
I-00184
ROMA
ITALY

Tél:39 640 694 216
Fax:39 640 694 232

BUNNIK N.J.J.
NETHERLANDS REMOTE SENSING BOARD

P.O. BOX 5023
NL-2600 GA
DELF
NETHERLANDS

Tél:31 15 69 11 11
Fax:31 15 61 89 62

CALABRESI G.
ESRIN/DEX
VIA GALILEO GALILEI
C.P. 64
I-00044
FRASCATI
ITALY

Tél:39 694 180 1
Fax:39 694 180 655

CANTONI M.
TELESPAZIO

VIA TIBURTINA, 965
I-00159
ROMA
ITALY

Tél:
Fax:39 6 40 796 202

CARL S.
DEPT. MATHEMATICS, STATISTICS & D.P.
TECHNICAL UNIVERSITY OF MUNICH

D-85350
FREISING
GERMANY

Tél:49 81 61 71 4040
Fax:49 81 61 71 4409

CARRETERO J.C.
PUERTOS DEL ESTADO
CLIMA MARITIMO
AVDA. PARTENON, 10
E-28042
MADRID
SPAIN

Tél:34 15 24 55 68
Fax:34 15 24 55 06

CASTERAD A.
SERVICIO DE INVESTIGACION AGRARIA
UNIDAD DE SUELOS Y RIEGOS
P.O. BOX 727
E-50080
ZARAGOZA
SPAIN

Tél:34 76 57 64 11
Fax:34 76 57 55 01

CHARUPPAT THONGCHAI
FOREST RESOURCES ANALYSES GROUP
TECHNICAL FORESTRY GROUP
PHAHOLYOTHIN ROAD
10900
BANGKOK
THAILAND

Tél:66 2
Fax:66 2 579 8611

CHATENIER M.
CAP GEMINI SESA
VIA DEI BERIO, 91

I-00155
ROME
ITALY

Tél:39 6 225 93514
Fax:39 6 225 1547

CIOLKOSZ A.
INSTITUTE OF GEODESY & CARTOGRAPHY
REMOTE SENSING CENTRE
UL. JASNA 2/4
00950
WARSAW
POLAND

Tél:4822277613
Fax:4822270328

CLARK C.
UNIVERSITY OF SHEFFIELD
DEPARTMENT OF GEOGRAPHY
WINTER STREET
S10 2TN
SHEFFIELD
U.K.

Tél:44 742 824 744
Fax:44 742 797 912

COMHAIRE A.-L.
LABORATOIRE DE GEOMORPHOLOGIE
UNIVERSITE DE LIEGE
PLACE DU 20 AOUT, 7
B-4000
LIEGE
BELGIUM

Tél:32 41 66 53 35
Fax:32 41 66 57 22

CORVES C.
UNIVERSITY OF EDINBURGH
DEPARTMENT OF GEOGRAPHY
DRUMMOND STREET
EH8 9XP
EDINBURGH
U.K.

Tél:44 31 650 2523
Fax:44 31 650 2524

D'ELIA S.
ESRIN/DEX
VIA GALILEO GALILEI
C.P. 64
I-00044
FRASCATI
ITALY

Tél:39 694 180 1
Fax:39 694 180 361

DABROWSKA-ZIELINSKA K.
INSTITUTE OF GEODESY & CARTOGRAPHY
REMOTE SENSING CENTRE
UL. JASNA 2/4
PL-00950
WARSAW
POLAND

Tél:4822270328
Fax:4822270328

DAVISON M.
VEGA SPACE SYSTEMS ENG. LTD.

ARDEN GROVE
AL5 4SJ HERTS.
HARPENDEN
U.K.

Tél:44 582 461 678
Fax:44 582 461 773

DE LA CRUZ A.
INFOCARTE S.A.
NUNEZ DE BALBOA, 115
2e J
E-28006
MADRID
SPAIN

Tél:34 15 64 13 56
Fax:34 15 63 11 47

DE ROOVER B.
UNIVERSITY OF GENT
LABORATORY OF REMOTE SENSING &
FOREST MANAGEMENT
COUPURE LINKS 653
B-9000 GENT
BELGIUM

Tél:32 92 64 61 09/8
Fax:32 92 64 62 40

DELPONT G.
BRGM
DEPT. TELEDETECTION
B.P. 6009
F-45060
ORLEANS CEDEX 2
FRANCE

Tél:33 38 64 34 34
Fax:33 38 64 35 18

DENOIRE B.J.
IBERSAT S.A.
CALLE ARAQUIL, 11

E-28023
MADRID
SPAIN

Tél:34 13 57 18 60
Fax:34 13 57 31 92

DESNOS Y-L.
ESTEC
XRI
POSTBUS 299
NL-2200 AG
NOORDWIJK
NETHERLANDS

Tél:31 17 19 849 27
Fax:31 17 19 174 00

DILLON M.
ESYS LTD.
BERKELEY HOUSE
LONDON SQUARE, CROSS LANES
SURREY GU1 1UE
GUILDFORD
U.K.

Tél:44 483 304 545
Fax:44 483 303 878

DOHERTY M.
ESRIN/DPE
VIA GALILEO GALILEI
C.P. 64
I-00044
FRASCATI
ITALY

Tél:39 694 180 1
Fax:39 694 180 361

DONADIO A.I.
ESPELSA
CALLE ACANTO 22 - 10

E-28045
MADRID
SPAIN

Tél:34 15 27 02 15
Fax:34 15 30 10 25

DREISER U.
WELTRAUM-INSTITUT BERLIN GmbH
LASSENSTR. 11-15
POSTFACH 33 06 69
D-14193
BERLIN
GERMANY

Tél:49 30 820 910
Fax:49 30 826 6101

DUCHOSOIS G.
EUROPEAN SPACE AGENCY
D/DEE
8-10 RUE MARIO NIKIS
F-75738 CEDEX
PARIS
FRANCE

Tél:42 73 72 84
Fax:42 73 76 74

EDWARDS A.
ESRIN/HELP DESK
VIA GALILEO GALILEI
C.P. 64
I-00044
FRASCATI
ITALY

Tél:39 694 180 1
Fax:39 694 180 361

ENGELIS T.
HELLENIC NATIONAL SPACE COMMITTEE
NATIONAL OBSERVATORY OF ATHENS
NCRS DEMOKRITOS
GR-11810
ATHENS
GREECE

Tél:30 1 346 4161
Fax:30 1 342 1019

ESPINO M.
LABORATORI D'ENGINYERIA MARITIMA
UNIVERSITAT POLITECNICA DE CATALUNYA
c/GRAN CAPITA S/N, MODUL D1
E-08034
BARCELONA
SPAIN

Tél:34 3 401 64 71
Fax:34 3 401 73 57

ESTABAN M.
PUERTOS DEL ESTADO
AVENIDA DEL PARTENON, 10
CAMPO DE LAS NACIONES
E-28042
MADRID
SPAIN

Tél:34 15 24 55 00
Fax:34 15 24 55 02/06

FEA M.
ESRIN
VIA GALILEO GALILEI
C.P. 64
I-00044
FRASCATI
ITALY

Tél:39 694 180 1
Fax:39 694 180 361

FELLAH K.
SERTIT/ENSPS
PARC D'INNOVATION
BOULEVARD SEBASTIEN BRANT
F-67400
ILLKIRCH
FRANCE

Tél:33 88 65 50 00
Fax:33 88 65 52 49

FERNANDEZ P.
INSTITUTO NACIONAL DE METEOROLOGIA
CAMINO DE LAS MORERAS S/N
E-28040
MADRID
SPAIN

Tél:34 15 81 96 68
Fax:34 15 81 98 46

FIGA J.
LABORATORI D'ENGINYERIA MARITIMA
UNIVERSITAT POLITECNICA DE CATALUNYA
c/GRAN CAPITA S/N, MODUL D1
E-08034
BARCELONA
SPAIN

Tél:34 3 401 64 71
Fax:34 3 401 73 57

FISSE G.
CISI INGENIERIE
OBSERVATION & RECONNAISSANCE
PAR SATELLITES (13 RUE VILLET)
B.P. 4042
31029 TOULOUSE CEDEX
FRANCE

Tél:33 61 17 66 66
Fax:33 61 54 13 39

FREMBGEN U.
DORNIER GmbH
SATELLITE SYSTEMS, EARTH OBSERVATION
POSTFACH 1420
D-88039
FRIEDRICHSHAFEN
GERMANY

Tél:49 7545 85732
Fax:49 7545 82206

FRIEAUFF D.
DORNIER GmbH
POSTFACH 1420
D-88039
FRIEDRICHSHAFEN
GERMANY

Tél:49 7545 85732
Fax:49 7545 82206

FUCHS U.
KAYSER-THREDE
DEPT. OF EARTH OBSERVATION
WOLFRATSHAUSER STR. 46
D-81379
MUNICH
GERMANY

Tél:49 89 724 95 146
Fax:49 89 724 95 291

FYALL J.
ESRIN/HELP DESK
VIA GALILEO GALILEI
C.P. 64
I-00044
FRASCATI
ITALY

Tél:39 694 180 1
Fax:39 694 180 361

GABRIEL D.
DORNIER GMBH
P.O. BOX 1420
ELECTRONIC SYSTEMS IMAGE PROCESSING
D-7990
FRIEDRICHSHAFEN 1
GERMANY

Tél:49 75 45 885 05
Fax:49 75 45 881 08

GARCIA M.A.
LABORATORI D'ENGINYERIA MARITIMA
UNIVERSITAT POLITECNICA DE CATALUNYA
c/GRAN CAPITA S/N, MODUL D1
E-08034
BARCELONA
SPAIN

Tél:34 3 401 64 71
Fax:34 3 401 73 57

GARGIR N.
SCOT CONSEIL
PARC DU CANAL
1 RUE HERMES
F-31520
RAMONVILLE SAINT AGNE
FRANCE

Tél:33 61 39 46 00
Fax:33 61 39 46 10

GEILE W.
MCR LABORATORY
UNIVERSITY OF BASEL
SPALENRING 145
CH-4055
BASEL
SWITZERLAND

Tél:41 61 272 64 80
Fax:41 61 272 69 23

GOMEZ V.
C.D.T.I.
PO. DE LA CASTELLANA, 141

E-28046
MADRID
SPAIN

Tél:3415815541
Fax:3415815584

GONZALEZ ALONSO F.
INIA-MAPA
CTRA. DE LA CORUNA, KM. 7
APARTADO 8111
E-28035
MADRID
SPAIN

Tél:34 13 47 68 28
Fax:

GONZALEZ-BARBUDO A.
C.D.T.I.
PO. DE LA CASTELLANA, 141

E-28046
MADRID
SPAIN

Tél:3415815541
Fax:3415815584

GRONVALL H.
FINNISH INSTITUTE OF MARINE RESEARCH
ICE SERVICE
P.O. BOX 166
SF-00141
HELSINKI
FINLAND

Tél:358 0 635 092
Fax:358 0 174 573

GUERRE L-F.
SPOT IMAGE

B.P. 4359
F-31030
TOULOUSE CEDEX
FRANCE

Tél:
Fax:61 28 18 59

GUIGNARD J.P.
ESRIN/DPE
VIA GALILEO GALILEI
C.P. 64
I-00044
FRASCATI
ITALY

Tél:39 694 180 722
Fax:39 694 180 321

GUYENNE D.
ESTEC
EPD
POSTBUS 299
NL-2200 AG
NOORDWIJK
NETHERLANDS

Tél:31 17 19 83 403
Fax:31 17 19 85 433

HABFAST C.
EUROPEAN SPACE AGENCY
CAB/PR
8-10 RUE MARIO NIKIS
F-75738 CEDEX
PARIS
FRANCE

Tél:42 73 74 16
Fax:42 73 75 60

HAJJI H.
METEOMER

R.N.7, QUARTIER LES BARESTES
F-83480
PUGET SUR ARGENS
FRANCE

Tél:94 45 66 11
Fax:94 45 68 23

HAKANSSON B.
SMHI
RESEARCH SECTION

S-601 76
NORRKOPING
SWEDEN

Tél:46 11 15 83 85
Fax:46 11 17 02 07/08

HALLIKAINEN M.
HELSINKI UNIVERSITY OF TECHNOLOGY
LABORATORY OF SPACE TECHNOLOGY
OTAKAARI 5A
SF-02150
ESPPO
FINLAND

Tél:35804512371
Fax:3580460224

HARMS J.
SCOT CONSEIL
PARC DU CANAL
1 RUE HERMES
F-31520
RAMONVILLE SAINT AGNE
FRANCE

Tél:33 61 39 46 00
Fax:33 61 39 46 10

HERLAND E.-A.
TECHNICAL RESEARCH CENTRE OF FINLAND
INSTRUMENT LABORATORY, SECTION R-S
METALLIMIEHENKUJA 10, P.O.BOX 13031 VTT
SF 02100
ESPPO
FINLAND

Tél:358 0 456 1
Fax:358 0 456 4496

HERRERO J.
SERVICIO DE INVESTIGACION AGRARIA
UNIDAD DE SUELOS Y RIEGOS
P.O. BOX 727
E-50080
ZARAGOZA
SPAIN

Tél:34 76 57 64 11
Fax:34 76 57 55 01

HOOD V.
EUROPEAN SPACE AGENCY
ISP/I
8-10 RUE MARIO NIKIS
F-75738 CEDEX
PARIS
FRANCE

Tél:42 73 74 43
Fax:42 73 75 60

HOWES S.
ESYS LTD.
BERKELEY HOUSE
LONDON SQUARE, CROSS LANES
SURREY GU1 1UE
GUILDFORD
U.K.

Tél:44 483 304 545
Fax:44 483 303 878

INGMANN P.
ESTEC
OEE/VRO
POSTBUS 299
NL-2200 AG
NOORDWIJK
NETHERLANDS

Tél:31 17 19 844 59
Fax:31 17 19 174 00

IPPOLITO E.
ESRIN/HELP DESK
VIA GALILEO GALILEI
C.P. 64
I-00044
FRASCATI
ITALY

Tél:39 694 180 1
Fax:39 694 180 361

JENSEN W.
ESRIN/DEX
VIA GALILEO GALILEI
C.P. 64
I-00044
FRASCATI
ITALY

Tél:39 694 180 602
Fax:39 694 180 361

JOHANNESSEN J.A.
ESTEC
OEE/VRO
POSTBUS 299
NL-2200 AG
NOORDWIJK
NETHERLANDS

Tél:31 17 19 859 59
Fax:31 17 19 174 00

KANNEN A.
DEUTSCHE PROJECT UNION GmbH

TECHNOLOGIE UND GEWERBEPARK
D-16225
EBERSWALDE-FINOW
GERMANY

Tél:49 3334 59253
Fax:49 3334 59245

KING Ch.
BRGM
DEPARTEMENT TELEDETECTION
B.P. 6009
F-45060 CEDEX 2
ORLEANS-LA-SOURCE
FRANCE

Tél:33 38 64 34 34
Fax:33 38 64 35 18/31 64

KIRCHHOF W.
DLR
NE-OE-FO
POSTFACH 11 16
D-82230
WESSLING
GERMANY

Tél:49 81 53 28 877
Fax:49 81 53 28 1349

KLAEDTKE Dr.
INSTITUTE OF NAVIGATION
UNIVERSITY OF STUTTGART
KEPLERSTRASSE 11
D-70174
STUTTGART
GERMANY

Tél:49 711 121 3412
Fax:49 711 121 2755

KOHL H.
CEE/JRC
INST. FOR REMOTE SENSING APPLICATIONS
TP.441
I-21020
ISPRA
ITALY

Tél:39 332 785 449
Fax:39 332 789 074

KOHLHAMMER G.
ESRIN/DEX
VIA GALILEO GALILEI
C.P. 64
I-00044
FRASCATI
ITALY

Tél:39 694 180 1
Fax:39 694 180 361

KRAEMER O.
GEOSCAN GmbH

GELBER STERN 1
D-31134
HILDESHEIM
GERMANY

Tél:49 5121 15 09 0
Fax:49 5121 76 90 15

LANAJA J-M.
ESCUELA TECNICA SUPERIOR DE INGENIEROS
INDUSTRIALES
LAGOAS-MARCOSENDE No 9, APARTADO 62
E-36200
VIGO
SPAIN

Tél:34 86 812 205
Fax:34 86 812 201

LANDMARK F.
TROMSOE SATELLITE STATION

N-9005
TROMSOE

Tél:47 77 68 48 17
Fax:47 77 65 78 68

LASNIER P.
METEOMER
QUARTIER LES BARETES
R.N. 7
F-83480
PUGET-SUR-ARGENS
FRANCE

Tél:3394456611
Fax:3944566823

LEHNER S.
DLR
WT-DA-FE
POSTFACH 11 16
D-82230
OBERPFAFFENHOFEN
GERMANY

Tél:49 81 53 28 28 95
Fax:49 81 53 28 28 1445

LICHTENEGGER J.
ESRIN/DEX
VIA GALILEO GALILEI
C.P. 64
I-00044
FRASCATI
ITALY

Tél:39 694 180 1
Fax:39 694 180 361

LOEFFLER E.
ESRIN/PR
VIA GALILEO GALILEI
C.P. 64
I-00044
FRASCATI
ITALY

Tél:39 694 180 1
Fax:39 694 180 257

LOHMANN P.
GEOSCAN GmbH
GELBER STERN 1
D-31134
HILDESHEIM
GERMANY

Tél:49 5121 15 09 0
Fax:49 5121 15 09 15

LOIZZO R.
A.S.I.
CGS
LOCALITA' TERLECCHIA
P.O. BOX 155
75100 MATERA
ITALY

Tél:39 835 377 201
Fax:39 835 339 005

LOMBARDI F.
EURIMAGE
DIRECTOR OF SALES
VIA D'ONOFRIO 212
I-00184
ROMA
ITALY

Tél:39 640 694 237
Fax:39 640 694 232

LOPEZ EPIFANIO D.
UNIVERSITY OF THE PHILIPPINES
DEPT. OF GEODETIC ENGINEERING

DILIMAN
QUESON CITY
PHILIPPINES

Tél:63 2 97 6061 x.5534
Fax:63 2 99 3144

LOUET J.
ESTEC
OEE/NW
POSTBUS 299
NL-2200 AG
NOORDWIJK
NETHERLANDS

Tél:31 17 19 844 55
Fax:31 17 19 195 02

LUCARELLI F.
UNIVERSITA DI NAPOLI
FACOLTA DI ECONOMIA E COMMERCIO
VIA ONTELLA
MONTE S. ANGELO
NAPOLI 80126
ITALY

Tél:39 81 675 097
Fax:39 81 675 094

MANSO M.
INSTITUTO NACIONAL DE METEOROLOGIA
CAMINO DE LAS MORERAS S/N

E-28040
MADRID
SPAIN

Tél:34 15 81 98 65
Fax:34 15 81 98 46

MARANESI M.
EURIMAGE
MANAGING DIRECTOR
VIA D'ONOFRIO 212
I-00184
ROMA
ITALY

Tél:39 640 694 237
Fax:39 640 694 232

MARELLI L.
ESRIN/DPE
VIA GALILEO GALILEI
C.P. 64
I-00044
FRASCATI
ITALY

Tél:39 694 180 388
Fax:39 694 180 361

MARINELLI L.
GEOIMAGE
ESPACES DE SOPHIA, BAT. M9
80 RUE DES LUCIOLES
F-06560
VALBONNE
FRANCE

Tél:33 93 00 40 00
Fax:33 93 00 40 01

MARTIN Ph.
EUROPEAN SPACE AGENCY
D/OEE
8-10 RUE MARIO NIKIS
F-75738 CEDEX
PARIS
FRANCE

Tél:42 73 76 57
Fax:42 73 76 74

MARTINEZ A.
INISEL ESPACIO
S. OBSERVACIONALES
AVDA. BURGOS, 8 bis 3, APDO. 2144
E-28036
MADRID
SPAIN

Tél:34 13 96 33 11
Fax:34 13 96 32 22

MASON D.C.
UNIVERSITY OF READING
DEPARTMENT OF GEOGRAPHY
WHITEKNIGHTS, PO BOX 227
RG6 2AB
READING
U.K.

Tél:44 734 318 743
Fax:44 734 755 865

MASSONNET D.
CNES
RADAR SYSTEMS PERFORMANCES DEPT.
18 AVENUE EDOUARD BELIN
F-31055
TOULOUSE CEDEX
FRANCE

Tél:61 27 34 18
Fax:61 27 31 67

MATTHEWS J.
SCHOOL OF OCEAN SCIENCES
UNIVERSITY OF WALES
MENAI BRIDGE
LL59 5EY
GWYNEDD
U.K.

Tél:44 248 382 586
Fax:44 248 716 367

MAUSER W.
UNIVERSITY OF MUNICH
INSTITUT FUER GEOGRAPHIE
LUISENSTRASSE 37
D-80333
MUNCHEN
GERMANY

Tél:49895203322 OR 320
Fax:49895203321

MEHL H.
LUDWIG-MAXIMILIANS-UNIVERSITY
AGF
LUISENSTRASSE 37
D-80333
MUNICH
GERMANY

Tél:49 89 520 34 25
Fax:49 89 520 33 93

MELIS M.
SPACE ENGINEERING S.r.l.
VIA DEI BERIO, 91

I-00155
ROMA
ITALY

Tél:39 6 225 95227
Fax:39 6 769 015

MILES M.
NANSEN ENVIRONMENTAL REMOTE
SENSING CENTRE
EDVARD GRIEGSVEI 3A
N-3057
SOLHEIMSVIK/BERGEN
NORWAY

Tél:4755297288
Fax:4755200050

MUNIER P.
SPOT IMAGE

B.P. 4359
31030 CEDEX
TOULOUSE
FRANCE

Tél:61 27 46 08
Fax:61 28 18 59

MURRAY C.N.
CEC
JOINT RESEARCH CENTRE
I-21020
VA.
ISPRA
ITALY

Tél:39 332 785 591
Fax:

NIELSEN P.
DANISH METEOROLOGICAL INSTITUTE

LYNGBYVEJ 100
DK-2100
COPENHAGEN Ø
DENMARK

Tél:45 39 15 73 44
Fax:45 39 15 73 00

NORMAND M.
CEMAGREF
HYDROLOGIE
B.P. 121
F-92185
ANTONY CEDEX
FRANCE

Tél:33 40 96 60 54
Fax:33 40 96 61 99

NOWAK M.
WESTERN EUROPEAN UNION
APARTADO DE CORREOS No. 11
MADRID
E-28850
TORREJON DE ARDOZ
SPAIN

Tél:34 16 77 77 59
Fax:34 16 77 72 28

O'CLERIGH E.
NRSC LTD.
DELTA HOUSE
SOUTHWOOD
GU14 6TW
FARNBOROUGH, HANTS.
U.K.

Tél:44 252 541 464
Fax:44 252 375 016

OCAMPO-TORRES F.J.
CICSE
DEPTO. DE OCEANOGRAFIA FISICA
APDO. POSTAL 2732
ENSENADA, B.C
TIJUANA-ENSENADA
MEXICO

Tél:52 617 450 50-53
Fax:52 617 448 48

OPRESCU N.
T.U. OF CIVIL ENGINEERING BUCAREST
REMOTE SENSING LABORATORY
B-DUL LACUL TEI 123, SECT. 2
CODE 72302
BUCHAREST 38
ROMANIA

Tél:40 1 312 8793
Fax:40 1 650 4222

ORIOL E.
ESRIN/DEX
VIA GALILEO GALILEI
C.P. 64
I-00044
FRASCATI
ITALY

Tél:39 694 180 1
Fax:39 694 180 361

ORTEGA E.
MINAS DE ALMADEN Y ARRAYANES, S.A.
DPTO. DE GEOLOGIA Y TELEDETECCION
CERCDO DE SAN TEODORO S/N
E-13400
ALMADEN
ITALY

Tél:34 26 71 04 00
Fax:34 26 71 04 37

OSTERRIETH A.
SPPS
8 RUE DE LA SCIENCE
B-1040
BRUSSELS
BELGIUM

Tél:
Fax:32 22 30 59 12

OSTOS P.J.
ESPELTA
CALLE ACANTO 22 - 10

E-28045
MADRID
SPAIN

Tél:34 15 27 02 15
Fax:34 15 30 10 25

OZER A.
UNIVERSITE DE LIEGE
GEOMORPHOLOGIE ET GEOLOGIE
DU QUATERNAIRE
PLACE DU 20-AOUT, 7
B-4000 LIEGE
BELGIUM

Tél:32 41 66 53 35
Fax:32 41 66 57 22

OZER P.
LABORATOIRE DE GEOMORPHOLOGIE
UNIVERSITE DE LIEGE
PLACE DU 20 AOUT, 7
B-4000
LIEGE
BELGIUM

Tél:32 41 66 53 35
Fax:32 41 66 57 22

PACI G.
ESRIN/DEX
VIA GALILEO GALILEI
C.P. 64
I-00044
FRASCATI
ITALY

Tél:39 694 180 1
Fax:39 694 180 361

PAPPALOPRE M.
UNIVERSITY OF BARI
DEPT. OF GEOLOGY & GEOPHYSICS
VIA ORABONA 4

I-70100
ITALY

Tél:39 80 242 571
Fax:39 80 242 625

PARAVANI F.
EURIMAGE
SALES MANAGER
VIA D'ONOFRIO 212
I-00184
ROMA
ITALY

Tél:39 640 694 216
Fax:39 640 694 232

PARLOW E.
MCR LABORATORY
UNIVERSITY OF BASEL
SPALENRING 145
CH-4055
BASEL
SWITZERLAND

Tél:41 61 272 64 80
Fax:41 61 272 69 23

PARTINGTON K.C.
GEC-MARCONI RESEARCH CENTRE
WEST HANNINGFIELD ROAD
GREAT BADDOW
ESSEX CM2 8HN
CHELMSFORD
U.K.

Tél:44 245 473 331
Fax:44 245 475 244

PASQUALI G.
TESIS S.P.A.
VIA S. BARGELLINI, 4

ROMA
ITALY

Tél:39 6 43 93 485
Fax:39 6 43 96 685

PASQUARIELLO G.
IESI-CNR
VIA AMENDOLA 166/5
I-70126

BARI
ITALY

Tél:39 80 548 1612
Fax:39 80 548 4311

PATTERSON T.
ESRIN/HELP DESK
VIA GALILEO GALILEI
C.P. 64
I-00044
FRASCATI
ITALY

Tél:39 694 180 1
Fax:39 694 180 361

PEDERSEN F.B.
DANISH METEOROLOGICAL INSTITUTE

LYNGBYVEJ 100
DK-2100
COPENHAGEN O
DENMARK

Tél:45 39 15 73 44
Fax:45 39 15 73 00

PELLEMANS A.
RIJKSWATERSTAAT
SURVEY DEPARTMENT
P.O. BOX 5023
NL-2600 GA
DELFT
NETHERLANDS

Tél:31 15 691 364
Fax:31 15 618 962

PEREZ GOMEZ B.
PUERTOS DEL ESTADO
AVENIDA DEL PARTENON, 10
CAMPO DE LAS NACIONES
E-28042
MADRID
SPAIN

Tél:34 15 24 55 00
Fax:34 15 24 55 02/06

PEREZ PICAZO F.
ESPELSA
CALLE ACANTO 22 - 10
E-28045
MADRID
SPAIN

Tél:34 15 27 02 15
Fax:34 15 30 10 25

PERLANT F.
ISTAR
CAMPUS II BAT.C
3 AV. DE L'EUROPE, PARC DU CANAL
F-31400
TOULOUSE
FRANCE

Tél:33 62 19 19 20
Fax:33 61 73 81 81

PETIT M.
ORSTOM
SEAS DEPT.
B.P. 172
97492 LA REUNION
SAINTE CLOTILDE
FRANCE

Tél:262 295 629
Fax:262 284 879

PONS I.
SYSAME
LES ALGORITHMES
ROUTE DE LUCIOLES
06560
SOPHIA ANTIPOlis
FRANCE

Tél:93 65 33 55
Fax:93 65 24 19

PONSARD C.
UNIVERSITE CATHOLIQUE DE LOUVAIN
LABO. DE TELECOM & TELEDETECTION
BATIMENT MAXWELL
B-1348
LOUVAIN-LA-NEUVE
BELGIUM

Tél:32 10 47 23 00
Fax:32 10 47 20 89

POUILQUEN Ms. S.
IFREMER
CENTRE DE BREST
B.P. 70
F-29280
PLOUZANE
FRANCE

Tél:98 22 44 92
Fax:98 22 45 33

PRISCO G.
WESTERN EUROPEAN UNION
APARTADO DE CORREOS No. 11
MADRID
E-28850
TORREJON DE ARDOZ
SPAIN

Tél:34 16 77 77 59
Fax:34 16 77 72 28

PROENCA M.
GEOMETRAL
QUINTA GRANDE
RUA E, LOTE 62 - R/C
P-2700
AMADORA
PORTUGAL

Tél:351 1 471 15 62
Fax:351 1 471 52 13

PUCH C.
INTA
DIV. DE INVESTIGACIONES ESPACIALES
CARRETERA DE AJALVIR, P.K. 4
E-28850 MADRID
TORREJON DE ARDOZ
SPAIN

Tél:34 16 27 06 53
Fax:34 16 27 09 45

PUIGDEFABREGAS J.
LABORATORI D'ENGINYERIA MARITIMA
UNIVERSITAT POLITECNICA DE CATALUNYA
C/GRAN CAPITA S/N, MODUL D1
E-08034
BARCELONA
SPAIN

Tél:34 3 401 64 71
Fax:34 3 401 73 57

QUEFFEULOU P.
IFREMER
CENTRE DE BREST
B.P. 70
F-29280
PLOUZANE
FRANCE

Tél:98 22 42 94
Fax:98 22 45 33

RAMSAY B.
ICE SERVICES ENVIRONMENT CANADA
373 SUSSEX DRIVE
3rd FLOOR, BLOCK "E"
ONT. K1A 0H3
OTTAWA
CANADA

Tél:613 996 4671
Fax:613 563 8480

RANGSIKANBHUM T.
NATIONAL RESEARCH COUNCIL
THAILAND REMOTE SENSING CENTER
196 PHAHONYOTHIN ROAD
10900
BANGKOK
THAILAND

Tél:662 562 0428
Fax:662 561 3035

RAST M.
ESTEC
OEE/VR
POSTBUS 299
NL-2200 AG
NOORDWIJK
NETHERLANDS

Tél:31 17 19 865 55
Fax:31 17 19 174 00

READINGS C.
ESTEC
OEE/VR
POSTBUS 299
NL-2200 AG
NOORDWIJK
NETHERLANDS

Tél:31 17 19 856 73
Fax:31 17 19 174 00

ROQUES J.-M.
CISI INGENIERIE
OBSERVATION & RECONNAISSANCE
PAR SATELLITES (13 RUE VILLETT)
B.P. 4042
31029 TOULOUSE CEDEX
FRANCE

Tél:33 61 17 66 66
Fax:33 61 54 13 39

ROSSIGNOL S.
RADARSAT INTERNATIONAL
3851 SHELL ROAD
SUITE 200
B.C. V6X 2W2
RICHMOND
CANADA

Tél:604 231 4910
Fax:604 231 4900

ROUZE M.
CNES

18, AVENUE EDOUARD BELIN
F-31055
TOULOUSE Cedex
FRANCE

Tél:61 28 25 61
Fax:61 28 40 13

RUDANT J.P.
UNIVERSITE P & M CURIE
GEOLOGIE STRUCTURALE TELEDETECTION
BOITE 129, TOUR 2616, 1er.et.
4, PLACE JUSSIEU
F-75252 PARIS CEDEX 05
FRANCE

Tél:33144275087
Fax:33144275085

SANCHEZ IRIE C.
IBERSAT S.A.
CALLE ARAQUIL, 11

E-28023
MADRID
SPAIN

Tél:34 13 57 18 60
Fax:34 13 57 31 92

SANZ GONZALEZ R.
SPANISH HOLDING OF HARBOURS
AVDA. PARTENON, 10

E-28042
MADRID

Tél:34 15 24 55 00
Fax:34 15 24 55 06

SCALES D.
DFD
DLR
P.O. BOX 11 16
D-82234
WESSLING
GERMANY

Tél:49 81 53 28 13 77
Fax:49 81 53 28 14 45

SCHMIDT K.
DARA GmbH
GS-A/AN1
POSTFACH 30 03 64
D-53183
BONN
GERMANY

Tél:49 228 447 571
Fax:49 228 447 700

SCHOENEMANN B.
ESTEC
OEE/JW
POSTBUS 299
NL-2200 AG
NOORDWIJK
NETHERLANDS

Tél:31 17 19 865 55
Fax:31 17 19 174 00

SCHRIMPF W.
JOINT RESEARCH CENTRE
T.P. 690

I-21020
ISPRA
ITALY

Tél:39 332 785 352
Fax:39 332 789 648

SCHULZE O.
 UNIVERSITY OF HANNOVER
 INST. F. METEOROLOGIE & KLIMATOLOGIE
 HERRENHAUSER STRASSE 2
 D-30419
 HANNOVER
 GERMANY

Tél:49 511 762 4413
 Fax:49 511 762 4418

SEMPERE J-P.
 IGN ESPACE
 PARC TECHNOLOGIQUE DU CANAL
 24 RUE HERMES
 31527 CEDEX
 RAMONVILLE
 FRANCE

Tél:62 19 18 18
 Fax:61 75 03 17

SHARMAN M.J.
 CEC
 DG XII, D-4 SPACE
 200, RUE DE LA LOI
 B-1049
 BRUXELLES
 BELGIUM

Tél:322 265 9798
 Fax:322 235 0146

SHOKR M.
 ATMOSPHERIC ENVIRONMENT SERVICE
 4905 DUFFERIN ST.
 ONTARIO
 M3H 5T4
 NORTH YORK
 CANADA

Tél:4167394906
 Fax:4167394221

SIEGERT F.
 ZOOLOGISCHES INSTITUT
 UNIVERSITY OF MUNICH
 LUISENSTR. 14
 D-8033
 MUNICH
 GERMANY

Tél:49 89 5902 442
 Fax:49 89 5902 450

SIMON M.
 INTA
 DIV. DE INVESTIGACIONES ESPACIALES
 CARRETERA DE AJALVIR, P.K. 4
 E-28850 MADRID
 TORREJON DE ARDOZ
 SPAIN

Tél:34 16 27 03 83
 Fax:34 16 27 09 45

SKOELV A.
 NDRE
 DIVISION FOR ELECTRONICS
 P.O. BOX 25
 N-2007
 KJELLER
 NORWAY

Tél:47 63 80 74 68
 Fax:47 63 80 72 12

SLOGGETT D.
 EOS LTD.
 BROADMEAD
 FARNHAM BUSINESS PARK
 GU9 8QL
 FARNHAM, SURREY
 U.K.

Tél:44252721444
 Fax:44252712552

SOLE-SUGRANES L.
 INSTITUTE OF EARTH SCIENCES
 (JAUME ALMERA) CSIC
 CALLE MARTI I FRANQUES, S/N
 E-08028
 BARCELONA
 SPAIN

Tél:34 33 30 27 16
 Fax:34 34 11 00 12

SOMMA R.
 ALENIA SPAZIO S.P.A.
 VIA SACCOMURO 24
 I-00131
 ROME
 ITALY

Tél:39 641 51 20 14
 Fax:39 641 91 39 1

STOFFELEN A.
 KNMI
 P.O. BOX 201
 NL-3730 AE
 DE BILT
 NETHERLANDS

Tél:31 30 206 585
 Fax:31 30 210 407

STRUETING Klaus
 BSH - ICE SERVICE
 BERNHARD-NOCHT-STRASSE 78
 P.O.BOX 301220
 D-20305
 HAMBURG
 GERMANY

Tél:494031903221
 Fax:494031905032

SUNDE J.
NORWEGIAN METEOROLOGICAL INSTITUTE
P.O. BOX 43
BLINDERN
N-0313
OSLO
NORWAY

Tél:47 22 96 32 42
Fax:47 22 96 31 33

SUPAN KARNCHANASUTHAM
OFFICE OF AGRICULTURAL ECONOMICS
PHAHOLYOTHIN ROAD

BANGKOK 10900
CHATUCHAK
THAILAND

Tél:662 579 8545
Fax:622 579 0617

SYLOS-LABINI G.
A.S.I.
CGS
LOCALITA' TERLECCHIA
P.O. BOX 155
75100 MATERA
ITALY

Tél:39 835 377 201
Fax:39 835 339 005

TACK W.
WEU SATELLITE CENTRE
AVDA. DE CADIZ
ED. 457
E-28850
TORREJON DE ARDOZ
SPAIN

Tél:34 16 77 77 59
Fax:34 16 77 77 28

TAPP Carole
EUROPEAN SPACE AGENCY
D/OEE
8-10 RUE MARIO NIKIS
F-75738 CEDEX
PARIS
FRANCE

Tél:42 73 76 54
Fax:42 73 75 60

THOMAS G.
BNSC
BRIDGE PLACE
88/89 ECCLESTON SQUARE
SW1V 1PT
LONDON
U.K.

Tél:44 71 215 0790
Fax:44 71 821 5387

THOMAS M.
UNIVERSITY OF HANNOVER
INST. FUER METEOROLOGIE & KLIMATOLOGIE
HERRENHAUSER STRASSE 2
D-30419
HANNOVER 21
GERMANY

Tél:49 511 762 4413
Fax:49 511 762 4418

TOURON H.
WEU SATELLITE CENTRE
AVDA. DE CADIZ
ED. 457
E-28850
TORREJON DE ARDOZ
SPAIN

Tél:34 16 77 77 59
Fax:34 16 77 77 28

TYCHSEN J.
DANMARKS MILJØUNDERSØGELSER
FREDERIKSBORGVEJ 399
P.O. BOX 358
DK-4000
ROSKILDE
DENMARK

Tél:45 46 30 12 00
Fax:45 46 30 11 14

URDIROZ A.
SPOT IMAGE
B.P. 4359
31030 CEDEX
TOULOUSE
FRANCE

Tél:61 27 46 08
Fax:61 28 18 59

VALEUR H.H.
DANISH METEOROLOGICAL INSTITUTE
OBSERVATION DEPT/OCEANOGRAPHY
LYNGBYVEJ 100
DK-2100
COPENHAGEN O
DENMARK

Tél:45 39 15 73 44
Fax:45 39 15 73 00

VAN DE VELDE L.
LABORATORIUM PHYSICAL GEOGRAPHY
UNIVERSITY OF GENT
KRIJGSLAAN 281/58
B-9000
GENT
BELGIUM

Tél:32 91 64 46 88
Fax:32 91 64 49 97

VAN GENDEREN J.L.
ITC
CONSULTING & RESEARCH PROJECTS BUREAU
P.O. BOX 6
NL 7500 AA
ENSCHDEDE
NETHERLANDS

Tél:31 53 874 254
Fax:31 53 874 436

VAN HALSEMA D.
TNO DEFENCE RESEARCH
PHYSICS & ELECTRONICS LABORATORY
P.O. BOX 96864
NL-2509 JG
THE HAGUE
NETHERLANDS

Tél:31 70 326 4221
Fax:31 70 328 0961

VARGAS CUERVO G.
UNIVERSITE P & M CURIE
DEPARTEMENT DE GEOTECTONIQUE
BOITE 129
4 PLACE JUSSIEU, TOUR 26, 1er et.
75252 PARIS CEDEX 05
FRANCE

Tél:33143 26 82 46
Fax:33144 27 50 85

VERNEMMEN C.
LABORATORIUM PHYSICAL GEOGRAPHY
UNIVERSITY OF GENT
KRIJGSLAAN 281/S8
B-9000
GENT
BELGIUM

Tél:32 92 64 47 59
Fax:32 92 64 49 70

VERRALL D. Ms.
EARTH OBSERVERATION SCIENCES
BROADMEDE, FARNHAM BUSINESS PARK
WEYDON LANE
GU9 8QL
FARNHAM, SURREY
U.K.

Tél:44 252 721 444
Fax:44 252 712 552

VIVAS WHITE P.
INSTITUTO GEOGRAFICO NACIONAL
CALLE GENERAL IBANEZ DE IBAYO, 3

E-28003
MADRID
SPAIN

Tél:34 15 33 28 00
Fax:34 15 34 95 36

WAGNER M.J.
EURIMAGE
EDITOR
VIA D'ONOFRIO, 212
I-00184
FRASCATI
ITALY

Tél:39 640 694 216
Fax:39 640 694 232

WEIMANN A.
GERMAN AEROSPACE ESTABLISHMENT
INSTITUTE FOR SPACE SENSOR TECHNOLOGY
RUDOWER CHAUSSEE 5
D-12484
BERLIN
GERMANY

Tél:493069545648
Fax:493069545642

WENSINK G.J.
DELFT HYDRAULICS
P.O. BOX 152
NL-8300 AD

EMMELOORD
NETHERLANDS

Tél:3152742922
Fax:3152743573

WINKLER P.
FOMI INSTITUTE OF GEODESY,
CARTOGRAPHY & REMOTE SENSING
BOSNYAK TER 5
1149
BUDAPEST
HUNGARY

Tél:36 1 163 6669
Fax:36 1 252 7918

WOODING M.G.
REMOTE SENSING APPLS. CONSULTANTS
MANSFIELD PARK
MEDSTEAD
HANTS. GU34 5PZ
ALTON
U.K.

Tél:44 420 561 377
Fax:44 420 561 388



